Proceedings

International Conference on Nuclear Science and Technology

Nuclear Society Of Iran | Atomic Energy Organization of Iran | Nuclear Sciences and Technologies Research Institute

Papers on:

Radiation Applications (Industry, Medical And Environment)

1

*In this booklet, you will find the selected papers presented at the **First International Conference on Nuclear Science and Technology**, held from May 6-8, 2024, in Isfahan, Iran.*
We hope you find it informative and enjoyable!

ICNST 2024

Contact and Accessibility
icnst2024.com
registration@icnst2024.com


بسم الله الرحمن الرحيم

The Conference President's Message
ICNST 2024

Attendees, guests, and colleagues

I would like to warmly welcome you to the first International Conference on Nuclear Science and Technology (ICNST 2024). It has been a real honor and privilege to serve as the president of this conference. The conference this year has brought together an incredible diversity of authors and speakers from universities, government, and industry to share ideas and new perspectives on a wide range of radiation applications, nuclear reactors, particle accelerators, radiation measurements, fusion and plasma, stable and radioactive isotopes, radiation safety and security, nuclear agriculture, fuel cycle, lasers, education and training and nuclear governance.

Climate change, a new topic which has been added to this year's agenda as an important worldwide issue. a matter that has been brought up as a critical concern at the majority of IAEA conferences and nuclear scientific assemblies in recent years.

Panel discussions and exhibitions are being introduced as side activities in an attempt to keep this scientific meeting from becoming one-dimensional and increase its effectiveness.

More than 520 complete papers have been approved for this conference; when combined with the additional panels, get-togethers, and side activities, it is anticipated that over 1000 people will attend in person in the historical and touristic city of Isfahan. We look forward to welcoming participants to share their practical ideas and to enjoy an academical and cultural three days in Isfahan.

I'll close by wishing you everyone an incredible, instructive, and transformative experience during ICNST2024 and I hope that this conference can pave the route for academic materials to be used in industry and everyday life.

Prof. Javad Karimi-Sabet
President of ICNST2024
Javad Karimi-Sabet

welcome statment of scientific secretary ICNST 2024

"In the name of God, the Merciful,

Prior to giving the stage to address this distinguished forum, let me take this opportunity to express our deep gratitude, on behalf of all attendees, for His Excellency Mr. Islami's scientific, educational, and motivational remarks, as well as for his excellent organization of this conference.

I would also like to express our appreciation to His Excellency Dr. Mortazavi, Governor-General of Isfahan Province, for his constructive and useful support in enabling this meeting to take place.

This is a great pleasure and honor to extend a warm greeting to each and every one of you for the International Conference on Nuclear Science and Technology, scheduled from May 6th to May 8th, 2024, in the historic city of Isfahan, Iran.

With the aim of advancing our knowledge of nuclear science and technology, this conference is a major global convergence of experts, researchers, and practitioners. It is a platform for the sharing of creative concepts, the presentation of state-of-the-art research, and the formation of cooperative alliances.

As the scientific secretary of this prestigious event, I am particularly excited about the diverse array of participants expected to grace us with their presence. From the esteemed scientists and engineers of Russian universities and research centers to representatives from Islamic countries, friendly nations, and beyond, this conference promises to be a melting pot of perspectives, experiences, and expertise.

The extensive coverage of this conference is another aspect of its uniqueness. We have nearly 900 participants representing 22 countries around the world. Of the 900 participants, 620 are authors covering 13 major topics. There are 421 papers for oral and poster presentations, with additional documents for publication in ISC journals. There will be 3 plenary sessions, 16 panel discussions, 20 parallel oral presentation sessions, and 3 poster sessions.

Prof. Hosein Afarideh
Scientific Secretariat of ICNST2024

Organizers

Nuclear Society Of Iran (NSI)

Atomic Energy Organization of Iran (AEOI)

Nuclear Science and Technology Research Institute (NSTRI)

Scientific Partnership

International Atomic Energy Agency (IAEA)

Isfahan University

Sharif University

Kurchatov Institute

Amirkabir University of Technology (Tehran Polytechnique)

Shahid Beheshti University

Isfahan University of Technology

Shiraz University

Islamic Azad University

K. N. Toosi University of Technology

Ferdowsi University of Mashhad

Kerman Graduate University of Technology

Sahand University of Technology

University of Tabriz

Islamic World Scieence Citation Center

Journal of Nuclear Science and Technology (JonSat)

Radiation Physics and Engineering journal

Nuclear Watch

Cooperative Organization

Isfahan Governorate

Isfahan Municipality

Abbasi Hotel

Iran Atomic Energy Production & Development Co.

Iran's Nuclear Raw Materials & Fuel Production Co.

Radiation Application Development Co.

Ofogh Consulting Engineers Co.

Nuclear Power Plant Safety Development & Promotion Co.

Nuclear Power Plant Engineering & Construction Co.

Engineering & Design of Industrial Simulator Co.

Energy Industry Development Engineering Co

Atomic Power Plant Pepair & support

Nuclear Reactors Fuel Co.

Iran Radioactive Waste Management Co.

Mesbah Energy Co.

Iran Gharb Industrial, Mining and Energy Co.

Pars Isotope Co.

Center for Laser Science & Technology of Iran

Centrifuge Production of Iran Co.

Plasma Technology Development Co.

Rasa Technology and Innovation Center

Behyaar Sanaat Sepahan Co.

Nuclear Data Base of Iran (NDB)

Parto think tank

International Conference Alerts

Local Scientific Board

RAW	NAME	ROLE	AFFILIATION
1	**Prof. Hossein Afarideh**	**Chairman of Local Scientific Board**	**Amirkabir University of Technology (Tehran Polytechnique)(AUT)**
2	**Prof. Mohammad Ghanadi Maragheh**	**Member of The Local Scientific Board**	**Nuclear Science and Technology Research Institute of Iran (NSTRI)**
3	**Prof. Mohammad Lamei Rashti**	**Member of The Local Scientific Board**	**Nuclear Science and Technology Research Institute of Iran (NSTRI)**
4	**Prof. Mohammad Bagher Ghofrani**	**Member of The Local Scientific Board**	**Sharif University of Technology (SUT)**
5	**Prof. Hosein Faghihian**	**Member of The Local Scientific Board**	**University of Isfahan (UI)**
6	**Prof. Javad Rahighi**	**Member of The Local Scientific Board**	**Institute for Research in Fundamental Sciences (IPM)**
7	**Prof. Seyed Amirhossein Feghhi**	**Member of The Local Scientific Board**	**Shahid Beheshti University (SBU)**

Scientific Committee

RAW	NAME	ROLE	AFFILIATION
1	**Prof. Ali Akbar Salehi**	**Member of The Scientific Committe**	**Sharif University of Technology (SUT)**
2	**Prof. Seyyed Javad Ahmadi**	**Member of The Scientific Committe**	**Nuclear Science and Technology Research Institute of Iran (NSTRI)**
3	**Prof. Farhoud Ziaee**	**Member of The Scientific Committe**	**Nuclear Science and Technology Research Institute of Iran (NSTRI)**
4	**Prof. Saeed Hamidi**	**Member of The Scientific Committe**	**University of Arak**
5	**Prof. Seyedzafarollah Kalantari**	**Member of The Scientific Committe**	**Isfahan University of Technology (IUT)**
6	**Prof. Naser Bagheri Moghaddam**	**Member of The Scientific Committe**	**National Research Institute for Science Policy (NRISP)**
7	**Prof. Naser Vosoghi**	**Member of The Scientific Committe**	**Sharif University of Technology (SUT)**
8	**Prof. Seied Rabi Mahdavi**	**Member of The Scientific Committe**	**Iran University of Medical Sciences**
9	**Prof. Meisam Torab Mostaedi**	**Member of The Scientific Committe**	**Nuclear Science and Technology Research Institute of Iran (NSTRI)**
10	**Prof. Fereydoun Abbasi Davani**	**Member of The Scientific Committe**	**Shahid Beheshti University (SBU)**
11	**Prof. Seyed Farhad Masoudi**	**Member of The Scientific Committe**	**K.N.Toosi University of Technology**
12	**Prof. Rasool Ruknizadeh**	**Member of The Scientific Committe**	**University of Isfahan (UI)**
13	**Prof. Gholamreza Raeesali**	**Member of The Scientific Committe**	**Nuclear Science and Technology Research Institute of Iran (NSTRI)**
14	**Prof. Asghar Sedighzadeh**	**Member of The Scientific Committe**	
15	**Prof. Hossein Kazeminejad**	**Member of The Scientific Committe**	**Nuclear Science and Technology Research Institute of Iran (NSTRI)**

RAW	NAME	ROLE	Affiliation
16	**Prof. Hossein Khalafi**	**Member of The Scientific Committe**	**Nuclear Science and Technology Research Institute of Iran (NSTRI)**
17	**Prof. Seyyed Jaber Safdari**	**Member of The Scientific Committe**	**Nuclear Science and Technology Research Institute of Iran (NSTRI)**
18	**Prof. Omid Reza Kakuee**	**Member of The Scientific Committe**	**Nuclear Science and Technology Research Institute of Iran (NSTRI)**
19	**Prof. Alireza Keshtkar**	**Member of The Scientific Committe**	**Nuclear Science and Technology Research Institute of Iran (NSTRI)**
20	**Prof. Fereshte Haj esmail Beigi**	**Member of The Scientific Committe**	**Nuclear Science and Technology Research Institute of Iran (NSTRI)**
21	**Prof. Masoud Mahjour-shafiei**	**Member of The Scientific Committe**	**Nuclear Science and Technology Research Institute of Iran (NSTRI)**
22	**Prof. Mahmoud Payami Shabestar**	**Member of The Scientific Committe**	**Nuclear Science and Technology Research Institute of Iran (NSTRI)**
23	**Prof. Ali Bahrami Samani**	**Member of The Scientific Committe**	**Nuclear Science and Technology Research Institute of Iran (NSTRI)**
24	**Dr. Farhanaz Motamedi**	**Member of The Scientific Committe**	**Nuclear Science and Technology Research Institute of Iran (NSTRI)**
25	**Dr. Faezeh Rahmani**	**Member of The Scientific Committe**	**K.N.Toosi University of Technology**
26	**Dr. Ebrahim Moghiseh**	**Member of The Scientific Committe**	**Nuclear Science and Technology Research Institute of Iran (NSTRI)**
27	**Dr. Iraj Jabari**	**Member of The Scientific Committe**	**University of Isfahan (UI)**
28	**Dr. Nima Ghal-Eh**	**Member of The Scientific Committe**	**Ferdowsi University of Mashhad**
29	**Dr. Mitra Athari Alaf**	**Member of The Scientific Committe**	**Islamic Azad University Science and Research Branch**
30	**Dr. Gholamreza Etaati**	**Member of The Scientific Committe**	
31	**Dr. Amir Movafeghi**	**Member of The Scientific Committe**	**Nuclear Science and Technology Research Institute of Iran (NSTRI)**

Executive Committee

RAW	NAME	ROLE
1	**Dr. Farshad Ghasemi**	**Chairman of the Executive Committee**
2	**Dr. Ehsan Molazadeh**	**Member of The Executive Committee**
3	**Dr. Seyyed Ghasem Biniaz**	**Member of The Executive Committee**
4	**Mr. Aliakbar Aminidoust**	**Member of The Executive Committee**
5	**Mr. Mohammad Hosein Arkannia**	**Member of The Executive Committee**
6	**Ms. Fatemeh Zamani**	**Member of The Executive Committee**
7	**Ms. Mahia Pazoki**	**Member of The Executive Committee**
8	**Mr. Hosein Maleki**	**Member of The Executive Committee**

Radiation Radiation Applications (Industry, Medical And Environment)

Radiation Applications (Industry, Medical And Environment)

ICNST 2024
International Conference on Nuclear Science and Technology
6- 8 MAY 2024 | Isfahan, Iran

Concrete shields with attenuating and neutron absorbing components (Paper ID : 1226)

Alipoor M.R[1*], Eshghi M.[1]

[1]*Department of Physics, Imam Hossein University, Tehran, Iran.*

Abstract

The neutron shielding capacity of concrete samples by adding boron and iron carbide at different rates in the energy range of neutron sources was investigated in this study. In order to investigate the shielding capacities of concrete samples, the total macroscopic cross section and Mean Free Path, the cross-section of removing fast neutrons, the deposited energy, the thickness required to reduce the neutron intensity to 0.01, and the different interactions on the neutron against radiation using It was analyzed by the theoretical method and Geant4 Montecarlo simulation tool. The results showed that increasing the amount of boron carbide in the studied sample, compared to the samples without boron carbide, reduced the number of neutrons. By using different thicknesses and energies, the neutron shielding property of the samples was analyzed for the neutron transfer test. The results showed that the sample containing boron carbide (MF3) has a 10% better performance than the other investigated samples for absorbing and moderating neutrons. Finally, the effective thickness for the moderating and absorption of neutrons was calculated, which showed a reduction of 4 cm in shielding thickness.

Keywords: Neutron shielding, Concrete, components, Montecarlo, simulation.

INTRODUCTION

Research reactors are known as one of the main sources of neutron production in the world, which have many and varied applications. In recent years, technological progress has led to the production of new research reactors for various purposes, such as the production of medical radioisotopes for the diagnosis and treatment of diseases and industrial radioisotopes for the production of semiconductors widely used in the electronics industry [1-3]. However, this increase has raised concerns about the risks associated with the use of radioactive equipment and sources and its impact on the surrounding environment. It is very important to follow the radiation protection safety guidelines to reduce the risks of dangerous radiation. The use of radiation shielding materials is critical to minimize the risks of ionizing radiation and reduce radiation damage to extend the life of device components [4-8]. Materials with high protective performance should be used in radiation environments to avoid the effects of radiation. Considering the quantities affecting the protective properties such as density, chemical properties (such as lack of corrosion and brittleness) and the

thickness of the produced material is necessary for data communication in analytical and numerical calculations [9]. In many realistic cases, neutrons are moderated not only by a hydrogen environment but also by an internal non-hydrogen shield. Elements with low atomic number (hydrogen, carbon, oxygen) are usually used as shielding materials to slow down fast neutrons [10-13]. In places where the neutron flux is high, element Boron (B) is effectively used to control and reduce the speed of thermal neutrons with fast neutron absorption properties. Also, carbon (C) and beryllium (Be), with their thermal neutron scattering and absorption cross sections, are the most suitable moderators for thermal neutrons [14, 15]. Due to the development of neutron-based fission and fusion reactors, the need for high-performance shielding materials has increased. Neutron shielding materials may also contain high atomic number elements and multi-element layers. Concrete is a useful material in radiation protection due to its high stability and cost-effectiveness. To reduce the radiation dose, many researchers have produced new materials by adding different elements to concrete. Production of a new concrete with a mixture of neutron absorbing materials reduces the thickness of the concrete to a minimum level and increases the radiation protection efficiency of the material. Materials and compounds containing cement are usually used in the construction sector, and the primary binding material for concrete is cement [16, 17]. To strengthen the radiation protection properties of concrete, researchers are looking for cost-effective materials that can be used for radiation protection. In recent years, pulverized eggshell waste, recycled pulverized oysters and scallop shells, palm oil, waste glass and many other alternative materials have been successfully used in cement production, and the search for new materials continues [18-20]. In terms of radiation shielding properties, cementitious compounds are naturally considered good shielding. However, this feature alone is not sufficient for radiation protection. Concrete compositions containing high-density cement can effectively act as a barrier against radiation. Portland cement can be used in nuclear reactor safety walls, nuclear containment structures and radiation isolation walls. In this way, it prevents the passage of radiation and prevents it from leaking into the surrounding environment [21, 22]. Portland cement can be modified by adding different raw materials to increase its radiation protection properties. Lead is a high-density metal that prevents the passage of radiation. It can improve radiation shielding capabilities by incorporating lead powder or lead-containing aggregates into Portland cement. [23-25]. By adding boron compounds to Portland cement, neutron absorption and radiation protection can be improved. For example, boron compounds such as boric acid or borax can be used. Borax, a salt of boric acid, can help absorb neutrons and protect against radiation. Addition of borax to Portland cement can increase the radiation protection properties. Silica fume is a

byproduct with high silica content in the form of fine particles. When added to Portland cement, it increases the density of concrete and reduces radiation transmission [26-28]. Iron ore can be used as a raw material due to the presence of iron oxide. When iron oxide is added to cement, it absorbs radiation [29, 31]. These raw materials are standard options used to enhance the radiation protection properties of Portland cement. These minerals contribute to its unique properties, including increased radiation protection. One of the most prominent features of these minerals is its exceptional ability to weaken ionizing radiation. This feature distinguishes it from other common cement additives that lack this specialized feature. Minerals have a higher density compared to conventional cement additives. This higher density is useful for radiation protection, as denser materials are more effective at stopping or attenuating ionizing radiation. Mineral-containing concrete shows lower flammability and modulus, which can help produce more cost-effective cement. This feature reduces the baking temperature during production and ultimately saves energy and reduces production costs. Minerals are relatively abundant and can often be obtained in bulk. The unique properties of minerals make them very versatile in different applications. While its main application may be in radiation protection, it can also be used in other specialized environments where its properties, such as increased density and structural integrity, are useful [32-34]. Therefore, based on the findings of other researchers, it is clear that the use of minerals rich in alumina and iron as an alternative raw material in cement production will open new horizons in new concretes. In this study, the properties of neutron shields, mineral concretes combined with boron carbide and upgraded mineral concretes will be investigated.

RESEARCH THEORIES

The neutron shielding efficiencies of compounds have been compared based on an equivalent absorption cross-section called a fast neutron effective removal cross-section, Σ_R [35, 36]. It is a linear attenuation coefficient given in cm^{-1} and is defined as a probability that a fast energy neutron undergoes a collision, which removes it from the group of un-collided neutrons. The concept of this phenomenon is based on the presence of hydrogen as it is the main moderator that dominates the attenuation of neutrons. Calculation of fast neutron effective removal cross-sections is by analogy to the calculation of mass attenuation coefficients of neutron according to the equation (1).

$$\sum_R = \sum_i W_i (\Sigma i / \rho)_i \quad (1)$$

where: W_i partial density of i^{th} constituent, Σ_R/ρ fast neutron mass removal coefficient of i^{th} constituent. The fast neutron mass removal cross-section of constituents is related to the microscopic nuclear properties and varies smoothly with the atomic weight. The value can be calculated using empirical equations or measured. For most elements and some compounds, experimental and theoretical values of the fast neutron mass removal cross-sections have been published [37]. Additionally, in order to estimate the neutron shielding efficiency of concrete in a more detailed way, a method based on macroscopic cross-sections for a different interaction has been used. In this method, instead of fast neutron attenuation cross-sections, a database of neutron scattering lengths and cross-sections that includes the thermal neutron microscopic cross-section as well is used [38, 39]. Thus, the macroscopic neutron scattering cross-section or the macroscopic thermal neutron absorption cross-section and finally their sum named the total macroscopic neutron cross-section have been calculated using equation (2):

$$\sum_j = \sum_i W_i(^{\Sigma j}/_{\rho})_i \qquad (2)$$

where: W_i partial density of i^{th} constituent, $\Sigma j/\rho$ neutron mass attenuation coefficient of i^{th} constituent for a specific interaction (j).

GEANT4

The neutron shielding property of the samples was calculated by Geant4 Montecarlo tool. For these simulation calculations, sample density and type of particles (neutrons) were first defined in Geant4 simulation tool. Then the weight fraction was defined according to the mass of the sample in the simulation tool. After these definitions, 1 million neutrons with different energies were bombarded on the prepared target sample. To calculate all the quantities related to neutrons, the physics of the hadron list available in the Geant4 simulation tool was used. The neutron radiation shielding property of the samples in different thicknesses (15 -30 cm) was also calculated to determine the thickness effect. The calculated quantities for the samples were performed at the specified energy (2.8, 4, 4.1, 4.2 and 4.5 MeV) [40, 41].

Results and discussion

The compositions of the four heavy concretes considered in this study as an alternative to conventional cement clay, a meta-schist material characterized by high silicon and iron, are listed in Table 1. In the calculation section, the aim is to investigate the difference in the neutron shielding capacity of iron, silicon

and boron compounds to estimate the length of neutron attenuation, neutron transmission through simulation tools.

Table 1. The Chemical properties of shielding materials.

Properties (%)	Sample Cement			
	MB	MF1	MF2	MF3
H	0.32	0.26	0.27	0.27
B	0.16	--	--	0.2
O	36.37	36.58	36.55	36.54
C	--	--	0.9	0.11
Na	0.53	0.19	0.18	0.18
Mg	0.3	0.3	0.3	0.3
Al	0.57	0.57	0.57	0.57
Si	13.12	13.2	0.39	13.18
P	0.38	0.39	0.15	0.39
S	0.13	0.13	13.19	0.13
Cl	0.01	0.01	0.01	0.01
K	0.18	0.18	0.18	0.18
Fe	42.39	42.62	42.59	41.58
Ca	5.54	5.57	5.57	5.56
Density ($g.cm^{-3}$)	3.053	3.069	3.164	2.855

The neutron, because of its neutral charge, has a relatively high penetration power in matter. Unlike charged particles, neutrons will not be impeded by the atomic coulombic barrier of the material through which the neutrons travel and the neutron will consequently not lose energy directly via ionization. However, neutrons will interact with the nuclei of matter. There are several possible interactions of neutrons with nuclei. Among these are elastic scattering, inelastic scattering, neutron capture and nonelastic. To check the performance of a neutron shield, all these interactions must be taken into account. A neutron shield must have a high absorption rate for neutrons and reduce the scattering of incident neutrons. The results for various interactions that occur on incident neutrons such as neutron absorption and neutron transport, neutron inelastic and scattering are shown in Table 2. It can be seen that with the addition of very low content of B_4C to the MF3 sample, the number of transition neutrons decreases. Also, the number of inelastic neutrons will increase, which will decrease the energy of neutrons.

Table 2. 1 million neutrons gun to 5 cm thickness of samples at 4.5 MeV energy.

Interaction	Sample			
	MB	MF1	MF2	MF3
Elastic	432863	429656	429633	410009
Inelastic	100118	100413	114537	95529
Transport	466883	469795	455705	494331
Capture	136	136	125	131
Total	1000000	1000000	1000000	1000000

For materials with a high total cross-section, the mean free path is very short, and neutron absorption occurs mostly on the material's surface. This surface absorption is called self-shielding because the outer layers of atoms shield the inner layers. According to Figure 1, the MF3 sample has a higher cross-sectional area than the other investigated samples. By decreasing the mean free path, neutrons are more absorbed in less thicknesses and there is no need for thick shielding.

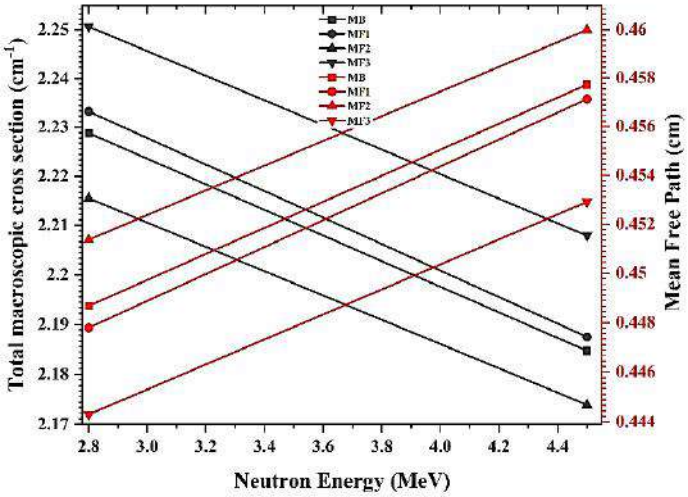

Fig. 1. Results of total macroscopic cross section and Mean Free Path in terms of neutron energy for samples.

For neutron shielding, calculations of the effective cross-section of fast neutron removal are shown in Figure 2. As shown in Figure 2, the results of the calculated Σ_R/ρ values show that hydrogen, carbon and boron atoms can affect the interaction mechanisms of neutrons with the microscopic cross-section. The main role of fast neutron speed reduction mechanisms shows that neutron absorption by boron and carbon increases the cross section of fast neutron removal. This can be attributed to the fact that sample MF3 is richer in

hydrogen and boron atoms than the other samples shown in Table 1. In addition, increasing the concentration of boron atoms in the sample increases the absorption of neutrons, and hence the total cross-sectional area and the effective cross-section of fast neutron removal increase, so the shielding efficiency also increases. This means that the MF3 sample is the most suitable in the field of fast neutron shielding.

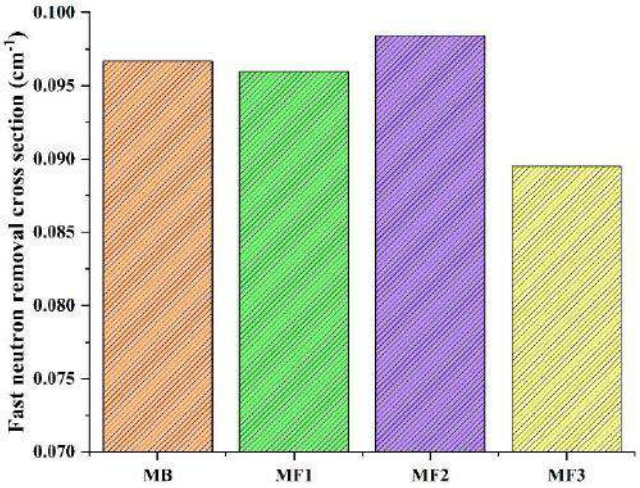

Fig. 2. Effective fast neutron removal cross section for samples.

Neutrons are indirectly ionizing radiation, but generally neutrons have more biological effectiveness per unit of absorbed dose than gamma rays and X-rays. Neutrons deliver the radiation dose to specimens via the energy transfer from neutrons to charged particles, such as electrons, protons, and nuclei. This is where the amount of energy transferred to the sample will be important. According to Figure 3, the energy of 2.8 MeV volts, the amount of energy transferred to the MF3 sample is more than other samples. While with the increase of energy, the energy transferred to the MB sample is more than the others.

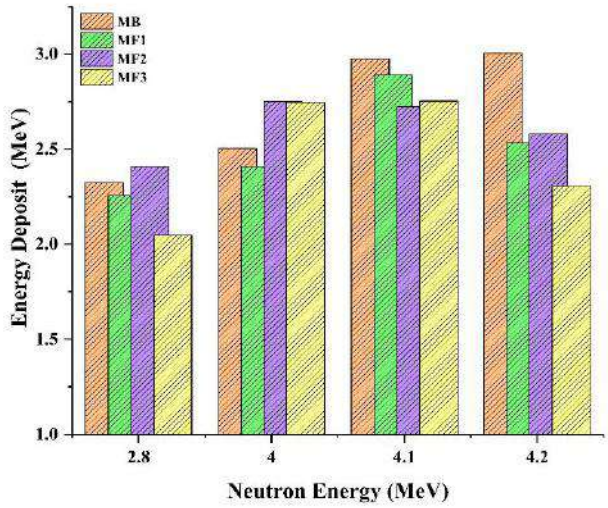

Fig. 3. Energy Deposit for Sample.

In Figure 4, the thicknesses of the samples corresponding to the transmission coefficient of 0.01 for the energy of 2.8 and 4.5 MeV are drawn. When the thickness of the sample exceeds 20 cm, we will have the required thickness to reduce one hundredth of the neutron intensity at 2.8 MeV energy. Also, when the thickness of the sample exceeds 35 cm, we will have the required thickness to reduce one hundredth of the neutron intensity at 4.5 MeV energy. This increase is due to considering the cumulative effects of neutrons and the maximum attenuation of fast and thermal neutrons. After this thickness, the intensity of neutrons decreases to the minimum level and the secondary particles resulting from neutron absorption are also absorbed in the shield. The results show that the MF3 sample has a lower thickness than the other samples in each energy.

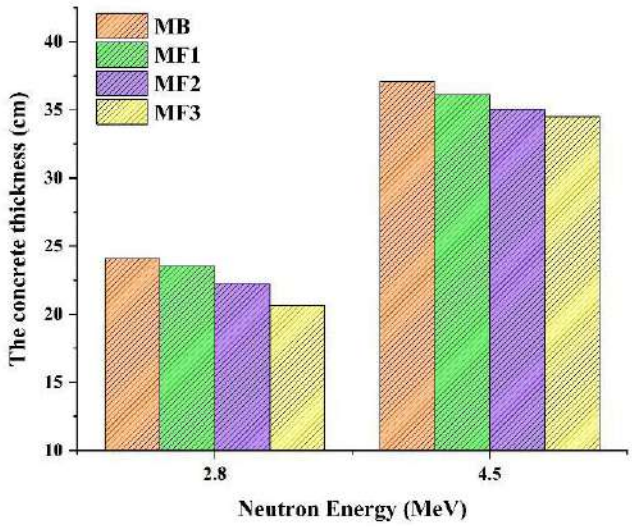

Fig. 4. Shielding thickness required for different neutron energy.

Conclusions

The results of this study indicate that the estimation of fast neutron removal cross-section, macroscopic cross-section and energy deposit is useful for determining shielding performance. As a result, the results obtained from this work showed how effective the boron element can be in moderating the neutrons. Next, due to safety restrictions, the safe thickness was also calculated for safe use in the equipment which shows a reduction of 4 cm in thickness. Finally, the results show that MF3 concrete reaches ١٠ precent better performance than normal concrete. This shows that the composition and microstructure of MF 3 concrete can optimize the damping properties for protective applications. Also, the calculation results showed that MF3 concrete has extraordinary values for removing fast neutrons and may exceed the value determined for common concretes.

References

Porras, I., Praena, J., De Saavedra, F. A., Pedrosa-Rivera, M., Torres-Sánchez and et al (2020). BNCT research activities at the Granada group and the project NeMeSis: Neutrons for medicine and sciences, towards an accelerator-based facility for new BNCT therapies, medical isotope production and other scientific neutron applications. Applied Radiation and Isotopes, 165: 109247.

Shehada, A., Кривобоков, В. П. and Головков, В. М. (2021). Evaluating the dependency of neutron spectra and absorbed dose rates on the collimation field size in fast neutron therapy. Heliyon, 7(11), e08274.

Li, J. and Zheng, S. (2023). Feasibility study to byproduce medical radioisotopes in a fusion reactor. Molecules, 28(5): 2040.

Dickson, E. D. And Hamby, D. (2014). Experimental shielding evaluation of the radiation protection provided by the structurally significant components of residential structures. Journal of Radiological Protection, 34(1): 201–221.

Karatasakis, A. and Brilakis, E. S. (2018). Shields and garb for decreasing radiation exposure in the cath lab. Expert Review of Medical Devices, 15(9): 683–688.

Wang, K., Ma, L., Yang, C., Bian, Z., Zhang, D., Cui, S., Wang, M., Chen, Z. and Li, X. (2023). Recent Progress in GD-Containing Materials for Neutron shielding Applications: A review. Materials, 16(12):4305.

Chen, Y. and Yan, B. (2023). The technology of shielding design for nuclear reactor: A review. Progress in Nuclear Energy, 161: 104741.

Ahmadi, M., Zanganeh, V., Bagheri, S. and Karami, H. (2023). Effect of substitution of Zirconium dioxide by Tin(IV) oxide on radiation shielding and properties of used in therapeutic environments. Optik, 278:170538.

Windsor, C. G., Morgan, J. and Buxton, P. (2015). Heat deposition into the superconducting central column of a spherical tokamak fusion plant. Nuclear Fusion, 55(2): 023014.

Hayashi, T., Tobita, K., Nakamori, Y. and Orimo, S. I. (2009). Advanced neutron shielding material using zirconium borohydride and zirconium hydride. Journal of Nuclear Materials, 386–388: 119–121.

Shultis, J. K. and Faw, R. (2010). Radiation shielding and radiological protection. In Springer eBooks (pp. 1313–1448).

Ahmadi, M., Vahid, Z. and Darush, N. (2024). Investigated mechanical, physical parameters and Gamma-Neutron radiation shielding of the rare earth (Er_2O_3/CeO_2) doped barium borate glass: Role of the melting time and temperature. Radiation Physics and Chemistry, 217, 111450.

Neu, R., Dux, R., Kallenbach, A., Pütterich, T., Balden, M., Fuchs, J., Herrmann, A., Maggi, C. F. and et al. (2005). Tungsten: an option for divertor and main chamber plasma facing components in future fusion devices. Nuclear Fusion, 45(3): 209–218.

Hila, F. C., Jecong, J., Dingle, C. a. M., Geraldino, G. C., Hila, A. M. J. and Guillermo, N. R. D. (2021). Generation of fast neutron removal cross sections using a multi-layered spherical shell model. Radiation Physics and Chemistry, 189:109735.

Jiang, Q., Wang, H., Ma, B., Wang, Y. and Zhao, F. (2005). Fabrication of B_4C particulate reinforced magnesium matrix composite by powder metallurgy. Journal of Alloys and Compounds, 386(1–2):177–181.

Abdullah, M. a. H., Rashid, R. S. M., Amran, M., Hejazii, F., Azreen, N. M., Fediuk, R., Voo, Y. L., Vatin, N. and Idris, M. I. (2022). Recent trends in advanced radiation shielding concrete for construction of facilities: Materials and properties. Polymers, 14(14): 2830.

Han, B., Zhang, L. and Ou, J. (2017). Radiation shielding concrete. In Springer eBooks (pp. 329–337).

Jiang, X., Xiao, R., Bai, Y., Huang, B. and Ma, Y. (2022). Influence of waste glass powder as a supplementary cementitious material (SCM) on physical and mechanical properties of cement paste under high temperatures. Journal of Cleaner Production, 340: 130778.

Her, S., Park, J., Li, P. and Bae, S. (2022). Feasibility study on utilization of pulverized eggshell waste as an alternative to limestone in raw materials for Portland cement clinker production. Construction and Building Materials, 324: 126589.

Zhou, M., Yang, T., Li, J., Bing, Q., Qiu, W., Li, B., Shu, B., Gong, J., Guo, L. and Li, Y. (2023). Preparation and performance Study of Radiation-Proof Ultra-High-Performance concrete. Coatings, 13(5): 906.

Piotrowski, T., Romero, M. J. M., Prochoń, P., López-Alonso, M., Michalczyk, R., Gran, A. U. O., Ciupiński, Ł., Becerril, S., Józefiak, K., Qiu, Y., Ansorge, M., Chohan, H. and Wojtkowska, M. (2024). Optimization and evaluation of structural and shielding concrete for IFMIF-DONES. Nuclear Materials and Energy, 101597.

Erkoyuncu, İ., Demirkol, İ., Akman, F., Dilsiz, K., Kaçal and Polat, H. (2024a). A detailed investigation of gamma and neutron shielding capabilities of concrete doped with bronze and boron carbide. Radiation Physics and Chemistry, 215:111358.

Holmes, R. R., Hart, M. and Kevern, J. T. (2017). Heavy metal removal capacity of individual components of permeable reactive concrete. Journal of Contaminant Hydrology, 196:52–61.

Fode, T. A., Jande, Y. a. C. and Kivevele, T. (2023). Effects of different supplementary cementitious materials on durability and mechanical properties of cement composite – Comprehensive review. Heliyon, 9(7):17924.

Chidiac, S., El-Samrah, M. G., Reda, M. A. and Abdel-Rahman, M. A. (2021). Mechanical and radiation shielding properties of concrete containing commercial boron carbide powder. Construction and Building Materials, 313: 125466.

Korkmaz, A. V., Can, Ö. and Kayiran, H. F. (2022). The effect of boron waste on the radiation shielding properties of cement. Arabian Journal of Geosciences, 15(1):1-5.

Sanjuán, M. Á., Menéndez, E. and Recino, H. (2022). Mechanical performance of Portland cement, coarse silica fume, and limestone (PC-SF-LS) Ternary Portland Cements. Materials, 15(8): 2933.

Beaucour, A., Pliya, P., Faleschini, F., Njinwoua, R., Pellegrino, C. and Noumowé, A. (2020). Influence of elevated temperature on properties of radiation shielding concrete with electric arc furnace slag as coarse aggregate. Construction and Building Materials, 256: 119385.

Tyagi, G., Singhal, A., Routroy, S., Bhunia, D. and Lahoti, M. (2021). Radiation Shielding Concrete with alternate constituents: An approach to address multiple hazards. Journal of Hazardous Materials, 404: 124201.

Borucka-Lipska, J., Brzozowski, P., Błyszko, J., Bednarek, R. and Horszczaruk, E. (2020). Effects of Elevated Temperatures on the Properties of Cement Mortars with the Iron Oxides Concentrate. Materials, 14(1):148.

Kaur, A., Sahani, G., Mudgal, M., Chouhan, R., Srivastava, A. K. and Pawaskar, P. (2023). studies on radiation shielding properties of newly developed high-density concrete for advanced radiotherapy facilities. Radiation Protection Dosimetry, 199(5): 399–409.

Marschke, S. F., Rish, W. and Mauro, J. (2019). Radiation exposures from the beneficial use of alumina production residue. Journal of the Air & Waste Management Association, 69(12):1479–1489.

Korkmaz, A.V. and Hacıfazlıoğlu, H. (2019). çimento üretiminde kil taşina alternatif bir hammadde: meta şist. Bilimsel Madencilik Dergisi, 58(2): 95–110.

Seenappa, L., Manjunatha, H., Chandrika, B., Sridhar, K. and Hanumantharayappa, C. (2018). Gamma, X-ray and neutron interaction parameters of Mg–Gd–Y–Zn–Zr alloys. Radiation Physics and Chemistry, 150: 199–206.

Tekın, H., Kavaz, E., Papachristodoulou, A., Kamislioglu, M., Ağar, O., Guclu, E. A., Kılıcoglu, O. and Sayyed, M. (2019). Characterization of SiO2–PbO–CdO–Ga2O3 glasses for comprehensive nuclear shielding performance: Alpha, proton, gamma, neutron radiation. Ceramics International, 45(15):19206–19222.

Dong, M., Xue, X., Elmahroug, Y., Sayyed, M. and Zaid, M. H. M. (2019). Investigation of shielding parameters of some boron containing resources for gamma ray and fast neutron. Results in Physics, 13: 102129.

Her, S., Park, T., Zalnezhad, E. and Bae, S. C. (2021). Synthesis and characterization of cement clinker using recycled pulverized oyster and scallop shell as limestone substitutes. Journal of Cleaner Production, 278: 123987.

Knop, Y. and Peled, A. (2018). Sustainable Blended Cements—Influences of packing density on cement paste chemical efficiency. Materials, 11(4): 625.

Tamayo, P., Thomas, C., Rico, J., Pérez, S. P. M. and Mañanes, Á. (2022). Radiation shielding properties of siderurgical aggregate concrete. Construction and Building Materials, 319: 126098.

Akhdar, H. and Alshehri, M. (2023). Geant4 Simulation of Photon- and Neutron-Shielding Capabilities of Biopolymer Blends of Poly(lactic acid) and Poly(hydroxybutyrate). Polymers, 15(21): 4257.

Cadini, F., Bolst, D., Guatelli, S., Beltran, C., Jackson, M. and Rosenfeld, A. B. (2016). Neutron shielding for a new projected proton therapy facility: A Geant4 simulation study. Physica Medica, 32(12): 1862–1871.

ICNST 2024 International Conference on Nuclear Science and Technology
6- 8 MAY 2024 | Isfahan, Iran

Heavy metal oxide glasses as gamma-rays and neutron shielding material (Paper ID : 1227)

Alipoor M.R[1*], Eshghi M.[1]

[1]*Department of Physics, Imam Hossein Comprehensive University, Tehran, Iran.*

Abstract

Gamma-ray shielding parameters for borate glass samples reinforced with niobium and lanthanum are reported. We have simulated mass attenuation coefficients between 15 keV and 10 MeV using Geant4 Monte Carlo simulation tool. The maximum values of linear attenuation coefficient were reported at energy less than 0.6 MeV. The half-value layer decreased due to the addition of Nb_2O_5 and La_2O_3, but the values of half-value layer for glasses containing, Nb_2O_5 and La_2O_3 are lower than the half-value layer for samples 1 and 4. Glass 2 and 4 is the best attenuator in this study due to the lowest half-value layer of this sample. Also, the obtained results showed that glass containing 2.5% Nb_2O_5 and La_2O_3, a thickness equal to 35 cm, is required to reduce photons with energy of 10 megaelectron volts by one tenth. While for a sample free of Nb_2O_5 and La_2O_3, at the same energy, a sample with a thickness of 38 cm is required. Finally, we have calculated the of removal cross section for fast neutron for glass samples. The of removal cross section for fast neutron showed that sample 3 has a better performance for removal fast neutron.

Keywords: Gamma-ray, Neutron, Shielding, Glass, Geant4, simulation.

INTRODUCTION

Among the studies of different health care sectors, medical radiation is still a significant issue for medical center staff and researchers in sub-fields of medicine such as radiation therapy and diagnostic radiology. In addition to the benefits of radiation, concerns about radiation exposure cannot be ignored [1]. These effects cause gene remodeling that leads to organ dysfunction to cause diseases such as cancer and similarly, ionization effects in materials can lead to device dysfunction and other radiation damage. Depending on the severity and other related factors, these effects may cause irreparable economic losses and even death [2]. The use of shields in radiation applications is an accepted way to protect instruments, their components, to protect people and other environmental components from uncontrolled radiation without limiting radiation activity. The development of reliable radiation shields often requires the use of specialized elements that have a high ability to absorb and weaken the radiation beams, especially gamma photons [3]. Considering the increasing use of active gamma ray isotopes in various fields, it is necessary to study the interaction of

gamma rays in order to identify suitable materials in terms of density and composition in order to reduce radiation effects [4]. Therefore, the density and atomic number of the elements are the primary factors that have the greatest influence on choosing the right shield. In this regard, lead (Pb) and its derivatives, such as cement and steel, are common materials used for protective applications. But materials containing lead are known to have negative effects on humans and the environment [5, 6]. Therefore, various materials such as alloys, polymers and glasses are proposed as alternatives to concrete and lead-based materials [7-9]. The reason for choosing glass is because of its distinctive features such as high optical clarity, excellent formability and the ability to change the composition to improve its properties to form different glass structures. Such properties justify glass materials for use in basic applications, for example in display panels and windows. Borate glasses are characterized by strong bond formation, reduced thermal expansion, increased flexibility and low melting point. All these features make borate glasses easy to work with and prepare for various applications including optical fibers, filters, communication devices, lasers and most importantly, its use in reducing ionizing radiation [10, 11]. Many studies have been conducted for various lead-free glass systems that can be used for radiation protection in hospitals and diagnostic laboratories. The new glasses, one of which is lanthanum oxide, have an extremely high refractive index and very low dispersion, and are used in camera lenses, military binoculars, and other military equipment to correct spherical and chromatic aberrations [12]. Glass containing La_2O_3 will be transparent and colorless due to its high refractive index, have high density and high atomic number, so they are very suitable for use in radiation shielding applications. Lanthanum oxide, by adding oxide modifiers such as sodium oxide (Na_2O) and barium oxide (BaO) to increase moisture resistance, reduce melting point and increase the stability of the glass network, plays a role in modifying the optical absorption of borate glass. Borate glass with added barium oxide, an alkaline earth metal, is an excellent radiation shielding material because it has a good mass attenuation coefficient, effective atomic number values, high density, and most importantly, is non-toxic compared to lead [13-15]. On the other hand, Niobium pentoxide, which is also known as niobium oxide, belongs to the group of metal oxides and is a white and odorless powder. Niobium oxide (Nb_2O_5) is used in the production of optical glass and filters for photographic lenses, copiers and glasses. Also, they have high density and high atomic number, so it will be very suitable for use in radiation shielding applications [16]. Therefore, the aim of the present study, to investigate the different protective properties of ionizing radiation, a new composition of lead-free borate glasses reinforced with lanthanum oxides and niobium oxide in different concentrations for its use in radiation protection.

RESEARCH THEORIES

When a parallel beam of mono-energetic gamma radiation is allowed to penetrate through a material of thickness, x(cm) the intensity of the incident radiation degrades due to different interaction processes viz., photoelectric effect, Compton scattering and Rayleigh scattering in the intermediate energy range used in the present study. The equation (1) can be arranged to determine the linear attenuation coefficient as follows: [17]:

$$\boldsymbol{I = I_0 e^{-\mu x}} \quad (1)$$

where **x** is the thickness of the sample, I represent the intensity of transmitted photons and I_0 denotes the intensity of the initial photons.

Where μ (cm^{-1}) is called linear attenuation coefficient of the sample under investigation. The symbols I and I_o representing the intensity under the photo-peak with and without the material in the photon beam. The equation (2) can be arranged to determine the mass attenuation coefficient as follows: [17]:

$$\boldsymbol{\mu_m = \frac{\mu}{\rho} = \frac{1}{\rho x} \ln \frac{I}{I_0}} \quad (2)$$

Simulation with Geant4 Tool

Experiments in particle and beam physics studies involve complex processes, and hence it is convenient to perform simulation modeling before starting experiments. The geometry of the experiment and the design of the detectors used in these experiments are of great importance. The large size of the detector, which increases its sensitivity, increases the cost of detecting complex events. In radiation shielding studies, it greatly facilitates the transport of radiation events within shielding materials, provides basic information to the user, and guides the design of new materials [18]. Figure 1 shows the narrow beam geometry of the Geant4 simulation tool, which consists of a gamma source impinging on a glass plate. Gamma photon energy is determined using the GPS spectrum definition in the energy range of 0.15 to 10 MeV. Also, glass samples are modeled according to their atomic number, mass number, element weight fraction and density. In this work, ten million photons are fired from the energy source to hit the glass sample target. Then the transmitted photons are recorded using a detector. Eventually, the mass attenuation coefficients values of the studied glasses were calculated based on the Beer-Lambert law.

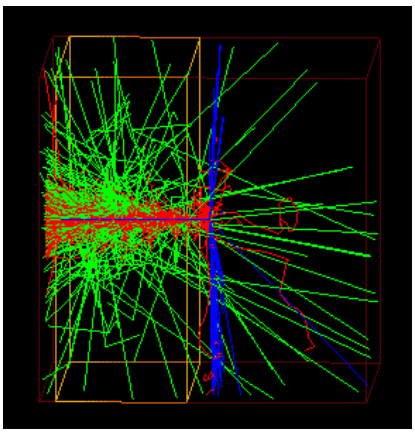

Fig. 1. Simulated geometry in Geant4 tool to determine gamma shielding properties in glasses.

Results and Discussion

The compositions of heavy metal oxide glass considered in this study as an alternative to conventional glass, characterized by the addition of Lanthanum and Niobium oxides, are listed in Table 1. In the calculation section, the aim is to investigate the difference in the gamma shielding capacity of Lanthanum, Niobium compounds with borate glasses to estimate the attenuation length and gamma absorption through simulation tools.

Table 1. Chemical compositions of glass samples.

Chemical Composition (%)	Sample			
	Glass 1	Glass 2	Glass 3	Glass 4
B_2O_3	60	55	55	55
Bi_2O_3	10	10	10	10
Al_2O_3	10	10	10	10
ZnO	10	10	10	10
Li_2O	10	10	10	10
La_2O_3	--	2.5	5	--
Nb_2O_5	--	2.5	--	5
Density ($g.cm^{-3}$)	3.527	3.682	3.729	3.634

The mass attenuation coefficients (MAC) of the glasses were determined using the Geant4 toolbox. The results obtained from mass attenuation coefficients in the energy range of 0.015 to 15 MeV are shown according to Figure 2. It can be seen that the mass attenuation coefficient of the existing glasses depends

on the gamma energy and also on its compositions. For low energy photons (0.015-0.5 MeV), the mass attenuation coefficient is significant due to the dominance of photoelectric absorption in this energy range. Moreover, some abrupt discontinuities can be seen in the Fig. 2 due to the photoelectric effect near the absorption K-edge of La, Bi and Nb elements at 38.92 keV, 90.52 keV and 18.98 keV, respectively. This very slight increase in the energy related to the absorption edge of Niobium and Bismuth causes more photon energy to be absorbed by the orbital electron, which can be used for protection in this energy range. Also, due to this absorption, secondary particles will have less energy. Among our suggested glasses, glass 4 and 2 have a higher mass attenuation coefficient, because both have a higher weight fraction than the other two samples.

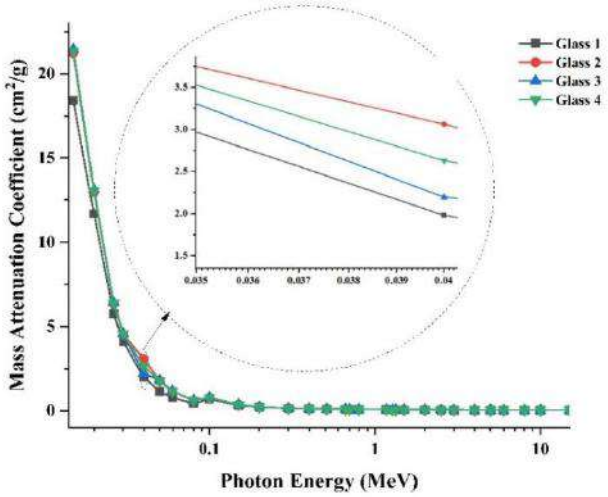

Fig. 2. Variations of mass attenuation coefficients with respect to a function of photon energy in the Samples.

The linear attenuation coefficients (LAC) for gamma rays in the studied glasses are qualitatively plotted in Figure ۳. As Figure ۳ shows, with increasing energy, the values of linear attenuation coefficient decrease for all glasses. Therefore, the value of the attenuation coefficients of glass 2 and 4 reaches a maximum at 0.015 MeV and a minimum at 10 MeV. This process is predicted by the behavior of photoelectric effect, Compton scattering and pair production cross section according to gamma ray energy. These processes are dominated by gamma photon interactions with glasses at these energies. In addition, the dominance of photoelectric absorption (a process that completely absorbs photons at low energies below 0.6 MeV) explains the relatively higher in this energy range. The Compton process, which is effective at later energies, does not completely absorb the photons, but slows them down. In comparison, glass 2 has the highest

possible μ at all energies, while glass 1 has the lowest μ. The high atomic number of lanthanum and niobium along with bismuth oxide, which is a good absorber for gamma photons, causes the photon attenuation characteristics of these glasses to increase.

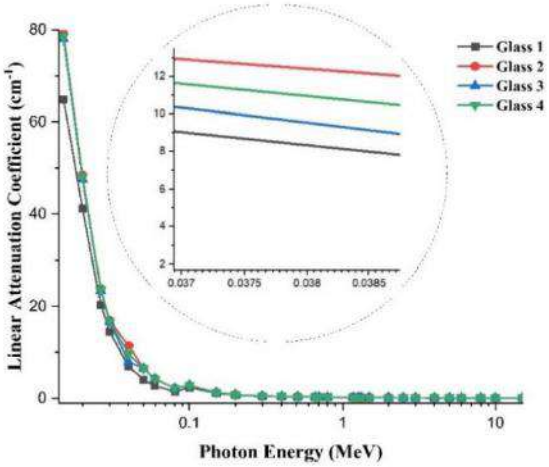

Fig. 3. Variations of linear attenuation coefficient (μ) with respect to a function of photon energy in the Samples.

Plotting the reduction of gamma radiation inside a glass sample in terms of MFP can give meaningful information. Given that it was obtained for low MFP, more interactions between photons and materials can be inferred, resulting in better performance. As the photon energy increases, the MFP increases very quickly, so in shielding applications, it is better to increase the thickness of the glass because the gamma rays can penetrate deep into the glass. In addition, Figure 4 shows that the existing glass has better properties than borate glass with bismuth oxide (Glass 1).

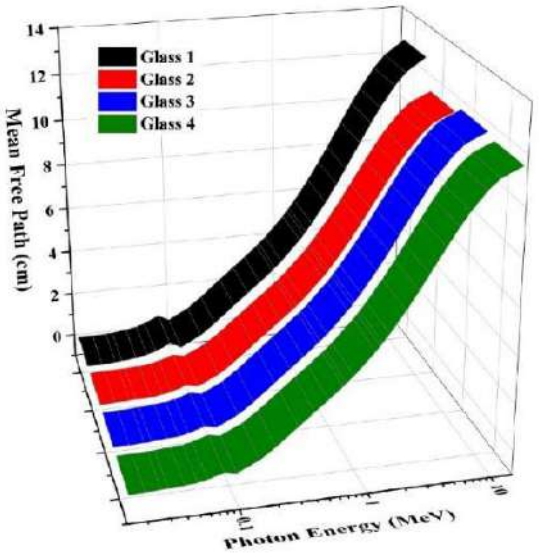

Fig. 4. Comparison of the values of mean free path with respect to a function of photon energy in the samples.

The half value layer HVL values of the present glasses are calculated and plotted in Figure 5. It can be seen from Figure 5 that the HVL values of the glasses present at low photon energies are very small (0.511 MeV). Then, HVL values increase with the increase of photon energy and the maximum thickness, which is about 3.5 cm, is observed at about 1.333 MeV for all studied glasses. These findings show that high-energy photons have a greater capacity to penetrate the shield. With increasing energy and increasing density values and increasing μ/ρ, the HVL values determined for the samples increased in energy of cobalt, cesium and sodium sources in niobium and lanthanum content samples.

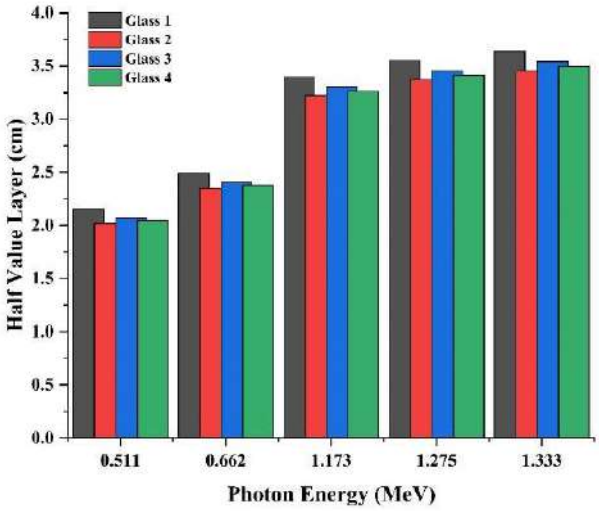

Fig. 5. The values of half value layer with respect to a function of photon energy in the samples.

In addition, we can estimate the coverage at an even deeper layer, for example a tenth, using the concept of the tenth value layer. For this reason, we calculated the tenth value layer (TVL) for the samples and plotted the results in Figure 6. After that, the TVL values of the present glasses increase with increasing photon energy. The low value of TVL in the low-energy region indicates that the surface of La_2O_3 and Nb_2O_5 significantly affects the capacity of these glasses to reduce radiation, which is consistent with the important role of the photoelectric effect. At higher energies, the content of La_2O_3 and Nb_2O_5 has a great effect on TVL. The required thickness should be as small as possible to select the ideal material sample. It has been found that glass 2 and 4, which has the composition structure of La_2O_3 and Nb_2O_5, has the lowest TVL values compared to other glass samples. Under these research conditions, the behavior of the samples is satisfactorily explained by the inverse relationship between LAC and TVL. Therefore, glass density has an

inverse relationship with TVL. As seen in Figure 5, the increase of La_2O_3 and Nb_2O_5 increases the density. At the same energy, it requires a relatively thinner layer of glass to shield the high-energy photons.

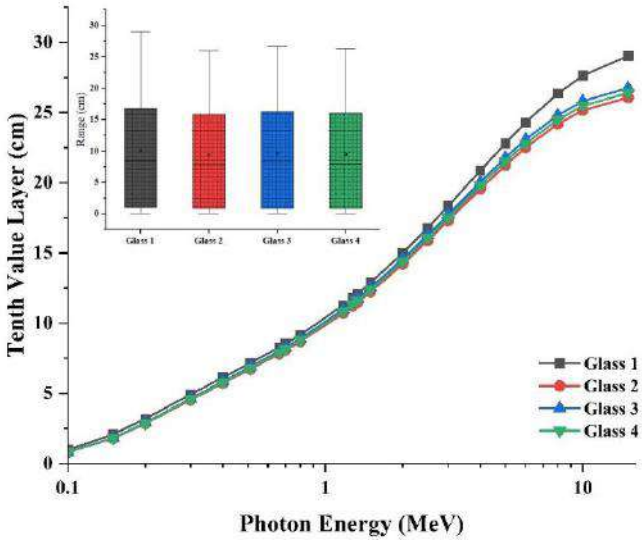

Fig. 6. Tenth value layer with respect to a function of photon energy in the samples.

The cross-section of the fast neutron removal of the present glasses is shown in Figure 7. The total exclusion cross section (Σ_R) for fast neutrons for glass 3 has the highest Σ_R values. While glass 2 has the lowest Σ_R values among the present glasses. Although Li and O have the highest mass exclusion cross sections for fast neutrons among the elements in glasses. It seems that the increase in the density of glass due to the addition of Nb_2O_5, La_2O_3 increases the frequency of fast neutron collisions and hence the cross section of fast neutron removal. Therefore, the optimal glass structure for fast neutron modulation is found in glass 3.

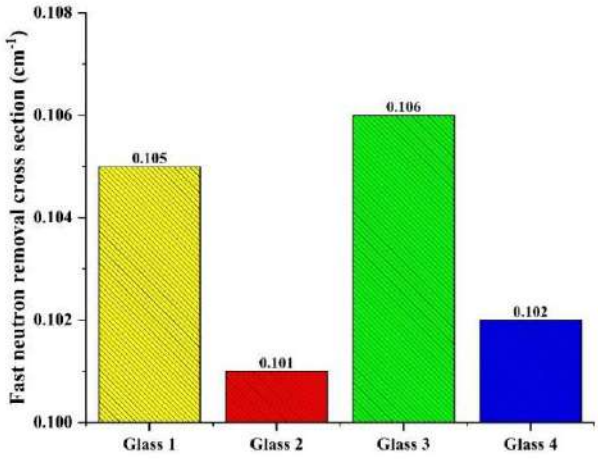

Fig. 7. Variations of removal cross section (Σ_R) for the glasses for fast neutron.

Conclusions

Gamma-ray shielding parameters are reported for four samples using Geant4 code. We simulated the MAC between 15 keV and ١٠ MeV using the Geanr4 code. The maximum linear attenuation coefficients values were found in the low energy range (less than 0.6 MeV). Linear attenuation coefficients decrease with increasing energy and it had the highest value for glass 2 and 4. HVL increased due to the addition of Nb_2O_5 and La_2O_3. HVL values for glasses 1 and 3 are lower than HVL for glasses 2 and 4. Glass 3 did not perform well even with a higher density than other samples. Samples 2 and 4 are the best attenuators in this study due to the lowest HVL and TVL values in the samples. A 35 cm thick glass 2 is needed to reduce the photon surface carrying energy of 10 MeV by a factor of one Tenth, while 1 requires a 38 cm thick sample for this purpose with the same energy. The results showed that lanthanide glass has a slightly lower TVL than other glasses and is more suitable for use as a transparent radiation shield.

References

Gomaa, H. M., Saudi, H. A., Yahia, I., Ibrahim, M. and Zahran, H. (2022). Influence of exchanging CeO_2 with Cu_2O_3 on structural matrix, shielding, and linear/nonlinear optical parameters of the cerium-sodium borate glass. Optik, 249: 168267.

Obaid, S. S., Gaikwad, D. and Pawar, P. P. (2018). Determination of gamma ray shielding parameters of rocks and concrete. Radiation Physics and Chemistry, 144: 356–360.

Kaur, P., Singh, K. J., Kurudirek, M. and Thakur, S. (2019). Study of environment friendly bismuth incorporated lithium borate glass system for structural, gamma-ray and fast neutron shielding properties. Molecular and Biomolecular Spectroscopy, 223: 117309.

Saudi, H. A., Tekın, H., Zakaly, H. M., Issa, S. A., Süsoy, G. and Zhukovsky, M. (2021). The impact of samarium (III) oxide on structural, optical and radiation shielding properties of thallium-borate glasses: Experimental and numerical investigation. Optical Materials, 114: 110948.

Al-Buriahi and Singh, V. P. (2020). Comparison of shielding properties of various marble concretes using Geant4 simulation and experimental data. Journal of the Australian Ceramic Society, 56(3): 1127–1133.

Al-Buriahi, El-Agawany, F., Sriwunkum, C., Akyıldırım, H., Arslan, H., Tonguç, B. T., El-Mallawany, R. and Rammah, Y. S. (2020). Influence of Bi_2O_3/PbO on nuclear shielding characteristics of lead-zinc-tellurite glasses. Physica B: Condensed Matter, 581: 411946.

ALMisned, G., Zakaly, H. M., Issa, S. A., Ene, A., Kılıç, G., Bawazeer, O., Almatar, A., Shamsi, D., Rabaa, E., Sideig, Z. and Tekın, H. (2021). Gamma-Ray Protection Properties of Bismuth-Silicate Glasses

against Some Diagnostic Nuclear Medicine Radioisotopes: A Comprehensive Study. Materials, 14(21): 6668.

Alzahrani, J. S., Alrowaili, Z., Olarinoye, I., Katubi, K. M. and Al-Buriahi. (2023). Effect of ZNO on radiation shielding performance and gamma dose of boron silicate glasses. Silicon, 16(1): 105–113.

Kaur, P., Singh, D. and Singh, T. (2016). Heavy metal oxide glasses as gamma rays shielding material. Nuclear Engineering and Design, 307: 364–376.

Al-Buriahi, Arslan, H., Tekın, H., Singh, V. P. and Tonguç, B. T. (2020). MoO_3-TeO_2 glass system for gamma ray shielding applications. Materials Research Express, 7(2): 025202.

Elbashir, B., Sayyed, M., Dong, M., Elmahroug, Y., Lakshminarayana, G. and Kityk, I. (2019). Characterization of Bi_2O_3ZnO B_2O_3 and TeO_2-ZnO CdO Li_2O V_2O_5 glass systems for shielding gamma radiation using MCNP5 and Geant4 codes. Journal of Physics and Chemistry of Solids, 126:112–123.

Henaish, A. (2022). Enhancement of Optical Properties of Borate Glass Doped with Vanadium Oxide. Juniper Online Journal Material Science, 6(5):555700.

Kebaïli, I., Sayyed, M., Boukhris, I. and Al-Buriahi. (2020). Gamma-ray shielding parameters of lithium borotellurite glasses using Geant4 code. Applied Physics A, 126(7): 536.

Samdani, M., Basha, B., Alomairy, S., Kebaïli, I., Sekhar, K. C., Alrowaili, Z., Eke, C., Olarinoye, I. and Al-Buriahi. (2024). Gamma shielding performance of B2O3/BaO-based glassy system: Synthesis and simulation study. Radiation Physics and Chemistry, 214: 111301.

Zenhom, K., Ebrahem, N. M., Mohammad, S. And Saudi, H. A. (2023). Role of La_2O_3 in enhancement the properties of the BaO–B_2O_3 glass system: optical and radiation shielding study. Optical and Quantum Electronics, 56(2):1-16.

Shaaban, K. S., Althagafi, T. M., Ashour, A., Alalawi, A., Al-Buriahi and Ibraheem, A. A. (2024b). The role of Nb_2O_5 on structural, mechanical, and gamma-ray shielding characteristics of lithium molybdenum borate glasses. Radiation Physics and Chemistry, 216:111440.

Alipoor, M.R, Eshghi, M.(202٤). A Comprehensive Study of Gamma-rays Shielding Features of Binary Compounds. Progress in Physics of Applied Materials, ٤(١): ٥٩-٦٧.

Savchenko, A. A., Khudyakova, A. and Wagner, W. (2024). Geant4 implementation of axial channeling radiation in classical description. Nuclear Instruments and Methods in Physics Research Section A: Accelerators, Spectrometers, Detectors and Associated Equipment, 1060: 169057.

ICNST 2024 International Conference on Nuclear Science and Technology
6- 8 MAY 2024 | Isfahan, Iran

Evaluation of Bremsstrahlung photon pollution inside the MIRD Phantom at electron therapy (Paper ID : 1229)

Hoseini M. Correspond* , Hamidi S. Co-Author

Faculty of Science, Arak University, Arak, Iran

Abstract

Much research is being conducted on the Bremsstrahlung photon contamination in medical linear accelerators. This work aims to evaluate Bremsstrahlung photon pollution inside the MIRD Phantom. In this work, Bremsstrahlung photon contamination in the ELEKTA Precise linear accelerator at Ayat-O-lah Khansari Hospital is measured by thermo luminescence detectors and calculated by MCNPX simulation. Comparison between the measured and calculated dose of produced Bremsstrahlung photons at 15MeV energy has shown a good agreement, so it will be possible to calculate Bremsstrahlung photon dose inside the MIRD Phantom with MCNPX. It was understood that in radiation therapy of neck tumors by 15 MeV electrons, the maximum rate of Bremsstrahlung photon dose will be produced at the pharynx position, and its average dose is 72.7 mSv. The MCNPX code offers an excellent tool to simulate absorbed doses in radiotherapy. So, it will be possible to have a comprehensive photon contamination plan produced during the electron therapy for a different part of the body with Monte Carlo codes.

Keywords: Bremsstrahlung contamination, Thermo luminescence dosimetry, Medical linear accelerator, Electron therapy, MCNPX, Humanoid Phantom.

Introduction

High-energy electrons have been used in radiation therapy since the 1950s. The electrons' most clinically practical energy limit is 6 to 20 MeV for treating superficial tumors like skin, lip, head, and neck cancers [1]. Having a finite range is an advantage of electron beam irradiation. This issue causes a sharp drop-off in the dose beyond the tumor. Also, a distinct advantage of electron beams is dose uniformity in the target volume [1,2].

The generation of suitable clinical electron beam imports a challenge to accelerator manufacturers [3]. Clinical electron beams contain an admixture of Bremsstrahlung photons produced in various structures in the accelerator head, such as the ion chamber, the dual scattering foil, the electron applicator, and the irradiated patient or Phantom. Therefore, the rate of producing Bremsstrahlung radiation is greatly affected by the thickness and atomic number of these elements [4,5,6].

It must be considered that electron beams parameter produced by various LINACs show the difference between manufacturers, so it is essential to know the amount of leakage and scattered radiation in electron

therapy by different LINACs [7,8]. Hence many studies have been done on various LINACs; some cases are mentioned briefly in the following. Characteristics of Bremsstrahlung in electron beams were performed on a Varian 2300CD LINAC. The maximum bremsstrahlung dose was estimated to be less than 10% of the maximum electron dose [6]. The result of the Monte Carlo investigation of electron beam output factors versus the size of the square cutout for the Siemens MD2 accelerator showed that the dose contribution from contaminant photons depends on energy and cutout size [9]. In other research, the dose distribution in whole-body superficial electron therapy was investigated**,** and the Bremsstrahlung dose has been studied as a function of the number of fields used [10].

Research theories

This study evaluates Bremsstrahlung photon pollution caused by the ELEKTA Precise linear accelerator. First, the production of Bremsstrahlung radiation is calculated with MCNPX and measured experimentally by thermo luminescence detectors at 15MeV energy. As there is a suitable match between simulation and experimental data, Bremsstrahlung photon contamination dose is calculated in different parts of the patient's body Phantom with MCNPX.

Experimental

1. MCNP Simulation and Experimental Measurements in Radiotherapy

Monte Carlo codes are the most accurate methods for predicting dose distribution and accumulation in the tissue at radiotherapy [8]. This study simulated the radiation transport of photons and electrons using the MCNPX 2.4.0 Monte Carlo code.

This simulation has been done for the electron mode of the ELEKTA Precise medical linear accelerator at Ayat-O-lah Khansari Hospital. The head of the ELEKTA Precise machine for electron mode has a primary scattering foil, primary collimator, secondary scattering foil, monitor unit chamber, mirror, X and Y jaws, and the electron applicator. This simulation was done for 15MeV energy and a 10cm×10cm applicator. A circular disk with a 1mm diameter was considered for simulating the electron source. The energy spectra of the electron source were modeled as a Gaussian function with FWHM = 10% for 15 MeV energy. The cylindrical polyethylene phantom with a 5cm radius and 5cm high thermo luminescence detectors, patient bed, and treatment room were simulated. The cut-off energy for transporting electrons and photons was considered 0.01 MeV in simulations. For calculating the absorbed photon dose, tally F6 was used. This tally gives the amount in the unit of MeV/g per particle. The total photon dose rate in the mSv range (equivalent

dose) can be calculated by considering the unit conversion and activity of the source. A schematic of the radiotherapy room, its different parts, and the place of simulated TLDs are shown in Fig. 1.

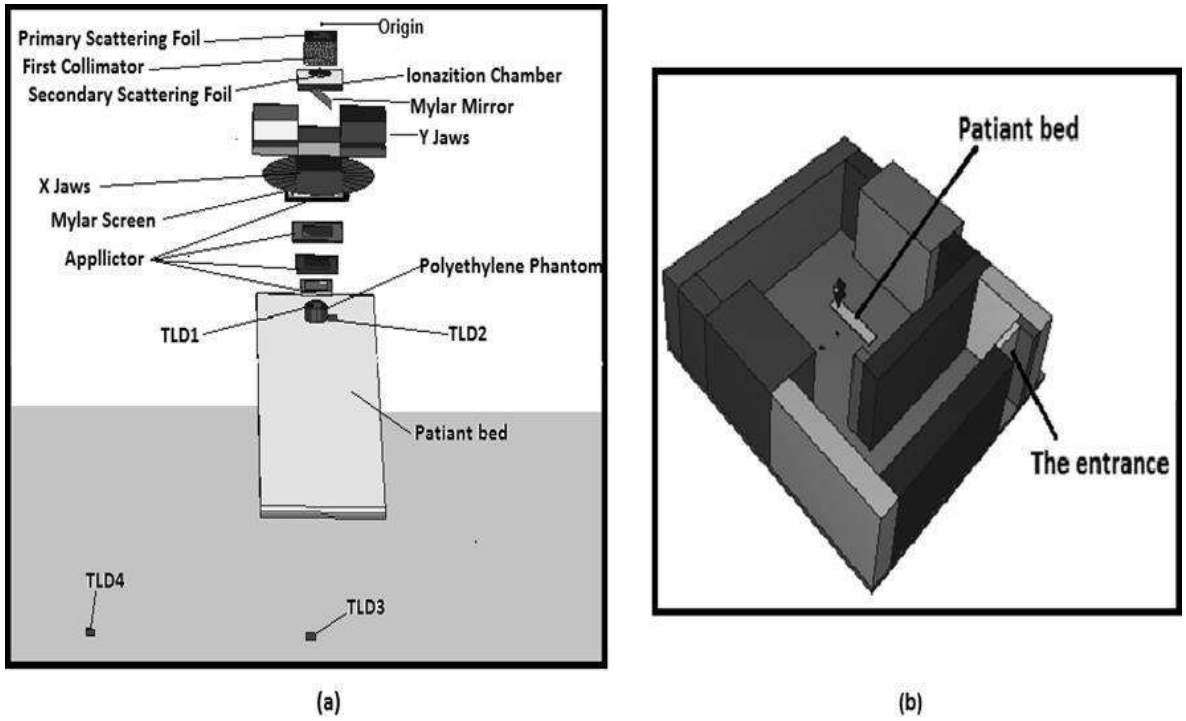

Fig. 1. a) 3D view of the simulated geometry of different parts of the treatment room in 15MeVenergy. b) 3D view of the simulated geometry of Ayat-O-lah Khansari Hospital radiotherapy room**.**

To validate the obtained results through simulation, the Bremsstrahlung contamination is empirically measured by using five TLD-700 at arbitrary points. The TLD-700 is a lithium fluoride (LiF) thermo luminescence detector made by the US Harshaw Company. It is the most commonly used TLD material for personnel dosimetry. LiF TLDs have a comprehensive dose response of ~0.01 mSv to 1.05 Sv. Another advantage of LiF TLDs is that their adequate atomic number is close to that of human tissue; therefore, the dose to the dosimeter is close to the human tissue dose over a wide range of energy. These TLDs are designed as rectangular cubes with 0.9mm×3mm×3mm dimensions [11]. The experiment used a cylindrical polyethylene phantom with a 5cm radius, 5cm high, and 10cm×10cm applicator. To calculate Bremsstrahlung photon contamination in 15 MeV, 5 TLD-700 were used around the Phantom and the patient bed. One of the TLDs was chosen as an environmental dosimeter. The location of other TLDs is shown in Fig. 1.(a). LINAC setup was: Dose rate= 300 mu/min, SSD= 100 cm, and monitor unit= 100mu. The average measurement error of TLDs is around 10%.

2. MCNP Model of the MIRD Phantom

Using of humanoid phantoms has been popular for many different uses in radiotherapy. Such Phantom allows calculating of dose distribution in other organs of the body. In this work, for calculating the rate of producing Bremsstrahlung dose in other parts of the body in electron therapy of neck and head cancer, the MIRD Phantom was used. The MIRD Phantom is provided by the Massachusetts Institute of Technology, Department of Nuclear Engineering. It represents a male 170 cm tall, which contains different body organs such as the lung, stomach, kidney, spleen, brain, skin, etc. It has been simulated with three different materials, the part of soft tissue, the bones, and the lungs. Fig. 2. shows our simulation's MIRD Phantom on the patient bed.

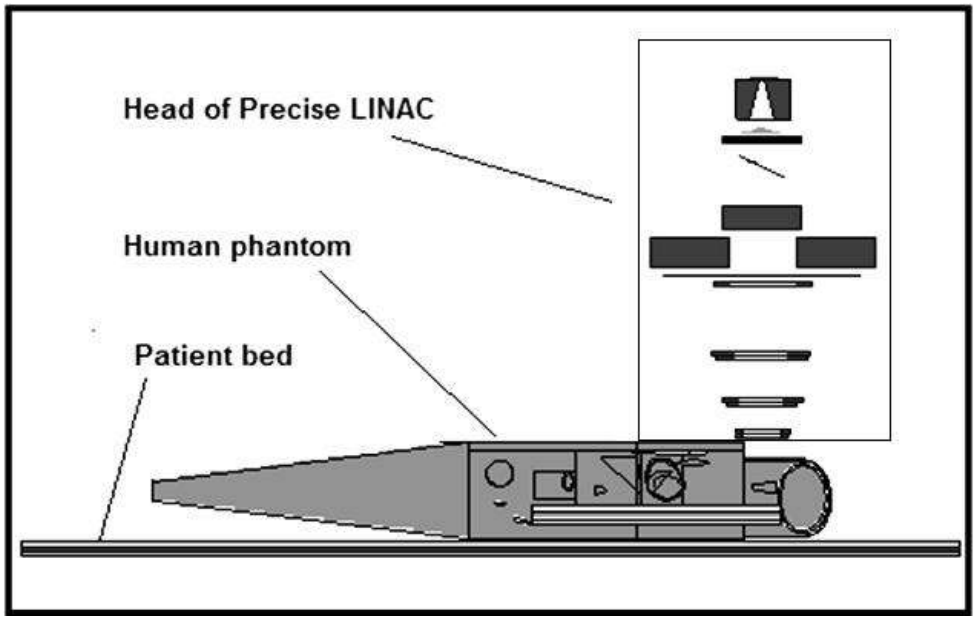

Fig. 2. Simulation of the MIRD Phantom on the patient bed in the radiotherapy room.

Results and discussion

The Bremsstrahlung contamination caused by the electron beam of the ELEKTA Precise linear accelerator at Ayat-O-lah Khan sari Hospital at different points is measured experimentally and simulated with MCNPX for 15 MeV energy. Results are calculated in a time unit and shown in Table 1. As shown in Table 1, the rate of producing Bremsstrahlung radiation in simulation and experimental data for a cylindrical polyethylene phantom shows a similar trend for these arbitrary points. This suitable match allows us to calculate the Bremsstrahlung photon contamination dose for different internal organs of the MIRD Phantom with MCNPX. The results of the calculation for the reference field (10×10 cm^2 applicator) in different parts of the MIRD Phantom are shown in Table 2. It was realized that in electron therapy for head and neck

tumors, the maximum rate of this unwanted dose would be produced at the pharynx of a patient with an average of 72.7 mSv at 15 MeV energy.

Table 1. Comparison of experimental and simulation results at 15MeV in different locations of the radiotherapy room.

TLD-700 characteristic	location of the TLD-700 according to the distance from origin(cm)	Average of the Bremsstrahlung absorbed dose in simulation (mSv)	Average of the Bremsstrahlung absorbed dose in the experiment (mSv)
1	100.52	27.5	40.52
2	105.8	6.49	5.72
3	225.52	1.96	0.721
4	246.48	0.09	0.034

Table 2. Average of the Bremsstrahlung absorbed dose for different organs of MIRD Phantom at 15MeV energy.

Body organ	Average of the Bremsstrahlung photon absorb dose (mSv)	Average of the Electron absorb dose (mSv)
BRAIN	5.62	6.99
HEAD	42	242.1
PHARYNX	72.7	123.6
THYROID	11.5	12.2
THYMUS	3.99	4.55
LUNG	0.062	0.065
LIVER	0.65	0.684
SPLEEN	0.482	0.484
STOMACH	0.447	0.472
PANCREAS	0.43	0.432
KIDNEY	0.242	0.259
LARGE INTESTINE	0.519	0.551
SMALL INTESTINE	0.314	0.324
BLADDER	0.027	0.03
BONE MARROW	2.27	2.92

SKIN	2.12	7.47
TRUNK	4.93	6.90

The ratio of Bremsstrahlung photon dose to the irradiated electron dose at each part of the MIRD Phantom is shown in Fig. 3. It is clear that the penetrating power of electrons is low, approximately a few mm range in tissue. So, the electrons with a good approximation penetrate the depth of neck tissue and loss their energies by absorbing in tissues. Because the intensity of the incident electron dose is very high in the head and neck, the ratio of the Bremsstrahlung photon dose to the electron dose will be small in these regions. This ratio remarkably increased with increasing distance from the place of treatment (neck) toward other parts of the body such as the lungs, stomach, kidneys, and so on. It will occur because the electrons scattering compared to photons scattering is much more, and the depth of their influence is much less. Some portions of this produced Bremsstrahlung photon dose is due to penetrating electron dose. The main contribution came from the penetrating photons produced and scattered in other body parts toward these areas.

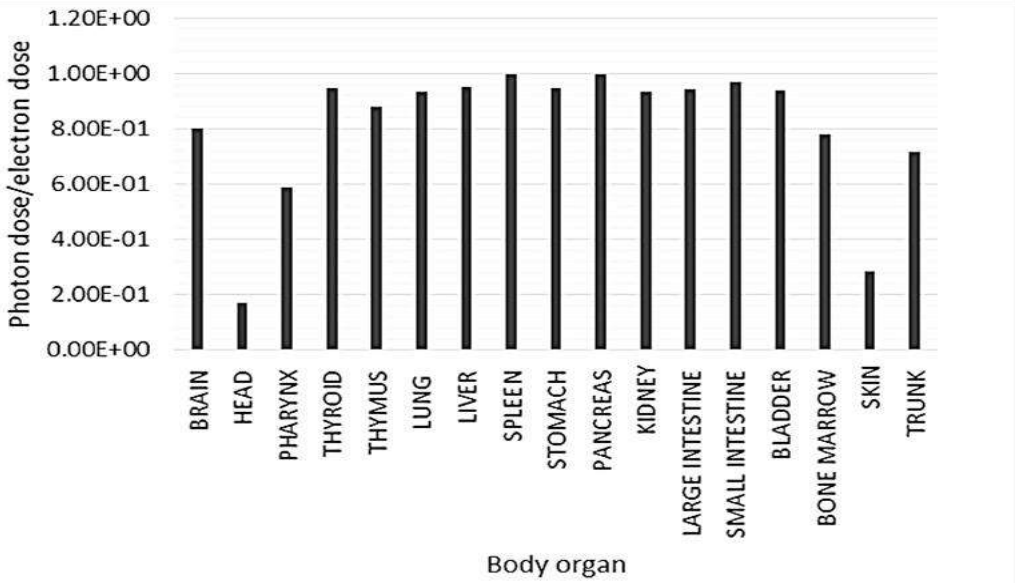

Fig. 3. The ratio of Bremsstrahlung photon dose to the irradiated electron dose at each part of the humanoid Phantom in electron therapy at 15 MeV energy.

Conclusions

This study was intended to evaluate Bremsstrahlung pollution inside the MIRD Phantom at electron therapy with Precise LINAC. The MCNPX code offers an excellent tool to calculate absorbed doses in radiotherapy. In electron therapy for neck and head tumors, the top portion of the Bremsstrahlung photon dose will be

produced at the pharynx position with an average of 72.7 mSv at 15 MeV energy. Then it will be possible to have a comprehensive photon contamination plan produced during the electron therapy for a different part of the body with Monte Carlo codes.

References

[1] Khan, F. M., & Gibbons, J. P. (2019). Khan's the physics of radiation therapy. Lippincott Williams & Wilkins.

[2] Klein, E. E. (2008). Electron-beam therapy: dosimetry, planning, and techniques. Perez and Brady's principles and practice of radiation oncology, 5th edition. Philadelphia, PA: Lippincott Williams & Wilkins, 190-217.

[3] Karimi, A. H., Mirian, S. F., Mahmoudi, F., Geraily, G., Vega-Carrillo, H. R., & Mohiuddin, M. (2022). Feasibility of 18-MV grid therapy from radiation protection aspects: unwanted dose and fatal cancer risk caused by photoneutrons and scattered photons. Computer methods and programs in biomedicine, 213, 106524.

[4] Hogstrom, K. R., & Almond, P. R. (2006). Review of electron beam therapy physics. Physics in Medicine & Biology, 51(13), R455.

[5] El-Khatib, E. E., Scrimger, J., & Murray, B. (1991). Reduction of the bremsstrahlung component of clinical electron beams: implications for electron arc therapy and total skin electron irradiation. Physics in Medicine & Biology, 36(1), 111.

[6] Alabdoaburas, M. M., Mege, J. P., Chavaudra, J., Bezin, J. V., Veres, A., de Vathaire, F., ... & Diallo, I. (2015). Experimental assessment of out-of-field dose components in high energy electron beams used in external beam radiotherapy. Journal of applied clinical medical physics, 16(6), 435-448.

[7] Chang, K. P., Wang, Z. W., & Shiau, A. C. (2014). Determining optimization of the initial parameters in Monte Carlo simulation for linear accelerator radiotherapy. Radiation Physics and Chemistry, 95, 161-165.

[8] Nedaie, H. A., Mosleh-Shirazi, M. A., Shariary, M., Gharaati, H., & Allahverdi, M. (2006). Monte Carlo study of electron dose distributions produced by the elekta precise linear accelerator. Reports of Practical Oncology and Radiotherapy, 11(6), 287-292.

[9] Zhang, G. G., Rogers, D. W., Cygler, J. E., & Mackie, T. R. (1999). Monte Carlo investigation of electron beam output factors versus size of square cutout. Medical physics, 26(5), 743-750.

[10] Bjärngard, B. E., Chen, G. T., Piontek, R. W., & Svensson, G. K. (1977). Analysis of dose distributions in whole body superficial electron therapy. International Journal of Radiation Oncology* Biology* Physics, 2(3-4), 319-324.

[11] Attix, F. H. (2008). Introduction to radiological physics and radiation dosimetry. John Wiley & Son

ICNST 2024 International Conference on Nuclear Science and Technology
6- 8 MAY 2024 | Isfahan, Iran

An investigation into the impact of LET on the Single Event Burnout (SEB) sensitivity of a 3.3 kV PiN diode (Paper ID : 1232)

Soleimaninia M.*

Nuclear Science and Technology Research Institute, Atomic Energy Organization of Iran, Tehran, Iran

Abstract

High-voltage semiconductor devices are prone to Single Event Burnout (SEB) due to the interactions of Galactic Cosmic Rays (GCR). SEB is a permanent failure which is initiated by the passage of a single particle during turn-off state of the device. In this paper, SEB in a PiN diode induced by various ions in space studied through simulation. The studied ion's LET determined by SRIM. Also, the electrical properties of the device due to irradiation studied by Silvaco TCAD tool. The key indicator of the SEB occurrence is the threshold voltage of SEB (V_{SEB}). Therefore, the correlation between the ion's LET and V_{SEB} has been investigated.The results indicate that the most sensitive region is in the middle of the device and SEB is caused by avalanche multiplication of ion-generated carriers. Furthermore, it is found that the V_{SEB} decreased from 3200 V to 2100 V, when the LET increased from 0.19 to 58 MeV.cm^2/mg for He and Ta, respectively. Therefore, ions with higher values of LET can burnout the device in the lower V_{SEB} and make the device more sensitive to SEB.

Keyword: Single Event Burnout (SEB), Linear Energy Transfer (LET), PiN diode, Silvaco TCAD, SRIM, Threshold Voltage of SEB (V_{SEB}).

Introduction

Modern Space technology has developed during the last decades and the power demand for space platforms has continuously increased. The future space platform's power should reliably work in space for more than 30 years without maintenance [1]. In 2016, NASA highlighted the high-power electric propulsion as the first priority of future space technologies. These technologies use high-power devices which should work in space environments for decades [2].

High-power semiconductor devices are essential in modern spacecraft and propulsion systems. The device's performance may be degraded under space radiation. There are charged ions with energy up to 10^{20} eV in space [3]. Interaction of electronic devices with ionizing radiation may affect their performance, leading to their failure. Reliability of these systems is very important because of the high costs of space applications. When electronic devices are exposed to radiation, they may lose their correct performance due to

cumulative or Single Event Effects (SEEs). Cumulative effects are gradual effects which take place during the whole lifetime of the electronic devices which are exposed in the radiation environment. These effects can be categorized into Total Ionizing Dose (TID) and Displacement Damage (DD). On the other hand, SEEs are stochastic events which cause the perturbation of the behavior of electronic devices or systems because of the passing of a single ionizing particle. SEE is divided into two categories of soft error and hard error. Single Event Burnout (SEB) is a destructive form of SEE (hard error) which can disrupt the power devices exposed to radiation. SEB is a widely recognized problem for space applications. It occurs in the high-voltage devices when they are in OFF-state. SEB was first observed in power MOSFETs in 1986 [4]. But, after that it was reported that power diodes may also experience this phenomenon due to heavy ion strikes [5]. In recent years, many investigations conducted to understand the SEB mechanisms and also hardening approach in different power devices to reduce the vulnerability of these devices against radiation [6-10].

The investigations showed that as the applied voltage of electronic devices increases, the probability of failure and malfunctions due to SEB are increasing due to the interactions with galactic charged particles in space [11,12]. The key parameter of the SEB sensitivity of the device is the threshold voltage (V_{SEB}), which related to the ability of the device to resist against SEB [13]. Scheick et al. point that the V_{SEB} may be much lower than the breakdown voltage (V_{BD}) of the device and it could be different under irradiation of different ions [14]. According to experimental results of Martinez et al. for p-GaN gate HEMT, V_{SEB} probably would have been lower for heavier ions [15].

Obtaining SEB data test for semiconductor devices is an expensive, challenging and time-consuming task, because of the destructive nature of the test. But simulations tools provide an opportunity to investigate the behavior of the device due to irradiation. Silvaco TCAD is one of these tools which is based on the finite-element methods for solving the equations.

In this paper, simulations performed using Silvaco TCAD to understand the electrical properties of a PiN diode during irradiation. PiN diode is considered because of the presence of P-i-N structure in all high voltage semiconductor devices. To this perpose, the sensitive injection position and the V_{SEB} of each ion were conducted and then, the correlation between different values of LET and V_{SEB} was studied.

Materials and methods

The PiN diode with the voltage breakdown (V_{BD}) of 3.3 kV is adopted in this work. Simulations using Victory module of Silvaco TCAD tool were performed to study the device behavior under irradiation of different ions. This tool is based on the finite-element methods and solves the Poisson's and carrier continuity partial differential equations for the device. The key models used in the simulation, include the SRH[1] recombination model, the Auger recombination model, the impact ionization model and the electric-field dependent model. Doping levels and dimensions which are used in the PiN diode simulations are given in Table 1. As the particle passes through the material, it deposits part or all of its energy through direct or indirect ionization, and a column of electron-hole pairs is created along its track. According to the Bethe-Bloch equation, the LET value firstly increases with energy and then, decreases after a peak value [16].

Table 1. The parameters used in the diode simulation

Region	Length (μm)	Doping (cm^{-3})
n^+	20	$1*10^{18}$
(i-layer) $\boldsymbol{n^-}$	300	$3*10^{13}$
P^+	20	$1*10^{18}$

To understand the relation between the V_{SEB} and LET, different ions with relatively high flux in the space were selected. The studied ions are He, O, Ne, Si, Fe, Cu, Br, Kr, and Ta. To consider the same condition for the studied ions in this study, it was supposed that all of them pass completely through the device. So, for the same range of ions, the energy and LET in the silicon were calculated using SRIM. Then, the electrical simulations were performed to obtain the most sensitive region in the device and also to observe the effect of the heavy ion strike on the PiN diode behavior. The V_{SEB} at a given LET value can be obtained by gradually increasing cathode voltage and observing its transient current. The results have been shown in the following section.

Results and discussion

The simulated 2D diode structure has been shown in Fig. 1. After the ion strikes the device, some electron-hole pairs will be generated. Because of the electric field, the strike-induced electron-hole pairs

[1] Shockley-Read-Hall

separate. Electrons flow to the cathode, while holes flow to the anode. The current density of electron and holes around cathode and anode after incidence into the PiN diode is shown in Fig. 2 (a, b).

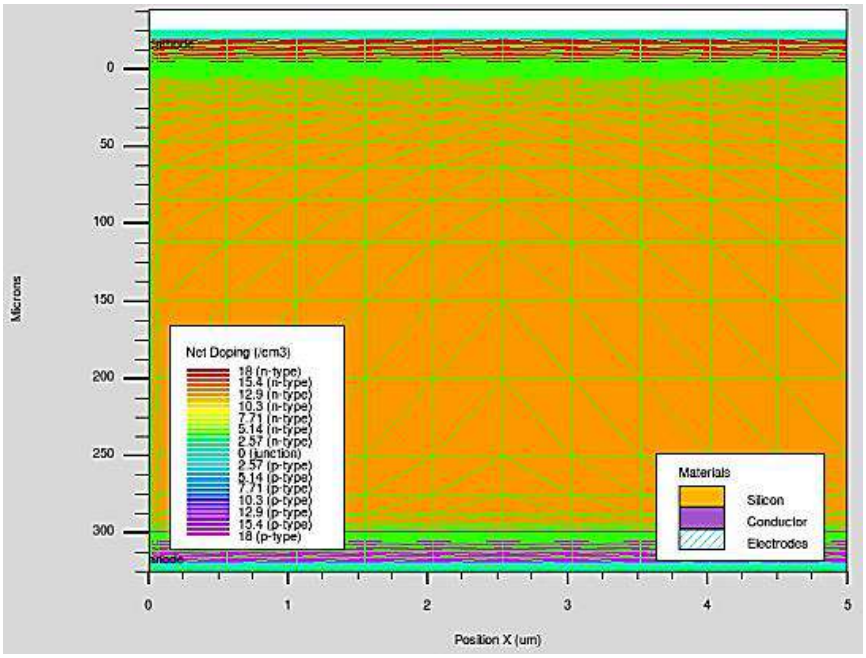

Fig. 1. The simulated structure of PiN diode using Sivaco TCAD tool.

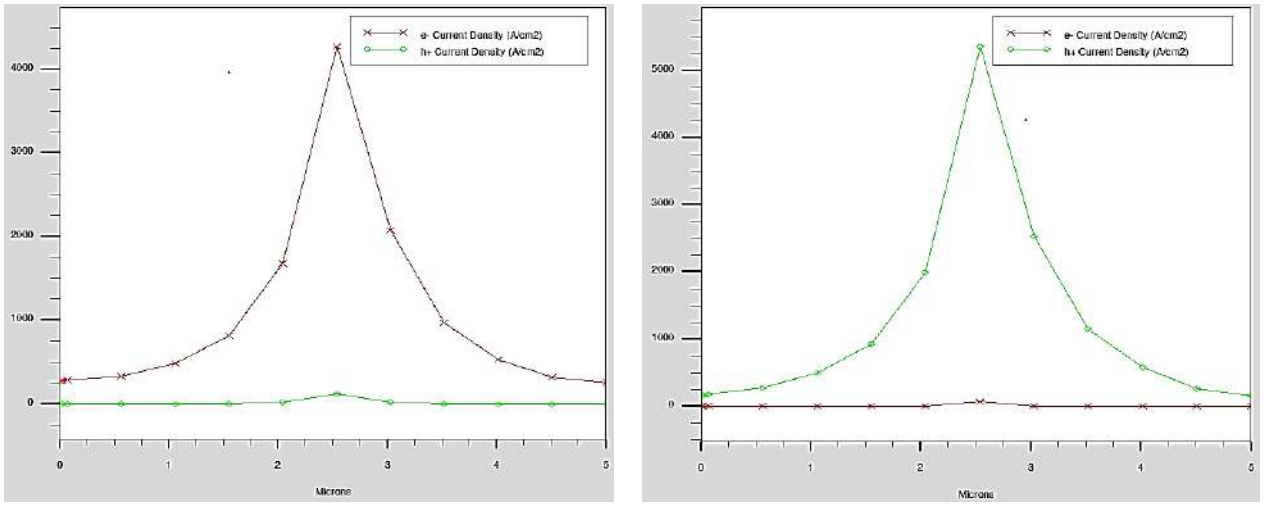

(a) (b)

Fig. 2. The current density of the generated electron and holes around the (a) cathode and (b) anode after ion strike. The strike location is in x=2.5 µm.

To investigate the most sensitive region, the ion with different values of LET was struck into the different locations in the PiN diode. The most sensitive region is defined by the minimum LET value which is triggering SEB. Fig. 3, shows the minimum LET which leads to SEB in the device versus position. The

results indicate that the most sensitive region is in the middle of the device, where the device is most likely to burnout when the ion with lower LET strikes on it.

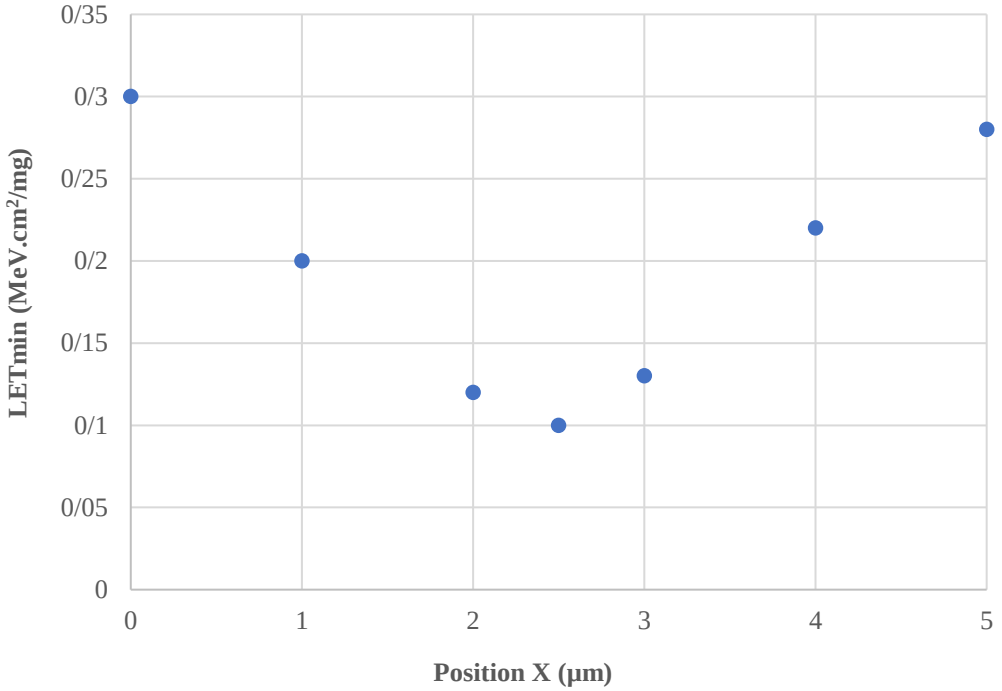

Fig. 3. The sensitivity of different positions in the PiN diode.

The transient behavior of the cathode current in the device after ion strike has been shown in Fig. 4. This figure is due to the ion strike with two values of LET=13.6 MeV.cm^2/mg and LET=27.2 MeV.cm^2/mg. according to the simulation results, the current pulse after ion strike for LET=13.6 MeV.cm^2/mg, falls back to zero and the device recovers. So, no SEB has occurred. But for LET=27.2 MeV.cm^2/mg, as can be observed, the current increases enormously and in this case the device burnout. Occurrence of SEB is due to the presence of a strong electric field after the particle strike and the multiplication of ion-generated carriers.

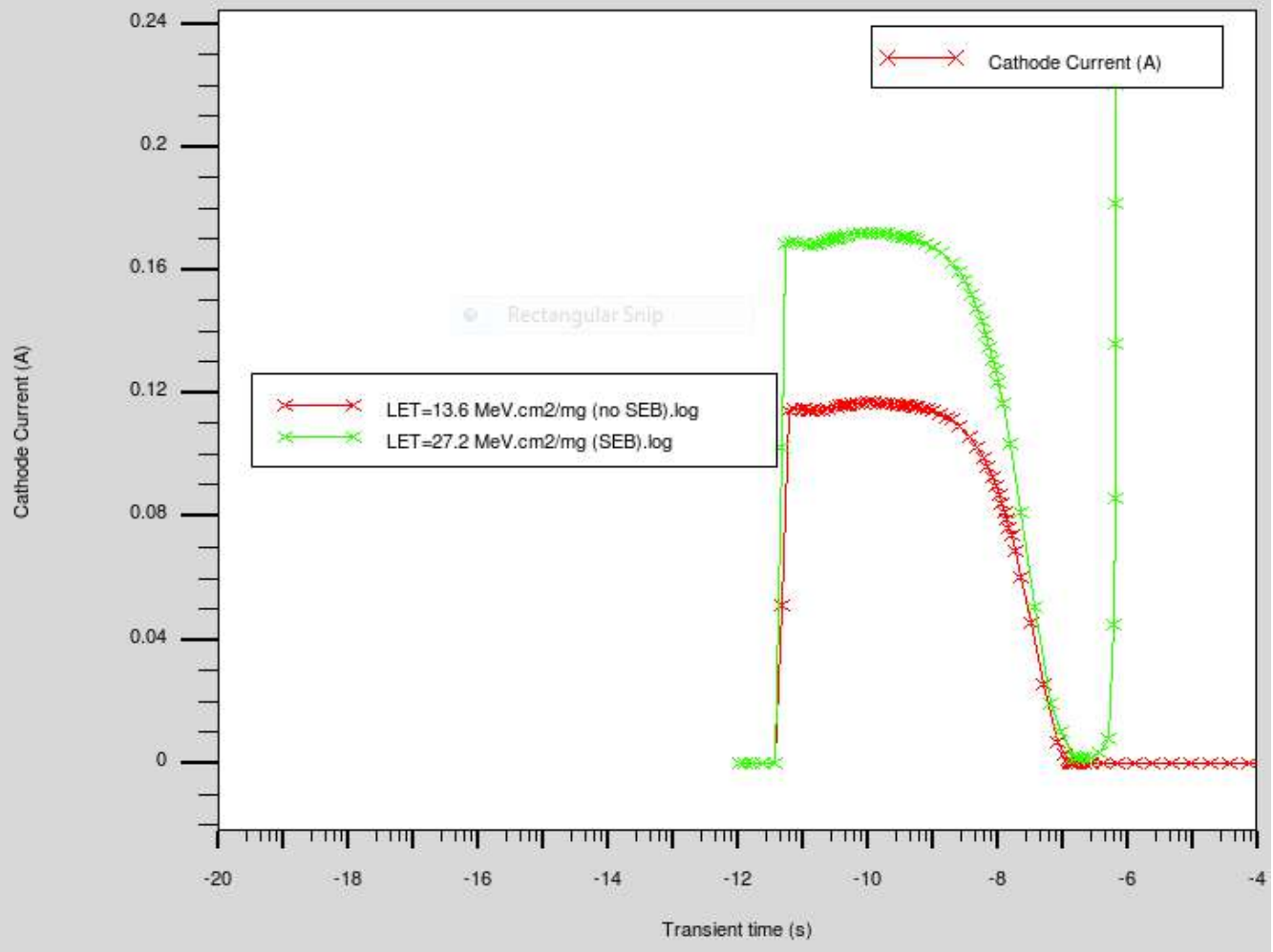

Fig. 4. Cathode transient current as a result of ion strike with two values of LET. LET= 13.6 MeV.cm^2/mg and LET=27.2 MeV.cm^2/mg.

In order to investigate the correlation between V_{SEB} and LET, the transient current for different biases less than the breakdown voltage has been simulated by irradiation of the ions in the middle of the device as the most sensitive region. The results have been shown in Table 2, which indicate that the V_{SEB} is different under irradiation of different values of LET. As can be observed in the table 2, the V_{SEB} of He, Cu, and Ta ions obtained 3200 V, 2500 V, and 2100 V respectively. The results indicate that the V_{SEB} decreases with the increase of LET value. This was predictable, because of the more energy deposition in the device and more carrier generation due to the higher values of LET, more multiplication occurs.

Therefore, the ion with higher LET value possesses lower V_{SEB}. It means that the sensitivity of the device to the occurrence of SEB increases when the ions with higher LET strikes on it. The similar result has been recently obtained for GaN HEMT power devices [13].

Ion	Energy	LET in Silicon (MeV.cm^2/mg)	V_{SEB} (V)
Ta	4.7 GeV	58	2100
Kr	2 GeV	19.5	2450
Br	1.8 GeV	18.7	2480
Cu	1.4 GeV	13.6	2500
Fe	1.2 GeV	11.4	2600
Si	500 MeV	4.4	2800
Ne	300 MeV	2.5	3000
O	250 MeV	1.8	3100
He	25 MeV	0.19	3200

Table 2. Relationship of V_{SEB} and LET value of different ions.

Conclusion

In this work, a simulation study on the SEB induced in a PiN diode has been conducted to investigate the impact of LET value on the SEB sensitivity of the device. In order to understand the correlation between the ion's LET and threshold voltage of SEB (V_{SEB}), firstly, SRIM has been adopted to determine the LET of the studied ions in the silicon. Then, the transient behavior of the device has been studied using Silvaco TCAD tool. The results demonstrate that the PiN diode is most sensitive to the ions injected in the middle of the device. SEB is caused by avalanche multiplication of ion-generated carriers. Furthermore, it is found that the V_{SEB} decreases from 3200 V for He to 2100 V for Ta, under irradiation of ions with higher values of LET. Therefore, ions with higher values of LET can burnout the device in lower voltage and make it more sensitive to SEB.

References

[1] Gollapudi, Srikanth, and Ichiro Omura. "Altitude dependent failure rate calculation for high power semiconductor devices in aviation electronics." Japanese Journal of Applied Physics 60, no. SB (2021): SBBD19.

[2] Khurelbaatar, Luvsanbat, Turtogtokh Tumenjargal, Begzsuren Tumendemberel, Otgonbaatar Myagmar, Srikanth Gollapudi, Ichiro Omura, and Erdenebaatar Dashdondog. "Space radiation induced failure rate calculation method using energy deposition probability function for high-voltage semiconductor device." Materials Today Communications 35 (2023): 105499.

[3] W. Kaindl, H.-J. Schulze, G. Wachutka, G. Soelkner, Reliability of power electronics devices against cosmic radiation-induced failure, Microelectron. Reliab. 44 (9–11) (2004) 1399–1406.

[4] A.E.Waskiewicz, J.W.Groninger, V.H.Strahan, D.M.Long, IEEE Trans. Electron Devices 33, 1710 (1986).

[5] H. Kabza et al., "Cosmic radiation as a cause for power device failure and possible countermeasures". in Proc. 6th Int. Symp. Power Semiconductor Devices ICs (ISPSD), Davos, Switzerland, 1994, pp. 9–12

[6] W. Kaindl, H.-J. Schulze, G. Wachutka, G. Soelkner, "Reliability of power electronics devices against cosmic radiation-induced failure", Microelectron. Reliab. 44 (9–11) (2004) 1399–1406.

[7] F. Xin-Xing, Y. Wang, X. Luo, M-T. Bao, C-H. Yu, and X-Ji. Li, "Research of single-event burnout and hardened GaN MISFET with embedded PN junction." Microelectronics Reliability 110 (2020): 113699.

[8] L. Jiang, J. Liu, X. Tian, H. Chen, Y. Tang, Y. Bai, Ch. Li, and X. Liu. "Impact of varied buffer layer designs on single-event response of 1.2-kV SiC power MOSFETs." IEEE Transactions on Electron Devices 67, no. 9 (2020): 3698-3704.

[9] M. Pocaterra, and C. Mauro. "Single event burnout failures caused in silicon carbide power devices by alpha particles emitted from radionuclides." e-Prime-Advances in Electrical Engineering, Electronics and Energy (2023): 100203.

[10] Srivastava, Ajay K., Nitu Saini, Puspita Chatterjee, Thresia Michael, and Shilpa Patyal. "TCAD simulation of the mixed irradiated n-MCz Si detector: Impact on space charges, electric field distribution." Nuclear Instruments and Methods in Physics Research Section A: Accelerators, Spectrometers, Detectors and Associated Equipment 1049 (2023): 168031.

[11] Mukund R. Patel, Spacecraft Power Systems, CRC Press, New York, 2004.

[12] Clay S. Mayberry, Dave S. Glaister Kitt, C. Reinhart, Space power technology in power management and distribution electronics, J. Spacecr. Rockets (1998) 837–844.

[13] Wu, Wangran, Wenting Xu, Kai Qu, Guangan Yang, Zuoxu Yu, and Weifeng Sun. "Comprehensive investigation on different ions of geostationary orbit induced single event burnout in GaN HEMT power devices." Microelectronics Reliability 149 (2023): 115187.

[14] L. Scheick, Determination of single-event effect application requirements for enhancement mode gallium nitride HEMTs for use in power distribution circuits, IEEE Trans. Nucl. Sci. 61 (6) (2014) 2881–2888, https://doi.org/10.1109/ TNS.2014.2365545.

[15] M.J. Martinez, M.P. King, A.G. Baca, A.A. Allerman, A.A. Armstrong, B.A. Klein, E. A. Douglas, R.J. Kaplar, S.E. Swanson, Radiation response of AlGaN-channel HEMTs, IEEE Trans. Nucl. Sci. 66 (1) (2019) 344–351, https://doi.org/10.1109/ TNS.2018.2885526. Jan.

[16] D.R. Grimes, D.R. Warren, M. Partridge, An approximate analytical solution of the Bethe equation for charged particles in the radiotherapeutic energy range, Sci. Rep. 7 (2017) 9781, https://doi.org/10.1038/s41598-017-10554-0. Aug.

Evaluation the impact of detector crystal on SPECT performance (Paper ID : 1233)

Pouya abasi javdan*[1], Mohammad Babaei Ghane[1], Alireza sadremomtaz[1]

[1]*University of Guilan, Rasht, Iran*

Abstract

The Sensitivity of SPECT relies on both Collimator and Detector Crystals. To design an optimal Scanner, a comprehensive study of the impact of both is crucial. Therefore, the aim of this study is to investigate the impact of CZT, NaI, LuAP, and BGO on Sensitivity and Scatter Fraction. To achieve this objective, a whole-body SPECT Scanner was simulated and validated using the GATE Monte Carlo toolkit. Sensitivity and Scatter Fraction were evaluated based on the NEMA NU-1 2018 standard. The results indicate that LuAP and BGO exhibit approximately 17.5% and 11.2% higher Sensitivity, respectively, compared to CZT Crystal. Additionally, these Crystals show an increase of 18.6% and 35.5% in Scattering Fraction compared to CZT. Furthermore, we concluded that Nal(TI) Crystal performed worse both in terms of Sensitivity and Scattering Fraction compared to the utilized Crystals. In conclusion, based on the results, LuAP and BGO demonstrate better performance in this energy range.

Keywords: SPECT – Monte Carlo simulation – NEMA – Sensitivity

INTRODUCTION

Single photon emission computed tomography (SPECT) is an effect metabolic and functional imaging technique, and is increasingly used as a quantitative imaging tool in recent years [1]. SPECT have a wide variety of useful diagnostic applications such as bone scanning for metabolic bone diseases, myocardial perfusion for heart diseases, and neurotransmitter brain imaging for brain diseases, etc. They are also widely used in pre-clinical for drug and disease researches [1,2]. Most of the commercial SPECT systems are built with cost-effective, large size monolithic Nal(TI) scintillators by an array of large conventional PMTs using the well-known Anger logic principle [3]. This common design is inexpensive to manufacture, and robust as using few output electronica channels. However, there are some fundamental limitations

such as relatively long image acquisition time due to the low Sensitivity and count rate limited by signal pile up, and poor intrinsic spatial resolution due to the scintillation

photons spread in the large size scintillator [4]. In the last decades, many researchers have been attempting to develop compact SPECT detectors using different scintillators with high Sensitivity, good energy resolution as well as high spatial resolution [5]. Currently, the most widely used scintillation Crystals for SPECT include thallium-doped sodium iodide (Nal(TI)), and (CZT) telluride zinc cadmium [6]. In this paper, we simulated and validated a whole-body SPECT Scanner using the GATE Monte Carlo toolbox and investigated the effect of CZT, NaI, LuAP, and BGO Crystals on the Sensitivity and Scattering Fraction of the Scanner. We adhered to the NEMA NU1-2018 standard throughout our study.

Materials and Method

System Description and GATE Simulation

To achieve the mentioned goal a whole-body SPECT Scanner was simulated and validated using the GATE Monte Carlo (v.9.3) toolkit (Fig.1-a). The simulated Scanner Detector array consists of 32448 Crystals and 8 heads. Each head has a Detector area of 179.2 mm × 128 mm with 1.6 mm × 1.6 mm pixels with a thickness of 5 mm. The Crystals have an active area of 1833 square mm. The Collimator is made of Tungsten-Alloy (W 91%, Ni 6%, Pb 3%) with a thickness of 25 mm and has a rectangular array. The diameter of the holes is 1.28 mm and the thickness of the septa is 0.32 mm. The Collimator provides good Sensitivity both for energies above 140 keV and for low energies of 170 keV and also has a good Scattering Fraction (Fig.1-b). The supplementary information of the simulated Scanner is provided in Table 1. The key system performance characteristics including Sensitivity and Scatter Fraction have been evaluated according to the NEMA NU 1-2018 specifications. As mentioned, in this study, 4 Crystals of CZT, Nal(TI), LuAP and BGO were Simulated to evaluate the Sensitivity and Scattering Fraction, and the properties of each of the selected candidate materials are shown in Table 2[7].

Table 1. Simulated Scanner specifications

Parameter		Design
Detector	Number of detector heads	8
Detector heads radial position		185 mm for brain 240 mm for torso (this work)
Detector thickness		5 mm
Detector head size		179.2 mm × 128 mm
Full detector area		1833 cm^2
Pixel pitch		1.6 mm
	Number of pixels per head	112 × 80
Collimator	Collimator hole shape	Rectangular
Collimator material		Tungsten-Alloy W 91%, Ni 6%, Pb 3%
Collimator density		17.3g/cm^3
Collimator length		25mm
Collimator hole size		1.28 mm
Septal thickness		0.32 mm

Table 2. Comparison of CZT, Nal(TI), LuAP, and BGO characteristics in nuclear medicine.

Crystal	Nal(TI)	CZT	LuAP	BGO
Effective Atomic Number	56	50	65	74
Density (g/cm^3)	3.67	6.2	8.34	7.13
Photon Yield (Ph/MeV)	38000	----	10000 - 12000	8000 - 10000

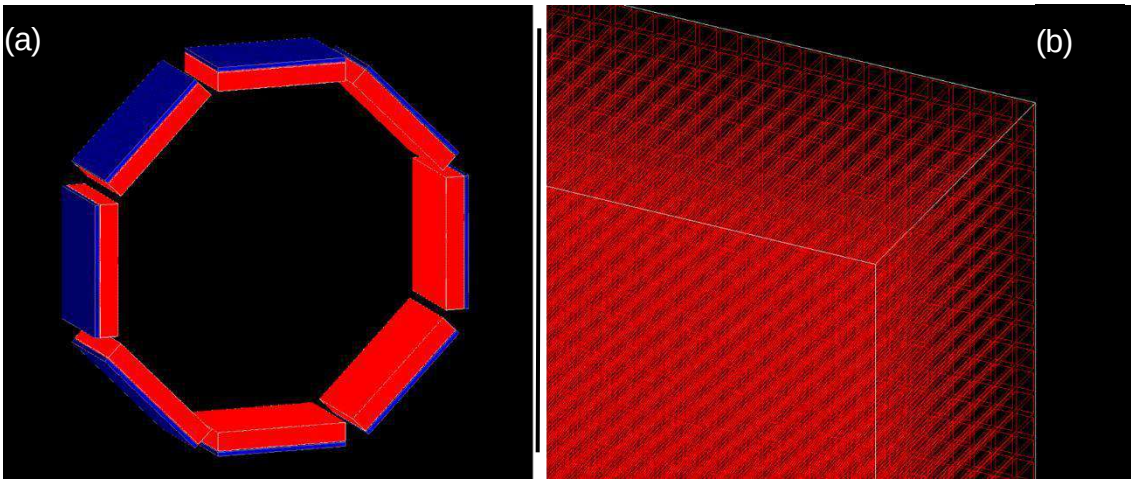

Fig. 1. (a) System geometry as simulated in Geant4 application for tomographic emission (GATE). (b) close-up of single detector head.

Sensitivity Calculation

The volume Sensitivity measurement gives the number of events detected by the SPECT system per second per unit of concentration of radionuclide uniformly distributed [8]. The result depends, among other things, on the efficiency of Collimator, the energy window setting, the energy resolution of the detector, the Crystal thickness, and the radionuclide [2]. We defined the total Sensitivity, *S*, of our system, and the Sensitivity to selected counts, *S′*, as:

$$S = \frac{C}{T \times A} \qquad \text{Eq. 1}$$

$$S' = \frac{C'}{T \times A} \qquad \text{Eq. 2}$$

where C is the number of detected counts independent of the energy, C′ is the number of selected counts in the photopeak region, T is the time in seconds, and A is the total activity of the subject [4]. The Sensitivity for a Point Source placed in the air at the center of Scanner has been calculated for two radionuclides ^{99m}Tc and ^{177}Lu.

Scatter Fraction

Scatter Fraction is a metric commonly used in nuclear medicine imaging to quantify the level of Scattered radiation relative to the total detected radiation. It represents the ratio of Scattered counts to the total counts detected by the imaging system. A lower Scatter Fraction indicates better image quality, as it suggests less interference from Scattered photons and thus improved contrast and spatial resolution in the reconstructed images [9]. The Scatter Fraction, k, can be written in terms of broad-beam (including Scatter) and narrow-beam (excluding scatter) counts as [10]:

$$K = \frac{C_{broad} - C_{narrow}}{C_{broad}} \qquad \text{Eq. 3}$$

Results

Sensitiviy

In the initial phase, the Sensitivity of the Simulation system was confirmed with the study by Yunsuk Hoh and colleagues, showing a relative difference of less than 1% [6]. The Sensitivities, as defined in Eq 1 and Eq 2, were calculated by the centered Point Source for ^{99m}Tc and ^{177}Lu (Fig 2 (. Sensitivity is lower for ^{177}Lu due to the lower branching ratio and the higher energy of the gamma-rays, which have a lower photoelectric cross-section [5]. In addition, it has been observed that the Sensitivities of BGO and LuAP Crystals are superior to those of NaI and CZT Crystals. This can be attributed to several factors. Firstly, BGO and LuAP Crystals exhibit higher stopping power for gamma-rays compared to NaI and CZT Crystals [2]. Secondly, they have better energy resolution characteristics, allowing for more precise determination of gamma-ray energies [2,11]. Thirdly, their decay time properties are more

favorable, resulting in reduced detector dead time and improved temporal resolution [11]. Overall, these factors contribute to enhanced Sensitivity and performance of BGO and LuAP Crystals in gamma- ray detection applications [12].

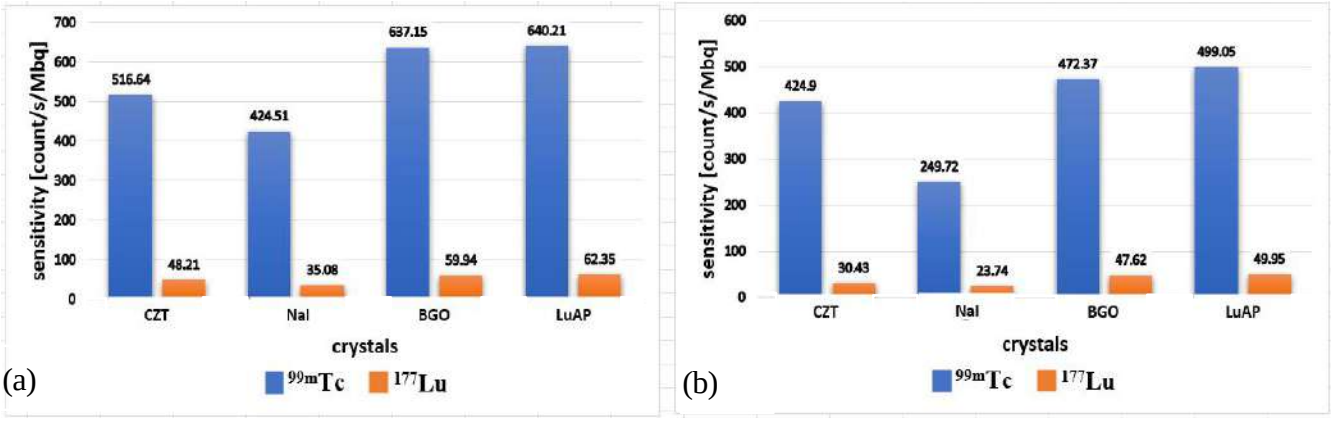

Fig. 2. (a) Sensitivities obtained without the presence of a Collimator. (b) Sensitivities obtained in the presence of a Collimator.

Scattering Fraction

The Scattering Fraction was calculated for 4 Crystals of CZT, NaI, LuAP and BGO with ^{99m}Tc and the results are reported in Table 3. It can be seen that CZT has a lower Scattering Fraction than other Crystals. This can be attributed to its higher atomic number and density, which result in increased absorption of Scattered photons within the Crystal volume, thereby reducing their contribution to the detected signal [13].

Table 3. Scatter Fraction results for CZT, NaI(TI), LuAP and BGO Crystals.

Crystals	NaI(TI)	CZT	LuAP	BGO
Scattering Fraction	41%	17.7%	21%	24%
Uncertainty	0.8%	0.9%	0.5%	0.6%

Conclusion

In this paper, a whole-body SPECT imaging system equipped with specialized tungsten Collimators is Simulated. The study assesses its efficacy in whole body imaging employing ^{99m}Tc and ^{177}Lu radionuclides. It is noteworthy that ^{99m}Tc demonstrates better performance compared to ^{177}Lu in the Simulated Scanner. The lower performance of ^{177}Lu is attributed to its lower branching ratio and higher energy gamma rays, which have a lower photoelectric cross section. Additionally, the findings indicate that LuAP and BGO Crystals exhibit approximately 17.5% and 11.2% higher Sensitivities compared to CZT Crystal, respectively. Several factors contribute to these conclusions. Firstly, the intrinsic properties of LuAP and BGO Crystals, such as high light yield and fast decay time, make them efficient in absorbing and converting incident radiation into detectable signals. This characteristic is particularly crucial in scenarios requiring rapid and accurate detection. Furthermore, the excellent energy resolution demonstrated by LuAP and BGO Crystals enhances their Sensitivity and enables precise detection of various radiation energies, essential in applications where distinguishing between radiation types or identifying specific isotopes is necessary. Additionally, the stability and robustness of LuAP and BGO Crystals against temperature variations and environmental factors contribute to their superior Sensitivity compared to CZT and NaI Crystals. This resilience ensures consistent performance across diverse operating conditions and enhances their reliability in practical deployment. Moreover, advancements in Crystal growth techniques and manufacturing processes have enabled the production of large size and high quality LuAP and BGO Crystals, expanding their applicability in various radiation detection systems while maintaining their Sensitivity advantages. Finally, the Scatter Fraction of LuAP and BGO increased by 18.6% and 35.5% compared to CZT due to their high effective atomic number andhighdensity.

References

Madsen, M. T. (2007). Recent advances in SPECT imaging. Journal of Nuclear Medicine, 48(4), 661- 673.

Wu, J., & Liu, C. (2019). Recent advances in cardiac SPECT instrumentation and imaging methods. Physics in Medicine & Biology, 64(6), 06TR01.

Yang, J., Shi, L., Wang, R., Miller, E. J., Sinusas, A. J., Liu, C., ... & Seo, Y. (2021). Direct attenuation correction using deep learning for cardiac SPECT: a feasibility study. Journal of Nuclear Medicine, 62(11), 1645-1652.

Van den Wyngaert, T., Elvas, F., De Schepper, S., Kennedy, J. A., & Israel, O. (2020). SPECT/CT: standing on the shoulders of giants, it is time to reach for the sky!. Journal of Nuclear Medicine, 61(9), 1284-1291.

Weng, F., Bagchi, S., Zan, Y., Huang, Q., & Seo, Y. (2016). An energy-optimized collimator design for a CZT-based SPECT camera. Nuclear Instruments and Methods in Physics Research Section A: Accelerators, Spectrometers, Detectors and Associated Equipment, 806, 330-339.

Huh, Y., Caravaca, J., Kim, J., Cui, Y., Huang, Q., Gullberg, G., & Seo, Y. (2023). Simulation studies of a full-ring, CZT SPECT system for whole-body imaging of 99mTc and 177Lu. Medical physics, 50(6), 3726-3737.

Rudenkov, A., Kisel, V., Yasukevich, A., Hovhannesyan, K., Petrosyan, A., & Kuleshov, N. (2021, June). Picosecond and Femtosecond Mode-Locked Lasers Based on Yb: LuAP Crystal. In 2021 Conference on Lasers and Electro-Optics Europe & European Quantum Electronics Conference (CLEO/Europe-EQEC) (pp. 1-1). IEEE.

Meikle, S. R., Hutton, B. F., & Bailey, D. L. (1994). A transmission-dependent method for scatter correction in SPECT. Journal of Nuclear Medicine, 35(2), 360-367.

Floyd Jr, C. E., Baker, J. A., Lo, J. Y., & Ravin, C. E. (1992). Measurement of scatter fractions in clinical bedside radiography. Radiology, 183(3), 857-861.

Myronakis, M. E., & Darambara, D. G. (2011). Monte Carlo investigation of charge-transport effects on energy resolution and detection efficiency of pixelated CZT detectors for SPECT/PET applications. Medical physics, 38(1), 455-467.

Holstensson, M., Erlandsson, K., Poludniowski, G., Ben-Haim, S., & Hutton, B. F. (2015). Model- based correction for scatter and tailing effects in simultaneous 99mTc and 123I imaging for a CdZnTe cardiac SPECT camera. Physics in Medicine & Biology, 60(8), 3045.

Weber, S., Christ, D., Kurzeja, M., Engels, R., Kemmerling, G., & Halling, H. (2003). Comparison of LuYAP, LSO, and BGO as scintillators for high resolution PET detectors. IEEE Transactions on Nuclear Science, 50(5), 1370-1372..

Kobayashi, H., Ryu, Y., Baldocchi, D. D., Welles, J. M., & Norman, J. M. (2013). On the correct estimation of gap fraction: How to remove scattered radiation in gap fraction measurements?. Agricultural and Forest Meteorology, 174, 170-183.

ICNST 2024 International Conference on Nuclear Science and Technology
6- 8 MAY 2024 | Isfahan, Iran

Dosimetry Investigation of a Novel Yttrium-90 Disc Brachytherapy Source in the Eye Phantom Using GATE Monte Carlo Code (Paper ID : 1238)

Fardi Z. and Taherparvar P.*

Department of Physics, University of Guilan, Rasht, Guilan, Iran

Abstract

In this study, dose distribution was calculated by Monte Carlo simulation for a novel, high dose rate beta-emitting disc source (Liberty Vision Yttrium-90 Disc, or LV Y-90 Disc) during treatment of uveal melanoma. Hereby, a LV ^{90}Y disc with 6 mm diameter simulated by GATE Monte Carlo simulation code. An eye phantom includes different substructures sclera, choroid, retina, cornea, vitreous, optic nerve, lens, cornea, anterior chamber, and a tumor with thickness of 1.6 mm, width of 4.1 mm and a base diameter (Length) of 2.9 mm, was modeled using the GATE code. The ICRU-72 standard beta spectrum of the ^{90}Y source was used, and for validation of this source used in this study using GATE code, the ^{90}Y source was verified as an isotropic point source centered in a water phantom. Then, the disc source central axis depth dose was calculated in the water phantom, and compared with reference experimental, and simulation results. After validating in the water phantom, the depth dose along the central axis of the disc source was also calculated in the eye phantom. Furthermore, the received dose in the eye structures was also calculated.

Keywords: Monte Carlo simulation, Uveal melanoma, Disc source, ^{90}Y source, GATE.

INTRODUCTION

Uveal melanoma is the most common primary intraocular malignancy occurring in the uveal layer of the eye, which includes the choroid, ciliary body, and iris [1]. Typically, the sources used for plaque brachytherapy are ^{106}Ru/^{106}Rh, ^{90}Sr/^{90}Y or ^{125}I (or much less often ^{103}Pd and ^{131}Cs), despite the availability of many other radioisotopes for treatment. Eye plaque brachytherapy for eye melanoma treatment with ^{106}Ru/^{106}Rh plaque is commonly used in Europe and Asia [2] and ^{90}Sr/ ^{90}Y beta emitting HDR source is utilized in England. The beta emitting applicators of ^{90}Sr/^{90}Y sources contains two radionuclides in secular equilibrium, which was permanently attached at the end of the plaque. Recently, some studies have been conducted on the Yttrium-90 (^{90}Y) beta emitting brachytherapy source, which has several distinctive features including singular, discrete, disc shaped source, and capable of being assembled into clinical applicators used in eye melanoma brachytherapy. Beta radiation from the ^{90}Y source is widely used for

treatment of cholangio carcinoma, colon metastases, renal cell carcinoma, and metastatic choroidal melanoma [3]. This beta emitter high dose-rate ^{90}Y source can deliver up to 800 Gy/h at 1 mm from the surface of the source in water environment, which makes it possible to reduce the time of treatment to a few minutes [4]. First clinical implementation of ^{90}Y disc brachytherapy were performed by Finger et al. in 2023. They showed ^{90}Y brachytherapy source, as high-dose rate (HDR) source, could be utilized by medical physicists, radiation oncologists, and ophthalmic surgeons [5]. In 2023 Chang et al. simulated a ^{90}Y disc source with 6 mm in diameter. They calculated the dose distribution using GATE/GEANT4 Monte Carlo simulations for episcleral brachytherapy and provide a lookup table for treatment planning. The results of Monte Carlo simulation were compared with the experimental results using Gafchromic EBT-3 film [4]. In this study, GATE/GEANT4 Monte Carlo code was used to simulate a new ^{90}Y disc source with 6 mm in diameter. For validation purposes, the simulated dose distribution results of the disc source were compared with the simulation and experimental results of the Chang et al. [4]. Then, in order to accurately investigate dosimetry calculations of eye plaques and dose deposition into the tumor and internal structures of the eye, a human eye phantom was designed including a choroid melanoma with the thickness of 1.6 mm, width of 4.1 and the length of 2.9 mm, by GATE Monte Carlo code. The designed eye phantom also included sclera, choroid, retina, vitreous, lens, anterior chamber, cornea, and optic nerve. From this, we calculated the percentage of the received dose by the eye components relative to the tumor due to the ^{90}Y disc source attached to the human eye phantom.

Material and Methods

The ^{90}Y is a beta-emitting radioisotope which produced by neutron activation of ^{89}Y and decays by beta emission with a maximum energy of E = 2.28 MeV, mean energy of electrons 0.933 MeV and a half-life of $T_{1/2}$ = 64.1 h. The ^{90}Y beta spectrum used in the simulations was taken from the ICRU report 72 [6]. The energy spectrum of ^{90}Y is shown in Figure 1.

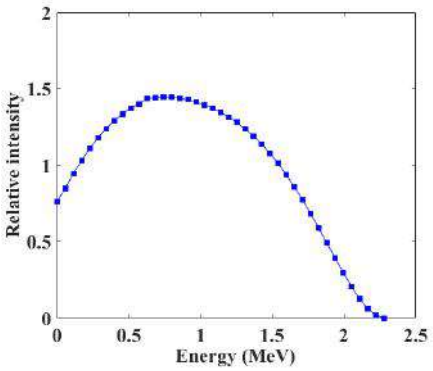

Fig. 1. The beta energy spectra of ^{90}Y used in our simulation [4].

The new ^{90}Y disc source

Currently, the LV ^{90}Y disc source for episcleral brachytherapy is available in 6 mm diameter, and the sources with the 8 mm and 10 mm diameter coming soon [4]. This new ^{90}Y disc with various diameters (6 mm, 8 mm, and 10 mm) are shown in Figure 2-a. The detailed structure of the 6 mm LV ^{90}Y disc source illustrates in Figure 2-b. This source consists of a titanium cylinder with 6 mm radius and 1 mm thickness. The disc internal section was made of a cylinder with 5.5 mm diameter and 0.5 mm length which consists of two parts ^{90}Y source and air. Top and side view of 6 mm disc source simulated by GATE Monte Carlo simulation code is shown in Figure 2-c.

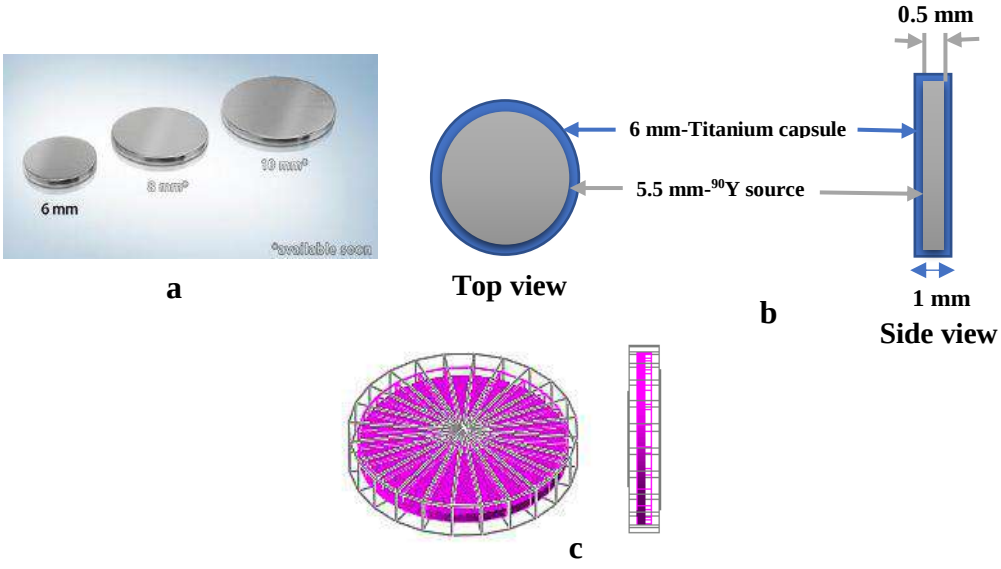

Fig. 2. (a) Demonstration of three commercially available ^{90}Y disc sources with diameters of 6 mm, 8 mm, and 10 mm. (b) Detailed structure of the disc source with 6 mm diameter (c) Top and side view of 6 mm disc source simulated by GATE Monte Carlo simulation code.

Eye Model Description

A model of adult human eye phantom consisting of sclera, choroid, retina, vitreous, lens, aqueous humor, cornea, and optic nerve has been designed in this study by GATE code. In the designed phantom, we have considered a spherical shell of 24 mm as sclera, was constructed using concentric spheres which are nearly 1 mm thickness for the choroid, retina, and vitreous. Based on the information reported in the first clinical

study of implementation of ^{90}Y disc brachytherapy [5], a choroidal melanoma has been designed with the thickness of 1.6 mm, width of 4.1, and the length of 2.9 mm, which is situated above the eye and on the inner surface of the sclera. The eye lens is defined as an ellipsoidal shape with 8 mm, and 9 mm in equatorial diameters and 2.5 mm in polar diameter, which has been placed at the posterior part of the anterior chamber. The cornea is the transparent front part of the eye and the geometric region bounded by the cornea inner wall and the anterior curved segment of the lens is known as the anterior chamber. For optic nerve geometry simulation, a cylindrical shell with diameters of 5 mm, and 6 mm, was considered. Three different views of the eye phantom designed in this study are shown in the Figure 3-a. Figure 3-b, which shows the position of the disc source on the exterior surface of the sclera in the eye model with a 1.6 mm apex height. It was placed in the lateral segment of the eyeball.

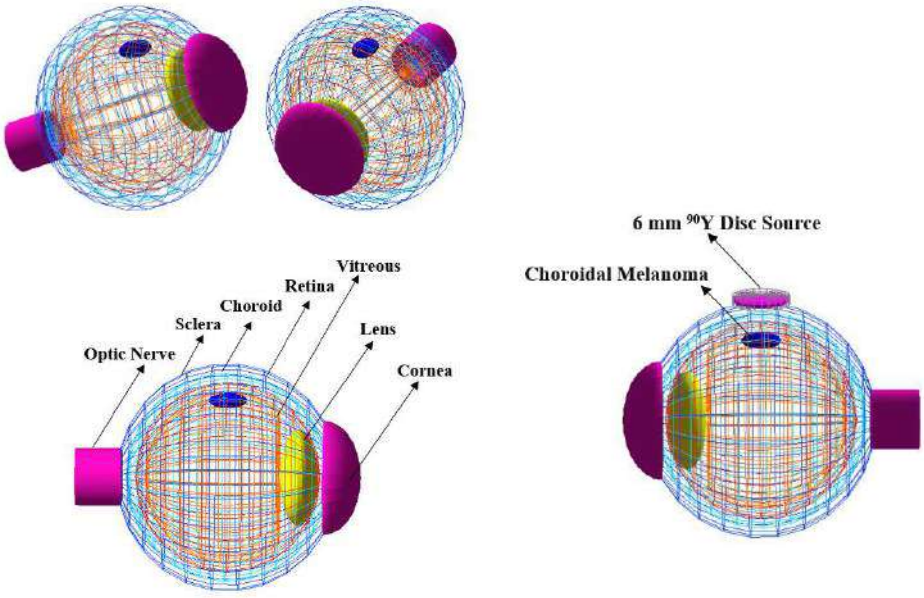

Fig. 3. (a) The simulated human eye phantom by GATE Monte Carlo code. (b) The simulated eye phantom along with the ^{90}Y disc source.

In our study the simulations were performed with GATE Monte Carlo cod version 9.2, which is based on GEANT4 version 10.7 [7-10] Monte Carlo code. The GATE standard physics List_Opt3 was used and production range cuts were set to 1 µm for photons particles, 10 µm for electrons and, 1 mm for positrons. Linear interpolated spectrum was applied to simulate continuous energy spectrum of the source. For dosimetry calculation in the eye phantom, the deposited dose was scored at the cubic voxel level with the *Dose Actor*, and associated uncertainties were calculated with the *Dose Actor Uncertainty*. In order to run simulations with GATE code, random number generator was chosen *Mersenne Twister*.

Results and discussion

Validation of the ^{90}Y source

The first step and before any meaningful simulations in our study, to specify and validate ^{90}Y energy spectrum, a ^{90}Y source was considered and simulated in the GATE code, and the resulting spectrum compare with those offered by the ICRU-72 [6]. Therefore, the ^{90}Y betta source was simulated as an isotropic point source centered in a spherical water phantom with a radius of 20 cm. the energy spectrum was scored in a file with *Root* format using *Energy Spectrum Actor* in the GATE code. For this purpose, 2×10^7 simulation histories were performed to obtain the least statistical uncertainty (< 1%). Comparison of the ^{90}Y energy spectrum in the water phantom, which is calculated by GATE code, with the data presented by ICRU-72 [6] is shown in Figure 4. There is a good agreement between our simulation results and ICRU data, with an average difference of about 0.83%. Dose distribution due to a ^{90}Y point source centered in the water phantom was calculated in the voxels with $0.25\times0.25\times0.25$ mm^3 dimensions, as a function of distance from the center of the source. The simulation results were compared with ICRU-72 [6]. As seen in the Figure 2-b, a good agreement was found between our results (normalized to *100*% at 2 mm depth) and ICRU-72 up to 8 mm.

Dosimetry calculations

To calculate the percentage depth dose of the plaque, a 20 cm × 20 cm × 20 cm cube of air was created as simulation world in GATE code. The plaque was placed in the center of the world volume and a cylindrical water phantom with 10 mm in diameter and 10 mm in height was generated in front of it. In order to record the dose at different depths to the center of the source, cubic voxels with dimensions of $0.5 \times 0.5 \times 0.5$ mm^3 was defined along the central axis of the applicator by GATE Monte Carlo code.

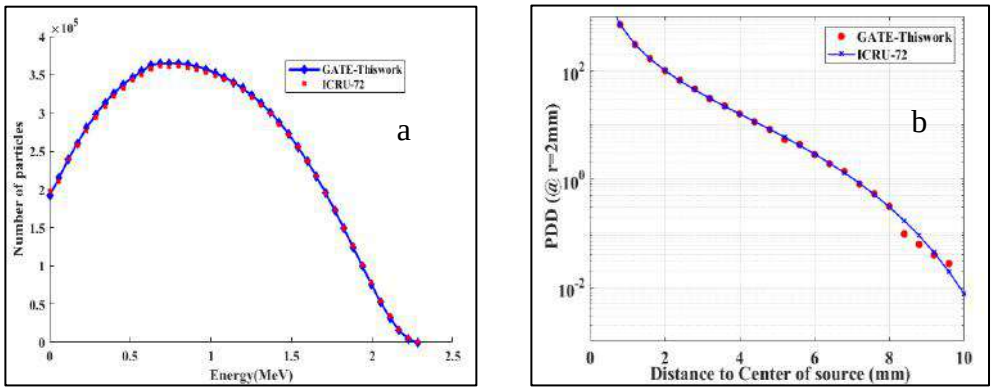

Fig. 4. (a) Comparison energy spectrum of ^{90}Y calculated by GATE code with the data presented by ICRU-72 (b) Comparison of the ^{90}Y point-source percentage depth dose as a function of depth from the source center with Table 4.3 of ICRU-72 [6].

Figure 5 shows the calculated percentage depth dose in the cylindrical water phantom compared with those calculated data by Chang et al. [4] and reported data for ^{131}Cs by Zhang et al. [11]. There is a good agreement between GATE results for relative depth dose and previously reported data by Chang et al. [4]. Table 1 shows the percentage of the received dose by the eye components such as sclera, choroid, retina, vitreous, optic nerve, cornea, anterior chamber, and lens, relative to the received dose in the tumor due to the ^{90}Y disc source attached to the eye phantom. The first eye substructure in front of the eye plaque brachytherapy is sclera which will receive the highest dose compared to other eye structures. A closer look at results shows that by receiving 100% of the dose in the tumor volume the delivered dose at the sclera will be 8.867% m.aximum dose. The lens as the most radiosensitive eye component receive just 0.008% maximum dose (dose at tumor volume). For this tumor location, the radation effect on the optic nerve, anterior chamber, and cornea was negligible, since doses to these structures were already very low. For a tumor with 1.6 mm in thickness the treatment time calculated using the dose rate from the Monte Carlo simulation, is 3.65 min considering a prescription dose of 30 Gy at tumor apex. While the ABS (**American Brachytherapy Society**) for ^{125}I brachytherapy source suggests the treatment time 3 to 7 consecutive days considering a prescription dose of 85 Gy at tumor apex [12].

a dose rate of 0.60–1.05 Gy/h delivering the total dose in 3 to 7 consecutive days. Figure 6 shows the received dose to each component of the eye. As can be seen in this Figure, the maximum dose will be received by the tumor, while other eye structures will receive less dose, which indicates the appropriate performance of the simulated Liberty Vision Yttrium-90 disc plaque.

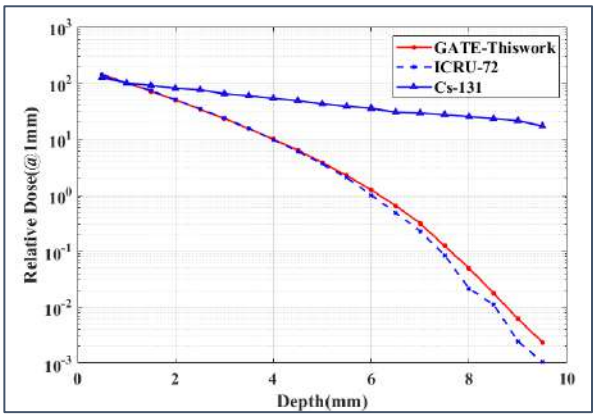

Fig. 5. The comparison of the plaque central axis depth dose between this work and the work by Chang et al. [4] and reported data for ^{131}Cs by Zhang et al. [11]

Table 1. The percentage of the received dose by each of the different tissues of the eye relative to the received dose in the tumor

Eye components	(Dose/ Tumor dose)×100
Sclera	8.867
Choroid	5.335
Retina	3.121
Vitreous	2.142
Tumor	100.000
Lens	0.008
Anterior chamber	0.004
Cornea	0.004
Optic nerve	0.007

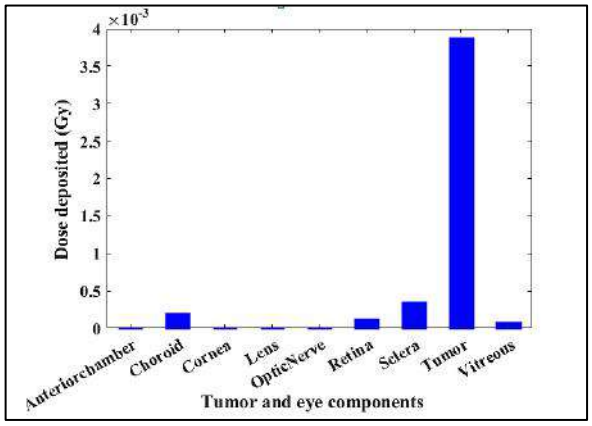

Fig. 6. The received dose in the tumor and other components of the eye due to the ^{90}Y disc source

Conclusions

In this study, using GATE Monte Carlo simulations, at first the clinical parameters of the new ^{90}Y source required for the treatment planning of eye brachytherapy have been investigated. The energy spectrum and dose distribution due to a ^{90}Y point source were calculated in water phantom and were compared with data presented in the literature. In order to increase the accuracy in dose calculation of the disc source, an eye phantom consisting of sclera, choroid, retina, vitreous, lens, aqueous humor, cornea, and optic nerve has been designed by GATE Monte Carlo code. The percentage depth dose curve along with dose deposition in different eye structures were calculated in the eye phantom. Our results show that the simulated plaque can be well used in the treatment of the eye tumors.

References

[1] S.T. Chiu-Tsao, M.A. Astrahan, P.T. Finger, D.S. Followill, A.S. Meigooni, C.S. Melhus, F. Mourtada, M.E. Napolitano, R. Nath, M.J. Rivard, Dosimetry of 125I and 103Pd COMS eye plaques for intraocular tumors: Report of Task Group 129 by the AAPM and ABS, Medical physics, 39 (2012) 6161-6184.

[2] B. Tarlan, H. Kiratli, Current treatment of choroidal melanoma, Expert Review of Ophthalmology, 7 (2012) 189-195.

[3] R. Salem, G.E. Johnson, E. Kim, A. Riaz, V. Bishay, E. Boucher, K. Fowers, R. Lewandowski, S.A. Padia, Yttrium-90 radioembolization for the treatment of solitary, unresectable HCC: the LEGACY study, Hepatology, 74 (2021) 2342-2352.

[4] X. Chang, L. Huang, J. Liu, Y. Cao, J. Chang, Monte Carlo dosimetry of a novel Yttrium-90 disc source for episcleral brachytherapy, Journal of Applied Clinical Medical Physics, 24 (2023) e14140.

[5] P.T. Finger, R. Stewart, M.J. Rivard, R.J. Beers, J. Kamen, S. Lama, K.J. Chin, K. Mohney, T.S. Welles, W.A. Sauerwein, First clinical implementation of Yttrium-90 Disc Brachytherapy after FDA clearance, Brachytherapy, 22 (2023) 416-427.

[6] W.G. Cross, C.G. Soares, S. Vynckier, K. Weaver, Dosimetry of beta rays and low-energy photons for brachytherapy with sealed sources, ICRU Report 72, DOI (2004).

[7] G.P. Cirrone, G. Cuttone, F. Di Rosa, S.E. Mazzaglia, F. Romano, A. Attili, F. Bourhaleb, G. Russo, P. Kataniemi, A. Heikkinen, Hadrontherapy: an Open Source, Geant4-based application for proton-ion

therapy studies, 2009 IEEE Nuclear Science Symposium Conference Record (NSS/MIC), IEEE, 2009, pp. 4186-4189.

[8] S. Agostinelli, J. Allison, K.a. Amako, J. Apostolakis, H. Araujo, P. Arce, M. Asai, D. Axen, S. Banerjee, G. Barrand, GEANT4—a simulation toolkit, Nuclear instruments and methods in physics research section A: Accelerators, Spectrometers, Detectors and Associated Equipment, 506 (2003) 250-303.

[9] J. Allison, K. Amako, J. Apostolakis, H. Araujo, P.A. Dubois, M. Asai, G. Barrand, R. Capra, S. Chauvie, R. Chytracek, Geant4 developments and applications, IEEE Transactions on nuclear science, 53 (2006) 270-278.

[10] J. Allison, K. Amako, J. Apostolakis, P. Arce, M. Asai, T. Aso, E. Bagli, A. Bagulya, S. Banerjee, G. Barrand, Recent developments in Geant4, Nuclear instruments and methods in physics research section A: Accelerators, Spectrometers, Detectors and Associated Equipment, 835 (2016) 186-225.

[11] H. Zhang, D. Martin, S.-T. Chiu-Tsao, A. Meigooni, B.R. Thomadsen, A comprehensive dosimetric comparison between 131Cs and 125I brachytherapy sources for COMS eye plaque implant, Brachytherapy, 9 (2010) 362-372.

[12] S. Nag, J.M. Quivey, J.D. Earle, D. Followill, J. Fontanesi, P.T. Finger, A.B. Society, The American Brachytherapy Society recommendations for brachytherapy of uveal melanomas, International Journal of Radiation Oncology* Biology* Physics, 56 (2003) 544-555.

Dosimetry of the X-Ray radiation device using TLD dosimeters and GAF Chromic films and comparison with MCNPX (Paper ID : 1242)

Tohidi T. *, Ghahremani M.R., Rahmatallahpur Sh., Salamat Bakhash M.H., Yeganeh M.

Northwest Research Complex (Bonab), Radiation Application Research School, Nuclear Science and Technology Research Institute, Tehran, Iran

Abstract

Due to the widespread use of X-ray irradiation systems in medicine, industry, and agriculture, research in design, construction and dosimetry of these devices is under development. These irradiation systems have received increased attention in recent years. In this work, using the arrangement of four X-ray tubes around the cylindrical irradiation chamber, a low dose uniformity was obtained. The thermoluminescent dosimeter (TLD) is used as a radiation dosimeter and can be used as environmental and staff personnel monitoring. The TLD measures ionizing radiation exposure by a process in which the amount of radiation collected by the dosimeter is converted in visible light when the crystal is heated. The practical dosimetry was carried out using TLD (GR 200) dosimeters in different areas of the irradiation chamber and simulated using MCNPX software code. Also, the isodoses obtained from MCNPX software code were compared using practical GAF Chromic films, and similar results were obtained.

Keywords: X-ray irradiation system, Dosimetry, TLD dosimeter, GAF Chromic film, MCNPX

INTRODUCTION

Ionizing rays, including gamma rays, X rays, and electron particles, break down molecules and change the chemical, physical, or biological properties of the materials exposed to radiation [1]. Therefore, ionizing radiation can polymerize plastics, kill pathogens and microorganisms, and damage DNA molecules, leading to applications in industry, food processing, sterilizing health products, and sterilizing insects. All ionizing radiations generally have similar effects on the irradiated material because they have similar relative biological effectiveness [2]. Recently, it has become more difficult to purchase and transport small-scale stand-alone gamma irradiation systems. For example, Nordion Canada has stopped producing its Cobalt-

60 springs. Additionally, the international transportation of radioactive isotopes has become a problem. This has

caused the Joint Division of Nuclear Techniques of FAO and International Atomic Energy Agency in Food and Agriculture to look for other types of irradiation that could be suitable for low-dose research work [3].

Based on the general requirements of research applications, such as easy localization, easy operation with minimal training, and the ability to work continuously for several hours, it seems reasonable that low-energy X-rays would be suitable for these purposes. The main mechanisms of photon-matter interaction in the X-ray energy range are photoelectric absorption, Compton scattering and coherent scattering. In these processes, the photon is either absorbed or scattered by an atom and can transfer some, none or all of its energy to the irradiated material.

There are three types of ionizing radiation generally used in radiation processing, namely gamma radiation, X radiation and electrons. All have generally similar effects on the irradiated materials (since they have similar relative biological effectiveness), and in particular on the irradiated insects. In many different fields of radiation application, precise measurement of relative or absolute dose is very important. There are different ways to do this. In any dosimetry method, it is very important to check the accuracy, correctness and uncertainty of the measurement. The use of TLD and Gafchromic film as a dosimeter requires the application and evaluation of a specific protocol in reading these dosimeters and their accurate calibration [4].

In this study the practical dosimetry was conducted using TLD (GR 200) dosimeters, and then simulated using the MCNPX software code. Additionally, the isodoses obtained from the MCNPX software code were compared to practical results from GAF Chromic films, yielding similar results.

EXPERIMENTAL

The X-ray tube device consists of four RAXON120HPB type X-ray tubes with the following specifications:

X-ray Tube Voltage: 60-120 kV, X-ray Tube Current: 0.1-2 mA in continuous mode.

The radiation chamber, made of aluminum with a diameter of 10 cm, is symmetrically positioned in the middle of the tubes and rotates with a rotating mechanism. Irradiation time is controlled by a digital timer, automatically stopping the irradiation of the sample after the specified time.

In this study, practical dosimetry was conducted using TLD tablet dosimeters (GR 200) with a diameter of 3 mm and a thickness of 1 mm. The readings of these dosimeters were performed by PartoPaish Equipment Company. Additionally, GAF Chromic films with Ashland TM specifications (EBT3) were utilized to assess dose uniformity. Calibration was conducted using data provided in [5]. The irradiation chamber was simulated using MCNPX software data (Fig.1).

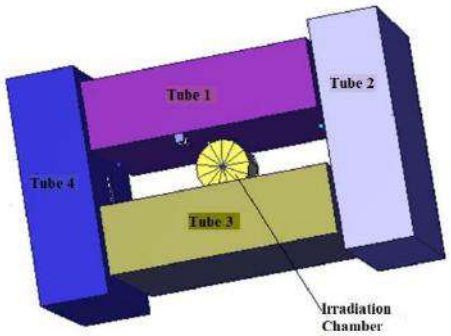

Fig. 1. Schematic placement of the chamber and tubes within the radiation system

Results and discussion

The dose inside the radiation chamber of the manufactured device was determined using two methods: practical measurement and Calculation with MCNPX software.

Practical Measurement: The dose inside the radiation chamber of the X-Ray radiation device (refer to Fig. 2) was measured using a TLD (GR-200) dosimeter. The results obtained are presented in Table 1 (in an air environment) and Table 2 (equivalent to tissue). The practical dosimetry results within the radiation chamber of the X-Ray radiation system, utilizing TLD (GR-200) dosimeters at 120 kV and 1.5 mA, irradiated for 5 minutes, were conducted in an air environment.

Table 1. The dose measurement inside the radiation chamber of the X-ray radiation system

TLD Location (NO)	kV	mA	Dose (Gy)	Dose Rate (Gy/h)	
5	120	1.5	6.63	79.56	
6	120	1.5	1.35	16.2	
7	120	1.5	8.15	97.8	
8	120	1.5	1.68	20.16	
9	120	1.5	7.63	91.56	TLD plate is inserted between 2 layer of 1 mm Al layer
10	120	1.5	0		BKG

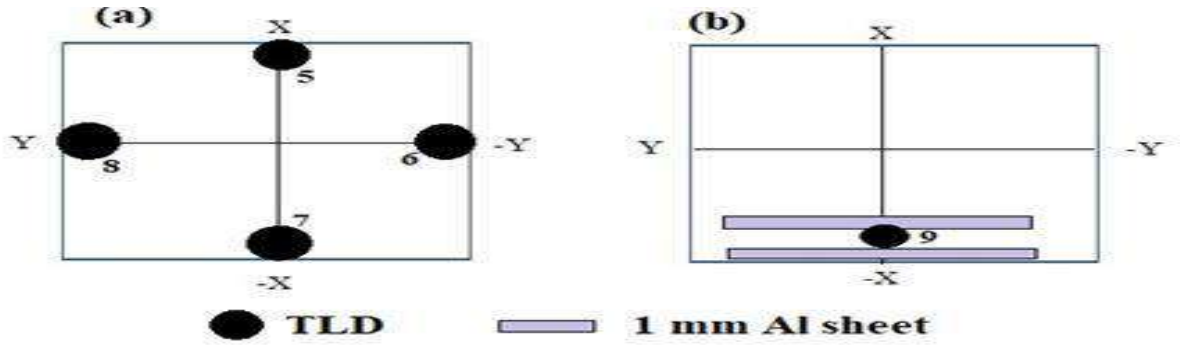

Fig. 2: Shows the placement of the dosimeters inside the radiation chamber at a voltage and current of (a) 120 kV and 1.5 mA, and (b) 120 kV and 1.5 mA. Additionally, two aluminum sheets with a thickness of 1 mm are included in the setup.

The practical results of dosimetry inside the radiation chamber of the X-ray radiation system were obtained using TLD (GR200) dosimeters. The system operated at a voltage of 100 kV and a current of 1 mA for a duration of 15 minutes. The irradiation took place in a medium equivalent to tissue with a density of 0.98. The results can be found in table 2 (refer to Fig. 3).

Table 2. The dose amount measured inside the radiation chamber of the X-ray radiation system with a voltage and current of 100 kV and 1mA.

NO	Dose(Gy)	Dose Rate (Gy/h)	TLD Location (cm)	
			X	Y
1	1.28	5.12	-4	0
2	1.49	5.96	-2	0
3	1.82	7.28	0	0
4	1.83	7.32	2	0
5	1.44	5.76	4	0
6	1.86	7.44	0	2
7	1.76	7.04	0	4
8	1.78	7.12	2	2
9	1.87	7.48	4	4
10	0		BKG	

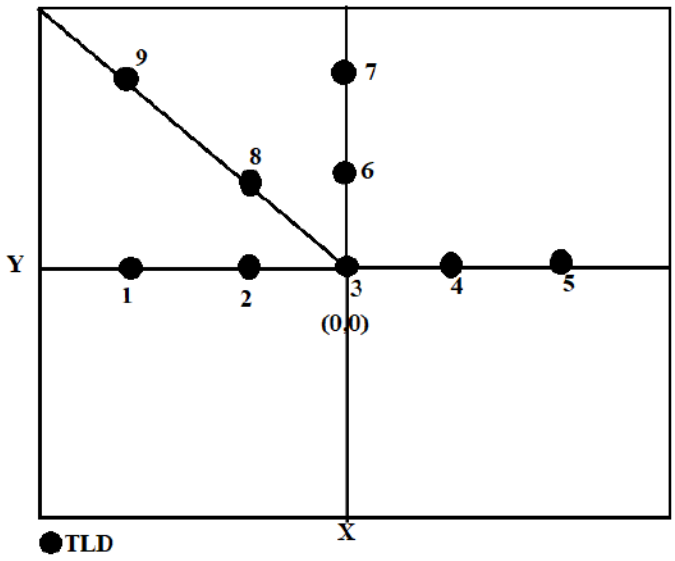

Fig. 3: Shows the placement of the dosimeters within the radiation chamber with a voltage and current of 100 kV and 1mA.

The dose amount inside the radiation chamber of the radiation device was calculated using MCNPX software for a working voltage of 120 kV in a water environment. The results are as follows:

The dose amount for each particle was 1.4E-12 ±0.0016 (rem/h)/ (photons/cm^2.s). This was determined by considering the current in mA and converting 1% of electron particles to X-rays as specified by the

manufacturer (RAXON tubes). By converting the current into electric charge and taking into account that the maximum current of each tube is 2 mA and that 4 tubes are used, we can calculate the following:

$$\dot{D} = (1.4 * 10^{-12}) * 4 * (2 * 10^{-3}) * 10^{-2} * (6.2 * 10^{18})\ rem/h$$

$$\dot{D} = 696\ rem/h$$

Therefore, the maximum applied dose in water according to MCNP software calculations will be equal to:

$$\dot{D} = 6.96\ Gy/h$$

We also measured the dose uniformity in rotating mode using Gaf-chromic film.

We used an Epson scanner to scan the films and utilized Matlab software to extract the image array. As shown in [5], the three main colors have the same response. Therefore, using Matlab, we extracted only the red color to gain an understanding of dose uniformity.

The resulting films are displayed in Fig. 4, showing graphs with lines indicating the relative strength (density) of film exposure through the center of the chamber in the axial (z) direction (see Fig. 5). The DUR ratio in the axial direction is approximately 1.1.

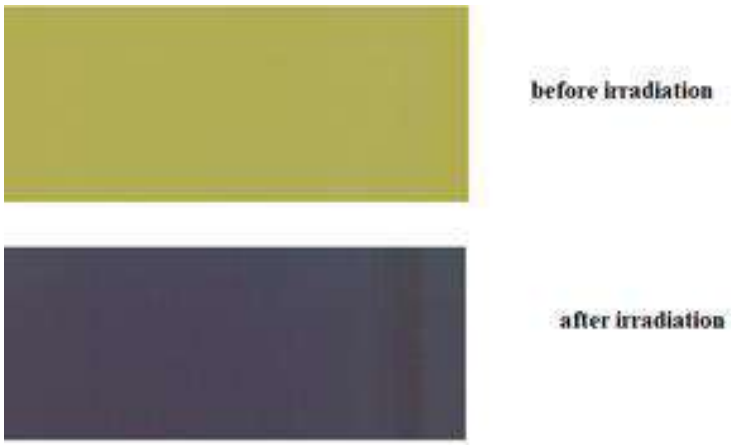

Fig. 4: The Gaf-chromic films before and after irradiation

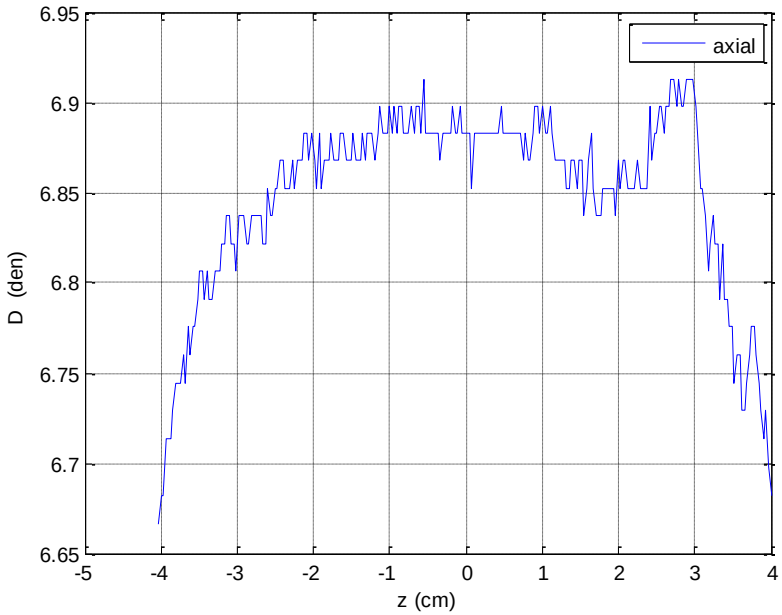

Fig. 5: Shows the dose uniformity in the rotating mode in the axial (z) direction

Conclusion

In this study, we conducted a practical measurement of an x-ray irradiation chamber using TLD and Gaf chromic films. The results indicate that the dose uniformity in the chamber is less than 1.3, and even less than 1.1 in the z-direction of the chamber.

References

[1] Bakri A., Mehta K. and Lance D.R. (2005). Sterilizing Insects with Ionizing Radiation. In: Dyck V.A., Hendrichs J., Robinson A. (eds) Sterile Insect Technique. Springer, Dordrecht.

[2] Mehta K. (2017). Technical Specification for an X-ray System for the Irradiation of Insects for the Sterile Insect Technique and Other Related Technologies, Joint FAO/IAEA Programme of Nuclear Techniques in Food and Agriculture. IAEA, Vienna, Austria.

[3] Codex Alimentarius (2003). Code of practice for radiation processing of food (CAC/RCP 19-1979). Codex Alimentarius . pp 6. Food and Agricuture Organization, Rome.

[4] Van B., Dewaraja Y.K., Niedbala J.T., Rosebush G., Kazmierski M., Hubers D., Mikell J.K., Wilderman S.J. (2023). Experimental validation of Monte Carlo dosimetry for therapeutic beta emitters with radiochromic film in a 3D-printed phantom. Medical Physics, 50(1):540-556.

[5] Massillon-JL G., Chiu-Tsao S.T., Domingo-Munoz I., Chan F.M. (2012) Energy Dependence of the New Gafchromic EBT3 Film: Dose Response Curves for 50 KV, 6 and 15 MV X-Ray Beams. International Journal of Medical Physics, Clinical Engineering and Radiation Oncology, 1(2):60-65.

ICNST 2024
International Conference on Nuclear Science and Technology
6- 8 MAY 2024 | Isfahan, Iran

Investigating the Effect of Radiation on Crosslinking Behavior of Polypropylene Blends Containing Recycled Polypropylene (Paper ID : 1243)

Rafiei-Sarmazdeh. Z[1*], M. Torab-Mostaedi[1], M. Asadollahzadeh[1], R. Torkaman[1]

[1]*Nuclear Fuel Cycle School, Nuclear Science and Technology Research Institute, Po. Box:14399-51113, Tehran, Iran*

Abstract

This study investigates the effect of radiation on the crosslinking behavior of polypropylene blends containing recycled polypropylene. The polymer blends based on virgin polypropylene were prepared using 0, 5, and 10 wt.% of waste polypropylene (WPP) using the melt mixing method in the presence of 2 wt.% of trimethylolpropane trimethacrylate (TMPTMA) as a cross-linking promoter, and then using electron beam were irradiated at a dose of 40 kGy. The results show that in a dose of 40 kGy, the amount of melt flow index (MFI) for polymer blends containing 0, 5, and 10 wt.% of WPP is 0, 0, and 0.01 g/10 min, respectively, indicating the occurrence of radiation crosslinking in the presence of TMPTMA. The MFI test is also validated by the gel content findings. The crosslinking promoters form more radicals faster than polymers alone, thus lowering radiation doses is required to occur crosslinking and achieve the desired properties. The study aims to provide insights into the potential applications of radiation technology in polypropylene recycling.

Keywords: Radiation effect, Polypropylene, Crosslinking, Polymer blend

INTRODUCTION

Approximately 8% of global solid waste consists of plastic debris, with polypropylene (PP) accounting for nearly half of that amount. As a result, there is growing concern over the negative impacts of plastic pollution on ecosystems and human health. By implementing effective recycling methods, we can reduce the volume of waste entering landfills or oceans, conserve natural resources, lower greenhouse gas emissions associated with virgin production, and create new economic opportunities [1, 2].

Polypropylene (PP) is an indispensable thermoplastic material widely utilized across various industries due to its lightweight nature, excellent chemical resistance, and ease of processing. However, the inherent limitations of PP - such as low impact strength and poor thermal stability - have led to further discarding

of this polymer and increasing its waste volume. This situation has prompted researchers to explore strategies to recycle waste PP (WPP) and enhance its performance [3, 4].

Crosslinking refers to the formation of covalent bonds between polymer chains, which results in enhanced mechanical properties and increased stability against degradation. Conventional crosslinking processes often involve high temperatures and pressures, making them energy-intensive and unsuitable for incorporating WPP, due to the oxidative destruction of the polypropylene structure resulting from thermal processing. In contrast, radiation-induced crosslinking offers a more environmentally friendly alternative by utilizing non-thermal means to achieve similar improvements in polymer characteristics without compromising the integrity of WPP [5, 6].

Irradiation of polypropylene without any additives primarily results in a significant decrease in molecular weight due to chain scission. However, crosslinking in composites and polymer blends containing polypropylene can be initiated by the formation of radicals that are reactive enough to separate hydrogen from the main chain of polyolefin. The conducted research shows that the addition of a suitable crosslinking agent, such as multi-functional bismalimide, acrylate, and methacrylate esters, plays an important role in achieving the cross-linking reaction instead of chain scission [7-9]. Meanwhile, trimethylpropane trimethylacrylate (TMPTMA) is one of the most common cross-linking agents used as a multifunctional methacrylate compound in the irradiation process.

This research will focus on evaluating the effects of electron irradiation on the crosslinking behavior of PP blended with varying amounts of WPP under controlled conditions. The resulting changes in properties will be analyzed using standard testing procedures and state-of-the-art characterization techniques. Ultimately, this study aims to offer valuable insights into the potential of radiation-induced crosslinking as a feasible method for upcycling WPP and creating environmentally friendly polypropylene (PP) composites.

EXPERIMENTAL

Materials and Characterization

Virgin PP (ZR230 C, Parslen PP) had a melting index (MI) of 0.35 g/10 min and a density of g/cm3, supplied by Zarshimi Company. WPP was collected from factories with pipe grading. The multifunctional crosslinking agent trimethylolpropane triacrylate (TMPTA) was purchased from Sigma-Aldrich.

A two-roll mixer model PM-3000 from the Brabander company, manufactured in Germany, was utilized to mix the components. The molded samples were prepared using a P200P Laboratory Platen Press manufactured by Dr. Kolin in Germany. TT200 Rhodotron electron accelerator, with an electric potential difference of 10 MeV and a current of 10 mA, at the Central Iran-Yazd Research Complex, was used to irradiate the samples. Gel content was measured using the Soxhlet method in accordance with the ASTM D2765 standard. The gel fraction of the samples is determined using equation (1).

$$Gel\ Content\ (\%) = Wa/Wb \times 100 \qquad \text{equation (1)}$$

where Wa is the weight of samples after extraction and Wb is the weight of samples before extraction. The flowability of the composites in the molten state was assessed using the melt flow index (MFI) test. MFI measurements were conducted following the ASTM D1238 standard using a Zwick model 4100 plastometer (manufactured in Germany) fitted with a capillary tube measuring 50.8 mm in diameter, 9.55 mm in internal diameter, and 162 mm in length. MFI values indicates the amount of composite material melted and delivered over a 10-minute period at a constant temperature of 230°C and under a load of 2.16 kg.

Preparation and irradiation of WPP/PP blends

All the samples were mixed using a roller mixer at a temperature of 175°C and a speed of 30 rpm for 6 minutes to ensure thorough mixing. At first, after melting polypropylene, WPP in content of 0, 5, and 10 wt.% and TMPTMA in the amount of 2 wt.% were added to the molten PP and mixed for 6 min. TMPTMA, as a cross-linking agent, induces the formation of cross-linking networks in the PP matrix by releasing monomer free radicals during irradiation. The utilization of crosslinking agents in the composite structure decreases the amount of received dose and minimizes the degradation of polypropylene.

Table 1 summarizes the formulation of the manufactured samples. Composite plates measuring 7x8 cm^2 were molded at a temperature of 175°C and a pressure of 2.5 MPa. Afterward, the prepared composite samples were exposed to electron irradiation with a dose of 40 kGy in the air atmosphere, resulting in the production of recycled polypropylene (RPP).

Table 1. Formulation of composites prepared with varying content of WPP

No.	Sample Code	PP Content (%)	WPP Content (%)	TMPTMA Content (%)	Absorbed Dose (kGy)
1	RPP0	98	0	2	0
2	RPP5	93	5	2	0
3	RPP10	88	10	2	0
4	i-RPP0	98	0	2	40
5	i-RPP5	93	5	2	40
6	i-RPP10	88	10	2	40

Results and discussion

Melt flow index

Fig. 1 illustrates the impact of electron radiation on the MFI index of mixed samples containing WPP. The melt index for PP is 0.35 g/10 min. Without irradiation, adding WPP to the PP matrix and increasing its content leads to an increase in MFI value. After a single thermal processing, the non-irradiated RPP0 sample demonstrates a more than 70% increase in the MFI value. Only the RPP5 sample shows a slight decrease in MFI compared to the RPP0 sample. The reason for this can be attributed to the presence of WPP. Waste polypropylene can develop cross-links in addition to undergoing oxidative reactions caused by prolonged exposure to air and heat. The presence of crosslinked structures reduces the melt flow index compared to non-irradiated RPP0. By increasing the content of WPP, the scission of the chains in the WPP structure shows a greater effect in competition with cross-linked structures, leading to an increase in MFI.

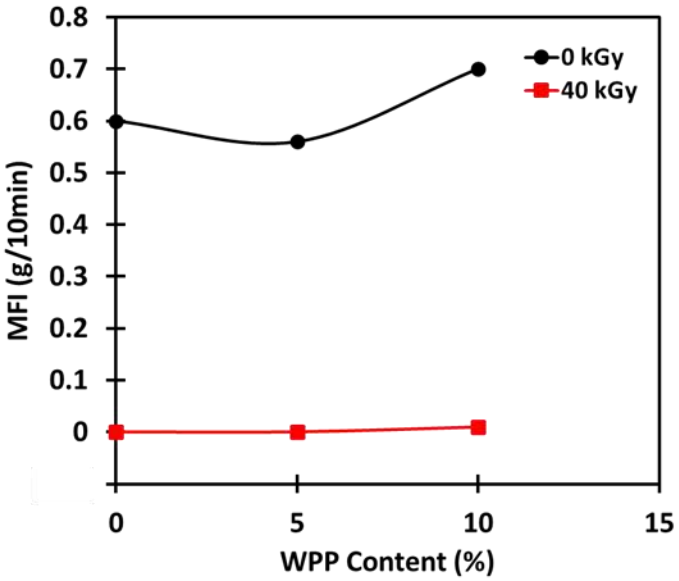

Fig.1 the melt flow index as a function of WPP content at two different absorbed doses (0 and 40 kGy). **The MFI value for i-RPP0 and i-RPP5 could not be measured and is considered as zero in the curve.

In non-irradiated samples, MFI increases with the rise in the content of WPP, indicating oxidative degradation and chain scission. However, when the samples are irradiated, the MFI value in the prepared formulations is significantly reduced compared to the non-irradiated RPP. This reduction indicates the formation of cross-links due to the irradiation of the samples, for which the value could not be measured for samples i-RPP0 and i-RPP5. It should be noted that in the graph (Figure 1), the value is considered zero for these two samples. By increasing the content of WPP, the molten polymer blends flowed more easily, and the MFI value reached 0.01 for the sample containing 10 wt.% of WPP.

It can be concluded that in the absence of irradiation, the thermal processing of PP and the addition of WPP lead to an increase in MFI due to the destruction of the polymer chains and the reduction in chain length. On the other hand, radiation processing creates cross-links throughout the polymer blends, reducing the negative effects of increasing WPP and thermal processing of the composite to a great extent. It also decreases the rate of MFI increase with rising WPP content.

The analysis of the results reveals that in all irradiated recycled samples (i-RPP0, i-RPP5, and i-RPP10), a high amount of crosslinks is formed at a dose of 40 kGy. These crosslinks impede the polymer from flowing at a temperature of 230°C.

Gel content

To determine the effect of radiation-induced cross-links in radiation, the gel content test was performed on samples containing WPP, and the results are presented in Table 3. Without irradiation, the gel content of PP, and RPP blends is zero [49]. The results show that PP blends in the presence of TMPTMA cross-linking agent can effectively gel at a dose of 40 kGy. Sample RPP0 exhibits a maximum gel content of 37.9% at 40 kGy. In the presence of 5 wt.% WPP, the gel content of i-RPP5 is approximately 33%. The presence of WPP led to a slight decrease in the gel content compared to the i-RPP0 sample. This decrease is attributed to the destructed structure caused by the presence of WPP. In the presence of 10 wt.% of WPP, the gel content slightly increases and reaches 34%. According to Charlesby and Pinner, cross-link formation occurs preferentially in amorphous regions. Therefore, the high density of cross-linking in the amorphous domains of WPP causes the formation of chemical bonds between PP and WPP. The presence of these bonds increases the surface adhesion, which can also affect the mechanical properties [55]. The obtained results confirm the findings of the MFI test.

Table. 2 Gel content of mixed PP/rPP samples irradiated at a dose of 40 kGy

No.	Sample Code	Absorbed Dose (kGy)	Gel Content (%)
1	i-RPP0	40	37.92
2	i-RPP5	40	32.66
3	i-RPP10	40	34.40

Mechanism of Crosslinking Promoter

TMPTMA serves as a cross-linking promoter and a multi-functional monomer (A). It can protect the polymer matrix (RH_2) from radiolytic decomposition by transferring charge and energy during irradiation (reaction 1 and 2).

$$RH_2^{*\bullet} + A \rightarrow RH_2 + A^{*\bullet} \quad \text{(reaction 1)}$$

$$RH_2^{*} + A \rightarrow RH_2 + A^{*} \quad \text{(reaction 2)}$$

On the other hand, this compound can react with cations, electrons, or free radicals, thereby altering the progression of the subsequent reaction chain. In the case of a polymeric matrix with a multi-functional agent, the energy absorption follows the "law of mixtures." This means that the total energy absorbed by

each component of the mixture is proportional to the relative amounts of orbital electrons of each component per unit volume. In practical terms, it is very close to the weight fraction of the component. However, it is not uncommon to observe disproportionately large radiolytic changes in the smaller components of a mixture. This is typically the outcome of the smaller component's involvement in energy and charge transfer reactions [10].

Polyfunctional agents help achieve cross-linking at a lower radiation level without significant degradation of the base polymers [11-13]. The structure of a polymer matrix can be influenced by the presence of species produced during thermal oxidation and/or radiation-induced cross-linking [7, 14]. In the presence of radiation, these agents can form highly reactive radicals that can homopolymerize or bond to the unsaturated branches of polymer chains through the "ene" reaction mechanism. Hence, the created network can be strengthened, and the cross-linking density can be increased through the linking of such additives among the polymer chains [10].

Conclusions

This study has examined the crosslinking behavior of electron beam-irradiated polypropylene blends containing recycled polypropylene. The application of electron beam irradiation could induce crosslinking networks in all PP blends, as evidenced by the decrease in MFI value and the analysis of the gel content result. The irradiation and the addition of TMPTMA have significantly decreased the MFI of all i-RPP blends. During irradiation, the monomer free radicals released from TMPTMA would interact with the polymeric free radicals generated by the irradiation, leading to the formation of crosslinking networks within the PP matrix. The crosslinking networks formed could restrict the mobility of macromolecular chains of PP from flowing during heating throughout the entire mixed polymer matrix. The gel content results also confirm the MFI test.

References

[1] Hopewell, J., Dvorak, R., & Kosior, E. (2009). Plastics recycling: challenges and opportunities. Philosophical Transactions of the Royal Society B: Biological Sciences, 364(1526), 2115-2126.

[2] Maitlo, G., Ali, I., Maitlo, H. A., Ali, S., Unar, I. N., Ahmad, M. B. And et al (2022). Plastic Waste Recycling, Applications, and Future Prospects for a Sustainable Environment. Sustainability, 14(18).

[3] Stoian, S. A., Gabor, A. R., Albu, A.-M., Nicolae, C. A., Raditoiu, V., & Panaitescu, D. M. (2019). Recycled polypropylene with improved thermal stability and melt processability. Journal of Thermal Analysis and Calorimetry, 138(4), 2469-2480.

[4] Matias, Á. A., Lima, M. S., Pereira, J., Pereira, P., Barros, R., Coelho, J. F. J., & Serra, A. C. (2020). Use of recycled polypropylene/poly(ethylene terephthalate) blends to manufacture water pipes: An industrial scale study. Waste Management, 101, 250-258.

[5] Spenadel, L. (1979). Radiation crosslinking of polymer blends. Radiation Physics and Chemistry (1977), 14(3), 683-697.

[6] Chodák, I. (1999). Crosslinking of polypropylene. In J. Karger-Kocsis (Ed.), Polypropylene: An A-Z reference (pp. 128-134). Dordrecht: Springer Netherlands.

[7] Ali, Z. I., Youssef, H. A., Said, H. M., & Saleh, H. H. (2006). Influence of electron beam irradiation and polyfunctional monomer loading on the physico-chemical properties of polyethylene/polypropylene blends. Advances in Polymer Technology, 25(3), 208-217.

[8] Chodak, I. (2004). Improving the Properties of Polyolefin Waste by Reactive Processing. Polymer-Plastics Technology and Engineering, 43(6), 1769-1777.

[9] Shukushima, S., Hayami, H., Ito, T., & Nishimoto, S.-i. (2001). Modification of radiation cross-linked polypropylene. Radiation Physics and Chemistry, 60(4), 489-493.

[10] Mittal, V. (2012). Functional polymer blends: synthesis, properties, and performance: CRC Press.

[11] Chattopadhyay, S., Chaki, T. K., & Bhowmick, A. K. (2001). Structural characterization of electron-beam crosslinked thermoplastic elastomeric films from blends of polyethylene and ethylene-vinyl acetate copolymers. Journal of Applied Polymer Science, 81(8), 1936-1950.

[12] Dworjanyn, P., Garnett, J., Khan, M., Maojun, X., & Reig, M. (1994). Radiation Physics and Chemistry, 42, 31.

[13] McGinnis, V. D. (1986). Encyclopedia of Polymer Science and Technology. In (Vol. 445). New York: John Wiley & Sons.

[14] Böhm, G. G. (1973). The radiation chemistry of elastomers, 2: 195.

ICNST 2024 International Conference on Nuclear Science and Technology
6- 8 MAY 2024 | Isfahan, Iran

Synthesis and characterization of carboxymethyl cellulose/acrylic acid superabsorbent hydrogel by gamma irradiation (Paper ID : 1247)

Mahsa Radmehr[1], Ahmad Poursattar Marjani[1], Azam Akhavan[2,] *, Farahnaz Nasiri[2]
[1] *Department of Organic Chemistry, Faculty of Chemistry, Urmia University, Urmia, Iran*
[2] *Radiation Applications Research School, Nuclear Science and Technology Research Institute, Tehran, Iran*

Abstract

Superabsorbent hydrogels (SAP) are hydrophilic polymers with a 3D network that can absorb and store large amounts of water and aqueous solutions. SAPs are widely used in various applications such as drug delivery, hygiene products, agriculture, etc. Ionizing radiation is a very suitable technique for the preparation of hygiene products. Natural polymers, such as biodegradable and non-toxic polymers with high molecular weight, have been widely used in making SAPs. In this research acrylic acid (AA) was partially neutralized with sodium hydroxide then it was added to carboxymethyl cellulose (CMC) aqueous solution with different concentrations, 0.5, 1 and 2%. Gamma irradiation was applied to synthesize CMC/AA hydrogels at 5 to 20 kGy absorbed doses. FTIR infrared spectroscopy was used to determine the functional group of gel structure in SAPs formation. Also, the effect of radiation dose and different neutralization percentage of acrylic acid on the gel content, swelling behavior and absorption under load (AUL) in water and saline solution were investigated.

Keywords: Superabsorbent, Carboxymethyl cellulose, Gamma radiation, acrylic acid.

INTRODUCTION

Superabsorbent polymers (SAP) are a class of three-dimensional, hydrophilic, functional polymeric network systems that can absorb large amounts of water, including those with good water retention capacity, even under high pressure or temperature [1]. Usually, ionic functional groups along the cross-linked polymer chains encourage the diffusion of water within the network without allowing the substance to dissolve in water [2]. SAPs are widely used in various applications such as drug delivery, hygiene, foods, cosmetics, and agriculture[3].

Superabsorbents with eco-friendly properties and biodegradability are finding increasing interest in the academic and industrial fields [4]. Todays, superabsorbents are prepared with a natural polymer, such as cellulose, starch, chitosan, alginate, carrageenan, and gellan gum[5].

Ionizing radiation is a very convenient technique for the preparation of SAPs. An initiator, catalyst, and cross-linker are not required in radiation processing because ionizing radiation is highly energetic[6].

Radiation processing has many advantages, such as ease of process control, and the technology is environmentally friendly because it leaves no residue or environmental pollutants [7, 8].

A demand for biopolymers derived from feedstock, such as cellulose, has recently arisen. Compared to petroleum-based polymers, these biopolymers have the advantages of high hydrophilicity, sustainability, biodegradation properties, and non-toxic base components [9],[10]. Biopolymers can be made from carboxymethylcellulose (CMC), which has a naturally occurring polysaccharide cellulose base. CMC, a linear glycosidic macromolecule consisting of β- (1→4)-linked D-glucose, is the most popular and the cheapest cellulose ether that can also be used for this purpose. It is an anionic linear polymer in which the original H atoms on the cellulose hydroxyl groups are replaced by a carboxymethyl substituent $–CH_2COO$ [11, 12]. CMC hydrogel has been prepared by gamma radiation in the presence of mono- and divalent salts (NaCl and $CaCl_2$),The result showed that swelling properties depend on the radiation dose and the ionic strength of the salts [13]. However, a single study on carboxymethylcellulose/acrylic acid SAPs prepared by a radiation method is insufficient to understand this process thoroughly. Thus, this study has reported the synthesis of SAPs by copolymerizing acrylic acid with CMC using a γ-ray irradiation technique. The effect of radiation dose and acrylic acid concentration on the prepared hydrogels' properties were investigated. The hydrogels were characterized with respect to gel content, swelling properties, and Fourier transform infra-red (FTIR) spectroscopy.

EXPERIMENTAL

Materials

Carboxymethylcellulose (purity 99.5%), obtained from Sigma Aldrich Co (Product NO 419273), was used without further purification. Acrylic acid (purity 99.5%) was purchased from Merck and was stored in a refrigerator before use. sodium hydroxide (NaOH 84%) was obtained from Merck and used for neutralization. Sodium chloride (NaCl) was also purchased from Merck. Distilled water was used in the polymerization and swelling experiments. All the reagents were analytical grade used without purification.

Characterization

Free swelling capacity (FSC)

To measure swelling, a free absorption measurement test in deionized water and a physiological serum solution (0.9% sodium chloride solution) was used using the tea bag method. 0.1 g (W_1) of superabsorbent in 500 g of deionized water (or saline water 0.9 %) was placed for half an hour until the sample reached equilibrium swelling. Then the bag was taken out of the liquid, the excess liquid was removed by hanging the bag for a specific time, and the bag was weighed (W_2). The same steps were followed for the bag

without the sample to serve as blank, and it was also weighed (W_0). Absorption capacity or equilibrium swelling (g/g) was calculated from the following equation:

$$FSC= (W_2- W_0)/ W_1 \quad (1)$$

Absorption under load (AUL)

In order to measure Absorbency under load (AUL) of SAP (absorption rate of 0.9% sodium chloride solution by the superabsorbent sample which is under 0.3 psi pressure), a glass strainer (diameter 80 mm and height 7 mm) was put in the Petri dish and the strainer or fabric net was closed by a metal fastener to the end of the glass cylinder (with an inner diameter of 63 mm, an outer diameter of 67 mm, and a height of 50 mm) and placed on the glass strainer. Then, 0.5 grams of superabsorbent was uniformly distributed inside the cylinder (on a cloth net located on a glass strainer) and a Teflon piston with a diameter of 63 mm was placed on the superabsorbent particles so that the pressure was 0.3 psi. applied to the sample. At the end, salt water was poured into the Petri dish so that the filter was immersed in the solution. To prevent surface evaporation of saline solution and changing its concentration, the entire device was covered. After 60 minutes, the swollen sample under pressure was weighed and the numerical value of AUL was determined from equation 2 [14]. Where W_1 and W_2 are the weights of dried hydrogel and swollen hydrogel.

$$AUL=(W_2-W_1)/W_1 \quad (2)$$

Determination of Gel Fraction

The SAP samples dried to constant weight (W_i) were immersed in distilled water for 24 h. They were removed from the distilled water, and then dried to a constant weight (W_1) in a vacuum oven. The gel fraction was calculated as follows:

$$\text{Gel fraction (\%)} = W_1/ W_i \times 100 \quad (3)$$

Where W_1 is the weight of the dry sample after extraction in water, and W_i is the initial weight of the dry sample.

Preparation of SAPs

CMC (0.5,1,2 % wt) mixed with distilled water in a beaker (250 mL) was stirred with a stirrer for one hour at room temperature. Then, various concentrations of acrylic acid were added to the solution above and

partially neutralized by NaOH. The mixture was poured into glass test tubes, sealed, and finally irradiated by γ-rays with radiation doses of 5, 10,15 and 20 kGy at room temperature (~27 ºC). The CMC/acrylic acid SAP obtained in a cylindrical shape was cut into small pieces, dried.

Results and discussion

FT-IR Spectra of SAP and Identification

FT-IR spectroscopic analysis was used to show the nature of bond formation in hydrogen moieties and cross-linking in anhydroglucose units. The FT-IR spectrum of pure CMC powder and CMC/AAc combined hydrogel was shown in Figure 1. Pure CMC had absorption bands related to O-H stretching at 3461 cm^{-1} as well as intramolecular and intermolecular hydrogen bonds in cellulose, -CH_2- stretching on anhydroglucose units at 2922 cm^{-1}, C=O carbonyl stretching in the anhydroglucose unit of the cellulose at 1642 cm^{-1}, C-OH in in-plane bending at 1418 cm^{-1}, –OH bending vibration at 1322 cm^{-1}, C=O stretching from an asymmetric oxygen bridge at 1157 $cm^{-1,}$ and ring stretching at 905 cm^{-1}. These values were consistent with those reported by Rim Dusit et al. [15]. and Wang et al. [16]. As shown in Figure 1, the characteristic absorption bands of CMC at 1064.42 and 1157.024 cm-1 were obviously weakened after the reaction in the CMC/AAc composite hydrogel. In the spectrum (blue color), the new band at 1728.92 cm-1 (C=O stretch of –COOH groups) showed the C=O stretch of the carbonyl group of acrylic acid, which was not present in the CMC spectrum (red spectrum). The band shift towards a less obvious wavenumber at 1629.75 cm-1 (which was at 1642.97 cm-1 for CMC) for CMC/AAc SAPs indicates the formation of copolymer hydrogels. These results also indicate that AAc monomers were grafted onto the CMC backbone.

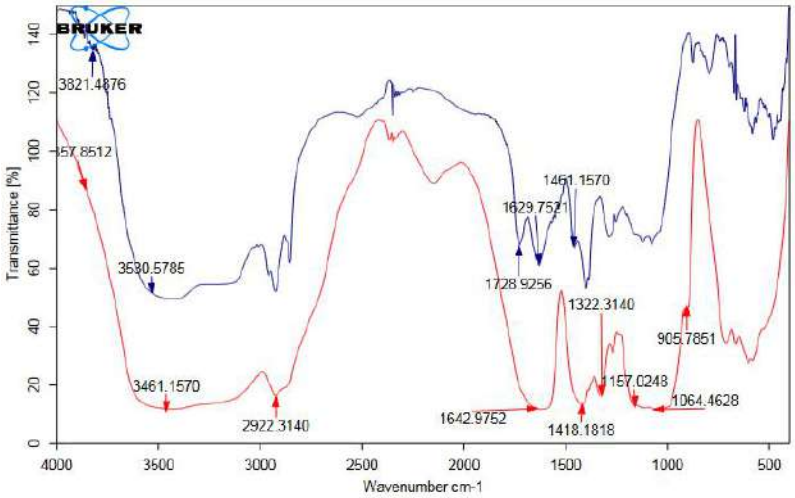

Figure1: Infrared spectroscopy, CMC powder (red color spectrum), and SAPs from CMC/AAc (blue color spectrum).

Gel Fraction of SAP

The gel fraction of SAP prepared from the CMC/AAc blend with the various radiation doses and the variation of the CMC content in the feed solution is shown in Figure 2. In the radiation dose of 5 kGy, no dried gel is formed; with increasing radiation dose the gel fraction of SAP increases (Figure 2). The maximum value of the gel fraction is obtained at the 15 kGy radiation dose. From Figure 2, it can be observed that a slight decreasing trend of the gel fraction occurred after irradiation at 15 kGy. This result might be due to the degradation of the cellulose molecules. In addition, the gel fraction increased with an increase of CMC content in the feed solution, and it increased from 73 to 78% following the variation of the CMC concentration from 0.5 to 2% at a radiation dose of 15 kGy. When an aqueous solution of CMC/AAc is irradiated with gamma rays, free radicals are generated on the CMC and AAc. Random reactions of these radicals lead to formation of a graft copolymer of CMC and AAc. When the radiation dose increases beyond a certain value, the polymer chains become cross-linked, and a gel-like material is obtained.

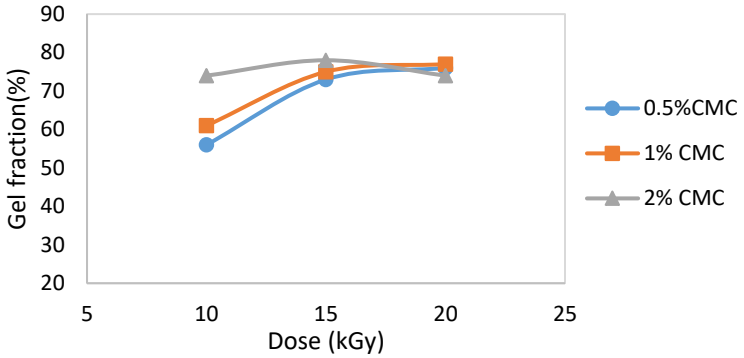

Figure 2: Effect of radiation dose and concentration of AAc on gel fraction of CMC/AAc SAP

Water absorption of SAP

The effects of the radiation dose and the concentration of AAc on the water absorption of SAP prepared from CMC/AAc are shown in Figure 3. The results show that with increasing CMC percent in solutions both the water and saline solution absorption increase due to increasing of hydroxyl groups in the CMC. When the samples are irradiated from 10 to 20 kGy the water and saline solution absorption of the SAP decrease in solutions contain 1 and 2% CMC. This result might be due to the increased cross-linked density with the increase in the radiation dose. for the solution with 0.5% CMC increasing dose lead to increasing

water and saline solution absorption. Measured water and salt absorption were reported 437 and 76 g/g respectively for the 0.5% CMC best sample, which occurred at a dose of 20 kGy.

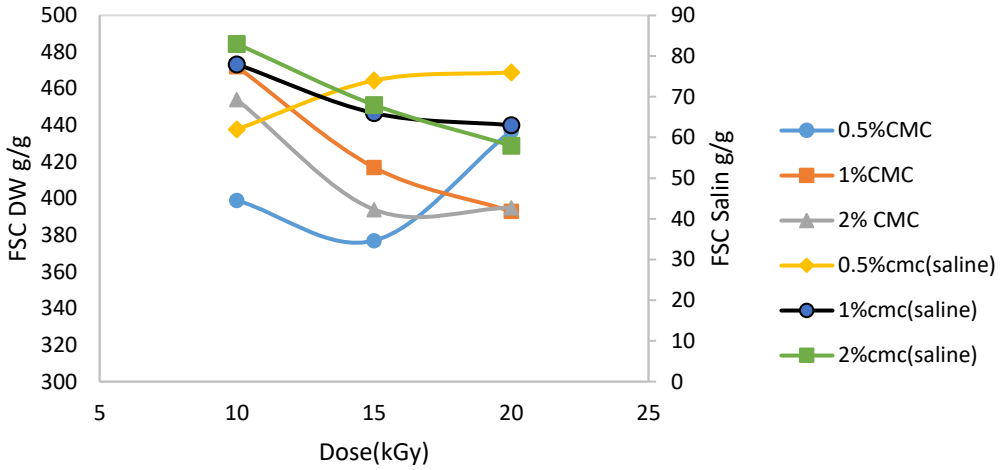

Figure 3: Effect of radiation and concentration of CMC on water absorption of SAPs

Absorption under load (AUL)

The Absorbency under load (AUL) test measures the capacity of the SAP sample to absorb fluid under specific pressures. Figure 4 displays that with increasing the CMC content the AUL decreases. By raise in the irradiation dose and subsequently content of cross-link density the AUL has been significantly increased between 15.36 and 25 g/g. For the 0.5% CMC, which has the best saline solution FSC, the AUL is 24.6 g/g which occurred at a dose of 20 kGy.

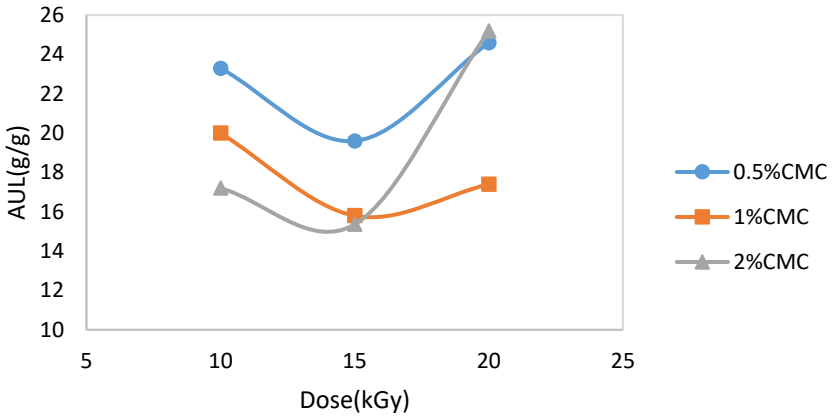

Figure 4: Effect of radiation dose and concentration of CMC on AUL

CONCLUSION

The synthesis of SAP from a CMC/AAc blend can be performed with a radiation processing technique using a Co-60 gamma source. With respect to gel fraction, a 20 kGy radiation dose can be considered suitable for the preparation of SAP from a CMC/AAc blend. The grafting of AAc on to CMC confirmed by FTIR. The addition of CMC increases the FSC in water, however according to AUL results the best properties is observed in SAP with 0.5% CMC. Therefore, it can be concluded that CMC/AAc SAPs synthesized with radiation method may be used in drug delivery, dressings, and baby diapers.

References

[1] F. Esposito, M. A. Del Nobile, G. Mensitieri, and L. Nicolais, 1996, "Water sorption in cellulose-based hydrogels," *J. Appl. Polym. Sci.*, Vol. 60, No. 13, pp. 2403–2407.

[2] K. M. Raju, M. P. Raju, and Y. M. Mohan, 2003, "Synthesis of superabsorbent copolymers as water manageable materials," *Polym. Int.*, Vol. 52, No. 5, pp. 768–772

[3] H. Y. Zhou, Y. P. Zhang, W. F. Zhang, and X. G. Chen, 2011, "Biocompatibility and characteristics of injectable chitosan-based thermosensitive hydrogel for drug delivery," *Carbohydr. Polym.*, Vol. 83, No. 4, pp. 1643–1651.

[4] N. Q. Hien, D. Van Phu, N. N. Duy, and H. T. Huy, 2005, "Radiation grafting of acrylic acid onto partially deacetylated chitin for metal ion adsorbent," Nucl. Instrum. Methods Phys. Res. Sect. B Beam Interact. Mater. *At.*, Vol. 236, No. 1–4, pp. 606–610.

[5] L. Pérez-Álvarez, L. Ruiz-Rubio, E. Lizundia, and J. L. Vilas-Vilela, 2019, "Polysaccharide-based superabsorbents: synthesis, properties, and applications," Cellul.-Based Superabsorbent Hydrogels, pp. 1393–1431.

[6] E. Jabbari and S. Nozari, 2000, "Swelling behavior of acrylic acid hydrogels prepared by γ-radiation crosslinking of polyacrylic acid in aqueous solution," Eur. Polym. J., Vol. 36, No. 12, pp. 2685–2692.

[7] J. M. Rosiak and P. Ulański, 1999, "Synthesis of hydrogels by irradiation of polymers in aqueous solution," Radiat. Phys. Chem., Vol. 55, No. 2, pp. 139–151.

[8] B. Fei, R. A. Wach, H. Mitomo, F. Yoshii, and T. Kume, 2000, "Hydrogel of biodegradable cellulose derivatives. I. Radiation-induced crosslinking of CMC," J. Appl. Polym. Sci., Vol. 78, No. 2, pp. 278–283.

[9] J. D. Stahl, M. D. Cameron, J. Haselbach, and S. D. Aust, 2000, "Biodegradation of superabsorbent polymers in soil," Environ. Sci. Pollut. Res., Vol. 7, No. 2, pp. 83–88

[10] S. A. Weerawarna, 2024, 2014 "Method for making biodegradable superabsorbent particles, Vol 60, No. 5, pp 432

[11] A. Baar, W. Kulicke, K. Szablikowski, and R. Kiesewetter, 1994, "Nuclear magnetic resonance spectroscopic characterization of carboxymethylcellulose," Macromol. Chem. Phys., Vol. 195, No. 5, pp. 1483–1492.

[12] T. Heinze, 1998, "New ionic polymers by cellulose functionalization," Macromol. Chem. Phys., Vol. 199, No. 11, pp. 2341–2364.

[13] S. Sultana, M. Islam, N. Dafaderd, M. Haque, N. Nagasawa, and M. Tamadat, 2024, "Effect of mono- and divalent salts on the properties of carboxymethylcellulose hydrogel", Vol 200, No. 2, pp 234-431.

[14] M. M. Zohourian and K. Kabiri, 2024 "Superabsorbent polymer materials: a review," 2008, Accessed: Vol.100, No.3, pp 564.

[15] S. Rimdusit, S. Jingjid, S. Damrongsakkul, S. Tiptipakorn, and T. Takeichi, 2008, "Biodegradability and property characterizations of methyl cellulose: effect of nanocompositing and chemical crosslinking," Carbohydr. Polym., Vol. 72, No. 3, pp. 444–455.

[16] X.-L. Wang, K.-K. Yang, Y.-Z. Wang, D.-Y. Wang, and Z. Yang, 2004, "Crystallization and morphology of a novel biodegradable polymer system: poly (1, 4-dioxan-2-one)/starch blends," Acta Mater., Vol. 52, No. 16, pp. 4899–4905.

ICNST 2024 International Conference on Nuclear Science and Technology
6- 8 MAY 2024 | Isfahan, Iran

Integration of Compressed Sensing Principles in Collimator Design for Neutron Imaging Systems: A Monte Carlo Simulation Study (Paper ID : 1249)

Mehrabi M.[1*], Salek N.[2], Vosoughi S.[1], Beigzadeh A.[1]

[1]*Radiation Application Research School, Nuclear Science and Technology Research Institute (NSTRI), Tehran, Iran*
[2]*Nuclear Fuel Research School, Nuclear Science and Technology Research Institute (NSTRI), Tehran, Iran*

Abstract

The application of compressed sensing theory has been widely employed in signal processing within various imaging systems. This study aims to integrate compressed sensing principles into the design of collimators in neutron imaging system. To establish a proof-of-concept experimental setup, the Monte Carlo N-Particle Transport Code (MCNP) was utilized. Extensive simulations were conducted to determine crucial parameters such as the water height necessary to stop thermal neutrons emitted by a ^{252}Cf source, dimensions of the collimator array, suitable collimator material, and optimal collimator size for the experiment. The simulations involved a cylindrical water tank and a collimator array consisting of a 2×2 configuration of channels. Three different materials were simulated to identify the most effective composition for the collimator. The array configuration was defined as a randomized combination of air-filled and water-filled channels. MCNP was employed to tally neutron counts for each configuration, with 300 configurations for a 23×23 array and 100 configurations for an 11×11 array. MATLAB, utilizing a non-negative least squares approach, was employed to construct images of the source corresponding to different collimator array sizes. Additionally, a rectangular tank MCNP model was created, incorporating an 11×11 collimator array. Multiple images were generated to observe the minimum number of measurements, denoted as K, required for accurate image quality. Based on these simulations, an imaging system comprising a 250-gallon tank filled with water and an array of 1.27 cm 11×11 polyvinyl chloride (PVC) pipes were chosen for assembly. In contrast to the conventional raster scan method, which necessitates K to be equivalent to the total number of pixels (K=121 for the 11×11 case), it was discovered that the shape and location of the source can be obtained with K representing only 50% of the total pixels.

Keywords: Compressed Sensing, Collimator Design, Monte Carlo Simulation, Accurate Image Quality.

INTRODUCTION

In conventional imaging methods, a large number of measurements are required to reproduce an image with a high level of accuracy [1]. However, recent advancements in compressed sensing theory have shown that it is possible to obtain meaningful information with a significantly reduced number of

measurements [2]. Compressed sensing theory, also known as compressive sensing, is a revolutionary approach in signal processing and image reconstruction that enables the acquisition and reconstruction of high-quality signals and images from a small number of measurements or samples [3]. It is based on the fundamental principle that many signals and images of interest have a sparse or compressible representation in a certain domain or basis [4].

Traditional signal processing techniques typically require a large number of samples to accurately reconstruct a signal or image. However, compressed sensing takes advantage of the sparsity or compressibility of signals and images to significantly reduce the number of measurements needed for reconstruction [5]. This has important implications in various fields such as medical imaging, remote sensing, and wireless communication, where acquiring a large number of measurements may be costly or time-consuming.

The key idea behind compressed sensing is to acquire linear projections of the signal or image using a random or pseudo-random measurement matrix. These projections capture a compressed version of the underlying signal or image, which can then be reconstructed using specialized algorithms [6]. The reconstruction algorithms exploit the sparsity or compressibility of the signal or image to recover the original data accurately. This approach has been successfully applied in various signal processing and data storage applications, but its potential in the field of nuclear imaging remains largely unexplored [7].

The objective of this study is to investigate the integration of compressed sensing principles into the design of neutron source imaging systems [8]. By incorporating these principles into the collimator design, we aim to enhance the efficiency and effectiveness of neutron imaging techniques for nuclear security applications.

Neutron source imaging would be helpful in the efforts to monitor contraband nuclear materials transportation at shipping ports or land borders. Traditional neutron detection methods provide limited information about the source, making it challenging to determine the appropriate response level. By visualizing the shape and size of the neutron source, we can better assess the threat and respond accordingly.

The proposed imaging system offers several advantages over conventional methods. Firstly, it requires only one or two neutron detectors to capture images of fast neutron sources, significantly minimizing the complexity and cost of the system. Additionally, the materials used in this system are inexpensive and readily available, making it feasible for widespread implementation. This imaging technique can also be employed in nuclear installations for comparing neutron image signatures, thereby enhancing nuclear safeguards measures.

The fundamental principle that allows compressed sensing technique to work is the fact that mathematically, signals obtained by measurements using compressed sensing can be translated into another set of signals that collectively form the image signals, x. Compressive sensing works because x

is required to be s-sparse, which means that x can be represented using only s non-zero coefficients. As x is plotted as an image, lighter shades in x would represent the possible positions with stronger neutron intensity. Therefore, if a neutron source is present when the imaging takes place, x would be an s-sparse set of signals as it is expected that the neutron source is the dominant neutron emitter that would stand out from the surrounding.

The translation process utilizes incoherence of a sensing matrix, A, which maps x to the measured signals, b, the neutron counts. In linear algebra, coherence of a matrix is defined as the largest absolute normalized inner product between its different columns and this characterizes the dependence between the matrix columns. A small value of coherence (higher incoherence) would result in a better likelihood for successful signal recovery. To ensure incoherence, the sensing matrix is required to have randomness as a property. Solving for x would eventually produce a $2D$ resemblance that identifies the shape and location of the imaged neutron source.

Image reconstruction is performed using the non-negative least squares (NNLS) method, which imposes the constraint that the sparse entries of the image signals must be non-negative [9]. This assumption is based on the premise that only positive values indicate the presence of a neutron source, while other surrounding materials do not generate radioactive signals. By solving the equations $Ax=b$, where A represents the sensing matrix and b denotes the measured neutron counts, the image signals can be accurately recovered using the lsqnonneg function in MATLAB.

To determine the optimal collimator design, extensive Monte Carlo N-Particle Transport Code (MCNP) simulations were conducted. These simulations involved varying the dimensions, materials, and configurations of the collimator array. Neutron counts were tallied for each configuration, and the resulting images were reconstructed using the NNLS method. The findings from these simulations have informed the decision to proceed with the assembly of an imaging system consisting of a water-filled 250-gallon tank and a polyvinyl chloride (PVC) collimator array.

In conclusion, this research aims to optimize the experimental design for compressed sensing neutron source imaging. By incorporating compressed sensing principles into the collimator design and utilizing MCNP simulations, we can enhance the efficiency and accuracy of neutron imaging systems. The proposed imaging technique has significant implications for nuclear security applications, enabling the detection and characterization of contraband nuclear materials with improved precision and cost-effectiveness.

RESEARCH THEORIES

Monte Carlo N-Particle Transport (MCNP) Simulations

To optimize the experimental design for compressed sensing neutron source imaging, Monte Carlo N-Particle Transport Code (MCNP) simulations were conducted. The initial simulations involved a cylindrical water tank, where the height of water necessary to stop thermal neutrons emitted from a ^{252}Cf source was determined. The MCNP program utilized the F_1 tally to measure neutron counts as they crossed a designated surface. This tally was placed underneath the tank to capture direct streaming neutrons from the source for image reconstruction. Various sizes of the F_1 tally surface were examined to minimize in-scattering from external neutrons. The collimator, comprising a 2×2 array, was introduced

vertically into the model at the center of the tank. Simulations were performed using three different materials for the collimator: stainless steel, polyvinyl chloride (PVC), and aluminum. By comparing the results, the most suitable collimator material was identified. Once the appropriate material was identified, an array size of 23 × 23 (0.316 cm × 0.514 cm × 100 cm) was arbitrarily chosen. A ring source was positioned at 50 cm above the water surface and was defined as a 1 μCi ^{252}Cf fission source emitting 4.31 × 10^{3} ns^{-1}. A ring source was chosen so that the image quality could be evaluated by the easiness of source shape and position identification. After the image produced using 23 × 23 array size was evaluated, the array size was reduced by half to see if there was any difference in the image quality. An acceptable image quality difference would mean that smaller array size may be employed as it would result in a more practical experiment. Another model with an 11 × 11 array size (0.635 cm × 0.912 cm × 100 cm) was simulated using of a 100 μCi of the same neutron source as one of the variance reduction methods in ensuring accurate MCNP results. Figure 1 shows the configuration of proposed imaging system.

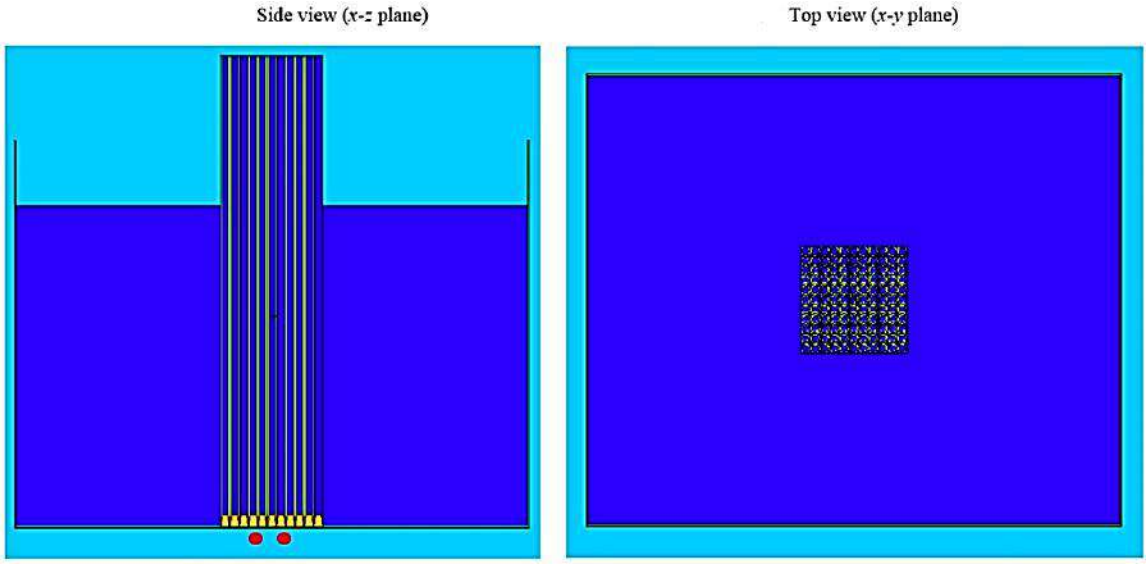

Fig. 1. Illustration of the proposed neutron source imaging system displayed using the MCNP Visual Editor software.

Image Reconstruction

A MATLAB code was created to extract the array configurations from the MCNP input files and to rewrite in an Excel spread sheet where each array configuration is stored as the row entry of the spreadsheet. The extracted data forms matrix A, which is therefore a 300 × 529 matrix for the 23 × 23 array and 100 × 121 for the 11 × 11 array. The $F1$ tally results were also extracted from the corresponding output files and rewritten as the row entry in another spreadsheet. These entries in a new Excel sheet makes matrix b. Here, b is a 300 × 1 matrix for the 23 × 23 array and 100 × 1 for the 11 × 11 array.

$$\min || x ||_1 \text{ subject to } Ax = b \quad (1)$$

Image reconstruction in compressed sensing is usually solved using l1-minimization. There are a few variations of l1-minimization technique, depending on the type of problem to be solved. The earliest code was developed using MATLAB program and is known as the l1- MAGIC program [10]. An example of one way to solve for $x = b/A$ by l1-minimization is shown by Eq. (1), which is known as basis pursuit. If a nonnegative vector, x, is recovered by l1-minimization, then it is the unique nonnegative vector that satisfies $Ax = b$. Therefore, x can also be recovered by NNLS by solving for $x = b/A$ and minimizing the $l2$ of the difference between b and the inner product of A and x as shown in Eq. (2). If the image, x, is nonnegative and sparse, the use of NNLS will typically solve for x if the NNLS uses the active Lawson Hanson algorithm.

$$\min || b - Ax ||_2 \text{ subject to } z \geq 0 \quad (2)$$

Solving for Eq. (2) using an active set is possible by solving an unconstrained least-square problem that includes only inactive variables, if the active variables are known [11]. This is done by attempting to find the nonnegative solution with some variables being assigned to zero. These variables are called an active set because of their non-negativity constraints being activated. The active set is modified by a single variable in each iteration and finally the unconstrained least-square problem is solved without the active set [12]. The lsqnonneg function in MATLAB executes the Lawson–Hanson algorithm that employs this active-set technique [13].

The recovered signal matrix, x, is shown as a gray-scaled image using the imagesc command in MATLAB. For the 11 × 11 rectangular data, images were constructed with various numbers of measurements, K, starting from 100 and reduced to 30 with an interval of 10 measurements. The purpose of this was to observe the effect of K value on image quality.

RESULTS AND DISCUSSION

The image of the neutron source corresponding to different collimator array sizes was constructed using the non-negative least squares (NNLS) method in MATLAB. An MCNP model was created with a rectangular tank and a collimator array to generate multiple images based on the number of measurements, K. The minimum value of K required for accurate image quality was determined through this process.

The initial simulations revealed that a water height of 100 cm is required to effectively stop all thermal neutrons at the bottom of the cylindrical water tank. This was observed through the zero value of the MCNP

tally output for thermal neutrons. To prevent in-scattering from the sides of the tank into the $F1$ tally surface, it was necessary for the array to be smaller than 25.3 cm by 25.3 cm.

Introducing a different material into the tank could potentially lead to some neutrons reaching the $F1$ tally surface due to its lower neutron absorption cross section compared to water. Given that most of the thermal neutrons should be absorbed by the determined water height, the ideal material would allow for minimal neutrons to reach the $F1$ tally surface. Stainless steel emerged as the most effective collimator material, resulting in minimal neutron travel through the collimator compared to PVC and aluminum. However, the use of PVC as the collimator material only resulted in a slight average count rate increase of 0.17 ± 0.09 ns^{-1}. Considering the cost-effectiveness of PVC pipes compared to stainless steel pipes, PVC was chosen as the collimator material for the proof-of-concept experiment.

With the prescribed requirements, the successful reconstruction of the neutron source image was achieved using a 23×23 array size and all measurements (K=300). Although reducing the array size to 11×11 led to a lower resolution in the reconstructed image, as expected with all measurements (K=100), the image quality remained sufficient for source localization and shape identification. The reconstructed image, x, was generated using the *lsqnonneg* function in MATLAB, with matrices A and b as inputs. The choice of using the NNLS technique to solve for x was based on its speed and availability in MATLAB.

A comparison of the images produced by the 23×23 array and the 11×11 array is illustrated in Figure 2. It was determined that an 11×11 array size would be suitable and practical for a physical experiment. Consequently, a new MCNP model was built to accommodate a rectangular 250-gallon water tank with these specifications. The images produced as a function of K are depicted in Figure 3, which clearly shows that image quality significantly degraded below K=60. To enable better comparison of image quality as a function of K, the source shape and location were modified to a larger ring placed in the middle of the collimator.

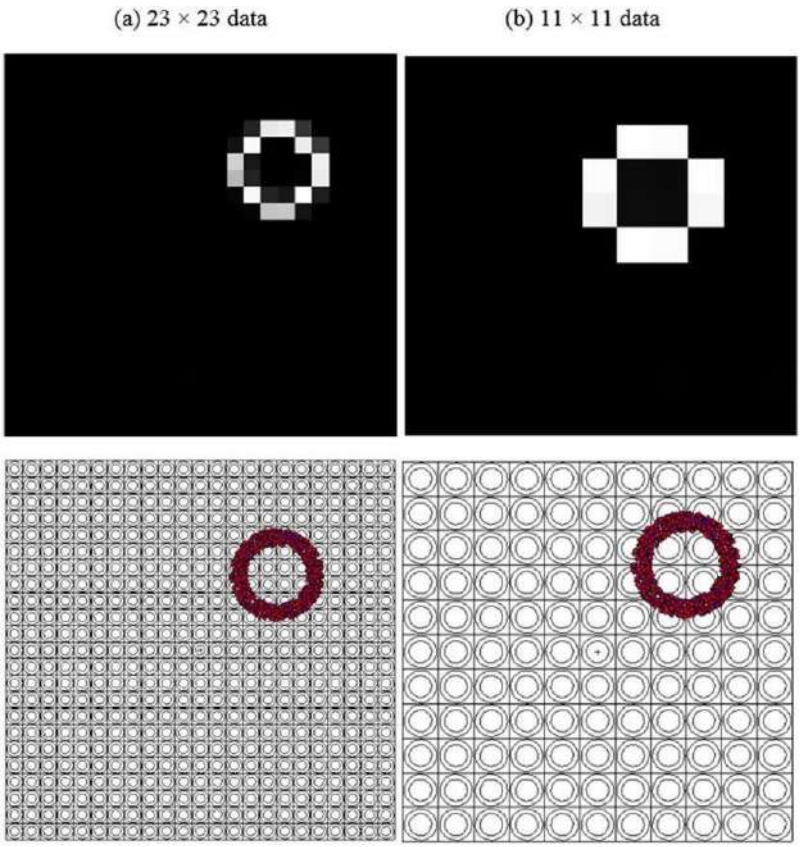

Fig. 2. (a) the image generated using 23×23 simulation data with K=300, and (b) the image produced using 11×11 simulation data with K=100. The presence of a dotted plot in the bottom figures represents the source plot displayed using the MCNP Visual Editor software, providing a top view of the array.

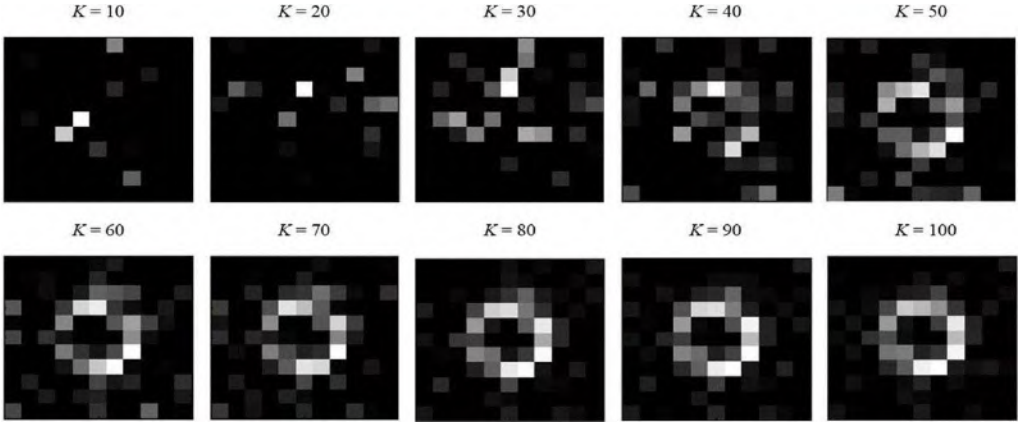

Fig. 3. Images obtained using varying K values during the simulation of a circular source positioned at the core of a rectangular container featuring an 11×11 grid.

In cases where measurements have low count rates, it is expected that there will be a large relative error in b, resulting in significant uncertainties in x. Ideally, determining the minimum K would require multiple reconstructions from various data sets, each containing measurements for 100 configurations. However, the

current simulations serve as a benchmark for the actual experiment. It is anticipated that the source shape or location will start becoming visible with a minimum of K=50 measurements. For final design optimization, multiple data set reconstructions will be implemented in the future.

The MCNP simulations for the rectangular water tank indicate that for a ring source strength of 100 μCi with a ^{252}Cf fission spectrum, the average total number of neutrons crossing the bottom of the tank for all configurations is 2.58 ± 1.6 ns^{-1}. Assuming a neutron background of 0.5 ns^{-1} and a detector efficiency of 0.01, a 10-minute measurement for one configuration would yield an expected average count of 15.5 ± 3.9, with an expected background count of 3.0 ± 1.7. These measurements are statistically distinct from each other within 2σ, indicating that a 10-minute count is sufficient for analysis through the image reconstruction process.

CONCLUSIONS

The results of the MCNP simulations demonstrate that employing an 11×11 array comprising PVC pipes would be both practical and adequate for conducting a physical experiment aimed at reconstructing neutron source images. The simulations revealed that image quality, enabling accurate determination of the neutron source's shape and location, can be achieved with as few as 50% of the total pixels compared to the conventional raster scan method. This breakthrough holds significant value in developing a system that is cost-effective and highly efficient in localizing and identifying the shape of a neutron source.

Notably, this system stands out for its affordability, as it can be constructed using readily available materials such as water, PVC pipes, a water tank, and a water pumping system.

References

[1] Wood, M.L., 2020. Variability and standardization of quantitative imaging. *Investigative Radiology*, *55*(9), pp.617-618.

[2] Li, X. and Voroninski, V., 2013. Sparse signal recovery from quadratic measurements via convex programming. *SIAM Journal on Mathematical Analysis*, *45*(5), pp.3019-3033.

[3] Candès, E.J., 2006, August. Compressive sampling. In Proceedings of the international congress of mathematicians (Vol. 3, pp. 1433-1452).

[4] Candès, E.J. and Wakin, M.B., 2008. An introduction to compressive sampling. IEEE signal processing magazine, 25(2), pp.21-30.

[5] Pope, G., 2009. Compressive sensing: A summary of reconstruction algorithms (Master's thesis, ETH, Swiss Federal Institute of Technology Zurich, Department of Computer Science).

[6] Pamula, V.R., Van Hoof, C., Verhelst, M., Pamula, V.R., Van Hoof, C. and Verhelst, M., 2019. Introduction to Compressive Sampling (CS). Analog-and-Algorithm-Assisted Ultra-low Power Biosignal

Acquisition Systems, pp.33-53.
[7] Anuar, N., Marianno, C. and McClarren, R.G., 2020. Employing MCNP to optimize experimental design for compressed sensing neutron source imaging. *Nuclear Instruments and Methods in Physics Research Section A: Accelerators, Spectrometers, Detectors and Associated Equipment*, *954*, p.161446.
[8] Garza, D.T., 2019. Design and Analysis of a Spatial Neutron Modulator for Neutron Imaging via Compressive Sensing.
[9] Vila, J.P. and Schniter, P., 2014. An empirical-Bayes approach to recovering linearly constrained non-negative sparse signals. *IEEE Transactions on Signal Processing*, *62*(18), pp.4689-4703.
[10] Candes, E. and Romberg, J., 2005. l1-magic: Recovery of sparse signals via convex programming. URL: www. acm. caltech. edu/l1magic/downloads/l1magic. pdf, 4(14), p.16.
[11] Chen, J., Richard, C., Bermudez, J.C.M. and Honeine, P., 2011. Nonnegative least-mean-square algorithm. IEEE Transactions on Signal Processing, 59(11), pp.5225-5235.
[12] Myre, J.M., Frahm, E., Lilja, D.J. and Saar, M.O., 2017. TNT-NN: a fast active set method for solving large non-negative least squares problems. Procedia Computer Science, 108, pp.755-764.
[13] Foucart, S. and Koslicki, D., 2014. Sparse recovery by means of nonnegative least squares. IEEE Signal Processing Letters, 21(4), pp.498-502.

ICNST 2024
International Conference on Nuclear Science and Technology
6- 8 MAY 2024 | Isfahan, Iran

Determining the appropriate dose of gamma irradiation for the sterilization of Cannabis sativa L. seeds (Paper ID : 1256)

Ghahramani M.R.*, Azarbahram F., Tohidi T., Salamat bakhsh M.H, Yeghaneh M.

Northwest Research Complex (Bonab), Radiation Application Research School, Nuclear Science and Technology Research Institute, Tehran, Iran

Abstract

Considering that the permission to import seeds of some medicinal plants containing narcotic drugs to most countries relies on ensuring the sterility and non-sprouting of these plants, this research investigated the effects of different doses of gamma irradiation on the physiology and germination of cannabis seeds for sterilization. Gamma irradiation using Cobalt 60 at a rate of 60 Gy/minute with 13 levels of gamma irradiation (0, 30, 60, 90, 120, 150, 180, 240, 300, 360, 500, 600, and 900 Gy) was utilized. The samples were completely randomized with 3 replications in each sample. The results indicated that gamma irradiation affects some characteristics of seed germination. Doses above 120 Gy significantly reduced the number of healthy seedlings compared to other levels, with the average stem length decreasing to 1/3 of healthy ones. It was found that germination percentage was not a suitable criterion for determining the sterilization dose, as most seeds germinated after irradiation but died shortly after. A dose of 150 Gy was identified as the most suitable for sterilizing cannabis seeds.

Keywords: Radiation sterilization, Cannabis Irradiation, Dose determination

INTRODUCTION

Cannabis, with the scientific name Cannabis sativa L., is an herbaceous, annual plant belonging to the Cannabacea family. The seeds of this plant have a significant amount of oil and unsaturated fatty acids, and the fiber in it is used in paper and textile industries. Tetrahydrocannabinol and cannabidiol are among the most important cannabinoid compounds of this plant, which are of great importance due to their known medicinal properties, but due to legal obstacles to planting, it has not yet found its main place among plants, especially in Iran. This plant usually has two bases and the male and female flowers of this plant are located on separate bases and generally the male flowers appear a little earlier than the female flowers. Of course, there are also single base and hermaphrodite figures. This plant has clawed leaves with five to seven serrated leaflets and has different varieties and shapes with a strong and pleasant smell and its height reaches 1 to 3 meters. This plant is spring and is cultivated in different regions from early to mid-spring if the weather conditions and temperature are favorable. The highest water requirement for this plant is in the rapid growth stage (the stage of the emergence of five leaves until the production of buds), which naturally absorbs the highest amount of nutrients, and in this stage, it requires a large amount of nutrients and high temperature. After water, the type of soil and the method of land preparation are the factors that determine the yield. One of the methods that can cause non-germination or sterilization of seeds with low cost is irradiation with gamma rays. Although gamma ray irradiation has wide applications in agriculture, medicine and industry, its application in the field of new plant breeding has been limited due to reasons such as not knowing the appropriate dose for plants. In order to succeed in the sterilization of seed plants, the appropriate dose must be determined first. To determine the best radiation dose, two points should be considered, first, the applied dose should not be so high that it kills the plants, and next, it should be selected so that the irradiated seeds do not reach the flowering stage. Gamma rays are among the ionizing rays that lead to the production of free radicals in the cell. Depending on the level of radiation, free radicals can lead to morphological, anatomical, biochemical, physiological changes or damage to important cell components. These effects include changes in the plant's cellular structure and metabolism (for example, expansion of the thylakoid membrane, changes in the efficiency of photosynthesis and the functioning of the antioxidant system, and the accumulation of phenolic compounds). Irradiation of plant seeds through the production of free radicals and oxidation of atoms causes disturbance in protein synthesis and gas exchange and disruption of hormonal balance and on the other hand it affects the activity of enzymes. Previous studies show that these rays cause inhibition of metabolic pathways, changes in growth and development, and damage to DNA. Reactive oxygen species in very small amounts lead to the expression of basic genes inside the plant cell, but due to the induction of ionizing radiation, the amount of reactive oxygen species increases and the balance and homeostasis of the

cells are disturbed. This disturbance leads to the reduction of electron transfer in the electron transfer chain, which is caused by the reduction of the reducing agent in the Calvin cycle. This situation also subsequently leads to photo-oxidation by increasing the flow of electrons towards oxygen and producing hydrogen peroxide and hydroxyl radicals. These active reactive species are responsible for causing damage to photosynthetic organs, the effect of mutagenic treatments is generally measured by parameters such as germination percentage, seedling length and seed germ. The percentage of germination is not a good measure to determine the dose effect, because most of the seeds germinate after irradiation, but they die after some time.

EXPERIMENTAL

In this study, cannabis seeds were prepared from Afghanistan and then divided into 13 groups as follows:

1- Control group

2- The seeds that were irradiated with the dose of 30 Gy.

3- The seeds that were irradiated with the dose of 60 Gy.

4- The seeds that were irradiated with the dose of 90 Gy.

5- The seeds that were irradiated with the dose of 120 Gy.

6- The seeds that were irradiated with the dose of 150 Gy.

7- The seeds that were irradiated with the dose of 180 Gy.

8- The seeds that were irradiated with the dose of 240 Gy.

9- The seeds that were irradiated with the dose of 300 Gy.

10- The seeds that were irradiated with the dose of 360 Gy.

11- The seeds that were irradiated with the dose of 500 Gy.

12- The seeds that were irradiated with the dose of 600 Gy.

13- The seeds that were irradiated with the dose of 900 Gy.

The seeds, with the exception of the control sample, were irradiated using the portable seed products irradiation system located in Salimi Industrial Town at the specified doses. Next, the treated seeds were transported to the laboratory along with the control seeds and planted in separate growth beds. To ensure consistent results, 72 seeds from each group were planted in each growth bed. The seeds were monitored daily, and consistent light and temperature conditions were maintained for germination.

Results and discussion

After one month, the results were checked and listed in the Table 1 and Figure 1.

Table 1. Mean comparison of 72 cannabis seeds in each sample at varying doses

Sample	No. Of sprouts	healthy seedlings No.	Plastid seedlings No.	Leaflets No.	Stem length
Control sample	68	65	3	6	15
30 Gy	60	17	43	6	11.3
60 Gy	55	11	44	6	8
90 GY	60	25	35*	4	6.8
120 Gy	56	18	38*	4	5.9
150 Gy	58	2*	56*	4	4
180 Gy	64	5*	59*	4	3.3
240 Gy	47	1*	46	2	3*
300 Gy	48	0*	48	2	2.2*
360 Gy	46	0*	46	2	2*
500 Gy	44	0*	44	2	2*
600 Gy	50	2*	48	2	2.5*
900 GY	46	2*	44	2	2.4*

* Significant at $p < 0.05$ level vs. non-irradiated seeds (control).

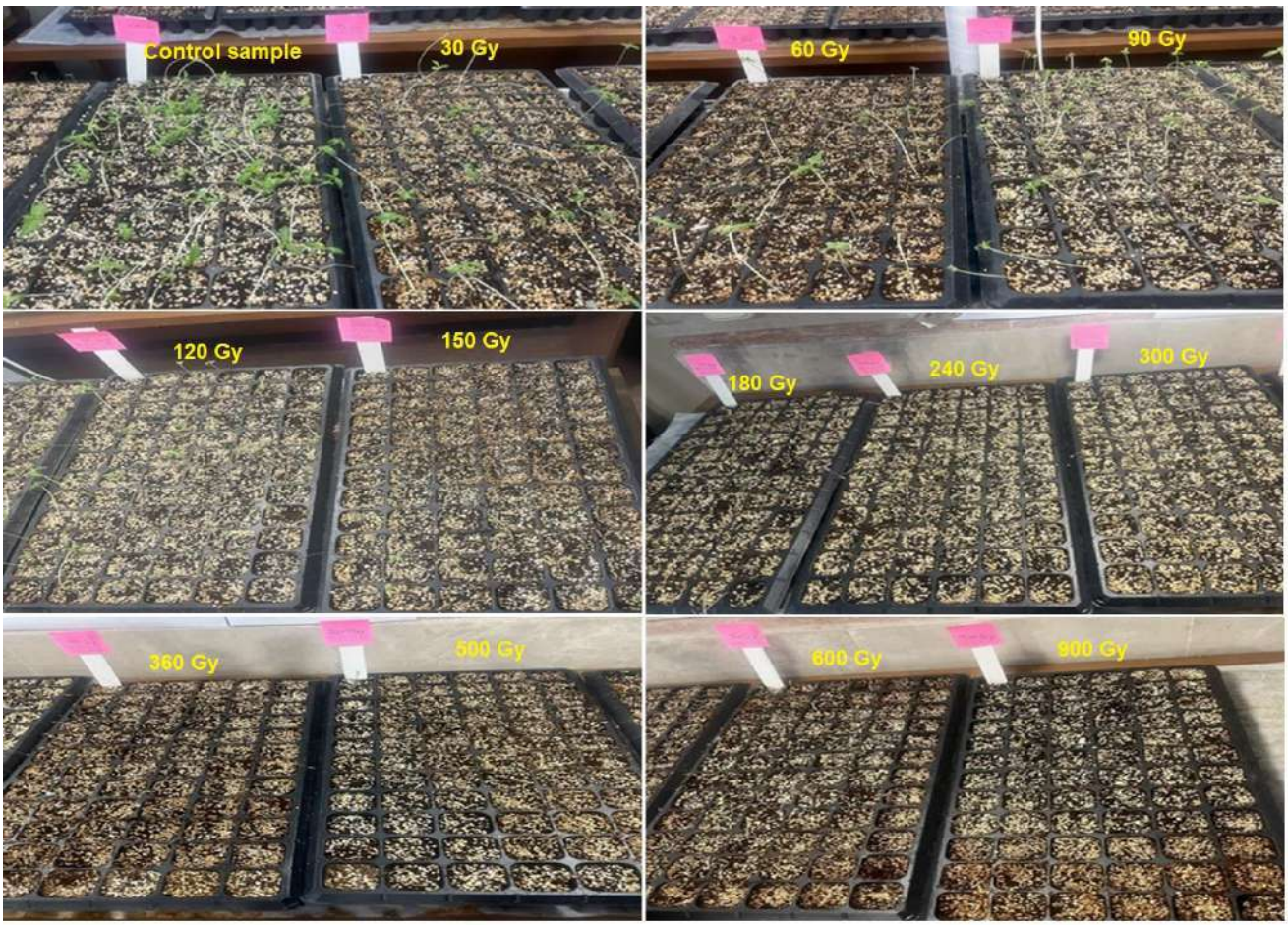

Fig. 1: Images related to the results of cannabis growth in both the control group and the treatment groups

Conclusions

In this study, the impact of gamma radiation at varying doses on the physiology and germination of cannabis seeds for sterilization purposes was examined. The findings revealed that exposing cannabis seeds to gamma rays alters certain germination characteristics. Specifically, doses exceeding 120 Gy notably decreased the number of healthy seedlings compared to lower doses. Additionally, the average stem length decreased by more than 1/3.

References

[1] Alizadeh .A, et al. Effect of seed irradiation with low dosed of gamma ray on some seedling emergence and morphological parameters of two species of Bromus tomentellus and Agropyron elongatum. *Watershed Management Research Journal*, 2015; 28(1): 10-16. doi: 10.22092/wmej.2015.107043

[2] Hazekamp A. Evaluating the Effects of Gamma-Irradiation for Decontamination of Medicinal Cannabis. Front Pharmacol. 2016 Apr 27;7:108. doi: 10.3389/fphar.2016.00108. PMID: 27199751; PMCID: PMC4847121.

[3] Majumdar, C.G.; ElSohly, M.A.; Ibrahim, E.A.; Elhendawy, M.A.; Stanford, D.; Chandra, S.; Wanas, A.S.; Radwan, M.M. Effect of Gamma Irradiation on Cannabinoid, Terpene, and Moisture Content of Cannabis Biomass. *Molecules* **2023**, *28*, 7710. https://doi.org/10.3390/molecules28237710

Irradiation of agricultural products utilizing self-shielded gamma irradiator systems (Paper ID : 1271)

M. Monshizadeh[1], A. Soleymani[1], M. Yahaghi[1], A. Farrokhizadeh[1], E. Javadi[1], M. Khosravani[1], H. Sayyar[1], M. S. Islami[1], A. Salehizadeh[1], H. R. Saravani[1], R. Roozehdar Mogaddam[1], O. Haghighi[1], A. Taheri[1,2*] and S.P. Shirmardi[1,2]

[1]*Iran Radiation Application Development Company (IRAD Co.) – Atomic Energy Organization of Iran, Tehran – I.R. of Iran, PO Box: 14395-836*

[2]*Radiation Application Research School, Nuclear Science and Technology Research Institute, Tehran, Iran, PO Box: 14395-836*

Abstract

To enhance the longevity and minimize wastage of agricultural products, an effective method involves the use of gamma irradiation to eliminate harmful microorganisms, insects, and pests. To facilitate this process, a self-shielded gamma irradiation system "IRAD-0113-01" was designed and constructed specifically for treating grains and legumes using ^{60}Co radioactive sources with an activity level of 50 kCi. The system operates by feeding agricultural products in bulk through an input funnel equipped with a conveyor belt. Under the influence of gravitational force, the products are guided through a spiral path, ultimately leading them into the cask or irradiation chamber for exposure to gamma radiation. The mechanical structure of the system is robust, capable of withstanding loads of up to 140kN.

A notable feature of this system is the unique design of the entrance chamber, which takes the form of a step rather than a spiral. This innovative design significantly reduces the amount of lead material required for effective shielding by approximately 2 tons when compared to a similar irradiation system developed in Hungary. The system demonstrates efficient output, with a mass flow rate of around 1 ton per hour for wheat when irradiated with a dose of 200 Gy. The achieved dose uniformity ratio of 2 meets the acceptable standards for industrial radiation applications, ensuring consistent and reliable results. By utilizing this self-shielded gamma irradiation system, the shelf life of agricultural products can be extended, minimizing the risk of spoilage and reducing wastage. Furthermore, the eradication of harmful contaminants contributes to improved food safety and quality, benefiting both producers and consumers alike.

In this paper, permissible dose limit based on the existing standards were reviewed. The simulation and experimental results show that all the parts of the self-shielded irradiation system have a gamma dose of less than $20\mu Sv/h$, which is fully compliant with the ANSHI standard and therefore makes the system suitable for operation.

Keywords: Irradiation, Gamma-ray, Self-shielded system, ^{60}Co, Dose uniformity ratio.

INTRODUCTION

Nowadays, irradiation is one of the methods of preserving food and agricultural products. Using gamma rays is one of the most important and widely used food irradiation techniques. Gamma rays are electromagnetic radiation from excited nuclei of ^{60}Co or ^{137}Cs. Gamma radiation, the cheapest type of radiation, is essential in preserving food and agricultural products. Irradiation with gamma rays is a physical method of food processing [1].

Food or agricultural products are exposed to ionizing radiation for a certain period of time. The goals of irradiation include increasing food durability, reducing microbial, fungal, and parasitic contamination, reducing food product waste, and preventing contamination of food products and the environment. In agriculture, one of the most important reasons for using irradiation is to fight insect infestation and reduce the waste of grains and legumes. These wastes are around 5-10% worldwide, while in countries with hot climates, these wastes can reach up to 50%. The most widespread pest control method uses chemical pesticides for grains and legumes. However, this pest control method leads to environmental pollution and pesticide residues in seeds and requires special measures for the safety and health of operators. Irradiation with gamma rays can eliminate insects, parasites, and pathogens from agricultural products [2]. The use of radiation means that disinfectants, which are not only toxic but also cause cancer in the long run, are not used. In other words, irradiation of foods with relatively low doses causes the killing or sterilization of all the different developmental stages of common grain pests, even the eggs inside the seeds. Dried fruits, vegetables, and nuts are always subject to insect attack. Some of these products, especially fruits, can only be disinfected using radiation, and chemical methods or physical agents cannot be used.

Among the problems that using these pesticides brings, we can point out the resistance of pests to pesticides, environmental pollution, remaining phosphine residues in seeds, and as a result, causing poisoning in humans and other mammals, the unaffordability of using these disinfectants as well as limiting the use of methyl bromide since 2005 in developed countries and since 2015 in developing countries. Considering these problems and based on the approval of the Environmental protection agency and United Nations Standing Committee on Nutrition, food irradiation can be a suitable alternative to pesticides. Also, irradiation in low doses prevents the germination of potato, onion, garlic, ginger, and chestnut tubers. These conditions have led to the development of radiation methods to eliminate grain pests, which requires the determination of appropriate radiation doses. Also, obtaining a license from public health institutions is needed for the industrial use of the irradiation process [3]. Research in eliminating grain pests with radiation has been carried out since the 1950s. These studies began in 1955 at the Scientific Research Institute of Grains and Agricultural Products of the USSR Ministry of Interior (VNIIZ) in collaboration with the Institute of Biophysics of the USSR Academy of Sciences. After the Soviet Union, in 1963, the United States of America approved the irradiation of wheat and its products with a dose of 20-50 krads. Following these two leading countries, grain irradiation is carried out in Ukraine, Brazil, Thailand, Serbia, China, India, Pakistan, Japan, Argentina, Belgium, Bulgaria, Chile, France, and Poland [1,2].

The Iran Radiation Application Development Company (IRAD Co.) has carried out the design and construction project of a gamma self-shielded radiation system. The gamma self-shielded radiation system, model IRAD-0113-01, is a grains and legumes irradiation system with a 50-500 Gy dose. This system can irradiate grains and legumes in low doses, cause disinfection and control the germination of products. It can also reduce storage pests and increase product durability by reducing microbial contamination and eliminating microorganisms that infect and destroy agricultural products. This system can irradiate legumes such as peas, cobs, lentils, beans, corn, wheat, and rice. One can also use the portable gamma irradiation system for dry fruits such as walnuts, almonds, pistachios, hazelnuts, etc. In this paper, the limits of the permitted dose based on the relevant standards will be examined.

MATHERIALS AND METHODS

To irradiate grains and legumes, first, these products enter the stepped spiral from the upper part of the system (the funnel) and then the irradiation chamber. The products are irradiated while passing through the chamber and exit from the system's lower part (product exit point). In addition to the product's characteristics (density, type of product, etc.), the dose received by the product depends on the duration of the product's presence (speed of product passing through the irradiation chamber) in the irradiation chamber. This is done by Mardon (spiral) at the place of product exit. The rotation speed of Mardon determines the output flow rate of the product inside the system, and by changing it, the absorption dose of the product can be changed. the complete schematic view of the gamma self-shielded radiation system is shown in Figure 1. The type of design is such that it can withstand 140 kN loads. Also, a step ladder was used in order to reduce the amount of lead by at least 2 tons.

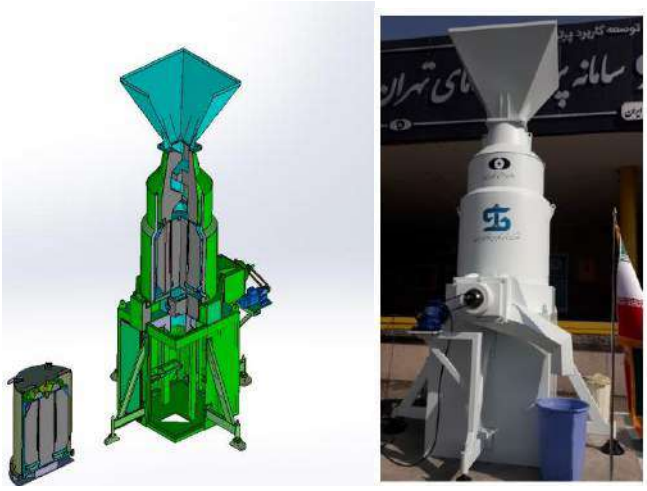

Fig. 1. Schematic view of the gamma self-shielded radiation system.

This system is a gamma radiation device of self-maintaining type in a dry tank. This device includes ^{60}Co radiation sources of the self-shielded chamber type, and the maximum activity of the system is limited to 1.85 PBq. The sources used in this system are supplied in standard dimensions and specific activity by suppliers from different countries with this technology. In the Gamma 36 self-shielded system, there is a location to place source pencils, which will be arranged based on the activity of the sources and the dose distribution in the radiation chamber. A typical ^{60}Co source pencil is sealed with a zirconium sheath in a stainless steel sheath and typically has an activity of about 8,000 to 12,000 Ci per pencil. Each pencil has a length of 45.2 cm and a diameter of 1.1 cm. Pencils are placed in the radiation chamber equipped with a special lead shield. The inner diameter of the steel chamber (where products pass through and are irradiated) is 300 mm, and the diameter of the ring on which the pencils are located is 304 mm. Due to the symmetrical arrangement of the radiating rods, a dose space with cylindrical symmetry is obtained.

RESULT AND DISCUSSION

The design of the gamma self-shielded irradiation system is based on shielding calculations with the help of Monte Carlo codes to make sure that the dose rate does not exceed the permissible value provided in the standard and to measure the uniformity of the dose inside the radiation chamber. The arrangement of pencils is one of the effective factors for creating symmetry and standard dose uniformity. Other factors such as activity and density of products are effective in creating standard dose uniformity ratio. Figure 2 shows the dose distribution contour plot for the product density of 1 g/cm^3 and 18 ^{60}Co source pencil placed in the irradiation cask.

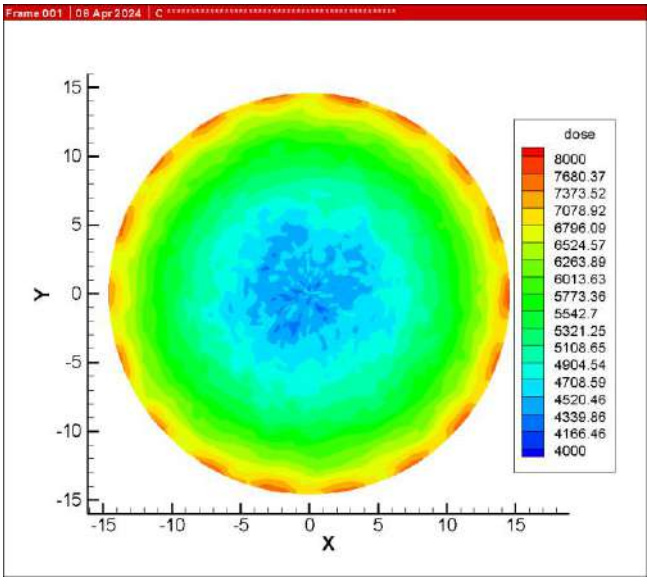

Fig. 2. dose distribution contour plot inside the cask.

According to the calculations and considering that the product passes through the middle of the chamber, a special arrangement should be made for the uniformity of the dose with an activity of 50 kCi and dose ratio be obtained 2.

the evaluation and calculation of the distribution of the gamma dose rate of biological shielding of the gamma self-shielded radiation system are carried out according to the Permissible dose limits in ANSI/HPS N43.7-2018 [4,5].

Different parts of the system are made of different materials, including lead as biological shield, SS-316L stainless steel for the source chamber, upper entrance funnel, vertical spiral path, typical steel for the outer walls of the biological shield, and the device, screws, bases and primary columns of the device and shafts. During irradiation, the irradiation chamber, the vertical spiral path, the carriage, and the Mardon are filled with grains and legumes.

The limits of the allowed dose and the equivalent dose rate for different modes of operation of radiation systems with a dry source maintaining chamber are stated in the ANSI/HPS N43.7-2018 standard. As shown in figure 3, we will investigate the dose of the gamma self- shielded system at a distance of 5 cm from the surface. Table 1 shows the dose for different areas of the gamma self-protection system.

Fig. 3. Dosimetry of different regions of the gamma self- shielded system

According to the experimental dose measurement, the allowed limits in the system's design have been met according to the gamma self-shielded radiation standard, and the gamma dose rate is within the allowed limits.

Table 1. Dose rate in different positions of the system

Position	Photon dose rate [µSv/h]
Above the system On the vertical spiral inlet	1.31
In front of the end of the Mardon shaft	0.28
Behind the cover of the location of the carriage and Mardon	15.62
Under the table and next to the on/off lead cylinder	20.10
	18.75
In front of the product outlet	15.02

CONCLUTION

ANSI/HPS N43.7-2018 standard titled "Design and safe use of dry self-shielded radiation systems" has been used in the design, construction and installation of this gamma self-shielded radiation system. The said standard is used for self-shielded radiation systems including closed gamma or beta sources.

It is worth mentioning that the radioactive springs of this device are loaded after transporting the device and installing it in the place, and the device will never be transported together with the source, so the design and construction of this device is not covered by the regulations of safe transportation of radioactive materials. The permissible dose limits are stated in the ANSI/HPS N43.7-2018 standard, and the equivalent dose rates are different in various modes of irradiation within the cask. According to the permissible limits in the standard, the standard dose rate for operation mode must be less than $20\mu Sv/h$ According to the above table and the simulation results for the operating mode of the gamma self-shielded radiation system, the permissible limits have been observed in the design of the said system and the gamma dose rate is within the permissible limits.

References

[1] Piri, I., Babayan, M., Tavassoli, A., & Javaheri, M. (2011). The use of gamma irradiation in agriculture. African Journal of Microbiology Research, 5(32), 5806-5811.

[2] Jan, S., Parween, T., Siddiqi, T. O., & Mahmooduzzafar. (2012). Effect of gamma radiation on morphological, biochemical, and physiological aspects of plants and plant products. *Environmental Reviews*, *20*(1), 17-39.

[3] Piri, I., Babayan, M., Tavassoli, A., & Javaheri, M. (2011). The use of gamma irradiation in agriculture. African Journal of Microbiology Research, 5(32), 5806-5811.

[4] McCaffrey, J. P., Shen, H., Downton, B., & Mainegra-Hing, E. (2007). Radiation attenuation by lead and nonlead materials used in radiation shielding garments. *Medical physics*, *34*(2), 530-537.

[5] American National Standards Institute. Sampling and monitoring releases of airborne radioactive substances from the stacks and ducts of nuclear facilities. McLean, VA: Health Physics Society; ANSI/HPS N13.1-2018.

ICNST 2024
International Conference on Nuclear Science and Technology
6- 8 MAY 2024 | Isfahan, Iran

Simulation and Validation of a 6 MV Elekta Compact Accelerator Head (Paper ID : 1276)

Karimi-Shahri K.[1*]
[1]*Department of Physics, Faculty of Science, University of Birjand, Birjand, Iran*

Abstract

The purpose of this study was to simulate the 6 MV Elekta Compact accelerator head installed in Iran- Mehr radiotherapy and oncology hospital (Birjand-Iran) using MCNPX2.6 Monte Carlo code. The simulation aimed to validate the accuracy of the model by comparing the simulated results with the measured percent depth dose (PDD) at 10 ×10 cm^2 field and dose profile at 10 cm depth, which were obtained using a water phantom and Baldwin-farmer ionization chamber provided by PTW company. The main components of the linac's head, including the target, primary collimator, flattening filter, and secondary collimators, were simulated. A phase space file generation process involved the using of SSW (surface source write) and SSR (surface source read) cards to capture the particle source information. In this case, the horizontal plane was positioned 100 cm below the tungsten target. A significant number particle, specially 10^7 particles (photons and electrons), that traversed the surface were then recorded in a binary phase space file for use as an SSR card. The deposited energy of photons and electrons was recorded using a mesh tally (type 3) to calculate the PDD and beam dose profile. The model's accuracy was evaluated by comparing the simulated results with the measured data, using relative error as the evaluation metric. The optimum energy of the initial electron beam was determined by analyzing the PDD curves. The full-width half-maximum (FWHM) of the electron source was adjusted based on the dose profile curves. After computing the PDD curves for electron beam energies ranging from 5.5 to 6.5 MeV with a step of 0.1 MeV, an electron energy of 5.8 MeV was determined to be the best match. To obtain the optimum FWHM, the profile dose curves were analyzed by varying the FWHM from 0.4 to 0.5 cm with a step of 0.01 cm. The optimum FWHM value of 0.44 cm was obtained. Different field sizes were simulated by adjusting the secondary collimators, and rotation matrices were obtained and used in the TRCL card. The simulated field sizes included 8×8, 10×10, 12×12, 15×15, 20×20, 25×25, 30×30, and 40×40 cm^2.

Keywords: 6 MV linear accelerator, Elekta Compact, percent depth dose, MCNPX Monte Carlo code, Dose profile.

INTRODUCTION

Radiotherapy is a crucial component in treating over 50% of cancer types and is utilized in 40% of cancer patients alongside other treatments [1]. In external radiotherapy, linear accelerator (linac) devices are

commonly used to generate beams from a source positioned at a specific distance from the body [2]. The choice of accelerator with a known energy is influenced by factors such as tumor depth, extent, and location [3]. Accurate treatment planning is essential for ensuring a reliable dose distribution, and Monte Carlo codes are valuable tools in this process. The Monte Carlo method is widely recognized for its accuracy in predicting radiation fields produced by linacs, offering valuable data that may be challenging to measure directly [4,5]. Although the Monte Carlo method can be time-consuming, improvements in computer technology and variance reduction techniques are enhancing its feasibility for dose calculations [6,7]. Each type of accelerator has unique beam properties influenced by component design and material variances [8]. Even identical accelerators may exhibit differing beam characteristics due to adjustments made during field installation [9]. Achieving precise alignment between modeled beam properties and those of the actual reference accelerator can be challenging and time-consuming [10]. The final beam output is influenced by the geometric parameters of components, the materials utilized, and the initial electron source parameters within the model. [11]. This linac has been simulated by several Monte Carlo codes, such as GATE [12], PENELOPE [13], BEAMnrc/EGSnrc [14,9], and GEANT4[15]. This paper focuses on establishing a Monte Carlo model of a 6 MV Elekta Compact accelerator head at Iran- Mehr radiotherapy and oncology hospital in Birjand, Iran, using the MCNPX2.6 [16] program. The alignment of the model beam with the actual beam is confirmed by analyzing the percentage depth dose (PDD) and dose profile evaluations.

RESEARCH THEORIES

The head of Elekta Compact linac was simulated using the MCNPX2.6.0 code [16]. Figure 1 represents a 3D view of the simulated components. The main simulated components of linac's head included target, primary collimator, flatting filter, and secondary collimators. Also, a cubic water phantom with a dimension of $62.5\times62.5\times51.5$ cm^3 was simulated at a distance of 100 cm SSD. A phase space file generation process involved the utilization of SSW and SSR cards to capture the particle source information. In this case, the horizontal plane was positioned 100 cm below the tungsten target. A significant number particle, specially 10^7 particles (photons and electrons), that traversed the surface were then recorded in a binary phase space file for use as an SSR card. The energy cut-off was defined as 0.5 and 0.1 MeV for electron and photon, respectively. Electrons stopped by target, a bremsstrahlung X-ray is generated. This X-rays spectrum can be considered as a photon source that its spectrum changes through different parts of the accelerator head. Two physics cards (PHYS: E and PHYS: P) were used to control bremsstrahlung X-rays. Different field sizes

were simulated by adjusting the secondary collimators, and rotation matrices were obtained and used in the TRCL card.

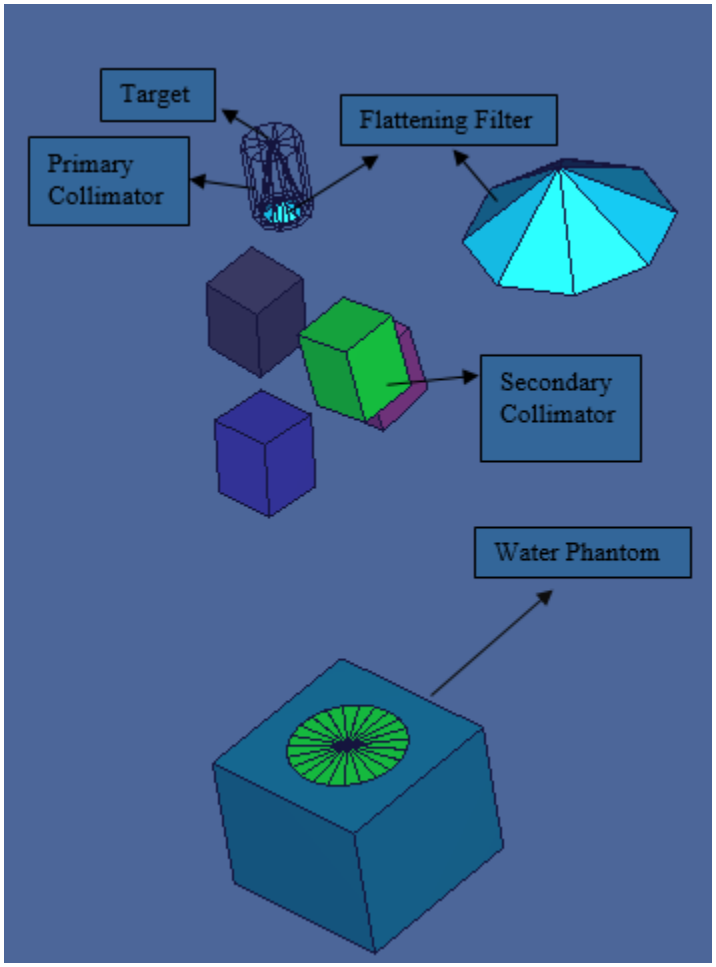

Fig. 1. 3D view of simulated linac of the 6 MV, Elekta Compact.

EXPERIMENTAL

The optimum energy and radial intensity of the incident beam were obtained through matching the MCNPX derived PDD and dose profile data with those obtained by experimental measurements. PDD relates the absorbed dose at any depth (D_d) to a depth at which the absorbed dose is a maximum(D_0) [17]. PDD was calculated based on equation 1.

$$PDD = \frac{D_d}{D_0} \times 100 \qquad (1)$$

The variation of dose occurring on a line perpendicular to the central beam axis at a certain depth is known as the dose profile. To calculate the PDD and dose profiles, mesh tally (type 3) was used to record the deposited energy of photons and electrons within cube with dimensions 2×2×0.2 cm^3. The obtained date converted to suitable format and then PDD was calculated.

Measurements were performed using a water phantom and Baldwin-farmer an ionization chamber provided by PTW company at 10×10 cm^2 field for dose profile PDD at 10 cm depth. The PDD curves of 8×8, 10×10, 12×12, 15×15, 20×20, 25×25, 30×30, and 40×40 cm^2 were measured.

All simulations were done by a server system with the following specifications: Intel(R) Xenon(R) (Intel Corp., Santa Clara, CA), CPU 2.70 GHz and 2.69 GHz (two processors), 70.00 GB RAM, and Windows7 (64 bit) (Microsoft Corp., Redmond, WA). For the calculations, 2×10^9 particles were tracked to decrease the statistical uncertainty to less than 3%.

Results and discussion

Determine the Incident Electron Energy through PDD Curves

Although the nominal energy of the device is known as 6 MV, however, the characteristics of the primary electron beam for each device must be determined precisely. Studies have shown that the flux of the initial electron source follows a Gaussian distribution [18] that the mean energy and FWHM should be determined. By using the PDD curve, the optimal energy can be identified as it plays a significant rule in the production of bromstrahlung X-rays influences the absorbed dose value in the phantom. Therefore, the PDD was obtained for an energy range from 5.5 to 6.5 with a step of 0.1 at 10×10 cm^2 field, and then compared with the measured values in each case. The percentage of relative difference was calculated at different depths based on equation 2.

$$^{2}\ RD = \frac{D_i(measurment) - D_i(MC)}{D_i(measurment)} \times 100 \qquad (2)$$

The best energy with the smallest relative difference was determined to be 6.1 MeV. Figures 2a and 2b show the PDD curve for energy 6.1 MeV(2a) and the corresponding relative difference(2b), respectively.

[2] Relative Difference(RD)

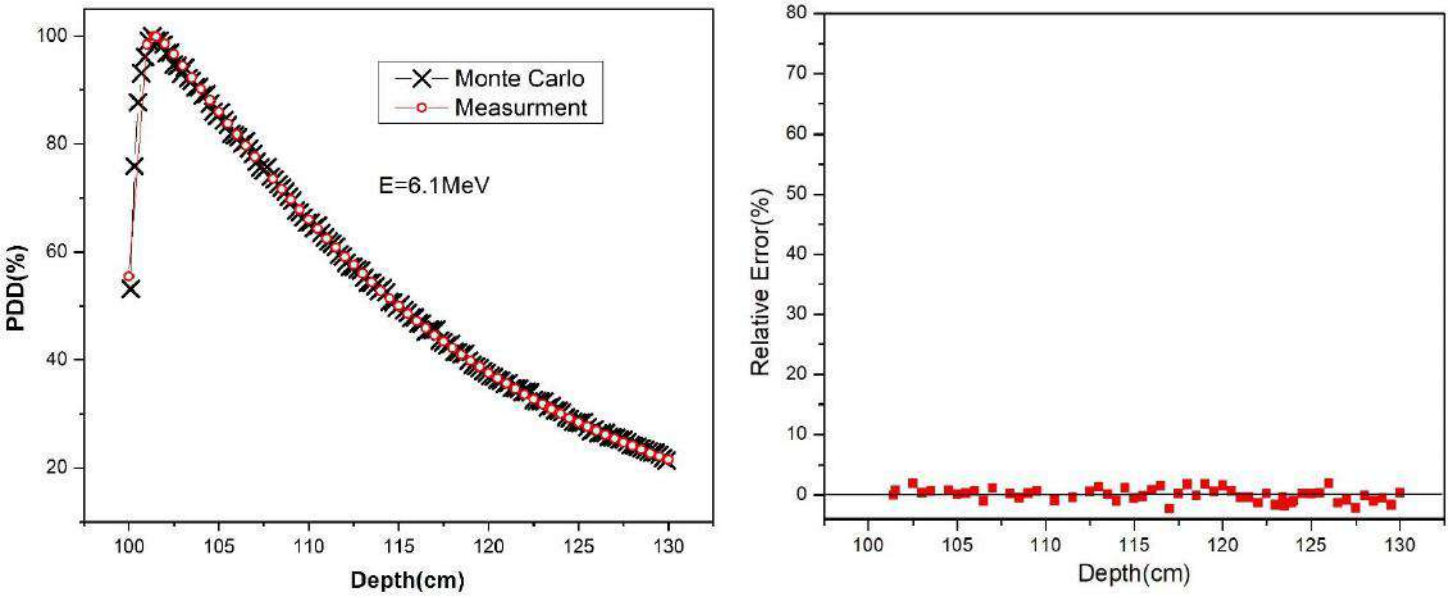

Fig. 2. PDD(a) and relative error (b) curves for 6.1 MeV energy

Determine the FWHM of the Incident Electron Source

The FWHM of the electron source was determined using the dose profile curve. The dose profile curves were calculated with a change in the FWHM parameter from 0.1 to 0.2 with a step of 0.01 for a constant energy value of 6.1 MeV. At each step, the calculated data were compared with the experimental data. The dose profile data was calculated and measured at a depth of 10 cm in the phantom, considering a field size of 10×10 cm^2 and a SSD of 100 cm. Analysis revealed the optimal FWHM value to be 0.44 cm. Figure 3 illustrates the comparison of dose profile percentage obtained from measurements and MC calculations for an energy of 6.1 MeV and FWHM of 0.44 cm. As seen in the figure, the dose profile is formed from a flat region equal to the field dimensions and at the field edges where the dose change gradient is high in that area. The study indicated that varying FWHM values have minimal effect on the flat region but signifacantly affect the penumbra region at the field edges. This finding aligns with previou sresearch by Lu[9]. With an increase in FWHM, the dose gradient decreased at the field edges.

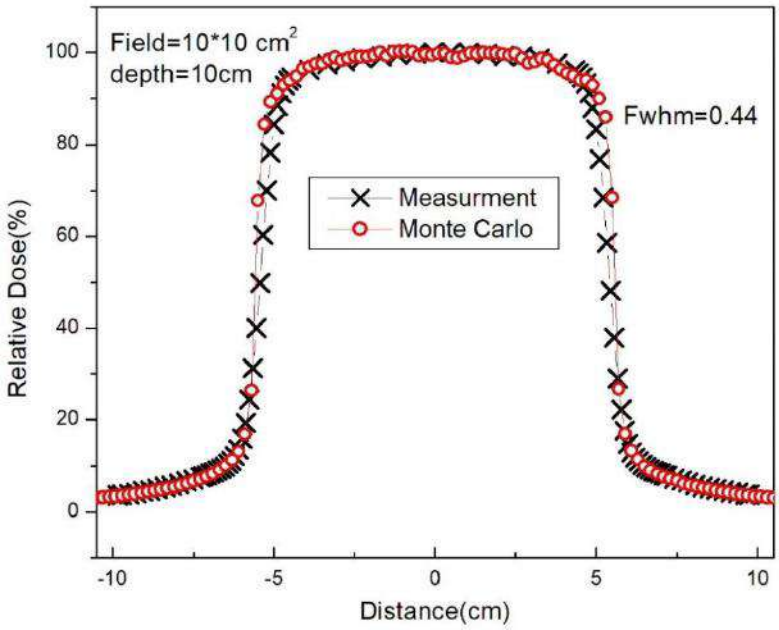

Fig. 3. the percentage of dose profile obtained from measurements and MC calculations for energy of 6.1 MeV and FWHM of 0.44 cm

The PDD curves for different fields

Using secondary callimators, different fields were adjusted, and PDD for different fields was calculated. Figures 4a and 4b show comparing the results of PDD with the measured data in the fields including 8×8, 10×10,12×12, 15×15cm^2 (4a), 20×20 ,25×25, 30×30, and 40×40 cm^2 (4b).

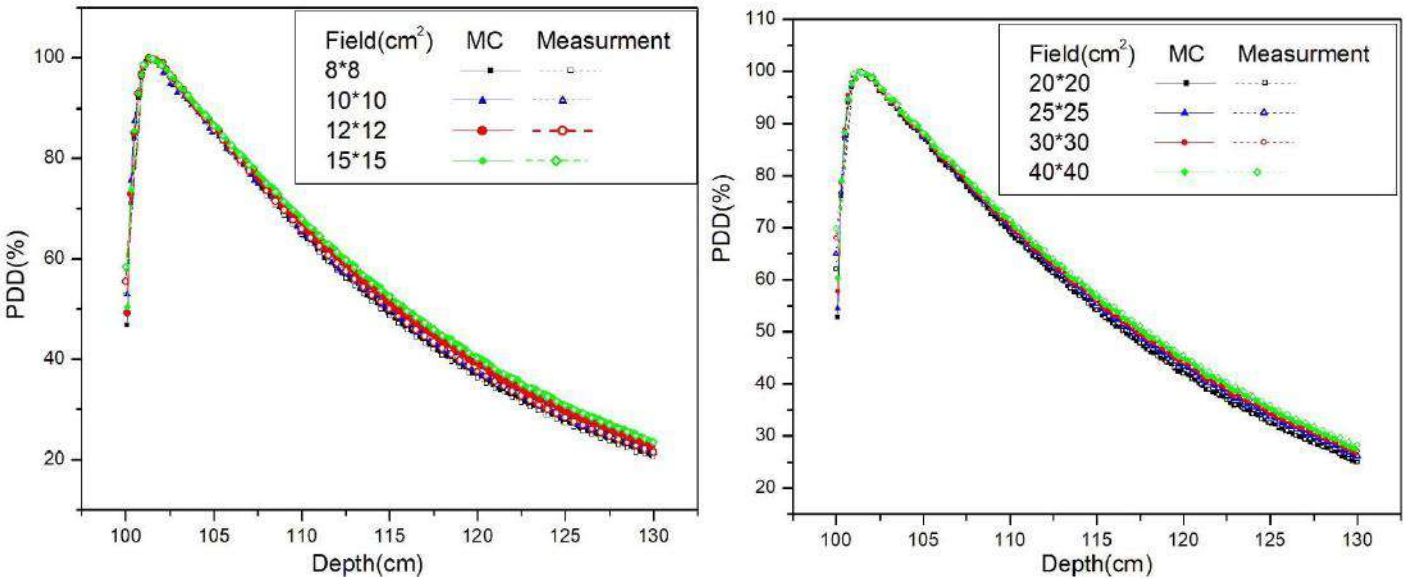

Fig. 4. PDD curve for different fields

Results indicate that a very good match between MC and measured data in the different fields.

Conclusions

In this study, the head of 6MV Elekta Compact linac was modeled using the MCNPX Monte Carlo code. The model's accuracy was confirmed through the comparison with measured PDD and dose profile curves. The optimum energy and FWHM values of incident electron beam were determined to be 6.1 MeV ad 0.44 cm, respectively. The obtained beam agrees well with measured data of PDD data for different fields.

Acknowledgements

The author extends gratitude to Ms. Rezaei, a physicist at the Iran-Mehr Radiotherapy and Oncology Hospital, for her assistance, as well as the support provided by the High-Performance Computing Center of the University of Birjand.

References

[1] Evans, E. and Staffurth, J. (2018).Principles of Cancer Treatment by Radiotherapy. Surgery(Oxford),36(3):111-116.

[2] Leszczynski, K. and Boyko, S. (1997). On the controversies surrounding the origins of radiation therapy. Radiotherapy and oncology, 42(3): 213-217.

[3] Andreo, P. (2018). Monte Carlo simulations in radiotherapy dosimetry. Radiation Oncology, 13(1): 1-15.

[4] Razghandi, S., Karimi-Shahri, K., & Firoozabadi, M. M. (2023). Dosimetric effects of different hip prosthesis materials during pelvic radiotherapy using high energy photons. Radiation Physics and Chemistry, 212:111134.

[5] Ahnesjö, A., and Aspradakis, M. M. (1999). Dose calculations for external photon beams in radiotherapy. Physics in Medicine & Biology, 44(11), 36024.

[6] Fippel, M. (1999). Fast Monte Carlo dose calculation for photon beams based on the VMC electron algorithm. Medical physics, 26(8), 1466-1475.

[7] Ma, C. M., Pawlicki, T., Jiang, S. B., Li, J. S., Deng, J., Mok, E., ... and Boyer, A. L. (2000). Monte Carlo verification of IMRT dose distributions from a commercial treatment planning optimization system. Physics in Medicine & Biology, 45(9): 2483.

[8] Chetty, I. J., Curran, B., Cygler, J. E., DeMarco, J. J., Ezzell, G., Faddegon, B. A., ... & Siebers, J. V. (2007). Report of the AAPM Task Group No. 105: Issues associated with clinical implementation of Monte Carlo-based photon and electron external beam treatment planning. Medical physics, 34(12): 4818-4853.

[9] Lu, S.X. and Deng,H.J. (2022) Monte Carlo Modeling and Verification of 6 MV Linear Accelerator. World Journal of Engineering and Technology,10(2):213-223.

[10] Angal-Kalinin, D., Bainbridge, A., Brynes, A. D., Buckley, R. K., Buckley, S. R., Burt, G. C., ... andWolski, A. (2020). Design, specifications, and first beam measurements of the compact linear accelerator for research and applications front end. Physical Review Accelerators and Beams, 23(4): 044801.

[11] Sadoughi, H. R., Nasseri, S., Momennezhad, M., Sadeghi, H. R., and Bahreyni-Toosi, M. H. (2014). A comparison between GATE and MCNPX Monte Carlo codes in simulation of medical linear accelerator. Journal of medical signals and sensors, 4(1), 10.

[12] Durán-Nava, O. E., Torres-García, E., Oros-Pantoja, R., and Hernández-Oviedo, J. O. (2019). Monte Carlo simulation and experimental evaluation of dose distributions produced by a 6 MV medical linear accelerator. In Journal of Physics: Conference Series, 1221(1): 012079.

[13] Al-Saleh, W. M., and Hugtenburg, R. P. (2023). Monte Carlo modelling of a 6 MV Elekta linear accelerator for in-field and out-of-field dosimetry. Radiation Physics and Chemistry, 203: 110584.

[14] Zareie, N., Rezaie, M.R. and Jomehzadeh, A., Phase space calculation of 6-MV Elekta compact linear accelerator by GEANT4 simulation.28th national conference on nuclear scient & thechnology 2022.

[15] Pelowitz, D.B., (2005). MCNPX^{TM} users manual. Los Alamos Natl. Lab. Los Alamos.5,369.

[16] Khan, F. M. (Ed.). (2010). The physics of radiation therapy. Lippincott Williams & Wilkins.

[17] Assalmi, M., & Diaf, E. Y. (2023). Effect of the Gaussian distribution parameters of the electron beam generated at the target on the simulated x-ray dose. Biomedical Physics & Engineering Express, 9(3), 035013.

ICNST 2024 International Conference on Nuclear Science and Technology
6- 8 MAY 2024 | Isfahan, Iran

Thickness Measurement of Thin Plastic Sample using 147Pm and 85Kr Beta Sources (Paper ID : 1280)

Sadeghi K.[1], Tajik M.[1*], Islami Rad S. Z.[2]

[1]*School of Physics, Damghan University, Damghan, Iran*

[2]*Department of Physics, Faculty of Science, University of Qom*

Abstract

Beta radiation sources are often used in the production of very thin plastic in industry. One such source of interest is ^{147}Pm, which is used to measure the thickness of materials such as plastic in the micrometer range. However, the short half-life of ^{147}Pm poses a challenge for its industrial application. Therefore, this study investigates the feasibility of using 85Kr sources as an alternative for the production of very thin plastics in the micrometer range. The aim of the study is to determine the theoretical and experimental error limits in the production of 20 µm thick plastics using ^{147}Pm and ^{85}Kr sources. The results show that the decrease in the number of beta particles count for ^{85}Kr and ^{147}Pm sources is 0.084% and 0.8%, respectively, when the thickness is increased from 20 to 20.5 µm. Furthermore, the maximum difference in the number of beta particles count emitted by the ^{147}Pm source between simulation and experimental methods is 0.15% for a plastic absorber with a thickness of 20.5 µm. This difference increases to 0.19% when the ^{85}Kr beta particle source is used. Overall, this study provides valuable insight into the potential use of ^{85}Kr sources for the production of very thin plastics. The results highlight the importance of considering error margins and variations in the number of beta particles count when determining the thickness of materials in industrial applications.

Keywords: ^{147}Pm, ^{85}Kr, Thin plastic sample, Beta gauging, Thickness

INTRODUCTION

Nuclear radiation, such as beta radiation, is widely used in industry, e.g. in the analysis of materials. One of the applications of nuclear radiation, including beta radiation, is the production of materials with a precise thickness, e.g. plastics [1]. For this reason, thickness gauges have been developed for quality control in the manufacturing process. One of the most common applications of beta radiation is online thickness gauges. These are devices that continuously and contactlessly check the thickness of BOPP (biaxially oriented

polypropylene) sheets. These gauging devices are very common in the industry. One of their most common applications is gauging the thickness of this type of sheet.

A beta thickness gauge consists of two main parts (the radioactive source and the radiation detector) and a system that processes the data from the detector [2]. Both the ^{147}Pm and ^{85}Kr isotopes are beta-emitting radioactive elements used in industry for low-energy applications. ^{147}Pm has a half-life of 2.62 years and an energy range up to 224 keV (with an average energy of 61 keV), while ^{85}Kr has a half-life of 10.76 years and an energy range up to 687 keV (with an average energy of 251 keV) [3, 4]. ^{147}Pm is often used to gauge the thickness of thin plastics (about one micrometre).

Due to limitations such as the short half-life of the ^{147}Pm source, the ^{85}Kr source was used in this research to produce plastics with a thickness of about 20 micrometres. Considering the high half-life of the ^{85}Kr source, for the preparation of thin plastics in the production line, the concerns caused by the need for early replacement are solved, which is very important in the production line. In addition, it is effective in accurately measuring plastic thickness due to the reduction in the intensity of the source and the resulting error [4, 5].

^{147}Pm is a radioactive isotope produced indirectly by neutron irradiation on ^{146}Pm. Access to a high-energy neutron flux is required to produce ^{146}Pm, so it is possible to produce the isotope ^{146}Pm using the target element. ^{146}Pm can be produced in a particle accelerator by the fission of heavy nuclei such as uranium by high-energy particles. the ^{85}Kr source is also produced indirectly by the ^{86}Kr isotope decomposition method or by irradiating the ^{84}Kr isotope with high-energy neutrons. In contrast to ^{146}Pm, which does not found in nature, the isotopes ^{84}Kr and ^{86}Kr isotopes exist in nature in reasonable quantities. Therefore, the production of ^{85}Kr is less complicated than that of ^{147}Pm, which does not exist in nature and requires a two- or multi-step process to produce. Considering the probable limitations in the production of ^{147}Pm and the short half-life of this source, this study theoretically and experimentally investigated the performance of two beta radiation sources, ^{147}Pm and ^{85}Kr, produced to control the standard thickness of thin plastic from the plastics industry [6, 7].

RESEARCH THEORIES

The thickness of plastic samples can be gauged by the rate of passage of electrons through the sample and their absorption in the sample. Due to the interaction of beta particles with absorbing materials, some particles pass through the sample and some particles are also absorbed by the material. Due to the interaction of beta particles with absorbing material, some particles pass through the material and some particles are also

absorbed by the material. As the thickness of the material increases, the probability of beta particles being absorbed also increases. Using Lambert's law, it is possible to determine the decrease in intensity of the beta particles emitted from the source after interaction with the material and the thickness of the material.

This law is as equation (1):

$$I = I_0 e^{-\mu x} \quad (1)$$

In equation (1), I is the intensity of the source emitting beta particles, I0 is the initial intensity, μ is the linear absorption coefficient of the material, and x is the thickness. The mass absorption coefficient of the material can be calculated using the experimental equation (2):

$$\mu(\frac{m^2}{kg}) = 1.7E_{max}^{-1.14} \quad (2)$$

In equation (2), Emax is the maximum energy of the beta particle emitted by the source [1, 8]. By applying equations (1) and (2), it is possible to determine the rate of passage of the beta rays of ^{147}Pm and ^{85}Kr through the thickness of the plastic sample and the absorption in it in the range of 20 to 20.5 μm.

To calculate the number of beta particles passing through the BOPP plastic absorber after losing some energy and changing direction, MCNPX software was used [9]. To evaluate the suitability of the ^{85}Kr source as an alternative to the ^{147}Pm beta radiation source, the change in the number of beta particles after their interaction with the plastic material is first measured. BOPP sheet with a thickness of 20-20.5 μm and a density of 0.91 g/cm^3 was exposed to beta radiation from ^{85}Kr and ^{147}Pm sources. The energy spectra are shown in Figures 1 and 2 and follow the setup in Figure 3.

Since the ^{147}Pm source is commonly used to gauge the thickness of plastics up to 20 μm, the thickness of 20 μm was chosen as the standard thickness and the count rate was examined by increasing it by +0.5 μm relative to the standard thickness value. The setup used by the MCNPX software for the simulation is shown in Figure 3. In the simulation using the MCNPX software, the thickness of the plastic sample was increased from 20 to 20.5 μm (adding 0.05 μm to the previous thickness at each step) and the variation in the number of beta particles passing through the plastic sample and emitted from the ^{147}Pm source was investigated.

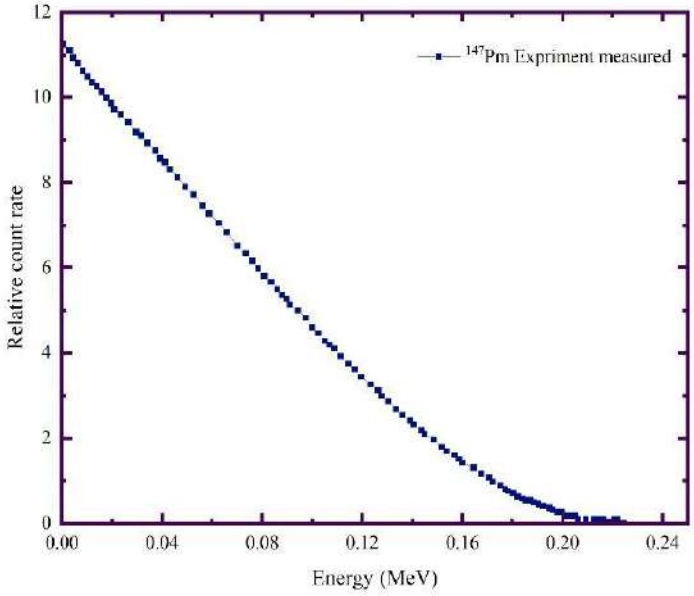

Fig. 1. The energy spectrum of the ^{147}Pm beta emitter source [4].

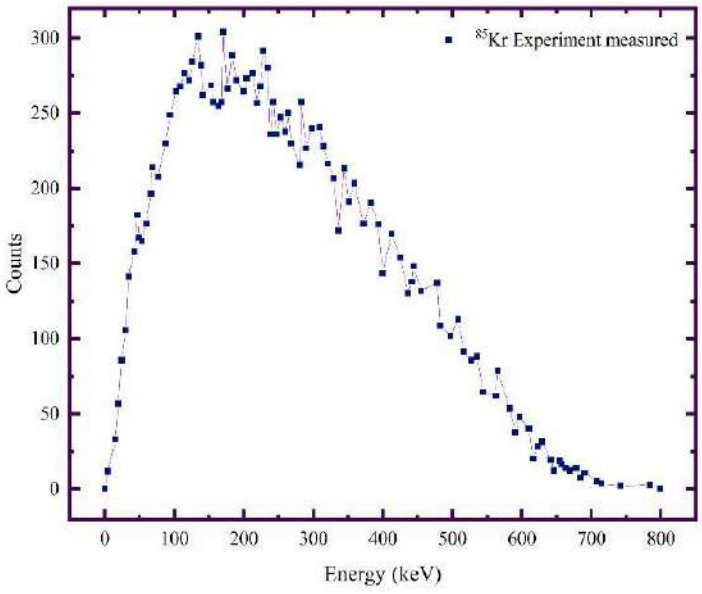

Fig. 2. The energy spectrum of the beta emitter source of ^{85}Kr [3].

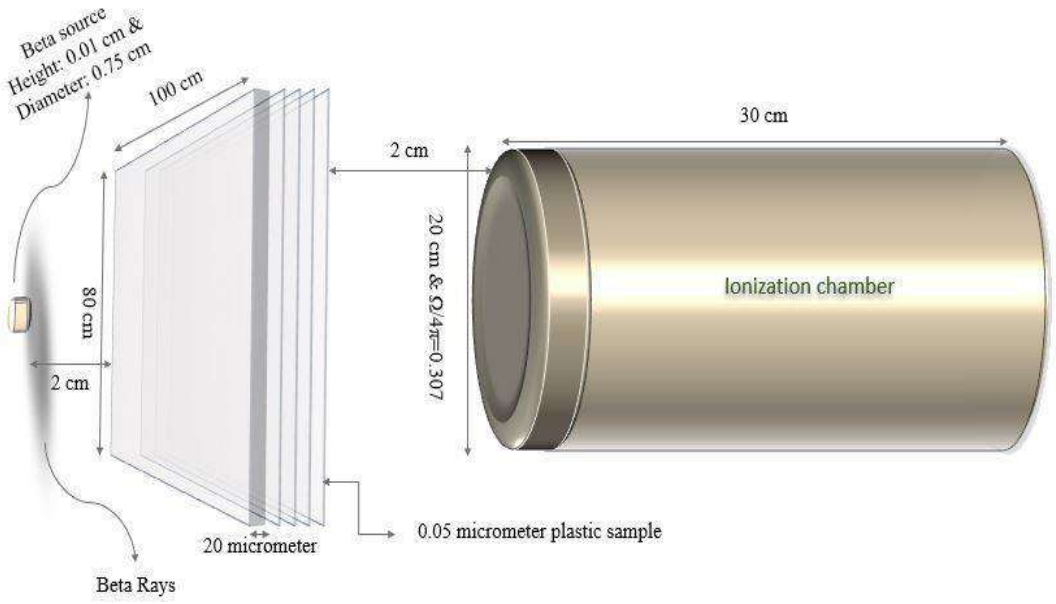

Fig. 3. Simulated arrangement for the determination of the beta particles passing flux.

EXPERIMENTAL

Beta sources are used for online thickness gauging, which is one of the most common applications of these sources. The beta thickness gauge used in this study, model BT-3000, is manufactured by JASCH. The radiation source and the ion chamber detector are the two main elements of this thickness gauge (Figure 1). The thickness of the plastic sheet is gauged by placing it between the source and the detector. The measurement principle is based on the attenuation of the low-energy beta radiation emitted by a nuclear source when it passes through a plastic sheet. The thickness is determined by sensing the energy changes of the beta particles emitted by a source with a certain intensity. The measurement is continuous and online. The thickness parameter is constantly gauged and checked by control systems. Any deviations from the specified values are detected immediately. All measurement results are evaluated and displayed graphically on the monitor. The plastic sheet used in this study is of the BOPP type and has a density of 0.91 gr/cm^3 and a standard thickness of 20 µm. To gauge the thickness of the plastic sheet in this study, low-energy beta radiation sources of ^{147}Pm and ^{85}Kr with intensities of 300 and 500 mCi, respectively, and an ion chamber detector with a length and radius of 30 and 10 cm, respectively, were used. According to the simulation setup, plastic samples with different thicknesses from 20 to 20.5 µm were placed between the source and the

detector. The measurements were performed three times for 180 seconds for each sample and then averaged. The results of the measurements for the sources ^{147}Pm and ^{85}Kr are shown in Figure 5.

Fig. 4. beta thickness gauge set up.

Results and discussion

Figure 5 shows how the flux of beta particles from ^{85}Kr and ^{147}Pm sources decreases as they pass through different plastic thicknesses. The absorption coefficient of the plastic sample was considered for two experimentals and the analytical methods (taking into account the energy spectrum of the source) using equations 1 and 2.

Figure 5 shows that the flux of beta particles passing through the ^{147}Pm source decreases more than in the ^{85}Kr source. The reason for this discrepancy lies in the different energy of the particles released from the two sources, which results in the particles from the ^{147}Pm source having a higher stopping power in the plastic sample. In addition, the flux of beta particles with an energy of 224 keV decreases by 0.42% after passing 20.5 μm of the sample thickness. This discrepancy between the analytical and experimental results is due to the use of the highest energy for the calculation data. The flux of beta particles from the ^{85}Kr source decreases by about 0.084%. This figure is obtained by applying equations 1 and 2 to the particles emitted from ^{85}Kr with an energy of 687 keV, i.e. about 0.12%. To contrast the reduction in beta particle flux measured by the detector in the laboratory environment, the corresponding setup was considered based on theoretical calculations. Figure 6 shows how the flux of beta particles from ^{85}Kr and ^{147}Pm sources decreases as they pass through the plastic absorber. The figure compares the results of the Monte Carlo simulation and the experimental methods. The detector measured the number of beta particles for different plastic sample thicknesses exposed to ^{85}Kr and ^{147}Pm beta sources (using both the simulation and the experimental method).

The simulation and the experimental methods provided similar qualitative results for flux variations depending on the thickness of the plastic sample between 20 and 20.5, although there were slight discrepancies. This discrepancy results from neglecting the details of the measurement simulation, neglecting the backscattering electron impacts in the laboratory and the measurement error due to the movement of the roller supporting the plastic sheet. The experimental results show that the number of beta particles decreases by 0.084 and 0.8% for ^{85}Kr and ^{147}Pm sources, respectively, when the thickness of the sample is between 20 and 20.5 micrometres. When the thickness of the plastic absorber is 20.5 micrometres, the simulation and experimental approaches result in a maximum discrepancy of 0.15% in the number of beta particles of the ^{147}Pm source. The discrepancy increases to 0.19% for the ^{85}Kr source.

Figure 7 illustrates how the electron flux of the krypton source decreases as it passes through the plastic sample. The electron flux of the promethium source decreases to 0.8% of its initial value in the simulation setup after passing through 20.5 μm of plastic. The electron flux of the krypton source can be determined under comparable conditions.

Figure 7 shows that the variation in the thickness of the plastic sample (starting from the standard thickness of 20 micrometres), which causes a 0.8% decrease in the electron flux of the krypton beta source, is 1.6 micrometres.

The variation of beta particle flux of ^{85}Kr and ^{147}Pm sources as a function of thickness from 20 to 20.5 in some half-lifes is shown in Figures 8 and 9. Equations (1) and (2) were used to calculate this variation. When ^{147}Pm is used as the beta source for 18 half-lifes in the manufacturing process, the calculated variation in counts is approximately 1238. The relative error in gauging the plastic thickness in the manufacturing process with a deviation of 0.5 micrometres from the standard thickness of 20 micrometres is approximately 2.84% for this order of magnitude of counts. To gauge the thickness with an error less than 2%, the source should be used for less than 16 half-lifes. If ^{85}Kr is used as a source for less than one half-life to gauge the thickness of thin plastic around 20 microns, the gauging error is less than 0.02%. Using the ^{85}Kr source instead of the ^{147}Pm source can reduce the error in gauging the thickness of thin plastic if the ^{147}Pm source has been used for up to 18 half-lifes in the manufacturing process and no new ^{147}Pm source is available.

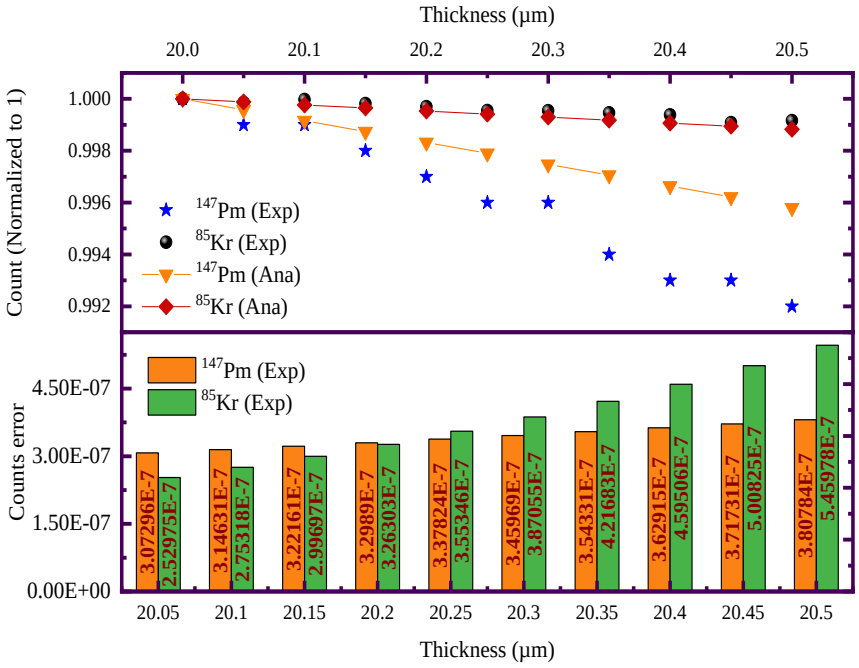

Fig. 5. Comparison of the experimental and analytical results (equation (1, 2)) of the beta particles passing flux of 20 to 20.5 µm thick plastic samples using the ^{147}Pm and ^{85}Kr sources.

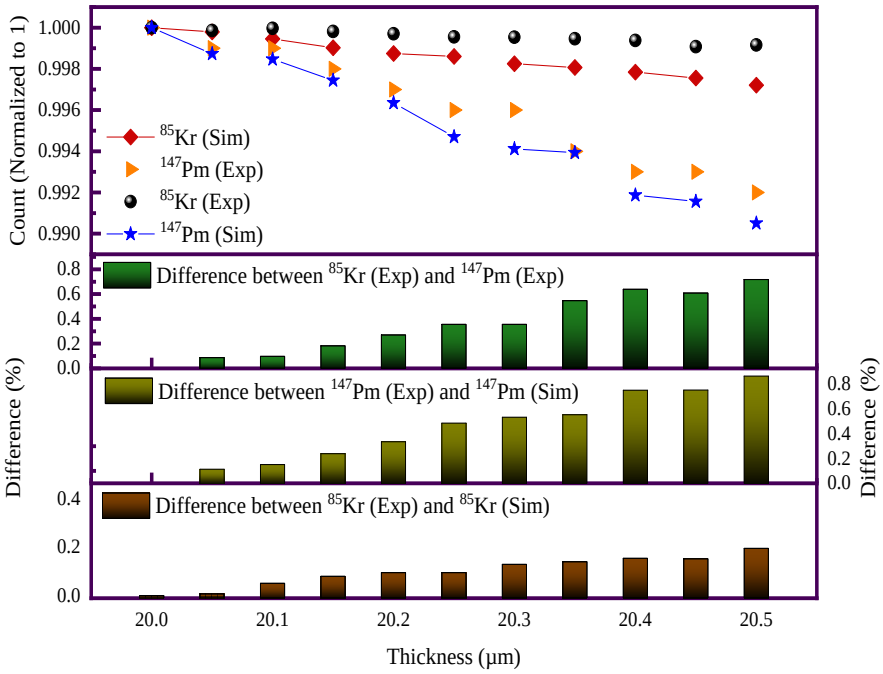

Fig. 6. Comparison of simulation and experimental results of beta particle flux from a thickness of 20 to 20.5 µm of a plastic sample using ^{147}Pm and ^{85}Kr sources.

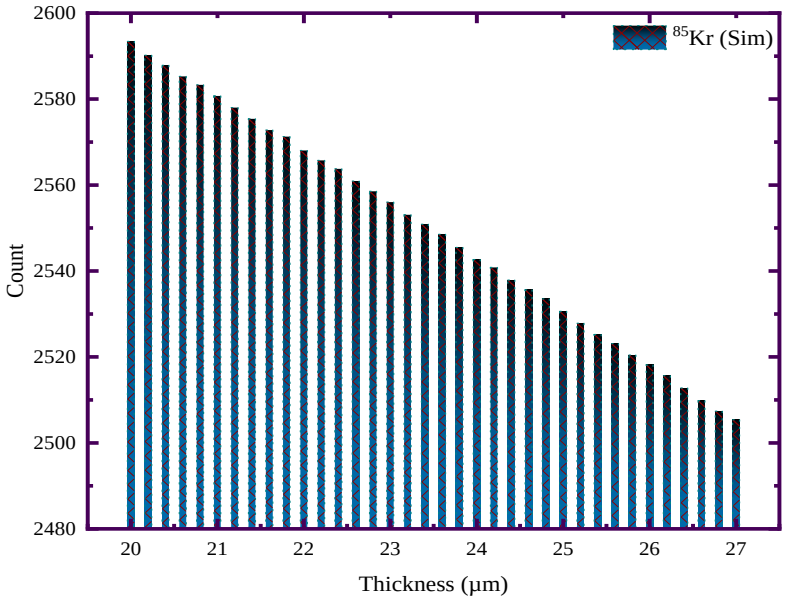

Fig. 7. The magnitude of the beta particle flux when the plastic sample is 20 to 27 µm thick using an ^{85}Kr source.

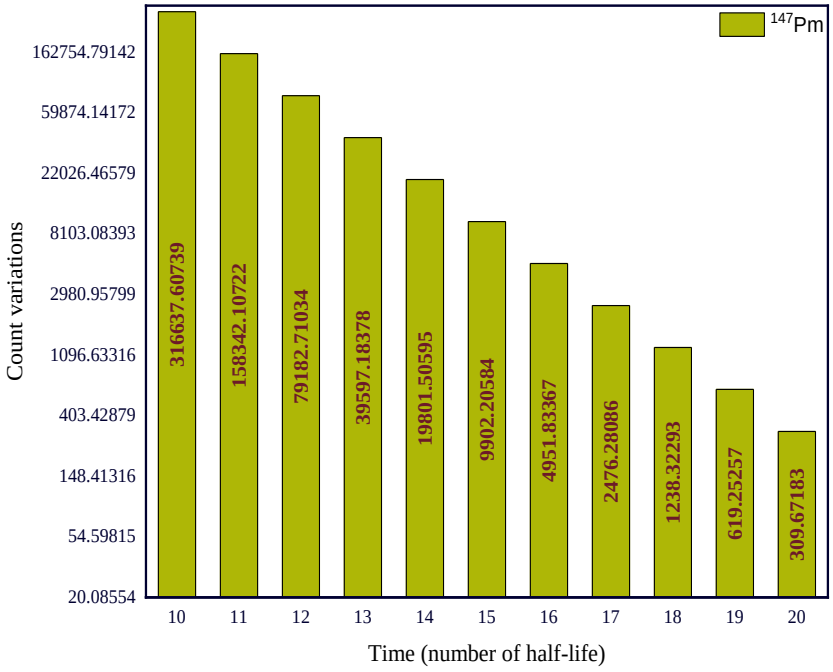

Fig. 8. Changes in beta particle flux from a thickness of 20.5 µm to a thickness of 20 µm in several half-lifes of the ^{147}Pm source.

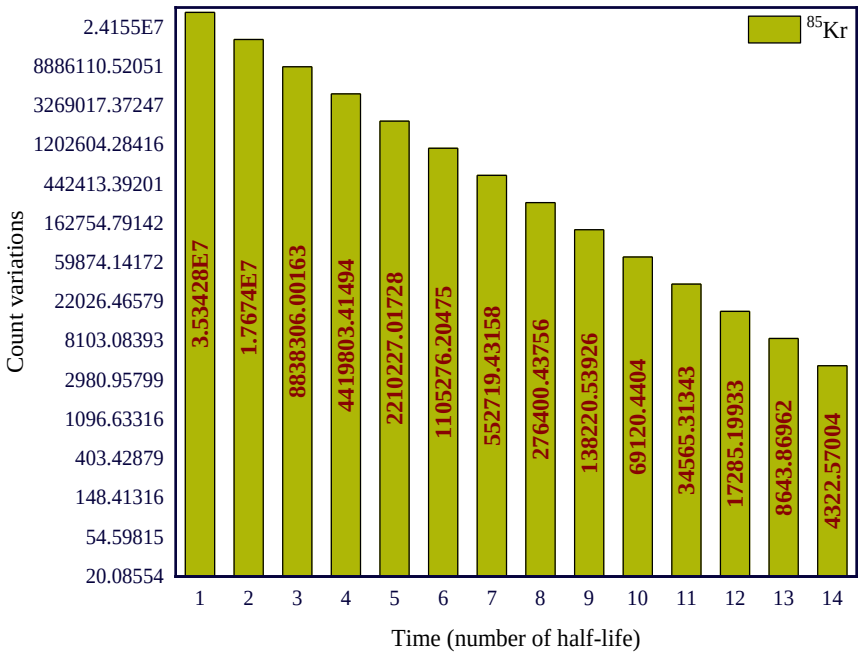

Fig. 9. Changes in the passing flux of beta particles from a thickness of 20.5 µm to a thickness of 20 µm in several half-lifes of the ^{85}Kr source.

Conclusions

In this study, the strategy of using the ^{85}Kr beta source as an alternative to the old (used) ^{147}Pm beta source for the thickness measurement of thin plastics was investigated. The results of the investigations showed that the error in measuring the thickness of thin plastics is influenced by the activity of the source and the time of its use. In order to measure the plastic thickness with a deviation of 0.5 µm from the standard thickness of 20 with an error of less than 2%, the promethium source should be used for less than 16 half-lives. This error rate was determined for the ^{85}Kr source in the 14th half-life of this source. If the ^{147}Pm source has been used for more than 16 half-lives in the production process and no new ^{147}Pm source is available, using the ^{85}Kr source instead of the ^{147}Pm source can reduce the error in measuring the thickness of thin plastic by 0.02%.

References

[1] S. Dönmez, A. Arjhangmehr, M. Mohammadzadeh, S. A. H. Feghhi, and S. Tasouji Hassanpour, "Beta-backscattering thickness-meter design and evaluation with fuzzy TOPSIS method," *Nukleonika*, vol. 59, no. 2, pp. 53–59, Jul. 2014,

[2] S. Ülkü, D. Balköse, E. Arkiş, and M. Sipahioğlu, "A study of chemical and physical changes during biaxially oriented polypropylene film production," *J. Polym. Eng.*, vol. 23, no. 6, pp. 437–456, Nov.

2003,

[3] J. Zeng *et al.*, "Development of a well-type phoswich detector for low concentration Krypton-85 measurement," *Nucl. Instruments Methods Phys. Res. Sect. A Accel. Spectrometers, Detect. Assoc. Equip.*, vol. 1013, p. 165634, Oct. 2021,

[4] A. Endo, Y. Yamaguchi, and K. F. Eckerman, "Nuclear decay data for dosimetry calculation. Revised data of ICRP Publication 38," 2005,

[5] R. P. Gardner, W. A. Metwally, and A. Shehata, "A semi-empirical model for a 90Sr beta-particle transmission thickness gauge for aluminum alloys," *Nucl. Instruments Methods Phys. Res. Sect. B Beam Interact. with Mater. Atoms*, vol. 213, pp. 357–363, Jan. 2004,

[6] S. I. Sukhoruchkin and Z. N. Soroko, *Excited Nuclear States for Cs-145 (Caesium)*, vol. 25. 2013.

[7] S. E. Hosseini, M. Ghannadi-Maragheh, A. Bahrami-Samani, and S. Shirvani-Arani, "Evaluation of promethium-147 production by irradiating natural neodymium using medium-flux Tehran research reactor," *J. Radioanal. Nucl. Chem.*, vol. 326, no. 1, pp. 465–474, 2020,

[8] S. Dönmez, *Radiation Detection and Measurement*. 2017.

[9] D. B. Pelowitz, "MCNPX User'S Manual Version 2.6.0," *Los Alamos Natl. Lab.*, 2008.

ICNST 2024 International Conference on Nuclear Science and Technology
6- 8 MAY 2024 | Isfahan, Iran

Measurement of radon exhalation rate from building materials: The case of Mashhad-Khorasan Region Iran (Paper ID : 1286)

Zabihinpour M [1*], Khaniki Z[2], Mohammadi S[3]

[1,2,3]*Department of Physics, Payame Noor University, Tehran, IRAN*

Abstract

The release of radon gas from soil, water and building materials in closed environments exposes residents to this radioactive gas. Although humans use building materials as a protective barrier against the natural radiation of the open space (terrestrial and cosmic), the radionuclide compounds released from some materials used in buildings cause an increase in indoor radon concentration. Therefore, measuring the amount of radon exhalation from building materials is very important for public health. Also, although radon is the most important factor and source of natural radiation and its high concentration level in the indoor air of closed environments can cause a significant health risk, the main daughter nuclei of radon, ^{214}Po and ^{218}Po, have a high ability to cause lung cancer in humans. As a result, public attention and concern regarding the release of radon from building materials used in the indoor environment has increased and many efforts have been made to evaluate and control indoor radon concentration.

In this research, the surface diffusion coefficient of radon from three samples of widely used building materials in the Khorasan region was measured and calculated using the active method in the closed chamber of the Sarad-RTM1689 equipment. The exhalation rate for these samples was in the range of undetectable insignificant values up to 4.85 Bq m $^{-2}$ h $^{-1}$. The highest surface exhalation rate was observed in granite samples, while the clay brick sample showed a radon exhalation rate lower than the detection threshold (0.05 Bq m $^{-2}$ h $^{-1}$). Our results can offer to choose suitable building materials for a safe indoor environment for residents.

Keywords: radon, exhalation rate, indoor concentration, building materials.

INTRODUCTION

From the point of view of radiology, the new and current human lifestyle, which is sometimes accompanied by quarantine or isolation conditions like during the COVID-19 epidemic, can increase the risk of exposure to natural radiation as a result, the possibility of lung cancer increases. According to the World Health

Organization (WHO), 3% to 14% of lung cancer deaths are related to long-term exposure and living in an environment with a high concentration of radon gas [1]. Therefore, it is necessary to prevent, reduce, and control the radon exhalation rate from building materials [2]. Radon gas is released from the decay of radium nuclei (^{226}Ra) and depend on the granularity and size of the pores or fine cracks in the building materials [3]. The occurrence, rejection, and effect of (^{226}Ra) can be found in building materials, but determining the amount of radon exhalation rate is not easily possible from the activity of (^{226}Ra) [4]. Therefore, the actual measurement of the radon exhalation rate should be done to estimate the radiological risk associated with building materials. In particular, building materials with magmatic origin (melted materials under the earth's crust) such as granites are classified as important sources of radon [5-8]. Recent laws in the construction of residential, commercial, and industrial buildings in our country, like in other parts of the world, have paid special attention to energy saving and thermal efficiency, and as a result, indoor radon increases by reducing the rate of air conditioning [9]. On the other hand, although some research is available on the measurement of radon gas emissions from water supply sources in Iran, there are few official and comprehensive reports on radon monitoring and its emission rate from building materials in different regions of Iran including Khorasan [10-14]. The main goal of this research is to evaluate the radon exhalation rate from common building materials such as concrete, concrete block, and granite used in the residential area of Mashhad city in Razavi Khorasan.

MATERIALS AND METHODS

The investigated building materials included concrete cylindrical samples, granite stone, concrete blocks and clay bricks (Figure 1). The reason for choosing these materials was the huge use of these materials in most of the buildings under construction. To obtain reliable and accurate data, an attempt was made to select samples from pure materials. The samples were dried overnight at 100°C in an oven to remove water from their pores. Concrete blocks are often used in external walls, clay bricks in internal porcelain walls, cylindrical concrete samples (with a combination of sand, lime, cement and water with a density between 1018 and 1600 kg/m3) in the foundation and columns and Granite stones are used in the floor of the building. These materials were randomly selected from building materials stores and local markets.

Figure (1): Selected building materials: concrete blocks, concrete cylinders, clay bricks and granite stones (figure pointer 1). and Mashhad city, Taken from Google map (map pointer 2).

EXPERIMENTAL SETUP

The measurement of radon and thoron and its products are always based on detecting the type of alpha, beta or gamma rays that are emitted from them. All of these rays cause various effects such as local defects, currents or electrical pulses when they collide with matter Therefore, different tools and methods can be used to record these emissions. One of the most widely used methods is the closed chamber method, in which the desired quantity is evaluated by sucking the volume of trapped air above the surface of the sample to be evaluated and passing it through the appropriate detector during a predetermined period of time. [15-19]. Among other methods is the open chamber method, in which the environmental conditions and its effect on the evaluation cannot be controlled [20,21]. According to the registration of the desired isotope and the power of time resolution, other methods, including the cover sample method, can be used to determine the activity (226Ra) [22] Among these methods, the first one is the most used and recommended. Because in the closed chamber method, it is possible to control the parameters of the environment (such as humidity, pressure and temperature) as well as the inherent parameters of the experimental set (including the rate of leakage, the rate of back emission and natural background radiation) [23].

The test settings and the placement of the equipment inside the closed chamber are specified and shown in Figure 2. The closed chamber is made of six sheets of colorless glass with a cross section of 80 x 30 square centimeters, a height of 50 centimeters, and a thickness of 1 centimeter. To stick them, waterproof silicone glue is used and its corners are sealed with special glue. The seam was tested by filling it with water, and no water seepage or seepage around the chamber or along the joints after 3 days. The net volume of the chamber was 0.1250 cubic meters. The volume of RTM1689 inner cell and tubes was 0.0008 cubic meters. The volume of instruments related to the measurement was 0.0020 cubic meters. The free volume of V_n compartment was different according to the sample volume. These values can be considered from 0.1000 cubic meters to 0.1140 cubic meters. The measurement of radon concentration was carried out using RTM1689 solid state alpha detector made in the German Sarad company (Figure 2).

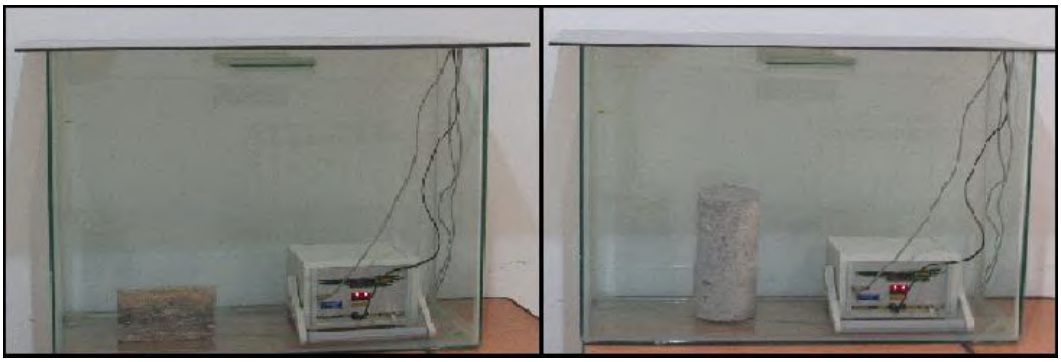

Figure (2): Showing the equipment settings of the RTM1689 device and the samples inside the closed chamber to measure the Rn concentration of the samples.

RN ACCUMULATION

After the sample is well insulated inside the chamber, the concentration of radon gas released from the sample inside the closed chamber is measured. Radon concentration curve, usually given in Bqm^{-3}, It increases until it tends to the equilibrium concentration [15] (See Figure 3). An equilibrium state occurs when the rate of radon gas production and emission is equal to the rate of radon loss due to natural decay, ventilation and back emission. The time required to reach the equilibrium concentration depends on the type of substance and test conditions, which took more than two weeks for the samples examined in the present study. By ensuring that the environmental parameters (temperature, elevation and pressure) are constant, the increase in C_{Rn} can be described as follows:

$$\frac{\partial C_{Rn}}{\partial t} = -\lambda_e C_{Rn} + \frac{EA}{V_n} + \lambda_n C_{Bg} \quad (1)$$

$$\lambda_e = \lambda_{Rn} + \lambda_L + \lambda_{Bd} \quad (2)$$

Where, λ_e (h^{-1}) is the effective rate which includes, the natural radon decay λ_{Rn} (h^{-1}), the chamber leakage rate λ_L (h^{-1}), and the back diffusion rate λ_{Bd} (h^{-1}). E represents the Rn exhalation. A (m^2) is the exhalation area of the sample. C_{Bg} (Bq m^{-3}) represents the laboratory background contribution as a result of the chamber leakage. If the free volume Vn (m^3) of the closed chamber is at least ten times bigger than the sample pores, Rn accumulated outside the sample does not return to the sample, thus the back diffusion effect can be neglected [21,24,25]. The closed chamber volume in the present work meets this condition, therefore, there is no loss due to back diffusion, giving $\lambda_{Bd} = 0$**.**

At time t = 0, the initial Rn concentration C_i (Bq m^{-3}) is equal to C_{Rn} (Bq m^{-3}), and the solution to Eq (1) is:

$$C_{Rn}(t) = C_i e^{-\lambda_e t} + \left(\frac{EA}{V_n \lambda_e} + \frac{\lambda_L C_{Bg}}{\lambda_e}\right)\left(1 - e^{-\lambda_e t}\right) \quad (3)$$

After a long period, the CR_n relationship will become the equilibrium state concentration as follows:

$$C_{eq} \cong \frac{EA + \lambda_L C_{Bg} V_n}{V_n \lambda_e} \quad (4)$$

Hence, Eq. (3) can be written as:

$$C_{Rn}(t) = C_i e^{-\lambda_e t} + C_{eq}(1 - e^{-\lambda_e t}) \quad (5)$$

Figure 3 shows the accumulation curve of Rn for a selected sample of the concrete cylinder sample. C_{eq} was calculated according to the experimental data and λ_e was calculated by fitting the data using Equation 5. From the relevant data sets, C_{eq} and le were found as:

$\lambda_e = (0.0195 \pm 0.0003) h^{-1}$, $C_{eq} = (146 \pm 11) Bq\ m^{-3}$

By inserting the value of λ_e obtained in equation 2, the value of λ_l is calculated as follows:

$\lambda_l = (0.0120 \pm 0.0002) h^{-}$

Which parameter λ_l includes the air exit and entrance to the chamber.

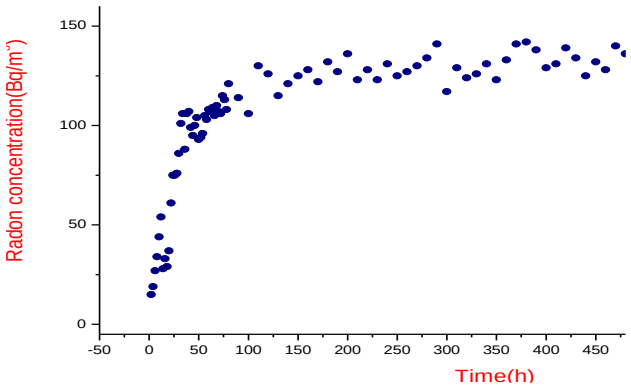

Figure (3): Rn concentration variation curve as a function of time for the concrete cylinder sample.

RADON LEAKAGE

To ensure the leakage rate of the chamber, several collapse tests were performed. A sample was placed inside the chamber and the chamber was well sealed, and after a few weeks, the sample was put aside and sealed again. If the operation is performed carefully in a short perio, some of the gas already accumulated in the chamber remains [15]. if this radon concentration inside the chamber is denoted by C_{dec}, we have for its changes:

$$\frac{\partial C_{dec}}{\partial t} = -\lambda_{Rn} C_{dec} - \lambda_L C_{dec} - \lambda_L C_{Bg} \tag{6}$$

C_{Bg} (Bq m^{-3}) is the fraction of the laboratory background that enters due to leakage. The solution to Eq. (6) can be expressed as:

$$C_{dec}(t) = C_0 e^{-\lambda_{dec} t} + \frac{\lambda_L}{\lambda_{dec}} C_{Bg}\left(1 - e^{-\lambda_{dec} t}\right) \tag{7}$$

At time t = 0, the concentration of Rn C_{dec} is equal to the initial Rn concentration C_0 (Bq m^{-3}). The effective decay rate λ_{dec} (h^{-1}) is equal to (8), where λ_{Rn} (h^{-1}) is the radon decay rate and λ_L (h^{-1}) is the chamber leakage rate.

$$\lambda_{dec} = \lambda_{Rn} + \lambda_L \tag{8}$$

The optimal values of the radon surface diffusion rate coefficient (E) and the chamber leakage coefficient (λ_L) can be obtained by comparing the experimental data with the three-dimensional diagram of the radon concentration changes inside the chamber with the changes of these parameters, which are obtained from the

computer simulation for time (Figure 4). The results of this method for the Sample concrete cylinder at t=10h were obtained as follows:

E= (1.95±0.18) Bq.m^{-2}h^{-1} , λ_L =(0.0120±0.0002)h^{-1}

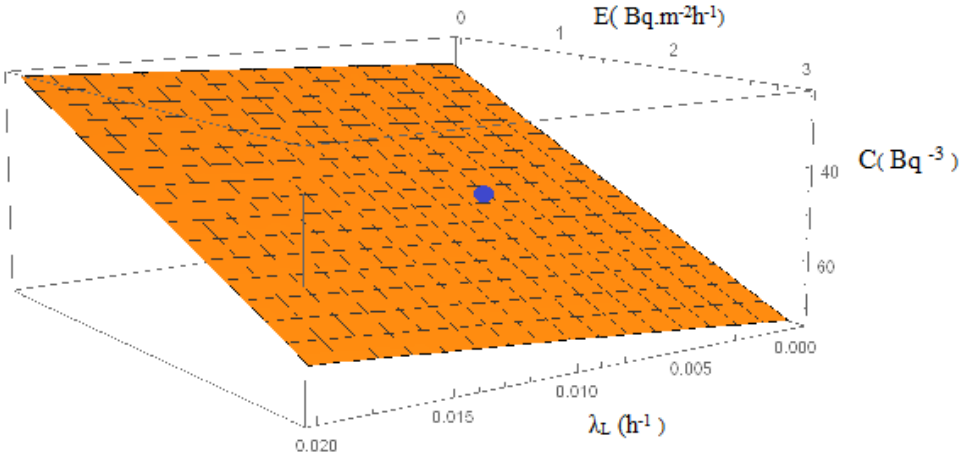

Figure (4): Three-dimensional diagram of changes in radon concentration inside the chamber with variations in radon surface diffusion rate (E) and chamber leakage coefficient (λL) obtained from computer simulation for time t=10h for the concrete cylinder sample provided. The red dot represents the radon concentration at this time in an experimental study.

Results and discussion

The Rn emission rate (E) is defined as the net amount of Rn that escapes from the building material per time unit. Exactly, E is defined as the radon activity measured in Becquerel (Bq) per hour (h^{-1}). There are two forms to express E, considering the exposed surface area (A) or the mass of the building material (m). In the first case, E is noted as the surface exhalation rate (E_A) expressed in Bq. m^{-2}. h^{-1}. The second case, as mass exhalation rate (E_m) expressed in Bq. kg^{-1}. h^{-1}. In the present work, it will be defined by E_A value which is calculated by the following equation:

$$E_A = \frac{C^*_{eq} V_n \lambda_{Rn}}{A} \quad (9)$$

The parameter C_{eq} was corrected as C^*_{eq}, heeding the loss due to the chamber leakage. To ensure the results obtained for the surface diffusion coefficient, the data obtained for different coefficients can be put in equation 3 and the experimental test can be simulated in the desired time with computer numerical methods. The matching of this curve with the curve of experimental changes will prove the correctness of the data. Figure 5 is an example of this simulated curve under the same conditions as the experimental test in Figure 3, and their clear agreement shows the correctness of the radon surface diffusion coefficient obtained for the concrete cylinder sample. Table 1 shows the values of the surface emission rate of radon of the studied samples.

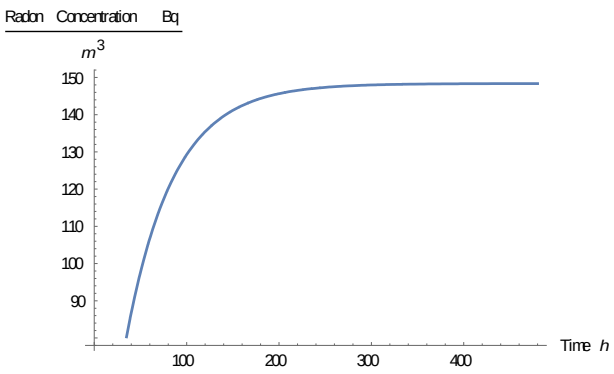

Figure (5): The graph of changes in the rate of radon surface emission for the concrete cylinder sample obtained through computer simulation.

The maximum radon exhalation rate was observed in granite samples. Among the results obtained from the samples, the radon exhalation rate of the examined clay bricks was undetectable, which means their radon surface emission rate can be ignored. The values measured in this research are consistent with the values reported in other works [6,7,16].

Table1. The exhalation rate of sample building materials and their use in the building.

Description	Application	E_A ($Bq\ m^{-2}\ h^{-1}$)	measurement error ($Bq\ m^{-2}\ h^{-1}$)
clay brick	Internal Walls	Less than detection threshold	-
Granite	Floor	4.85	0.54
concrete cylinder	Columns and foundation	1.95	0.18

Conclusions

Radon gas is an inert, colorless, odorless, and radioactive gas whose high concentrations in the residential environment can cause serious problems for human health. Building materials can be the most important factor in radon exhalation in residential buildings. In this research, the surface diffusion coefficient of radon from commonly used samples of construction materials in the Mashhad, Khorasan Razavi region, which included concrete cylinders, granite stones, and clay bricks, was investigated. The radon surface diffusion coefficient of these three samples was measured and calculated using the active method and in a closed chamber with the Sarad-RTM1689 radon meter. The radon surface diffusion coefficient of these three samples is shown in Table 1, In the range of measurable values by this device, 1.95 $Bq\ m^{-2}\ h^{-1}$ was obtained for the cement cylinder and 4.85 $Bq\ m^{-2}\ h^{-1}$ for granite stone. Observing the highest rate of radon surface emission in granite samples, as other researchers in this field have already reported, is a clear sign of not using this stone in residential buildings, especially with a low ventilation coefficient with outdoor. Also, these results can offer effective help in choosing suitable building materials for the safe indoor environment of the residents [26,27].

References

[1] WHO (2009). Handbook on indoor radon: a public health perspective, World Health. Organization.

[2] WHO (2015). Protection of the public against exposure indoors due to radon and other natural sources of radiation. specific safety guide, Tech. rep., World Health Organization.

[3] Ujic´, P. and C˘ elikovic´, I. and Kandic, A. and Vukanac, I. And Juraševic´, M. And Dragosavac, D. and Z˘unic´, Z.S. (2010). Internal exposure from building materials exhaling 222rn and 220rn as compared to external exposure due to their natural radioactivity content, Applied Radiation and Isotopes, 68 (1):201–206.

[4] Dentoni, V. and Da Pelo, S. and Aghdam, M.M. and Randaccio, P. and Loi, A. and Careddu, N. Bernardini, A. (2020). Natural radioactivity and radon exhalation rate of Sardinian dimension stones, Construction and Building Materials, 247:118377.

[5] Bruno, R.C. (1983). Sources of indoor radon in houses: A review, Journal of the Air Pollution Control Association, 33 (2):105–109.

[6] Stoulos, S. And Manolopoulou, M. and Papastefanou, C. (2003). Assessment of natural radiation exposure and radon exhalation from building materials in Greece, Journal of Environmental Radioactivity, 69(3):225–240.

[7] Righi, S. and Bruzzi, L. (2006) Natural radioactivity and radon exhalation in building materials used in Italian dwellings, Journal of Environmental Radioactivity, 88(2):158–170.

[8] Hassan, N.M. and Ishikawa, T. and Hosoda, M. and Sorimachi, A. Tokonami, S. and Fukushi, M. and Sahoo, S. K. (2010) Assessment of the natural radioactivity using two techniques for the measurement of radionuclide concentration in building materials used in japan, Journal of Radioanalytical and Nuclear Chemistry, 283(1)15–21.

[9] Zabihinpour, S.M. and Mowlavi, A.A. and Azadegan, B. (2018). The role of natural ventilation on reducing indoor radon concentration, Journal of Radiation Safety and Measurement, 7(4):1–10.

[10] Asgharizadeh, F. and Ghannadi Maragheh, M. and Salimi, B. And Sedgh Gouya, E. (2014). Dose rate calculation caused by natural radioactivity in granite samples used as building materials in Iran, Journal of Radiation Safety and Measurement, 3(2):27–33.

[11] Zareie, N. and Rezaie Rayeni Nejad, M.R. (2023). Department of Nuclear Engineering, Faculty of Sciences and Modern Technologies, Graduate University of Advanced Technology, Kerman, Iran, Estimation of radiation hazards caused by granite in the villages of Dehsiahan, Khanaman and Mani in Rafsanjan city of Kerman province, Journal of Radiation Safety and Measurement, 11(4):25–32.

[12] Asgharizadeh, F. and Esmailnezhad, M. and Pourdeh, P. and Moatar, F. and Sadigzadeh, A. and Sedgh Gouya, E. and Nasiri, P. (2013). Measurement and comparison of radioactivity concentration of radon indoor air of buildings faced by granite and carbonate, Journal of Radiation Safety and Measurement, 2(1):11–14.

[13] Binesh, A. and Mowlavi, A.A. and Mohammadi, S. (2012). Estimation of the effective dose from radon ingestion and inhalation in drinking water sources of Mashhad, Iran, Iran. J. Radiat. Res., 10(1):37–41.

[14] Poor habib, Z. and Binesh, A. and Mohammadi, S. (2019). A study on heavy radioactive pollution: Radon and Radium in streams and drinking water of Ramsar region by measured Prassi system, Iranian Physics Research Journal, 11(4):397–403.

[15] Chao, C.Y. and Tung, T.C. and Chan, D.W. and Burnett, J. (1997). Determination of radon emanation and back diffusion characteristics of building materials in small chamber tests, Building and Environment, 32(4):355–362.

[16] Tuccimei, P. and Moroni, M. and Norcia, D. (2006). Simultaneous determination of 222rn and 220rn exhalation rates from building materials used in central italy with accumulation chambers and a continuous solid state alpha detector: influence of particle size, humidity and precursors concentration, Applied Radiation and Isotopes, 64(2):254–263.

[17] Keller, G. And Hoffmann, B. and Feigenspan, T. (2001). Radon permeability and radon exhalation of building materials, Science of the Total Environment, 272(1–3):85–89.

[18] Zhang, L. and Lei, X. and Guo, Q. and Wang, S. and Ma, X. and Shi, Z. (2012). Accurate measurement of the radon exhalation rate of building materials using the closed chamber method, Journal of Radiological Protection, 32(3):315.

[19] Kovler, K. and Perevalov, A. and Steiner, V. and Rabkin, E. (2004). Determination of the radon diffusion length in building materials using electrets and activated carbon, Health Physics, 86(5):505–516.

[20] Andersen, C.E. (1999). Radon-222 exhalation from Danish building materials, Verlag nicht ermittelbar.

[21] Petropoulos, N. and Anagnostakis, M. and Simopoulos, S. (2001). Building materials radon exhalation rate: Erricca intercomparison exercise results, Science of the Total Environment, 272(1–3):109–118.

[22] Chen, J. and Rahman, N.M. Atiya, I.A. (2010). Radon exhalation from building materials for decorative use, Journal of Environmental Radioactivity, 101(4):317–322.

[23] Friedmann, H. and Nuccetelli, C. and Michalik, B. and Anagnostakis, M. and Xhixha, G. and Kovler, K. and de With, G. and Gascó, C. and Schroeyers, W. and Trevisi, R. (2017). Measurement of norm, Naturally Occurring Radioactive Materials in Construction, Elsevier.

[24] Samuelsson, C. And Pettersson, H. (1984). Exhalation of 222rn from porous materials, Radiation Protection Dosimetry, 7(1–4):95–100.

[25] Samuelsson, C. The closed-can exhalation method for measuring radon, Journal of Research of the National Institute of Standards and Technology, 95(2).

[26] El-Dine, N. W. and El-Shershaby, A. and Ahmed, F. And Abdel-Haleem, A. S. (2001). Measurement of radioactivity and radon exhalation rate in different kinds of marbles and granites. Applied Radiation and Isotopes, 55(6):853-860.

[27] Shoqwara, F. and Dwaikat, N. And Saffarini, G. (2013). Measurement of radon exhalation rate from building materials. Res Rev J Physics, 2(1):10-19.

ICNST 2024 International Conference on Nuclear Science and Technology
6- 8 MAY 2024 | Isfahan, Iran

A fisibility study on design and fabrication an anthropomorphic head phantom using 3D printer (Paper ID : 1287)

Khoshhal A.R.*, Esmaili Torshabi A., Habibi M.

Department of Nuclear Engineering, Graduate University of Advanced Technology, Kerman, Iran

Abstract

Despite the increasing expansion of radiation therapy and diagnostic radiation centers in the country to treat and increase the quality level of treatment of various diseases, we are still facing challenges such as dosimetry, calibration and quality control of radiation therapy and diagnostic radiation devices. In this sense, it is important to prepare and make a suitable phantom. Phantoms are used in dosimetry due to their density and effective atomic number similar to body tissues. Among the phantoms prepared for dosimetry purposes is the Rando phantom. The main purpose of this study is to determine the feasibility of the materials for making the anthropomorphic head phantom (AHP) head and neck phantom using a Digital Light Processing (DLP) 3D printer, as well as the design of the whole human body phantom with the lowest cost. The dimensions of different parts of the phantom were extracted from CT-Scan images and were designed using SolidWork, Meshmixer and Ultimaker Cura. In this study, the use of Thermoplastic polyurethane (TPU) resin equivalent to soft tissue and bone tissue were investigated. Considering that the density of soft tissue and skull bone is 1 $^{gr}/_{cm^3}$ and 1.6-1.7 $^{gr}/_{cm^3}$, the density of these two resins is 1 $^{gr}/_{cm^3}$ and 1.6 $^{gr}/_{cm^3}$. In order to verify the accuracy of our developped phanom a Monte Carlo based simulation assessment was done using GEANT4 code. Final results show that there is good agreement between our phantom in comparison with other common available phantoms.

Keywords: anthropomorphic phantom, 3D printer, internal dosimetry, Monte Carlo simulation

INTRODUCTION

Phantom is a numerical and physical model that shows the characteristics of several anatomical structures needed by humans. Phantoms are used for dosimetry purposes, calibration and quality control of radiation therapy devices.

In internal dosimetry, due to the unavailability of internal organs and tissues and the presence of various radiations, it is not possible to perform the dosimetry in a practical way only if the detector is placed instead of the desired organ or tissue, which is not possible. During radiation therapy with any radiation, it is always

necessary to stop the absorption of excess dose by a normal tissue. On the other hand, measuring and evaluating the absorbed dose is an important issue. Therefore, before practical treatment, a new phantom modeling may be very useful for dose calculation. [1]

In this sense, it is important to prepare and make a suitable phantom.

External beam radiation therapy is a standard-of-care cancer treatment method used to deliver localized radiation to known tumor sites. However, it is often limited by the toxicity of normal tissue to tissues that are anatomically close to the tumor. Head and neck cancer is a disease in which the tumor is often associated with vital normal tissues (spinal cord, brainstem, visual structures, etc.). [2]

Radiation therapy plays an important role in the treatment of head and neck cancer with a high probability of tumor control and a low probability of normal tissue complications. In image-guided radiotherapy to the head and neck absorbed dose to vital organs such as the lens, parotid gland and thyroid gland are of concern because they have already received doses from the course of radiotherapy. Phantoms are used to measure the absorbed dose during the treatment process and prevent extra dose to the sensitive tissue. [3]

Phantoms are used in dosimeters due to their density and effective atomic number similar to body tissues. One of the phantoms prepared for dosimetry purposes is Rando phantom. The head phantom allows us to place different sized dosimeters in many locations of the phantom volume. The human head has heterogeneous characteristics with distinct dielectric properties of head tissues due to corresponding components such as water, fat and protein. Due to the distinctive characteristics of head tissues, researchers have developed different categories of head phantoms for imaging purposes. For example, a heterogeneous phantom, a 3D printed phantom, a four-shell diffusion phantom, a plaster phantom, a reconfigurable phantom, and a head-sized phantom. The fabricated head phantom allows us to place different sized dosimeters in many locations of the phantom volume. The head phantom is made based on three-dimensional arrangements filled with numerous biochemical compounds, whose density and effective atomic number are similar to body tissue. Currently, several imaging technologies such as computed tomography scanning, magnetic resonance imaging, X-ray mammography, ultrasound, and positron emission tomography are used to detect brain abnormalities in the human head in the medical research system.

Low energy photons can be dangerous to human organs, tissues or DNA, RNA. Significant phantom materials that can be used in diagnostic radiology, radiation protection, radiation dosimetry, and dose estimation were reviewed for some essential radiation application values. The interaction of gamma ray

photons with matter has always been one of the fields of great interest among researchers due to its usefulness in medical imaging, radiation therapy, energy production, and food science. A thorough understanding of the interactions is necessary to accurately measure and control gamma radiation in various applications in order to minimize the risks of exposure and maximize their benefits. [4]

Low-energy photons are widely used in the medical field for various purposes such as medical imaging, radiography, and radiotherapy, as well as for radiation protection, radiation dosimetry, and dose estimation. Therefore, understanding their interactions is essential because low-energy photons are more damaging than high-energy photons. Phantom materials are artificial materials designed to mimic human tissues and have values of mass attenuation coefficients and effective atomic number similar to real human tissues. These can be made of various materials such as polymers, gels, plastics and even real tissue.

In the research of Josefine Cederhag and et al., their purpose was to establish the correlation between thermoluminescence dosimeters (TLDs) and Gafchromic film to measure absorbed doses and compare the minimum, maximum and average absorbed doses in larger areas of interest and in different organs and tissues of the skull to draw during cone beam computed tomography (CBCT). The result of their work was this: TLD positioning could not cover several organ sites. For this, only measurements of the absorbed dose from the film were available. [5]

In the research of Durer Iskanderani et al., the aim of this study was to map and compare the distribution of absorbed doses with Gaffochromic film for panoramic radiography and cone beam CT scans (CBCT) of the temporomandibular joint (TMJ) using adults and children phantoms. The result of their work was that the absorbed doses differed significantly between and in the radiosensitive tissues. The bone surface and salivary glands received the highest absorbed dose compared to other tissues in both panoramic and CBCT examinations of the TMJ. [6]

Although there are various reports for making phantoms using different 3D printers including fused-deposition-modeling 3D printers and also using different materials [7,8], but in our opinion, these methods have defects such as the presence of holes, non-uniformity of the produced product, long manufacturing time and high cost. Therefore, we investigated the possibility of using DLP 3D printer as well as TUP resins which are available and cheap to make this phantom. In addition to these things, we investigated factors such as cost reduction, construction time, and accuracy in design and achieved significant progress. Also, our results are very close to the real results.

In this research, we first used the GEANT4 simulation code to compare soft tissue and bone tissue with resins in terms of some factors (such as density, effective atomic number, etc.). Then, using CT-scan images and GEANT 4, we extracted the exact dimensions of the skull and designed the skull with Meshmixer, Ultimaker Cura and Solid work software and analyzed the results.

EXPERIMENTAL

GEANT4 simulation code

In the first part of this research, using the Monte Carlo method and the GEANT 4 simulation code, the target volume was defined in dimensions of 5 cm × 5 cm × 3 cm and the dimensions of the detector are 25 cm^2. The ingredients of this target were primarily skull bone and soft tissue. Then, the amount of rays reaching the detector was checked by using photon beam emission with a width of 2 cm. The numbers of this survey were registered as a reference. In the next step, the target volume of two TPU resins is considered to be equivalent to bone tissue and soft tissue. (Fig.1.)

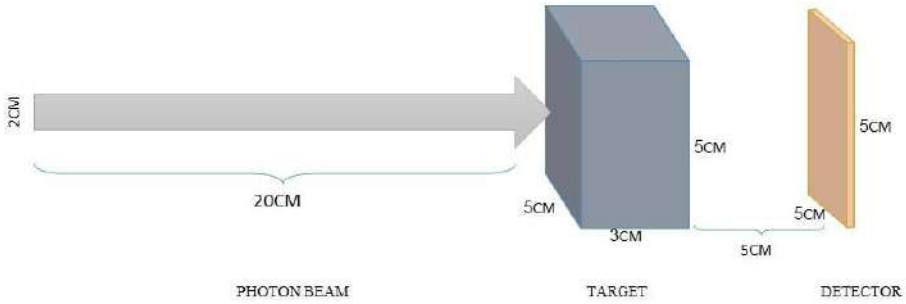

Fig.1. The Photon Beam, Target volume and Detector

In the next section, the dimensions of the target volume have been changed to 10cm × 10cm × 10 cm and the dimensions of the detector are 100 cm^2. The ingredients of this volume are defined as in the first part, firstly the skull bone and soft tissue as a reference, and in the next step, two TPU resins. Then, by using proton beam emission with a width of 2 cm, the depth of penetration of the beam into the target with different materials was investigated. (Fig.2.)

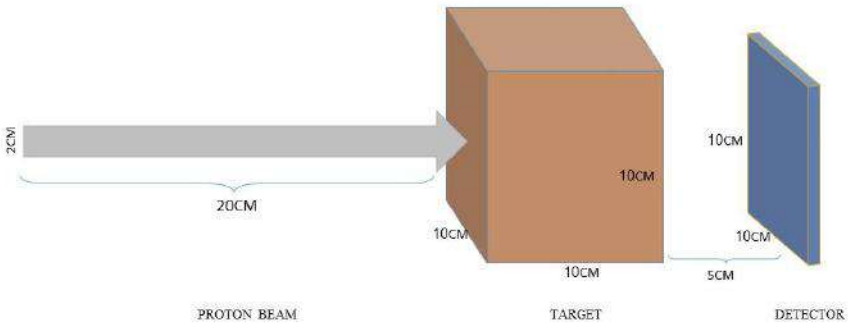

Fig.2. The Proton Beam, Target volume and Detector

Also in this simulation code, all the constituent elements of resins, soft tissue and bone tissue are defined and all physical and chemical properties as well as the most important factors such as density and effective atomic number related to them were applied.

Phantom design

Here, we used head CT-SCAN images and extracted the desired phantom dimensions from the images using GEANT4 code. Then we designed the phantom using Ultimaker Cura, Meshmixer and Solid work software. In designing the phantom from the outside to the inside, the first layer was considered as the skin layer on the skull, the second layer as the skull bone and the inner soft tissue layer. (Fig. 3 and 4)

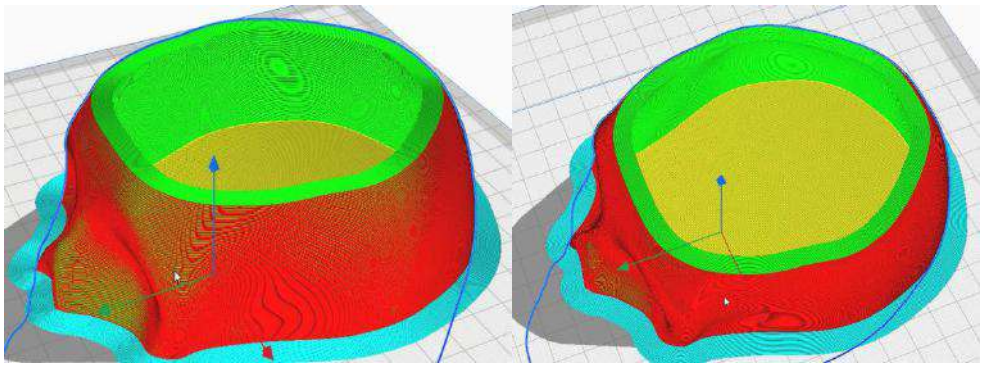

Fig. 3. Phantom design using Ultimaker Cura software (Red is Skin and equal to soft tissue, green is skull bone and yellow is soft tissue)

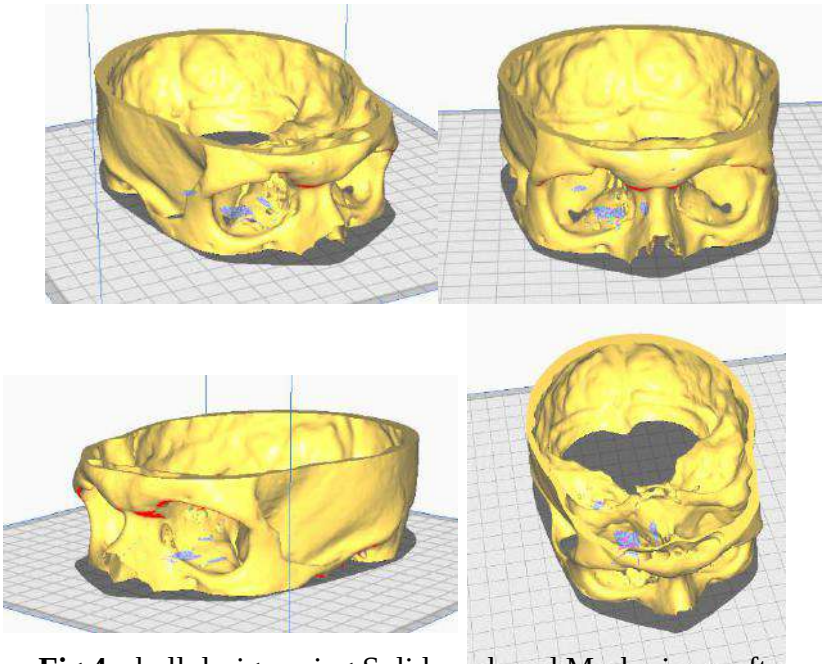

Fig.4. skull design using Solid work and Meshmixer software

In the last part of the research, we investigated the fabrication of the AHP phantom using a DLP 3D printer. Its prototype was made using Fused deposition modeling (FDM) 3D printer and is shown in Figure 5.

Fig. 5. Skull of AHD Prototype using FDM 3D printer

Results and discussion

In the first part of the simulation using the GEANT4 code, by comparing the number of particles that reached to the detector that had passed through the reference materials and two resins, the results at Table 1 showed that the use of two resins in this research is very favorable and have similar results to the reference results. According to Table 1, the percentage of particles that reached the detector in bone tissue and TPU resin is 54.59 % and 55.66 %, and this value for soft tissue and TPU resin is 66.6 % and 67.09 %.

Table 1. The percent of particles that reached to the detector

	Skull bone (Density: 1.6 $^{gr}/_{cm^3}$)	**TPU resin** (Density: 1.6 $^{gr}/_{cm^3}$)	**Soft Tissue** (Density: 1 $^{gr}/_{cm^3}$)	**TPU resin** (Density: 1 $^{gr}/_{cm^3}$)
particles (%)	54.59	55.66	66.6	67.09

Also, after checking the Bragg curve and the penetration depth of the particles in the second part of the simulation, the results showed that the penetration depth of the proton beam in the two resins is almost the same as the penetration depth in the reference tissues, which is shown in figure 5 and 6. In this figures, it can be seen that the penetration depth in bone tissue and TPU resin is 55 mm and 56 mm, and this value for soft tissue and TPU resin is 77 mm and 78 mm.

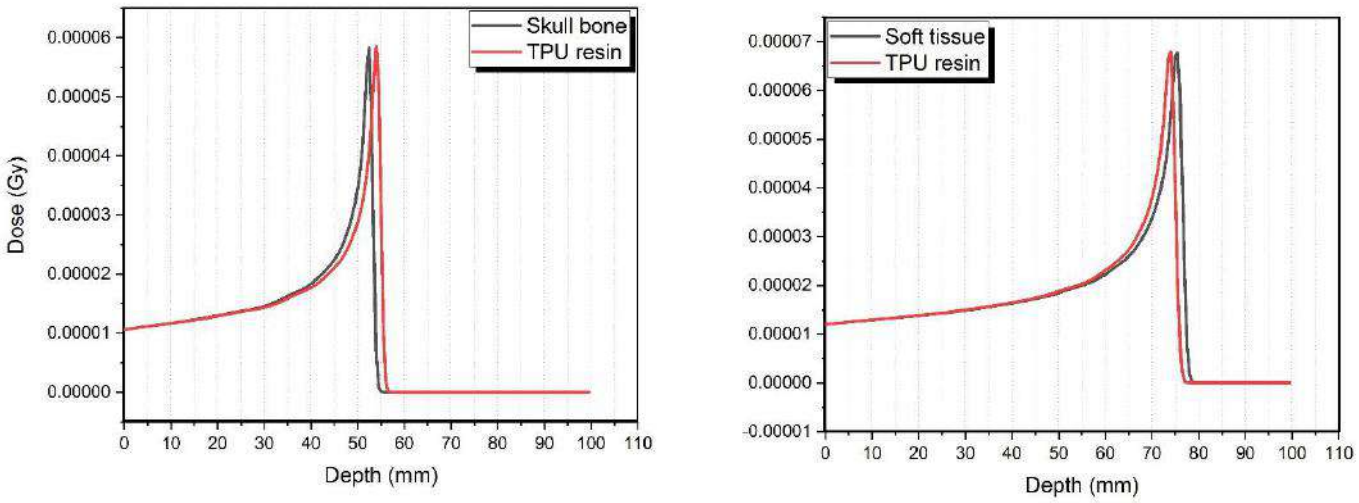

Fig. 5. The Bragg curve of results

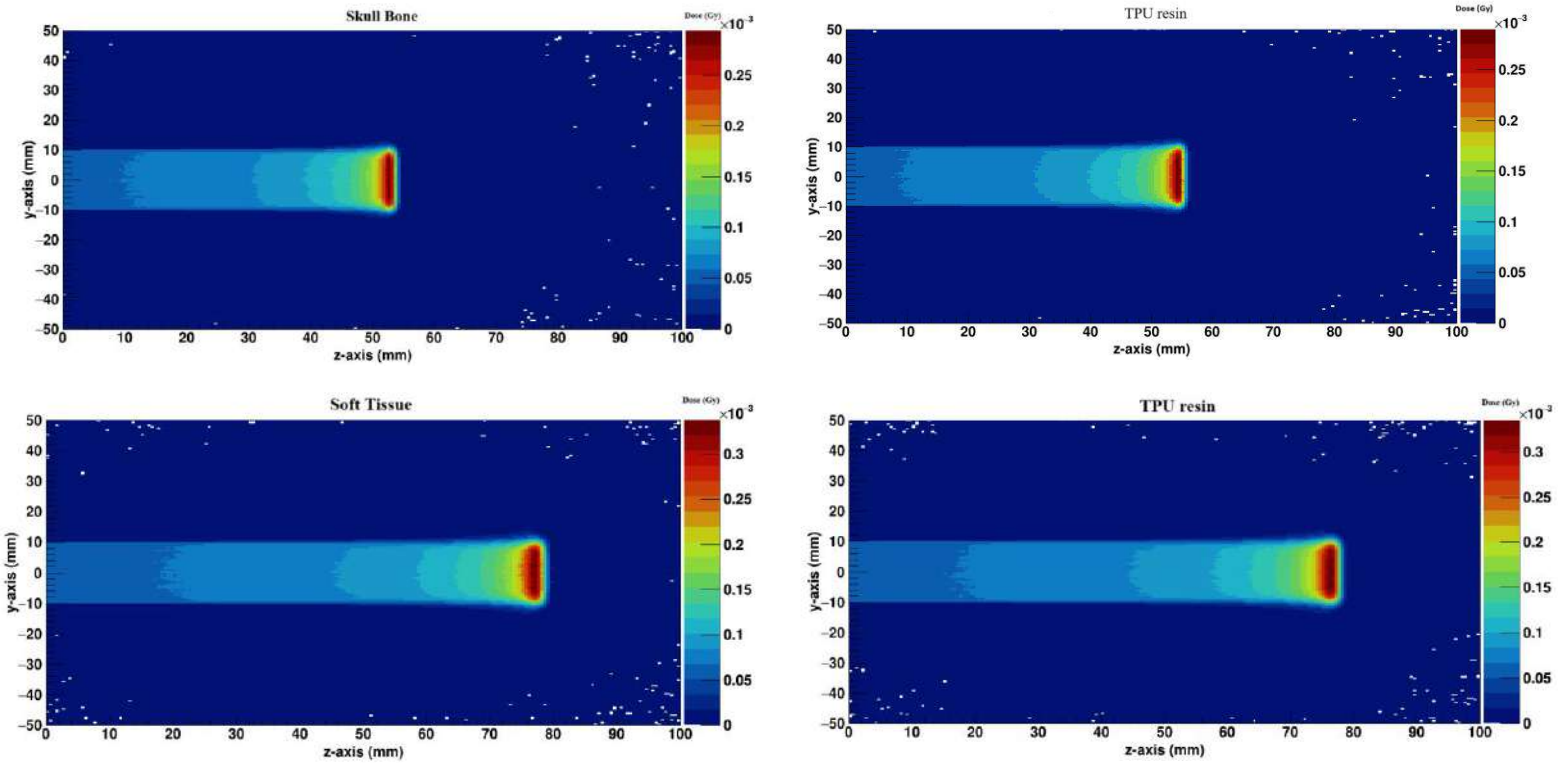

Fig. 6. Proton penetration depth in the target volume

In future research after the development of this product, we will examine the dosimetry results using the AHP phantom compared to a reference phantom (e.g. Rando phantom).

Since the density of lung tissue is 0.6 g/cm^3, we will face limitations and challenges to make this part of the phantom.

Conclusions

Phantoms are the anatomical structure of the whole human body and are used in dosimetry, quality control and calibration of radiation therapy and diagnostic radiation devices. One of the methods of making phantoms is using 3D printers. In this research, the possibility of making a phantom using a DLP 3D printer and TUP resins with different densities was investigated. The desired dimensions were extracted from CT scan images. Factors such as density and effective atomic number were applied in the GEANT4 simulation code. The simulated volumes were exposed to photon beam and proton beam irradiation. According to the results obtained from the number of particles reaching the detector, there is only a 1.07% difference in the number of photons reaching the skull bone and the equivalent TPU resin, and there is a 0.49% difference for the soft tissue and the equivalent TPU resin. Also, the penetration rate of the proton beam in the soft tissue and skull bone is only one millimeter different from their equivalent TPU resins. Therefore, our selected resins are suitable for making phantoms due to their availability and low cost. The novelty of our research, after careful design and selection of suitable resin, it was possible to make a phantom and a new method to make it has been introduced. It is suggested to use 3D printers and newer materials to make this phantom. The construction of this phantom is in our future plans and the results will be reported in the next investigations.

References

[1] Shirazi, S.A.M., Pazirandeh, A., Jahanfarnia, G. and Allaf, M.A., 2017. Presenting and simulating an innovative model of liver phantom and applying two methods for dosimetry of it in neutron radiation therapy. Reports of Practical Oncology & Radiotherapy, 22(1), pp.42-51.

[2] Adam, D.P., Grudzinski, J.J., Marsh, I.R., Hill, P.M., Cho, S.Y., Bradshaw, T.J., Longcor, J., Burr, A., Bruce, J.Y., Harari, P.M. and Bednarz, B.P., 2024. Voxel-level dosimetry for combined Iodine-131 radiopharmaceutical therapy and external beam radiotherapy treatment paradigms of head and neck cancer. International Journal of Radiation Oncology* Biology* Physics.

[3] Paduka, S., Thongsawad, S., Janthawanno, P., Khaeongrod, R., Ketphan, K. and Saiyo, N., 2024. Assessment of organ doses from head and neck cone-beam computed tomography (CBCT) in adaptive radiation therapy: A phantom study. Radiation Physics and Chemistry, 215, p.111338.

[4] Büyükyıldız, M., Kaur, P., Thakur, S. and Atlı, R., 2024. Study of phantom materials close to 1 keV photon energy for radiation applications. Radiation Physics and Chemistry, 215, p.111375.

[5] Cederhag, J., Kadesjö, N., Nilsson, M., Alstergren, P., Shi, X.Q. and Hellén-Halme, K., 2023. Comparison of absorbed doses and organ doses measured with thermoluminescent dosimeters and Gafchromic film for cone beam computed tomography examination of the posterior mandibular region in a head phantom. Oral surgery, oral medicine, oral pathology and oral radiology, 136(6), pp.769-776. [6] Iskanderani, D., Nilsson, M., Alstergren, P. and Hellén-Halme, K., 2020. Dose distributions in adult and child head phantoms for panoramic and cone beam computed tomography imaging of the temporomandibular joint. Oral surgery, oral medicine, oral pathology and oral radiology, 130(2), pp.200-208.

[7] Tran-Gia, J., Schlögl, S. and Lassmann, M., 2016. Design and fabrication of kidney phantoms for internal radiation dosimetry using 3D printing technology. Journal of Nuclear Medicine, 57(12), pp.1998-2005.

[8] Tino, R.B., Yeo, A.U., Brandt, M., Leary, M. and Kron, T., 2022. A customizable anthropomorphic phantom for dosimetric verification of 3D-printed lung, tissue, and bone density materials. Medical Physics, 49(1), pp.52-69.

ICNST 2024
International Conference on Nuclear Science and Technology
6- 8 MAY 2024 | Isfahan, Iran

GEANT4 simulation for calculating the permissible distance of rescuers without radiation protection equipment during the fall of nuclear level gauge radioactive sources (Paper ID : 1288)

Zaidabadi nejad.M*, Babamohammadi.Sh, Khoshhal.A.R
Department of Nuclear Engineering, Graduate University of Advanced Technology, Kerman, Iran

Abstract

Determining the continuous level of materials using nuclear technology in places where conventional methods are not responsive, provides important information for many industries, including iron processing factories. In this technology, it is tried to determine information related to the surface of materials by using the interaction of gamma rays with these materials. In the Kerman iron mining and industrial company, in order to monitor the online feeding of the iron processing plant line, it uses a nuclear level gauge with three Co60 sources, which have activities of 28.5, 28.5 and 30.5 mCi.

The use of nuclear precision instruments should be such that the risk of radioactive radiation does not threaten the heath of the personnel and rescuers at the site, either during normal operation or during an accident. Therefore, in this study, the Accident of the fall of all three radioactive sources of this level gauge due to the collision of the on-site overhead crane with them and Exiting the source from the holding chamber in order to investigate the safe distance of rescuers without protective equipment against the radiation present at the scene of the accident has been done. So that the results can be used to develop strategies to deal with this Accident. For this purpose, the desired sources and phantom of the human body were designed in GEANT4 code, and then by placing the phantom at different distances of 20 to 250 cm from this sources, the absorbed dose rate at different distances from the sources in the important human organs was obtained. The results showed that at a distance of 250 cm, the average absorption dose of the whole body will be 0.01 msv/h, so the rescuers are not allowed to cross this distance without using personal equipment and to provide aid, the area around the sources must be isolated up to this radius.

Keywords: Nuclear level gauge, Phantom, GEANT4, Absored dose rate

INTRODUCTION

Kerman province is the second largest province of the country after Khorasan province, where large mines and important steel factories are located. Iron mining and industrial companies of Kerman province play an important role in the policy making and management of the region. Due to the continuous presence of personnel and employees in the environment of the iron processing production line as a result of the accident,

it is necessary to investigate the dangers caused by the radiation of cobalt 60 element. Research shows that cobalt 60 is used in many technologies and provides many benefits to the daily operations of industry. [1] In similar research, it can be said that cobalt 60 source is used for oil and gas well logs, as well as in multiphase flowmeter technology in oil and gas production facilities, and in transition rocks for reservoirs in refineries, x-ray fluorescence, XRF, and sulfur gauges in laboratories. [2] The use of radiation sources has increased significantly since the last 20 years due to the advances in the special technology of ionizing rays that today the use of ionizing radiation sources in many industries including automotive, semiconductors, oil and petrochemicals, Cement, iron processing company, detergents, paper, etc. are used [2]. Dealing with radiation sources (ionizing rays) with the purposes of radiation protection is achieved by complying with national and international radiation protection regulations [3]. Measuring the volume or the level of the contents of the open air has been neglected in many industries and scientific applications. In most of these cases, it is not possible to observe the fluid, or continuous measurement and constant control of the amount of fluid is needed. Therefore, for achieve these purpose, level sensors have come to help the industry. In terms of technology, there are different methods for measuring the level of units. including: visible glass, moving glass, floating sensors, use of liquid weight measurement and tank (load cell), use of bubblers, use of differential pressure sensors, use of radar waves, use of light and laser waves, use of radioactive rays, acoustic and ultrasonic sensors, the use of inductive sensors, capacitive probes and other cases. [4]

In different methods, the level is measured either single-point or continuously. In point measurement, the material level is monitored at a predetermined point to prevent the overflow or complete emptying of the tanks, and continuous measurement also monitors the amount of material level in the tank constantly and without interruption.[5] Point and continuous level measurement systems in many industries including oil and gas exploration and extraction, oil and gas refineries, petrochemical and chemical industries, pharmaceutical, cement, mining, papermaking, electricity and power, food and water industries and sewage is used. [6]

Harmful tissue reactions, cancer as a result of radiation hazards due to high dose radiations. [7] Considering this issue, investigation and study on radiation consequences can have a significant impact on radiation protection in medicine, research and future industry [8].

This research describes the permissible distance against ionizing rays with three Cobalt 60 sources at distances of 20, 50 and 100 cm. that the personnel and employees can pass by observing the allowed distance

without using personal equipment and assistance. Finally, with the definition of an adult male phantom approved by the MIRD committee, according to the spectrum of radiation from three sources of cobalt 60 at different distances, the amount of absorbed dose in different and important organs of the body was calculated using GEANT4.

Materials and Method

Method section

Two detectors and three Cobalt 60 sources with 28.5, 28.5 and 30.5 mCi activity are used in Kerman Province Mining and Industry Company for nuclear level measurement. In this method, detectors and sources are located around the tube of the level gauge. When the iron ore passes through this tube, it will change the count of the detector output. Now, in this study, the Accident of the fall of all three radioactive sources of this level gauge due to the collision of the on-site overhead crane with them and Exiting the source from the holding chamber in order to investigate the safe distance of rescuers without protective equipment against the radiation present at the scene of the accident has been done. The schematic can be seen from Figure 1, where three sources are placed at different distances from the phantom.

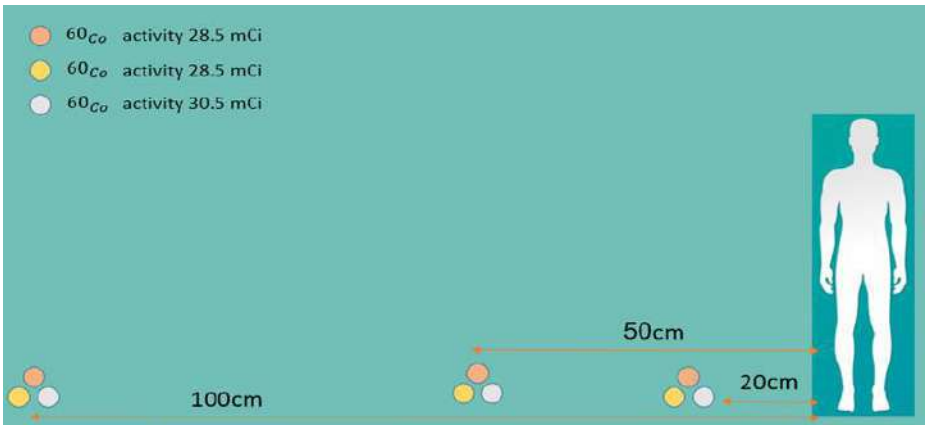

Fig. 1. Schematic placement of three Cobalt 60 sources at different distances

Simulation

In this research, the amount of absorbed dose received by several important organs of the body was evaluated and calculated by using GEANT4 calculation code. To write this code, three cobalt 60 sources were defined

at different distances from the adult phantom. At a distance from 20 to 250 cm, three sources of cobalt 60 with activity 28.5, 28.5 and 30.5 were placed. In each of these intervals, the amount of absorbed dose reached to the phantom was evaluated in the GEANT4 code. The image of the adult human phantom in the GEANT4 code that has been simulated can be seen from Figure 2.

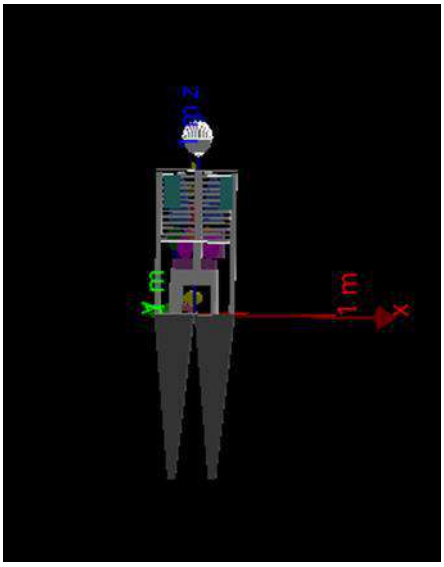

Fig. 2. Adult human phantom designed in GEANT4 code

Monte Carlo simulation is a precise method to confirm the results, develop and optimize a typical experiment. Geant4 code derived from (Geometry and Tracking), is a Monte Carlo simulation tool written in C++ programming language and is based on the transport of various types of particles in the environment. GEANT4 has extensive libraries containing the cross section (probability of interaction) of different particles and in different environments. One of the prominent features of this code is its high capability in designing geometry, physics of particle interaction and radiation source. In this research, the material, geometry, and spring were introduced using tools, and in this code, an adult male phantom with a height of 180 cm was coded and designed to check the absorbed dose to different organs of the phantom body.

Results and discussion

The calculations and results were done by the GEANT4 code, the results of the absorbed dose reached to each body organ at different distances are shown in Table 1. Table one shows cobalt 60 with three sources with activities of 28.5, 28.5 and 30.5 at a distance from 20 to 250 cm from the phantom. The amount of absorbed dose in terms of millisilverts per hour for each organ is shown in Table 1.

Table 1. The absorption dose of some of the most important organs of the body with cobalt 60 source with three sources with activities of 28.5, 28.5 and 30.5 at a distance from 20 to 100 cm from the phantom

Organs	Absorbed dose (mSv/h) 20 cm	Absorbed dose (mSv/h) 50cm	Absorbed dose (mSv/h) 100cm
Brain	5.5	0.841	0.29
Thyroid	7.68	1.103	0.43
Heart	8.83	2.11	0.52
Right Adrenal	11.71	3.308	0.59
Left Adrenal	11.53	3.33	0.57
Liver	6.19	3.074	0.609
Left Lung	7.3	2.93	0.55
Right Lung	8.05	2.86	0.57
Left Arm	12.36	3.99	1.000072
Right Arm	12.46	4.03	1.00006
Spleen	8.24	2.907	0.57
Left Clavicle	6.38	1.407	0.49
Right Clavicle	6.93	1.45	0.54
Left Kidney	10.93	3.82	1.009
Right Kidney	10.51	3.93	1.007
Left Leg	26.46	5.43	1.98
Right Leg	26.32	5.42	2.1
Thymus	10.61	3.56	0.48
Stomach	18.86	3.98	0.73
Left Scapula	6.41	1.094	0.39
Right Scapula	6.13	1.23	0.36
Left Testis	17.007	3.98	0.82
Right Testis	19.88	4.003	0.86
Pancreas	12.28	2.85	0.62
Pelvis	18.91	4.11	0.707

Bladder	19.24	4.21	0.73
Small Intestine	17.62	3.61	0.66
Large Intestine	17.99	3.89	0.63
Lower Large Intestine	18.63	4	0.66

The results of this research, according to Table 1, show that at a distance of 20 cm, the amount of total dose reached to the body is higher than at a distance of 50 and 100 cm, and the highest amount of dose received is the leg organ. Also, the results show that at a distance of 100 cm, the total absorbed dose is 1.072 mSv/h, which is higher than the permissible limit for radiation workers who are exposed to X-rays. Also simulation for 150, 200 , 250 cm was done and the result of these was shown in table 2.

Table 2. The average absorbed dose reached to body organs at different from 20 to 250 cm

The average absorbed dose (mSv/h)					
20cm	**50 cm**	**100cm**	**150cm**	**200cm**	250cm
19.69	4.30	1.07	0.26	0.063	0.01

Also, the results are shown as a chart in Figure 3. According to these charts, the brain organ, as the farthest organ from the source, received the lowest dose, and the leg organ, as the closest organ to the source, received the highest dose. The displacements in the graphs are due to the different distances of the source, which changes the amount of ray reaching the phantom at different distances according to the angular change.

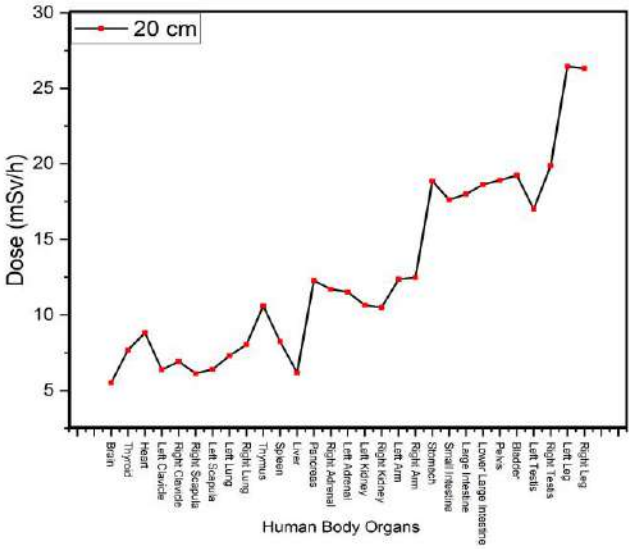
20 cm
Dose (mSv/h)
Human Body Organs
Brain
Thyroid
Heart
Left Clavicle
Right Clavicle
Right Scapula
Left Scapula
Left Lung
Right Lung
Thymus
Spleen
Liver
Pancreas
Right Adrenal
Left Adrenal
Left Kidney
Right Kidney
Left Arm
Right Arm
Stomach
Small Intestine
Large Intestine
Lower Large Intestine
Pelvis
Bladder
Left Testis
Right Testis
Left Leg
Right Leg

(A)

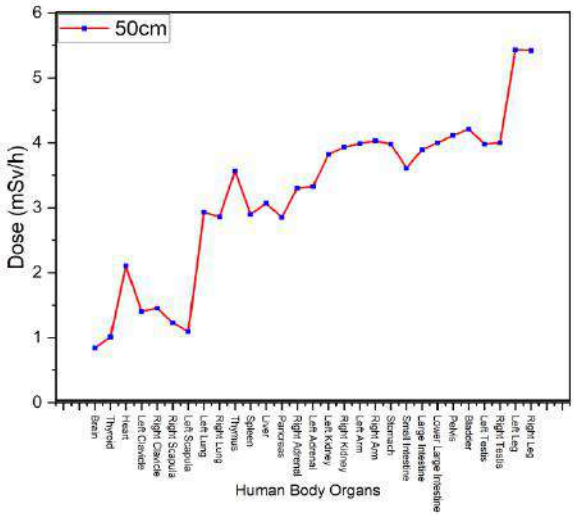
50cm
Dose (mSv/h)
Human Body Organs
Brain
thyroid
Heart
Left Clavicle
Right Clavicle
Right Scapula
Left Scapula
Left Lung
Right Lung
Thymus
Spleen
Liver
Pancreas
Right Adrenal
Left Adrenal
Left Kidney
Right Kidney
Left Arm
Right Arm
Stomach
Small Intestine
Large Intestine
Lower Large Intestine
Pelvis
Bladder
Left Testis
Right Testis
Left Leg
Right Leg

(B)

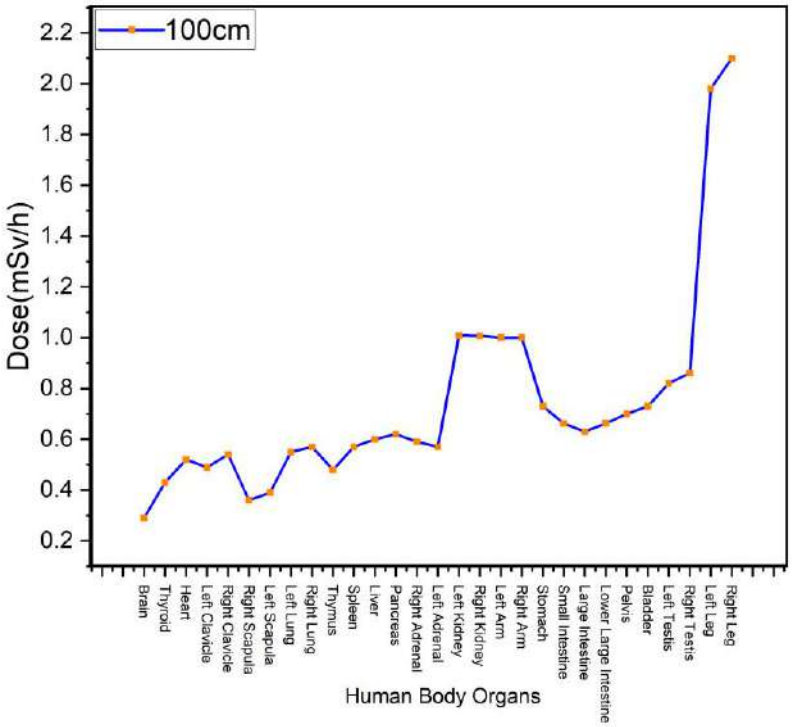

(C)

Fig. 3. Graphs of absorbed dose from head to foot at distances of 10 cm (A), 50 cm (B) and 100 cm (C)

Conclusions

In order to maintain the health of employees, personnel and rescue workers in iron ore processing industrial mines in Kerman province, the absorbed dose from sources of ionizing radiation was investigated in this paper during the accidents. The average absorbed dose at different intervals is given in Table 2. As can be seen in Table 2, the results obtained with the GEANT4 code showed that the amount of dose reached at different distances up to 200 cm is higher than the permissible limit. The permissible absorbed dose for radiation workers is 0.003 mSv/h per hour. According to the results and studies obtained at a distance of more than 250 cm, the absorption dose is within the permissible limit. Therefore, it is recommended that

radiologists and rescuers follow protective and safety measures against radiation in order to maintain their health during this incident.

References

[1]El Sadani R. A. M. (2001): Heavy Weight Concrete, M. Sc Thesis, Structural Engineering Department, Faculty of Engineering Ain Shams University, Cairo, Egypt.

[2] Abu-Jarad, F., 2009. The application of radiation sources in the oil and gas industry and shortages in their services. Atoms for Peace: an International Journal, 2(4), pp.338-349.

[3] Jones, C.G., 2005. A review of the history of US radiation protection regulations, recommendations, and standards. Health physics, 88(2), pp.105-124.

[4]Dunn, W., 2005. Introduction to instrumentation, sensors, and process control. Artech.

[5]Carlson, D.R., 1977. Level and density measurement using non-contact nuclear gauges. Measurement and Control, 10(3), pp.83-87.

[6] Xie, X.C., Zhang, Y.Y., Guo, Y.J. and Lai, W.C., 2019. Research on the passive nuclear level gauge. Radiation Effects and Defects in Solids, 174(9-10), pp.915-927.

[7] IAEA, I., 2005. TECDOC-1459-Technical Data on Nucleonic Gauges.

[8] Falahati, M., Vaziri, M.R., Beigzadeh, A.M. and Afarideh, H., 2018. Design, modelling and construction of a continuous nuclear gauge for measuring the fluid levels. Journal of Instrumentation, 13(02), p.P02028.

ICNST 2024
International Conference on Nuclear Science and Technology
6- 8 MAY 2024 | Isfahan, Iran

Simulation the fall of a radioactive source from an industrial densitometer due to an earthquake using the GEANT4 code to calculate the personal Absorbed dose (Paper ID : 1289)

Zaidabadi nejad.M*, Khoshhal.A.R, Babamohammadi.Sh
Department of Nuclear Engineering, Graduate University of Advanced Technology, Kerman, Iran

Abstract

Nuclear methods are widely used in advanced industrial measurement systems. The nuclear densitometer is one of the most accurate methods of density measurement, which is based on detecting the attenuated flux of a gamma-ray source with a certain activity. Due to its high speed and being online, this method has become a very suitable alternative to the usual time-consuming and expensive analysis methods. Using this method in iron processing industries has reduced costs and increased efficiency. In the Kerman iron mining and industrial company, a nuclear densitometer with a Cs137 source, which has an activity of 100 mCi, is used to check the presence or absence of iron concentrate in the exhaust dust of iron processing plants. The use of precision nuclear instruments should be such that the risk of radioactive radiation does not threaten the Health of the personal at the site, either during normal operation or during an accident. Therefore, in this paper, the fall of the radioactive source of this densitometer due to an earthquake and its exit from the holding chamber has been investigated in order to calculate the absorbed dose by the personnel at distances of 10, 50 and 100 cm from the source. So that the results can be used to develop strategies to deal with this Accident. For this purpose, the desired source and also the phantom of the human body were designed in the GEANT4 code, and by placing the phantom at different distances from this source, the absorbed dose in the important human organs was obtained. The results showed that the average absorbed dose of the whole body at distances of 10, 50, 100 and 170 cm is 24.27, 1.3617, 0.21 and 0.0077 msv/h, respectively, which distance more than 170 cm, the dose is allowed.

Keywords: Phantom, Nuclear Densitometer, Absorbed dose, GEANT4

INTRODUCTION

Nuclear instruments are widely used by various industries for measuring product quality, optimizing processes, energy storage, irradiating materials, monitoring physical processes, and other applications due to their many economic advantages [1-2]. The first industrial use of these tools was reported more than fifty years ago, and since then their use has expanded widely [3]. In these tools, there is no need for direct contact with the materials under test, and therefore they can be used to monitor difficult processes, such as identifying

materials with very high temperatures or toxic and dangerous materials and packaged products that can be opened around the protection [4]. In addition, beta, gamma and X-ray radiations, which are often used in these tools, do not damage the material and do not change their physical properties or appearance. Due to these countless advantages, radioisotope sources and nuclear tools have maintained their practical position in the industrial and scientific fields in competition with other alternative tools [5]. Nuclear measuring instruments often operate automatically and are used in a portable or stationary and installed form. All these tools include a source that acts as a radiation source. Also, there is at least one detector in them that measures the intensity of the radiation beam after it interacts with the material [6].

The nuclear densitometer is a type of measuring device that can be used for measurement by radiometric and non-contact methods. The nuclear densitometer device is installed on the pipe. This type of device can be made in any shape and size, and there is no limit to its size and shape. In general, nuclear gamma ray densitometry is one of the most accurate measurement methods that is widely used in the industry [7]. The nuclear densitometer can be used in the fields of oil product relationship in the transmission line and also to determine the mass flow rate in combination with the flow meter [8].

In the nuclear densitometer of Kerman Mining and Iron Industry Company, the source of cesium 137, which has an activity of 100 mCi, is used [9]. Radiation hazards due to high dose radiation sometimes cause harmful tissue reactions, cancer, etc. Investigation and study of radiation consequences can have a significant impact on radiation protection in medicine, research and future industry [1,4].

Due to the high activity of cesium 137 in Kerman Mining and Iron Industry Company, the risk of radioactive radiation threatens the health of employees and personnel at the place of iron ore processing operations when the source falls due to natural events such as an earthquake or an accident of a source falling from a container. For this purpose, in this research, the dangers of radiation after the occurrence of these incidents were investigated and the amount of absorbed dose by different organs of the human body has been evaluated using the GEANT4 calculation code at distances of 10, 50, 100 and 170 cm from the source of cesium 137. became.

Material and Method

To measure the density by nuclear methods in Kerman Iron Mining and Industry Company, the pipe is tested between the detector and a source of cesium 137, which is counted every time iron passes through this path of the detector, as a result, the presence and passage of iron can be found. In this research, with the aim of cesium 137 falling to the ground due to an accident such as an earthquake, the amount of radioactive radiation

hazards caused by this source at distances of 10, 50,100 and 170 cm has been investigated using the GEANT4 calculation code. In Figure 1, you can see the schematic of the location of the Cs 137 source with an activity of 100 mCi.

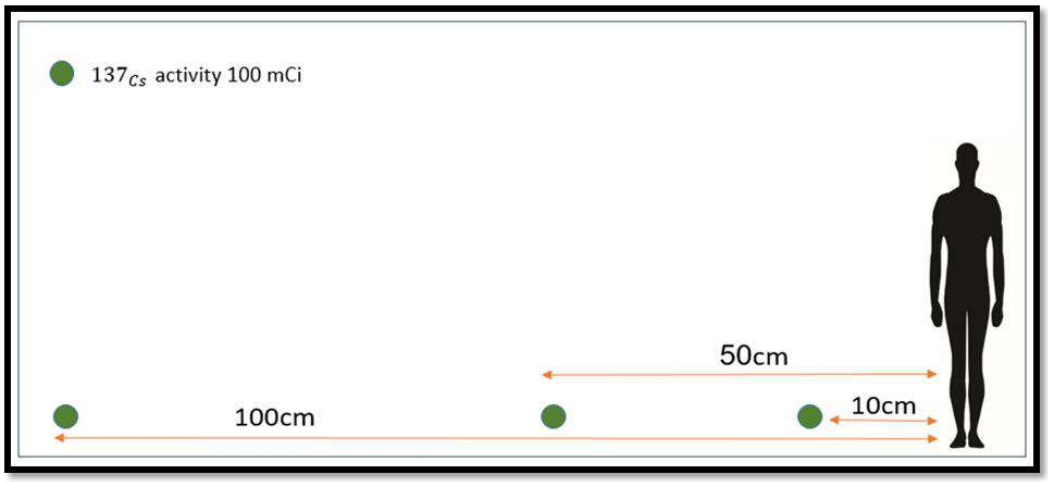

Fig. 1. Schematic of placement of Cs137 at different distances from the human body

GEANT4 (GEometry ANd Tracking 4) is an object-oriented Monte Carlo simulation toolbox that has been developed in collaboration with many world scientists [10]. GEANT4 is a simulation tool for the passage of particles through matter. This computational code includes a full spectrum including tracking and physics and geometry models [11]. In this article, using this calculation code, which is widely used in radiation protection, the amount of dose received from Cesium 137 at different distances was investigated and evaluated. In this research, Cesium spring 137 was considered as a point source. In Figure 2, you can see the image designed with the GEANT4 code of the adult human phantom at distances of 10, 50 ,100 and 170 cm with the code.

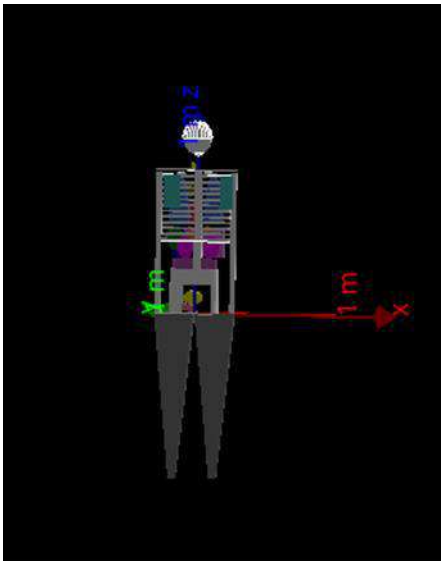

Fig. 2. Adult human phantom simulated with GEANT4 code

Results and discussion

After checking the output of the GEANT4 simulation code, the results of absorbed dose to different organs of the phantom by the cesium 137 source are shown in Table No. 1. In this table, the amount of absorbed dose at distances of 10, 50, 100 and 170 cm from the phantom is calculated in terms of mSv/h.

According to what was expected, the results of this research show that at a distance of 10 cm from the source, we have the highest absorbed dose in different organs of the human phantom. According to the results obtained at distances of 10, 50, 100 and 170 cm, the total absorption development is 24.27 (mSv/h), 1.3617 (mSv/h), 0.21 (mSv/h) and 0.0077(mSv/h), respectively. According to the obtained results, the absorption explanation obtained in the distances calculated by the GEANT code is higher than the permissible limit.

Table 1. The amount of dose absorbed by the source of cesium 137 to different organs of the phantom

Organs	Absorbed dose (mSv/h) 10cm	Absorbed dose (mSv/h) 50cm	Absorbed dose (mSv/h) 100cm
Brain	9.24	0.6633	0.024
Thyroid	12.81	1.00084	0.053
Heart	13.12	1.0014	0.085
Right Adrenal	16.42	1.0105	0.087
Left Adrenal	16.99	1.0106	0.0893
Liver	14.302	1.0093	0.0793
Left Lung	12.5002	1.01003	0.731
Right Lung	12.67	1.01	0.069
Left Arm	18.51	1.1034	0.125
Right Arm	19.405	1.1032	0.184
Spleen	13.32	1.0308	0.0654
Left Clavicle	13.21	0.93	0.0595
Right Clavicle	13.41	0.949	0.0582
Left Kidney	17.75	1.13	0.1801
Right Kidney	18.88	1.168	0.1790
Left Leg	28.722	1.971	0.295
Right Leg	28.721	1.104	0.297
Thymus	12.18	1.0709	0.0687
Stomach	18.32	0.995	0.125
Left Scapula	12.94	0.916	0.0458
Right Scapula	12.83	0.92	0.0401
Left Testis	20.11	1.19	0.118
Right Testis	20.13	1.18	0.1506
Pancreas	16.94	0.85	0.0795
Pelvis	19.075	1.051	0.171
Bladder	19.802	1.015	0.1706
Small Intestine	18.14	0.991	0.1105
Large Intestine	18.906	0.98	0.1192
Lower Large Intestine	19.15	0.99	0.1201

Also, the results are shown as a diagram in Figure 3. The brain organ, as the farthest organ from the source , received the lowest dose, and the leg organ, as the closest organ to the source, received the highest dose due to the presence of the spring on the ground, the highest dose to the leg organ and the lowest dose to the brain organ due to The distance of the skull (the height of the phantom is 180 cm) is entered from the ground. The displacements in the graphs are due to the different distances of the source, which changes the amount of ray reaching the phantom at different distances according to the angular change.

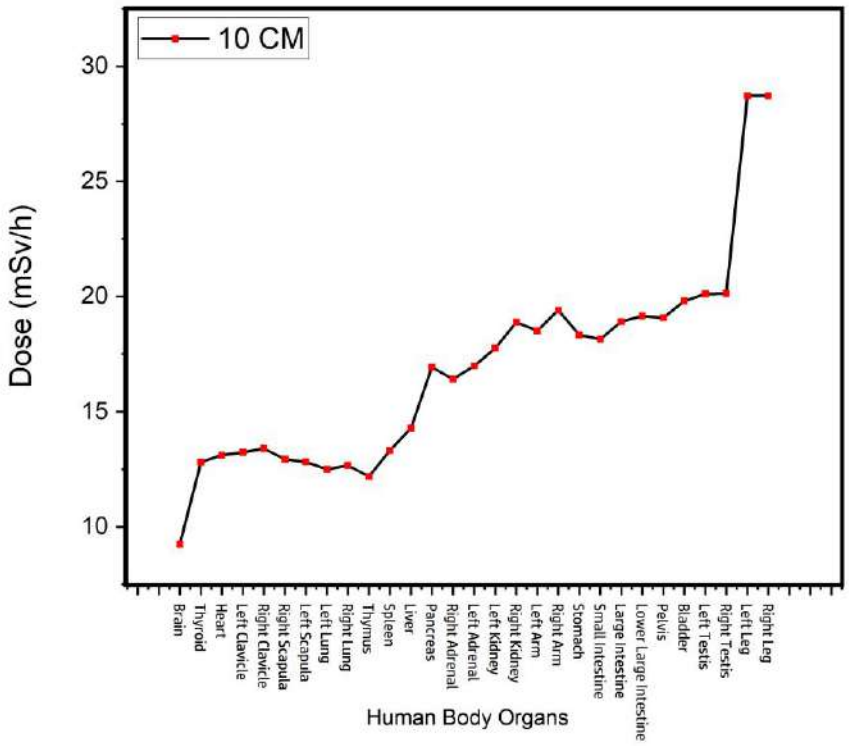

(A)

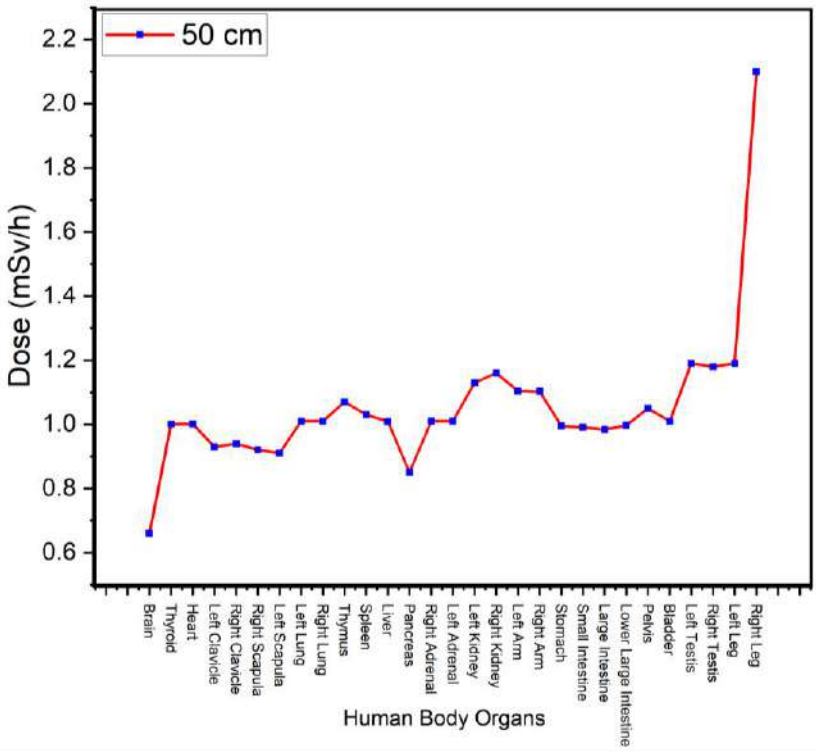

(B)

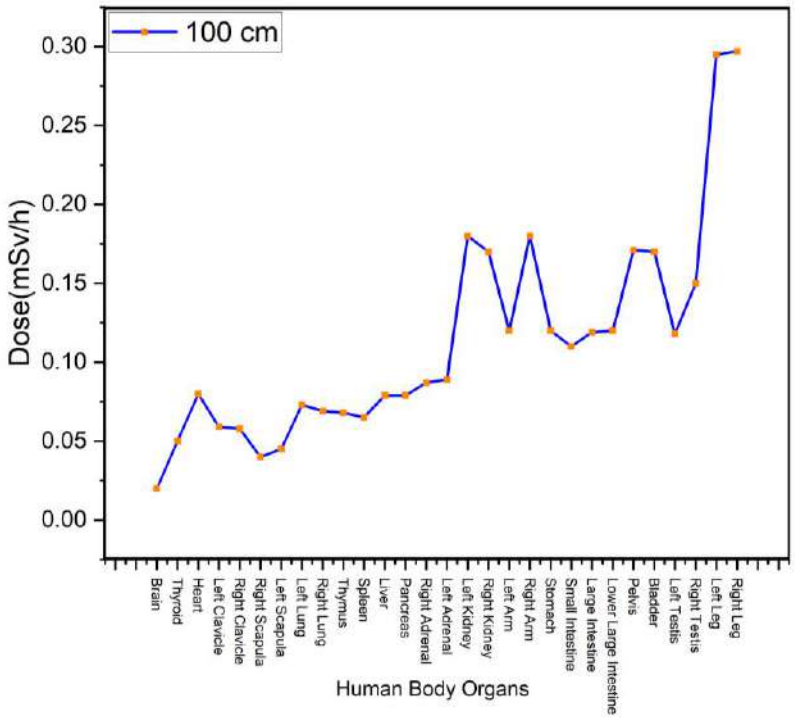

(C)

Fig. 3. Graphs of absorbed dose from head to foot at distances of 10 cm (A), 50 cm (B) and 100 cm (C)

Conclusions

In this research, the amount of absorption dose with cesium 137 source with 100 millicury activity in source falls Accident at different organs of the phantom has been obtained at 10, 50, 100 and 170 cm different levels. According to the results, in each of these intervals, the received dose is higher than the permissible limit. Simulation at a distance of 170 cm showed that this distance is within the allowable limit. It is recommended that radiation workers and rescuers are not allowed to provide aid during this accident up to a distance of 170 <X without observing safety issues, and it is necessary to observe protective and safety measures against radiation in order to maintain their health.

References

[1] I A E A (IAEA); "Technical Data on Nucleonic Gauges", IAEA-TECDOC-1459 (2005) 1

[2] W Boyes, "Instrumentation Reference Book"; Butterworth-Heinemann (2009).

[3] I A E A (IAEA); "Manual on Nuclear Gauges", IAEA-PRSM-3 (1996) 1.

[4] M Falahati, M R Vaziri, A M Beigzadeh, and H Afarideh, J. Instrum. 13, 02 (2018) 02028.

[5] P K Bhatnagar and A Nagaratnam, Defence. Sci. J. 37 (1987) 339.

[6] M B Holstad, "Gamma-Ray Scatter Methods Applied to Industrial Measurement Systems", Ph. D. Thesis, University of Bergen (2004)

[7] Taylor D, Kansara M. A theory of the nuclear densimeter. Soil Science. 1967 Jul 1;104(1):25-34.

[8] Chen Z, Ahmed RM, Miska SZ, Takach NE, Yu M, Pickell MB, Hallman J. Experimental study on cuttings transport with foam under simulated horizontal downhole conditions. InSPE/IADC Drilling Conference and Exhibition 2006 Feb 21 (pp. SPE-99201). SPE.

[9] Khorsandi M, Feghhi SA. Design and construction of a prototype gamma-ray densitometer for petroleum products monitoring applications. Measurement. 2011 Nov 1;44(9):1512-5.

[10] Agostinelli S, Allison J, Amako KA, Apostolakis J, Araujo H, Arce P, Asai M, Axen D, Banerjee S, Barrand GJ, Behner F. GEANT4—a simulation toolkit. Nuclear instruments and methods in physics research section A: Accelerators, Spectrometers, Detectors and Associated Equipment. 2003 Jul 1;506(3):250-303.

[11] Carrier JF, Archambault L, Beaulieu L, Roy R. Validation of GEANT4, an object-oriented Monte Carlo toolkit, for simulations in medical physics. Medical physics. 2004 Mar;31(3):484-92.

[12] Cember, H., 1969. Introduction to health physics. Introduction to health physics.

ICNST 2024
International Conference on Nuclear Science and Technology
6- 8 MAY 2024 | Isfahan, Iran

Investigating the distribution of indoor radon concentration in a residential typical building (Paper ID : 1293)

Zabihinpour M [1*], Mohammadi S [2].

[1,2] Department of physics, Payame Noor University, Tehran, IRAN

Abstract

Radon is a radioactive gas that nowadays is considered one of the most harmful natural factors in residential areas all over the world. After cigarettes, radon gas is considered to be the biggest cause of lung cancer. Therefore, it is very important to study the measurement of radon concentration in different parts of the building. In this research, by choosing a sample building, the distribution of radon concentration in different regions is modelled by using Computational Fluid Dynamics (CDF) in two conditions, non-ventilation and natural ventilation. Then the results measured by a continuous work radon detector have been compared in a similar condition. Also, to confirm the results, the average radon concentration in the building and for different conditions was compared with the data obtained from the analytical method. The results show that the modelling performed in a non-ventilation method with an error of less than 15% is consistent with the experimental data. Also in natural ventilation conditions, the experimental results confirm the numerical modelling results. On the other hand, the results derived from the analytical solution in both non-ventilation and natural ventilation conditions confirm the results obtained from the simulation of the distribution of radon concentration. Our emphasis on this study is to determine the proper location of sleeping, sitting, and standing in a building, to reduce the dose received from radon gas.

Keywords: Radon, Natural ventilation, Computational Fluid Dynamics (CFD), Analytical method.

INTRODUCTION

People in developed countries, on average, spend more than 85% of their time indoors, such as in houses, offices, schools, and so on. Although the building is considered as a shelter for protecting against heat, cold, sunshine, noise, etc., the people, however, these shelters are not safe enough as they may contain pollutants in the indoor environment. Pollutants affect the quality of the indoor atmosphere which may damage human health. Unfortunately, there are many kinds of pollutants that are rising constantly [1].

Studies have shown that after cigarettes, radon (222Rn) is the major cause of lung cancer (UNSCEAR, 2000) and is one of the most harmful pollutants in the domestic environment of many countries, including

Scandinavia, the United Kingdom, and the United States. It is estimated that half of the dose the public receives is from radon and its progeny. And that radon is responsible for more than 3,000 and 21,000 annual lung cancer deaths in the UK and the United States, respectively [2-3].

In recent years, with further identification of the internal damage caused by radon in human health, the development of more precise research seems necessary, especially with the expansion of closed ventilation systems such as fan coils, chillers, radiators, floor heating and air conditioners in residential, offices and educational places. According to many research activities, the average radon content in residential houses is about 48 Bq/m^3, and in open environments is about 15 Bq/m^3. But the very important point is that this amount can vary considerably in different places [4].

In addition, using traditional methods of measuring indoor radon, one can only see the average raw material provided for a whole building or for one room in a period of one year. The lack of information in such methods is not acceptable in terms of the safety principles of indoor air quality.

The World Health Organization also insists on having information concerned with the rate of radioactive elements such as radon that may be carcinogenic [5].

In other words, most of the research performed, up to the present, on indoor radon has been measured and the average air concentration is calculated in a few buildings. Although this information is useful in terms of finding areas and buildings potentially with potential internal radon risk factors, it is not enough in the prediction of the real risk for their residents. For example, the exact location of breathing during sleeping or sitting and also during daily activities is very important, so they should be taken into account with more efficiency compared to the areas that are not frequently used by the inhabitants. Therefore, in recent studies, the focus is on measuring, as well as finding an acceptable pattern of radon distribution, taking into account all existing physical parameters, including ventilation conditions at specified times and also for places that are more important in our current studies. The need to continuously measure internal radon using solid-state detectors to determine the level and distribution of radon concentration in residential environments was emphasized [6].

Many scientists investigated the effect of physical factors such as temperature variations, humidity, geological characteristics, and rainfall on the average internal radon concentration [7-9].

By using Computational Fluid Dynamics (CFD), the method of distribution of radon concentration based on the physical characteristics of the room and also the proper ventilation effect on reducing indoor radon concentration has been checked and reported [10-13].

In this study, the distribution of radon concentration in different locations and also in different physical conditions was investigated by selecting a suitable sample building, from March 2017 to January 2018. Due to the dynamical complexity of radon distribution in the interior of the buildings, in addition to the usual measurements, the computational fluid dynamics method was used. Determining the required parameters, by using the Fluent software, the distribution of radon concentration in the specified building was simulated. To validate the derived model, the data obtained from the numerical solution for the specified points were compared with the results obtained from the analytical solution and also the data from measurement obtained by using a high-precision continuous radon detector work.

EXPERIMENTAL

Sample Building

In this work, a study was conducted to investigate the effect of various physical factors on the distribution of radon concentration in the interior of a one-story building in Shandiz-Iran. This building is situated on an almost ground floor and is connected to three areas: salon, kitchen and bedroom, toilet and bathroom are located outside the main building. The total area of the building is about 48 m^3 and the height of the roof is 3 m (Figure 1).

The salon's area is about 24 m^2 and the entrance door of the building is 120 cm wide and 190 cm high in the eastern corner of the southern wall, and below which is a gap of approximately 4 cm along the width of the door, which can be used as natural ventilation. The bedroom and the kitchen are similar in size with a length of 4 m and a width of 3 m parallel to the northern part of the building. Also, according to Figure 1, there are two similar windows with dimensions of 100 to 50 cm and 2 m above the floor in the middle of the northern wall of the bedroom and kitchen. The walls, roofs, and floors of the entire building are covered with tiles and ceramics with a low radon emission rate. On the other hand, there are some small but deep gaps in the walls. These gaps are the main source of radon entry to the building and are depicted in Figure 1, Gap1 to Gap4.

Measuring chamber

To determine the rate of radon emission at given surfaces, a cubic measuring chamber has been used that except for its open face; five other faces are coated with an impenetrable plastic material. During measuring the output flux, a Radon Meter device is placed inside the chamber. Dimensions of our chamber are 45cm×45cm×25cm and with the existence of a measuring device inside the chamber, the volume of empty space is roughly .032 m^3. The area of open surface is 0.16 m^2.

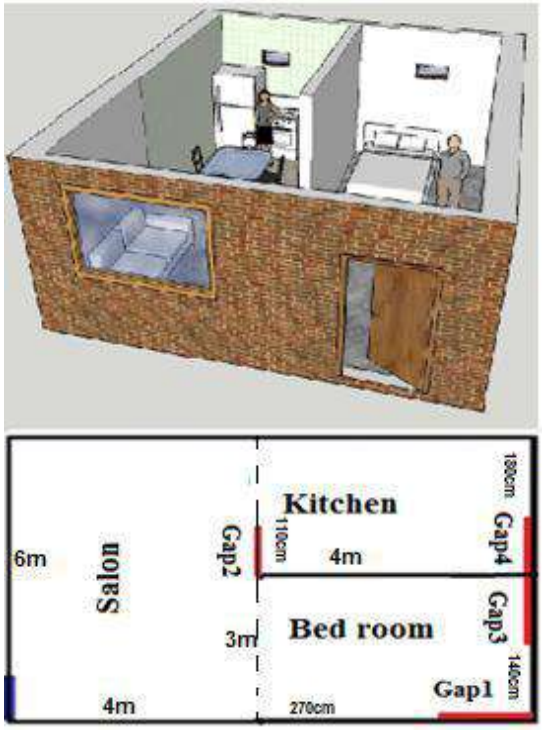

Figure 1. 3D Model (top) and Sample Building Map (bottom).

Measuring device

In order to measure the radon concentration in this study, we used the Radon Meter Model 2-1688 RTM made by the German company Sarad. It is a portable electronic measuring device that can simultaneously measure and record pressure, temperature, relative humidity, and Thoron concentration. In addition, it has the ability to operate in two fast and slow modes (higher precision). The most important feature of this device is its rapid response to variations in radon concentration compared to other devices or other measuring methods.

RESEARCH THEORIES

Method of Active measurement

In order to focus our research on the critical points affecting human health, four important heights of the floor, at which often an adult human being with a normal stature, breathes a mixture of air and Radon were selected (Figure 2-top) and, accordingly, the Radon concentration was measured at each stage for 16 sample points in different areas of the building (Figure 2-bottom) and compared with the data obtained from fluid dynamics (CFD). At each stage, the measurements continued to reach a stable equilibrium state (at least three half-lives). Also, the number of boundary conditions used in the Fluent, such as the temperature of the walls,

ceiling, and floor inside, as well as the pressure and temperature of the air outside the building, were measured several times and their averages were used in our study. These quantities are presented in Table 1.

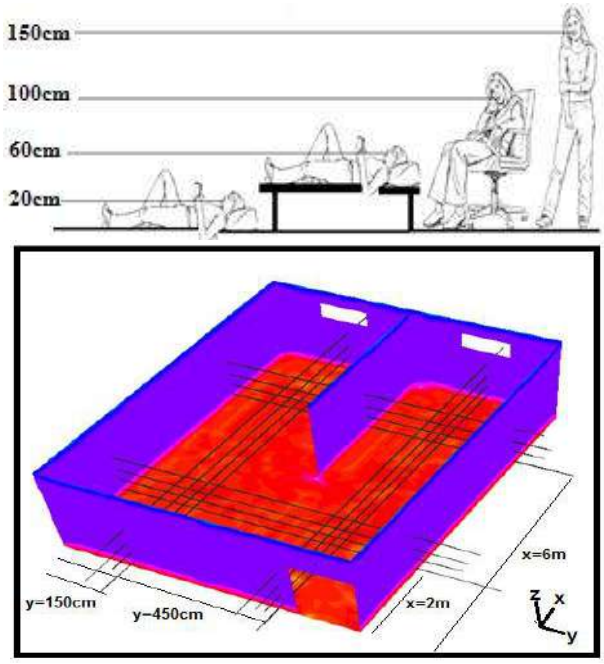

Figure 2. Important respiratory heights for an adult human being with a normal stature (top) and a view of the 16 selected sample points that are located at the intersection of the drawing lines (bottom).

Method of Computational Fluid Dynamics (CFD)

Using the finite-volume method of conservation laws, numerical equations were solved by using powerful Fluent software. The general form of conservation laws in fluid flux for a small controlled volume, which depends on variable C is:

$$\frac{\partial(\rho C)}{\partial t} + \nabla.(\rho CV) = \nabla.(\rho D \nabla C) + S_C \qquad (1)$$

The first term on the left of this equation is the time rate of the variations of the fluid element C (unbalanced effect). The second term is the pure flux of the variable C outside the fluid element (motion effect), the first term on the right shows the rate of C variation as a result of the diffusion, and finally the last term is the source of C production, which in fact shows the rate of flux change due to the C production.

All equations used in this method are derived from equation (1). The quantities are introduced in Table 1, and the equations used in this method are introduced in Table 2. Fluent software uses the laminar flow models in solving equations. That is for calculations, we consider adhesion forces in the areas neighbor to the walls,

and forces of viscosity in the areas remote from the walls, The non-organized networks govern the solutions of our equations. The advantage of using this type of network can be significant in reducing computational costs compared to the organized networks.

It should also be noted that to simplify the numerical modeling, several limitations have been used in this research as the following:

1. The effect of the presence of residents and furniture in the building is neglected.
2. All gases in the building are assumed ideal.
3. Due to the lack of access to realistic changes in the temperature of the walls, floor, and ceiling during simulation, their average values are used as a constant.

Table 1. Quantities used in measurements and CFDs.

Symbols and Abbreviations			
κ	kenetic energy	E	Radon exhalation rate(Bq$m^{-2}s^{-1}$)
λ_v	Air change rate	K	Thermal Conductivity(w/m-k)
λ_{Rn}	Radon decay constant (s^{-1} or h^{-1})	G	Radon generation rate (Bq m^{-3} s^{-1})
C_p	Specific heat capacity (J kg^{-1} K^{-1})	ε	Turbulent dissipation rate (m^2 s^{-3})
ν	Kinematic viscosity (m2 s^{-1})	S	Source term
u v w	Velocity components in x, y, and z coordinates (m s^{-1})	V	Velocity vector(m/s)
A	Surface (m^2)	ρ	Density (kq/$m^{3)}$
M_w	Molecular weight(kmol/kg)	D_e	radon difference (Pa)
RH	Relative humidity	T	Temperature (·C)
C	Radon concentration (Bq m^{-3})	Δp	Pressure Deference (Pa)
L	Characteristic length(m)	V	Velocity (m/s)
ρ_s	Density of the soil grain	Re	Reynolds number
f	Radon emanation coefficient	A_{Ra}	Radium activity (Bq/kg)
CFD	Computational fluid dynamics	CRM	Continuous radon monitor
F_B	Body force vector	T	Temperature (K)

D	Effective diffusion coefficient (m^2s^{-1})	V	Volume (m^3)

Analytical solution method

A well-known analytical model was used to estimate the radon concentration in the sample building. In this model, radon concentration is increased by the release of radon through slabs and all surfaces in the building,

On the other hand, the radionuclide decay and ventilation reduce this quantity. The final equation to determine the internal concentration of radon in a room with the volume V, is presented [14-15].

$$C_i(t) = C_0 e^{-\lambda t} + \frac{EA}{V\lambda}(1 - e^{-\lambda t}) \qquad (2)$$

where C_i is the internal radon concentration at time t (h), C_0 is the initial radon concentration at t = 0 in terms of Bqm^{-3}, $E(Bqm^{-2}h^{-1})$ is the radon input flux, or the radon emission rate from the soil and building materials, $A(m^2)$ is the area of the surface through which the radon gas is released, $V(m^3)$ is the volume of the closed room or the test chamber and $\lambda(h^{-1})$ is the total radon decay rate that is given by the equation: $\lambda = \lambda_{Rn} + \lambda_V$

Where λ_{Rn} is the radon decay constant, and λ_V is the air ventilation rate from the room or compartment. Therefore, the most important variables in determining the internal radon concentration are the radon input flux entering the room and also the room ventilation coefficient. Therefore, in the event of blockage of all air ventilation systems, in the case of stable equilibrium, the equation 2 can be rewritten as:

$$C_{Max} = \frac{EA}{V\lambda_{Rn}} \qquad (3)$$

By inserting radon emission data from different gaps (Table 1) and the volume of the building, the average radon content in the building is derived by using relation 3[16].

Table 2. Equations used in CFD for numerical solution.

Expression	Equation
$\frac{D(\rho)}{Dt} = \frac{\partial \rho}{\partial t} + \nabla.(\rho V) =$ $\frac{\partial \rho}{\partial t} + \frac{\partial}{\partial x}(\rho u) + \frac{\partial}{\partial y}(\rho v) + \frac{\partial}{\partial z}(\rho w) = 0$	The mass conservation equation
$\nabla.(V) = \frac{\partial}{\partial x}(u) + \frac{\partial}{\partial y}(v) + \frac{\partial}{\partial z}(w) = 0$	The mass conservation equation-in the steady state condition

$\frac{\rho D(V)}{Dt} = -\nabla P + \mu\nabla^2 V + F_B$	The momentum conservation equation
$\frac{\rho D(u)}{Dt} = \frac{\partial(\rho u)}{\partial t} + \nabla.(\rho u V) = -\frac{\partial P}{\partial x} + \mu\left(\frac{\partial^2 u}{\partial x^2} + \frac{\partial^2 u}{\partial y^2} + \frac{\partial^2 u}{\partial z^2}\right)$ $\frac{\rho D(v)}{Dt} = \frac{\partial(\rho v)}{\partial t} + \nabla.(\rho v V) = -\frac{\partial P}{\partial y} + \mu\left(\frac{\partial^2 v}{\partial x^2} + \frac{\partial^2 v}{\partial y^2} + \frac{\partial^2 v}{\partial z^2}\right)$ $\frac{\rho D(w)}{Dt} = \frac{\partial(\rho w)}{\partial t} + \nabla.(\rho w V) = -\frac{\partial P}{\partial z} + \mu\left(\frac{\partial^2 w}{\partial x^2} + \frac{\partial^2 w}{\partial y^2} + \frac{\partial^2 w}{\partial z^2}\right) + \rho g$	The simplified forms of the momentum equations- in the x, y and z directions.
$\frac{\partial(\rho C_p T)}{\partial t} + \nabla.(\rho C_p T V) = \nabla.(k\nabla T) + S_e$	The energy conservation equation
$\frac{\partial C}{\partial t} = \nabla.(D\nabla C) + \nabla.CV - \lambda_{Rn} C + G = 0$	Conservation equation – In steady state and incompressible flow
$\frac{\partial(\rho C)}{\partial t} + \nabla.(\rho C V) = \nabla.(\rho D\nabla C) + S_C$	Radon transport equation
$\frac{\partial(\rho C)}{\partial t} + \nabla.(\rho C V) = \nabla.(\rho D\nabla C)$	Radon transport equation- no radon generation and decay in the air, $SC = 0$
$\nabla.(CV) = \nabla.(D\nabla C)$	Radon transport equation - For steady state conditions and constant radon density

Results and discussion

During the period from March 2017 to January 2018, radon concentration was measured at different points in the building in different periods, and, according to its conditions, numerical solutions were performed both with Fluent software and with an analytical solution. Each complete cycle includes at least 10 days with no ventilation and 4 days with a condition with specific ventilation rates. In the followings, we explain various surveys for a typical period.

Border Conditions

All indoor air ventilation systems were completely blocked for about 10 days (860,000s). Although during this period, we saw temperature variations of around 10 ° C in the air outside the building for a full day and night, the wall temperature inside the building was almost constant. According to our measurements, the

average temperature of the northern, southern, eastern, and western walls, as well as the temperature of the ceiling and floor was 16, 17, 17, 19, 16, and 15 $^{\circ}C$ respectively.

Radon Entrance Rate

The floors and walls in the sample building are completely insulated in this study, and apart from the four gaps in the floor, labeled as Gap1 to Gap 4 in Figure 1, the radon emission rate released from other surfaces can be ignored. The radon emission rate of these gaps was measured for different months of the year, using a measuring chamber and a continuous measuring device, both described previously. Putting all required measured data in Equation 2, the average values are tabulated in Table 3.

Table 3. Radon emission rates from slots.

/Gap Parameter	Gap1	Gap2	Gap3	Gap4
Location	Bed room	Hall	Bed room	Kitchen
Area(m^2)	4.9×10^{-2}	5.1×10^{-2}	3.2×10^{-2}	2.8×10^{-2}
E (Bq/m^2s)	0.48	0.64	0.42	0.39

Non-ventilation condition

Modeling plates based on CFD at x=2 m and x=6 m are shown in Figure 3 about the boundary conditions of the sample state and after 800,000 seconds of blocking all air ventilation routes. The intersection of these plates with the lines perpendicular to them at selected heights specifies the density at the corresponding points. The results of this simulation are compared with the data obtained from the measurement and are tabulated in Table 4. The maximum difference observed in these cases is about 15%, indicating a relatively good coincidence of the CDF model with experimental results.

Also, Figure 4 shows the contour variation of radon concentration at a height of 1.5 m from the floor at the same conditions. The average of these values and also the average of the data obtained from measurement are compared with the average concentration derived from the analytical solution of Equation 3. The results are tabulated in Table 5. As can be seen, the experimental and analytical results are consistent with the simulated results.

Effect of Ventilation

In order to investigate the effect of ventilation on the concentration and the distribution of indoor radon concentration, opening the gap under the main door and windows on the northern walls allows the entrance of fresh air into the building.

The average temperature of the intake air during this period was 14°C and the radon concentration in the building could be ignored.

During this period, meteorological data shows that for most of the time, the direction of the airflow outside the building was south-north, so, during the ventilation, it was assumed that fresh air entered the building from the gap under the main door, and exit from the windows on the northern side of the building.

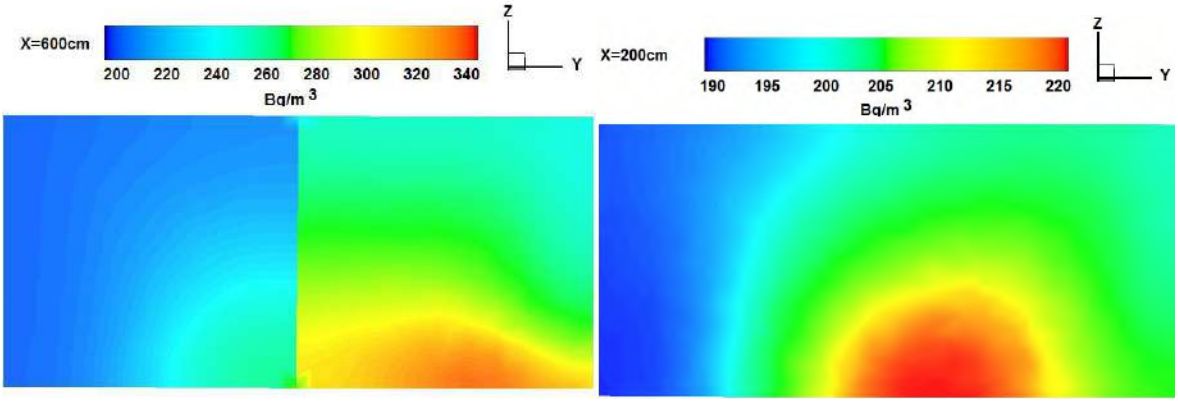

Figure 3. Radon concentration contours in x=2 m (top figure) and in x=6 m (bottom figure) for a closed room mode.

Table 4. Radon concentration in 16 sample building samples based on numerical solution and measured in closed room mode.

	Coordinate(cm)			**C(Bq/m^3)**	
	X	Y	Z	Numerical	**Measurement**
1	200	150	20	199	**228±31**
2	200	150	60	196	**219±28**
3	200	150	100	195	**202±23**
4	200	150	150	194	**187±19**
5	200	450	20	215	**241±37**
6	200	450	60	211	**229±24**
7	200	450	100	208	**221±22**
8	200	450	150	206	**211±21**
9	600	150	20	227	**241±27**
10	600	150	60	221	**244±25**
11	600	150	100	218	**237±21**
12	600	150	150	214	**234±27**

13	600	450	20	334	**385±39**
14	600	450	60	316	**341±29**
15	600	450	100	296	**317±32**
16	600	450	150	274	**294±27**

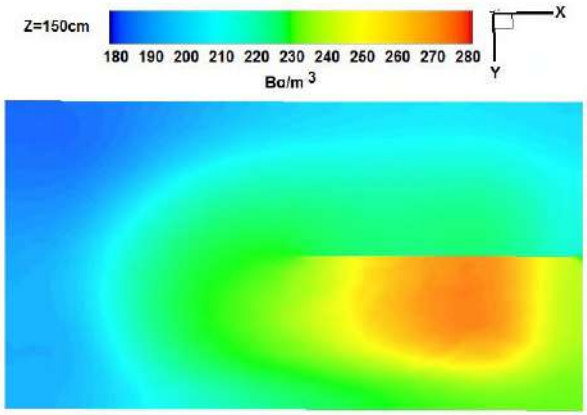

Figure 4. Radon concentration contours at a height of 1.5 meters from the floor in non-ventilation conditions.

Table 5. Data obtained from measurement methods, analytical and numerical solutions for radon average concentration in the building after a 10-day period without ventilation.

Calculation Method	Analytical Solution	Numerical Solution	Measurement
C(Bq/m^3)	272±38	238	252±29

By inserting the measured data obtained from the temperature changes in the corresponding thermodynamic equations used in these cases, the air velocity and the ventilation coefficients in each case were calculated separately.

These patterns show a mean velocity of approximately 40 mm /s in a typical period, for airflow from the main door. Also, the ventilation rate equivalent to this velocity, (according to the given air inlet and also the volume of the room) is $\lambda_V = 3.3\times10^{-5}\frac{1}{s}$.

Similar to the non-ventilated mode, the contours simulated from radon concentration using the Fluent software at x=2 m and x=6 m were used to calculate radon concentration at these points. (Figure 7)

The data obtained from this modeling with the results obtained from measurements over a 4-day period (100,000s) after the start of the natural ventilation, is presented in Table 6. There is a good consistency between the results of modelling and those obtained from experimental data.

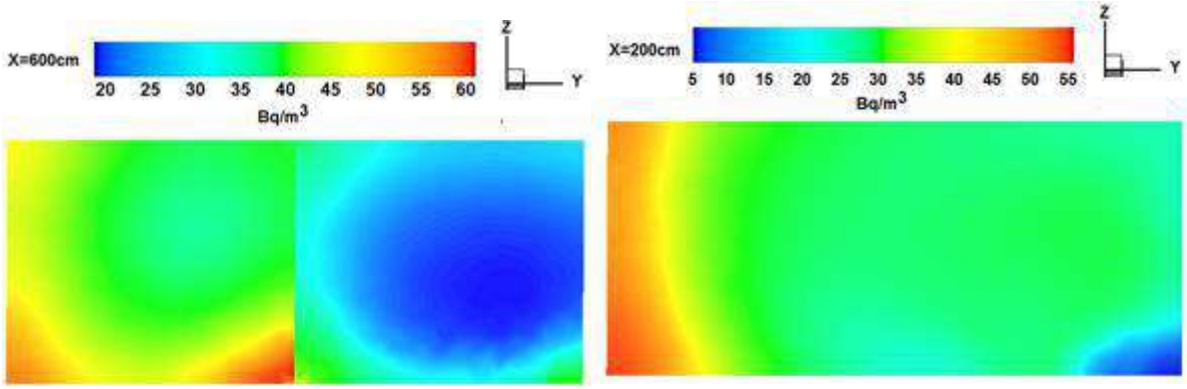

Figure 5. Radon concentration contours at x = 2m (top figure) and x = 6m (bottom figure) for a 4 day period of continuous natural ventilation.

Also, Figure 6 shows the radon concentration contour at a height of 1.5 meters from the floor, after the same period of ventilation, from which we can obtain the mean value of radon concentration in the room. Also, by inserting the ventilation coefficient in Equation 5, the predicted analytical value was obtained at a stable equilibrium. Our results are indicated in Table 7.

Table 6. Radon concentration in 16 sample points in the building based on numerical solution and measurement for a 4 day period of natural ventilation.

	Coordinate(cm)			**C(Bq/m^3)**	
	X	Y	Z	Numerical	**Measurement**
1	200	150	20	39.5	**43±4**
2	200	150	60	35.9	**47±9**
3	200	150	100	34.1	**42±8**
4	200	150	150	33.2	**39±7**
5	200	450	20	24.7	**31±7**
6	200	450	60	25.6	**29±5**
7	200	450	100	26.9	**33±7**
8	200	450	150	27.4	**34±7**
9	600	150	20	44.8	**51±8**
10	600	150	60	40.8	**43±6**
11	600	150	100	37.2	**42±7**
12	600	150	150	34.1	**41±7**
13	600	450	20	27.9	**32±6**
14	600	450	60	20.8	**28±6**
15	600	450	100	19.6	**24±5**
16	600	450	150	19.5	**21±3**

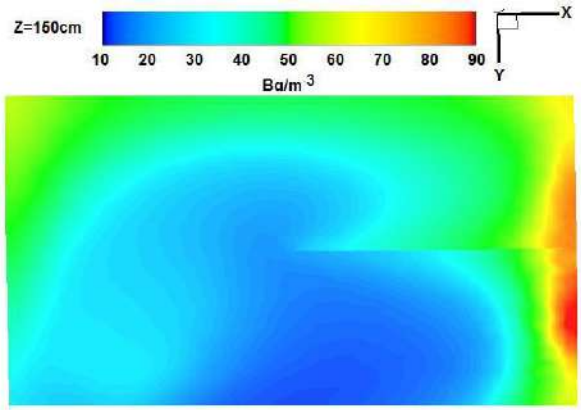

Figure 6. Radon concentration contours at 1.5 meters height from the floor for a 4-day period of natural ventilation.

Table 7. Data obtained from measurement methods, analytical solution, and numerical solution for average radon concentration in the building for a 4-day period of natural ventilation.

Calculation Method	Analytical Solution	Numerical Solution	Measurement
C(Bq/m^3)	17±2	16.1	23±4

Temperature Effect

Figure 7 (solid curve) shows the effect of temperature variations on radon concentration in natural ventilation conditions. As it is seen, the radon concentration decreases by reducing the average temperature difference between internal and external environments. The results derived by other scientists (dashed curve) also confirm this behavior [13].

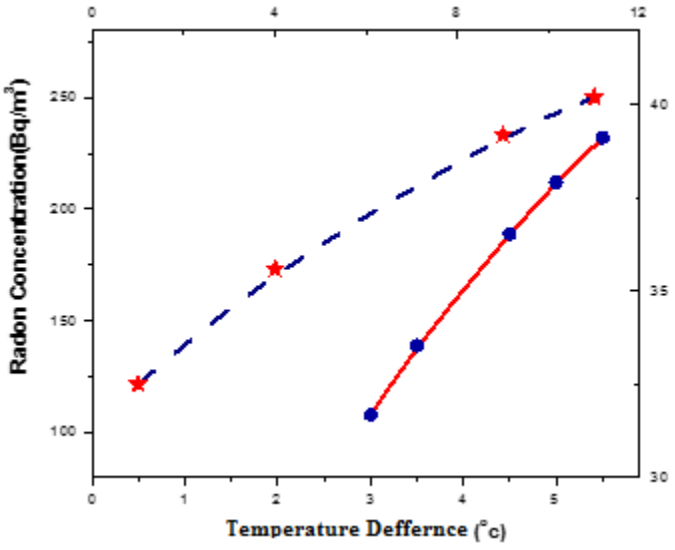

Figure 7. The variations in radon concentration versus temperature differences between Internal and External Environments in Natural Ventilation, the solid curve is the current study, the dashed curve is Rabi et al. work, 2017.

Height Effect

The accuracy of our results in this study shows that by increasing height from the floor, the concentration of radon decreases. Figure 8, shows a sample of these variations for the mid-point of the bedroom in a natural ventilation condition in our research (solid curve) and also in other research (dashed curve). An increase in the slope of these variations is observed by decreasing height in both distributions (Akbari and Oman, 2015). [11].

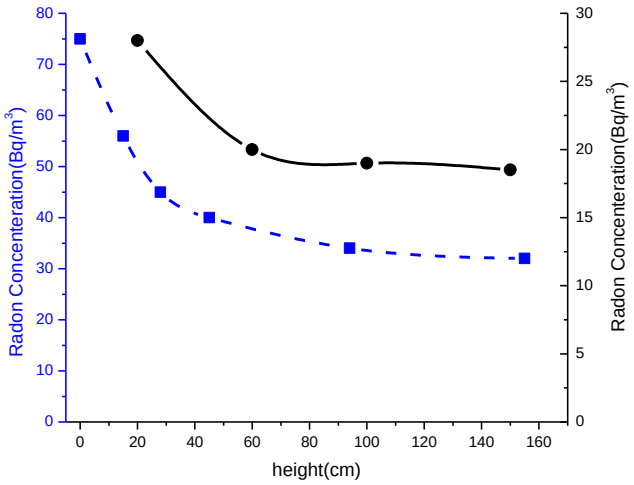

Figure 8. The variation of radon concentration versus height difference from the floor in natural ventilation, the solid curve is Current study, dashed curve belongs to Akbari and Oman work.

Conclusion

We have used in this paper, a 3D model of CFD for research and development concerned with the distribution of radon concentration in a typical building. In the case that, all the building ventilation routes were closed for a 10-day period, the results obtained (Table 4) show that the maximum difference between the simulated and experimental data is about 15%.

On the other hand, the data show that, although in all areas, radon concentrations are greater than the permissible value (100 Bq/m^3), the person sleeping on the ground or in a bed with the location of his head in the middle of the bedroom receives a radiation dose almost twice as much as the person standing on the right side of the hall.

On the other hand, Table 5 shows that the average data obtained from these two methods has at most, a 14% discrepancy with the results obtained from the numerical solutions in similar conditions. This indicates an acceptable accuracy for the simulated model.

Also, the data in Table 6 shows that although the results of numerical modeling and experimental data (after 4-days of natural ventilation with the assumption that fresh air entered the building from the gap under the main door, and exited from the windows on the northern side of the building)

Have 20-30%, discrepancy in 7 points out of 16 points, but there is a good consistency between the two methods for the remaining 9 points.

More clarification of the data indicates that after the 4-day period of natural ventilation, although the radon concentration is declared permissible, in all parts of the building, but radon concentration at 20 cm high in the middle of the kitchen was about 142 percent more than the radon concentration in the place where one was standing in the middle of the bedroom.

Also, the average values of the numerical solution in natural ventilation are almost consistent with the average values of the analytical solution., but the average values of experimental data are about 35% higher than those for numerical solution (Table 7). There are three reasons for such discrepancy:

1. On experimental averaging, only data at a height of 1.5 m and less was used, so the absence of radon concentration data at higher altitudes increases the mean value.

2. In all calculations made in this paper, the release of radon from other areas of the building has been ignored due to the low radon emission factors of those surfaces, but the sum of these small quantities of radon released throughout the entire period is probably more significant, so that it can affect the experimental measurements (as seen in most experimental data in Tables 4 and 6).

3. The presence of a background error of a few Bq/m^3b may lead to a larger error in measuring the lower radon concentration regions.

Also, as expected and shown in Figure 7 (solid curve), by increasing ventilation time, as well as by reducing the difference between indoor and outdoor temperature, radon concentration is also reduced. In this regard, although the average air velocity during the natural ventilation period is assumed to be constant for simplicity, we know that this variable is reduced by decreasing the temperature difference between the two environments. This is also consistent with the results obtained by Rabi et al.

Furthermore, the results of this study show that radon concentration decreases by increasing altitude, and as shown in Figure 8 (solid curve) it has the maximum gradient near the floor. It has also been reported by Oman and colleagues, how to reduce radon concentration by increasing the height from the floor of the building. (Figure 8 - dashed curve)

Finally, it should be acknowledged that due to the risk of indoor radon affecting human's health, with the development of the necessary hardware and software, more research activities are needed to consider the impact of air conditioning equipment, furniture, etc., on the human body. Achieving more precise experimental measurements will enable us to find radon distribution models for each building in order to find the critical points where the radon concentration is considerable. Also, by using the results of these researches, buildings can be designed in such a way that their residents receive a lower annual effective dose.

Note: This research did not receive any specific grant from funding agencies in the public, commercial, or not-for-profit sectors.

References

[1] Thompson, R. E., Nelson, D. F., Popkin, J. H., &Popkin, Z. (2008). Case-control study of lung cancer risk from residential radon exposure in Worcester County, Massachusetts. *Health Physics*, *94*(3), 228-241.

[2] United Nations, Scientific Committee on the Effects of Atomic Radiation. (2000). *Sources and effects of ionizing radiation: sources* (Vol. 1). United Nations Publications.

[3] Baldelli, P., McCullagh, J., Phelan, N., & Flanagan, F. (2010). Comprehensive dose survey of breast screening in Ireland. *Radiation protection dosimetry*, *145*(1), 52 -60.

[4]EPA, Assessment of risks from radon in homes (2003). https://www.epa.gov/sites/production/files/2015-05/documents/402-r-03-003.pdf

[5] Steck, D. J., Field, R. W., & Lynch, C. F. (1999). Exposure to atmospheric radon. *Environmental Health Perspectives*, *107*(2), 123.

[6] Oufni, L., & Misdaq, M. A. (2001). Radon emanation in a limestone cave using CR-39 and LR-115 solid state nuclear track detectors. *Journal of Radioanalytical and Nuclear Chemistry*, *250*(2), 309-313.

[7] Singh, K., Singh, M., Singh, S., Sahota, H. S., & Papp, Z. (2005). Variation of radon (222Rn) progeny concentrations in outdoor air as a function of time, temperature and relative humidity. *Radiation Measurements*, *39*(2), 213-217.

[8] Murty, V. R. K., King, J. G., Karunakara, N., &Raju, V. C. C. (2010). Indoor and outdoor radon levels and its diurnal variations in Botswana. *Nuclear Instruments and Methods in Physics Research Section A: Accelerators, Spectrometers, Detectors and Associated Equipment*, *619*(1-3), 446-448.

[9] Xie, D., Liao, M., Wang, H., &Kearfott, K. J. (2017). A study of diurnal and short-term variations of indoor radon concentrations at the University of Michigan, USA and their correlations with environmental factors. *Indoor and Built Environment*, *26*(8), 1051-1061.

[10] Chauhan, N., Chauhan, R. P., Joshi, M., Agarwal, T. K., Aggarwal, P., &Sahoo, B. K. (2014). Study of indoor radon distribution using measurements and CFD modeling. *Journal of environmental radioactivity*, *136*, 105-111.

[11] Akbari, K., & Oman, R. (2013). Impacts of heat recovery ventilators on energy savings and indoor radon in a swedish detached house. *WSEAS Transactions on Environment and Development*, *9*(1), 24-34.

[12] Lee, J. E., Park, H. C., Choi, H. S., Cho, S. Y., Jeong, T. Y., & Roh, S. C. (2016). A numerical study on the performance evaluation of ventilation systems for indoor radon reduction. *Korean Journal of Chemical Engineering*, *33*(3), 782-794.

[13] Rabi, R., &Oufni, L. (2017). Study of radon dispersion in typical dwelling using CFD modeling combined with passive-active measurements. *Radiation Physics and Chemistry*, *139*, 40-48.

[14] Clavensjö, B., & Åkerblom, G. (1994). *The radon book: Measures against radon*, The Swedish Council for Building Research, Stockholm.

[15] Petropoulos, N. P., Anagnostakis, M. J., &Simopoulos, S. E. (2001). Building materials radon exhalation rate: ERRICCA intercomparison exercise results. *Science of the total environment*, *272*(1-3), 109-118.

[16] Gupta, Mamta, Verma, K.D., Mahur, A.K., Prasad, R., & Sonkawade, R.G. (2013). Measurement of radon activity, exhalation rate and radiation dose in fly ash and coal samples from NTPC, Badarpur, Delhi, India. India: Aggarwal College.

ICNST 2024 International Conference on Nuclear Science and Technology
6- 8 MAY 2024 | Isfahan, Iran

Specific Activity and Effective Dose Measurement of Thorium-232 and its daughter nuclei for a Gas Light Mantle (Paper ID : 1296)

Kafaei N. Co-Author[1], Noshad H. Correspondent[*2]

[1] *Department of Physics, University of Tehran, Tehran, Iran*

[2*] *Department of Physics and Energy Engineering, Amirkabir University of Technology (Tehran Polytechnic), Tehran, Iran*

Abstract

In this paper, a sample in the form of a circular disk from a gas light mantle are prepared and the effects of its radioactive radiation are investigated. To this end, the spectrum of the gamma rays emitted from the disk is recorded by using gamma spectroscopy and the HPGe detector. The results are obtained by Monte Carlo simulation for a disk with a thickness of 1.3 cm and a diameter of 4.7 cm along with a detector with a diameter of 5.9 cm. Some photoelectric peaks in the spectrum such as 643, 727, 795, 861, 911, and 969 keV corresponding to daughter nuclei of ^{208}Tl, ^{228}Ac, and ^{214}Bi for ^{232}Th are identified. By analyzing the photopeaks corresponding to these daughter nuclei, the average specific activity for ^{232}Th in the gas light mantle is measured to be 0.20 ± 0.015 kBq/g. This amount of activity is equivalent to an affective dose of 12.31 mSv/year not recommended for safety reasons prescribed by the ICRP.

Keywords: Gas light mantle, Gamma spectroscopy, Thorium-232, Monte Carlo

INTRODUCTION

Thorium is present in most soils and rocks in very small amounts. The abundance of this element is three times as much as the uranium. ^{232}Th is the most abundant isotope of the element with a half-life of 14.5 billion years [1]. The pure form of this metal element is silvery color and maintains its luminance for several months. Thorium oxide (ThO_2) with a melting point of 3300 °C has one of the highest melting points among all oxides [2]. If this metal is heated in the air, it will ignite and burn with bright white light. For this reason, thorium is used in gas light mantles [3-5]. Carl Auer von Welsbach was the first person to use a mixture of 99% ThO_2 and 1% CeO_2 to create a bright white light in a gas lamp [6].

Gamma spectroscopy for the samples made of the gas light mantle has been carried out for ^{232}Th and its daughter nuclei, ^{224}Ra, ^{228}Ra, ^{212}Pb and ^{212}Bi with activity of 2.40 kBq [3]. Furthermore, the levels of radioactivity for ^{232}Th are estimated to be 1.410 ± 0.140 kBq from the content of ^{228}Ac for 11 mantles made

by different countries using gamma spectroscopy technique. [7]. Moreover, Doretti et al. determined specific activity of ^{232}Th to be equal to 4.047 kBq/g in a gas lamp mantle with an alpha spectroscopy method [8]. Investigation on two gas mantles, claimed to be non-radioactive, based on Instrumental Neutron Activation Analysis (INAA), gamma spectroscopy and Liquid Scintillation Counting (LSC) has been reported the presence of Th-content in these mantles with the activities of 796 Bq and 1054 Bq in the samples with 195 ± 1 mg and 258.7 ± 0.4 mg, respectively [6].

Due to the emission of alpha particles and gamma rays, long-term exposure to ^{232}Th causes radio toxicity, which can be disturbing. The maximum permissible concentration of thorium in air is reported to be 3.7×10^{-2} Bq/ml air [9]. The annual intake limit for ^{232}Th with specific activity of 4 kBq/g is 170 mg, which is equivalent to an effective dose of 20 mSv per year [10].

Poisoning caused by thorium can occur through inhalation, ingestion, open wounds, and skin absorption. Most thorium enters the body as a hydrolyzed salt polymerized providing colloidal particles that are accumulated in the liver, spleen and bone marrow cells [10-12]. If inhaled, it will accumulate in the lungs [10]. Because of the biological half-life of thorium in humans, 2 years in the liver, 5 years in the lung and 20 years in the skeleton, it is expected to cause health effects through alpha emissions and chemical interaction in the organs [10]. Cancer of blood vessels, liver, kidneys, and other organs can occur when exposed to thorium for 11 to 37 years as a radioactive environment [12]. The ^{232}Th injection in mice causes neural changes and cholinergic function, which may result in inducing oxidative stress in different regions of the brain [13]. Moreover, effects such as Down's syndrome, mental retardation, and point mutations in the ultraviolet region due to the occurrence of ^{232}Th and ^{238}U normal radionuclides were reported as a long-term effect in high background radiation areas (1-45 mSv/year) on liver carcinogenesis [14].

Today's, in developed countries, the use of free-thorium mantles is commonplace due to the risks of the use of radioactive heavy metals. In Australia in November 1992, the National Health and Medical Research Council announced that thorium-containing mantles should have a warning sign [15].

In this paper, due to the frequent use of the gas light mantle and the well-known biological effects of thorium on health human, we have determined specific activity released from ^{232}Th in a gas light mantle to inform the harmful effects that may result from this radionuclide. For this purpose, we have used gamma spectroscopy method to identify daughter nuclei of ^{232}Th. We have characterized the parameters corresponding to a radioactive disk by Monte Carlo simulation technique. The values of radiation dose that can affect the human's organs have also been specified. Hence, the paper is organized as follows. In Sec. 2,

the experimental method is discussed. Data analysis is also represented in sub-Sec. 2.1. The results have been presented in Sec. 3, with the sub-Sec. 3.1 and 3.2, respectively, which can obtain the corresponding radioactivity and dosimetric data.

EXPERIMENT

To measure of specific activity of ^{232}Th in a gas light mantle, three gas light mantles are prepared as a circular disk with a thickness of 1.3cm and diameter of 4.7 cm. The disk is then placed in front of a high purity germanium (HPGe) detector with a aperture diameter of 5.9 cm and a resolution of 1.98 keV in energy of 1408 keV so that, the front surface of the disk was up to 5 cm. The gamma spectra delivered from this disk have been recorded by a multi-channel analyzer with 8192 channels. A standard point source of ^{152}Eu with activity of 19 kBq has been used to calibrate energy and efficiency of the detector at a distance of 6.3 cm. The counting time of gamma rays released from the disk was approximately 4 hours and dead time of the detector was about 1%.

Data Analysis

To measure the efficiency of the detector against gamma rays emitted from the disk, we have determined efficiency for a standard point source form Eq. (1) as follows:

$$\varepsilon_0 = \frac{s\lambda}{fA[1-\exp(-\lambda t_c)]}, \quad (1)$$

where *s*, λ, *f*, *A* and ε_0 denote to pure surface under photoelectric peak, decay constant, branching ratio, activity at the beginning of the count and point source efficiency, respectively. The term of t_c is counting time of the detector.

In this experiment, the ^{232}Th activity in the disk has been obtained from Eq. (2) for several photoelectric peaks seen in the spectrum as below:

$$A = \frac{s\lambda}{\gamma\varepsilon_0\frac{\Omega'}{\Omega}[1-\exp(-\lambda t_c)]}, \quad (2)$$

where Ω' and Ω stand for the solid angles corresponding to disk and the point source, respectively. The solid angle for a point source can be calculated as [16]:

$$\Omega = 2\pi\left(1-\frac{d}{\sqrt{d^2+R_d^2}}\right), \quad (3)$$

where d and R_d represent the distance from the detector and the radius of the detector, respectively. The amount of Ω' in the distance from disk to detector is shown in Fig. (1) obtained by using the Monte Carlo simulation for a disk with a thickness of 1.3 cm and a diameter of 4.7 cm along with a detector with diameter of 5.9 cm.

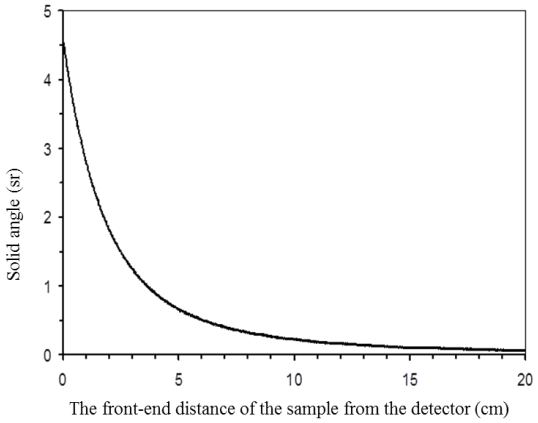

Fig. 1. Monte Carlo simulation for solid angle of a disk with thickness of 1.3 cm and a diameter of 4.7 cm along with a detector with diameter of 5.9 cm.

Results and Discussion

In this work, some photoelectric peaks in the spectrum such as 643, 727, 795, 861, 911 and 969 keV were identified corresponding to daughter nuclei of ^{208}Tl, ^{228}Ac and ^{214}Bi [1]. Considering parameters associated to each daughter nuclei, radioactivity measurement and dosimetry have been carried out.

Radioactivity

The gamma spectrum emitted from the mantle at a distance of 5 cm from the detector in a semi-logarithmic scale is shown in Fig. (2)

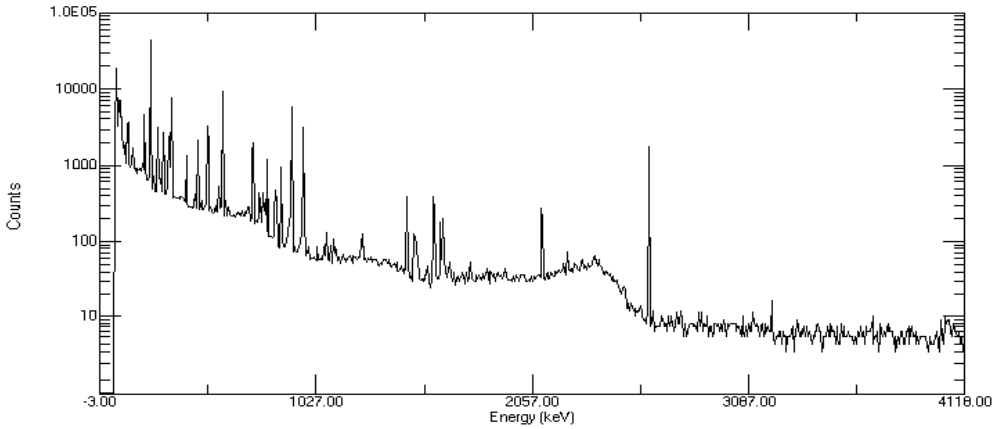

Fig. 2. The gamma spectrum of a gas light mantle. The photoelectric peaks corresponding to daughter nuclei in decay chain of ^{232}Th are shown in the figure.

The photoelectric peaks of the daughter nuclei in the decay chain of ^{232}Th are also seen in this picture. A number of these daughter nuclei, their photoelectric energy and branching ratio are presented in Table 1. Considering the parameters for each daughter nuclei, the disk activity has been determined by using Eqs. (2) and (3). Activities of each of these daughter nuclei are presented in Table 1. The average of these activities with an approximate error of 8% has been attained to be 1.1 kBq. A part of this error is due to systematic error related to measurement of sample dimensions and solid angle while the other part result from statistical error related to counting.

Table 1. Daughter nuclei of ^{232}Th, their photoelectric energies and branching ratios.

Daughter nuclei	Energy (keV)	Branching ratio (%)	Activity (Bq)
^{228}Ac	463	4.5	1122
^{214}Bi	727	7.35	1087
^{228}Ac	795	4.34	1123
^{208}Tl	861	4.55	1065
^{228}Ac	911	26.6	1160
^{228}Ac	969	**16. 23**	1020

It is worth noting that the actual activity, in general, depends not only on the age of the mantle, but also on the amount of ^{232}Th in the mantle [3].

2. Dosimetry

Given the fact that these substances accumulate in the liver, lungs, spleen, and bone marrow (red) due to the absorption or inhalation of thorium and its daughter nuclei, now we present the quantities corresponding to absorbed, equivalent and effective doses by these organs.

The absorbed dose is energy of radiation R absorbed per unit mass of tissue T. The dose equivalent, H_T, in a specified organ is also defined by $H_T = W_R D_{T.R}$, where $D_{T.R}$ and W_R stand for values of the absorbed dose in a tissue T by radiation R and the corresponding radiation weighting factor, respectively. The effective dose is given by $E = \sum_T W_T H_T$ that is sum of equivalent doses to organs and tissues exposed, each multiplied by the appropriate tissue weighting factor W_T. Considering $W_R = 20$ [17] and $W_T = 0.12$ for bone marrow (red) and lung and equal to 0.05 for liver and spleen [18] the absorbed, equivalent and effective doses related to these organs are calculated. The results are shown in Tables 2-5. In all the calculations, we have assumed that someone uses a gas lamp for an hour per day. The total effective dose of these organs is 12.31 mSv. Evidently, the value of the total effective dose increases for longer exposure time of the sample. Considering the limit of the public effective dose as 1 mSv/year prescribed by the ICRP [19], the hazardous of the gas light mantle due to ThO_2 is confirmed.

Compared to Doretti's results [8] based on alpha spectroscopy to identify daughter nuclei of ^{232}Th in a gas light mantle, this work has been carried out with more precision due to the use of gamma spectroscopy. In addition, Saı¨dou et al. reported that alpha spectrometry has sensitivity, with a detection limit (1–5 mBq/kg) typically 1000 times lower than gamma spectrometry for ^{232}Th [20].

Table 2. The deposited dose in liver with $m = 1.7\,\mathrm{kg}$.

Daughter Nuclei	Energy (keV)	Activity (Bq)	Absorbed Dose (mGy)	Equivalent Dose (mSv)	Effective Dose (mSv)
^{228}Ac	463	1122	0.06	1.28	**0.06**
^{214}Bi	727	1087	0.10	1.96	**0.10**
^{228}Ac	795	1123	0.11	2.2	**0.11**
^{208}Tl	861	1065	0.11	2.2	**0.11**
^{228}Ac	911	1160	0.13	2.6	**0.13**
^{228}Ac	969	1020	**0.12**	**2.4**	**0.12**

Table 3. The deposited dose in lung with $m = 1\text{kg}$.

Daughter Nuclei	Energy (keV)	Activity (Bq)	Absorbed Dose (mGy)	Equivalent Dose (mSv)	Effective Dose (mSv)
^{228}Ac	463	1122	0.10	2	**0.24**
^{214}Bi	727	1087	0.17	3.4	**0.40**
^{228}Ac	795	1123	0.19	3.8	**0.46**
^{208}Tl	861	1065	0.19	3.8	**0.46**
^{228}Ac	911	1160	0.22	4.4	**0.53**
^{228}Ac	969	1020	**0.21**	**4.2**	**0.50**

Table 4. The deposited dose in bone marrow (red) with $m = 1.5$ kg.

Daughter Nuclei	Energy (keV)	Activity (Bq)	Absorbed Dose (mGy)	Equivalent Dose (mSv)	Effective Dose (mSv)
^{228}Ac	463	1122	0.07	1.5	**0.18**
^{214}Bi	727	1087	0.11	2.2	**0.26**
^{228}Ac	795	1123	0.13	2.6	**0.31**
^{208}Tl	861	1065	0.13	2.6	**0.31**
^{228}Ac	911	1160	0.15	3	**0.36**
^{228}Ac	969	1020	**0.14**	**2.8**	**0.34**

Table 5. The deposited dose in spleen with $m = 0.15$ kg.

Daughter Nuclei	Energy (keV)	Activity (Bq)	Absorbed Dose (mGy)	Equivalent Dose (mSv)	Effective Dose (mSv)
^{228}Ac	463	1122	0.73	14.6	**0.73**
^{214}Bi	727	1087	1.1	22	**1.1**
^{228}Ac	795	1123	1.3	26	**1.3**
^{208}Tl	861	1065	1.3	26	**1.3**
^{228}Ac	911	1160	1.5	30	**1.5**
^{228}Ac	969	1020	**1.4**	28	**1.4**

In addition, activity of ^{232}Th has been calculated using gamma spectroscopy by a Ge(Li) detector with an 8% absolute efficiency [3]. In the last experiment, the activity of ^{232}Th has been specified indirectly from the activity of ^{228}Th. Moreover, Etsuko et al. estimated activity of ^{232}Th from the ^{228}Ac activity using gamma spectroscopy by using an HPGe detector with a relative efficiency of 32.7% [7]. Determination of ^{232}Th activity via these procedures is feasible only within about 3 years after extraction, since after this time the ^{228}Ac to ^{228}Th activity ratio stays almost constant with time [3, 8].

Conclusion

In this work, a sample of the gas light mantle was studied in order to investigate the effects of radioactive radiation. The presence of the photopeaks originated from the daughter nuclei of ^{232}Th such as ^{208}Tl, ^{228}Ac and ^{214}Bi were recorded by gamma spectroscopy technique using the HPGe detector. Afterwards, the average specific activity for ^{232}Th in the gas light mantle was calculated via the analytical formula as well as the Monte Carlo simulation to be equal to 0.20 ± 0.015 kBq/g. Moreover, as this radioactive substance can affect the lung, spleen, liver and bone marrow, the dose absorbed by someone who is exposed to the radiation for one hour per day was determined with the total effective dose of 12.31 mSv. Especial care was taken the experiment to be carried out with high accuracy. Comparison between the results obtained in this measurement and the value reported by the ICRP demonstrates that use of the gas light mantles can be harmful due to the radiation damage; and consequently, is not recommended.

References

[1] Firestone, R. B. Shirley, V. Baglin, C. Chu, S. F. and Zipkin, J. (1996). Table of Isotopes, 8th edn. Vol. II," ed: John Wiley & sons inc., New York.

[2] Emsley, J. (2011). Nature's building blocks: an AZ guide to the elements: Oxford University Press.

[3] Luetzelschwab, J. W. and Googins, S. W. (1984). Radioactivity released from burning gas lantern mantles, Health physics, 46, 873-881.

[4] Aksoy, A. Al-Jarallah, M. and Abu-Jarad, F. (1997). Measurements of thorium content and radioactivity in gas mantles, Arabian Journal for Science and Engineering, 22, 25-35.

[5] Al-Jarallah, M. Al-Arfaj, A.-R. Aksoy A. , and Abu-Jarad, F. (1998). Chemical analysis of thorium content in gas mantles, Arabian Journal for Science and Engineering, 23, 17-21.

[6] Poljanc, K. Steinhauser, G. Sterba, J. H. Buchtela, K. and Bichler, M. (2007). Beyond low-level activity: on a “non-radioactive” gas mantle, Science of the total environment, 374, 36-42.

[7] Furuta, E. Yoshizawa, Y. and Aburai, T. (2000). Comparisons between radioactive and non-radioactive gas lantern mantles, Journal of Radiological Protection, 20, 423.

[8] Doretti, L. Ferrara, D. and Barison, G. (1990). Determination of thorium isotopes in gas lantern mantles by alpha-spectrometry," Journal of Radioanalytical and Nuclear Chemistry, 141, 203-208.

[9] Carson, B. L. (2018). Toxicology Biological Monitoring of Metals in Humans: 0: CRC Press.

[10] Kumar, A. Ali, M. and Pandey B. N. (2013). Understanding the biological effects of thorium and developing efficient strategies for its decorporation and mitigation," Barc Newsletter, 335, 55-60.

[11] Kumar, A. Mishra, P. Ghosh, S. Sharma, P. Ali, M. Pandey, B. et al. (2008).Thorium-induced oxidative stress mediated toxicity in mice and its abrogation by diethylenetriamine pentaacetate, International journal of radiation biology, 84, 337-349.

[12] Carson, B. Ellis, H. and McCann, J. (1986). Toxicology and biological monitoring of metals in humans, Chelsea, MI: Lewis, 71, 133.

[13] Kumar, A. Ali, M. Mishra, P. Pandey, B. Sharma, P. and Mishra, K. P. (2009). Thorium-induced neurobehavioural and neurochemical alterations in Swiss mice, International journal of radiation biology, 85, 338-347.

[14] Pandey, B. N. Kumar, A. Tiwari, P. and K. Mishra, K. P. (2010). Radiobiological basis in management of accidental radiation exposure, International journal of radiation biology, 86, 613-635.

[15] Mortazavi, S. Rahmani, S. Rahnama, A. Saeed-Pour, A. Nouri, E. Hosseini, N. et al., (2009). The stimulatory effects of topical application of radioactive lantern mantle powder on wound healing, Dose-Response, 7, dose-response. 08-022. Mortazavi.

[16] Tsoulfanidis, N. (2010). Measurement and detection of radiation: CRC press.

[17] Hwang, S. T. (1977). Quantities and Units in radiation Dosimetry," Journal of Radiation Protection and Research, 2, 38-46

[18] Quantities and Units in Radiation Protection Dosimetry, ICRU report 51, 1993.

[19] Mountford, P. J. and Temperton, D. H. (1992). Recommendations of the international commission on radiologialprotection (ICRP) 1990Eropean Journal of Nuclear Medicine, 19, 77-79.

[20] Bochud, F. Laedermann, J. P. Njock, M. K. and Froidevaux, P. (2008) A comparison of alpha and gamma spectrometry for environmental natural radioactivity surveys, Applied Radiation and Isotopes, 66, 215-222.

ICNST 2024 International Conference on Nuclear Science and Technology
6- 8 MAY 2024 | Isfahan, Iran

Assessment of Natural Radioactive Materials in Soil and Water Samples from the City of Kazeroon, Fars province, Iran (Paper ID : 1313)

Leila Puyan[1], Sedigheh Sina[1, 2, *], Kamal Hadad[1], Mohammad Hossein Sadeghi[1], Zahra Rakeb[1]

[1] *Nuclear Engineering Department, School of Mechanical Engineering, Shiraz University, Shiraz, Iran*

[2] *Radiation Research Center, School of Mechanical Engineering, Shiraz University, Shiraz, Iran*

Abstract

The study aims to assess the concentrations of Naturally Occurring Radioactive Materials (NORM) in soil and water samples collected from Kazeroon, Iran, using gamma spectrometry. The investigation focuses on radioactive isotopes, including Ra-226, Th-232, K-40, and U-238, to understand their presence in the environment and potential implications for human health. Six distinct soil sampling points encircling Kazeroon were randomly selected to ensure representative data collection. Additionally, water samples were gathered from three urban drinking wells and five springs located on the city's periphery. The application of gamma spectrometry, coupled with meticulous accounting for background radiation and calibration procedures, facilitated accurate measurements. The results revealed varying concentrations of radioactive isotopes in soil samples, ranging from 5.92 to 212.57 Bq/kg. This variability can be attributed to the geological composition of the region. Strikingly, all water samples exhibited concentrations of radioactive isotopes below the minimum detectable limit, indicating minimal levels of natural radioactivity in the water sources of Kazeroon. In conclusion, this study underscores the importance of assessing NORM concentrations in the environment, particularly within urban areas. The research outcomes provide valuable insights into the distribution of radioactive materials in soil and water, emphasizing the need for ongoing monitoring and potential mitigation strategies. By contributing to the understanding of natural radioactivity levels, the study highlights the relevance of considering radiation exposure in urban planning and environmental management efforts. Ultimately, this research enhances our knowledge of the intricate interactions between natural radioactivity, human health, and the environment.

Keywords: NORM, Gamma spectrometry, Radiation exposure, Urban development

INTRODUCTION

The presence of Naturally Occurring Radioactive Materials (NORM) in the environment is a subject of considerable scientific and public health interest. NORM encompasses a variety of radioactive elements found in the Earth's crust, including uranium (U-238), thorium (Th-232), potassium (K-40), and their decay products, such as radium (Ra-226). These elements are ubiquitous in soil and water, contributing to background radiation levels experienced by all living organisms. The study of NORM is crucial due to its implications for environmental health, public safety, and regulatory compliance. Understanding the distribution and concentration of NORM can help assess potential risks to human health and guide the development of strategies to mitigate adverse effects.

Kazeroon, a city in the Fars province of Iran, is characterized by diverse geological formations, making it an area of interest for studying the concentration of NORM. The region's unique geology, including its soil and water resources, may influence the distribution and levels of NORM. Given the significance of agriculture and urban development in Kazeroon, assessing the levels of NORM is essential for ensuring the safety and health of its population and environment. Previous studies have highlighted the importance of monitoring NORM in various regions, emphasizing the need for localized assessments to understand regional variations in natural radioactivity [1,2].

The objectives of this essay are to:

1. Provide an overview of NORM and their importance in environmental and public health contexts.

2. Highlight the significance of studying NORM in the specific context of Kazeroon, Iran, considering its unique geological and socio-economic characteristics.

3. Assess the concentration of key NORM elements (U, Th, K, and Ra) in soil and water samples collected from various locations within Kazeroon. This assessment aims to establish baseline levels of natural radioactivity, contributing to the broader understanding of environmental radiation and its implications for human health and safety.

This study contributes to the growing body of knowledge on natural radioactivity, offering insights into the distribution of NORM in a region where such data are scarce. By identifying areas with elevated levels of

natural radioactivity, this research can inform risk assessment and management strategies, ensuring the well-being of the community and the integrity of the environment in Kazeroon.

RESEARCH THEORIES

Definition and Sources of NORM

NORM refer to radioactive substances found in the Earth's crust. These materials include elements such as U-238, Th-232, K-40, and their decay products, notably Ra-226. NORM can be found in varying concentrations in soil, water, air, and even in building materials, contributing to the natural background radiation that all living organisms are exposed to. The primary sources of NORM are igneous and sedimentary rocks from which these radioactive elements are gradually released into the environment through weathering processes [3,4].

Historical Perspective on NORM Studies in Urban Areas

The study of NORM and its impact on urban areas has evolved significantly over the past few decades. Initially, the focus was primarily on occupational exposure in industries such as mining and oil and gas, where workers might be exposed to elevated levels of NORM. However, as understanding of the widespread presence of NORM grew, researchers began to investigate its implications for the general population, particularly in urban settings. Urban areas are of specific interest due to the concentration of population and the potential for enhanced exposure through building materials and infrastructure that may contain NORM, such as concrete, bricks, and water supply systems [2,5].

Importance of Assessing NORM in Environmental Health and Safety

Assessing the levels of NORM in the environment is crucial for several reasons. Firstly, it helps in understanding the baseline levels of natural radioactivity to which populations are exposed. This knowledge is essential for public health, as prolonged exposure to elevated levels of radiation can increase the risk of cancer and other health issues. Secondly, assessing NORM is vital for environmental protection. It enables the identification of areas with naturally high levels of radioactivity, guiding land use and urban planning decisions to mitigate exposure risks. Lastly, knowledge of NORM concentrations supports regulatory bodies in developing guidelines and safety standards to protect workers and the public from potential radiation hazards [2,4].

Understanding NORM's distribution and impact is integral to ensuring environmental health and safety. As urban areas continue to grow, and as human activities disturb natural materials, the importance of monitoring and managing exposure to NORM becomes increasingly significant.

METHODS

Overview of Gamma Spectrometry and Its Application in NORM Assessment

Gamma spectrometry is a widely used analytical technique for identifying and quantifying radioactive isotopes in various materials. It operates on the principle of detecting and measuring the energy and intensity of gamma rays emitted by radioactive substances. This method is particularly effective for assessing NORM due to its sensitivity, accuracy, and non-destructive nature. Gamma spectrometry allows for the precise determination of radionuclides such as U-238, Th-232, K-40, and Ra-226 in environmental samples [1,6].

Description of Soil and Water Sampling Procedures

Soil Sampling: Soil samples were collected from predetermined locations within the study area to ensure a representative distribution of sampling points. A stratified random sampling approach was adopted to cover different land uses and geological features. At each sampling site, the top 15 cm of soil was collected using a stainless-steel auger, as this layer is most relevant to human exposure. The collected samples were then air-dried, homogenized, and sieved through a 2 mm mesh to remove large particles and organic debris, preparing them for analysis [7].

Water Sampling: Water samples were collected from both surface and groundwater sources, including rivers, lakes, and wells. Sampling involved collecting water in pre-cleaned polyethylene bottles, which were rinsed with the water being sampled before filling. The samples were then transported to the laboratory under cool conditions. Prior to gamma spectrometry analysis, water samples underwent a pre-concentration process to increase the detectability of low-level radionuclides [8].

Calibration and Background Radiation Accounting Methods

Calibration of the gamma spectrometry system is essential for accurate measurement of radioactivity in samples. Calibration was performed using standard reference materials with known activity concentrations of the radionuclides of interest. This process ensures that the system's measurements are accurate and reproducible. Additionally, to account for background radiation, which includes cosmic rays and natural

radioactivity from the laboratory environment, background measurements were taken with an empty detector or with a blank sample. These background counts were subtracted from the sample counts to obtain the net activity concentrations of the radionuclides in the samples [1,6]. The methodology outlined provides a robust framework for the accurate assessment of NORM in soil and water samples. By employing gamma spectrometry, coupled with rigorous sampling and calibration procedures, this approach ensures reliable quantification of natural radioactivity in the environment. The minimum detectable activity (MDA) of our measurement system was carefully determined through calibration procedures using standard reference materials and accounting for background radiation. To perform energy calibration, at first, we placed Cs-137, Co-60, Am-241 and Ba-131 springs which have specific energies on the system and obtained the channel-energy calibration chart. In order to count samples with different geometry and dimensions, it is necessary to first perform the efficiency calibration for the detector. For the calibration of yield of soil samples, from the standard sources of the International Atomic Energy Agency, such as RGU for the calibration of uranium and its chain elements, RGTh for the calibration of thorium and its chain elements, and RGK for the calibration of potassium, as well as soil-6 for the calibration of Cs-137 and System quality control was used. The efficiency calibration of liquid samples was also done by a composite standard liquid sample. Figure 1 and 2 shows the calibration curve of the samples.

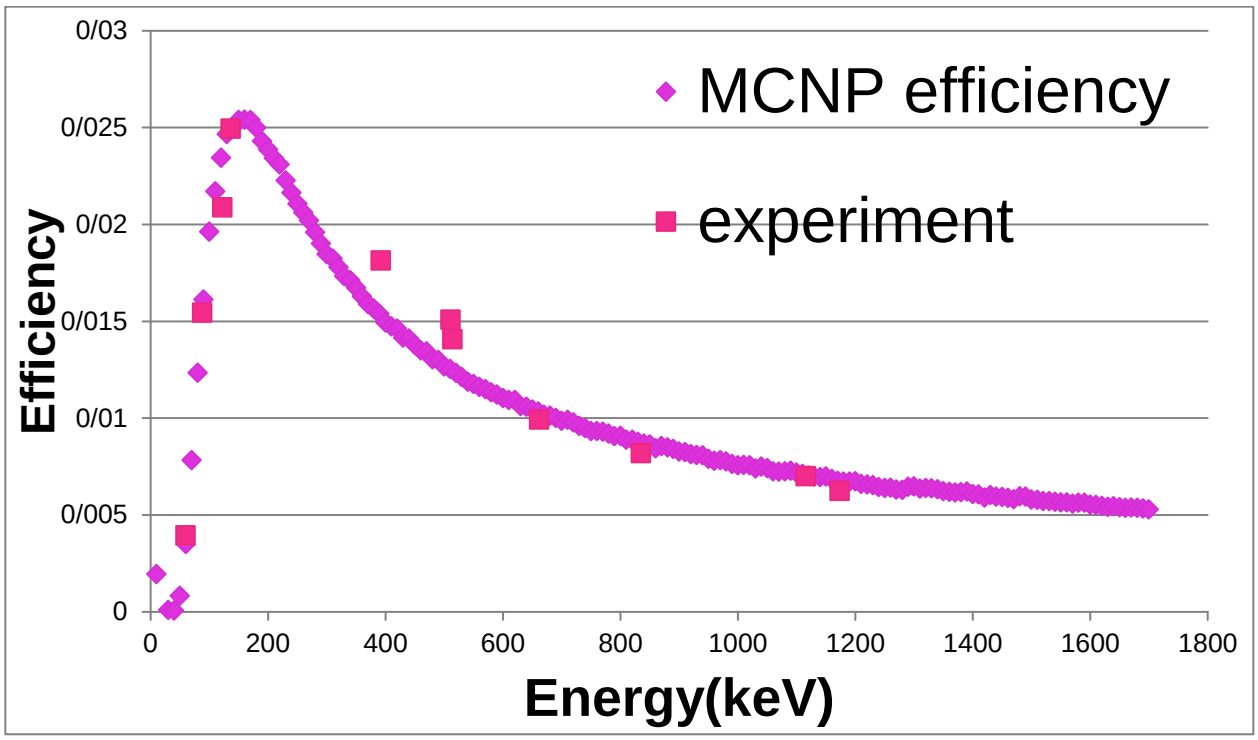

Fig. 1. Calibration efficiency curve for water sample

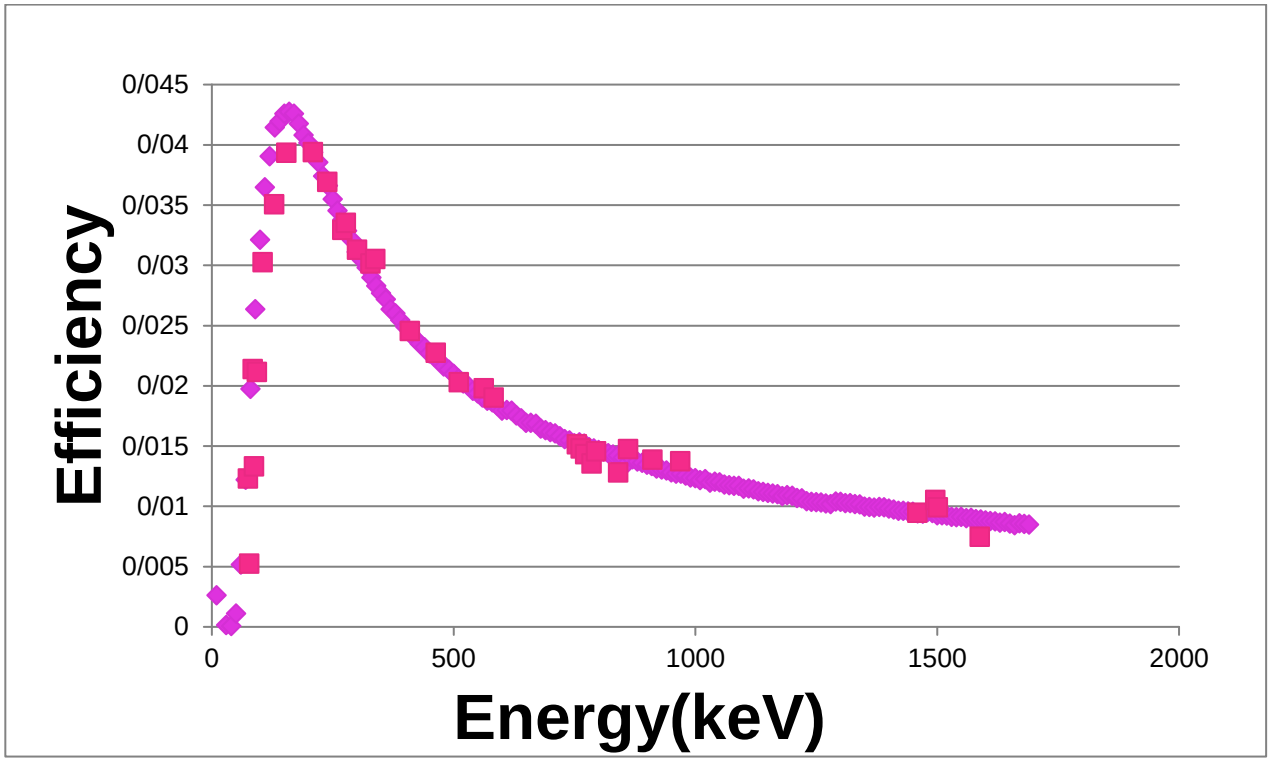

Fig. 2. Calibration efficiency curve for soil sample

RESULTS AND DISCUSSION

The gamma spectrometry analysis of soil samples collected from various locations around Kazeroon revealed the presence of NORM, including uranium (U), thorium (Th), potassium (K), and radium (Ra). The concentrations of these radionuclides varied across different sampling sites, reflecting the heterogeneity of the geological composition in the area. The average concentrations were found to be within the expected range for natural soils, with uranium (U-238) at 5.92 Bq/kg, thorium (Th-232) at 6.25 Bq/kg, potassium (K-40) at 212.57 Bq/kg, and radium (Ra-226) at 30.33 Bq/kg. These values are consistent with global averages reported in literature for soils, indicating that the soil in Kazeroon does not exhibit unusually high levels of radioactivity [2]. Table 1 shows the concentration for soil samples.

Table 1. Corrected concentration for soil samples

		Ra-226	Th-232	Cs-137	K-40	U-238	U-235
Sample 1	Bq	19.18	6.54	0.24	233.63	4.71	1
	Bq/kg	31.96	10.91	0.4	389.39	7.85	1.66
Sample 2	Bq	22.35	2.56	0.42	105.51	2.3	0.87
	Bq/kg	34.39	3.95	0.65	162.32	3.53	1.34
Sample 3	Bq	19.96	6.04	2.24	162.22	3.14	0.61
	Bq/kg	32.19	9.74	3.61	261.64	5.07	0.98
Sample 4	Bq	19.95	0.87	0.31	72.87	4.65	0.84
	Bq/kg	28.09	1.22	0.44	102.63	6.55	1.18
Sample 5	Bq	18.2	6.09	2.42	148.47	5.62	1.08
	Bq/kg	25.64	8.58	3.41	209.11	7.91	1.52
Sample 6	Bq	17.75	1.86	0.16	90.23	2.76	0.27
	Bq/kg	29.58	3.1	0.27	150.38	4.59	0.44

Water samples from both drinking water wells within the urban area and springs in the periphery of Kazeroon were analyzed for their NORM content. The concentrations of radioactive isotopes in all water samples were found to be below the minimum detectable limits for gamma spectrometry, suggesting that the water sources in Kazeroon are not significantly impacted by natural radioactivity. This finding is in line with the World Health Organization's guidelines for drinking water quality, which specify permissible levels of radionuclides in drinking water [9]. The absence of detectable levels of NORM in water sources is a positive indicator of the water quality in Kazeroon, with minimal risk posed by radioactivity to public health through water consumption. This suggests that the residents of Kazeroon are exposed to radiation levels from NORM that

are within safe limits for public health. The low levels of NORM in water further contribute to the overall assessment that the environmental exposure to natural radioactivity in Kazeroon does not pose a significant health risk to the population. These results are crucial for informing public health policies and environmental management practices in the region, ensuring that the health and safety of the community are safeguarded against potential radiological hazards.

The results of the study conducted in Kazeroon, Iran, indicate that the concentrations of NORM in soil and water samples are within safe limits when compared to global and national benchmarks for radiation exposure.

The variability in NORM concentrations observed in the soil samples from Kazeroon can be attributed to the region's geological composition. Kazeroon's diverse geological formations, including sedimentary rocks that are known to contain higher concentrations of uranium and thorium, play a significant role in the distribution of NORM. Studies have shown that areas with significant sedimentary rock formations tend to exhibit higher natural radioactivity levels due to the presence of these radionuclides [3]. Understanding the geological context is crucial for interpreting the variability in NORM concentrations and assessing potential exposure risks.

The findings of this study have significant implications for environmental health and safety in Kazeroon. The low levels of NORM in soil and water suggest minimal risk to public health from radiation exposure. However, the study underscores the importance of considering natural radioactivity in environmental health assessments and urban planning. Long-term exposure to even low levels of radiation can have cumulative health effects, making it essential to monitor and manage NORM exposure [10].

Incorporating NORM assessment into urban planning and environmental management strategies is vital for sustainable development. The data obtained from this study can inform land use planning, construction practices, and water resource management in Kazeroon. For instance, areas with slightly elevated NORM levels might be designated for non-residential use, or specific construction materials could be chosen to minimize indoor radon levels, a decay product of uranium found in soil.

NORM assessment plays a critical role in urban planning by identifying areas where natural radioactivity may impact public health and the environment. This information is essential for making informed decisions

about land use, infrastructure development, and environmental conservation, ensuring that urban expansion does not inadvertently increase exposure to natural radiation.

Mitigation strategies for managing NORM exposure include regulatory measures to limit the use of materials with high NORM concentrations, public education on minimizing exposure, and environmental remediation techniques. For example, improving ventilation in buildings can reduce indoor radon levels, while proper water treatment processes can remove radionuclides from drinking water [9].

Continuous monitoring of environmental radioactivity is crucial for detecting changes in NORM concentrations and assessing the effectiveness of mitigation strategies. Regular monitoring can help identify emerging risks and ensure that public health measures are updated in response to new data. This proactive approach is essential for protecting public health and the environment from the potential risks associated with natural radioactivity [2].

CONCLUSIONS

The comprehensive assessment of NORM in soil and water samples from Kazeroon, Fars province, Iran, has yielded significant insights into the environmental radioactivity of the region. The key findings from this study indicate that the concentrations of radioactive isotopes such as uranium (U), thorium (Th), potassium (K), and radium (Ra) in soil samples are within expected natural ranges. Similarly, the analysis of water sources revealed that the levels of NORM are below detectable limits, suggesting minimal risk to public health from water consumption. These results are significant as they provide reassurance regarding the environmental safety and public health implications for the inhabitants of Kazeroon. However, the study also underscores the importance of continuous monitoring and management of natural radioactivity, particularly in urban areas undergoing rapid development and expansion. The findings serve as a valuable baseline for future research and can inform urban development strategies to ensure that growth is sustainable and does not inadvertently increase exposure to natural radiation.

Recommendations for Future Research and Urban Development Strategies

1. Continuous Monitoring: Implement regular monitoring programs to track changes in NORM concentrations in soil and water, ensuring early detection of any shifts in environmental radioactivity levels.

2. Public Health Studies: Conduct epidemiological studies to investigate potential health effects associated with long-term exposure to low levels of natural radioactivity, enhancing our understanding of the risk to public health.

3. Urban Planning: Integrate NORM assessment into urban planning and development processes, using the data to guide land use decisions, building material selection, and infrastructure development to minimize radiation exposure.

4. Public Awareness: Develop public education campaigns to raise awareness about natural radioactivity, its sources, and effective measures to reduce exposure, empowering the community to make informed decisions about their health and safety.

5. Research on Mitigation Strategies: Invest in research to explore innovative technologies and strategies for mitigating exposure to NORM, including advancements in building design, water treatment, and environmental remediation.

In conclusion, the study conducted in Kazeroon provides a foundational understanding of the levels of natural radioactivity in the region, contributing to the body of knowledge necessary for informed decision-making regarding environmental health and urban development. The proactive management of NORM exposure, guided by continuous research and monitoring, will be crucial in safeguarding the health and well-being of the inhabitants of Kazeroon and ensuring the sustainable development of the area.

References

1. Erdi-Krausz, G., Matolin, M., Minty, B., Nicolet, J.P., Reford, W.S., Schetselaar, E.M. (2003). Guidelines for Radioelement Mapping Using Gamma Ray Spectrometry Data: Also as Open Access e-Book. International Atomic Energy Agency (IAEA).

2. United Nations Scientific Committee on the Effects of Atomic Radiation (UNSCEAR) (2000). Sources and Effects of Ionizing Radiation. UNSCEAR 2000 Report to General Assembly with Scientific Annex, New York, United Nations, 1.

3. Eisenbud, M., Gesell, T.F. (1997). Environmental Radioactivity from Natural, Industrial and Military Sources: From Natural, Industrial and Military Sources. Elsevier.

4. Tsurikov, N. (2018). Management of NORM Residues: Practical Aspects. In Proceedings of the International Symposium on Naturally Occurring Radioactive Material (NORM VIII).

5. Tzortzis, M., Svoukis, E., Tsertos, H. (2004). A comprehensive study of natural gamma radioactivity levels and associated dose rates from surface soils in Cyprus. Radiation Protection Dosimetry, 109(3):217-224.

6. Gilmore, G. (2008). Practical Gamma-Ray Spectroscopy. John Wiley & Sons.

7. Krishnamoorthy, T.M. (2003). Collection and preparation of lake sediments for dating and trace element analysis by nuclear techniques. Collection and Preparation of Bottom Sediment Samples for Analysis of Radionuclides and Trace Elements, 63.

8. Ješkovský, M., Kaizer, J., KontuĺI., Lujanienė, G., Müllerová, M., Povinec, P.P. (2019). Analysis of environmental radionuclides. In Handbook of Radioactivity Analysis: Volume 2, Elsevier, 137-261.

9. Edition, F. (2011). Guidelines for drinking-water quality. WHO Chronicle, 38(4):104-108.

10. Haridasan, P.P. (2014). IAEA safety standards and guidance on exposure to Naturally Occurring Radioactive Material (NORM).

ICNST 2024
International Conference on Nuclear Science and Technology
6- 8 MAY 2024 | Isfahan, Iran

Enhancing Recovery Efficiency: Crafting a Radiochemical Purification Panel for the Zn-65 Radioisotope Tracer and Stable Zn Isotopes (Paper ID : 1316)

Behrouz Shirazi Tirani*, Alireza Grayeli, Amin Dayanti

Physics and Accelerators Research School, Nuclear Sciences and Technology Research Institute, P. O. Box 1498-31465, Karaj, Iran

Abstract:

In this scientific paper, unique copper metal targets were employed for a brief proton bombardment of a few minutes. The specific energy utilized was 12.5 million electron volts, and the nuclear reaction ^{65}Cu(p, n)^{65}Zn was harnessed to synthesize the radioisotope Zn-65. After a fortnight's wait, during which most unwanted radioisotopes decayed, the targets underwent a meticulous recovery and purification process to isolate the coveted Zn-65 radioisotope. The procedure commenced with a combined recovery method, where the copper targets underwent an acid wash with a concentrated hydrochloric acid solution, fortified with a touch of hydrogen peroxide. This initial step was designed to eliminate as much copper chemical impurity as possible through a Fast Electroplating operation. Subsequently, the solution obtained was subjected to chemical purification using a cylindrical Plexiglas column. This column, with its 3-centimeter inner diameter and 15-centimeter height, was packed with the ion exchange resin "Dowex 1x8 100-200 mesh in Cl^- form." Hydrochloric acid solutions of varying concentrations were then passed through the column at a steady pace of roughly 3 mL per minute. The meticulous recovery process yielded impressive results. Through gamma spectroscopic analysis of samples at different stages, it was determined that the overall recovery yield for the produced Zn-65 radioisotope was approximately 91.78%. Furthermore, the losses attributed to the Fast Electroplating operation (Electrolysis) and chromatographic separation with the resin column were quantified at 2.5% and 4.82%, respectively. The concentration and enhancement of specific activity were also addressed, with a minimal loss of 0.29%.

Keywords: enriched zinc isotopes, radioisotope zinc-65, tracer, chemical purification, recovery rate

1. Introduction:

The employment of zinc-65 as a radioisotope tracer with a half-life of 244 days has proven invaluable for studying and enhancing the intricate and costly stages of chemical purification for stable and enriched zinc isotopes. This method's reliability and cost-effectiveness stem from the indistinguishable chemical behavior

between stable isotopes and radioisotopes of the same element. Thus, by utilizing zinc-65, scientists can efficiently navigate the purification process, making it one of the most vital and efficient techniques available today.

In this intricate research endeavor, the production of a suitable detector commenced with the synthesis of zinc-65 radioisotopes. This was achieved through the strategic proton bombardment of copper metal targets, utilizing an energy of 12.5 million electron volts, and the optimization of the nuclear reaction $^{65}Cu(p, n)^{65}Zn$. With the zinc-65 radioisotopes in hand, the focus shifted to recovery and chemical purification. The initial stage involved a Fast Electroplating operation, meticulously designed to eliminate the significant copper chemical impurity that arises during the washing of proton-bombarded copper targets. In the subsequent stage, final purification was accomplished using the ion exchange resin "Dowex 1x8 100-200 mesh in Cl^- form," ensuring the desired level of purity for the zinc-65 radioisotopes.

2. Experimental procedure:

2-1 Production of Zn-65 radioisotope by proton bombardment of copper targets:

The production of the Zn-65 radioisotope is a delicate process that involves the strategic use of the $^{Nat.}Cu(p, x)^{65}Zn$ nuclear reaction. During this method, specific copper metal targets undergo an intense proton bombardment with an energy of 12.5 million electron volts. This bombardment is carefully timed to last for several minutes[1-7].

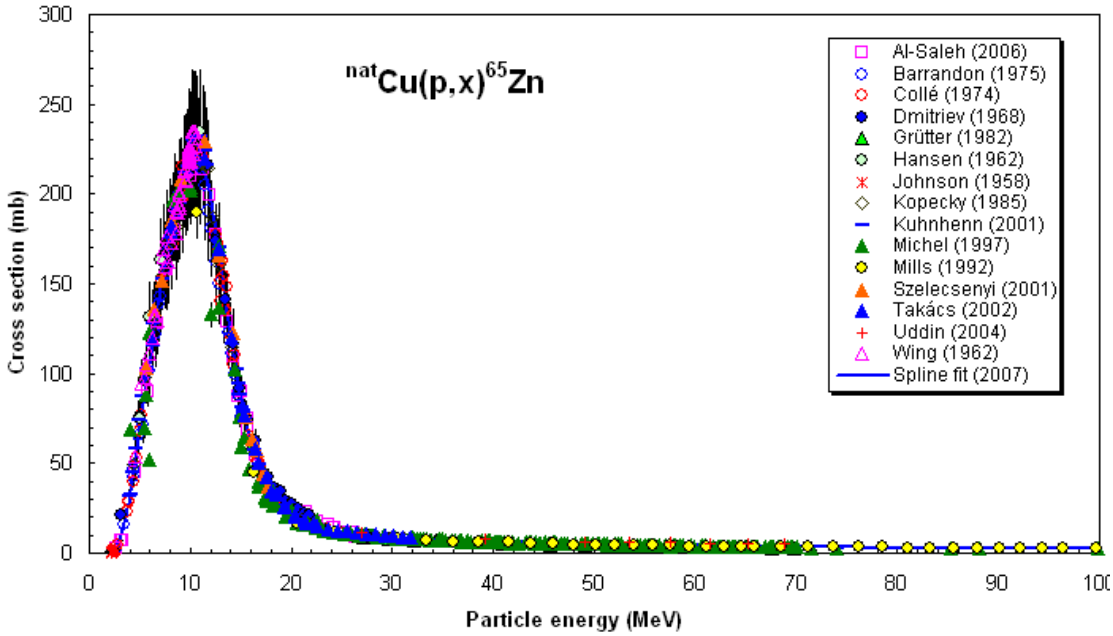

Chart 1. A Visual Guide to the Efficiency of the ^{Nat}.Cu(p, x)^{65}Zn Nuclear Reaction

Once the proton bombardment is complete, the copper target is carefully transferred to a primary hot cell, where it rests in a corner for a period of up to two weeks. This crucial cooling period allows for the destruction of most radioactive impurities, ensuring the purity and integrity of the desired Zn-65 radioisotope[1-2, 8].

2-2 Washing and recovering the bombarded surface of the copper target:

The delicate process of dissolving the bombarded surface of the copper target involves a precise mixture of 9 normal hydrochloric acid and a few drops of hydrogen peroxide. This careful formulation prepares the resulting solution for its crucial next step.

2-3 Fast Electroplating operation to remove major impurities of copper from the solution containing Zn-65 radioisotope:

In the intricate process of recovering the Zn-65 radioisotope through acid washing of the bombarded copper target surface, a significant copper chemical impurity arises. To address this challenge, a preliminary step is introduced to remove the major copper impurity through Fast Electroplating. Prior to electrolysis, the solution undergoes careful preparation. The constant current method is employed to maintain a controlled voltage range during electrolysis, facilitating the selective separation of copper. A comparison of the standard

potential of copper and zinc reveals copper's greater propensity for reduction in solutions containing ions of both elements. [9].

$$Cu^{2+} + 2e^{-} \Leftrightarrow Cu \qquad E^{\circ} = +0.337 \text{ Volt}$$

$$Zn^{2+} + 2e^{-} \Leftrightarrow Zn \qquad E^{\circ} = -0.763 \text{ Volt}$$

Figure 1. Electrolysis operation to remove copper impurity.

2-4 Recovery and purification of Zn-65 radioisotope solution obtained using ion exchange resin "Dowex 1x8 100-200 mesh in Cl^- form"

2-4-1 The solution, approximately 180 mL in volume, contains the bombarded and meticulously dissolved copper layer from the previous step. This solution is carefully passed over a Plexiglas column, with an inner diameter of 3 centimeters and a height of 15 centimeters, at a steady rate of approximately 3 mL per minute. The column is meticulously packed with the ion exchange resin Dowex 1x8 100-200 mesh in Cl^- form, which plays a crucial role in the purification process. As the solution passes through the column, the radioisotope Zn-65 and some impurities are effectively

absorbed by the resin's surfaces. It is imperative to prepare the resin column just before introducing the radioactive solution by first passing a 4 normal hydrochloric acid solution of 30 mL through it.

2-4-2 To separate the chemical and radiochemical impurities, including copper, from the resin surfaces, a 2 normal hydrochloric acid solution of 50 mL is carefully passed through the resin column. This process, conducted at the same controlled speed, ensures that the impurities are efficiently collected in a complex form within the solution beneath the column.

2-4-3 To maximize the recovery of the Zn-65 radioisotope, a 0.005 normal hydrochloric acid solution of 150 mL is meticulously passed through the resin column. Maintaining the same controlled speed, this process ensures that the radioisotope is efficiently separated from the resin surfaces and collected as a complex in the solution beneath the column.

2-4-4 To further enhance the recovery of the Zn-65 radioisotope and neutralize any residual acidity within the resin column, a crucial step is introduced. Approximately 30 mL of distilled water is carefully passed through the resin column, ensuring that any remaining acidic solution is neutralized and the resin is freed from any acidic remnants. The solution collected beneath the column during this step is then combined with the solution from the previous step, ensuring a comprehensive recovery process.

2-4-5 To elevate the specific activity of the Zn-65 radioisotope, the entire volume of the solution from the previous two steps is carefully transferred to a 250-milliliter beaker. This beaker is then placed under a hood, where the solution undergoes a gentle evaporation process at a temperature of approximately 60 degrees Celsius. This controlled evaporation reduces the solution's volume to approximately 20 milliliters, thus increasing the concentration and specific activity of the coveted Zn-65 radioisotope. [7-10].

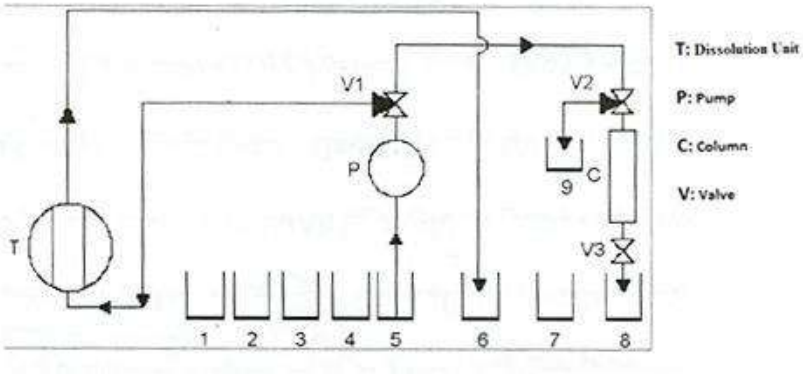

Figure 2. Schematic diagram of the semi-automatic device for radiochemical separation of Zn-65 radioisotope.

3. Results and Discussion:

Table No. 1 encapsulates the comprehensive details gathered throughout the various stages of chemical purification of the Zn-65 radioisotope. It is essential to highlight that this research involves tracking the 1115 KeV energy associated with the radioisotope. The level beneath this energy peak serves as a measuring scale for analysis. Although the counting time remains consistent for all samples, the varying quantities and total solution volumes in each step must be considered when interpreting the results. By utilizing the direct relationship between the "Area" parameter and the activity value of Zn-65, the losses of the Zn-65 radioisotope during each stage can be accurately calculated. This calculation takes into account the actual area of each stage, which is influenced by the differing solution volumes and can be determined using the provided formula.

$$\text{Area}_{\text{Real in each stage}} = \text{Area}_{\text{sample of that stage}} \times [\text{Total volume of solution in that stage} / \text{Sample volume}]$$

Table 1. The characteristics of the samples, the actual area and the percentage of radioactive presence in the different stages of the chemical treatment of Zn-65 radioisotope.

Specifications of the sample solution	The Area of Sample	The Sample counting time (seconds)	The weight of sample (gr.)	The total volume of solution in each step (mL)	The actual Area of every step	The Percent existence Zinc-65 in solution
The primary active solution before electrolysis operation.	1365	6000	0.196	80	557142.85	100
The active solution after electrolysis operation.	1082	6000	10282.04	180	1521562.50	94.80
The electrolysis Waste solution.	62	6000	0.119	200	104201.68	2.92
The active prototype solution passed through the column.	50	6000	0.340	180	26470.58	3.12
The active HCl 2 N solution passed through the column.	26	6000	0.131	50	9923.66	1.70
The active HCl 0.005 N solution and water passed through the column.	967	6000	0.155	180	1122967.74	92.07
The active Final Condensed HCl solution containing	3097	6000	0.166	20	10282.04	91.78

radioisotope Zn-65.

4. Conclusion:

The comprehensive analysis of the obtained results reveals a total recovery yield of 91.78% for the Zn-65 radioisotope after undergoing the various stages of chemical purification. This calculation also allows for the determination of the loss amount of this coveted radioisotope during the purification process.

Table 2. Percentage of Zn-65 radioisotope losses at the end of each stage of chemical treatment

Zinc-65 radioisotope losses.

Number	The Name of chemical treatment step of zinc-65 radioisotope	Zinc-65 radioisotope losses (in percent)
1	Electric sedimentation (electrolysis)	5.20
2	Chromatographic separation with resin column	4.82
3	Condensation and increase of specific activity	0.29

5. References:

1. Lahiri S, Banerjee S, Das NR (1997) Simultaneous production of carrier-free ^{65}Zn and ^{66,67,68}Ga in particle activated copper target and their separation with TOA. Appl Radiat Isot 48:15-18.

2. Kurt A. Kraus and George E. Moore; Anion exchange studies: The Divalent Transition Elements Manganese to Zinc in Hydrochloric Acid; Sept. 2, 1952.

3. Blann M, Bislinghoff J (Nov 5, 1991) Code Alice/Livermore 91. Lawrence Livermore National Laboratory, Internal Report, UCID-19614.

4. International Atomic Energy Agency (IAEA), Nuclear Data Services- http://www-nds.iaea.org,

5. Ziegler JF, Biersack JP, Littmark U (2000) The code of SRIM - the Stopping and Range of Ions in Matter, January 1, 2000, Version 2000.

6. Winkel P.V., End of Mission Report, 1995, IAEA, Mission, Project, IRA/4/019/07, July 9-24.

7. S. M. Haji Saeed, h. Afrideh, A. Sattari, b. Akbari, M. Shafi'i, b. Fateh, b. Shirazi, Kh. Ardane, M. Mirzaei, "Galium-67 Citrate Radiopharmaceutical", 1376, Nuclear Energy Journal, No. 21, 39-36, (in Persian).

8. Shirazi B, Fateh B "Production of a prototype ^{68}Ge/^{68}Ga generator", ^{5}th International Conference on Isotopes, 25-29 April 2005, Brussels- Belgium.

9. H.Nourkojouri, and P.Sarabadani "Selective Separation of $^{68}Zn^{+2}$ from other Metal Ions by Chemical Procedure" Proceeding of First International Congress of Chemistry and Chemical Engineering", Shahid Beheshty University, Tehran 183 (1993).

10. Behrouz Shirazi, Khosro Ardane, "Radiochemical separation of gallium-67 radioisotope from zinc and copper metal impurities using Amberlite XAD-7 absorption resin, March 1385, Iran Nuclear Conference -, Isfahan Universit

ICNST 2024 International Conference on Nuclear Science and Technology
6- 8 MAY 2024 | Isfahan, Iran

Feasibility of improving the irradiation of topaz stones by using neutron absorbing filters to reduce their activity in Tehran research reactor (Paper ID : 1318)

S. Saeid Mousavi[1*], Hamid Jafari[1], M.R. Kardan[2], Zohreh Gholamzadeh[2]

[1]*Application of rays, Faculty of Nuclear Engineering, Shahid Beheshti University, Tehran, Iran.*

[2]*Reactor and Nuclear Safety Research Institute, Atomic Energy Organization, Tehran, Iran.*

Abstract

Topaz stone is known and used as a precious stone. It is possible to give topaz stones beauty, transparency, and better coloring by performing a series of processes. This process is done by neutron bombardment and gamma irradiation. Irradiation of topaz is one of the commercial applications of research reactors. In this research, neutrons produced in the Tehran research reactor (TRR) are used to color topaz stones. The main factor in creating color centers in this process is fast neutrons. However, the presence of thermal neutrons during the irradiation of topaz stones activates the impurities in them. This research aims to reduce the activity of topaz stones by using thermal neutron absorber filters during irradiation. The thermal, epithermal, and fast neutron fluxes in topaz have been investigated in this regard. The required calculation has been carried out by MCNPX code. In this research, Cadmium(Cd), Tantalum (Ta), and boron carbide (B_4C) materials were used as absorbent filters and according to the desired thickness, it has a good effect in reducing the radioactivity of topaz stones. The results showed that the Ta filter can reduce the thermal neutron flux by more than 40%, and with the reduction of the thermal neutron flux, the activity level also decreases.

Keywords: Activity, Topaz, MCNPX, Absorbing filter, TRR

INTRODUCTION

In general, the name gem or precious stone is used for a group of minerals that are distinguished from other minerals and stones by having some characteristics such as beauty, hardness, durability, and transparency. The demand for precious and semi-precious stones, including topaz, with better and more ideal colors and clarity than what it provides, has created a group that seeks solutions to improve the appearance and the quality of the color and strength of the stones. and find ways. Some of these improvement actions are

sustainable and some are unstable. The topaz stone will have a higher price after the treatment and color change than before irradiation. The process of improvement is called an operation after which the appearance of precious stones, such as their color, clarity, hardness, and value, is improved [1,2].

This color change is caused by neutron bombardment by neutron generators (research reactor), gamma rays, high-energy electrons produced by the accelerator, or a combination of them. The change and enhancement of color by neutrons create a deeper blue color than irradiation with only gamma or electrons in topaz stones, and in this sense, neutrons are better for irradiation [3]. Research reactors produce neutrons and these neutrons are in the range of thermal, epithermal, and fast energy. For the healing process, we need fast neutrons so that this process is done correctly and the color of the topaz stones changes, but during the prototyping process, the thermal neutrons make the topaz stones radioactive [4].

One of the factors that cause color change in topaz stones is the presence of color centers in their structures. The color center is a defect in the crystal lattice, which must be created to cause color change in topaz stones. The existence of these fast neutrons causes a defect in the crystal lattices and finally creates color centers that change the color of the topaz stones and the healing process is performed [5].

Topaz stones are irradiated in research reactors of other countries such as Egypt, Kazakhstan, Brazil, Indonesia, Uzbekistan, and Thailand. In Egypt's ETRR-2 reactor, aluminum containers are used to irradiate topaz stones, and a total of 4-6 kg of topaz is placed inside these containers. To reduce the thermal neutrons inside the containers, they use a boron carbide filter or materials containing boron. Boron-10 has a high absorption cross-section of thermal neutrons. In Egypt's ETRR-2 reactor, if there is a thermal neutron absorber filter for the irradiation of topaz stones, the irradiation of topazes will reach below the permissible limit after 6-18 months, and if there is no thermal neutron absorber filter, after 20-29 months, topaz radioactivity reaches less than the permissible limit [6].

The chemical formula of topaz stone is $Al_2SiO_4(F.OH)_2$ [6]. The main elements in topaz stone are aluminum, silicon, oxygen, and fluorine, which have a half-life of about a few minutes and a few seconds. Thermal neutrons irradiate the main elements, but because they have a small half-life, after passing at least 5 times their half-life, the risk of irradiation does not include these and they will not be dangerous.

In general, in addition to the main elements mentioned, topaz stones have a series of impurities, the types of these impurities will be different according to the types of topaz stones that are extracted from different mines. These impurities have a longer half-life thermal neutrons activate these impurities and cause topaz stones to radiate. Due to the long half-lives of a series of impurities and the irradiation of topaz stones by

thermal neutrons, it makes it impossible for the stones to be delivered quickly to the consumer, and a lot of time must be spent, and these stones are stored in the warehouse with Specific and appropriate protection should be maintained so that the radioactivity of the stones reaches the permissible limit. It is not economical to spend a lot of time to reduce the activity of topaz stones. However, a method for irradiating topaz stones should be used that keeps the flux of rapidly produced neutrons constant and the flux of thermal and super-thermal neutrons is reduced as much as possible so that after less time passes, the irradiation of the stones reaches the permissible limit and can be He offered these stones in the market [7].

The process of irradiating topaz stones industrially is being implemented in the Tehran Research Reactor (TRR). The goal and innovation of this research is to achieve a suitable method according to the conditions to reduce the radioactivity of topaz stones, which topazes enter the market after spending less time and can lead to the development of this industry in Iran [7].

Materials and methods

Characteristics of the core of the TRR

TRR is a pool type, the central core of this reactor is located in an 8-meter deep pool with a capacity of 500,000 liters of light water. The moderator and coolant of this research reactor is light water and it is used for research, training, radiation, and radiopharmaceutical production purposes. The concrete pool filled with light water consists of two parts, the reactor core can be operated in each of those two parts. On the wall of one of these two parts, laboratory equipment such as 7 beam tubes with different cross-sections, pneumatic rabbit tubes, and thermal columns are placed. In addition, it is possible to irradiate the sample in special irradiation chambers inside the core and at the periphery of the core. The reflector of this type of reactor is of graphite type and has inhomogeneous solid fuel of plate type. The core of the reactor has fuel elements of the MTR type, which are placed inside the grid plate. On the screen, there are 54 positions for the placement of fuel complexes in a regular $\mathbf{9 \times 6}$ rectangular arrangement. By placing the fuel complexes in their place on this plate, the core complex is formed. The fuel of this reactor is low-enriched uranium oxide (LEU), which includes standard fuel elements (SFE) with a height of 63 cm. Both types of fuel elements have $\boldsymbol{U_3O_8 - Al}$ fuel plates with 20% richness, which are placed in SFE type, 19 fuel plates, and in CFE type, 14 fuel plates. Each CFE element includes two $\boldsymbol{Cd - In - Ag}$ control blades that are used to control the core's

reactivity and regulate the neutron flux [8-11]. Some graphite reflectors are placed around the core to reduce neutron leakage from the core [12-14].Figure 1, shows the layout of the heart of the TRR, along with the different positions for irradiation, as well as the fuel plates and the graphite box, simulated by the MCNPX code.

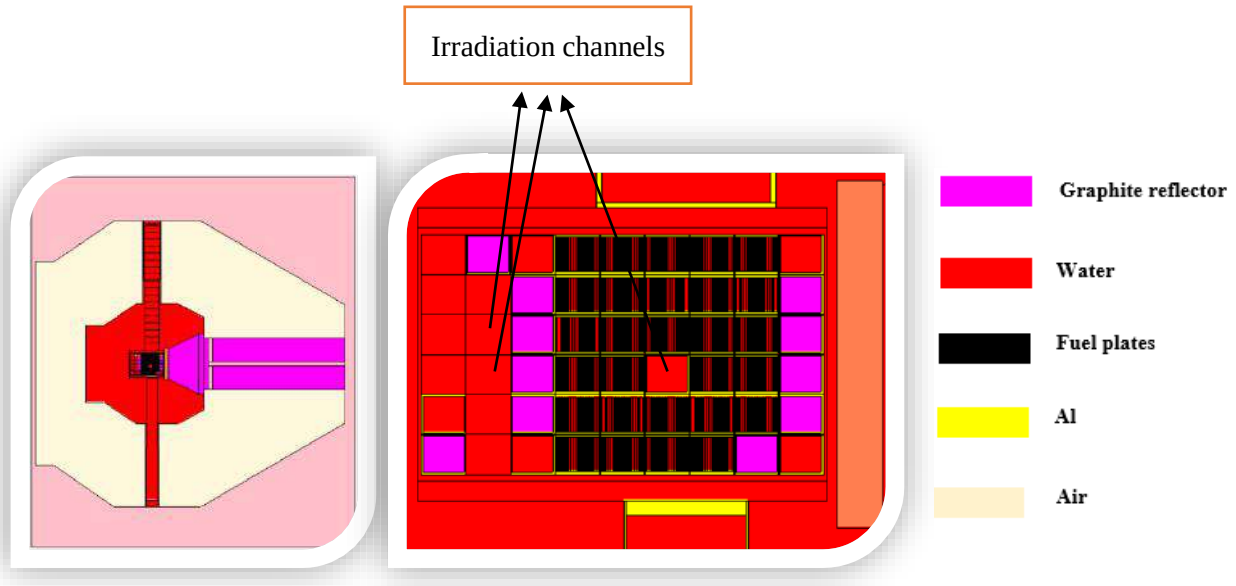

Fig. 1. Layout of the core of the TRR along with different irradiation positions.

Description of irradiation in code MCNPX

For irradiating topaz stones, two rectangular cube boxes with dimensions of $\mathbf{5\ cm\ x\ 5\ cm\ x\ 27\ cm}$ have been used. Topazs are placed in these containers and simulated by MCNPX code. Irradiation boxes are placed vertically on top of each other and placed in the irradiation channel of the edge of the core and simulated. In this research, thermal neutron absorber filters such as Cd, B_4C, and Ta have been used separately in thicknesses of 1 mm, 2 mm, and 3 mm in the wall of the irradiation box and the amount of neutron flux and also the residual energy caused by It has been calculated from neutron and gamma if filters are used. The

cooling of topaz stones during irradiation in all modes is light water. Neutron flux calculations are divided into 3 categories and performed for the following 3 energy groups:

0 – 0.4 eV	(Thermal)
0.4 eV – 1 keV	(Epithermal)
1 keV – 20 MeV	(Fast)

Figure 2 indicates the box containing topaz. The wall of the box is only aluminum. The boxes are placed vertically on top of each other and radiated. Figure 3 shows the box containing topaz along with neutron-absorbing filters.

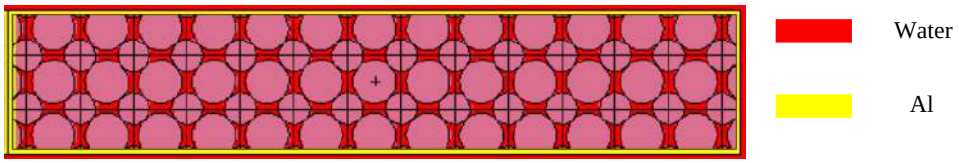

Fig.2. Irradiation box containing topaz and water with aluminum wall

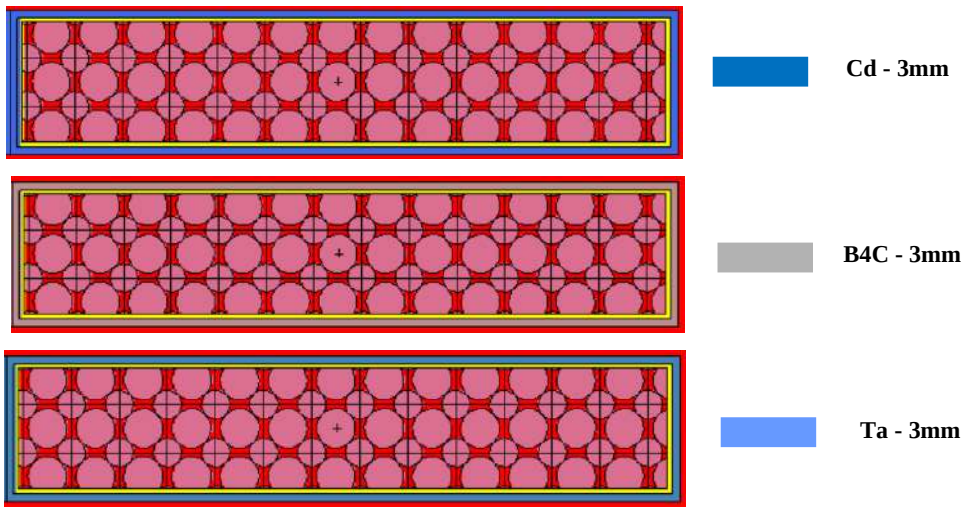

Fig.3. Boxes containing topaz with neutron absorbing filters.

In the MCNPX code, the track length estimator (F4) was used to calculate the average volume flux of neutrons at each neutron energy range. To calculate the residual energy caused by neutrons and gammas, heat deposited tally (F6) was used. The statistical error in all the results obtained from the simulation calculations was less than 2%.

Calculations have been done on both irradiation boxes in the desired channel. Figure 4 shows the location of boxes containing topaz for irradiation.

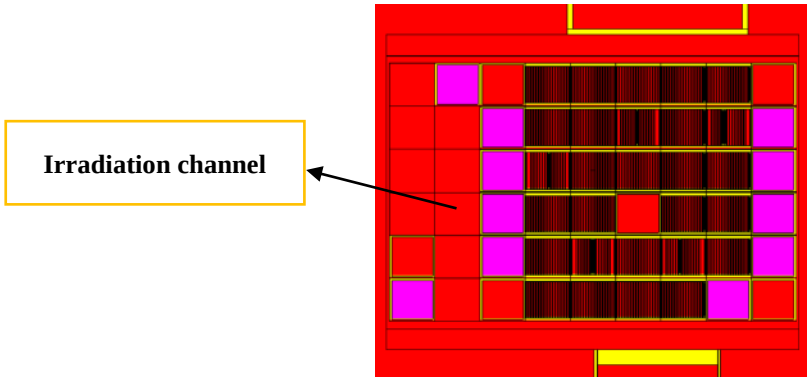

Fig.4. The simulated Irradiation channel of boxes containing topaz

Figure 5 shows the cross-sections of B-10, Ta-181, and Cd-113 isotopes. In the graphs of the figure, the vertical axis shows the cross-sectional (barns) area value and the horizontal axis shows the energy (MeV) value.

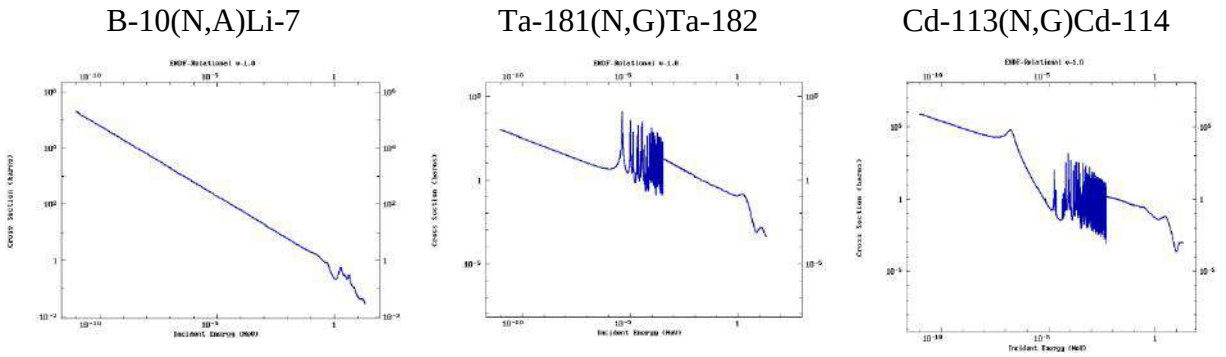

Fig.5. The total neutron cross-section of isotopes B-10, Ta-181, and Cd-113 [15].

Results and discussion

The neutron flux distribution was calculated for all 3 ranges of thermal, epithermal, and fast energy. The desired irradiation boxes were placed vertically on top of each other in the irradiation channel at the edge of the core, i.e. behind the graphite boxes as shown in Figure 4.

In the simulation, the topaz box is made of aluminum with a thickness of 2 mm. In the following cases, B_4C, Cd, and Ta filters with thicknesses of 1 mm, 2 mm, and 3 mm are considered on this aluminum wall and the calculations are examined. The cooling of topaz stones during irradiation is light water.

The cooling of topaz stones during irradiation is the light water in the reactor pool. Table 1 summarizes the amount of thermal neutron flux for boxes with different filters in the irradiation channel of the core periphery.

Table 1. Distribution of thermal neutron flux in the irradiation channel of the core periphery

Material / Thickness(mm)	Thermal neutron flux ($n/cm^2.s$)	Material / Thickness(mm)	Thermal neutron flux ($n/cm^2.s$)
Al-2mm	2.44402E+13 2.50938E+13	Al-2mm/ B_4C-2mm	7.17648E+11 7.14065E+11
Al-2mm/ Cd-1mm	1.41721E+12 1.41376E+12	Al-2mm/ B_4C-3mm	5.92036E+11 5.76058E+11
Al-2mm/ Cd-2mm	1.34267E+12 1.27643E+12	Al-2mm/ Ta-1mm	1.20184E+13 1.20727E+13
Al-2mm/ Cd-3mm	1.29231E+12 1.26022E+12	Al-2mm/ Ta-2mm	8.47934E+12 8.40188E+12
Al-2mm/ B_4C-1mm	1.12524E+12 1.17674E+12	Al-2mm/ Ta-3mm	5.51164E+12 5.46123E+12

According to the results, by increasing the thickness of the filters from 1 mm to 3 mm, the amount of thermal neutron flux has decreased well. The B_4C filter has a better performance in reducing the thermal neutron flux than the other investigated filters.

The amount of epithermal and fast neutron fluxes for boxes with different filters in the irradiation channel of the core periphery are given in Tables 2 and 3 respectively.

Table 2. Distribution of epithermal neutron flux in the irradiation channel of the core periphery

Material / Thickness (mm)	Epithermal neutron flux (n/cm^2.s)	Material / Thickness (mm)	Epithermal neutron flux (n/cm^2.s)
Al-2mm	3.51817E+12 3.62478E+12	Al-2mm/ B_4C-2mm	2.46008E+12 2.50351E+12
Al-2mm/ Cd-1mm	3.42689E+12 3.45378E+12	Al-2mm/ B_4C-3mm	2.22387E+12 2.23860E+12
Al-2mm/ Cd-2mm	3.39711E+12 3.39651E+12	Al-2mm/ Ta-1mm	3.11762E+12 3.07709E+12
Al-2mm/ Cd-3mm	3.41714E+12 3.41465E+12	Al-2mm/ Ta-2mm	2.92973E+12 2.86456E+12
Al-2mm/ B_4C-1mm	2.81911E+12 2.81301E+12	Al-2mm/ Ta-3mm	2.72465E+12 2.71367E+12

Table 3. Distribution of fast neutron flux in the irradiation channel of the core periphery

Material / Thickness(mm)	Fast neutron flux (n/cm^2.s)	Material / Thickness(mm)	Fast neutron flux (n/cm^2.s)
Al-2mm	3.87097E+12 3.94663E+12	Al-2mm/ B_4C-2mm	3.87589E+12 3.92417E+12
Al-2mm/ Cd-1mm	3.90715E+12 3.94593E+12	Al-2mm/ B_4C-3mm	3.94890E+12 3.99256E+12
Al-2mm/ Cd-2mm	3.92286E+12 3.97781E+12	Al-2mm/ Ta-1mm	3.84276E+12 3.89301E+12
Al-2mm/ Cd-3mm	3.99398E+12 4.07447E+12	Al-2mm/ Ta-2mm	3.99556E+12 3.90425E+12
Al-2mm/ B_4C-1mm	3.88149E+12 3.89204E+12	Al-2mm/ Ta-3mm	4.15538E+12 4.03895E+12

According to the results, the flux of fast neutrons for the case of box topaz with Ta-3mm filter is higher than B4C and Cd filters and has increased by 8% compared to the case without filter.

Tables 4 and 5 reperesent the amount of residual heat caused by neutron and gamma in topaz stones in different filters in the wall respectively.

Table 4. Residual heat caused by neutrons in the irradiation channel of the core periphery

Material / Thickness (mm)	Neutron residual heat (W)	Material / Thickness (mm)	Neutron residual heat (W)
Al-2mm	24.7 24.7	Al-2mm/ B_4C-2mm	23.8 24.2
Al-2mm/ Cd-1mm	23.7 23.8	Al-2mm/ B_4C-3mm	24.4 24.3
Al-2mm/ Cd-2mm	23.6 23.8	Al-2mm/ Ta-1mm	24.1 23.9
Al-2mm/ Cd-3mm	23.9 24.6	Al-2mm/ Ta-2mm	24.2 24.4
Al-2mm/ B_4C-1mm	23.7 23.9	Al-2mm/ Ta-3mm	24 24.1

In the case of using neutron absorber filters and also increasing the thickness of these filters, there is no special change in the residual heat caused by neutrons. According to the results in Table 5, if using a Cd filter up to 3 mm thick, the amount of residual heat reduction caused by gammas is higher than the other mentioned filters and there are about 50% changes compared to the basic state.

Table 5. Residual heat caused by gammas in the irradiation channel of the core periphery

Material / Thickness (mm)	Gamma residual heat (W)	Material / Thickness (mm)	Gamma residual heat (W)
Al-2mm	244.2 248.3	Al-2mm/ B_4C-2mm	203.3 213.1
Al-2mm/ Cd-1mm	177.8 178	Al-2mm/ B_4C-3mm	206.5 208.2
Al-2mm/ Cd-2mm	167 169	Al-2mm/ Ta-1mm	241 242.3
Al-2mm/ Cd-3mm	159.3 161.5	Al-2mm/ Ta-2mm	230.7 231.9
Al-2mm/ B_4C-1mm	213.1 209	Al-2mm/ Ta-3mm	225.6 227

Conclusions

The use of TRR for neutron irradiating and improving the color of topaz stones requires design requirements to reduce their activity. According to the results obtained from the simulation by MCNPX code, among the investigated thermal neutron absorber filters, the B_4C filter performed better. The flux of thermal neutrons decreased 50% by adding 1 mm to the thickness of the B_4C filter. The thermal neutron flux ratio of topaz box stones with aluminum wall to box with B_4C-3mm filter is equal to (40.73). The amount of epithermal neutron flux has decreased more with the addition of the Ta filter. Finally, it has changed and decreased the flux by 30% compared to the basic state without the filter. If the Cd filter is used, the deposit heat caused by gamma has decreased by 50%, but if other filters are used, this item has not changed significantly. It can be concluded that the presence of B_4C in the topaz box wall is very effective in reducing the thermal neutron flux and the activity of topaz stones.

References

[1] Nelson, K., Baum, J.W., 1993. Health risk assessment of irradiated topaz. U.S. Nuclear Regulatory Commission.

[2] M. Kaveh. Measuring and studying the effects of irradiation on the color change and crystal structure of stones. 2013.

[3] S. Salama, A.I. Helal and M.A. Gomaa, Radioactivity of the Treated Topaz,2012.

[4] Jian Zhang, Taijin Lu, Manjun Wang, and Hua Chen, the radioactive decay pattern of blue topaz treated by neutron irradiation, 2011.

[5] Shamshad Ahmed, Value addition in diamonds and other gemstones by nuclear radiation: the phobias and safety considerations,2009.

[6] Nader M.A. Mohamed, M.A. Gaheen, Design of fast neutron channels for topaz irradiation,2016.

[7] S. S. Mousavi, Hamid Jafari , M. R. Kardan , Zohreh Gholamzadeh. Feasibility of optimization of Topaz radiation in order to reduce the activity of Topaz stones in Tehran research Reactor. 2023.

[8] AEOI, Safety Analysis Report of Tehran Research Reactor, Atomic Energy Organization of Iran, (2009).

[9] M.H.C. Dastjerdi, H. Khalafi, Design of a thermal neutron beam for a new neutron imaging facility at Tehran research reactor, Physics Procedia, 69, 92-95 (2015).

[10] A. Lashkari, et al, Neutronic analysis for Tehran Research Reactor mixed-core, Prog. Nucl. Energy, 60, 31–37 (2012).

[11] N. Zandi, Study on a new design of Tehran Research Reactor for radionuclide production based on fast neutrons using MCNPX code, Applied Radiation and Isotopes, 132, 67-71 (2018).

[12] H. Khalafi, M. Gharib, Optimization of 60Co production using neutron flux trap in the Tehran research r

[13] M.R. Aboudzadeh, et al, Preparation and Characterization of Chitosancapped Radioactive Gold Nanoparticles: Neutron Irradiation Impact on Structural Propertie. Safety Analysis Report for the Tehran Research Reactor (HEU), Tehran-Iran, (13, 339-345.AEOI, 1966) (2015).

[14] Z. Zarei, M. Amin Mozafari, S. Mohammadi, M. Hasanzadeh. Design of irradiation box of topaz stones and its neutronic and thermal analysis in Tehran Research Reactor. 2022.

[15] https://www-nds.iaea.org/exfor/endf.htm.

ICNST 2024
International Conference on Nuclear Science and Technology
6- 8 MAY 2024 | Isfahan, Iran

Investigating effective factors in the radiolabeling of carbon- based quantum dots with technetium-99m (Paper ID : 1320)

Mazaheri Tehrani M[1]*., Erfani M[1]., Guodarzi M[1].

[1]*Radiation Application Research School, Nuclear Science and Technology Research Institute, Tehran, Iran*

Abstract

In recent years, nano-based radiopharmaceuticals have shown potential for cancer diagnosis and treatment. Quantum dots (QDs) are semiconductor nanoparticles with size <10 nm that exhibit specific optical and electronic properties. In this study, the effect of parameters (temperature, pH, amount of initial ligand and reducer agent...) and optimum conditions on radiolabeling yield of biocompatible QDs with ^{99m}Tc radioisotope were investigated. Various amounts of QDs (15-30 mg) were used in the radiolabeling process to reach the high radiochemical purity. The percentage of $^{99m}TcO_4^-$ in the reaction mixture was followed by a radio-thin layer chromatography (Radio-TLC) method. The radiolabeling was performed in the presence of $SnCl_2$ solution as a reducer agent in the range of 40-100 μg at 90-95°C. The pH of the reaction was adjusted in the range of pH 5.5-6. By optimizing the labeling conditions, the radiochemical purity was obtained in the range of 60 to 98.0 %. According to the obtained results, the QDs particles would be able to bind with technetium-99m under the controlled conditions for *in vivo* applications in nuclear imaging.

Keywords: Carbon quantum dots; Technetium-99m; Cancer; Radiochemical purity; Radiolabeling.

INTRODUCTION

The application of nanotechnology in nuclear medicine has led to the development of new radiopharmaceuticals in molecular imaging. Meanwhile, the preparation of radiopharmaceuticals based on quantum dots has attracted considerable attention for bioimaging applications [1, 3]. Quantum dots, as zero-dimensional nanomaterials, are semiconductor fluorescent nanocrystals in the size range between 1 and 10 nm with special optical and electronic properties [4-6]. Typically, these common fluorescent materials suffer from low depth penetration and background autofluorescence in cellular imaging [5,6]. To overcome the inherent limitations of fluorescent nanoprobes, radioisotopes have been combined with various nanomaterials, including quantum dots (QDs). In fact, the incorporation of characteristics related to the size of nanomaterials and the sensitivity of radioisotopes in nuclear imaging techniques discloses an appealing field in the development of new probes for the diagnosis and treatment of various cancers. After preparation and subsequent administration of the radiolabeled QDs in living models, *in vivo* biodistribution could be non-invasively monitored by molecular imaging techniques such as single photon emission computed tomography (SPECT), positron emission tomography (PET), Cerenkov luminescence (CL), Cerenkov

resonance energy transfer (CRET), etc. [6-8]. These techniques are now used to visualize and measure changes in cellular metabolic processes in the preclinical and/or clinical phase. In this study, biocompatible or free-metal QDs such as graphene quantum dots (GQDs) were used as nanoprobes for radiolabeling with technetium-99m. ^{99m}Tc is the most widely used in nuclear diagnostic procedures [3-6]. Several methods can be followed in order to radiolabel QDs efficiently with ^{99m}Tc. Regardless of which method is used, the entire radiolabeling process is usually affected by various factors including temperature, pH, radioactive dose, amount of ligand, reducing agents [3]. In this study, we investigated the impression of some factors on the radiolabeling of QDs with Technetium-99m. The optimization of experimental conditions was carried out to obtain the high radiochemical purity of stable radiolabeled QDs.

EXPERIMENTAL

Materials and Instruments

All chemicals were consumed without further purification. Solvents were analytical grade and purchased from Sigma-Aldrich. Natural graphite powder was purchased from Merck (Germany). De-ionized (DI) water (18.2 MΩ) from purification system was utilized for the whole experiment. For radiolabeling, 99m-Technetium pertechnetate was available from a commercially ^{99m}Mo /^{99m}Tc generator (Iran, Tehran, Pars Isotope Co.). Radio-TLC tests were performed using a radio- thin layer chromatography (Radio-TLC) scanner (Raytest-GITA, Germany). A sodium iodide well counter (EG&G/ORTEC, model 4001M) was used for quantitative gamma counting of the radiolabeled samples. The fluorescence intensity (PL) of the prepared GQD were recorded using FL-Arn 20 spectrofluorometer (Iran) with a xenon lamp and quartz cuvette (path length of 1 cm) at different temperatures.

Methods

Optimization studies

In the optimization studies for radiolabeling of QDs with technetium-99m, the following parameters were sequentially tested: the ligand QDs concentration, the amount of reducing agent, the pH, and the other effective factors in quantum dot labeling. The QDs concentration varied from 15 to 30 mg/mL in acetate buffer. Acetate buffer (0.5 M) was prepared with 0.41 g of sodium acetate [= 8.9×10^{-3} mol, MW: 82.0343 g] that was dissolved in 10 mL distilled water. Also, The pH of the reaction mixture was adjusted by NaOH (0.5 M) and HCl (N) to obtain desired values. Stock solution of $SnCl_2.2H_2O$ in 10 mL HCl (0.1 N) was prepared and for quantification, either 40-100 μg was added to each sample. 5 mCi of the fresh $^{99m}TcO_4^-$

solution (from $^{99}Mo/^{99m}Tc$ generator) was added to the reaction mixture in all experiments. All experiments were performed in triplicate to ensure the accuracy of the results.

Synthesis of QDs

GQDs as a ligand for conjugation to Technetium-99m in this study were synthesized from graphene powder and characterized based on the method of Qi et al., as previously reported [9]. Briefly, graphene powder (10 mg) was oxidized in a thick mixture of H_2SO_4: H_2O_2 (7:3 v/v) at 80 °C for 30 min. Then the mixture was diluted with deionized water (250 mL) and the pH was adjusted to neutrality with NaOH solution (N). The colloidal solution was dialyzed in a dialysis bag (1000 molar mass cutoff) for 5 days to remove the salt. Finally, the GQDs powders were obtained by freeze-drying with high performance [9].

Radiolabeling of QDs with Technetium-99m

The radiolabeling process was directed with a certain amount of GQDs in the presence of $SnCl_2.2H_2O$ and fresh $^{99m}TcO_4^-$ solution. In order to determine the radiochemical purity of ^{99m}Tc radiolabeled QDs, Radio-TLC test was performed using Whatman paper No. 1 strips (2×10 cm^2) in two solvent systems containing acetone and a mixture of [H_2O: EtOH: ammonia solution 25 % (5:2:1 v/v)] as mobile phase. The ^{99m}Tc activity was measured as previously described using an automated gamma counter. Also, radiolabeling efficiency was calculated relative to the total amount of ^{99m}Tc added to each sample.

RESULTS & DISCUSSION

In this study, GQD_S were synthesized using a heating method at 80 °C to induce the chemical oxidation process. Any substance for medical applications must be safe and compatible with biological systems. Based on the previously reported littrature, GQDs compared to colloidal semiconductors and graphene oxide (GO) is biocompatible and non-cytotoxic [10-12]. This claim was also confirmed by Ros's experiment, where the small size of GQDs demonstrated good biocompatibility and ability to pass through the ultrafiltration barrier in an *in vitro* model [13]. Also, in the MTT assay results by Li et al., (2019) treated HL-7702 cells with GQDs (200 μg ml^{-1}) for 24 h showed high cell viability [14]. However, these properties make GODs ideal candidates for the application in various fields such as drug delivery systems, bio-imaging, therapeutics, and theranostics [15]. In the following, the GQDs were radiolabelled with ^{99m}Tc. The entire radiolabeling process is usually affected by different factors, including temperature, pH, total volume, the amount of ligand, and the amount of reducing agent. In this study, it was found that the radiolabeling efficiency was strongly influenced by the pH value. As shown in **Fig. 1**, in the acidic range, the yield of the radiolabeling was apparently low and negligible (13.45 %- 53.76 %). This means that there is no measurable amount of ^{99m}Tc-

GQDs. Moreover, further increasing the pH above 7 resulted in lower radiolabeling efficiency under the conditions used. The highest radiolabeling efficiency was obtained at pH = 6 (97.08 %) and remained almost unchanged between pH 6 and 7. To optimize the reducing agent concentration in order to extract free $^{99m}TcO_4^-$, various amounts of the stannous chloride stock solution in the range of 40 µg to 100 µg were added to the radiolabeling mixture, and the percentage of $^{99m}TcO_4^-$ was followed by Radio-TLC. Results showed that 100 µg of the $SnCl_2.2H_2O$ solution (40 mg $SnCl_2.2H_2O$/10 mL of HCl 0.1 N) extracted nearly all $^{99m}TcO_4^-$ (**Fig. 2**). The radiochemical purity reached (98.0 %) in 100 µg of $SnCl_2.2H_2O$ and remained almost constant with further increase of reducing agent.

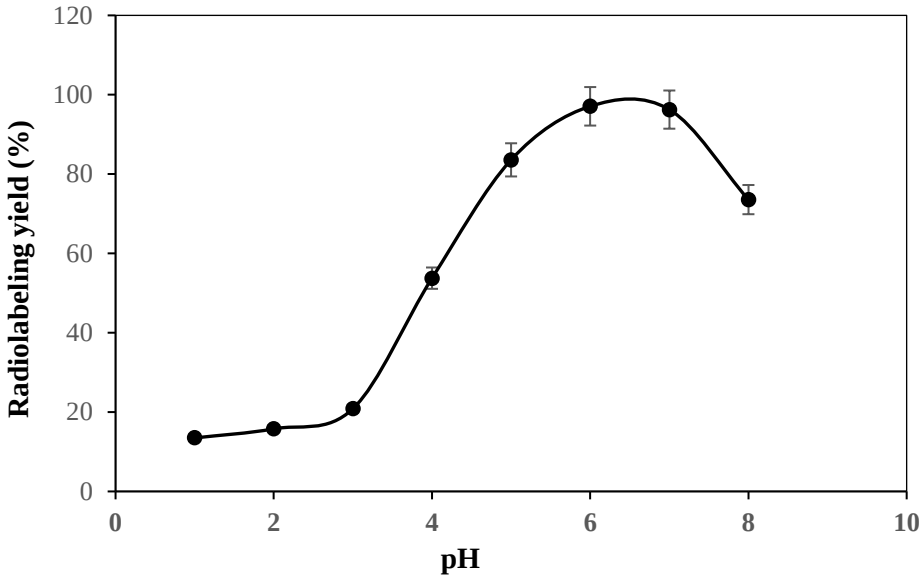

Fig. 1. The effect of pH on the radiolabeling yield of GQDs with Technetium-99m.

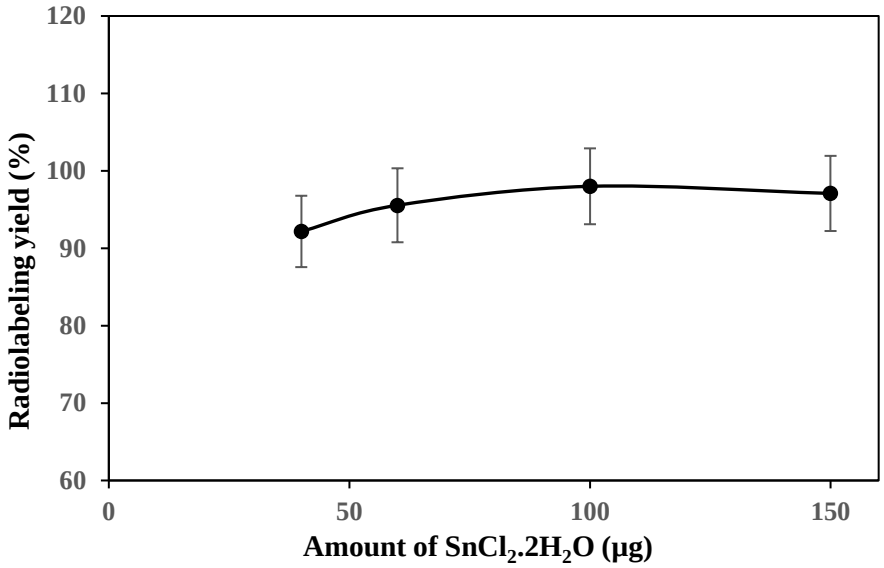

Fig. 2. The effect of reducer agent amount on the radiolabeling yield of GQDs with Technetium-99m.

Different concentrations of initial composition were used in the radiolabeling process to reach the high radiochemical purity. Various amounts of the ligand (10-30 mg) were used to find the optimal amount. The radiolabeling efficiency increases with the amount of QDs up to 20 mg/mL. The results showed that by keeping the values of the test factors constant, the radiolabeling could be increase up to 98.0 % with 30 mg/ml GQD as a ligand. With the greater amounts than 30 mg a small decline of the yield of radiolabeling was observed (**Fig. 3**).

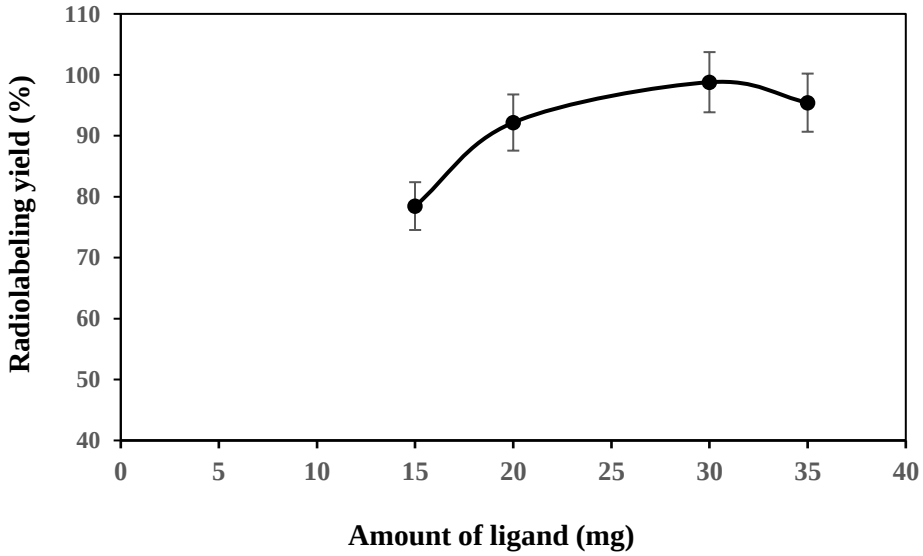

Fig. 3. The effect of ligand concentration on the radiolabeling yield of GQDs with Technetium-99m.

In the following, the radiolabeling was done in the temperature ranges from 25°C to 100 °C under all optimized factors in a sealed vial for 20 min. The results showed that high temperature and magnetic stirring conditions increase the percentage of radiolabeling from 53.76 % to 0.98.0 % and the reaction proceeds better at a higher temperature (**Fig.4**).

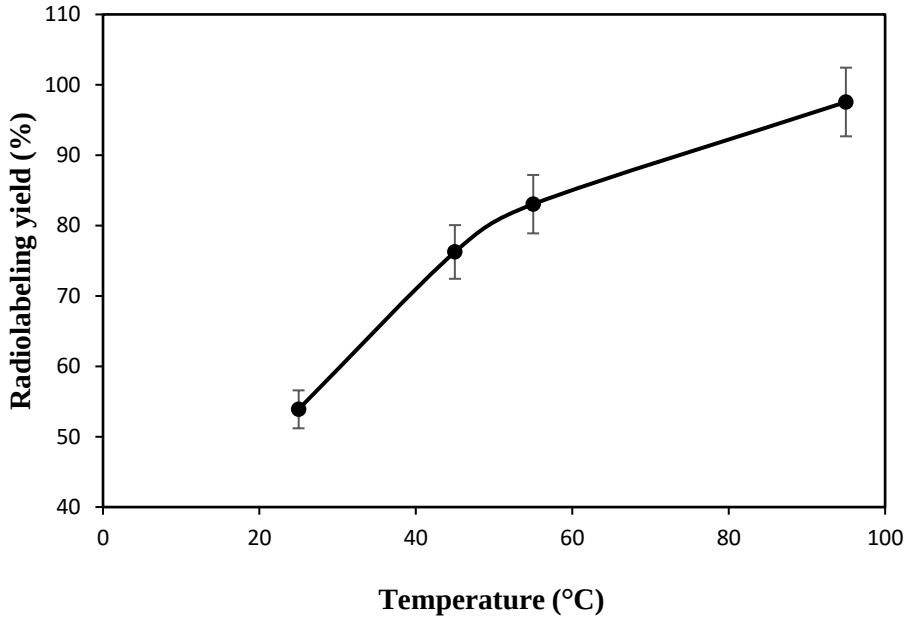

Fig. 4. The effect of temperature on the radiolabeling yield of GQDs with Technetium-99m.

It has been observed that optical properties of CQDs are affected by various factors such as temperature. Therefore, the optical stability (photostability) of developed GQDs was investigated after 5, 10,15 and 20 h at 25 °C. The results showed that there was no significant change in fluorescence intensity (PI) after 20 hours. As shown in **Fig.5**, this finding indicates the excellent photostability of GQDs at room temperature. In addition, the optical stability of the developed GQDs was investigated at different temperatures 25, 50, 75, and 95 °C in **Fig. 6**. The results showed that by increasing the temperature from 25 to 95 °C, approximately 5% of the initial fluorescence intensity decreased. However, so far, a lot of research has been done regarding the stability of quantum dots with different results. In 2014, Wang et al., noticed that the emission of the prepared CQDs, strongly affected by temperature. In this study, the fluorescence intensity decreased by 52% when the temperature changed from 15 to 90°C [16]. In another study also by Lin et al., (2017) in different heating tests, observations showed that the initial intensity of N-CDs was preserved from 25 to 65 °C and even with increase of temperature from 75 to 95°C a small of intensity inceasment (2%) was obtained [17].

Therefore, according to our results from the optical stability of the prepared GQDs, it is possible to radiolabel GQDs with Technetium-99m at 90-95°C within 20 min.

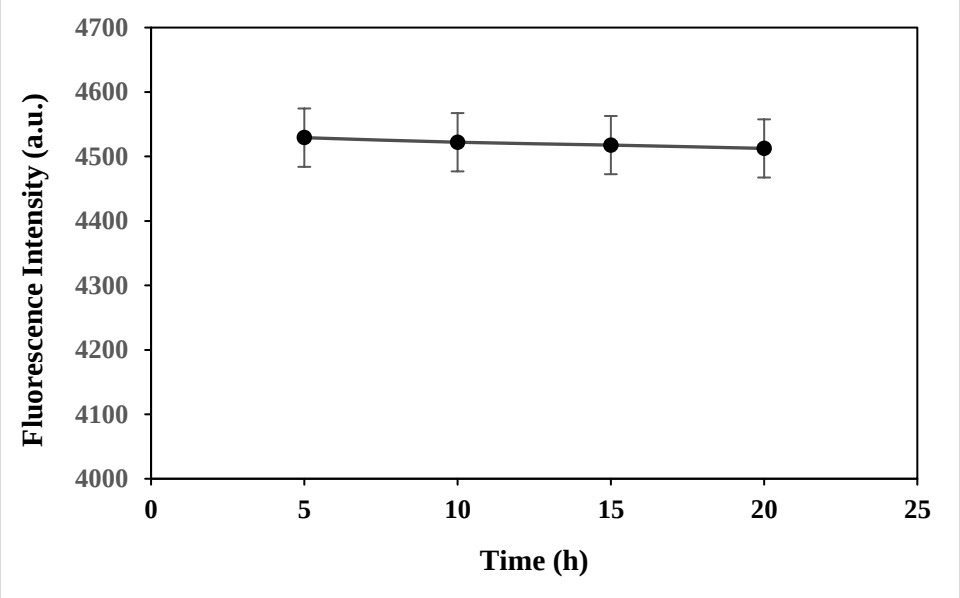

Fig.5. The photostability of GQDs in diferrent times at room temperature.

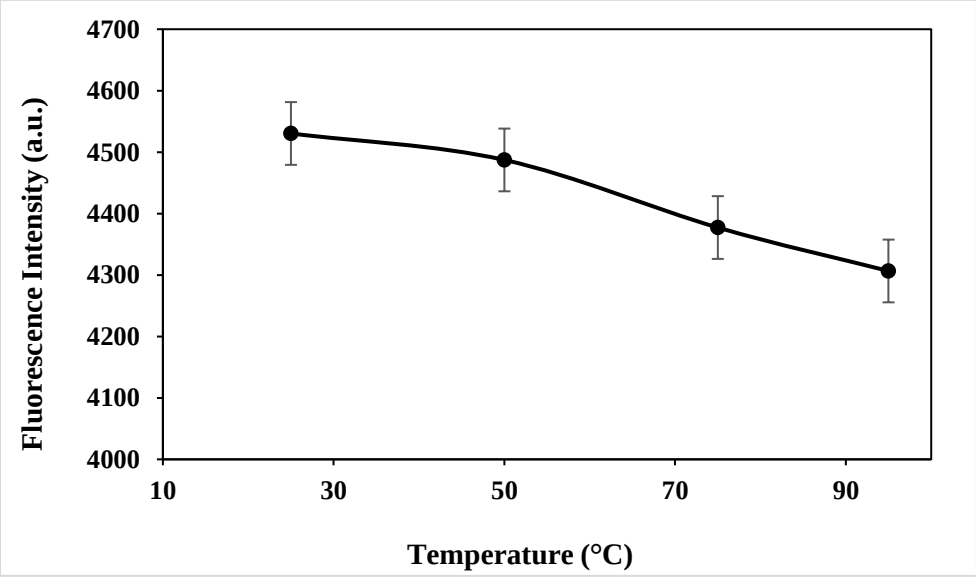

Fig.6. The photostability of GQDs at diferrent temperatures rangeing from 25 to 95°C.

CONCLUSION

In this study, we have investigated the ^{99m}Tc radiolabeling efficiency of GQDs nano-based radiopharmaceuticals through the means of a Radio-TLC method. To optimize the condition, the effect of variable factors on the radiolabeling process was examined. As our results showed, the high radiochemical purity (RCP %) up to 98.0 % was obtained with 30 mg/mL of GQDs (pH= 6) in the presence of 100 µg of reducer agent for 20 min at 90-95 °C. In general, ^{99m}Tc- radiolabeled GQD could be introduced as a suitable candidate for *in vivo* nuclear imaging.

ACKNOWLEDGEMENTS

We greatly appreciate the support of this work by the Research Councils of Nuclear Science and Technology Research Institute (Tehran, Iran).

REFERENCES

[1] Zhu, Y., Hong H., Zhi Ping X., Li Z., Cai W. (2013). Quantum dot-based nanoprobes for in vivo targeted imaging. Current Molecular Medicine,13(10): 1549-1567.

[2] Geszke-Moritz, M. and Moritz, M. (2013). Quantum dots as versatile probes in medical sciences: synthesis, modification and properties. Materials Science & engineering. C, 33(3):1008-1021.

[3] Pijeira, M.S.O., Viltres, H., Kozempel J., Sakmár M., Vlk, M., İlem-Özdemir, D., et al. (2022). Radiolabeled nanomaterials for biomedical applications: radiopharmacy in the era of nanotechnology. EJNMMI Radiopharmacy and Chemistry,7(1):8.

[4] Chakravarty, R., Goel, S., Dash, A., CAI, W. (2017). Radiolabeled inorganic nanoparticles for positron emission. Quarterly Journal of Nuclear Medicine and Molecular Imaging, 61(2): 181-204.

[5] Guo, W., Sun, W., Jacobson, Q., Yan, X., Min, K., Srivatsan, A., Niu, G., Kiesewetter, D., Chang, J., Chen, X. (2015). Intrinsically radioactive [^{64}Cu]CuInS/ZnS quantum dots for PET and optical imaging: improved radiochemical stability and controllable Cerenkov luminescence. ACS Nanomaterials, 27:9(1):488-95.

[6] Farzin, L., Sheibani, S., Moassesi, M.E., Shamsipur M. (2018). An overview of nanoscale radionuclides and radiolabeled nanomaterials commonly used for nuclear molecular imaging and therapeutic functions. Journal of Biomedical Materials Research Part A, 9999:1-35.

[7] Fernández-Barahona, I., Muñoz-Hernando, M., Pellico, J., Ruiz-Cabello, J., Herranz, F. (2018). Molecular imaging with ^{68}Ga radio-nanomaterials: shedding light on nanoparticles. Applied Sciences, 8:1098.

[8] Psimadasa, D., Bouziotisb, P., Georgouliasa, P., Valotassioua, V., Tsotakosb, T., Loudos G. (2013). Radiolabeling approaches of nanoparticles with ^{99m}Tc. Contrast Media Molecular Imaging, 8: 333-339.

[9] Qi, B., Hu, H., Bao, L., Zhang, Z., Tang, B., Ying Peng, Y.,Wang, B.S., Pang, D. (2015). An efficient edge-functionalization method to tune the photoluminescence of graphene quantum dots. Nanoscale, 7: 5969-5973.

[10] Henna, T.K., Pramod, K. (2020). Graphene quantum dots redefine nanobiomedicine. Materials Science and Engineering: C, 110: 110651.

[11] Shinde, S., Patil1, A., Gaikwad R. (2022). Graphene Quantum Dots: a pharmaceutical review. Asian journal of pharmaceutical sciences, 12: 2231-5683.

[12] Liang, L., Peng, X., Sun, F., Kong, Z., Shen, J. (2021). A review on the cytotoxicity of graphene quantum dots: from experiment to simulation. Nanoscale Advances, 3: 904-917.

[13] Hadad, C., González-Domínguez, J. M. Armelloni, S., Mattinzoli, D., Ikehata, M., Istif, A., Ostric, A., Cellesi, F., Alfieri, C. M., Messa, P.(2020). Graphene quantum dots: From efficient preparation to safe renal excretion, Nano Research, 1-10.

[14] Li, J., Zhang, X., Jiang, J., Wang, Y., Jiang, H., Zhang, J., Nie, X., Liu, B. (2019). Systematic assessment of the toxicity and potential mechanism of graphene derivatives in vitro and *in vivo*, Toxicological Sciences, 167: 269-281.

[15] Cui, Y., Liu, L., Shi, M., Wang, Y., Meng, X., Chen, Y., Huang, Q., Liu, C. (2024) A review of advances in graphene quantum dots: from preparation and modification methods to application. Journal of Carbon Research, 10(1), 7.

[16] Wang, Y., and Hu, A. (2014). Carbon quantum dots: synthesis, properties and applications, Journal of Materials Chemistry C, 2: 6921-6939.

[17] Liu, Y., Zhou, L., Li, Y., Deng R., Zhang, H. (2017). Highly fluorescent nitrogen-doped carbon dots with excellent thermal and photo stability applied as invisible ink for loading important information and anti-counterfeiting. Nanoscale, 9: 491-496.

ICNST 2024 International Conference on Nuclear Science and Technology
6- 8 MAY 2024 | Isfahan, Iran

The Impact of Configuration on Neutron Beam Monitoring System Counts (Paper ID : 1332)

Sadeghi K., Tajik M.*

School of Physics, Damghan University, Damghan, Iran

Abstract

A neutron monitoring system using a cylindrical proportional gas detector has been developed and simulated with the MCNPX code. This system is specifically designed for nuclear laboratories that use neutron sources for teaching and research purposes. To achieve this goal, BF_3 gas detector with a cylindrical geometry of 31.11 cm height and 1.27 cm radius was considered. The simulation results were then used to experimentally test the monitoring system with different moderators such as water, paraffin and polyethylene. These measurements were performed with a 4.3 Ci neutron source commonly used in neutron activation facilities. The simulation results showed that the effects of the thickness and type of moderator on the counts and pulse height spectrum of the neutron monitoring system are consistent with the experimental results. Also, the comparison between the measurement and simulation results shows that an online neutron monitoring system, with BF_3 gas detectors, can reliably monitor the neutron flux background radiation within a laboratory environment.

Keywords: Monitoring system, BF_3 detector, Moderator, Neutron

INTRODUCTION

^{10}B can be a very suitable element for the detection of thermal neutrons, as it has a very high cross-section for thermal neutrons. Considering that neutron sources are used in education, research, industry and some medical and agricultural fields where the emitted neutrons have an energy range from thermal to fast, it is necessary to use a detector with high neutron detection efficiency to measure the neutron flux in these field [1]. To increase the detection efficiency of neutrons emitted from a source such as ^{241}Am-Be, the neutrons

must be sufficiently moderated before reaching the detector. Neutron detection with BF_3 is based on the reaction shown in equation 1;

$$ {}^{1}_{0}n + {}^{10}_{5}B \rightarrow \begin{cases} \alpha + {}^{7}_{3}Li + 2{,}79MeV\ (6{,}1\%)\ \text{(ground state)} \\ \alpha + {}^{7}_{3}Li^{*} + 2{,}31MeV(93{,}9\%)\ \ \text{(excited state)} \end{cases} \quad (1) $$

The branching implies that the reaction product ^{7}Li can remain either in its ground state or in its first excited state. When thermal neutrons (0.025 eV) are used to generate the reaction, about 94% of all reactions proceed to the excited state, while only 6% proceed to the ground state. The energy of the particles produced in this reaction, including lithium and alpha, is 0.84 MeV and 1.47 MeV respectively. The cross section of this reaction is very high for thermal neutrons (3837 barn to 0.025 MeV [1].

Experiments and Monte Carlo simulations were used to investigate the properties of proportional counters. Lippold et al. performed Monte Carlo simulations for neutron moisture gauges [2]. In 2004, Saegusa et al. calculated and measured the energy responses of three types of Japanese neutron dose- equivalent metres [3]. The energy responses were calculated for neutrons from radionuclide sources and for thermal neutrons, monoenergetic neutrons with energies up to 15.2 MeV. Nasir et al. investigated the relationship between the response of the BF_3 detector and the detector size and reflector thickness [4].

The design and development of an efficient neutron monitoring system using various common neutron detectors has been studied in different fields for many years. As is well known, the measurement of neutron flux is very important for radiation protection and radiation detection [5–13]. In 1966, Yamashita et al. investigated the dependence of the efficiency of a BF_3 detector without a moderator and with moderators, including paraffin and polyethylene, on the energy of isotropic neutrons from 1eV to 10 MeV. These studies showed that the BF_3 detector with paraffin moderator in combination with a lead filter has the highest efficiency [8]. In 2011, Castro et al. tested the efficiency of the BF_3 neutron detector using the MCNPX code. In this study, the neutron detector efficiency of BF_3 was calculated theoretically and experimentally by using paraffin plates as a retarder for 241Am-Be source neutrons [9]. In 2013, Cardinans et al. used the MCNPX code and experimental experiments to investigate the effects of paraffin and polyethylene retarders on the efficiency of the BF_3 detector and determined the optimal thickness of these retarders to increase the efficiency of the BF_3 detector [10]. In 2017, Orima et al. calculated the effects of the pressure and diameter of the BF_3 detector on the efficiency of the neutron detector using the MCNPX code [11].

With a radiation activity greater than 1Ci, ^{241}Am-Be sources are frequently used in education, research, medicine and industry. It is necessary to use a neutron monitoring system to measure the neutron count in neutron radiation environments immediately and under various working conditions in order to comply with

the rules and standards of radiation protection and the health of researchers and employees in these centers and to minimize the risks of neutron radiation. It is necessary to study the effective parameters in determining the counts of a neutron monitoring system in order to improve and optimize these systems.

The neutron monitoring system considered in this study includes a neutron detector and a configuration of moderators to improve the efficiency of the system. According to the ^{241}Am-Be neutron source considered for this study, a BF_3 detector was chosen. The use of a moderator to thermalize fast neutrons is necessary to improve the efficiency of a monitoring system in detecting neutron fluxes. Therefore, a suitable moderator should be used in this monitoring system to decelerate the neutrons.

In this study, the Monte Carlo code MCNPX [12] is used to simulate a neutron monitoring system. It is investigated which parameters are most effective in optimizing a neutron monitoring system. The role of moderator thickness and material in determining the minimum counts obtained from single-energy and ^{241}Am-Be neutron sources is calculated in these studies. An experimental monitoring system was used to test the obtained theoretical results. For this purpose, layers of various moderators with various thicknesses around the detector were considered and the variation of the thermal neutron flux was calculated qualitatively and quantitatively. The results of these simulation calculations are compared with the experimental results obtained from the detection pulse height measurement.

RESEARCH THEORIES

Monte Carlo Simulation of neutron monitoring system

The MCNPX code was used to calculate the parameters of the monitoring system, such as the reaction rate and the flux of thermal neutrons. The main components of the system, including a cylindrical BF_3 with a diameter of 2.54 cm and a length of 31.11 cm, a moderating layer and a 4.3-Ci Am-Be source, were simulated in MCNPX for this purpose.

Other research [13, 14] has shown that hydrogenated and lightweight materials, especially organic materials, are effective moderators of fast neutrons. For this reason, the moderator for the monitoring system was

selected from five hydrogenated organic materials: paraffin, polycarbonate, polyethylene, polystyrene and polypropylene, as well as water. Table 1 lists the different materials used in the neutron monitoring system, as well as their physical properties. The BF_3 detector was placed in the center of the nested cylinders. Through the simulation procedure, various thicknesses of moderators were poured into these cylinders.

Table 1. Specifications of the moderators used in the neutron monitoring system.

	Material					
	Paraffin	Polycarbonate	Polyethylene	Polypropylene	Polystyrene	Water
Chemical Formula	$C_{25}H_{52}$	$C_{16}H_{14}O_3$	C_2H_4	C_3H_6	C_8H_8	H_2O
Density ($\frac{gr}{cm^3}$)	0.93	1.2	0.95	0.9	1.06	1

The configuration of the moderator and the position of the BF_3 detector in relation to the moderator and the source are shown in Fig. 1. The radii of the cylinders differ by 1 cm, and a distance of 20 cm was considered between the source and the detector. The neutrons from the Am-Be source are used to irradiate the monitoring system shown in Fig. 1. The cylinders containing moderator are arranged in such a way that the probability of thermal neutrons reaching the detector position increases.

For the calculation of the flux and reaction rate, 10^7 neutron particle histories were used in the simulation process, resulting in an error of less than 1%, and 10^8 neutron histories were used for the calculation of the pulse height spectra. Different tallies were used to calculate the optimal thickness of the most suitable moderator in the monitoring system. The average neutron flux was calculated using the F4:N tally card, and the reaction rate (n , α) was calculated using this card and the FM4 tally card. The pulse height spectrum of the BF_3 detector in the neutron monitoring system was calculated with the Physics, Cut-Off, FM4, F6, F8 and FT8 tally cards.

The reaction rate and flux of thermal neutrons in the detector were investigated as a function of the thickness of the moderator. For this purpose, different thicknesses of Paraffin, polycarbonate, polyethylene, polystyrene, porpolyethylene and water in the range of 1 to 10 cm were investigated. The optimum thickness

at which the highest reaction rate is observed is determined by examining these variation trends. The effects of moderator thickness and moderator type on the pulse height spectra of the detector in the monitoring system were also investigated. We can determine the best thickness to increase the efficiency of the monitoring system by examining the pulse height spectra for different configurations of moderators.

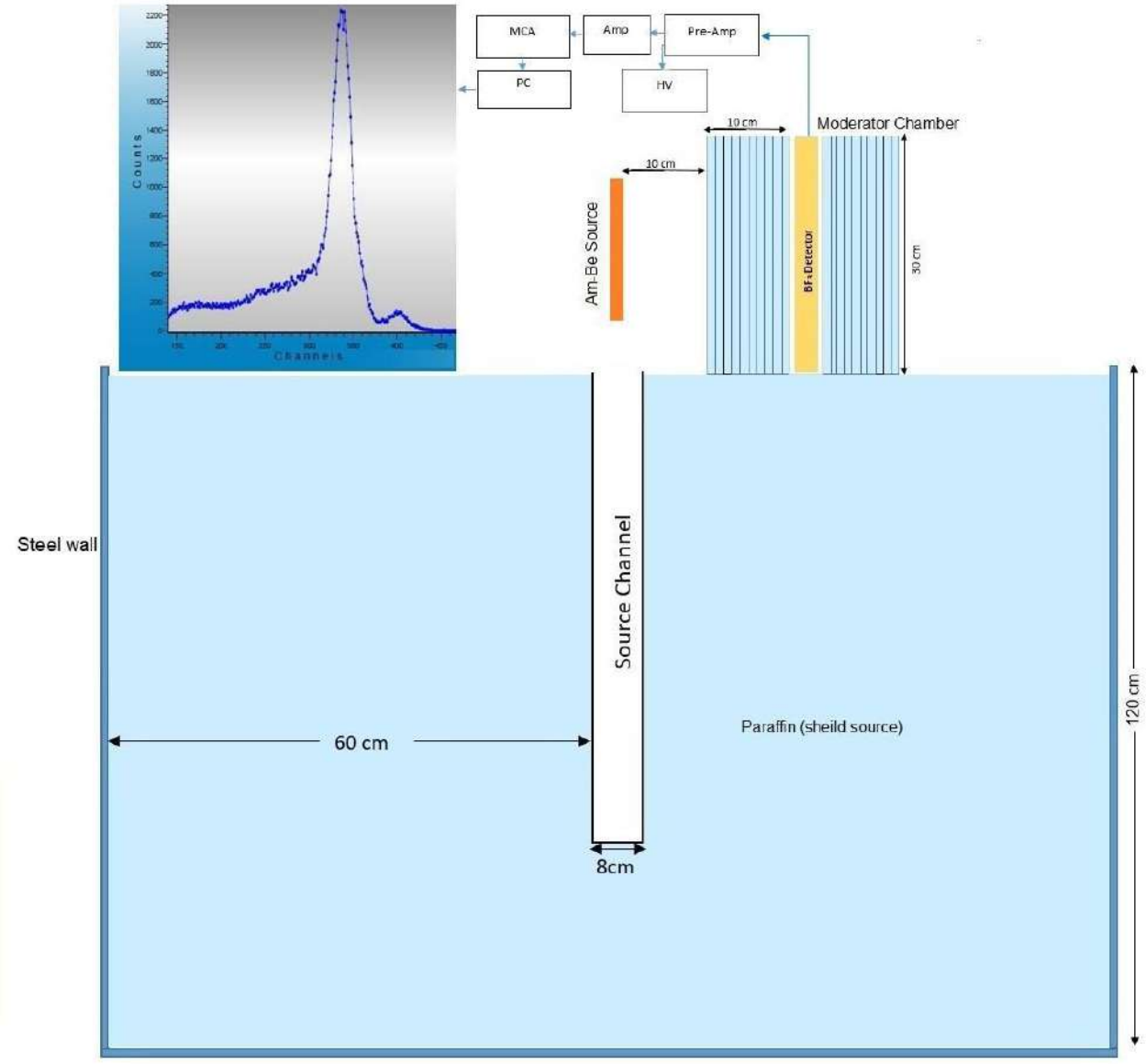

Fig. 1. Configuration of the neutron monitoring system for simulation and experiments.

EXPERIMENTAL

In order to confirm the simulation results, the simulation results should be tested and examined in a real laboratory, which corresponds to the simulation procedure carried out in the virtual laboratory (MCNPX). The neutron monitoring system consists of a BF_3 neutron detector model 2029 [15], ^{241}Am-Be neutron source (4.3 Ci), high voltage model NHQ105M (FASTComTec. Company), preamplifier model 3000 (IAP-Iran), AMP spectroscopy model 3600 (IAP-Iran), Multi Parameter Analyzer model 4201 (IAP-Iran). DAS data collection software (IAP-Iran), Cylindrical chamber made of aluminum with a thickness of 2 mm, which has a height of 35 cm and a radius of 15 cm. When the neutron monitoring system was set up, the detector was located 20 cm away from the ^{241}Am-Be neutron source.

To confirm the effect of the thickness and type of the moderator on the counts of the neutron monitoring system, the pulse height and counts of the BF_3 detector were investigated using the laboratory configuration shown in Figs. 1 and 2(b). According to Fig. 2(b), the BF_3 detector embedded in the chamber containing the moderator was exposed to neutron radiation from the Am-Be source. Using the electronic configuration as shown in Fig. 1 and applying a voltage of 940 volts (working voltage of the detector) and filling the cylindrical layers step by step with the moderator material, the counts and the pulse height spectrum of charged particles generated by the interaction of neutrons with BF_3 nuclei were measured for the layers of cylindrical moderators with a radius of 1-10 cm. The experimental setup of the neutron monitoring system designed in this study is shown in Figs. 1 and 2(b).

The pulse height of the BF_3 detector was investigated using the laboratory configuration shown in Fig. 1 to confirm the effects of the thickness and type of moderator on the counts of the neutron monitoring system. The BF_3 detector embedded in the chamber containing the moderator was exposed to neutron radiation from the ^{241}Am-Be source as shown in Fig. 1. The counts and the pulse height spectrum of the charged particles produced by neutron interactions with BF_3 nuclei were measured for the layers of cylindrical moderators with a radius of 1-10 cm. The electronic configuration shown in Fig. 1 and a voltage of 940 volts (working voltage of the detector) were used and the cylindrical layers were filled step by step with the moderator material.

The moderator was placed in the first cylindrical layer of the chamber. It was then placed in the exact position in front of the neutron source. In the second stage, the detector was placed in the innermost layer of the cylindrical chamber. In the third stage, a voltage of 940 volts was applied to the BF_3 detector. In the fourth stage, the source was placed in front of the monitoring system. The pulse height and the counts were measured for a thickness of one centimeter from the moderator over a period of 300 seconds.

The pulse height and counts from the ^{241}Am-Be source were measured using a monitoring device that increased each centimeter of the moderator thickness to nine centimeters during a 300-second period. These measurements were taken for all thicknesses of water, paraffin and polyethylene moderators. The software then displays a graph of the counts in relation to the channel, called the detector pulse height spectrum.

(b)

Fig. 2. (a) View of the BF_3 neutron detector (LND-2029) and the preamplifier, (b) Experimental setup. a: ^{241}Am-Be neutron source, b: paraffin, c: Neutron shielding, d: Preamplifier, e: Neutron monitoring chamber, f: Position of the BF_3 detector in the neutron monitoring system.

Results and discussion

Simulation results

Fig. 2 (a) and (b) show a qualitative study of the variation trend of the reaction rate and the flux of thermal neutrons in the detector to change as a function of the moderator thickness. Fig. 3(a) shows that the reaction rate and thermal neutron flux increase for all moderators with increasing thickness from 1 to 4.5 cm, but this increase is different: a rapid increase for paraffin, polypropylene and polyethylene moderators, a moderate increase for water and a slow increase for the three polycarbonate and polystyrene materials.

The reaction rate and the flux of thermal neutrons in the detector change practically constantly as a function of the thickness of the moderator (Fig. 2 (a) and (b)) for paraffin, polypropylene, polyethylene and water at a thickness of 6-7 cm. The decreasing variation trend of the reaction rate and the flux of thermal neutrons in the detector as a function of the thickness of the moderator can be observed for moderators such as paraffin, polyethylene, polypropylene and water with a thickness of 6-10 cm and moderators such as polycarbonate and polystyrene with a thickness of 7 to 10 cm (Fig. 3). For the materials paraffin, polyethylene, polypropylene and water, this decreasing tendency is significantly faster than for polycarbonate and polystyrene. According to Fig. 3, there are three qualitative ranges in the variations of the reaction rate and the neutron flux in the monitoring system versus the thickness of the moderator.

Fig. 3 shows that the reaction rate and the flux of thermal neutrons are higher for paraffin, water, polyethylene and polypropylene than for the other moderators. These materials have been labeled as Materials I. These materials behave almost identically to the neutron moderator, but also have a better performance. The results show that paraffin and then polyethylene perform best in the monitoring system. The best detection thickness is 7 cm, based on the highest reaction rate and thermal neutron flux.

Due to the functional limitations of paraffin, polyethylene is generally used instead of paraffin for the monitoring system. According to a comparative quantitative study, the 6-7 cm thick paraffin moderator offers the highest reaction rate and the highest flux of thermal neutrons among the moderators. The optimum thickness is determined by the highest reaction rate.

Fig. 3 shows that the second category of materials (Materials II), which includes polycarbonate and polystyrene, performs poorly compared to the materials in the first category (Materials I). Therefore, these materials should not be used in a monitoring system.

The reason for the difference in the optimal thickness of the moderators lies in the fact that materials containing only H and C have much better moderating properties than materials containing multiple elements of oxygen (O), so materials with the highest hydrogen-to-carbon ratio have the best moderating properties.

Since paraffin performs best in the pulse height spectrum of the BF_3 detector, the pulse height spectrum of the neutron monitoring system was compared for paraffin and water in various thicknesses.

The distribution of the thermal neutron flux within the neutron monitoring system (BF_3 detector and the surrounding moderator) was calculated for three moderators: Water, polyethylene and paraffin, for thicknesses of 1 cm, 7 cm and 10 cm in Fig. 4. The position of the detector in these figures is 0 to 30 cm in height and -1.25 to 1.25 cm in length, respectively. According to these figures, the maximum thermal neutron flux is associated with the position of the detector and a moderator thickness of 7 cm.

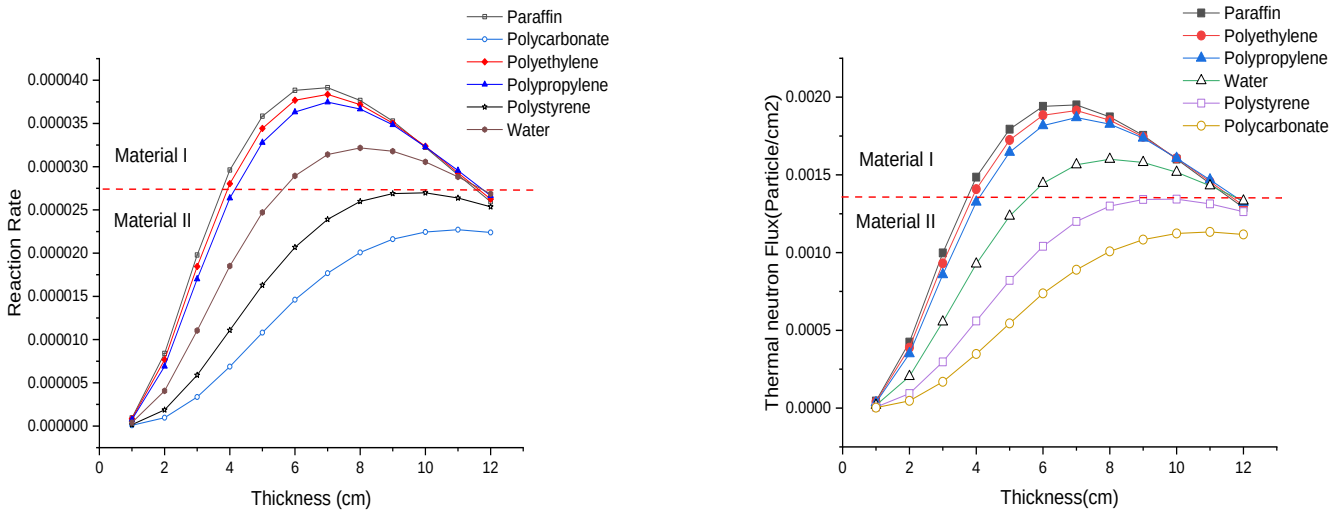

Fig. 3. Variation of the reaction rate and thermal neutron flux in BF_3 as a function of the thickness of the moderator for different materials in the monitoring system using the MCNPX code.

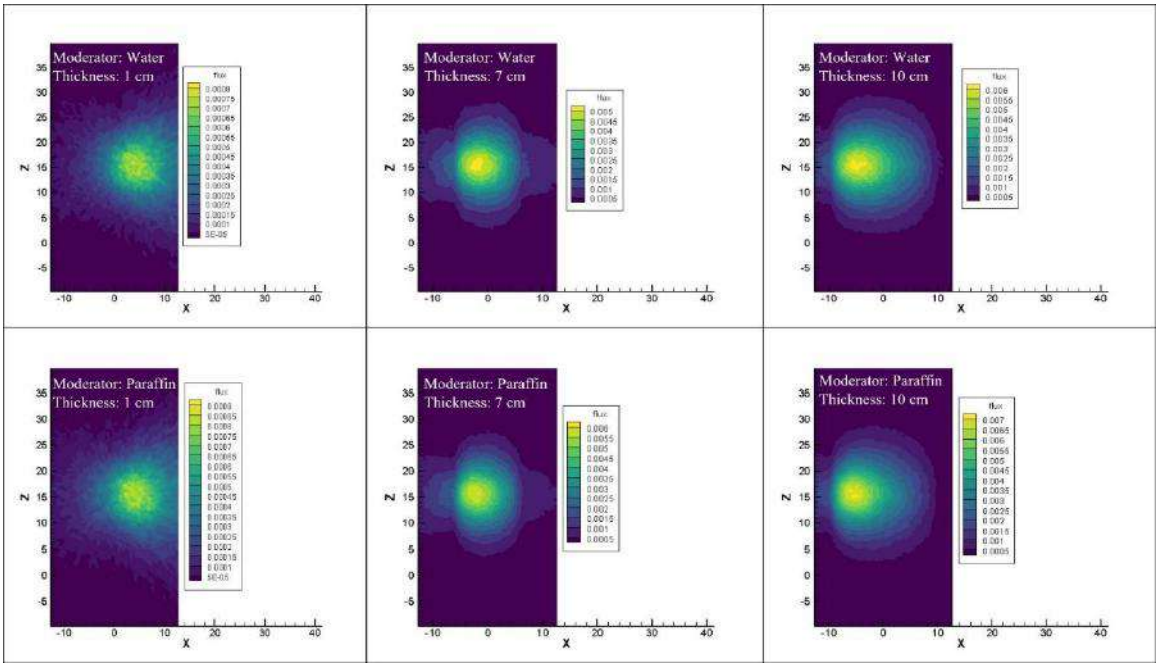

Fig. 4. Thermal neutron flux for the moderators of water and paraffin with a thickness of 1 cm, 7 cm and 10 cm in the neutron monitoring system.

Experimental results

Fig. 5 shows good agreement between the experimental and simulated spectra (except in the lower amplitude range). The pulse height spectra and counts obtained from the monitoring system for paraffin and water moderators and radii of 1-10 cm were measured according to the structure of the moderator chamber considered in the experiment. Fig. 6 shows the results of this measurement. As can be seen in this graph, the intensity of the peaks and continuum of the spectrum increases as the thickness of the moderator increases from 1 cm to 7 cm, which means that the counts increase while the intensity of the peaks and continuum decreases from 7 cm to 8 cm. These experimental results confirm the simulation results.

The results of the experiment were compared for water and paraffin moderators under the condition that the moderator chamber was filled with moderator in a radius of 4 cm and 5 cm. The results of this comparison are shown in Fig. 7 (a) and (b). The results of these experimental comparisons are in complete agreement with those of the simulation. Since the simulation results for the water and paraffin moderators were confirmed by the experimental results, a polyethylene housing with a cylindrical geometry and a thickness of about 7 cm was designed to house the detector, the preamplifier and the single-channel analyzer (SCA). The BF_3 detector is housed inside the polyethylene moderator. The neutron counts and pulse height associated

with the charged particles generated in the detector were measured with this specially designed monitoring system.

Four experimental steps were carried out to assess the effectiveness of a neutron monitoring system. In the first two experiments, the source was placed inside a paraffin shield (Fig. 1). The pulse height spectrum of the charged particles and the neutron counts recorded by the neutron monitoring system with polyethylene moderator (I) and without moderator (II) for the ^{241}Am-Be source inside the paraffin shield were measured in the first and second experiments. In the third and fourth experiments, the ^{241}Am-Be source was removed from the shield and the pulse height spectra of the charged particles and the counts obtained from a neutron monitoring system with and without a polyethylene moderator (I) and without a moderator (II) were measured.

The data from the first and second experiments in Table 2 show that the monitoring system with polyethylene moderator effectively measures the background neutrons from a shielded source with a cylindrical housing with a radius of 60 cm and a height of 120 cm in a laboratory environment. The use of polyethylene as a moderator increased the recorded counts in this experiment by 60%. The results of the third and fourth experiments in Table 2 show that the measurements of the neutron counts in the monitoring system with polyethylene moderator are very different from the results of the monitoring system without moderator.

Table 2. The counting of the neutron monitoring system with polyethylene moderator (state I) and without moderator (state II) for the case of source ^{241}Am-Be.

Source inside the paraffin shield		Source outside the paraffin shield	
Count of State I	Count of Sate II	Count of State I	Count of Sate II
1310	823	32991	823

The thermal neutron flux increased by 4000% when the moderator was used, as shown by a quantitative comparison of the results in Table 2. In the case of the ^{241}Am-Be source inside and outside the paraffin shielding, the flux of thermal neutrons is almost the same in the case of the monitoring system without moderator, as shown by the results of the third and fourth experiments in Table 2. These comparisons show that polyethylene performs excellently in the monitoring system.

The simulation and experimental results of the counts of the neutron monitoring system for the moderators of water, polyethylene and paraffin with a thickness of 7 cm are shown in Fig. 8. The experimental and simulated results agree well in this comparison. Quantitative analyses show that the experimental values

obtained at a thickness of 7 cm deviate from the simulated results by about 1.6%. Since pure paraffin has a low melting point and water is liquid at room temperature, the use of these two materials in a monitoring system requires the use of a container, which increases construction costs and the risk of liquid leakage. However, since polyethylene can be prepared in the desired geometric shapes, any dimensions and at a reasonable price, it may be the best option for the moderator of a neutron monitoring system.

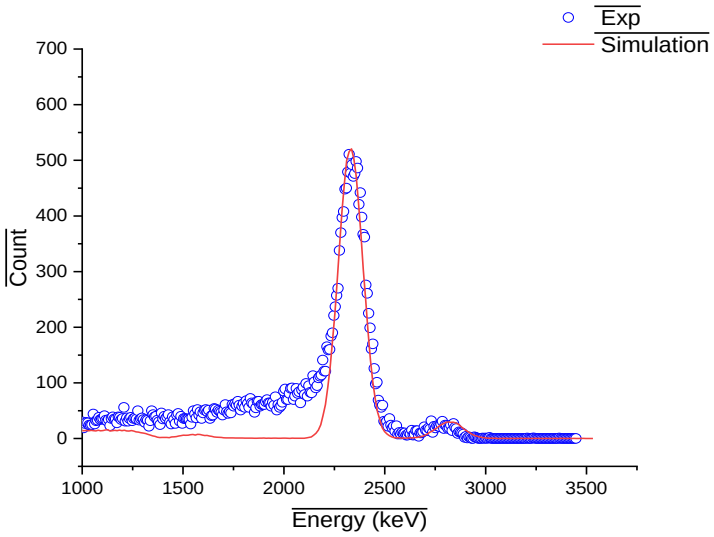

Fig. 5. Experimental vs. Monte Carlo simulations (MCNPX) of the pulse height spectrum for the case of paraffin moderator with a thickness of 1 cm in the monitoring system.

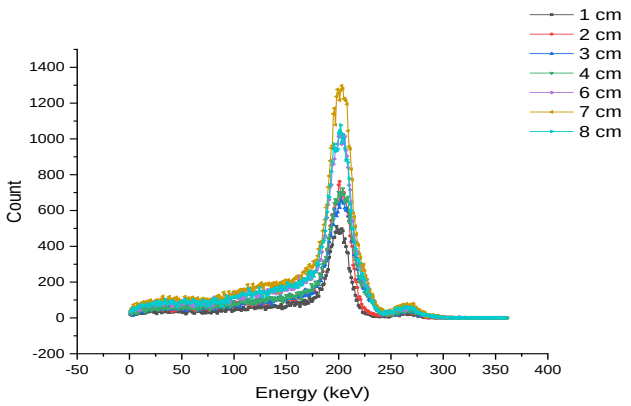

Fig. 6. BF_3 detector pulse height spectrum for the case of paraffin moderator with a thickness of 1 - 4 cm and 6 - 8 cm in the monitoring system.

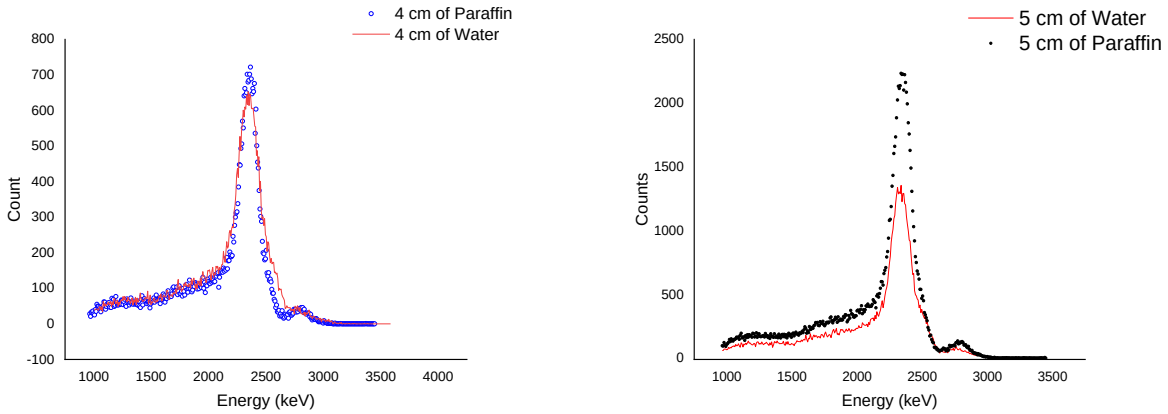

(a) (b)

Fig. 7. BF_3 detector pulse height spectrum for the case of paraffin moderator with a thickness of (a) 4 cm and (b) 5 cm.

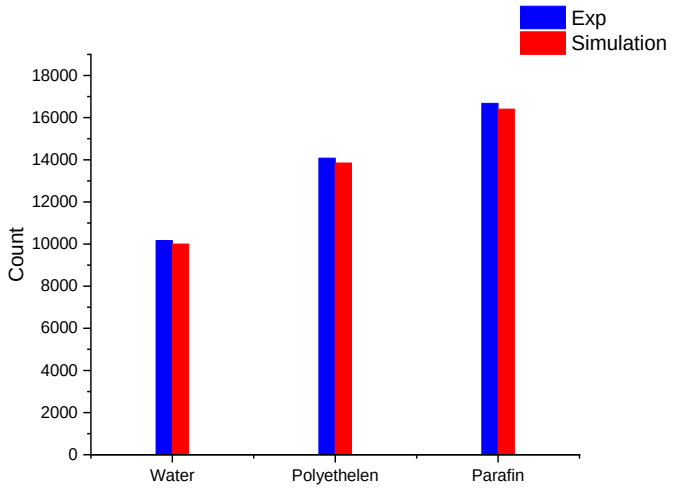

Fig.8. Comparison of the simulation and experimental results of the neutron monitoring system counts for the moderators of water, polyethylene and paraffin with a thickness of 7 cm.

Conclusions

The effect of the thickness and type of moderator on the reaction rate and neutron flux magnitudes were calculated to effectively estimate the number of neutrons detected in the environment. For the neutrons of ^{241}Am-Be, the calculations show that the optimum thickness of the moderator in the designed monitoring system is about 7 cm. According to the simulation results, the three moderators paraffin, polyethylene and water have the best performance in the neutron flux monitoring system. An experimental neutron monitoring system was built in accordance with the designs of the monitoring system used in the modeling procedure, and the neutron pulse height spectrum and neutron counts were measured. The effect of moderator thickness and moderator type on the neutron counts and pulse height spectrum of the neutron monitoring system is consistent with the simulation results, as shown by the experimental data. The neutron monitoring system with a polyethylene moderator with a thickness of approx. 7 cm measures the background counts of the beam environment well, even if the source is located inside a paraffin shield.

References

[1] G. F. Knoll and H. W. Kraner, Radiation Detection and Measurement, vol. 69, no. 4. John Wiley & Sons, 1981.

[2] W. J. Lippold, A. Carnesale, and R. P. Gardner, “A Monte Carlo simulation of the surface-type neutron moisture gauge,” Nucl. Eng. Des., vol. 10, no. 3, pp. 373–380, 1969,

[3] J. Saegusa, M. Yoshizawa, Y. Tanimura, M. Yoshida, T. Yamano, and H. Nakaoka, "Evaluation of energy responses for neutron dose-equivalent meters made in Japan," Nucl. Instruments Methods Phys. Res. Sect. A Accel. Spectrometers, Detect. Assoc. Equip., vol. 516, no. 1, pp. 193–202, 2004,

[4] R. Nasir, F. Aziz, S. M. Mirza, and N. M. Mirza, "Experimental and theoretical study of BF3 detector response for thermal neutrons in reflecting materials," Nucl. Eng. Technol., vol. 50, no. 3, pp. 439–445, 2018,

[5] V. Kovaltchouk and R. MacHrafi, "Monte Carlo simulations of response functions for gas filled and scintillator detectors with MCNPX code," Ann. Nucl. Energy, vol. 38, no. 4, pp. 788–793, 2011,

[6] D. Rezaei-Ochbelagh, "Comparison of 3He and BF 3 neutron detectors used to detect hydrogenous material buried in soil," Radiat. Phys. Chem., vol. 81, no. 4, pp. 379–382, 2012,

[7] A. Lintereur et al., "3He and BF3 neutron detector pressure effect and model comparison," Nucl. Instruments Methods Phys. Res. Sect. A Accel. Spectrometers, Detect. Assoc. Equip., vol. 652, no. 1, pp. 347–350, 2011,

[8] M. Yamashita, L. D. Stephens, A. R. Smith, and H. W. Patterson, "Detection Efficiency of Bare and Moderated BF3-Gas-Filled Proportional Counters for Isotropic Neutron Fluxes," J. Nucl. Sci. Technol., vol. 3, no. 8, pp. 343–353, 1966,

[9] V. A. Castro, T. A. Cavalieri, P. T.D. Siqueira, G. G. Fedorenko, P. R. P. Coelho, and T. M. Filho, "MCNP to study the BF-3 detection efficiency," Int. Nucl. Atl. Conf., vol. 7, no. 1, 2011.

[10] J. P. N. Cardenas et al., "Experimental and MCNP studies of Paraffin and Polyethylene in Neutron Moderation and BF3 Detector Efficiency," in 2013 3rd International Conference on Advancements in Nuclear Instrumentation, Measurement Methods and Their Applications, ANIMMA 2013, IEEE, 2013, pp. 1–5.

[11] B. Oryema, M. A. M. Nader, and S. A. E. Agamy, "Response function estimation for in-core BF-3 and He-3 neutron detectors using MCNPX - case study of Opal reactor," Adv. Appl. Sci. Res., vol. 8, no. 3, pp. 76–89, 2017.

[12] D. B. Pelowitz, "MCNPX user's manual, version 2.6. 0, LA-CP-07-1473," Los Alamos Natl. Lab. Los Alamos, 2008.

[13] S. C. Gujrathi and J. M. D'Auria, "The attenuation of fast neutrons in shielding materials," Nucl. Instruments Methods, vol. 100, no. 3, pp. 445–452, 1972,

[14] H. Y. Kang, C. J. Park, K. S. Seo, and J. S. Yoon, "Evaluation of neutron shielding effects on various

materials by using a Cf-252 source," J. Korean Phys. Soc., vol. 52, no. 6, pp. 1744–1747, 2008,

[15] https://www.lndinc.com/products/neutron-detectors/25169-2-2/.

ICNST 2024 International Conference on Nuclear Science and Technology
6- 8 MAY 2024 | Isfahan, Iran

Investigating the Impact of Detector Crystals on Biograph Vision Quadra Total Body PET Scanner Performance: A GATE Monte Carlo Study (Paper ID : 1334)

Ghanbari Khanghah M.[1*], Babaei Ghane M.[1] ,Sadremomtaz A.[1]

[1] *Department of Physics, Faculty of Science University of Guilan, Rasht, Iran*

Abstract

Total body PET scanners offer numerous advantages, including higher sensitivity over whole-body scanners. The choice of the detector crystal plays an important role in maximizing the performance of these scanners. The objective of this research is to compare the sensitivity, scatter fraction, and noise equivalent count rate (NECR) of a total body PET scanner using LSO, LYSO, BGO, and NaI crystals to evaluate their impact on the scanner. To achieve this aim, the Siemens Biograph Vision Quadra PET scanner with a 106 cm axial field of view was simulated and validated using the GATE Monte Carlo simulation toolkit. Sensitivity, scatter fraction, and NECR were evaluated according to NEMA NU2-2018 standards. The results demonstrated better sensitivity for the BGO crystal, both in the center and off-center of the field of view, with 384.5 and 335.9 Kcps/MBq, respectively. However, NaI demonstrated the least sensitivity for 511KeV annihilation photons with 44 and 38.15 Kcps/MBq in the center and off-center of the field of view, respectively. Scatter fractions, on the other hand, were 35.83%, 36.05%, 36.42%, and 37.29% for LSO, BGO, LYSO, and NaI, respectively. Also, NECR peaks for BGO, LYSO, LSO, and NaI have been obtained as 19107.3 kBq/ml, 22452.8 kBq/ml, 23050.14 kBq/ml, and 24078.8 kBq/ml, respectively. In conclusion, the BGO crystal has demonstrated better NECR and sensitivity in comparison with others, while NaI, under the same conditions as other crystals, resulted in performance degradation, concluding that it is not suitable for PET due to its low detection efficiency for 511 keV annihilation photons, as expected.

Keywords: PET, NEMA NU2-2018, GATE, Sensitivity, Monte-Carlo

INTRODUCTION

Total-body PET scanners offer improved disease detection due to their long axial fields of view, which increase sensitivity and reduced scan time. This enables them to find smaller abnormalities, potentially leading to earlier and more accurate diagnoses [1,2]. High number of crystal usage has led to a significant cost increase.To optimize system costs, it is recommended to investigate substituting expensive crystals with more affordable options [3,4]. LSO and LYSO, which are popular scintillation crystals in PET

scanners, both incorporate cerium (Ce) to enhance their light detection abilities [5].While both serve the

same purpose, LYSO boasts a simpler and more cost-effective growth process due to the inclusion of yttrium (^{39}Y) [6]. Despite the potential of BGO with its high density, its lower light output and longer decay time compared to LSO and LYSO limit its use in PET[7]. Similarly, NaI(Tl) suffers from poor stopping power despite its exceptional light output, hindering its effectiveness in PET applications[8]. Therefore, our primary goal is to investigate the feasibility of utilizing alternative scintillating crystals that can deliver sufficient performance while achieving cost efficiencies within the system.

MATERIALS AND METHODE

System description and GATE simulation

In pursuit of this objective, the Biograph Vision Quadra PET scanner, an advanced medical imaging scanner designed by Siemens Healthineers, has been simulated. As brifly described in (Table 1) Biograph Vision Quadra PET is a cylindrical scanner with 82 cm diameter and 106 cm height. This scanner employs silicon photomultiplier-based detectors with dimensions of 3.2×3.2×20.0 mm lutetium-oxoorthosilicate (LSO) crystals. Each detector block comprises eight mini-blocks in 2×4 array, each mini-blocks containing 25 crystals in 5×5 array. The scanner consists of 32 detector rings, each with 38 detector blocks, providing an axial field of view (AFOV) of 106 [10]. (Fig. 1) shows the geometry of this scanner.

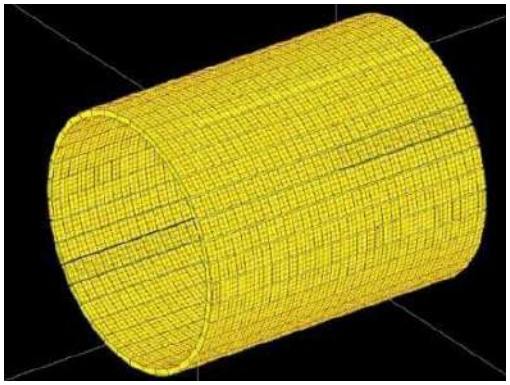

Fig. 1 GATE visualised of simulated Biograph Vision Quadra PET scanner

Table 1. Biograph Vision Quadra scanner specifications

Parameters	Content	Unit
Crystal size	3.2×3.2×20	mm
Crystals per SiPM(mini-block)	5×5	-
Detector blocks per ring	38	-
Detector ring diameter	82	cm
Energy window	[435-585]	KeV
PET Axial FOV	106	cm
SiPM array size	16×16	mm
Mini-blocks per detector block	2×4	-
Detector rings	32	-
Coincidence time window	4.7	ns
PET Transaxial FOV	78	cm
Image plane spacing	1.65	mm

GATE Monte Carlo Simulation

Monte Carlo (MC) tools provide a powerful toolkit for modeling and simulating PET scanner. The GATE/GEANT4 framework, a sophisticated software tool, was employed to conduct Monte Carlo (MC) simulations for evaluating PET scanner performance. GEANT4 library, is chosen for the physics processes simulation, which includes radioactive-decay and electromagnetic processes modeling. This list encompasses processes ranging from 0 TeV to 100 TeV and supports the simulation of various particle sources. In this research, GATE version 8.2 was employed for modeling and simulation.The geometric features of the simulated scanners are according to (Table 1).

Performance characrization

NEMA performance tests are serving as the standard benchmark for assessing PET and SPECT scanners and for comparing scanner performanc . This study employs the most recent version of NEMA standards for PET scanners, NEMA NU 2-2018, to validate the Siemens Biograph Vision and to compare crucial performance aspects including sensitivity, scatter fraction, and NECR[12].

To measure scanner sensitivity across different source positions, a 70 cm polyethylene capillary filled with 5MBq of 18F solution served as the source.This source was surrounded by five concentric aluminum sleeves with varying degrees of damping (Fig.2.A). The count rate was measured by sequentially removing each sleeve, allowing for the extrapolation of sensitivity at the center and a 10 cm radial offset. For the measurement of scatter fraction (SF) and NECR , were utilized a polyethylene cylinder measuring 20.3

cm in diameter and 70 cm in length. Within this cylinder, a 3 mm wide and 70 cm long polyethylene

capillary was inserted, containing 4 MBq of 18F[13]. Positioned along the cylinder's center, the capillary was offset radially by 45 mm (Fig.2.B).

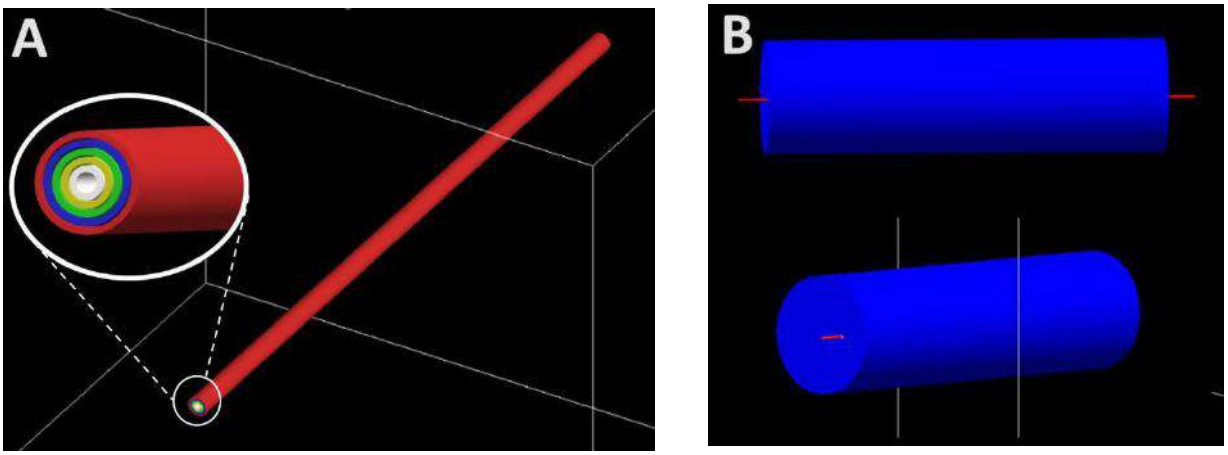

Fig.2 Simulated geometry of NEMA NU phantoms: A) sensitivity B) scatter fraction and NECR

Results

Biograph Vision Quadra PET performance was evaluated using NEMA NU 2-2018 standards. According to (Fig.3) the sensitivity of the scanner was determined as follows: LSO crystal exhibit a calculated sensitivity of 320.6 kcps/MBq at the center of the AFOV. This sensitivity decreases to 285 kcps/MBq at 10 cm.The other observed sensitivities were: LYSO crystals (110.4 kcps/MBq and 96.43 kcps/MBq), BGO (384.5 kcps/MBq and 335.9 kcps/MBq), and NaI (44 kcps/MBq and 38.18 kcps/MBq) crystals, respectively.

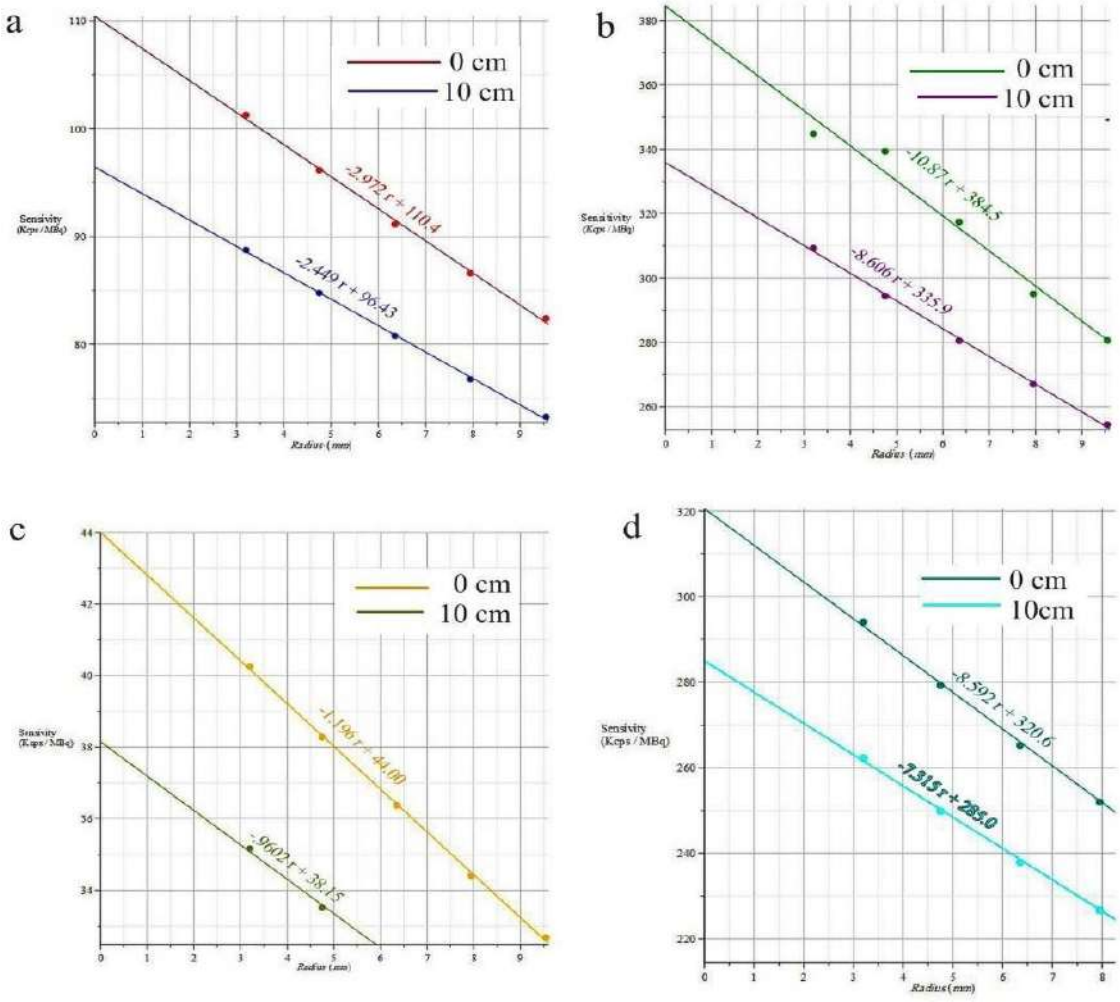

Fig.3 Total sensitivity plots at the center of AFOV and at a 10 cm offset position for the crystals a) LYSO, b) BGO, c) NaI, and d) LSO.

LSO, LYSO, BGO and NaI crystals showed the dispersion fraction of 35.83, 36.42, 36.05% and 37.29%, respectively. (Fig.4) shows a comparison of the simulated and measured count rates versus increasing activity concentration in the Scatter Fraction (SF) phantom.The lowest NECR peak was observed with BGO crystal at the activity concentration of 19107.3 kBq/ml . The peak NECR values for the other crystals were as follows: 22452.8 kBq/ml for LYSO, 23050.1 kBq/ml for LSO, and 24078.8 kBq/ml for NaI.(Table 2) summarizes the performance characterization of the Biograph Vision Quadra scanner.

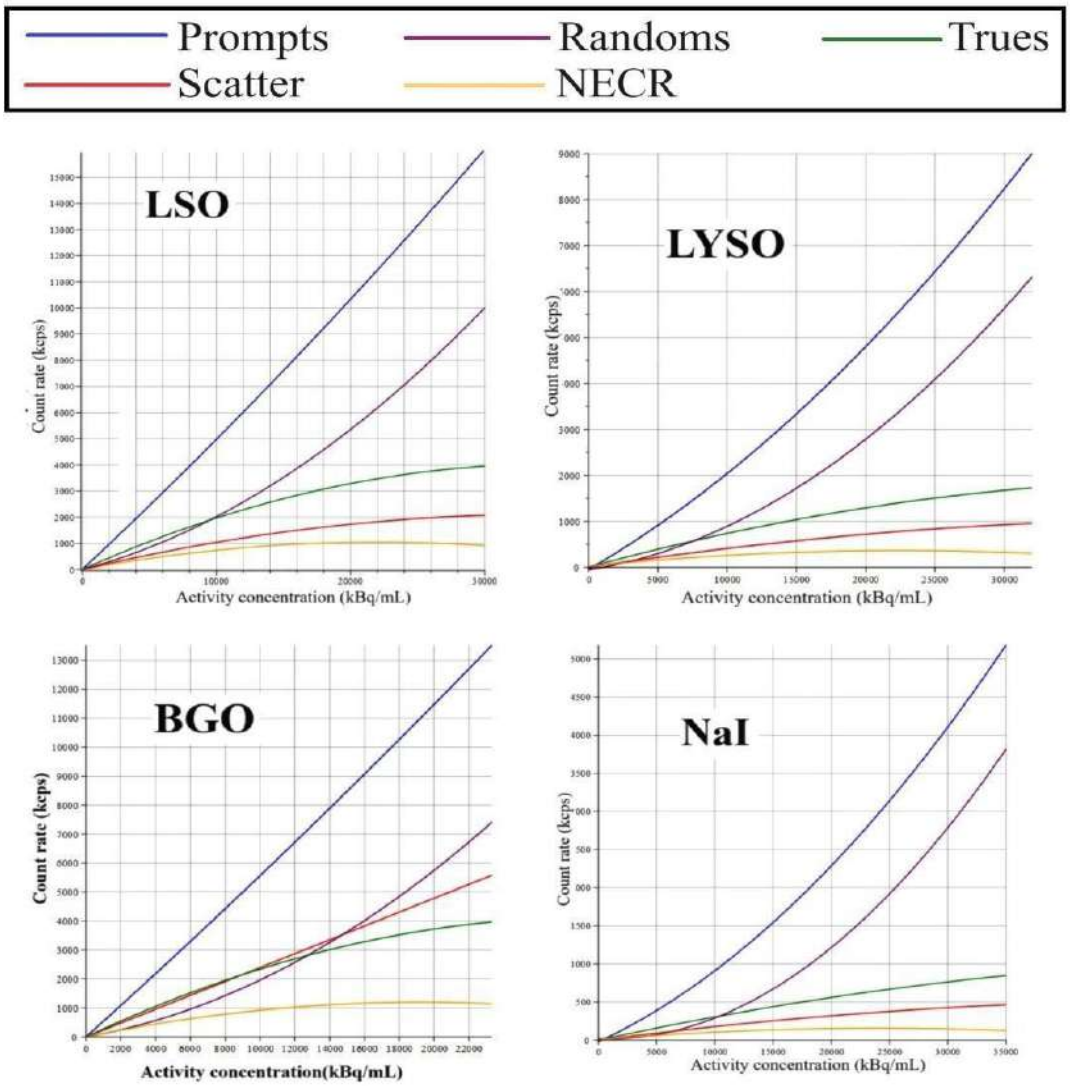

Fig.4 plots of prompts, randoms, trues, scatter and NECR rates for LSO,LYSO,BGO,NaI crystals.

Table 2. The results of the performance comparison of LSO, LYSO, BGO, and NaI

		LSO	LYSO	BGO	NaI	unit
Sensitivity	At centre	320.6	110.4	384.5	44	kcps/MBq
At 10 offset		285	96.43	335.9	38.15	kcps/MBq
Scatter Fraction		35.8	36.42	36.05	37.29	%
NECR peak		23050.14	22452.8	19107.3	24078.8	kBq/ml

Discussion

Performance characteristics comparison of the Biograph Vision Quadra scanner between LSO, LYSO, BGO, NaI crystals were investigated. Simulations were conducted for each crystal, and the scanner sensitivity, scatter fraction, and NECR were measured. The BGO showed a significant 19% improvement in sensitivity compared to LSO. This superior performance can be ascribed to BGO's enhanced photon detection capabilities, resulting in the generation of higher images quality.As anticipated, the NaI crystal exhibited the lowest sensitivity due to its lower linear attenuation coefficient compared to the other crystals. LSO (Lutetium Lanthanum Orthosilicate) and LYSO (Lutetium Yttrium Orthosilicate) are two common scintillator crystals employed in PET scanners. While LSO and LYSO share a similar crystal structure, the key difference lies in the substitution of lutetium with yttrium in LYSO. This seemingly minor change has a significant impact on the light yield of the crystal, ultimately affecting its sensitivity. LSO crystals generally exhibit a higher light yield compared to LYSO crystals. This means that for the same incoming photon, LSO produces more photons, leading to a stronger signal and higher sensitivity. The presence of yttrium in LYSO's structure is a primary factor contributing to its reduced light yield. A high accuracy of the scatter fraction provided by Biograph vision Quadra scanner is observed, with a deviation from the experimental values lower than 4%. Therefore, The calculated scattering fraction from the simulations is in good accord with the perusals of George A. Prenosil et al [10]. Interestingly, measurements of the scattering fraction indicate that these crystals do not differ much from each other. in closer examination of (Table.3) reveals a statistically , albeit slight, superiority of the LSO crystal.

Count rate performance is a critical NEMA measurement that evaluates a PET scanner's capability to accurately measure highly radioactive sources. This is achieved by considering the noise introduced by subtracting random and scattered counts from the total signal. The NECR curve (Fig.4) exhibits a linear

behavior up to 10000 kBq/mL, followed by a drop after reaching its peak . This happens when count rate reaches the maximum total events throughput.

Conclusions

The aim of this study was to identify suitable and cost-effective crystal alternatives for this scanner, leading to optimization of its Performance. NaI has been recognized as the most cost-effective crystal for imaging scanners, but due to its low light output and sensitivity, it is not a suitable replacement. In contrast ,BGO scintillators, showed superior sensitivity compared to LSO , LYSO and NaI scintillators. Among the evaluated materials,Considering sensitivity, scatter fraction and NECR , BGO was identified as the optimal replacement material for the Biograph Vision Quadra scanner. Additionally, BGO crystal is much more cost-effective compared to LSO and LYSO crystals.

References

Badawi, R. D., Shi, H., Hu, P., Chen, S., Xu, T., Price, P. M., ... & Cherry, S. R. (2019). First human imaging studies with the EXPLORER total-body PET scanner. Journal of Nuclear Medicine, 60(3), 299- 303.

Surti, S., Pantel, A. R., & Karp, J. S. (2020). Total body PET: why, how, what for?. IEEE transactions on radiation and plasma medical sciences, 4(3), 283-292.

Moskal, P., & Stępień, E. (2020). Prospects and clinical perspectives of total-body PET imaging using plastic scintillators. PET clinics, 15(4), 439-452.

Cherry, S. R., Badawi, R. D., Karp, J. S., Moses, W. W., Price, P., & Jones, T. (2017). Total-body imaging: transforming the role of positron emission tomography. Science translational medicine, 9(381), eaaf6169.

Pepin, C. M., Bérard, P., Perrot, A. L., Pépin, C., Houde, D., Lecomte, R., ... & Dautet, H. (2004). Properties of LYSO and recent LSO scintillators for phoswich PET detectors. IEEE Transactions on Nuclear Science, 51(3), 789-795.

Qin, L., Li, H., Lu, S., Ding, D., & Ren, G. (2005). Growth and characteristics of LYSO (Lu2 (1− x− y) Y2xSiO5: Cey) scintillation crystals. Journal of crystal growth, 281(2-4), 518-524.

Moszyński, M., Gresset, C., Vacher, J., & Odru, R. (1981). Timing properties of BGO scintillator. Nuclear Instruments and Methods in Physics Research, 188(2), 403-409.

Sæterstøl, J. (2010). Characterization of scintillation crystals for positron emission Tomography. no. June.

Saha, G. B., & Gopal, B. (2005). Basics of PET imaging: physics, chemistry, and regulations (p. 21). New York: Springer.

Prenosil, G. A., Sari, H., Fürstner, M., Afshar-Oromieh, A., Shi, K., Rominger, A., & Hentschel, M. (2022). Performance characteristics of the biograph vision quadra PET/CT system with a long axial field of view using the NEMA NU 2-2018 standard. Journal of nuclear medicine, 63(3), 476-484.

Jan, S., Santin, G., Strul, D., Staelens, S., Assié, K., Autret, D., ... & Morel, C. (2004). GATE: a simulation toolkit for PET and SPECT. Physics in Medicine & Biology, 49(19), 4543.

National Electrical Manufacturers Association, & NEMA, N. (2018). NU 2-2018-Performance Measurements of Positron Emission Tomographs. Rosslyn, USA: National Electrical Manufacturers Association.

Abi-Akl, M., Dadgar, M., Toufique, Y., Bouhali, O., & Vandenberghe, S. (2023). Monte Carlo simulation of the system performance of a long axial field-of-view PET based on monolithic LYSO detectors. EJNMMI physics, 10(1), 37.

ICNST 2024 International Conference on Nuclear Science and Technology
6- 8 MAY 2024 | Isfahan, Iran

Tritium production in MNSR research reactor (Paper ID : 1335)

Pazoki M.[1*], Ebrahimzadeh R.[2], Choopan Dastjerdi M.H[3], Mokhtari J[3], Jafari M[3], Jafari H[1]

[1]*Department of Radiation Application, Shahid Beheshti University, Tehran, Iran*

[2] *Reactor and Nuclear Safety, Nuclear Science and Technology Research Institute, Atomic Energy Organization of Iran, Tehran, Iran, Atomic Energy Organization of Iran, Tehran, Iran,*

[3] *Nuclear Science and Technology Research Institute, Esfahan, Iran*

Abstract

It is well-known that industrial radiation processing is based on the use of radiation as an energy source to cause specific chemical, physical and biological changes. On the other hand, isotope applications in industry, either as sealed sources or tracers, rely on the measurement of physical signals that monitor properties of interest. Tritium or hydrogen-3 (symbol T or 3H) is a rare and radioactive isotope of hydrogen with a long half-life which is widely used as trace in different science branches such as pharmacy, biology, chemistry, physics, … studies. The present work theoretically and experimentally investigated 3H production in MNSR 30 kW reactor as a tracer source for the mentioned studies. 2 cc heavy water target was used in simulation and experiment schedules to produces ^{3}H product. The sample placement uncertainty fwas also carried out and according its results, the best position for irradiating sample, is the bottom of the channel. The obtained results showed, MCNPX code could be powerfully used to estimate ^{3}H product activity before the experiment.

Keywords: MNSR reactor, 3H production, Simulation, MCNPX code, Activity measurement

INTRODUCTION

Tritium or hydrogen-3 (3H) is a rare and radioactive isotope of hydrogen with a half-life of ~12.3 years. Tritium is used as the energy source in radio-luminescent lights for watches, gun sights, numerous instruments and tools, and even novelty items such as self-illuminating key chains. It is used in a medical and scientific setting as a radioactive tracer. Tritium is also used as a nuclear fusion fuel, along with more abundant deuterium, in tokamak reactors. Tritium was produced in special heavy water reactors at the Savannah River Site until their closures in 1988 in United States. From 1955 to 1996, 225 kg of tritium was produced in the

United States [1]. Also, tritium (3H) is used as a tracer in seepage studies through hydraulic structures [2].

As a naturally occurring isotope and as an injected tracer tritium has been found to be useful in meteorology, cosmology, geohydrology, biology, agriculture, and medical sciences both in aqueous and organic forms. In self-luminous compounds, paints and plastics the radioisotopic power of tritium (0.26 w/g) is found to be useful. Several biochemically significant tritium labelled compounds have been produced for use in industry and research [3].

Hydrogen isotopes are a unique tool for identifying and understanding biological and chemical processes. Hydrogen isotope labeling allows the direct investigation of an excess mass or radioactive label in an organic molecule without altering its chemical structure, physical properties, or biological activity. In the case of tritium (3H), in particular, there has been an increase in use, especially in drug discovery. Because of the long half-life (12.3 years) of tritium, decay correction is not necessary during analysis. Therefore, once a 3H tracer is prepared, it can be stored for long periods of time if radiolytic decay is minimized [4].

RESEARCH THEORIES

Before heavy water irradiation, the target was modeled using MCNPX2.7 computational code to estimate the 3H product yield theoretically. MCNPX code is used to model any complicated geometry in detail while the code has ability to transport 34 particles consisted of neutron, photon, proton, alpha, … [5].

The Iranian miniature neutron source reactor (MNSR) is a low temperature and pool type reactor. It is a small and safe nuclear facility, and the core design embodies highly enriched uranium (90.2 w/o U235) as fuel, light water as moderator, coolant and shield, and metal beryllium as reflector [6]. The mentioned computational code was used to model the research reactor as well as the target geometry at the irradiation position (Fig.1).

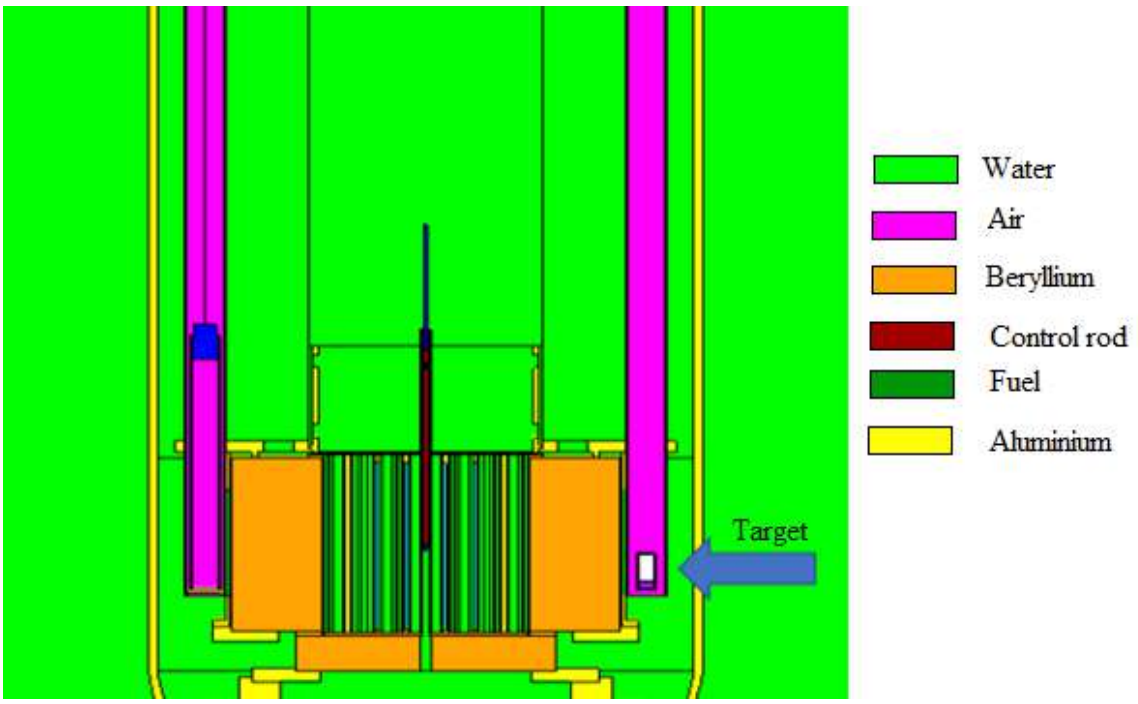

Fig. 1. Simulation of MNSR core using MCNPX code

The buildup of different isotopes inside the core during the reactor core operation is calculated using BURN card of the used computational code. CINDER code of MCNPX originally developed to calculate the material balance process can be described at any time by the following depletion equation:

$$\frac{dN_i}{dt} = \sum_j \gamma_{ij}\,\sigma_{f,j}\,N_j\varphi + \sum_k \sigma_{c,k\to i}\,N_k\varphi + \sum_l \lambda_{l\to i}\,N_l - (\,\sigma_{f,i}N_{ji}\varphi + \sigma_{a,i}N_{ji}\varphi + \lambda_i\,N_l\,) \quad (4)$$

Where $\frac{dN_i}{dt}$= time rate of change in concentration of isotope i, $\sum_j \gamma_{ij}\,\sigma_{f,j}\,N_j\varphi$ = production rate per unit volume of isotope i from fission of all fissionable nuclides,

$\sum_k \sigma_{c,k\to i}\,N_k\varphi$ = production rate per unit volume of isotope i from neutron transmutation of all isotopes including (n,γ), (n,2n), etc., $\sum_l \lambda_{l\to i}\,N_l$ = production rate per unit volume of isotope i from decay of all isotopes including β^-, β^+, α, γ, etc., $\sigma_{f,i}N_{ji}\varphi$ = removal rate per unit volume of isotope i by fission, $\sigma_{a,i}N_{ji}\varphi$ = removal rate per unit volume of isotope i by neutron absorption (excluding fission), $\lambda_i\,N_l$ = removal rate per unit of isotope i by decay [7].

Meanwhile, we must examine any potential uncertainties in this experiment. The location of the sample is one of the most important candidate uncertainties. To this aim, different positions and distances from the default sample position- which has been using for every irradiations- was taken under examination.

EXPERIMENTAL

To produce 3H, 2 cc heavy water was poured inside a vial according to Fig.2.

Fig. 2. The used vials involved heavy water as the target for 3H production

Burn-up card was used to calculate the activity in the sample after 4 hours of irradiation at 15 kW power at the bottom of the PGNAA channel. Vials of heavy water were irradiated for 4 hours using the reactor beam and finally analyzed using beta spectroscopy method. Spectroscopy in this experiment was performed using a liquid scintillation detector. The calculated activity of 3H was compared with the measured value.

Results and discussion

Table 1. Comparison of the calculated and measured 3H activities of the heavy water irradiation.

Parameter	3H product activity (nCi)	Deposited heat by neutrons (W)	Deposited heat by photons (W)
Theoretical	12.96	0.00106±0.00006	0.00322±0.00009
Experimental	2.92	—	—

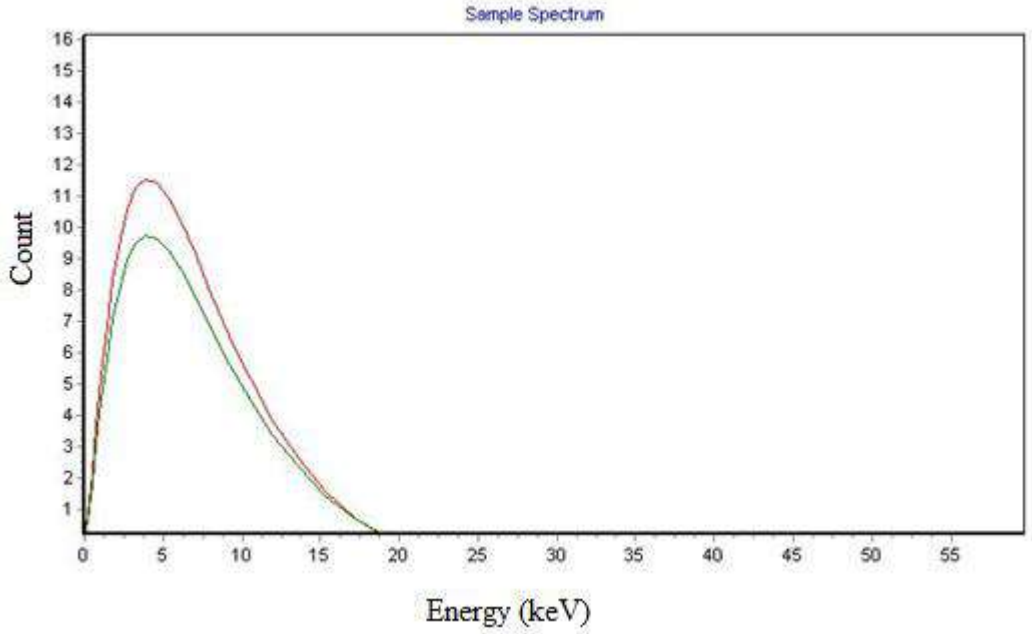

Fig.3 The spectra obtained from the irradiated heavy water samples**.**

Additionally, the impact of the sample's position on the quantity of tritium produced is depicted in the linear graphic in Fig.4.

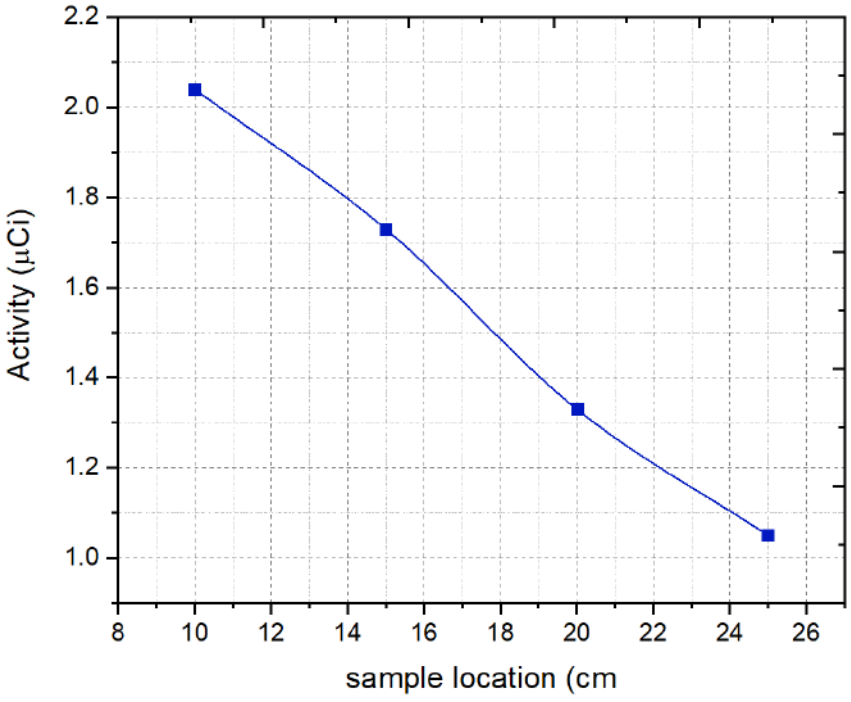

Fig.4 The tritium activity generated relative to the sample position.

The location of the sample is actually a distance from irradiation position. The Sample is typically positioned parallel to the reactor core at the end of this channel. Thus, this is obvious that the further the sample will be from the bottom of the channel, the lesser the tritium activity will be.

Conclusions

It is commonly recognized that the use of isotopes in industry—as either sources or tracers—depends on the monitoring of physical signals that track relevant features. Tritium, also known as hydrogen-3 (symbol T or 3H), is a long-lived form of hydrogen that is frequently employed as a trace in a variety of scientific fields. As a tracer source, the current work examined 3H generation in an MNSR 30 kW reactor both theoretically and practically. In simulation and experiment programs, a 2-cc heavy water target was employed to create 3H. On the other hand, there are always a variety of uncertainties that might hugely affect the infinite result of any experiments. Here, in the current work, we try to consider some of those possible uncertainties to examine such as the sample position and deuterium purity percentage. As the surveys showed, the commonly used position for sample irradiation is the best place with the utmost gain in results.

References

[1] IAEA (2014). Applications of Research Reactors, IAEA Nuclear Energy Series No. NP-T-5.3. Technical report, IAEA,Vienna.

[2] Shang, J. and Huang, P. (2010). Modeling of ac dielectric barrier discharge. Journal of Applied Physics, 107(11):113302.

[3] Miramonti, L. (2002). A plastic scintillator detector for beta particles. Radiation Measurements, 35(4):347–354.

[4] Zerriffi, Hisham (January 1996). Tritium: The environmental, health, budgetary, and strategic effects of the Department of Energy's decision to produce tritium (Report). Institute for Energy and Environmental Research. Retrieved 15 September 2010.

[5] Rolland Andrade ∗, Sudipta Bhowmick, Archana K. Pun, Application of tritium (3H) as a tracer in seepage studies through hydraulic structures, HydroResearch 5 (2022) 48–53

[6] Murthy, T.S. Iyengar, T.S., Applications of tritium in industry and research Symposium on tritium - measurements and applications; Bombay (India); 22-23 Feb 1990

[7] Jens Atzrodt,* Volker Derdau,* William J. Kerr,* and Marc Reid, Deuterium- and Tritium-Labelled Compounds: Applications in the Life Sciences, Angew. Chem. Int. Ed. 2018, 57, 1758 – 1784

[8] D.B. Pelowitz, MCNPXTM user's manual. Los Alamos National Laboratory, Los Alamos. 2005.

[9] M.L. Fensin, Development of the MCNPX depletion capability: A Monte Carlo linked depletion method that automates the coupling between MCNPX and CINDER90 for high fidelity burnup calculations. University of Florida. 2008.

[10] Chengzhan, G., Yongchun, G., 1994. Safety Analysis report for miniature neutron source reactor (MNSR). China Institute of Atomic Energy Report RPT4-S-430- SIAE/SA, RC, FL, RP.

ICNST 2024
International Conference on Nuclear Science and Technology
6- 8 MAY 2024 | Isfahan, Iran

A Geant4-DNA study of DNA damages produced by alpha particles in an arrangement of the chromatin fibers (Paper ID : 1336)

Azizi Ganjgah A.[1], Taherparvar P.[1*]
[1]*Department of Physics, Faculty of Science, University of Guilan, Guilan, Iran*

Abstract

Charged particle radiation can impact cells by damaging DNA strands, leading to direct and indirect single-strand breaks (SSB) and double-strand breaks (DSB), which can result in cell death and the mitotic failure. In this study, we constructed various levels of a precise atomic DNA model in the Geant4-DNA Monte Carlo simulation toolkit, containing chromatin loops (flower). This atomic model was placed inside the cell nucleus with a length of 2 μm. Then, the number of direct and indirect SSB, DSB, and the dose deposition caused by the monoenergetic alpha beams at the energy levels of 0.1–1 MeV in 0.3 MeV steps were calculated. Our results indicated that increasing the energies led to an increase in dose deposition and then increase in the SSBs and DSBs values (with a small positive slope). Based on the results, the 1 MeV alpha beams are more effective for the inhibition of cells in tumor region.

Keywords: Geant4-DNA, DNA damage, SSB, DSB, alpha beams

INTRODUCTION

High LET particles, such as alpha particles, can induce intense ionization along their paths, initiating a chain of events that lead to biological changes through direct interaction with biological targets and DNA damage. Understanding high LET processes in radiobiology is crucial for optimizing hadron therapy. It is also essential to comprehend the mechanism of DNA damage through energy deposition to maximize damage to the target cell and minimize damage to normal tissues [1]. In biological research, DNA molecules are considered the most vital among cell constituents due to their role as carriers of genetic information, making them a primary factor in radiation-induced cell death. The types of DNA damage can usually be grouped into single-strand breaks (SSBs) and double-strand breaks (DSBs), significantly influencing the biological effect of exposure to ionizing radiation [2]. Various studies have been conducted on computational approaches for calculating DNA breaks based on the Track

Structure (TS). Monte Carlo TS codes have become crucial tools for modeling the interaction of ionizing particles with DNA, enhancing the understanding of radiation track structure and its connection to DNA damage [3]. In this way, Geant4-DNA specializes in comprehensive physics and chemistry models to simulate the interactions of radiation with geometrical structures of the biological medium based on the TS approach. The present study aims to investigate the direct and indirect radiation effects of monoenergetic alpha particles at energy levels ranging from 0.1 to 1 MeV in 0.3 MeV steps using Geant4-DNA. The number of SSB, SSB yield (SSBY), DSB, DSB yield (DSBY), and dose values for different energies were calculated for alpha particles.

Materials and Methods

The Geant4-DNA version 11.1.1 has been used to simulate the interaction of particles at the molecular scale. This study considered a cell nucleus with a length of 2 μm and unit-density liquid water. Focusing on the cell nucleus as the irradiation target, the monoenergetic alpha beams with energies of 0.1, to 1 MeV (in 0.3 MeV steps), based on the Ahmadi Ganjeh et al. [1] suggestion, were irradiated along the Z direction and at the entrance of the cell nucleus. Constructing chromatin fiber was performed based on the study by Ahmadi Ganjeh et al [4]. In this way, the nucleotide pair was defined as a base pair (bp), consisting 63 atoms. The properties of atoms such as chemical element, position, and base of nitrogen are considered based on the information provided by Bernal and co-workers [5]. Following a double helix of 154 bp construction by rotating each bp by +36°, the nucleosome was made by folding two double-helical loops around a sphere (histone). After constructing the nucleosomes, chromatin fibers were formed by six nucleosomes per level, forming a supra helix with a pitch of 7.11 nm and an external diameter of 31.38 nm. The repetition of this structure resulted in the formation of a chromatin fiber. According to the research by Santos et al. [6], four chromatin fibers are utilized to create loops arranged in a diamond shape. This "simple loop" consists of 55.44 kbp and can be employed to create another level of compaction, as seen in the fibroblast depiction resembling a "Flower" (Figure 1) and comprising 0.388 Mbp. The present study assessed DNA damage by evaluating direct and indirect SSBs and DSBs. An energy threshold of 17.5 eV was utilized for the Physical and Chemical stages. In water, indirect damage in the chemical stage produced radicals and molecules, including H_2O_2, H_2, H, H^+, OH^-, OH, and e_{aq}-, in water. The

hydroxyl radical (OH) interacts more with sugar and base groups in DNA than others. The probability of strand break production in the DNA by hydroxyl radicals is 13%. The SSBs occur if the energy deposited in the DNA exceeds the threshold value of 17.5 eV. On the other hand, the DSBs are counted when two SSBs occur on the two strands within a distance of less than 10 base pairs. The G4EmDNAPhysics_option6 and G4EmDNAChemistry_option3 physics lists were used to simulate the physical and chemical stages, respectively. The simulation includes 10^6 primary particles, with the statistical error in the results being less than 1%.

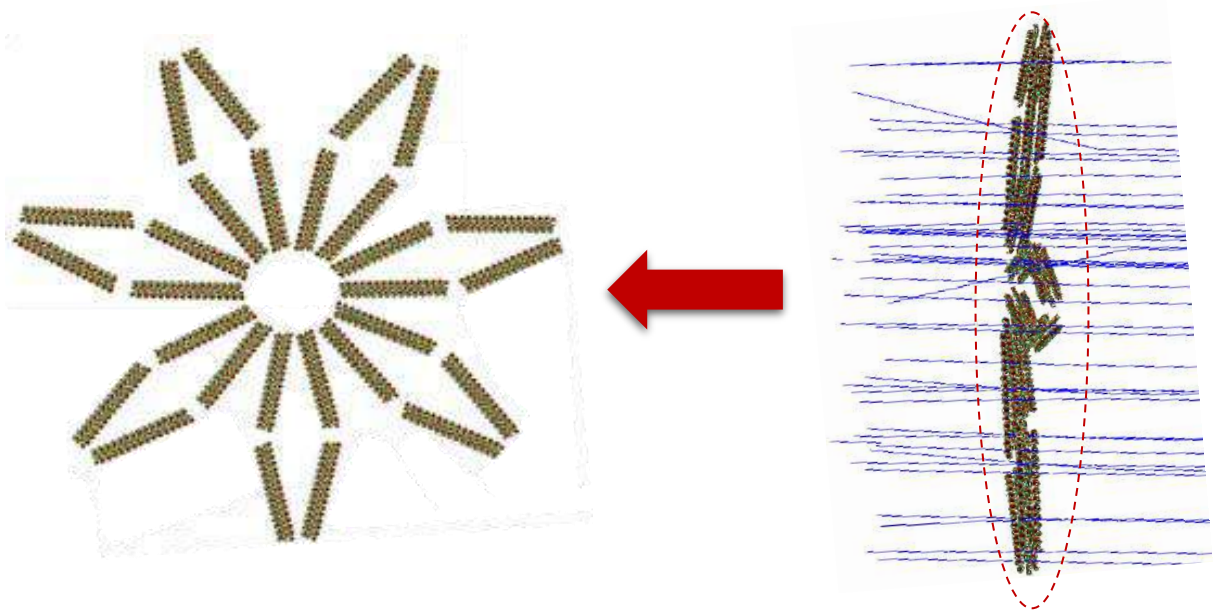

Fig. 1. A 3D view of Flower constructed in the Geant4 toolkit.

Results and discussion

To verify and validate our simulation, the direct and indirect SSBs and DSBs of the 1-bna model irradiated with four radionuclides (^{99m}Tc, ^{111}In, ^{123}I, and ^{125}I) originating from the physical and chemical stages were compared with the values reported by Zafarghandi et al [7]. According to the data in Table 1, it is observed that the differences between the results obtained in this study and those presented by Zafarghandi et al. amount to approximately 4.76%, 3.45%, 4.85%, and 6.1% for SSBs, as well as 10.9%, 13.66%, 1.96%, and 3.84% for DSBs for ^{125}I, ^{111}In, ^{99m}Tc, and ^{123}I, respectively. Generally, there is a good agreement between our results

and the corresponding literature since the average magnitude of the differences is below about 5% and 8% for SSBs and DSBs, respectively.

Table 1. Comparison of the total number of SSBs and DSBs (direct and indirect) per decay between the findings of this study and those of Zafarghandi et al, at a distance of 2.5 nm for ^{125}I, ^{111}In, ^{99m}Tc, and ^{123}I.

Radionuclides	SSB per decay (this study)	SSB per decay (Zafarghandi et al)	DSB per decay (this study)	DSB per decay (Zafarghandi et al)
^{125}I	3.36	3.2	1.91	1.7
^{111}In	2.90	2.8	1.20	1.39
^{99m}Tc	1.05	1	0.51	0.5
^{125}I	1.06	1	0.52	0.5

Moreover, the range (μm) and LET (keV/μm) of alpha particles in the medium are shown in Table 2. Results show that as alpha particles energy increases, LET decreases and subsequently range increases. Table 3 shows the number of direct and indirect SSB, SSBY, DSB, DSBY, and the dose caused by 0.1, 0.4, 0.7, and 1 MeV alpha beams. Compared to 1 MeV alpha beams, SSB (DSB) they were decreased by 70% (88%), 30% (31%), and 11% (1%) for 0.1, 0.4, and 0.7 MeV alpha beams. These values were 65%, 18%, and 1% for the dose deposition. The number of SSB (DSB) per absorbed dose per bps is defined as SSBY (DSBY) in terms of $(GbpGy)^{-1}$. In comparison to 1 MeV alpha beams, SSBY (DSBY) values were reduced by 13% (66%), 12% (14%), and 9% (1%) for 0.1, 0.4, and 0.7 MeV alpha energies. As can be seen in Table 3, the greatest levels of SSBs and DSBs are seen for to particles at the energy of 1 MeV. It is because of the alpha range was smaller than the cell nucleus size, which was 2 μm in this study, and the whole energy was deposited inside the cells. Furthermore, the 1 MeV alpha particles, due to higher LET, deposit more energy per unit path length directly into the DNA, resulting in a higher probability of causing damage such as SSBs, DSBs, SSBY, and DSBY compared to 0.1, 0.4, and 0.7 MeV alpha particles. This energy level allows 1 MeV alpha beam to penetrate cell membranes and reach the nucleus effectively.

Table 2. The range (μm) and LET (keV/μm) of 0.1, 0.4, 0.7, and 1 MeV alpha particle in water

Energy (MeV)	Range (μm)	LET (keV/μm)
0.1	1.616	1.823
0.4	3.213	0.61
0.7	4.428	0.377
1	5.647	0.278

Table 3. The number of direct and indirect SSB, DSB, and the dose for 0.1-1 MeV alpha beams

Energy (MeV)	SSB (Direct and Indirect)	SSBY $(GbpGy)^{-1}$	DSB (Direct and Indirect)	DSBY $(GbpGy)^{-1}$	Dose (Gy)
0.1	6686	2.71×10^{-5}	356	1.44×10^{-6}	6.48×10^{11}
0.4	15804	2.73×10^{-5}	2133	3.69×10^{-6}	1.52×10^{12}
0.7	20031	2.84×10^{-5}	3074	4.28×10^{-6}	1.85×10^{12}
1	22518	3.12×10^{-5}	3106	4.3×10^{-6}	1.86×10^{12}

Conclusions

The study established the relationships between alpha energy and resulting SSBs, DSBs, SSBY, and DSBY, which can be attributed to the particle range and local energy deposition patterns. Our simulation results show that 1 MeV alpha beam irradiation is more effective than 0.1, 0.4, and 0.7 MeV energies. In comparison with the alpha particle with energies of 0.1, 0.4, and 0.7 MeV, the 1 MeV alpha particles have longer particle ranges, dispersing absorbed doses over larger cellular volumes and interacting with higher DNA fragments near their origin to cause more significant clustered damage. In addition, the particle range was smaller than the cell nucleus, and the energy of the particles was deposited entirely in the cell region.

References

[1] Ahmadi Ganjeh, Z., et al. (2020). Simulation of direct DNA damages caused by alpha particles versus protons. Nuclear Inst. and Methods in Physics Research B, 473: 10-15.

[2] Date, H., et al. (2007). Ionization and excitation collision processes of electrons in liquid water. Nuclear Instruments and Methods in Physics Research B, 265 (2): 515-520.

[3] Garty, G., et al. (2010). Grosswendt, A nanodosimetric model of radiation-induced clustered DNA damage yields. physical biology medical. 55: 761–781.

[4] Ahmadi Ganjeh, Z., et al. (2021). Simulation of direct DNA damages caused by alpha particles versus protons. Radiation Physics and Chemistry, 179: 109249.

[5] Bernal, M.A., et al. (2013). An atomistic geometrical model of the B-DNA configuration for DNA–radiation interaction simulations. Computer Physics Communications. 184(12): 2840–2847.

[6] Santos, M. D., et al. (2014). Influence of the chromatin density on the number of direct clustered damages calculated for proton and alpha irradiations using a Monte Carlo code. Progress in Nuclear Science and Technology. 4: 449-453.

[7] Shamsai Zafarghandi, M., et al. (2020). Calculation of direct and indirect damages of Auger electron-emitting radionuclides based on the atomic geometric model: A simulation study using Geant4-DNA toolkit. Nuclear Inst. and Methods in Physics Research B. 483: 22-28.

ICNST 2024
International Conference on Nuclear Science and Technology
6- 8 MAY 2024 | Isfahan, Iran

Design and simulation of neutron/gamma shielding for coincidence Doppler Broadening Spectroscopy based on neutron generator using 113Cd (n,ɣ) 114Cd nuclear reaction (Paper ID : 1337)

A. Samei[a], A. Biganeh[b], D. Sardari[a], B. Shakery Jouybari[b*]

Corresponding Author E-mail: bshakeri@aeoi.org.ir

[a] *Faculty of Engineering, Science and Research Branch, Islamic Azad University, P.O. Box 14515-775.*

[b]*Physics & Accelerators Research School, Nuclear Science and Technology Research Institute, P. O. Box 14395-836, Tehran, Iran.*

Abstract

Coincidence Doppler Broadening Spectroscopy (CDBS) is a non-destructive test for defect identification in metal alloys, semiconductors, and polymers. The standard positron source for the CDBS technique is ^{22}Na with a positron endpoint energy of 540 keV which can penetrate up to 100 µm depth of metals. So, this is impossible to test the industrial thick samples using conventional CDBS. In this paper, we developed the neutron generator-based CDBS to generate positrons inside the sample using the pair-production mechanism. The technique was established based on the generation of high energy gamma-rays via a ^{113}Cd (n,ɣ) nuclear reaction using a 150 KV deuteron-deuteron neutron generator. Experimentally, the challenge is that CDBS needs high-resolution and low-level background gamma spectroscopy using an HPGe detector for fine measurement of the momentum of the annihilated electrons. However, the HPGe detector is exposed to a high level of gamma radiations produced by neutron capture reaction, and fast neutrons of the electrostatic accelerator that decrease the quality of the gamma spectrum. Moreover, the interaction of neutrons with Ge crystal leads to the degradation of the detector energy resolution after long-time operation. So, to increase the quality of the gamma spectroscopy and to save detectors against fast neutrons, effective neutron-gamma shielding of the detector is needed. In this work, different configurations of the neutron-gamma shielding and neutron moderators were designed and simulated by the MCNP code and the most promising was constructed for the neutron-driven CDBS experiment. The performance of the neutron moderator was experimentally tested and verified using the foil activation technique.

Keywords: Neutron-gamma shielding, CDBS, positron annihilation, neutron generator, MCNP simulation.

Introduction

Positron Annihilation Spectroscopy (PAS) is a well-established technique for the investigation of the free volume size, the concentration of defects, and their chemical environments in metals, liquids, polymers, and semiconductors [1]. Experimentally, PAS includes two main techniques:

Coincidence Doppler Broadening Spectroscopy (CDBS) which measures the energy of positron annihilation radiation with a high energy resolution gamma spectrometer. The initial momentum of the annihilating electrons that participate in the positron annihilation radiation leads to a small shift ($\Delta E = P_l c/2$). Where P_l is the longitudinal momentum of the annihilated electrons and c is the light velocity. The measured momentum reflects the chemical environment of positron annihilation sites [2].

Positron Annihilation Lifetime Spectroscopy (PALS) that precisely determines the positron lifetime using a high timing resolution spectrometer. The positron lifetime inside the material and its intensity is an indications of free volume size.

The standard positron source for PAS is ^{22}Na ($T_{1/2}$ =2.6 years) with an endpoint energy of 540 keV. The range of the positron (x) with the maximum energy (E_{max}) in a sample with a Z-atomic number and density of ρ follows the empirical equation (1):

$$P(x) = \alpha e^{-\alpha Z} \qquad (1)$$

Where α is defined by equation (2):

$$\alpha = 16 \frac{\rho \left(\frac{g}{cm^3}\right)}{E_{max}^{1.4}\ (MeV)} \qquad (2)$$

According to equations 1 and 2, the maximum penetration depth of positron for alloys is 100-200 µm, leaving the analysis of thick industrial samples out of reach. However, the generation of positrons inside the material via electron-positron pair-production induced by high-energy photons is a new approach that enables PAS to analyze the thick samples. So far, various techniques have been presented for the generation of high-energy photons:

Using LINAC accelerator for production of high energy Bremsstrahlung radiation [3].

Launching the photo neutron reaction (ɣ,n) using the Bremsstrahlung reaction and using the produced neutron for activation of a neutron-poor target [4].

Generation of high energy gamma-ray via ^{19}F (p, αɣ) ^{16}O or ^{27}Al (p, ɣ) nuclear reaction [5,6].

Initiation of ^{113}Cd (n,ɣ) ^{114}Cd nuclear reaction using the thermal neutrons [7].

In our previous paper, a 2.5 MeV Van de Graaff accelerator was used to generate the high energy gamma-ray via ^{19}F (p, αɣ) ^{16}O nuclear reaction for CDBS analysis of five steel alloys preloaded during uniaxial tension test. The shift in the 511 keV gamma line versus the strain values was demonstrated [5]. However, doing the experiment using this technique is time-consuming (3 hours per sample). To obtain a higher yield of high-energy gamma-ray, we are going to change the nuclear reaction to ^{113}Cd (n,ɣ) ^{114}Cd. In this work, the design and simulation of the gamma-driven CDBS based on a D-D neutron generator is investigated and discussed.

Description of the presented technique

The neutron physics laboratory of the Nuclear Science and Technology Research Institute (NSTRI) is equipped with a 150 kV electrostatic accelerator. The machine can accelerate both the hydrogen and deuteron particles. Figure 1 shows the accelerator. In this work, we used the D-D reaction for the production of neutrons. The average energy of the produced neutrons is about 2.45 MeV and the flux of the fast and thermal neutrons is 10^7 and 10^4 $n.cm^{-2}.s^{-1}$, respectively. For gamma-driven CDBS, high energy gamma-rays with suitable reaction yield are needed for the production of positron inside the material. Although there are many isotopes that produce prompt gamma radiation via (n,ɣ) reaction, there are a few isotopes that produce high-energy gamma rays with appropriate yield for the production of positrons. We used ^{113}Cd (n,ɣ) ^{114}Cd due to its natural abundance (12.33%), the high cross-section for (n,ɣ), and generation of high-energy gamma rays (up to 9.1 MeV).

Figure 1. The 150 kV electrostatic accelerator that is used for the generation of neutrons via D-D reaction.

Figure 2. shows the cross-section versus the neutron energy for ^{113}Cd (n,ɣ) ^{114}Cd reaction reported [8]. According to the reported data in Figure 2, the cross-section is high enough for thermal neutrons (~10^5 barns) and decreases significantly by an increase in neutron energy. So, the fast neutrons of the accelerator should be thermalized to obtain the maximum yield of the reaction. Moreover, CDBS needs high-resolution HPGe detector for measurement of the longitudinal momentum of the electrons. However, the fast neutrons lead to the degradation of the HPGe performance. In the next section, a Monte Carlo N-Particle (MCNP) simulation is performed to design a suitable moderator and neutron gamma shield for the HPGe detector.

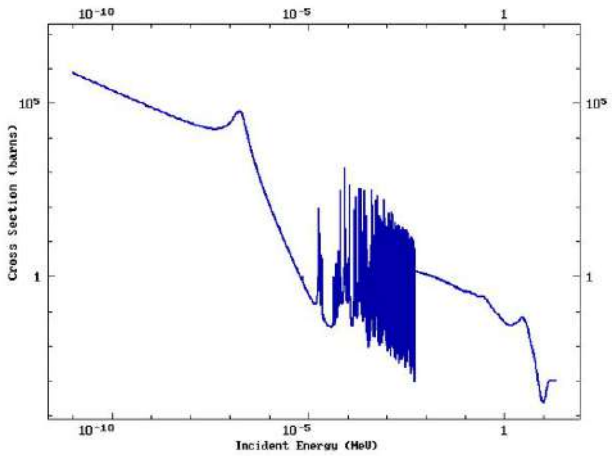

Figure 2. The cross-section versus the neutron energy of (n,ɣ) reaction for ^{113}Cd [8].

Simulation by MCNP

Figure 3 shows the neutron generator-based gamma-driven CDBS simulated by the MCNP code. In this setup, the fast neutrons generated by the accelerator are thermalized by a polyethylene moderator. The 5 and 30% borated polyethylene are used to capture the thermalized neutrons around the acceleration tube. The reason for using to types of borated polyethylene is that 5% borated polyethylene in the inner part can moderate the fast neutron besides the absorption of moderated neutrons and the 30% borated neutron efficiently absorbs the thermal neutrons at the outer layer. The lead shield absorbs the gamma-ray produced by the polyethylene and borated resin. The thermalized neutrons initiate the ^{113}Cd (n,ɣ) ^{114}Cd nuclear reaction, and the produced gamma rays irradiate the sample. The gamma rays produce positrons in the sample and the positron annihilation radiation is measured by HPGe and NaI (Tl) detectors in coincidence mode. The measurement in coincidence mode not only increases the peak-to-Compton ratio but also confirms that the annihilation radiation significantly relates to the positron annihilation in the sample.

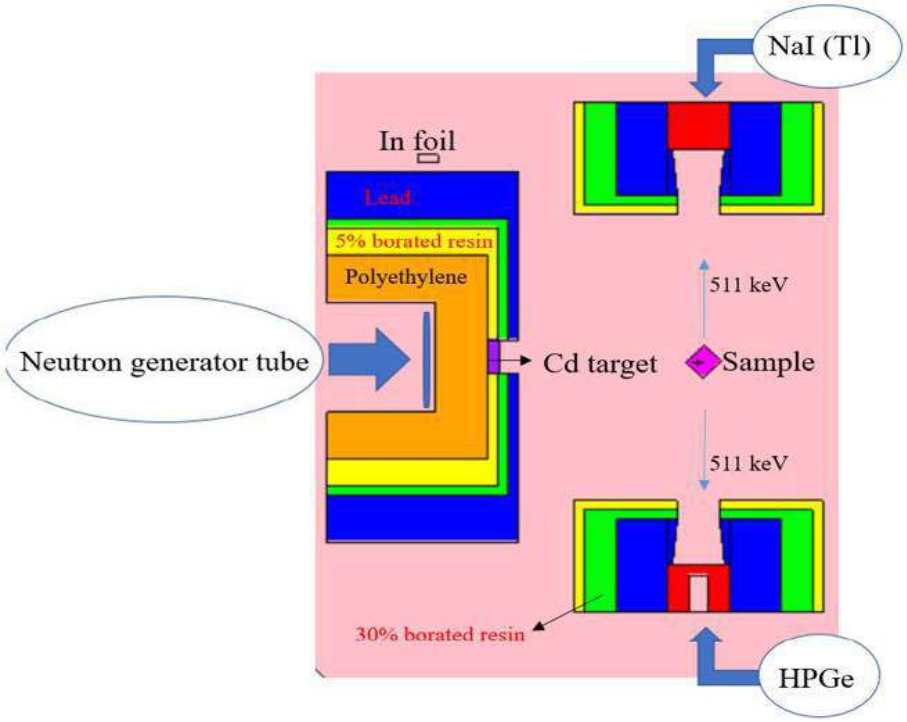

Figure 3. The configuration of neutron-based gamma-driven CDBS experiment simulated by MCNP.

4. Results and discussion

Moderator

Moderators are materials that reduce the speed of neutrons. Moderators must have a high scattering cross section for fast neutrons and a low absorption cross section for thermal neutrons. It should also have a low mass number so that it loses a lot of energy in every collision. Materials that can be used as moderator are hydrogen and carbon in paraffin, water, polyethylene, graphite, and their combinations. In this work, we used polyethylene as a moderator due to its low price and excellent machinability. To obtain the optimum thermal neutron flux at the position of the Cd target, the fast and thermal neutron flux were simulated for different thicknesses of polyethylene. Figure 4 shows the fast and thermal neutron flux for different thicknesses of polyethylene. The results show that the thermal neutron flux increases up to 5 cm of polyethylene and then decreases significantly. We selected 5 cm polyethylene as an appropriate thickness for the moderator. According to the simulation, the polyethylene moderator was designed and made. Figure 5 shows the moderator that is made in different thicknesses. The results of thermal neutron flux measured by foil activation technique for different thicknesses of polyethylene will be presented in the next section.

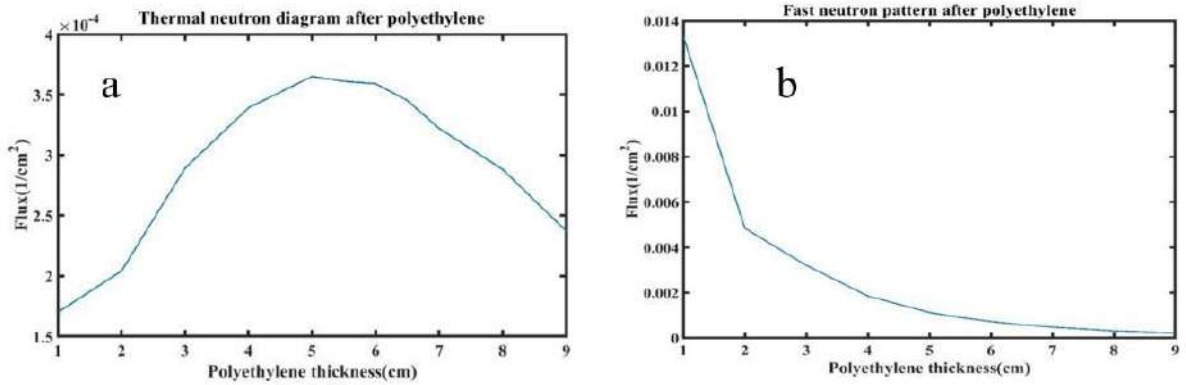

Figure 4. The calculated of, a) Thermal neutron flux and b) fast neutron flux for various thickness of polyethylene.

Figure 5. The polyethylene moderator made for the installation on the neutron generator.

Borated resin for neutron absorption around the vacuum tube

Absorbing the thermal neutron requires the use of a suitable absorber that has a high thermal neutron absorption cross-section. Materials such as boron and its compounds, such as boron carbide, polyethylene borate, and lithium-containing materials are candidates for use as an absorber. Since fast neutrons do not stop easily, one should look for materials that have an elastic scattering cross-section surface as well as a high absorption cross-section surface. In this work, we used B_4C as the neutron absorber. We used two compounds: 5% boron to absorb the fast neutrons and a small amount of boron to convert them into gamma and the next layer consists of resin with 30% boron, which again absorbs neutrons. To optimum the appropriate thickness for the borated resin, the simulation of the thermal neutron flux was performed for 5% and 30% borated resin with different thicknesses. The results of the simulation are shown in Figure 6. According to the results of the simulation, 3 and 1cm thickness were selected for 5% and 30% borated resin.

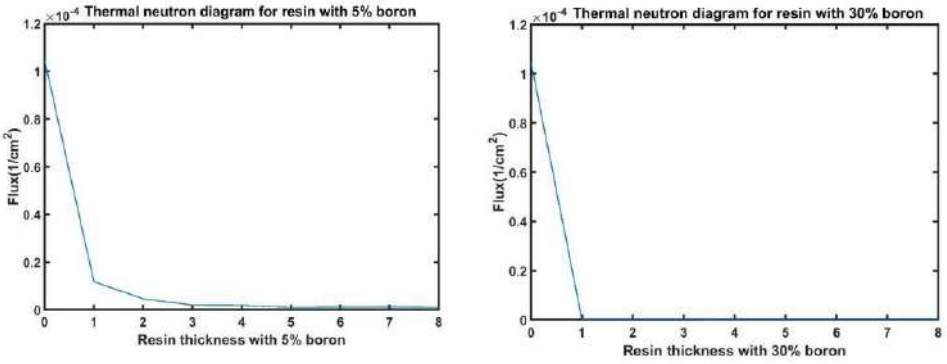

Figure 6. Thermal neutron flux for different thickness of borated resin.

HPGe detector shield

As mentioned before, the CDBS experiment needs high resolution detector for precise measurement of the longitudinal momentum of the annihilated electrons. However, performing high-resolution gamma spectroscopy in the neutron field is challenging due to the destructive effect of the fast neutrons on the HPGe crystal. The configuration of the HPGe detector shield is shown in Figure 7. The shield design was optimized so as to minimize the dose in the detector. Figure 8 shows the detector dose rate in the HPGe detector for different thicknesses of lead. According to the simulation, 5 cm lead was selected as an appropriate value for lead shielding. So, the HPGe shield consists of 5 cm lead in the first layer, 3 cm of 5% borated resin in the second layer, and 1cm of 30% borated resin in the last layer.

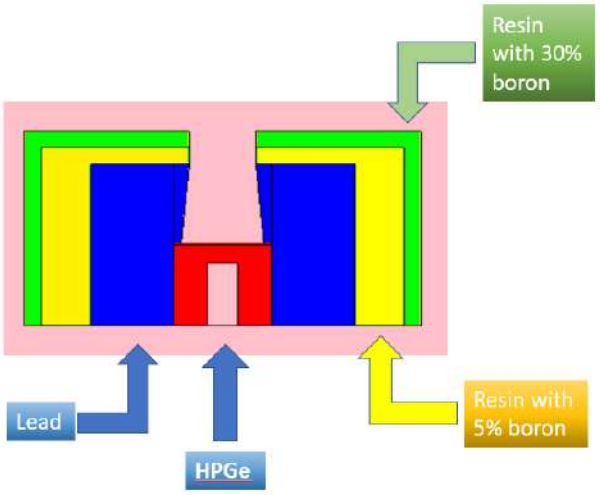

Figure 7. The configuration of the shield designed for the HPGe detector.

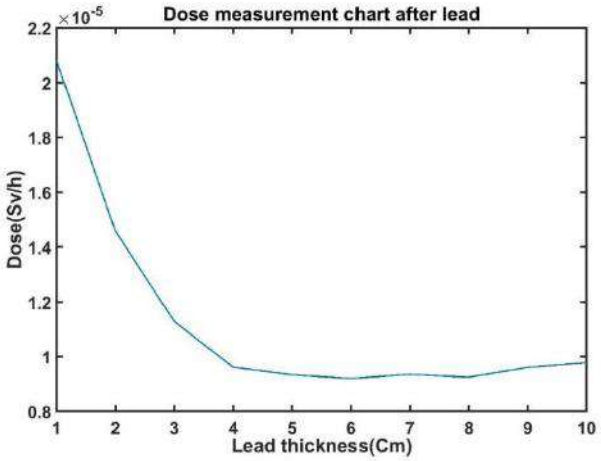

Figure 8. Calculation of the dose rate (Sv/hour) for different thickness of lead.

Measurement of the thermal and fast neutron flux at the Cd target position

The measurement of the fast and thermal neutron flux at the position of the target was done using the neutron generator at NSTRI using the indium foil activation technique [9]. The polyethylene moderator was placed at the end of the accelerator tube and the indium foil was placed on the moderator. For each thickness, the indium foil was irradiated for 2 hours by the neutron generator at 300 μA deuteron beam current. Then, the activated foil was placed on a 20% efficiency HPGe detector for gamma spectroscopy. Figure 9 shows the gamma-ray spectroscopy of the activated indium foil recorded for 1 hour. The gamma lines of 336 and 1293 keV were used to determine the flux of the fast and thermal neutrons, respectively [10]. Figure 10 shows the thermal neutron flux measured by the indium foil activation technique for

different thicknesses of moderator. According to the results of the experimental data, the maximum thermal neutron flux is achievable at 5 cm of the moderator which is in complete agreement with the results of simulations.

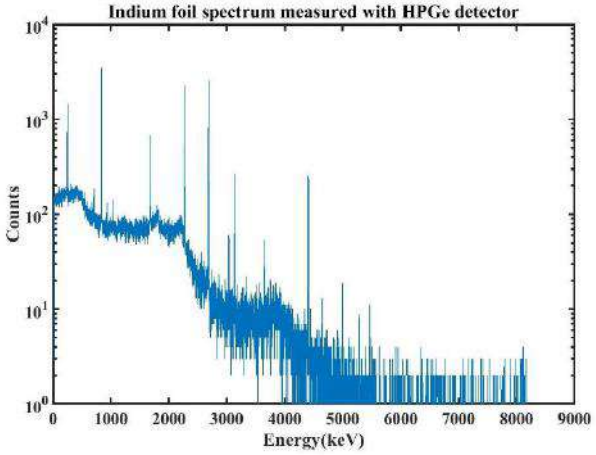

Figure 9. The gamma-ray spectroscopy of the activated indium foil.

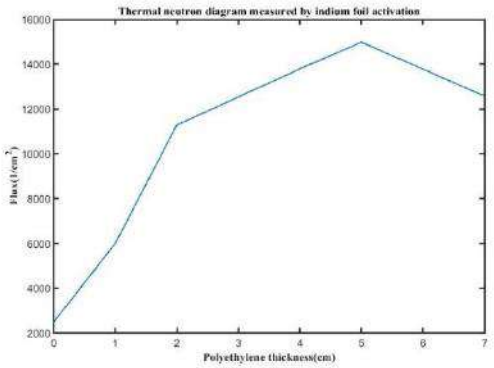

Figure 10. Thermal neutron flux measured using indium foil for different polyethylene thickness.

Conclusion

In this work, the concept of positron annihilation spectroscopy using the neutron generator was described. The configuration of the experiment was simulated by the MCNP code and the optimum value for the moderator thickness was obtained. The results of the simulation were in agreement with the measurement of neutron flux performed using the indium foil activation method. The shield of the HPGe detector was simulated so as to minimize the dose rate in the detector. Thanks to the high yield of high-energy gamma rays using ^{113}Cd (n,ɣ) ^{114}Cd nuclear reaction, we expect to improve the sensitivity of the accelerator-based PAS technique. Further

to this work, we are going to establish the first neutron generator-based CDBS spectrometer for the volumetric assay of defects in high-Z thick alloys.

References

[1] Biganeh, A., et al. "Development of a 2D digital coincidence Doppler broadening spectrometer." Journal of Instrumentation 14.02 (2019): P02017.

[2]Biganeh, A., et al. "Positron annihilation lifetime and Doppler broadening spectroscopy of polymers." Radiation Physics and Chemistry 166 (2020): 108461.

[3] F.A. Selim, et al., Doppler broadening measurements of positron annihilation using bremsstrahlung radiation, Nuclear Instruments and Methods in Physics Research Section B: Beam Interactions with Materials and Atoms 192 (1-2) (2002) 197–201.

[4] D.P. Wells, et al., Gamma-induced positron annihilation spectroscopy and application to radiation-damaged alloys, Nuclear Instruments and Methods in Physics Research Section A: Accelerators, Spectrometers, Detectors and Associated Equipment 562 (2) (2006) 688–691.

[5] Biganeh, A., et al. "Ion beam-based coincidence Doppler broadening spectroscopy of positron annihilation radiation: The experiences of Tehran Van de Graaff lab." Nuclear Instruments and Methods in Physics Research Section B: Beam Interactions with Materials and Atoms 518 (2022): 15-22.

[6] M.J. Kenny, J.R. Bird, E. Clayton, Proton induced γ-ray yields, Nuclear Instruments and Methods 168 (1-3) (1980) 115–120.

[7] Schut, H., et al. “Performance of an intense nuclear-reactor based positron beam.”Materials Science Forum. Vol. 363. Trans Tech Publications Ltd. Zurich-Uetikon. Switzerland. 2001.

[8] https://www-nds.iaea.org/exfor/endf.html.

[9] Forrest Brown, Brian Kiedrowski, Jeffrey Bull, “MCNP5-1.60 Release Notes”, LAUR-10-06235 (2010).

[10] Greenfield, Moses A., Roscoe L. Koontz, and Alan A. Jarrett. "Computing absolute thermal neutron flux from measurements made with indium foils." Nuclear Science and Engineering 4.4 (1958): 563-569.

Assessment of Pseudo-CT Images derived from MRI using U-Net and Attention U-Net Networks (Paper ID : 1338)

Alireza Sadremomtaz[1*], Seyedeh Sajedeh Mousavi Eshkiki[2]

Faculty of Sciences, University of Guilan, Rasht, Iran

Abstract

Deep convolutional neural networks have exhibited robust and dependable PET attenuation correction (AC) as an alternative to traditional AC methodologies in integrated PET/MRI systems. The integration of PET with Magnetic Resonance Imaging (MR) in hybrid PET/MR scanners presents a challenge for attenuation correction due to the inherent limitation of MRI images in providing information on tissue attenuation coefficients. Recently, there has been a utilization of deep neural networks to generate pseudo-CT images, facilitating the extraction of attenuation coefficients from MRI data. This study delves into an investigation of the efficacy of the U-NET and Attention U-NET neural networks in the assessment of pseudo-CT images derived from MRI data. The Attention U-NET network has exhibited a noteworthy enhancement, with Mean Squared Error (MSE) and Mean Absolute Error (MAE) values improving by 16% and 6%, respectively, in comparison to the U-NET network. This advancement highlights the potential of neural networks in refining accuracy in pseudo-CT generation, contributing to the optimization of PET/MR hybrid imaging.

Keywords: Pseudo-CT, deep neural network, U_NET, Attention U_NET

Introduction

The integration of positron emission tomography (PET) and magnetic resonance imaging (MRI) has shown promise in delivering comprehensive functional and anatomical information. Despite the potential benefits such as reduced radiation exposure and enhanced image quality, the adoption of PET-MRI systems in routine clinical practice has been limited [1,2]. A significant hurdle lies in addressing attenuation correction, which is essential for PET image reconstruction, especially when employing MRI-based attenuation

correction (AC) methods. The advent of deep learning (DL) has showcased substantial potential in both computer vision and medical imaging domains [3]. DL methodologies offer the capability to generate synthetic CT images from MR images for the prediction of attenuation correction (AC) maps [4, 5, 6]. However, these approaches typically necessitate structural images, and their accuracy may be constrained by image artifacts and inter-modality co-registration errors. In 2017, Han introduced a 2D deep convolutional neural network (CNN) that directly learns a mapping function for translating a 2D MR image slice into its corresponding 2D CT image slice, closely adhering to the U-Net architecture [7]. In 2018, Oktay introduced a novel attention gate (AG) model tailored for medical imaging applications, aiming to autonomously prioritize target structures of diverse shapes and sizes. Utilizing AGs during model training enables the implicit learning of mechanisms to attenuate extraneous regions within input images, thereby accentuating pertinent features conducive to the task at hand [8]. This article evaluates the performance and suitability of both standard U-Net and Attention U-Net architectures for translating MRI images to pseudo-CT images, a critical step in PET-MRI imaging. While the standard U-Net remains a robust and widely used architecture, the Attention U-Net demonstrates enhanced adaptability and performance, particularly in scenarios with intricate structures or requiring precise feature localization. Ultimately, the choice between the two architectures depends on the characteristics of the dataset. This research sheds light on the potential of attention mechanisms in improving PET-MRI imaging and highlights the importance of leveraging advanced deep learning techniques for enhancing medical imaging modalities.

Materials and Methods

Imaging dataset

The imaging dataset utilized in this study was sourced from the CERMEP-IDB-MRXFDG [9], encompassing data from thirty-nine participants who underwent [18F] FDG PET/CT and MRI scans. These scans yielded [18F] FDG PET, T1 weighted MRI, FLAIR MRI, and CT images. The dataset exists in three distinct formats: 1) DICOM, 2) NIFTI and 3) NIFTI normalized (images normalized to MNI space). This study focused on data from twenty patients, each contributing 178 slices of paired CT and MRI scans. All images were normalized to MNI space. MRI sequences were captured using a Siemens Sonata 1.5 T scanner with specific

parameters: TR 2400 ms, TE 3.55 ms, inversion time 1000 ms, and flip angle 8°. These images were reconstructed into a 160 ×192 × 192 matrix with voxel dimensions of 1.2 ×1.2 ×1.2 **mm³** (axial field of view 230.4 mm). CT data were obtained using a Siemens Biograph mCT64 scanner, acquiring low-dose CT images for attenuation

correction at a tube voltage of 100 keV. These images were reconstructed into a 512×512×233 matrix with a voxel size of 0.6 ×0.6 ×1.5 **mm³** (axial field of view 349.5 mm).

Preprocessing

Data preprocessing is a vital step in deep learning frameworks, refining data before inputting it into the network. For MRI and CT images, two key preprocessing steps are crucial: resizing and normalization. Resizing ensures uniformity in image dimensions, making processing seamless across different models. Both MRI and CT images are resized to (256, 208, 1), ensuring consistency and simplifying subsequent analysis. Normalization is essential for standardizing image intensity. Pixel values are scaled to the range [0, 1] This ensures uniformity in data representation across the dataset. Python version 3.10 is used for these preprocessing tasks.

Network architecture

The U-Net architecture, initially designed for biomedical image segmentation, has become widely utilized in convolutional neural network (CNN) frameworks. It features a symmetrical hierarchical structure comprising an encoder and a decoder component, incorporating skip connections for pixel-wise prediction. This study undertakes the development and comparison of a 2D standard U-Net and an Attention U-Net model tailored to directly learn a mapping function converting a 2D MR slice to its corresponding 2D CT image. The primary distinction lies in their treatment of spatial information integration: while the standard U-Net merges spatial data using skip connections, potentially leading to suboptimal feature representation, the Attention U-Net incorporates attention layers within skip connections to actively suppress activation in non-essential regions. Trained on a dataset comprising paired 2D MR and CT slices, the model reconstructs synthetic CT predictions progressively, aligning the final output with input image dimensions. The encoding segment extracts intricate features from input MR images, while the decoding segment facilitates pseudo-CT prediction reconstruction. with

convolutions followed by nonlinear activation functions to generate feature representations. The input images are sized at 256 × 208 pixels and one channel (grayscale image). The encoder comprises repeated applications of two 3 × 3 convolutions with 2- pixel strides, except for the last block, which includes a single convolutional layer. A ReLU activation layer and dropout operation are applied. The second convolutional layer is followed by a ReLU activation layer and a 2 × 2 max-pooling operation, reducing the spatial size to minimize computational cost and memory usage. The number of convolutional filters increases from 16 to 256 across blocks, enabling discernment of hierarchical relationships in MR images.

Training the network

The U-Net models proposed in this study are equipped with 2D convolutions and exclusively support 2D input images. Following data preprocessing, the combined number of 2D images across all datasets amounted to approximately 6732 slices for both MRI and CT images. The model's trainable parameters, comprising weights and biases, were initialized utilizing the variance scaling distribution technique. To optimize model performance, the Adam optimization algorithm was employed with a learning rate of 0.0001, aiming to minimize the Mean Absolute Error (MAE) loss function for both networks. The training encompassed 100 epochs, resulting in a total of 9900 iterations for the attention U-Net and 8800 iterations for the standard U-Net. This epoch count was determined sufficient to attain convergence in training loss. Evaluation of the quality of generated CT images produced by the standard U-Net and attention U-Net architectures involved a thorough analysis against ground-truth images, utilizing four pixel-wise metrics: Mean Absolute Error (MAE), Mean Squared Error (MSE), Peak Signal-to-Noise Ratio (PSNR), and Structural Similarity Index (SSIM). These metrics offer a comprehensive assessment, encompassing both quantitative and qualitative disparities that emulate human perception.

Results and discussion

The assessment of CT image quality generated by both the standard U-Net and attention U-Net architectures was conducted through a comprehensive evaluation against ground- truth images, employing four pixel-wise metrics. These metrics provide a holistic assessment,

encompassing both quantitative and qualitative aspects akin to human perception. The quantitative evaluation of pseudo-CT images in comparison to ground- truth images is delineated in Table 1, showcasing the performance of each network on the test dataset across the MSE, MAE, SSIM, and PSNR evaluation metrics. Lower MAE/MSE values and higher PSNR/SSIM values signify superior outcomes, wherein the attention U- Net demonstrates enhanced performance across all metrics.

Table 1. Quantitative results of pseudo-CT images using standard U-Net compared with the attention U-Net images evaluated using PSNR, MAE, MSE, and SSIM metrics on the test dataset.

	PSNR	MAE	MSE	SSIM
Standard U-Net	15.263±4.006	0.141±0.083	0.049±0.033	0.485±0.27
Attention U-Net	16.275±9.423	0.134±0.081	0.042±0.032	0.513±0.239

The findings of pseudo-CT images produced by standard U-Net and attention U-Net architectures are delineated. Visual comparisons between pseudo-CT images and their corresponding ground-truth counterparts are illustrated in Figure 1, representing a single example patient within the testing dataset. Notably, upon visual examination, pseudo-CT images generated by the attention U-Net exhibit enhanced fidelity, closely resembling their authentic counterparts to the extent of being nearly indistinguishable.

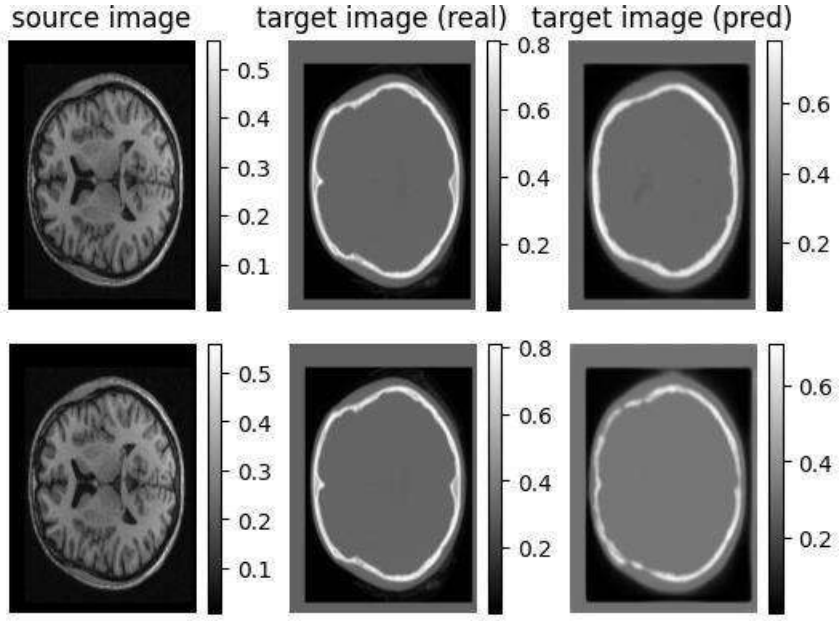

Fig. 1. The comparison of pseudo-CT images generated using a standard U-Net (bottom) and attention U-Net (top) for one subject on a test dataset. From left to right: input MR image (source image); ground-truth/real CT image (real image); pseudo-CT image (predicted image), as can be seen, attention U-Net predicts better pseudo-CT image.

Figure 2 depicts the learning curves of both U-Net models utilized in our study. Observing the graph, it is evident that both standard U-Net and attention U-Net exhibit comparable performance across both the training and validation datasets. The training curves exhibit a consistent downward trajectory until reaching stabilization, indicative of convergence within the selected 100 epochs. thereby underscoring the robust generalizability of our model for MRI to pseudo-CT translation. Moreover, this observation indicates that both models were adequately fitted to the data.

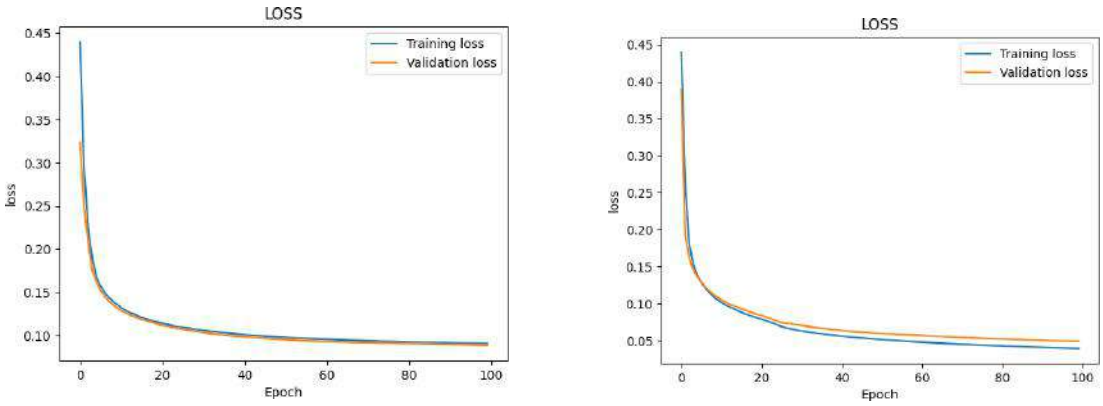

Fig. 2. A plot of the training loss versus validation loss over the number of epochs for standard U- Net (left) and attention U-Net (right). The training learning curve shows the goodness of the model's learning, whereas the validation learning curve shows the goodness of the model's generalization.

Conclusions

PET-MRI integration holds promise in medical imaging despite challenges like attenuation correction. DL, particularly U-Net architectures, offer solutions by generating pseudo-CT images from MRIs. Our study compares standard U-Net and Attention U-Net models, finding Attention U-Net excels in complex scenarios.

References

Ehman, E. C., Johnson, G. B., Villanueva-Meyer, J. E., Cha, S., Leynes, A. P., Larson, P. E. Z., & Hope, T. A. (2017). PET/MRI: where might it replace PET/CT?. Journal of Magnetic Resonance Imaging, 46(5), 1247-1262.

Zhu, T., Das, S., & Wong, T. Z. (2017). Integration of PET/MR hybrid imaging into radiation therapy treatment. Magnetic Resonance Imaging Clinics, 25(2), 377-430.

Burgos, N., Cardoso, M. J., Modat, M., Pedemonte, S., Dickson, J., Barnes, A., ... & Ourselin, S. (2013). Attenuation correction synthesis for hybrid PET-MR scanners. In Medical Image Computing and Computer-Assisted Intervention–MICCAI 2013: 16th International Conference, Nagoya, Japan, September 22-26, 2013, Proceedings, Part I 16 (pp. 147-154). Springer Berlin Heidelberg.

Yang, X., Wang, T., Lei, Y., Higgins, K., Liu, T., Shim, H., ... & Nye, J. A. (2019). MRI-based attenuation correction for brain PET/MRI based on anatomic signature and

machine learning. Physics in Medicine & Biology, 64(2), 025001.

Dong, X., Wang, T., Lei, Y., Higgins, K., Liu, T., Curran, W. J., ... & Yang, X. (2019). Synthetic CT generation from non-attenuation corrected PET images for whole-body PET imaging. Physics in Medicine & Biology, 64(21), 215016.

Spuhler, K. D., Gardus, J., Gao, Y., DeLorenzo, C., Parsey, R., & Huang, C. (2019). Synthesis of patient-specific transmission data for PET attenuation correction for PET/MRI neuroimaging using a convolutional neural network. Journal of nuclear medicine, 60(4), 555-560.

Han, X. (2017). MR-based synthetic CT generation using a deep convolutional neural network method. Medical physics, 44(4), 1408-1419.

Oktay, O., Schlemper, J., Folgoc, L. L., Lee, M., Heinrich, M., Misawa, K., ... & Rueckert, D. (2018). Attention u-net: Learning where to look for the pancreas. arXiv preprint arXiv:1804.03999.

Mérida, I., Jung, J., Bouvard, S., Le Bars, D., Lancelot, S., Lavenne, F., ... & Costes,

N. (2021). CERMEP-IDB-MRXFDG: a database of 37 normal adult human brain [18F] FDG PET, T1 and FLAIR MRI, and CT images available for research. EJNMMI research, 11(1), 1-10.

Ronneberger, O., Fischer, P., & Brox, T. (2015). U-net: Convolutional networks for biomedical image segmentation. In Medical Image Computing and Computer-Assisted Intervention–MICCAI 2015: 18th International Conference, Munich, Germany, October 5-9, 2015, Proceedings, Part III 18 (pp. 234-241). Springer International Publishing.

ICNST 2024
International Conference on Nuclear Science and Technology
6- 8 MAY 2024 | Isfahan, Iran

Theoretical calculations and experimental production of 89Zr: A new emerging PET radionuclide (Paper ID : 1339)

Zolghadri S.[1*], Mohammadpour-Ghazi F.[1], Yousefnia H.[1], Akbari L.[2]

[1] *Radiation Application Research School, Nuclear Science and Technology Research Institute, P.O.BOX: 14893-836, Tehran, Iran.*

[2] *Radiation Application Department, School of Mechanical Engineering, Shiraz University, Shiraz, Iran.*

ABSTRACT

Today, radionuclides are widely used in positron emission tomography (PET) procedures to detect various malignancies. ^{89}Zr, an emerging PET radionuclide with special physical properties, has been known as an ideal candidate for use in the procedure sometimes termed immunoPET. This study aimed to produce ^{89}Zr radionuclide with high specific activity, and high chemical, radiochemical, and radionuclide purities appropriate for the development of new radioimmunoconjugates. ^{89}Y(p,n)^{89}Zr nuclear reaction was considered the best choice for the production of ^{89}Zr radionuclide in a 30 MeV cyclotron. The level density model was considered to calculate the reaction cross sections using TALYS-1.8 and ALICE-91. 330 mg Y_2O_3 powder was pressed in an aluminum pellet (diameter = 11 mm; thickness = 0.8 mm) and was used as a target holder and the target was covered by a high-purity aluminum foil. $^{89}Y_2O_3$ pellet target was bombarded with 14 MeV proton energy for 125 µA.h. The irradiated target was washed with HCl solution (6 M) as the primary solvent. ^{89}Zr was separated from the target via ZR resin. The chemical purity of the final solution was checked by inductively coupled plasma spectrometry. The radiochemical purity assessed by a radionuclidic purity was assessed by an instant thin layer chromatography (ITLC) method. A high-purity germanium detector was utilized for radionuclide purity assessment. ^{89}Zr radionuclide was prepared with a high specific activity of 344.1 MBq/µg. The chemical purity assessment of the final solution showed the total amount of the metal ions < 0.1 ppm. The radiochemical purity of the solution was higher than 99%. The radionuclidic purity was measured more than 99.99 %. The results of this study showed the ^{89}Zr radionuclide can be produced with high chemical, radiochemical, and radionuclidic purities. These features as well as the possibility of high specific activity

production of ^{89}Zr promise the possible preparation of novel ^{89}Zr-based radiopharmaceuticals in the country.

Keywords: ^{89}Zr, positron emission tomography, TALYS, ALICE,

INTRODUCTION

In several fields, especially in medicine, radionuclides have been utilized, but positron emission tomography (PET) radionuclides with short half-lives like ^{11}C, ^{13}N, ^{15}O,^{18}F, etc., cannot be utilized for long-term PET studies, such as analyzing the kinetics of antibodies. For more than four decades, antibodies labeled with radioactive substances have been utilized to detect tumors. Recently, they have been explored as a promising area for molecular imaging. A technique called immunoPET combines monoclonal antibodies' high specificity for antigens with the high sensitivity of PET imaging to enable precise imaging of a broad range of illnesses, including tumors.

The unique physical characteristics of the ^{89}Zr radionuclide make it an excellent choice for immunoPET imaging, due to its long half-life ($T_{1/2}$ = 78.41 h) and low-energy positrons (EC = 76.6%, β^+ = 22.3%, $E_{max}(\beta^+)$ = 897 keV, $E_{ave}(\beta^+)$ = 397 keV, $R_{ave}(\beta^+)$ = 1.18 mm, E_γ = 908.9 keV, I_γ =100%) that result in high-resolution PET images. Additionally, ^{89}Zr-based radioligands are safer to handle, more stable in vivo, and provide higher image resolution with lower absorbed dose compared to ^{124}I-based radioligands, making it a more suitable choice for immunoPET imaging.

Trials based on ^{89}Zr-radiopharmaceuticals have been conducted using different compounds such as trastuzumab, bevacizumab, cetuximab, rituximab, NMOTO53OA, ibritumomab-tiuxetan, cmAb U36, and Hu-J591 MoAb, which have shown a remarkable ability to detect various types of tumors with high accuracy, resolution, and signal-to-noise ratio. Therefore, ^{89}Zr-based radioimmunopharmaceuticals can be considered the effective imaging tools for identifying tumor-associated antigens.

Zirconium-89 is typically generated through the bombardment of mono-isotopic natural yttrium using the ^{89}Y(p,n)^{89}Zr nuclear reaction method at a biomedical cyclotron. A small-scale experimental production of ^{89}Zr has been reported in the country, with a maximum activity of 74 MBq. The country has produced a small amount of ^{89}Zr experimentally, but they

have not reported the degree of purity in terms of chemical and radiochemical properties. For using this radionuclide in medical imaging, it is necessary to produce it with high levels of chemical, radiochemical, and radionuclide purity, and at an appropriate activity level to label it with antibodies, peptides, or other small molecules. Given the unique physical properties of ^{89}Zr, this recently emergimg radioactive isotope has become critical in creating new imaging agents for immunoPET procedures. The objective of this research was to generate ^{89}Zr with high specific activity, as well as high levels of chemical, radiochemical, and radionuclide purity suitable for the production of novel radioimmunoconjugates for medical applications.

MATERIALS AND METHODS

The computational studies were conducted using TALYS-1.8 and ALICE-91 codes. To produce ^{89}Zr, a 30 MeV Cyclone-30 was used, and the ZR resin was bought from TrisKem Co. (France). All chemical reagents, including Y_2O_3 powder with a 99.99% trace metals basis, were obtained from Sigma Aldrich (Heidelberg, Germany).

Radio-chromatography was conducted using Whatman No. 1 paper (Whatman, U.K.) and a thin-layer chromatography scanner (Bioscan AR2000, Paris, France). The N-type coaxial high-purity germanium (HPGe) detector (NIGC-4020) coupled with a multichannel analyzer card system (NIGC1040-, DSG, GMBH) was used to measure the activity of the samples.

Computational studies

The cross-section analysis of the ^{89}Y(p,n)^{89}Zr reaction was performed using TALYS-1.8 and ALICE-91 codes to identify the most effective energy range for ^{89}Zr production. The level density model was utilized in the computation of the cross-section.

Experimental studies

Production and quality control of [^{89}Zr]Zr-oxalic acid

The Y_2O_3 target was produced by pressing of 330 mg powder in an aluminum pellet with 11 mm diameter and 0.8 mm thickness. The target was irradiated by 14 MeV protons with a current of 25 μA for 5 h. The irradiated target was washed via a 6 M HCl solution for five times. A preconditioned column filled by 200 mg of ZR resin (TrisKem) used to separate the ^{89}Zr from natY target. The column was washed four times with a 2.5 mL of HCl solution and

2.5 mL of water, and eventually, 1.5 mL of 1.0 M oxalic acid solution was used to obtain [^{89}Zr] Zr-oxalate.

To assess the radionuclide purity of the final preparation, the activity of each sample was determined by calculating the area under the energy peak of a 908.9 keV gamma ray using Equation (1).

$$A = \frac{N}{\varepsilon \gamma t_s K_1 K_2 K_3 K_4 K_5} \quad (1)$$

Where ε is the efficiency of the detector in the photo-peak, γ is the probability of photo-peak emission, t_s is the live time of collecting the sample spectrum in seconds, k_1, k_2, k_3, k_4 and k_5 are the correction factors and N is the net area under the corresponding photo-peak and in the form of equation (2) is calculated:

$$N = N_s \frac{t_s}{t_b} N_b \quad (2)$$

Where N_s is the area under the net peak in the sample spectrum, N_b is the area of the corresponding net peak in the background spectrum, and t_s and t_b are the live time of collecting the sample spectrum and the background spectrum in seconds, respectively.

The final solution was analyzed for any chemical impurity using the ICP-OES method, and the radiochemical purity was examined through the instant thin-layer chromatography (ITLC) method. The mobile phase used for ITLC was 20 mM citric acid, and the Whatman paper was chosen as the stationary phase.

RESULTS and DISCUSSION

Computational studies

The cross-section of ^{89}Y(p, n)^{89}Zr reaction, calculated by Alice-91 and TALYS-1.8 codes cross (Fig.3), showed the maximum cross-section will occur approximately in proton energies between 13-15. However, other calculation for undesirable radionuclides that may produce by the proton irradiation of yttrium target, obtained by ALICE and TALYS codes, demonstrated the best proton energy for ^{89}Zr is below than 15 MeV.

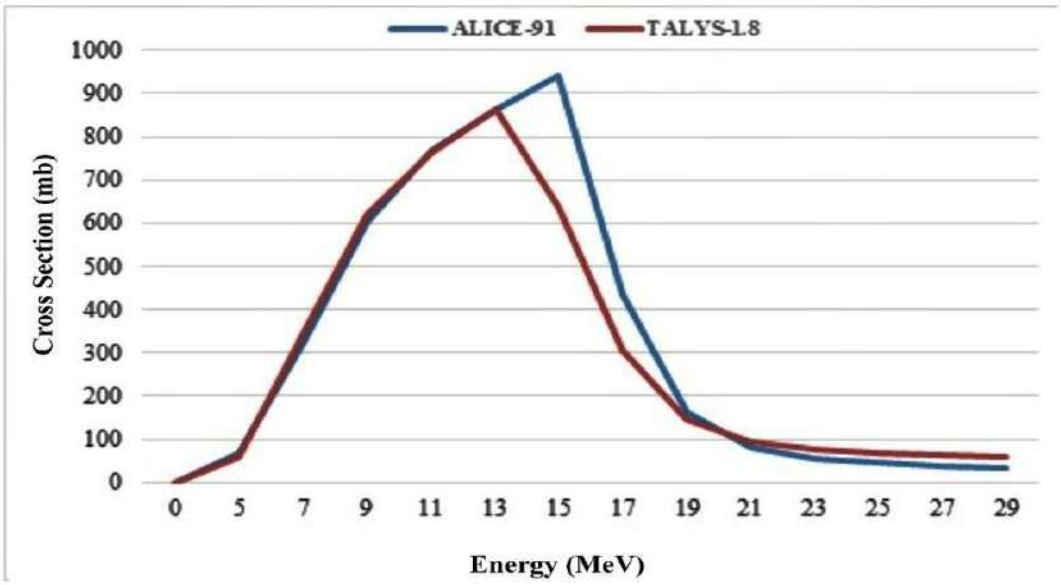

Fig. 1. ^{89}Y (p, n) ^{89}Zr reaction cross-sections obtained by Alice-91 and TALYS-1.8 codes.

Quality control of the final product

The gamma-ray spectrometry of the final product showed two significant photons originated from ^{89}Zr, and a radionuclide purity of over 99.99% was obtained (Fig. 2). The ICP-OES method was used to measure the quantity of metal ions demonstrated the total amount of metal ions was below 0.1 ppm. The ITLC method was utilized to investigate the radiochemical purity, which indicated that the purity level was over 99% (Fig.3).

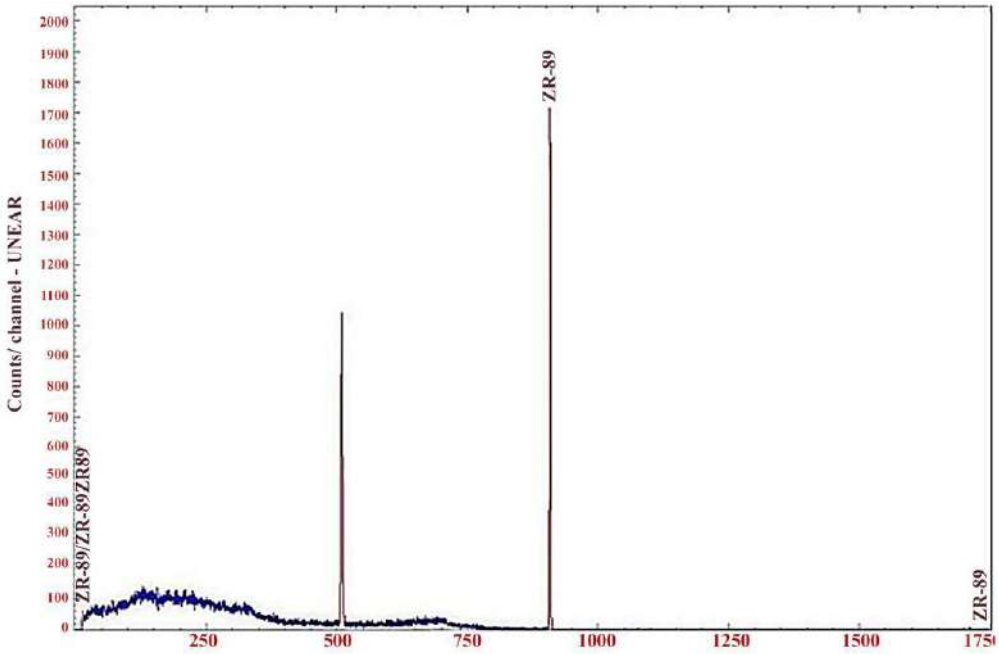

Fig. 2. Gamma spectrometry of the final [^{89}Zr] Zr-oxalate solution

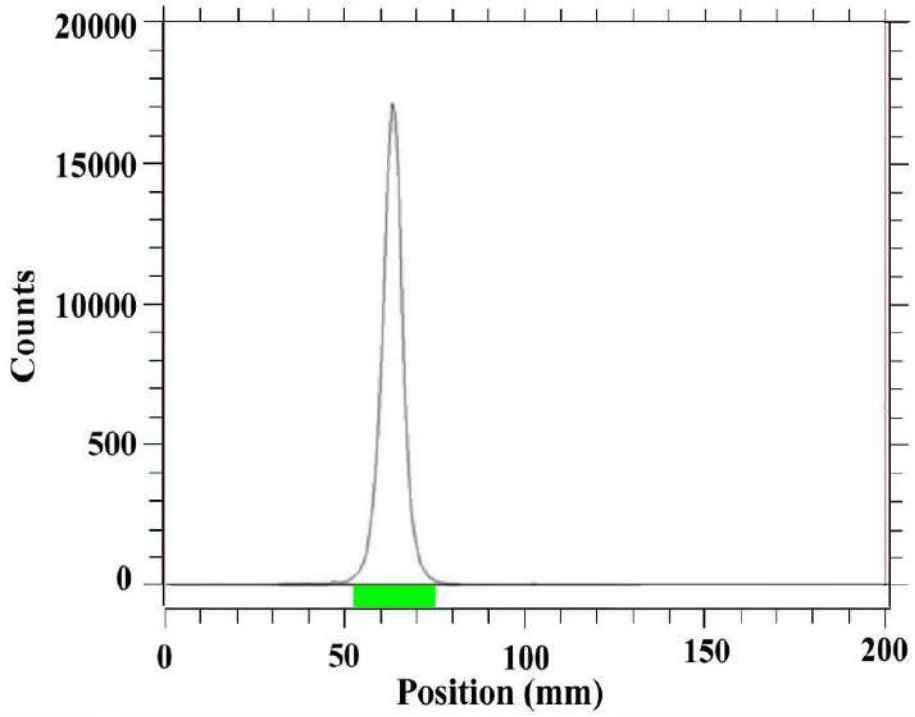

Figure 2. ITLC chromatogram of [^{89}Zr] Zr-oxalate solution using Whatman No.1 paper and 20 mM citric acid

CONCLUSION

The process of producing ^{89}Zr was carried out in this research study using a 30 MeV cyclotron through the ^{89}Y (p, n)^{89}Zr reaction. After five hours of proton bombardment of $^{89}Y_2O_3$ pellet target with a current of 25 µA, more than 3000 MBq ^{89}Zr was obtained with a radionuclidic purity above 99.99%, while the quantity of metal ions in the solution was less than 0.1 ppm. The study results confirmed that this process can be used to create high-purity ^{89}Zr-based radiopharmaceuticals with appropriate activity.

References

[1] Marengo, M., Lodi, F., Magi, S., Cicoria, G., Pancaldi, D., & Boschi, S. (2008). Assessment of radionuclidic impurities in 2-[18F] fluoro-2-deoxy-D-glucose ([18F] FDG) routine production. Applied Radiation and Isotopes, 66(3), 295-302.

[۲] Lodi, F., Rizzello, A., Trespidi, S., Di Pierro, D., Marengo, M., Farsad, M., ... & Boschi, S. (2008). Reliability and reproducibility of N-[11C] methyl-choline and L-(S-methyl-[11C]) methionine solid-phase synthesis: a useful and suitable method in clinical practice. Nuclear Medicine Communications, 29(8), 736-740.

[۳] Mohammadpour-Ghazi, F., Yousefnia, H., Zolghadri, S., Yarmohammadi, M., Alirezapour, B., Rahiminejad, A., & Aslani, G. (2023). Production of radioimmunoPET grade zirconium-89. Iranian Journal of Nuclear Medicine, 31(1), 20.

[٤] Burkhardt, C., Bühler, L., Viertl, D., & Stora, T. (2021). New isotopes for the treatment of pancreatic cancer in collaboration with CERN: a mini review. Frontiers in Medicine, 8, 674656.

[٥] Chomet, M., Van Dongen, G. A., & Vugts, D. J. (2021). State of the art in radiolabeling of antibodies with common and uncommon radiometals for preclinical and clinical immuno-PET. Bioconjugate chemistry, 32(7), 1315-1330.

[٦] Dammes, N., & Peer, D. (2020). Monoclonal antibody-based molecular imaging strategies and theranostic opportunities. Theranostics, 10(2), 938.

[۷] Firestone, R. B. (1986). Table of radioactive isotopes. Wiley.

[۸] Sadeghi, M., Enferadi, M., & Bakhtiari, M. (2012). Accelerator production of the positron emitter zirconium-89. Annals of Nuclear Energy, 41, 97-103.

[۹] Deri, M. A., Zeglis, B. M., Francesconi, L. C., & Lewis, J. S. (2013). PET imaging with 89Zr: from radiochemistry to the clinic. Nuclear medicine and biology, 40(1), 3-14.

[١٠] W Severin, G., W Engle, J., E Barnhart, T., & Nickles, R. J. (2011). 89Zr radiochemistry for positron emission tomography. Medicinal chemistry, 7(5), 389-394.

[١1] Van de Watering, F. C., Rijpkema, M., Perk, L., Brinkmann, U., Oyen, W. J., & Boerman, O. C. (2014). Zirconium-89 labeled antibodies: a new tool for molecular imaging in cancer patients. BioMed research international, 2014.

[1٢] Jauw, Y. W., Menke-van der Houven van Oordt, C. W., Hoekstra, O. S., Hendrikse, N. H., Vugts, D. J., Zijlstra, J. M., ... & van Dongen, G. A. (2016). Immuno-positron emission tomography with zirconium-89-labeled monoclonal antibodies in oncology: what can we learn from initial clinical trials?. Frontiers in pharmacology, 7, 131.

[1٣] Kasbollah, A., Eu, P., Cowell, S., & Deb, P. (2013). Review on production of 89Zr in a medical cyclotron for PET radiopharmaceuticals. Journal of nuclear medicine technology, 41(1), 35-41.

[1٤] Sharifian, M., Sadeghi, M., Alirezapour, B., Yarmohammadi, M., & Ardaneh, K. (2017). Modeling and experimental data of zirconium-89 production yield. Applied Radiation and Isotopes, 130, 206-210.

1. Currie, L. A. (2004). Quantifying uncertainty in nuclear analytical measurements.

ICNST 2024
International Conference on Nuclear Science and Technology
6- 8 MAY 2024 | Isfahan, Iran

Human absorbed dose estimation of 89Zr-Anti-EGFR complex based on tumor-bearing mice data (Paper ID : 1343)

Zolghadri S[1*]., Mohammadpour-Ghazi F[1]., Yousefnia H[1]., Karimian A[1]

[1] *Radiation Application Research School, Nuclear Science and Technology Research Institute, P.O.BOX: 14893-836, Tehran, Iran.*

Abstract

The early detection of cancer, as the most common cause of the death worldwide, can effectively reduce the mortality associated with this fatal disease. Monoclonal antibody-based radiopharmaceuticals are recognized as effective agents for the primary diagnosis of cancers. The estimation of human absorbed dose using animal data is a common first step and a prerequisite which largely satisfies the (International Commission on Radiological Protection) ICRP 62 recommendations. This research aimed to estimate the human absorbed dose of Cetuximab labeled ^{89}Zr as a new emerging radiopharmaceutical which can target several cancers overexpressed epidermal growth factor receptors (EGFRs). ^{89}Zr-Anti-EGFR complex was prepared at the optimized conditions with radiochemical purity > 99%. 100 µL (100 µCi) of the final prepared complex was injected into the EGFR expressing tumor-bearing mice. The absorbed dose of human organs was calculated according to the animals' data utilizing the radiation absorbed dose assessment resource (RADAR) and the relative mass extrapolation methods. The results demonstrated that the most remained activity in the mouse body accumulated in the tumor site. Considerable accumulation was also visible in other non-target organs like liver, kidney, spleen, and lung, similar to the other studies on the radiolabeled antibodies. The liver was received the highest absorbed dose (0.94 mGy.MBq-1). Generally, it can be concluded this radiopharmaceutical is a safe and suitable PET agent for imaging of EGFR-expressing tumors.

Keywords: ^{89}Zr, epidermal growth factor receptors, radiation absorbed dose assessment resource

INTRODUCTION

From the beginning of the 20th century, it became increasingly clear that early detection of many cancers leads to reduced metastasis, faster treatment, and a reduction in patient mortality. Monoclonal antibody(mAb) is obtained from a cell lineage created by white blood cells, and they trace back to their special parent cells. mAbs are used in the treatment of inflammatory and cancer diseases.

Cetuximab is a mAb used for treatment of metastatic colorectal and head and neck cancers. Furthermore, it can be used for the diagnosis and detection of tumors with epidermal growth factor receptors (EGFR) overexpression. So, cetuximab labeled with diagnostic radionuclides can produce effective agents for the primary diagnosis of cancers with EGFR expression.

Positron emission tomography (PET) imaging is a sensitive procedure which can give the information in cellular level. Positron-emitting radionuclides such as fluorine-18 (^{18}F) ($E_{\beta+max}$= 634 keV, half- life= 1.83 h), carbon-11 (^{11}C) ($E_{\beta+max}$= 960 keV, half- life= 20.36 min), zirconium-89 (^{89}Zr) ($E_{\beta+max}$= 902 keV, half- life= 3.27 days), gallium-68 (^{68}Ga) ($E_{\beta+max}$= 1899 keV, half- life= 67.83 min), and copper-64 (^{64}Cu) ($E_{\beta+max}$= 656 keV, half- life= 12.70 h) are widely used for PET imaging. Among the radionuclides used for PET imaging, ^{89}Zr has a good serum stability in complexation with mAbs.

The estimation of absorbed dose of a radiolabeled compound based on the animal data is the first step of developing new radiopharmaceuticals.

Also, the half-life of ^{89}Zr is long enough to matched with the half-life of mAbs, which allows for capturing images at late time points. and 89 Zr and the estimation of human absorbed dose using animal data is a common first step and a prerequisite that largely satisfies the (International Commission on Radiological Protection) ICRP 62 recommendations. This research aimed to estimate the human-absorbed dose of Cetuximab labeled ^{89}Zr as a new emerging.

EXPERIMENTAL

Quality control of ^{89}Zr

The radionuclidic purity of the final ^{89}Zr product was measured by an HPGe detector, showing the purity > 99.99 %. The radiochemical purity of the final solution was greater than 99%. Also, the chemical purity assessment demonstrated yttrium and aluminium impurities less than 0.1 ppm.

Labeling of DFO-Anti-EGFR with ^{89}Zr

Labelling of DFO-Cetuximab was performed in optimized conditions. Briefly, 1 M oxalic acid (200 µL) and 2 M Na_2CO_3 (100 µL) were added to a borosilicate vial containing 37 MBq [^{89}Zr]Zr oxalic acid. To obtained the optimized conditions, various amount of the cetuximab (0.5-2 mg) and HEPES buffer were added to the reaction vial and the radiochemical purity of the radiolabeled complex was investigated in different intervals by the RTLC (Whatman paper and 20 mM citric acid (pH=4.5). the final preparation was passed from the PD-10 column for further purification.

Stability studies of [^{89}Zr]-Anti-EGFR

The radiolabeled complex (150 µL) was added to the PBS buffer (4°C) and human serum (37°C) and stability was investigated by measuring the radiochemical purity in intervals times including 2, 4, 24, and 48 h.

Biodistribution and Imaging studies of [^{89}Zr]Zr-Anti-EGFR in the tumor-bearing mice

^{89}Zr-DFO-Anti-EGFR (100 µCi) was injected into the tumor-bearing nude mice. The mice were anatomized after injection at different intervals, and the activity of each organ was measured based on the energy peak of 908.9 keV gamma ray. The percentage of the injected dose per gram (%ID/g) for different organs was calculated by dividing the activity amount of each tissue (A) to the non-decay corrected injected activity and the mass of each organ.

$$\%ID=\frac{A}{\text{injected activity}\times\text{Tissue weight}_{(g)}}\times 100 \qquad (1)$$

Dosimetry studies

The accumulated activity in each human organ was estimated using the accumulated activity in each animal organ using Eq. 2, presented by Sparks et al.

$$\tilde{A}_{\text{human organ}}=\tilde{A}_{\text{animal organ}}\frac{\text{OrganMass}_{\text{human}}/\text{BodyMass}_{\text{human}}}{\text{OrganMass}_{\text{animal}}/\text{BodyMass}_{\text{animal}}} \qquad (2)$$

The human organ absorbed dose after ^{89}Zr-Anti-EGFR injection was estimated by the MIRD method using the dose factors (DFs) reported in OLINDA/EXM software (Version 2.1).

Results and discussion

Production and quality control of ^{89}Zr

The gamma spectrum of ^{89}Zr exhibited two primary photons that originated from ^{89}Zr. The radiochemical purity was demonstrated and it was > 99%. The ICP-OES method determined the amount of metal ions in the final solution. The total impurity level of metal ions in the final solution was less than 0.1 ppm.

Labeling optimization and stability studies

DFO-Cetuximab was labelled with ^{89}Zr at optimized conditions. Finally, the radiolabelled complex was prepared with radiochemical purity of higher than 99% by the RTLC method.

The stability of ^{89}Zr-DFO-Anti-EGFR in PBS buffer (in vitro) and freshly prepared human serum (ex vivo) was assessed for 48 h after preparation.The RCP in different intervals shows the purity higher than ٩٦% even after .h ٤٨

Dosimetry studies

The non-decay corrected percentage of injected activity per gram after injection of ^{89}Zr-DFO-Anti-EGFR has been demonstrated in Fig. 1. The equivalent absorbed dose of human organs after ^{89}Zr-DFO-Anti-EGFR injection has been indicated in Fig.2. The highest amount of the absorbed dose was observed in the liver with 0.94 mGy.MBq^{-1}.

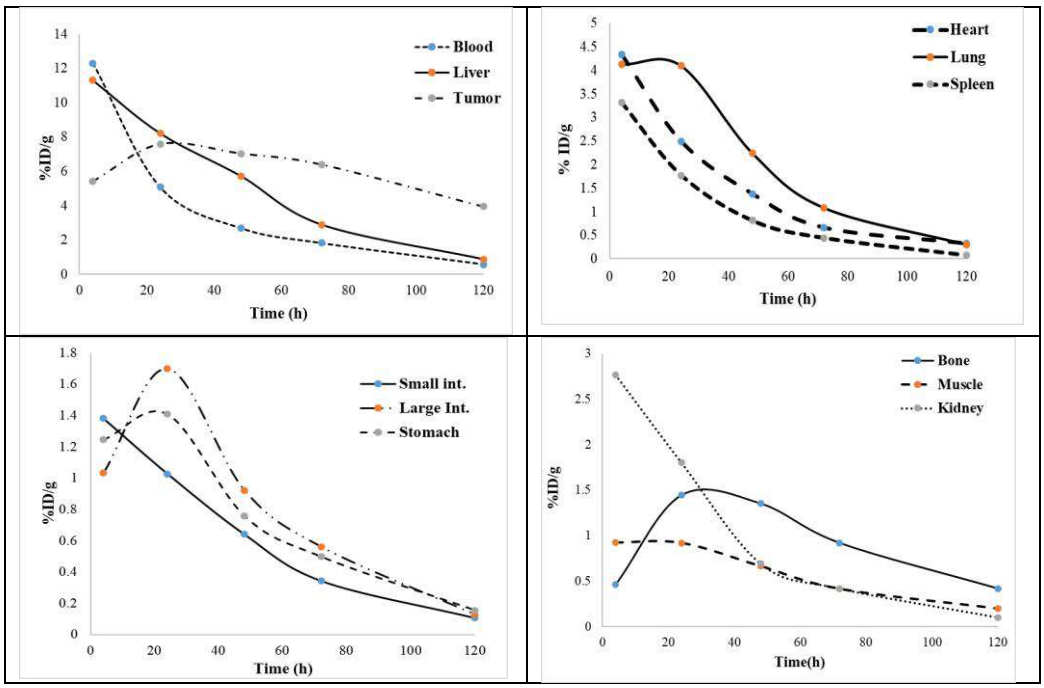

Fig.1. Non-decay corrected clearance curves of the animals' organs after injection of ^{89}Zr-DFO-nti-EGFR

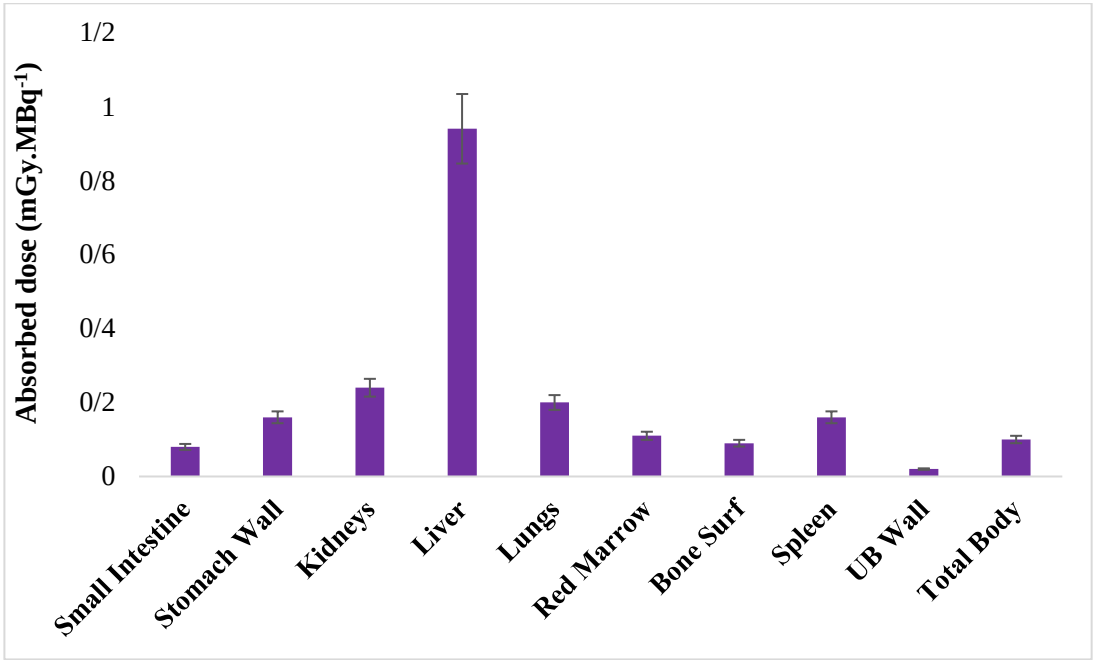

Fig.2. Equivalent absorbed dose of human organs after injection of ^{89}Zr-DFO- Anti-EGFR

Conclusions

In this study, [^{89}Zr]Zr-Anti-EGFR was prepared with radiochemical purity of >99% as an agent for PET imaging. The complex had high stability in PBS buffer and in human serum for at least 48 h. The absorbed dose of human organs was estimated based on the mice biodistribution data, showing liver is received the highest absorbed dose after injection of [^{89}Zr]Zr-Anti-EGFR and can be considered as the dose limiting organ

Acknowledgements

The authors would like to acknowledge the invaluable scientific and financial support of the International Atomic Energy Agency (IAEA) for this research under the Coordinated Research Project (Project Code; F22071, IAEA Research Contract No: 23763).

References

[1] Wender, R. C., Brawley, O. W., Fedewa, S. A., Gansler, T., & Smith, R. A. (2019). A blueprint for cancer screening and early detection: Advancing screening's contribution to cancer control. CA: a cancer journal for clinicians, 69(1), 50-79.

[٢] Waldmann, T. A. (1991). Monoclonal antibodies in diagnosis and therapy. Science, 252(5013), 1657-1662.

[1] Van Cutsem, E., Köhne, C. H., Hitre, E., Zaluski, J., Chang Chien, C. R., Makhson, A., ... & Rougier, P. (2009). Cetuximab and chemotherapy as initial treatment for metastatic colorectal cancer. New England Journal of Medicine, 360(14), 1408-1417.

[٣] Messersmith, W. A., & Ahnen, D. J. (2008). Targeting EGFR in colorectal cancer. New England Journal of Medicine, 359(17), 1834-1836.

[٤] Abrantes, A. M., Pires, A. S., Monteiro, L., Teixo, R., Neves, A. R., Tavares, N. T., ... & Botelho, M. F. (2020). Tumour functional imaging by PET. Biochimica et Biophysica Acta (BBA)-Molecular Basis of Disease, 1866(6), 165717.

[٥] Van de Watering, F. C., Rijpkema, M., Perk, L., Brinkmann, U., Oyen, W. J., & Boerman, O. C. (2014). Zirconium-89 labeled antibodies: a new tool for molecular imaging in cancer patients. BioMed research international, 2014.

[٦] Zhang, Y., Hong, H., & Cai, W. (2011). PET tracers based on Zirconium-89. Current radiopharmaceuticals, 4(2), 131-139.

[٧] Fischer, G., Seibold, U., Schirrmacher, R., Wängler, B., & Wängler, C. (2013). 89Zr, a radiometal nuclide with high potential for molecular imaging with PET: chemistry, applications and remaining challenges. Molecules, 18(6), 6469-6490.

[۸] Sparks RB, Aydogan B (1996) Comparison of the effectiveness of some common animal data scaling techniques in estimating human radiation dose, Proceedings of the Sixth International Radiopharmaceutical Dosimetry Symposium, Oak Ridge TN. Oak Ridge Associated Universities, p. 705.

[۹] Stabin MG, Sparks RB, Crowe E (2005) OLINDA/EXM: the Second-generation personal computer software for internal dose assessment in nuclear medicine. J Nucl Med. 46:1023-1027.

ICNST 2024
International Conference on Nuclear Science and Technology
6- 8 MAY 2024 | Isfahan, Iran

Recovery of residual traces of enriched cadmium from dissolved cadmium target solution by using ion exchange resins (Paper ID : 1355)

M. Mirzaei[1], S. Rasouli garmarodi[1], E. Maadi[2], S. Rajabifar [1]

[1] *Radiation Application Research School, Nuclear Science and Technology Research Institute, P.O. Box 11365-3486, Tehran, Iran*

[2] *Pars Isotope company, P.O. Box 143995-5416, Tehran, Iran*

Abstract

The use of ^{111}In in nuclear medicine for tumor imaging, labeling of lymphocytes, platelets, monoclonal antibodies and many others has been known for a long time. The most widely production route of ^{111}In is bombardment of highly enriched ^{112}Cd targets with protons relying on the nuclear reaction of ^{112}Cd (p, 2n)^{111}In. Cadmium targets for radioindium production are commonly prepared by electroplating thin layers of cadmium-112 over a copper substrate. After dissolving the surface of the irradiated cadmium target, the solution was passed through a cation exchange column, containing AG 50W-X8 resin, and indium was separated from cadmium and copper impurities by using a simple two stage procedure. In this work, a simple ion exchange procedure was developed for the recovery of remained enriched cadmium from natural copper impurity which can be used for the preparation of new targets. AG1-X8 resin was employed and several parameters which could affect the magnitude of separation of cadmium from copper, were examined. The amount of cadmium and copper ions in the final solution were measured by polarographic method. The results of experiments showed that cadmium ions were quantitatively recovered.

Keywords: enriched cadmium recovery, Indium-111, separation of cadmium from copper, ion exchange resin, nuclear medicine.

INTRODUCTION

The use of ^{111}In in diagnostic nuclear medicine has been known for a long time. It has favorable decay characteristics and emits two intense γ-rays that are in the preferred energy range for SPECT. Since its early application in labelling of blood platelets, useful for localization of inflammation, it has evolved into a tumor and receptor imaging agent when coupled to antibodies. Apart from its continued use for targeting neuroendocrine tumors, examples of ongoing new interests in clinical use of ^{111}In are still appearing [1,2]. Indium-111 can be produced by compact medical cyclotrons through the ^{111}Cd(p,n)^{111}In nuclear reaction, but a

significantly higher yield and lower impurities can be obtained through the irradiation of enriched ^{112}Cd by proton. Cadmium targets are commonly prepared by electroplating thin layers of cadmium-112 over a copper substrate [3-5]. When the enriched cadmium was used, separation of remained enriched cadmium from dissolved cadmium target solution could be important. Several chemical methods have been described for separation and purification of cadmium. Solvent extraction technique was used for separation of Cd from Cu targets [6-7]. In addition, ion-exchange resins were extensively used to separate Cd from Cu. Aardaneh et al. and Sadeghi et al. used AG1-X10 and AG1-X8 resins for the separation of nanogram amounts of cadmium (^{109}Cd) from other impurity (Ag, Cu) [8-9].

In this study, experiments were carried out to develop a more simple and efficient approach toward radiochemical separation of cadmium from copper. The ability of AG1- X8 resin was considered for this separation because cadmium forms many stable anionic complexes, at small amount of the reagent in the eluting medium.

EXPERIMENTAL

Reagents and equipment

A Metrohm 757 polarograph instrument was used for determination of cadmium and copper. The AG1-X8 strong base anion-exchange resin (100–200 mesh, Cl^- form) was supplied by Bio-Rad laboratories. All other chemicals were analytical grade and were purchased from Merck.

Ion-exchange chromatography

Indium-111 was produced by irradiating a target, made of enriched cadmium electroplated on a copper backing. The electroplated cadmium target on the copper substrate was dissolved with HBr until the cadmium layer dissolved completely. Through dissolving the target some copper is dissolved in the solution. Then the solution was passed through a cation exchange Dowex 50 WX8 resin, preconditioned by conc. HBr (Indium was adsorbed and cadmium and copper were passed). The resin was then washed by an HBr solution. In order to remove the unwanted impurities of Cd and Cu. ^{111}In was eluted with HCl 1 M as $^{111}InCl_3$. After separation of ^{111}In, the solution containing of the enriched cadmium and natural copper was evaporated almost to dryness. The residue was dissolved in HCl.

For separation of remained enriched cadmium from dissolved cadmium target solution, the Plexiglas column (a bed of 1.5 cm^2 i.d., 10 cm in length) was packed with the AG1-X8 (100–200 mesh, Cl^- form) anion-exchange resin and conditioned with 100 ml of 6 M HCl at a flow

rate of 2 ml/min using a peristaltic pump. In the second step, this solution was loaded onto a column was packed with AG1-X8 resin using the slurry-packing technique. ^{112}Cd is separated from copper on an anion-exchange column (Dowex 1×8). ^{112}Cd and copper was retained in the column. Eluant solutions of HBr, HCl and HNO_3 were used for the recovery of cadmium from the resin. The amount of cadmium and copper ions in the solutions before and after separation were measured by polarographic method. The process followed by washing resin with 50 ml of 2 M HCl for elution of copper ions.

RESULTS AND DISCUSSION

The effect of molarity of HCl on cadmium and copper adsorption on resin

As said before, after separation of ^{111}In, the solution containing of the enriched cadmium and natural copper was evaporated almost to dryness and then the residue was dissolved in HCl. The adjustment of HCl concentration is very important because the separation of various metal ions by anion exchange is based on the formation of metal chloride complex anions in HCl media and their different distribution coefficients between the resin phase. The chloride ion concentration in the aqueous phase and hence, the molarity of the hydrochloric acid has an intense influence on the separability of the complexes. The retention of ^{112}Cd and copper in different HCl concentrations were investigated. The results of experiments are shown that at low concentration of HCl adsorption of cadmium and copper on resin due to very poor formation probability of chloro complexes of Cd and Cu was negligible. 6 M HCl is the most suitable concentration because polarographic test on solution passed from column, indicates no copper and cadmium ions in that solution.

Effect of eluent type

Various eluents such as HBr, HCl and HNO_3 were examined to desorption of cadmium and copper from AG1-X8 (100–200 mesh, Cl- form) anion-exchange resin column. Based on the results, the recovery values for cadmium ions were quantitative (higher than 95%) with 1 M of HNO_3 acid and Copper was eluted with 2M HCl (20 ml) from column at the end of the separation process.

Table 1 .effect of eluent for elution of Cd

Eluent	Presence of cadmium in eluent
1 M HNO_3	Detected
2 M HNO_3	Detected
1 M HCl	Not detected
2 M HCl	Not detected
1 M HBr	Not detected
2 M HBr	Not detected

Flow rates

The influences of the flow rates of eluent solutions on the desorption of copper and cadmium were also investigated keeping other conditions constant. The effects of the flow rates of eluent solutions were quantitative in the range of 1.0–3.0 mL/min. Due to these data; all the studies were carried out at a flow rate of 2.0 mL/min.

Effect of resin weight

Different amounts of AG1-X8 (100–200 mesh, Cl- form) anion exchange resin was used for the adsorption of cadmium. The adsorption percentage increased with increasing amount of resin and the optimum weight for complete adsorption of cadmium was 5 g.

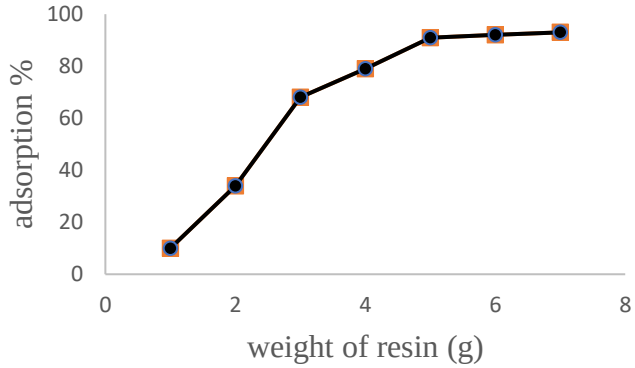

CONCLUSION

A new, simple, rapid, reliable and highly sensitive method was developed for recovery of remained enriched cadmium from dissolved cadmium target solution by using AG1-X8 anion exchange resin. ^{112}Cd can be quantitatively recovered and separated from copper with a recovery yield of greater than 95%. Thus, Cu can be washed efficiently from the column in the first stage using 2M HCl, and finally ^{112}Cd can be separated efficiently using 1 M HNO_3.

References

[1] International atomic energy agency, alternative radionuclide production with a cyclotron, No. 4, IAEA, Vienna (2021).

[2]. Cris, G., Cioroianu, N., Timaru, D., Andries, G., Căinap, C., Chis, V., Radiopharmaceuticals for PET and SPECT Imaging: A Literature Review over the Last Decade (2022) Int. J. Mol. Sci. 23: 5023.

[3]. Lahiri, S., Maiti, M., Ghosh,K., (2012) Production and separation of 111In: an important radionuclide in life sciences: a mini review, J Radioanal. Nucl. Chem, 297:309-318.

[4]. Ebrahimi, F., Jungclas, H., Happel, S., Ensinger, W., Béhé, M., Bombard, A. (2010) Application of Extraction Chromatography for the Preparation of High Purity ^{111}In for Medical Use 28:109-123.

[5]. Gao,J., Liao, Z., Liu,W.(2021) Simple and efficient method for producing high radio nuclidic purity 111In using enriched 112Cd target, Appl. Radiat. Isot., 176: 109828-109835.

[6]. Xie P., Li Z., Qu G., Zhang Y., Wang C., Zeng Y., Chen Y., (2023) The selective and sustainable separation of Cd (II) using C6MImT/[C6MIm]PF6 extractant Ecotoxicol Environ Saf 255: 114792.

[7]. Yee Lee L., Morad N., Ismail N., Talebi A., Rafatullah M., (2020) Optimization for Liquid-Liquid Extraction of Cd(II) over Cu(II) Ions from Aqueous Solutions Using Ionic Liquid Aliquat 336 with Tributyl Phosphate, Int J Mol Sci. 21(18): 6860.

[8]. Aardaneh K., Naidoo C., Steyn GF. (2008) Radiochemical separation of ^{109}Cd from a silver target. J Radioanal Nucl Chem, 276:831-834.

[9]. Sadeghi M., Karami H., Sarabadani, P., Bolourinovin, F., (2009) Separation of the no-carrier-added 109Cd from Ag, Cu and 65Zn by use of a precipitation and AG1-X8 resin, J Radioanal Nucl Chem 281:619–623.

Examining Low-Dose Radiation Therapy as a Promising Alternative for Alzheimer's Disease Treatment (Paper ID : 1358)

Bahar Shafi Naderi [1*], Seyed Mahmoud Reza Aghamiri[1]
[1]*Department of Medical Radiation Engineering, Shahid Beheshti University, P. O. Box 4716-19839, Tehran-Iran*

Abstract

Alzheimer's disease (AD) is a pressing global issue that causes progressive damage to brain cells, leading to memory and cognitive impairments in a significant portion of the global dementia population of 131.5 million individuals. Early detection is critical for effective AD treatment, as 10-15% of patients transition from the Mild cognitive impairment (MCI) stage to AD. However, the commonly prescribed cholinesterase inhibitors such as Galantamine, Rivastigmine, and Donepezil, which lack curative potential, are not recommended for MCI patients. While the modulation of neuroinflammation has been extensively studied, recent evidence suggests that Low-Dose Radiation Therapy (LD-RT) may have anti-amyloid and anti-inflammatory effects, warranting further investigation. This comprehensive review delves into the prospective utility of RT as a non-pharmacological modality for the treatment of AD, with a particular emphasis on critical parameters including cumulative dosage, fractionation schemes, and post-treatment surveillance intervals. While the efficacy of RT in all instances remains equivocal, the primary objective of this investigation is to elucidate novel radiotherapeutic strategies that have hitherto received scant attention within the realm of AD management.

Keywords: Alzheimer's Disease, Mild Cognitive Impairment, amyloid-beta aggregation, Low-Dose Radiation Therapy, non-pharmaceutical

1.Introduction

The prevalence of dementia is projected to reach 74.7 million individuals by 2030, with estimates indicating a rise to 131.5 million by 2050 as per the World Health Organization's findings [1] with this number being expected to double every 20 years . This escalation suggests a trend in which the number of cases is anticipated to double every two decades [2]. The primary pathological indicators of AD are extracellular amyloid β-peptide (Aβ) fibrils plaques as the main component of senile plaques, and intracellular neurofibrillary tangles (NFT) formed by phosphorylated tau protein [3].

The presence of specific hallmarks in certain brain regions can lead to dysfunction and inflammation, accelerating AD progression [4]. While pharmaceutical therapies are commonly

used to treat patients with AD, recent studies have also explored the potential use of RT - typically a mainstay treatment for cancer - as a novel and relatively understudied approach in the context of AD [5]. In AD treatment, the total dose administered is relatively low compared to oncological therapies, although the dose per fraction remains consistent with conventional doses ranging from 1.8 to 2 Gray (Gy) [5]. This review article explores the potential of radiotherapy as a non-pharmaceutical approach to treat AD, focusing on aspects such as total dosage, number of fractions, and follow-up duration. Although not all cases have yielded promising results, this research aims to shed light on current radiotherapy approaches that have been less discussed in the context of AD treatment. The remainder of this article is divided into three sections:

- Section 2 covers the three primary Neuropathological Hallmarks that contribute to AD, as well as the symptoms present at each stage of the disease progression.
- Section 3 categorizes various clinical (phases I, II, and III) and pre-clinical studies conducted to assess the efficacy of LDRT in Alzheimer's patients.
- Section 4 presents the conclusion drawn from the collected data.

2. Alzheimer's Disease's Neuropathological Hallmarks

Therapeutic approaches for AD can be classified into three main groups based on targeting these blood-based biomarkers: extracellular anti-amyloid beta, anti-tau protein, and anti-neuroinflammation interventions [3].

(2.1.) Amyloid-beta hypothesis

Aβ's identification as the primary component of constituent of meningovascular amyloid by George Glenner and Caine Wong in 1984 [6] was a breakthrough which marked a pivotal moment in the advancement of AD research, shedding light on its fundamental mechanism. Aβ plaques evolve through five phases in different brain regions [4]: 1. neocortex, 2. limbic regions including entorhinal cortex, subiculum, amygdala, and cingulate gyrus, 3. subcortical areas, brainstem, and 5. cerebellar cortex. In clinical settings, Aβ peptides are most frequently measured in the cerebrospinal fluid (CSF) or through brain imaging of Aβ fibrils with positron emission tomography (PET) using different Aβ-binding tracers [7].

(2.2.) Tau hypothesis

Alois Alzheimer (1907) was the first who described the NFT in the soma of cortical neurons in 51-years old women who had had a 5-year history of progressive dementia [8]. Tau is initially deposited in the medial temporal lobe memory system, spreading from the trans entorhinal cortex to the hippocampus and the Para hippocampal cortex and, finally, to other brain regions [9].

(2.3.) Neuroinflammation

A therapeutic intervention targeting Aβ clearance has shown effectiveness in reducing Aβ levels in animal and human studies but has not significantly altered the progression of Alzheimer's Disease, according to research [10]. Misfolded proteins bind to receptors on microglia and astroglia, triggering an immune response that includes inflammation [11]. Neuroinflammation is characterized by reactive astrocytes and activated microglia, which are involved in both the accumulation and removal of Aβ [12]. Neuroinflammation caused by increased expression of cytokines and activated microglia in the neurogenic zone of the dentate gyrus of the hippocampus [13]. According to the bi-phasic dose-response model [14], stimulating innate Adaptive Protection Systems (APS) helps organisms fight DNA damage from oxidative stress [15] at doses between 0.1 to 0.5 Gy, below the 3 Gy threshold in cancer radiotherapy [16]. Kaul et al. [17] found that LDRT has anti-inflammatory effects in animals and humans. RT is one of the numerous treatments known to have an anti-inflammatory effect [18]. Administering the dose in small fractions induced fewer negative effects in normal brain tissue [19].

(2.4.) Neuropsychiatric Symptoms in patients and stage-based pharmaceutical therapies

AD pathology involves synaptic and neuronal disruption [20], leading to progressive neuron loss, cognitive symptoms, including memory issues, and neuropsychiatric symptoms (NPS) [21]. Donepezil is the only acetylcholinesterase inhibitor that has been licensed for use in all stages of AD [22], other acetylcholinesterase inhibitors are: Tacrine, Rivastigmine and Galantamine. In 2024, a study led by Twitto-Greenberg et al. [23] delved into the effectiveness of utilizing a 9-cis beta-carotene (9CBC)-rich powder as a preventive treatment on two mouse models (Tg2576 and 5xFAD) of AD out of three. The study found improvements in memory and decreased Alzheimer's markers. In 2020, 441 drugs were in development for AD, targeting

Aβ (n = 72), followed by inflammation (n = 56), neurotransmitters and receptors (n = 49), and tau (n = 44) [24]. Some of the Food and Drug Administration (FDA)-approved pharmaceutical strategies for managing AD have been organized in Table 1. Based on the collected data, there is no clear correlation between the increase in administered dosage and the improvement in cognitive function among patients.

3. Case Study Reports of The Potential Therapeutic Effects of Low-Dose Ionizing Radiation in Alzheimer's Disease

The discovery of X-rays was followed by a variety of attempts to treat infectious diseases and various other non-cancer diseases with ionizing radiation [25]. RT, one of the main treatments for cancer, has

been recently studied in the context of AD. By disrupting hydrogen bonds [26] and depolymerizing radiation-sensitive molecules like glycosaminoglycan, LDRT induces an anti-amyloid effect on the beta-sheet structure of amyloid fibrils.

Table1. Some of the FDA-approved pharmaceutical strategies for managing Alzheimer's disease

Drug Name	**Drug Type**	**Number of Participants**			**Administrated Dose**	**Mechanism of Action**	**(Possible) Side Effects**	**Study Duration (month)**	**Results**	**Authors (year)**
		Treatment	Placebo	Total						
Aducanumab	Disease modifying treatment	1120	548	1638	3 or 6 (LD receivers) or 10 (HD receivers) mg/Kg*	Targets Beta-Amyloid	Headache and fall, dizziness, ARIA	17.95	71% decrease in amyloid PET SUVR	Budd Haeberlein et al. (2022) [27]
Lecanemab	Disease modifying treatment	898	897	1795	10 mg/Kg receivers	Targets Beta-Amyloid	Headache and fall, dizziness, ARIA	18	59.1% decrease in Centoloid brain amyloid burden	Van Dyck et al. (2023) [28]
Donepezil	Cognitive symptoms treatment	31	29	60	5 mg/day and 10 mg/day after 4 weeks	Cholinesterase Inhibitor	Diarrhea, nausea, headache, dizziness	6	Improvement in dual task gait speed and DTC	Montero-Odasso et al. (2019) [29]

Abbreviations: LD, Low Dose Receivers; HD, High Dose Receivers; SUVR, Standardized Uptake Value Ratio; DTC, Dual-task cost; *Kg of Body Weigh

(3.1.) Preclinical studies: Animal models and in-vitro investigations

In their study [Kim et al., 30], findings from in-vivo and in-vitro investigations indicate that low dose ionizing radiation (LDIR) not only targets pathogenic proteins like Aβ (in comparison to sham-treated 5XFAD mice, LDIR-treated 5XFAD mice exhibited significant decrease in Aβ-positive area in both cerebral cortex and hippocampus), but also induces a shift in microglial cell phenotype. This shift leads to a decrease in pro-inflammatory cytokines and an increase in anti-inflammatory cytokines within the 5xFAD mice brain tissue treated with LDRT, along with improvements in learning and memory skills [30]. Since 2016, several studies on LDRT for subjects with AD and animal models of AD were reported from several groups [31]. In their study published in [33, 34], Marples et al. discovered a substantial decrease in both the quantity and size of amyloid-beta plaques in male mice following head-only X-ray (160 kVp) with dose rate of 0.69 Gy/min fractionated irradiation. The reduction levels were as follows: 29.3% with a single 5Gy dose, 45.7% with a single 10Gy dose, 56.9% with a single 15 Gy dose, 50.6% with fractionated 1Gy daily for 10 days, and an impressive 72% with fractionated 2Gy daily for 10 days. Notably, significant differences were observed between the sham-RT group (group 1) and the group exposed to five fractions of 2Gy radiation (group 2) eight weeks post-treatment, with statistically significant results ($p = 0.002$ for reduced numbers, $p = 0.01$ for reduced plaque size). O'Banion et al. [18] discovered that male APP/PS1 mice exposed to 1 Gy 56Fe irradiation exhibited more severe cognitive impairment and reduced Aβ plaque deposition compared to non-irradiated APP/PS1 mice. Wilson and colleagues [13] observed a 20% reduction in Tau tangles and a significant decrease in amyloid-beta burden in the right side of the murine model at the study endpoint, which was 8 weeks after daily exposure to 5 Gy x 2 using a 2-beam treatment plan. The treatment beams were delivered using a variable collimator with size adjustments for each mouse [13]. However, another study [35] found no significant impact on the accumulation of amyloid-beta or tau. In their study, Yang et al. [36] examined the effectiveness of moderate total dose

in comparison to a conventional dose per fraction (5 x 2Gy), as well as a low single dose (5 x 0.6 Gy), in 5xFAD mice models. The researchers discovered a decrease in the size of Aβ, without any alterations in the quantity of them. These findings indicate anti-inflammatory effects through cytokine modifications. In their study [37], Kim et al. studied the effects of low-moderate dose ionizing radiation (LMDRI) on 5xFAD mouse models by giving them a total radiation dose of 9Gy. They found that while there was no notable change in Aβ

accumulation compared to the control group, there was improvement in synaptic degeneration, neuronal loss, and neuroinflammation in the hippocampal formation and cerebral cortex. A study conducted by Bellone et al. aimed to test the hypothesis that astronauts exposed to charged particles could experience neurological deficits similar to age-related neurodegenerative diseases [20]. They found that mice with Alzheimer's disease showed temporary cognitive deficits three months after exposure to 0.1 Gy of gamma radiation.

(3.2.) Clinical Studies: Observational Trials

The initial first case-reported article by Cuttler et al. In 2016 [16], highlighting the positive impact of 11 LDRT on an 81-year-old AD woman, along with subsequent follow-up articles on 2017 [38], 2018 [39] indicates its beneficial effects. A consequent pilot clinical phase I trial (NCT03597360) study on four participants on 2021 was conducted in which each participant received standard CT brain scans, performed on a General Electric LightSpeed VCT 64 detector scanner with helical mode and Slice thickness of 2.5 mm and three of them showed immediate recovery in qualitative terms, especially after the 0.08 Gy CT. In order to evaluate neurocognitive capacity, behavioral symptoms, and functional ability, this study incorporated three quantitative outcome measures [40]: The Severe Impairment Battery (SIB) [41], The Cohen-Mansfield Agitation Index (CMAI) [42] and AD Functional. In 2023, Rogers and colleagues [44] documented a positive change in mini-mental state examination (second edition) scores for three out of five patients, alongside an unchanged score for one patient, twelve months after undergoing low-dose whole brain radiation therapy (LD-WBRT) at a dosage of 2Gy per fraction over five days. In 2023, Kim et al. [5] conducted a study examining the efficacy of LDRT on five female patients diagnosed with amyloid plaques via amyloid positron emission tomography at baseline. Additionally, PET-CT scans, conducted with 379.5±12.7 Mega Becquerel (MBq) of 18F-florapanol acquired 30 to 60 minutes post-injection, and the post-treatment cognitive function tests revealed a temporary neurological improvement in 20% of patients after a 6-month follow-up. Since 2023, Kim et al. [42] have undertaken a phase II, multicenter, prospective, single-blinded, randomized controlled trial involving 60 patients who were randomly assigned to three groups: experimental I (24 cGy/6 fractions), experimental II (300 cGy/6 fractions), or a sham RT group (0 cGy/6 fractions). Mentioned research [5] initiative seeks fresh candidates with a history of prolonged use of traditional Alzheimer's medications exceeding a span of three months, alongside documented

amyloid aggregation within the cerebral regions as evidenced by positron emission tomography scans. The most recent findings, incorporating investigations involving low dose radiation therapy interventions, are consolidated within Table 2 for reference.

4. Conclusion

Contemporary pharmacotherapies for AD predominantly confer transitory amelioration of symptoms without halting the inexorable progression of the ailment, while concurrently engendering adverse reactions as documented in antecedent inquiries. Despite an extensive array of clinical assessments appraising pharmaceutical interventions, a substantial proportion have culminated in disillusionment, propelling an evaluation of LDRT as a non-pharmacological substitute within the quest for more efficacious treatments for Alzheimer's affliction. This scrutiny posits that through amalgamating extant dementia remedies with judicious LDRT administration as an established and innocuous medical modality, a heightened magnitude of therapeutic outcomes may be achievable, notwithstanding the imperative need for further empirical inquiry to elucidate enigmatic experimental outcomes and ascertain the efficacy and safety profile of this therapeutic regimen.

ICNST 2024
International Conference on Nuclear Science and Technology
6- 8 MAY 2024 | Isfahan, Iran

Exploring the Efficacy of Deep Learning Techniques in Comparing the Diagnostic Accuracy of Fluorine-18-Labeled (AV-45 and FDG) PET and MRI Scans for MCI to AD Conversion (Paper ID : 1360)

Bahar Shafi Naderi[1*], Seyed Mahmoud Reza Aghamiri[1]

[1]*Department of Medical Radiation Engineering, Shahid Beheshti University, Tehran, Iran*

Abstract

Alzheimer's Disease (AD) is a prevalent form of dementia, accounting for 60-80% of all neurodegenerative cases. AD leads to a progressive decline in cognitive abilities and functioning. Neuroimaging biomarkers offer valuable insights into the structural and functional aspects of the brain affected by this disease. Magnetic Resonance Imaging (MRI) reveals severe shrinkage in the hippocampus and cerebral cortex, along with ventricle enlargement. Positron Emission Tomography (PET) scans provide biochemical data such as glucose metabolism abnormalities, neuro-inflammation, and tau-protein aggregation.

This study aims to compare the accuracy of ^{18}F-labelled PET scans (Florbetapir and Fluorodeoxyglucose) with MPRAGE MRI scans in the early diagnosis of AD. Accurate diagnosis plays a crucial role in assessing the progression from Mild Cognitive Impairment (MCI) to AD. We utilized a dataset of 35 patients (17: MCI, 18:AD) obtained from the open-source Alzheimer's Disease Neuroimaging Initiative (ADNI) database, consisting of 18-fluorodeoxyglucose (FDG), 18F-florbetapir (AV-45) and MRI scans.

We utilized the Free surfer software to pre-process the images, and employed the U-Net, a Deep Learning architecture, to automatically segment the Region of Interest (ROIs) highlighting significant shrinkage in the hippocampus, an extension of the temporal lobe cortex. To address the issue of vanishing gradients in very deep neural networks, we employed the Residual Network (Res-Net) architecture.

Based on the findings, we achieved an accuracy achieved an accuracy of 98.3% for MRI data, indicating that it is a more precise modality for distinguishing between AD and MCI when compared to 18-F-FDG PET (93.5% accuracy) and ^{18}F-AV45 PET (89.8% accuracy). This research emphasizes the significance of MRI scans as an effective approach in early AD diagnosis for selecting appropriate assessment methods for patients with MCI.

Keywords: Alzheimer's Disease, Magnetic Resonance Imaging, Positron Emission Tomography, 18F-FDG, 18F-AV45, Deep Learning

Introduction

Early detection of AD is crucial for effective treatment and slowing disease progression. The neuropathological hallmarks of AD, including abnormal levels of amyloid plaques and tau protein accumulation in the cerebrospinal fluid and changes in brain volume, are believed to begin forming approximately 20 years (for amyloid beta build-up) and 15 years (for tau protein accumulation) before clinical symptoms appear. As a result, there is a widely acknowledged understanding that to enhance patients' chances of survival, it is imperative to provide accurate treatment and intervention for AD prior to the manifestation of advanced symptoms; in this pursuit, deep learning can assist us. It is important to note that not all individuals with MCI progress to AD, as only about 10-15% of MCI cases convert to AD per year [1, 2]. Although MRI does not have the capability to specifically identify molecules or directly detect histopathological markers of diseases, specialists often turn to FDG PET for this purpose after initially diagnosing a condition due to the difficulty in establishing a direct link between hypo-metabolism and AD pathology [3] which measures the decline in glucose concentration in the temporoparietal association cortex [4]. Clinical trials typically
use amyloid PET imaging, but PET scanners and amyloid tracers are not widely available geographically [5]. In preclinical stages, MRI is commonly used to visualize cerebral atrophy [6]. Due to the lack of contrast, small volume, and blurry edge outline in MRI images of this part of the brain's gray matter structure, accurate segmentation is challenging [7]. The pathology of AD is characterized by the disturbance of synaptic and neuronal function, resulting in the gradual decline of neurons and brain volume. Individuals with mild MCI and mild AD demonstrate decreased hippocampal volumes in comparison to controls. Furthermore, those with AD display even smaller hippocampal volumes compared to those with MCI.

Two representative axial plane MRI image from the 82.0 Male Normal Control (NC) (Left) and 84.9-year Male AD patient (Right) are shown in Fig.1. El-Assy et al. [8] introduced a unique methodology that utilizes two simplified Convolutional Neural Network (CNN) models connected in the classification layer. Each model features different pooling layers and filter sizes. Their research showed that reducing the filter sizes can significantly enhance the classification accuracy from 95% to 99.13%. This enhancement enables the models to better acquire task-specific features and leverage each other's strengths effectively. In another study, Soujanya et al. [9] evaluated the performance of four transfer learning CNN models on a Kaggle archive dataset containing 6400 MRI scans across four different classes. The models

tested were VGG-19 (accuracy: 89%), Inception-V3 (accuracy: 89%), ResNet-50 (accuracy: 68%), and Xception (accuracy: 87%). SUN et al. [10] (2020) introduced a technique that combines multi-order 3D U-NET and CNN on MRI images sourced from the Kaggle database, achieving an impressive accuracy of 98.45%. The image enhancement part includes median filtering and Histogram equalization processing, and the scale transformation includes removing excessive background image volume outside the brain tissue and pruning the image to a pre-selected size for network input 112 × 96 × 96. However, this model is hindered by high memory consumption and slow processing speed. Choi et al. [11] utilized a straight-forward CNN+Softmax as a first use of a voxel-based 3D CNN on multi-modal (FDG PET, AV-45 or 18F-Florebetapir) images without any requirement of feature extraction methods for quantification using auto-encoders or Boltzmann machine. The algorithm was implemented on 492 ADNI subjects, with co-registered FDG and AV-45 PET images and cortical regions segmented using Free surfer software. The detection accuracy for future cognitive decline was 94.2% for MCI converters versus non-converters, and 96% for distinguishing AD from NC. Xiao et al. [7] developed a novel SC-Net derived from U-Net, utilizing complete MRI images as training samples rather than cropped ones. This enhancement led to improved accuracy in hippocampal structural segmentation by preserving the original information of the hippocampus, resulting in a Dice Similarity Coefficient of 0.885.

In this paper, we focus on two primary objectives. Firstly, we leverage transfer learning and tackle the challenge of diminishing gradients in deep neural networks by employing the Residual Network architecture. We make use of this architecture as the foundation for the U-net encoder,

implementing up sampling in the decoder to improve segmentation of the hippocampal region of the brain. Secondly, we present an End-to-End approach for AD vs. MCI classification, with the goal of enhancing customized therapy and comparing them through demonstrating the efficacy of ^{18}F-AV45 PET/^{18}F-FDG PET/T1W MRI modalities individually. The organization of this paper is as follows:

-Experimental section provides an explanation of the materials and methods used, including data acquisition, data pre-processing, and the introduction of our proposed models for accomplishing two tasks related to AD diagnosis.

-Results and Discussion section showcases the experimental results, and finally

-Conclusion section presents the conclusion of our work.

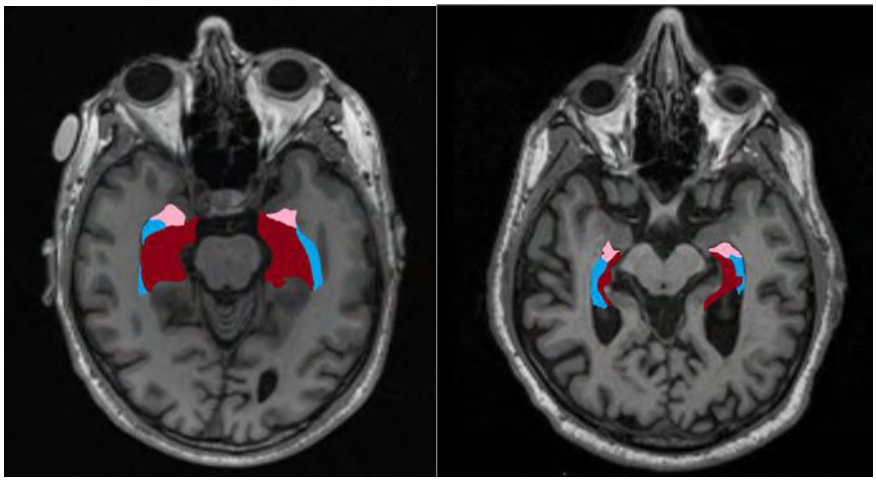

Fig.1. Two representative axial plane MRI image from the 82.0 Male Normal Control (NC) (Left) and 84.9-year Male AD patient (Right), enlargement in ventricles (blue) and hippocampus volume (red) and Amygdala (pink) shrinkage is evidently observed.

Experimental

I. Data Acquisition

We utilized a combined 3D NIfTI format dataset of 35 patients (17: MCI, 18:AD) from three modalities: 1) ^{18}F-FDG PET, 2) ^{18}F-AV45 PET and 3) MRI scans obtained from the open-source Alzheimer's Disease Neuroimaging Initiative (ADNI: https://adni.loni.usc.edu/) database [12]· FDG PET images were acquired 30 to 60 min and AV-45 PET images were acquired 50 to 70 min after the injection.

The ADNI was launched in 2003 as a public-private partnership, by the National Institute on Aging (NIA), the National Institute of Biomedical Imaging and Bioengineering (NIBIB), and the Food and Drug Administration (FDA), as a 5-year public private partnership led by Principal Investigator Michael W. Weiner,MD. The primary goal of ADNI has been to test whether serial MRI, PET, other biological markers, and clinical and neuropsychological assessment can be combined to measure the progression of MCI and early AD. We divided our data into three classes: 75% for training, 15% for evaluation and 10% for testing.

Patients are classified into MCI (Mini-Mental State Examination (MMSE) [13] scores between 24 and 30, (Clinical Dementia Rating) CDR [14] of 0.5) and AD (MMSE scores between 20 and 26, CDR of 0.5 or 1.0) based on their MMSE and CDR scores.

II. Data Pre-Processing

Image pre-processing, considered as a pivotal stage in medical image analysis, encompasses various image processing tasks aimed at converting raw data from acquired image scans into a suitable format for further utilization. Unreliable data can significantly hinder accuracy and potentially generate false predictions [15], therefore pre-processing plays a crucial role in enhancing the quality of biomarkers which prevent errors in experimental findings stemming. To ensure precise and meaningful outcomes, data must undergo pre-processing procedures before these biomarkers can be effectively applied [16].

Free Surfer2 [17] is a software package for the analysis and visualization of neuroimaging data from cross-sectional and longitudinal studies. It is developed by the Laboratory for Computational Neuroimaging at the Martinos Center for Biomedical Imaging. The ground truth was generated by Free surfer software, specifically applying Motion Correction and conform, non-uniformity normalization, Talairach transform computation, Intensity normalization, and skull stripping to eliminate noise for improving the model performance via the recon-all command. The pre-processing duration for each individual image ranged from 6 to 12 hours. 3D to 2D Image conversion and resized to 224 x 224 pixels was applied. Since we have small datasets, we implemented the data augmentation technique [18] during training our data, which helps us to increase the number of samples in our training dataset and to overcome the possible over-fitting problems. We generated augmented images from original slices thorough six techniques: Image segmentation was applied afterwards and resulting images was fed into ResNet-50 networks.

III. Medical Image Segmentation and Feature extraction with U-network (U-net)

In this research, we modified U-Net as whole brain extracted features lack distinctiveness and do not aid in diagnosis, potentially impacting the accuracy of AD detection. U-Net was proposed by Olaf Ranneberger et al. [19] for fast and precise biomedical image segmentation. Considering hippocampal atrophy as the most clinically useful marker for AD progression, U-Net creates an encoder-decoder structure for semantic segmentation using the concept of Fully Convolution Network (FCN) to restore image size and features [7]. By extracting feature information at each layer, the encoder reduces the spatial dimension, and the decoder gradually restores the target details and spatial dimension in accordance with the feature information [7], this can help the model achieve better accuracy by honing in on relevant features and patterns within the hippocampus that may be important for the disease analysis. To additionally enhance the feature data for classification, a characteristic vector is created on the basis of combining

the pixel intensity values of feature segmented images [25], and the mentioned characteristic vector is fed into a ResNet-50 classifier as detailed in following section. A U-Net construction is depicted in Fig.2.

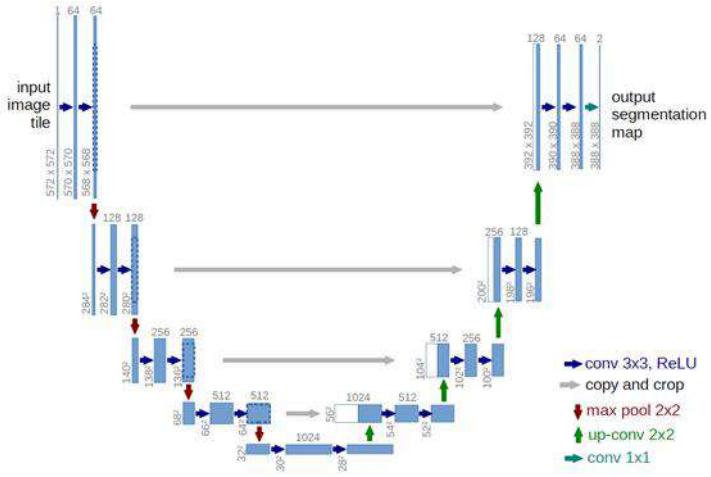

Fig. 2. U-net Architecture

IV. Medical Image Classification and Prediction with ResNet-50

Feature extraction in deep learning methods is particularly valuable when working with small datasets. To address challenges such as the need for extensive training data and appropriate optimization techniques in very deep neural networks, we utilized a pre-trained CNN model, ResNet-50, which features 50 layers including convolutional, pooling, and fully connected layers with residual blocks as its core innovation. This model was initially trained on the ImageNet dataset for binary classification but has been successfully applied to various other datasets. The Residual Network (ResNet) was introduced by He et al. [24] In 2015. Within a residual block, the input undergoes a sequence of convolutional layers, with the resulting output being combined with the original input before being processed through a non-linear activation function (Fig.3). For our study, we utilized Python 3.0 and the Google Collaboratory Pro platform for training and validating the classifier.

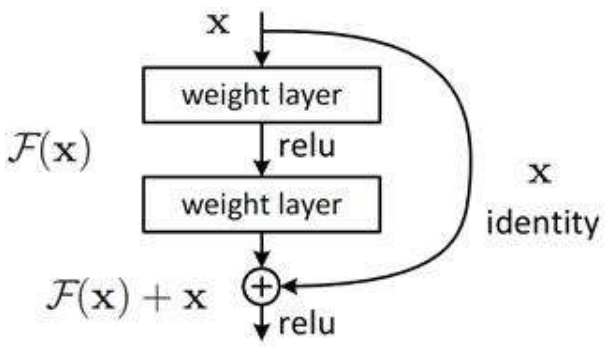

Fig. 3. Schematic of a residual block of the residual networ

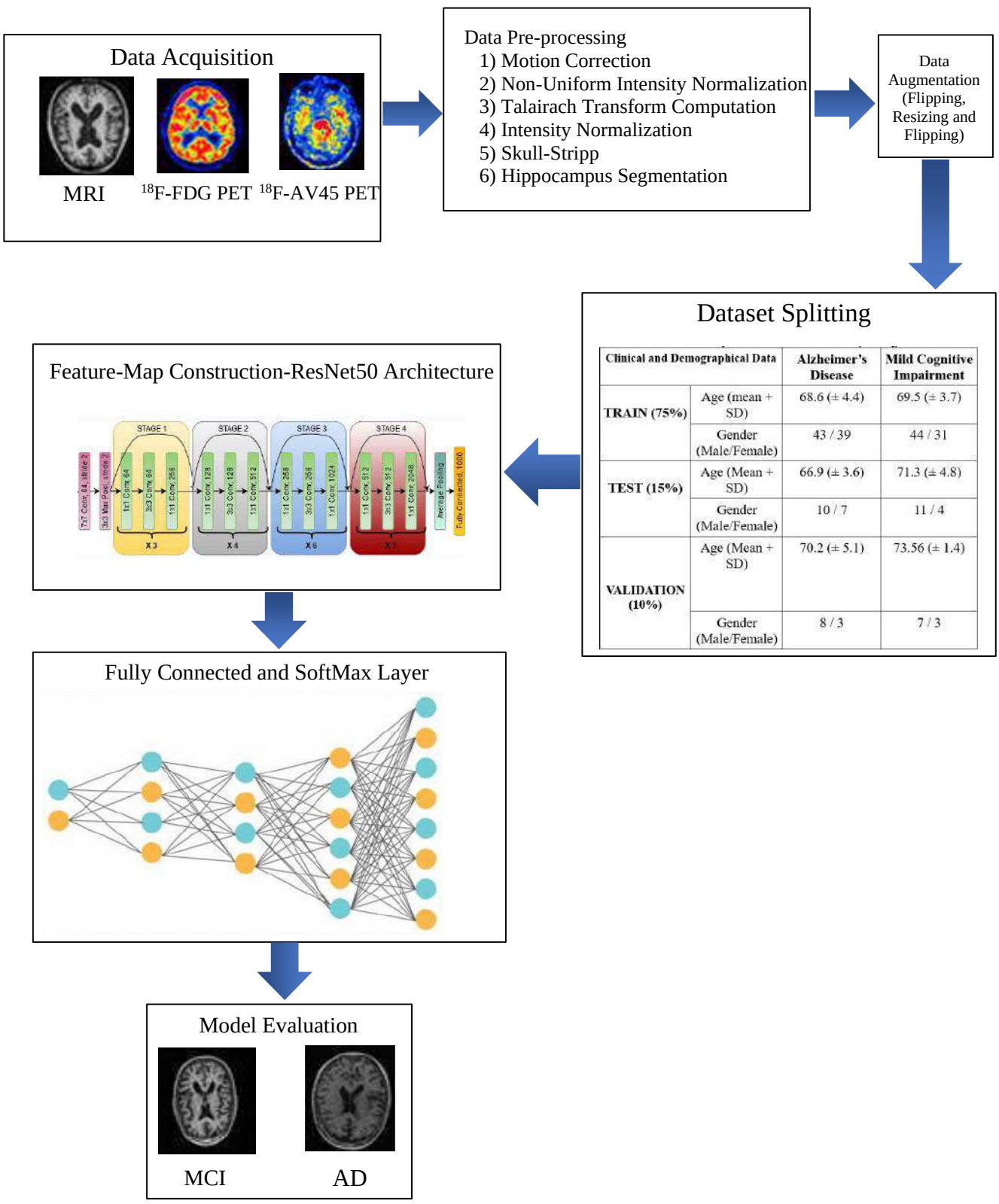

Clinical and Demographical Data		Alzheimer's Disease	Mild Cognitive Impairment
TRAIN (75%)	Age (mean + SD)	68.6 (± 4.4)	69.5 (± 3.7)
	Gender (Male/Female)	43 / 39	44 / 31
TEST (15%)	Age (Mean + SD)	66.9 (± 3.6)	71.3 (± 4.8)
	Gender (Male/Female)	10 / 7	11 / 4
VALIDATION (10%)	Age (Mean + SD)	70.2 (± 5.1)	73.56 (± 1.4)
	Gender (Male/Female)	8 / 3	7 / 3

Fig.4. Schematic Representation of proposed Model Framework

Results and Discussion

This study capitalizes on the utilization of segmented hippocampal Regions of Interest (ROIs) as input for the pre-trained transfer model ResNet50 in place of the holistic MRI image. This approach has shown enhanced classification efficacy as the distinctive attributes specific to each segmented MRI region serve as robust features for the labeling process. The initial step involved employing UNet to extract pertinent features from the pre-processed Alzheimer's Disease Neuroimaging Initiative (ADNI) dataset, followed by the utilization of ResNet50 for the classification of Mild Cognitive Impairment (MCI) and Alzheimer's Disease (AD) classes. Notably, differentiating between AD and MCI patients holds paramount significance for early identification and intervention. The ability to pinpoint individuals with MCI at an elevated risk of AD progression enables timely implementation of treatment and management strategies aimed at potentially decelerating disease advancement. Comparative analyses have demonstrated that the proposed UNet+ResNet50 model exhibits superior classification accuracy when juxtaposed against CNN-based architectures such as VGG19, InceptionV3, and Xception. Table 1 displays a comparison between Unet semantic segmentation of the hippocampal region of the brain and state-of-the-art studies utilizing the Dice Similarity Coefficient (DSC) parameter, while Table 2 outlines the results of comparing our classification outcomes with other similar studies using the accuracy parameter. DSC evaluates the spatial overlap between two segmentations (Equation 1), while Accuracy measures the proportion of correct predictions made by a model out of its total predictions (Equation 2). These criteria are defined as follows: True Positive (TP) occurs when a pixel is accurately identified as belonging to the hippocampus region, True Negative (TN) is when a pixel is correctly classified as not belonging to the hippocampus region, False Positive (FP) is when a pixel is incorrectly assigned as belonging to hippocampus region, and False Negative (FN) is when a pixel is incorrectly assigned as not belonging to hippocampus region.

$$\text{Dice similarity coefficient (DSC)} = \frac{2TP}{2TP+FP+FN} \quad (1)$$

$$\text{Accuracy} = \frac{TP+TN}{TP+TN+FP+FN} \quad (2)$$

Table 1. Comparing the Segmentation Performance to other studies

Authors	Database	Data Quantity	Modality	ROI	DSC
Pasini et al. [20] (2022)	Institutional database	102	^{18}F-FDG PET	Right Temporal Lobe	76 (±0.10)
				Left Temporal Lobe	77 (±0.10)
Jia et al. [21] (2020)	ADNI	146	MRI	Hippocampus	89.15
Sun et al. [10] (2024)	Kaggle [19]	6400	MRI	Hippocampus	98.45
Xiao et al. [7] (2023)	ADNI	240	MRI	Hippocampus	88.5
Toh et al. [22] (2023)	HarP	135	MRI	Hippocampus	85.41
Proposed work	ADNI	210	MRI	Hippocampus	98.6

Conclusion

Due to the intricate nature of the automatic segmentation of the hippocampus, which is attributed to the low signal contrast, small structural size, and inadequate image resolution [7], in this study we utilized a U-net architecture to effectively segment this specific area of the brain.

Our model outperformed previous models, achieving a Dice Similarity Coefficient (DSC) of 98.6%. In the next phase of our research, we assessed the predictive accuracy of disease progression using three modalities MRI, 18F-FDG, and 18F-florbetapir PET. Our findings revealed that MRI had the highest accuracy at 98.3%, followed by 18F-FDG and 18F-florbetapir PET at 93.5% and 89.8% respectively. MRI emerged as the most effective tool for forecasting the transition from MCI to AD, aiding experts in efficiently preventing and tailoring personalized treatments for AD by evaluating the morphological volume of relevant hippocampal regions while excluding non-informative areas.

In future endeavors, the model's precision can be enhanced through fine-tuning before the classification stage in post-processing. Moreover, given MRI's proven accuracy in identifying cortical and subcortical grey matter, white matter, and cerebrospinal fluid volume atrophy linked to AD pathology, incorporating segmentation of these regions into the findings is recommended.

References

[1] Guzmán-Vélez, E., Diez, I., Schoemaker, D., Pardilla-Delgado, E., Vila-Castelar, C., Fox-Fuller, J. T., ... & Quiroz, Y. T. (**2022**). Amyloid-β and tau pathologies relate to distinctive brain dysconnectomics in preclinical autosomal-dominant Alzheimer's disease. Proceedings of the National Academy of Sciences, 119(15), e2113641119.

[2] Goenka, N., & Tiwari, S. (**2021**). Deep learning for Alzheimer prediction using brain biomarkers. Artificial Intelligence Review, 54(7), 4827-4871.

[3] Dubois, B., Hampel, H., Feldman, H. H., Scheltens, P., Aisen, P., Andrieu, S., ... & Washington, D. C. (**2016**). Preclinical Alzheimer's disease: definition, natural history, and diagnostic criteria. Alzheimer's & Dementia, 12(3), 292-323.

[4] Khatri, U., & Kwon, G. R. (**2024**). RMTnet: Recurrence meet Transformer for Alzheimer's disease diagnosis using FDG-PET. Age, 79(6.13), 77-30.

[5] Heidebrink, J. L., & Paulson, H. L. (**2024**). Lessons Learned from Approval of Aducanumab for Alzheimer's Disease. Annual Review of Medicine, 75, 99-111.

[6] Johnson, K. A., Fox, N. C., Sperling, R. A., & Klunk, W. E. (**2012**). Brain imaging in Alzheimer disease. Cold Spring Harbor perspectives in medicine, 2(4), a006213.

[7] Xiao, X., Pan, D., & Yuan, J. SC-Net: A New U-Net Network for Hippocampus Segmentation.

[8] El-Assy, A. M., Amer, H. M., Ibrahim, H. M., & Mohamed, M. A. (**2024**). A novel CNN architecture for accurate early detection and classification of Alzheimer's disease using MRI data. Scientific Reports, 14(1), 3463.

[9] Soujanya, R., & Maganti, S. (**2024**). Deep Transfer Learning Models for Alzheimer's Disease Classification using MRI Images. International Journal of Intelligent Systems and Applications in Engineering, 12(1), 95-101.

[10] Ningsen, S. U. N., Yuan, Y. U. A. N., & Lanhua ZHANG, Z. H. (**2024**). Convolutional Neural Network Image Segmentation of Alzheimer's Disease Based on Multi-Order 3D U-NET.

[11] Choi, H., Jin, K. H., & Alzheimer's Disease Neuroimaging Initiative. (**2018**). Predicting cognitive decline with deep learning of brain metabolism and amyloid imaging. Behavioural brain research, 344, 103-109.

[12] All ADNI studies are searchable at: https://adni.loni.usc.edu/news-publications/publications/

For up-to-date information, see www.adni-info.org.

[13] Arevalo-Rodriguez, I., Smailagic, N., i Figuls, M. R., Ciapponi, A., Sanchez-Perez, E., Giannakou, A., ... & Cullum, S. (**2015**). Mini-Mental State Examination (MMSE) for the detection of Alzheimer's disease and other dementias in people with mild cognitive impairment (MCI). Cochrane Database of Systematic Reviews, (3).

[14] Morris, J. C. (**1997**). Clinical dementia rating: a reliable and valid diagnostic and staging measure for dementia of the Alzheimer type. International psychogeriatrics, 9(S1), 173-176.

[15] Maharana, K., Mondal, S., & Nemade, B. (**2022**). A review: Data pre-processing and data augmentation techniques. Global Transitions Proceedings, 3(1), 91-99.

[16] Shukla, A., Tiwari, R., & Tiwari, S. (**2023**). Review on alzheimer disease detection methods: Automatic pipelines and machine learning techniques. Sci, 5(1), 13.

[17] Fischl, B. (2012). FreeSurfer. Neuroimage, 62(2), 774-781.

[18] Van Dyk, D. A., & Meng, X. L. (**2001**). The art of data augmentation. Journal of Computational and Graphical Statistics, 10(1), 1-50.

[19] Ronneberger, O., Fischer, P., & Brox, T. (**2015**). U-net: Convolutional networks for biomedical image segmentation. In Medical Image Computing and Computer-Assisted Intervention–MICCAI 2015: 18th International Conference, Munich, Germany, October 5-9, 2015, Proceedings, Part III 18 (pp. 234-241). Springer International Publishing.

[20] Pasini, E., Genovesi, D., Rossi, C., De Santi, L. A., Positano, V., Giorgetti, A., & Santarelli, M. F. (**2022**). Convolution Neural Networks for the Automatic Segmentation of 18F-FDG PET Brain as an Aid to Alzheimer's Disease Diagnosis. Electronics, 11(14), 2260.

[21] Jia, C., Jia, C., & Yu, H. (**2020**, July). Combining Residual learning and U-Net for Hippocampus Segmentation of Brain MRI Volume Image. In Proceedings of the 2020 4th International Conference on Deep Learning Technologies (pp. 94-98).

[22] Toh, Y. S., & Hargreaves, C. A. (**2023**). Analysis of 2D and 3D Convolution Models for Volumetric Segmentation of the Human Hippocampus. Big Data and Cognitive Computing, 7(2), 82.

[23] Sachin Kumar, Sourabh Shastri. Alzheimer MRI Preprocessed Dataset. Kaggle. **2022**.
https://www.kaggle.com/datasets/sachinkumar413/alzheimer-mri-dataset;
https://www.kaggle.com/datasets/jboysen/mri-and-alzheimers;
https://catalog.data.gov/dataset/alzheimers-disease-and-healthy-aging-data

[24] He, K., Zhang, X., Ren, S., & Sun, J. (**2016**). Deep residual learning for image recognition. In Proceedings of the IEEE conference on computer vision and pattern recognition (pp. 770-778).

[25] Buvaneswari, P. R., & Gayathri, R. (**2021**). Deep learning-based segmentation in classification of Alzheimer's disease. Arabian Journal for Science and Engineering, 46(6), 5373-5383.

Operating/Underdevelopement 225Ac- Production-routes, and The Current status of the Clinical Development of Its Radiopharmaceuticals (Paper ID : 1361)

Simindokht Shirvani Arani*

Nuclear Science and Technology Research Institute, Tehran, Iran

Abstract

Highly attractive nuclear properties of ^{225}Ac and the reports on striking therapeutic efficacy of ^{225}Ac-labeled-PSMAs have stimulated a profound global interest in exploiting this radioisotope for targeted alpha therapy (TAT). As can be deducted from the reports and literatures, ^{225}Ac will follow the same market trend that is observed for ^{177}Lu. Considering today's patients' needs of 100 kBq/kg, the losses during transportation, labeling yields, and an average of 3 doses for a full treatment of a patient, the total needed activity for each patient at the end of bombardment will be about 30 to 35 MBq. This estimated value will annually increase and the industry or importation must guarantee the obligatory capacity to cover the rising future demand. The success story of applying ^{225}Ac-radiopharmaceuticals is already begun in country and the feasibility study for domestic production has started as well. In this paper the ^{225}Ac-production methods that have been introduced over recent years are reviewed, the probable issues and caution that have to be taken are addressed, and finally, a brief overview on the current status of the clinical development of ^{225}Ac-labelled compounds is also provided.

Keywords: Actinium-225, Production technology, Clinical status.

INTRODUCTION

^{225}Ac, a component of the ^{237}Np decay chain, no longer exists in nature but has been artificially synthesized. It possesses features that position it as a promising contender for nuclear medicine applications. With a half-life of 9.9 days, its disintegration follows a six-step decay chain, see the figure, resulting in the emission of multiple alpha particles. This property enhances its potential cytotoxicity compared to other α-emitters. The most recent study on radiotherapy development revealed that molecules labeled with ^{225}Ac are currently in development, with already even undergoing human testing. The first ^{225}Ac-labeled molecule has entered clinical phase III trials and may potentially reach the market by 2028. These molecules cover essential indications studied using beta-emitting radionuclides, and it's evident that each ^{177}Lu-labeled drug will be explored as an ^{225}Ac-labeled counterpart. ^{225}Ac-labeled drugs are following a

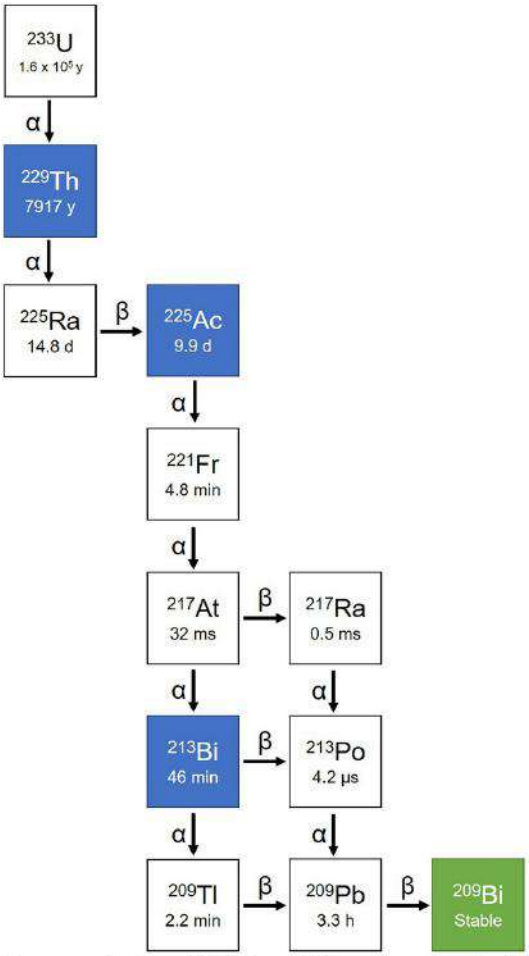

Decay chain of ^{225}Ac. ^{225}Ac decays to ^{209}Bi with seven intermediate radionuclide progenies, including ^{221}Fr, ^{217}At, ^{213}Bi, ^{209}Tl, ^{217}Ra, ^{213}Po, and ^{209}Pb. Among the decay chain ^{225}Ac and ^{213}Bi are medically relevant and intensively investigated.

similar trajectory to ^{177}Lu-labeled molecules, albeit with a 5-year delay having a high chance of reaching the market before 2030 [1].

Considering a global goal of treating half a million patients, this represents only 1% of the 5-year prevalence of cumulative cancers, which remains realistic when compared to surgical procedures, external radiotherapy, or chemotherapy. To evaluate additional requirements, the average patient dose of 100 kBq/kg is considered. For a complete treatment, each patient needs 30–36 MBq of ^{225}Ac at the end of bombardment, assuming an average of 3 doses. In other words, 3,000 GBq at the end of bombardment would adequately treat 100,000 patients annually [2]. The industry must ensure capacity for 5–6 times this yearly amount by 2032. In recent years, substantial investments have been made in developing large-scale Ac-225 production technologies. The key players in the alpha emitter market include Alpha Tau Medical Ltd., NorthStar Medical Radioisotopes, IBA Worldwide, RadioMedix, Orano Med, Bayer AG, Novartis International AG, Actinium Pharmaceuticals, Inc., Fusion Pharmaceuticals Inc., Eckert & Ziegler, Telix Pharmaceuticals Limited, Curium Pharma, AAA (Advanced Accelerator Applications), Isotopen Technologien München AG (ITM), Nordion (Canada) Inc., and it is predicted that North America is expected to dominate the global alpha emitter market from 2024 to 2033. These efforts aim to enable large-scale production of this radioisotope. The literature has documented various approaches for achieving this goal. The five applied technologies are outlined in the following section.

Additionally, a brief overview of the current status of clinical development for its radiopharmaceuticals is provided.

Current Approaches for ^{225}Ac Production in Operation and Development

1- Carrier-free ^{225}Ac is produced through the natural decay of ^{229}Th. Three sites (in the United States, Russia, and Germany) currently produce high-quality ^{225}Ac. While alternative routes may eventually surpass this generator route, for now, it remains the largest source of very clean ^{225}Ac.

2- ^{232}Th activation programs: in the United States and Canada have progressed well. This technology has the potential for very high capacity, allowing production of several terabecquerels per year. Unfortunately, the product remains contaminated with ^{227}Ac. The mixture can be used up to clinical phase II for development purposes, but cleaner forms of ^{225}Ac are preferred for routine applications and marketing. Clearly, the release of radioactive waste from patients in hospital waste tanks is a significant concern. European authorities may recommend avoiding ^{227}Ac, while in the United States, it must be included in radioactive waste, affecting decommissioning financial assurance.

3- The next technology involves the thorium activation process. During this process, ^{225}Ra, a by-product, can be easily separated from the mixture. This separation allows indirect access to clean ^{225}Ac through its decay. Unfortunately, the yields are limited to only 10% compared to the ^{225}Ac/^{227}Ac mix, resulting in high levels of waste and making it financially unattractive.

4- Accelerator production is another rout that works by irradiating ^{226}Ra targets using small cyclotrons. Several large-scale production sites are currently under construction, with support from companies in the United States and Europe. The goal is to eventually produce large amounts of ^{225}Ac per week, theoretically exceeding 4 TBq a month. However, for practical safety reasons, aiming for a tenth of this figure would be more feasible. Cooling of larger targets becomes the limiting factor in this approach.

5- The last approach has witnessed recent advancements, revealing that photo-conversion technology not only provides a means to produce exceptionally pure ^{225}Ac, but it also holds the potential for large-scale production. Construction of facilities utilizing this technology is underway in both the United States and Europe.

Probable issues and caution that have to be taken

Even if high capacity and reliable access to ^{225}Ac from 2025 onward is confirmed, the production of actinium still presents several other issues. While handling ^{232}Th doesn't seem problematic, obtaining larger quantities of ^{226}Ra remains uncertain. Companies are working on solutions, including accessing domestic stocks or extracting radium from older devices (such as paintings, radiotherapy tools, and older brachytherapy material). In the worst case, this issue should also be resolved by 2025. The need for Additional Safety Investments and handling ^{226}Ra is complex because it generates the gas ^{222}Rn, which is challenging to store and trap. As patient numbers increase, the demand for radium and radon production will rise, necessitating additional safety investments. Risk of explosion and contamination also should be considered. Cyclotron and photoconversion technologies face the risk of radium target explosion due to challenging cooling conditions. This limitation could lead to contamination with long-half-life radionuclides. Any capacity increase will be gradual, and the upper limit remains theoretical. As ^{225}Ac, an alpha-emitter, undergoes a 6-step decay cascade to stable ^{209}Bi, releasing 4 alpha particles and 2 beta particles sequentially, the potential toxicity and limited therapeutic efficacy is another challenge to be addressed. Therapeutic efficacy is restricted to the first emitted alpha particle, as recoil effects and chelator limitations prevent trapping of decay products. Daughter radionuclides release additional alpha and beta particles elsewhere in the body. Toxic effects are of high importance, because it defines the maximum tolerated dose level. Finally, it has to be noted that the handling of patients treated with ^{225}Ac poses a dilemma. These patients cannot be kept at therapeutic centers long enough to collect all their waste until full decay. While releasing this waste into nature is manageable for a small number of patients, it becomes problematic if millions of doses are used annually. This issue extends beyond ^{225}Ac and will also impact other long-half-life radionuclides like ^{131}I, ^{177}Lu, and ^{161}Tb. It highlights the need for next-generation radiotherapeutic agents with shorter half-lives, such as ^{67}Cu.

Clinical Development of Its Radiopharmaceuticals

Clinical researchers are actively exploring the applications of Ac-225 in treating human diseases. This radioisotope, when labeled with antibodies and peptides, shows promise in various therapeutic contexts. Let's delve into some notable examples: Ac-225 Labeled Antibodies for AML (Acute Myeloid Leukemia): ^{225}Ac-DOTA-anti-VAL-4, ^{225}Ac-DOTA-Hum195, ^{225}Ac-anti-CD33, etc., or for prostate Cancer Treatment including antibodies:^{225}Ac-

DOTA-hu11B6, ^{225}Ac-macropa-H-Tmab, ^{225}Ac-DOTA-hu5A10, …or peptides including: ^{225}Ac-PSMA617, ^{225}Ac-PSMA-DA1, ^{225}Ac-RPS-088, HER2 Receptor-Positive Cancer (Breast and Stomach): including antibodies: ^{225}Ac-DOTA-HER2-Nb, ^{225}Ac-DOTA-trastuzumab, ^{225}Ac-DOTA-HTAB004, etc., including peptides with Ac-225: ^{225}Ac-proteous-DOTA: Used for colorectal cancer.^{225}Ac-Macropa-RPS070: Effective against breast cancer, neuroblastoma, liver, and skin cancer. ^{225}Ac-DOTACycMSH: Aids in treating various cancers. However, a significant challenge lies in the limited understanding of Ac-225's coordination chemistry, hindering the development of effective chelation techniques for specific ions. Advancements in this field are crucial for enhancing the use of Ac-225-labeled compounds and small biomolecules in modern radiopharmaceuticals for clinical application [3,4].

However, over the past two decades, significant progress has occurred in the development of Actinium-225-labeled radiopharmaceuticals for treating various cancers, central nervous system disorders, and infections. Researchers have achieved this through advancements in production technology. Notably: A research-scale thorium generator now facilitates regular separation and purification of hundreds of MBq (mCi) of ^{225}Ac from a small stock of ^{233}U material at the Canadian Nuclear Laboratories (CNL). Additionally, three ^{229}Th generators in the United States, Germany, and Russia supply the majority of the global ^{225}Ac used in preclinical and clinical trials. Annually, approximately 74 GBq (2 Ci) of ^{225}Ac are accessible from these generators. While this quantity alone allows for about 10,000 treatments, the limited supply persists. Despite this challenge, the route continues to deliver high-quality material on schedule [5].

Discussion

Research on Ac-225 radiopharmaceuticals holds great promise for developing more effective therapies using alpha emitters, which exhibit significantly fewer side effects and discomforts. Clinical trials have consistently demonstrated that Ac-225 radiopharmaceuticals can effectively treat advanced malignancies. As new agents gain FDA approval and insurance coverage, the future of radiotheranostics looks bright. Ideally, a streamlined process would allow FDA clearance to align seamlessly with reimbursement approvals. Furthermore, effective strategies for precise targeting, achieving optimal radiolabeling yields, and developing suitable Ac-225 radiopharmaceuticals are essential. These radiopharmaceuticals induce double-stranded DNA breaks in tumors through α-particle emissions, which cancer cells

struggle to repair. Given their strong affinity for tumor-associated biomarkers, both antibodies and peptides emerge as prime candidates for molecularly targeted nuclear treatments. Notably, administering α-particle emitters to tumors, coupled with immunotherapy, holds the potential to trigger a systemic immune response. Despite the current global scarcity of Ac-225, ongoing research and development initiatives aim to address this limitation.

Conclusions

The global production capacity for ^{225}Ac is expected to a level allowing for the annual creation of at least 2 million patient doses. This favorable situation contrasts with the challenges faced by ^{177}Lu and ^{161}Tb, where reactor access poses limitations. Overall, the emergence of ^{225}Ac-labeled radiopharmaceuticals marks the beginning of a successful journey spanning over 15 years. Working with Ac-225 labeled radiopharmaceuticals presents several challenges that should be considered. These include the limited availability of the isotope, the difficulty in detecting alpha particles, and the high toxicity affecting activity handling and quality control (QC) analysis. To ensure clinical quality, cross-validation using different QC techniques is essential. Moreover, due to health physics and methodological considerations, producing GMP-grade radiopharmaceuticals is time-consuming and requires experienced personnel. Despite these challenges, patients treated with Ac-225 radionuclide therapy have shown exceptional benefits, making it an intriguing and encouraging treatment option for further investigation in well-designed clinical trials

References

[1] Implementing Ac-225 labelled radiopharmaceuticals: practical considerations and (pre-)clinical perspectives. Hooijman et al.EJNMMI Radiopharmacy and Chemistry (2024) 9:9.

[2] Perspectives for Actinium-225 Production at Commercial Scale, James T. Harvey, Current Radiopharmaceuticals, 2018, 11, 180-191,

[3] Production and supply of a-particleemitting radionuclides for targeted a-therapy.Radchenko V, Morgenstern A, Jalilian AJ, et al. J Nucl Med. 2021;62:1495–1503.

[4] Alpha-peptide receptor radionuclide therapy using actinium-225 labeled somatostatin receptor agonists and antagonists, REVIEW article Front. Med., 07 December 2022, Sec. Nuclear Medicine. Mengqi Shi et al. Volume 9 – 2022.

Experimental investigation of the effect of oxygen on the positron annihilation mechanisms in liquids (Paper ID : 1369)

Y. Abdollahi pour, O. Kakuee, D. Sardari, A. Biganeh[1*]

[1] *Faculty of Engineering, Science and Research Branch, Islamic Azad University, P.O. Box 14515-775, Tehran, Iran*

[2] *Physics & b Accelerators Research School, Nuclear Science and Technology Research Institute, P. O. Box 14395-836, Tehran, Iran.*

Abstract

Treatment of cancer patients requires high-sensitivity diagnostic techniques. Recently, the Society of Positron Annihilation Spectroscopy (PAS) has been working on hypoxia detection using positron lifetime and hopes to diagnose cancer at its initial phases. The accepted hypothesis for the use of positron as a biomarker of tumor hypoxia is that due to the distance between the blood vessels and the cancerous tissues, the oxygen concentration strongly decreases in cancerous tissues. The point that can put the PAS technique in the category of cancer diagnosis tools is its potential capability for oxygen-sensing in tissues. So, the partial pressure of oxygen in the patient's tissues can be measured from the Positron Annihilation Lifetime Spectroscopy (PALS). However, before the establishment of the positron lifetime imaging technique, the oxygen-sensing ability of the PALS should be confirmed in different chemical environments. In this paper, the mechanisms of positron annihilation in the deionized water and air-bubbled water samples were investigated via systematic experiments by our homemade Doppler Broadening Spectroscopy (DBS) and PALS spectrometer. Three mechanisms for positron annihilation in the investigated liquid samples including oxidation, Positronium conversion, and Positronium inhibition were described. The results of this work can contribute to the development of the PAS technique for clinical tumor diagnosis using the under-development J-PET scanner.

Keywords: Positronium, Lifetime, PAS, tumor, hypoxia.

INTRODUCTION

PAS is a well-established technique for the assessment of the sub-nanometer size of free volume and its concentration in polymers, metals, semiconductors, and liquids [1]. These days the Society of PAS is working on the analysis of biological samples [2,3]. Their purpose is to find a way to detect the cancerous tissues and the precise location of the altered tissues at the initial stages of molecular abnormalities in the initial state. The gold standard for the oncological diagnosis is histopathology. The histopathological research confirms that

cancerous tissues have lower oxygen concentrations than normal tissues due to their abnormal vasculature and increased metabolism [4]. This condition is called tumor hypoxia. This hypoxic environment not only affects the tumor's response to treatment but also promotes its progression and metastasis [5]. Therefore, measuring the oxygen concentration in tumors is crucial for understanding their biology and designing effective therapies. The point that conducts PAS to hypoxia detection is the potential oxygen-sensing ability of the PAS technique. Oxygen molecules can interact with positrons through various mechanisms, such as electron transfer, positronium formation, and direct positron annihilation. These interactions can affect the lifetime of the positron and the momentum distribution of the annihilation gamma rays. Moskal et al. at the Jagiellonian University of Krakow introduced a new scanner called J-PET for positronium (Ps) imaging of tissues [6]. This device is made of a large number of plastic scintillators which are capable of imaging the whole body with the Ortho-positronium (O-Ps) lifetime by reconstruction method. The feasibility study of the Ps imaging using positron annihilation lifetime spectroscopy has been investigated in [7]. The first positronium imaging of a cardiac myxoma phantom using the developed J-PET scanner was demonstrated by the J-PET group [8]. A simulation study of a novel preclinical total body imaging with the J-PET technology was investigated by Dadgar et al.[9].

However, before the establishment of the technique, the oxygen-sensing ability of the PAS should be investigated. In our previous work, we measured the parameters of the (PALS) and Coincidence Doppler Broadening Spectroscopy (CDBS) for four tissue-equivalent polymers[10]. The results of the PALS experiment confirmed that the positronium formation decreases with an increase in the oxygen concentration in the polymer content. The results of the DBS technique also confirmed that the Orbital Electron Momentum Spectrum (OEMS) is a signature of the characteristic elements and reflects the chemical environment of hydrocarbon sites. However, for samples with similar oxygen concentration, factors such as chemical environments, degree of crystallinity, and elementary free volumes influence the positron annihilation mechanisms and a limited number of experimental data has been reported to support the technique [11]. In this work, the positron annihilation parameters were investigated via systematic experiments using PALS and DBS for water samples.

Theoretical details

Standard PAS performs using ^{22}Na as a positron emitter source. Simultaneously by the emission of the positron from the source, a 1274 keV gamma also emits which is a signal for the birth of the electron. The positron with the endpoint energy of 540 keV penetrates inside the material and after thermalization, annihilates by the free electrons, valance, or core electrons of the material and provides the death signal. Measuring the time difference between the start and stop signals provides the positron lifetime inside the material. This technique is called PALS and reflects the size and concentration of the positron annihilation site. The other technique called DBS focuses on the measurement of the longitudinal momentum (P_l) of the annihilated electrons and provides valuable information about the chemical environments of positron annihilation sites.

For low electron density materials such as liquids and polymers, positrons can form an unstable hydrogen-like state atom called Positronium (Ps). According to the relative spin orientation of the electron and positronium, two states can exist:

The triple state with parallel spin (S=1 , M_S= -1,0,1) is called Ortho-Positronium (O-Ps) which has a lifetime of 142 ns in the vaccum and 1-5 ns in material and mainly decays to three-gamma. Due to the long lifetime of the O-Ps and its neutral charge, it can interact with core electrons and probe the chemical environment before its annihilation.

The singlet state with anti-parallel spin (S=0 , M_S= 0) is called Para-Positronium (P-Ps) with the characteristics self-annihilation lifetime of 0.125 ns. From the PAS point of view, the P-Ps self-annihilation has no information and does not make sense for material characterization.

Whether with a short or long lifetime, the fate for positron or positronium is the same: Annihilation with free, valence, or core electrons and generation of three or two gamma rays. The initial momentum of the electrons participating in the annihilation mechanism leads to an energy shift ($\Delta E = P_l c/2$) from the 511 keV gamma line. Where c is the light velocity. The DBS technique measures the ΔE using a high-resolution HPGe detector.

Experimental details

In this section, the PALS and DBS techniques are presented for water and air-bubbled samples.

PALS experiment

Figure 1. shows the setup of the PALS experiment. The PALS technique was performed using two face-to-face plastic scintillators (NE-102) at the Nuclear Science and Technology Research Institute (NSTRI) in Iran. The positron lifetime was measured using a fast-slow spectrometer. The timing resolution of the spectrometer was measured at 320 ps using the coincidence gamma line of ^{60}Co (1173 and 1332 keV). The time calibration was determined at 24 ps using a delay module. The positron source is a 1MBq ^{22}Na sandwiched between two 4 μm thick kapton foils. Kapton foils inhibit the formation of Ps inside the source and reduce the error in the calculation of the longest-lived component for the investigated sample. To avoid the penetration of water into the source, a sealed circular shape plexiglass with a hole in the center was made. Figure 2 shows how the source was sealed using plexiglass and O-rings. A 4×20×20 cm^3 container was filled with deionized water and the source was placed at the common axis of the detectors. The positron lifetime was measured for the deionized water and ai-bubbled water for 21 days and 10^6 events were recorded on the spectrum. Figure 3 shows the positron lifetime spectrum for the deionized water. The lifetime spectrum of each sample was decomposed to the sum of three-exponential decay in the form of $\sum_i (I_i/\tau_i) e^{-t/\tau_i}$ folded with the FWHM of the spectrometer using the LT-10 code [12]. Where $\tau_i(ns)$ and I_i (%) is the lifetime and the intensity of the ith mechanism for positron annihilation. For the PALS data analysis, 7 free parameters including three τ_i, three I_i, and τ_{Source} were considered. The lifetime of the positron in the source (τ_{Source}) was determined using the measurement of positron lifetime in a well-annealed Ni sample with the known lifetime of 110 ps. The shortest lifetime component (τ_1) and its intensity (I_1) originate from the P-Ps self-annihilation and does not make sense in our investigation. The medium-lived component (τ_2) and its intensity (I_2) are attributed to the positron annihilation with free and valence band electrons. The longest-lived component (τ_3) and its intensity (I_3) are due to the O-Ps annihilation via the pick-off mechanism. The results of the PALS data analysis are listed in Table 1.

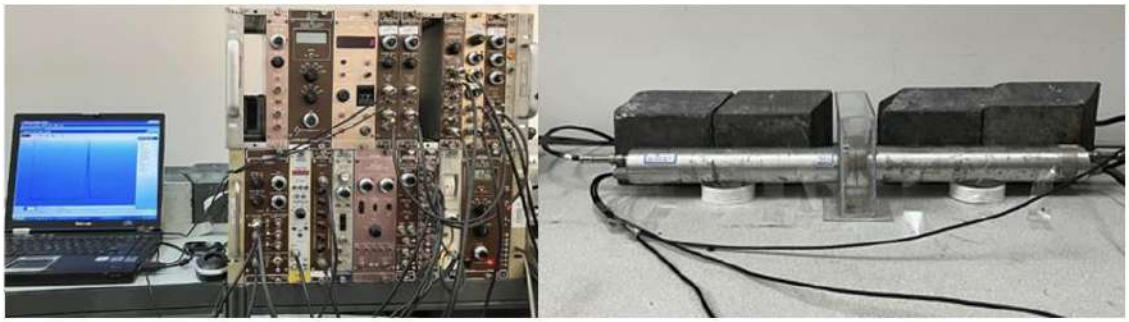

Figure 1. The setup of the PALS experiment.

Figure 2. The support is made to place the source inside the water.

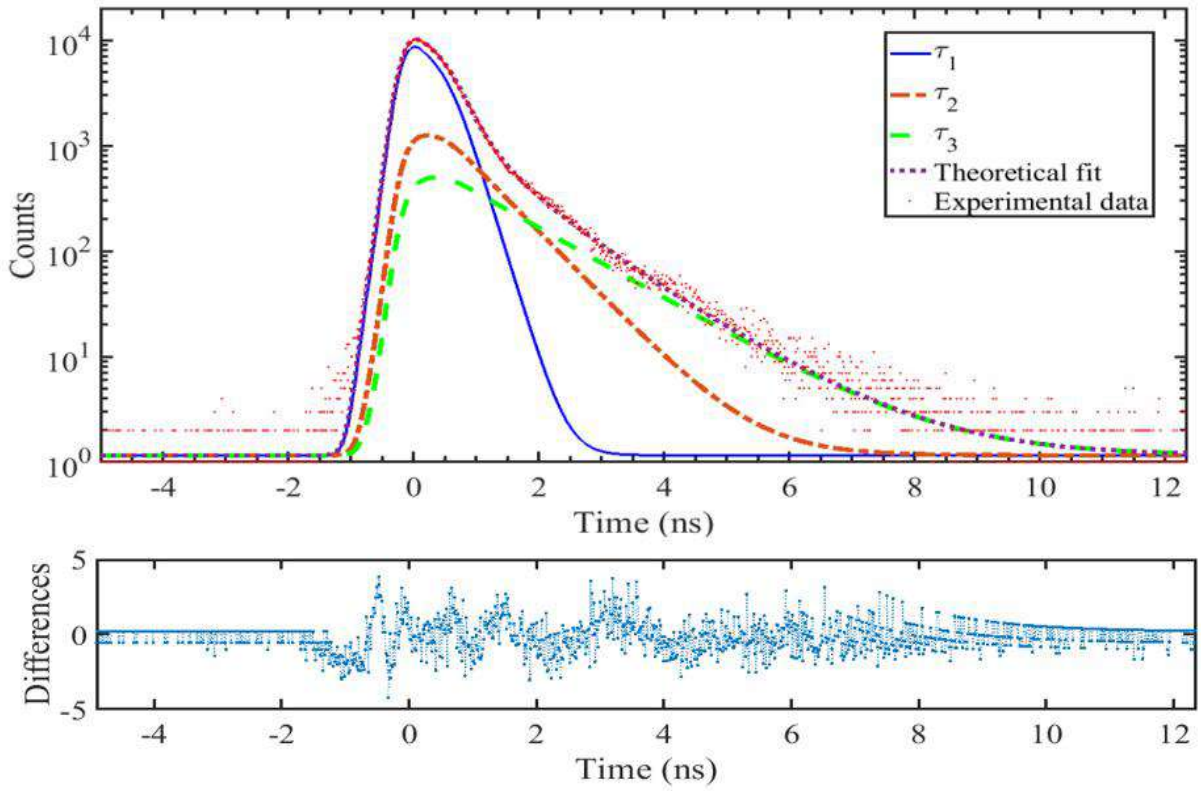

Figure 3. Positron lifetime spectrum of the deionized water (top) and the differences between the theoretical and experimental data (below).

DBS experiment

The setup of the DBS was established using an HPGe detector (Canberra 20200) and a waveform digitizer (CAEN DT5724). The digitizer samples directly at the preamplifier output of the detector and the analysis of the digitized signal performs by MC2 software. The digitizer is loaded by a Digital Pulse Height (PHA) algorithm that transforms the sampled data to pulse height. The PHA control software is used to manage the energy filter configuration to obtain the best energy resolution. The details of the optimum parameters for the pulse shape analysis

have been reported in our previous paper [13]. The FWHM of the HPGe detector was measured at 2.1 keV for the 662 keV gamma line of ^{137}Cs. For the DBS experiment, we used ^{64}Cu radioisotope ($T_{1/2} = 12.7\ h$) as the positron source with the positron endpoint energy of 653 keV. The ^{64}Cu was produced using ^{nat}Cu (n,ɣ) ^{64}Cu nuclear reaction at the Neutron Physics Laboratory (NPL) of the NSTRI. The ^{64}Cu was produced with 10 g of Copper (II) Nitrate ($Cu(NO_3)_2(H_2O)$) powder. The powder was poured into a plastic container and placed in front of the 5 Ci Am-Be neutron source. To increase the reaction yield, the fast neutrons were thermalized using a 5 cm thick polyethylene rod in front of the Am-Be window. The flux of the thermal neutrons was measured at 3×10^3 n.cm^{-2}s^{-1} at the target position using the foil activation technique. The irradiation time for the target was 63.5 hours and after 20 min cooling time for decay of short-lived radionuclide, the target was dissolved in 100 cc deionized water and placed in front of the HPGe detector for gamma spectroscopy. Figure 4 shows the activated copper nitrate solution made for DBS. The gamma-ray spectroscopy of the solution is shown in Figure 5. The DBS was performed for the deionized and air-bubbled water for 6 hours. The gamma-ray spectrum was analyzed using SP-1code [14]. Figure 6 shows the results of the DBS analysis by SP-1 code. The Doppler broadened spectrum of the positron annihilation radiation is often described by S and W-parameters [15]. The S-parameter reflects the contribution of positron annihilation with free and valence band electrons with $0<\Delta E<0.8$keV. Where ΔE is the energy shift from the 511 keV gamma line caused by the initial momentum of the annihilated electrons. The W-parameter describes the positron annihilation with core electrons with $1.5<\Delta E<3.8$keV. Since the probability of positron annihilation by core electrons is less than 10^{-4}, the measurement of the W-parameter needs a peak-to-compton ratio better than 10^5 which is achievable using 2D-CDBS and long time data acquisition. So, the W-parameter can not be reported in our work. The results of the DBS for the investigated samples are listed in Table 1.

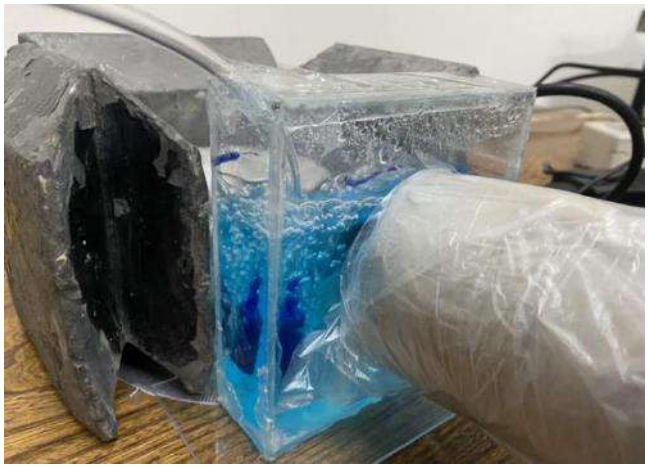

Figure 4. The activated Copper nitrate solution in the water in front of the HPGe detector. Bubbling in the sample has been done using an air pump.

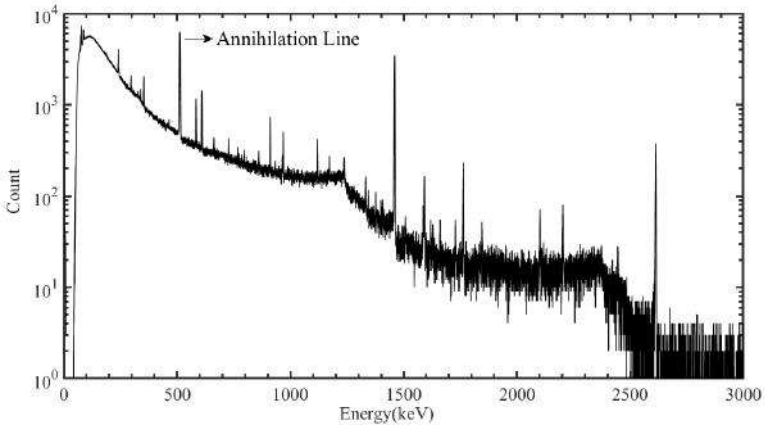

Figure 5. Gamma-ray spectrum of the activated copper nitrate solution used as the positron source for the DBS experiment. The positron annihilation line is shown in the spectrum.

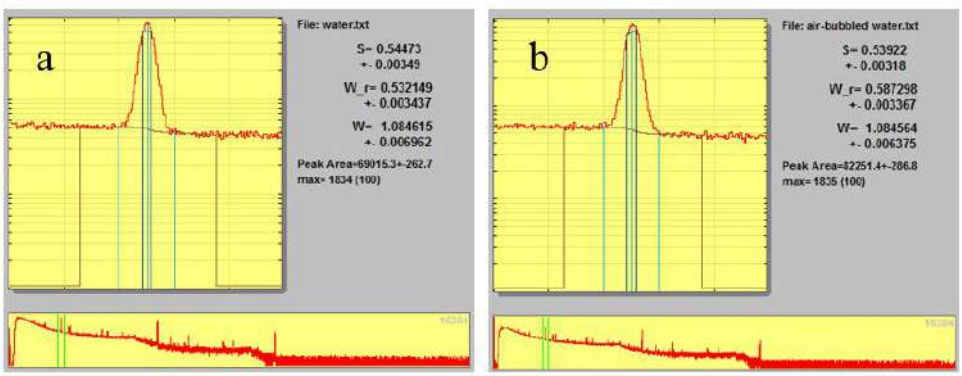

Figure 6. The result of DBS analysis by SP-1 code: a) water, b) Air-bubbled water.

Discussion on results

The results of the PALS and DBS for the investigated samples are listed in Table 1. According to the results of the PALS experiment, the intensity of the longest-lived component (I_3) is significantly (37%) reduced for the air-bubbled sample. Consequently, the intensity of the P-Ps self-annihilation is increased significantly. The S-parameter of the DBS experiment also is decreased for the air-bubbled sample. An important question that should be addressed is the reason for the O-Ps quenching for the air-bubbled sample. Two phenomena can be considered as the main reason for the reduction of O-Ps formation:

Positron shares an electron with the oxygen molecule and Positronium converts to positron with lower lifetime according to the (1):

$$Ps + O_2 \rightarrow e^+ + O_2^- \qquad (1)$$

An unpaired electron in the 2p orbital of the oxygen interacts with the electron of the O-Ps atom and transforms it to P-Ps with a lower lifetime according to (2). This phenomenon is called O-Ps to P-Ps conversion and first was described by Ferrel et al. in 1956 [16].

$$O\text{-}Ps + O_2 \rightarrow P\text{-}Ps + O_2 \qquad (2)$$

Table 1. The results of PALS and DBS. The $\boldsymbol{\chi^2}$ parameter describes the quality of the multi-exponential fitting.

Sample	$\boldsymbol{\tau_1}$ (ns)	$\boldsymbol{I_1}$(%)	$\boldsymbol{\tau_2}$ (ns)	$\boldsymbol{I_2}$(%)	$\boldsymbol{\tau_3}$ (ns)	$\boldsymbol{I_3}$(%)	$\boldsymbol{\chi^2}$	S-parameter
Water	0.22	71.72	0.71	17.85	1.28	10.41	0.94	0.54473
Air-bubbled water	0.26	75.28	0.86	16.85	1.3	7.53	1.47	0.53922

Conclusion

In this paper, the changes in the PAS parameters in the oxygen-content water samples were measured and described. The results show that the increase in the oxygen concentration leads to the quenching in the Positronium formation. The oxidation and conversion mechanisms were described as the main causes for the decrease in the O-Ps intensity for the air-bubbled sample. The results confirmed that the Positronium intensity is sensitive to the oxygen concentration in liquid samples.

The measurement of oxygen concentration by the PAS method using the under-construction J-PET scanner has several advantages over the other techniques:

Provides a non-invasive and quantitative measurement of hypoxia in the tumor cells.

Allows for the detection of hypoxic regions that are not visible on the other PET imaging techniques.

Can be used to monitor changes in hypoxia, during treatment, which can help assess treatment response and guide radiotherapy.

The results of this work can contribute to the development of data analysis techniques for the under-construction J-PET scanner at the Jagiellonian University in Krakow, Poland. After this work, we are going to measure the PAS parameter for the oxygen-degassed samples by argon-bubbling and for high oxygen concentration samples using hydrogen peroxide solutions.

References

[1] Biganeh, A., et al. "Positron annihilation lifetime and Doppler broadening spectroscopy of polymers." Radiation Physics and Chemistry 166 (2020): 108461.

[2] Bass, Steven D., et al. "Colloquium: Positronium physics and biomedical applications." Reviews of Modern Physics 95.2 (2023): 021002.

[3] Moskal, Paweł, et al. "Developing a novel positronium biomarker for cardiac myxoma imaging." EJNMMI physics 10.1 (2023): 22.

[4] Moskal, Paweł, and Ewa Ł. Stępień. "Positronium as a biomarker of hypoxia." Bio-Algorithms and Med-Systems 17.4 (2021): 311-319.

[5] Chaudary, Naz, and Richard P. Hill. "Hypoxia and metastasis." Clinical Cancer Research 13.7 (2007): 1947-1949.

[6] Bass, Steven D., et al. "Colloquium: Positronium physics and biomedical applications." Reviews of Modern Physics 95.2 (2023): 021002.

[7] Moskal, Pawel, et al. "Feasibility study of the positronium imaging with the J-PET tomograph." Physics in Medicine & Biology 64.5 (2019): 055017.

[8] Moskal, Paweł, et al. "Positronium imaging with the novel multiphoton PET scanner." Science Advances 7.42 (2021): eabh4394.

[9] Dadgar, Meysam, et al. "Investigation of novel preclinical Total Body PET designed with J-PET technology: a simulation study." IEEE Transactions on Radiation and Plasma Medical Sciences 7.2 (2022): 124-131.

[10] Zare, M., et al. "Positron Annihilation Spectroscopy of Oxygen Content Tissue-Equivalent Samples." Acta Physica Polonica, A. 142.3 (2022).

[11] Stepanov, P. S., et al. "Interaction of positronium with dissolved oxygen in liquids." Physical Chemistry Chemical Physics 22.9 (2020): 5123-5131.

[12] Giebel, Dawid, Kansy, Jerzy, 2012. LT10 program for solving basic problems connected with defect detection. Phys. Procedia 35, 122–127.

[13] Biganeh, A., et al. "Development of a 2D digital coincidence Doppler broadening spectrometer." Journal of Instrumentation 14.02 (2019): P02017.

[14] J. Dryzek, SP version 1.0, downloaded from www.positronannihilation.net/software.html.

[15] Biganeh, A., O. Kakuee, and H. Rafi-Kheiri. "Positron Annihilation Spectroscopy of KCl (Zn) crystals." Applied Radiation and Isotopes 166 (2020): 109330.

[16] Ferrell, Richard A. "Theory of positron annihilation in solids." Reviews of Modern Physics 28.3 (1956): 308.

The Predictive Power of Pre-treatment [68Ga]Ga PSMA-11 PET and Clinical Biomarkers in Tumor Lesion Dosimetry of [177Lu]Lu PSMA-617 Radioligand Therapy: A Machine Learning Approach (Paper ID : 1372)

Elmira Yazdani1, Mahboobeh Asadi2, Najme Karamzade-Ziarati2, Habibeh Vosoughi2, Parham Geramifar2,*

1Medical Physics Department, School of Medicine, Iran University of Medical Sciences, Tehran, Iran
2Research Center for Nuclear Medicine, Tehran University of Medical Sciences, Tehran, Iran

Abstract

Patients with metastatic castration-resistant prostate cancer (mCRPC) benefit from [^{177}Lu]Lu-prostate-specific membrane antigen (PSMA) radioligand therapy (RLT). Optimizing dosimetry enhances treatment efficacy by ensuring precise dose delivery to tumoral lesions. The primary purpose of this study was to develop machine learning (ML) models to predict therapeutic tumoral lesion doses for PSMA-RLT utilizing pre-treatment [^{68}Ga]Ga-PSMA-11 PET and clinical biomarkers. We analyzed 114 segmented tumoral lesions from 20 mCRPC patients who underwent [^{68}Ga]Ga-PSMA PET/CT scans (148 ± 16.92 *MBq* at 1 *h*) before receiving (6.8 ± 0.4 *GBq*) [^{177}Lu]Lu-PSMA-617 RLT. Post-therapy whole-body planar scans were acquired at ~4*h*, 48*h*, and 72*h*, along with a SPECT/CT at ~48*h*. A nuclear medicine clinician performed lesion segmentation on baseline PET/CT and was subsequently transferred to co-registered SPECT/CT images. The tumoral lesion features were calculated from [^{68}Ga]Ga-PSMA-11 PET using 3D Slicer v5.2.2 software. Post-therapy dosimetry was conducted using sequential whole-body planar and SPECT/CT images to calculate time-integrated activities (TIAs). Subsequently, tumoral lesion dose estimation was conducted through Monte Carlo (MC) simulations, utilizing the Geant4 application for tomographic emission (GATE) toolkit based on the medical internal radiation dose (MIRD) scheme. The study explored the correlation between tumoral lesion mean doses and both PET-derived features and clinical biomarkers. Several regression ML methods were employed to predict tumoral lesion doses using the pre-treatment data. The model's performance was assessed through tenfold cross-validation, utilizing coefficient of determination (R^2), mean absolute error (MAE), and root mean square error (RMSE) metrics. The mean estimated doses per unit administered activity of [^{177}Lu]Lu-PSMA-617 for tumoral lesion were 2.62 ± 2.47 (0.15-13.7) Gy/GBq. PET-SUV_{mean} demonstrated a significant correlation (p-value<0.01) with tumoral lesion doses (Spearman ρ=0.73), followed by PET-SUV_{max} and standardized additional metabolic (SAM). Regarding univariate analysis, the predictive efficacy of PET-SUV_{mean} in estimating post-treatment

tumoral lesion doses was superior, with an R^2=0.51, compared to PET-SUV_{max} and SAM, where R^2<0.51. An optimal random forest (RFR) model, incorporating selected features of SUV_{mean}, SUV_{max}, and SAM, demonstrated a higher performance in predicting tumoral lesion doses with R^2=0.83. By combining three selected imaging features with clinical biomarkers, we improved performance significantly, achieving an R^2=0.85 using the RFR algorithm. According to the preliminary findings, pre-treatment features have promising potential in predicting absorbed doses of [^{177}Lu]Lu-PSMA, thereby contributing to the advancement of personalized RLT. Developing a robust methodology for predicting doses could provide valuable assistance in the individualization of treatment planning in RLT.

Keywords: Dosimetry, Monte Carlo, PSMA RLT, PET/CT imaging, mCRPC, Machine-learning.

INTRODUCTION

The theragnostic principle in nuclear medicine, encapsulated by the phrase "We treat what we see, and we see what we treat", emphasizes the integration of diagnostic imaging and therapeutic intervention [1]. This approach involves the development of theragnostic pairs, comprising an imaging radiotracer for molecular targeting and staging, and its therapeutic counterpart, typically a beta- or alpha-emitter employed for tumoral lesion eradication [2]. Radioligand therapy (RLT) represents a cutting-edge paradigm in radiation oncology, aiming to administer highly targeted and destructive radiation doses through cancer-specific radiopharmaceuticals [3].

Prostate-specific membrane antigen (PSMA) is a trans-membrane glycoprotein that has significant overexpression in metastatic castration-resistant prostate cancer (mCRPC) [4]. The [^{177}Lu]Lu-PSMA-617 RLT has been specifically designed to administer beta-particle radiation to cells expressing PSMA and their adjacent microenvironment. Following the success of a phase III clinical trial, [^{177}Lu]Lu-PSMA-617 has obtained approval from the U.S. Food and Drug Administration (FDA) [3, 5]. This achievement underscores its effectiveness and marks a notable advancement in the field of targeted therapy for mCRPC. Despite the initial success of RLT, concerns persist regarding the balance between therapeutic efficacy and potential side effects. In the current protocol, patients are still treated with a fixed radiopharmaceutical activity and fraction interval [6]. To address these concerns, RLT treatments require careful planning before therapy initiation, similar to the individualized radiation dose planning seen in external beam radiotherapy (EBRT) or brachytherapy [7]. This emphasis on personalized

planning highlights the need to optimize therapeutic benefits while minimizing potential adverse effects [8].

Internal dosimetry plays a crucial role in radiopharmaceutical therapies (RPT) by estimating absorbed doses in both organs at risk (OAR) and tumoral lesions, allowing for the anticipation of biological effects [9]. Patient-specific dosimetry in RPTs involves considering patient-dependent factors (anatomy and radiopharmaceutical biodistribution), and patient-independent factors (radionuclide properties) [10]. In this regard, OARs and tumoral lesions pharmacokinetics can be assessed by a series of cross-sectional scans whether sequential single photon emission computed tomography/computed tomography (SPECT/CT) scans or sequential hybrid planar-SPECT/CT scans [9]. However, the process demands significant imaging time and effort, often proving impractical for routine clinical practice.

An alternative solution involves utilizing pre-treatment imaging to assess post-therapy absorbed doses. For managing mCRPC, the theragnostic pair of ^{68}Ga/^{177}Lu-PSMA is commonly used [9]. In the current clinical practice of [^{177}Lu]Lu-PSMA-617 RLT, pre-treatment [^{68}Ga]Ga-PSMA-HEBD-CC (PSMA-11) positron emission tomography (PET)/CT imaging is essential to determine candidate eligibility and verify adequate tumoral lesion PSMA expression [11]. In a narrative review, the potential of pre-treatment PET imaging in diverse applications of RPTs was assessed, including dose prediction, such as the power of [^{68}Ga]Ga-PSMA PET for dose prediction in [^{177}Lu]Lu-PSMA RLT [12]. Several studies have established correlations between [^{68}Ga]Ga-PSMA PET uptake and [^{177}Lu]Lu-PSMA mean absorbed doses [13-16]. In the research conducted by Xue et al. [17], machine learning (ML) models were employed to predict post-therapy absorbed doses for [^{177}Lu]Lu-PSMA RLT. However, relying on Hermes dosimetry software for dose estimation, the assessment was limited to OARs, excluding tumoral lesion absorbed dose prediction from their analysis.

In this study, we aimed to develop ML models to predict mean tumoral lesion absorbed doses delivered by [^{177}Lu]Lu-PSMA-617 RLT based on Monte Carlo (MC) dose estimation, pre-treatment [^{68}Ga]Ga-PSMA-11 PET imaging, and clinical biomarkers. Our objective was to determine if pharmacokinetic information of PSMA ligands over several days could be estimated through a single pre-treatment PET scan, eliminating the need for a series of post-therapy imaging sessions. This innovative approach holds promise for seamless integration into routine clinical protocols for efficient dosimetry-based treatment planning in RLT.

EXPERIMENTAL

Patient Cohorts

Patients with mCRPC who were treated with [^{177}Lu]Lu-PSMA-617 RLT screened at Center A through pre-treatment [^{68}Ga]Ga-PSMA-11 PET/CT within 2 months of treatment initiation for inclusion. Twenty patients (age: 68.28 ± 6.44 *yr*) met the eligibility criteria and were included. Among these patients, two individuals underwent [^{68}Ga]Ga-PSMA-11 PET/CT scans at other centers, namely Center B and Center C. The patients received an injection of the administered activity of [^{177}Lu]Lu-PSMA-617. The net injection dose (administered dose minus the remaining dose in the vial) was determined, which was approximately 6.8 ± 0.4 *GBq* for our cohorts. As part of an ongoing research study approved by the Institutional Review Board, all patients provided written informed consent to participate in the dosimetry investigation. The study involved serial whole-body planar imaging and one SPECT/CT imaging session after standard treatment. Each participant underwent whole-body planar at two or three time points, approximately at 4 *h*, 48 *h*, and 72 *h* as well as one SPECT/CT imaging at ~48 *h* post-injection.

Tumor Segmentation

All patients had multiple tumoral lesions (bone metastases, lymph node metastases, and soft tissue metastases). An experienced nuclear medicine clinician manually segmented up to eight index tumoral lesions larger than 2 *mL* on baseline PET/CT scans utilizing the "Segment Editor" module in 3D Slicer software v5.2.2. The inclusion criteria for these lesions were primarily determined by the anatomical size and clear margins, ensuring confidence in the manual segmentation process. Subsequently, the delineated index lesions were transferred to the SPECT/CT scans through co-registration. The segmentations underwent verification and adjustments by a second nuclear medicine clinician as needed. Fig. 1 illustrates the manual segmentation of a mCRPC patient in PET/CT and SPECT/CT images, presented in maximum intensity projection (MIP) views, with the image visualization conducted using LIFEx v.7.4 software.

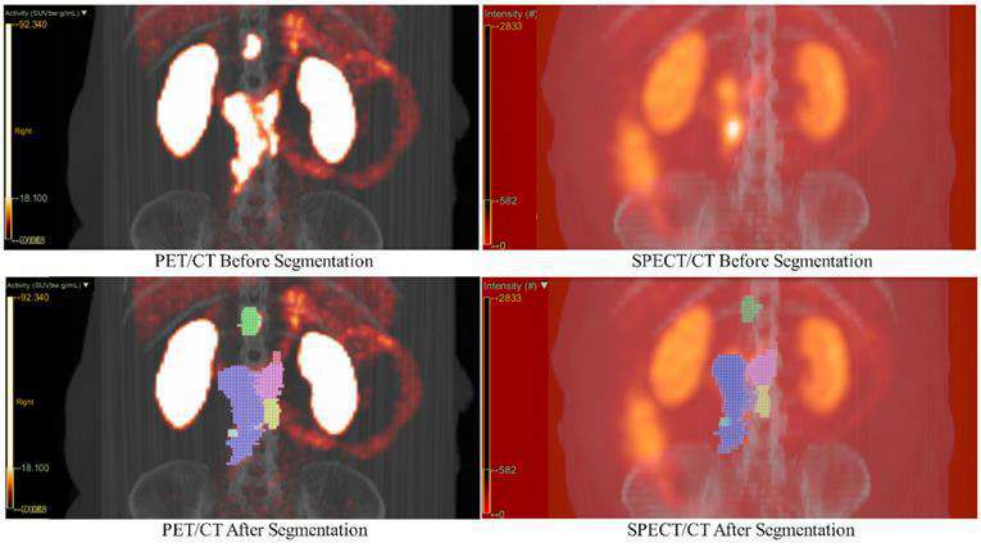

Fig. 1. PET/CT and SPECT/CT images of a mCRPC patient before (top) and after (down) manual segmentation in MIP views with image visualization conducted using LIFEx V.7.4 software.

[^{68}Ga]Ga-PSMA PET/CT Imaging and PET-derive Metrics

In our center, [^{68}Ga]Ga-PSMA-11 PET/CT imaging was conducted using a dedicated PET/CT system (Siemens BioGraph6 TruePoint). An average activity of 148 ± 16.92 *MBq* [^{68}Ga]Ga-PSMA-11 was intravenously administered. The data were reconstructed using vendor-specific recommended parameters. In all patients, a whole-body PET scan (skull to mid-thighs) in three-dimensional (3D) mode was performed, with scan times lasting 3 or 4 minutes per bed position. The scans started 45 to 60 minutes after tracer injection and were acquired with an image matrix size of 168 × 168 (pixel size 4.072 *mm*). All patients underwent a low-dose CT scan for attenuation correction of the PET emission data, encompassing the area from the skull to the mid-thigh. The low-dose CT scan parameters included a 512 × 512 matrix size (pixel size 0.97 *mm*), 110 kV_p, 80 *mA*, slice thickness of 5 *mm*, and a pitch of 1.5. The PET/CT scanners utilized at centers B and C were a Siemens BioGraph6 TruePoint TrueV and a BioGraph Horizon, respectively, equipped with identical features as those described for Center A. Although, Center C is equipped with a time of flight (TOF) algorithm in the reconstruction procedure.

Tumor volume and standard uptake value (SUV) metrics were extracted using the "PET Volume Statistics" module in the 3D Slicer software V5.2.2. Among the blood test biomarkers for mCRPC patients, we collected prostate-specific antigen (PSA, $\mu g/L$), alkaline phosphatase

(ALKP, *U/L*), and creatinine (Cr, *mg/dL*). Table 1 provides a comprehensive overview of the total variable set and their definitions, encompassing 6 morphological, 19 quantitative ^{68}Ga-PET, and 3 blood-test features.

Table 1. The comprehensive variable set in this study includes both PET and clinical features.

Feature type	Feature name		Feature Definition
Morphological-related	Volume		Volume of index tumors (segmented by nuclear medicine clinician)
	Total voxel		Total number of voxel
	Tumor Type	Bone Metastases	Bone metastases tumoral lesions (indicated by 1)
		Lymph Node Metastases	Lymph node metastases tumoral lesions (indicated by 2)
		Soft Tissue Metastases	Soft tissue metastases tumoral lesions (indicated by 3)
	Age		Patient's age (yr)
	Weight		Patient's weight (kg)
	Height		Patient's Height (cm)
SUV-related	SUV mean		Mean SUV value
	SUV min		Minimum SUV value
	SUV max		Maximum SUV value
	SUV TLG		Total lesion glycolysis [g]: SUV mean × metabolic tumor volume (MTV)
	Glycolysis Q1		Glycolysis Within First Quarter of Intensity Range [g]
	Glycolysis Q2		Glycolysis Within Second Quarter of Intensity Range [g]
	Glycolysis Q3		Glycolysis Within Third Quarter of Intensity Range [g]
	Glycolysis Q4		Glycolysis Within Fourth Quarter of Intensity Range [g]
	SUV std. dev.		Standard deviation of SUV value
	SUV median		Median SUV value
	SUV RMS		Root mean square SUV
	SUV SAM		Standardized additional metabolic activity SUV
	SUV SAMB		Standardized additional metabolic activity background SUV
	SUV 1st quartile		1st quartile SUV
	SUV 3rd quartile		3rd quartile SUV
	Q_1 distribution		Percent within the first quarter of intensity range [%]
	Q_2 distribution		Percent within the second quarter of intensity range [%]

	Q_3 distribution	Percent within the third quarter of intensity range [%]
	Q_4 distribution	Percent within the fourth quarter of intensity range [%]
Blood tests	PSA (*μg/L*)	A glycoprotein enzyme
	Cr (*mg/dL*)	A breakdown product of creatine phosphate resulting from muscle and protein metabolism.
	ALKP (*U/L*)	An enzyme that exists throughout the body

SPECT/CT and Whole-body Planar Imaging

Patient dosimetry for [^{177}Lu]Lu-PSMA-617 RLT involved serial post-therapy whole-body planar imaging sessions (post-void) at approximately 4 *h*, 48 *h*, and 72 *h*, along with a SPECT/CT scan at 48 *h* after the first RLT cycle. Fig. 2 illustrates a mCRPC case from the study with three whole-body planar images in anterior (A) and posterior (P) views on the left panels and a ~48 *h* SPECT/CT imaging (coronal and MIP views) on the right panel. A SPECT/CT imaging with a low-energy high-resolution (LEHR) collimator was conducted using a Siemens Symbia T_2 system. The imaging acquisition, utilizing auto-contour orbits, spanned 25 minutes in a single-bed configuration. In cases of widespread metastases, a two-bed configuration was implemented to ensure comprehensive coverage. The system demonstrated a sensitivity of 202 counts per minute per microcurie (*cpm/μCi*), providing a comprehensive imaging approach with the capability to capture detailed anatomical and functional information. This system is equipped with a dual-headed camera, generating 64 projections per head, each with a frame duration of 20 *fr/ sec*. The acquired images underwent reconstruction using ordered subset expectation maximization (OSEM) iterative reconstruction, employing eight iterations and eight subsets. Attenuation corrections were applied using CT scans, and a subsequent step involved applying a 5 *mm* Gaussian filter, resulting in an isotropic resolution of 4.79 *mm*. The whole-body planar and SPECT/CT acquisition parameters are provided in Table 2.

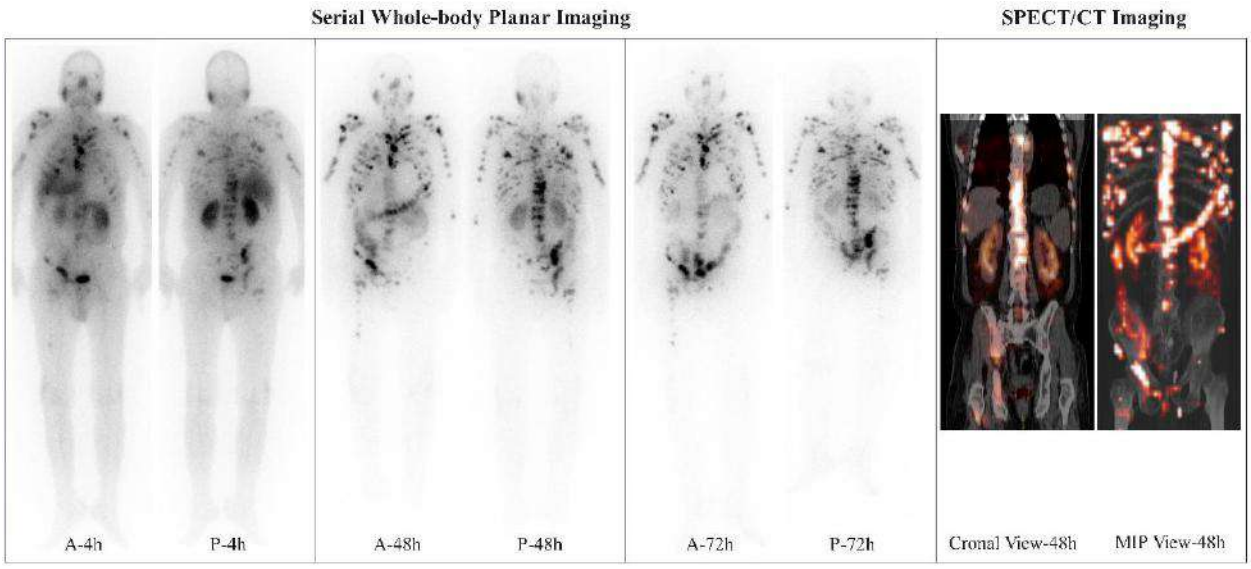

Fig. 2. Time-lapsed imaging in mCRPC post-RLT - Anterior (A) and posterior (P) whole-body planar images at ~4 *h*, 48 *h*, and 72 *h*, with a SPECT/CT at ~48 *h*, revealing the dynamic evolution of a patient in this study.

Table 2. SPECT/CT and whole-body planar imaging acquisition parameters.

Whole-body planar acquisition		**SPECT acquisition**		**CT acquisition**	
Parameter	**Value**	**Parameter**	**Value**	**Parameter**	**Value**
Matrix size	1024 × 256	Matrix size	128 × 128	Matrix size	512 × 512
Pixel size	2.4 *mm* × 2.4 *mm*	Voxel size	4.8 *mm* × 4.8 *mm* × 4.8 *mm*	Tube voltage and current	110 *kV* and 55 *mAs*
Scan time	17 *min*	Frame duration (*fr/sec*)	20	Pitch	1.5
Energy window	Center: 113, 15% photopeak, 10% both lower and upper scatter.	Collimator	LEHR, 113 *keV* [18]	Slice thickness and pixel size	5 mm and 0.97 mm

Calibration and Dosimetry Workflow

A calibration method was used to convert SPECT and whole-body planar images from counts to Becquerel (*Bq*) units [18, 19]. The calibration factor [*cps/ MBq*] is calculated by dividing the total counts in the reconstructed image by the product of scan time and activity [18]. To maintain consistency, we followed the patient protocol for acquisition, reconstruction, and essential corrections [18].

The dosimetry workflow is composed of the following steps:

In the preprocessing phase, CT images were resampled through Lanczos interpolation using the "Resize Image (BRAINS)" module in 3DSlicer v5.2.2 to ensure alignment with the resolution and dimensions of SPECT images. Whole-body planar images captured at ~4 *h*, 48 *h*, and 72 *h* post-RLT were co-registered using the "Transform Module" in 3DSlicer. Regions of interest (ROIs) encompassing the targets were delineated initially on the 4 *h* anterior scan. To maintain consistency in contouring and quantification, the ROIs from the initial segmentation were kept unchanged in size and shape, and manually relocated on the other anterior views, with a 180-degree reversal applied to posterior views.

In the process of quantifying activity, the conjugate view method was utilized. Absolute activity (in *MBq*) was calculated using the geometric-mean calculation method [20], as outlined by Equation 1:

$$A = \frac{1}{F}\sqrt{N_A N_P} \quad (1)$$

In the given equation, N_A and N_P denote the count numbers within the ROI for anterior and posterior images, respectively. The conversion factor (F) represents the ratio between whole-body counts and decay-corrected injected activity (counts per unit activity). This factor serves as the means for converting counts into activity. The 2D kinetics derived from whole-body planar in these ROIs were combined with the activity estimation from the SPECT scan conducted at ~48 *h*. The activity obtained from SPECT was employed to rescale the 2D-based time-activity curve (TAC) for each volume of interest (VOI) [21, 22]. To understand radiopharmaceutical behavior, these rescaled TACs with equally weighted activities underwent integration through a triple-exponential equation to calculate time-integrated activity (TIA) or $\tilde{A}$ values, representing the total disintegrations within each VOI [23].

The Geant4 Application for Tomographic Emission (GATE) is an open-source MC simulation

platform built upon the GEANT4 toolkit. It facilitates the user-friendly simulation of imaging scenarios across a diverse spectrum of nuclear medicine and radiation therapy applications. Using GATE (v 9.2, with Geant4 v11.0), we simulated patient-specific simulations to calculate 3D absorbed doses. This methodology provides a comprehensive simulation approach that integrates real-world imaging data with MC simulations to estimate absorbed doses. The MersenneTwister random seed was used during the MC simulation. Activity and density maps were derived from SPECT and CT images, respectively. Hounsfield Units (HU) were converted into materials and densities using the density and material tables developed by Schneider et al. [18]. A physics macro was used to simulate processes from both the emstandard opt3 and the RadioactiveDecay physics lists. The simulation utilized 10e9 primaries on a single CPU to provide voxelized S-values. Following the Pamphlet No. 21 methodology, the mean absorbed dose was calculated [24]. Based on medical internal radiation dose (MIRD) formalism, as shown in Equation 2, S-values from the GATE simulation and TIA values from TACs were merges to calculate the mean absorbed doses.

$$D(k \leftarrow T_D) = \sum_{r_S} \tilde{A}(\mathrm{h} \leftarrow T_D) S(\mathrm{k} \leftarrow \mathrm{h}), \quad (2)$$

In this equation, $D(\mathrm{k} \leftarrow \mathrm{T_D})$ is the mean absorbed dose to the target voxel in *Gy* over the dose-integration period ($\mathrm{T_D}$) which is usually taken as infinity. The symbols k and h represent target and source voxels, respectively. $\tilde{\mathrm{A}}(\mathrm{h} \leftarrow \mathrm{T_D})$ is TIA or the cumulated activity in *MBq.s*. $S(k \leftarrow h)$ represents the amount of radionuclide-specific dose absorbed by a target voxel k per unit of activity in a source voxel h (in *Gy/ MBq.s*) [9]. We calculated absorbed doses (in *Gy*), and also doses per administered activity (in *Gy/ GBq*) for tumoral lesions.

We calculated S-values for patient-specific geometries utilizing a voxel-based MC method through GATE simulation and a CT image for determining tissue properties [9]. In the case of ^{177}Lu, the S-value between a source voxel h and a target voxel k can be formulated as presented in Equation 3:

$$S_{^{177}Lu}(\mathrm{k} \leftarrow \mathrm{h}) = \frac{1}{m_k}\left[\sum_{\mathrm{i}\epsilon^{177}Lu,\mathrm{e}} \mathrm{E_i} Y_i \phi_e(\mathrm{k} \leftarrow \mathrm{h}, E_i) + \sum_{\mathrm{i}\epsilon^{177}Lu,\mathrm{ph}} \mathrm{E_i} Y_i \phi_{ph}(\mathrm{k} \leftarrow \mathrm{h}, E_i)\right], \quad (3)$$

Where m_k represents the mass of the target voxel, while ϕ denotes the absorbed fraction (AF), indicating the proportion of the energy emitted from voxel h that is absorbed in voxel k. AF

has been separated into components for electron emissions, encompassing β^- particles, conversion, and Auger electrons, as well as photon emissions, including gamma-photons and X-rays. The radionuclide-specific factors E_i and Y_i represent the mean energy emitted during a given nuclear transition and the yield of a given nuclear transition [9].

Feature Selection and Machine Learning Predictive Models

The dosimetry prediction models were meticulously developed by incorporating PET-derived features obtained from the pre-treatment scan using [^{68}Ga]Ga-PSMA-11, along with relevant clinical biomarkers. The ground truth for these models was established through the dosimetry data of targeted tumoral lesions. Various regression-type ML models were harnessed to accurately predict the absorbed doses of tumoral lesions during the initial treatment cycle of [^{177}Lu]Lu-PSMA-617 RLT.

To effectively reduce the dimensionality of our training dataset and choose robust features, we implemented a hierarchical feature selection strategy. As part of this process, imaging features that were not complementary to the data were discarded. Consequently, the goal was to identify the optimal combination of imaging features that yielded the highest performance between pre-treatment features and post-treatment absorbed doses. Subsequently, we integrated these selected imaging features with all available clinical biomarkers to find the best features. This combined dataset was then processed through multiple ML algorithms to identify the model that demonstrated superior performance.

The feature selection process begins with a univariate linear regression model, where each predictor variable is individually analyzed. The variable with the highest coefficient of determination (R^2), indicative of the best predictive performance, is selected. Following the selection of the best variable in the univariate analysis, bivariate regression models are created. Each bivariate model includes the initially selected variable along with another variable from the predictor set. We compared a cross-combination of all features with selected features to evaluate the second and third important imaging features in dose prediction. In the third step, the two best bivariate models that most increased predictive likelihood (with the highest R^2) were selected, forming the basis for a set of trivariate models to find the best feature combination for each of the ML regression algorithms that we tested for tumoral lesions.

Finally, utilizing multivariate analysis, we integrated the selected imaging features with selected clinical biomarkers to identify the optimal combination that demonstrated the highest R2 among all features.

The hierarchical feature selection algorithm was applied to six supervised ML regression algorithms, encompassing both linear and non-linear approaches, and underwent evaluation to find the best model. The regression ML algorithms include linear regression, k-nearest neighbors (KNN) regression, support vector regression (SVR), gradient boosting regression, decision tree regression, and random forest (RF) regression. These algorithms are regarded as cutting-edge solutions for both classification and regression tasks. Employing the Python programming language (v.3.11.5), the ML regression models were implemented through univariate, bivariate, and multivariate analyses.

We adopted the K-fold cross-validation method for 80% of the dataset (from Center A), initially dividing the dataset D into k mutually exclusive folds:

$$D = D_1 \cup D_2 \cup \cdots \cup D_k, \quad D_i \cup D_j = \phi \ (i \neq j), \tag{4}$$

The consistency of data distribution within each subset D_i was maintained through sampling. In each training iteration, one of the k subsets was designated as the holdout for the validation dataset to fine-tune hyperparameters, while the remaining k-1 subsets collectively serve as the training dataset. In this context, we selected a value of k equal to 10. Subsequently, the model's performance was assessed on a separate, independent 20% holdout test subset, evenly distributed from three centers. This final holdout subset was used to provide an unbiased estimate of the ML model's performance after the training/validation phase.

Statistics Analysis

In the statistical analysis, Spearman rank correlations between predictive features and tumoral lesion absorbed dose per unit administered activity were calculated, and Benjamini and Hochberg p-value corrections were applied. Q-values below 0.05 were considered to be significant. The model performance was assessed using CV tenfold R^2, mean-absolute-error (MAE), and root-mean-square-error (RMSE), in comparison to the ground truth.

RESULTS AND DISCUSSION

A total of 20 patients (age 68.28 ± 6.44 yr, range 63–89 yr) with 114 tumoral lesions larger than 2 mL (mean = 48.25 ± 80.54 mL, range: 2.09–373.42 mL) were included in this study. To reduce the absorbed dose calculation uncertainties owing to mis-registrations and partial volume effect (PVE), we excluded lesions smaller than 2 mL for the statistical analysis. The majority of studied tumoral lesions were found in the bone (94/114), while 16 lesions were lymph node metastases, and 4 lesions were found in soft tissues.

We used Python programming language (v.3.11.5) to generate the TAC and absorbed dose of tumoral lesions based on whole-body planar and SPECT/CT images. Fig. 3 illustrates an example of a TAC, the change of fraction of injected activity over time of tumoral lesions. Tumoral lesions represented a mean absorbed dose of 2.62 ± 2.47 Gy/ GBq (0.15–13.7 Gy/ GBq) based on data from 20 mCRPC patients included in this study.

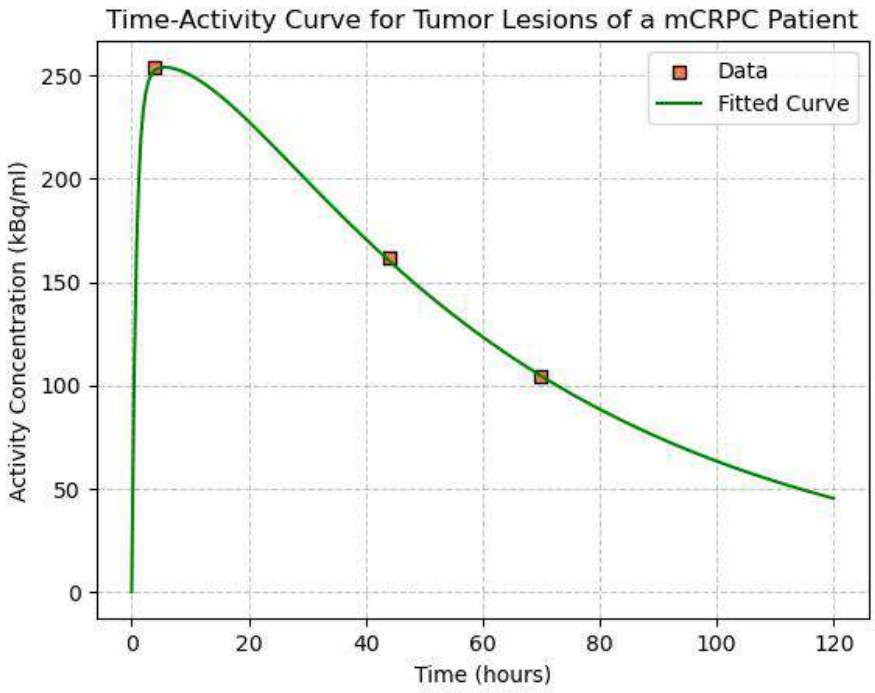

Fig. 3. TAC of tumoral lesions in a mCRPC case: orange rectangles depict serial whole-body planar imaging time-points rescaled to a SPECT/CT time-point, and the green curve represents the fitted tri-exponential model.

Using pre-treatment [^{68}Ga]Ga-PSMA-11 PET-derived features and clinical biomarkers, we evaluated six ML-based regression algorithms to predict the absorbed dose in tumoral lesions following the first treatment cycle of RLT. Based on MC simulations, we obtained the actual

dose values for each tumoral lesion, and we regarded them as the ground truth for every comparison with the predicted dose values generated by the ML models.

Fig. 4 illustrates the self and cross-correlation of all baseline features concerning the absorbed dose in tumoral lesions, as depicted by Spearman correlation coefficients (R), with a q-value below 0.05. As depicted in Fig. 5, there is a strong correlation between SUV_{mean} and absorbed dose (R = 0.73). Following closely is SUV_{max}, displaying a correlation of 0.69.

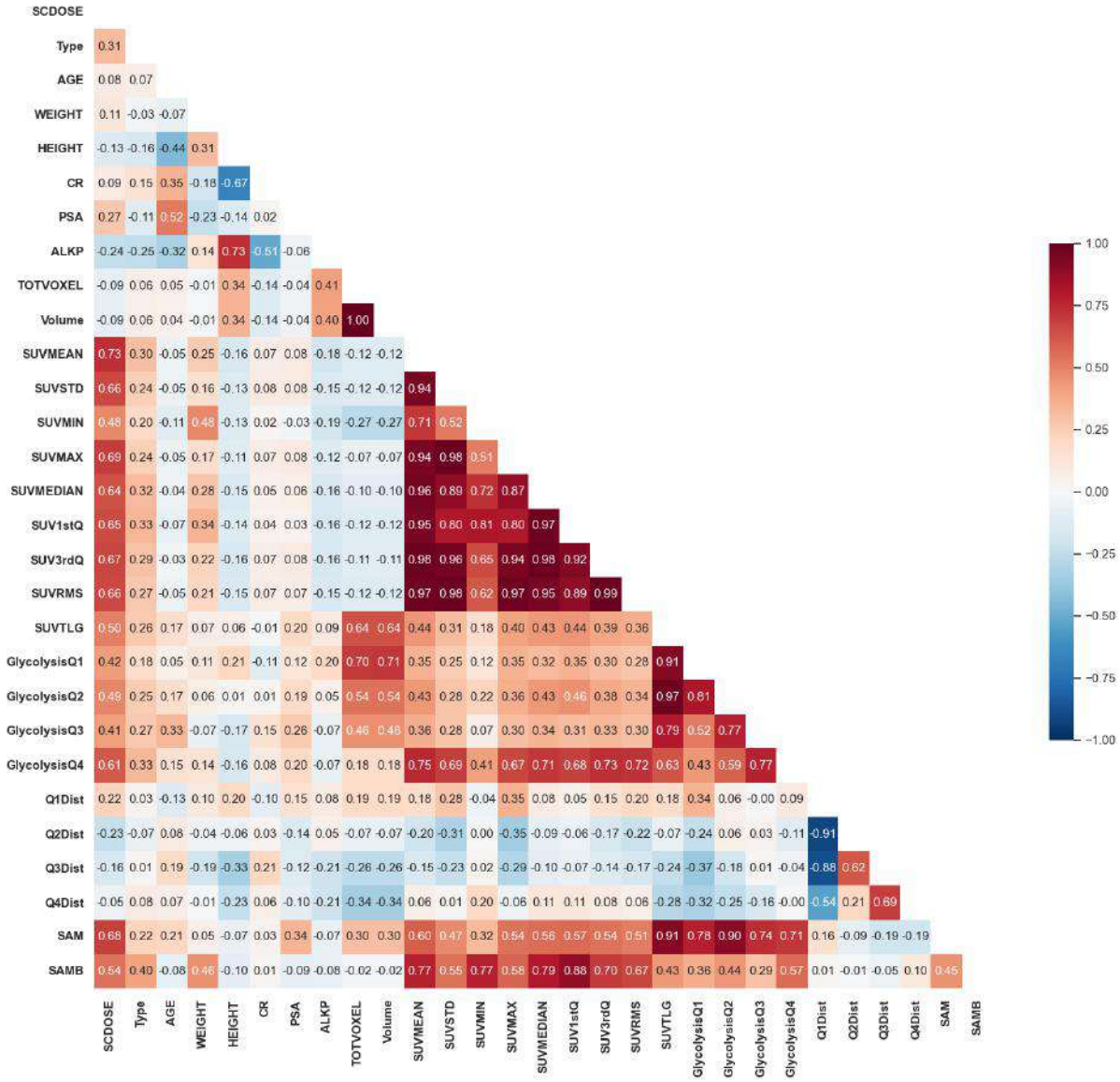

Fig. 4. Spearman rank self and cross-correlation of absorbed dose (SCDOSE) with pre-treatment parameters.

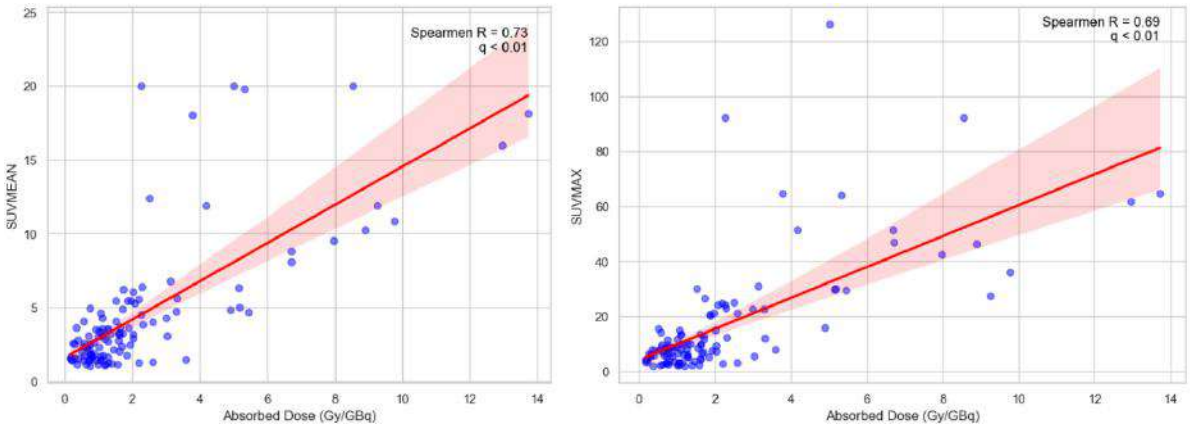

Fig. 5. Correlation between PET- SUV_{mean} and absorbed dose in *Gy/ GBq* (left panel) as well as PET-SUV_{max} and absorbed dose in *Gy/ GBq* (right panel).

A primary goal of this investigation was to identify features that enhance the utilization of pre-treatment data in predicting absorbed doses during the initial course of [^{177}Lu]Lu-PSMA-617 RLT. In Table 3, we present the final set of selected features for tumoral lesions, chosen from all PET-derived features. Also, Table 3 presents the model performance of the final selected prediction algorithms utilizing [^{68}Ga]Ga-PSMA-11 PET metrics. Additionally, the last row incorporates PET metrics combined with clinical biomarkers for a comprehensive evaluation. The quantitative metrics, including R^2, MAE, and RMSE, are reported based on calculations from a 10-fold cross-validation on a 20% hold-out test set. Following the proposed hierarchical feature-selection strategies, the linear univariate regression model selected SUV_{mean}, yielding an R^2 value of 0.51, an MAE of 1.47 *Gy/ GBq*, and an RMSE of 2.23 *Gy/ GBq*.

We conducted a comparative analysis, cross-combining all features with SUV_{mean}, to evaluate the significance of the second and third features in predicting absorbed doses. In a bivariate analysis, SUV_{mean} combined with SAM, as well as SUV_{mean} combined with SUV_{max}, emerged as the most effective predictors based on R^2 (0.71 and 0.8), MAE (1.13 and 0.98 *Gy/ GBq*), and RMSE (1.71 and 1.41 *Gy/ GBq*), as obtained from RF models. The optimum prediction performance utilizing PET-only features was attained through a trivariate RF algorithm comprising SUV_{mean}, SUV_{max}, and SAM, yielding $R^2 = 0.83$, MAE = 0.93 *Gy/ GBq*, and RMSE of 1.32 *Gy/ GBq* (refer to Table 3). Remarkably, utilizing a multivariate analysis, the cross-combination of the three chosen PET features with all clinical biomarkers led to the

identification of PSA and ALKP as pivotal among the clinical biomarkers. The final set of selected features, including SUV_{mean}, SUV_{max}, SAM, PSA, and ALKP, played a crucial role in achieving an impressive R^2 of 0.85, with an MAE of 0.93 *Gy/ GBq* and an RMSE of 1.24 *Gy/ GBq*, obtained through the implementation of a RF ML algorithm (Table 3, last row).

The comparison between predicted absorbed doses and measured absorbed doses from selected regression algorithms is depicted in Fig. 6. These predictions stem from the application of univariate linear model and RF models—encompassing bi/tri/multi-variate configurations, as detailed in Table 3. The graph meticulously compares these predictive outcomes against the actual delivered dose, ascertained through Lu-177 SPECT/CT scans.

Table 3. Performance of selected prediction algorithms using [^{68}Ga]Ga-PSMA-11 PET metrics and clinical biomarkers. Quantitative metrics (R^2, MAE, and RMSE) are reported based on 10-fold cross-validation with a 20% hold-out test set.

Model	**Features**	**R^2**	**MAE (*Gy/ GBq*)**	**RMSE (*Gy/ GBq*)**
Univariate: Linear	SUV_{mean}	0.51	1.47	2.23
Bivariate: RF	SUV_{mean}, SAM	0.71	1.13	1.71
	SUV_{mean}, SUV_{max}	0.80	0.98	1.41
Trivariate: RF	SUV_{mean}, SUV_{max}, SAM	0.83	0.93	1.32
Multivariate: RF	SUV_{mean}, SUV_{max}, SAM, PSA, and ALKP	0.85	0.93	1.24

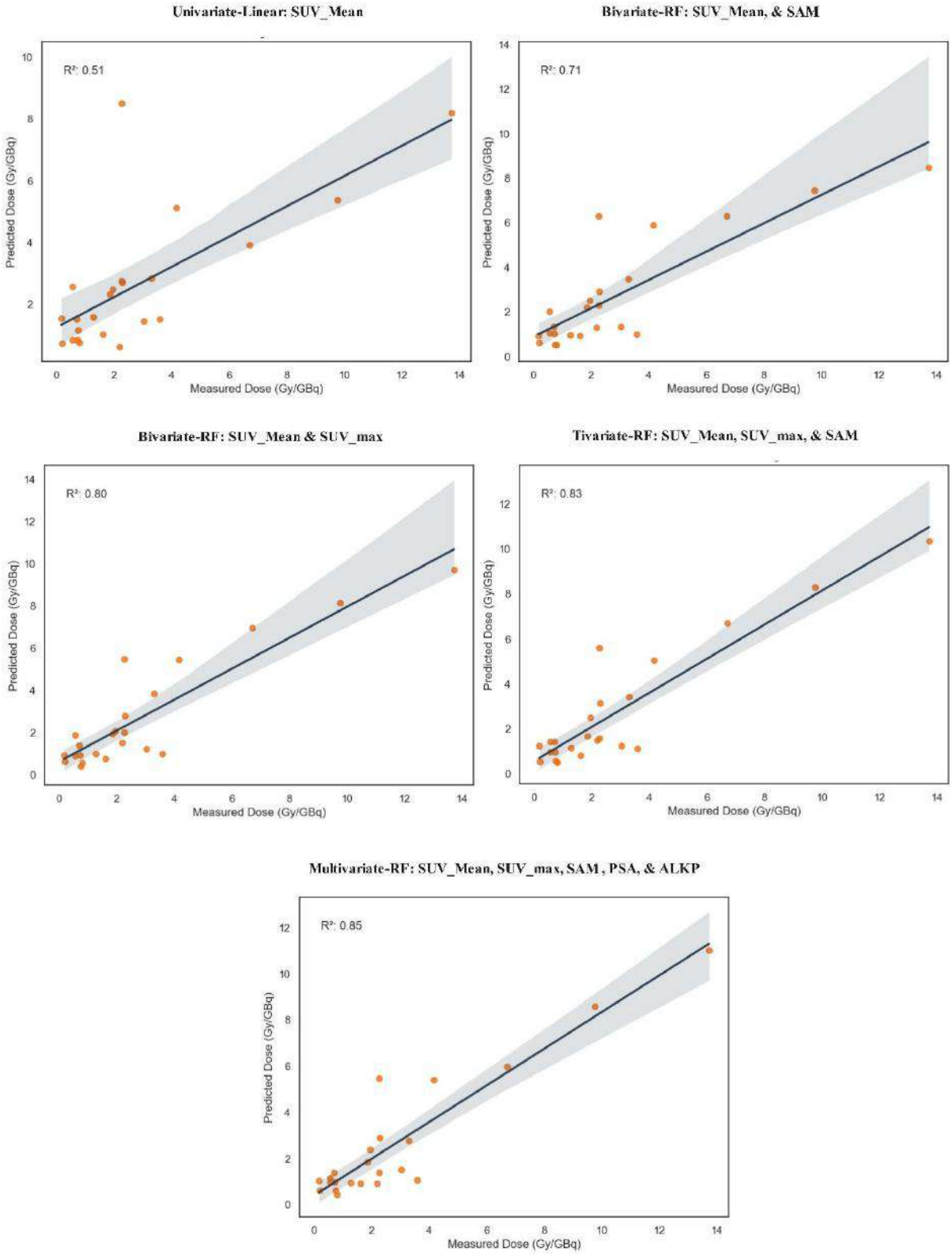

Fig. 6. Pre-treatment predicted absorbed dose using a univariate linear model and bi/tri/multi-variate RF models in Table 2 against measured absorbed dose in RLT.

Theranostics, the integration of diagnostics and therapeutics, emerges as a highly promising approach for the personalized management of advanced prostate cancer, particularly in mCRPC cases involving metastasis **[25, 26]**. The promising future of theranostics in prostate cancer management revolves around PSMA RLT, a crucial element in personalized treatment strategies, with a particular emphasis on the significant role of dose in its application [27]. It is important to calculate the appropriate administered activity for each fraction for mCRPC patients who undergo ~ 4-5 fractions of treatment. Identifying the optimal therapeutic absorbed dose in mCRPC early on can guide appropriate patient selection and treatment alterations for RLT.

Currently, PSMA-directed RLT involves administering a fixed activity to patients. Despite regulatory agencies and scientific societies typically advocating for treatment planning and dose application in RLT, there is currently no practical solution available [9, 18, 21, 22, 24]. In metastatic prostate cancer tumoral lesions, quantitative metrics derived from ^{68}Ga-PET have shown promise in assessing PSMA distribution. Despite this, few studies have examined the correlation between SUV features and absorbed doses/treatment outcomes [13-15, 17]. Further research is essential to establish conclusive findings in this regard.

Predicting absorbed doses in both tumoral lesions and OARs holds the potential to enhance treatment efficacy before treatment. This approach facilitates the creation of individualized treatment plans, allowing for the administration of patient-specific doses in RLT. This personalized strategy aims to maximize tumoral lesion irradiation while minimizing exposure to OARs. The present study aimed to assess the predictive capability of ^{68}Ga-PET-derived metrics, combined with available clinical biomarkers, in developing ML models for predicting absorbed doses in tumoral lesions. To enhance the accuracy of the models, training datasets were generated from MC simulations, offering reliable ground truth information.

There is a complex relationship between baseline PET-derived features and the administered absorbed dose. Distinctive variances arise in the pharmacokinetics and biodistribution of ^{68}Ga/^{177}Lu-PSMA theragnostic pairs. These variations are influenced by factors such as the diverse masses and chemical structures of administered radiopharmaceuticals, patient behavior, the presence of radioactive metabolites, and the impact of medications, among other factors [28]. In other words, the pre-therapy SUV, taken one hour after administration, provides a single-time point measurement primarily reflecting PSMA distribution. In contrast, the

absorbed dose is a cumulative measure over several days, considering the dynamic physiologic circulation and accumulation of a similar but not identical tracer, capturing a broader perspective of the radiation time course [17]. Moreover, therapeutic tracers, specifically [^{177}Lu]Lu-PSMA-617, are administered at substantially higher activity levels in contrast to imaging tracers like [^{68}Ga]Ga-PSMA-11. Despite sharing similarities in ligands, they are not identical. The underlying theragnostic principle, marked by analogous pharmacokinetics between imaging (PSMA-11) and therapy tracers (PSMA-617), streamlines the qualitative assessment of post-therapy doses before treatment [29].

Existing literature consistently suggests a noteworthy correlation between ^{68}Ga-SUV and ^{177}Lu-induced tumoral lesions absorbed doses [13, 14, 16, 17, 30, 31]. These studies have demonstrated that SUV values from pre-therapy PET imaging are correlated with post-therapy dose distribution. These correlations underscore the importance of incorporating pre-treatment information, aiding in the estimation of post-therapy dosimetry, and mitigating the likelihood of under- or over-estimation of diverse biodistributions.

Ezziddin et al. [30] for the first time demonstrated a robust correlation between [^{68}Ga]Ga-DOTATOC SUV-metrics and [^{177}Lu]Lu-Octreotate absorbed dose, with SUV_{mean} showing an R-value of 0.72 and SUV_{max} exhibiting an R-value of 0.71 [28]. Similarly, Hänscheid et al. [32] highlighted a significant correlation (R = 0.76) between PET-based SUV_{max} and the maximum absorbed dose administered to tumors in patients with meningioma [29]. Violet et al. [13], relying on PSMA PET screening, observed a correlation between whole-body tumor SUV_{mean} and mean absorbed dose, with a reported correlation coefficient (R) of 0.62. Xue et al. [17] conducted dosimetry prediction of OARs through the integration of pre-therapy PET imaging and blood test results. They offered an alternative solution leveraging ML techniques. Nevertheless, a limitation in their study was the inability to predict absorbed doses for tumoral lesions, attributed to the unavailability of the lesion phantom in the Hermes dosimetry tool.

In our assessment of the correlation between tumoral lesion PET-derived metrics and clinical biomarkers with absorbed doses during RLT, we identified a robust correlation, particularly with SUV_{mean} and absorbed doses (R = 0.73, Fig. 5). Additionally, we observed a noteworthy correlation between SUV_{max} and absorbed doses, with an R-value of 0.69 (Fig. 5). Expanding beyond a univariate analysis that demonstrated the predictive value of SUV_{mean} (R^2 = 0.51), we constructed bi/tri-variate models to improve prediction accuracy. A bivariate RFR model, utilizing only SUV_{mean} and SAM, exhibited strong predictive performance (R^2 = 0.71, MAE =

1.13 *Gy/ GBq*). Furthermore, another bivariate analysis incorporating SUV_{mean} and SUV_{max} achieved high predictive performance (R^2 = 0.8, MAE = 0.98 *Gy/ GBq*), with an RFR model identified as the most efficient among six different models. The optimal model performance was attained through a tri-variate RF model, exclusively incorporating PET-derived metrics, namely SUV_{mean}, SUV_{max}, and SAM, resulting in an impressive R^2 value of 0.83 and a low MAE of 0.93 *Gy/ GBq*. The correlation of all the selected features with the absorbed dose based on uni/bi-variate analysis is illustrated visually in Fig. 6. Moreover, we combined the three selected features from PET imaging with clinical biomarkers and improved the prediction performance (R^2 = 0.85, MAE = 0.93 *Gy/ GBq*). These observations could imply that clinical biomarkers, particularly blood test features such as PSA, might influence tumor behavior, potentially impacting the extent of PSMA tumor uptake and metabolism.

While our study yielded meaningful and promising outcomes, it faced certain limitations. First and foremost, the patient cohort was limited due to the high workload and time-consuming nature of the SPECT/CT or whole-body planar imaging in dosimetry workflow. The nuclear medicine center, where the study was conducted, had only one SPECT/CT system, contributing to the constraints on patient enrollment. Incorporating additional subjects may enhance the model's generalizability and robustness. Despite the development of ML methods, the limited data for training may limit their predictive power in the dosimetry prediction process. The reliability of dose estimation using ML can be improved by training and validation with additional data. Moreover, due to the non-mandatory nature of post-treatment scans, we were unable to obtain all whole-body planar post-treatment scans for a few patients. Our study is inherently limited by uncertainties associated with the nature of the dosimetry workflow. This includes challenges in quantitative imaging, encompassing aspects such as scatter/attenuation correction, segmentation, and calibration factor. Additionally, the study was constrained by uncertainties in multi-time point serial imaging, involving considerations such as time-series registration, time–activity curve parameters, and cumulated activity determination [33]. Furthermore, the simplification of post-therapy imaging, whether through the adoption of SPECT/ whole-body planar hybrid imaging, reduction in imaging time-points, or the approximation of particle transport algorithms, may contribute additional uncertainties to the overall dosimetry process.

In this investigation, PET/CT scans were gathered from a PET/CT scanner within our facility for 18 patients, and an additional two patients had their scans collected from PET/CT scanners

at different centers. This diverse data collection aims to enhance the generalizability of our model. Augmenting the data set from diverse nuclear medicine centers with potential variations in image reconstruction protocols and scanning parameters could enhance the model's ability to generalize. This strategy would make the findings more applicable to other studies. Moreover, in this investigation, we assessed and standardized the suggested prediction model specifically for the initial treatment cycles of each mCRPC patient. Our focus did not extend to exploring absorbed dose prediction across subsequent RLT cycles. However, the potential of the proposed model can be further harnessed in clinical dosimetry, enabling the prediction of absorbed doses for all treatment cycles. Given that manual segmentation stands out as the most time-consuming step in the internal dosimetry workflow, there is an opportunity to enhance efficiency by implementing semi-automatic or fully automatic segmentation procedures to streamline this process [34-38]. Furthermore, we can apply the same methodology to predict absorbed doses of OARs such as the liver, spleen, kidneys, and salivary glands.

The study emphasizes the performance of the ML-based model in predicting absorbed doses is significantly influenced by the choice of feature selection and regression model. Simple linear regression models are found to be less effective than non-linear ML models, such as RF regression, especially when dealing with limited data sets. The need for additional research is underscored to draw conclusive insights into the effective application of automated models in RPTs and the development of precise, patient-specific treatment plans for RLTs in mCRPC cases.

CONCLUSION

To ensure precise individualized dosimetry, it is essential to employ a precise planning agent before undergoing [^{177}Lu]Lu-PSMA-617 RLT. The preliminary findings described herein confirmed the feasibility of pre-treatment tumoral lesion dose prediction before the PSMA-RLT for patients with mCRPC. We assessed the use of [^{68}Ga]Ga-PSMA-11 PET-derived metrics in a multi-center framework and clinical biomarkers to predict tumoral lesion absorbed doses in [^{177}Lu]Lu-PSMA-617 RLT. Tumoral lesion SUV_{mean}, SUV_{max}, and SAM were found to accurately predict absorbed doses (R^2 = 0.85 and MAE = 0.93 *Gy/ GBq*, in 10-fold cross-validation). As a result of this approach, each cycle of therapy could be tailored for optimal activity levels to reduce radiation-induced tissue damage while enhancing tumor suppression. Validation on multi-center datasets will provide clinicians with a decision-support tool,

improve patient stratification, and optimize treatment response. To verify the validity of this model in routine clinical practice, investigators should examine more patient data than we analyzed in this study.

Abbreviations

AF: absorbed fraction; ALKP: alkaline phosphatase; CT: computed tomography; cpm: counts per minute; EBRT: external beam radiotherapy; FDA: Food and Drug Administration; GATE: Geant4 Application for Tomographic Emission; HU: Hounsfield units; KNN: k-nearest neighbors; LEHR: low-energy high-resolution; MC: Monte Carlo; mCRPC: metastatic castration-resistant prostate cancer; MIP: maximum intensity projection; MIRD: medical internal radiation dose; ML: machine learning; MTV: metabolic tumor volume; OAR: organs at risk; OSEM: ordered subset expectation maximization; PET: positron emission tomography; PSA: prostate-specific antigen; PSMA: prostate-specific membrane antigen; PVE: partial volume effect; RFR: random forest regression; RLT: radioligand therapy; ROI: regions of interest; RPT: radiopharmaceutical therapies; SAM: Standardized additional metabolic; SPECT: single photon emission computed tomography; STP: single time-point; SUV: standard uptake value; SVR: support vector regression; TAC: time-activity curve; TIA: time-integrated activity; TOF: time of flight; VOI: volume of interest

Acknowledgments

This work was supported by the School of Medicine, Iran University of Medical Sciences (IUMS), Grant number 25160.

Ethics Approval

The Ethics Committee of the Iran University of Medical Sciences (IUMS) approved this study under ethics approval IR.IUMS.FMD.REC.1401.505, with the patient's written informed consent.

Competing Interests

The author declares that there are no conflicts of interest.

References

1. Baum RP, Kulkarni HR. THERANOSTICS: from molecular imaging using Ga-68 labeled tracers and PET/CT to personalized radionuclide therapy-the Bad Berka experience. Theranostics. 2012;2(5):437.

2. Yordanova A, Eppard E, Kürpig S, Bundschuh RA, Schönberger S, Gonzalez-Carmona M, et al. Theranostics in nuclear medicine practice. OncoTargets and therapy. 2017:4821-8.

3. Sartor O, De Bono J, Chi KN, Fizazi K, Herrmann K, Rahbar K, et al. Lutetium-177–PSMA-617 for metastatic castration-resistant prostate cancer. New England Journal of Medicine. 2021;385(12):1091-103.

4. Kessel K, Bernemann C, Bögemann M, Rahbar K. Evolving castration resistance and prostate specific membrane antigen expression: implications for patient management. Cancers. 2021;13(14):3556.

5. Food U, Administration D. FDA approves Pluvicto for metastatic castration-resistant prostate cancer. 2022.

6. Flux GD, Sjogreen Gleisner K, Chiesa C, Lassmann M, Chouin N, Gear J, et al. From fixed activities to personalized treatments in radionuclide therapy: lost in translation? European Journal of Nuclear Medicine and Molecular Imaging. 2018;45:152-4.

7. Stokke C, Gabiña PM, Solný P, Cicone F, Sandström M, Gleisner KS, et al. Dosimetry-based treatment planning for molecular radiotherapy: a summary of the 2017 report from the Internal Dosimetry Task Force. EJNMMI physics. 2017;4(1):1-9.

8. Mokoala K, Lawal I, Lengana T, Kgatle M, Giesel FL, Vorster M, et al. PSMA theranostics: science and practice. Cancers. 2021;13(15):3904.

9. Sjögreen Gleisner K, Chouin N, Gabina PM, Cicone F, Gnesin S, Stokke C, et al. EANM dosimetry committee recommendations for dosimetry of 177Lu-labelled somatostatin-receptor-and PSMA-targeting ligands. European Journal of Nuclear Medicine and Molecular Imaging. 2022;49(6):1778-809.

10. O'Donoghue J, Zanzonico P, Humm J, Kesner A. Dosimetry in radiopharmaceutical therapy. Journal of Nuclear Medicine. 2022;63(10):1467-74.

11. Han S, Woo S, Kim YJ, Suh CH. Impact of 68Ga-PSMA PET on the management of patients with prostate cancer: a systematic review and meta-analysis. European urology. 2018;74(2):179-90.

12. Yazdani E, Geramifar P, Karamzade-Ziarati N, Sadeghi M, Amini P, Rahmim A. Radiomics and Artificial Intelligence in Radiotheranostics: A Review of Applications for Radioligands Targeting Somatostatin Receptors and Prostate-Specific Membrane Antigens. Diagnostics. 2024;14(2):181.

13. Violet J, Jackson P, Ferdinandus J, Sandhu S, Akhurst T, Iravani A, et al. Dosimetry of 177Lu-PSMA-617 in metastatic castration-resistant prostate cancer: correlations between pretherapeutic imaging and whole-body tumor dosimetry with treatment outcomes. Journal of nuclear medicine. 2019;60(4):517-23.

14. Wang J, Zang J, Wang H, Liu Q, Li F, Lin Y, et al. Pretherapeutic 68Ga-PSMA-617 PET may indicate the dosimetry of 177Lu-PSMA-617 and 177Lu-EB-PSMA-617 in main organs and tumor lesions. Clinical nuclear medicine. 2019;44(6):431.

15. Scarpa L, Buxbaum S, Kendler D, Fink K, Bektic J, Gruber L, et al. The 68Ga/177Lu theragnostic concept in PSMA targeting of castration-resistant prostate cancer: correlation of SUVmax values and absorbed dose estimates. European journal of nuclear medicine and molecular imaging. 2017;44(5):788-800.

16.Brosch-Lenz J, Colpo N, Bloise I, Hou X, Parulekar W, Dellar C, et al. Can we use pre-therapy PSMA PET/CT as a predictor for Lutetium-177-PSMA-617 therapy? Early experience from the Canadian Cancer Trials Group PR21 trial (NCT 04663997). Journal of Nuclear Medicine. 2023;64(supplement 1):P985-P.

17. Xue S, Gafita A, Dong C, Zhao Y, Tetteh G, Menze BH, et al. Application of machine learning to pretherapeutically estimate dosimetry in men with advanced prostate cancer treated with 177Lu-PSMA I&T therapy. European journal of nuclear medicine and molecular imaging. 2022:1-9.

18. Ljungberg M, Celler A, Konijnenberg MW, Eckerman KF, Dewaraja YK, Sjögreen-Gleisner K. MIRD pamphlet no. 26: joint EANM/MIRD guidelines for quantitative 177Lu SPECT applied for dosimetry of radiopharmaceutical therapy. Journal of nuclear medicine. 2016;57(1):151-62.

19. Delker A, Fendler WP, Kratochwil C, Brunegraf A, Gosewisch A, Gildehaus FJ, et al. Dosimetry for 177 Lu-DKFZ-PSMA-617: a new radiopharmaceutical for the treatment of

metastatic prostate cancer. European journal of nuclear medicine and molecular imaging. 2016;43:42-51.

20. Chatachot K, Shiratori S, Chaiwatanarat T, Khamwan K. Patient dosimetry of 177 Lu-PSMA I&T in metastatic prostate cancer treatment: the experience in Thailand. Annals of Nuclear Medicine. 2021;35:1193-202.

21. Siegel JA, Thomas SR, Stubbs JB, Stabin MG, Hays MT, Koral KF, et al. MIRD pamphlet no. 16: techniques for quantitative radiopharmaceutical biodistribution data acquisition and analysis for use in human radiation dose estimates. Journal of Nuclear Medicine. 1999;40(2):37S-61S.

22. Dewaraja YK, Frey EC, Sgouros G, Brill AB, Roberson P, Zanzonico PB, et al. MIRD pamphlet no. 23: quantitative SPECT for patient-specific 3-dimensional dosimetry in internal radionuclide therapy. Journal of Nuclear Medicine. 2012;53(8):1310-25.

23. Jackson P, McIntosh L, Hofman MS, Kong G, Hicks RJ. Rapid multiexponential curve fitting algorithm for voxel-based targeted radionuclide dosimetry. Medical Physics. 2020;47(9):4332-9.

24. Bolch WE, Eckerman KF, Sgouros G, Thomas SR. MIRD pamphlet no. 21: a generalized schema for radiopharmaceutical dosimetry—standardization of nomenclature. Journal of Nuclear Medicine. 2009;50(3):477-84.

25. O'Dwyer E, Bodei L, Morris MJ, editors. The role of theranostics in prostate cancer. Seminars in radiation oncology; 2021: Elsevier.

26. Farolfi A, Fendler W, Iravani A, Haberkorn U, Hicks R, Herrmann K, et al. Theranostics for advanced prostate cancer: current indications and future developments. European urology oncology. 2019;2(2):152-62.

27. Okamoto S, Thieme A, Allmann J, D'Alessandria C, Maurer T, Retz M, et al. Radiation dosimetry for 177Lu-PSMA I&T in metastatic castration-resistant prostate cancer: absorbed dose in normal organs and tumor lesions. Journal of Nuclear Medicine. 2017;58(3):445-50.

28. Miller C, Rousseau J, Ramogida CF, Celler A, Rahmim A, Uribe CF. Implications of physics, chemistry and biology for dosimetry calculations using theranostic pairs. Theranostics. 2022;12(1):232.

29. Fendler WP, Eiber M, Beheshti M, Bomanji J, Ceci F, Cho S, et al. 68 Ga-PSMA PET/CT: Joint EANM and SNMMI procedure guideline for prostate cancer imaging: version 1.0. European journal of nuclear medicine and molecular imaging. 2017;44:1014-24.

30. Ezziddin S, Lohmar J, Yong-Hing CJ, Sabet A, Ahmadzadehfar H, Kukuk G, et al. Does the pretherapeutic tumor SUV in 68Ga DOTATOC PET predict the absorbed dose of 177Lu octreotate? Clinical nuclear medicine. 2012;37(6):e141-e7.

31. Akhavanallaf A, Peterson AB, Fitzpatrick K, Roseland M, Wong KK, El-Naqa I, et al. The predictive value of pretherapy [68Ga] Ga-DOTA-TATE PET and biomarkers in [177Lu] Lu-PRRT tumor dosimetry. European Journal of Nuclear Medicine and Molecular Imaging. 2023:1-13.

32. Hänscheid H, Sweeney RA, Flentje M, Buck AK, Löhr M, Samnick S, et al. PET SUV correlates with radionuclide uptake in peptide receptor therapy in meningioma. European journal of nuclear medicine and molecular imaging. 2012;39:1284-8.

33. Gear JI, Cox MG, Gustafsson J, Gleisner KS, Murray I, Glatting G, et al. EANM practical guidance on uncertainty analysis for molecular radiotherapy absorbed dose calculations. European journal of nuclear medicine and molecular imaging. 2018;45:2456-74.

34. Moazemi S, Khurshid Z, Essler M, Schultz T, Bundschuh R. Automated detection of pathological lesions in PSMA PET/CT scans in prostate cancer patients: analyzing the relative importance of different groups of features. Nuklearmedizin-NuclearMedicine. 2019;58(02):L7.

35. Nazari M, Jiménez-Franco LD, Schroeder M, Kluge A, Bronzel M, Kimiaei S. Automated and robust organ segmentation for 3D-based internal dose calculation. EJNMMI research. 2021;11(1):1-13.

36. Nickols N, Anand A, Johnsson K, Brynolfsson J, Borreli P, Parikh N, et al. aPROMISE: a novel automated PROMISE platform to standardize evaluation of tumor burden in 18F-DCFPyL images of veterans with prostate cancer. Journal of Nuclear Medicine. 2022;63(2):233-9.

37. Yazdani E, Karamzadeh-Ziarati N, Cheshmi SS, Sadeghi M, Geramifar P, Vosoughi H, et al. Automated segmentation of lesions and organs at risk on [68Ga] Ga-PSMA-11 PET/CT images using self-supervised learning with Swin UNETR. Cancer Imaging. 2024;24(1):30.

38. Parhi S, Xue S, Gafita A, Eiber M, Rominger A, Afshar-Oromieh A, et al. Semi-automatic Segmentation of Metastatic Tumor Load for 177Lu-PSMA Therapy. Soc Nuclear Med; 2022.

ICNST 2024
International Conference on Nuclear Science and Technology
6- 8 MAY 2024 | Isfahan, Iran

Monte Carlo simulation of biological shielding for 90Sr/90Y generator (Paper ID : 1380)

Vosoughi S. Co-Author [1], Mehrabi M. Co-Author[1], Salek N. Correspondent [2*], Moazami HR. Co-Author[2]

Radiation Application Research School, Nuclear Science and Technology Research Institute (NSTRI), Box 14395-836, North Kargar Street, Tehran, Iran.
Nuclear Fuel Research School, Nuclear Science and Technology Research Institute (NSTRI), Box 14395-836, North Kargar Street, Tehran, Iran.

Abstract

Yttrium-90 is a pure beta emitter with a half-life of 64.1 hours and an average energy of 0.9367 MeV which decays to stable zirconium-90. Today, high-energy beta emitters such as yttrium-90 are increasingly used in nuclear medicine. Improving the targeted therapy with radionuclides requires effective protection of personnel and the general against the harmful effects of beta radiation and bremsstrahlung radiation caused by the interaction of energetic beta particles with shield material. In the shielding design for high-energy beta emitters, various characteristics of materials such as maximum beta range and bremsstrahlung yield should be considered. In this study, the simulation of the biological shielding for the in-house $^{90}Sr/^{90}Y$ generator (Pars Isotope Company) was performed by calculating the effective dose using the MCNP6 code. The results showed that polyethylene was the optimal material for efficient shielding against ^{90}Sr and ^{90}Y Beta radiation. Bremsstrahlung radiation can be further reduced by adding a layer of lead to the primary shielding material. Ultimately, the effective dose reduces from a certain value in mSv to µSv using a multi-layer shield configuration.

Keywords: Radiation shielding, $^{90}Sr/^{90}Y$ generator, MCNP6, Bremsstrahlung

INTRODUCTION

Targeted therapy with radionuclides (TRT) has attracted the attention of many nuclear researchers in recent years. Unlike conventional external beam radiation therapy, TRT causes less lateral damage to normal tissues and allows radiopharmaceuticals to be delivered to

neoplastic abnormalities, metastasized cells, and cell clusters and cause cancer treatment. This method is based on the use of molecules with high affinity (as carriers of radionuclides) to tumor cells [1]. The use of radionuclides has increased with the development of targeted radionuclide therapy and it has led to an increase in the demand for therapeutic radionuclides.

Yttrium-90 (half-life: 64.1 hours) as a pure beta emitter decays to stable zirconium-90 and produces the most beta energy among beta emitters. It is an important radionuclide in nuclear medicine and the treatment of bulky malignant tumors. The average and maximum penetration depths are 2.5 and 10 mm, respectively. Maximum beta energy is 2.27 MeV (100%) and the linear energy transfer is about 2keV/µm. It can be produced with two direct and indirect methods. In the direct method, ^{90}Y is produced from irradiation of the ^{89}Y target using thermal neutrons through the ^{89}Y(n,γ)^{90}Y reaction. The obtained radionuclide by this method is carrier-added (CA) and due to its low specific activity, it can be applied for different applications such as radio-synovectomy and brachytherapy. The carrier-free (CF) form of ^{90}Y used in TRT due to its high specific activity is obtained through the ^{90}Y/^{90}Sr radionuclide generator which is based on the indirect production method. In this method, ^{90}Sr is used as the parent radionuclide, and the daughter radionuclide (^{90}Y) is separated from it. The separation method currently used is the electrochemical separation method.

In the ^{90}Sr/^{90}Y generator, beta and bremsstrahlung radiations are produced. Although these radiations are useful for cancer treatment, they cause biological hazards for personnel. Depending on the amount of radiation, symptoms such as nausea, hair loss, hives, and skin irritations may appear. More intensive exposure may also lead to cancer and heart problems. Three factors of irradiation time, distance, and radiation protection should be considered for reducing hazards. Irradiation time should be minimized and since the radiation intensity is inversely proportional to the square of the distance, therefore a safe distance from the radiation source should be maintained. A biological shield is the most effective factor in reducing radiation intensity. Therefore, to reduce the personnel dose to a safe level, a suitable biological shield must be designed. The important factors in the design of the shield are the geometry and the type of material. To achieve the appropriate dose, the thickness of the device's shield must be sufficient and affordable in terms of cost. In this study, the simulation of the biological

shielding for the in-house $^{90}Sr/^{90}Y$ generator (Pars Isotope Company) was performed by calculating the effective dose using the MCNP6 code.

Material and Methods

In biological protection issues, the annual occupational dose limit is defined as the quantity of the effective dose of the whole body [2]. In this study, to calculate this quantity, flux to effective dose conversion coefficients provided by ICRU-57 have been used. These coefficients were defined using DE, DF, and logarithmic interpolation in the simulation.

MCNP6 is an effective code for simulating the interaction of radiation in different types of shielding materials [3,4]. This code considers the interaction of electrons through elastic and inelastic scattering, ionization, delta beam production, and bremsstrahlung radiation. The interaction of beta particles emitted from the decay of ^{90}Y with the nuclei of the shielding material causes the creation of bremsstrahlung radiation. Bremsstrahlung radiation may be generated from the shielding of the generator and lead to increased radiation exposure of related personnel. Therefore, the removal of bremsstrahlung radiation is very important in shielding, especially when the beta energy is very high. To estimate the total effective dose, the incident flux on the point detectors, in the appropriate energy ranges, has been calculated using the MCNP6 code. Knowing the flux, and the coefficients for converting the flux into the effective dose for the energy distribution, and considering all the particles, the amount of the effective dose for different materials is calculated according to equation (1):

$$E = \sum_{P}\left(\sum_{E} (E/\Phi)_{E,P}.\Phi_{E,\mathrm{p}} \right) \tag{1}$$

Result and discussion

Figure 1 presents the simulation results for three different materials, polyethylene, aluminum, and acrylic, used as beta radiation shields at various thicknesses. As evident from the figure, polyethylene demonstrates the best performance as a beta radiation shield. The selection of these three materials for simulation is justified by their widespread use as shielding materials for beta radiation.

In the case of beta radiation shielding, polyethylene, aluminum, and acrylic are commonly employed due to their favorable characteristics. Polyethylene is a widely used material for shielding purposes due to its high hydrogen content, which effectively attenuates beta particles. Aluminum, with its moderate

atomic number, offers a good compromise between shielding effectiveness and ease of handling. Moving on to the shielding of bremsstrahlung radiation, three other materials, bismuth, lead, and tungsten, were considered at different thicknesses, as shown in Figure 2. Lead, bismuth, and tungsten are commonly used for bremsstrahlung shielding due to their high atomic numbers and superior attenuation properties. As shown in Figure 2, the obtained results indicate that lead is the most effective material for shielding bremsstrahlung radiation.

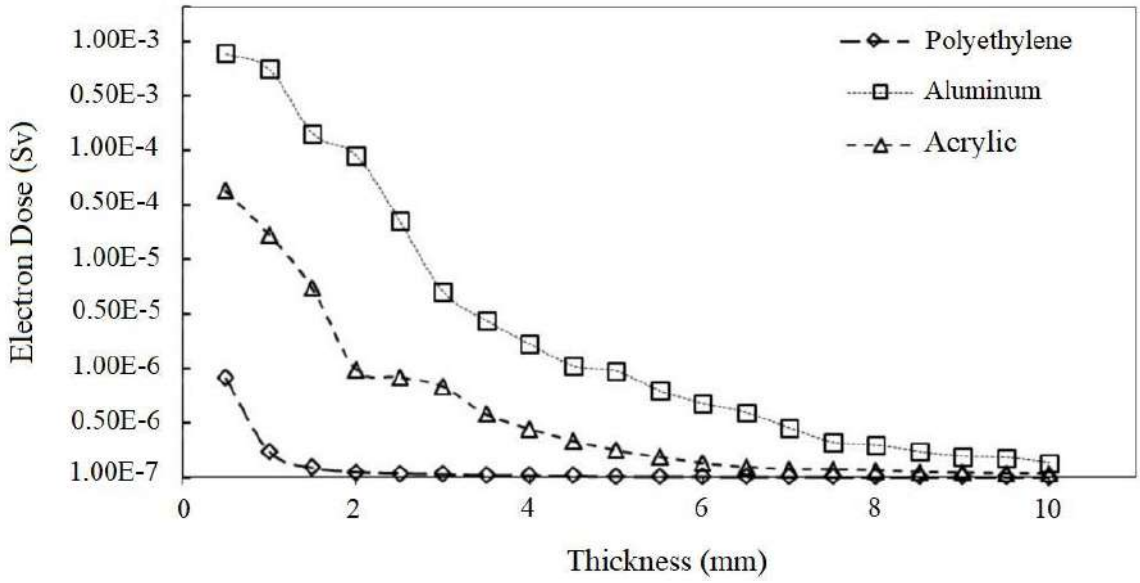

Figure 1: Comparison of beta radiation dose in different thicknesses of Polyethylene, Aluminum, and Acrylic shields

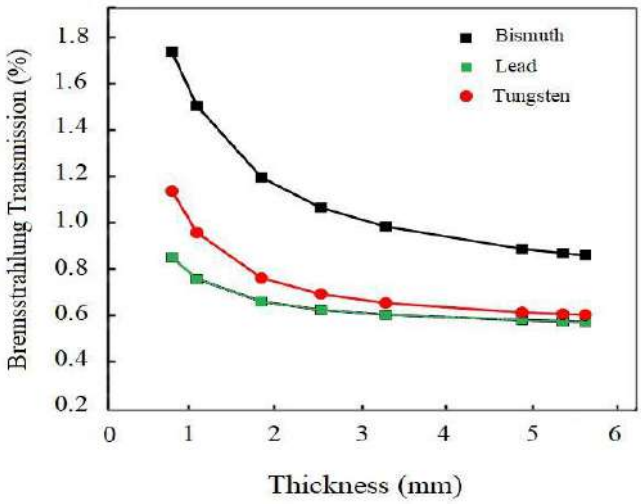

Figure 2: Percentage of bremsstrahlung radiation transmission through Bismuth, Lead, and Tungsten shields

Considering the results obtained, a combination of two layers, polyethylene and lead, was chosen for optimal shielding performance. This configuration resulted in a significant reduction in the effective dose, measured in 0.084 µSv.

Conclusions

In conclusion, the simulation results indicate that polyethylene is the optimal material for beta radiation shielding, while lead is the most effective material for bremsstrahlung shielding. Based on these findings, a multi-layer shield configuration consisting of polyethylene and lead was implemented, resulting in a substantial reduction in the effective dose to a safe level.

References

[1] Curcio, C. G., Vasile, C., Gianciotta, A., Casali, A., Gionfra, T., Rinaldi, M., ... & Sega, E. (1976). Short-term results of combined radioimmunotherapy in inoperable lung cancer. Tumori Journal, 62(6), 587-597.

[2] Seltborg, P., Polanski, A., Petrochenkov, S., Lopatkin, A., Gudowski, W., & Shvetsov, V. (2005). Radiation shielding of high-energy neutrons in SAD. Nuclear Instruments and Methods in Physics Research Section A: Accelerators, Spectrometers, Detectors and Associated Equipment, 550(1-2), 313-328.

[3] Sayyed, M. I., Mahmoud, K. A., Islam, S., Tashlykov, O. L., Lacomme, E., & Kaky, K. M. (2020). Application of the MCNP 5 code to simulate the shielding features of concrete samples with different aggregates. Radiation Physics and Chemistry, 174, 108925.

[4] Ozyurt, O., Altinsoy, N., Karaaslan, Ş. İ., Bora, A., Buyuk, B., & Erk, İ. (2018). Calculation of gamma-ray attenuation coefficients of some granite samples using a Monte Carlo simulation code. Radiation Physics and Chemistry, 144, 271-275.

ICNST 2024
International Conference on Nuclear Science and Technology
6- 8 MAY 2024 | Isfahan, Iran

The effect of current density in galvanostatic electrochemical separation of Radiopharmaceutical grade (_^90)Y from (_^90)Sr - Paper ID : 1384

Moazami H.R. Co-Author[1], Salek N. Correspondent [1*], Vosoughi S. Co-Author [2], khosronejad H. Co-Author [3]

Nuclear Fuel Research School, Nuclear Science and Technology Research Institute (NSTRI), Box 14395-836, North Kargar Street, Tehran, Iran.

Radiation Application Research School, Nuclear Science and Technology Research Institute (NSTRI), Box 14395-836, North Kargar Street, Tehran, Iran.

Pars isotope company, No.88, West 23rd St.Azadegan Blvd. South Sheykh Bahaie Ave. Tehran, Iran

Abstract

Radiopharmaceutical grade ^{90}Y was electrochemically separated from ^{90}Sr in galvanostatic mode. The separation was carried out in a two-electrode assembly composed of a central rod-shaped Pt electrode surrounded by a helical Pt wire electrode. The separation sequence was a) the loading of ^{90}Sr solution in the electrochemical cell and three-replicated accumulation of the impure ^{90}Yon the outer helical electrode. b) the loading of the cell with ^{nat}Sr solution and collection of the accumulated ^{90}Y on the central rod electrode by reversing the cell polarity and c) three replicated purifications of ^{90}Y by dissolution/electrodeposition cycles. To investigate the effect of current density, separations were conducted from a $5Ci$ feed solution in one-week periods at various applied currents ranging from 300 to 900 mA with 100 mA intervals. It was found that the applied current has a significant impact on the overall separation performance and parameters such as separation time, recovery, wasted activity, and final activity of the produced ^{90}Y Generally, separations at low applied currents, were time/activity consuming but gave higher final activities. For an applied current of 300mA, a final activity of 629.61 mCi was achieved but 37.46 % of the activity was wasted during the purification steps. On the contrary, high applied currents (800mA) allowed for faster separation with lower wasted activity (20.1 %).

Keywords: Ytrium-90, Strontium-90, generator, electrochemical separation, current.

INTRODUCTION

The ^{90}Y radionuclide is obtained from the ^{90}Sr/^{90}Y radionuclide generator for a wide range of therapeutic applications, especially in the treatment of cancers. Since yttrium-90 is a pure beta emitter with a high energy of 2.27 Mev and a half-life of 64.53 hours can be effective in the treatment of massive cancer tumors [1]. The average and maximum radiation penetration is 2.5 and 10 mm, respectively. This radionuclide has drawn a lot of interest because of its direct injection into the tumor and lack of gamma radiation, which lowers the quantity of undesired radiation of non-target tissues yttrium-90 can be labeled with antibodies and peptides and also has many therapeutic applications such as radioimmunoassay, radio-synovectomy, and bone pain palliation. Unlike other therapeutic radionuclides, there is unlimited potential for the use of ^{90}Y because its radionuclide parent ^{90}Sr is one of the main fission products and the annual global production of ^{90}Sr in nuclear reactors reaches several hundred megacuries [2-5]. Over the past three decades, to obtain a ^{90}Sr/^{90}Y generator, several isolation technologies have been reported. Most of these separation techniques involve multiple steps and use conventional separation methods such as solvent extraction, ion exchange, or extractive chromatography alone or in combination. However, none of these methods are acceptable for routine use in hospitals [5,6]. With commercial access to ^{90}Sr/^{90}Y electrochemical generator, it became possible to use this generator in radiopharmaceuticals regularly. The entire separation process uses simple electrochemistry and can be automated [7,8]. An electrochemical module, named the "^{90}Y -Kamdhenu" generator, was developed fully automatically by Dr. Joseph Komor and now is available in the Pars isotope company of Iran. Some optimization to best supply ^{90}Y radiopharmaceuticals to nuclear medical centers. This study investigated the significant effect of applied current on the parameters and overall performance of the separation, including the final activity of the produced, ^{90}Y recovery, wasted activity, and separation time.

EXPRIMENTAL

The optimization of current density was done on the ^{90}Sr/^{90}Y Kamadhenu generator available in the pars isotope company of IRAN. A two-electrode assembly with a central rod-shaped Pt electrode and a helical Pt wire electrode around it was used to perform the separation.

A) loading of the ^{90}Sr solution into the electrochemical cell and a three-repeated accumulation of the impure ^{90}Y on the outer helical electrode: The accumulation step is carried out in three

consecutive cycles of 45 minutes. The solution containing strontium-90 along with yttrium-90 is introduced into the electrochemical cell. Applying a potential to the electrodes, impure Y-90 is loaded onto the central electrode. In each cycle, an increase in activity occurs firstly, due to the electrochemical deposition of yttrium-90. In the time between cycles, the ^{90}Sr parent solution free of Yttrium-9 is drained from the electrochemical cell and then a fresh solution containing higher amounts of Yttrium-90 is injected into the cell.

B) filling the cell with ^{nat}Sr solution and collecting the accumulated ^{90}Y on the central rod electrode by reversing the cell polarity.:

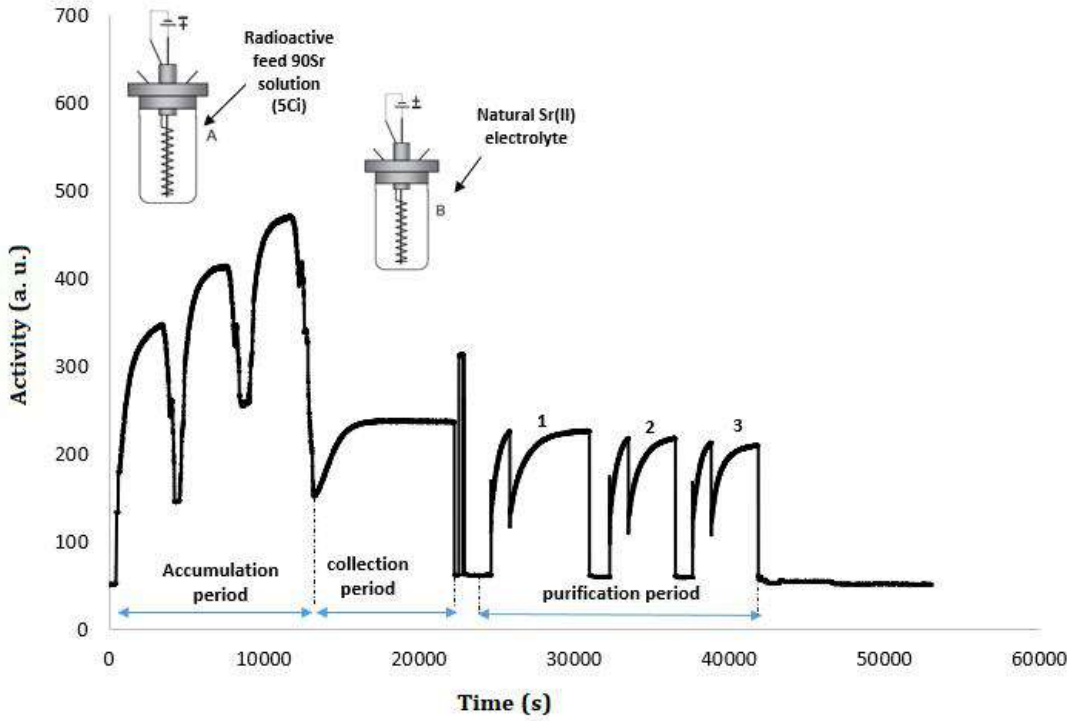

Fig. 1. Activity on central electrode

After the accumulation step, in the collection step, the electrolyte containing natural strontium is introduced into the cell. Yttrium-90 loaded on the electrode is diluted in natural strontium electrolyte and collected by re-applying the potential. The activity detected by the detector increases and reaches a stable plateau after a certain time. In the purification step, the central electrode containing the collected yttrium-90 is removed from the cell and the cell is washed. Then the electrolyte containing natural strontium is introduced into the cell.

C) Purification is done in three cycles of electrode polarity reversal. In each cycle, yttrium-90 deposited on the central electrode is removed and after changing the electrolyte, it is dissolved by changing the polarity. These reversals cause the precipitation/redissolution of yttrium-90 and the dilution of strontium-90 in natural strontium and its significant reduction in the final product. At the end, yttrium-90 free from strontium-90 impurity is dissolved in a hydrochloric acid solution by removing the central electrode and used for the marking stage.

Results and discussion

Optimization of the current density of all experiments was performed with a time interval of one week for the decay of ^{90}Sr and acceptable production of ^{90}Y. A constant current density was used for all steps of accumulation, collection, and purification. By changing this current in the range of 300 to 900 mA at intervals of 100 mA, the effect of this parameter on the results was followed. Figure 2 illustrates the detected activity versus time for different currents in the range of 300 to 900 mA.

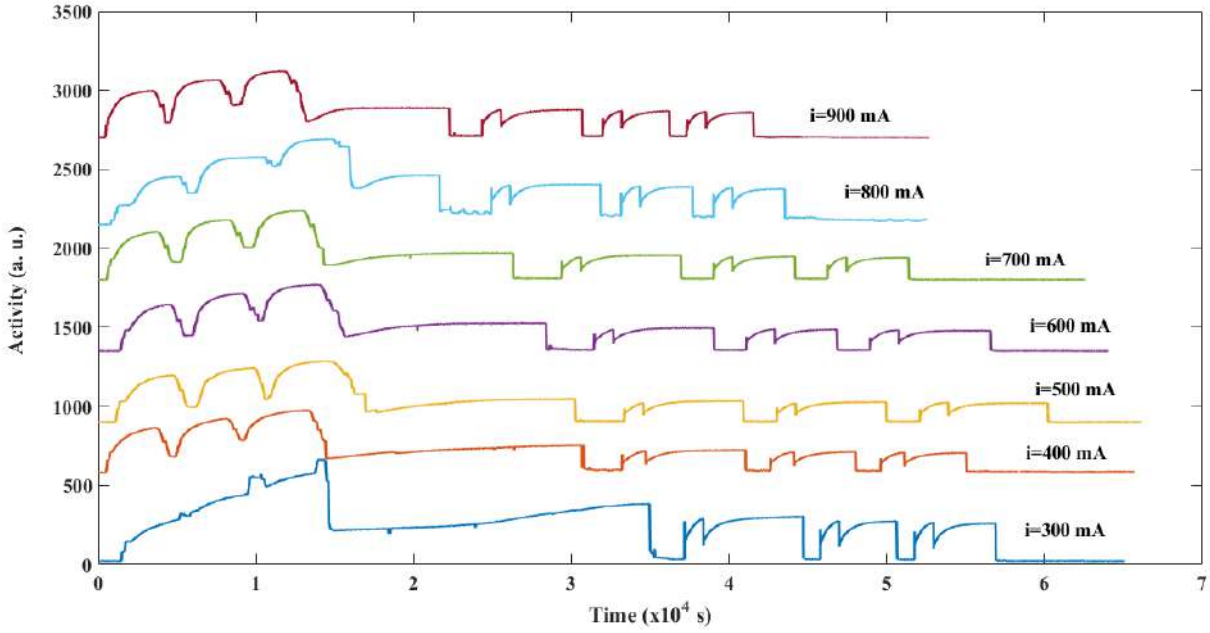

Fig. 2. Changes of detected activity versus time for different currents

Figure 3 shows the dependency of the accumulated activity as a function of the applied current.

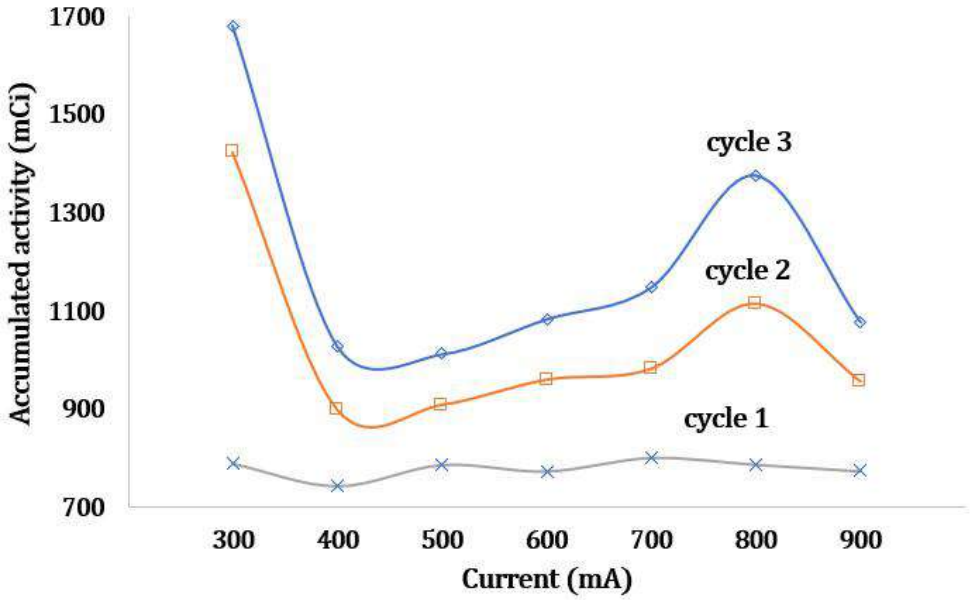

Fig. 3. The dependency of the accumulated activity as a function of the applied current

The cumulative activity curve in the first cycle is smooth and unaffected by the applied current. At 300 mA, the largest cumulative activity is observed in the second and third cycles. But as the current rises, it diminishes. At 800 mA, the activity once more approaches an extremum before declining. The complicated subordination of the accumulated activity to the applied current appears to result from the interaction of three factors: the applied current's Joule heating of the solution, the electrode reaction's overall kinetic profile, and the evolution of hydrogen. The electrode reaction's kinetics are adequate for the solution's slow deposition at extremely low currents, whereas hydrogen evolution and Joule heating have little effect. Hydrogen emission becomes more important with increasing current. Hydrogen emission has two harmful effects. The first effect includes reducing the cathode gain of the cell. In fact, with the evolution of hydrogen, the charge passing through the cell becomes an undesirable side reaction and the share of the charge used for the deposition of yttrium-90 decreases. Another harmful effect is the removal of ^{90}Y ions from the surface of the electrode due to the pressure resulting from the release of hydrogen gas. As the current increases further and the overall rate of reduction reactions increases, the accumulated activity increases once again, reaching a maximum at 800 mA. As the current increases excessively, Joule heating of the solution is likely. This Joule heating changes parameters such as reduction potential and solubility product, which are thermally dependent.

Conclusions

The effect of current on the performance of electrochemical separation of ^{90}Y was investigated. The results showed that the current has significant impact on the performance of the extraction. In the first cycle of accumulation, the activity showed a smooth current dependence indicating a monolayered deposition of ^{90}Y. In 2nd and 3rd cycles, the activity showed maxima at the lowest current (300mA) and local extremums at 800 mA. According to the obtained results, the optimized current depends on the production strategy. The application of low currents results in higher final activity, but the separation is time consuming and generates significant amount of radioactive waste. While, higher currents allow for faster separation and lower amount of waste with a slight reduction in activity.

Acknowledgments

The Pars isotope company's cooperation in presenting this work is gratefully acknowledged.

References

[1] Lange, G.; Herrmann, G.; Strassmann, F(1957) Preparation of strontium90-free yttrium-90 by electrolysis [in German]. J. Inorg. Nucl. Chem., 4,146–54.

[2] Hamaguchi, H.; Ikeda, N.; Kawashima, T (1958). Isolation of carrier free yttrium from the radioactive strontium-yttrium system by electrodeposition. Bunseki Kagaku, 7, 243–6.

[3]. Barrio, G., & Osso, J. A. (2007). Development of methodology for the preparation of 90S r-90 Y generators.

[4]. Skraba, W.J.; Arino, H.; Kramer, H.H (1978). A new ^{90}Sr/^{90}Y radioisotope generator. Int. J. Appl. Radiat. Isot., 29, 91-96.

[5] Chinol, M.; Hnatowich, D.J (1987). Generator-produced Yttrium-90 for radioimmunotherapy. J. Nucl. Med., 28, 1465-1470

[6] Malja, S., Schomacker, K., & Malja, E. (2000). Preparation of ^{90}Y by the ^{90}Sr-^{90}Y generator for medical purpose. Journal of Radioanalytical and Nuclear Chemistry, 245(2), 403-406.

[7]. Chakravarty, R., Pandey, U., Manolkar, R. B., Dash, A., Venkatesh, M., & Pillai, M. A. (2008). Development of an electrochemical ^{90}Sr–^{90}Y generator for separation of ^{90}Y suitable for targeted therapy. Nuclear medicine and biology, 35(2), 245-253.

[8]. Dash, A., & Chakravarty, R. (2014). Electrochemical separation: promises, opportunities, and challenges to develop next-generation radionuclide generators to meet clinical demands. Industrial & Engineering Chemistry Research, 53(10), 3766-3777.

ICNST 2024
International Conference on Nuclear Science and Technology
6- 8 MAY 2024 | Isfahan, Iran

Development of 64Cu-DOTA-(Tyr3)-octreotate for PET imaging of neuroendocrine tumors (Paper ID : 1387)

Zolghadri S.[1], Shafiei S.[1], Karimian A.[1], Yousefnia H. [1*]

[1] *Radiation Application Research School, Nuclear science and technology Research Institute, P.O.BOX: 14893-836, Tehran, Iran.*

Abstract

Neuroendocrine tumors (NETs) are the dangerious cancers originate from endocrine tissues which overexpress somatostatin receptors (SSRs) on the cell surfaces. The early diagnosis of the tumors cauld be very helpful for the treatment managment. Targeted radiopharmaceuticals can be effectively used for diagnosis of the tumors overexpressed SSRs. Positron emission tomography (PET) can provide the visualization and quantification of functions at the cellular or molecular level. Copper-64 (^{64}Cu) is known as one of the suitable PET radioisotopes for diagnosing and treating various types of cancers. This study aimed to develop ^{64}Cu-DOTA-(Tyr3)-octreotate as a new agent for PET imaging of NETs. Zinc-68 was bombarded via proton (30 MeV) to produce ^{64}Cu-DOTA-(Tyr3)-octreotate was labeled with ^{64}Cu at the optimized conditions. Radiochemical purity assessment was checked by HPLC and RTLC, and stability was measured up to 12 h in PBS buffer (**4**°C) and human serum (**37**°C). Biodistribution was investigated after injected ^{64}Cu-DOTA-(Tyr3)-octreotate (150 µL; 150 µCi) to tumor-bearing rats. The radiolabeled compound was produced with radiochemical purity >99% and specific activity of 22.4 GBq/mg. ^{64}Cu-DOTA-(Tyr3)-octreotate demonstrated high stability in vitro and in vivo. The biodistribution of the final complex in tumor-bearing rats showed high uptake of somatostatin-receptor-expressing organs and tumors. Preclinical studies of ^{64}Cu-DOTA-(Tyr3)-octreotate showed that the radiopharmaceutical has a high potential for domestic use in PET imaging of patients with NETs.

Keywords: ^{64}Cu, Neuroendocrine tumors, somatostatin receptors, Positron emission tomography, Octreotate

INTRODUCTION

Neuroendocrine tumors (NETs) are engendered from the secondary epithelial cell lines. NETs overexpress somatostatin receptors (SSRs) on the cell surfaces and originate from endocrine tissues including the respiratory tract, gastrointestinal tract, central nervous system, pharynx, genitourinary system, breast, skin, and thyroid gland. The early diagnosis of the tumors with the use of radiopharmaceuticals could be very helpful for treatment management [2].

Targeted radiopharmaceuticals can be effectively used for diagnosis of the tumors overexpressed SSRs or variants of NETs.

Positron emission tomography (PET) can provide the visualization and quantification of functions at the cellular or molecular level. ^{64}Cu, is a known radionuclide (half-life= 12.7 h, β+ = 0.653 MeV), labeled with peptides, proteins, antibodies and other biological molecules has been used for PET imaging to diagnose various types of cancers [6]. (Tyr3)-octreotate is a long peptide (eight amino acids) bonded with chelator DOTA which able to react with some radionuclides such as ^{64}Cu, ^{68}Ga, and ^{177}Lu for imaging and treatment.

Due to the especial physical characteristics of ^{64}Cu for PET imaging and high affinity of (Tyr3)-octreotate to target NETs, ^{64}Cu-DOTA-(Tyr3)-octreotate was developed in this study as a new agent for PET imaging of NETs in the country.

EXPERIMENTAL

Preparation and quality control of [^{64}Cu]$CuCl_2$

The Zinc-68(^{68}Zn) target (thickness = 100 μm) coated on high-purity gold was bombarded via proton in a 30 MeV Cyclotron (Cyclone-30, IBA, Belgium) to produce ^{64}Cu. The target was cooled (18 °C) and dissolved in 10 N HCl (15 mL) (Sigma Aldrich, Germany) including hydrogen peroxide (20 μL) (Sigma Aldrich, Germany). It crossed through a cation exchange column and was washed with 9 N HCl (25 mL) (Sigma Aldrich, Germany) to remove Zinc. Eventually, ^{64}Cu was washed with 2 N HCl (50 mL) (Sigma Aldrich, Germany). The radionuclide purity of [^{64}Cu]$CuCl_2$ was measured by a High purity germanium (HPGe) detector (NIGC-4020), and radiochemical purity assessment was checked by radio thin layer

chromatographic (RTLC) with two solvents. The chemical purity of the solvent was check by polarography method.

Optimized production and quality control of [^{64}Cu]Cu-DOTA-(Tyr3)-octreotate

The stock of (Tyr3)-octreotate peptide for labeling purposes was solved in 1 mL pure water (1mg/ml). To find optimized conditions, different parameters including peptide concentration, reaction time, reaction pH, etc. were changed, and in each case the radiochemical purity was determined by RTLC and HPLC methods.

Investigating the stability of [^{64}Cu]Cu-DOTA-(Tyr3)-octreotate

The final stability of the compound was checked in human blood serum (37℃) and PBS buffer (4℃) for 2, 4, 6, and 12 h by HPLC and RTLC methods.

Biodistribution and PET imaging studies of [^{64}Cu]Cu-DOTA-(Tyr3)-octreotate in tumor-bearing rats

Tumors were created by hypodermic injection (1×10^7/100 μL) cells till the average volume of tumors reached to 900±100mm^3. Compounds (150 μL; 150 μCi) were injected into the tumor-bearing rats (weigh= 140-160 gr; age= 8-10 weeks) by their tail veins; and after 2, 4, 12, and 24 h some organs such as bone, muscle, pancreas, heart, small intestine, large intestine, stomach, liver, lung, kidney, and spleen, were investigated. The percentage of injected dose per gram (ID/g%) for each organ was calculated by using Equation (1):

$$\frac{\mathbf{ID}}{\mathbf{g}}\% = \frac{\mathbf{A(t)}}{\mathbf{A_0 \times m}} \quad (1)$$

Where, A(t) is the organ activity in Time (t), A_0 is the injected activity and m is the organ mass. The images were taken at 4, and 24 h by a dual-head SPECT system. The useful field of view (UFOV) was 540 mm × 400 mm.

Results and discussion

Quality control of [^{64}Cu]$CuCl_2$

Radionuclide purity, radiochemical purity, and chemical purity were measured by a HPGe detector, RTLC (Fig.1), and polarographic techniques, respectively. Radionuclide purity was

greater than 99.9, and showed three energy peaks including 278 keV; 9%, 511 keV; 35%, and 1346 keV; 1% for ^{64}Cu. The radiochemical purity was greater than 99%, and it was estimated by two solvent systems such as 1 mM DTPA, and 10% ammonium acetate: methanol (1:1). The chemical purity assessment showed the impurities of the final product was less than 1 ppm.

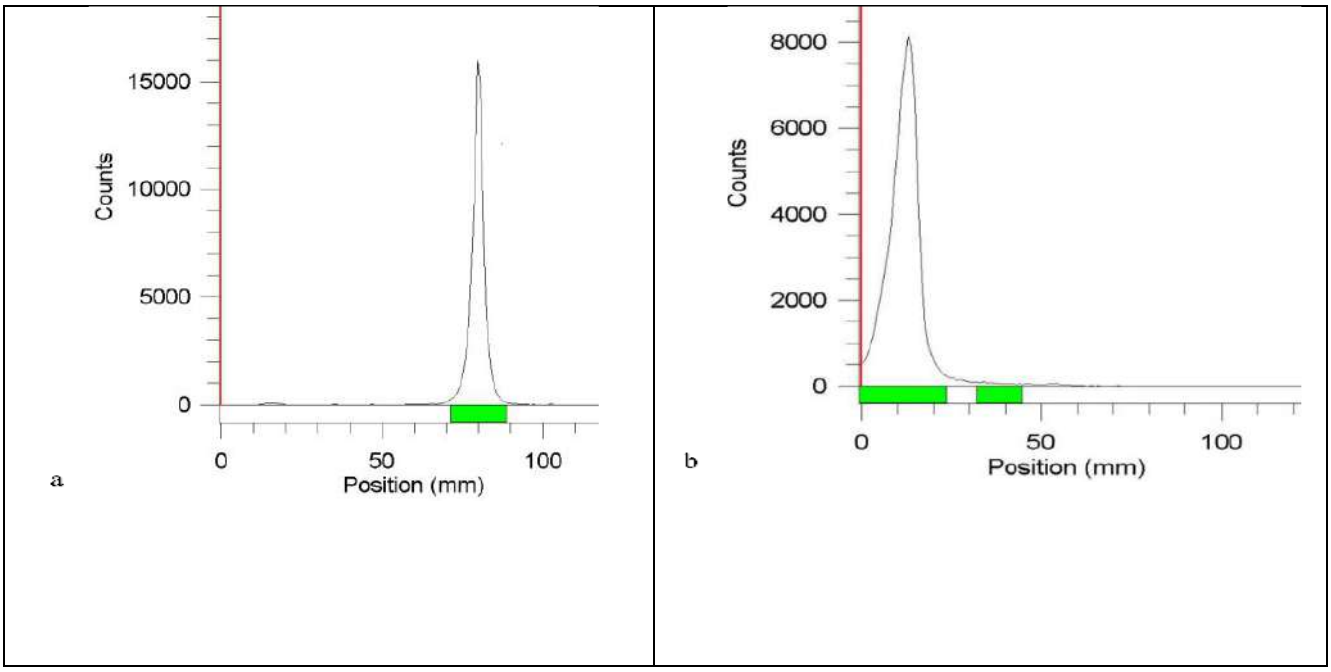

Fig 1. Radio chromatogram of [^{64}Cu]$CuCl_2$ a)1 mM DTPA and b 10% ammonium acetate: methanol ratio (1:1))

Quality control of [^{64}Cu]Cu-DOTA-(Tyr3)-octreotate

The optimized conditions for labeling were activity=10 mCi, Time =20 min, temperature =95°C, pH=5.5, and peptide concentration=15 µg. The radiochemical purity of the compound was measured by RTLC (ammonium acetate 10%: methanol) and HPLC methods, demonstrating the purity of greater than 99% (Figs. 2 & 3).

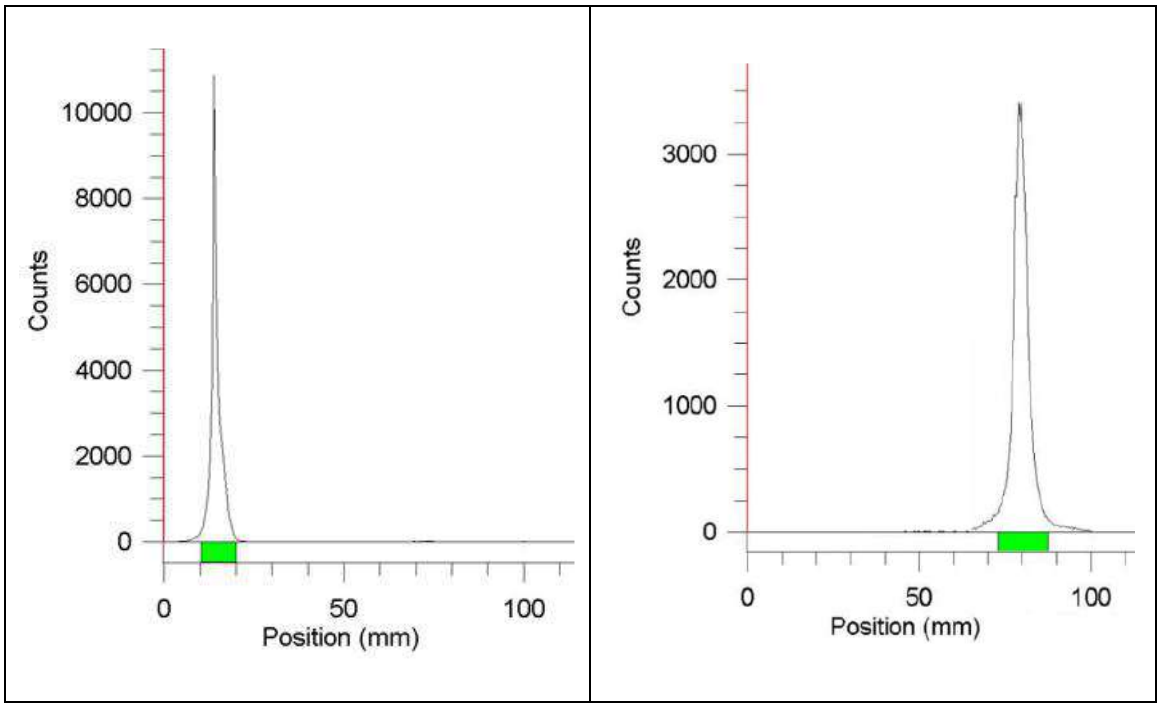

Fig 2. Radio chromatogram of [^{64}Cu]Cu- DOTA-(Tyr3)-octreotate in ammonium acetate 10%: methanol (30:70; V:V))

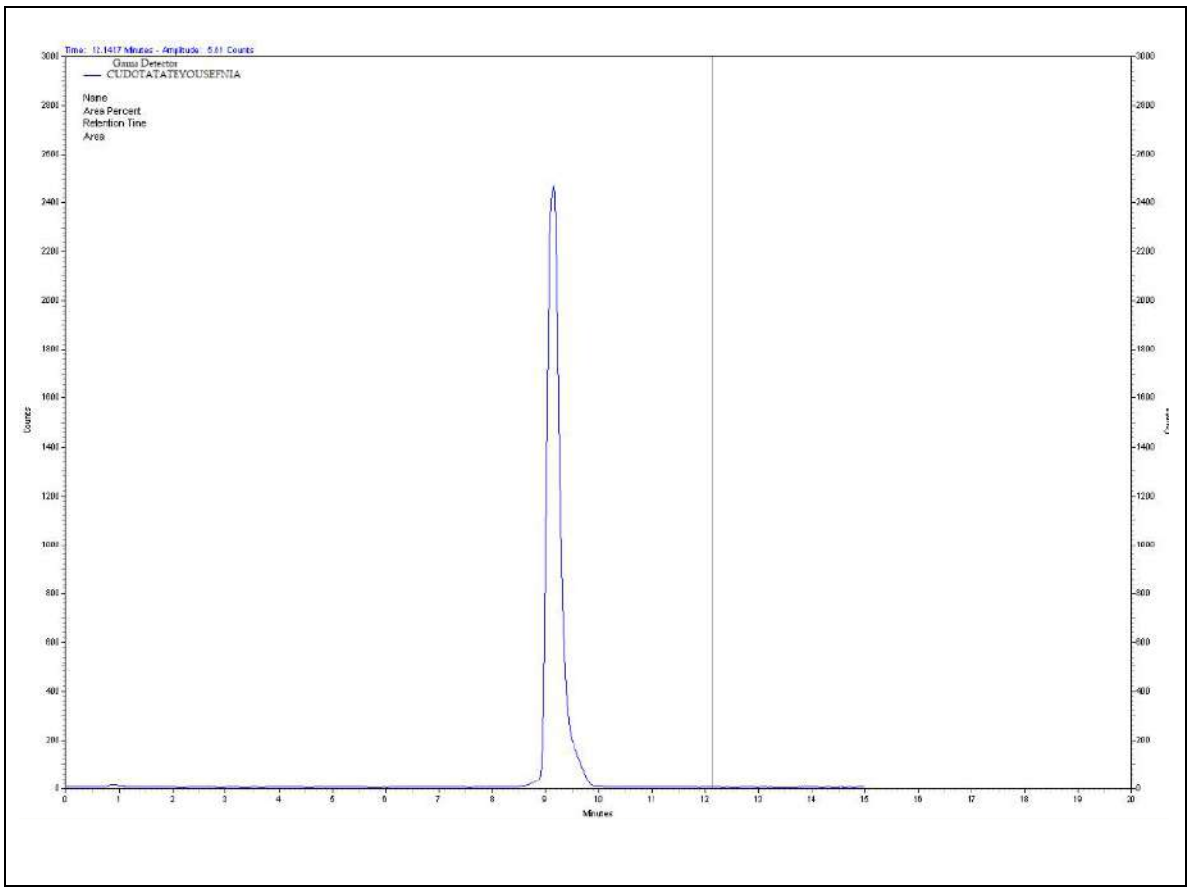

Fig 3. HPLC chromatogram of [^{64}Cu] Cu- DOTA-(Tyr3)-octreotate

Stability studies

The compound stability was measured showing the radiochemical purities of 95.5 %± 1.8% and 94.9% ± 1.7%, in PBS buffer (4 ˚C) and human blood serum (37 ˚C) after 12 h, respectively.

Biodistribution and imaging studies

The biodistribution of [^{64}Cu] Cu- DOTA-(Tyr3)-octreotate in tumor-bearing rats was investigated at 2, 4, 12, and 24 h after injection (Fig. 4). The images were taken after 4, and 24 h (Fig.5).

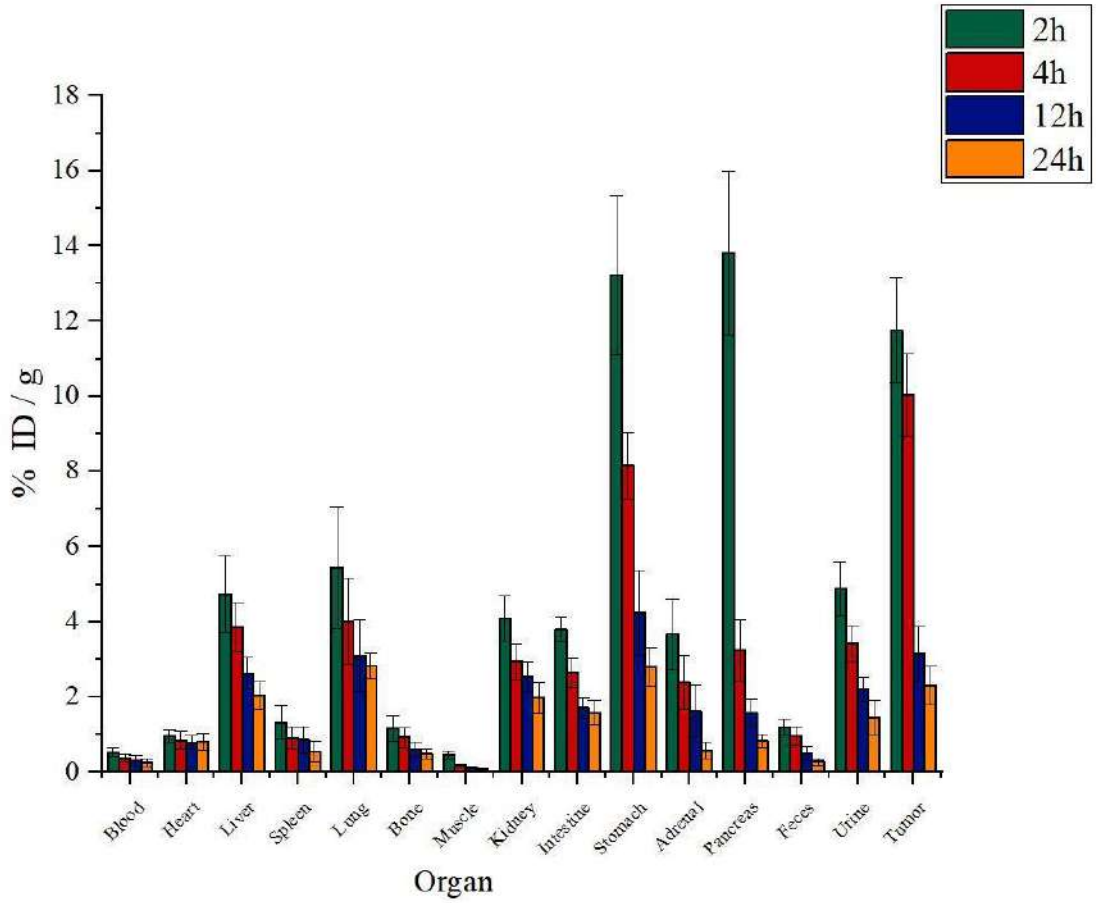

Fig. 4. Biodistribution of [^{64}Cu]Cu-DOTA-(Tyr3)-octreotate in tumor-bearing rats

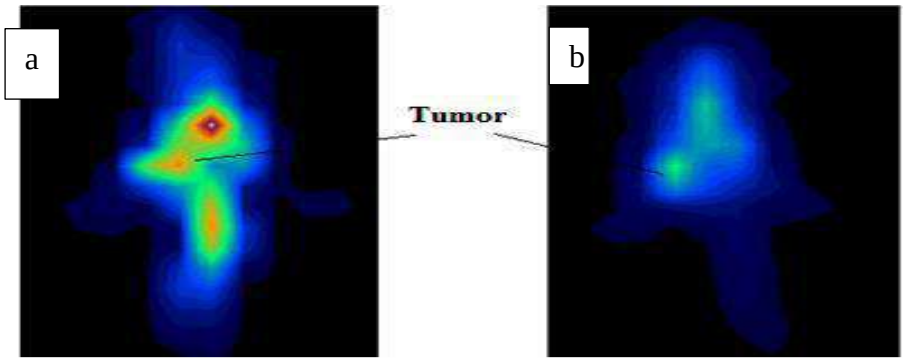

Fig. 5. Scintigraphy images of the tumor-bearing rats, 4 h (a) and 24 h (b) after injection of [^{64}Cu]Cu-DOTA-(Tyr3)-octreotate

Nowadays, radiopharmaceuticals according to peptides and antibodies have been developed for the targeted diagnosis and targeted therapy. DOTA-(Tyr3)-octreotate was labeled and used

with ^{68}Ga, ^{64}Cu, and 111In for PET and SPECT imaging 177Lu for therapy. ^{64}Cu has a longer physical half-life, which allows for imaging of smaller tumors within optimal time limits. This radiopharmaceutical is rapidly cleared from the blood, and highly accumulated in organs with somatostatin receptors, such as the pancreas. The accumulation of [^{64}Cu]Cu-DOTA-(Tyr3)-octreotate in the kidney, as well as the high accumulation of activity in the urine, indicate that the urinary tract is the primary route of excretion for the radiopharmaceutical, similar to the excretion of other radio peptides. These results are entirely consistent with the data from clinical trials of this radiopharmaceutical.

Conclusions

These preclinical studies suggested that the radiopharmaceutical has a high potential for use in PET imaging of patients with NETs.

Acknowledgements

The authors would like to thanks Nuclear Science and Technology Research Institute (NSTRI) for your financial support.

References

[1] Vahidfar, N., Farzanehfar, S., Abbasi, M., Mirzaei, S., Delpassand, E. S., Abbaspour, F., ... & Ahmadzadehfar, H. (2022). Diagnostic value of radiolabelled somatostatin analogues for neuroendocrine tumour diagnosis: the benefits and drawbacks of [^{64}Cu] Cu-DOTA-TOC. Cancers, 14(8), 1914.

[۲] Zolghadri, S., Badipa, F., Amraee, N., Alirezapour, B., Beiki, D., & Yousefnia, H. (2023). Development and evaluation of [64Cu] Cu-DOTATATE for clinical applications. Iranian Journal of Nuclear Medicine.

[۳] Oronsky, B., Ma, P. C., Morgensztern, D., & Carter, C. A. (2017). Nothing but NET: a review of neuroendocrine tumors and carcinomas. Neoplasia, 19(12), 991-1002.

[1] Lewington, V. J. (2003). Targeted radionuclide therapy for neuroendocrine tumours. Endocrine-related cancer, 10(4), 497-501.

[٤] Sakulpisuti, C., Charoenphun, P., & Chamroonrat, W. (2022). Positron emission tomography radiopharmaceuticals in differentiated thyroid cancer. Molecules, 27(15), 4936.

[٥ Shokeen, M., & Anderson, C. J. (2009). Molecular imaging of cancer with copper-64 radiopharmaceuticals and positron emission tomography (PET). Accounts of chemical research, 42(7), 832-841.

[٦] Papotti, M., & de Herder, W. W. (Eds.). (2015). Neuroendocrine Tumors: A Multidisciplinary Approach. Karger Medical and Scientific Publishers.

[٧] Strosberg, J., El-Haddad, G., Wolin, E., Hendifar, A., Yao, J., Chasen, B., ... & Krenning, E. (2017). Phase 3 trial of 177Lu-Dotatate for midgut neuroendocrine tumors. New England Journal of Medicine, 376(2), 125-135.

[٨] Johnbeck, C. B., Knigge, U., Loft, A., Berthelsen, A. K., Mortensen, J., Oturai, P., ... & Kjaer, A. (2017). Head-to-head comparison of 64Cu-DOTATATE and 68Ga-DOTATOC PET/CT: a prospective study of 59 patients with neuroendocrine tumors. Journal of Nuclear Medicine, 58(3), 451-457.

[٩] Aghanejad A, Jalilian A, Maus , Yousefnia H, Geramifar P, Beiki D. Optimized production and quality control of 68Ga-DOTATATE. Iran J Nucl Med. 2016 Jan;24(1):29-36.

[1٠] Yousefnia, H., Mousavi-Daramoroudi, M. S., Zolghadri, S., & Abbasi-Davani, F. (2016). Preparation and biodistribution assessment of low specific activity 177 Lu-DOTATOC for optimization studies. Iranian Journal of Nuclear Medicine, 24(2).

[1١] Pfeifer A, Knigge U, Binderup T, Mortensen J, Oturai P, Loft A, Berthelsen AK, Langer SW, Rasmussen P, Elema D, von Benzon E, Højgaard L, Kjaer A. 64Cu-DOTATATE PET for neuroendocrine tumors: a prospective head-to-head comparison with 111In-DTPA-Octreotide in 112 patients. J Nucl Med. 2015 Jun;56(6):847-54.

Investigation of early diagnosis of Leukaemia with trace elemental analysis utlising synchrotron radiation (Paper ID : 1392)

Yasaman Satvat*[1], Ehsan Salimi[1], Tayeb Kakavand[1]
Imam Khomeini International University, Qazvin, Iran

Abstract

The aim of this study is to determine the low concentration of potassium (K), chlorine (Cl), arsenic (As), phosphorus (P), manganese (Mn), iron (Fe), nickel (Ni), copper. (Cu), zinc (Zn), bromine (Br), strontium (Sr), iodine (I), cadmium (Cd), calcium (Ca) in hair and nails of leukemia patients and healthy volunteers using synchrotron x-ray fluorescence (SRXRF) spectroscopy, which was performed with 40 healthy and 40 unhealthy samples. All samples were cleaned, disinfected, cut to appropriate sizes and coded. According to the International Atomic Energy Agency (IAEA) protocol, the samples were washed three times using ethanol and distilled water to remove any contamination. In this research, X-ray fluorescence spectroscopy was used in the XRF/XAFS beamline in Sesami synchrotron facility. The results of the Mann-Whitney U test comparing the studied elements in the hair and nails of healthy and leukemia patients people compared to the control group showed that there is a significant difference between the healthy and leukemia patients group ($P>0.05$). Based on comparison of data means, the patient group had the highest accumulation of elements in hair and nails compared to the healthy group. In both groups, zinc (Zn) had the highest concentration. Also, the logistic regression results showed that the concentration of 5 elements arsenic, zinc, nickel, lead and iron have a significant relationship with leukemia.

Keywords: Trace element – Leukemia – Synchrotron radiation – XRF

1. INTRODUCTION

Today, cancer is one of the main causes of death in human societies [1,2], and blood cancers or leukemia constitute about 8% of all cancers in the human population and are known as the fifth most common cancer in the world [3]. Unfortunately, cancer occurs even among pediatric, and numerous studies have shown that the most common cancer in pediatric is leukemia, which accounts for 60% of cancers in children under the age of 15 [4]. Blood cancer or leukemia is a malignant progressive disease of the hematopoietic organs of the body, which is caused by the proliferation and incomplete development of white blood cells and bone marrow. Blood cancer is categorized into three main types: lymphoma, affecting lymphocyte cells and potentially

disrupting the immune system, leading to the transformation of abnormal cells; myeloma, targeting plasma cells, particularly hindering the production of natural antibodies and weakening the immune system; and leukemia, occurring in the blood and bone marrow, characterized by an excessive production of abnormal white blood cells, diminishing the ability to produce red blood cells and platelets. There are generally four types of leukemia: acute lymphoblastic leukemia (ALL), acute myeloid leukemia (AML), chronic lymphoid leukemia (CLL), and chronic myeloid leukemia (CML). Although the main cause of leukemia is still unknown, some environmental factors are known to be risk factors for this disease, including exposure to ionizing radiation, chemicals such as gasoline and pesticides, smoking, family history, and age [5]. This study examines the detection of leukemia by measuring elements in nails and hair using SESAME synchrotron x-ray fluorescence (SRXRF) spectroscopy. This method is considered as a low-cost, non-invasive and low-risk method. The stability of chemical compounds is one of the necessary conditions for the normal functioning of the body, and the deviation from the level of various microelements can lead to the emergence of disease or the risk of disease. There are a number of trace elements, including iron, iodine, zinc, copper, selenium, nickel and other elements, which are essential for the physiological activity of humans and animals. Several studies have shown that trace elements are closely related to tumor formation. Trace elements are a group of factors with multiple functions that are directly involved in cell proliferation, differentiation and maturation. Their increase or decrease may cause metabolic disorders in the body and cause disease and even tumor development [6].

2. Materials and method

2.1 Study Subjects

In this study, 40 hair samples and 40 nail samples from both leukemia patients and healthy groups (160 samples in total) were included in SRXRF analysis. The average age in the healthy and leukemia patients groups is 41.4 and 41.1 years old, respectively, and in terms of gender distribution, this population consists of 57.5% men and 42.5% women. Healthy samples are from people who did not show any symptoms of blood cancer during clinical and diagnostic tests, and cancer samples are from patients whose test results were positive. Patient samples were collected in collaboration with Shariati, Imam Khomeini and Taleghani Hospitals in Tehran, Iran, under the supervision of adult blood and cancer specialists over a period of approximately 8 months. In conducting this research, before collecting hair and nail samples,

the study protocol was approved by the Human Ethics Committee of Tehran University of Medical Sciences. Hair and nail samples were collected using ceramic scissors, in 4-5 cm sections of hair from the occipital area (back of the head) and as close to the scalp as possible. In case of hair dyeing, samples were taken from the roots at least two weeks after dyeing. According to the protocols, the samples were properly washed, sterilized and stored in zipped plastic bags at room temperature (20-25°C). Sample preparation procedures were performed in accordance with the IAEA protocol for X-ray fluorescence analysis [7].

2.2 Synchrotron

Synchrotron radiation is one of the most important and fascinating phenomena in physics and has many applications in various fields. This phenomenon, using accelerators, provides the possibility of producing electromagnetic radiation in a wide range from ultraviolet to x-rays. Synchrotron radiation is widely used in scientific and applied research due to its high energy properties and quantum photons produced. Synchrotron is a type of particle accelerator in the form of a circular ring that magnetically moves pregnancy particles in a curved path. While moving, these jets receive their energy from the magnetic field and are radiated as electromagnetic rays. These rays are in a range from ultraviolet light to X-rays and provide users with features such as focus, time discontinuity, high power, high accuracy and the ability to adjust various parameters. This technology is used in various fields, including biological sciences, medical imaging and in industry and engineering [8].

Synchrotron-based techniques, with their unique capabilities and characteristics, are vastly different from laboratory techniques. Synchrotron radiation is billions of times brighter than radiation produced by laboratory techniques, which enhances detection capability and analysis accuracy. In laboratory techniques, there is usually a need for sample preparation and processing before analysis. However, in synchrotron-based techniques, samples can be directly tested in the apparatus without the need for prior preparation, reducing time and cost and enabling the analysis of sensitive samples.This technique, compared to conventional XRFs used in laboratories with prices around tens of thousands of dollars, can cost hundreds of millions of dollars. Therefore, considering the unique features and mentioned advantages, synchrotron-based techniques serve as vital tools in scientific research, especially in more complex research areas such as materials physics, environmental sciences, molecular biology, and other advanced fields [4].

2.3 SESAME XAFS/XRF beam line

The XAFS/XRF beamline is one of the 8 active beams at the Sesame Synchrotron located in Amman, Jordan, dedicated to X-ray fluorescence spectroscopy (XRF) and X-ray absorption microstructure spectroscopy (XAFS) [8]. The beamline is built on bending magnets in the 8th cell of the BM 08 Sesame storage ring and allows the researchers to study the energy spectrum from 4.5 to 30 Kev with photon fluxes in the range of 10^9 to 10^{12}/s with stability have access the above provides [8-10].

In this beam line, three ionization chambers are used to measure the radiation intensity and the rays passing through the sample. Two ionization chambers are placed at the top and bottom of the sample, which measure the primary and secondary beam intensity, respectively. A third ionization chamber is also used as a reference. Measurement of the gas inside the chamber due to X-ray radiation provides information about the beam intensity, which is used for normalization and calibration purposes [8-10].

In this beam line, two types of SDD (Silicon Drift Detector) detectors are used to optimize the detection of X-ray fluorescence signals from samples with different concentrations of elements. The first detector is a multi-element SDD developed by INFN capable of detecting very low concentrations of elements (down to a few parts per million) and has 64 elements with a capacity of up to 15 million counts per second. The second detector is a single-element SDD used for samples with concentrations above 10 ppm with a lower count rate of about 1 million counts. Using both types of detectors in the Sesame beamline allows researchers to obtain more accurate and comprehensive data about the elemental composition of a sample, regardless of its concentration or complexity. This helps to optimize the analysis of XRF and XAFS data and leads to a better understanding of sample properties and characteristics [8-10].

2.4 Experimental procedure

In this experiment, an energy beam of 18 Kev with a flux of 10^9 to 10^{12} photons/s and dimensions of 2.8×0.3 mm^2 from an X-ray tube coupled with a 64-element silicon drift detector to excite several low-quantity elements. It was used in hair and nail samples. To maintain the strength and correct position of the nail and hair samples in the beam path, the holders were adjusted and fixed by Sesame synchrotron technicians. The incident beam and the detector were placed at an angle of 45 degrees to each other, and the samples were also set at an angle of 45 degrees to the incident photon beam to minimize signal attenuation effects. A standard distance of 2cm was considered between the sample and the detector, and all samples were placed in the analysis path for 300 seconds [11]. Fluorescence signals from trace elements

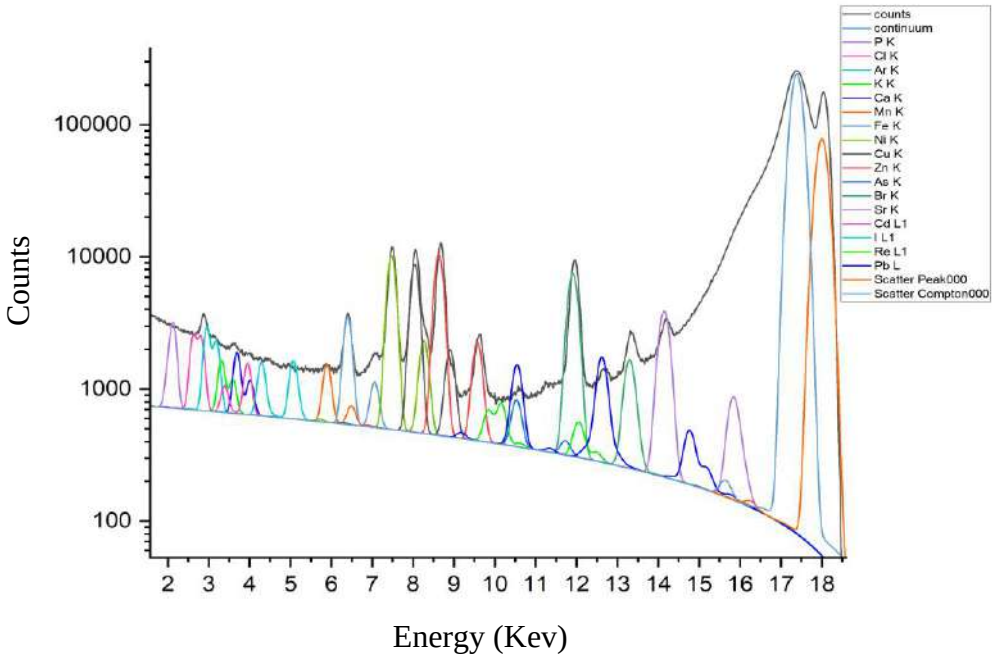

Fig. 1. Energy spectrum obtained from X-ray fluorescence measurement of a single nail clipping, with data fit by PyMca software. The black line represents the overall PyMca fit with contributions from various elements and the background continuum.

were detected using an SDD silicon drift detector. The standard deviation is obtained from the difference between the number of counts for each peak and the average number of counts for that peak and is used as a measure of data dispersion. In this analysis, elements of potassium, chlorine, arsenic, phosphorus, manganese, iron, nickel, copper, zinc, bromine, strontium, iodine, cadmium, rhenium, lead, argon, and calcium in hair and nail samples have been

examined. Each element is identified by a photopeak associated with its K or L fluorescence photon emission. Analysis results using this software are obtained in two ways, the area under the spectrum diagram and the mass concentration. In this software, the mass concentration is presented in milligrams to milliliters, and we changed the results to ppm. An example of the spectrum obtained is shown in Fig1.

3. Results

Using the Kolmogorov-Smirnov and Shapiro-Wilk tests, to investigate the concentration distribution of trace elements (potassium, chlorine, arsenic, phosphorus, manganese, iron, nickel, copper, zinc, bromine, strontium, iodine, cadmium, calcium) were analyzed in hair and nail samples of healthy people and people with leukemia. The results of the Kolmogorov-Smirnov and Shapiro-Wilk tests showed that the concentrations of the 14 studied elements in the hair and nail samples for healthy and sick people did not have a normal distribution, so the Mann-Whitney U test, which is a non-parametric test, was used to compare two independent groups. and the results showed that there are significant differences between the two groups.

3.1 Hair results

Among the studied elements for hair samples, only Rhenium (Re) had no significant difference between the two groups according to the reported error value of 0.192 ($P>0.05$). Based on the comparison of the average concentration of the studied elements, the patient group always had the highest value of elements accumulated in the hair compared to the healthy group. In the meantime, zinc (Zn) had the highest accumulation at 833.49 ppm, and phosphorus (P) had the lowest accumulation at 307.23 ppm in sick people. Also, zinc element had the highest accumulation at 640.09 ppm, and arsenic element had the lowest accumulation at 292.25 ppm in healthy people. Also, the phosphorus element was almost the same in healthy and sick people. It should be noted that the biggest difference in the average of the elements for the first three elements is related to iron (Fe) with a difference of 214.28 ppm, nickel (Ni) with a value of 194.27, zinc (Zn) with a value of 193.4 ppm and the lowest the difference related to phosphorus element (P) is 0.05.

3.2 Nail results

Based on the comparison of the averages, the patient group always had the highest value of accumulated elements in the nails compared to the healthy group. So that zinc element (Zn) with the amount of 682.75 ppm has the highest accumulation and arsenic element (As) with

the amount of 416.11 ppm has the lowest accumulation in the nails of sick people. It should be noted that the highest difference in the average concentration of the first three elements is related to zinc (Zn) with a difference of 66.95 ppm, manganese (Mn) with a difference of 64 ppm, nickel (Ni) with a difference of 58.75 ppm and the lowest difference It is related to the element strontium (Sr) at the rate of 26 ppm.

3.3 The Relationship Between Leukemia and the Studied Elements

In the continuation of the research, in order to investigate the relationship between the 14 studied elements and blood cancer, the logistic regression method was used and this investigation was done separately for hair and nail samples. In the section related to hair, five elements As, Zn, Ni, Pb and Fe were significantly related to leukemia. Among these five elements, the two elements Fe and As had the highest and lowest relationship with blood cancer with the odds of 1.55 and 0.53, respectively. These findings indicate the importance of these two elements in the diagnosis of leukemia and may be considered as important markers for this type of cancer. In the nail-related section, only two elements, namely Fe and Ni, were associated with leukemia. These results show the greater effect of these two elements in identifying leukemia in nail samples. This information can help doctors to be more accurate in diagnosing blood cancer and formulating an appropriate treatment plan. These results demonstrate the clinical importance of trace elements in the diagnosis and study of certain diseases such as blood cancer and lead to more targeted and efficient diagnosis and treatment paths. The analysis of these results is reported in Table 1.

Table 1. Investigating the relationship between elements in hair and nails with leukemia using logistic regression

Elements	Significance (sig)	Odds ratio (OR)
Hair		
As	0.00	0.53
Zn	0.00	0.99
Ni	0.01	1.26
Pb	0.02	0.96
Fe	0.00	1.55
Nail		
Fe	0.00	0.91
Ni	0.00	1.11

4. Discussion

In this study, the effect of 14 elements in hair and nail samples was investigated using Sesame Synchrotron and the results showed that there is a direct relationship between the increase in the concentration of 5 elements and acute leukemia.

The element arsenic is essential in very low levels as an essential element in some biochemical processes of the body. But as arsenic levels increase to higher levels, this element may become a toxic and harmful substance .[12] In this study, an increase in arsenic levels can be seen in people with acute leukemia. These results may indicate a possible role of arsenic in causing or accelerating the development of leukemia.

Zinc can act as an activator of some enzymes, there are 18 known zinc enzymes that require zinc for activation. These enzymes include DNA and RNA polymerases, protein synthesis enzymes and acids, which are widely present in the metabolism of the human body, the main ones are in the metabolism of sugar, protein, fat and acids. Research has shown that intracellular zinc maintains a constant balance. Not only zinc deficiency but also excess zinc can be toxic. Studies have shown that zinc intake can increase the abundance of metallothioneins mRNA, protect DNA and reduce the accumulation of reactive oxygen species (ROS). Conversely, zinc deficiency can inhibit MT and lead to ROS accumulation, which indicates a close relationship between oxidative stress and acute leukemia. Zinc deficiency can

lead to reduced immune function and reduce the size of immune organs and reduce immunity [13-15]. Many malignant tumors, including liver, stomach, bowel, lung, Hodgkin's lymphoma, leukemia, and kidney cancer, are significantly associated with imbalanced zinc levels. The tumor leads to the accumulation or expulsion of zinc in the liver and other tissues and organs, which leads to its increase in the blood; Some drugs for the expression of oncogenes can inhibit the synthesis of zinc absorption proteins and thus directly lead to a decrease in zinc levels in leukemia patients [16,17].

Nickel is considered as a low carcinogenic element. It has been observed that the nickel content in the urine of children with ALL is significantly increased. Previous research has found that nickel can induce cell contraction through an NADPH oxidase/ROS-dependent mechanism, which may be responsible for stimulating cell growth. be the root of cancer. In addition, urinary 8-hydroxy-2'-deoxyguanosine and nickel were significantly associated with increased risk of ALL [18]. In this research, we found that for both hair and nails, the amount of nickel in the group with leukemia is significantly higher than in the healthy group, and the increase in the amount of this element in the body is positively related to the risk of leukemia.

Lead has no useful purpose in the human body and its presence in the body can lead to toxic effects. Over the past decade, studies have shown that exposure to lead, even at very low levels, can cause serious adverse health effects, especially in young children. The main targets of lead toxicity are the hematopoietic system and the nervous system. This element has been classified by the International Agency for Research as a probable group two carcinogenic element for humans. In this study, we showed that the levels of lead in acute leukemia were high compared to the control group [19].

Cancer-related mechanisms suggest that iron is required as a cofactor for cell contraction and growth, and research has shown that iron deficiency reduces tumor cell viability. Iron can increase the production of reactive oxygen species, excess iron suppresses the body's immunity against destructive cells, and excess iron interacts with other micronutrients. Although iron is an essential nutrient, it is known that excess iron also leads to oxidative DNA damage. Excessive iron intake may predispose to breast tumorigenesis, as iron acts as a catalyst to generate reactive oxygen species and suppress host defense cells. In this research, the amount of iron in the hair samples is significantly higher than the control group [20].

5. Conclusion

The results obtained in this study indicate significant changes in the levels of various elements in patients with blood cancer compared to healthy individuals. Mann-Whitney U test results comparing the studied elements in the hair and nails of healthy and diseased individuals showed a significant difference between the healthy and patient groups. Based on the mean comparisons, the patient group had the highest accumulation of elements in both hair and nails compared to the healthy group. In both groups, Zinc (Zn) had the highest concentration. Additionally, logistic regression results indicated a significant association between the concentration of 5 elements (arsenic, zinc, nickel, lead, and iron) and blood cancer.

6. References

[1] Zhang, R., Li, L., Sultanbawa, Y., & Xu, Z. P. (2018). X-ray fluorescence imaging of metals and metalloids in biological systems. American journal of nuclear medicine and molecular imaging, 8(3), 169.

[2] Zand, A. M., Imani, S., Saadati, M. O. J. T. A. B. A., Borna, H., Ziaei, R., & Honari, H. O. S. S. E. I. N. (2010). Effect of age, gender and blood group on blood cancer types. Kowsar Medical Journal, 15(2), 111-4.

[3] Motevich, I. G., Strekal, N. D., Papko, N. M., Glebovich, M. I., Shulha, A. V., & Maskevich, S. A. (2015). Application of x-ray fluorescence analysis to determine the elemental composition of tissues from different ovarian neoplasms. Journal of Applied Spectroscopy, 82, 98-103.

[4] Rahimi, F., & Heidari, M. (2012). Time trend analysis of stomach cancer incidence in the west of Iran. Health and Development Journal, 1(2), 100-111.

[5] Maziar, A., Shahbazi-Gahrouei, D., Tavakoli, M. B., & Changizi, V. (2015). Non invasive XRF analysis of human hair for health state determination of breast tissue. Iranian Journal of Cancer Prevention, 8(6).

[6] Wang, J., Huang, P., Lang, C., Luo, Y., He, Z., & Chen, Y. (2023). The progress in the relationship between trace elements and acute lymphoblastic leukemia. Frontiers in Cell and Developmental Biology, 11, 1145563.

[7] Kolmogorov, Y., Kovaleva, V., & Gonchar, A. (2000). Analysis of trace elements in scalp hair of healthy people, hyperplasia and breast cancer patients with XRF method. Nuclear

Instruments and Methods in Physics Research Section A: Accelerators, Spectrometers, Detectors and Associated Equipment, 448(1-2), 457-460.

[8] https://www.sesame.org.jo/.

[9] Schopper, H. (2017). The light of SESAME: A dream becomes reality. La Rivista Del Nuovo Cimento, 40, 199-239.

[10] Günaydın, S., & Ozkendir, O. M. (2020). Synchrotron facilities for advanced scientific oriented research.

[11] Markowicz, A., Wegrzynek, D., Bamford, S., & Chinea-Cano, E. (2006). Activities in the IAEA X-ray fluorescence laboratory at Seibersdorf. X-Ray Spectrometry: An International Journal, 35(4), 207-214.

[12] Mayer, J. E., & Goldman, R. H. (2016). Arsenic and skin cancer in the USA: the current evidence regarding arsenic-contaminated drinking water. International journal of dermatology, 55(11), e585-e591.

[13] Jarosz, M., Olbert, M., Wyszogrodzka, G., Młyniec, K., & Librowski, T. (2017). Antioxidant and anti-inflammatory effects of zinc. Zinc-dependent NF-κB signaling. Inflammopharmacology, 25, 11-24.

[14] Aydemir, T. B., Blanchard, R. K., & Cousins, R. J. (2006). Zinc supplementation of young men alters metallothionein, zinc transporter, and cytokine gene expression in leukocyte populations. Proceedings of the National Academy of Sciences, 103(6), 1699-1704.

[15] Jing, L., Li, L., Zhao, J., Zhao, J., Sun, Z., & Peng, S. (2016). Zinc-induced metallothionein overexpression prevents doxorubicin toxicity in cardiomyocytes by regulating the peroxiredoxins. Xenobiotica, 46(8), 715-725.

[16] Kang, M., Zhao, L., Ren, M., Deng, M., & Li, C. (2015). Reduced metallothionein expression induced by Zinc deficiency results in apoptosis in hepatic stellate cell line LX-2. International journal of clinical and experimental medicine, 8(11), 20603.

[17] Gutiérrez-Vargas, R., Villasis-Keever, M. Á., Portilla-Robertson, J., Ascencio-Montiel, I. D. J., & Zapata-Tarrés, M. (2020). Effect of zinc on oropharyngeal mucositis in children with acute leukemia undergoing chemotherapy. Medicina Oral, Patología Oral y Cirugía Bucal, 25(6), e791.

[18] Yang, Y., Jin, X. M., Yan, C. H., Tian, Y., Tang, J. Y., & Shen, X. M. (2008). Urinary level of nickel and acute leukaemia in Chinese children. Toxicology and Industrial Health, 24(9), 603-610.

[19] Khuder, A., Bakir, M. A., Hasan, R., Mohammad, A., & Habil, K. (2014). Trace elements in scalp hair of leukaemia patients. Nukleonika, 59(3), 111-120.

[20] Moussa, R. S., Park, K. C., Kovacevic, Z., & Richardson, D. R. (2019). Ironing out the role of the cyclin-dependent kinase inhibitor, p21 in cancer: Novel iron chelating agents to target p21 expression and activity. Free Radical Biology and Medicine, 133, 276-294.

Investigation of the impact of using monolithic BGO crystal on Siemens Biograph Vision PET Scanner performance characterization (Paper ID : 1394)

Babaei Ghane M.[1*], Sadremomtaz A.[1], Saed M.[1]
[1] *Department of Physics, Faculty of Science, University of Guilan, Rasht, Iran*

Abstract

Positron emission tomography (PET) is a crucial imaging modality in the field of nuclear medicine, providing metabolic information about organs. Despite its benefits, comparing monolithic and pixelated crystals is an interesting study for optimizing PET performance, in addition to finding suitable materials for PET detectors, also As half of the building cost is related to the detector crystal, a potential solution is to replace crystals with monolithic, cost-efficient ones. Monolithic BGO provides an energy resolution of 15%, superior stopping power, a higher linear attenuation coefficient (0.96 over 0.87 cm^{-1} for 511 keV photons), and high resolution within the 2-3.5 mm range. The objective of this research is to investigate the impact of changing the pixelated LSO crystal with pixelated BGO and monolithic BGO on PET performance. To achieve this aim, Siemens Biograph Vision has been simulated and validated using the GATE Monte Carlo simulation toolkit with a 10-second scan time, and all physical processes have been included. Performance characterizations were evaluated based on NEMA NU 2-2018. The results indicate that the sensitivity of PET at the center and off-center of the field of view (FOV) outperforms in the presence of monolithic BGO with 17.6 and 16.3 ($\frac{kcps}{MBq}$), respectively, also monolithic BGO demonstrated slightly better sensitivity than pixelated BGO as expected due to energy resolution, high density and high stopping power of BGO and reduced crosstalk, and continuous light collection of a monolithic structure. Also, for a point source, the full width at half maximum (FWHM) was evaluated at 3.2 mm compared to 2.9 mm for LSO. Additionally, in the presence of BGO, the scatter fraction improved by 2.6%. In conclusion, changing the pixelated crystal with a monolithic could effectively reduce the overall cost of the scanner while maintaining system characterization or even improving it.

Keywords: PET, GATE Monte Carlo simulation, NEMA, sensitivity, scatter fraction

1. INTRODUCTION

Positron Emission Tomography (PET) is known as a non-invasive molecular imaging technique used to assess molecular targets in various diseases [1]. Over the years, there have been many advancements to improve PET scanners, including the advent of new scintillation materials and innovative image reconstruction algorithms [1], the introduction of fully 3D

acquisitions [2], time-of-flight (TOF) detection [3], and silicon photomultiplier (SiPM)-based detector developments [4].

PET detectors are designed to stop and measure the interaction of high-energy 511 keV annihilation photons [5]. The ideal scintillator for converting these photons into optical photons should possess specific properties such as high density and Z_{eff} for increased stopping power and photoelectric interactions, high light yield for excellent resolution, fast decay time to minimize dead time, and a refractive index similar to the photodetector for efficient light transmission [5]. Among all PET scintillators, BGO crystal is favored for its density, effective atomic number, stopping power, and cost efficiency.

Different materials have been explored for PET detector design, utilizing pixelated arrays or monolithic crystals, each with advantages and disadvantages. Pixelated scintillator crystal arrays are formed by coupling individual scintillator elements, or pixels, into a matrix. This pixelation process is important for achieving high light output and uniformity with minimal crosstalk. The intrinsic spatial resolution of pixelated PET detectors is influenced by detector resolution, annihilation photon collinearity variance, and positron range variance [6,7]. Monolithic scintillation crystals, on the other hand, are single continuous slabs of scintillation material [8]. They offer higher sensitivity, depth of interaction (DOI) measurement from the shape of the scintillation light distribution, continuous positioning of photon interactions, and lower cost [9].

Hence, comparing monolithic and pixelated crystals is an interesting study for optimizing PET performance, in addition to finding suitable materials for PET detectors [4,8]. So, the first aim of this study is to investigate the effect of scintillator material on the PET scanner's performance, followed by a comparison of monolithic and pixelated crystals. To achieve these objectives, the Siemens Biograph Vision [10,11] is simulated and validated using the Monte Carlo (MC) simulations. Then, the pixelated LSO was replaced with pixelated BGO, and the scanner's performance evaluated based on the NEMA NU 2-2018 guidelines. Finally, each sub-module of the scanner was replaced with a monolithic BGO to investigate the impact of monolithic scintillator crystals on the scanner's performance.

2. MATERIALS AND METHODS

2.1 PET Scanner Description

The Siemens Biograph Vision [10,11], as briefly described in Table 1, is a cylindrical PET scanner with a diameter of 82 cm and a height of 25.6 cm. It consists of 8 rings, with each ring made of 38 detector modules. Each module consists of 4 trans-axial × 2 axial sub-modules of a 5×5 LSO detector array. Each LSO crystal has dimensions of 3.2×3.2 mm^2 and a height of 20 mm. The crystal pitch is 3.2 mm. To investigate the impact of the presence of the monolithic detector crystal as illustrated in Figure 1, each 5×5 crystal array in the sub-module has been replaced with a single 16×16 mm^2 monolithic BGO crystal. Additionally, Table 1 provides an overview comparison of the two geometries and detector parameters.

Table 1. Description of initial Siemens Biograph Vision PET scanner Geometry and Simulation Parameters with Pixelated and Monolithic BGO Replacements

Parameter	**Biograph vision**		
Crystal	LSO	BGO	BGO
Crystal type	Pixelated	Pixelated	Monolithic
Crystal dimension(mm^3)	3.2×3.2×20	3.2×3.2×20	16×16×20
Crystal pitch(mm)	3.2	3.2	16
Crystal per sub-module	200	200	8
Number of rings	8	8	8
Number of modules per ring	38	38	38
Axial FOV(cm)	25.6	25.6	25.6
Scanner diameter(cm)	82	82	82
Coincidence window(ns)	4.7	4.7	5
Energy resolution	11.7%	15%	15%
Energy window(keV)	435-650	435-650	435-650
Light yield(photons/keV)	25000	10000	10000
Dead time(ns)	320 Paralyzable	370 Paralyzable	370 Paralyzable

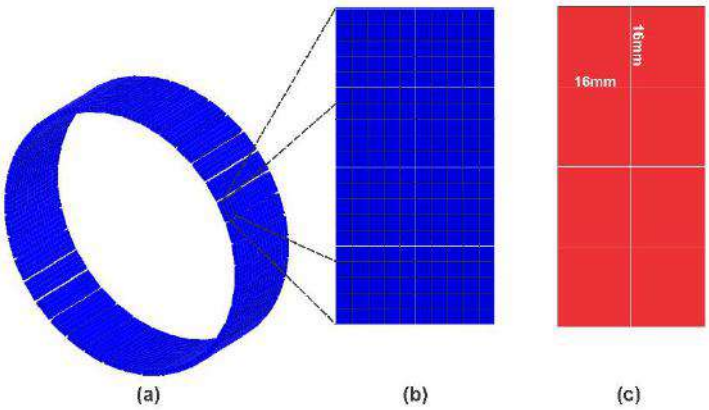

Fig.1 Schematic representation of the simulated Siemens Biograph Vision PET scanner (a), magnification of a single 64×32 mm detector module consisting of 4×2 sub-modules (b), and replacement of pixelated 3.2×3.2 mm LSO crystal with monolithic 16×16 mm BGO (c).

2.2 GATE Monte Carlo Simulation

To evaluate the performance of the PET scanner, MC simulations were performed using the advanced software called the GATE/GEANT4 framework. GATE is an open-source Monte Carlo simulation toolkit designed to model tomographic imaging systems, radiotherapy, and dosimetry [12-14]. In this research, GATE version 9.2 was employed for modeling and simulation, and the listed physics processes in Table 2 were applied in all simulations. Additionally, we considered a reference energy resolution and energy windows for each crystal in the GATE simulation (see Table 1). The geometric features of the simulated scanners are according to Table 1.

Table 2. Physical models and processes of particles utilized in the simulation.

Particles	Processes	Models
Gamma	Photoelectric effect	Standard model
	Compton scattering	Standard model
	Rayleigh scattering	Penelope model
Electron	Ionization	Standard model e^-
	Bremsstrahlung	Standard model e^-
	Multiple scattering	Multiple scattering e^-
Positron	Ionization	Standard model e^-
	Bremsstrahlung	Standard model e^-
	Multiple scattering	Multiple scattering e^-
	Positron annihilation	

2.3 Phantom Study

For the comparison of scanner performance, NEMA performance tests are conducted. They serve as the standard benchmark for evaluating the performance of PET and SPECT scanners and for comparing different scanners [15]. In this research, the latest version of NEMA standards for PET scanners, NEMA NU 2-2018 [16], is utilized to validate the Siemens Biograph Vision and compare key performance features such as sensitivity, scatter fraction, and spatial resolution.

To evaluate sensitivity, the NEMA NU 2-2018 proposed a phantom consisting of a 70 cm line source surrounded by 5 aluminum sleeves with inner/outer diameters of 3.9/6.4, 7.0/9.5, 10.2/12.7, 13.4/15.9, and 16.6/19.1 mm, respectively. These sleeves are added sequentially around the previous sleeve [16]. The simulated line source is a hollow polyethylene cylinder with an inner and outer diameter of 1 mm and 3 mm, respectively, filled with 4 MBq activity of ^{18}F. The phantom is placed in two positions: at the center of the scanner and a 10 cm radial offset. The scan time was set to 10 seconds. The sensitivity is determined using the following formula:

$$\boldsymbol{Sensitinity} = \frac{\boldsymbol{True}}{\boldsymbol{Activity \times Time}} \quad (1)$$

The system sensitivity was plotted against the number of aluminum sleeves (attenuation degree), and a fit was applied. This fit was then extrapolated to zero attenuation to deduce the system sensitivity.

The scatter fraction of the scanner is also evaluated based on the NEMA NU 2-2018 standards using the NEMA scatter phantom. The NEMA scatter phantom is a polyethylene cylinder with a density of 0.96 g/cm^3, 20 cm in diameter, and 70 cm in height, with a 6.4 mm diameter hole positioned at a 4.5 cm radial offset parallel to the center axis [16]. A simulated line source of ^{18}F with 5 MBq activity was placed within an 80 cm hollow polyethylene tube with an inside and outside diameter of 3.2 and 4.8 mm, respectively. The line source was then positioned within the hole of the phantom for 10 seconds of scan time. The scatter fraction is evaluated using the following formula:

$$\boldsymbol{Scatter\ Fraction} = \frac{\boldsymbol{Scatter}}{\boldsymbol{Scatter+True}} \quad (2)$$

The spatial resolution is expressed as the Full Width at Half Maximum (FWHM) of the reconstructed image of a point source measured across radial, tangential, and axial profiles [1]. For this purpose, using the NEMA NU 2-2018 protocol, a point source with a 1 mm diameter consisting of 3.9 MBq activity was placed at the center of the FOV for 30 seconds of scan time. The image was reconstructed using CASToR v 3.1 software with a grid size of 431×431 pixels and voxel size of 1.65×1.65×1.6 mm^3, employing 2 iterations and 19 subsets using the Maximum Likelihood Expectation Maximization (MLEM) algorithm with Gaussian post-filtering to ensure accurate image reconstruction [10].

3. RESULTS

Table 3 shows the comparison and validation of the sensitivity and scatter fraction of the Biograph Vision scanner with van Sluis et al. [11] experimental data and Sara Zain et al. [10] simulation data.

Table 3. The comparison of performance characterization of the simulated Biograph Vision scanner with experimental data (pixelated LSO crystal).

Parameter		Sara Zain et al	van Sluis et al.	Our study
Scatter fraction		34%	37%	39%
Sensitivity ($\frac{kcps}{MBq}$)	Center of FOV	16.0	16.4	16.5
	10 cm off-center	15.7	16.3	15.9

In Table 4, the scatter fraction, sensitivity, and spatial resolution of the scanner are reported for pixelated LSO, pixelated BGO, and monolithic BGO, evaluated using NEMA guidelines. The scatter fraction was evaluated using the NEMA scatter phantom. The sensitivity of all these scanners was evaluated in two positions using the proposed sensitivity phantom by NEMA. Figure 2 illustrates the system sensitivity per aluminum thickness extrapolated to zero attenuation for all these scanners at the center of FOV and 10 cm radial offset. The zero attenuation sensitivity is reported in Table 4. Figure 3 illustrates the reconstructed image of a point source, which was reconstructed using CASToR with 2 iterations and 19 subsets. The FWHMs of the reconstructed image are listed in Table 4 in three directions (radial, tangential, and axial).

Table .4. Simulation results of the comparison between pixelated LSO, pixelated BGO, and monolithic BGO.

Parameter		Pixelated LSO	pixelated BGO	Monolithic BGO
Scatter fraction		39%	37.8%	37.6%
FWHM	radial	2.9	3.2	3.4
	tangential	2.8	3.2	3.4
	axial	2.9	3.2	3.4
Sensitivity ($\frac{kcps}{MBq}$)	Center of FOV	16.5	17.2	17.6
	10cm off-center	15.9	16.1	16.3

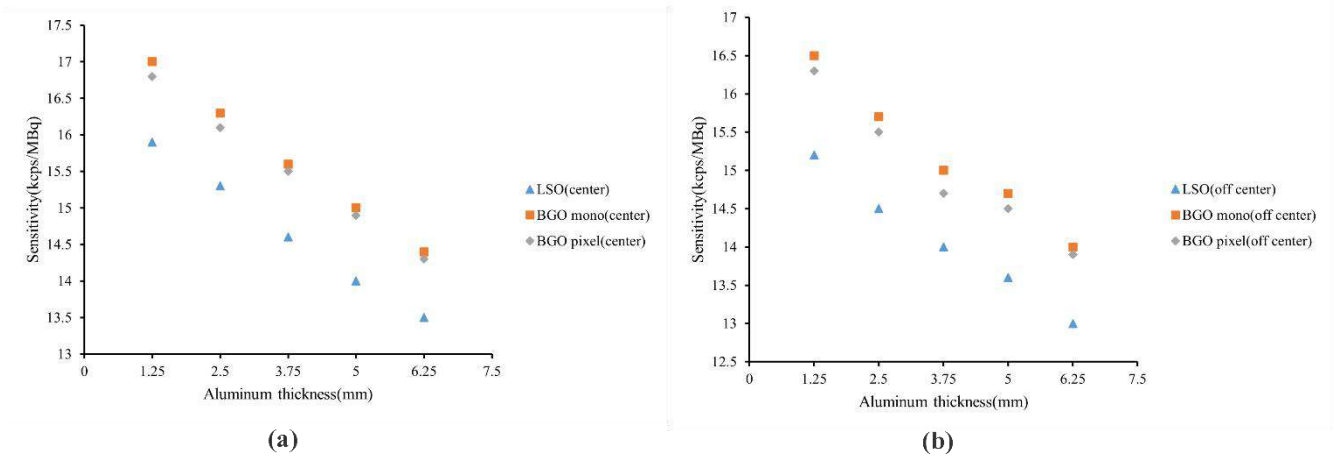

Fig. 2. System sensitivity per aluminum thickness extrapolated to zero attenuation for both LSO and BGO crystal at the center and 10 cm radial off-center of FOV.

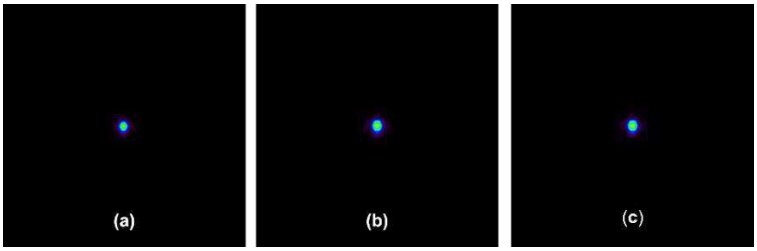

Fig. 3. Reconstructed images of the point source using CASToR in the presence of pixelated LSO (a), pixelated BGO (b), and monolithic BGO (c).

4. DISCUSSION

As shown in Table 3, a good agreement exists between our simulation results and the experimental findings of van Sluis et al. [11], and the simulation results of Zain et al [10]. The maximum error for sensitivity at the center and off-center of the FOV was approximately 2%, while for scatter fraction, the error was around 5%. These discrepancies may be attributed to uncertainties in simulation parameters, differences in experimental setups, and variations in physical processes.

As anticipated, BGO exhibited improved sensitivity compared to LSO, a benefit further enhanced with the monolithic approach. Referring to Table 4 and Figure 3, the monolithic BGO approach demonstrated approximately 7% and 6.5% higher sensitivity at the center of the field

of view and 10 cm radial offset, respectively, compared to pixelated LSO. Furthermore, monolithic BGO showed higher sensitivity than pixelated BGO. The use of monolithic BGO crystals also led to a 2.6% improvement in scatter fraction for the scanner. This enhancement is attributed to BGO's higher density, reduced crosstalk, and continuous light collection due to its monolithic structure [17].

However, it is worth noting that BGO resulted in lower spatial resolution compared to LSO. As depicted in Figure 4, the reconstructed image of the point source using LSO exhibited approximately 10% and 17% better spatial resolution compared to pixelated BGO and monolithic BGO, respectively. This is mainly due to LSO having approximately three times higher light yield, contributing to its superior spatial resolution capabilities. Additionally, the larger dimensions of monolithic crystals (16×16 mm) compared to pixelated LSO crystals (3.2×3.2 mm^2) led to poorer intrinsic spatial resolution. The continuous structure of monolithic crystals may also cause increased light sharing between adjacent crystals, resulting in a broadening of the scintillation light profile and reduced spatial resolution. Furthermore, the design of monolithic crystal modules may introduce complexities in the light collection process, further affecting spatial resolution.

Despite the lower spatial resolution with BGO and the monolithic approach, they offer advantages in terms of sensitivity. The higher sensitivity of BGO is particularly beneficial for applications where high sensitivity is crucial, such as low-dose imaging or dynamic studies [18]. Similarly, the monolithic approach provides improved sensitivity due to its continuous crystal structure, efficient light collection, and reduced crosstalk [18]. These trade-offs between sensitivity and spatial resolution underscore the importance of selecting the appropriate scintillator material and crystal approach based on the specific imaging requirements of the PET scanner.

5. CONCLUSION

The use of monolithic crystals instead of pixelated ones has been found to improve sensitivity in PET scanners. While monolithic crystals have weaker spatial resolution than pixelated crystals, they are more cost-efficient and can significantly reduce costs. Therefore, it is suggested that the adoption of monolithic crystals in PET detector design can lead to improved

sensitivity and lower costs. This has significant implications for the development of PET imaging technology.

References

[1] Ghabrial, A., Franklin, D., & Zaidi, H. (2018). A Monte Carlo simulation study of the impact of novel scintillation crystals on performance characteristics of PET scanners. Physica medica, 50, 37-45.

[2] Townsend, D. W., Geissbuhler, A., Defrise, M., Hoffman, E. J., Spinks, T. J., Bailey, D. L., & Jones, T. (1991). Fully three-dimensional reconstruction for a PET camera with retractable septa. IEEE Transactions on Medical Imaging, 10(4), 505-512.

[3] Vandenberghe, S., Mikhaylova, E., D'Hoe, E., Mollet, P., & Karp, J. S. (2016). Recent developments in time-of-flight PET. EJNMMI physics, 3, 1-30.

[4] Lewellen, T. K. (2008). Recent developments in PET detector technology. Physics in Medicine & Biology, 53(17), R287.

[5] Gonzalez-Montoro, A., Gonzalez, A. J., Pourashraf, S., Miyaoka, R. S., Bruyndonckx, P., Chinn, G., & Levin, C. S. (2021). Evolution of PET detectors and event positioning algorithms using monolithic scintillation crystals. IEEE Transactions on Radiation and Plasma Medical Sciences, 5(3), 282-305.

[6] Knoll, G. F. (2010). Radiation detection and measurement. John Wiley & Sons.

[7] Cherry, S. R., Sorenson, J. A., Phelps, M. E., & ScienceDirect (Online service). (2003). Physics in nuclear medicine (Vol. 3). Saunders.

[8] Cabello, J., Barrillon, P., Barrio, J., Bisogni, M. G., Del Guerra, A., Lacasta, C., & Llosá, G. (2013). High resolution detectors based on continuous crystals and SiPMs for small animal PET. Nuclear Instruments and Methods in Physics Research Section A: Accelerators, Spectrometers, Detectors and Associated Equipment, 718, 148-150.

[9] Enlow, E., & Abbaszadeh, S. (2023). State-of-the-art challenges and emerging technologies in radiation detection for nuclear medicine imaging: A review. Frontiers in Physics, 11, 1106546.

[10] Zein, S. A., Karakatsanis, N. A., Conti, M., & Nehmeh, S. A. (2020). Monte carlo simulation of the siemens biograph vision PET with extended axial field of view using sparse detector module rings configuration. IEEE Transactions on Radiation and Plasma Medical Sciences, 5(3), 331-342.

[11] Van Sluis, J., De Jong, J., Schaar, J., Noordzij, W., Van Snick, P., Dierckx, R., ... & Boellaard, R. (2019). Performance characteristics of the digital biograph vision PET/CT system. Journal of Nuclear Medicine, 60(7), 1031-1036.

[12] Saed, M., Sadremomtaz.A, and Mahani. H. (2023), A Monte Carlo study on quantification of scattering and edge penetration in a breast-dedicated SPECT scanner with lofthole collimation. Iranian Journal of Nuclear Medicine. **31**(2): p. 119-128.

[13] Saed. M, Sadremomtaz. A, and Mahani. H, (2022). Design and optimization of a breast-dedicated SPECT scanner with multi-lofthole collimation. Journal of Instrumentation. **17**(01): p. P01006.

[14] OpenGATE Collaboration. Available from: http://www.opengatecollaboration.org/.

[15] Perkins A, Stearns C, Chapman J, Kolthammer J. NEMA Standards Publication NU 2-2007: performance measurements of positron emission tomographs. Rosslyn USA: National Electrical Manufacturers Association (NEMA); 2007.

[16] National Electrical Manufacturers Association. (2018). Performance measurement of positron emission tomographs. NEMA Standards Publication NU 2-2018

[17] Abi-Akl, M., Dadgar, M., Toufique, Y., Bouhali, O., & Vandenberghe, S. (2023). Monte Carlo simulation of the system performance of a long axial field-of-view PET based on monolithic LYSO detectors. EJNMMI physics, 10(1), 1-13.

[18] Dadgar, M., Maebe, J., Abi Akl, M., Vervenne, B., & Vandenberghe, S. (2023). System characteristics comparison of the Walk-Through Total-Body PET and the Biograph Vision Quadra PET/CT.

ICNST 2024
International Conference on Nuclear Science and Technology
6- 8 MAY 2024 | Isfahan, Iran

Design of fast neutron box for topaz irradiation and coloring in Tehran research reactor (Paper ID : 1398)

S. Saeid Mousavi[1*], Hamid Jafari[1], M.R. Kardan[2], Z. Gholamzadeh[2]

[1]*Application of rays, Faculty of Nuclear Engineering, Shahid Beheshti University, Tehran, Iran.*

[2]*Reactor and Nuclear Safety Research Institute, Atomic Energy Organization, Tehran, Iran.*

Abstract

The purpose of this research is to design a box for irradiating topaz stones in Tehran research reactor (TRR). One of the cases of coloring and performing the improvement process is the use of fast neutrons in the research reactor. The presence of thermal neutrons during irradiation causes the impurities in topaz stones to become radioactive. Of course, the type of these impurities and the concentration of impurities in the stones will be different and this factor will affect the activity of the stones after irradiation. To reduce the flux of thermal neutrons, a thermal neutron absorber filter is used, and two air and water coolers are used for topaz during irradiation, and the amount of neutron flux and finally the activity created in both cases are compared. In this research, MCNPX code is used for geometry simulation and neutronic calculations, as well as ANSYS Fluent software for heat transfer calculations in the irradiation box. In this research, boron carbide (B_4C) is used as a thermal and epithermal neutron absorber filter, and lead (Pb) is used as a gamma absorber filter in the reactor pool. If lead is used, the residual heat caused by gammas in topaz stones changes and decreases by 60%.

Keywords: Topaz, ANSYS Fluent, MCNPX code, Activity

INTRODUCTION

Topaz is one of the precious stones. Precious stones are stones that are distinguished from other minerals and stones by having some characteristics such as beauty, hardness, durability and transparency. The demand for precious and semi-precious stones including topaz with better and clearer color and clarity is more and has more monetary value. There are ways to improve appearance, quality, color and clarity. Some improvement actions are sustainable and some are unstable. The improvement process with neutron bombardment is more stable and has deeper and more beautiful coloring [1,2].

This color change is caused by neutron bombardment by neutron generators (research reactor), gamma rays, high-energy electrons produced by the accelerator, or a combination of them. The change and enhancement of color by neutrons create a deeper blue color than irradiation with only gamma or electrons in topaz stones, and in this sense, neutrons are better for irradiation [3].

Research reactors produce neutrons and these neutrons are in the range of thermal, epithermal, and fast energy. For the healing process, we need fast neutrons so that this process is done correctly and the color of the topaz stones changes, but during the prototyping process, the thermal neutrons make the topaz stones radioactive [4].

The cause of color change in topaz stones is the creation of color centers within their crystal structure. The color center is a defect in the crystal structure that must be created to change the color of topaz stones. The cause of defects in the crystal structure of topaz stones is fast neutrons, and when this type of neutrons hits topaz stones, it changes their color and takes on a more beautiful color [5].

Citation

Topaz stones are irradiated in research reactors of other countries such as Egypt, Kazakhstan, Brazil, Indonesia, Uzbekistan, and Thailand. In Egypt's ETRR-2 reactor, aluminum containers are used to irradiate topaz stones, and a total of 4-6 kg of topaz is placed inside these containers. To reduce the thermal neutrons inside the containers, they use a boron carbide filter or materials containing boron. Boron-10 has a high absorption cross-section of thermal neutrons. In Egypt's ETRR-2 reactor, if there is a thermal neutron absorber filter for the irradiation of topaz stones, the irradiation of topazes will reach below the permissible limit after 6-18 months, and if there is no thermal neutron absorber filter, after 20-29 months, topaz radioactivity reaches less than the permissible limit [6].

One of the things that will affect the color change of topaz stones and their color stability is temperature. The temperature of topaz stones should be less than 150°C during irradiation, and a temperature above 300°C during irradiation will cause them to deteriorate and break. Therefore, it is necessary to use proper cooling during irradiation so that the temperature of topazes during irradiation is below 200 °C [4].

In the WWR-K reactor, a container similar to a capsule is used, the wall of which is made of an aluminum alloy. The height of the useful volume of this container is 50 mm and its useful

diameter is 46 mm. In the inner wall of the container, filters B_4C and Cd have been used to reduce the flux of thermal neutrons, it has reduced the flux of thermal neutrons as much as possible [7].

Reactor TRR1/M1-Thailand is also used for irradiating and enhancing the color of topaz stones. In this reactor, colorless topazes are placed in cylindrical containers, and the wall of the container is made of aluminum, and cadmium is used to filter thermal neutrons. The amount of flux is equal to $10^{11}\ \frac{n}{cm^2.s}$. The amount of topaz placed in the container for irradiation is equal to 300 g and they are irradiated in the core of the reactor for 72-12 hours [8].

The chemical formula of topaz stone is $Al_2SiO_4(F.OH)_2$ [6]. The main elements in topaz stone are aluminum, silicon, oxygen, and fluorine, which have a half-life of about a few minutes and a few seconds. Thermal neutrons irradiate the main elements, but because they have a small half-life, after passing at least 5 times their half-life, the risk of irradiation does not include these and they will not be dangerous [9].

In topaz stones, in addition to the main elements that were mentioned, according to the type of topaz, there are different types of impurities with different concentrations inside them. These radioisotopes have a longer half-life that thermal neutrons activate these radioisotopes and cause topaz stones to radiate. Due to the long half-life of some radioisotopes in topaz stone, after their activation, a long period of time must pass until the activity level is less than 74 Bq/g.

The process of irradiating topaz stones industrially is being implemented in the Tehran Research Reactor (TRR). The goal and innovation of this research is to achieve a suitable method according to the conditions to reduce the radioactivity of topaz stones, which topazes enter the market after spending less time and can lead to the development of this industry in Iran [9].

Materials and methods

Characteristics of the core of the TRR

TRR is a pool type, the central core of this reactor is located in a pool with a capacity of 500,000 liters of light water, the depth of this pool is 8 meters. The moderator and coolant of this

research reactor is light water and it is used for research, training, irradiation, and radiopharmaceutical production purposes. The concrete pool filled with light water consists of two parts, the reactor core can be operated in each of those two parts. On the wall of one of these two parts, laboratory equipment such as 7 beam tubes with different cross-sections, pneumatic rabbit tubes, and thermal columns are placed. In addition, it is possible to irradiate the sample in special irradiation chambers inside the core and at the periphery of the core. The reflector of this type of reactor is of graphite type and has inhomogeneous solid fuel of plate type. The core of the reactor has fuel elements of the MTR type, which are placed inside the grid plate. On the screen, there are 54 positions for the placement of fuel complexes in a regular $\mathbf{9 \times 6}$ rectangular arrangement. By placing the fuel complexes in their place on this plate, the core complex is formed. The fuel of this reactor is low-enriched uranium oxide (LEU), which includes standard fuel elements (SFE) with a height of 63 cm. Both types of fuel elements have $\boldsymbol{U_3O_8 - Al}$ fuel plates with 20% richness, which are placed in SFE type, 19 fuel plates, and in CFE type, 14 fuel plates. Each CFE element includes two $\boldsymbol{Cd - In - Ag}$ control blades that are used to control the core's reactivity and regulate the neutron flux [9-12]. Some graphite reflectors are placed around the core to reduce neutron leakage from the core [13-15].

Figure 1, shows the layout of the heart of the TRR, along with the different positions for irradiation, as well as the fuel plates and the graphite box, simulated by the MCNPX code.

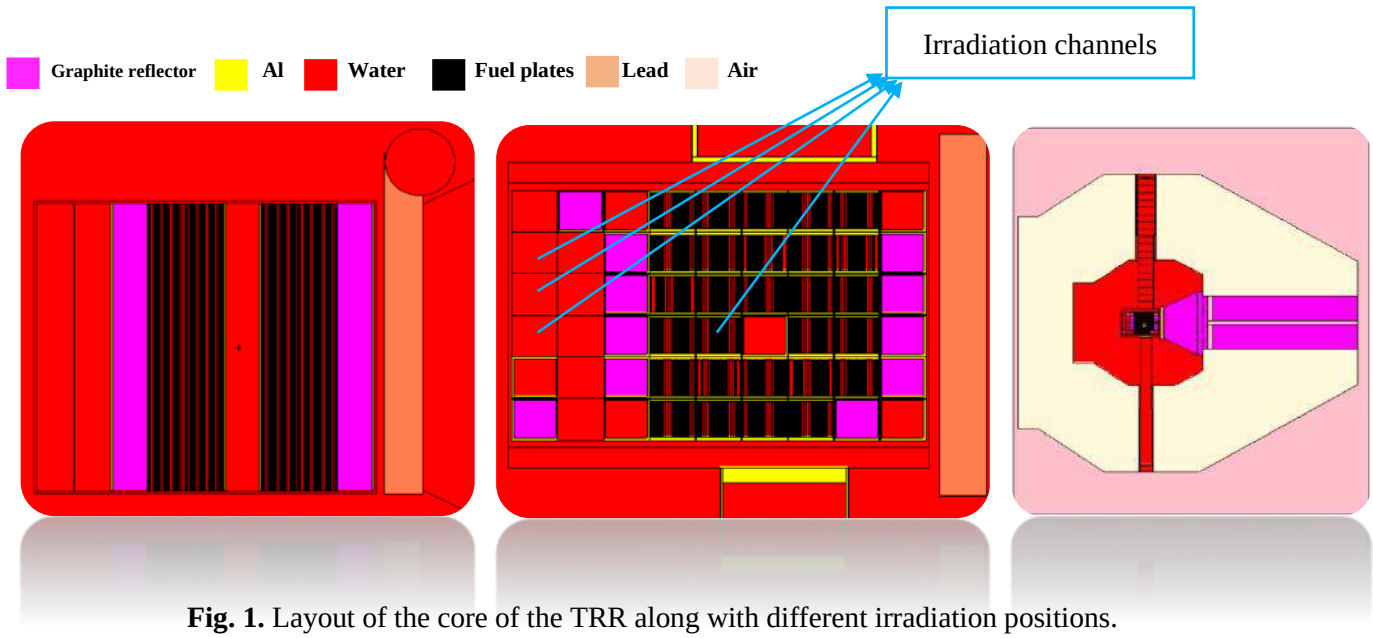

Fig. 1. Layout of the core of the TRR along with different irradiation positions.

Description of irradiation in code MCNPX, and ANSYS-Fluent

For irradiating topaz stones, two rectangular cube boxes with dimensions of $\mathbf{5\ cm\ x\ 5\ cm\ x\ 27\ cm}$ made of aluminum with a thickness of 2 mm have been used. Topazs are placed in these containers and simulated by MCNPX code. Irradiation boxes are placed vertically on top of each other and placed in the irradiation channel of the edge of the core and simulated. In this research, B_4C filter was used as thermal neutron absorber and lead material was used as gamma ray absorber on topaz aluminum box wall with thicknesses of 1 mm, 2 mm and 3 mm. Both boxes are placed vertically in the irradiation channel. In this research, two water and air coolers have been used in the simulations. The flux of thermal neutrons, epithermal neutrons and fast neutrons and residual heats caused by neutrons and gamma are compared. Neutron flux calculations have been done for the following 3 energy groups:

0 – 0.4 eV	(Thermal)
0.4 eV – 1 keV	(Epithermal)
1 keV – 20 MeV	(Fast)

Figure 2 indicates the box containing topaz. The wall of the box is only aluminum. The boxes are placed vertically on top of each other and radiated. Figure 3 shows the box containing topaz along with filters B_4C and Pb.

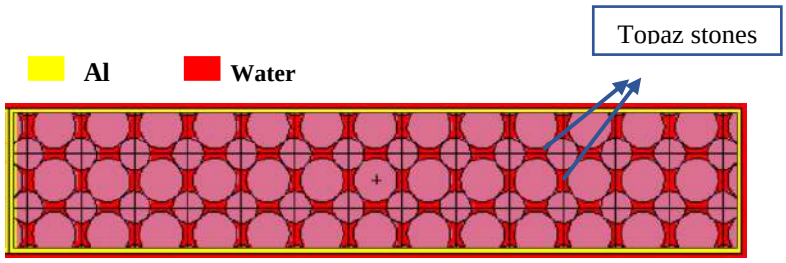

Fig.2. Irradiation box containing topaz and water with aluminum wall

Figure 3 shows the box containing topaz along with filters Pb and B_4C from a vertical view of the box.

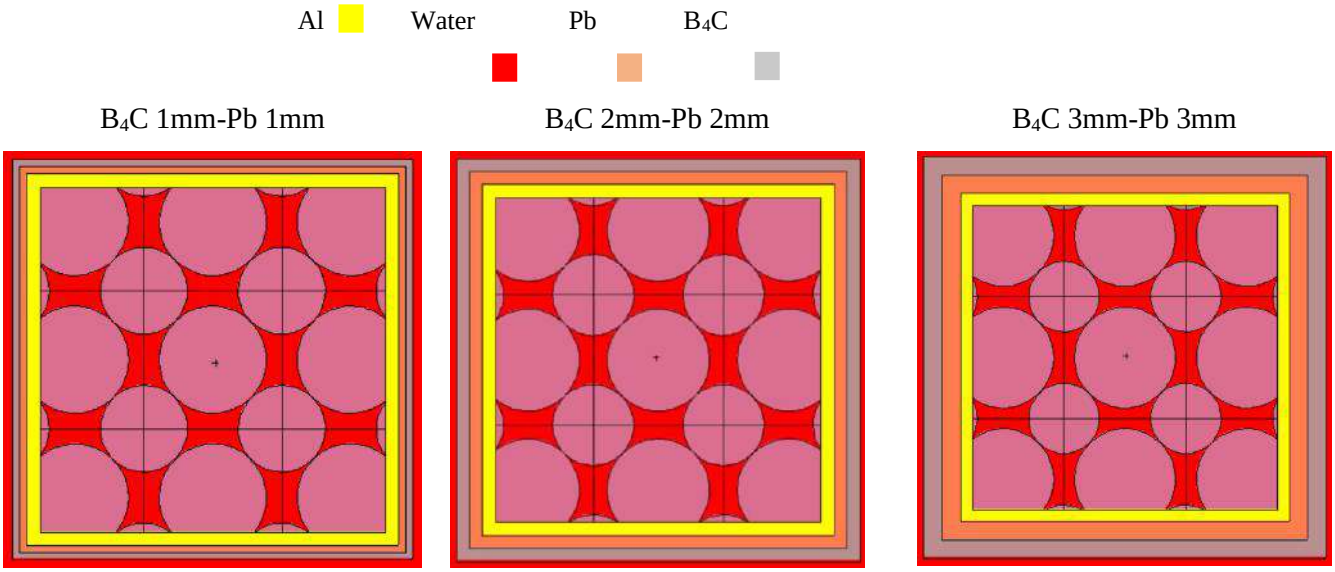

Fig.3. Boxes containing topaz with filters.

In the MCNPX code, the track length estimator (F4) was used to calculate the average volume flux of neutrons at each neutron energy range. To calculate the residual energy caused by neutrons and gammas, heat deposited tally (F6) was used. The BURN card in code MCNPX is used to calculate the activity of radioisotopes in topaz, and radioisotope Scandium (Sc-46) considered as topaz impurity.

The statistical error in all the results obtained from the simulation calculations was less than 4%.

Calculations have been done on both irradiation boxes in the desired channel. Figure 4 shows the location of boxes containing topaz for irradiation.

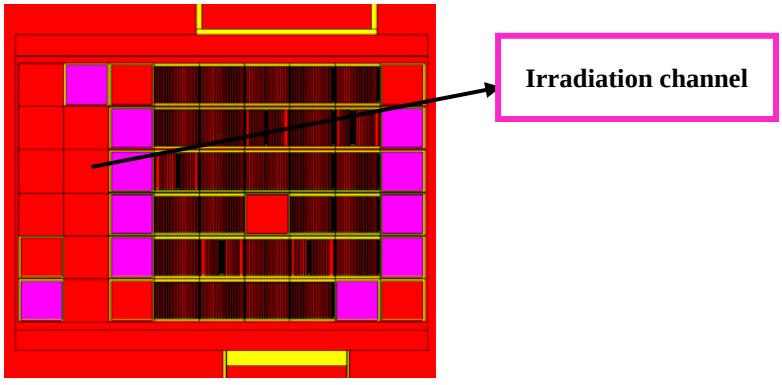

Fig.4. The simulated Irradiation channel of boxes containing topaz.

Fluent software is a fluid simulation software in industry that is used to predict fluid flow, heat and mass transfer, chemical reactions and other related phenomena. Fluent software is used for advanced fluid modeling to provide the most accurate solutions in the industry, regardless of modifying assumptions. With the help of this software, topaz irradiation boxes are simulated along with filters, And the temperature of the topaz stone at the central point of the box is calculated for two situations: 1) the box contains topaz and water. 2) The box contains topaz and air. Figure 5 shows an example of the simulation of an aluminum box containing topaz in two dimensions.

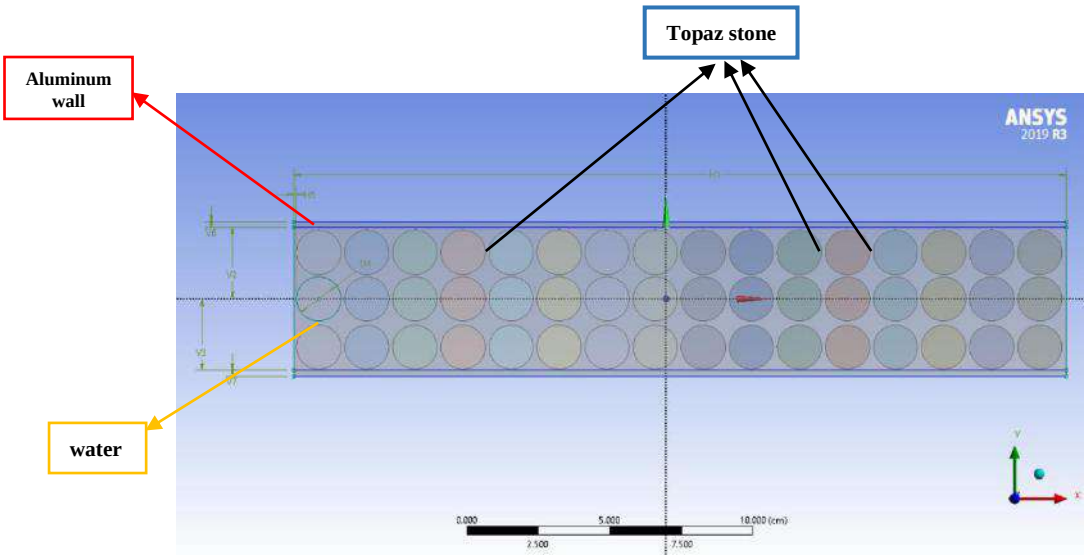

Fig.5. Simulation of aluminum box containing topaz in two dimensions in ANSYS-Fluent software

Results and discussion

The neutron flux distribution was calculated for all 3 ranges of thermal, epithermal, and fast energy. The desired irradiation boxes were placed vertically on top of each other in the irradiation channel at the edge of the core, behind the graphite boxes as shown in Figure 4.

In the topaz box simulation, it is made of aluminum with a thickness of 2 mm. In other cases, lead (Pb) and B_4C filters have been used at each stage, and the thickness of both filters has been increased, and calculations have been made and examined. In this research, two water and air coolers have been used and the calculations made are examined.

Tables

Table 1 summarizes the amount of thermal neutron flux for boxes with different filters in the irradiation channel of the core periphery.

Table 1. Distribution of thermal neutron flux in the irradiation channel of the core periphery

Material / Thickness(mm)/cooling	Thermal neutron flux ($n/cm^2.s$)	Material / Thickness(mm)/cooling	Thermal neutron flux ($n/cm^2.s$)
Al-2mm/Water	2.44E+13 2.51E+13	****	****
Pb1mm-B_4C1mm/Water	1.18E+12 1.15E+12	Pb1mm-B_4C1mm/Air	5.39E+11 5.5E+11
Pb2mm-B_4C2mm/Water	7.38E+11 7.67E+11	Pb2mm-B_4C2mm/Air	2.10E+11 2.46E+11
Pb3mm-B_4C3mm/Water	6.73E+11 6.90E+11	Pb3mm-B_4C3mm/Air	1.54E+11 1.59E+11

According to the results, with increasing the thickness of the B_4C filter from 1 mm to 3 mm, the amount of thermal neutron flux has decreased. If air cooling is used, the amount of thermal neutron flux is much lower than in the presence of water.

The amount of epithermal and fast neutron fluxes for boxes with different filters in the irradiation channel of the core periphery are given in Tables 2 and 3 respectively.

Table 2. Distribution of epithermal neutron flux in the radiation channel of the core periphery

Material / Thickness(mm)/cooling	Epithermal neutron flux ($n/cm^2.s$)	Material / Thickness(mm)/cooling	Epithermal neutron flux ($n/cm^2.s$)
Al-2mm/Water	3.52E+12 3.62E+12	****	****
Pb1mm-B_4C1mm/Water	2.87E+12 2.87E+12	Pb1mm-B_4C1mm/Air	2.83E+12 2.92E+12
Pb2mm-B_4C2mm/Water	2.55E+12 2.53E+12	Pb2mm-B_4C2mm/Air	2.45E+12 2.44E+12
Pb3mm-B_4C3mm/Water	2.45E+12 2.39E+12	Pb3mm-B_4C3mm/Air	2.20E+12 2.19E+12

According to the results, if a neutron absorber filter is used, the amount of epithermal neutron flux decreases.

Table 3. Distribution of fast neutron flux in the irradiation channel of the core periphery

Material / Thickness(mm)/cooling	Fast neutron flux ($n/cm^2.s$)	Material / Thickness(mm)/cooling	Fast neutron flux ($n/cm^2.s$)
Al-2mm/Water	3.87E+12 3.95E+12	****	****
Pb1mm-B_4C1mm/Water	3.93E+12 3.89E+12	Pb1mm-B_4C1mm/Air	4.34E+12 4.34E+12
Pb2mm-B_4C2mm/Water	4.07E+12 4.06E+12	Pb2mm-B_4C2mm/Air	4.55E+12 4.54E+12
Pb3mm-B_4C3mm/Water	4.32E+12 4.22E+12	Pb3mm-B_4C3mm/Air	4.64E+12 4.67E+12

According to the results, with increasing the thickness of the boron carbide filter, the amount of fast neutron flux increases. If air is used as a coolant, this amount of flux will increase. Tables 4 and 5 respectively the amount of residual heat caused by neutron and gamma in topaz stones in different filters in the wall respectively.

Table 4. Residual heat caused by neutrons in the radiation channel of the core periphery

Material / Thickness (mm)	Neutron residual heat (W)	Material / Thickness (mm)	Neutron residual heat (W)
Al-2mm/Water	24.7 24.7	****	****
Pb1mm-B_4C1mm/Water	23/6 23/8	Pb1mm-B_4C1mm/Air	26/3 26/2
Pb2mm-B_4C2mm/Water	24/7 24/6	Pb2mm-B_4C2mm/Air	27/3 27/3
Pb3mm-B_4C3mm/Water	25/6 25/3	Pb3mm-B_4C3mm/Air	27/5 27/5

Table 5. Residual heat caused by gammas in the radiation channel of the core periphery

Material / Thickness (mm)/cooling	Gamma residual heat (W)	Material / Thickness (mm)/cooling	Gamma residual heat (W)
Al-2mm/Water	244/2 248/3	****	****
Pb1mm-B_4C1mm/Water	164/5 167	Pb1mm-B_4C1mm/Air	170/5 170/2
Pb2mm-B_4C2mm/Water	150 150/5	Pb2mm-B_4C2mm/Air	153/5 150/5
Pb3mm-B_4C3mm/Water	138/5 134/5	Pb3mm-B_4C3mm/Air	137 139/3

According to the results of Table 5, with the increase in the thickness of the lead filter, the residual heat caused by gamma decreases and changes by 77%. Table 6 shows the activity of impurity in topaz stone. The cooling period after irradiation for the activity of scandium in topaz stone is 6 months.

Table 6. Activity of a topaz impurity sample

Material / Thickness (mm)/cooling	Activity Sc-46 (Bq/g)	Material / Thickness (mm)/cooling	Activity Sc-46 (Bq/g)
Al-2mm/Water	1.241E+08	***	***
Pb1mm-B_4C1mm/Water	9.653E+06	Pb1mm-B_4C1mm/Air	5.342E+06
Pb2mm-B_4C2mm/Water	5.804E+06	Pb2mm-B_4C2mm/Air	2.318E+06
Pb3mm-B_4C3mm/Water	4.656E+06	Pb3mm-B_4C3mm/Air	1.581E+06

According to the results of Table 6, by adding the thickness of the B_4C filter, the activity level has decreased well. If air is used as topaz cooling during irradiation, the activity is less than water cooling. Table 7 reports the temperature of topaz stones during irradiation which is simulated with ANSYS-Fluent software. The temperature of the topaz stone in the center of the irradiation box is reported as the highest temperature point.

Table 7. Temperature of topaz stones during irradiation

Material / Thickness (mm)/cooling	Temperature (^{0}C)	Material / Thickness (mm)/cooling	Temperature (^{0}C)
Al-2mm/Water	79	***	***
Pb1mm-B_4C1mm/Water	71	Pb1mm-B_4C1mm/Air	**> 450**
Pb2mm-B_4C2mm/Water	67	Pb2mm-B_4C2mm/Air	**> 400**
Pb3mm-B_4C3mm/Water	61	Pb3mm-B_4C3mm/Air	**> 350**

According to the results of Table 7, water has a better cooling effect than air and the heat transfer has been done well.

Conclusions

According to the results obtained from the simulation in code MCNPX, by adding to the thickness of filter B_4C, the amount of thermal neutron flux decreases well, and in the case of water cooling, these changes are about 75%. If air is used as a cooling agent for topaz, the amount of thermal neutron flux and the activity of topaz stones will be lower than if it is water. If air is used as a cooling agent, the temperature of topaz stones increases during irradiation and the temperature rises above 200 ^{0}C, and this temperature is not suitable for topaz stones, and it causes damage to topaz stones. If water is used as a coolant, heat transfer during radiation is done well and the temperature of topaz stones is below 100 ^{0}C, and there is no problem for topazes. It can be concluded that the presence of filter B_4C with a thickness of 3 mm has been very effective in reducing the thermal neutron flux and the activity of stones, as well as a lead (Pb) filter with a thickness of 3 mm in reducing the residual heat caused by gamma. The presence of water as a coolant has had a good effect in reducing the temperature of the stones.

References

[1] Nelson, K., Baum, J.W., 1993. Health risk assessment of irradiated topaz. U.S. Nuclear Regulatory Commission.

[2] M. Kaveh. Measuring and studying the effects of irradiation on the color change and crystal structure of stones. 2013.

[3] S. Salama, A.I. Helal and M.A. Gomaa, Radioactivity of the Treated Topaz,2012.

[4] Jian Zhang, Taijin Lu, Manjun Wang, and Hua Chen, the radioactive decay pattern of blue topaz treated by neutron irradiation, 2011.

[5] Shamshad Ahmed, Value addition in diamonds and other gemstones by nuclear radiation: the phobias and safety considerations,2009.

[6] Nader M.A. Mohamed, M.A. Gaheen, Design of fast neutron channels for topaz irradiation,2016.

[7] A.M. Akhanov, M.T. Aitkulov, D.S. Sairanbayev, Sh.Kh Gizatulin, N.K. Romanova , A. A. Shaimerdenov, Y.V. Chikhray, Zh Ualzhanov, T.K. Zholdybayev, Irradiation capsule design for neutron coloration of topaz in a WWR-K reactor,2022.

[8] K. TIYAPUN, N. KLAYSUBAN, S. BOONMARK, C. TIPPAYAKUL ,current status and future challenge of TRR-1/M1 Thai research reactor.

[9] S. S. Mousavi, Hamid Jafari , M. R. Kardan , Zohreh Gholamzadeh. Feasibility of optimization of Topaz radiation in order to reduce the activity of Topaz stones in Tehran research Reactor. 2023.

[9] AEOI, Safety Analysis Report of Tehran Research Reactor, Atomic Energy Organization of Iran, (2009).

[10] M.H.C. Dastjerdi, H. Khalafi, Design of a thermal neutron beam for a new neutron imaging facility at Tehran research reactor, Physics Procedia, 69, 92-95 (2015).

[11] A. Lashkari, et al, Neutronic analysis for Tehran Research Reactor mixed-core, Prog. Nucl. Energy, 60, 31–37 (2012).

[12] N. Zandi, Study on a new design of Tehran Research Reactor for radionuclide production based on fast neutrons using MCNPX code, Applied Radiation and Isotopes, 132, 67-71 (2018).

[13] H. Khalafi, M. Gharib, Optimization of 60Co production using neutron flux trap in the Tehran research r

[14] M.R. Aboudzadeh, et al, Preparation and Characterization of Chitosancapped Radioactive Gold Nanoparticles: Neutron Irradiation Impact on Structural Propertie. Safety Analysis Report for the Tehran Research Reactor (HEU), Tehran-Iran, (13, 339-345.AEOI, 1966) (2015).

[15] Z. Zarei, M. Amin Mozafari, S. Mohammadi, M. Hasanzadeh. Design of irradiation box of topaz stones and its neutronic and thermal analysis in Tehran Research Reac

Evaluation of heartbeat-induced dose variation to cardiovascular structures in left-sided breast cancer radiotherapy with DIBH (Paper ID : 1402)

Rafat-Motevalli N.[1,2], Miri-Hakimabad H.[1,2*], Hoseinian-Azghadi E.[1,2], Dayyani M.[2]

[1]*Physics Department, Faculty of Science, Ferdowsi University of Mashhad, Mashhad, Iran*

[2]*Research and Education Department, Mashhad Cancer Charity, Mashhad, Iran*

Abstract

Left-sided breast cancer patients undergoing radiation therapy have a higher risk of cardiac mortality. Advanced techniques like t-IMRT, t-VMAT, and deep inspiratory breath-hold (DIBH) can help reduce side effects by sparing organs at risk. Recent studies suggest considering dose parameters of the left ventricle (LV), left anterior descending artery (LAD), and mean heart dose for better results.

A retrospective study was conducted to evaluate the dose parameters of the heart and its substructures. The DIBH treatment plans of 12 patients with left-sided breast cancer (LSBC) were analyzed. The contours of the heart, LV, and LAD were regenerated. Then the 3D dose distribution was recalculated and compared the results with the QUANTEC criteria and recently proposed stricter criteria. Heart mean dose was <26 Gy for all plans. 8/12 plans met V25 criteria, all met V30. 2 plans had mean heart dose of 2.5 Gy but failed for LAD and LV. Only 1 plan met criteria for LV.

The study found that shifting LAD towards the posterior direction reduced its dose parameters compared to shifting it towards the anterior direction. However, none of the adjustments made met the required criteria. The investigation underlines the importance of strict criteria for critical heart substructures during treatment planning.

Keywords: breast cancer, radiation therapy, heart, DIBH, 3D-CRT

INTRODUCTION

Breast cancer is a prevalent cancer that affects women more than any other type of cancer. According to the World Health Organization, breast cancer is the most frequently occurring cancer in women worldwide and the second most common cancer overall. Fortunately, external beam radiation therapy has emerged as a highly effective treatment method for breast cancer. It greatly decreases the probability of local recurrence by 70-80%, thereby increasing the chances of long-term survival [1,2]. However, there are concerns about potential harm to healthy tissues, especially when irradiating the left side of the chest wall or breast. This is

because such treatment often involves exposure of the myocardium and coronary arteries, which may increase cardiac morbidity and mortality. Several studies have shown that careful consideration of the risks and benefits is essential when managing breast cancer [3-5]. According to recent studies, the number of deaths caused by heart disease has increased to 30% [6]. Patients with left-sided breast cancer (LSBC) face a higher risk of cardiac mortality than those with right-sided breast cancer [7-9].

Significant improvements have been made in radiation therapy, which has improved our ability to protect critical OARs. These advancements include innovative techniques like tangential intensity-modulated RT (t-IMRT), tangential volumetric modulated arc therapy (t-VMAT), and breath-controlled deep inspiratory breath hold (DIBH) [10]. Compared to conventional 3D-CRT, IMRT and VMAT techniques have resulted in greater dose conformity in the target area, resulting in better OAR sparing [11].

Our center has considered the mean heart dose criteria based on the QUANTEC value (reported in

Table 1) while planning the 3D-CRT treatments in DIBH conditions. Several studies have found that the mean heart dose criteria for cardiac structure is insufficient. Radiation therapy for breast cancer can increase the risk of major coronary events, even at low doses. The risk increases during the first five years after radiation therapy and continues into the third decade; the rate of major coronary events per Gray increases by 7.4%. If the mean heart doses remain under 2Gy, the event rates do not increase significantly [12]. According to studies conducted by Darby et al. and van den Bogaard et al., the risk of acute coronary events increased by 16.5% per Gy of mean heart dose within nine years of undergoing radiation therapy. The mean heart dose is a relevant parameter for predicting all-cause cardiac toxicities for other tumor types [9]. In patients with an estimated whole heart dose of 2.8Gy and 12.9Gy to 5% of the cardiac volume, Carr et al. discovered a statistically significant increase in coronary heart disease [13].

Arslan et al. conducted a study on the negative effects of breast radiotherapy on the heart, which are mainly caused by coronary artery disease. Patients with LSBC are at higher risk of cardiac toxicity. However, recent studies have shown that using the DIBH technique can be beneficial. In cases where DIBH is unavailable, contouring the heart and its lower anatomical regions as OARs can significantly reduce the heart, LV, and LAD dose, minimizing the risk of

cardiac toxicity. The study concludes that for centers without access to DIBH, contouring the heart and its lower anatomical regions as OARs is critical to reducing the risk of cardiac toxicity [14].

Recent studies indicate that minimizing the radiation dose to critical substructures of the heart during breast radiation therapy is essential to reduce long-term side effects. Regardless of the technique used, the lower anatomical regions of the heart should be considered as critical OARs [15]. Specifically, the dose parameters of the LV, the LAD, and the mean heart dose were proposed [16]. Consequently, the aim of this study is to retrospectively assess the mentioned dose parameters to heart substructures that were not considered during the treatment planning phase. Moreover, the results of our investigation were compared with two sets of criteria: firstly, the standard QUANTEC criteria, and secondly, a recently proposed strict criteria.

Materials and Methods

12 patients with LSBC who were previously treated with the DIBH technique using the 3D-CRT treatment plans have been selected. The prescription dose for these treatment plans was 50 Gy. The treatment plans were generated by means of the Prowess Panther software version 5.50 treatment planning system (P-TPS). The Limbus AI software was used to regenerate the contours of the heart, LV, and LAD on CT simulation images. The regenerated contours were then reviewed and approved by an expert radiation oncologist.

Considering the movement caused by the heartbeat, a symmetric 5 mm and 4 mm margin around LAD and LV was added respectively. After defining the margin, the maximum displacements of LAD were considered towards anterior and posterior directions. The dose parameters were then recalculated for the newly generated contours.

Table 1 lists the QUANTEC values for the heart. The DEGRO breast cancer expert panel recommends some constraints for a safe treatment plan. These constraints are as follows: mean heart dose <2.5 Gy; D_{mean}LV (mean dose LV) <3 Gy; $V5_{LV}$ (volume of LV receiving ≥5 Gy) <17%; $V23_{LV}$ (volume of LV receiving ≥23 Gy) <5%; D_{mean}LAD (mean dose LAD) <10 Gy; $V30_{LAD}$ (volume of LAD receiving ≥30 Gy) <2%; $V40_{LAD}$ (volume of LAD receiving ≥40 Gy) <1%. [16] These criteria are considered the stricter guidelines for evaluating the treatment plans.

Results and Discussion

The calculated dose for heart, LV, and LAD for 12 patients using P-TPS are as follows: mean doses of heart, LAD, and LV were obtained 1.5 to 11.5 Gy, 2 to 18.2 Gy, and 14.8 to 48.9 Gy, respectively (Fig. 1, Fig. 5), $V30_{LAD}$ and $V40_{LAD}$ were 23% to 96.4% and 17.2% to 100%, respectively (Fig. 2, Fig. 5), $V25_{Heart}$ and $V30_{Heart}$ were 3.4% to 20.03% and 2.87% to 19.13%, respectively (Fig. 3) and $V5_{LV}$ and $V23_{LV}$ were 6% to 46% and 2.5% to 35.5%, respectively (Fig. 4).

Various technical options are available to reduce the mean heart. Traditional methods like tangential IMRT or field-in-field approaches do not effectively spare the heart and lungs. However, multi-angle or rotational IMRT delivery, DIBH-based radiation therapy, prone positioning, and using a thermoplastic bra have shown promising results in reducing the dose to the heart and substructures. Partial-breast RT can also be considered for elderly patients with low-risk cancer [16-21].

Table 1. QUANTEC Summery for heart

Volume segmented	Irradiation type	Endpoint	Dose (Gy), or dose/volume parameters	Rate (%)	Note on dose/volume parameters
Pericardium	3D-CRT	pericarditis	Mean dose<26	<15	Based on single study
Pericardium	3D-CRT	pericarditis	V30<46%	<15	
Whole organ	3D-CRT	Long-term cardiac mortality	V25<10%	<1	Overly safe risk estimate based on model predictions

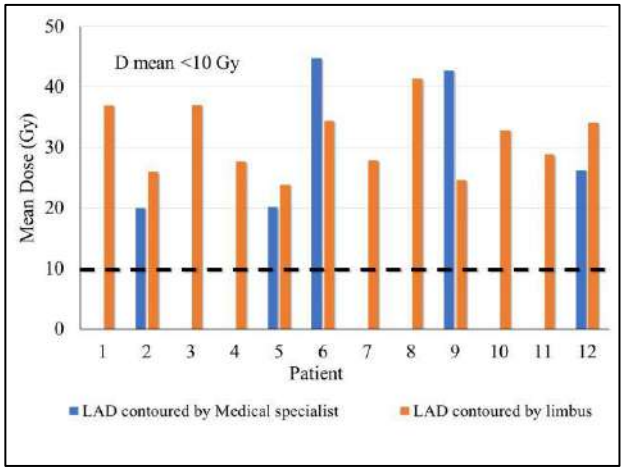

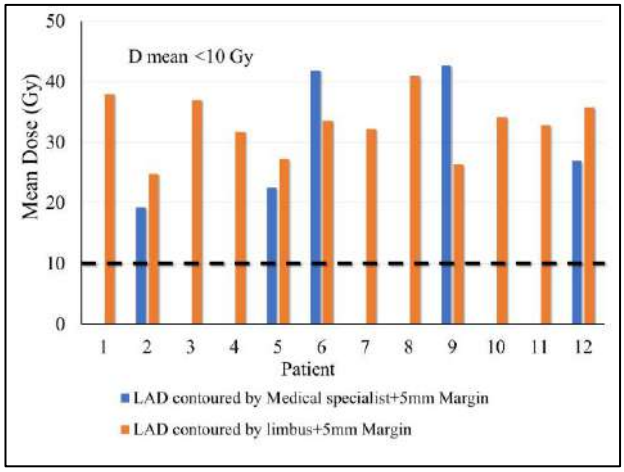

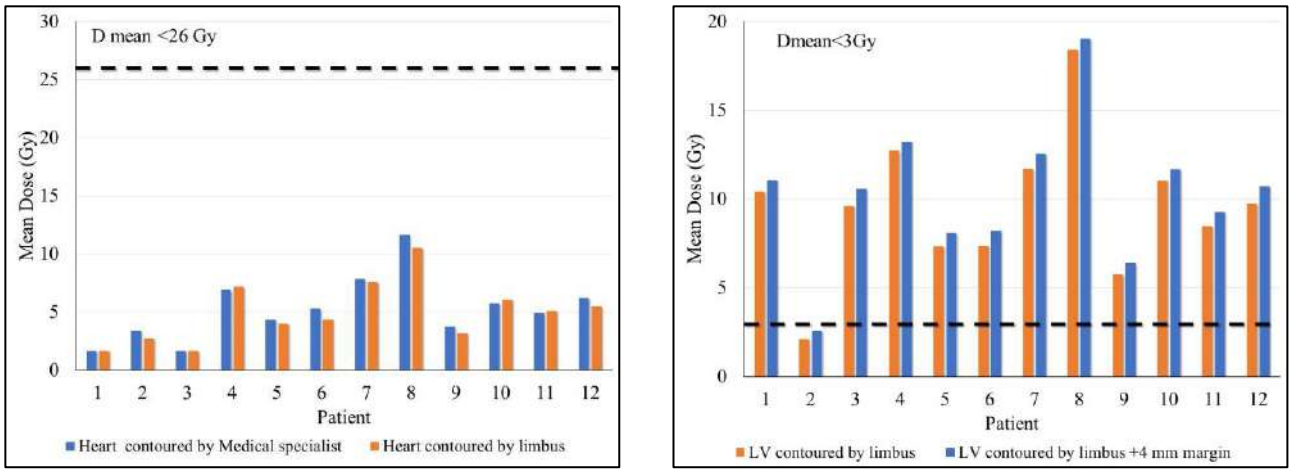

Fig. 1. Column charts for a mean dose of heart, LAD, and LV

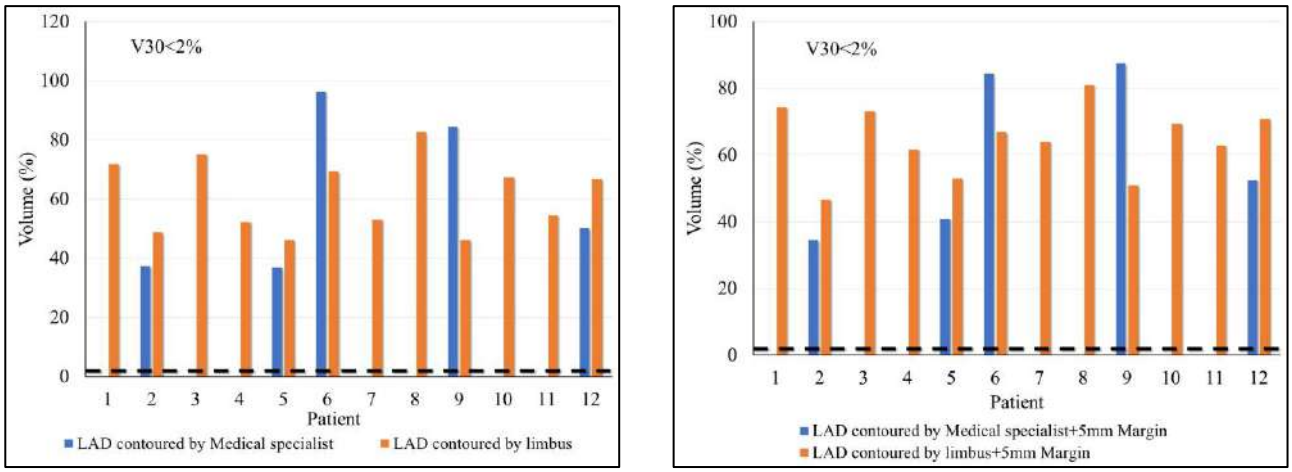

Fig. 2. Column charts for V30 and V40 of LAD (continued)

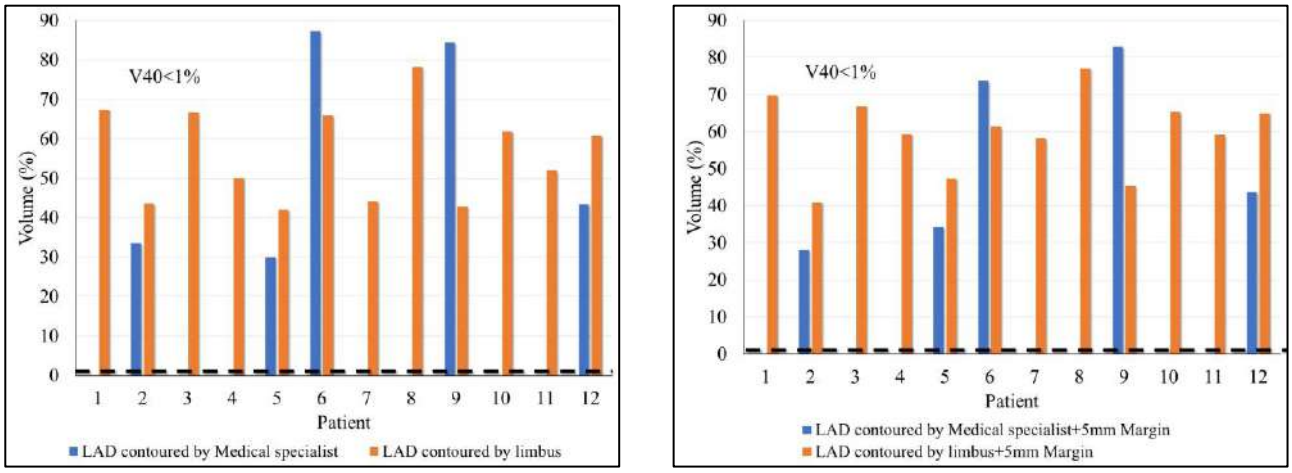

Fig. 2. Column charts for V30 and V40 of LAD

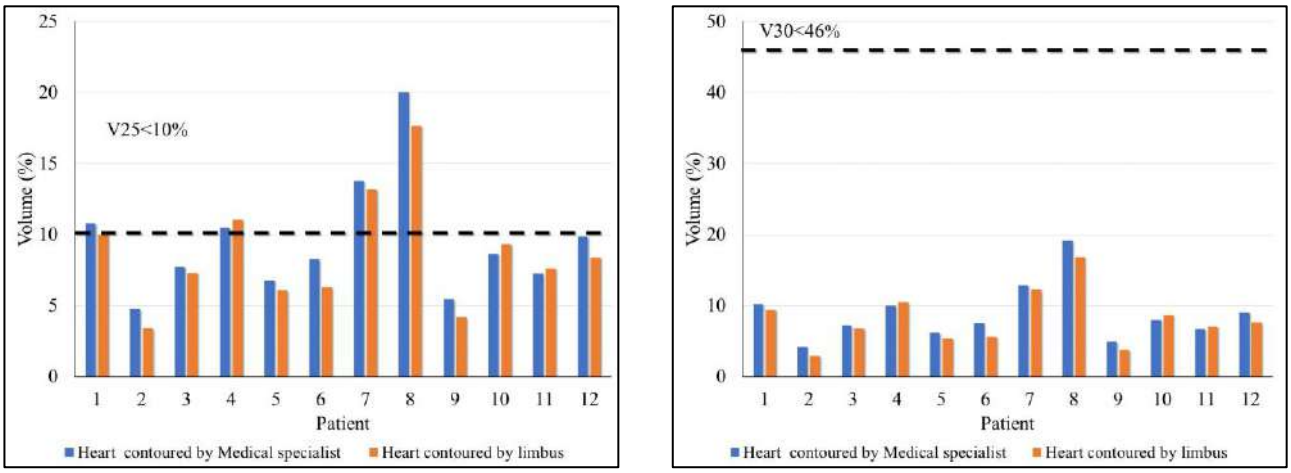

Fig. 3. Column charts for V25 and V30 of heart

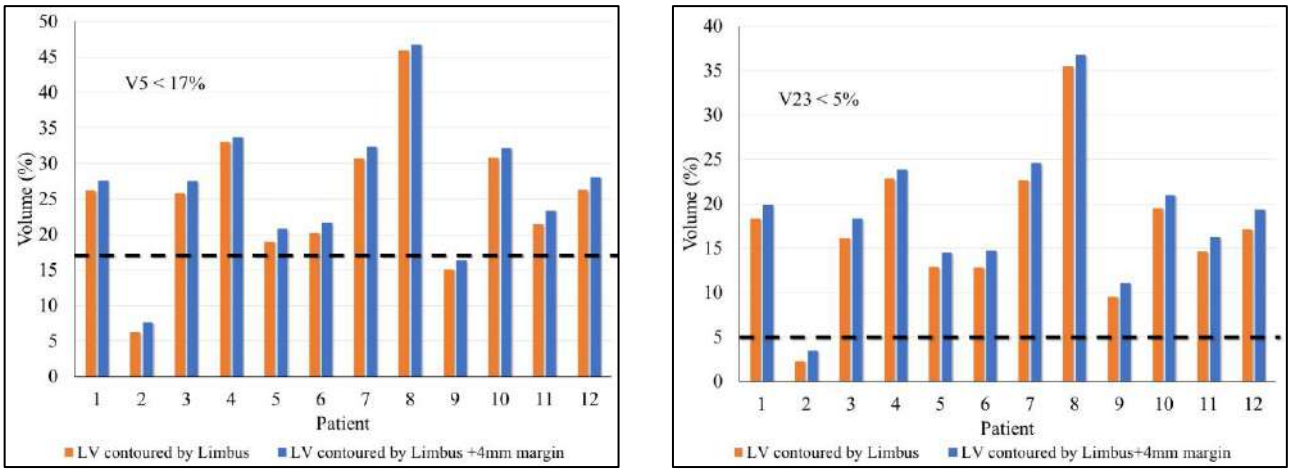

Fig. 4. Column charts for V5 and V23 of LV

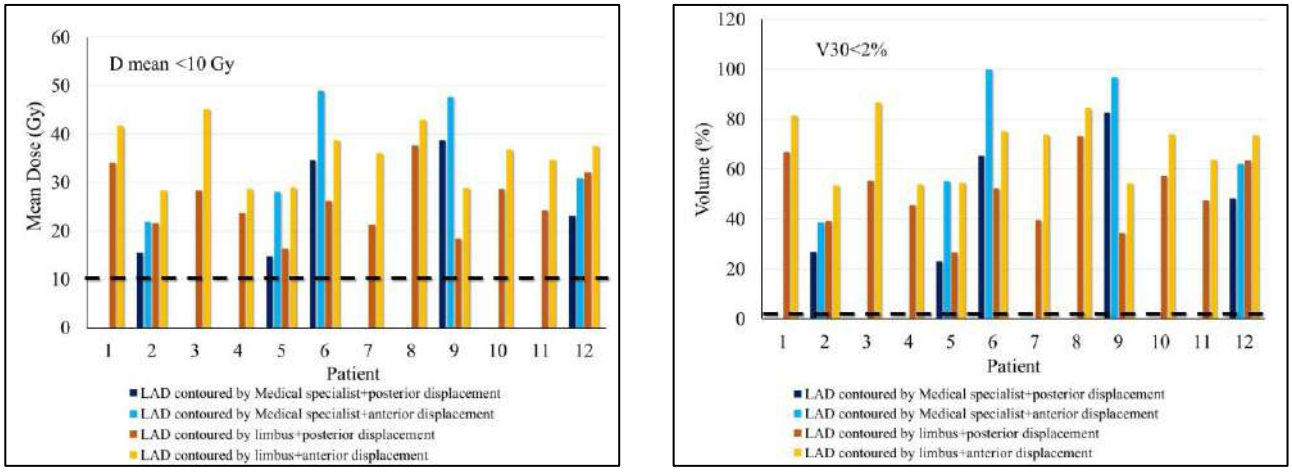

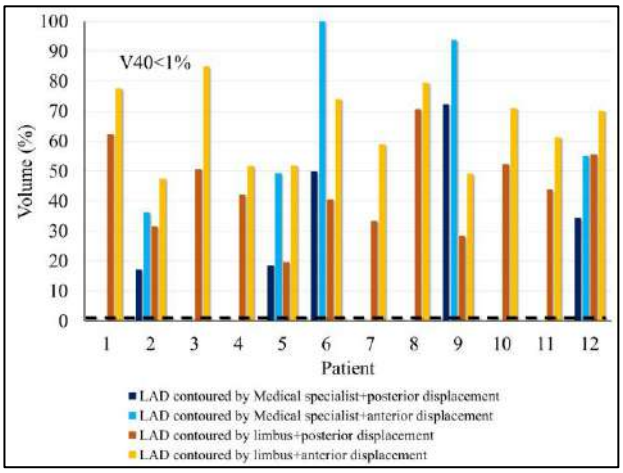

Fig. 5. Column charts for mean dose, V30, and V40 of LAD shifted contours.

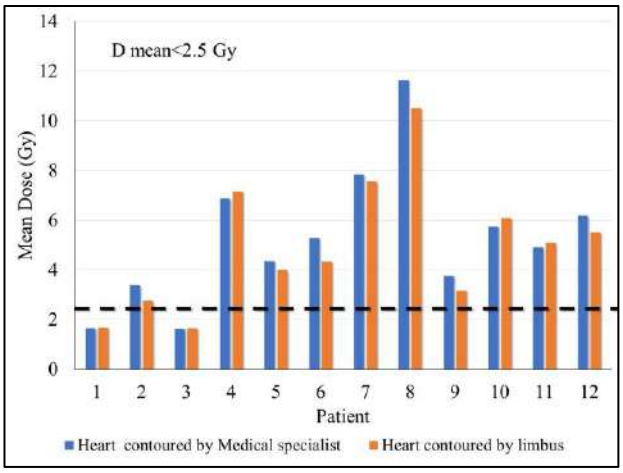

Fig. 6. Column charts for mean heart dose (recent studies recommended limitation for mean heart dose should be lower than 2.5 Gy)

The treatment plans of 12 patients were assessed, with our main focus on the mean heart dose, which was required to be lower than 26 Gy. This criterion was met for all plans. Table 1 was used for our evaluation, including V25 and V30 values of heart. The values of V25 for eight plans and V30 for all plans were found within the acceptable range.

Recent studies have recommended that the mean heart dose should not exceed 2.5 Gy [16], and only two treatment plans met this criterion (Fig. 6). However, the plans did not consider the restrictions for the LAD and LV substructures. None of the plans for LAD and only one for LV met the suggested criteria.

The present study examined the effect of posterior and anterior displacements of LAD contours on the dose parameter. Results revealed a significant reduction in the dose parameter for LAD contours moved towards the posterior direction compared to those moved anteriorly. This effect might be attributed to the LAD being situated farther away from the treatment field, thereby receiving a lower dose. However, none of the plans met the proposed criteria (Fig. 5). These findings have important implications for clinical practice as they underscore the need to assess LAD's position to optimize treatment outcomes carefully.

Conclusions

Breast radiation therapy may lead to severe heart toxicities, particularly for patients with left-sided breast cancer. However, with modern techniques, the heart can be effectively protected. Even when the heart mean dose is low, certain heart substructures, such as LV or LAD, may still be exposed to high doses of radiation. Upon retrospectively investigating the treatment plans of 12 patients, our study found that only 8 out of 12 treatment plans satisfied the V25 criteria and just 2 plans met the stricter mean heart dose of 2.5 Gy. Only 1 plan fulfilled the suggested criteria for LV. In conclusion, it is crucial to consider the LV and LAD as critical organs at risk (OARs) and to take into account the plan acceptance criteria for these substructures during the planning phase. Stricter criteria for the heart and its substructures are highly recommended, especially when advanced radiation therapy techniques such as IMRT and VMAT are employed.

References

[1] Clark, R. M., Whelan, T., Levine, M., Roberts, R., Willan, A., McCulloch, P., ... & Mahoney, L. J. (1996). Randomized clinical trial of breast irradiation following lumpectomy and axillary dissection for node-negative breast cancer: an update. JNCI: Journal of the National Cancer Institute, 88(22), 1659-1664.

[2] Fisher, B., Anderson, S., Redmond, C. K., Wolmark, N., Wickerham, D. L., & Cronin, W. M. (1995). Reanalysis and results after 12 years of follow-up in a randomized clinical trial comparing total mastectomy with lumpectomy with or without irradiation in the treatment of breast cancer. New England Journal of Medicine, 333(22), 1456-1461.

[3] Fisher, B., Anderson, S., Bryant, J., Margolese, R. G., Deutsch, M., Fisher, E. R., ... & Wolmark, N. (2002). Twenty-year follow-up of a randomized trial comparing total

mastectomy, lumpectomy, and lumpectomy plus irradiation for the treatment of invasive breast cancer. New England Journal of Medicine, 347(16), 1233-1241.

[4] Veronesi, U., Cascinelli, N., Mariani, L., Greco, M., Saccozzi, R., Luini, A., ... & Marubini, E. (2002). Twenty-year follow-up of a randomized study comparing breast-conserving surgery with radical mastectomy for early breast cancer. New England Journal of Medicine, 347(16), 1227-1232.

[5] van Dongen, J. A., Voogd, A. C., Fentiman, I. S., Legrand, C., Sylvester, R. J., Tong, D., ... & Bartelink, H. (2000). Long-term results of a randomized trial comparing breast-conserving therapy with mastectomy: European Organization for Research and Treatment of Cancer 10801 trial. Journal of the National Cancer Institute, 92(14), 1143-1150.

[6] Taylor, C., Correa, C., Duane, F. K., Aznar, M. C., Anderson, S. J., Bergh, J., ... & Early Breast Cancer Trialists' Collaborative Group. (2017). Estimating the risks of breast cancer radiotherapy: evidence from modern radiation doses to the lungs and heart and from previous randomized trials. Journal of Clinical Oncology, 35(15), 1641.

[7] Darby, S. C., McGale, P., Taylor, C. W., & Peto, R. (2005). Long-term mortality from heart disease and lung cancer after radiotherapy for early breast cancer: prospective cohort study of about 300 000 women in US SEER cancer registries. The Lancet Oncology, 6(8), 557-565.

[8] Roychoudhuri, R., Robinson, D., Putcha, V., Cuzick, J., Darby, S., & Møller, H. (2007). Increased cardiovascular mortality more than fifteen years after radiotherapy for breast cancer: a population-based study. BMC cancer, 7, 1-5.

[9] van den Bogaard, V. A., Ta, B. D., van der Schaaf, A., Bouma, A. B., Middag, A. M., Bantema-Joppe, E. J., ... & Crijns, A. P. (2017). Validation and modification of a prediction model for acute cardiac events in patients with breast cancer treated with radiotherapy based on three-dimensional dose distributions to cardiac substructures. Journal of Clinical Oncology, 35(11), 1171.

[10] Karpf, D., Sakka, M., Metzger, M., & Grabenbauer, G. G. (2019). Left breast irradiation with tangential intensity modulated radiotherapy (t-IMRT) versus tangential volumetric modulated arc therapy (t-VMAT): trade-offs between secondary cancer induction risk and optimal target coverage. Radiation Oncology, 14, 1-11.

[11] Mansouri, S., Naim, A., Glaria, L., & Marsiglia, H. (2014). Dosimetric evaluation of 3-D conformal and intensity-modulated radiotherapy for breast cancer after conservative surgery. Asian Pacific journal of cancer prevention, 15(11), 4727-4732.

[12] Darby, S. C., Ewertz, M., McGale, P., Bennet, A. M., Blom-Goldman, U., Brønnum, D., ... & Hall, P. (2013). Risk of ischemic heart disease in women after radiotherapy for breast cancer. New England Journal of Medicine, 368(11), 987-998.

[13] Carr, Z. A., Land, C. E., Kleinerman, R. A., Weinstock, R. W., Stovall, M., Griem, M. L., & Mabuchi, K. (2005). Coronary heart disease after radiotherapy for peptic ulcer disease. International Journal of Radiation Oncology* Biology* Physics, 61(3), 842-850.

[14] Arslan, A., Aktas, E., Sengul, B., & Tekin, B. (2021). Dosimetric evaluation of left ventricle and left anterior descending artery in left breast radiotherapy. La radiologia medica, 126, 14-21.

[15] Feng, M., Moran, J. M., Koelling, T., Chughtai, A., Chan, J. L., Freedman, L., ... & Pierce, L. J. (2011). Development and validation of a heart atlas to study cardiac exposure to radiation following treatment for breast cancer. International Journal of Radiation Oncology* Biology* Physics, 79(1), 10-18.

[16] Piroth, M. D., Baumann, R., Budach, W., Dunst, J., Feyer, P., Fietkau, R., ... & Sauer, R. (2019). Heart toxicity from breast cancer radiotherapy: current findings, assessment, and prevention. Strahlentherapie und Onkologie, 195(1), 1.

[17] Pignol, J. P., Olivotto, I., Rakovitch, E., Gardner, S., Sixel, K., Beckham, W., ... & Paszat, L. (2008). A multicenter randomized trial of breast intensity-modulated radiation therapy to reduce acute radiation dermatitis. *Journal of Clinical Oncology*, *26*(13), 2085-2092.

[18] Lohr, F., El-Haddad, M., Dobler, B., Grau, R., Wertz, H. J., Kraus-Tiefenbacher, U., ... & Wenz, F. (2009). Potential effect of robust and simple IMRT approach for left-sided breast cancer on cardiac mortality. International Journal of Radiation Oncology* Biology* Physics, 74(1), 73-80.

[19] Boda-Heggemann, J., Knopf, A. C., Simeonova-Chergou, A., Wertz, H., Stieler, F., Jahnke, A., ... & Lohr, F. (2016). Deep inspiration breath hold—based radiation therapy: a clinical review. International Journal of Radiation Oncology* Biology* Physics, 94(3), 478-492.

[20] Corradini, S., Ballhausen, H., Weingandt, H., Freislederer, P., Schönecker, S., Niyazi, M., ... & Belka, C. (2018). Left-sided breast cancer and risks of secondary lung cancer and ischemic heart disease. Strahlentherapie und Onkologie, 194(3), 196-205.

[21] Coles, C. E., Griffin, C. L., Kirby, A. M., Titley, J., Agrawal, R. K., Alhasso, A., ... & Thompson, A. (2017). Partial-breast radiotherapy after breast conservation surgery for patients

with early breast cancer (UK IMPORT LOW trial): 5-year results from a multicentre, randomised, controlled, phase 3, non-inferiority trial. *The Lancet*, *390*(10099), 1048-1060.

Determination of photon and electron fluence spectral variation for a 6 MV medical linear accelerator by Monte Carlo simulation (Paper ID : 1408)

Khodabandeh-Baygi V. [1, 2], Rafat-Motavalli L. [1, 2*], Hoseinian-Azghadi E.[1, 2]

[1]*Physics Department, Faculty of Science, Ferdowsi University of Mashhad, Mashhad, Iran*
[2] *Research and Education Department, Mashhad Cancer Charity, Mashhad, Iran*

Abstract

External beam radiation therapy can expose patients to unintended sources of radiation such as patient scattering, collimator scattering, and leakage from the machine head. These sources can contribute to out-of-field doses that have the potential to induce long-term adverse effects and secondary cancers, even at relatively low doses. To better evaluate the secondary effects of modern radiotherapy treatments and determine the impact of spectral variations on energy-dependent dosimeters, it is first necessary to understand the photon and electron energy spectra in the beam-bordering and out-of-field regions. This study aimed to evaluate the photon and electron fluence spectra as well as mean energies beyond the field edge and the corresponding spectra on in-field regions for several small radiotherapy fields. Phase-space files of a 6 MV photon beam produced by a Varian TrueBeam™ linac for eight small circular fields of 0.75 cm, 1.0 cm, 2 cm, 2.5 cm, 3 cm, 3.5 cm, 4 cm, and 5 cm and for the reference 10 cm field at SSD = 100 cm were generated using the BEAMnrc code. The photon and electron fluences in each field were calculated at 0.125, 1. 5, and 10 cm water depth and several off-axis distances using FLURZnrc. The study found that the photon fluence spectra strongly depend on spatial positions and vary significantly as a function of depths, off-axis distances, and field size. Compared to the spectrum within the field, the spectrum outside of the field showed greater variations. Changes in depth caused a more significant difference in the shapes of photon spectra since beyond D_{max}, the photon spectra were significantly weighted towards the low-energy photons. Furthermore, the behavior of electrons is depth-dependent beyond the field edge, where the mean electron energy at depth near the surface is greater than in-field regions, especially in small fields. This is due to the relatively high linear energy transfer (LET) of these electrons and primary electron beam leaking from the linac head, leading to surface dose enhancement. Thus, when assessing the dose delivered to a patient's skin, it is necessary to consider these electrons from a radiological protection perspective.

Keywords Peripheral radiation, Monte Carlo simulation, Varian TrueBeam™, secondary cancer

Introduction

Technological advancements have made radiation therapy an effective treatment for cancer. However, these advanced technologies require longer beam-on time and more MUs to deliver highly conformal doses, which results in increased irradiation exposure to patients due to machine head and collimator leakage. Consequently, the out-of-field doses may be higher than desirable, increasing the risk of long-term adverse effects and secondary cancers for patients [1-4]. Diallo et al. discovered that the majority of second cancers emerge in the margin of the irradiated target or the beam bordering region [5]. Thus, to determine the risks of secondary cancers due to the out-of-field doses, it is important to identify the peripheral low-absorbed dose received by healthy organs surrounding the tumor. Furthermore, healthy tissues near a tumor are affected differently by radiation depending on low-energy radiations (electrons and photons) commonly present outside the field edge [6]. On the other hand, accurate dose measurement requires energy-dependent dosimeters, which can lead to discrepancies in absorbed dose measurements outside the radiotherapy fields. Dosimeters calibrated within the beam central axis can mislead dose measurement outside the field due to their energy dependence. Therefore, to calibrate dosimeters properly, it is also necessary to determine the type of photon energy spectrum in the out-of-field region. Thus, Precise knowledge of the beam spectra characteristics, such as mean electron and photon energy in small radiotherapy fields, would allow for better evaluation of the biological effect on healthy organs and appropriate correction factors for energy-dependent dosimeters. Previous studies clearly indicate that there are significant variations in the photon energy spectra of radiotherapy beams. These variations are highly pronounced in small field sizes, particularly in intensity-modulated radiation therapy (IMRT) [2]. Concerning the small field size, to the best of our knowledge, there are few studies where electron and photon energy spectra in water have been evaluated both inside and outside of the radiation field. This is a highly complex undertaking because the energy spectrum outside the field changes as a function of field size, depth, and distance from the central axis [2]. To overcome this challenge, most researchers have used Monte Carlo methods, as this method has already been proven effective and accurate in simulating in-field doses, making them useful in calculating out-of-field doses [1, 2, 7]. We undertook the current study to

investigate the variability in the energy spectrum and mean energies of a 6 MV Varian TrueBeam™ as a function of the field size and measurement location for small radiotherapy fields to evaluate the secondary effects of modern radiotherapy treatments and determine the impact of spectral variations on energy-dependent dosimeters.

Research Theories

Varian TrueBeam™ linear accelerator (Varian Oncology Systems, Palo Alto, CA) operating in a 6 MV photon beam has been modeled by BEAMnrc Monte Carlo code [8]. The model geometry incorporated all beam-line components, including a 120-leaf Multileaf collimator (MLC), and other structural components. The IAEA phase-space files (PSF) generated from the machine head were used as inputs for a component module to simulate photon and electron spectra of a 6 MV photon beam for circular field sizes ranging from 0.75 to 5 cm (i.e. 0.75 cm, 1.0cm,2cm,2.5cm,3cm,3.5cm,4cm,and 5 cm) and for the reference field of 10 cm [9]. The photon and electron fluences were calculated at 0.125, 1.5, 5, and 10 cm water depth and several off-axis distances using the FLURZnrc module of the EGSnrc [8]. In all simulations, the calculation was performed at SSD = 100 cm and the electron cut-off (ECUT) and photon cut-off (PCUT) energies were defined at 0.521 MeV and 0.01 MeV, respectively. Also, the photon and electron fluence spectra were scored within cylindrical voxels of 0.5 cm height and variable radius of 0.15 cm for 0.7 cm field size to 0.5 cm for larger ones. The particle flux was tallied for each simulation using a logarithmic energy binning structure from 10 keV to 6 MeV. It should be noted that while the BEAMnrc code allows the simulation of square fields using the secondary collimators, the FLURZnrc module of the EGSnrc Monte Carlo code only allows cylindrical geometries to be converted into equivalent circular fields. Table 1. presents the diameters of circular fields that correspond to their square equivalent at the phantom surface.

Table 2. The equivalent square field sizes.

Length of the square field (cm)	Diameter of the equivalent circular field (cm)
0.7	0.75
0.9	1.0
1.8	2.0
2.2	2.5
2.7	3.0
3.1	3.5
3.6	4.0
4.5	5.0
10	10

Results and discussion

Photon fluence spectra

The normalized energy photon fluence for the circular field of 5 cm is presented in Figure 1. The results demonstrate that changes in depth caused a considerable difference in the shapes of photon spectra since, beyond D_{max}, the photon spectra were weighted towards the low-energy photons (photon energies below 100 keV). It is also essential to consider the variations of photon spectra in an off-axis distance for a given water depth, where as the distance away from the central axis increased, the photon energy spectra became softer. Also, regarding Fig.1. changes in depth show a more pronounced difference in the photon spectra than increased distance away from the central axis for out-of-field regions. The reason behind this behavior is attributed to the increased number of Compton scattering as the water volume becomes larger. A further feature of the photon spectra (Fig. 1) is the narrow peak at 0.511 MeV due to positron annihilation, which occurred predominately in the high-energy atomic number components, independent of the water depth.

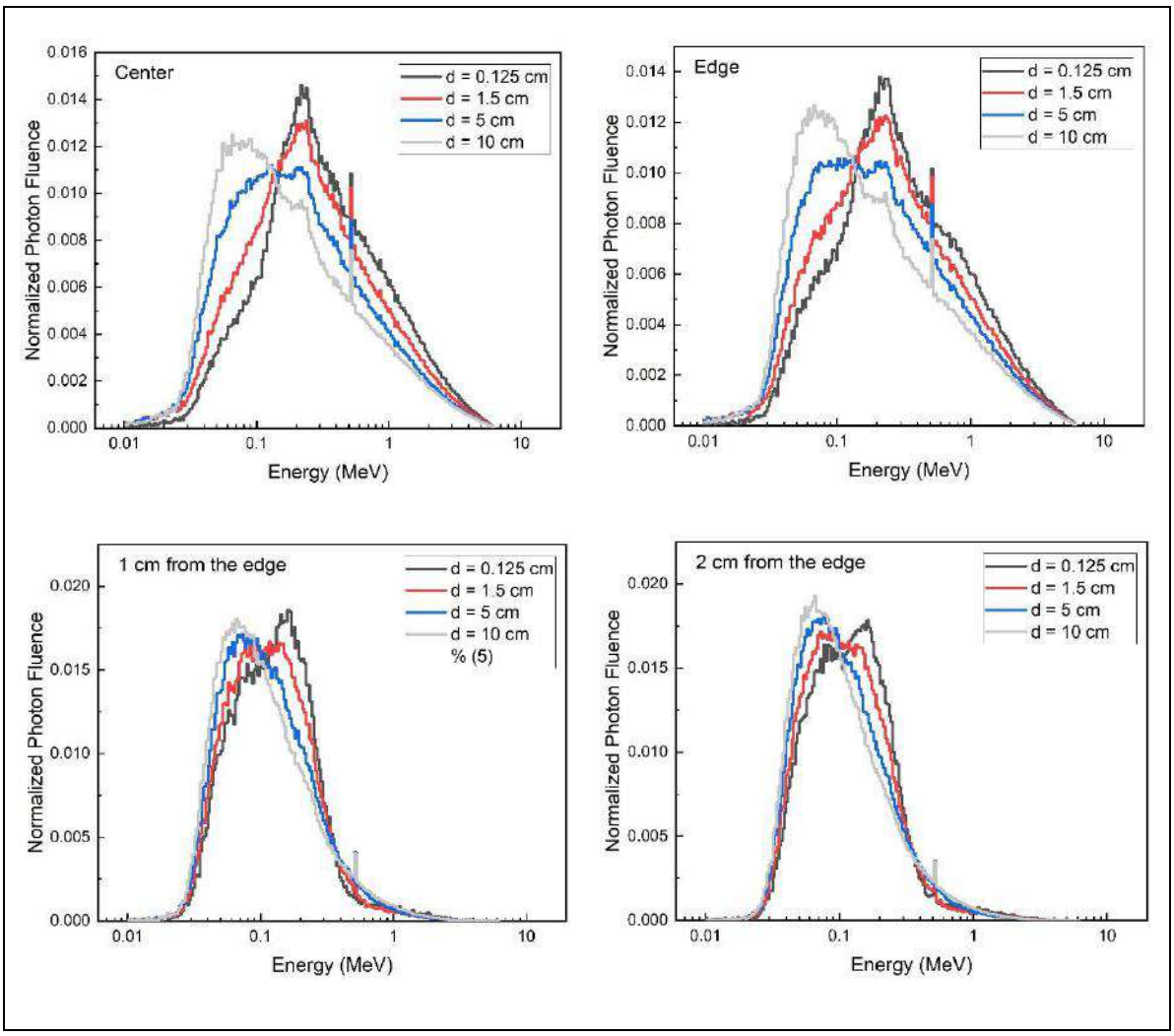

Fig. 1. Normalized photon fluence as a function of photon energy at several depth and four off-axis distances for a 5 cm circular field size.

The calculation of the mean photon energies in all spectra was carried out as a function of both depth and off-axis distances. Figures 2. and 3. present the mean photon energy as a function of depth at the central axis for different field sizes, and the mean photon energy as a function of off-axis distances for circular field sizes of 0.75, 2, 5, 10 cm and several depths, respectively. Figure 2. reveals that the mean photon energy in the central axis at different water depths varies with the field size. Note that in the central axis of small field sizes, mean photon energies at shallow depths, i.e. 0.125 and 1.5 cm water depths are similar, whereas, in the 10 cm field size, the differences are more considerable. The similarity of the photon spectra at different depths is due to the lack of charged particle equilibrium (CPE) in the vertical direction of the beams. Furthermore, unlike small fields where the mean photon energy in the central beam axis rises as the depth increases, in the 10 cm field size, the mean photon energy decreases with the water

depth. The reason behind this could be the significant contribution of low-energy photons that are scattered at a specific depth. That is, deeper depths leading to a larger volume of water where the primary beam interacts to produce more Compton photons; this ultimately results in a softer photon-energy spectrum. The current findings suggest that the photons scattered within the water phantom at a given depth hold greater significance than those originating from the phantom's surface.

Figure 3. indicates that within the radiation field, the mean photon energy decreases as the field size increases, and it is due to more contribution of scattered photons as the field size increases. On the other hand, for a given field size, increasing the depth leads to a higher mean photon energy, especially for smaller fields. However, an inverse trend is observed outside the field edge, where the mean photon energy decreases as we move away from the field edge, reaches a minimum, and then increases as the field size increases. This result can be attributed to the rapid decline in low-energy photon fluence with the distance from its origin. The increase in the number of scattered photons generally associated with an increase in field size produced a decrease in mean energy with field size at any particular position. These findings demonstrate a correlation between the mean photon energy and the field size, which can be useful in the development of radiation therapy planning techniques.

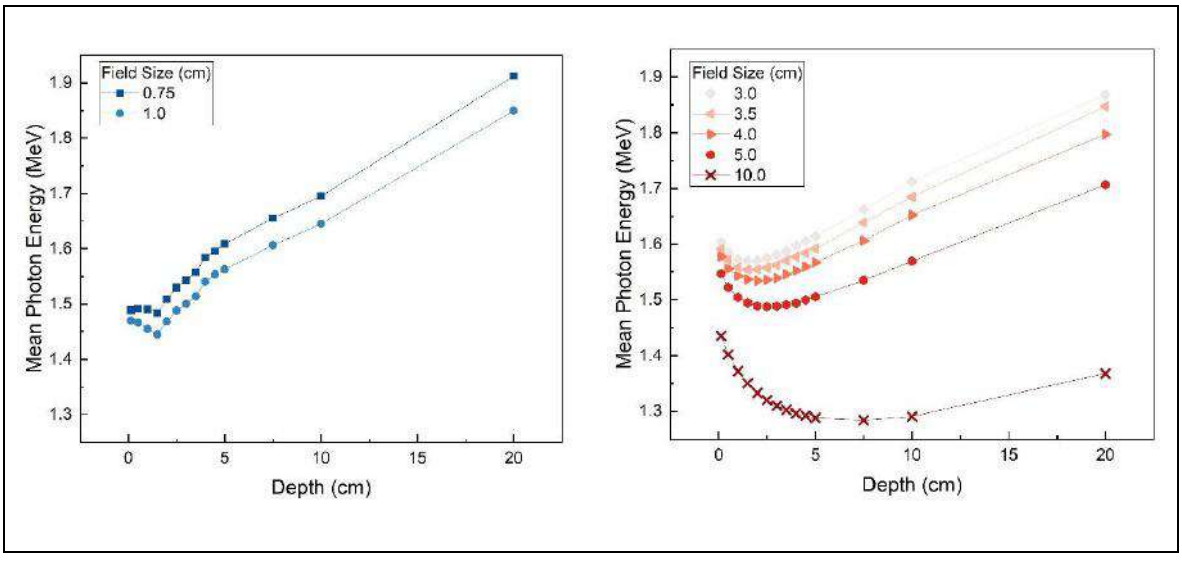

Fig. 2. Mean photon energy as a function of depth for several square field sizes at the field center

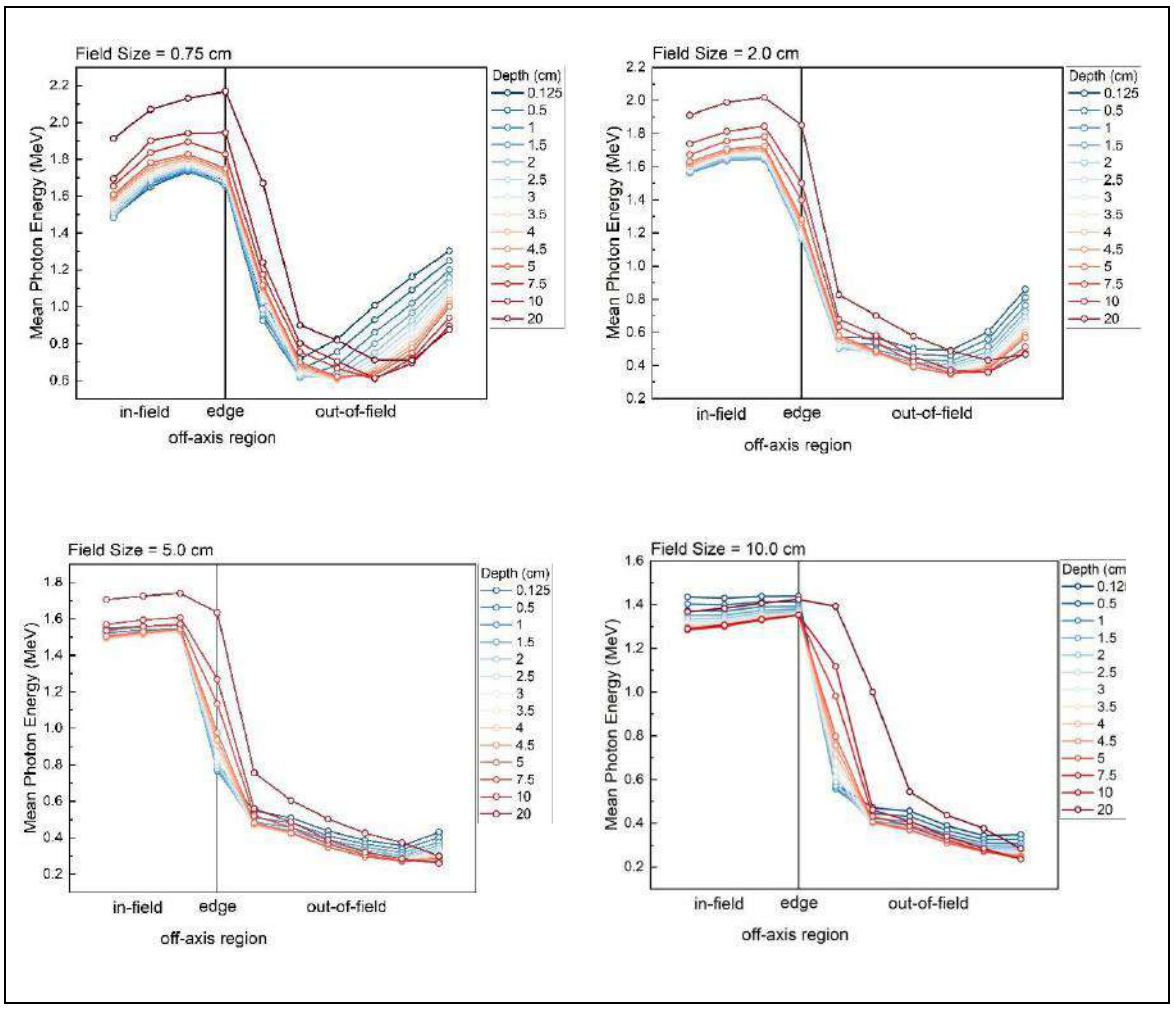

Fig. 3. Mean photon energy as a function of off-axis distances for field sizes of 0.75, 2, 5 and 10 cm and several depths.

Electron fluence spectra

Figure 4. shows the mean electron energy as a function of distance from the center of the field for two circular field sizes: a small field of 0.75 cm and a larger 10 cm field. The data reveals that, for a given field size, the mean electron energy consistently increases with depth inside the field, while similar to photons, the mean electron energy decreases with increasing field size in the central axis and the edge of the fields. Xicohténcatl-Hernández et al. found that there is a significant difference in the total electron fluence between the 4.5 and 0.7 cm^2 field sizes at depths of 1.35 cm and 9.85 cm in the central axis, with a difference of approximately 21% and 30%, respectively [6].

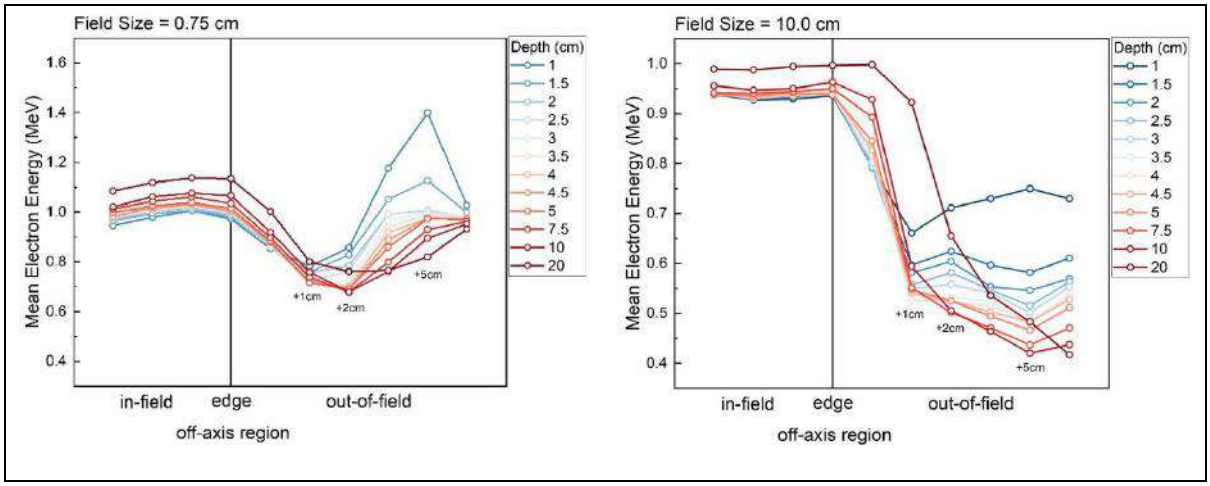

Fig. 4. Mean electron energy as a function of off-axis distances and several depths for 0.75 and 10 cm circular field sizes.

However, outside the field, the behavior of electrons is depth-dependent. The mean electron energy beyond the field edge displays a different pattern with both a minimum and a maximum value, which depends on the field size and the water depth. This is due to the increase in the scattering radiation outside the field boundaries. Ultimately, at larger off-axis distances, it seems that the electron mean energy reaches a constant value, i.e. at about 10 cm from the central axis, the mean electron energy was nearly constant for a 0.75 cm field size. Concerning the data shown in Figure 4. at 1 and 2 cm beyond the field edge, the mean electron energies are higher than those for photons. This could possibly be attributed to the primary electrons that are leaked from the linac head, causing contamination. This result is of prominent importance due to the relatively high LET of these electrons, which may have a significant impact on the healthy tissue surrounding the tumor volume, despite the delivered dose being considered small. This is why it is crucial to consider these electrons from a radiation protection standpoint to ensure the protection of the patient's skin during radiotherapy treatment using linear accelerators.

Conclusion

We have investigated the photon and electron spectral variation and mean energies for beam-bordering, out-of-field regions and the corresponding spectra inside the field for several small radiotherapy fields produced by a 6 MV Varian TrueBeam™ accelerator. This study found that the photon fluence spectra strongly depend on spatial positions and vary significantly as

a function of depths, off-axis distances, and field sizes. The out-of-field spectrum shows significant variations, which are crucial to consider when calibrating energy-dependent dosimeters. It is also observed that the mean photon energy clearly drop off outside the 6 MV photon beam at all depths. Also, the behavior of electrons is depth-dependent beyond the field edge, where the mean electron energy at depth near the surface is greater than in-field regions, especially in small fields. These high LET electrons should be considered as they affect healthy organs surrounding the tumor and leading to surface dose enhancement. Thus, the outcome of this study will enable us to assess with greater accuracy the potential long-term effects attributable to secondary.

References

[1] Kry, S.F., et al. (2007). A Monte Carlo model for out-of-field dose calculation from high-energy photon therapy. Medical physics, 34(9): 3489-3499.

[2] Scarboro, S.B., et al. (2011). Variations in photon energy spectra of a 6 MV beam and their impact on TLD response. Medical physics, 38(5): 2619-2628.

[3] Jang, S.Y., et al. (2007). Variations in energy spectra and water-to-material stopping-power ratios in three-dimensional conformal and intensity-modulated photon fields. Medical physics, 34(4):1388-1397.

[4] Huang, J.Y., et al. (2013). Accuracy and sources of error of out-of field dose calculations by a commercial treatment planning system for intensity-modulated radiation therapy treatments. Journal of applied clinical medical physics, 14(2):186-197.

[5] Diallo, I., et al. (2009). Frequency distribution of second solid cancer locations in relation to the irradiated volume among 115 patients treated for childhood cancer. International Journal of Radiation Oncology Biology Physics, 74(3): 876-883.

[6] Xicohténcatl-Hernández, N., A. Moreno-Ramirez, and G. Massillon-Jl,. (2021). Electron and Photon Energy Spectra Outside of 6 MV X-ray Small Radiotherapy Field Edges Produced by a Varian iX Linac. Frontiers in Physics, 9.

[7] Sardari, D., et al. (2010). Measurement of depth-dose of linear accelerator and simulation by use of Geant4 computer code. Reports of practical oncology and radiotherapy, 15(3): 64-68.

[8] Kawrakow, I. and D.W.O. Rogers, The EGSnrc code system: Monte Carlo simulation of electron and photon transport.

[9] https://www-nds.iaea.org/phsp/photon/Varian_TrueBeam_6MV.

Effect of covering nickel-copper ferromagnetic core on the efficiency of iodine-125 adsorption in the thermo-brachytherapy seeds (Paper ID : 1410)

ICNST 2024
International Conference on Nuclear Science and Technology
6- 8 MAY 2024 | Isfahan, Iran

Optimization of galvanostatic electrochemical separation of Radiopharmaceutical grade (_^90)Y from (_^90)Sr by independent adjustment of accumulation and collection currents (Paper ID : 1411)

Moazami H. R. Co-Author[1], Salek N. Correspondent [1*], Mehrabi M. Co-Author [2].

Nuclear Fuel Research School, Nuclear Science and Technology Research Institute (NSTRI), Box 14395-836, North Kargar Street, Tehran, Iran.

Radiation Application Research School, Nuclear Science and Technology Research Institute (NSTRI), Box 14395-836, North Kargar Street, Tehran, Iran.

Abstract

According to high radiotoxicity of ^{90}Sr, development of highly specific separation methods for ^{90}Y from ^{90}Sr is a challenge. In this work, radiopharmaceutical grade ^{90}Sr was separated from ^{90}Sr by means of galvanostatic electrochemical separation. A two-electrode electrochemical cell comprising a central rod-shape Pt electrode and a helical Pt wire electrode was used for the separation. ^{90}Sr solution at an initial activity of 5Ci was loaded into the electrochemical cell and ^{90}Y was accumulated on the outer helical electrode at a constant current of 300 mA. then, the electrochemical cell was loaded with ^{nat}Sr solution and collection of the accumulated ^{90}Y on the central rod electrode was carried out by a reversed polarity at different currents ranging from 600 to 1500 mA. Finally, the collected 90Y was purified at the same current for three times. The results showed that the independent adjustment of accumulation and collection currents is an excellent approach for fast, selective and efficient separation of ^{90}Y from ^{90}Sr. At the optimized conditions, ^{90}Y was separated from ^{90}Sr with a final activity of 709 mCi.

Keywords: Yttrium-90, Strontium-90, generator, electrochemical separation, current.

INTRODUCTION

Yttrium-90 ($T_{\frac{1}{2}}$: 64.1 h; Eb_{max}: 2.28 MeV) is an interesting therapeutic radioisotope with several established radiopharmaceuticals[1]. As a pure β– particle emitter, it can be prepared by the neutron irradiation of ^{89}Y in a nuclear reactor or by the decay of ^{90}Sr. Because of the small neutron capture cross-section (0.001 b) of ^{89}Y, Yttrium-90 produced from a reactor has very low specific activity. According to the this limitation, ^{90}Y is separated from ^{90}Sr ($T_{1/2}$: 28.8 a) which is a major fission product with estimated annual world production of 600

megacuries[2-5]. Currently, a small number of countries have the capabilities for large scale sepaeation of ^{90}Sr from spent nuclear fuel. For example, there is a high level facility for separation of ^{90}Sr at Mayak, Russian Federation. Another facility was set up at the Pacific Northwest National Laboratory, United States of America (USA), for the recovery of (1500 Ci) of pure ^{90}Sr [1,2]. Since yttrium-90 has a high energy of 2.27 Mev and a half-life of 64.53 hours, it can be effective in the treatment of massive cancer tumors. with average and maximum radiation penetrations of 2.5 and 10 mm, respectively. A well-known application of ^{90}Y is the treatment of liver cancer by the process called radioembolization. In this treatment, a thin flexible tube is used to inject ^{90}Y labeled tiny beads into the main blood vessel that carries blood to the liver. The beads are accumulated in the tumor and in blood vessels near the tumor giving off high energy β radiation. This specifically destroys the blood vessels that the tumor needs to grow along with radiotherapy of the cancer cells. Yttrium-90 can also be labeled with many antibodies and peptides resulting in numerous therapeutic applications such as radioimmunoassay, radio-synovectomy, and bone pain palliation. The most important challenges in the separation of ^{90}Y for therapeutic uses is its very high radionuclidic purity (>99.998%). ^{90}Sr is the most probable contaminant, which is a bone seeker with a maximum permissible body burden (MPBB) of only 74 kBq (2 µCi). According to the United States Pharmacopeia (USP), the content of ^{90}Sr is only 740 KBq per 37 GBq (or 20 µCi per Ci) of ^{90}Y at the date of expiration. The content of ^{90}Sr in the monograph for ^{90}Y-ibritumomab tiuxetan (Zevalin) injection is the same. Hence, the radionuclidic purity of ^{90}Y should be greater than 99.998%. in other words, the contamination of ^{90}Sr should be less than 2×10^{-3} % or 20 ppm. Several techniques have been reported for the separation ^{90}Y from ^{90}Sr including solvent extraction, ion exchange, supported liquid membrane extraction or extractive chromatography. Most of these separation techniques involve multiple steps and use conventional separation methods. However, none of the above mentioned methods are suitable for routine use [5,6]. The electrochemical generator offers several advantages including simple automation, low radioactive waste and negligible usage of chemicals. A minimal amount of ^{90}Sr is lost during the operation of an electrochemical generator. It was named under the Indian goddess ‘Kamadhenu’ because of this unique feature that allows for virtually indefinite ‘milking’ the generator [7,8]. This instrument is commercially available by “ELEX commerce” company and it is used by Pars Isotope Company for the production of ^{90}Y. in this work, independent

currents were applied for accumulation and collection/purification steps and the effect of parameters on the performance of the separation was investigated.

EXPRIMENTAL

The electrochemical system for the separation of ^{90}Y from ^{90}Sr has been comprehensively described in the literature [7-9]. The process involves electrolysis of a mixture of ^{90}Sr and ^{90}Y in nitrate form using two platinum electrodes. In the first step, called the accumulation step, the ^{90}Y is deposited on the cathode, which is a helical platinum wire surrounding the central rod-shape anode. The thickness of the Pt wires used as anode and cathode was 1mm. In this work, this step was carried out three times at a constant current of 300 mA for a fix time of 45 min for each accumulation. In the second step, called the collection step, the cell was loaded with $^{nat}Sr(NO_3)_2$ electrolyte and the ^{90}Y was collected on the central rod-shaped Pt electrode by reversing the polarity of the electrodes. In fact, in this step, the central electrode is cathode and the outer helical electrode is anode, and ^{90}Y is leached and deposited on the fresh cathode. After the collection, the central electrode is removed and subjected to three replicated purification periods. Purification is done in three cycles of electrode polarity reversal. In each cycle, ^{90}Y deposited on the central electrode was removed and it was redissolved by changing the polarity after refilling the electrolyte. These replicated reversals result in the precipitation/redissolution of ^{90}Y and the dilution of surface adsorbed ^{90}Sr in natural strontium. This may cause significant reduction of ^{90}Sr in the final product. Finally, the purified ^{90}Y was dissolved in a hydrochloric acid solution by removing the central electrode. The effect of the current used in collection and purification steps was investigated by varying this parameter from 600 to 1500 mA. A beta-particle detector equipped with a slit colimator eas used to monitor the deposition of 90Y during the whole process. All experiments were carried out with one-week intervals.

Results and discussion

In this work, 8 replicated accumulation runs were performed at an accumulation current of 300mA. For each run, three 45min accumulation cycle were applied and the activity at the end of each cycle was recorded. Figure 1 shows the results. As can be seen, the accumulated activity shows an oscillating nature between each run. This means that any efficient separation run extracts the majority of the decayed ^{90}Y from the feed solution resulting in the decrease of the

accumulated activity the next run. On the other hand, for any poor separation a significant amount of ^{90}Y remains in the feed solution that may lead to an efficient separation in the following run. According to the results, the one-week interval of the separation runs in not adequate to generate stable amounts of ^{90}Y between the runs.

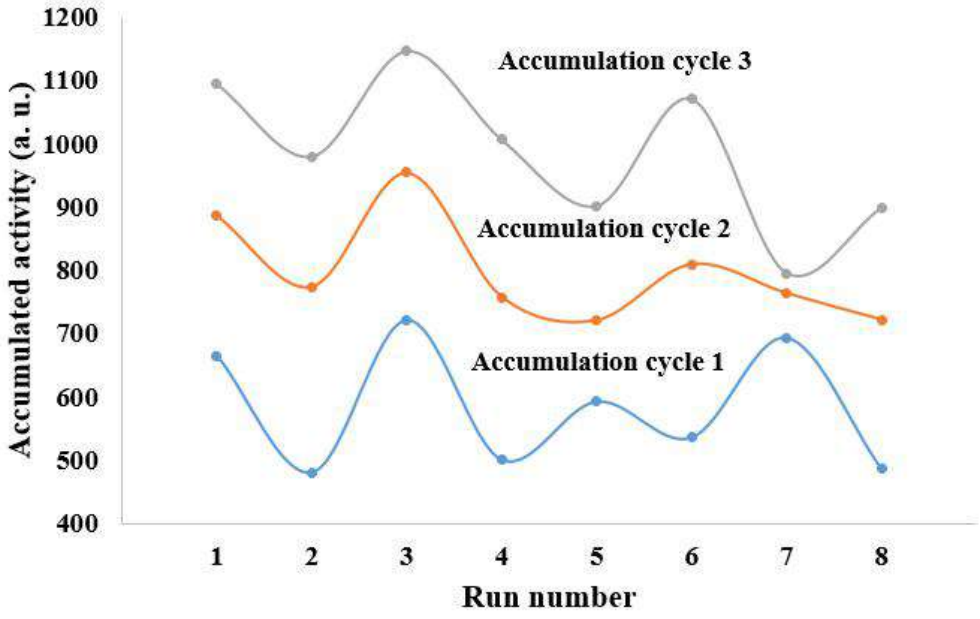

Fig. 1. The accumulated activity for 8 accumulation runs including 3 cycles

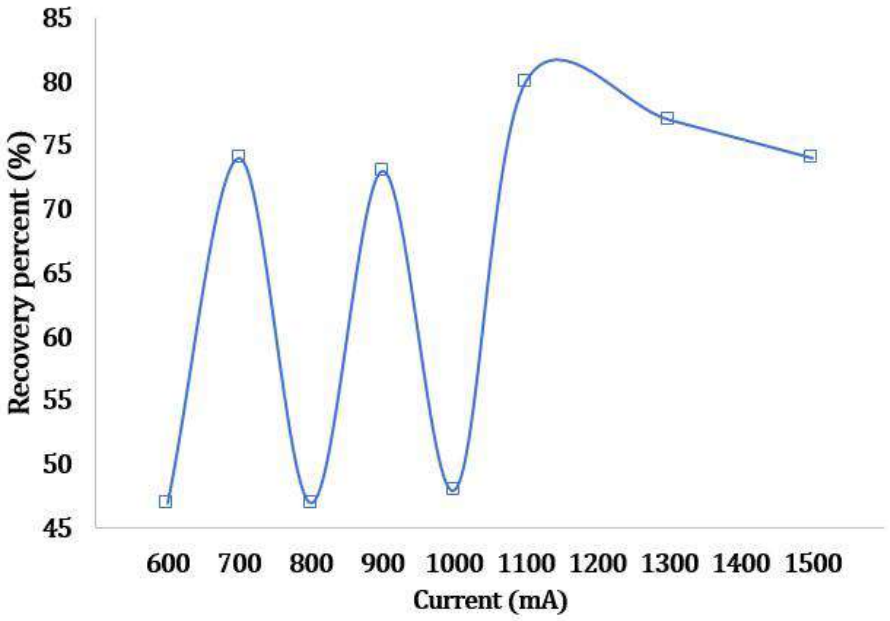

Fig. 2. The recovery as a function of collection current

Figure 2 shows the recovery of the separation as a function of the applied collection current. As can be seen, for collection currents from 600 to 1000 mA, the recovery also shows oscillating pattern, but in the opposite direction as compared to activity values. In other words, when accumulation step has low efficiency, the percent of the collected activity is high. This indicates that the capacity of the electrochemical cell for the collection of accumulated ^{90}Y in medium current range is limited. At the current of 1100 mA, the percent recovery reaches a maximum of 80 % and decreases for higher currents. It can be attributed to the incorporation of unwanted phenomena such as hydrogen evolution and joule heating.

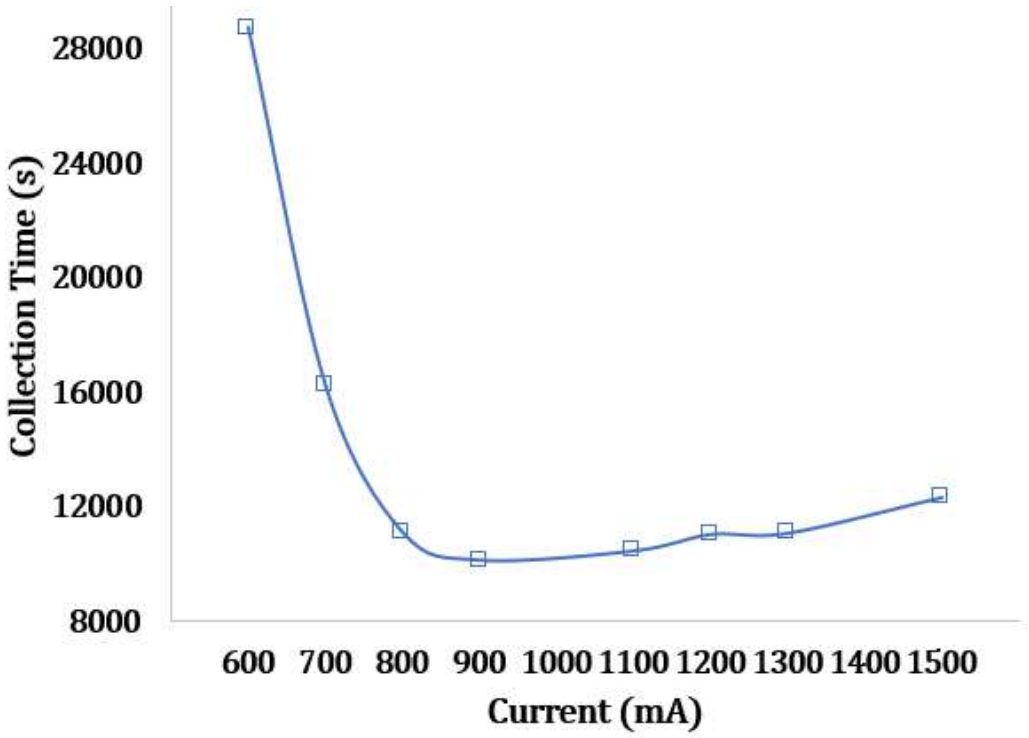

Fig. 3. The collection time as a function of collection current

The collection time was measured as a function of the applied collection current as shown in figure 3. The collection time showed a steep fall for currents from 600 to 900 mA as the outcome of an improvement in kinetics of the electrodeposition process. At higher currents, the collection time slightly increased due to the reduction of the cathodic efficiency. This reduction is in accordance with the results of Figure 2.

Conclusions

In this work, the accumulation current was held constant and the collection/purification currents were independently adjusted. The results showed that even at a fixed accumulation current, the accumulated activity follows an oscillating pattern which is ascribed to the limited supply of the decayed ^{90}Y. It assumes that precise management of the separation interval is needed to achieve a sustainable and reliable production of ^{90}Y. The results also showed that higher currents may lead to higher recoveries and faster separation in spite of reduction of cathodic efficiency. In summary, independent adjustment of the accumulation current on one hand and collection/purification current, on the other hand is recommended.

Acknowledgments

The Pars isotope company's cooperation in presenting this work is gratefully acknowledged.

References

[ss] Therapetic Radionuclide Generators: ^{90}Sr/^{90}Y AND ^{188}W/^{188}Re GENERATORS, (2009) Technical Reports Series No. 427, International Atomic Energy Agency, Vienna, Austria.

[1] Lange, G.; Herrmann, G.; Strassmann, F(1957) Preparation of strontium90-free yttrium-90 by electrolysis [in German]. J. Inorg. Nucl. Chem., 4,146–54.

[2] Hamaguchi, H.; Ikeda, N.; Kawashima, T (1958). Isolation of carrier free yttrium from the radioactive strontium-yttrium system by electrodeposition. Bunseki Kagaku, 7, 243–6.

[3]. Barrio, G., & Osso, J. A. (2007). Development of methodology for the preparation of 90S r-90 Y generators.

[4]. Skraba, W.J.; Arino, H.; Kramer, H.H (1978). A new ^{90}Sr/^{90}Y radioisotope generator. Int. J. Appl. Radiat. Isot., 29, 91-96.

[5] Chinol, M.; Hnatowich, D.J (1987). Generator-produced Yttrium-90 for radioimmunotherapy. J. Nucl. Med., 28, 1465-1470

[6] Malja, S., Schomacker, K., & Malja, E. (2000). Preparation of ^{90}Y by the ^{90}Sr-^{90}Y generator for medical purpose. Journal of Radioanalytical and Nuclear Chemistry, 245(2), 403-406.

[7]. Chakravarty, R., Pandey, U., Manolkar, R. B., Dash, A., Venkatesh, M., & Pillai, M. A. (2008). Development of an electrochemical ^{90}Sr–^{90}Y generator for separation of ^{90}Y suitable for targeted therapy. Nuclear medicine and biology, 35(2), 245-253.

[8]. Dash, A., & Chakravarty, R. (2014). Electrochemical separation: promises, opportunities, and challenges to develop next-generation radionuclide generators to meet clinical demands. Industrial & Engineering Chemistry Research, 53(10), 3766-3777.

[9] Pichestapong, P., Sriwiang, W., & Injarean, U. (2016). Separation of Yttrium-90 from Strontium-90 by extraction chromatography using combined Sr resin and RE resin. Energy Procedia, 89, 366-372.

ICNST 2024
International Conference on Nuclear Science and Technology
6- 8 MAY 2024 | Isfahan, Iran

Preliminary evaluation of Radiotheranostic couple preparation consisting 177Lu/68Ga-3BP in Iran (Paper ID : 1415)

Somayeh Akbari-Karadeh[1], Seyed Mahmoud Reza Aghamiri[1*], Simindokht Shirvani-Arani[2], Parisa Tajer-Mohammad-Ghazvini[2], Ali Bahrami-Samani[2], Seyed Milad Miremad[2], Mohammadreza Davarpanah[3,] Bagher Azizkalantari[3], Mahdi samizadeh[3], Yaser Hossein Tavakoli[3], Afshar Gravand[3], Naser Soltani[3]

[1]*Department of Medical Radiation Engineering, Shahid Beheshti University, Tehran, Iran*
[2]*Nuclear Fuel Cycle Research School, Nuclear Science and Technology Research Institute, Tehran, Iran*
[3]*Pars Isotope Company, Tehran, Iran*

Abstract

In recent years, nuclear medicine has witnessed extensive research on new peptide receptors labeled with diagnostic and therapeutic radiopharmaceuticals. Among these, neurotensin receptors (NTR1) stand out as promising targets in theranostics. These receptors are highly expressed in various malignant cancers, including those affecting the colon and pancreas.The objective of this study is to introduce NTR1 antagonists, specifically 3BP-227, along with its radiolabeled compound. Notably, this marks the first time such a radiotheranostic couple—using ^{177}Lu/^{68}Ga—has been explored in Iran. The synthesized 3BP-227 purity, assessed through Analytical High-Performance Liquid Chromatography (HPLC), exceeded 97%. Radiolabeling of 3BP-227 using ^{177}Lu/^{68}Ga was verified using Instant Thin-Layer Chromatography (ITLC). The radiochemical purity was more than 80% for the ^{177}Lu-3BP-227 formulation and more than 97% for the ^{68}Ga-3BP-227 formulation. Subsequent studies will delve into optimal labeling conditions and preclinical investigations. Should the final results prove positive, 3BP-227 could serve as an ideal targeting moiety.Its extended retention time within tumors makes it a promising candidate for radiotheranostic applications across various cancers, including pancreatic ductal adenocarcinoma, prostate cancer, colorectal cancer, breast cancer, and small cell lung cancer.

Keywords: Neurotensin Receptors, ^{177}Lu/^{68}Ga -3BP-227, Theranostic.

Introduction

Theranostics is an emerging and expanding field that seamlessly integrates treatment and diagnosis. In nuclear medicine, this technique employs radiopharmaceuticals attached to the same molecular target for both imaging and therapy. The goal is to selectively deliver radionuclides to tumor cells at the cellular level while minimizing harm to healthy tissues [1, 2].

The beauty of theranostics lies in its ability to individualize treatment planning for each patient. This personalized approach forms the bedrock of what we call 'personalized nuclear medicine'. By prescribing the appropriate dose of radiopharmaceuticals based on safety and efficacy considerations, we optimize outcomes. In practice, theranostics often involve a diagnostic radioisotope paired with a therapeutic radioisotope. These isotopes typically share similar chemical properties and are used alongside targeted carriers. Consequently, theranostic applications have spurred the development of novel peptides as carriers, combined with diagnostic/therapeutic radioisotope pairs for precise localization within cancer cells [3].

Two noteworthy radionuclides used as theranostic couples are ^{68}Ga and ^{177}Lu. These isotopes exhibit similar chemical behavior. Chelating agents, such as DOTA, enable complexation, allowing a single biologically active molecule to serve both diagnostic and therapeutic purposes[4, 5]. ^{68}Ga has garnered significant attention in molecular imaging studies due to its superior resolution and heightened sensitivity as a PET imaging agent. With a short half-life ($T_{1/2}$ = 67.83 min) and suitable energy ($E\beta^+$ = 1.899 MeV), it decays to ^{68}Zn emitting 88.88% positrons and 11.11% electrons [5].

On the other hand, ^{177}Lu, with a half-life of 6.71 days, undergoes β^- decay to stable ^{177}Hf with a maximum energy of 497 keV[6].

NEUROTENSIN (NTS), a fascinating player, serves as a neuro-transmitter/modulator in the central nervous system. Its physiological and biological functions continue to captivate researchers[7].

3BP-227 is a DOTA-conjugated NTR1 antagonist that has recently been developed. It can be labeled with various therapeutic and diagnostic radionuclides for theranostic purposes. In 2016, Schulz et al. labeled 3BP-227, 3BP-228, and 3BP-483 with ^{111}In. They evaluated and compared these compounds based on their imaging performance and biodistribution profiles in tumor-bearing mice. The study concluded that ^{111}In-3BP-227 exhibits higher accumulation in tumors and lower absorption in normal tissues. The primary objective of this research was to label 3BP-227 using ^{177}Lu and ^{68}Ga for theranostic applications.

EXPERIMENTAL

All the chemicals utilized in this study were prepared by Pars Isotope Company. Specifically: HEPES (4-(2-hydroxyethyl)-1-piperazineethanesulfonic acid) Gentisic acid buffer, Sodium acetate. These chemicals were procured from Merck (Germany). The 3BP-227 used in the

experiment had previously been conjugated with the DOTA chelator by Pars Isotope Company.

To assess the purity of the synthesized peptide, we employed an Analytical High-Performance Liquid Chromatography (HPLC) device. Additionally, radiolabeling of 3BP-227 was carried out using buffers with varying concentrations. Finally, Instant Thin-Layer Chromatography (ITLC) was employed to verify the radiochemical purity.

Labeling of 3BP-227 with ^{68}Ga

^{68}Ga was freshly extracted from the ^{68}Ge/^{68}Ga generator. Throughout the process, we employed HEPES buffer. Specifically, we added an activity amount of 40-50 mCi of ^{68}Ga to 40-50 µL of the 3BP-227-DOTA composition, which was dissolved in 400-500 µL HEPES buffer solution. The mixture was then heated to a temperature of 95°C.

Labeling of 3BP-227 with ^{177}Lu

We procured ^{177}Lu from RIAR JSC (ROSATOM Scientific Division), which has been confirmed as the State Scientific Center according to the relevant Order of the Government of the Russian Federation. The process involved adding an activity amount of 50-60 mCi of ^{177}Lu to 40-50 µL of the 3BP-227-DOTA composition. This composition was dissolved in a solution containing gentisic acid buffer and sodium acetate, after which it was heated to a temperature of 95°C.

Quality control

We conducted quality control assessments using Reverse-Phase Thin-Layer Chromatography (RTLC). Specifically:

For the RTLC method, we used a mobile phase consisting of Ammonium acetate/Methanol (50:50) (1 M) as mobile phase A and sodium citrate 0.1 M with pH=5 as mobile phase B.

We employed ITLC-SG as the stationary phase in the device.

Results and discussion

In the obtained RTLC spectrum:

The ^{68}Ga/3BP-227 radiochemical yield exceeded 97% (Table 1).

The RTLC spectrum from ^{177}Lu/3BP-227 indicated an estimated labeling amount of more than 80% (Table 2).

These results align with a study by Schulz et al., where Instant Thin-Layer Chromatography confirmed high radiochemical purity (≥97%) for ^{111}In-3BP-227[7].

Also, in another study done by Schulz et al., the radiolabeling efficiency of ^{177}Lu-3BP-227 was more than 95%[8].

Table 1.TLC values of ^{68}Ga/3BP-227

	R/F	%Area
Reg #1	0.003	2.88 %
Reg #2	0.043	97.12 %

Table 2.TLC values of ^{177}Lu/3BP-227

	R/F	%Area
Reg #1	0.02	99.54 %
Reg #2	1.149	0.46 %

Conclusions

This study explored the labeling of the novel target 3BP-227 with the radiotheranostic couple ^{177}Lu/^{68}Ga. The HPLC results validate the purity of the synthesized peptide. Moreover, the high yield of the resulting labeled compound suggests that 3BP-227/^{177}Lu/^{68}Ga possesses favorable characteristics as a promising theranostic agent for personalized nuclear medicine. In future phases of this project, we will investigate the stability of the labeled combination and conduct preclinical studies.

*

This manuscript is part of the PhD thesis by S. Akbari-Karadeh.

References

[1] S. Navalkissoor, G. Gnanasegaran, and R. Baum, "Theranostics and precision medicine special feature," ed: The British Institute of Radiology., 2018.

[2] C. Miller, J. Rousseau, C. F. Ramogida, A. Celler, A. Rahmim, and C. F. Uribe, "Implications of physics, chemistry and biology for dosimetry calculations using theranostic pairs," *Theranostics*, vol. 12, no. 1, p. 232, 2022.

[3] S. Banerjee, M. Pillai, and F. Knapp, "Lutetium-177 therapeutic radiopharmaceuticals: linking chemistry, radiochemistry, and practical applications," *Chemical reviews,* vol. 115, no. 8, pp. 2934-2974, 2015.

[4] I. Velikyan, "Prospective of 68Ga-radiopharmaceutical development," *Theranostics,* vol. 4, no. 1, p. 47, 2014.

[5] R. A. Leonte *et al.*, "Preparation and Preliminary Evaluation of Neurotensin Radiolabelled with 68Ga and 177Lu as Potential Theranostic Agent for Colon Cancer," *Pharmaceutics,* vol. 13, no. 4, p. 506, 2021.

[6] M. Pillai, S. Chakraborty, T. Das, M. Venkatesh, and N. Ramamoorthy, "Production logistics of 177Lu for radionuclide therapy," *Applied radiation and isotopes,* vol. 59, no. 2-3, pp. 109-118, 2003.

[7] J. Schulz *et al.*, "Comparative evaluation of the biodistribution profiles of a series of nonpeptidic neurotensin receptor-1 antagonists reveals a promising candidate for theranostic applications," *Journal of Nuclear Medicine,* vol. 57, no. 7, pp. 1120-1123, 2016.

[8] J. Schulz *et al.*, "Proof of therapeutic efficacy of a 177Lu-labeled neurotensin receptor 1 antagonist in a colon carcinoma xenograft model," *Journal of Nuclear Medicine,* vol. 58, no. 6, pp. 936-941, 2017.

ICNST 2024
International Conference on Nuclear Science and Technology
6- 8 MAY 2024 | Isfahan, Iran

Evaluation of the effects of tissue density on the distribution of positron-emitting isotopes for monitoring the proton range in proton therapy (Paper ID : 1416)

Gharib Sh. and Taherparvar P.*

Department of Physics, University of Guilan, Rasht, Guilan, Iran

Abstract

The Bragg peak located at the end of the proton beam range is one of the great advantages of proton therapy compared to common radiation therapy. Because of the high concentration of the deposited dose at the Bragg peak and its position uncertainties, it is very important to predict the proton range accurately in order to ensure that the tumor receives the prescribed dose and that organs at risk are not exposed to radiation. In this paper, the correlation between the proton dose distribution and the spatial distribution of positron-emitting radioisotopes resulting from the interaction of proton beams - with energies of 90, 120, 150, and 180 MeV - with PMMA phantom was investigated by GATE Monte Carlo code. For evaluation of the effects of tissue density on the distribution of positron-emitting isotopes, fat, lung, and bone tissues were placed inside the PMMA phantom and the simulations were re-run. The results showed that for all four proton beam energies, using the spatial distribution of positron emitting radionuclides, the proton range can be estimated with reasonable accuracy. Furthermore, the results showed that the production efficiency of the radioisotopes depends on the density of the passing medium. Then, heterogeneous tissues cause shift in the position of the proton range, which its monitoring can be determined by detecting the radionuclides production along the beam path.

Keywords: Proton therapy, Proton range, Positron-emitting isotope, GATE

INTRODUCTION

The main advantage of proton therapy over conventional radiation therapy with photons is the unique dose distribution of the proton beam; the proton beam dose distribution curve has a low entrance dose and a sharp peak at the end of the proton beam range which is known as Bragg-peak [1]. This physical advantage allows for a precise local dose distribution in the target tumor volume while minimizing the over spill of radiation on the healthy tissue [2]. Uncertainties affecting beam range have created a challenge for medical physicists and radiation oncologists to exploit the finite beam range. The beam-range uncertainty could cause the Bragg peak to overshoot or undershoot the tumor and damage adjacent healthy tissue. Although proton therapy systems can select the energy of the proton beam with high accuracy, various sources

of range uncertainty have been identified, such as inhomogeneities and x-ray computed tomography (CT) artifacts, conversion of Hounsfield units to proton stopping power, anatomical variations (weight change, tumor shrinkage), incorrect patient position, and internal organ motion. All of these sources can create a maximum uncertainty of 10−15 mm [3]. Over the past decades, significant research efforts have been conducted worldwide to develop in-vivo beam range verification methods. Prompt gamma (PG) imaging is one of the beam range monitoring methods. This method is based on detecting high energy gamma rays that are emitted almost immediately from the decay of excited nuclear products [4]. Although this method is very promising for the future, it is currently impractical because of the lack of appropriate systems to detect these gamma rays with high efficiency and spatial resolution in a clinical setting. The currently more practical method is positron emission tomography (PET) imaging [5]. This method is based on detecting of 511 keV coincident photon pairs from the decay of positron-emitting isotopes produced as a result of proton-nuclear interactions [4]. Hereby, in this research, by simulating proton beams with energies of 90, 120, 150, and 180 MeV and their interaction with a homogeneous PMMA cylindrical phantom using the GATE code, the correlation between the proton dose distribution curve and the spatial distribution curve of positron-emitting isotopes was investigated. Then, lung, fat, and bone tissues were placed in the path of the proton beam inside the phantom to investigate the effect of heterogeneous tissue on the proton dose distribution curve and the distribution curve of positron-emitting isotopes.

Material and Methods

In this research, the simulations were performed in two stages using GATE Monte Carlo code as follows:

In the first step, a PMMA homogeneous cylindrical phantom with a density of 1.195 gr/cm3, a diameter of 38 mm, and a height of 290 mm along its central axis (along the Z axis) was simulated (Figure 1). Then, cylindrical proton beams with a diameter of 5 mm and uniform energy distribution with energies of 90, 120, 150, and 180 MeV and moving in the direction of the Z (phantom axis) were defined. The distance between the source and the phantom was 380 mm. In order to calculate the depth dose of the beam in the direction of beam movement and to evaluate the spatial distribution of positron-emitting isotopes, the phantom was divided into

290 parts in the axial direction. The simulations were performed with the QGSP_BIC_HP_EMZ physics list.

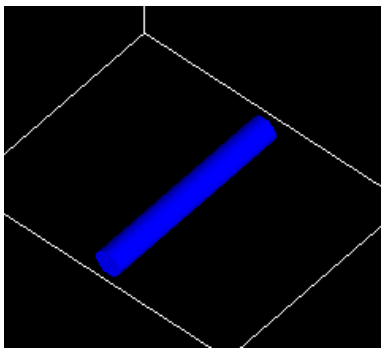

Fig. 1. A view of PMMA phantom.

In the second stage, in order to investigate the effect of heterogeneous tissue on the proton depth dose distribution curve and the spatial distribution curve of positron-emitting isotopes, we placed 2 cm thick cylindrical plates of different lung, fat, and bone tissues with densities of 0.26, 0.95, and 1.85 gr/cm^3 respectively, in the path of the proton beam inside the PMMA phantom. In this configuration, we used a proton beam with an energy of 180 MeV. Two scenarios were considered for the simulations: (1) A single plane of each tissue in the PMMA phantom. (2) All three plates were placed back-to-back in the PMMA phantom to investigate the effect of composite inhomogeneity. Figure 2 shows the simulation setup of the two scenarios considered.

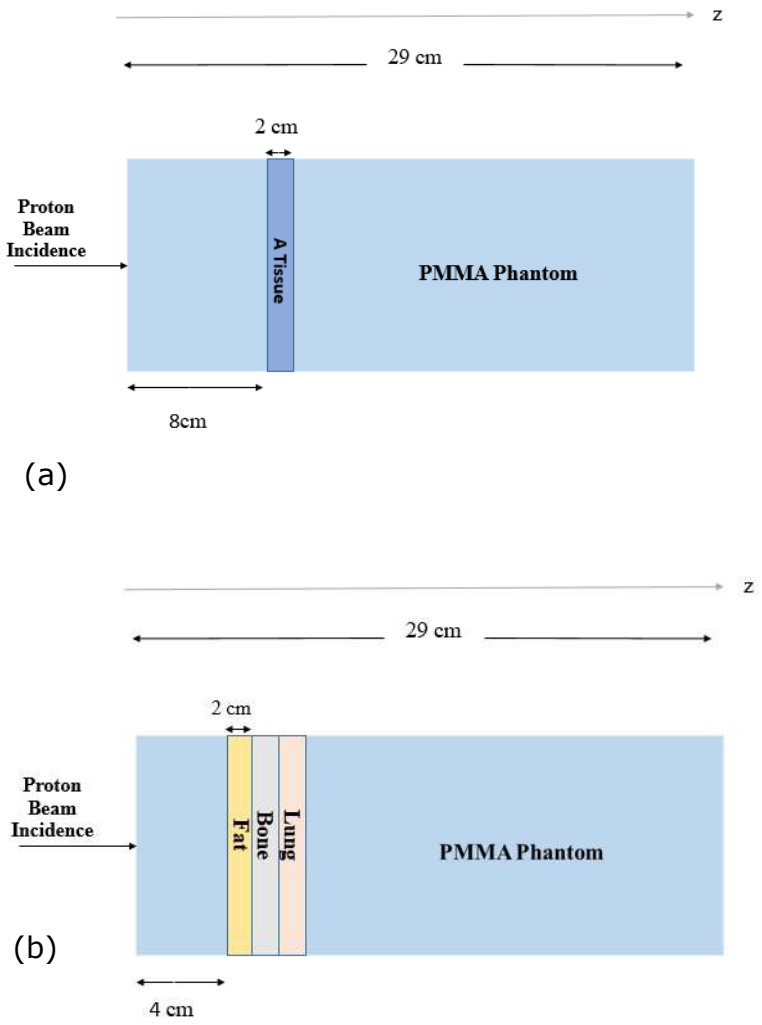

Fig. 2. Geometrical simulation setup of the PMMA Phantom with 2 cm plates of lung, fat, and bone. Two scenarios are considered: a single plate of each tissue is placed in the PMMA phantom in the same position for each tissue (a), and the plates of tissues are placed back-to-back in the PMMA phantom (b).

In post-simulation data analysis, the proton beam range (R) was defined as the point with 80% Bragg peak distal fall-off along the beam path in the phantom. The spatial distribution range

of positron-emitting isotopes (R_{PER}) was defined as the position with 80% efficiency fall-off of positron-emitting isotopes along the beam in the phantom. The difference R-R_{PER}, denoted as Δ fall-off, was used to quantify the correlation between the proton dose distribution curve and the spatial distribution curve of positron-emitting isotopes.

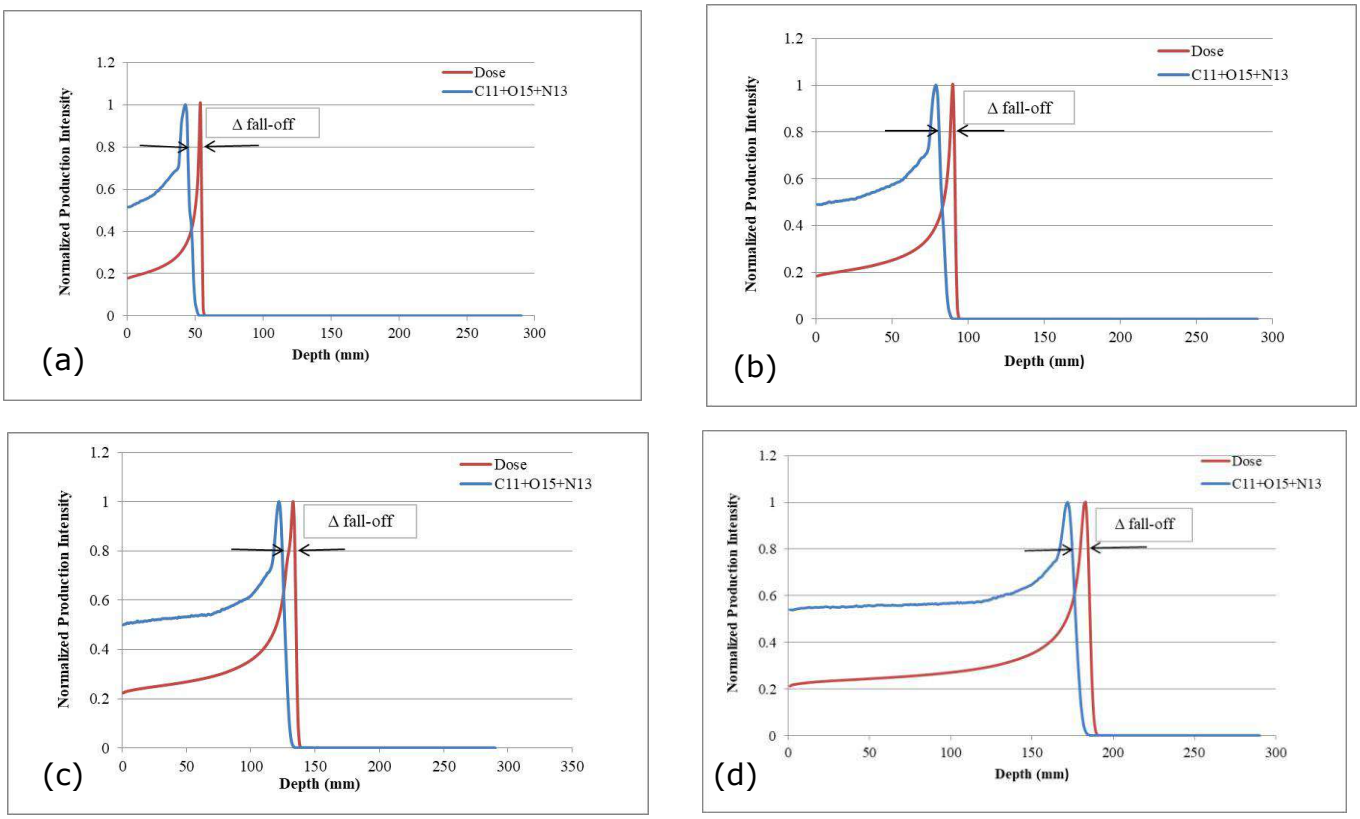

Fig. 3. Spatial distribution curve of positron-emitting isotopes resulting from the interaction of a proton beam with energy 90 MeV (a), 120 MeV (b), 150 MeV (c), and 180 MeV (d) with a PMMA phantom, along with the associated scaled dose distribution curve.

Results

By drawing the dose distribution curves, the proton range was obtained for proton beams with energies of 90, 120, 150, and 180 MeV at distances of 55, 91, 135, and 185 mm from the entrance of the phantom, respectively**.** Then, in order to evaluate the correlation between the spatial distribution of positron-emitting isotopes with proton-beams range, spatial distribution curves related to the production of three abundant positron-emitting isotopes ^{11}C, ^{15}O, and ^{13}N in the PMMA phantom were drawn for proton beams with energies of 90, 120, 150, and 180

MeV (Figure 3-a, b, c, and d respectively). The spatial distribution range of positron-emitting isotopes produced for proton beams with energies of 90, 120, 150, and 180 MeV was measured at 45, 81, 125, and 175 mm from the entrance of the phantom, respectively. Therefore, for all four energies of the proton beams, the quantity Δ fall-off was determined as a constant value of 10 mm.

Dose distribution curves of 180 MeV proton beam in PMMA phantom with single plates of fat, lung, bone, and all three plates back-to-back, with the spatial distribution curve of production of three related positron-emitting isotopes are shown in figures 4-a, b, c, and d, respectively. In the figures, the change in the production efficiency of isotopes in the plate's positions are clearly visible, which shows a close correspondence with the change of the dose deposition in the plate's position. It can be observed that the production efficiency of positron-emitting isotopes, depends on the composition of materials and density of the medium traversed by the proton beam . Results show that the production efficiency increases with the increasing of the tissues density. In order to calculate the amount of Δ fall-off, Table 1 lists the range of 180 MeV proton beam in the PMMA phantom and the range of positron-emitting isotopes with the placement of different tissue plates .

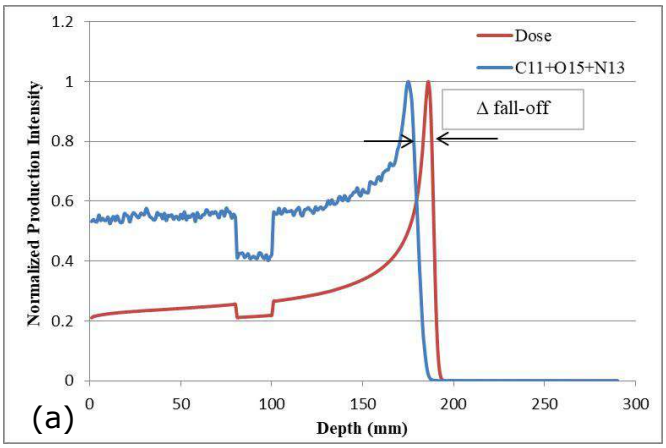

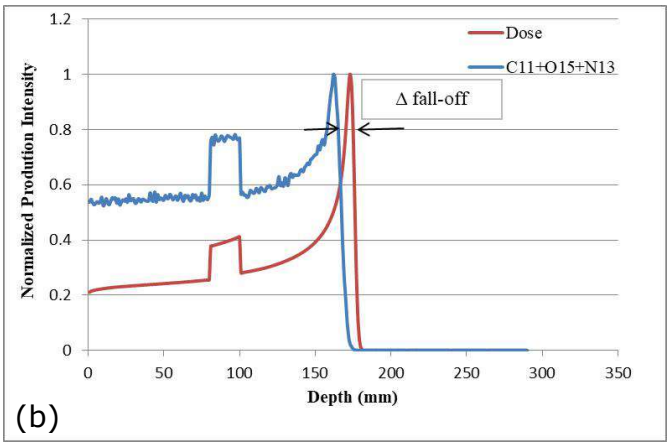

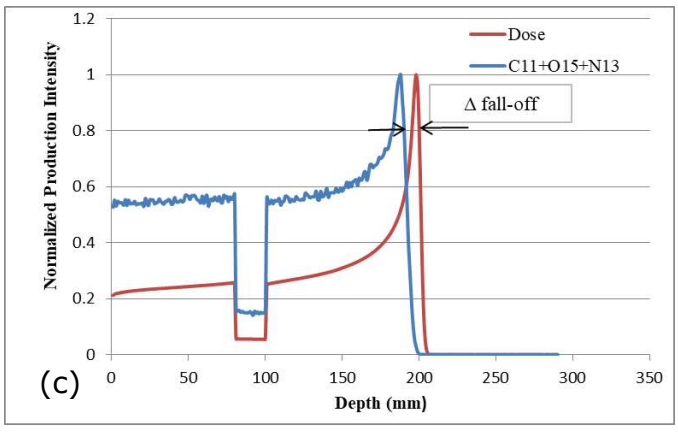

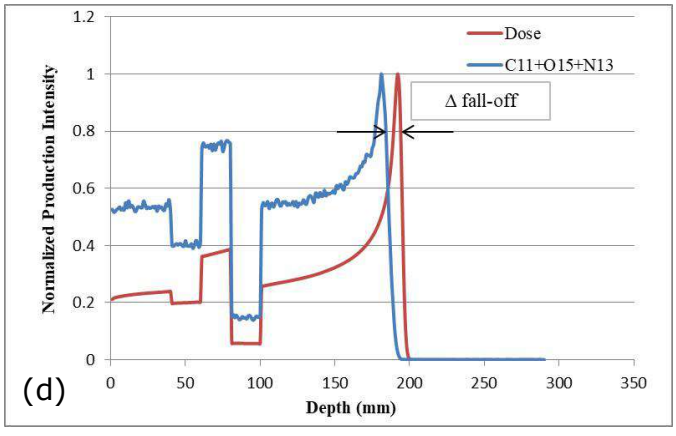

Fig. 4. Spatial distribution curve of positron-emitting isotopes in PMMA phantom with a single plate of fat (a) bone (b) lung (c) and all three plates back-to-back (d) along with scaled dose distribution curve of 180 MeV proton beam.

Table 1. Comparison of R shifts and R_{PER} between the plate-embedded PMMA phantom and the homogeneous PMMA phantom during the 180 MeV proton beam irradiation.

Phantom	R (mm)	R_{PER} (mm)	Shift in Proton Beam Range (mm)	Δ fall-off (mm)
PMMA (homogeneous)	185	175	_	10
Fat plate	188	178	3	10
Bone plate	176	166	-9	10
Lung plate	200	190	15	10
All tissue plates	194	184	9	10

For all cases, the Δ fall-off values was constant and about 10mm. Results were same as the value obtained in the first stage of the simulation, which the homogeneous PMMA phantom was used. As can be observed in Table 1, the heterogeneous plates cause a shift in the position of the proton range, which can be tracked with the same 10 mm accuracy using the spatial distribution of positron-emitting isotopes.

Conclusions

In this paper, in order to monitor the proton range by use of the PET imaging system during proton therapy, the correlation between the spatial distribution of positron-emitting isotopes and the proton dose distribution curve was evaluated by simulating the interaction of proton beams with energies of 90, 120, 150, and 180 MeV with a homogeneous PMMA phantom with GATE Monte Carlo code. The results showed that the spatial distribution curve of positron-emitting isotopes has a good correlation with the proton dose distribution curve. For all four energies of the proton beam, the range of the proton beam can be estimated with an accuracy

of 10 mm using the spatial distribution curve of positron-emitting isotopes. Then, to investigate the effect of heterogeneous tissue on the proton dose distribution curve and the spatial distribution curve of positron-emitting isotopes, heterogeneous plates of lung, fat, and bone tissues were placed inside the PMMA phantom. The results showed that the existence of different heterogeneous tissues leads to the same shift of the proton dose distribution curve and the spatial distribution curve of positron emitting isotopes. In addition to, the results showed that the production efficiency of positron-emitting isotopes depends on the density of the medium traversed by the proton beam, and the production efficiency increases with density.

References

[1]. Dendoowen et al. (2015). Short-lived positron emitters in beam-on PET imaging during proton therapy. Phys. Med. Biol. 60(23): 8923–47.

[2] Melek et al. (2019). Characterization of prompt gamma ray emmision for in vivo range verification in particle therapy: A simulation study.Physica Medica. 62: 20-32.

[3] Smeets, et al. (2012). Prompt gamma imaging with slit camera for real-time range control in proton therapy. Phys. Med. Biol. 57(11): 3371-405.

[4] Zarifi, et al. (2019). Characterization of prompt gamma ray emission for in vivo range verification in particle therapy: A simulation study. Physica Medica. 62: 20-32.

[5] Paganetti, H. and Fakhri, G EI. (2015). Monitoring proton therapy with PET. Br J Radiol. 88(1051): 20150173.

ICNST 2024
International Conference on Nuclear Science and Technology
6- 8 MAY 2024 | Isfahan, Iran

Calculating the effects of alternative materials as microdosimeter wall and their optimal thickness on the neutron microdosimetry spectra (Paper ID : 1417)

Jahanfar S. [1*], Tavakoli-Anbaran H. [2]

[1] *Faculty of Physics and Nuclear Engineering, Shahrood University of Technology, Shahrood, Iran*

Abstract

This study attempts to design and develop microdosimeters with optimal accuracy based on alternative materials for wall microdosimeters in order to make an accurate microdosimeter for Shahrood University of Technology with simple, accessible, and inexpensive alternative materials. All effects on neutron microdosimetric spectra were studied. In this research, using the Geant4-10-4 code we simulated neutrons with energies of 0.1, 1, and 10 MeV for two point and beam sources. In order to compare between different states microdosimetric quantities and distributions included of frequency-mean lineal energy, dose-mean lineal energy, mean quality factor, absorbed dose, and these statistical uncertainties in each case were calculated and reported. Also, we calculated the optimal thickness of the microdosimetric wall. It was observed that for microdosimetric walls, polyethylene, and polypropylene, in addition to tissue-equivalent solids such as A-150 plastic are suitable. Also, it was observed that the thickness of 1.2 to 6 mm of the microdosimetric wall is suitable for neutron microdosimeters up to 10 MeV energy. Therefore, we were able to use another alternative material to make this precise and practical device without changing the microdosimetric spectra. Using the results of alternative materials, the prototype of this microdosimeter built and tested at Shahrood University of Technology.

Keywords: Neutron Microdosimeter; Microdosimetric Spectra; Tissue-Equivalent Material, Optimal thickness, Alternative materials.

INTRODUCTION

Microdosimeters are a tool used to measure the dose in body tissues, and since it is not possible to measure in the tissue and on a human sample, so from tissue-equivalent materials such as A-150 plastic for making walls of microdosimeters are used. Tissue-equivalent materials may be fabricated to simulate a wide variety of tissues and organs [1,2].

The lineal energy y is an important microdosimetric quantity that $y = \frac{\varepsilon_1}{\bar{\iota}}$ obtained from the quotient of $\varepsilon_1$by $\bar{\iota}$. ε_1 is the energy imparted in the target in a single event, and $\bar{\iota}$ is the mean chord length, and unit y is expressed as $keV/\mu m$ [3-10]. In Cauchy's theorem for a convex

object, the mean chord length is 4V/S, where V and S are the volume and surface of the site, respectively. Lineal energy distribution f(y) is the probability density of lineal energy and f(y)dy is the probability of lineal energy being in the event of an interval of $[y, y+dy]$ [1,11] and the dose probability density is $d(y)=\frac{y}{\bar{y}_F}f(y)$, that $\bar{y}_F$ is known as the frequency-mean lineal energy $\bar{y}_F=\int_0^\infty yf(y)dy$ [12-15]. Also, the dose-mean lineal energy defines $\bar{y}_D=\int_0^\infty yd(y)dy$ [16-20], and mean quality factor or $\bar{Q}$ is $\bar{Q}=\frac{1}{D_t}\int D(y)Q(y)dy$, $Q(y)$is a quality factor and D(y) is the distribution of absorbed dose in y, that it implies $D(y)=D_t dy$ [21,22]. The absorbed dose measurement, D_t, by a tissue-equivalent proportional counter (TEPC) is done by measuring the energy imparted in a gas cavity of a TEPC as follows:

$$D_t(Gy)=\frac{d\bar{\varepsilon}}{dm}=\frac{1.602e{-}13}{m_g}\sum_i n_i\varepsilon_i=\frac{1.602e{-}13}{m_g}\frac{2d_t}{3}\sum_i N_i y_i$$

Where $1.602e-13$ is a conversion constant (Gy-g/keV), y_i the average lineal energy of bin "i" and N_i the number of events in that bin, m_g is a mass of the tissue-equivalent gas and d_t is a tissue cavity diameter (μm) simulated by the TEPC [23] which in this study is 2 microns.

Since the for sites with 2 μm dimensions of tissue, the quality factors should be determined using the relationship between the quality factor and LET (L) by approximating $y\approx L$, [24] in the ICRP publication 60 $Q(y)$ defined as follows [25]:

$$Q(L\approx y)=\begin{cases}1 & L<10\frac{keV}{\mu m}\\ 0{,}32L-2{,}2 & 10\frac{keV}{\mu m}\le L\le 100\frac{keV}{\mu m}\\ \frac{300}{\sqrt{L}} & L>100\frac{keV}{\mu m}\end{cases}$$

And the Bragg-Gray relation in microdosimeters is as follows:

$$\Delta E_t=\left(\frac{S}{\rho}\right)_t\rho_t d_t=\left(\frac{S}{\rho}\right)_g\rho_g d_g=\Delta E_g$$

Where ΔE_t , ΔE_g are the average deposited energy from charged particles in body tissue and gas, respectively[1,12].

Microdosimeters are usually proportional counters with spherical or cylindrical cavities that are used with tissue-equivalent walls and tissue-equivalent gas to simulate microscopic tissue [12,26].

The purpose of this research is simulation to make an accurate microdosimeter for the Shahrood University of Technology with simple, accessible, and inexpensive materials. For this purpose, in this study, we considered the alternative materials for the design of a wall of microdosimeters and the optimal design for the two neutron point and beam sources. In the following, it has been observed which other compounds and under what conditions can be used to make these microdosimeters.

MATERIALS AND METHODS

The aim is to optimize the microdosimeter design with alternative materials and with appropriate accuracy. We considered a microdosimeter with a 2-micron site of A-150 tissue-equivalent plastic with a thickness of 5 mm. The microdosimetric cavity is a right cylinder of 2.5 cm, which is filled with propane based tissue equivalent gas with a density of 0.00008 g/cm^3.

In this research, we examined in addition to this substance what other alternative materials can be used. Therefore, considering the composition of A-150 tissue-equivalent plastic and the abundance of hydrogen and carbon in it, the initial assumption was that polyethylene and polypropylene compounds are similar to this plastic and can be used in microdosimetric walls. Using the Geant4-10-4 code [27], we wrote a program and calculated the microdosimetric spectra for this microdosimeter for the two neutron point and beam sources at three energies of 0.1, 1, and 10 MeV for these materials.

It is also worth noting that we should keep in mind that the thickness of the microdosimetric wall should be in accordance with the microdosimetric relation and the Bragg-Gray cavity in such a way that the balance of the charged particles should be preserved. In microdosimeters, the thickness of the microdosimetric wall is calculated based on the range of the largest charged particles in that material. Given that this particle is a proton particle, we consider the proton range of the 10-MeV in A-150 tissue-equivalent plastic. Also, by using the Geant4-10-4 code, we obtained the optimal thickness of the microdosimetric wall.

In order to compare between different states, frequency-mean lineal energy, dose-mean lineal energy, mean quality factor, absorbed dose, and these statistical uncertainties in each case were calculated and reported. Therefore, in the following, the optimization of the above cases along with the results are expressed in exact detail.

Results and discussion

Figures 1 to 3 compared microdosimetric spectra between alternative materials, such as polyethylene and polypropylene, and A-150 tissue-equivalent plastic for neutron point and beam sources at three energies of 0.1, 1, and 10 MeV using Geant4 code.

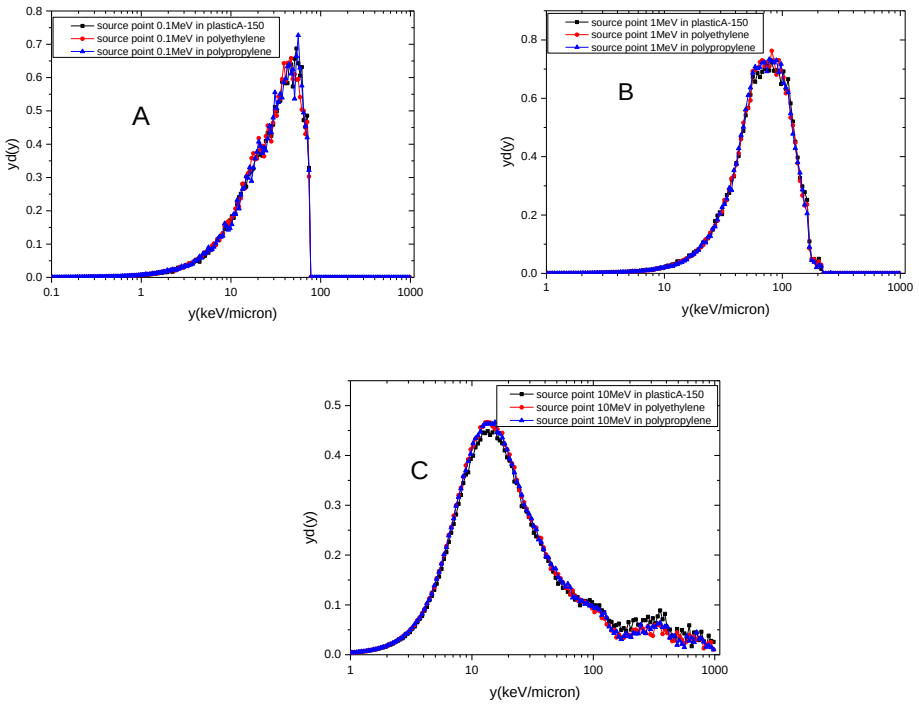

Fig. 1. Microdosimetric spectra of neutron sources for wall with three different materials in A-150 tissue-equivalent plastic (black curve) and polyethylene (red curve) and polypropylene (blue curve) for the beam source a) at 0.1 b) 1 and c) 10 MeV energies.

In order to compare between different states of this section, frequency-mean lineal energy, dose-mean lineal energy, mean quality factor, absorbed dose, and these statistical uncertainties in each case were calculated and reported in Table 1. Figure 1 and this table show that polyethylene and polypropylene can be good alternatives to A-150 tissue-equivalent plastic. Only at an energy of 10 MeV, the dose-mean lineal energy in A-150 tissue-equivalent plastic, polyethylene, and polypropylene is slightly different. Also, Figure 2 it can be seen that microdosimetric spectra differ in two states of neutron beam and point sources. In the neutron beam sources, since the neutron rays radiate perpendicular to the microdosimetric wall, the probability of interaction in particular lineal energy (y[$keV/\mu m$]) increases, and therefore the intensity or amount of yd(y) in this lineal energy increases compared to the point source, cause the microdosimetric spectrum more concentrated in this state. But in the case of a point source,

given that the rays are radiated at all angles, there is a microdosimetric spectrum in the range of more lineal energies.

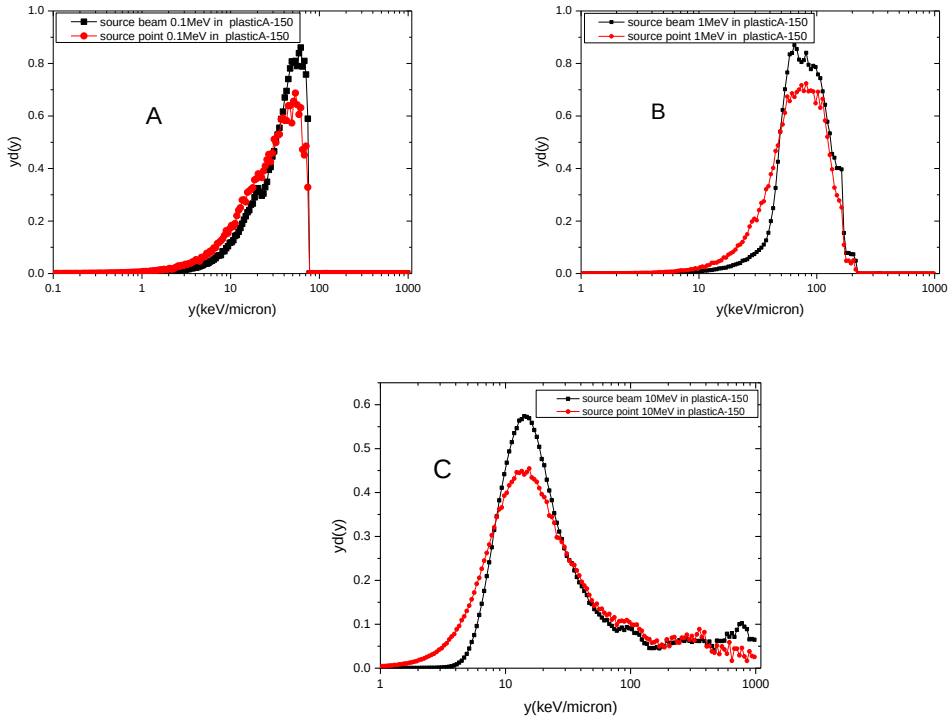

Fig. 2. Comparison of microdosimetric spectra for neutron beam source (black curve) and point source (red curve) in A-150 tissue-equivalent plastic at the energy of a) 0.1 b)1, and c)10 MeV.

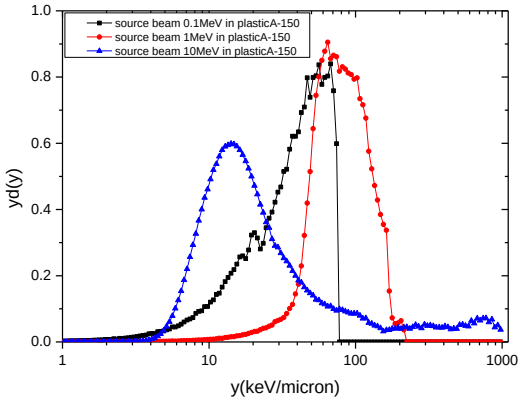

Fig. 3. Comparison of microdosimetric spectra of neutron beam in A-150 tissue-equivalent plastic at 0.1 MeV energy, black curve, and 1 MeV energy, red curve, and 10 MeV energy, blue curve.

Figure 3 also shows the microdosimetric spectra of neutrons in A-150 tissue-equivalent plastic at three different energies of the neutron beam**.**

Table 1. Compare between frequency-mean lineal energy, dose-mean lineal energy, mean quality factor, absorbed dose, and these statistical uncertainties in alternative materials as microdosimeter wall.

	A-150		Polyethylene		Polypropylene	
Beam /Point source and energy[MeV]	$\bar{y}_f\left[\frac{keV}{\mu m}\right]$	$\frac{\sigma_{\bar{y}_f}}{\bar{y}_f}$	$\bar{y}_f\left[\frac{keV}{\mu m}\right]$	$\frac{\sigma_{\bar{y}_f}}{\bar{y}_f}$	$\bar{y}_f\left[\frac{keV}{\mu m}\right]$	$\frac{\sigma_{\bar{y}_f}}{\bar{y}_f}$
beam .1	21.4501	0.0031	20.7737	0.0032	21.0243	0.0031
beam 1	64.1335	0.0016	65.3817	0.0014	65.3453	0.0014
beam 10	16.2675	0.0019	16.1438	0.0015	16.1629	0.0015
point .1	13.4833	0.0064	12.7439	0.0065	13.0439	0.0065
point 1	48.8211	0.0033	49.3475	0.0030	49.3383	0.0029
point 10	11.0400	0.0028	11.399·	0.0022	11.4941	0.0022
Beam /Point source and energy[MeV]	$\bar{y}_d\left[\frac{keV}{\mu m}\right]$	$\frac{\sigma_{\bar{y}_d}}{\bar{y}_d}$	$\bar{y}_d\left[\frac{keV}{\mu m}\right]$	$\frac{\sigma_{\bar{y}_d}}{\bar{y}_d}$	$\bar{y}_d\left[\frac{keV}{\mu m}\right]$	$\frac{\sigma_{\bar{y}_d}}{\bar{y}_d}$
beam .1	39.1934	0.0023	38.9154	0.0023	39.0241	0.0023
beam 1	84.7139	0.0017	84.5540	0.0015	84.3949	0.0015
beam 10	81.4196	0.0127	67.0359	0.0122	66.5477	0.0121
point .1	33.1057	0.0053	32.4679	0.0054	32.9519	0.0053
point 1	75.1232	0.0032	74.5152	0.0029	74.2383	0.0029
point 10	61.8263	0.0196	51.5584	0.0184	51.7242	0.0180
Beam /Point source and energy[MeV]	$\bar{Q}$	$\frac{\sigma_{\bar{Q}}}{\bar{Q}}$	$\bar{Q}$	$\frac{\sigma_{\bar{Q}}}{\bar{Q}}$	$\bar{Q}$	$\frac{\sigma_{\bar{Q}}}{\bar{Q}}$
beam .1	10.4195	0.0027	10.3344	0.0028	10.3685	0.0028
beam 1	20.9979	0.0009	21.1667	0.0005	21.1425	0.0008
beam 10	6.9420	0.0026	6.5502	0.0023	6.5619	0.0023
point .1	8.5588	0.0064	8.3629	0.0066	8.5154	0.0065
point 1	18.9326	0.0021	18.9284	0.0019	18.9128	0.0019
point 10	7.0416	0.0043	6.5526	0.0039	6.6174	0.0039
Beam /Point source and energy[MeV]	$D_t[Gy]$	$\frac{\sigma_{D_t}}{D_t}$	$D_t[Gy]$	$\frac{\sigma_{D_t}}{D_t}$	$D_t[Gy]$	$\frac{\sigma_{D_t}}{D_t}$
beam .1	2.6375	0.0045	2.5379	0.0047	2.5896	0.0046
beam 1	10.7514	0.0033	13.0309	0.0030	13.1016	0.0030
beam 10	25.9134	0.0021	32.1889	0.0017	32.2309	0.0017
point .1	1.3457	0.0083	1.3249	0.0167	1.3174	0.0084
point 1	6.7751	0.0056	8.1486	0.0051	8.2188	0.0051
point 10	18.6782	0.0031	23.0654	0.0025	23.1598	0.0025

In order to investigate the equilibrium and optimal thickness of the microdosimetric wall, the microdosimetric spectra were simulated in different thicknesses such as 0.5, 0.85, 1.2, 2, 4, 5, and 6 mm from polyethylene for the same number of particles using the Geant code at 10 MeV neutron beam source; the results are plotted in Figure 4 and compared together. Also,

frequency-mean lineal energy, dose-mean lineal energy, mean quality factor, absorbed dose, and these statistical uncertainties in each case were calculated and reported in Table 2.

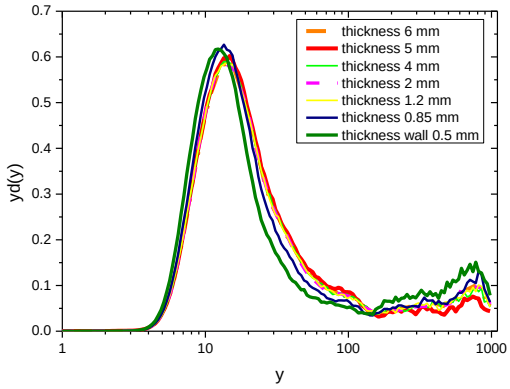

Fig. 4. The effect of different wall thicknesses in the microdosimetric spectra.

Table 2. Frequency-mean lineal energy, dose-mean lineal energy, mean quality factor, absorbed dose, and these statistical uncertainties in each case in different thicknesses as microdosimeter wall.

Thickness wall [mm]	$\bar{y}_f\left[\frac{keV}{\mu m}\right]$	$\frac{\sigma_{\bar{y}_f}}{\bar{y}_f}$	$\bar{y}_d\left[\frac{keV}{\mu m}\right]$	$\frac{\sigma_{\bar{y}_d}}{\bar{y}_d}$
0.50	15.5752	0.0024	104.2120	0.0126
0.85	16.1306	0.0018	86.7713	0.0120
1.20	16.7746	0.0016	80.3201	0.0115
2.00	16.7161	0.0017	80.8329	0.0116
4.00	16.5450	0.0016	78.1301	0.0116
6.00	16.3980	0.0017	79.7708	0.0116
Thickness wall [mm]	D_t[Gy]	$\frac{\sigma_{D_t}}{D_t}$	$\bar{Q}$	$\frac{\sigma_{\bar{Q}}}{\bar{Q}}$
0.50	22.6041	0.0026	6.2210	0.0033
0.85	30.2230	0.0020	6.2441	0.0026
1.20	33.4536	0.0018	6.6246	0.0023
2.00	33.3513	0.0019	6.6111	0.0023
4.00	32.9903	0.0018	6.6408	0.0023
6.00	32.5629	0.0019	6.6572	0.0023

According to Figure 4 and Table 2, since the thickness of the microdosimetric wall should be in accordance with the microdosimetric relation and the Bragg-Gray cavity, and the balance of the charged particles should be preserved, the microdosimetric wall with thicknesses of 1.2 mm to 6 mm is suitable for neutrons with 10 MeV energy. If the thickness is less than this optimal value, the charged particle balance will not be established, and if the thickness is much higher than this value, the amount of output flux is less. Therefore, the counting rate of the microdosimeter decreases so that the microdosimeter should be exposed to radiation for more

time. So, placing much higher thicknesses is not recommended. In order to investigate this effect, the microdosimetric spectra were calculated in several cases for the same number of particles using the Geant code.

Conclusions

For the calculation of the accurate doses of cells and tissues in the body, the use of microdosimetry is essential. The purpose of this study is to design an optimal microdosimeter with alternative materials. Therefore, various studies have been performed on alternative materials for two neutron point and beam sources with three energies of 0.1, 1, and 10 MeV. It was observed that polyethylene and polypropylene are suitable alternatives instead of A-150 tissue-equivalent plastic for the making of microdosimetric walls. We also calculated the optimal thickness of the microdosimetric wall. It was observed that the thickness of 1.2 to 6 mm of the microdosimetric wall is suitable for neutron microdosimeters up to 10 MeV energy. It should be noted that using the results of these simulations, a prototype of this microdosimeter built and tested at Shahrood University of Technology.

References

[1] Rossi, H. H. and Zaider, M. (2011). Microdosimetry and Its Applications, Springer.

[2] Jahanfar, S. and Tavakoli-Anbaran H. (2019). Extracting fairly accurate proton range formulas for use in microdosimetry, Revista Mexicana de F´ısica 65 (5) 566–572.

[3] Rosenfeld, A. B., Bradley, P. D., Cornelius, I., Kaplan, G. I., Allen, B. J., Flanz, J. B. et.al. (2000). A new silicon detector for microdosimetry applications in proton therapy, IEEE Transactions on Nuclear Science volume 47 issue 4.

[4] Lindborg, L.and Waker, A. (2017). Microdosimetry Experimental Methods anApplications CRC Press, Taylor & Francis Group.

[5] Northum, J. D., Guetersloh, S. B. and Braby, L. A. (2012). FLUKA Capabilities for Microdosimetric Analysis, radiation research 177, 117–123.

[6] Cornelius, I., Rosenfeld, A.and Bradley, P. (2002). Simulations of silicon microdosimetry measurements in fast neutron therapy, Australasian Physical & Engineering Sciences in Medicine Volume 25 Number 4.

[7] Reniers, B., Vynckier, S.and Verhaegen, F. (2004). Theoretical analysis of microdosimetric spectra and cluster formation for 103Pd and 125I photon emitters, Phys. Med. Biol. 49.

[8] Tsuda, S., Sato, T., Takahashi, F., Satoh D., Endo, A., Sasaki, S., Namito, Y., Iwase, H., Ban, S.and Takada, M. (2010). Measurement of microdosimetric spectra with a wall-less tissue-equivalent proportional counter for a 290 MeV/u 12C beam, Phys. Med. Biol. 55.

[9] Guardiola, C., Bachiller-Perea, D., M. Mate Kole, E, Fleta, C., David Quirion, De Marzi, L., Gómez, F. (2023). First experimental measurements of 2D microdosimetry maps in proton therapy, Med Phys. 50: 570–581.

[10] M DeCunha, J., Newpower, M. and Mohan, R., (2023). GPU-accelerated calculation of proton

microdosimetric spectra as a function of target size, proton energy, and bounding volume size, Phys. Med. Biol. 68, 165012.

[11] Bolst, D., Guatelli, S., Tran, L. T., Chartier, L., Lerch, M. L., Matsufuji, N. and Rosenfeld, A. B. (2017). Correction factors to convert microdosimetry measurements in silicon to tissue in 12C ion therapy, Phys. Med. Biol. 62.

[12] ICRU. Microdosimetry, report 36, International commission on radiation units and measurements, Bethesda-Maryland, USA (1983).

[13] Rosenfeld Anatoly, B. (2016). Novel detectors for silicon based microdosimetry, their concepts and applications, Nuclear instruments and methods in physics research A 809.

[14] Kliauga, Paul j. and Rossi, H. H. (1982). Studies with encapsulated sources of 125I III. Microdosimetry using a non-metallic wall-less proportional counter, International Journal of Radiation Oncology *Biology *Physics volume 8 issue 1.

[15] Burigo, L., Pshenichnov, I., Mishustin, I. and Bleicher, M. (2013). Microdosimetry of radiation field from a therapeutic 12C beam in water: A study with Geant4 toolkit, Nuclear Instruments and Methods in Physics Research Section B: Beam Interactions with Materials and Atoms, vol 310.

[16] Arghya Chattaraj, Palani Selvam, T.and Datta, D. (2018) investigation of applicability of pure propane gas for microdosimetry at neutron fields: A monte carlo study, Radiation Protection Dosimetry, pp. 1–13.

[17] Pan, C.Y., Huang, Y.W., Cheng, K.H., Chao, T.C. and Tung, C.J. (2015). Microdosimetry spectra and relative biological effectiveness of 15 and 30 MeV proton beams, Applied Radiation and Isotopes 97, 101–105.

[18] Chattaraj, A., and Palani Selvam, T. (2023). Microdosimetry-based investigation of biological effectiveness of 252Cf brachytherapy source: TOPAS Monte Carlo study, Physics

in Medicine & Biology 68, 225005.

[19] Papadopoulos, A., Kyriakou, I., Matsuya, Y., Incerti, S., Daglis, Ioannis A. and Emfietzoglou, D, (2022). Microdosimetry Study of Proton Quality Factor Using Analytic Model Calculations, Appl. Sci. 12, 8950.

[20] Braby, L. a., Conte, V., Dingfelder, M., Goodhead, d. T., Pinsky, L. S., Rosenfeld, B., Sato, T., Waker, a. J., Guatelli, S., Magrin, G., Menzel, h.-G., Brandan, M.-E., and Olko, P. (2023). CRU REPORT 98, STOChaSTIC NaTURE Of RadIaTION INTERaCTIONS: MICROdOSIMETRy, International Commission on Radiation Units & Measurements.

[21] The Quality Factor in Radiation Protection (Report 40), International Commission on Radiation Units and Measurements, 4 April (1986).

[22] Kellerer, A. M. and Hahn, A. (1988). Considerations on a Revision of the Quality Factor, Radiation Research 114, 480-488.

[23] Si-Young Chang and Bong-Hwan Kim (2008). Understanding of the Microdosimetric Quantities Obtained by a TEPC, Journal of nuclear science and technology, Supplement 5, p. 213–216.

[24] Moslehi, A., Raisali, G.and Lamehi, M. (2016). Simulation and experimental study of an indigenously designed and constructed THGEM-based microdosimeter for dose-equivalent measurement, Radiation Measurements 86, 56e62.

[25] ICRP 60, Annals of the ICRP, Published on behalf of the lnternational Commission on Radiological Protection, (1990).

[26] Waker, A. J. (1995). principles of experimental microdosimetry, radiation protection dosimetry, Vol 61 No 4, 297-308.

[27] Geant4 a simulation toolkit, Book for Application Developers Release 10.4, Geant4 Collaboration, Rev1.0: Dec 8th, (2017).

Advances in gamma spectroscopy: mapping NaI(Tl) spectra to HPGe spectra using multi-output regressor-chain structure based on SVR (Paper ID : 1420)

Saeidi Z.[1], Afarideh H. [1*], Ghergherehchi M.[2]

[1]*Department of Physics and Energy Engineering, Amirkabir University of Technology, Tehran, Iran*

[2]*Department of Electrical and Computer Engineering, Sungkyunkwan University, Suwon, Republic of Korea*

Abstract

This paper proposes a novel approach for generating high-resolution energy spectra using cost-effective Sodium iodide Thallium activated (NaI(Tl)) detectors. It employ a multi-output regression chain structure based on support vector regression (SVR) to map NaI(Tl) spectra to their corresponding HPGe spectra. The suggested framework utilizes a regression chain strategy to enhance regression models that lack support for multi-output regression. This involves initially employing one regressor for each energy channel of the HPGe spectrum. Subsequently, multiple regressors are integrated to forecast all energy channels of HPGe spectrum. Each regressor in the chain receives the entire NaI spectrum as input. Then, for each subsequent regressor, input is further augmented by concatenating the outputs of all preceding regressors in the chain. Despite being trained on a limited radioisotope library, the model exhibits exceptional performance across diverse measured test spectra containing multiple radioisotopes. Among the various kernel functions employed (linear, radial basis function (RBF), and polynomial), the RBF and polynomial kernels yielded superior performance compared to the linear kernel. By enabling HPGe spectrum prediction using NaI(Tl) detectors, this study highlights a significant advancement in radiation detection capabilities, addressing cost and operational considerations.

Keywords: multi-output regression, NaI detector, HPGe detector, gamma spectrscopy, support vector regression, radioisotope

INTRODUCTION

Gamma-ray spectroscopy, a cornerstone technique in diverse scientific fields like nuclear physics, environmental monitoring, and material characterization, finds wide application in environmental radiation monitoring, radioactive mineral exploration, radiation therapy, and food safety inspection [1-5]. It entails analyzing the energy distribution of gamma rays emitted

by atomic nuclei, offering valuable insights into their composition and structure [6]. HPGe detectors have excellent energy resolution, which means that they can distinguish between gamma rays with very similar energies. But, their high cost, complex manufacturing process, and need for cryogenic cooling at -196°C (77 K) limit their widespread application [6]. Sodium iodide Thallium activated (NaI(Tl)) detectors are prevalent due to their high efficiency and cost-effectiveness; however, their energy resolution falls short compared to high-purity germanium (HPGe) detectors [6-8]. This limitation impedes the precise identification and quantification of closely spaced gamma-ray peaks, particularly in complex spectra due to energy peak overlapping.

Several methods address the challenge of energy peak overlap in NaI detector gamma spectra, including deconvolution, curve fitting, and wavelet transformation (e.g., [9-11]). Deconvolution of low-resolution detector spectra, such as those obtained from NaI(Tl) detectors, has long been a significant challenge in gamma spectrometry and various security applications. These approaches often involve complex algorithms with numerous parameters requiring individual optimization for each specific application. Recently, fully connected neural networks (FCNNs) have emerged as a promising alternative due to their relatively simpler computational structures, faster response times, and higher flexibility. FCNNs enable the conversion of spectra acquired with inexpensive and user-friendly NaI detectors into the high-resolution counterparts typically obtained from HPGe detectors [12]. This method eliminates the need for HPGe detectors while transforming spectrum decomposition into a parameter-free, multi-output regression task.

FCNN model proposed by Saeidi et al. [12] demonstrated the capability of AI models in recognizing and transforming gamma-ray spectrum patterns from various detectors. However, these constructed spectra exhibit additional peaks. Training such models necessitates the creation of datasets encompassing multiple radioisotope spectra with varying contributions. This study presents a novel model designed to enhance the predicted HPGe spectrum of multiple radioisotopes solely utilizing their individual spectra. Considering the multi-output regression nature of NaI to HPGe spectrum mapping, a multi-output chain regression architecture is implemented, leveraging the support vector regression machine learning algorithm [13] and employing the problem transformation method [14].

RESEARCH THEORIES

Multi-output regression

Multi-output regression is a technique employed to predict two or more continuous numerical outcomes simultaneously based on a single input instance. One common strategy to achieve this simultaneous prediction is by decomposing the multi-output regression problem into multiple single-output regression problems [14]. A method for implementing this decomposition is the Ensemble of regressor chains [15]. This model leverages multiple single-output regressors in a sequential manner. Each subsequent regressor's prediction is dependent upon the outputs of the preceding regressors. The framework of the chained regression model for training and testing is illustrated in Figure 1. Training process utilizes n regressors as follows:

_ The first regressor get [x_train] as the input, and t_1 as target, resulting in y_1 as the output and built regressor 1.
_ The second regressor get [x_train, y1] as the input, and t_2 as target, resulting in y_2 as the output and built regressor 2.
⋮
_The n_{th} regressor get [x_train, y_1, y_2, ..., y_{n-1}] as the input, and t_n as target, Resulting in y_n as the output and built regressor n.

In the context of gamma spectroscopy, $x_{\_train}$ signifies the complete NaI spectrum. Each energy channel within the HPGe spectrum is denoted by t_i, with t_1 representing the first channel. Notably, t_1 serves as the target variable for the initial regressor. This pattern systematically extends to all subsequent energy channels (t_2, t_3, ..., t_n) of the HPGe spectrum, where each channel acts as the target variable for a corresponding regressor. Consequently, an HPGe spectrum containing n energy channels, mathematically represented as [t_1, t_2,..., t_{n-1}, t_n], undergoes training using a set of n regressors. As a result, the final model output, corresponding to the predicted HPGe spectrum, is constructed as [y_1, y_2, ..., y_{n-1}, y_n]. During the testing phase, when the model encounters a new, unseen instance ($x_{\_test}$), the n regressors developed during training are utilized to forecast the output, yielding [$\overline{y_1}$ $\overline{y_2}$ ⋯ $\overline{y_n}$].

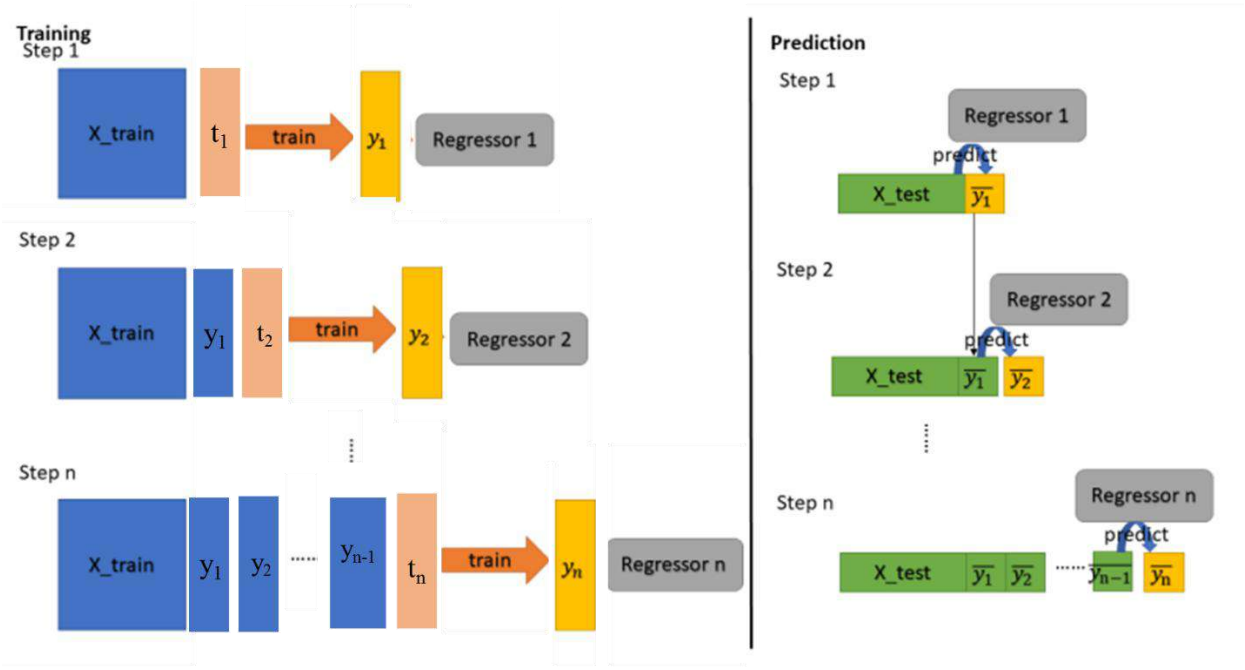

Fig. 1. regression chain Framework for training and testing steps.

EXPERIMENTAL

Experimental Setup

A gamma-ray spectroscopy system, consisting of a detector, high voltage power supply, pulse shaping amplifier, and multi-channel analyzer, was used for data acquisition. Two experimental setups were employed, utilizing ORTEC HPGe (model GEM-40190) and NaI(Tl) (Amcrys 10 S 10/3. VD(p), PA) detectors. To optimize detectors performance and achieve the minimum FWHM, amplifier settings like shaping time, coarse gain, fine gain, and pole-zero cancellation were carefully adjusted. Furthermore, the positioning of the sources in front of the detectors was determined in such a manner that the count rate exceeded 1000 counts per second, and the dead time for measuring all samples was kept below 1% (5 seconds). Also, acquisition time ensured the statistical error remained below 1.0%. Notably, HPGe detector exhibited a superior FWHM of 2.3 keV compared to 74 keV obtained with a NaI(Tl) detector for the 1332 KeV gamma-ray peak of ^{60}Co. (see Ref. [12] for details).

Dataset creation

To train the model, a dataset encompassing spectra from both NaI(Tl) and HPGe detectors was necessary. This involved measuring the individual spectra of ^{60}Co (1.035 $\pm$ 0.02 µCi as of 18

Jan 2012), ^{22}Na (0.795 ± 0.02 µCi as of 18 Jan 2012), ^{152}Eu (1.005 ± 0.03 µCi as of 20 Apr 2013), ^{137}Cs (1.115 ± 0.02 µCi as of 18 Jan 2012), and ^{133}Ba (1.15 ± 0.02 µCi as of 18 Jan 2012), along with spectra from various combinations of these radioisotopes, using both detectors. The background spectrum was also measured and subsequently subtracted from all spectra within the dataset. To prepare the data for model input, the spectra were first normalized to the integral. Subsequently, the single radioisotope spectra (including 5 samples) were employed to train the model, while the multiple radioisotope spectra (including 26 samples) were utilized to evaluate model performance.

Results and discussion

This study evaluated the performance of the regression chain model using the experimental test dataset, which comprised gamma-ray spectra acquired from various combinations of radioisotopes measured by Sodium Iodide detector. Figure 2 exemplifies the input spectra and corresponding model outputs, employing various kernel functions, including linear, RBF, and polynomial for several samples within the dataset. Also, the equivalent spectra obtained through measurements with the HPGe detector illustrated for comparing with resulting output. These samples contained the following radioisotopes: (a) Barium-133 and Cesium-137 (b) Cobalt-60 and Sodium-22, (c) Barium-133, Cesium-137 and Cobalt-60, (d) Europium-152, Cobalt-60, Sodium-22, (e) Barium-133, Cesium-137, Cobalt-60, and Sodium-22, (f) Barium-133, Europium-152, Cesium-137, Cobalt-60, and Sodium-22.

The gamma spectrum of Barium-133 exhibits characteristic energy peaks at 80.9979, 276.3989, 302.8508, 356.0129, and 383.8485 keV, each with a significant branching ratio. While the NaI detector struggles to resolve these peaks due to limitations in its energy resolution, the HPGe detector readily distinguishes them. The proposed models, utilizing Radial Basis Function (RBF) and polynomial kernels, effectively learned the transformation between the Barium-133 spectra acquired with both detectors, even when combined with other radioisotopes, as demonstrated in Figures 2a, 2c, and 2f.

Figure 2b exemplifies the models' performance for the combined spectrum of Cobalt-60 and Sodium-22. The Cobalt-60 spectrum exhibits characteristic energy peaks at 1173 keV and 1332.5 keV, whereas Sodium-22 energy peaks at 511 keV and 1274 keV. In the combined NaI spectrum, the second peak of Sodium-22 significantly overlaps with the Cobalt-60 peaks, rendering it indistinguishable. Remarkably, the proposed model, despite never encountering

this combined state previously, successfully disentangled these overlapping peaks in the simulated HPGe spectrum, generating a result closely resembling the genuine HPGe spectrum.

Europium-152 has many energy peaks that significantly overlap with those of Barium-133 at lower energies and with Cobalt-60 and Sodium-22 at higher energies. Figure 2d shows the combination of Europium-152 with Cobalt-60 and Sodium-22, and Figure 2f shows their combination with Barium-133. The complexity of the NaI spectra in these combinations is evident, yet the RBF and polynomial models demonstrate their capability in generating HPGe spectra with well-resolved, distinct energy peaks.

As illustrated in Figures 2a-f, the proposed SVR-based regression chain model did not perform acceptably for any of the samples with the linear kernel function. The RBF and polynomial kernel functions showed almost identical and excellent performance for constructing the desired HPGe spectrum. It successfully transforms the input NaI spectra into the desired HPGe spectra, even for complex combinations of radioisotopes. Notably, the model accomplishes this feat using only the spectra of single radioisotopes, demonstrating significantly greater performance compared to previous methods requiring substantially larger datasets (e.g., over 3000 samples for FCNN). Furthermore, the proposed model exhibits a reduction in extra positive peaks and reversed peaks compared to the FCNN model.

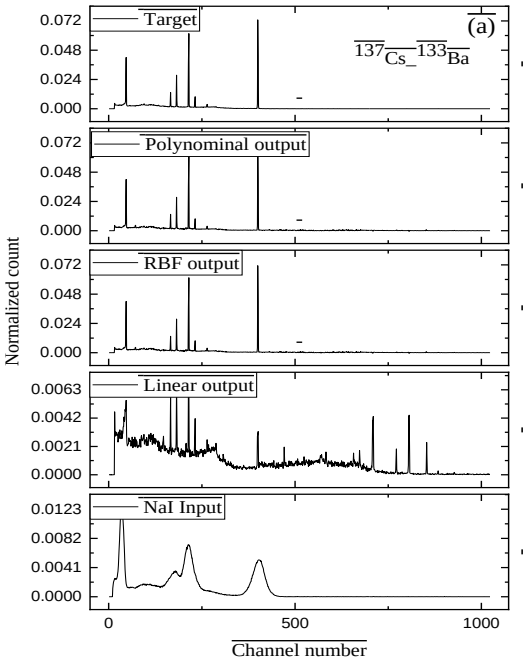
Target
(a)
137Cs_133Ba
Polynominal output
RBF output
Linear output
NaI Input
Normalized count
Channel number

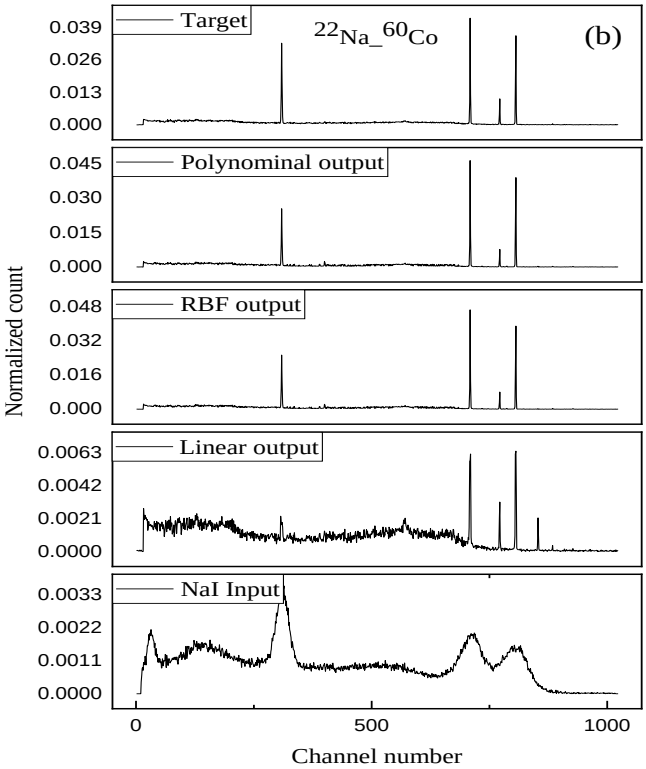
Target
22Na_60Co
(b)
Polynominal output
RBF output
Linear output
NaI Input
Normalized count
Channel number

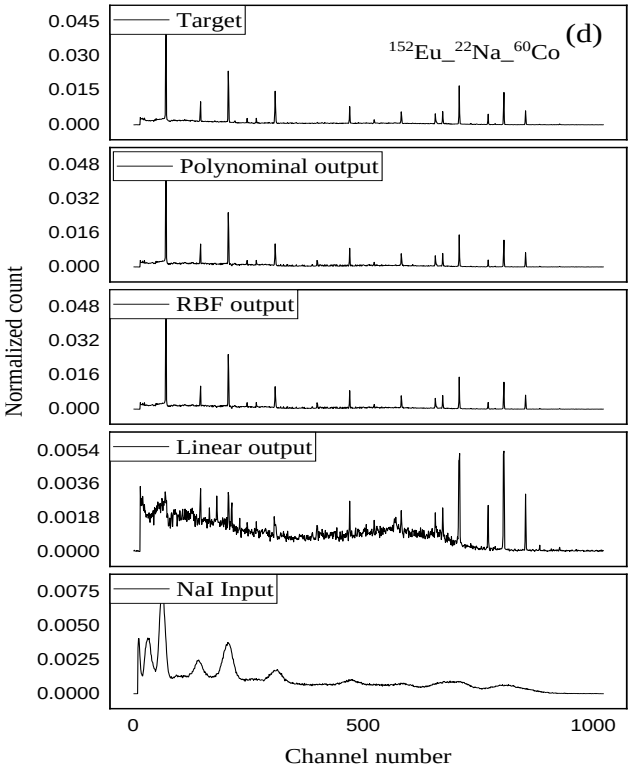
Target
^{152}Eu_^{22}Na_^{60}Co
(d)
Polynominal output
RBF output
Linear output
NaI Input
Normalized count
Channel number

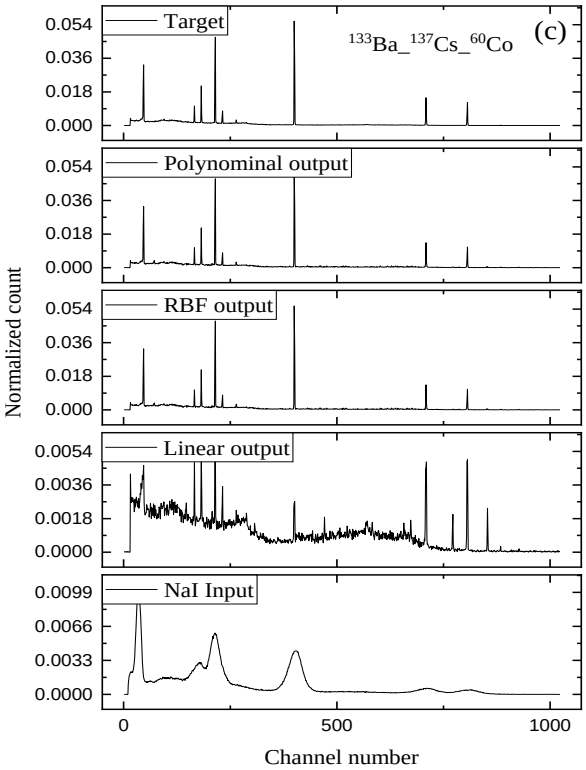
Target
^{133}Ba_^{137}Cs_^{60}Co
(c)
Polynominal output
RBF output
Linear output
NaI Input
Normalized count
Channel number

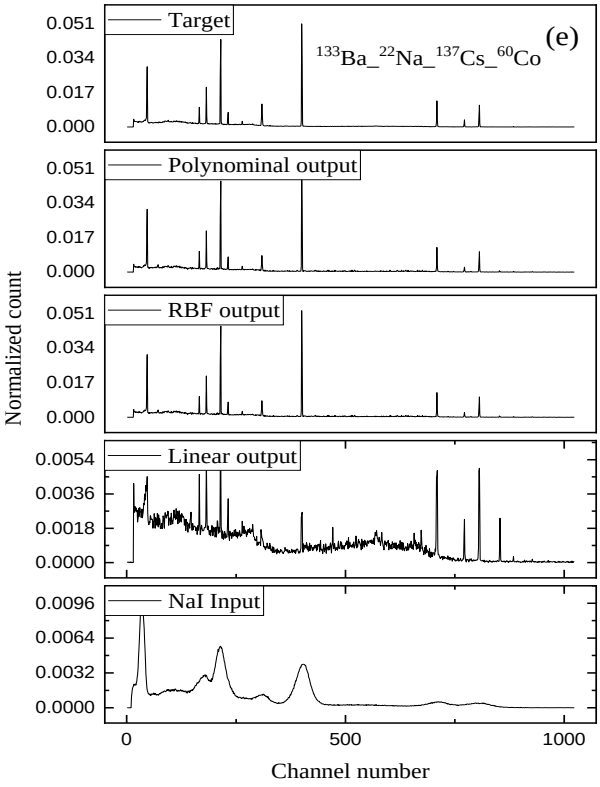
Target
(e)
^{133}Ba_^{22}Na_^{137}Cs_^{60}Co
Polynominal output
RBF output
Linear output
NaI Input
Normalized count
Channel number

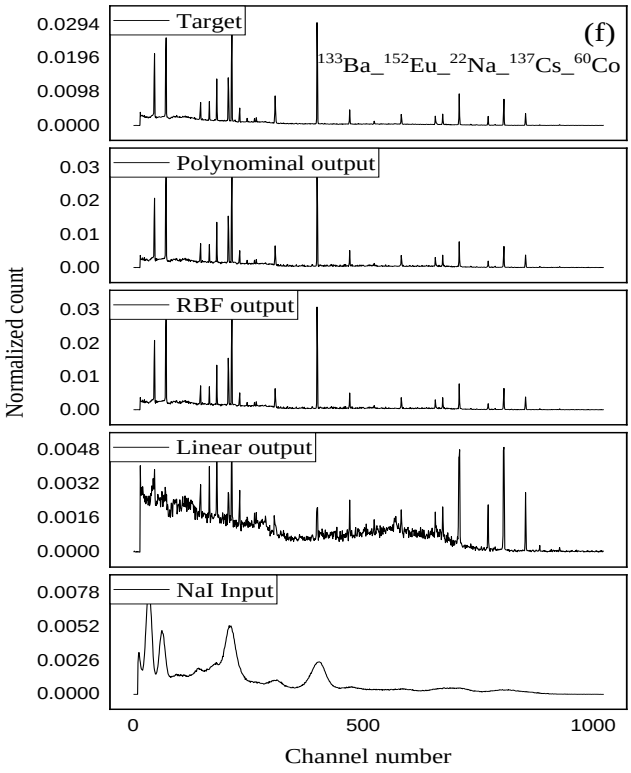
Target
(f)
^{133}Ba_^{152}Eu_^{22}Na_^{137}Cs_^{60}Co
Polynominal output
RBF output
Linear output
NaI Input
Normalized count
Channel number

Fig. 2. The input NaI spectra and corresponding model outputs for radioisotopes: (a) ^{133}Ba and ^{137}Cs (b) ^{60}Co and ^{22}Na, (c) ^{133}Ba, ^{137}Cs and ^{60}Co, (d) ^{152}Eu, ^{60}Co, and ^{22}Na, (e) ^{133}Ba, ^{137}Cs, ^{60}Co, and ^{22}Na, (f) ^{133}Ba, ^{152}Eu, ^{137}Cs, ^{60}Co, and ^{22}Na.

The resulting normalized HPGe spectrum encapsulates valuable information that can be utilized for identifying energy peaks associated with the unknown sample, radioisotope identification, and determining the contribution of each radioisotope in a multi-radioisotope spectrum. However, the current model is not suitable for activation measurements. Future work will focus on calculating real counts, enabling the obtained spectrum to be utilized for activity calculations.

Conclusions

This paper proposed a novel idea to convert the low resolution NaI spectra to the high resolution HPGe spectra using multi-output regression chain structure based on support vector regression. The model exhibited excellent result using RBF and polynominal kernels, despite limitations with the linear kernel function. The NaI spectra of different combinations of radioisotopes have many energy peaks, which more overlapping than the spectra of single radioisotopes. However, the proposed model, although trained only with the spectra of single radioisotopes (5 training samples), showed excellent performance for a dataset of various combinations of radioisotopes (26 test samples). In future work, the performance of the model can be further investigated for more radioisotopes, and more complex combination states can be created by changing the measurement conditions and the model can be optimized for them.

The methodology presented in this work: using NaI detectors for prediction of HPGe spectra, offers several advantages, including: 1. Cost-effectiveness: NaI(Tl) detectors are considerably cheaper than HPGe detectors, making them a more accessible option for various applications. 2. User-friendliness: NaI(Tl) detectors are generally easier to operate and maintain compared to HPGe detectors, requiring less specialized expertise. 3. Enhanced peak identification and quantification: Improved resolution enables the separation of overlapping peaks, leading to more accurate identification and quantification of individual gamma-ray emitters. 4. Reduced analysis time: The use of constructed HPGe spectrum can significantly reduce analysis time compared to relying solely on NaI measurements.

Future work will focus on investigating the model's performance with an even wider range of radioisotopes and exploring the creation of more complex combination states by altering measurement conditions and subsequently optimizing the model for these scenarios.

References

Gordon R.G. (2008). Practical gamma-ray spectrometry, John Wiley & Sons.

Cresswell A.J, Sanderson D.CW., Katsuhiko Y. (2018) assessment of the calibration of gamma spectrometry systems in forest environments. Journal of Environmental Radioactivity. 181:70–7.

Maacha L., Jaffal M., Jarni A., Kchikach A., Mouguina E.M. (2017). A contribution of airborne magnetic, gamma ray spectrometric data in understanding the structure of the

Central Jebilet Hercynian massif and implications for mining. Journal of African Earth Sciences 134:389–403.

Söderström M., Eriksson Jan. (2013) Gamma-ray spectrometry and geological maps as tools for cadmium risk assessment in arable soils. Geoderma 192:323–34.

Khan H.M., Chaudhry Z.S., Ismail M., Khan K. (2010). Assessment of radionuclides, trace metals and radionuclide transfer from soil to food of Jhangar Valley (Pakistan) using gamma-ray spectrometry. Water, Air, & Soil Pollution 213(1–4):353–62.

Hung, N.Q., Chuong, H.D., Vuong, L.Q., Thanh, T.T., Tao, C.V., (2016). Intercomparison NaI(Tl) and HPGe spectrometry to studies of natural radioactivity on geological samples. Journal of Environmental Radioactivity, 164:197–201.

Knoll, G.F. (2010). Radiation detection and measurement. John Wiley & Sons.

Debertin, K., and Helmer, R.G. (1988). Gamma- and X-ray spectrometry with semiconductor detectors. North-Holland.

Kong, H., Ye, F., Lu, X., Guo, L., Tian, J. (2005). Deconvolution of overlapped peaks based on the exponentially modified Gaussian model in comprehensive two-dimensional gas chromatography. Journal of Chromatography. A. 1086:160–164.

Hu, Y., Wei, L., Hu, J. (2005). Resolving overlapped spectra with curve fitting. Spectrochimica Acta Part A. 62: 16–21.

Liu, M., Dong, Z., Xin, G., Sun Y., Qu, R. (2018). An improved method based on a new wavelet transform for overlapped peak detection on spectrum obtained by portable Raman system. Chemometrics and Intelligent Laboratory Systems. 182: 1–8.

Saeidi, Z., Afarideh, H., Ghergherehchi, M. (2024). Utilizing artificial neural networks to convert gamma-ray spectra from NaI(Tl) detectors to HPGe detector gamma-ray spectra, Annals of Nuclear Energy. 200:110368.

Drucker, H., Burges, C. C., Kaufman, L. A., Smola, J., Vapnik, V. N. (1997). Support Vector Regression Machines. Advances in Neural Information Processing Systems. 9, NIPS 155–161, MIT Press.

Borchani, H., Varando, G., Bielza, C. (2015). A survey on multi-output regression. WIREs Data Mining and Knowledge Discovery. 5:216–233.

Mao T, Lee S, Ou Y, Mih A. (2021). Transport multi-mode choice prediction using a hybrid multi-output regression modelling. doi:10.13140/RG.2.2.29663.74405.

ICNST 2024
International Conference on Nuclear Science and Technology
6- 8 MAY 2024 | Isfahan, Iran

Feasibility study of ruthenium-106 production through neutron activation method of natural target (Paper ID : 1426)

Kanani Kh. Correspondent1*, Feghhi S. A. H.1, Shirvani-Arani S.2, Bahrami-Samani A.2, Miremad S. M. Co-Author2

1Nuclear Engineering, Shahid Beheshti University, Tehran, Iran
2Nuclear Science and Technology Research Institute (NSTRI), Tehran, Iran

Abstract

Radioisotope ruthenium-106 (106Ru) plays a crucial role in ophthalmic brachytherapy, particularly for treating eye tumors like uveal melanomas. This radioisotope can be generated through 235U-fission using thermal neutron or neutron activation process. In this study, we assessed the feasibility of 106Ru production by neutron irradiation of natural ruthenium targets. The numerical solution is employed to the one-group Bateman equations using MATLAB, along with Monte Carlo simulations via the MCNPX (Monte Carlo N-Particle eXtended) code. Our investigation also focused on the impurities produced during this process and the factors influencing 106Ru production rates. The key findings are as follows, to produce 34.3 μCi of 106Ru from 1 g of natural ruthenium, a neutron flux of 5×1015n.cm-2.s-1 and 6 days of irradiation time are required. The primary impurity encountered is 103Ru, which can be mitigated by extending the delay-decay period.

Keywords: ^{106}Ru production, Neutron Activation, Bateman Equations, MATLAB, MCNPX

Introduction

Ruthenium is a rare transition metal belonging to the Platinum group metals (PGMs) of the periodic table [1]. Among the known radioisotopes of ruthenium, the most stable ones are ^{106}Ru (1.02 years), ^{103}Ru (39.24 days), and ^{97}Ru (2.83 days), respectively [2]. ^{106}Ru radioisotope is widely used to prepare eye plaques for the treatment of eye tumors in brachytherapy [3,4]. The nuclear industry is a rich source of ^{106}Ru and ruthenium is one of the fission products of ^{235}U in nuclear reactors, while the fission yield of ruthenium for ^{235}U is 0.004015 [2]. The amount of ruthenium produced during the reprocessing of spent fuel varies according to the type of reactor, fuel, level of fuel burning, cooling time after burning, and etc [5,6]. ^{106}Ru is commercially obtained by neutron irradiation of enriched ^{235}U in the production of ^{99}Mo process. ^{106}Ru will be isolated from the waste by different methods following the isolation of ^{99}Mo and the decay of ^{103}Ru. Currently, only a handful of reactors worldwide are capable of producing ^{99}Mo. Hence, alternative strategies for producing this key radioisotope in medicine are being explored [7]. In this study, a new method based on neutron activation reaction was investigated to produce ^{106}Ru. ^{106}Ru can be produced by using neutron sources and creating an activation reaction in which by absorbing thermal neutrons in the target nucleus and creating (n, γ) reaction, creates activity and produces a new nucleus [8]. Therefore, irradiating natural ruthenium with thermal neutrons and according to the thermal neutron absorption cross-section, leads to the neutron capture reaction and the production of successive radioisotopes, hence a decay chain of different radioisotopes is created, which finally after the beta decay of ^{106}Tc and

neutron capture by ^{105}Ru will lead to produce ^{106}Ru. Meanwhile, impurities such as radioisotopes of other nuclei and other radioisotopes of ruthenium are also produced, which due to the long half-life of ^{106}Ru and considering a long-term delay-decay period, they will decay and the purity of the produced ^{106}Ru will be increased. In this work, 1 g natural ruthenium is irradiated for 6 days by a thermal neutron flux of 5×10^{13} n.cm^{-2}.s^{-1} (thermal neutron flux of Tehran Research Reactor). Bateman's equations related to the production-decay chain of produced radioisotopes are numerically solved to calculate the activity and amount of produced ^{106}Ru and other impurities caused by other radioisotopes of ruthenium and radioisotopes of other elements. Theoretical calculations and Bateman's equations solution are done in MATLAB software using the dsolve command while taking into account the effective factors in the amount of produced ^{106}Ru such as irradiation time, thermal neutron flux, ^{104}Ru enrichment, and the amount of natural ruthenium under thermal neutron irradiation. The optimal values for each factor to achieve sufficient activity of ^{106}Ru for the preparation of ruthenium eye plaques were obtained. Also, to validate the theoretical calculations, the Tehran research reactor was simulated using the MCNP Monte Carlo code, and the amount of ^{106}Ru was carried out by the activation method with the above conditions.

2. Materials and Methods

2.1. Natural Ruthenium Target

Natural ruthenium with atomic number 44, has seven stable isotopes ^{96}Ru (5.52%), ^{98}Ru (1.88%), ^{99}Ru (12.7%), ^{100}Ru (12.6%), ^{101}Ru (17%), ^{102}Ru (31.6%) and ^{104}Ru (18.7%). The number of target atoms to be irradiated has a direct effect on the production rate of ^{106}Ru by neutron activation method. The ^{104}Ru is the closest stable isotope to the ^{106}Ru radioisotope which will be converted to the ^{106}Ru after 2 steps (first ^{104}Ru turns into ^{105}Ru and then ^{105}Ru turns into ^{106}Ru) by neutron irradiation. The thermal neutron absorption cross-section of ^{104}Ru for (n, γ) reaction is 0.49 barn [2]. So such, enriched ruthenium with ^{104}Ru in comparison to natural ruthenium has a significant effect in increasing the production of ^{106}Ru and also reducing the production of impurities such as ^{97}Ru, ^{105}Ru radioisotopes, and in particular, ^{103}Ru radioisotope. Hence, a highly enriched ^{104}Ru is needed to produce ^{106}Ru with high activity and purity. ^{104}Ru can be enriched up to 98% [9]. In this study, in section 3.4, enriched ^{104}Ru of 80% has been used in theoretical calculations for economic efficiency.

2.2. Method

2.2.1. Theoretical calculations by solving Bateman's equations

The calculations are done based on the schematic of the decay chain and the numbering of radioisotopes under thermal neutron irradiation and the produced products according to Figure 1.

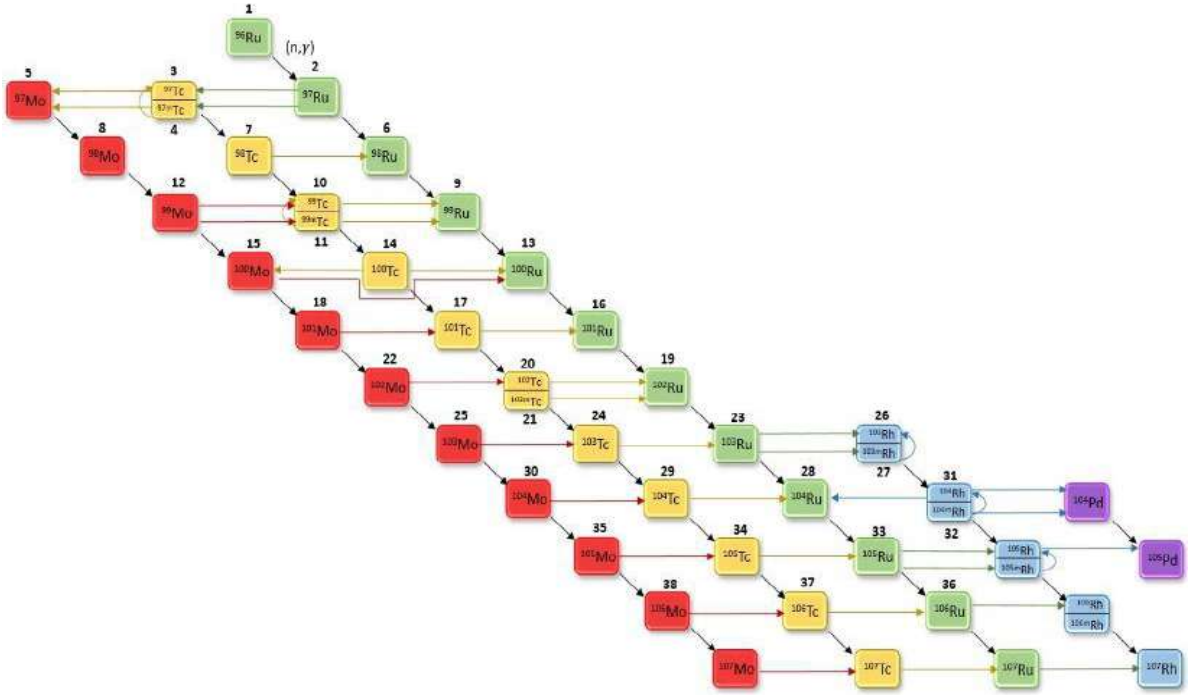

Fig. 1. Production-decay schematic of produced isotopes and radioisotopes by neutron activation
The activity of the produced isotopes has been calculated based on the general equations of the production of target nuclei and their decay into daughter nuclei. The differential equations of production and decay of radionuclides based on Figure 1 are as follows.

$$\frac{dN_1(t)}{dt} = -\sigma_{1,2}\varphi N_1(t) \qquad (1)$$

$$\frac{dN_{20}(t)}{dt} = (0{,}5)\sigma_{17,20}\varphi N_{17}(t) - \sigma_{20,24}\varphi N_{20}(t) - \lambda_{20}N_{20}(t) + \lambda_{22}N_{22}(t) \qquad (20)$$

$$\frac{dN_2(t)}{dt} = \sigma_{1,2}\varphi N_1(t) - \sigma_{2,6}\varphi N_2(t) - \lambda_2 N_2(t) \quad (2)$$

$$\frac{dN_3(t)}{dt} = 0{,}9996\lambda_2 N_2(t) + 0{,}9606\lambda_4 N_4(t) - \lambda_3 N_3(t) - \sigma_{3,7}\varphi N_3(t) \quad (3)$$

$$\frac{dN_4(t)}{dt} = -\sigma_{4,7}\varphi N_4(t) + 0{,}0003618\lambda_2 N_2(t) - \lambda_4 N_4(t) \quad (4)$$

$$\frac{dN_5(t)}{dt} = -\sigma_{5,8}\varphi N_5(t) + \lambda_3 N_3(t) + 0{,}0394\lambda_4 N_4(t) \quad (5)$$

$$\frac{dN_6(t)}{dt} = \sigma_{2,6}\varphi N_2(t) - \sigma_{6,9}\varphi N_6(t) + \lambda_7 N_7(t) \quad (6)$$

$$\frac{dN_7(t)}{dt} = \sigma_{3,7}\varphi N_3(t) + \sigma_{4,7}\varphi N_4(t) - \sigma_{7,10}\varphi N_7(t) - \lambda_7 N_7(t) \quad (7)$$

$$\frac{dN_8(t)}{dt} = \sigma_{5,8}\varphi N_5(t) - \sigma_{8,12}\varphi N_8(t) \quad (8)$$

$$\frac{dN_{21}(t)}{dt} = (0{,}5)\sigma_{17,20}\varphi N_{17}(t) - \sigma_{21,24}\varphi N_{21}(t) - \lambda_{21} N_{21}(t) \quad (21)$$

$$\frac{dN_{22}(t)}{dt} = \sigma_{18,22}\varphi N_{18}(t) - \sigma_{22,25}\varphi N_{22}(t) - \lambda_{22} N_{22}(t) \quad (22)$$

$$\frac{dN_{23}(t)}{dt} = \sigma_{19,23}\varphi N_{19}(t) - \sigma_{23,28}\varphi N_{23}(t) - \lambda_{23} N_{23}(t) + \lambda_{24} N_{24}(t) \quad (23)$$

$$\frac{dN_{24}(t)}{dt} = \sigma_{20,24}\varphi N_{20}(t) + \sigma_{21,24}\varphi N_{21}(t) - \sigma_{24,29}\varphi N_{24}(t) - \lambda_{24} N_{24}(t) + \lambda_{25} N_{25} \quad (24)$$

$$\frac{dN_{25}(t)}{dt} = \sigma_{22,25}\varphi N_{22}(t) - \sigma_{25,30}\varphi N_{25}(t) - \lambda_{25} N_{25}(t) \quad (25)$$

$$\frac{dN_{26}(t)}{dt} = -\sigma_{26,31}\varphi N_{26}(t) + \lambda_{27} N_{27}(t) + 0{,}011741\lambda_{23} N_{23}(t) \quad (26)$$

$$\frac{dN_{27}(t)}{dt} = -\sigma_{27,31}\varphi N_{27}(t) - \lambda_{27} N_{27}(t) + 0{,}988259\lambda_{23} N_{23}(t) \quad (27)$$

$$\frac{dN_9(t)}{dt} = \sigma_{6,9}\varphi N_6(t) - \sigma_{9,13}\varphi N_9(t) + \lambda_{10}N_{10}(t) + 0{,}000037\lambda_{11}N_{11}(t) \quad (9)$$

$$\frac{dN_{10}(t)}{dt} = (0{,}5)\sigma_{7,10}\varphi N_7(t) - \sigma_{10,14}\varphi N_{10}(t) - \lambda_{10}N_{10}(t) + 0{,}1211\lambda_{12}N_{12}(t) + 0{,}9999\lambda_{11}N_{11}(t) \quad (10)$$

$$\frac{dN_{11}(t)}{dt} = (0{,}5)\sigma_{7,10}\varphi N_7(t) - \sigma_{11,14}\varphi N_{11}(t) - \lambda_{11}N_{11}(t) + 0{,}8788\lambda_{12}N_{12}(t) \quad (11)$$

$$\frac{dN_{12}(t)}{dt} = \sigma_{8,12}\varphi N_8(t) - \sigma_{12,15}\varphi N_{12}(t) - \lambda_{12}N_{12}(t) \quad (12)$$

$$\frac{dN_{13}(t)}{dt} = \sigma_{9,13}\varphi N_9(t) - \sigma_{13,16}\varphi N_{13}(t) + 0{,}999982\lambda_{14}N_{14}(t) + \lambda_{15}N_{15}(t) \quad (13)$$

$$\frac{dN_{28}(t)}{dt} = \sigma_{23,28}\varphi N_{23}(t) - \sigma_{28,33}\varphi N_{28}(t) + 0{,}0045\lambda_{31}N_{31}(t) + \lambda_{29}N_{29}(t) \quad (28)$$

$$\frac{dN_{29}(t)}{dt} = \sigma_{24,29}\varphi N_{24}(t) - \sigma_{29,34}\varphi N_{29}(t) - \lambda_{29}N_{29}(t) + \lambda_{30}N_{30}(t) \quad (29)$$

$$\frac{dN_{30}(t)}{dt} = \sigma_{25,30}\varphi N_{25}(t) - \sigma_{30,35}\varphi N_{30}(t) - \lambda_{30}N_{30}(t) \quad (30)$$

$$\frac{dN_{31}(t)}{dt} = (0{,}5)\sigma_{26,31}\varphi N_{26}(t) + (0{,}5)\sigma_{27,31}\varphi N_{27}(t) - \sigma_{31}\varphi N_{31}(t) + 0{,}9987\lambda_{32}N_{32}(t) - \lambda_{31}N_{31}(t) \quad (31)$$

$$\frac{dN_{32}(t)}{dt} = (0{,}5)\sigma_{26,31}\varphi N_{26}(t) + (0{,}5)\sigma_{27,31}\varphi N_{27}(t) - \sigma_{32}\varphi N_{32}(t) - \lambda_{32}N_{32}(t) \quad (32)$$

$$\frac{dN_{14}(t)}{dt} = \sigma_{10,14}\varphi N_{10}(t) + \sigma_{11,14}\varphi N_{11}(t) - \sigma_{14,17}\varphi N_{14}(t) - \lambda_{14}N_{14}(t) \quad (14)$$

$$\frac{dN_{15}(t)}{dt} = \sigma_{12,15}\varphi N_{12}(t) - \sigma_{15,18}\varphi N_{15}(t) - \lambda_{15}N_{15}(t) \quad (15)$$

$$\frac{dN_{16}(t)}{dt} = \sigma_{13,16}\varphi N_{13}(t) - \sigma_{16,19}\varphi N_{16}(t) + \lambda_{17}N_{17}(t) \quad (16)$$

$$\frac{dN_{17}(t)}{dt} = \sigma_{14,17}\varphi N_{14}(t) - \sigma_{17,20}\varphi N_{17}(t) - \lambda_{17}N_{17}(t) + \lambda_{18}N_{18}(t) \quad (17)$$

$$\frac{dN_{18}(t)}{dt} = \sigma_{15,18}\varphi N_{15}(t) - \sigma_{18,22}\varphi N_{18}(t) - \lambda_{18}N_{18}(t) \quad (18)$$

$$\frac{dN_{19}(t)}{dt} = \sigma_{16,19}\varphi N_{16}(t) - \sigma_{19,23}\varphi N_{19}(t) + \lambda_{20}N_{20}(t) + \lambda_{21}N_{21}(t) \quad (19)$$

$$\frac{dN_{33}(t)}{dt} = \sigma_{28,33}\varphi N_{28}(t) - \sigma_{33,36}\varphi N_{33}(t) - \lambda_{33}N_{33}(t) + \lambda_{34}N_{34}(t) \quad (33)$$

$$\frac{dN_{34}(t)}{dt} = \sigma_{29,34}\varphi N_{29}(t) - \sigma_{34,37}\varphi N_{34}(t) - \lambda_{34}N_{34}(t) + \lambda_{35}N_{35}(t) \quad (34)$$

$$\frac{dN_{35}(t)}{dt} = \sigma_{30,35}\varphi N_{30}(t) - \sigma_{35,38}\varphi N_{35}(t) - \lambda_{35}N_{35}(t) \quad (35)$$

$$\frac{dN_{36}(t)}{dt} = \sigma_{33,36}\varphi N_{33}(t) - \sigma_{36}\varphi N_{36}(t) - \lambda_{36}N_{36}(t) + \lambda_{37}N_{37}(t) \quad (36)$$

$$\frac{dN_{37}(t)}{dt} = \sigma_{34,37}\varphi N_{34}(t) - \sigma_{37}\varphi N_{37}(t) - \lambda_{37}N_{37}(t) + \lambda_{38}N_{38}(t) \quad (37)$$

$$\frac{dN_{38}(t)}{dt} = \sigma_{35,38}\varphi N_{35}(t) - \sigma_{38}\varphi N_{38}(t) - \lambda_{38}N_{38}(t) \quad (38)$$

In the above equations, $N_i(t)$ is the number of nuclei of each nuclide at time t. The cross-section of neutron absorption by each nucleus i and the production of the next nuclide i+1

is denoted by $\sigma_{i,i+1}$. λ_i is the decay constant of each nuclide. The decay constants used in equations 1 to 38 have been extracted from the ENDF/B-VIII.0 library [2]. Due to the unavailability of (n, γ) reaction information for some isotopes in the ENDF library, the cross sections have been extracted from the TENDL- 2019 library [10] of Janis.

The number of nuclei of each radionuclide in terms of time is obtained by simultaneously solving equations 1 to 38 and calculating the values of $N_i(t)$ using MATLAB software. The activity of each radionuclide is calculated by using the relation $A_i(t)=\lambda_i.N_i(t)$. Theoretical calculations based on the irradiation of 1 g natural ruthenium by 5×10^{13} n.cm^{-2}.s^{-1}thermal neutron flux during irradiation times of 1, 2, 3, 5, 7/5, 10, 17 hours, and then 1 day to 6 days with steps of 0.25 days have been done. After irradiation, the process of producing nuclei through the neutron activation reaction will be stopped, but the process of producing nuclei that are produced from the decay of the mother nuclei continues. The number of nuclei of ^{97}Ru, ^{103}Ru, ^{105}Ru, and ^{106}Ru is obtained after the end of irradiation and during the cooling times of 1, 3, 6, and 12 months after irradiation by using equations 39 to 48.

$$\frac{dN_2(t)}{dt} = -\lambda_2 N_2(t) \quad (39)$$

$$\frac{dN_{23}(t)}{dt} = \lambda_{24} N_{24}(t) - \lambda_{23} N_{23}(t) \quad (40)$$

$$\frac{dN_{24}(t)}{dt} = \lambda_{25} N_{25}(t) - \lambda_{24} N_{24}(t) \quad (41)$$

$$\frac{dN_{34}(t)}{dt} = \lambda_{35} N_{35}(t) - \lambda_{34} N_{34}(t) \quad (44)$$

$$\frac{dN_{35}(t)}{dt} = -\lambda_{35} N_{35}(t) \quad (45)$$

$$\frac{dN_{36}(t)}{dt} = \lambda_{37} N_{37}(t) - \lambda_{36} N_{36}(t) \quad (46)$$

$$\frac{dN_{25}(t)}{dt} = -\lambda_{25}N_{25}(t) \quad (42)$$

$$\frac{dN_{33}(t)}{dt} = \lambda_{34}N_{34}(t) - \lambda_{33}N_{33}(t) \quad (43)$$

$$\frac{dN_{37}(t)}{dt} = \lambda_{38}N_{38}(t) - \lambda_{37}N_{37}(t) \quad (47)$$

$$\frac{dN_{38}(t)}{dt} = -\lambda_{38}N_{38}(t) \quad (48)$$

According to equations 1 to 38, not only the ^{104}Ru enrichment effect, but 3 other parameters like thermal neutron flux, irradiation duration, and the amount of ruthenium under irradiation are important to produce ^{106}Ru. The effect of enrichment and the amount of irradiated ruthenium are linear to produce all isotopes and radioisotopes in equations 1 to 38. Therefore, to feasibility of producing ^{106}Ru with the neutron activation method, only the effect of increasing the thermal neutron flux and duration time of irradiation on the production of ^{106}Ru are investigated.

2.2.2. Monte Carlo Calculation with MCNPX code

The core of the Tehran research reactor was simulated by using the MCNPX Monte Carlo code. To perform Monte Carlo simulations according to the theoretical calculations, a quartz glass containing 1 g of natural ruthenium was placed in an aluminum can. An aluminum can was placed in one of the channels of the core of the reactor with a thermal neutron flux of 5×10^{13} $cm^{-2}.s^{-1}$ for 6 days of irradiation.

3. Results and Discussion

3.1. The results of theoretical calculations

The activity of ^{106}Ru, ^{105}Ru, ^{103}Ru, and ^{97}Ru radioisotopes obtained by theoretical calculations (using Bateman's equations) and immediately after the end of irradiation is shown in Figure 2.

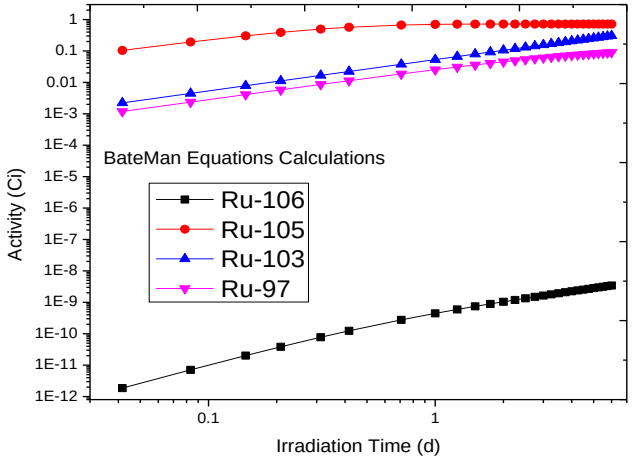

Fig. 2. The activity of ruthenium radioisotopes obtained by theoretical calculations (Bateman's equations)

Figure 2 shows the activity of ^{106}Ru after 6 days of irradiation with 1 g natural ruthenium and 5×10^{13} n.cm^{-2}.s^{-1} thermal neutron flux is very low (few nCi) to prepare any kind of ruthenium plaques. On the other hand, the activity of impurities, i.e. ^{103}Ru and ^{105}Ru, is very high (hundreds mCi). Since the effect of increasing the abundance of ^{104}Ru and the amount of irradiated ruthenium is linear, only the effect of increasing the flux and time of irradiation has been investigated to increase the activity of produced ^{106}Ru.

3.2. The results of Monte Carlo simulations

To validate the results of theoretical calculations, simulations are performed using MCNPX code, with the same situation used in theoretical calculations. The activity of ruthenium radioisotopes resulting from MCNP simulations and immediately after the end of irradiation is shown in Figure 3.

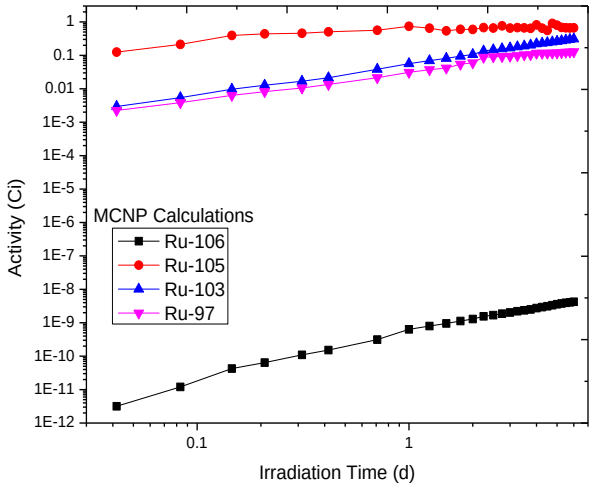

Fig. 3. The activity of ruthenium radioisotopes obtained with MCNP simulations

Figure 3 shows that the activity of ^{106}Ru obtained by the MCNP code is very low (few nCi). Also, the activity of impurities, i.e., ^{103}Ru and ^{105}Ru, after 6 days of irradiation is very high (hundreds mCi). To validate the results of solving Bateman's equations, the results of theoretical calculations and MCNP simulations are compared in Section 3.3.

3.3. Comparison of the results of theoretical calculations and Monte Carlo simulation

To well comparison of the results of simulation and theoretical calculations, the activity of ruthenium radioisotopes is shown separately in Figure 4.

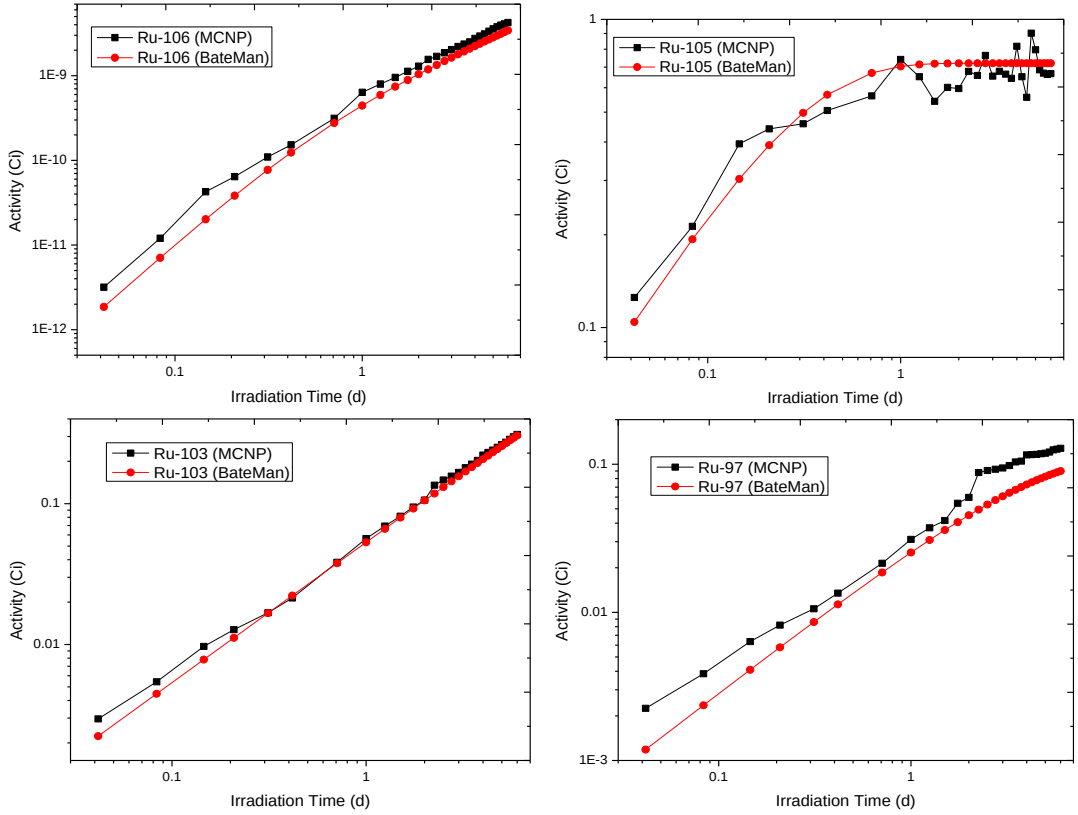

Fig. 4. Comparing the activity of ruthenium radioisotopes obtained by MCNP and solving Batman's equations

Figure 4 shows that there is a good agreement between the activity obtained by theoretical calculations and MCNP simulation for each radioisotope. On average, the

difference between theoretical calculations and MCNP calculations for ^{106}Ru, ^{105}Ru, ^{103}Ru, and ^{97}Ru radioisotopes is less than 20%, 10%, 5%, and 30% respectively. The main difference can be due to the libraries used in the MCNP code. This difference increases during short irradiation times, which is due to statistical errors. By increasing the irradiation time and as a result, increasing the activity of ruthenium radioisotopes, the difference between the theoretical calculation and MCNP decreases significantly.

3.4. The feasibility of production

High-flux thermal neutron reactors in the world have a maximum flux of 5×10^{15} n.cm^{-2}.s^{-1} (SM reactor in Russia [11]) and the Tehran research reactor in Iran has a range of flux around 5×10^{13} n.cm^{-2}.s^{-1} to 8×10^{13} n.cm^{-2}.s^{-1}. Hence, to investigate the effect of flux variation on the production of ^{106}Ru, equations 1 to 38 are solved in different fluxes of 1×10^{13} n.cm^{-2}.s^{-1}, 5×10^{13} n.cm^{-2}.s^{-1}, 8×10^{13} n.cm^{-2}.s^{-1}, 1×10^{14} n.cm^{-2}.s^{-1}, 5×10^{14} n.cm^{-2}.s^{-1}, 1×10^{15} n.cm^{-2}.s^{-1}, and 5×10^{15} n.cm^{-2}.s^{-1} with 1 g natural ruthenium and 6 days of irradiation. The results are shown in Figure 5.

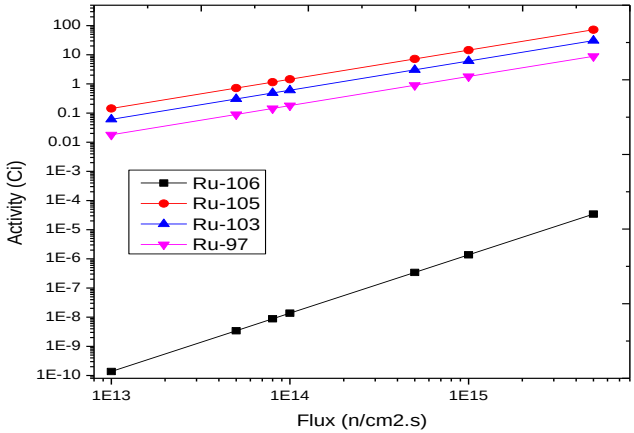

Fig. 5. The variation of ruthenium isotopes activity in terms of neutron flux

The slope of the curves in Figure 5 shows that increasing the flux causes a greater increase in the production of ^{106}Ru compared to other ruthenium radioisotopes. Hence, by increasing the flux from 5×10^{13} n.cm^{-2}.s^{-1} to 5×10^{15} n.cm^{-2}.s^{-1}, the ^{106}Ru and ^{103}Ru activity are increased from 3.43 nCi and 305 mCi to 34.3 µCi and 30.5 Ci, respectively. It shows that by increasing the thermal neutron flux by 10^2 times, the production of ^{106}Ru will be increased up to 10^4 times while the production of other radioisotopes of ruthenium will be increased up to 10^2 times. This is because the number of isotopes that lead to the production of ^{106}Ru, is higher than the isotopes that lead to produce other radioisotopes of ruthenium. It should be noted that such an increase in the flux leads to an increase in the production of other radioisotopes in the chain by 10^2 to 10^{20} times. But due to the small amount production of them and their short half-life, they will decay very fast and it will not lead to produce high activity of them. Among these produced radioisotopes, only 5 of them have a high half-life. Due to their small amount of production, their activity will be less than a

few μCi. The activity of these radioisotopes with both thermal neutron fluxes of 5×10^{13} $n.cm^{-2}.s^{-1}$ and 5×10^{15} $n.cm^{-2}.s^{-1}$ after 6 days of irradiation of 1 g natural ruthenium is given in Table 1.

Table 1. The activity of radioisotopes with a long half-life in the production-decay chain

Radioisotope	**Half-Life**	**Activity (nCi) With 5×10^{13} $n.cm^{-2}.s^{-1}$ flux**	**Activity (nCi) With 5×10^{15} $n.cm^{-2}.s^{-1}$ flux**
^{97}Tc	4.21 y	0.15	14.6
^{97m}Tc	91 d	902	89000
^{98}Tc	4.2 y	2.4×10^{-5}	0.236
^{99}Tc	2.11 y	2.75×10^{-9}	2.67×10^{-3}
^{100}Mo	7.3 y	1.26×10^{-35}	1.25×10^{-27}

To investigate the effect of irradiation time on the production of ^{106}Ru, the variation of ruthenium radioisotope activity in terms of irradiation time is investigated for 1 g natural ruthenium at 5×10^{13} $n.cm^{-2}.s^{-1}$ neutron flux during 1, 6, 15 days, and 1 to 12 months irradiation. The results for each radioisotope are shown in Figure 6.

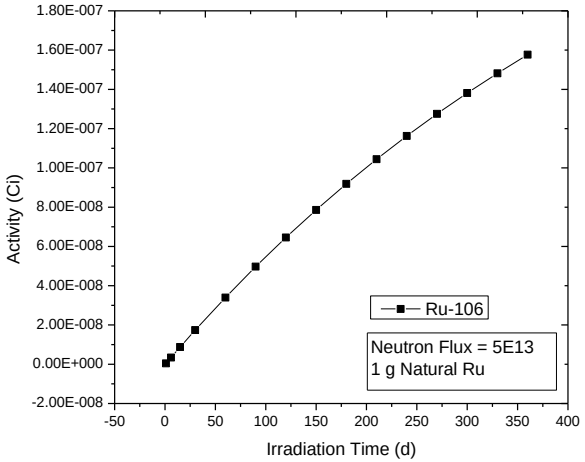
Activity (Ci)
Irradiation Time (d)
Ru-106
Neutron Flux = 5E13
1 g Natural Ru

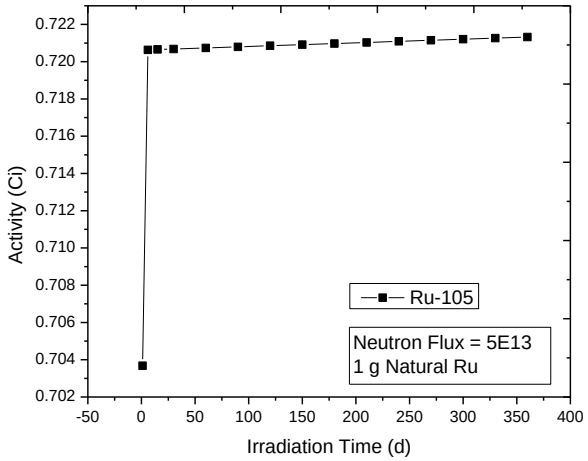
Activity (Ci)
Irradiation Time (d)
Ru-105
Neutron Flux = 5E13
1 g Natural Ru

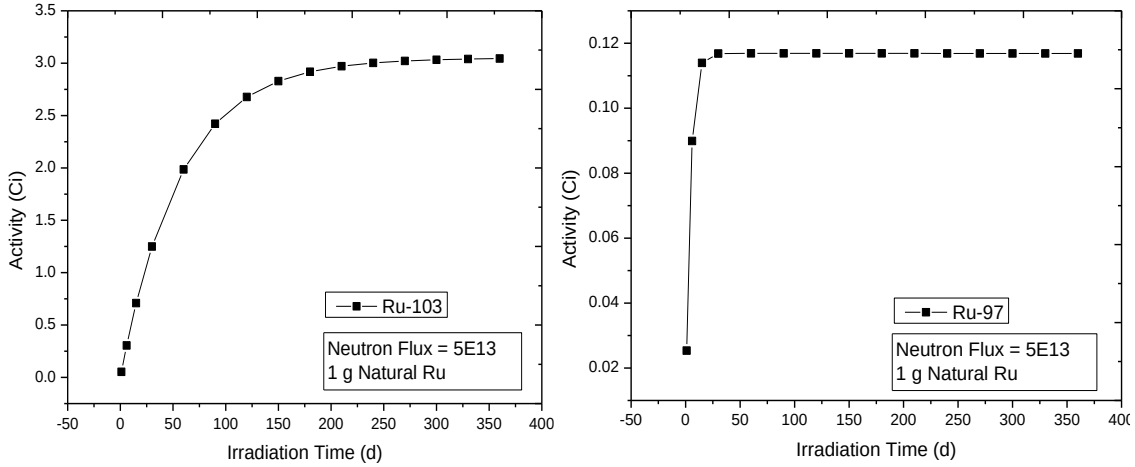

Fig. 6. variation of ruthenium radioisotope activity in terms of irradiation time

Figure 6 shows that by increasing irradiation time, no activity increase is observed for ^{105}Ru after 6 days, ^{97}Ru after 15 days, and ^{103}Ru after 4 months of irradiation. But ^{106}Ru activity is increasing continuously by increasing irradiation time.

Considering that the effect of increasing the amount of irradiated ruthenium and the enrichment of ^{104}Ru on the production of ^{106}Ru by neutron activation method is completely linear, the produced activity for each radioisotope of ruthenium in different conditions of irradiation time, flux, enrichment, and the amount of irradiated ruthenium is calculated and listed in Table 2.

Table 2. Ruthenium radioisotopes activity in different conditions of irradiation time, flux, enrichment, and amount of ruthenium under irradiation

^{106}Ru Activity (Ci)				Irradiation time (month)	Flux (n.cm^{-2}.s^{-1})
80% Enriched Ruthenium		Natural Ruthenium			
100 g	1 g	100 g	1 g		
2.14×10^{-5}	2.14×10^{-7}	4.97×10^{-6}	4.97×10^{-8}	**3**	**5×10^{13}**
3.95×10^{-5}	3.95×10^{-7}	9.19×10^{-6}	9.19×10^{-8}	**6**	
6.79×10^{-5}	6.79×10^{-7}	1.58×10^{-5}	1.58×10^{-7}	**12**	
5.47×10^{-5}	5.47×10^{-7}	1.27×10^{-5}	1.27×10^{-7}	**3**	**8×10^{13}**
1.01×10^{-4}	1.01×10^{-6}	2.35×10^{-5}	2.35×10^{-7}	**6**	
1.74×10^{-4}	1.74×10^{-6}	4.04×10^{-5}	4.04×10^{-7}	**12**	
2.14×10^{-1}	2.14×10^{-3}	4.97×10^{-2}	4.97×10^{-4}	**3**	**5×10^{15}**
3.95×10^{-1}	3.95×10^{-3}	9.19×10^{-2}	9.19×10^{-4}	**6**	
6.79×10^{-1}	6.79×10^{-3}	1.58×10^{-1}	1.58×10^{-3}	**12**	

The results show by increasing the amount of ruthenium to 100 g, enrichment of ^{104}Ru to 80%, with thermal neutron flux of 5×10^{15} n.cm^{-2}.s^{-1} and 12 months irradiation time, ^{106}Ru activity will be 679 mCi, while the activity of impurities, i.e., ^{97}Ru, ^{103}Ru and ^{105}Ru will be 268 Ci, 7.08×10^{3} Ci and 3.1×10^{4} Ci, respectively. Due to the short half-life of ^{105}Ru and ^{97}Ru, they will decay completely after a few days (for ^{105}Ru) and a few months (for ^{97}Ru). The inventory of produced radioisotopes of ruthenium by 12-months irradiation of 100 g enriched ^{104}Ru (80%) under 5×10^{15} n.cm^{-2}.s^{-1} thermal neutron flux with 1, 6, 12, 18, 24, 30, 36, 42, and 48 months cooling times is calculated by using equations 39 to 48, to investigate the suitable decay-delay time to remove ^{103}Ru impurity. the results are shown in Figure 7.

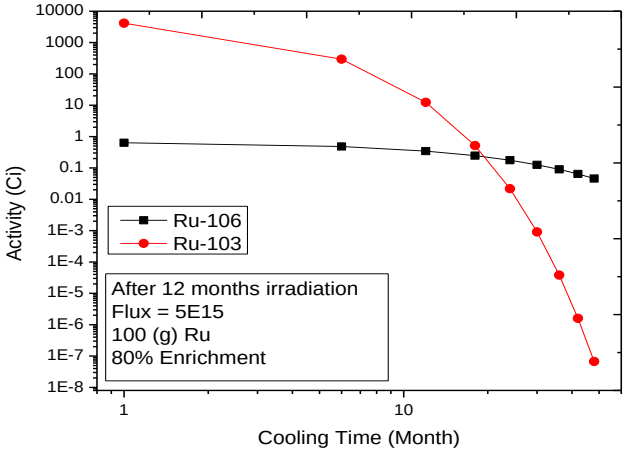

Fig. 7. The activity of ruthenium radioisotopes at different cooling times after 12 months irradiating 100 g enriched ^{104}Ru (80%) under 5×10^{15} n.cm^{-2}.s^{-1} thermal neutron flux

The obtained results in Figure 7 show that the ^{106}Ru and ^{103}Ru activity is 90.18 mCi and 38.22 µCi, respectively with 36 months of delay-decay time. Therefore, after 36 months of the end of irradiation, the activity of ^{103}Ru impurity will be negligible.

Conclusion

The increasing use of ^{106}Ru for the preparation of eye plaques used in brachytherapy to treat eye cancers makes the need to produce high-purity ^{106}Ru more important than ever. In this article, a new method is introduced to investigate the feasibility of high purity and activity ^{106}Ru production using neutron activation reaction. The activity and inventory of produced radioisotopes in the production-decay chain were calculated by numerically solving Bateman's equations using MATLAB software. Furthermore, the results of

solving Bateman's equations were validated using the MCNPX code. According to the obtained results, a good agreement was observed between the results of theoretical calculations and simulation for each radionuclide. Efficient parameters were determined to increase the production of ^{106}Ru. The results showed that the effect of increasing the enrichment of ^{104}Ru and the amount of irradiated ruthenium leads to the increase of produced ^{106}Ru in a completely linear manner. Increasing the flux causes a greater increase in the production of ^{106}Ru compared to other ruthenium radioisotopes. Also, the increase in flux leads to an increase in the production of other radioisotopes in the chain. But due to their small amount of production or their short half-life, they decay quickly and it will not lead to produce high activity of them. With an increase in the irradiation time, there was no increase in the production rate of other ruthenium radioisotopes, while the production of ^{106}Ru is increasing continuously by increasing irradiation time. By choosing the appropriate decay-delay time, other produced impurities decay and high purity ^{106}Ru can be obtained.

Reference

[1] Zuba, I., Zuba, M., Piotrowski, M., Pawlukojć, A., Ruthenium as an important element in nuclear energy and cancer treatment, Applied Radiation and Isotopes, https[2] Evaluated Nuclear Data File (ENDF), https://www-nds.iaea.org.

[2] Hoedl S.A., Updegraaff W.D., The production of Medical Isotopes without Nuclear reactors or Uranium Enrichment, on-line supplement

[3] Rieber M.S., Anzelloti A., Sanchez-Delgado R.A., Rieber M., Tumor apoptosis induced by ruthenium(II)-ketoconazole is enhanced in nonsusceptible carcinoma by monoclonal antibody to EGF receptor, International Journal of Cancer 112 (3) (2004) 376-384

[4] P. Swain, S. Annapoorani, R. Srinivasan, C. Mallika, U.K. Mudali, R. Natarajan, Separation of ruthenium from simulated nuclear waste in nitric acid medium using n-paraffin hydrocarbon, Sep. Sci. Technol. 49 (2014) 112–120.

[5] P. Swain, C. Mallika, R. Srinivasan, U.K. Mudali, R. Natarajan, Separation and recovery of ruthenium: a review, J. Radioanal. Nucl. Chem. 298 (2013) 781–796.

[6] Magdalena Blicharska • Barbara Bartos´ •Seweryn Krajewski • Aleksander Bilewicz. "Separation of fission produced 106Ru from simulated high level nuclear wastes for production of brachytherapy sources" J Radioanal Nucl Chem, 2013, DOI 10.1007/s10967-013-2570-3

[7] Michael D. Glascock, "An Overview of Neutron Activation Analysis" University of Missouri ResearchReactor (MURR), 2005.

[8] National Isotope Development Center. www. https://www.isotopes.gov

[9] TALYS-based Evaluated Nuclear Data Library (TENDL), https://www-nds.iaea.org.

[10] http://www-naweb.iaea.org/napc/physics/research_reactors

://doi.org/10.1016/j.apradiso.2020.109176.

ICNST 2024
International Conference on Nuclear Science and Technology
6- 8 MAY 2024 | Isfahan, Iran

Radiotherapy dosimetry audit for 6 MV photon beam (Paper ID : 1428)

Nourmandi-pour H.[1], Rafat-Motavalli L.[1,2*], Hoseinian-Azghadi E.[1,2]
[1]*Physics Department, Faculty of Science, Ferdowsi University of Mashhad, Mashhad, Iran*
[2]*Research and Education Department, Mashhad Cancer Charity, Mashhad, Iran*

Abstract

The efficacy of radiation therapy is highly dependent on the precision and accuracy of its delivery, as it directly influences the treatment outcomes of patients receiving this modality. As such, healthcare providers must adopt optimal radiation delivery techniques to ensure that patients receive the highest standard of care possible. Dosimetry audit is a crucial step in ensuring quality and safety in radiation therapy, both nationally and internationally.

To this end, all linear accelerator machines used clinically to treat patients are subject to an on-site dosimetry audit by a team dedicated exclusively to radiotherapy audits. In this study, we audited (Level III) our in-house Monte Carlo (MC) modeling of a clinically used linear accelerator machine, performing high-accuracy 3D conformal radiation therapy (3DCRT).

The present study encompasses the MC simulation of the CIRS thorax phantom model 002LFC along with multiple scenarios pertaining to eight clinical tests utilizing a 6 MV photon beam. The MCNPX code version 2.6.0 has been employed to carry out the simulations. The study results indicate that the Monte Carlo (MC) model used in the research is in good agreement with the measured data. The dose differences at all the measurement points were within the agreement criteria set by the IAEA-1583-TECDOC. This benchmarked MC model can be used to independently verify clinical 3DCRT plans.

Keywords: Audit, Radiotherapy, Dosimetry, Monte Carlo

INTRODUCTION

The success of radiation therapy is greatly influenced by the accuracy and precision of its delivery, as it directly impacts the treatment outcomes of patients undergoing this procedure. Dosimetry audits provide an effective means to verify the quality of various dosimetry methods, as inadequate clinical dosimetry methods can negatively impact patient control and result in complications post-treatment, thereby affecting the patient's survival and quality of life. The significance of dosimetry audits in clinical trials has been well established [1-4], and such audits are being conducted globally [5].

Validation of a treatment planning system's dose calculation algorithm is a complex task that most hospitals cannot perform. To address this issue, the International Atomic Energy Agency (IAEA) has created a set of practical tests for dosimetry calculations. These tests are defined in a technical document called IAEA-TECDOC-1583. The audit dosimetry tests are designed to mimic the normal treatment planning process. A special phantom, known as the CIRS THORAX LFC002, is used during the audit to perform dosimetry tests. During audits, different types of dosimeters are utilized, such as optically stimulated luminescence detectors [6-8], ionization chambers [9-11], radiochromic film [12], and electronic portal imaging devices [13, 14]. The choice of dosimeter can impact the precision of the result and the time frame required to obtain it. In this particular study, we have simulated ionization chambers as dosimeters.

The Level III dosimetry audit, also known as the end-to-end test, for 3D-conformal radiotherapy (3D-CRT) was conducted using primary standard calibrated dosimeters and an on-site audit approach by a dedicated audit team. In recent years, Monte Carlo (MC) methods have become increasingly popular for solving radiation dosimetry problems. These methods have various applications, such as calculating dose values and simulating treatment planning in radiotherapy. Thanks to today's powerful computing codes, it is

possible to simulate exact 3D geometries, including the linear accelerator head, ionization chambers, and special phantoms, to predict patient treatment. This study aims to conduct a dosimetry audit for the benchmarked model of the 6 MV beam of the Siemens Artiste linear accelerator and validate the model's accuracy in terms of dose calculation for 3D-CRT plans.

MATERIALS AND METHODS:

Phantom and treatment couch:

In this study, a pseudo-human phantom named LFC002 CIRS THORAX was used for clinical test measurements. The CIRS phantom has an oval shape with dimensions of 30 cm × 30 cm × 20 cm. In terms of proportion, density and two-dimensional structure, the phantom represents an average human body. This phantom has a body of plastic water, lung and bone with specific electron density of 1.04 $\frac{gr}{cm^3}$, 0.21 $\frac{gr}{cm^3}$ and 1.60 $\frac{gr}{cm^3}$. Inside the phantom, there are 10 holes to hold the replaceable rods, and the ionization chambers are placed inside the replaceable rods. The CIRS phantom with all the above specifications was fully simulated using MCNP code version 2.6.0.

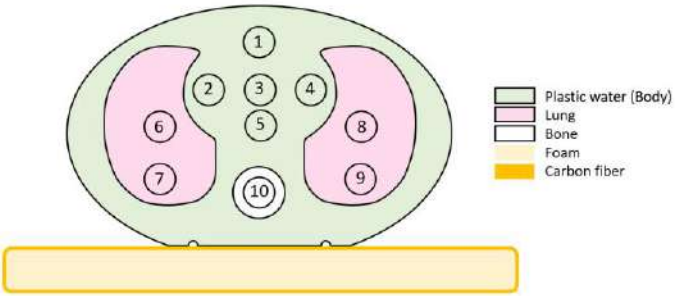

Fig. 1. A schematic view of simulated CIRS THORAX phantom and treatment couch

This study also simulated the precise geometry of the treatment couch. The couch consists of an inner foam material with a density of 0.075 g/cm³ and an outer layer made of carbon fiber with a density of 1.7 g/cm³. The outer layer is 50 cm × 30 cm × 4 cm and has a thickness of 1.8 mm (as shown in Fig. 1). The couch was placed beneath the phantom.

Clinical tests:

The International Atomic Energy Agency recommends a series of dosimetry audit tests in its IAEA-TECDOC-1583 guideline. These tests help confirm various therapeutic techniques used in clinical practice. In this study, the Nuclear Physics Department of Ferdowsi University of Mashhad simulated several of the dosimetry tests available in IAEA-TECDOC-1583 using the MCNPX code version 2.6. The research team also provided the initial phase space file related to the accelerator head for this study. This phase space file underwent validation in our previous study that is currently undergoing peer review. The data related to the Monte Carlo model validation can be requested by contacting the corresponding author.

Monte Carlo Calculations:

To ensure less statistical error and an easier process, the Monte Carlo program was run in two steps. First, the simulation of MLCs and jaws, along with the primary phase space file, was conducted separately. The secondary phase space was then created for specific fields, including 10×10, 10×15, and 8×15 cm^2. In the second step, the absorbed dose values were determined for specific tests. This was achieved by simulating the phantom, couch, and gantry rotation at specific angles. The phase space obtained from the previous step was used in this simulation process. The tally output from MCNP was converted to absorbed dose (PGY) using the following equation:

$$Dose[pGy] = Tally\left[\frac{Mev}{g}.\frac{1}{particle}\right] \times 160.218\left[\frac{pGy}{Mev}\right] \times C\left[\frac{particle}{MU}\right] \times MU$$

Where C is the normalization factor and equals to 7.53897×10^{13} $(particle/MU)$ for our Monte Carlo model. After running each calculation for each specific field at least ten times, the number of statistical errors was reduced to less than 3%. To evaluate the deviation between the measured dose values and the MC-based dose values, the following formula was used.

$$\text{Error } [\%] = \frac{100 \times (D_{CAL} - D_{MEAS})}{D_{MEAS\ REF}}$$

where D_{CAL} is the calculated dose, D_{MEAS} is the measured dose, and $D_{MEAS,REF}$ is the measured dose to the reference point.

Results and Discussion

Monte Carlo-based doses were evaluated for eight tests and 28 points and then compared with the measured doses. The statistical uncertainties for the data points situated within the field region were less than 1%, whereas the statistical error for points located outside the field was less than 4%.

The dose values for three points (3, 9, and 10) related to Case 1 of TECDOC-1583 have been calculated using the Monte Carlo (MC) method. These values are presented in Table 1 alongside the measured doses. The table also shows the agreement criteria, the deviation between the MC-calculated and measured doses, and the pass/fail status. As seen from Table 1, all MC-calculated doses have passed the criteria. The deviation between the calculated and measured doses for test 1 was between 0.08% and 2.5%, which satisfies the agreement criteria.

Table 1. The MC-based and measured doses for test 1 for the TECDOC-1583. It also displays the agreement criteria, the deviation between MC-based and measured doses, and the pass/fail status.

TEST 1	MC base dose (Gy)	Measured dose (Gy)	Agreement criteria (%)	Deviation (%)	Pass/fail
Point 3	2.024±0.020	2.020±0.011	2	0.08	PASS
Point 9	0.185±0.008	0.177±0.002	4	0.39	PASS
Point 10	1.220±0.015	1.270±0.007	3	2.5	PASS

Table2 . The MC-based and measured doses for test 1 for the TECDOC-1583. It also displays the agreement criteria, the deviation between MC-based and measured doses, and the pass/fail status.

TEST 4		MC base dose (Gy)	Measured dose (Gy)	Agreement criteria (%)	Deviation (%)	Pass/fail
Point 5	F1 (G0)	2.016±۰/۰۱۹	2.034±0.011	2	0.89	PASS
	F2 (G90)	2.002±0.۰۱۹	2.048±0.011	3	2.22	PASS
	F3 (G180)	1.934±0.۱۹۱	1.979±0.010	3	0.71	PASS
	F4 (G270)	1.981±0.۰۰9	2.055±0.011	3	3.61	FAIL
	SUM	7.933±0.۰٦٦	8.116±0.021	3	2.26	PASS
	F1 (G0)	0.125±0.006	0.122±0.001	4	0.14	PASS
	F2 (G90)	1.391±0.024	1.377±0.007	3	0.69	PASS

Point 6	F3 (G180)	0.167±0.008	0.153±0.001	4	0.71	PASS
	F4 (G270)	2.758±0.015	2.798±0.015	3	1.93	PASS
	SUM	4.441±0.135	4.450±0.016	3	0.1	PASS
Point 10	F1 (G0)	1.426±0.014	1.492±0.008	3	3.23	FAIL
	F2 (G90)	0.147±0.003	0.150±0.001	4	0.15	PASS
	F3 (G180)	2.687±0.020	2.829±0.015	3	2.5	PASS
	F4 (G270)	0.148±0.002	0.151±0.001	4	0.12	PASS
	SUM	4.409±0.055	4.621±0.017	3	2.61	PASS

The doses calculated by MC for points 5, 6, and 10 for case 4 were evaluated for four individual fields. The deviation between the calculated and measured doses at point 5 ranged from 0.71% to 3.61%. This deviation passed the agreement criteria in almost all points except for the fourth field, where it was slightly higher than the agreement value. The deviation between the calculated and measured doses at point 6 was found to be between 0.1 and 1.93, and it passed the agreement criteria well. For point 10, the deviations ranged from 0.12% to 3.23%, and it passed the criteria for three fields but failed for one field.

During the study, 26 out of the total 28 items were successfully passed, while two items failed during test 4. The cause of the failure may be attributed to the slight discrepancy between the simulated materials of replaceable rods in the simulation and the actual measurement. However, the discrepancies were only about 0.2% - 0.6%, which is

considered acceptable. To address this issue, we plan to modify the simulated material of the CIRS phantom in our future work.

Conclusions

We audited the Monte Carlo model of the 6 MV beam for the Siemens Artiste linear accelerator. Our calculations passed for 26 out of 28 points. However, in two points, our calculations did not pass the agreement criteria. Our future work includes plans to modify the simulated CIRS phantom to improve its conformity. Overall, we have successfully benchmarked our MC model of the linear accelerator head by conducting a level III dosimetry audit for 3D-CRT plans.

References

[1] Kron, T., Haworth, A., & Williams, I. (2013, June). Dosimetry for audit and clinical trials: challenges and requirements. In Journal of Physics: Conference Series (Vol. 444, No. 1, p. 012014). IOP Publishing.

[2] Ibbott, G. S., Haworth, A., & Followill, D. S. (2013). Quality assurance for clinical trials. Frontiers in oncology, 3, 311.

[3] Palmer, A., Mzenda, B., Kearton, J., & Wills, R. (2011). Analysis of regional radiotherapy dosimetry audit data and recommendations for future audits. The British journal of radiology, 84(1004), 733-742.

[4] Pettersen, M. N., Aird, E., & Olsen, D. R. (2008). Quality assurance of dosimetry and the impact on sample size in randomized clinical trials. Radiotherapy and Oncology, 86(2), 195-199.

[5] Izewska, J., Lechner, W., & Wesolowska, P. (2018). Global availability of dosimetry audits in radiotherapy: The IAEA dosimetry audit networks database. Physics and Imaging in Radiation Oncology, 5, 1-4.

[6] Kry, S. F., Dromgoole, L., Alvarez, P., Leif, J., Molineu, A., Taylor, P., & Followill, D. S. (2017). Radiation therapy deficiencies identified during on-site dosimetry visits by the imaging and radiation oncology core Houston quality assurance center. International Journal of Radiation Oncology* Biology* Physics, 99(5), 1094-1100.

[7] Lehmann, J., Dunn, L., Lye, J. E., Kenny, J. W., Alves, A. D., Cole, A., ... & Williams, I. M. (2014). Angular dependence of the response of the nanoDot OSLD system for measurements at depth in clinical megavoltage beams. Medical physics, 41(6Part1), 061712.

[8] Kerns, J. R., Kry, S. F., Sahoo, N., Followill, D. S., & Ibbott, G. S. (2011). Angular dependence of the nanoDot OSL dosimeter. Medical physics, 38(7), 3955-3962.

[9] de Prez, L., Heukelom, S., Jansen, B., Jansen, W., van de Kamer, J., van Klink, W., ... & Wittkämper, F. (2018). An on-site dosimetry audit for high-energy electron beams. Physics and Imaging in Radiation Oncology, 5, 44-51

[10] Lye, J., Kenny, J., Lehmann, J., Dunn, L., Kron, T., Alves, A., ... & Williams, I. (2014). A 2D ion chamber array audit of wedged and asymmetric fields in an inhomogeneous lung phantom. Medical physics, 41(10), 101712.

[11] Hussein, M., Tsang, Y., Thomas, R. A., Gouldstone, C., Maughan, D., Snaith, J. A., ... & Clark, C. H. (2013). A methodology for dosimetry audit of rotational radiotherapy using a commercial detector array. Radiotherapy and Oncology, 108(1), 78-85.

[12] Das, I. J. (Ed.). (2017). Radiochromic film: role and applications in radiation dosimetry. CRC Press.

[13] Miri, N., Lehmann, J., Legge, K., Vial, P., & Greer, P. B. (2017). Virtual EPID standard phantom audit (VESPA) for remote IMRT and VMAT credentialing. Physics in Medicine & Biology, 62(11), 4293.

[14] Miri, N., Lehmann, J., Legge, K., Zwan, B. J., Vial, P., & Greer, P. B. (2017). Remote dosimetric auditing for intensity modulated radiotherapy: a pilot study. Physics and Imaging in Radiation Oncology, 4, 26-31.

[15] Lehmann, J., Alves, A., Dunn, L., Shaw, M., Kenny, J., Keehan, S., ... & Lye, J. (2018). Dosimetric end-to-end tests in a national audit of 3D conformal radiotherapy. Physics and imaging in radiation oncology, 6, 5-11.

[16] Andreo, P. (1991). Monte Carlo techniques in medical radiation physics. Physics in Medicine & Biology, 36(7), 861.

[17] Seco, J., & Verhaegen, F. (Eds.). (2013). Monte Carlo techniques in radiation therapy (p. 20). Boca Raton, FL:: CRC press.

[18] Andreo, P., Burns, D. T., Nahum, A. E., Seuntjens, J., & Attix, F. H. (2017). Fundamentals of ionizing radiation dosimetry. John Wiley & Sons.

ICNST 2024
International Conference on Nuclear Science and Technology
6- 8 MAY 2024 | Isfahan, Iran

An estimation of 106Ru inventory in the high level liquid waste (HLLW) of Iran's 99Mo production industrial facility (Paper ID : 1430)

Kanani Kh.[1,*], Feghhi S. A. H.[1], Shirvani-Arani S.[2], Bahrami-Samani A.[2], Miremad S. M.[2]
[1]*Nuclear Engineering, Shahid Beheshti University, Tehran, Iran*
[2]*Nuclear Science and Technology Research Institute (NSTRI), Tehran, Iran*

Abstract

A high-level liquid waste (HLLW) consisting of various fission products is produced at the ^{99}Mo industrial production facility. Radioisotope ^{106}Ru, as a widely used radioisotope in ophthalmic brachytherapy for the treatment of retinoblastoma and uveal melanoma eye tumors, is one of the valuable radioisotopes that could be isolated from this waste. In this paper, the amount of elemental ruthenium (amount of both stable isotopes and radioisotopes of ruthenium element) in HLLW of industrial ^{99}Mo production in Iran was evaluated by simulation using MCNPX (Monte Carlo N-Particle eXtended) code. The results show that the HLLW resulting from a production cycle, can be a suitable source of ^{106}Ru after a cooling time of over 3 years. Also, around 184 and 48 ^{106}Ru-eye plaques with an average activity of 0.32 mCi can be prepared from HLLW with 3 and 5 years cooling time, respectively.

Keywords: ^{106}Ru eye plaque, High level liquid waste, ^{99}Mo production, MCNPX

1. Introduction

Brachytherapy is one of the treatment methods for uveal melanomas by using eye plaques. For more than 30 years, ophthalmologists have favored Ru-106 Eye Applicators due to their superior design and technical features. Today they are considered as the first choice for treatment with ergonomic design [1]. Brachytherapy of uveal melanoma with ruthenium applicator has advantages such as excellent local control and eye protection with low recurrence. ^{106}Ru applicators were introduced by Prof. Peter Lomatzech in the 1960s and have since been widely used by many ophthalmic oncologists [2]. Owing to the long half-life of ^{106}Ru (1.02 y) [3], the applicators can be used multiple times over a one-year period. They require no assembly, just sterilization before use. Up to 50 cycles are permitted [1]. The main advantage of ^{106}Ru compared to other isotopes is better preservation of vision in the treated eye and less damage to the healthy parts of the eye due to the limited range of its radiation [2]. ^{106}Ru is a beta emitter with a maximum energy of 39 keV and an average energy of 10 keV, which decays to ^{106}Rh. ^{106}Rh is a beta emitter with a half-life of 36 seconds, maximum energy of 3.54 MeV, and an average energy 1.5 MeV decays to ^{106}Pd [3]. The low energy of the emitted beta causes a particularly limited range of beta radiation, delivering a sufficient dose to the tumor while minimizing collateral damage to healthy parts of the eye. ^{106}Ru plaques are also used to treat superficial tumors up to a depth of 5 mm. The high dose gradient of these applicators makes it possible to concentrate the dose inside the tumor and minimize the dose delivering the critical and sensitive structures of the eye. For this reason, in the treatment of small and medium-sized tumors with a thickness of less than 5 mm, these beta emitter eye applicators are preferred

[4,5]. Wilkinson et al showed that for the treatment of thin melanoma, ^{106}Ru plaques usually deliver the dose to a smaller volume and with less side scatter than ^{125}I plaques of the same size. Also, for a given tumor, modeling treatment with ^{106}Ru plaque gives statistically significant smaller doses to the optic disc and macula. This feature is useful when assessing the risks of radiation retinopathy and radiation optic neuropathy [6]. ^{106}Ru brachytherapy for uveal melanoma provides excellent local control rates and eye preservation with a relatively low recurrence rate. As in most centres, the first choice for treating choroidal and uveal melanoma at the Liverpool Ocular Oncology Centre is brachytherapy. ^{106}Ru plaques have been used there since the service was established by Professor Bertil Damato in 1993, with excellent results [1]. There is enough experience resulting more than 25 years of using this method of treatment, and the number of hospitals that use this method to treat intraocular melanomas is increasing day by day [7]. The first step to localize the production of such plaques is the production and extraction of ^{106}Ru radioisotope. One of the methods of producing ^{106}Ru is fission. The fission yield of this radioisotope for ^{235}U is 0.004015 which is about 93.42 and 93.51 percent less than the fission yield of ^{99}Mo and ^{137}Cs, respectively [3]. So, it would not be cost-effective to use targets containing ^{235}U specifically to extract ^{106}Ru. Waste from spent fuel recycling facilities and HLLW waste from ^{99}Mo production facilities are two sources containing ^{106}Ru from which the extraction process can be carried out. Currently, Iran is not allowed to reprocess, but it is planning to produce ^{99}Mo by fission method on an industrial scale. In the domestic production process of ^{99}Mo with the modified Amur method, LEU targets

are irradiated in the Tehran research reactor for 6 days with power of 4 MW and then, after passing a 1-day cooling period, enter the respective hot cells to perform the process. Here, targets are dissolved in concentrated acid through a special mechanism. After the temperature of the solution reaches the ambient temperature, the solution containing various actinides and fission products is loaded into the alumina column. At this step, molybdenum and a small percentage of impurities (which includes about 40% of Ru) are trapped in the alumina column and the other fission fragments pass through it and enter the HLLW. This waste with a long cooling period is a suitable option for the production process of ^{106}Ru.

Calculation of the activity and production rate of radioisotopes produced in the fission or neutron activation process can be done by using calculation codes such as ORIGEN and MCNP. The ORIGEN code was created by famous and reputable nuclear institution in United States, Oak Ridge National Laboratory (ORNL) was written at ORNL in the late 1960s and early in 1970s by Bell and Nichols [8]. ORIGEN is a widely used deterministic computer code to solve Bateman equations, and is capable of determine isotopic composition balance submitted by a neutron flux over the time [9]. This code also can be used for calculating the buildup, decay, and processing of radioactive materials. ORIGEN (Oak Ridge Isotope Generation code) calculates time-dependent concentrations, activities, and radiation source terms for a large number of isotopes simultaneously generated or depleted by neutron transmutation, fission, and radioactive decay [10-12].

The particle radiation transport code MCNP, which stands for Monte Carlo N-Particle, is a general purpose three dimensional simulation tool that transports 37 different particle types by using Monte Carlo method, for criticality, shielding, dosimetry, detector response, and many other applications [13]. Monte Carlo Method is a type of computational algorithms that depend on recurring random sampling in computation of results. In all its application Monte Carlo Method has yielded better results than any other method that can be used. The stochastic process used by Monte Carlo Method gives a model of a problem that would otherwise have been hard to solve given discrete solutions. As such, Monte Carlo is can be defined as a simulation method that describes a system of an experimental method [14,15]. During years, different versions of MCNP were created, such as MCNP4B, MCNP4C, MCNP5, MCNPX 2.6.B, MCNP6, MCNPX that each one of them provided more capabilities for particle transport than the previous version [13,16-18]. The MCNP6 code incorporates a more complete set of transport physics and features than any previous member of the MCNP family of codes [13]. The results of MCNP calculations are more accurate and reliable due to the use of the Monte Carlo method than the results of the ORIGEN code that is a deterministic code. Another advantages of the MCNP code is that it can be run in parallel using MPI (Message Passing Interface) [19] and is easy to use to perform complex geometry calculations compared to conventional neutron transport deterministic computer codes such as ORIGEN [20].

In this article, an attempt will be made to evaluate an estimation of ^{106}Ru inventory in the high level liquid waste (HLLW) of Iran's ^{99}Mo production industrial facilities by

simulation using MCNPX Monte Carlo code. The inventory of fission and activation products along with the produced actinides, especially the inventory ^{106}Ru and its other produced isotopes and radioisotopes will be calculated after the end of irradiation and during different cooling periods. the optimal conditions for reducing impurities and increasing the purity of ^{106}Ru will be determined. At the end, the possibility of preparing ^{106}Ru eye plaques using ^{106}Ru extracted from such waste will be evaluated.

2. Materials and Methods

2.1. Target batch and radiation mechanism

In order to meet the demand of medical centers for ^{99}Mo (about 100-120 Ci 6-day per week), it is necessary to irradiate 9 native LEU targets in each weekly production cycle. Each LEU target contains 3 g ^{235}U with enrichment of 19.75% ± 0.2 and the chemical form of U_3O_8-Al_x is placed in an aluminum sheath with dimensions of 205 × 51 × 1.5 mm.

Table 1. Mini plates characteristics

Unit	Final LEU mini plate	Charactristic
mm	167×38.5×0.7	Meat dimention
	U_3O_8-Al_x	Chemical formula
%	19.75% ± 0.2	Uranium enrichment
g	3	^{235}U Mass
g	5.2	Al amount in meat
g	23.2	Meat mass
g	30.1	Al mass in sheath
mm	205 × 51 × 1.5	Mini plate dimention
g	53.3	Mini plate total mass

The targets are fixed in place in a holder similar to Figure 1, and the holder assembly and 9 LEU targets form a batch.

Fig. 1. Holder for irradiation 9 mini plates

The described batch above is placed in the center of the irradiation channel, in the core of the Tehran research reactor, and is irradiated with a specified power for the necessary time. The core of the Tehran research reactor is made of a 6 × 9 array, including rectangular cubes with approximate dimensions of 7 × 8 × 60 cm (effective). In this article, the following arrangement is used to perform calculations in the MCNPX code. In this arrangement of the core, the standard fuel complexes are characterized by two types, A and NRF. The geometric characteristics of both types of fuel are in according to the standard fuel of Tehran reactor and the NRF010 fuel is fresh and with 20% enrichment. Two types of fuel, ASO and NRF, have been used for control complexes.

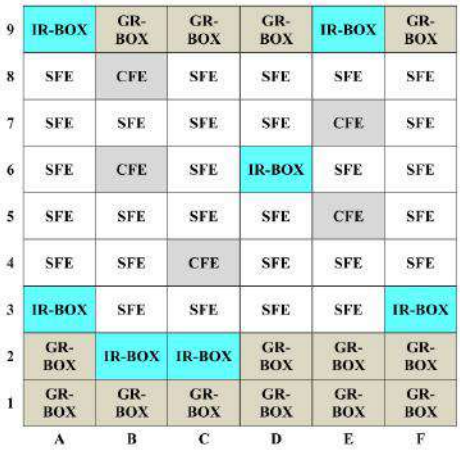

Fig. 2. Tehran reearch reactor core aray simulated by MCNPx code

Neutronic parameters as well as the reactivity of core 70 in critical state were calculated using MCNPX code and the results showed that shutdown margin (pcm) and safety reactivity factor (SRF) are more than 3000 and more than 1.5, respectively. The exit of SR control rods was considered to be about 57% and RR control rod to be about 45.9%. In this situation, the multiplication factor is equal to 0.99822. In this article, channel D6 and operating power of 4 MW were selected for batch irradiation. It should be noted that the calculations in this article focus on the estimation of fission and activation products along with actinides, especially ^{106}Ru and its other produced isotopes and radioisotopes in hot targets, but neutronic parameters of the core or thermos hydraulic analyzes related to the loading of targets are not important.

2.2. HLLW in ^{99}Mo production facilities

Figure 2 shows the production chain of ^{99}Mo. It illustrates that the processing facility consists of different parts. The generated waste in ^{99}Mo production facilities from fission is categorized in Figure 3.

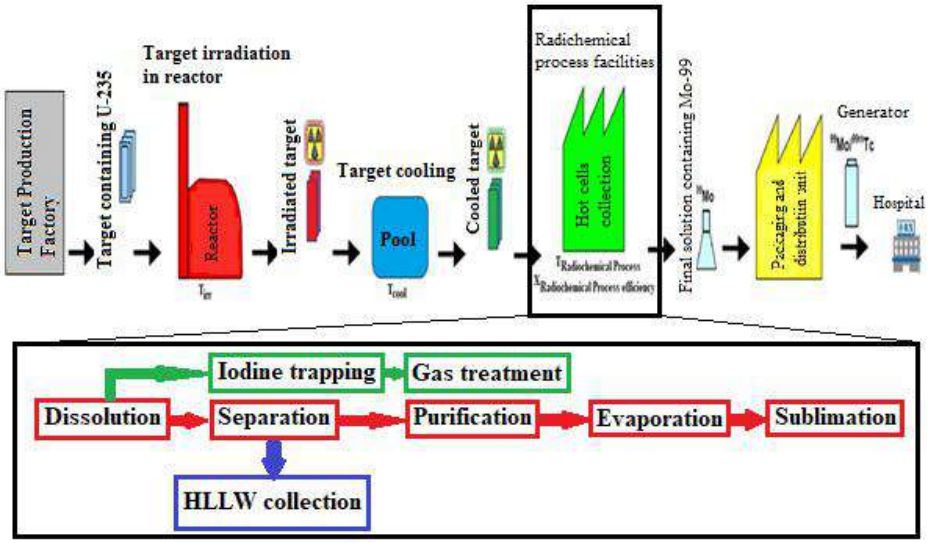

Fig. 2. ^{99}Mo Production chain

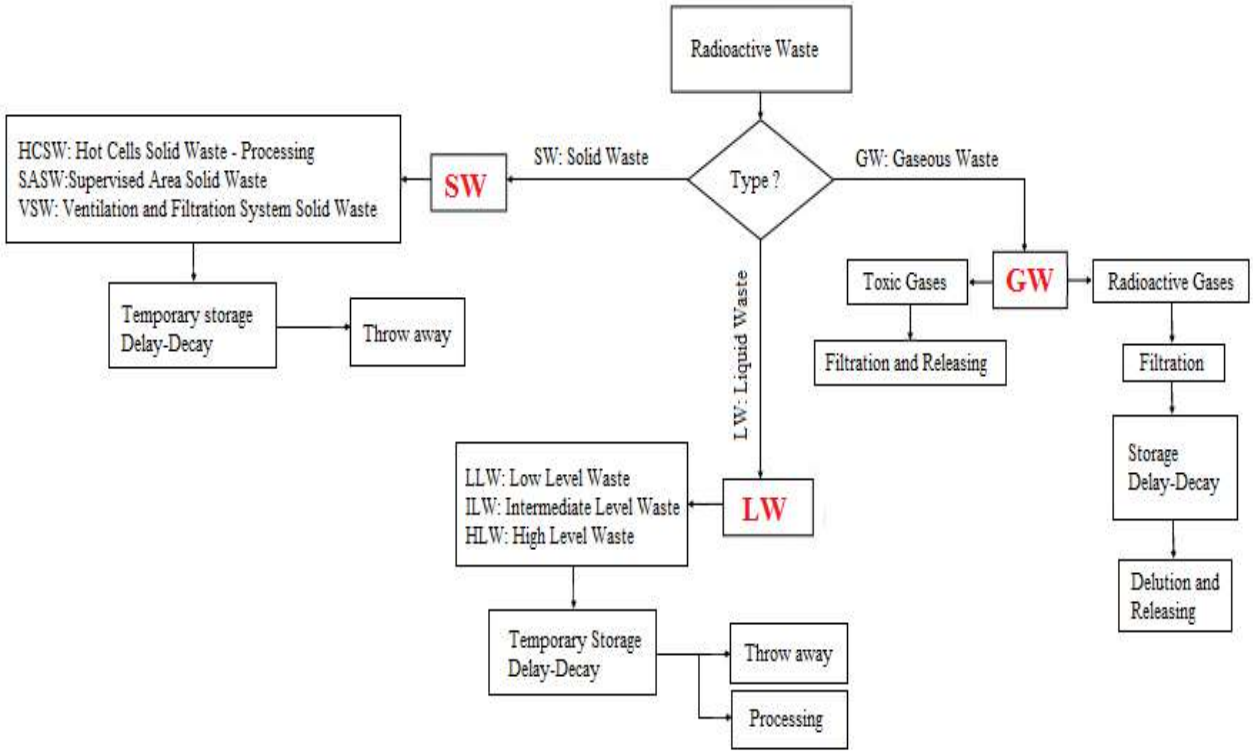

Fig. 3. Wastes in ^{99}Mo Production facilities

The HLLW is produced in the ^{99}Mo production facility, in the separation unit, after loading the solution resulting from dissolution and washing the separation column with nitric acid. The estimated volume of this waste is about 13 liters, which includes most of the fission fragments. The experimental studies of the production process show that out of 100% of ruthenium present in hot targets, about 25% enters the iodine trapping and gas purification section in gaseous form. A total of 15% will also be present in other liquid wastes or in the

separation column. In other words, only 60% of the produced ruthenium in hot targets will be collected in HLLW.

2.3. Method

After simulating the core of the Tehran Research Reactor using MCNPX code, the batch set in channel D6 was added to the geometry (Figure 4).

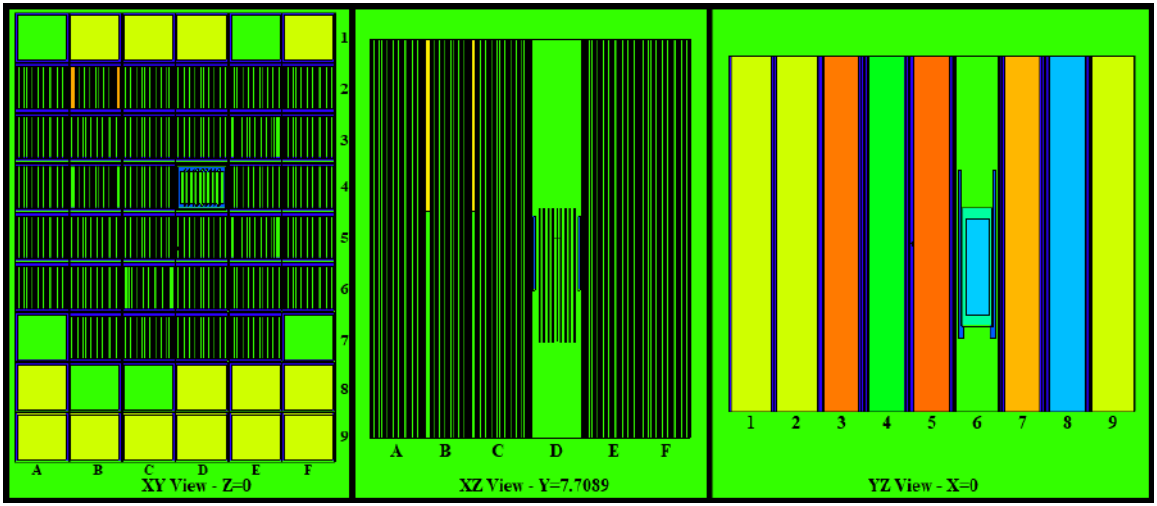

Fig. 3. Reactor core geometry simulated by MCNPx code with bstch ser placed in channel D6

By using the BURN card, the inventory of meat and LEU targets sheaths in the batch (9 LEU targets) was calculated after 6 days of irradiation with an operating power of 4 MW,

1-day cooling time (the beginning of the process), 1-day radiochemical process time (the end of the process (HLLW=0) and start collecting in reservoirs), and then, 30, 360, 1080 and 1800 days after collection in reservoirs. The inventory of isotopes and radioisotopes of ruthenium in HLLW was calculated and analyzed with the assumption of 60% probability of presence in the specified periods. In this work, the quality of the ^{106}Ru purity (by removing the other ruthenium radioisotopes) and the amount of mass specific activity were evaluated to prepare one of the models of eye plaques made by the Bebig company, considering three ranges of maximum, medium and minimum activity. The models of eye plaques made by this company are given in Table 2. To prepare a typical plaque, in the relevant calculations, the efficiency of extracting ^{106}Ru from HLLW and manufacturing process was assumed to be about 50% with high purity. The maximum activity required to prepare each plaque is also given in Table 2.

Table 2. The maximum activity of ^{106}Ru required to prepare any type of plaque

Maximum activity required for preparing by considering 50% efficiency (mCi)	Maximum activity (mCi)	Maximum activity (MBq)	Nominal activity (MBq)	radius of curvature (mm)	Diameter (mm)	Type
0.64	0.32	11.8	7.4	12	11.6	CCZ
0.64	0.32	11.8	7.4	12	11.6	CCY

0.64	0.32	11.8	7.4	12	11.6	CCX
0.36	0.18	6.6	4.1	12	11.6	CXS
1.18	0.59	21.9	13.7	12	15.3	CCA
1.82	0.91	33.8	21.1	12	17.9	CCD
2.22	1.11	41.4	25.9	12	20.2	CCB
3.2	1.6	59.2	37	13	22.3	CGD
3.49	1.74	64.5	40.3	13	24.8	CCC
1.72	0.86	32	20	12	19.8	COB
1.96	0.98	36.2	22.6	14	25.4	COD
0.92	0.46	17.1	10.7	12	19.8	COE
2.72	1.36	50.4	31.5	14	25.4	COC
0.86	0.43	16	١٠	12	15.3	CIA
1.64	0.82	30.2	18.9	12	20.2	CIB

3. Results and Discussion

Table 3 shows the possible radioisotopes of ruthenium in the HLLW waste generated during one run at the ^{99}Mo industrial production facility in Iran. This inventory is shown for different delay-decay times after HLLW storage (t=0) and 60% probability of presence in HLLW.

Table 3. Possible ruthenium radioisotopes present in HLLW of ^{99}Mo industrial production facilities in Iran

Activity (Ci) in HLLW per number of days after collection in reservoir					Half-Life (s)	Ru Radioisotopes
1800	1080	360	30	0		
1.476E-12	3.0012E-07	0.09954	33.744	57.312	3390941	^{103}Ru
0.030744	0.11778	0.45114	0.8352	0.8832	32123520	^{106}Ru
1.1256E-13	1.1262E-13	1.1262E-13	1.1262E-13	0.10752	15984	^{105}Ru
0	0	0	7.746E-22	1.0068E-18	244512	^{97}Ru

Table 3 shows that at the beginning and right after the storage of the mentioned waste, the ^{103}Ru activity is extremely higher than ^{105}Ru and ^{106}Ru radioisotopes. This is due to the higher fission yield of ^{103}Ru (fission yield of ^{103}Ru, ^{105}Ru and ^{106}Ru radioisotopes is 0.030309, 0.009642 and 0.004015, respectively [3]). Also, the results show that the production of ^{97}Ru can be ignored. With the start of the delay-decay period, the reduction of ^{106}Ru is done slowly due to its higher half-life, while the ^{105}Ru activity is almost zero after the 30-day delay-decay time. After a one-year storage period, the activity ^{106}Ru/^{103}Ru ratio will be 4.53. Some important characteristics of HLLW that should be considered for extracting ^{106}Ru are given in the table 4 for different delay-decay periods after storage (t=0).

Table 4. Characteristics of extracted ruthenium from HLLW in different delay-decay periods

Volume specific activity ^{106}Ru) ((Ci)/HNO_3(cc)	Mass specific activity ^{106}Ru) (Ci)/Total (Ru(g)	Concentration of Ru	^{106}Ru/^{103}Ru activity ratio	Amount of Ru (mg)	Time (day)
6.79E-05	96.49	0.704	0.015	9.153	At the begining of storage
6.42E-05	99.31	0.647	0.025	8.41	30
3.47E-05	62.20	0.558	4.53	7.253	360
9.06E-06	16.47	0.550	392443	7.15	1080

2.36E-06	4.32	0.548	20829268293	7.124	1800

Since high purity is important for radioisotope production in eye plaque brachytherapy applications, it can be stated that the HLLW of ^{99}Mo facilities with a storage period of at least 3 years can be a suitable option for the production of ^{106}Ru. Although, longer storage periods, for example 5 years, leads to an increase in the ^{106}Ru/^{103}Ru activity ratio, while the concentration of the ruthenium element in the waste remains almost constant, it results a lower mass and volume specific activity, which the extraction process of ^{106}Ru is not economical. Table 5 shows the number of eye plaques with three levels of maximum, medium and minimum activity that can be produced from two HLLW wastes with a storage period of approximately 3 and 5 years. It shows that in the worst case, from a HLLW with a long storage period of 5 years, 8 plaques with CCC model, which have the highest activity, can be produced.

Table 5. The number of eye plaques with three levels of maximum, medium and minimum activity can be made from two HLLW wastes with a storage period of approximately 3 and 5 years

The number of plaques that can be prepared		Waste volume required in each extraction process (cc)		^{106}Ru activity to be extracted in a selected amount of waste to prepare plaques	Plaque activity (mCi)	Plaque type	Activity range
HLLW-1800	HLLW-1080	HLLW-1800	HLLW-1080				
8	33	1474	385	3.486	1.743	CCC	Max
48	184	270	70	0.638	0.319	CCZ-CCY-CCX	Mid
86	330	151	39	0.356	0.178	CXS	Min

4. Conclusion

Using of ^{106}Ru eye plaques for the treatment of eye tumors in brachytherapy is increasing. Extraction of pure ^{106}Ru from fission wastes is the first step to prepare such plaques. In this article, the feasibility of producing and extracting pure ^{106}Ru radioisotope to prepare ^{106}Ru eye plaques with three levels of minimum, medium and maximum activity was evaluated by using the HLLW produced in ^{99}Mo industrial production facilities in Iran. The Tehran research reactor was simulated with the MCNPx code and the batch containing 9 LEU targets was irradiated for 6 days with power of 4 MW. The HLLW produced after the ^{99}Mo separation process was collected in the reservoir and the inventory of fission and activation products along with actinides, especially ^{106}Ru and its other isotopes and radioisotopes in hot targets was estimated. The inventory and activity of possible ruthenium radioisotopes in HLLW waste were calculated for different delay-decay times after HLLW storage (t=0) and the probability of 60% presence in HLLW waste. The results showed that the activity

of ^{103}Ru is significantly higher than ^{105}Ru and ^{106}Ru radioisotopes at the beginning of waste storage. By applying longer decay-delay periods, due to the shorter half-life of other ruthenium radioisotopes compared to ^{106}Ru, the impurities of ^{106}Ru decay and will be removed. So that after 1 and 3 years of HLLW storage, the ^{106}Ru/^{103}Ru activity ratio was obtained 4.53 and 392443, respectively. Thus, by applying a 3-year delay-decay period, 33, 184, and 330 ^{106}Ru eye plaques can be prepared with maximum, medium, and minimum activity, respectively.

References

[1] Ophthalmic Brachytherapy, Ru-106 eye applicators and I-125 ophthalmic seeds, Eckert & Ziegler, Germany, www.bebig.com.

[2] Jager MJ, Desjardins L, Kivelن T, Damato BE (eds), "Ruthenium- 106 Brachytherapy", Current Concepts in Uveal Melanoma, Dev Ophthalmol. Basel, Karger, 2012, vol 49, pp 27–40.

[3] Evaluated Nuclear Data File (ENDF), htps://www-nds.iaea.org.

[4] Thomson R, Rogers D. Monte Carlo dosimetry for I125 and P103d eye plaque brachytherapy with various seed models. Medical physics. 2010;37(1):368-76.

[5] Barbosa N, da Rosa L, Facure A, Braz D. Brachytherapy treatment simulation of strontium-90 and ruthenium-106 plaques on small size posterior uveal melanoma using MCNPX code. Radiation Physics and Chemistry. 2014; 95:224-6.

[6] The British Journal of Radiology, 81 (2008), Comparison of Ru-106 and I-125 plaques for treatment of shallow choroidal melanoma lesions, Wilkinson DA, Kolar M, Fleming PA, Singh AD.

[7] Mowlavi AA, Yazdani M. Monte Carlo simulation of two 106Ru eye plaques in a new mathematical human eye model. Iranian Journal of Nuclear Medicine. 2008;16(2):16-22.

[8] Kazimi, Mujid S.; Pilat, Edward E., "Systems Analysis of the Nuclear Fuel Cycle", "ORIGEN 2.1", 22.351-Spring2003, local: IMSCP-MD5-109dfed10fae0745513a0569e5327a2f, http://hdl.handle.net/1721.1/39662

[9] Daniel C, Claubia P, André C, Maria A F V, "GB -A PRELIMINARY LINKING CODE BETWEEN MCNP4C AND ORIGEN2.1 - DEN/UFMG VERSION" 2009 International Nuclear Atlantic Conference - INAC 2009. ISBN: 978-85-99141-03-8

[10] Gokhan Yesilyurt, Kevin T. Clarno, and Ian C. Gauld, "MODULAR ORIGEN-S FOR MULTI-PHYSICS CODE SYSTEMS", International Conference on Mathematics and Computational Methods Applied to Nuclear Science and Engineering (M&C 2011), Latin American Section (LAS) / American Nuclear Society (ANS), May 8-12, 2011, ISBN 978-85-63688-00-2

[11] Ariff Shah Ismail*, Khaironie Mohd Takip, Muhammad Khairul Ariff Mustafa, Abul Adli Anwar, "RTP: RADIONUCLIDES INVENTORIES CALCULATION USING ORIGEN CODE', Malaysian Nuclear Agency, Bangi, 43000, Kajang, Selangor Darul Ehsan, Malaysia

[12] Oak Ridge National Laboratory (ORNL). (2002). ORIGEN 2.2 Isotope Generation and Depletion Code. Tennessee

[13] Goorley, T., et al. Features of MCNP6. Ann. Nucl. Energy (2015), http://dx.doi.org/10.1016/j.anucene.2015.02.020

[14] Shultis J., Faw R. An MCNP Primer. URL: https://www.mne.kstate.edu/ jks/MCNPprmr.pdf.

[15] Mohammad Qadr Hiwa, "THE USE OF THE MCNP CODE FOR RADIATION DAMAGE CALCULATIONS", DOI: https://doi.org/10.15688/mpcm.jvolsu.2021.1.5

[16] Hughes, H.G., Waters, L.S., 1996. ''Many-Particle MCNP'', Memo, XTM: 96–91. Los Alamos National Laboratory.

[17] Hughes, H.G., Prael, R.E., Little, R.C., 1997a. ''MCNPX – The LAHET/MCNP Code Merger,'' Memo XTM-RN 97-012. Los Alamos National Laboratory.

[18] Hughes, H.G. et al., 1997b. ''MCNPXTM – The LAHETTM/MCNPTM Code Merger'', LAUR-97-1638, Los Alamos National Laboratory. In: Presented at SARE-3, Simulation of Accelerator Radiation Environments, Tsukuba, Japan, May 7–9, 1997.

[19] Walker DW. An embarrassingly parallel framework for running EGSnrc / BEAMnrc / DOSXYZnrc, FLUKA, MCNP / MCNPX, GEANT4 and PENELOPE on grid and cluster computers 2015.

[20] Fibra Rhoma Firmanda, "Conversion of ORIGEN2 Output for MCNP6 Calculation", 2020 Annual Nuclear Safety Seminar (SKN). ISSN: 1412-3258 © 2020 BAPETEN – FMIPA UI 197

ICNST 2024
International Conference on Nuclear Science and Technology
6- 8 MAY 2024 | Isfahan, Iran

The role of artificial intelligence in radiotherapy (Paper ID : 1441)

Kamyab S.[1], Rafat-Motavalli L.[1,2*], Miri-Hakimabad H.[1,2], Hoseinian-Azghadi E.[1,2]
[1]*Physics Department, Faculty of Science, Ferdowsi University of Mashhad, Mashhad, Iran*
[2]*Research and Education Department, Mashhad Cancer Charity, Mashhad, Iran*

Abstract

Radiotherapy is a highly complex medical treatment that involves several steps. To ensure proper quality assurance, each step of the radiotherapy process is subjected to rigorous testing and verification. For each patient receiving radiotherapy, a treatment plan is prepared using treatment planning system (TPS), and the patient is then irradiated based on the plan. The purpose of implementing artificial intelligence (AI) in radiotherapy is to verify the quality assurance of dose calculations and treatment plans suggested by TPS, as well as to optimize the treatment plan. In the present review, we have undertaken a comprehensive search using pertinent key terms, such as "artificial intelligence," "dose prediction," and "quality assurance," to provide an overview of the role of AI in radiotherapy. The search was conducted from 2020 to the present and has yielded a total of 169 relevant articles, which have been meticulously reviewed and analyzed. The insights gleaned from this review shed light on the current state of AI research in radiotherapy. Selection process identified articles that use CT images, RT structure, RT plan, dose prescription, and beam shaping features to predict 3D dose, DVH, and specific dose points in tissue. Various AI networks have been used to achieve the study's goals, with deep learning networks receiving more attention. These networks have more hidden layers,

resulting in highly accurate outputs. Convolutional networks are more suitable for processing computed tomography images. Among these networks, U-Net, Res-Net, and Dense-Net are commonly used because of their ability to quickly process a large amount of data. The U-Net networks take input data and reduce its volume while retaining the basic features. They then deliver the output in the same size as the input to the user. This allows them to process large amounts of data quickly and with minimal errors.

Keywords: radiotherapy, artificial intelligence, quality assurance, deep learning, U-Net network

INTRODUCTION

Cancer remains one of the leading causes of premature mortality globally. In fact, it is ranked as either the first or second leading cause of premature death (between ages 30 and 69) in a total of 134 out of 183 countries. Notably, it also ranks third or fourth in 49 other countries.[1] According to statistics from GLOBOCAN, there were 137,198 new cases of cancer in Iran in 2022.[2] Figure 1 presents a graph with statistics for all cancer types.

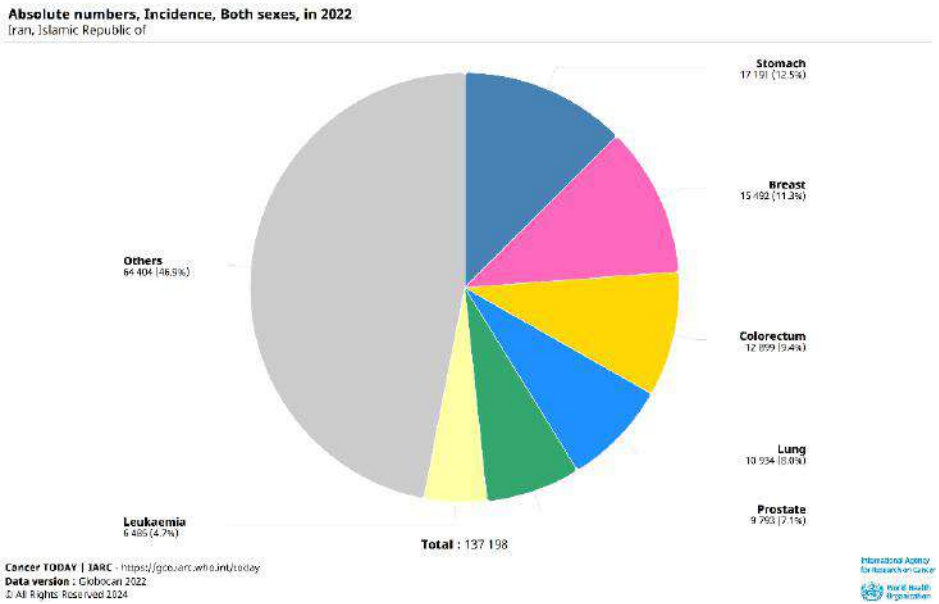

Fig. 1. The incidence of cancer in 2020 in Iran

Cancer can be treated through a variety of methods such as surgery, chemotherapy, radiotherapy, or a combination of these. Radiotherapy is one of the most effective cancer treatments available today, and almost 50% of patients receive radiotherapy as a part of their treatment.[3] External radiotherapy is a widely used method in the field of radiation therapy. Intensity-modulated radiation therapy (IMRT) and volumetric-modulated arc therapy (VMAT) are two notable techniques employed in external radiotherapy. Creating an effective treatment plan is a complex process that involves significant effort from both treatment planners and radiation oncologists. The quality of the resulting treatment plan is highly dependent on the personal experience of the professionals involved, and modifying

and recalculating the plan can be a time-consuming task.[4] In the two mentioned treatment methods, the physician first contours the boundary of the tumor volume and the surrounding healthy tissues in the CT images. In the next step, the planner designs a treatment plan according to the information received from the physician, and then, according to this plan, the patient is exposed to radiation.[5] Each step of the radiotherapy process is subjected to rigorous testing and verification to ensure proper quality assurance. Various steps of radiation treatment, such as contouring images, treatment planning, dosimetry, quality assurance of dose calculations, and optimizing the treatment plan can be improved with AI. This study aims to review the role of AI in the dose calculations. The present study aims to investigate the role of AI in the field of dose calculations. By virtue of its ability to learn and perceive, AI can predict doses without actually performing the calculations. This feature of AI not only reduces errors but also saves time.

Search strategy

We have conducted a thorough investigation to explore the impact of AI on radiotherapy. Firstly, we searched the Google Scholar database from 2020 onwards using the keywords "artificial intelligence", "dose prediction" and "quality assurance". The search yielded 169 articles that covered all aspects of radiotherapy, such as medical image contouring, treatment design, dosimetry, and quality assurance review. To conduct a more in-depth analysis of the articles, only those that utilized AI network architecture with input features such as CT images, RT structures, RT plans, dose prescriptions, and beam shaping features,

and output features such as 3D dose prediction, DVH, and specific dose points in the tissue were considered.

Reviewed topics

AI is a data-driven agent designed to imitate human intelligence, and the origin of AI can be traced back to the invention of robots. John McCarthy coined the term "Artificial Intelligence" in 1955 and defined it as "the science and engineering of building intelligent machines".[7] AI is a vast field that comprises several sub-branches, each having a different network architecture. Figure 2 shows the subsets of AI.

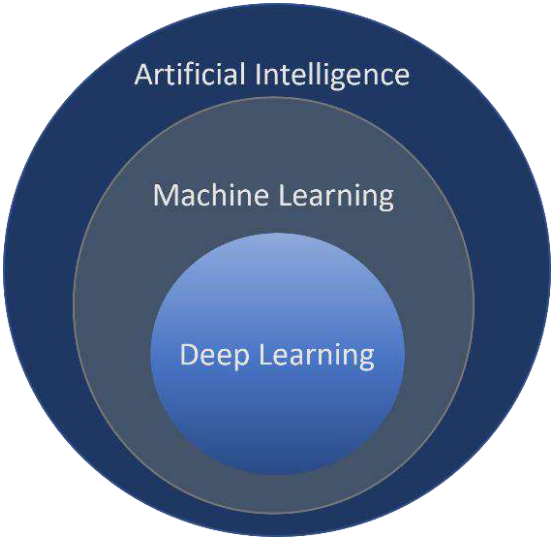

Fig. 2. Subcategories of AI

Machine learning (ML) is a subset of AI that enables machines to be trained through algorithms and statistical techniques with data and achieve AI to predict the outcome, so the end result, with more experience or training, improves. [8] Supervised ML methods can be used to automatically segment images by analyzing previously labeled data and constructing image representations using predefined filters. However, while machine learning techniques are more efficient with image samples and have more complex structures, they are often less accurate than deep learning (DL) techniques. [9]

Neural networks were formed after simulating the human brain to understand multiple information. In 1943, McCulloch and Pitts tried to understand how the brain can produce complex patterns using interconnected stem cells called neurons.[10] Unlike ML, where the user must determine useful features for the segmentation process, with DL, useful features are determined by the network without human intervention. [11] Figure 3 shows the difference in feature extraction between machine learning and deep learning.

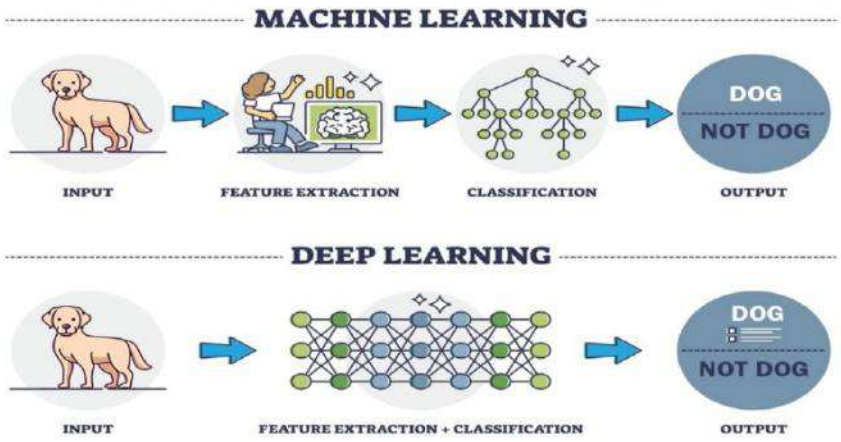

Fig. 3. Feature extraction difference between machine learning and deep learning

The name of convolutional neural networks (CNN) is derived from the mathematical linear operation between matrices called convolution. CNNs are a type of DL that entered the field of AI to process image structures. In the algorithms of CNNs, the main features are preserved and made into a form that makes their processing easier; then they are transferred to the next layer. CNNs are a good choice for big data. Each CNN includes three types of main layers: 1) convolutional layers, 2) pooling layers, 3) fully connected layers, each layer has its own task.[12] Figure 4 shows different layers of a CNN.

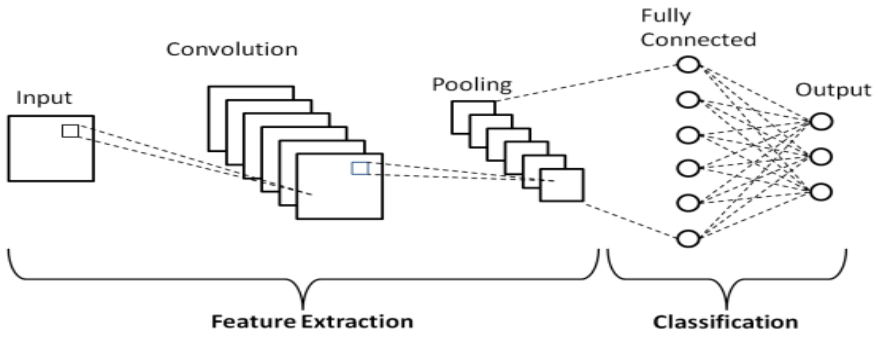

Fig. 4. Hidden layers of a convolutional neural network

U-Nets have shown great success in segmenting medical images and denoising captured images.[13] In this architectural network, the input data is first placed in a decreasing path, which leads to a reduction in dimensions, and the more layers there are, the more features are considered, and then, in an incremental path, the output is delivered to the user in the dimensions of the input. Figure 5 shows a view of the U-Net network architecture. In this way, a large data volume can be processed in the shortest possible time without losing its important and essential features. Throughout history, themes like Dense-Net, Res-Net, etc., have been added to the U-Net architecture network to improve user-specific targeted performance.[14] Figure 6 presents a schematic representation of the U-Net multi-shot approach proposed for segmenting areas affected by COVID-19.

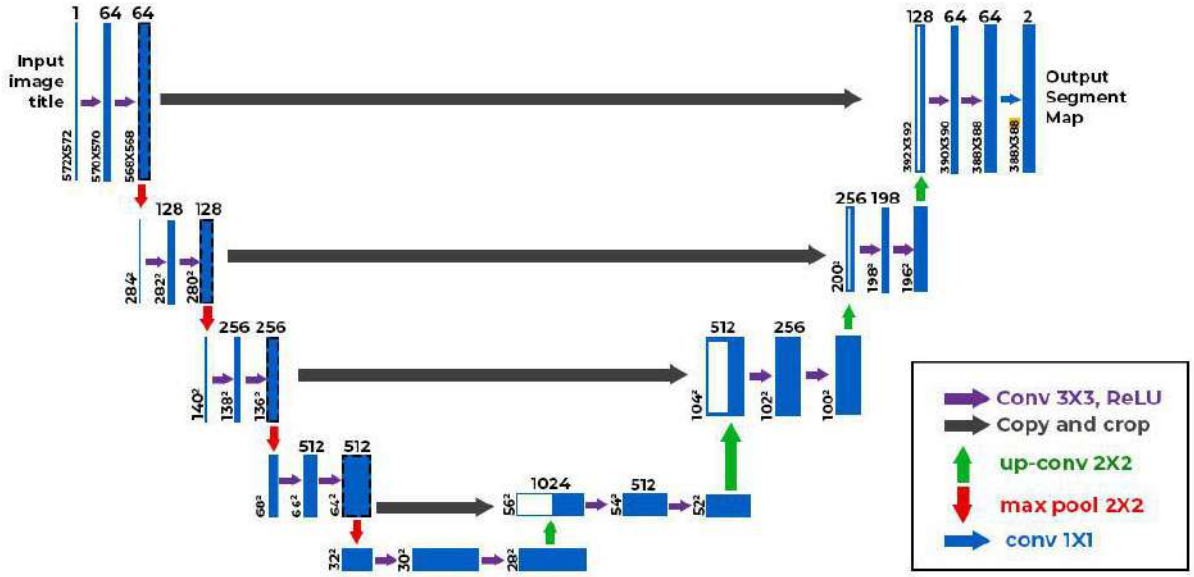

Fig. 5. U-Net architecture network

The Monte Carlo method is a technique used to estimate dose. However, due to its iterative nature and stochastic estimation of numerous probability density functions, it takes a long time to compute. Monte Carlo simulations are typically used to generate large sets of training and validation data for AI from CT images and treatment plans. Both AI and Monte Carlo methods have very small dose calculation errors, but the processing time is significantly different. AI processing time is usually a few minutes, while Monte Carlo processing time can take a few hours.[15]

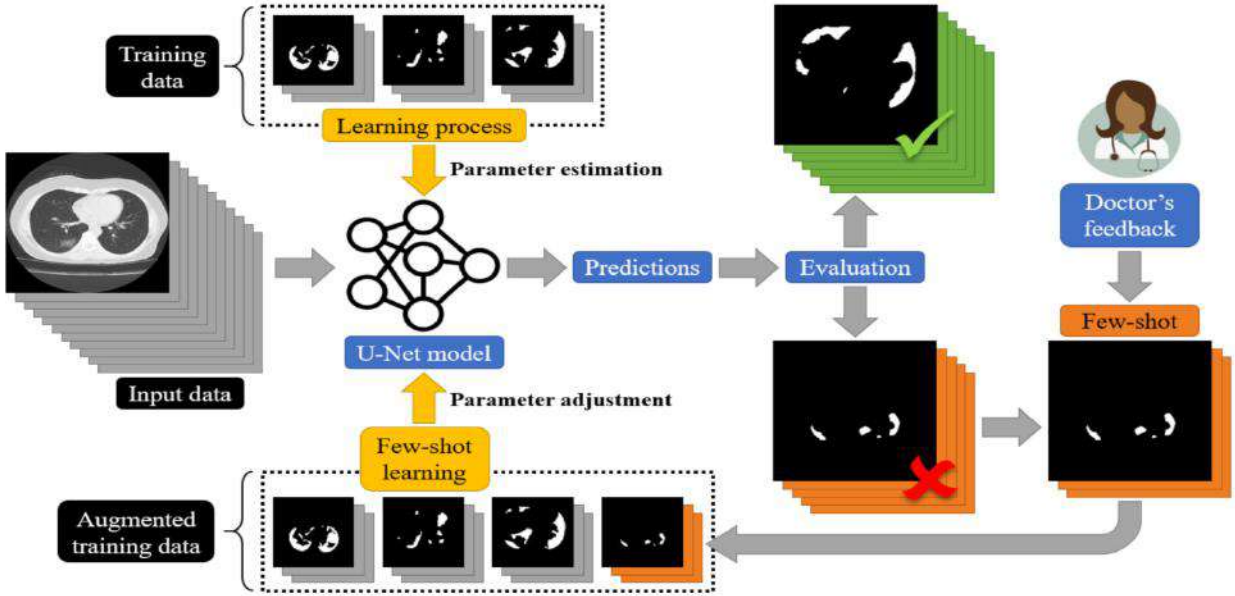

Fig. 6. A schematic representation of the proposed few-shot U-Net for the segmentation of COVID-19 infected areas

Results

Table 1 contains a summary of all the articles that were chosen for this study. In this table, we have first mentioned the name of the author of the article and the year of its publication. In the next part, we have given the name of the architecture network of AI used in each article. Also, for each article, we have specified the input and output of each program, and finally, we have placed the result of each research for review and comparison in the last column of the table. Table 1 shows that the CT image is a common input among all network

architectures, making it reasonable to use convolutional layers. The table indicates that only deep learning architectures have been employed, with U-Net receiving greater emphasis.

Discussion

The present study was conducted in order to investigate the role of artificial intelligence and compare its different network architectures in radiotherapy. The results of the study on the articles that have researched in this field showed that the U-Net architecture network has a better ability to process radiotherapy program data than other artificial intelligence architecture networks. U-Net is a convolutional neural network, so it can be used for image data, and since it reduces the volume of data during processing, it is used for large volumes of data.

Table 1. The list of selected articles that have been researched in the field of AI in radiation therapy from 2020 onwards.

reference	year	network	Training sets	input	Output	result

Lingpeng Zeng et al. [16]	2023	modified U-Net	307 cancer patients underwent VMAT, randomly divided into 246 and 61 cases for training and testing	CT, radiotherapy dose images exported from the treatment planning system, MDose distribution	high-quality voxel-wise prePSQA dose distribution	qualitative and quantitative experimental results show that the proposed prediction method could achieve comparable or better performance on MDose prediction over other approaches in terms of spatial dose distribution, dose–volume histogram metrics, gamma passing rates, mean absolute error, root mean square error, and structural similarity. Significance
Gong Changfei et al. [17]	2022	modified U-net	208 head-and-neck (H&N) cancer patients underwent VMAT	CT images, RT structures, and RT dose exported from TPS	patient-specific quality assurance (PSQA)	The prediction model was able to achieve a good agreement between predicted, measured, and TPS doses

Zhongsheng Zou et al. [18]	2024	modified DL	300 cancer patients who underwent VMAT between 2018 and 2021, in which 240 cases were randomly selected for training, and 60 for testing	CT images, radiotherapy dose exported from the treatment planning system, and MDose distribution extracted from the verification system	Pretreatment patient-specific quality assurance (prePSQA)	The IVPSQA model obtained high-quality 3D prePSQA dose distribution maps in head and neck, chest, and abdomen cases, and outperformed the existing U-Net-based prediction approaches in terms of dose difference maps and horizontal profiles comparison
Yang, X et al. [19]	2022	uncertainty-aware dual-task deep learning (UDDL)	245 multi-site fixed-field IMRT radiotherapy plans	feature information such as the MLC positions and MU weights of each control point	uncertainty-guided man–machine integrated pQA (UgMi-pQA)	this method can balance the efficiency and safety of the automatic pQA models and promote their clinical application
Yufeng Cao et al.[20]	2023	CNN	152 patients with brain metastases	CT images and tumor and OAR contours were	predict dose prescription	clinical parameters improved the overall prediction accuracy by 20 %
Michael Lempart et al. [21]	2021	modified U-Net	160 patients	CT images, and their corresponding binary segmentation masks of the PTV, body and OAR	dose distribution prediction	Triplet-based training improved VMAT dose distribution predictions when compared to 2D
Liu, Y et al. [22]	2021	3D Dense-U-Net	124 NPC patients	CT and contour masks	dose distributions	Increasing the height (Y direction) of training patch size can improve the dose prediction accuracy of tiny

								OARs and the whole body
Wenliang Yu et.al. [23]	2023	3DResUNet and 3DUNet	254 patients with cervical cancer		CT images, contours of the PTV and the OARs		dose distributions and DVH parameters of OARs and PTV between the prediction and clinical truth	In conclusion, in comparison with the 3DUNet model, the predicted edge dose of the body in the 3DResUNet model is closer to the dose distribution of TPS. With the adding the residual block, 3DResUNet improved the dose prediction of PTV
Xiaoyan Kui et.al. [24]	2024	C3D and HD-UNet, SP-DiffDose	320 patients		CT images, PTV segmentation, OARs segmentation, and the dose distribution from clinical plans, with OARs including the heart, lungs, and spinal cord		quantify the disparities between predicted and actual dose, the consistency of DVH curves, and the uniformity of dose distribution	These contemporary approaches encompass a variety of strategies, such as input augmentation techniques, U-Net based models, GAN methods, and other deep learning approaches.

Conclusion

The implementation of AI has proven to be beneficial in the treatment of cancer. At the beginning of using AI in radiotherapy, basic architectures such as machine learning networks were employed. In recent times, with the advancement of AI and the development of new network architectures capable of processing large amounts of data and learning with higher accuracy to minimize errors, the U-Net network has emerged as the best architecture for use in radiotherapy. One of the important features of this network, which is used in radiotherapy, is its convolutional layers. This is essential because one of the inputs is medical tomography images. Additionally, these networks are capable of processing large volumes of data quickly without losing any useful features. However, human ingenuity knows no bounds in enhancing U-Net networks to achieve maximum efficiency in minimum time.

References

[1] Stewart, B. W., & Kleihues, P. (Eds.). (2003). World cancer report (Vol. 57). Lyon: IARC press.

[2] https://gco.iarc.who.int/today/en/dataviz/pie?mode=cancer&types=0&sexes=0&populations=900

[3] Baskar, R., & Itahana, K. (2017). Radiation therapy and cancer control in developing countries: Can we save more lives?. International journal of medical sciences, 14(1), 13.

[4] Nguyen, D., Long, T., Jia, X., Lu, W., Gu, X., Iqbal, Z., & Jiang, S. (2019). A feasibility study for predicting optimal radiation therapy dose distributions of prostate cancer patients from patient anatomy using deep learning. Scientific reports, 9(1), 1076.

[5] Shepard, D. M., Earl, M. A., Li, X. A., Naqvi, S., & Yu, C. (2002). Direct aperture optimization: a turnkey solution for step-and-shoot IMRT. Medical physics, 29(6), 1007-1018.

[6] Zhu, Q. (2021). A Deep-Learning-Based Multi-Segment VMAT Plan Generation from Patient Anatomy for Prostate Simultaneous Integrated Boost (SIB) Cases: A Feasibility Study of Prostate Radiotherapy Application (Doctoral dissertation, Duke University).

[7] Hamet, P., & Tremblay, J. (2017). Artificial intelligence in medicine. Metabolism, 69, S36-S40.

[8] Nguyen, G., Dlugolinsky, S., Bobák, M., Tran, V., López García, Á., Heredia, I., ... & Hluchý, L. (2019). Machine learning and deep learning frameworks and libraries for large-scale data mining: a survey. Artificial Intelligence Review, 52, 77-124.

[9] Seo, H., Badiei Khuzani, M., Vasudevan, V., Huang, C., Ren, H., Xiao, R., ... & Xing, L. (2020). Machine learning techniques for biomedical image segmentation: an overview of technical aspects and introduction to state-of-art applications. Medical physics, 47(5), e148-e167.

[10] McCulloch, W. S., & Pitts, W. (1943). A logical calculus of the ideas immanent in nervous activity. The bulletin of mathematical biophysics, 5, 115-133.

[11] Fu, Y., Zhang, H., Morris, E. D., Glide-Hurst, C. K., Pai, S., Traverso, A., ... & Yang, X. (2021). Artificial intelligence in radiation therapy. IEEE Transactions on Radiation and Plasma Medical Sciences, 6(2), 158-181.

[12] Albawi, S., Mohammed, T. A., & Al-Zawi, S. (2017, August). Understanding of a convolutional neural network. In 2017 international conference on engineering and technology (ICET) (pp. 1-6). Ieee.

[13] Katz, Noam. "CommUnet: U-net decoder for convolutional codes in communication." arXiv preprint arXiv:2004.10057 (2020).

[14] Ronneberger, O., Fischer, P., & Brox, T. (2015). U-net: Convolutional networks for biomedical image segmentation. In Medical Image Computing and Computer-Assisted Intervention–MICCAI 2015: 18th International Conference, Munich, Germany, October 5-9, 2015, Proceedings, Part III 18 (pp. 234-241). Springer International Publishing.

[15] Sarrut, D., Etxebeste, A., Munoz, E., Krah, N., & Letang, J. M. (2021). Artificial intelligence for Monte Carlo simulation in medical physics. Frontiers in Physics, 9, 738112.

[16] Zeng, L., Zhang, M., Zhang, Y., Zou, Z., Guan, Y., Huang, B., ... & Gong, C. (2023). TransQA: deep hybrid transformer network for measurement-guided volumetric dose prediction of pre-treatment patient-specific quality assurance. Physics in Medicine & Biology, 68(20), 205010.

[17] Gong, C., Zhu, K., Lin, C., Han, C., Lu, Z., Chen, Y., ... & Jin, X. (2022). Efficient dose–volume histogram–based pretreatment patient-specific quality assurance methodology with combined deep learning and machine learning models for volumetric modulated arc radiotherapy. Medical Physics, 49(12), 7779-7790.

[18] Zou, Z., Gong, C., Zeng, L., Guan, Y., Huang, B., Yu, X., ... & Zhang, M. (2024). Invertible and Variable Augmented Network for Pretreatment Patient-Specific Quality Assurance Dose Prediction. Journal of Imaging Informatics in Medicine, 1-12.

[19] Yang, X., Li, S., Shao, Q., Cao, Y., Yang, Z., & Zhao, Y. Q. (2022). Uncertainty-guided man–machine integrated patient-specific quality assurance. Radiotherapy and Oncology, 173, 1-9.

[20] Cao, Y., Kunaprayoon, D., Xu, J., & Ren, L. (2023). AI-assisted clinical decision making (CDM) for dose prescription in radiosurgery of brain metastases using three-path three-dimensional CNN. Clinical and Translational Radiation Oncology, 39, 100565.

[21] Lempart, M., Benedek, H., Gustafsson, C. J., Nilsson, M., Eliasson, N., Bäck, S., ... & Olsson, L. E. (2021). Volumetric modulated arc therapy dose prediction and deliverable treatment plan generation for prostate cancer patients using a densely connected deep learning model. Physics and imaging in radiation oncology, 19, 112-119.

[22] Liu, Y., Chen, Z., Wang, J., Wang, X., Qu, B., Ma, L., ... & Xu, S. (2021). Dose prediction using a three-dimensional convolutional neural network for nasopharyngeal carcinoma with tomotherapy. Frontiers in Oncology, 11, 752007.

[23] Yu, W., Xiao, C., Xu, J., Jin, J., Jin, X., & Shen, L. (2023). Direct Dose Prediction With Deep Learning for Postoperative Cervical Cancer Underwent Volumetric Modulated Arc Therapy. Technology in Cancer Research & Treatment, 22, 15330338231167039.

[24] Kui, X., Liu, F., Yang, M., Wang, H., Liu, C., Huang, D., ... & Zou, B. (2024). A Review of Dose Prediction Methods for Tumor Radiation Therapy. Meta-Radiology, 100057. Kui, X., Liu, F., Yang, M., Wang, H., Liu, C., Huang, D., ... & Zou, B. (2024). A Review of Dose Prediction Methods for Tumor Radiation Therapy. Meta-Radiology, 100057.

Calculating Effect of dimensions on neutron microdosimetry spectra (Paper ID : 1446)

Jahanfar S. [1*], Tavakoli-Anbaran H. [2]

[1] *Faculty of Physics and Nuclear Engineering, Shahrood University of Technology, Shahrood, Iran*

Abstract

In order to the study effect of dimensions of the microdosimetric spectra, Using the Geant4-10-4 code, the sites with different dimensions such as 0.5, 1, 2, 3, and 4 microns were also simulated for neutron beam source in three energies 0.1, 1, and 10 MeV, and all effects on neutron microdosimetric spectra were studied. To compare between different dimensions microdosimetric quantities and distributions included of frequency-mean lineal energy, dose-mean lineal energy, mean quality factor, absorbed dose, and these statistical uncertainties in each case were calculated and reported. It is observed, that by increasing the dimensions of the site and consequently increasing mean chord length, lineal energy decreases. Therefore, the microdosimetric spectrum moves to lower lineal energies. For 0.1 MeV neutron energy, the total deposited energy of the proton remains constant at sites larger than 1 micron. Therefore, it is expected that for sites 2, 3, and 4 microns, the maximum observed value of y using the theoretical calculations with the values obtained using the geant4 code are in good agreement. The range of back-scattered protons on the 0.5-micron site is larger than the size of the site. So it deposits only part of its energy on this site. As a result, both energy imparted and mean chord length in the relation y change for this site, which the maximum obtained value does not follow the process of other sites. For neutrons with energies of 1 and 10 MeV, the range of backscattered protons will be greater than the dimensions of the largest site (4-micron site). Therefore, in these energies, both energy imparted and mean chord length change in the relation y, and cannot be compared to 0.1 MeV neutron energy. Also, it is observed that at energies of 0.1 and 1 MeV, with increasing the dimensions of the site, the amount of frequency-mean lineal energy and dose-mean lineal energy decreases, and at 10 MeV energy, the amount of these quantities increases.

Keywords: Neutron Microdosimeter; Microdosimetric Spectra; Tissue-Equivalent Material, Dimension site.

INTRODUCTION

The dose at the macroscopic scale is an average macroscopic quantity and in many situations, the absorbed dose is inadequate to describe the radiation action in biology. At microscopic dimensions, the mechanisms and effects are dominated by inhomogeneous microscopic properties [1,2]. Therefore, at the cells or at the DNA level understanding the radiation requires microdosimetric analysis [3].

For a detailed understanding of the mechanism of the radiation effects, microdosimetry requires the microscopic patterns of the interactions and the energy deposition of radiation that provide a better

understanding of the fundamental mechanisms of radiation in biological systems such as improvement and minimum of environmental and occupational hazards, etc. [1, 2].

The quantity of the lineal energy y is an important microdosimetric quantity obtained from the quotient of ε_1 by $\bar{\iota}$ in the following relation:

$$y = \frac{\varepsilon_1}{\bar{\iota}}$$

In this relation, ε_1 is the energy imparted in the target in a single event, and $\bar{\iota}$ is the mean chord length. Unit y is expressed as $keV/\mu m$ [4-11]. Cauchy's theorem for a convex object states: the mean chord length is 4V/S. V and S are the volume and surface of the site, respectively. Lineal energy distribution f(y) is the probability density of lineal energy and f(y)dy is the probability of lineal energy being in the event of an interval of $[y. y + dy]$ [12,13].

The dose probability density is defined as below:

$$d(y) = \frac{y}{\bar{y}_F} f(y)$$

In the above relation, $\bar{y}_F$ frequency-mean lineal energy is as follows [14-17].

$$\bar{y}_F = \int_0^\infty yf(y)dy$$

Also, the dose-mean lineal energy defines as follows [18-22].

$$\bar{y}_D = \int_0^\infty yd(y)dy$$

Since any irradiation entails a range of values of lineal energy, it is necessary to evaluate the quantity:

$$\bar{Q} = \frac{1}{D_t} \int D(y)Q(y)dy$$

Where $\bar{Q}$ is mean quality factor, $Q(y)$ is a quality factor and D(y) is the distribution of absorbed dose in y, that it implies [23,24]:

$$D(y) = D_t dy$$

The absorbed dose measurement, D_t, by a tissue-equivalent proportional counter (TEPC) is done by measuring the energy imparted in a gas cavity of a TEPC as follows:

$$D_t(Gy) = \frac{d\bar{\varepsilon}}{dm} = \frac{1.602e{-}13}{m_g} \sum_i n_i \varepsilon_i = \frac{1.602e{-}13}{m_g} \frac{2d_t}{3} \sum_i N_i y_i$$

Where $1.602e-13$ is a conversion constant (Gy-g/keV), y_i the average lineal energy of bin "i" and N_i the number of events in that bin, m_g is a mass of the tissue-equivalent gas and d_t is a tissue cavity diameter (μm) simulated by the TEPC [25] which in this study is 2 microns.

Since the for sites with 2 μm dimensions of tissue, the quality factors should be determined using the relationship between the quality factor and LET (L) by approximating $y \approx L$, [26] in the ICRP publication 60 $Q(y)$ defined as follows [27]:

$$Q(L \approx y) = \begin{cases} 1 & L < 10\frac{keV}{\mu m} \\ 0{,}32L - 2{,}2 & 10\frac{keV}{\mu m} \leq L \leq 100\frac{keV}{\mu m} \\ \frac{300}{\sqrt{L}} & L > 100\frac{keV}{\mu m} \end{cases}$$

Microdosimeters are usually proportional counters with spherical or cylindrical cavities that are used with tissue-equivalent walls and gas to simulate microscopic tissue [14,28]. Walls of tissue-equivalent proportional counters build conductive plastics like A-150 tissue-equivalent plastic that can be readily modelled and can be used to build complex and sensitive structures [12]. According to the different applications of microdosimetry, in this study, we examined the effect of dimensions on neutron microdosimetric spectra. There are two ways to investigate the effect of dimensions, one of which is not optimal due to the need for a lot of time and costs, and we used the optimal method in this article, which is described in detail below.

MATERIALS AND METHODS

In this study, the microdosimetric cavity is a right cylinder with a diameter of 2.5 cm, which is filled with propane based tissue equivalent gas with a density of 0.00008 g/cm^3 which is equivalent to 2 micron site. Its wall is made of A-150 tissue-equivalent plastic with a thickness of 5 mm. Using the simulation of the Geant4-10-4 code, we calculated the microdosimetric spectra in this microdosimeter for the neutron beam source at three energies of 0.1, 1, and 10 MeV.

There are two ways to investigate the dimensions of the microdosimeter. Method A: Make microdosimeters with different geometric dimensions, this method requires spending time in simulation and building and spending a lot of costs to make microdosimeters, and it is not an optimal method. The second method: to provide conditions so that with the same geometrical dimensions, different microdosimetric dimensions can be obtained. In this method, by applying and correctly calculating the gas density and pressure, microdosimeters with different dimensions can be simulated, designed, and manufactured with the same geometric dimensions. We have used the second method in this article.

In order to study the effect of dimensions, the microdosimetric spectra were also calculated and plotted on the sites with different dimensions such as 0.5, 1, 2, 3, and 4 microns. Table 1 shows the relationship between site density and dimensions for the sites mentioned above.

Table 1. The relationship between site density and dimensions for the sites with different dimensions.

Density$[g/cm^3]$	Dimension site $[\mu m]$	$\bar{\iota}\,[\mu m]$
2.00E-05	0.5	0.3333
4.00E-05	1.0	0.6667
8.00E-05	2.0	1.3333
1.20E-04	3.0	2.0000
1.60E-04	4.0	2.6667

The frequency-mean lineal energy, dose-mean lineal energy, mean quality factor, absorbed dose, and these statistical uncertainties in each case were calculated and reported.

Results and discussion

Impact of different sites on the microdosimetric spectra for neutron beam source in three energies 0.1, 1, and 10 MeV in different sites such as 0.5, 1,2, 3, and 4 microns simulated and plotted in Figure 1. In Table 2 frequency-mean lineal energy, dose-mean lineal energy, mean quality factor, absorbed dose, and these statistical uncertainties in each case are calculated and reported.

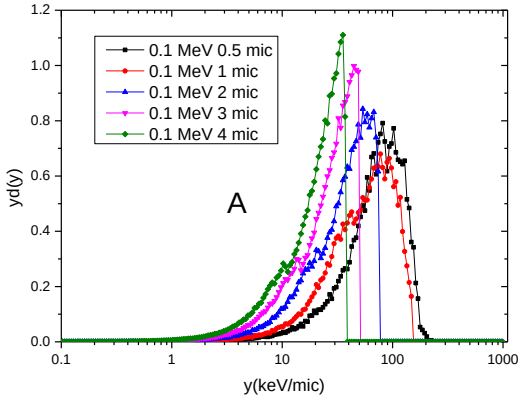

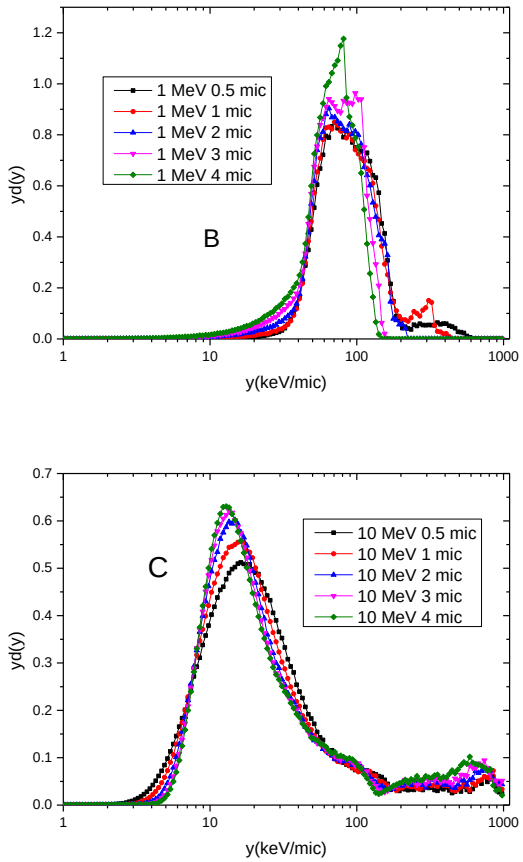

Fig. 1. Impact of different sites on the microdosimetric spectra for neutron beam source in three energies a) 0.1 b) 1 and c) 10 MeV. Black, red, blue, magenta, and olive curve are 0.5, 1,2, 3, and 4-micron sites respectively.

According to this figure, in sites where the maximum range of charged particles is less than the dimensions of the site, the total particle energy $\varepsilon_1$deposits on the site, therefore, by increasing the dimensions of the site and consequently $\bar{\iota}$, $y = \frac{\varepsilon_1}{\bar{\iota}}$ decreases. Therefore, the microdosimetric spectrum moves to lower lineal energies. For 0.1 MeV neutron energy, the maximum energy of the backscattered protons is 0.1 MeV, which the range of these protons is smaller than the size of the 1-micron site. Therefore, the total energy of the proton remains constant at sites larger than 1 micron.

Table 2. Compared to frequency-mean lineal energy, dose-mean lineal energy, mean quality factor, absorbed dose, and these statistical uncertainties on sites with different dimensions.

	10 MeV		1 MeV		0.1 MeV	
Dimension site $[\mu m]$	$\bar{y}_f\left[\frac{keV}{\mu m}\right]$	$\frac{\sigma_{\bar{y}_f}}{\bar{y}_f}$	$\bar{y}_f\left[\frac{keV}{\mu m}\right]$	$\frac{\sigma_{\bar{y}_f}}{\bar{y}_f}$	$\bar{y}_f\left[\frac{keV}{\mu m}\right]$	$\frac{\sigma_{\bar{y}_f}}{\bar{y}_f}$
0.5	15.6390	0.0014	77.4284	0.0017	41.5005	0.0062
1.0	15.8738	0.0014	74.1350	0.0017	31.5737	0.0047
2.0	16.1435	0.0015	65.3817	0.0014	20.7737	0.0032
3.0	16.3950	0.0016	57.8348	0.0014	15.0437	0.0025
4.0	16.5820	0.0016	51.8217	0.0014	11.7086	0.0022
Dimension site $[\mu m]$	$\bar{y}_d\left[\frac{keV}{\mu m}\right]$	$\frac{\sigma_{\bar{y}_d}}{\bar{y}_d}$	$\bar{y}_d\left[\frac{keV}{\mu m}\right]$	$\frac{\sigma_{\bar{y}_d}}{\bar{y}_d}$	$\bar{y}_d\left[\frac{keV}{\mu m}\right]$	$\frac{\sigma_{\bar{y}_d}}{\bar{y}_d}$
0.5	56.8787	0.0127	102.0333	0.0041	77.7120	0.0050
1.0	61.0972	0.0127	98.4177	0.0030	61.9579	0.0041
2.0	67.0092	0.0122	84.5540	0.0015	38.9154	0.0023
3.0	72.9105	0.0115	75.5976	0.0011	27.5044	0.0018
4.0	75.1546	0.0106	69.3884	0.0010	21.1480	0.0015
Dimension site $[\mu m]$	$\bar{Q}$	$\frac{\sigma_{\bar{Q}}}{\bar{Q}}$	$\bar{Q}$	$\frac{\sigma_{\bar{Q}}}{\bar{Q}}$	$\bar{Q}$	$\frac{\sigma_{\bar{Q}}}{\bar{Q}}$
0.5	6.7014	0.0022	21.7553	0.0008	19.3080	0.0033
1.0	6.5443	0.0023	21.4668	0.0008	16.3547	0.0036
2.0	6.5501	0.0023	21.1667	0.0008	10.3344	0.0028
3.0	6.6281	0.0023	20.5394	0.0009	6.7425	0.0022
4.0	6.7120	0.0023	19.3503	0.0009	4.7829	0.0020
Dimension site $[\mu m]$	$D_t[Gy]$	$\frac{\sigma_{D_t}}{D_t}$	$D_t[Gy]$	$\frac{\sigma_{D_t}}{D_t}$	$D_t[Gy]$	$\frac{\sigma_{D_t}}{D_t}$
0.5	30.7751	0.0016	11.9888	0.0035	1.3362	0.0091
1.0	31.4199	0.0017	12.5813	0.0033	1.9629	0.0067
2.0	32.1882	0.0017	13.0309	0.0030	2.5379	0.0047
3.0	32.8592	0.0018	13.2413	0.0028	2.7315	0.0038
4.0	33.3882	0.0018	13.4075	0.0027	2.8275	0.0033

According to Figure 1 on a site of 1 micron, the maximum lineal energy is y=154.882 $keV/\mu m$. Therefore, according to the above explanations, it is expected that for sites 2, 3, and 4 of a micron, the maximum value of y will be observed in y=154.882/2=77.441 $keV/\mu m$, y=154.882/3=51.627 $keV/\mu m$. and y=154.882/4=38.721 $keV/\mu m$ respectively. These values with the values obtained using the geant4 code are in good agreement. But the range of back-scattered protons on the 0.5-micron site is larger than the size of the site. So it deposits only part of its energy on this site. As a result, both ε_1 and $\bar{\iota}$ the relation to y change for this site, and the maximum value of y=234.423 $keV/\mu m$ is obtained, which does not follow the process of other sites.

According to Figures 1 b, c, for neutrons with energies of 1 and 10 MeV, the range of backscattered protons will be greater than the dimensions of the largest site (4-micron site).

Therefore, in these energies, both ε_1 and $\bar{\iota}$ change in the y relationship, and therefore cannot be compared to 0.1 MeV neutron energy. In Table 2 we compared frequency-mean lineal energy, dose-mean lineal energy, mean quality factor, absorbed dose, and these statistical uncertainties on sites with different dimensions from 0.5 to 4 microns. According to this table, it is observed that at energies of 0.1 and 1 MeV, with increasing the dimensions of the site, the amount of frequency-mean lineal energy and dose-mean lineal energy decreases, and at 10 MeV energy, the amount of these quantities increases.

Conclusions

Microdosimetry is the physical description of microscopic patterns of dose distribution. For the calculation of the accurate doses in the body, the use of microdosimetry is essential. In this study, the effect of different dimensions on microdosimetric spectra was studied. Therefore, various studies have been performed for neutron beam sources with three energies of 0.1, 1, and 10 MeV. In 0.1 MeV energy, since the range of backscattered protons on the 1, 2, 3, 4 micron sites is less than the size of the site, maximum lineal energy is obtained by dividing the maximum lineal energy at the one-micron site by the dimensions of the site. These values with the obtained values using the Geant4 code are in good agreement.

It should be noted that using the results of these simulations, a prototype of this microdosimeter is being built and tested at Shahrood University of Technology.

References

[1] Chipara, M. (20050). Mater. Res. Soc. Symp. Proc. Vol. 851, Materials Research Society.

[2] Bjarngard, B. E. and Attix, F. H. (1987). The dosimetry of ionizing radiation, Volume II, Harcourt Brace Jovanovich.

[3] Olko, P. (2007). Microdosimetry, track structure and the response of thermoluminescence detectors, Radiation Measurements 41.

[4] Rosenfeld, A. B., Bradley, P. D., Cornelius, I., Kaplan, G. I., Allen, B. J., Flanz, J. B. et.al. (2000). A new silicon detector for microdosimetry applications in proton therapy, IEEE Transactions on Nuclear Science volume 47 issue 4.

[5] Lindborg L. and Waker A. (2017). Microdosimetry Experimental Methods and Applications, CRC Press, Taylor & Francis Group.

[6] Northum, J. D., Guetersloh, S. B. and Braby L. A. (2012). FLUKA Capabilities for Microdosimetric Analysis, radiation research 177, 117–123.

[7] Cornelius I., Rosenfeld, A. and Bradley, P. (2002). Simulations of silicon microdosimetry measurements in fast neutron therapy, Australasian Physical & Engineering Sciences in Medicine Volume 25 Number 4.

[8] Reniers, B., Vynckier, S.and Verhaegen, F. (2004). Theoretical analysis of microdosimetric spectra and cluster formation for 103Pd and 125I photon emitters, Phys. Med. Biol. 49.

[9] Tsuda, S., Sato, T., Takahashi, F., Satoh, D., Endo, A., Sasaki, S., Namito, Y., Iwase, H., Ban, S.and Takada, M. (2010). Measurement of microdosimetric spectra with a wall-less tissue-equivalent proportional counter for a 290 MeV/u 12C beam, Phys. Med. Biol. 55.

[10] Guardiola, C., Bachiller-Perea, D., M. Mate Kole, E, Fleta, C., David Quirion, De Marzi, L., Gómez, F. (2023). First experimental measurements of 2D microdosimetry maps in proton therapy, Med Phys. 50: 570–581.

[11] M DeCunha, J., Newpower, M. and Mohan, R., (2023). GPU-accelerated calculation of proton microdosimetric spectra as a function of target size, proton energy, and bounding volume size, Phys. Med. Biol. 68, 165012

[12] Rossi, H. H. and Zaider, M. (2011). Microdosimetry and Its Applications, Springer.

[13] Bolst, D., Guatelli, S., Tran, L. T., Chartier, L., Lerch, M. L., Matsufuji, N. and Rosenfeld, A. B. (2017). Correction factors to convert microdosimetry measurements in silicon to tissue in 12C ion therapy, Phys. Med. Biol. 62.

[14] ICRU. Microdosimetry, report 36, International commission on radiation units and measurements, Bethesda-Maryland, USA (1983).

[15] Rosenfeld Anatoly, B. (2016). Novel detectors for silicon based microdosimetry, their concepts and applications, Nuclear instruments and methods in physics research A 809.

[16] Kliauga, Paul. J. and Rossi, H. H. (1982). Studies with encapsulated sources of 125I III. Microdosimetry using a non-metallic wall-less proportional counter, International Journal of Radiation Oncology *Biology *Physics volume 8 issue 11.

[17] Burigo, L., Pshenichnov, I., Mishustin, I. and Bleicher, M. (2013). Microdosimetry of radiation field from a therapeutic 12C beam in water: A study with Geant4 toolkit, Nuclear Instruments and Methods in Physics Research Section B: Beam Interactions with Materials and Atoms, vol 310.

[18] Arghya Chattaraj, Palani Selvam, T. and Datta, D. (2018). investigation of applicability of pure propane gas for microdosimetry at neutron fields: A monte carlo study, Radiation Protection Dosimetry, pp. 1–13.

[19] Pan, C.Y., Huang, Y.W., Cheng, K.H., Chao, T.C. and Tung, C.J. (2015). Microdosimetry spectra and relative biological effectiveness of 15 and 30 MeV proton beams, Applied Radiation and Isotopes 97, 101–105.

[20] Chattaraj, A., and Palani Selvam, T. (2023). Microdosimetry-based investigation of biological effectiveness of 252Cf brachytherapy source: TOPAS Monte Carlo study, Physics in Medicine & Biology 68, 225005.

[21] Papadopoulos, A., Kyriakou, I., Matsuya, Y., Incerti, S., Daglis, Ioannis A. and Emfietzoglou, D, (2022). Microdosimetry Study of Proton Quality Factor Using Analytic Model Calculations, Appl. Sci. 12, 8950.

[22] Braby, L. a., Conte, V., Dingfelder, M., Goodhead, d. T., Pinsky, L. S., Rosenfeld, B., Sato, T., Waker, a. J., Guatelli, S., Magrin, G., Menzel, h.-G., Brandan, M.-E., and Olko, P. (2023). CRU REPORT 98, STOChaSTIC NaTURE Of RadIaTION INTERaCTIONS: MICROdOSIMETRy, International Commission on Radiation Units & Measurements.

[23] The Quality Factor in Radiation Protection (Report 40), International Commission on Radiation Units and Measurements, (1986).

[24] Kellerer, A. M. and Hahn, A. (1988). Considerations on a Revision of the Quality Factor, Radiation Research 114, 480-488.

[25] Si-Young Chang and Bong-Hwan Kim (2008). Understanding of the Microdosimetric Quantities Obtained by a TEPC, Journal of nuclear science and technology, Supplement 5, p. 213–216.

[26] Moslehi, A., Raisali, G.and Lamehi, M. (2016). Simulation and experimental study of an indigenously designed and constructed THGEM-based microdosimeter for dose-equivalent measurement, Radiation Measurements 86, 56e62.

[27] ICRP 60, Annals of the ICRP, Published on behalf of the lnternational Commission on Radiological Protection, (1990).

[28] Waker, A. J. (1995). Principles of experimental microdosimetry, radiation protection dosimetry, Vol61 No 4, 297-308.

ICNST 2024
International Conference on Nuclear Science and Technology
6- 8 MAY 2024 | Isfahan, Iran

Determining the dead layer and thickness of the HPGe detector window using MCNP6 and Geant4 code and comparing with experimental results (Paper ID : 1452)

Kiyani A.[1*], Salehi M.[2], Mohebian M.[3], Nazari J.[4]
[1,3]*Nuclear Physics, Arak University, Arak, Iran*
[2] *Nuclear Physics, Kashan University, Kashan, Iran*
[4] *Electrical Engineering, Azad University, Tehran, Iran*

Abstract:

The photopeak efficiency of High-Purity Germanium (HPGe) detectors is a crucial parameter that depends on various measurement conditions, including the source-to-detector geometry, photon energy, and detector characteristics such as dead layer thickness (DL), end cap thickness, crystal absorption cross-section, window, active detector volume, and other factors. Precise assessment of the effectiveness of detecting the photopeak in a radiation spectrum is essential for determining the amount of radioactivity present in samples from the environment. Simulation approaches are essential because they provide an alternative when obtaining standard sources for different types of samples is challenging. This article presents experimental measurements of absolute efficiency using reference materials RGU-1, RGTh-1, and RGK-1. The measurements were conducted using coaxial germanium detectors with a relative efficiency of 30%. The obtained data were then compared with simulated data from MCNP6 and Geant4. The comparison revealed a high level of agreement between the experimental and simulated data. Moreover, we used modeling tools and charts to determine the ideal thickness and material for the detector window. We determined the most favorable window thickness to be 0.06 millimeters. Thus, by employing Monte Carlo simulation codes and considering the precise attributes of the measurement equipment in the input program, it is possible to accurately compute the photopeak efficiency under different conditions without conducting experimental measurements.

Keywords: HPGe detector-, dead layer-, Geant4 and MCNP Monte Carlo code-, photopeak efficiency

INTRODUCTION:

Semiconductor detectors, including germanium and silicon, together with scintillation detectors, are employed to quantify radiation levels in environmental samples. Out of these options, high-purity germanium semiconductor detectors are preferred because of their high efficiency and precise ability to differentiate energy levels when compared to other detectors[1]. In order to quantify the radiation levels in samples, it is important to ascertain the efficacy of the detectors. Direct measurement can be accomplished by utilizing relative and absolute standards, empirical calculations, semi-empirical calculations employing different parameters of the detectors or interaction processes, and Monte Carlo simulations[2]. In order to accurately calculate efficiency, it is necessary to have comprehensive understanding of detector parameters. This includes knowledge of the composition and geometry of detector materials, information about attenuation coefficients and material densities for efficiency calculations, as well as an understanding of semiconductor effects such as particle interaction with electrodes and Coulombic fields[3]. Monte Carlo simulation (MC) approaches can be used when there is accurate knowledge on the composition and geometry of the detector. Currently, there are other techniques available, such as MCNP6 and GEANT4, which can be used to trace the movement of gamma -rays[3, 4]. These methods enable more precise calculations of detector efficiency and better understanding of measurement data. Monte Carlo programming methods offer various advantages, such as the ability to quickly compute the absolute efficiency of the detector-sample system. Using solely the information regarding the composition of the detector and the standard sample, one can readily compute the efficiency of the detector-sample system. Multiple variables impact the performance curve of a detector sample, which might have an impact on computational outcomes. The factors that need to be considered are the thickness of the window, the diameter and length of the crystal, the volume of the active detector, the distance between the tip of the collimator and the detector crystal, and the thickness of the dead layer (both front and lateral). Precise outcomes from calculations require accurate information regarding these components. Within a germanium detector with a p-type lithium diffusion junction, the diffusion of lithium into the germanium results in the formation of a layer where the collection efficiency of the accumulated charge is completely absent[5]. Measuring the thickness of the dead layer is a complex task, and manufacturers occasionally offer consumers with comprehensive details regarding the dead layer thickness. Nevertheless, simulation techniques can be employed to ascertain the thickness of the dead layer[6, 7]. Several research studies have been carried out to ascertain the thickness of the dead layer[8, 9]. This effort aimed to determine the most effective dead layer thickness and window thickness for BSI HPGe detectors (Baltic Scientific Instruments). To do this, two simulation methods were employed: Monte Carlo simulations using MCNP6

and Geant4 tools. These research have been undertaken to enhance the efficiency and precision of measurements, and their findings can be applied in the development and refinement of radiation detection systems. The present study seeks to examine the properties of HPGe detectors, namely the dead layer thickness and window thickness, and their impact on efficiency in two simulation techniques, MCNP6 and Geant4. These investigations were conducted to evaluate the influence of these properties on the performance of detectors in detecting and measuring radioactive materials. This data can enhance the precision and effectiveness of measurements, as well as optimize the design of detectors.

RESEARCH THEORIES:

The codes MCNP6 and Geant4 were utilized to compute the theoretical calculations. The computation process is described in a distinct manner below.

--MCNP6 Simulation:

The MCNP6 computer code was utilized to simulate the transportation of several forms of radiation by the Monte Carlo approach. This package incorporates diverse cross-section libraries that enable the simulation of many forms of radiation interactions in materials with varying geometries. Indeed, the MCNP code can tally pulses within a certain energy range, ranging from E_1 to E_2, and record these pulses in a designated cell that represents the active volume of a detector. These recorded pulses are then stored for subsequent analysis. One can determine the quantity of particles within the energy range of E_1 to E_2 that the source has effectively scattered and moved to the active detector volume by using the Tally F8 (Tally Pulse Height) card in the MCNP code. To find the experimental yield at energy 1E, divide the net peak area in the energy range E_1-ΔE to E_1+ΔE by the sample's activity, which is the number of particles that come from the source. The output value of Tally F8 corresponds to the detector efficiency at energy E_1 within the energy range of ΔE_1 [10]. To accurately simulate the efficiency of the sample-detector system, it is essential to have detailed knowledge about the components and structure of both the reference sample and the detector. Comprehensive information regarding the organization of containers that carry the reference samples, as well as the activity and detection system in the reference , is available[6].

--Geant4 Simulation:

The CERN laboratory produced Geant4, which is open-source simulation software. This software was created with the C++ programming language and offers comprehensive functionalities for modeling and

simulating particle interactions with matter. Geant4 utilizes geometric and physical techniques to ascertain the trajectory and behavior of particles as they contact matter, which contributes to its high level of technical robustness. The simulation in this article utilized Geant4 software version 11.1.1. The G4EmStandardPhysics_option4 package has been used to model electromagnetic interactions. The choice of this package is based on its exceptional accuracy and precision in computing physics at low energies. The GPS (General Particle Source) type has been utilized with defined characteristics to model particle emission from the source. This method employs a spherically symmetric model to simulate the emission of particles. The code does not have any filters to analyze the spectrum within the active detector volume. The process of extracting the spectrum has been carried out utilizing the Event class. [11, 12].

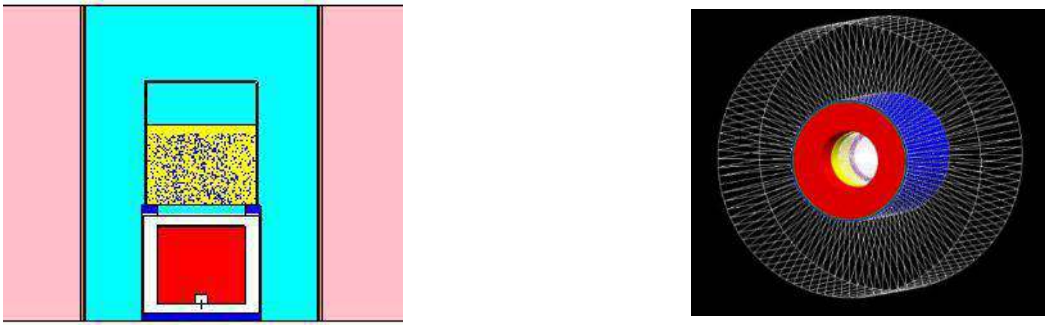

a) b)

Fig. 1. HPGe detector simulations (a) MCNP (b) Geant4

EXPERIMENTAL

Constructing the performance curve empirically requires using gamma standard sources. Reference materials (RMs) are highly valuable due to their distinct cores that possess a specified half-life and are reasonably cost-effective to manufacture[13]. Radioactive materials (RMs) contain radioactive nuclei that produce gamma photons with energy varying from 46.5 keV ^{210}Pb to ^{208}Tl 2614 keV[14]. The Atomic Energy Organization distributed reference materials in cylindrical canisters, with each container weighting 300 grams. After applying a sample code (such as VS, CS, and Sb), the specimens were rendered waterproof by using aquarium glue and then stored in the laboratory for at least 50 days. After a duration of 65.69 days, there is a 99.99 percent probability that the samples will achieve equilibrium. The samples reach equilibrium within a 50-day period, with an accuracy of less than 0.01 percent. Therefore, to guarantee the stability of samples for a prolonged duration, they are stored in the laboratory for a minimum of 50 days. The samples were examined with the Lsrmbsi software (Spectroscopy of the samples) for a duration of

86400 seconds. This phase is crucial for the Gaussian development of the photopeak peaks. As the count rate below the peak rises, the intrinsic relative counting inaccuracy diminishes. The spectrum processing was performed using the Gamma Vision 32 Master2 software.

Table 1. HPGe detector characteristics form BSI

Air (outside the detector and sample)	7.65	from the bottom) 19.1 (of the crystal	-
Active volume of the detector	5.9	from the bottom) 5.2 (of the crystal	-
Void (space between the germanium crystal and the aluminum window)	5.9	0.6	-
Void (cavity or pore)	0.74	4.55	-
Aluminum window	5.9	0.06	-
Aluminum holder	3.95	5.93	0.1
Germanium layer	5.9	from the) 5.035 (bottom of the crystal	0.165(0.01)

Results and discussion

Using RMs and the Maestro II Gamma Vision 32 software, it was possible to obtain the performance values for the available energy in these reference materials. The performance of the detector using reference materials (RMs) can be shown in Table 3 of the reference[6]. The performance curve was generated using the Matlab software based on the data presented in Table 3. Equation (1) represents the correlation between performance and energy in the form of a Gaussian function [15]

$$Eff = a_1 e^{-(\frac{E-b_1}{c_1})^2} + a_2 e^{-(\frac{E-b_2}{c_2})^2} \qquad (1)$$

The variables a_1, b_1, c_1, a_2, b_2, and c_2 are responsible for representing the values 1.666, 292.200, 107.600, 300.407, 695.1, and 935 respectively. Kilo-electron volts (keV) serve to measure both the experimental efficiency and the energy of gamma radiation.

The efficacy of the detector-sample system was assessed using Geant4 simulation methods for various thicknesses of the detector window. The outcomes of the computations are presented inTable2. Figure3 illustrates the correlation between efficiency and energy across different thicknesses.

Table 2. Measured values in simulation and experimental.

Energy	Efficiency			Correction Factor (CF)	
	.Experimental.	Geant4	MCNP	$Geant4/_{Exp}$	$MCNP/_{Exp}$
63.29	0.008402	0.01339	0.012813	1.593709	1.525024
295.22	0.028606	0.029935	0.031378	1.046448	1.096906
338.32	0.02513	0.026702	0.027797	1.062535	1.106124
351.93	0.025346	0.025433	0.026891	1.003442	1.060972
583.19	0.014627	0.016257	0.017254	1.111454	1.179565
609.31	0.015127	0.015481	0.01664	1.023421	1.100013
911.25	0.011289	0.011374	0.012013	1.00752	1.064124
1460.83	0.008009	0.007683	0.00825	0.959356	1.030163

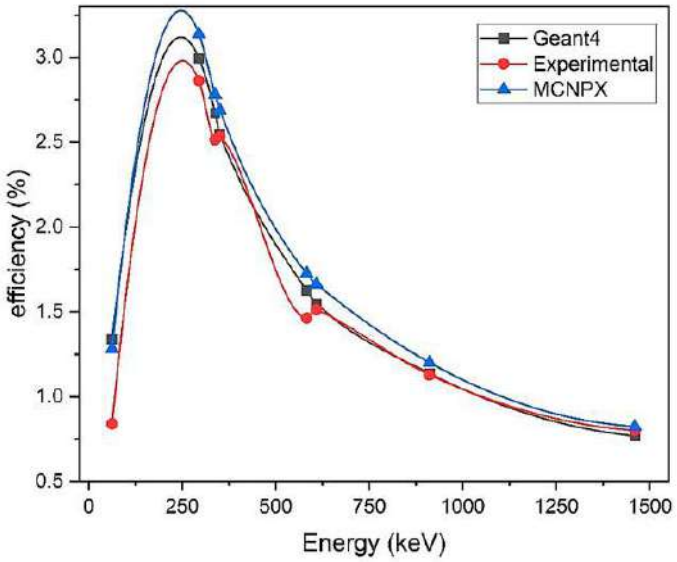

Fig. 2. Efficiency vs. Energy Plot (Simulation vs. Experimental Comparison)

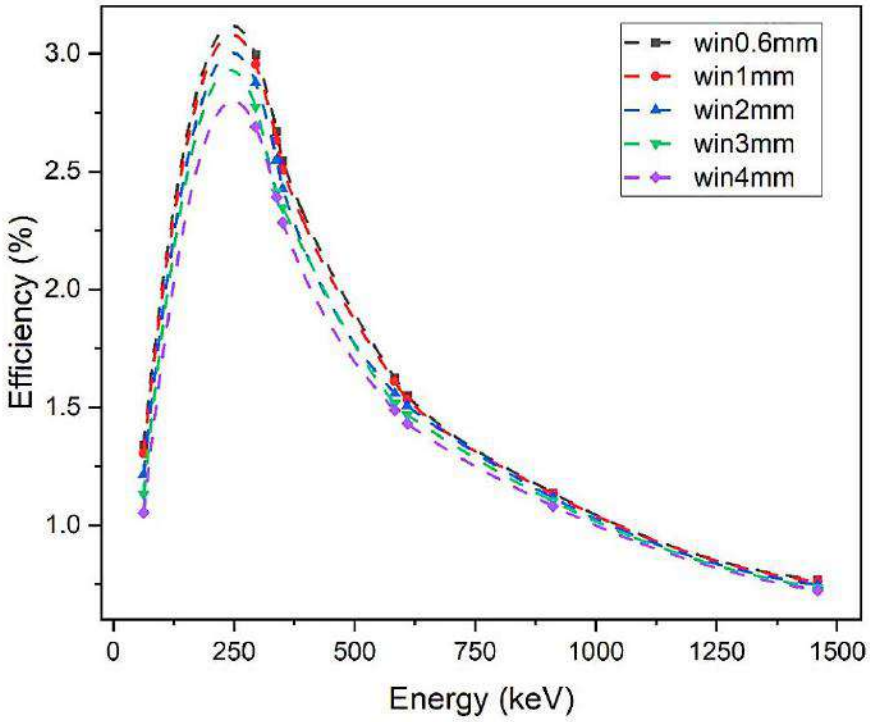

Fig. 3. Efficiency variations as a function of energy for different thicknesses of the window using Geant4 method.

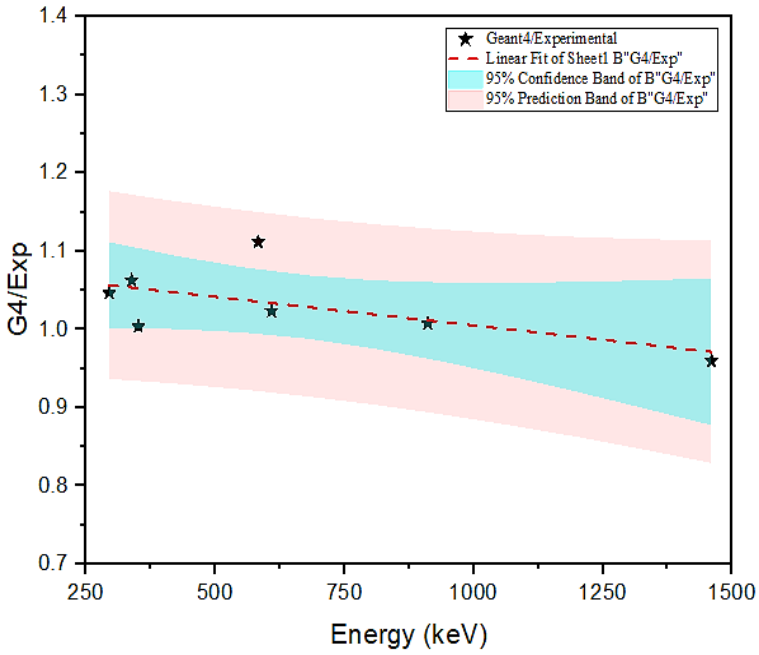

Fig. 4. relative differences in efficiency ratings between the experiment and the Geant4 simulation

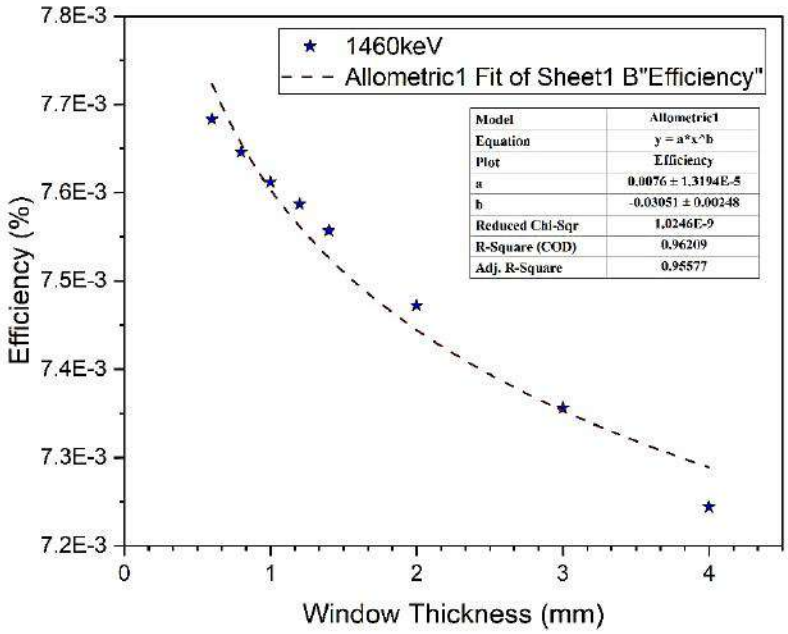

Fig. 5. Illustrates the variations in efficiency concerning window thickness at an energy level of 1460 MeV .

Conclusions

The data presented in Table 2 shows an accurate correlation between the simulated data acquired by MCNP6 and Geant4 and the experimental data. According to an analysis using the Geant4 technique, the thickness of the window has an impact on its efficiency at lower energy levels. However, when energy levels are increased, the effectiveness remains nearly constant regardless of the thickness. Figure 3 illustrates the fluctuations in energy efficiency across five different window thicknesses, specifically 0.6 to 4 millimeters. At lower energy levels, the effectiveness of the narrower window aligns with the Geant4 simulation outcome (0.00133). However, at a thickness of 4 millimeters, it diverges from this number. Conversely, as the energy levels rise, the efficiency diverges from the Geant4 simulation outcome (0.0076) for window thicknesses of greater thickness; however, it tends to approximate this number when the thickness reaches 0.6 millimeters. The efficiency differences in relation to energy for two different window thicknesses, namely 0.6 and 0.8 millimeters, are depicted in Figure 4. The observed correlation between thinner and closely spaced thicknesses and their efficiency indicates a notable degree of concurrence. The previous paragraph explains that the most effective type of graph for displaying efficiency statistics is a

power function plot. The graph demonstrates that a power function with the equation $y=0.0076\ x^{(-0.03051)}$ may model efficiency, and it has a linear regression coefficient of $R^2=0.95$.

References

[1] Tsoulfanidis, N., & Landsberger, S. (2021). *Measurement and detection of radiation*. CRC press.

[2] Harb, S., Salahel Din, K., & Abbady, A. (2008). Study of efficiency calibrations of HPGe detectors for radioactivity measurements of environmental samples.

[3] Briesmeister, J. F. (1993). MCNP-A General Monte Carlo N-Particle Transport Code, Version4A. *LA-12625*.

[4] Allison, J., Amako, K., Apostolakis, J., Araujo, H., Dubois, P., & Asai, M. (2003). Geant4-a simulation toolkit. *Nucl. Instrum. Meth. A*, *506*(3), 250-303.

[5] Campbell, J., & McNelles, L. (1974). Americium-241 as a low-energy photon intensity standard. *Nuclear Instruments and Methods*, *117*(2), 519-532.

[6] Mohebian, M., Pourimani, R., & Modarresi, S. (2019). Using MCNP simulation for self-absorption correction in HPGe spectrometry of soil samples. *Iranian Journal of Science and Technology, Transactions A: Science*, *43*, 3047-3052.

[7] Vasconcelos, D. C., Pereira, C., Gallardo, S., Santos, T., & Rocha, Z. (2011). Efficiency simulation of a HPGe detector for the environmental radioactivity laboratory/CDTN using a MCNP-gammavision method.

[8] Demir, D., Eroğlu, M., & Turşucu, A. (2013). Studying of characteristics of the HPGe detector for radioactivity measurements. *Journal of Instrumentation*, *8*(10), P10027.

[9] Ješkovský, M., Javorník, A., Breier, R., Slučiak, J., & Povinec, P. P. (2019). Experimental and Monte Carlo determination of HPGe detector efficiency. *Journal of Radioanalytical and Nuclear Chemistry*, *322*, 1863-1869.

[10] Pourimani, R., & Mohebian, M. (2021). Study of background correction of gamma-ray spectrometry using reference materials. *Iranian Journal of Science and Technology, Transactions A: Science*, *45*(2), 733-736.

[11] Geant4. (2023). Geant4 User's Guide for Toolkit Developers, Release, 11.1.1.

[12] Incerti. (Incerti). Cern Wiki for GEANT4, 2023.
https://twiki.cern.ch/twiki/bin/view/Geant4/LowePhysicsLists

[13] Nir-El, Y. (1998). Application of reference materials in the accurate calibration of the detection efficiency of a low-level gamma-ray spectrometry assembly for environmental samples. *Journal of Radioanalytical and Nuclear Chemistry*, *227*, 67-74.

[14] Oddone, M., Giordani, L., Giacobbo, F., Mariani, M., & Morandi, S. (2008). Practical considerations regarding high resolution gamma-spectrometry measurements of naturally occurring radioactive samples. *Journal of Radioanalytical and Nuclear Chemistry*, *277*(3), 579-585.

[15] Guide, M. U. J. T. M. I. (1998). Matlab Users Guide.

ICNST 2024
International Conference on Nuclear Science and Technology
6- 8 MAY 2024 | Isfahan, Iran

Development of superheated emulsion detector for thermal neutrons (Paper ID : 1466)

Sara Sadat Madani Kouchak[1], Dariush Rezaei Ochbelagh[1,*], Peiman Rezaeian[2], Majid Abdouss[3]

[1] *Department of Physics and Energy Engineering, Amirkabir University of Technology, Tehran, Iran.*

[2] *Radiation Applications Research School, Nuclear Science and Technology Research Institute, AEOI, Tehran, Iran.*

[3] *Department of Chemistry, Amirkabir University of Technology, Tehran, Iran.*

Abstract

Considering the need and wide application of neutron detectors in the nuclear industry, their design and construction is considered a necessity. Since the efficiency of superheated emulsion detectors for thermal neutrons is low, in this research, Freon-12 superheated emulsion detector has been developed to detect thermal neutrons. For this purpose, using 3.4% (by weight) lithium chloride salt, a superheated emulsion detector was made in the neutron laboratory of Amirkabir Faculty of Technology, and its performance was investigated. In addition to fast neutrons, the manufactured sample is also sensitive to thermal neutrons. Also, by using the Am-Be neutron source, the response of the superheated Freon-12 emulsion detector containing lithium ion was compared with the response of the superheated Freon-12 emulsion detector in the thermal neutron field. The sensitivity of the developed detector to thermal neutrons was determined to be 3.2 bubbles/μSv and it was found to be increased compared to the values reported by other researchers.

Keywords: Superheated emulsion detector, Thermal neutron, Sensitivity of detector, LiCl.

INTRODUCTION

A superheated emulsion detector (SED) is a collection of tiny superheated liquid halocarbon droplets suspended in an immiscible viscoelastic gel. Since the late 1970s, when Apfel introduced the superheated droplet detector [1], it has been widely employed as a tool for monitoring, dosimetry, and spectroscopy in the fast neutrons field. A good neutron detector should possess the capability to detect a wide range of neutron energies. Although the SED offers various benefits such as ease of preparation, direct reading, low cost, insensitivity to gamma-ray, portability, the ability of passive usage, and ease to use, its sensitivity to thermal neutrons is negligible [2].

Several ^{6}Li-based SEDs, including SDD-C318 [3] and BDT [4], have been developed for thermal neutron detection. Due to the limitations imposed by their chemical formulas, it is difficult to modify the ^{6}Li concentration in order to improve the sensitivity of these SEDs for thermal neutron detection. Also, among the halocarbons, only Freon-12 (CCl_2F_2) demonstrates little sensitivity to thermal neutrons [5]. As a result, the SED containing Freon-12 is a suitable choice for adding lithium compounds.

In this study, we have used Freon-12 as a superheated liquid in the detector. Using experimental and simulation results, samples made of ordinary SED and lithium-bearing SED were studied. The results show the improvement of the response of the lithium-bearing SED in the thermal neutrons field, hence the developed detector is a suitable alternative to the simple type and can be used in a wide range of energy of thermal to fast neutrons. Also, the sensitivity of the lithium-bearing SED was compared with the sensitivity of the commercial sample BDT.

RESEARCH THEORIES

Lithium-bearing SED thermal neutron energy responses are proportional to the exoergic ^{35}Cl(n,p)^{35}S and ^{6}Li(n,α)^{3}H capture reactions. Based on Sitze's [6] thermal spike theory, the formation of bubbles in SEDs can be explained. As a result of thermal neutron interactions with lithium in the host medium and chlorine in the superheated liquid, alpha, and sulfur particles are produced, respectively. Due to the deposit of the kinetic energy of these charged particles into the droplet, a sequence of small vapor bubbles of different sizes is formed along the radiation path. If the radius of the bubbles exceeds the critical radius (r_c), the bubbles will grow until the entire droplet evaporates and becomes an observable bubble. If the radius of the bubbles is smaller than the critical radius (r_c), they shrink back to liquid due to surface tension. The amount of energy and the critical size for bubble formation depends on the composition of the detector. As illustrated in Figure 1, the critical radius(r_c) is calculated based on the surface tension $\gamma(T)$ ($N.m^{-1}$) of the liquid at temperature T, the difference ΔP (Pa) between the superheated liquid's vapor pressure (P_v), and the external pressure on the viscoelastic gel's surface (P_o), which are as follows:

$$r_c = \frac{2\gamma(T)}{\Delta P} = \frac{2\gamma(T)}{(P_v - P_o)} \qquad (1)$$

The minimum energy required to form a vapor bubble with a critical radius using classical thermodynamics is:

$$W = \frac{16\pi\gamma^3(T)}{3(P_v - P_0)^2} \qquad (2)$$

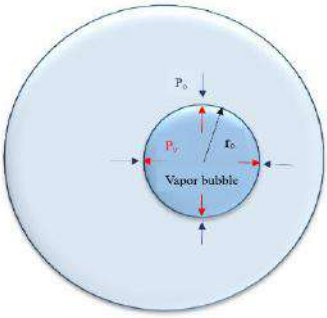

Fig 1. Schematic diagram of the pressure associated with a droplet surrounded by gel shows an SED

A charged particle's deposited energy is proportional to its stopping power (dE/dx). Only a small percentage of the energy deposited by the charged particles at a distance of $2r_c$ contributes to bubble formation [7], as defined by the thermodynamic efficiency of nucleation (η). Therefore, the condition for bubble formation is:

$$\eta(2r_c)\left(\frac{dE}{dx}\right) \geq W \qquad (3)$$

In Table 1, the physical parameters of Freon-12 are listed at ambient pressure (P_o =1atm), where the efficiency factor is taken as η=4% .

Table 1. Physical parameters of Freon-12 (CCl_2F_2) at 25℃ [8] [9]

Parameter	Freon-12 (CCl_2F_2)
Temperature (T) [℃]	25

Density (ρ) $[g.cm^{-3}]$	1.311
Surface tension $\left(\gamma(T)\right)$ $[dyn\ cm^{-1}]$	9.013
Vapor pressure (P_v) $[atm]$	6.43
Degree of superheated $(\Delta P = P_v - P_0\ )$ $[atm]$	5.43
Critical radius $(r_c = 2\gamma(T)/\Delta P)$ $[\mu m]$	0.0328
The minimum energy required to transform a microbubble into a visible bubble $\left(W = \frac{16\pi(\gamma(T))^3}{3(\Delta P)^2}\right)$ $[keV]$	0.253
Minimum energy required for bubble formation $(E_{min} = W/\eta)$ $[keV]$	6.32
$\left(\frac{dE}{dx} \geq \frac{W}{2\eta r_c}\right)$ $[keV\ \mu m^{-1}]$	$dE/dx \geq 96.417$

Different charged particles deposit different amounts of energy due to their different linear collisional stopping powers. It is possible to calculate their energy deposited at a given distance based on its stopping power. Table 2 presents the stopping power and the range of charged particles from ^{6}Li and ^{35}Cl interactions in Freon-12 (ρ=1.311 gcm^{-3} at 25 °C) as calculated using the SRIM code [10].

Table 2. The stopping power and the range of charged particles in SED calculated by SRIM code

Density: 1.311 g/cm^3	Freon-12 (CCl_2F_2)			
Reaction	$^{6}_{3}Li(n,\alpha)^{3}_{1}H$		$^{35}_{17}Cl(n,p)^{35}_{16}S$	
Products	A	$^{3}_{1}H$	P	$^{35}_{16}S$
Energy (MeV)	2.05	2.73	0.598	0.017
Range (μm)	13.36	76.53	14.89	0.0463
Stopping power (keV/μm)	139.2	24.02	28.01	42.98

According to Table 2, sulfur ion can lead to the formation of bubbles by depositing its energy at a distance of less than $2r_c$, and if alpha is produced up to a distance of 10.16 microns from the drop, it can deposit the energy necessary for the formation of bubble inside the drop [11].

EXPERIMENTAL

Two types of detectors, ordinary SED and lithium-bearing SED were fabricated to investigate their response to a thermal neutron field. All chemical materials required to prepare the host medium for detectors were provided by MERCK company and Freon-12 was supplied by ISCOEN company. In this study, ordinary SEDs were prepared according to the method described by Raisali et al [12]. To prepare the host medium for the lithium-bearing SED, the solution of 35% polyacrylamide, 3.4% LiCl, and saturated CsCl was applied. Droplets were homogeneously distributed in the gel by adjusting the density of the host medium to Freon-12's density.

In the 13x100mm screw cap test tube, 3 ml of the mixture was transferred, and 0.01 ml of Ammonium Persulfate solution (10% w/v) was added as the initiator. A water aspirator degassed the test tube, and then 0.01 ml of Tetramethylenediamine (TEMED) was added before sealing. The test tube was then frozen in the dry ice-ethanol bath. In the next step, 0.02 ml of liquid Freon-12 was transferred to the test tube using an adjustable volume micropipette, sealed, and placed in an ice bath until liquefied. The Freon-12 liquid was broken down and dispersed in the gel with a vortex shaker at 2,600 rpm. To deactivate SED against neutron radiation, an additional amount of Freon-12 was added to pressurize the gel medium. Lastly, the test tube was sealed and put in an ice water bath to complete the polymerization process.

During the emulsification process, where the superheated liquid is stirred or shared in a gel medium to form an emulsion, various sizes of drops can be formed [13]. Also, the larger droplets have a greater probability of vaporization than the smaller ones [14]. In Fig. 2, droplet sizes were measured using a digital microscope in randomly selected slices of the gel. It can be observed that superheated droplets of non-uniform size were dispersed in the gel. As a result, the bubble size will be different. Since droplet size determines bubble size, not neutron energy [15], bubbles of different sizes are expected to appear after irradiation.

Fig.2. The droplet sizes are non-uniform

To irradiate SEDs, an Am-Be neutron source with activity 15ci and emission rate 3.3 x 10^7 $n.s^{-1}$ was used in the neutron laboratory at Amirkabir University of Technology. Stainless-steel cylindrical containers with a diameter of 4.02 cm and a height of 13.72 cm held the source. It was placed at the center of a cylindrical steel tank filled with water, measuring 1.5 meters high and 77 cm diameter. According to Fig. 3, iron cylinders were arranged in the water around the source at different distances from each other. These cylinders were used to irradiate SEDs with thermal neutrons.

Fig. 3. Am–Be source is placed at the center of the iron tank containing water

The laboratory temperature during irradiation was 25℃. To activate SED, excess Freon-12 was released and SED temperatures dropped due to Freon-12 evaporation. After half an hour in the radiation room, the detector temperatures reached equilibrium with room temperature. By simultaneously exposing both types of SEDs to thermal neutrons, their response was investigated. According to the research done by Rezaei et al [11] on the proportionality of the number of bubbles formed in the fabricated SED with the neutron flux, the detector's sensitivity can be estimated. The SED sensitivity, expressed in bubbles/μSv, is calculated as follows [16]:

$$S = \frac{N}{H^*(10)} \qquad (4)$$

Where N represents the number of bubbles recorded by the detector when exposed to the ambient dose equivalent H*(10) [16]. The H*(10) was estimated using the conversion coefficients of neutron fluence into ambient dose equivalent based on ICRP publication 74, in MCNP code with DE and DF card and tally command F4. [17].

Results and discussion

To compare the performance of the fabricated SEDs, their responses were determined at different distances from the neutron source. For this purpose, the ordinary and lithium-bearing SED was simultaneously placed at distances of 15, 25, 35, and 45 cm from the source. Hence, iron cylinders were selected in the water tank around the source in the mentioned intervals. These places are illustrated in Figure 4. After thermal neutron exposure, the number of bubbles formed was counted with the naked eye. The four SEDs for each distance were considered in order to minimize measurement uncertainty and avoid bubble overlap.

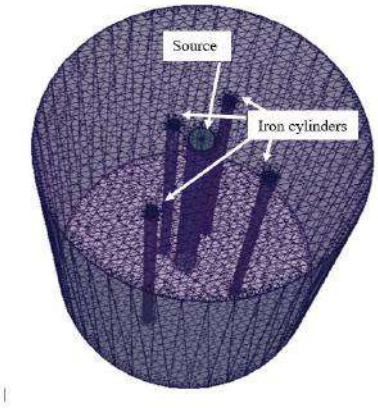

Fig. 4. Schematic view of the source, cylinders, and detector's location in Monte Carlo calculation

Figure 5 show, respectively, (a) the fabricated Li-bearing SED with additional freon in an inactive state, (b) the SED after the extra freon is removed and before irradiation, and (c) the SED with bubbles appearing after irradiation.

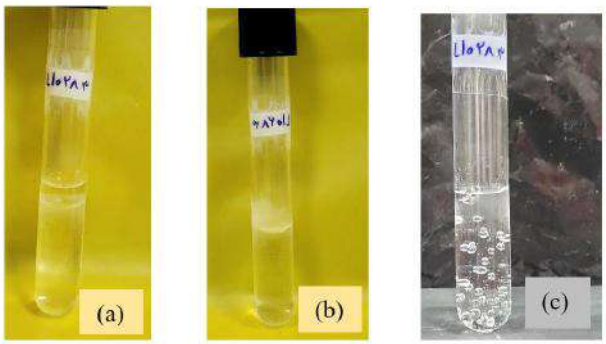

Fig. 5. (a). Inactive Li-bearing SED, (b) Active Li-bearing SED before irradiation, (c) Li-bearing SED after irradiation

The response of fabricated SEDs to a thermal neutron field at room temperature is provided in Table 3. In addition, In the fifth row, the flux reported by Rezaei et al. [11] is presented in the desired locations, which has been validated. In this way, the MCNP code was implemented using the geometry and data used by Rezaei et al., [11] as well as the conversion coefficients of neutron fluence into ambient dose equivalent based on the ICRP 74 publication, which are presented in the final row as ambient dose equivalents.

Table 3. the number of bubble formation in ordinary SED and Li-bearing SED in different distance of Am-Be source at given irradiation time

Distance (cm)	15	25	35	45
Time of irradiation (s)	600	600	1200	1200
Average number of bubbles in ordinary SED	5.00±1.00	4.00±1.50	2.00±0.50	1.00±0.50
Average number of bubbles in Li-bearing SED	73.00±23.01	18.00±2.62	4.00±0.70	3.00±0.01
Flux ($n/cm^2.s$)	262.70×10^2	53.70×10^2	10.90×10^2	3.15×10^2
Ambient dose equivalent (μSv)	83.20	13.74	1.37	0.40

As can be observed, in both types of SEDs, fewer bubbles were formed with increasing distance. Furthermore, lithium-bearing SEDs form more bubbles than ordinary SEDs due to the presence of lithium in the host medium. These differences are shown in Fig. 6.

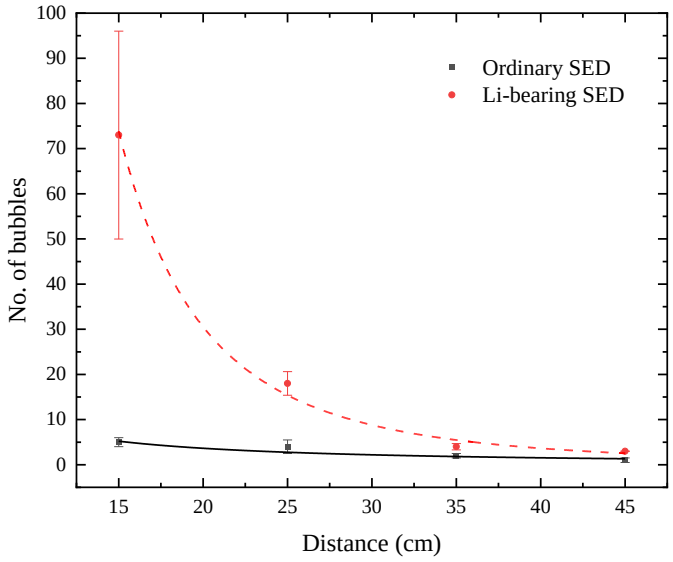

Fig. 6. Response variation of ordinary SEDs and lithium-bearing SEDs in a thermal neutron field

Figure 7 illustrates the trend of Li-bearing SED response changes and ambient dose equivalent according to the distance from the neutron source. Their distributions are well aligned, as can be seen. Based on equation (4), the sensitivity of the detector was measured at the desired locations and its value was estimated to be around 3.2 bubbles/mSv on average. Other researchers have reported various BDT sensitivity values listed in Table 4.

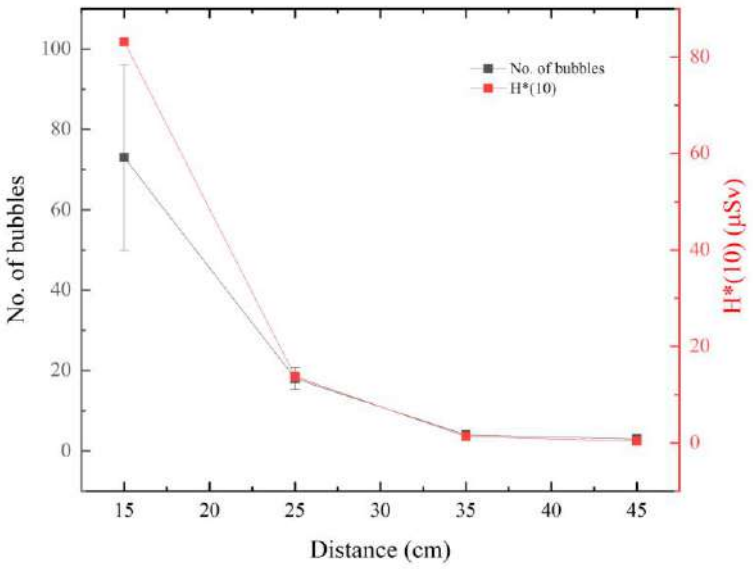

Fig. 7. The Li-bearing SED response and the amounts of ambient dose equivalent in a thermal neutron field

Table 4. SED sensitivity compared to reported values of BDT

Sensitivity (bubbles/μSv)	Ref	
0.2-0.5	[18]	ICRP 74
2.7	[19]	NCRP 38
2-3	[20]	
0.37-0.41	[16]	NCRP 38
3.2	This work	ICRP74

The sensitivity of the SEDs to thermal neutrons is determined by the amount of lithium and the number of drops [21]. The Li-bearing SED sensitivity is higher than the BDT sensitivity reported by researchers. There are several reasons for this difference.

Due to the various read-out methods, the number of bubbles counted at Li-bearing SED is higher because the automatic reader used at BDT does not count the bubbles located at the curved end of the detector, which explains their smaller sensitivity [4].

The BDT sensitivity was calculated by averaging the sensitivities at 5 different temperatures (20, 24, 28, 35, and 37 ℃), while the Li-bearing SED sensitivity was determined at a temperature [18].

The Li-bearing SED sensitivity is based on the fluence to ambient dose equivalent conversion coefficients of ICRP 74. In contrast, BDT used different coefficients based on NCRP 38 or ICRP 51 [18].

The host medium of Li-bearing SED is a gel, while the BDT host medium is a firm polymer. the procedure of bubble formation in the gel is faster than in polymer [22]. Hence more bubbles are formed in Li-bearing SED compared to BDT.

Conclusions

Two types of ordinary SED and Li-bearing SED were fabricated and the response of two detectors to a thermal neutron field was investigated. An increased response was observed for the Li-bearing SED. In addition, by computing the ambient dose equivalent, the sensitivity of this detector was estimated, and it was compared with the value reported for the commercial model BDT. The results show that Li-bearing

SED is more sensitive than BDT. This can be caused by the difference in the type of the host medium, bubble recording methods, and conversion coefficients utilized to determine the ambient dose equivalent.

Considering the effect of the number of droplets on the sensitivity of the detector, increasing the volume of freon-12 can be implemented in order to improve the sensitivity of this detector to thermal neutrons.

Acknowledgements

The authors gratefully acknowledge Mr. Ali Elhampour, Mr. Soroush Mohtashami, Mr. Mostafa Kabir, and Mr. Mahdi Sahraian for their assistance during this research work. The authors are also thankful to the neutron laboratory at the Amirkabir University of Technology for providing the Am–Be source.

References

[1] R. E. Apfel, "The superheated drop detector," *Nucl. Instrum. Methods*, vol. 162, no. 1-3, pp. 603-608, 1979.

[2] R. E. Apfel, "Photon-insensitive, thermal to fast neutron detector," *Nucl. Instrum. Methods*, vol. 179, no. 3, pp. 615-616, 1981.

[3] Y. Liu, *Simultaneous fast and slow neutron with superheated droplet detector and real-time readout system*, 2017.

[4] "A combined use of the BD-PND and BDT bubble detectors in neutron dosimetry," *Radiation Measurements* , vol. 29, no. 5, pp. 573-577, 1998.

[5] Robert E. APFEL and S.C. ROY, "Investigation on the applicability of superheated drop detectors in neutron dosimetry," *Nuclear Instruments and Methods in Physics Research*, vol. 219, no. 3, pp. 582-587, 1984.

[6] F. Seitz, "On the theory of the bubble chamber, 1 (1) (1958) 2.," *The physics of fluid*, vol. 1, no. 1, pp. 2-13, 1958.

[7] R.E. Apfel, S.C. Roy, Y.-C. Lo, "Prediction of the minimum neutron energy to nucleate vapor bubble in superheated liquids," *Physical review A* , vol. 31, no. 5, pp. 3794-3198, 1985.

[8] W. Lim, C.K. Wang, "Computational studies of neutron response function for a neutron spectrometer which uses Freon-12, -22, and -115 superheated liquids," *Nucl. Instrum. Methods* , vol. 335, no. 1-2, pp. 243-247, 1993.

[9] "E.I. du Pont de Nemours & Co., Thermodynamic properties of DuPont™ Freon® 12 (R-12) refrigerants".

[10] James F. Ziegler, M.D. Zigler, J.P. Biersack, "SRIM-The stopping and range of ions in matter," *Nucl. Instrum. Methods B,* vol. 268, no. 11-12, pp. 1818-1823, 2010.

[11] S. S. Madani Kouchak, D. Rezaei Ochbelagh, P. Rezaeian, M.Abdouss, "Fabrication of a superheated emulsion based on Freon-12 and LiCl suitable for thermal neutrons detection," Nuclear Engineering and Technology, 2023.

[12] P. Rezaeian, G. Raisali, A. Akhavan, H. Ghods, B. Hajizadeh, "Development of a new pressure dependent threshold superheated drop detector for neutrons," *Nuclear Instruments and Methods in Physics Research Section A,* vol. 776, pp. 50-56, 2015.

[13] R. Sarkar, B.K. Chatterjee, B. Roy, S.C. Roy, "Size distribution ofdrops in superheated drop detectors," *Radiation Physics and Chemistry* , vol. 71, pp. 735-736, 2004.

[14] Prasanna Kumar Mondal, Rupa Sarkar, Barun Kumar Chatterjee, "Response of Superheated Droplet Detector (SDD) and Bubble Detector (BD) to interrupted irradiations," *Nuclear Instruments and Methods in Physics Research A* , vol. 857, pp. 111-114, 2017.

[15] D. Ponraju, H. Krishnan, S. Viswanathan and R. Indira, "Preliminary results on bubble detector as personal neutron dosimeter," *Radiation Protection Dosimetry* , vol. 144, no. 1, pp. 177-181, 2011.

[16] M. CHEMTOB*, R. DOLLO**, C. COQUEMA*, J. CHARY*, C. GINISTY, "Essais de dosimètres neutrons à bulles, modèle BD 100 R-PND et modèle BDT," *Radioprotection,* vol. 30, no. 1, pp. 61-78, 1995.

[17] Conversion Coefficients for use in Radiological Protection against External Radiation., vol. 26, ICRP Publication 74, 1996.

[18] F. Vanhavere, M. Coeck, R. Noulty, "The BDT bubble neutron detector for personal dosimetry," in *European IRPA congress 2002*, Italy, 2002.

[19] A. Di Fulvio, C. Domingo, M. De San Pedro, ,E.D'Agostino, M. Caresana, L. Tana, F.d'Errico., "Superheated emulsions and track etch detectors for photoneutron measurements," *Radiation Measurements* , vol. 57, pp. 1-10, 2013.

[20] M Weinstein, B Ben-Shachar, U German, S Merling, R Srebro, "Experimental data for some characteristics of the bubble neutron," 2002.

[21] Mommen, S., & De Saint-Hubert, M., "Fabricatie en kalibratie van superheated droplet detectors (SDD's) voor neutronendosimetrie," 2017.

[22] L.K. Pan, C.-K.C. Wang, "Superheated-liquid-droplet technique for measuring alpha decays in uranium solutions," *Nuclear Instruments and Methods in Physics Research A* , vol. 420, pp. 345-355, 1999.

[23] R. Sarkar, B.K. Chatterjee, B. Roy, S.C. Roy, "Radiation detection by using superheated droplets," *Radiation Physics and Chemistry* , vol. 75, pp. 2186-2194, 2006.

[24] F. Vanhavere, F. d'Errico, "Standardisation of superheated drop and bubble detectors," *Radiation Protection Dosimetry*, vol. 101, no. 1-4, pp. 283-287, 2002.

ICNST 2024
International Conference on Nuclear Science and Technology
6- 8 MAY 2024 | Isfahan, Iran

Defect measurment in radiography of welding objects by image processing and curvelet transform (Paper ID : 1475)

Effat Yahaghi[1], Amir-Ahmad Shojaee[2], Behnam Arezabak[2], Behrouz Rokrok[3], Aboutaleb Kermani[2], Amir Movafeghi[3]

[1]Department of Physics, Imam Khomeini International University, Qazvin, Iran
[2]NDT labs., Iran Nuclear Regulatory Authority, Atomic Energy Organization of Iran, Tehran, Iran
[3]Reactor and Nuclear Safety School, Nuclear Science & Technology Research Institute (NSTRI), Tehran, Iran

Abstract

Defect measurement in radiography of welding objects and improved visualization of the defects are very important tasks for welding inspection. One of the most widely used Non-Destructive Testing methods is the industrial radiography testing, which is used to check internal and volumetric defects of heat affected zone (HAZ) in weldments. In this method, X- or gamma rays are used for obtaining industrial radiography images. Radiography can be carried out by conventional films or by digital radiography methods. Due to the inherent scattering of the photons and some other phenomena such as noise of the system, the radiographs are suffered from some amount of blurriness. Therefore, it is necessary to use image processing to increase the contrast of the radiographs and help to radiography interpreter for a better identification of the defective areas. In this research, curvelet transformations have been used to improve the quality of the radiographic images and for the sizing of the defects. This transformation is a new type of multi-scale analysis algorithm that has been developed to solve the basic problems of wavelet transformations in detecting the edges and the curves region. The size of Duplex IQI (DIQI) and conventional IQI lines are also used to measure the defect size. The results show that curvelet transformation is effective in extracting the information of the edges of the radiographs, and for the sizing of defect measurements by two mentioned methods on these reconstructed images are remarkably close to each other.

Keywords: X-ray imaging, industrial radiography, defects measurement, image processing, Curvelet method

INTRODUCTION

Welding defects caused by various factors will cause problems and as a result, a lot of costs. When the pipes are loaded in high pressure and heat, small cracks and small defects cause serious damage to the pipe, and these defects cause many life and financial risks. Radiography testing (RT) method is one of the approved methods among non-destructive tests [1]. In transmission mode of industrial radiography, an X-ray or gamma source is placed on one side of the object being studied, and a detector is placed on the other side of the object. Industrial RT can be implemented by three methods: radiography with the conventional films, computed radiography (CR) and digital radiography (DR). In CR; instead of traditional X-ray; film, cassettes with a phosphor plate use photo-stimulated luminescence

screens to capture the radiographs. DR using flat panel detectors produces a digital radiograph instantly on a computer. This technique uses x-ray sensitive plates to capture data during object examination, and immediately transfer the data to a computer without the use of an intermediate cassette [2-3].

In x-ray systems, there is intrinsic noise such as photon scattering, and also electronic equipment and data acquisition systems noise that cause blurriness in the radiograph. The blurriness of the radiograph makes the edges of the image not well defined and during inspection experts of radiography determine the size of the defects with difficulties [4-7].

Although it is not possible to completely eliminate the noise in the radiographs, the radiograph quality can be improved by noise removal algorithm [5-6]. There are a variety of image processing methods to improve the quality of radiographs, such as median smoothing, Gaussian smoothing, and wavelet methods. Wavelet Transform decomposes a function into a set of wavelets, that a wavelet is a wave-like oscillation that is localized in time. Lilly et.al [7] introduced the generalized morse wavelets as a superfamily of analytic wavelets and Cunha L. [8] explained theory, design and applications of the Non subsampled Contourlet transform. Kiapasha et al. [9] estimated the wall thickness of pipes using digital radiography and three wavelet methods. They used the wavelet transform (WT), Gabor Filters (GF) and shearlet transform (ST) with the background-removing algorithm. Curvelet transformation is a new type of multi-scale analysis algorithm that is developed to solve the fundamental problems of wavelet transformations in the detection of edges and curves [10,11]. It is used in data compression, pattern recognition, and other applications. There are different image processing methods that are more complicated but it is better define the feature of the images. One of these methods is Curvelets algorithm that is a non-adaptive technique for multi-scale object representation. A curvelet transform differs from other directional wavelet transforms in that the degree of localization in orientation varies with scale. For a wavelet transform, the squared error is as $O(1/n)$ for n wavelet. The curvelet transform allows it to achieve $O(\log n)^3/n^2$) [8-9].

The study reported the application of a curvelet algorithm to radiographs of the welded plates with the aim of improved visualization of the defects. The curvelet was applied to radiographs with unknown type noise, and quantity of the noise was estimated as background of the radiographs. Then the background was subtracted from the original radiographic images to form the final processed images, and the defects size ware measured by Image Quality Indicator (IQI) and Duplex IQI (DIQI).

RESEARCH THEORIES

The Curvelet transform is a multiscale directional transform and a higher dimensional of the Wavelet transform which allows an optimal non adaptive representation of edges designed to represent images at different scales and

different angles. The curved singularities are approximated with some coefficients and in a non-adaptive representation named "curvelets". The curvelets remain coherent waveforms under the action of the wave equation in a smooth medium [10,11]. Wavelet transform in signal analysis considers a family of dilated and translated function: $\boldsymbol{\Psi_{j,k} = 2^{j/2}\Psi\left(2^{j}\cdot(-k)\right), j,k\epsilon Z}$, generated by one mother wavelet $\boldsymbol{\Psi\epsilon L^2(R)}$, and being an orthonormal basis of L^2 (R). Then, each signal $f\,\epsilon\boldsymbol{L^2(R)}$ represented in a wavelet expansion [8]

$$\boldsymbol{f = \sum_{j,k} C_{j,k}(f)\Psi_{j,k}} \qquad (1)$$

where $\boldsymbol{C_{j,k}(f) = \langle f.\Psi_{j,k}\rangle}$ are the wavelet coefficients. Here $\langle\cdot.\cdot\rangle$ denotes the scalar product in $\boldsymbol{L^2(R)}$. It is necessary to transfer this process to two-dimensional mode for image analysis and to include a special non-rotation in it. Therefore, based on the basic elements, a basic curvelet $\boldsymbol{\Psi}$ is generated. Using the translations, dilations and rotations of $\boldsymbol{\Psi}$, the Curvelet family will be created. Therefore, the curvelet construction is now based on the following two main ideas [10-11]. 1) Consider polar coordinates in frequency domain. 2) Construct curvelet elements being locally supported near wedges according to Fig. 2, where the number of wedges is $\boldsymbol{N_j = 4\cdot 2^{\lceil j/2\rceil}}$ at the scale 2^{-j} , i.e., it doubles in each second circular ring. The advantage of curvelet transform are: Better sparse representation of the object along with the edges is possible. Good image reconstruction is possible under difficult conditions. In wave propagators an optimal-sparse representation is possible.

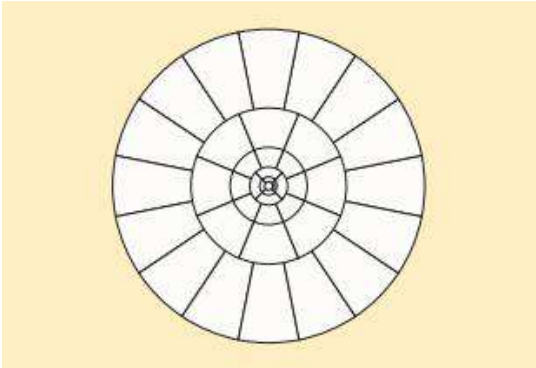

Fig.1 Tiling of the frequency domain into wedges for curvelet construction [10].

Applying curvelet transformation to radiographs of the welded plates can be summarized as follows [8-9]:

1. Reading the image,

2. Obtaining a fast digital curvelet conversion based on wrapping and obtaining the curvelet coefficients for background removal method.

3. Thresholding applied on the curvelet coefficients,

4. Obtaining the inverse fast digital curvelet transform from the obtained threshold coefficients and obtaining the improved image.

5. Subtracting the main image to the output of the curvelet transformation algorithm [7-9].

EXPERIMENTAL

Radiographic images were acquired of many welded plates using an X-ray machine and computed radiography (CR)), a photograph of the welded plate examined is shown in Fig. 2-a. the dimensions of plates are 10cm x 20cm. The X-ray beam was set to 160 kV and 1500 mAs, the source-to-film distance (SFD) was set to about 100 cm, and a thin lead plate was placed behind the CR plate to reduce the noise associated with the detection of back-scattered radiation. The X-ray image acquisition set-up for transmitted mode was shown in Fig. 2-b. The CR plates were scanned with a laser scanner of a nominal diameter of 50 μm in accordance to standard procedures [12–14] and IQI and DIQI were used to determine the image quality.

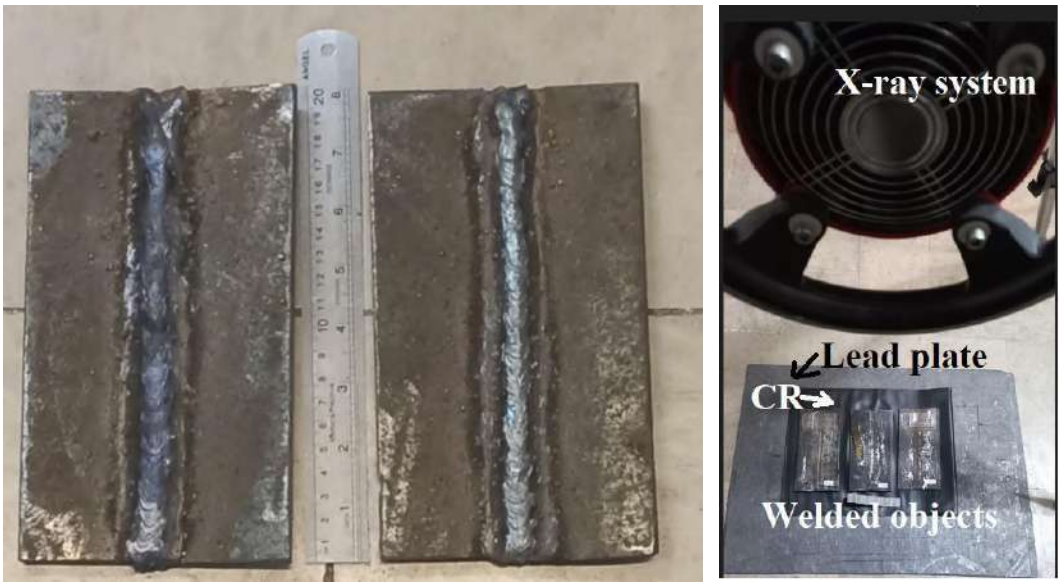

a b

Fig. 2. (a) a photograph of welded plates, (b) The X-ray image acquisition set-up for transmitted mode

Some standard images from one of the industrial radiography databanks, i.e. GDXray is used for comparison of the results [15].

Results and discussion

In this study, the curvelet transformation methods were employed to the acquired welded plates. The radiographs were procured as described in 'experimental section'. In Fig. 3, two typical digitized radiographs of the welded plates were shown. The radiograph of plates are very blurry due to scattered x-ray and noise, the radiograph are foggy and the defects region is hardly recognizable. To remove the blurriness and detecting the defect region, the reconstructed images was presented buy curvelet algorithm in Fig. 4. The fog level of the radiograph is unknown, therefore, we used the curvelet algorithm for background removal. First, a smoothed image was reconstructed with the change of parameters in the algorithm according to 'research theory section'. Then the smoothed part is subtracted to the original radiograph. We consider j=5 and k=10 for the best reconstruction. The comparison of Figs .3 and 4 shows that the edges are sharper and the defects areas (the markers 'C', 'I', 'G','K' 'L' and 'M') , the IQI lines (the markers'A', 'D', 'F' and 'H'), DIQI ('B' and 'G') of the lead ruler (the marker 'E') are better seen in the reconstructed images. The defect region such as the crack and pores are visualized in the reconstructed images.

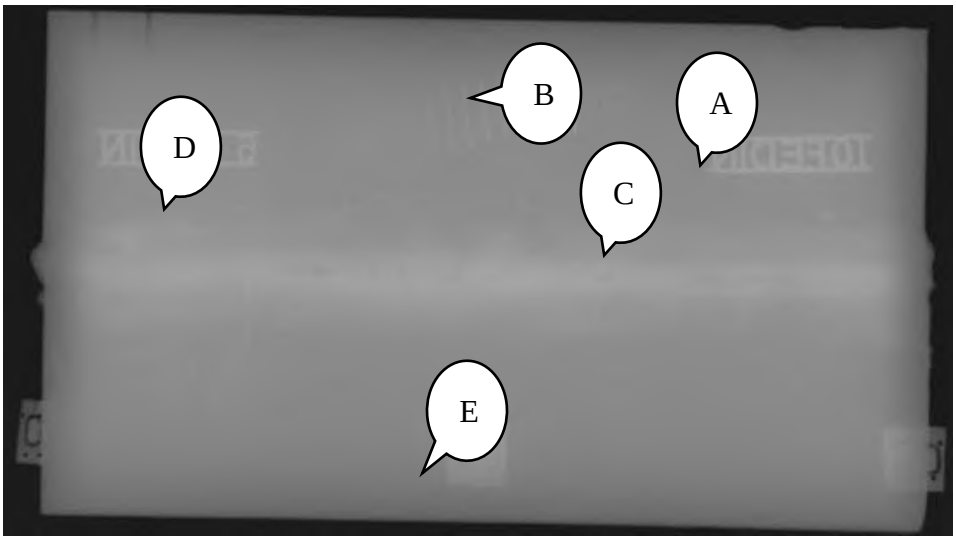

a

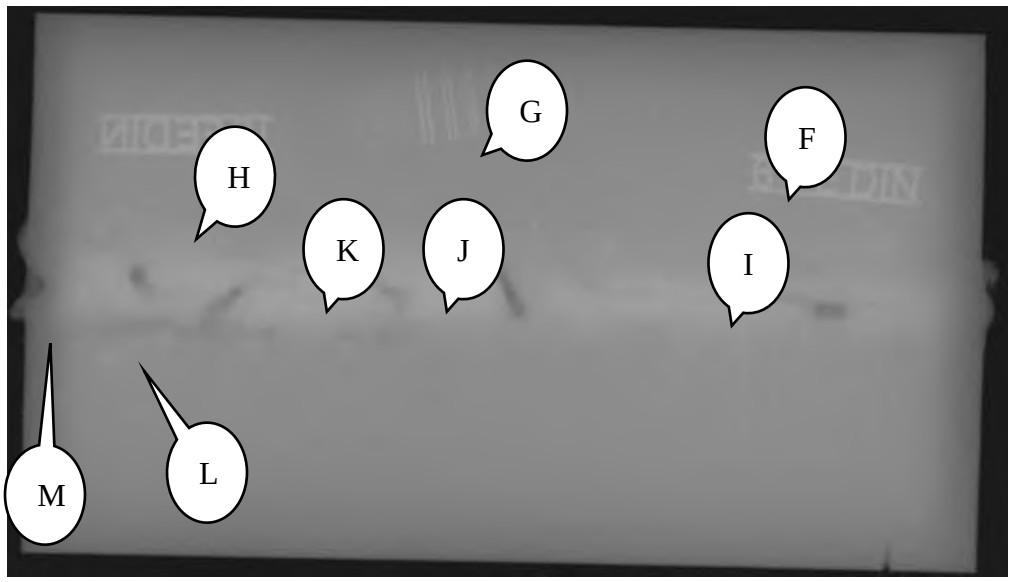

b

Fig. 3. two typical digitized radiographs of the welded plates a) plate1 b) plate 2

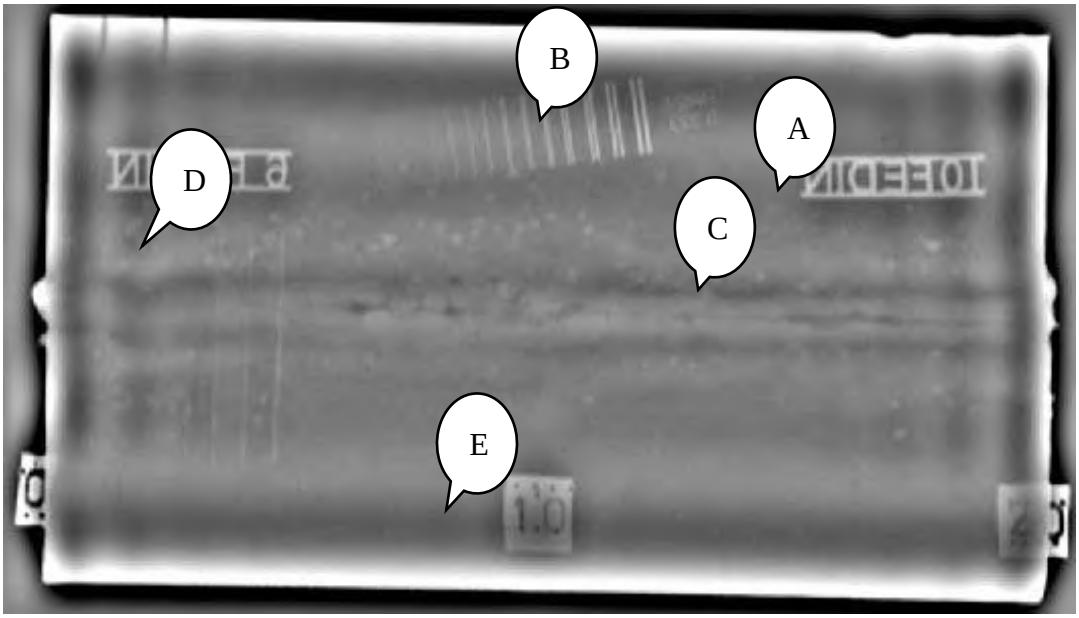

a

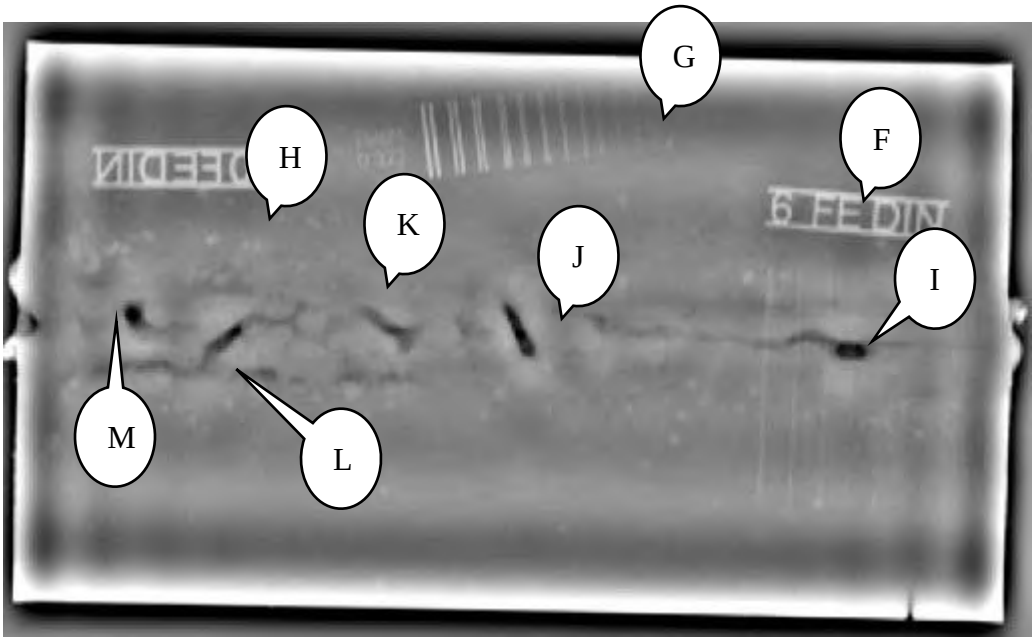

b

Fig. 4. the reconstructed images for radiograph of a) plate1 b) plate 2

For evaluated the size of defects, we use to the distance to the first and the second lines in the IQI and DIQI. Considering that the distance between these lines is 5 mm according to Standard ASTM E-747-17 [10], the defects dimensions were calculated by measuring the pixels in the length and width of the defects and comparing them with the pixels between the first and second lines (Table. 1).

Table 1. The sizes of each defect (mm)

	Plate1		Plate2			
	Marker C	Marker I	Marker J	Marker K	Marker L	Marker M
IQI	0.80 x14.16	6.13 x3.136	9.50 x4.32	5.91 x10.90	6.36 x6.18	2.95 x2.04
DIQI	0.71 x12.14	6.75 x4.00	10.50 x4.75	6.50 x12.00	7.00 x7.50	3.25 x2.25

It should be noted that any mathematical algorithm can show different features of images. In some algorithms, the extracted features may not have a significant difference in the outputs. The output of curvelet transform is compared with the wavelet Transform (WT) in Fig.5 for a radiograph of the welded objects. The crack

regions is visible on the left side of the radiograph in Fig.5-a and the IQI region are not visible on the image. The reconstructed images by the curvelet transform and WT are shown in Figs. 5-b and c. The comparison of two Figs.5 b and c shows that the crack and IQI regions are more clear than the original radiograph, the curved areas in the root welding are more distinct on the curvelet image.

Conclusions

In this research, the size of the defects in the welded plates were measured with the curvelet method and scaling using IQI and DIQI. The results show that the curvelet method has a suitable ability to detect the edges. The defect region is clear by detecting the faded edges. The defect size was calculated using known distance between the first and second lined in IQI and DIQI. The results show that the obtained sizes are close to each other. The difference between measured sizes is due to the user's error in measuring the number of pixels on the image.

a

b c

Fig. 5. a) the original radiograph [15], b) the reconstructed image for the curvelet transform and c) WT

Acknowledgements

The authors thank the metal workshop of NSTRI for providing the welded test pieces.

References

[1] Yahaghi, E., Movafeghi, A., Mirzapour, M., Rokrok, B. (2020). Defect detections in industrial radiography images by a multi-scale LMMSE estimation scheme, Radiation Physics and Chemistry, 168, 108560

[2] Mery, D., Pieringer Ch. (2021). Computer Vision for X-Ray Testing, ISBN : 978-3-030-56768-2, Springer.

[3] Wei, Y., Liu, X, and Liu Y. (2022). Research on the application of high-efficiency detectors into the detection of prohibited item in X-ray images Journal: Applied Intelligence, 52, r 5, 4807, DOI: 10.1007/s10489-021-02582-1.

[4] Zhang, H. and Yu, X. (2016). Quantitative analysis method of pipeline defects based on optimized RBF neural network, Sustain. Comput. Inf, 20, 203–209.

[5] Kasban, H., Zahran, O., Arafa, H., El-Kordy, M., Elaraby, S.M., and Abd El-Samie, F.E.(2011). Welding defect detection from radiography images with a cepstral approach, NDT & E Int, 44(2), 226–231.

[6] Getreuer, P. (2012). Total variation deconvolution using split Bregman, Image Process. Online, , 2, pp. 158–174.

[7] Lilly, J.M., Olhede, S.C. (2012). Generalized Morse wavelets as a superfamily of analytic wavelets. IEEE Transactions on Signal Processing, 60(11), 6036–6041.

[8] Cunha L., Zhou J., and Do M. N., 2006, The Non subsampled Contourlet transform: theory, design and applications, IEEE Trans. on Image Processing, 15, 10, 3089-3101.

[9] Kiapasha, Z., Yahaghi, E., M., Monem, S., Nekoei, J. (2020). Wall Thickness Measurement of Pipes Using Digital Radiography and Three Wavelet Methods, Journal of Nondestructive Evaluation,39:10, https://doi.org/10.1007/s10921-020-0654-x.

[10] Miri, M. S., Mahloojifar, A. (2011) Retinal image analysis using curvelet transform and multistructure elements morphology by reconstruction, IEEE Transactions on Biomedical Engineering, Vol. 58, No. 5, pp. 1183–1192

[11] Candes, E. J., Demanet, L., Donoho, D. L., Ying, L. (2006), Fast Discrete Curvelet Transforms, SIAM Multiscale Model. Simul, 5(3), 861-899.

[12] ASTM E-747 (2017). Standard Practice for Design, Manufacture and Material Grouping Classification of Wire Image Quality Indicators (IQI) Used for Radiology.

[13] ISO 16371-2 (2017). Non-destructive testing – Industrial computed radiography with storage phosphor imaging plates – Part 2: General principles for testing of metallic materials using X-rays and gamma rays, International Organization for Standardization, Switzerland,.

[14] ISO 16371-1 (2011). Non-destructive testing – Image quality of radiographs – Part 5: Determination of the image unsharpness value using duplex wire-type image quality indicators, International Organization for Standardization, Switzerland.

[15] Mery D., Riffo V., Zscherpel U. , et al, (2015). GDXray: The Database of X-ray Images for Nondestructive Testing,, J. of Nondestructive Evaluation, 34(4),. DOI:10.1007/s10921-015-0315-7.

Investigating the effect of megavoltage energy photon beams on the radiosensitivity level of cervical cancer cells in presence of dextran-coated iron oxide nanoparticles (Paper ID : 1476)

Abstract

Purpose: Use of nanotechnology is increasing in various fields of medical sciences including diagnosis and treatment. Iron nanoparticles have been proposed as contrast material in medical imaging and as physical radiation sensitizers in radiation therapy due to their high atomic number. The aim of this in-vitro study was to investigate the energy effect of photon beams on the radiosensitivity effect o created in cervical cancer cells (HeLa cells) in the presence of dextran conjugated iron oxide nanoparticles.

Materials and methods: HeLa cervical cancer cells were cultured as a monolayer and the cellular toxicity of the nanoparticles was performed on them at different concentrations and incubation periods. Then, in order to investigate the radiosensitivity effect of the nanoparticles (at concentrations of 20 and 50 μg/ml) on these cells, MTT assay method was used. Irradiations were performed in different doses using 6 and 18 megavoltage photon beams.

Results: No significant cytotoxicity was observed in treatment of the cells with the nanoparticles in concentrations up to 50 μg/ml ($P>0.05$). Irradiating the cells with 18 MV photons in presence of the nanoparticles showed more radiosensitization effect relative to 6 MV photons ($P<0.05$). Dextran coated iron oxide nanoparticles showed more radiosensitivity effect at a higher concentration value. Dose enhancement factor values at concentrations of 20 and 50 μg/ml for 6 and 18 MV photon beam irradiations were obtained 1.19±0.15 &1.61±0.11, and 1.49±0.11 & 2.25±0.44, respectively.

Conclusion: Using dextran coated iron oxide nanoparticles in accompany with megavoltage photon beams irradiations significantly enhances radiation cell-killing effect, which can be considered in radiation therapy of cancer.

Keywords: Radiotherapy, Radiosensitivity, Iron oxide nanoparticles, Dextran, Cervical cancer.

Introduction

Cancer is one of the main causes of death in worldwide [1]. The cervical cancer is the most common cancer in women [2]. Radiation therapy uses ionizing radiation especially high energy photon beams to destroy the cancer cells [3]. One of the main problems in this method is non-specific toxicity to cancer cells [4]. Reducing radiation dose of normal tissues without reduction in tumoral tissues absorbed dose is desirable goal which can reduce the radiation side effects [5]. Use of radiosensitizers in cancer cells is one way of

increasing the radiation dose just in cancer cells without exceeding the maximum tolerable dose in healthy tissues [4]. In field of radiosensitization of nanoparticles, more studies have been done using metal nanoparticles such as gold nanoparticles, silver and other nanoparticles [6-11]; and relatively few studies have been performed using iron oxide nanoparticles [12]. Iron oxide nanoparticles (IONs) compared to other nanoparticles can be easily synthesized with a good control on their size, composition and shape [13]. Radiosensitization of IONs under the photon beams irradiations is due to the higher atomic number of Iron (Z= 26) compared with the effective atomic number of tissue (Z=7.5) which will increase the probability of absorption processes and secondary electrons [14]. These charged particles can result local damage to the DNA of cancer cells and are the main and most important objectives for biological effects [12,15,16]. In orthovoltage X-ray irradiations, dose enhancement is mainly due to increase in photoelectric interactions with these materials [17]. For higher-energy photons, the primary model of energy transfer to biological material, are Compton and pair production interactions [18]. The impact of energy of ionizing radiation in the radiosensitivity enhancement of iron oxide nanoparticles especially in energies more than 6MV have not been comprehensively done. The aim of this in-vitro study was investigating the radiosensitivity effect of dextran coated iron oxide nanoparticles on cervical cancerous HeLa cells which irradiated with megavoltage (6 and 18 MV) photon beams.

Materials and method

Dextran-coated iron oxide nanoparticles

Dextran-coated iron oxide nanoparticles (DIONs) were purchased from Sharif-Teb System (Tehran, Iran) which were synthesized by co-precipitation method [19]. TEM image of dextran-coated iron oxide nanoparticles is shown in Figure 1.

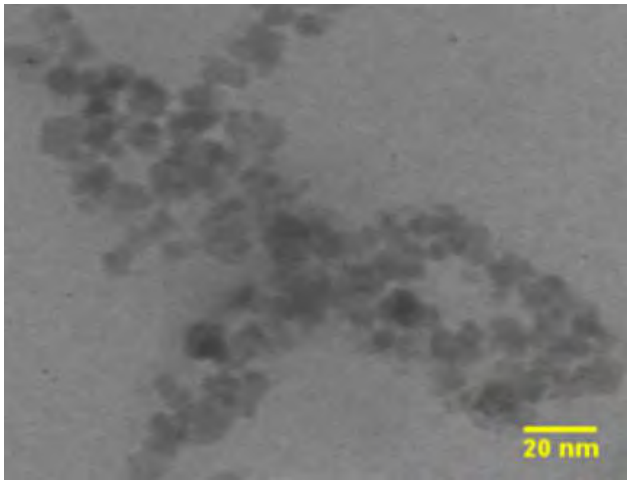

Figure 1. TEM image of dextran-coated iron oxide nanoparticles.

Cell Culture

HeLa cells were purchased from Pasteur institute (Tehran, Iran). These cells were cultured as monolayer in Dulbecco's Minimum Essential Media (DMEM) (Lonza, Switzerland) containing 10% fetal bovine serum (Lonza, Switzerland) and 100 µg/ml penicillin/streptomycin and incubated at 37 °C containing 5% carbon dioxide and 85% humidity in T-75 flasks. Cells growth curve was plotted based on daily counting living cells in 10 days by Trypan blue staining and also the approximate time which the cells reach to logarithmic phase were obtained. Before seeding in 96-well plates, the cells were cultured in T-75 flasks; and then when they reaches to more than about 70 percent confluency, they were detached by Trypsin-EDTA solution (Lonza, Switzerland) from the bottom flask and manually counted by phase contrast microscopy and Neubauer chamber. About 5000 cells/well were seeded in the plates.

Cytotoxicity assay

In order to study the cytotoxicity effect of the dextran coated iron oxide nanoparticles on the cells, 5× 103 HeLa cells were cultured in 96-well plates. The nanoparticles were incubated with the cells at different concentrations including 0, 1, 5, 10, 20 and 50 µg /ml. MTT (3- (4,5-dimethylthiazol-2-yl) -2,5-diphenyltetrazolium bromide, a tetrazol) assays were performed for all the cells groups after 6, 12 and 24 hours of incubation. In MTT assay, tetrazolium solution (5 mg/ml) was prepared and filtered with 0.22 µm (Korea, SPL); then 20 µl of the solution was added to the wells and incubated for 4 hours at 37 °C. 4 wells were used for each concentration. After the aforementioned time, tetrazolium is metabolized and purple formazan crystals formed inside living cells. Then the supernatant of the wells drained off and 100 µl DMSO was added to each well until violet color solutions to be created. Then the optical density of the wells which is a criterion of cells viability level were measured by an ELISA reader (USA, Awareness) at 570 nm wavelength.

Irradiations

Irradiations were performed using a linear accelerator (ELEKTA, England) in Imam-Reza hospital of Kermanshah (Iran). For measuring the radiosensitivity enhancement of the nanoparticles, 5 103 HeLa cells per well was plated in 96-well plates and incubated with the dextran-coated iron oxide nanoparticles for 24 hours at concentrations of 20 and 50 µg/ml. Then the plates were washed three times with PBS and fresh culture media were added; after that the plates transferred to the hospital via a portable incubator and were irradiated in presence or absence of the nanoparticles with different doses (0, 2, 4, 6, and 8 Gy) of 6 and 18 MV photon beams. Treatment groups were consisted of radiation alone (in which the cells irradiated without before incubation with the nanoparticles) and radiation plus DIONs (irradiation with prior

incubation of the nanoparticles), and also the control group (cells only, or no radiation and no nanoparticles) all were cultured in 96-well plates and were placed under the same environmental conditions. After 48 hours of irradiations MTT assay were performed for all groups. The experiments were repeated at least three times for each energy and concentration of the DIONs; and the results are reported as mean± standard deviation.

Statistical Analysis

All experiments were repeated at least three times and each experiment was done in triplicates. Results of 1-sample K-S statistical test showed that distribution of data were not normal. There were significant differences in mean survival rates between the treated groups using Kruskal-Wallis. Mann-Whitney tests also were used to compare the difference between each two independent groups.

Results

Cytotoxicity of dextran coated iron oxide nanoparticles

The results of cytotoxicity assessment of the nanoparticles on the HeLa cells showed significant difference between treated groups (in which the cells incubated with different concentrations of the nanoparticles including 1, 5, 10, 20 and 50 µg /ml for 6, 12 and 24 hours) and their control group ($p < 0.05$). Cells survival rates in all groups which obtained using MTT assay are shown in Figure 2.

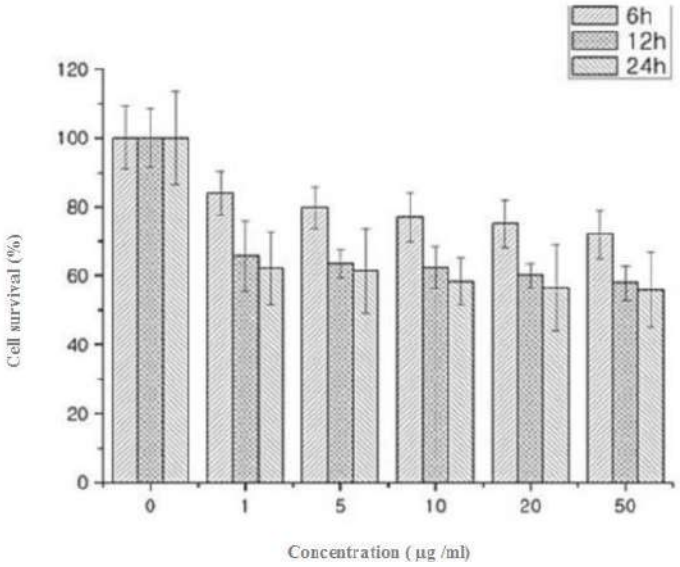

Figure 2. Cytotoxicity of the nanoparticles on the HeLa cell line. The cells incubated with different concentrations (0, 1, 5, 10, 20 and 50 µg/ml) of dextran coated iron oxide nanoparticles for 6, 12 and 24 hours.

Radiosensitivity enhancement by the nanoparticles

HeLa cells survival rate versus radiation absorbed dose of 6 and 18 MV photon beams is shown in Figures 3& 4. Regarding to these figures, DIONs at concentrations of 20& 50 µg/ml can enhance the radiosensitivity of HeLa cells. Significant differences were observed in cells survival rates between the groups irradiated with 6 and 18 MV in presence of the nanoparticles (at concentrations of 20 & 50 µg/ml) at all doses ($p < 0.05$). In other words, average percentage of cell survival was decreased at constant concentration (20 or 50 µg/ml) with increasing photon beamṡ energy from 6 to 18 MV.

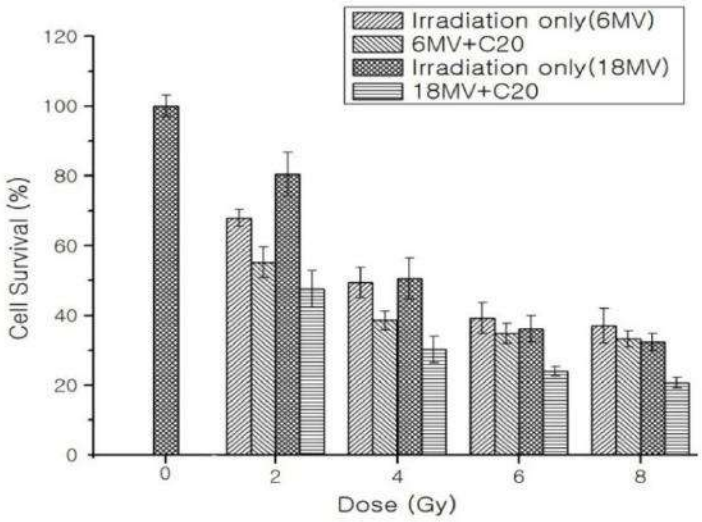

Figure 3. Comparison of the HeLa cells survival percentage which irradiated with 6 and 18 MV photon beams with and without prior incubation of the nanoparticles at concentration of 20 µg/ml.

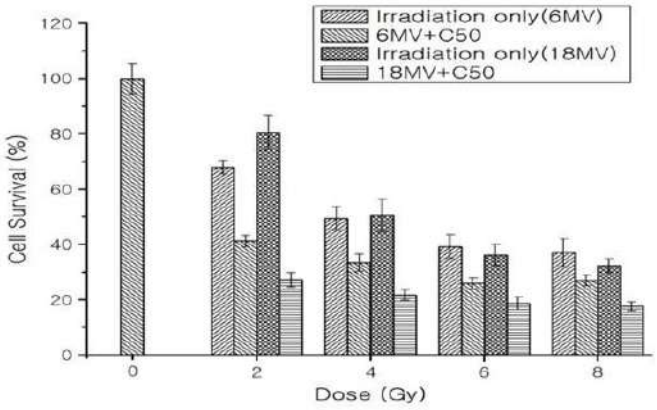

Figure 4. Comparison of the HeLa cells survival percentage which irradiated with 6 and 18 MV photon beams with and without prior incubation of the nanoparticles at concentration of 50 µg/ml.

A comparison of the dose enhancement factor (DEF) values induced by the DIONs in Hela cells which irradiated with different doses of 6 & 18 MV photons is shown in Figure 5. The DEF values were calculated from dividing the cellṡ mean survival percentage of irradiation only (without nanoparticles) group by that of irradiation plus nanoparticles group. Enhancement of the radiosensitivity of the cells due to presence of the nanoparticles (which is indicated with DEF value) in 18 MV irradiations is relatively more than it in 6 MV irradiations.

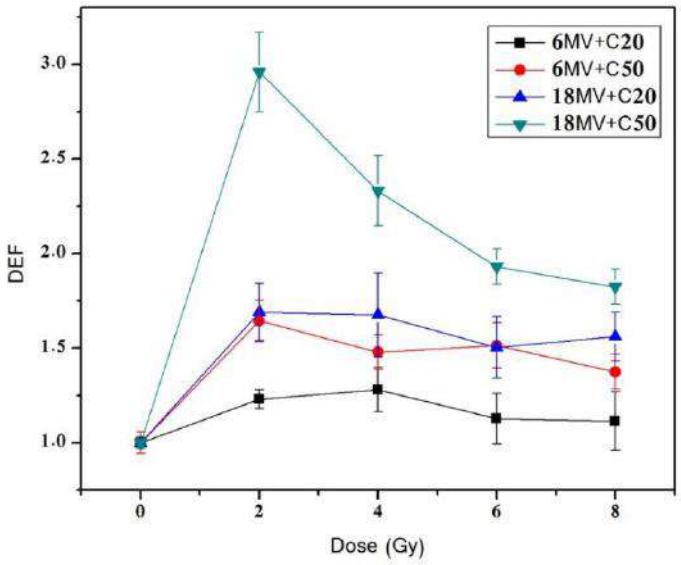

Figure 5. Comparison of the dose enhancement factor values in the cells which incubated with the nanoparticles (20& 50 μg/ml) and irradiated with 6 and 18 MV photon beams.

Discussion

Dextran coated iron oxide nanoparticles enhanced the radiosensitivity of cancerous HeLa cells. Based on the enhanced permeability and retention (EPR) effect, nanoparticles with a selective absorption method accumulate in tumor cells [7,37]. Positively charged surfaces of nanoparticles facilitate penetration of nanoparticles to the cells and cause cell damage through electrostatic interactions [38]. The main effects of radiation for killing the tumoral cells are DNA damages and chemical interactions caused by free radicals which are produced by the radiation [13]. The presence of high atomic number nanoparticles such as the DIONs inside the cells can increase damages to the cells and consequently lead to cell death. Also our study showed that these nanoparticles can be toxic for cancerous HeLa cells. As reported in previous studies, cytotoxicity of nanoparticles depends on many parameters including type, size and concentration surface

modification of nanoparticles as well as their incubation time and cell line [20-22]. A study has compared the cytotoxicity of several metal oxide nanoparticles in-vitro shows that iron oxide nanoparticles at concentrations of less than 100 μg/ml are safe and non-toxic [21]. The fracture of dextran and exposure the iron grains to cellular components and accumulation of them has been reported as a main reason for observed cytotoxicity of dextran coated iron nanoparticles [23].

However, we checked the effect of nanoparticles concentration and incubation time period in cytotoxicity level induced by the DIONs on HeLa cell line; this section was performed to obtain the optimum parameters (concentration and incubation time) in the main study. The main objective of present study was investigating the radiosensitization enhancement by these nanoparticles on cancerous cells in megavoltage photon beams irradiations, especially high energy photons. Some studies have focused on radiosensitization effect of high-Z nanoparticles especially gold nanoparticles [8,9,24,25], in orthovoltage and low MeV photon irradiations. In the case of orthovoltage X-ray irradiation, radiosensitization enhancement effect is due to increase in photoelectric interactions with these high-Z materials [26]. In interaction of megavoltage photons with materials such as tissue elements, important probable processes are Compton scattering, photoelectric, and pair production. If materials like tissue that often has a low atomic number are irradiated with 6 MV photons, Compton process will be the dominant interaction; however, with increasing photon energy over 6 MV the probability of pair production will be more significant [17,26,27]. The differences between the probabilities of various interactions in collision of photons with the tissue and gold and other metals such as iron are due to differences in their atomic number. Iron atomic number is 26 while the effective atomic number of tissue is about 7.4 [17]. As mentioned above, Compton interaction is dominant process in collision of 6 MV photons with tissue, however there are still the significant probabilities of photoelectric and also pair production interactions [17]. The occurrence probabilities of photoelectric and pair production interactions varies as Z^3/E^3 and Z^2, respectively [28]. Considering a given energy of photon (e.g. 6 or 18 MV beams) and under same conditions, photoelectric events in iron is $(26/7.4)^3$ or 43 times more than it in soft tissue. Irradiation the cells with 18 MV photon beams in presence of the DIONs also leads to more absorbed energy due to increase in pair production interactions (which varies as Z^2) and therefore more biological damage occurs in the cells. However, a considerable number of DIONs must be entered into the cells for having the significant increase in photon absorption by photoelectric or pair production interactions and consequently increasing the radiosensitivity of the cells. Most of former studies in the field of enhancing radiosensitivity of cancer cells in radiobiology have performed using gold nanoparticles [7,8,24,25,29]. However, in a similar study to our work, the DEF value of about 1.2 has been

reported due to use of dextran-coated iron oxide nanoparticles in DU-145 cancer cells accompany with megavoltage photon (6 MV) irradiations [12]. In present study, the average level of DEF in different radiation dose irradiations with 6 & 18MV was obtained as 1.19±0.15, 1.6±0.11 at concentration of 20 µg/ml, respectively; and 1.49±0.11, 2.25±0.44 at concentration of 50 µg/ml, respectively for HeLa cells. Generally, various factors including cell line, type, size, concentration, and coating of nanoparticles, as well as beam quality affect the dose enhancement induced by nanoparticles [12,30-32]. According to our results and in consistency with the other works [12,30], the DEF level increases with increasing the concentration of the nanoparticles. This can be due to further entry of the nanoparticles into the cells in higher concentrations; where a greater number of the high-Z nanoparticles in the cells during irradiation leads to more probability of interaction with photons and consequently production of more free radicals and secondary electrons [33-35].These agents increase the damage to DNA of the cells [36]. In comparison 6 and 18 MV results, we can say that enhancement of the radiosensitivity of the cells due to presence of the nanoparticles in 18 MV irradiations is significantly more than (averagely 1.35 and 1.5 at concentrations of 20 and 50 µg/ml, respectively) it in 6 MV irradiations. As previously mentioned, an increase in pair production as absorption processes in 18 MV irradiations than 6MV seems to be the cause of this difference. It also has reported that the probability of pair production events in interaction 18 MV photons with gold and aluminum is approximately 2.5 times greater than it via 6 MV photons [17]. The use of none-toxic concentrations of DIONs inside cancer cells that have high atomic number relative to tissues, will increase the efficiency of cancer treatment. In other words using these nanoparticles selectively in cancer cells, we will able to decrease the prescribed doses of radiation and consequently decrease the radiation dose to normal tissues which is the major concern in radiotherapy. This less radiation to healthy tissues surrounding the tumoral tissue led to lower side effects of ionizing radiation in normal organ at risk.

Conclusion

Using dextran-coated iron oxide nanoparticles in accompany with megavoltage photon beams irradiations significantly enhances radiation cell-killing effect, which can be considered in the treatment of cancer.

Acknowledgments

The authors gratefully acknowledge the Research Council of Kermanshah University of Medical Sciences for the financial support (Grant Number: 93148). This work was performed in partial fulfillment of the requirements for the master of science degree of Hossein Mafakheri, in the School of Medicine, Kermanshah University of Medical Sciences, Kermanshah, Iran.

Conflict of interest: The authors declare no conflict of interest.

References

1.Ting G, Chang C-H, Wang H-E. Cancer nanotargeted radiopharmaceuticals for tumor imaging and therapy. Anticancer research. 2009;29(10):4107-18.

2.Siegel R, Naishadham D, Jemal A. Cancer statistics, 2013. CA: a cancer journal for clinicians. 2013;63(1):11-30.

3.Khan FM, Gerbi BJ. Treatment planning in radiation oncology: Wolters Kluwer Health/Lippincott Williams & Wilkins; 2012.

4.Hall EJ, Giaccia AJ. Radiobiology for the Radiologist: Lippincott Williams & Wilkins; 2006.

5.Andreyev H. Gastrointestinal problems after pelvic radiotherapy: the past, the present and the future. Clinical Oncology. 2007;19(10):790-9.

6.Babaei M, Ganjalikhani M. The potential effectiveness of nanoparticles as radio sensitizers for radiotherapy. Bioimpacts. 2014;4(1):15.

7.Hainfeld JF, Dilmanian FA, Zhong Z, Slatkin DN, Kalef-Ezra JA, Smilowitz HM. Gold nanoparticles enhance the radiation therapy of a murine squamous cell carcinoma. Physics in medicine and biology. 2010;55(11):3045.

8.Jain S, Coulter JA, Hounsell AR, Butterworth KT, McMahon SJ, Hyland WB, et al. Cell-specific radiosensitization by gold nanoparticles at megavoltage radiation energies. International Journal of Radiation Oncology Biology Physics. 2011;79(2):531-9.

9.Khoshgard K, Hashemi B, Arbabi A, Rasaee MJ, Soleimani M. Radiosensitization effect of folate-conjugated gold nanoparticles on HeLa cancer cells under orthovoltage superficial radiotherapy techniques. Physics in medicine and biology. 2014;59(9):2249.

10.Rezaei-Tavirani M, Dolat E, Hasanzadeh H, Seyyedi S-S, Semnani V, Sobhi S. TiO2 Nanoparticle as a sensitizer drug in radiotherapy: in vitro study. Iranian Journal of Cancer Prevention. 2013;6:37-44.

11.Su X-Y, Liu P-D, Wu H, Gu N. Enhancement of radiosensitization by metal-based nanoparticles in cancer radiation therapy. Cancer biology & medicine. 2014;11(2):86-91.

12.Khoei S, Mahdavi SR, Fakhimikabir H, Shakeri-Zadeh A, Hashemian A. The role of iron oxide nanoparticles in the radiosensitization of human prostate carcinoma cell line DU145 at megavoltage radiation energies. International journal of radiation biology. 2014;90(5):351-6.

13.Gupta AK, Gupta M. Synthesis and surface engineering of iron oxide nanoparticles for biomedical applications. Biomaterials. 2005;26(18):3995-4021.

14.Brun E, Sanche L, Sicard-Roselli C. Parameters governing gold nanoparticle X-ray radiosensitization of DNA in solution. Colloids and Surfaces B: Biointerfaces. 2009;72(1):128-34.

15.Liu Y, Liu X, Jin X, He P, Zheng X, Dai Z, et al. The dependence of radiation enhancement effect on the concentration of gold nanoparticles exposed to low-and high-LET radiations. Physica Medica. 2015;31(3):210-8.

16.Wu X, Tan Y, Mao H, Zhang M. Toxic effects of iron oxide nanoparticles on human umbilical vein endothelial cells. Int J Nanomedicine. 2010;5:385-99.

17.Alkhatib A, Watanabe Y, Broadhurst JH. The local enhancement of radiation dose from photons of MeV energies obtained by introducing materials of high atomic number into the treatment region. Medical physics. 2009;36(8):3543-8.

18.Hubbell J. Review of photon interaction cross section data in the medical and biological context. Physics in medicine and biology. 1999;44(1):R1.

19.Gnanaprakash G, Mahadevan S, Jayakumar T, Kalyanasundaram P, Philip J, Raj B. Effect of initial pH and temperature of iron salt solutions on formation of magnetite nanoparticles. Materials chemistry and Physics. 2007;103(1):168-75.

20.Jeng HA, Swanson J. Toxicity of metal oxide nanoparticles in mammalian cells. Journal of Environmental Science and Health Part A. 2006;41(12):2699-711.

21.Karlsson HL, Gustafsson J, Cronholm P, Möller L. Size-dependent toxicity of metal oxide particles—a comparison between nano-and micrometer size. Toxicology letters. 2009;188(2):112-8.

22.Kim JS, Yoon T-J, Yu KN, Kim BG, Park SJ, Kim HW, et al. Toxicity and tissue distribution of magnetic nanoparticles in mice. Toxicological Sciences. 2006;89(1):338-47.

23.Berry CC, Wells S, Charles S, Curtis AS. Dextran and albumin derivatised iron oxide nanoparticles: influence on fibroblasts in vitro. Biomaterials. 2003;24(25):4551-7.

24.McMahon SJ, Mendenhall MH, Jain S, Currell F. Radiotherapy in the presence of contrast agents: a general figure of merit and its application to gold nanoparticles. Physics in medicine and biology. 2008;53(20):5635.

25.Regulla D, Hieber L, Seidenbusch M. Physical and biological interface dose effects in tissue due to X-ray-induced release of secondary radiation from metallic gold surfaces. Radiation research. 1998;150(1):92-100.

[26].Retif P, Pinel S, Toussaint M, Frochot C, Chouikrat R, Bastogne T, et al. Nanoparticles for radiation therapy enhancement: the key parameters. Theranostics. 2015;5(9):1030.

27.Karlsson HL, Cronholm P, Gustafsson J, Moller L. Copper oxide nanoparticles are highly toxic: a comparison between metal oxide nanoparticles and carbon nanotubes. Chemical research in toxicology. 2008;21(9):1726-32.

28.Hainfeld JF, Dilmanian FA, Slatkin DN, Smilowitz HM. Radiotherapy enhancement with gold nanoparticles. Journal of Pharmacy and Pharmacology. 2008;60(8):977-85.

29.Copland JA, Eghtedari M, Popov VL, Kotov N, Mamedova N, Motamedi M, et al. Bioconjugated gold nanoparticles as a molecular based contrast agent: implications for imaging of deep tumors using optoacoustic tomography. Molecular Imaging & Biology. 2004;6(5):341-9.

30.Algethami M, Geso M, Piva T, Blencowe A, Lu L, Ai K, et al. Radiation dose enhancement using Bi2S3 nanoparticles in cultured mouse PC3 prostate and B16 melanoma cells. NanoWorld Journal. 2015;1(3):97-102.

31.Luchette M, Korideck H, Makrigiorgos M, Tillement O, Berbeco R. Radiation dose enhancement of gadolinium-based AGuIX nanoparticles on HeLa cells. Nanomedicine: Nanotechnology, Biology and Medicine. 2014;10(8):1751-5.

32.Mousavi M, Nedaei HA, Khoei S, Eynali S, Khoshgard K, Robatjazi M, et al. Enhancement of radiosensitivity of melanoma cells by pegylated gold nanoparticles under irradiation of megavoltage electrons. International Journal of Radiation Biology. 2016:1-8.

33.Jeynes J, Merchant M, Spindler A, Wera A, Kirkby K. Investigation of gold nanoparticle radiosensitization mechanisms using a free radical scavenger and protons of different energies. Physics in medicine and biology. 2014;59(21):6431.

34.Le Sech C, Kobayashi K, Usami N, Furusawa Y, Porcel E, Lacombe S. Comment on? Therapeutic application of metallic nanoparticles combined with particle-induced x-ray emission effect? Nanotechnology. 2012;23(7):078001.

35.Praetorius NP, Mandal TK. Engineered nanoparticles in cancer therapy. Recent Patents on Drug Delivery & Formulation. 2007;1(1):37-51.

36.Yao X, Huang C, Chen X, Zheng Y, Sanche L. Chemical radiosensitivity of DNA induced by gold nanoparticles. Journal of biomedical nanotechnology. 2015;11(3):478-85.

37.Maeda H. The enhanced permeability and retention (EPR) effect in tumor vasculature: the key role of tumor-selective macromolecular drug targeting. Advances in enzyme regulation. 2001;41(1):189-207.

38.Selim KK, Xing Z-C, Choi M-J, Chang Y, Guo H, Kang I-K. Reduced cytotoxicity of insulin-immobilized CdS quantum dots using PEG as a spacer. Nanoscale research letters. 2011;6(1):528.

Dietary Trichoderma spp. mutants improved some immune and antioxidant indicators in rainbow trout (Oncorhynchus mykiss) fingerlings (Paper ID : 1479)

Fereshteh Zeraat Pisheh[1], Marzieh Heidarieh[*2], Alireza Mirvaghefi[1], Samira Shahbazi[2], Farhad Konyeh[1]
[1] *Department of Fisheries, Faculty of Natural Resources, University of Tehran, Karaj, Iran*
[2] *Nuclear Science and Technology Research Institute, Tehran, Iran*

Abstract

Scientists are currently exploring potential methods to increase food production while simultaneously ensuring environmental safety. One promising approach involves the utilization of *Trichoderma* spp., which has demonstrated the ability to enhance plant growth. Recent research has examined the impact of exposing *Trichoderma afroharzianum* and *Trichoderma lixii* to a 250 Gy dose of gamma radiation utilizing the Issoledovatle Gamma cell PX-30 device, which operates with Cobalt-60, to augment their growth-promoting potential. Subsequently, the effects of gamma-irradiated *Trichoderma* spp. on rainbow trout fingerlings were evaluated. Ninety rainbow trout fingerlings, with an average weight of 61 ± 0.5 grams, which were separated into three groups: *T. Afroharzianum* (TM-1), *T. Lixii* (TM-2), and a control group (CL). The fish were fed for six weeks in a 300-liter tank. The outcomes revealed a noteworthy discrepancy in the antioxidant levels between the control and the treated groups. TM-2 exhibited the highest antioxidant levels, while TM-1 exhibited the highest safety indicators, which were significantly distinct from the other treatments. As a result, the study suggests that gamma-irradiated *Trichoderma afroharzianum* and *Trichoderma lixii* have the potential to improve certain antioxidant and immunity responses in rainbow trout (*Oncorhynchus mykiss*) fingerlings.

Keywords: *Trichoderma* spp., immune indicators, antioxidant parameters, rainbow trout fingerlings, gamma irradiated.

INTRODUCTION

The escalation of the global population has engendered a concomitant demand for protein, resulting in a rise in the consumption of aquatic products, particularly fish [1]. Aquaculture production has emerged as the fastest-growing sector in the global economy, posting an average annual growth rate of 11% over the past two decades [2]. Cold-water fish has been the primary source of global fish production and has been extensively cultivated in various regions, including our country [3,4]. Rainbow trout, the most commonly cultivated fish globally, provides a valuable model for studying the toxicity level of some agents due to its susceptibility to pollution and genetic similarities to humans. This species has been extensively used for

research in diverse fields such as carcinogenesis, toxicology, comparative immunology, disease ecology, physiology, and nutrition [5].

Trichoderma are possibly the most widely used biocontrol agents worldwide. The *Trichoderma* spp. Is highly effective in controlling soil-borne fungi, as well as other pathogenic organisms, including bacteria, protozoa, nematodes, and viruses [6].

Recent research aims to determine the sensitivity of immune and antioxidant responses in rainbow trout (Oncorhynchus mykiss) fingerlings to gamma-irradiated Trichoderma afroharzianum and Trichoderma lixii.

EXPERIMENTAL

Fish

90 pieces of rainbow trout, with an average weight of 61 ± 0.5 grams, were purchased from a fish farm located in Yasouj, Iran, and transported to the Bushehr Persian Gulf Research Institute. The fish were acclimated for two weeks in 300-liter fiberglass tanks.

Following the acclimatization period, the fish were randomly assigned to nine 300-liter tanks, with three replicates for each treatment. Spores of gamma-irradiated *T. afroharzianum* (TM-1) and *T. lixii* (TM-2) were added to the feed, and the feed was sprayed with 4 ml of vegetable oils and then exposed to open air until it dried. The feed for each treatment was stored separately in a plastic container in the refrigerator (4 °C). The control (CL) group's diet underwent all stages of food preparation, except for the addition of Trichoderma spores to its food.

Throughout the six-week experimental period, tanks were changed daily by 90% of the water, and oxygen and temperature were measured daily in two stages using a portable device (BodyGuard®, Denmark), and pH with a Hana® device (made in China). The fish were fed twice daily with the commercial feed of Kimiagaran Nutrition Company, Iran, whose approximate analysis is provided in Table 1. The fish were fed at the rate of 2% of their body weight.

Table 1. Approximate analysis of commercial feed for rainbow trout

Compositions	raw materials (%)
Protein	48-52
Fat	9-13

Humidity	12
ash	11-15
Phosphorus	4/1-1

Gamma irradiated Trichoderma spp.

Spore suspension (107 mL-1) of *T. afroharzianum* and *T. lixii* 65 (Th65) isolate (WT) was spread on Water-Agar (WA) plates and then irradiated with gamma cell (Co- 60, activity 2500 Curry, rate dose of 0.23 Gy. Second-1 by the dose of 250 at the Nuclear Science and Technology Research Institute of Iran and incubated at 4 ºC [6].

Determination of the activity of antioxidant enzymes in serum

The activity of extracellular superoxide dismutase-3 (SOD-3) and total antioxidant capacity was measured in the serum of the studied fish using commercial kits (Biorex, UK).

Analysis of serum lysozyme activity

The method presented by Kumari (2006) with some modifications was used to determine the amount of serum lysozyme. Firstly, 25 microliters of serum were added to 96-well ELISA plates. Then, 150 microliters of Micrococcus lysodicticus suspension, which was prepared in 0.02 M sodium citrate buffer with a pH of 5.5, were added. The initial optical absorption was measured at a wavelength of 450 nm, and after being stored at room temperature for 4 minutes, the optical absorption was measured again. Sigma's lyophilized egg white lysozyme was used to create a standard curve [7].

Complement test (ACH50)

For every 0.5 microliters of serum diluted in (EGTA-MG-GVB 10Mm) {veronal buffer containing 10 mmol of ethylene glycol tetraacetic acid, 10 mmol of magnesium dichloride, and 0.1% gelatin}, 200 microliters of sheep erythrocyte suspension (cell ml-1108 × 2.5) was added in 10 mM EGTA-MG-GVB buffer. The prepared dilutions were incubated at 15°C for 90 minutes. Hemolytic activity was increased by adding 2.8 ml of 10 mM AD buffer. T. E-gelatin-veronal buffer (10mM EDTA-GVB) (veronal buffer containing 10mmol ethylene diamine tetra, acetic acid (EDTA), and 0.1% gelatin) was stopped. After centrifugation, the supernatant was read at a wavelength of 414 nm by a spectrophotometer. Lysis percentage (y) was obtained by dividing the red wavelength by 100% lysis (lysis in distilled water). The logarithmic graph of y/1-y points and the photo of the dilution were drawn on the logarithmic plane, and then the photo of the dilution that had 50% hemolysis was read as ACH50 (unit ml-1) from the obtained curve [8].

Statistical analysis of data

The Kolmogorov-Smirnov test was used to measure the normal distribution of the data. To compare the means between treatments, a one-way analysis of variance test was conducted. The level of significance was determined through Duncan's test, with a confidence level of 5%. Data analysis was carried out using SPSS 22 statistical software on Windows, and graphs were drawn using Excel 19 software.

Results and discussion

The results of the total antioxidant capacity assessment revealed that the TM-4 group exhibited the highest level of antioxidants, while the control group had the lowest level during the initial phase. Similarly, the superoxide dismutase assessment indicated that the TM-4 treatment group demonstrated the highest level of antioxidants, and there was a significant difference among all groups ($p<0.05$). Conversely, the control group showed the lowest level of antioxidants. These findings suggest that the TM-4 treatment has a more significant impact on antioxidant levels compared to the control group, and further research in this area is warranted.

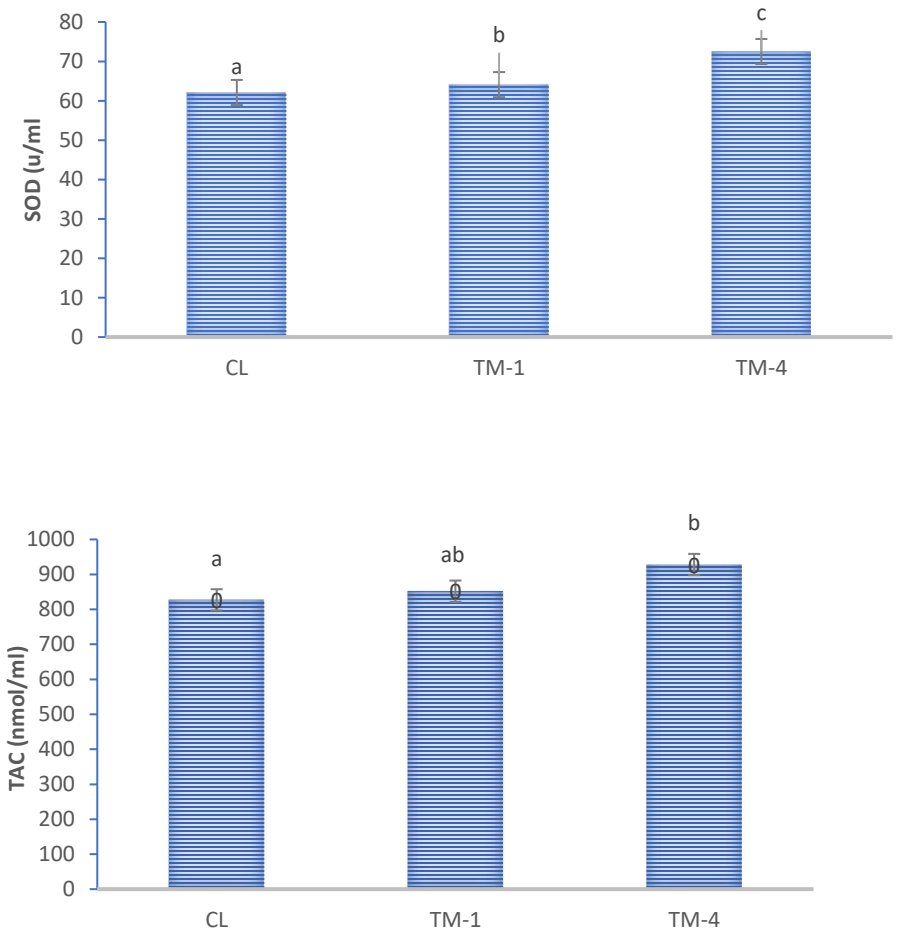

Fig. 1. The results of antioxidant indices (TAC and SOD) of rainbow trout fed with gamma-irradiated Trichoderma spp. During six weeks.

Significant differences were observed in complement levels among the groups. The lowest amount of complement was observed in the zero group and the highest amount was observed in the TM-1 group. A significant difference was observed between TM-4 and TM-1 groups. Also, the observation of the level of lysozyme showed that there is a significant difference between the control group and other groups. In other words, the lowest amount was observed in the zero group. The amount of lysozyme showed that there was a significant difference between the TM-3 and TM-1 groups, and the highest amount was visible in the TM-1 group.

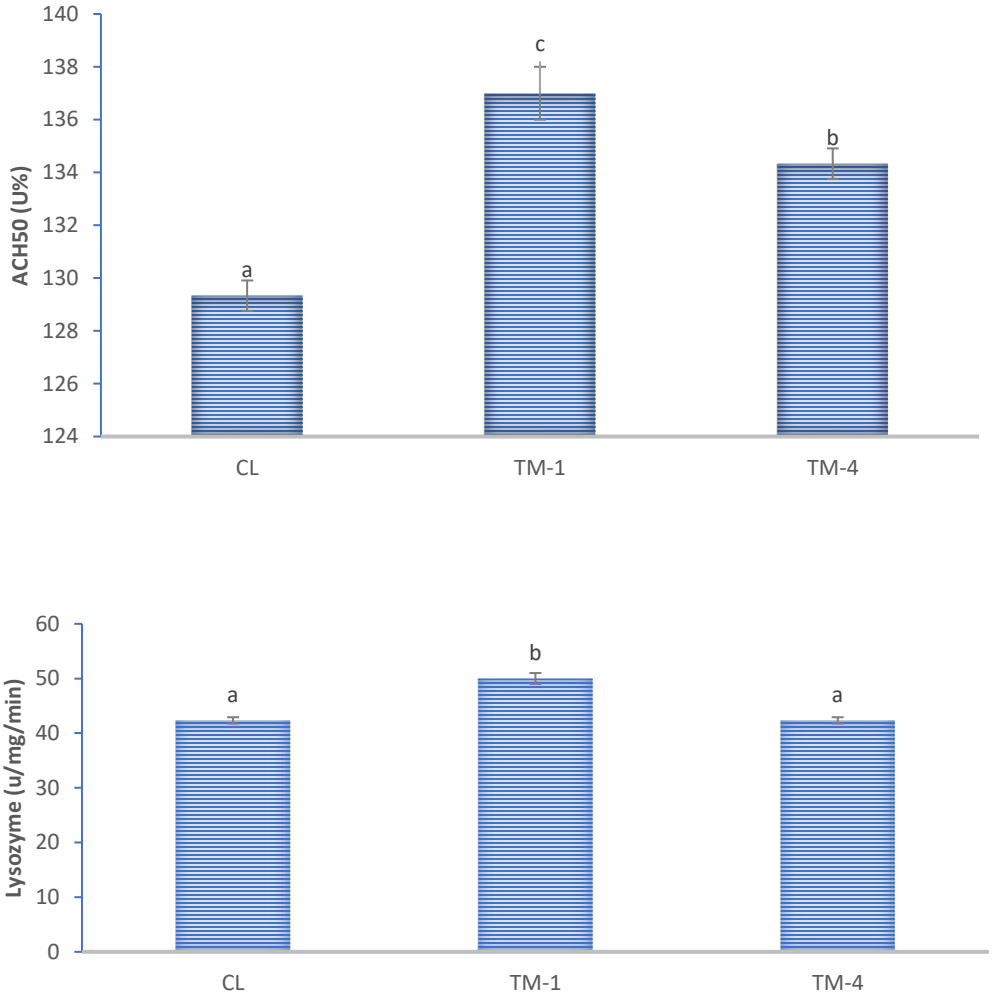

Fig. 2. The immunity responses (Lysozyme and ACH50) of rainbow trout fed with gamma irradiated *Trichoderma* spp. during six weeks.

Discussion

Innate immunity in fish is created by three physical, cellular, and chemical factors. Lysozyme, some proteins of the complement system are part of chemical agents. The complement system in mammals is a collection of 35 types of serum proteins that have a very close and controlled relationship with each other and other molecules of the immune system [9]. The complement system proteins between fishes and mammals have a great similarity, as revealed by studies on the immune system of fishes [10]. The greatest effects of gamma-irradiated *Trichoderma* spp. on complement system proteins (ACH50) were seen in the TM-3 treatment group. Complements are proteins of the acute phase (C-reactive protein) of the immune system and their concentration usually changes after cell necrosis and tissue death. Furthermore, the change

in the level of complements as an acute phase response of the immune system is considered a type of generalized systemic response that can be related to inflammation and innate immune response [11]. A decrease in plasma total complement protein levels can make fish susceptible to bacterial infections. The change of complement activity is very important as a part of the non-specific immune system of fish, and its high level of activity indicates the health of the fish. In most cases, the production of complement protein is done by liver macrophages, on the other hand, the liver is the body's detoxification center, and xenogenic compounds (compounds, drugs, and external factors) pass through the liver. Therefore, high levels of toxic substances will be found in the liver, which has locally affected the liver macrophages and prevented the production of complement proteins by them.

Lysozyme is released by white blood cells and secreted in various tissues and blood circulation, it is found in mucous secretions, gills, kidney tissues, spleen and digestive system, and blood serum of fishes and can break the glycosidic bonds of the peptidoglycan layer in the cell wall of bacteria [12]. The decrease in the level of lysozyme in the fish exposed to any toxin clearly shows the effect of diazinon in weakening the immune system. Therefore, these fish will be more sensitive to the occurrence of bacterial infections. In this study, there is no significant difference between the fed groups or an increase between the TM-3 and other groups, the level of lysozyme also indicates the effect of different species of *Trichoderma* spp. in measuring the immune system. The decrease in the level of lysozyme activity in grass carp (*Ctenopharingodon idella*) exposed to diazinon also confirms this [13].

Oxidative stress is one of the most common physiological effects of toxic substances in fish [14, 15, 16]. Fish possess antioxidant defense enzymes such as superoxide dismutase and catalase, which the superoxide dismutase enzyme act as the first line of defense against free radicals. It breaks down hydrogen peroxide into water and oxygen. However, its effectiveness is limited, and pollutants can reduce its capacity. In such cases, non-enzymatic antioxidant compounds such as vitamins play a crucial role in preventing the formation of free radicals [17]. Antioxidant enzymes such as superoxide dismutase, glutathione peroxidase, and glutathione are sensitive to toxic substances and can be used as an indicator of toxicity. Superoxide dismutase converts superoxide ions into hydrogen peroxide, which is then neutralized by glutathione peroxidase and turned into water [18]. In the first stage of the study, the highest amount of antioxidants was measured in the treatment groups fed with gamma-irradiated *Trichoderma* spp.

Compared to the control group, a significant increase was observed in the TM-3 and TM-4 groups, which was consistent with the results of the final stage. Similar to the present study in *Japanese medaka* and *Oryzias latips*, catalase, superoxide activity, and dismutase increased after exposure to BPA [19]. The study

suggests that gamma-irradiated *Trichoderma* spp. has the potential to improve certain antioxidant and immunity responses in rainbow trout (Oncorhynchus mykiss) fingerlings.

Conclusions

In conclusion, our study indicates that gamma-irradiated Trichoderma spp. may enhance specific antioxidant and immune responses in rainbow trout fingerlings.

Acknowledgments

The authors are grateful to the Research affairs of Nuclear Science and Technology Research Institute, Tehran, Iran and University of Tehran, Tehran, Iran.

References

[1] Gholampour Azizi, A.; Hosseinifard, M.; Rouhi, S.; Moqtadar, H. (2013). Investigation and identification of fungal skin contamination of Caspian Sea salmon (Salmo trutta caspius) in fish farms of Mazandaran province. Quarterly scientific journal of animal biology. 53-45.

[2] Ghorbanzadeh, R.; Nazari, S. (2013). Statistical Yearbook of Iranian Fisheries Organization. Iran Fisheries Organization, Tehran, Iran. 47-35.

[3] Mousavi, H., Hoosseinifard, S. M., Khosravi, A. R., Soltani, M. and Yosefian, M. (2007). Isolation and identification of parasite and saprophyte fungi from fungal affected eggs of the rainbow trout (*Oncorhynchus mykiss*) in Mazandaran province. Journal of Veterinary Research, 62(2): 163-168.

[4] Vathoqi, G.; Mustajir, b. (2013). Freshwater fish. Tehran University Press, Tehran, Iran.

[5] Pia Santacroce Maria, M. C., Conversano, E., Casalino, O., Lai, C., Centoducati, G. and Crescenzo, G. (2008). Aflatoxins in aquatic species: metabolism, toxicity and perspectives. Reviews in Fish Biology and Fisheries, 18: 99–130.

[6] Shahbazfar, A.A., Heidarieh, M., Shahbazi, S. and Askari, H. (2023). Trichoderma harzianum as fungicide and symbiont: is it safe for human and animals? Veterinary Research Forum, 14(11):604-614.

[7] Kumari, J., Sahoo, P.K., Swain, T., Sahoo, S.K., Sahu, A.K. and Mohanty, B.R. (2006). Seasonal variation in the innate immune parameters of the Asian catfish Clarias batrachus. Aquaculture, 252(2–4):121-127.

[8] Matsuyama, H., Tanaka, K., Nakao, M. and Yano, T. (1988). Characterization of the alternative complement pathway of carp. Developmental & Comparative Immunology,12(2): 403-408.

[9] Nesargikar, P. N., Spiller, B. and Chavez, R. (2012). The complement system: history, pathways, cascade and inhibitors. European journal of microbiology & immunology, 2(2):103–111.

[10] Holland, M.C. and Lambris, J.D. (2002). The complement system in teleosts. Fish and Shellfish Immunology, 12(5): 399-420.

[11] Szalai, A. J., van Ginkel, F. W., Wang, Y., McGhee, J. R. and Volanakis, J. E. (2000). Complement-Dependent Acute-Phase Expression of C-Reactive Protein and Serum Amyloid P-Component. Journal of Immunology, 165 (2): 1030–1035.

[12] Ghafoori, Z., Heidari, B., Farzadfar, F. and Aghamaali, M. (2014). Variations of serum and mucus lysozyme activity and total protein content in the male and female *Caspian kutum* (Rutilus frisii kutum, Kamensky 1901) during reproductive period. Fish & Shellfish Immunology, 37(1): 139-146.

[13] Soltani, M. (2012). free fish diseases Tehran University Press, Tehran, Iran. .272-263.

[14] Lee, J. W., Kim, J. H., Lee, D. C., Lim, H. J. and Kang, J. C. (2022). Toxic Effects on Oxidative Stress, Neurotoxicity, Stress, and Immune Responses in Juvenile Olive Flounder, Paralichthys olivaceus, Exposed to Waterborne Hexavalent Chromium. Biology, 11(5):766.

[15] Menon, S.V., Kumar, A., Middha, S.K., Paital, B., Mathur, S., Johnson, R., Kademan, A., Usha, T., Hemavathi, K.N., Dayal, S., Ramalingam, N., Subaramaniyam, U., Sahoo, D.K. and Asthana, M. (2023). Water physicochemical factors and oxidative stress physiology in fish, a review. Frontiers in Environmental Science, 11:1240813.

[16] Hossein Hoseinifar, S.H., Yousefi, S., Van Doan, H., Ashouri, Gh., Gioacchini, G., Maradonna, F. and Carnevali, O. (2021). Oxidative Stress and Antioxidant Defense in Fish: The Implications of Probiotic, Prebiotic, and Synbiotics. Reviews in Fisheries Science & Aquaculture, 29(2): 198-217.

[17] Yousef, M. I., El Hendy, H. A., El-Demerdash, F. M. and Elagamy, E. I. (2002). Dietary zinc deficiency induced-changes in the activity of enzymes and the levels of free radicals, lipids and protein electrophoretic behavior in growing rats. Toxicology, 175(1-3): 223-234.

[18] Fridovich, I. (1972). Superoxide radical and superoxide dismutase. Accounts of Chemical Research, 5(10):321-326.

[19] Minghong, T. and Yuanyuan, L. (2019). Spatial and temporal variation of cropland at the global level from 1992 to 2015. Journal of Resources and Ecology, 10(3): 235-245.

ICNST 2024
International Conference on Nuclear Science and Technology
6- 8 MAY 2024 | Isfahan, Iran

Primary evaluation of selected mutant lines derived from mutation induction in local rice varieties (Paper ID : 1485)

Ebadi A.A. [1*] Rahemi, M.R. [2] Khoshkdaman M. [1] Mohammadi M. [1]

[1]*Rice Research Institute of Iran (RRII), Agricultural Research Education and Extension Organization (AREEO), Rasht, Iran.*

[2]*Nuclear Science and Technology Research Institute (NSTRI), Nuclear Agriculture Research School, Karaj, Iran.*

Abstract

Preparation of promising lines for obtaining new cultivars is one of the important steps in breeding programs. For this purpose, in this research, the 25 mutant lines derived from local varieties, Hashemi (3 mutant lines), Binam (3 mutant lines), Alikazemi (11 mutant lines) and Dilamani (8 mutant lines) along with the 4 mentioned parents were evaluated based on randomized complete block design with four replications in the Rice Research Institute during the 2020 crop year. In this study, agricultural characteristics including grain yield, panicles per plant, hundred grain weight, plant height, panicle length and days to 50% flowering, physical and chemical characteristics of grain such as amylose content, gelatinization temperature and head rice yielding was measured. The results showed that the mean square of the genotypes for all traits was significant at the 1% probability level, which indicates the existence of significant genetic differences between the genotypes in terms of the evaluated traits. 15 mutant lines (7 Dilmani mutant lines, 4 Alikazemi mutant lines, 2 Hashemi mutant lines, and 2 Binam mutant lines) were selected based on yield traits and other desirable quantitative and qualitative traits to be tested for stability and adaptability in the coming years.

Keywords: Rice, Mutation, Primary evaluation.

INTRODUCTION

Rice (Oryza sativa L.) is one of the most important crops and provides for daily meals for over half of the worldwide population [1]. Rice plays an important role in providing food and nutritional security and eradicating poverty. The average of total rice growing area in Iran is 791 Thousand hectares with 3.6 million tons of paddy production [2]. Increasing the genetic base of rice is an essential requirement for a rice improvement program, considering conventional techniques have not been able to resolve these

problems due to its narrow genetic base. The shortest possible method is induced mutation technique [1]. The most important thing in mutation breeding is the process of identifying individuals with a target mutation, specifically in mutant screening and mutant confirmation [4].

From a number of studies that have been conducted show mutation techniques are very useful in improving rice plants, especially for characters controlled by closely linked genes that are difficult to break by gene recombination [5]. Induced mutation has been used in rice more than any other crop as confirmed by for over 873 rice mutant varieties listed in the FAO/IAEA Mutant Varieties Database [6].

Nahvi et al. [8] selected 7 lines from 14 lines in the preliminary performance comparison test. After evaluating the compatibility of these lines in regional experiments, finally, line 424 was selected and introduced as a dwarf variety in 2013 [9]. Mohaddesi [10] evaluated 15 rice lines in terms of yield and agricultural traits in a preliminary performance comparison test, and selected some of these lines for regional tests, one of which was later introduced as the Tisa variety [17].

A number of 56 mutant lines were evaluated in both normal and drought stress conditions in Iran Rice Research Institute-Rasht. Among these lines, 14 mutant lines that had the highest grain yield under normal and drought stress conditions were selected [11]. The number of 14 mutant lines were evaluated in 3 locations in Rasht, Chepressar station and Fars during two crop years (2014-2015). After statistical analysis, 2 mutant lines obtained from Hashemi and one local Tarem mutant line were selected as stable lines [12]. These two lines with the names of Kian and Hasti were introduced as cultivars tolerant to drought stress.

Ebadi et al. [13] selected 22 blast-tolerant mutant lines that had better agronomic characteristics than the parents by creating mutations in the local cultivars Hashemi, Dilmani, Binam and Ali Kazemi. Ebadi et al. [14] selected 18 mutant lines with superior characteristics by creating mutations in the local varieties of Hashemi, Dilmani, Binam and Ali Kazemi. These lines were evaluated in this research.

Materials and Methods

In this research, 25 mutant lines (generation M6) drived from the mutation of local cultivars Hashemi (3 mutant lines), Binam (3 mutant lines), Ali Kazemi (7 mutant lines) and Dilmani (8 mutant lines) were used [13,14]. These lines along with the 4 mentioned parents were evaluated based on randomized complete block design with four replications in the field of the Rice Research Institute of Iran (RRII)-Rasht during

the 2019 crop year. The area of each plot was 4 square meters and the distance between the plants was 20 cm on the row and 20 cm between the rows. The seeds were sown in April and transplanted in May at the stage of 4-5 leaves. All agricultural operations such as fertilizer, weed control, and pest control were carried out according to the institute's technical recommendations. In this study, agricultural characteristics including grain yield, number of panicles per plant, hundred grains weight, plant height, panicle length and number of days to full maturity were measured. Also, the physical and chemical characteristics of the grain such as grain length and width elongation after cooking, amylose content based on Juliano method [15], gelatinization temperature based on Little et al., method [16] and head rice yielding were also measured after harvesting. The collected data were analyzed using SAS ver9.4 statistical software. Also, mean comparisons between measured traits were done using Tukey's test.

Results and discussion

The effect of block was not significant for all traits, except the length of the panicle, the number of filled grains per panicle and the weight of one hundred grains. The effect of genotypes for all traits was significant at the 1% probability level. The values of the coefficient of variation ranged from 1.29 to 16.91, which indicated the good and acceptable accuracy of the experiment.

The mean comparison between genotypes by Tukey's method at the 5% probability level is shown in Tables 1 and 2. The average days to 50% flowering varied from 80 to 107 days. The shortest length of growth period belonged to line DM6-60-32 and the longest length of growth period belonged to line BM6-310-16 (table 1).

The average of plant height of the studied lines varied between 123.25 and 155.75 cm. The highest amount of plant height belonged to Binam variety. The shortest line in this research was line DM6-60-3. After that, DM6-65-2, DM6-300-39, DM6-80-5, DM6-300-40 and DM6-300-2 lines respectively had the shortest plant height, which together and with DM6-60-3 line There was no significant difference (Table 1).

The highest average number of panicles per plant belonged to the line HM6-60-1 with an average of 17.75, which had a statistically significant difference with only three cultivars Hashemi, Dilmani and Ali Kazemi. The lowest average number of panicles per plant was 11.25 and belonged to Ali Kazemi variety. The AM6-290-1 line with an average panicle length of 31.62 cm and the DM6-60-3 line with an average panicle

length of 25.12 cm had the highest and lowest average panicle length among the studied genotypes, respectively (Table 1).

The range of changes of the average filled grain for the examined genotypes was between 78 and 136, belonging to Dilmani variety and line DM6-300-4, respectively. Among the studied genotypes, DM6-65-2 with an average number of unfilled grains of 28 and Ali Kazemi with 6.75 had the highest and lowest number of unfilled grains, respectively. Among the studied genotypes, HM6-60-2 line had the highest average weight of 100 grains with an average of 3.04 grams, and the lowest average weight of 100 grains belonged to Dilmani cultivar with an average of 2.04 grams (Table 1).

Comparison of the average of studied genotypes in terms of grain yield showed that although line DM6-300-2 had the highest amount of grain yield (5221 kg/ha), but this value was not statistically significantly different from more than half of the investigated lines. But there was a significant difference with the Hashemi, Dilmani, Ali Kazemi and Binam cultivars. Dilmani cultivar had the lowest grain yield with 3713 kg/ha (Table 1).

Line DM6-300-4 with an average of 65.31% of head rice yielding had the highest amount of this trait and it was statistically significantly different from other lines in this study. The lowest average of this trait belonged to line AM6-290-1 with a value of 35.21%. Lines AM6-290-1 (30/96) and BM6-55-2 (29/34) had the highest mean percentage of crumb rice. In contrast, line DM6-300-4 had the lowest average percentage of crumb rice, equivalent to 8.72%. The highest value of total rice yielding belonged to line DM6-300-4 and the lowest value belonged to line BM6-310-16 with values of 74.34% and 62.61%, respectively (Table 2).

Line DM6-60-2 with amylose content of 22.25% had the highest average value of this trait. The lowest amount of amylose belonged to AM6-260-13 genotype and was equal to 17.75%. Most of the lines in this research had moderate amylose (20-23%) and therefore have good cooking quality. Genotypes DM6-65-2 (4/32), AM6-50-5 (4/28), BM6-50-1 (4/22), BM6-55-2 and AM6-290-5 (4/15) had the highest mean of Gelatinization temperature trait. Dilmani cultivar had the lowest average gelatinization temperature (3.25). Since cultivars with medium gelatinization temperature (range 3 to 5) are in the group of good quality cultivars, therefore, many of the genotypes in this research are among the desirable lines in terms of this trait (Table 2).

Table 1- Average comparison between genotypes for grain yield traits and grain yield components

Lines	days to 50% flowering	Plant height (cm)	Panicles per plant	Panicle lenght (cm)	Filled grain	Unfilled grain	100 grains weight (gr)	Grain yield (Kg/ha)
AM6-260-1	82.5e-h	143.5c-e	16.2a-c	30a-e	98.7j-n	17b-e	2.75gh	4488 b-f
AM6-260-11	96.5c	141.7d-f	15.0 a-d	29.6b-e	115.8b-i	12.7c-i	2.68h-j	4516 b-f
AM6-260-13	97c	149.7a-c	16.7a-c	30.6a-c	107.5e-k	13c-i	2.77gh	4321 c-g
AM6-290-1	97.5bc	146b-e	16.5a-c	31.6a	96.5k-n	9.2g-i	2.82e-g	4740 a-e
AM6-290-15	81.5gh	141.2d-g	14.7a-d	28.2e-h	129.5a-c	11e-i	2.92b-d	4772 a-c
AM6-290-2	86e	155a	17.2a-c	30.5a-c	121.2b-e	13.7c-h	3.01ab	4243 c-g
AM6-290-5	85e-g	155.5a	16.7a-c	30.0b-e	120.7b-f	15e-j	3.02ab	4251 c-g
AM6-320-2	81.5gh	149.5a-c	16.7a-c	30.9ab	98j-n	17.8b-d	2.62jk	4765 a-d
AM6-50-2	85e-g	141.2d-g	15.7a-d	30.2a-d	95.5k-n	12.5c-i	3.01ab	5192 a
AM6-50-4	86e	145.5b-e	15a-d	30.9ab	105.8c-i	15c-g	2.91c-e	4640 a-e
AM650-5	82l-n	143.2c-e	17.5ab	28.5d-g	106.2g-l	10.7e-i	2.62lm	4781 a-c
BM6310-16	106a	152ab	16.2a-c	28.2e-h	122.2a-d	11.2e-i	2.74g-i	4545 b-e
BM6-50-1	84.5e-g	147.5b-d	16.5a-c	28.9c-g	123.5a-d	12.2a-b	2.89d-f	4766 a-c
BM6-55-2	84.5e-g	149.7a-c	16.7a-c	28.2e-h	107f-k	10.2f-i	2.94a-d	4628a-e
DM6-300-2	80.5h	129ij	16.7a-c	25.1k	103.5h-m	10.7e-i	2.48l	5221 a
DM6-300-39	101 b	125j	16a-c	25.4jk	91.2m-o	12d-i	2.69h-j	4774 a-c
DM6-300-4	81.5gh	135.2f-i	16.7a-c	26.2i-k	136a	15e-j	2.34m	4754 a-e
DM6-300-40	99bc	126.2j	16.5a-c	26.5h-k	92.7l-o	12.2c-i	2.29mn	4467 b-f
DM6-300-7	81.5gh	133.5hi	16.7a-c	25.4jk	107f-k	10.7e-i	2.65i-k	4803 a-c
DM6-60-3	80.5h	129kl	17.2a-c	25.1k	118b-g	11.7d-i	2.90d-f	4556 b-e
DM6-65-2	81.5gh	123.2j	16.5a-c	26.0jk	86no	28a	2.94a-d	4534 b-e
DM6-80-5	81.5gh	125.5j	16.7a-c	27.12g-i	103.8h-m	15.2c-g	2.55kl	4656 a-e
HM6-60-1	82.5e-h	144c-e	17.7a	28.9c-g	96.2k-n	13.8c-h	2.94a-d	4878 ab
HM6-60-2	82.2f-h	134.5g-i	15.2a-d	28.6d-g	103i-m	16.5b-f	3.04a	4773 a-c
HM6-60-7	98bc	135.5f-i	16.2a-c	29.8b-f	101.8i-m	12.7c-i	2.93b-d	5199 a
AliKazemi	90.5d	142.2e-h	11.2e	30 a-e	115.5d-j	6.7i	2.90d-f	4140 e-g
Binam	97c	157.7a	14.5b-d	27.6f-i	128.5a-c	18.5a-c	2.81fg	4135 e-g
Dilamani	82.2ef	141.2d-g	12.6de	26.6h-k	78.7o	7.5hi	2.04o	3884 g
Hashemi	92.2d	146.2b-e	14.5c-e	30.5a-c	117.2b-h	9.2g-i	2.23n	4045 fg

In each column, the averages with same letters are not significantly different with Tukey's test at the 5%

Table 6- Average comparison between genotypes for cooking and eating quality traits

Lines	Head rice yielding %	Crumb rice %	Total rice yielding %	Amylose content%	Gelatinization temperature
AM6-260-1	66.6gh	12.70m	53.92d	20.30d-f	4.14ab
AM6-260-11	67.02f-h	15.12l	51.90e	18.38hi	3.95ab
AM6-260-13	70.32cd	18.45h-j	51.86e	17.75i	4.00ab
AM6-290-1	66.17h	30.96a	35.21k	18.75g-i	3.98ab
AM6-290-15	70.75b-d	11.00n	59.75bc	19.25f-i	3.90ab
AM6-290-2	66.43 gh	18.70g-j	47.72gh	20.40d-f	3.98ab
AM6-290-5	68.30d-h	20.37ef	47.93gh	20.00e-g	4.15ab
AM6-320-2	69.11d-g	47.82i-k	51.28ef	19.25f-i	4.00ab
AM6-50-2	69.79d-f	12.59m	56.98cd	19.25f-i	3.82ab
AM6-50-4	67.29e-h	20.51ef	46.78hi	20.00e-g	3.95ab
AM650-5	70.75b-d	10.00no	60.75b	19.45f-h	4.27a
BM6310-16	62.62i	11.13n	51.48e	22.00a-c	3.98ab
BM6-50-1	69.79d-f	11.23n	58.55c	21.12a-e	4.22ab
BM6-55-2	66.46gh	26.34bc	40.12j	21.30a-e	4.22ab
DM6-300-2	7047b-d	11.57n	58.90bc	21.67a-d	3.82ab
DM6-300-39	72.74a-c	19.90e-h	52.84de	21.78a-d	4.02ab
DM6-300-4	74.27a	8.72o	65.55a	21.50a-e	4.05ab
DM6-300-40	70.15c-e	10.65n	59.50bc	21.40a-e	3.98ab
DM6-300-7	73.26ab	15.06l	58.20c	21.25a-e	3.82ab
DM6-60-3	68.25d-h	8.75o	59.50bc	21.47a-e	3.62ab
DM6-65-2	68.5d-h	10.06n	58.44c	22.00a-c	4.27a
DM6-80-5	68.80d-h	17.22jk	51.51e	22.10ab	3.80ab
HM6-60-1	68.61d-h	19.13f-i	49.48fg	20.70b-f	3.95ab
HM6-60-2	68.20d-h	11.65n	56.54cd	22.25a	3.78ab
HM6-60-7	70.34ce	12.86m	57.48cd	22.00a-c	3.55ab
AliKazemi	70.37cd	19.84fi	50.53ef	18.50g-i	3.52ab
Binam	68.80d-h	18.09i-k	50.71ef	21.08a-e	3.25b
Dilamani	68.46d-h	17.16jk	51.30ef	20.50c-f	3.25b
Hashemi	69.09d-g	19.54fi	49.55fg	20.38d-f	3.60ab

In each column, the averages with same letters are not significantly different with Tukey's test at the 5% probability level.

Conclusion

According to the total measured characteristics and with emphasis on yield, plant height, length of growth period and cooking and eating quality, 15 lines were selected from among the studied genotypes to be evaluated in compatibility tests.

References

[1] FAOSTAT. Crop Prospects and Food Situation. In Rome: Food and Agriculture Organization of the United Nation. Available online: http://faostat.fao.org (accessed on 7 December 2019).

[2] Anonymous (2022). Cereals in the mirror of statistics. Department of Statistics and Information of the Ministry of Jihad and Agriculture.

[3] Cheema, A. A. (2006) Mutation breeding for rice improvement in Pakistan: achievements and

impact Plant Mutation Reports 1 1 36-39.

[4] Forster B P, Shu Q Y 2012 Plant mutagenesis in crop improvement: basic terms and applications. In: Shu QY, Forster BP. Nakagawa H. editors Plant mutation breeding and biotechnology CABI Wallingford.

[5] El-Degwy I S 2013 Mutation induced genetic variability in rice (Oryza sativa L.) Intl J Agri Crop Sci 5 23 2789-2794.

[6] MVD 202316 Mutant variety database. http://mvd.iaea.org/. Accessed on June 20. 2022.

[7] Viana, V.E.; Pegoraro, C.; Busanello, C. and de Oliveira, A.C.(2019). Mutagenesis in rice: The basic for breeding a new super plant. Front. Plant. Sci. 2019, 10, 1329.

[8] Nahvi, M. (1995). The final report of the investigation of rice cultivars and lines in the preliminary performance comparison test. Publications of rice research institute of Iran. 38 pages.

[9] Nahvi, M., Allahgholipour, M. Mohammad Salehi, M. S. (2002). Studying the compatibility and sustainability of rice in different regions of Gilan province. Seed and Plant Journal, 18 (1):1-13.

[10] Mohaddesi, A. (2013). Evaluation of rice lines in a preliminary performance comparison experiment. The final report of the research project. Publications of the rice research institute of Iran. Registration number 453.

[11] Ebadi, A. A. and Halajian, M.T. (2013). Development of rice plants tolerant to drought stress using mutation breeding and proteomics techniques. Final report under registration number 46845 - Rice Research Institute of Iran - Rasht.

[12] Ebadi, A. A., Halajian, M.T., Qudsi, M. and Mohammadi, M. (2015). Preliminary evaluation of selective mutant lines resulting from the mutation of local and improved rice cultivars. Final report under registration number 5104- Rice Research Institute of Iran-Rasht.

[13] Ebadi, A. A. and Rahmi M. R. (2021) Preliminary evaluation of selected mutant lines resulting from the mutation of local cultivars. Final report under registration number 62986 - Rice Research Institute of Iran– Rasht.

[14] Ebadi, A., Eskandari, A., and Elah Qalipour, M. (1400) Production of rice lines tolerant to cold stress through physical mutation. Final report under registration number 59350 - Rice Research Institute – Rasht.

[15] Juliano, B. O. (1971). A simplified assay for milled-rice amylose. Cereal science today, 16(10): 334-340.

[16] Little, R.R., Hilder, G.B. and Dawson, E.H. (1958). Differentioal effect of dilute alkali of 25 varieties of milled white rice. Cereal chemistery. 350: 111-126.

ICNST 2024
International Conference on Nuclear Science and Technology
6- 8 MAY 2024 | Isfahan, Iran

Simulation of Neutron flux Distribution of Ra-Be Neutron Source using Monte Carlo Method (Paper ID : 1486)

Mohammadi F., Shafaei M.A
[1]*Department physic, Institute, Yazd, Iran*

Abstract

Using MCNPX to determine axial neutron fluxes of the seven channels irradiation sites of 3 mCi of radium is tended for physics experiments on artificial radioactivity and irradiation facility in nuclear physics laboratory at (Yazd-University). Neutron source are used in nuclear physics research and in practical applications such as neutron logging and neutron diffraction analysis, and classified into three groups nuclear fission reactors, radioisotopes, and particle accelerators. In general, a neutron emitter is less than an isotope source such as ^{226}Ra, ^{239}Pu, ^{210}Po, ^{241}Am formed, which particles alpha emits when it hits elements with a low atomic number such as 9 and neutrons are produced through (α,n) reaction. Source a neutron that has a high radiation activity is inside a container that a retarding medium, for example (C_{25} H_{52}, H_2 O or paraffin). Ra-Be source in the interior of the shielded laboratory is sealed emanation tight into a brazed nickel and it's eccentrically off the axis of the lead cylinder. Lead thickness and distance shield are so designed that the gamma-dose rate from the source remains small enough in all directions. The seven irradiation channels are arranged vertically within the paraffin block.

Keywords: Ra-Be source, thermal neutron, flux, MCNP[1] code

INTRODUCTION

Neutron activation analysis (NAA[2]) is a sensitive non destructive method for determining the elemental composition of a simple. Nuclear reactors are frequently used for NAA because of their high neutron flux compared to the neutron source isotopes. The development of nuclear instrumentation to perform in neutron activation analysis using thermal, epithermal and fast neutrons, can be useful for studies elements in a variety of simples matrices outside the reactor premises. Installation of the neutron source ^{226}Ra-Be facility installed at department of physics Faculty of University of Yazd, Iran "Figs.1" , by company LEYBOLD HEREUS GMBH, Federal Republic of Germany by license No.NW 8/66[1].

[1] Monte Carlo N-Particle
[2] Neutron Activation Analysis

Fig. 1. Picture of source ^{226}Ra-^{9}Be of Yazd University

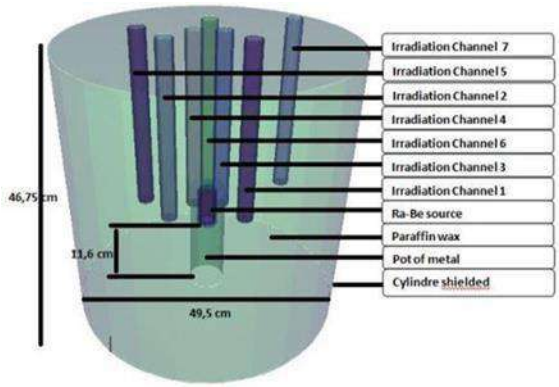

Fig. 2. Schematic of Ra-Be neutron source assembly

The seven irradiation channels (each 30 cm long, 3 cm of diameter) are arranged vertically within the paraffin block Figure 1. The sheetmetal pot with source, lead cylinder and paraffin wax is surrounded by a distance shield of 49.5 cm diameter joined to in by a sold steel construction irradiation channels Nos. 1, 2, 3 and 4 are in a circle of 7 cm radius about the Ra-Be source, irradiation channels Nos. 5 and 6 are 14 cm away the source and irradiation channel No. 7 is about 20 cm from the preparation “Figs.2, 3”.

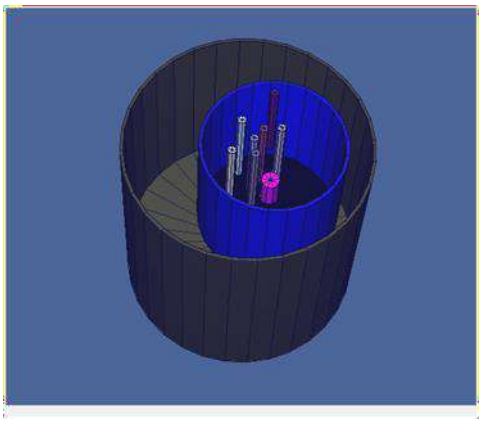

Fig. 3. Schematic of Ra-Be neutron source assembly

RADIOISOTOPE SOURCES

Neutron sources are characterized by a number of factors which include intensity (number of neutron emitted per seconds), energy distribution, Angular distribution, neutron polarization and mode of emission (continuous or pulsed), Neutron source are used in nuclear physics research and in practical applications such as neutron logging and neutron diffraction analysis, and classified into three groups nuclear fission reactors, radioisotopes, and particle accelerators. There are two main types of radioisotope neutron sources, direct and indirect. Direct refers to radioisotope sources that emit neutrons in their natura has a half-life of 2.645 years, and 3.09 % of decays are by spontaneous fission [3]. . Indirect radioisotope neutron sources refer to sources that rely on a charged particle emitting radionuclide and a stable target nuclide to produce neutrons through a nuclear reaction.l decay processes. Californium-252 is the most widely used direct radioisotope neutron source. ^{252}Cf The most common indirect radioisotope neutron source is the Ra-Be source. There, ^{226}Ra with a half-life of 1,599 years has two major alpha-particles located at 4.784 MeV (94.5 %) and 4.601 MeV (5.5 %) [4], the neutron producing reaction is:

$$^{4}\alpha + {}^{9}Be \rightarrow {}^{12}C + {}^{1}n$$

2 4 6 0

^{226}Ra -^{9}Be which is a mechanical mixture in weight of beryllium to radium with energy spectrum up to about 12 MeV shows is not a mono energetic source “Fig.4” [5].

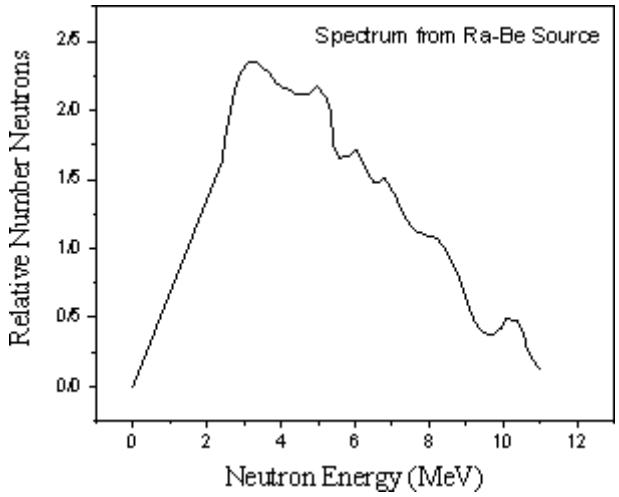

Fig.4. The spectrum of neutrons in the ^{226}Ra-^{9}Be source in terms of energy

FLUX CALCULATION

In The neutron fluxes investigated in this work are thermal, epithermal and fast according to the MCNPX input file prepared, the thermal neutron flux energy ranges from (0 to 6.25 $\times 10^{-1}$) MeV, the epithermal neutron flux energy ranges from (6.25 $\times 10^{-7}$ to 8.21$\times 10^{-1}$) MeV and the fast neutron flux ranges from (8.21 $\times 10^{-1}$ to 20.00) MeV. In this work, making 1 $\times 10^{6}$ particle histories monitored in the MCNPX simulation. Axial tallies were created in the seven irradiation channels for the source design. The axial neutron flux was determined by dividing the irradiation channels into 6 at an interval of 5 cm for each channel 1 to 7. The average neutron flux in the volume of each of the division of the channels was determined by using F4: N tally card or cell flux tally card as described in the MCNPX manual [6].

Results and discussion

The The results performed during the calculated with the MCNPX code from the tallies retrieved from the output file are normalized with formula (1) using the MS-Excel and interpreted into graphs as shown in figures (5 to 11 axial flux) :

$$\phi = \frac{Tally \times Source\ strength}{Valume\ of\ select\ cell} \quad \left(\frac{n}{cm^2 \cdot m}\right) \qquad (1)$$

The MCNPX simulation was run for the neutron flux profile in the whole irradiation channel. The

thermal, epithermal and fast neutron fluxes were determined including their uncertainties as evaluated by MCNPX code.

The flux thermal, epithermal and fast growing exponentially axially from the bottom of the source with a maximum increase in the center of the source, and starts to pour down from the exponentially source to very low values along of irradiation channel.

The channels (1, 2, 3 and 4) the neutron flux more intense and the maximum intensity of the flux thermal, epithermal and fast respectively 2200, 1700 and 1200 n/cm^2 s are almost equal in each channels irradiation 1 to 4, and then the tubes 5 and 6 the maximum intensity of the flux thermal, epithermal and fast respectively 1200, 390 and 90 n/cm^2 s then the neutron flux decreases almost half the channel 7 at a flow rate near zero fast neutrons respectively 150, 30 and 5 n/cm^2 s The MCNPX simulation was run for the neutron flux profile in the whole irradiation channel. The thermal, epithermal and fast neutron fluxes were determined including their uncertainties as evaluated by MCNPX code.

The results performed during the calculated with the MCNPX code from the tallies The average thermal flux in the irradiation site 1, 2, 3 and 4 is tow times that of irradiation sites 5 and 6 and 12 times that of irradiation 7. This indicates that as the distance from the source increases the thermal neutron flux decreases as a result of leakage and absorption. The average epithermal flux in the irradiation site 1, 2, 3 and 4 is four times that of the irradiation site 5 and 6 and big values in irradiation channel 7, that of irradiation channel 5 and 6.The neutron flux distribution along of the irradiation channels are as shown Figs. 5,6,7,8,9,10 and 11 for irradiation site 1, 2, 3,4,5,6 and 7 respectively.This validate the fact that as distance from the source in the paraffin increases the percentage thermal neutron flux increases whereas the percentage epithermal and fast neutron fluxes decreases.

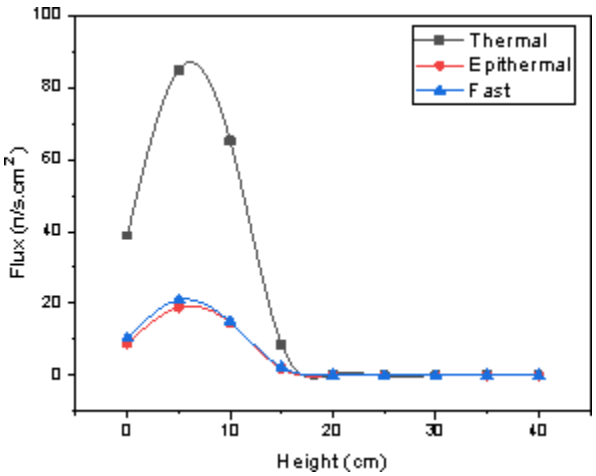

Fig. 5. Axial Profile Flux distribution of channel 1

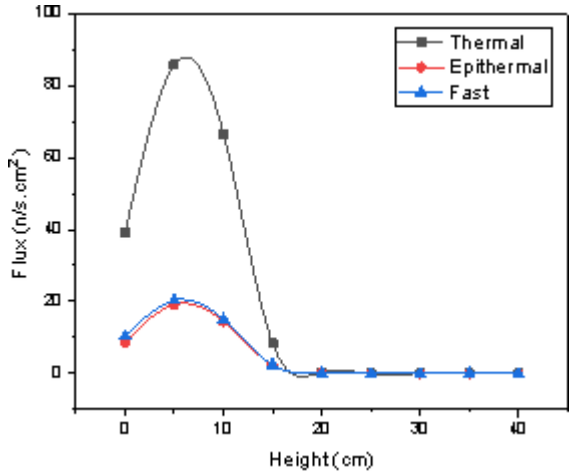

Fig. 6. Axial Profile Flux distribution of channel 2

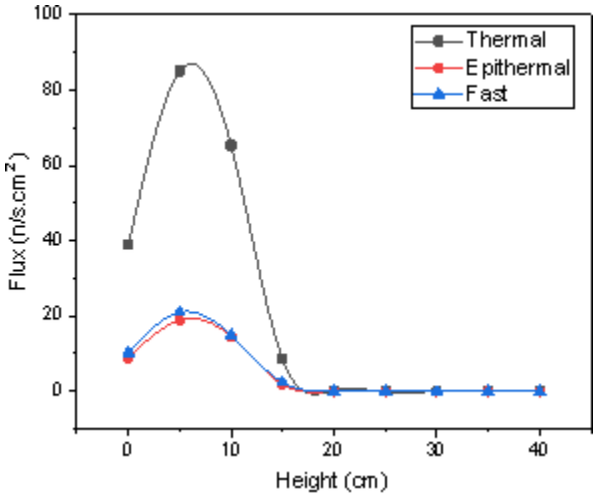

Fig. 7. Axial Profile Flux distribution of channel 3

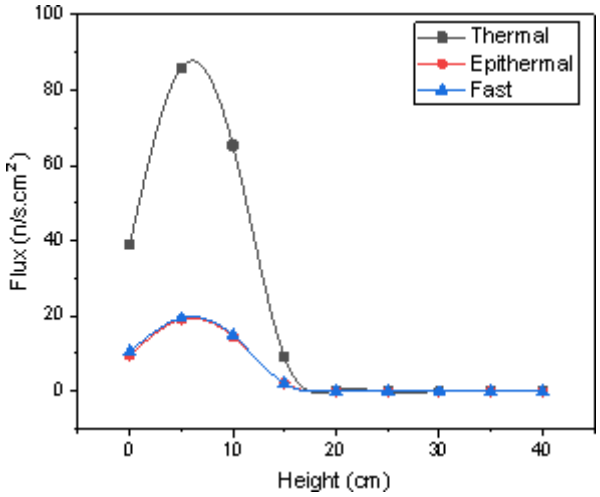

Fig. 8. Axial Profile Flux distribution of channel 4

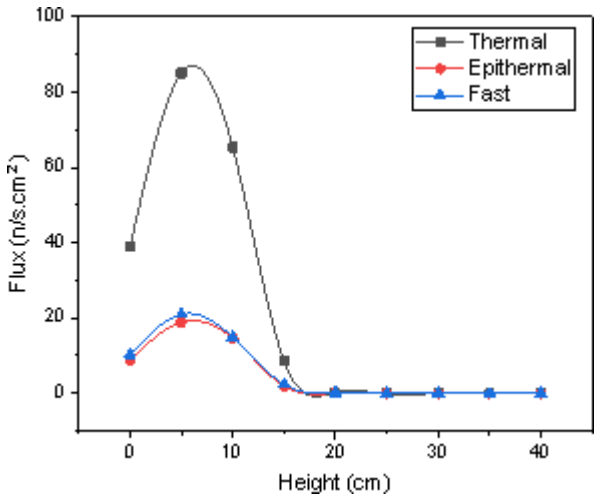

Fig. 9. Axial Profile Flux distribution of channel 5

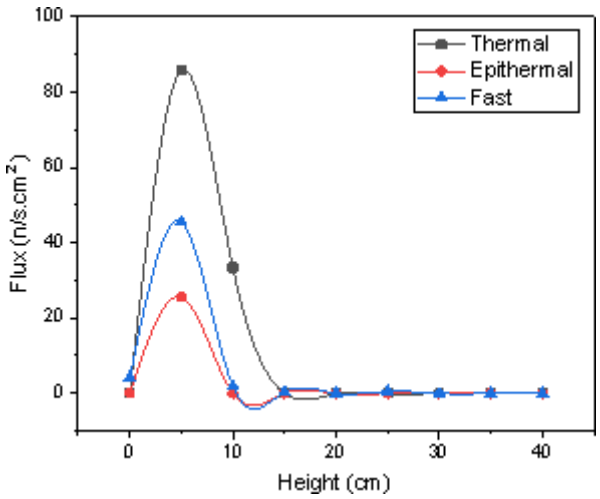

Fig. 10. Axial Profile Flux distribution of channel

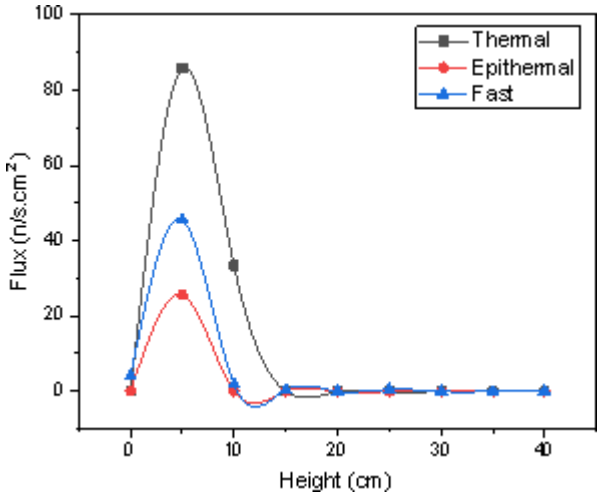

Fig. 11. Axial Profile Flux distribution of channel 7

Conclusions

Ra-Be neutron source was simulated using MCNP code, the characteristics of neutron flux in seven radiation channels were determined, which can be concluded that with increasing distance from the source, the amount of neutron flux decreases and with increasing distance from the source, The average percentage of thermal flux increases, but as a result, superthermal and fast neutron flux decreases. Also, the neutron flux has been measured in all 7 channels, which shows that certain ranges of the energy of the increase of neutrons are observed.

Supplementary information

I am grateful to Ayatollah Khamenei for his good support and prayers.

References

NW 8/66 License of source Radium-Beryllium producted by company LEYBOLD-HEREUS GMBH the Federal Republic of Germany

Peeples, Cody Ryan, Alternative to Am– Be Neutron Source for the Compensated Neutron Porosity Log, North Carolina State University, Master of Science, Raleigh, North Carolina 2007

Norman E Holden, Reciniello, Richard N.; Hu, Jih-Perng; Rorer, David C, Radiation Dosimetry of a Graphite Moderated Radium-Beryllium Source, World Scientific Publishing Co. Pte Ltd. ISBN

#9789812705563, June 2003, Pages 484-488.

Meyerhof, W.E. and W.E. Meyerhof, Elements of nuclear physics. Vol. 174. 1967: McGraw-Hill

New York.

RBM Sogbadji, RG Abrefah, BJB Nyarko, EHK Akaho, H.C. Odoi, S. Attakorah-Birinkorang, The design of a multisource americium–beryllium (Am–Be) neutron irradiation facility using MCNP for the neutronic performance calculation, Applied Radiation and Isotopes, April 2014, Volume 90, Pages 192– 196

Initial MCNP-6 Release Overview MCNP-6, Monte Carlo N–Particle Transport Code System Including MCNP6.1, MCNP5-1.60, MCNPX-2.7.0 and Data Libraries, Los Alamos National Laboratory, August 2013,LA-UR-13-22934

Evaluation of compatibility and stability of rice promising mutant lines originated from local variety (Paper ID : 1487)

Ebadi A.A. [1*] Rahemi, M.R. [2] Khoshkdaman M. [1] Majidi F. [1] Mohammadi M. [1]

[1]*Rice Research Institute of Iran (RRII), Agricultural Research Education and Extension Organization (AREEO), Rasht, Iran.*

[2]*Nuclear Science and Technology Research Institute (NSTRI), Nuclear Agriculture Research School, Karaj, Iran.*

Abstract

During the introduction of the new variety, studying and measuring the adaptability and stability of improved lines in different environmental conditions is very important in plant breeding programs. The stability of the 15 mutant lines derived from local varieties with five control varieties (Hashemi, Deylamani, Binam, AliKazemi and Hasti) were evaluated in three places: Rasht, Shahid Shiroodi Research and Fouman in complete randomized block design with 3 replications in two years (2021 and 2022). The results of analysis of variance in all locations and years separately showed significant differences between the studied genotypes for most of the evaluated traits. Based on combined variance analysis, there was a significant difference between genotypes at the level of 1% for the traits of number of days to 50% of flowering, plant height, tiller number, 100-seed weight and yield, and at the level of 5% for the traits of c panicle length, number of filled and unfilled seeds. The interaction effect of place in genotype was significant only for tiller number and yield at the 1% level. The interaction effect of year in genotype was significant only in the number of days to 50% of flowering and the number of filled grains at the level of 1%. The triple interaction effect was significant at the 1% level for all traits except the trait of number of days to 50% of flowering. Based on the comparison of the average traits in the examined genotypes, the three genotypes DM300-39, DM300-40 and DM60-3, in addition to having an average yield of over 6 tons per hectare, had a shorter plant height, earlier than the other genotypes and even the local cultivars. In stability analysis, these three lines were the stable lines in the investigated environments. Therefore, these three lines were selected to be used in promotional research projects as variety introductions.

Key words: Rice, Combined analysis, Stability analysis, Yield.

INTRODUCTION

Supplying daily calories from cereal grains is one of the cheapest sources of energy. Rice has a special place among cereals in Iran. In such a way that it accounts for most of the food of the Iranian people, especially in the provinces of Guilan and Mazandaran. According to the statistics of the Ministry of Jihad-e-Agriculture, in the crop year 2022-2023, about 84.77 million tons of crops were produced, of which the share of cereal grain was 25%. According to the report of the Ministry of Jihad-e-Agriculture, Mazandaran and Guilan, with 331,000 and 246,000 hectares respectively, have the largest area under rice cultivation (more than 72% of the total area under rice cultivation in the country). In total, with the production of 2.6 million tons of paddy (more than 70% of the total paddy production in the country), they are the main producer of rice in the country [1].

The introduction of mutant cultivars and their commercial use dates back to the 1960s. There were 78 mutant rice varieties released from 1966 to 1990 in China [2]. Also, 77 new cultivars were released from 1991 to 2004. Gamma rays have been used for this purpose, and the properties of the mutant varieties have been resistance to diseases and increased grain quality [3]. In Indonesia, the Atomia1 cultivar was released in 1982 [4]. There were 10 rice cultivar released from 1990 to 2002 In Vietnam by mutation breeding methods[5].

Genotype × environment interactions causes significant differences between genotypes in different environments [6]. One of the slowness of the process of improving and introducing cultivars in different regions is the presence of genotype × environment interaction effects [7]. Without examining and recognizing these effects, the conclusions of the breeding and agronomic experiments are not very valid. The reasons for the interaction between genotype and environment have been discussed in many articles [8].

By evaluating 25 mutant lines in the form of a preliminary performance comparison test, 15 lines that were superior to the rest were selected. The compatibility and stability of these 15 selected lines were evaluated in this research [9].

Materials and Methods

The number of 15 pure advanced mutant lines [9] along with Hasti, Hashemi, Ali Kazemi and Dilmani cultivars were evaluated in three regions (Foman, Rasht and Tankabon) in the form of a

completely randomized block design in 3 replications for 2 years. The size of each plot is 20 square meters and transplanting was done with a distance of 20 x 20 cm in the stage of 4-5 leaves. Nutrition management as well as pest and disease control of rice was done to accurately assess the yield potential and based on technical recommendations. During the growing season, necessary measurements of plant height and number of tillers were made at the time of harvest. At the end of the growing season, in order to measure the grain yield, sampling was done in each plot after removing the borders. After measuring grain moisture, grain yield was calculated based on 14% moisture. Also, the number of 10 main stem panicles in each plot was randomly selected and after measuring the length of the panicles, its average was considered as the panicle length in each plot. After that, the number of filled and unfilled grains in each panicle was counted and their average was calculated. The weight of one hundred grains was measured by randomly selecting 100 grains and weighing them using a scale with an accuracy of 0.001 grams. The traits related to grain quality, including the amylose content according to the method of Juliano [10], gelatinization temperature according to the method of Little et al., [11], were evaluated. Statistical analysis of the data, including testing the normality of the data distribution, Bartlett's test to check the homogeneity of the variance of the errors, analysis of variance and comparison of the means, was performed using SAS v9.4 software. Stability and uniformity test were performed based on GGE biplot using R software and the most stable lines were selected.

Results and discussion

Due to the different response of genotypes to different years and places, the data obtained from the experiment in one year and one place cannot be a suitable criterion for comparison and selection. and to be used to select and introduce new improved cultivars. Due to the interaction between genotype and environment, it is necessary to investigate the performance of varieties in a wide range of environmental changes in different places and years in order to increase the efficiency related to the selection and introduction of cultivars using the obtained results. Considering the homogeneity of the experimental errors related to three locations and two years based on Bartlett's test for the measured traits, a combined analysis of the experiments of three locations and two years was performed. The effect of year and place was not significant for all traits except for the number of days until 50% of flowering. But the interaction effect of year-place was significant for all traits except the number of days to 50% of flowering and hundred seed weight. The significance of this interaction indicated the fluctuation of the difference in figures from year to year and place to place.

Based on combined variance analysis, there was a significant difference between genotypes at the level of 1% for the traits of number of days to 50% of flowering, plant height, number of tillers, 100-grain weight and yield, and at the level of 5% for the traits of panicle length, number of filled and unfilled grains. The interaction effect of place in genotype was significant only for two traits, number of tillers and grain yield, at the level of 1%, and it was not significant for the rest of the studied traits. The interaction effect of year in genotype was also significant only in two traits: number of days to 50% flowering and number of filled grains at the level of 1%, and this interaction effect was not significant in other investigated traits. The triple interaction effect of genotype × year × location was significant at the 1% level for all traits except the trait of number of days to 50% of flowering.

Comparison of the means of genotype

Due to the significance of the main effect of genotype in all studied traits and in order to identify and introduce the superior genotypes in terms of the studied traits, a comparison of the average main effect of genotype was done. Genotypes DM60-3, DM300-39, DM300-40, DM80-5 and Dilmani were the earliest genotypes and Binam, BM310-16, HM60-7 and BM50-1 were the latest genotypes. The shortest genotypes were DM65-2, DM60-3, DM300-40, DM300-39 and DM300-2 and the tallest genotypes were Dilmani, Binam, BM50-1, Ali Kazemi and Hashemi. The longest panicle length was observed in Hasti, AM260-11, AM50-2 and AM50-5 genotypes and the shortest panicle length was observed in DM300-40, DM300-2, DM300-39 and DM300-4 genotypes. The highest number of filled grains per panicle was observed in BM310-16, BM50-1, HM60-7 and DM300-40 genotypes and the lowest of them was observed in DM300-2, DM80-5, Hashemi and DM65-2 genotypes. The highest value of 100-grain weight trait was observed in Hasti, DM80-5, HM60-2, and AM290-15 genotypes, and the lowest value of this trait was observed in Dilmani, DM300-40, DM300-39, DM300-4, and Hashemi genotypes. The highest grain yield was observed in genotypes DM300-39, AM50-2, DM300-40, HM60-7, BM310-16 and DM60-3 with the amount of 6424, 6358, 6206, 6188, 6095 and 6077 kg per hectare, respectively (Table 1). In total, the three genotypes DM300-39, DM300-40 and DM60-3, in addition to having a yield of more than 6 tons per hectare, have a shorter plant height and are earlier compared to the rest of the studied lines.

Table 1. Comparison of the means main effect of genotype for the investigated traits in three locations and two years

Genotype	G. No.	Number of days to 50% flowering	Plant height (cm)	Tiller No.	Panicle length (cm)	Filled grain	Unfilled grain	100-grain weight (gr)	Grain Yield (Kg/ha)
AM50-2	G1	88.50cd	137.2a-c	12.74b	30.71a-c	105.7ab	9.32cd	2.89b-d	6358ab

AM50-5	G2	88.50cd	133.8a-c	13.45b	31.13a-c	109.0ab	6.85d	2.80d-f	5928a-d
AM290-	G3	85.67de	133.1a-c	13.62b	30.51a-c	102.3ab	7.50cd	2.91a-c	5999a-d
HM60-2	G4	84.00de	131.2bc	15.34ab	29.89 a-	103.0ab	8.10cd	2.93a-c	5980a-d
BM50-1	G5	94.00ab	149.8ab	12.44b	29.66 a-	118.7a	10.95b-	2.84c-e	5615d
DM60-3	G6	81.00e	118.8c	14.85ab	26.95 a-	101.4ab	16.02a	2.80d-f	6077a-d
DM65-2	G7	88.33cd	93.3d	14.22ab	28.17 a-	97.9ab	14.03ab	2.72fg	4611e
DM80-5	G8	82.50e	124.6c	14.39ab	27.28 a-	95.8ab	11.49bc	2.95ab	5643cd
DM300-2	G9	83.00e	124.0c	17.94a	26.04bc	89.7b	8.59cd	2.69g	5857a-d
DM300-4	G1	83.50de	124.7c	14.81ab	26.33a-c	106.5ab	10.00b-	2.56hi	5684cd
AM260-	G1	85.017de	134.1a-c	13.37b	31.84ab	109.2ab	9.76b-d	2.85cd	5710cd
HM60-7	G1	94.33ab	145.2ab	11.92b	28.61a-c	116.3ab	11.10b-	2.87b-d	6188a-d
BM310-	G1	94.67ab	145.1ab	13.39b	28.26a-c	121.0a	11.22bc	2.80d-f	6094a-d
DM300-	G1	81.50e	123.4c	15.57ab	26.05bc	105.4ab	9.31cd	2.54hi	6424a
DM300-	G1	82.17e	121.9c	15.63ab	25.74c	109.7ab	8.08cd	2.53hi	6206a-c
Dylamani	G1	82.83e	151.6a	14.02ab	26.98a-c	105.2ab	10.31b-	2.47i	4446e
Bibam	G1	97.00a	151.1a	12.09b	29.61a-c	99.9ab	10.58b-	2.75e-g	4510e
Hashemi	G1	84.33de	146.3ab	14.39ab	29.85a-c	96.0ab	7.27cd	2.57h	4292e
Alikazem	G1	86.17c-e	147.7ab	13.65b	30.71a-c	106.3ab	9.52b-d	2.90a-c	4309e
Hasti	G2	91.00bc	131.5bc	14.26ab	31.94a	105.7ab	8.37cd	2.99a	5817b-d

Means with different letters have a significant difference at the 5% level with Tukey's test.

Stability analysis

Based on the analysis of GGE bi-plot for the performance of the first main component (genotype main effect) 57.4% and the second (genotype × environment interaction effect) 21.5% and in total 78.9% of the changes in the data were justified (Fig. 1). If most of the available variation is not explained by the sum of the first and second principal components, it will indicate the complex nature of the genotype × environment interaction [12]. Jadhav et al., [13] investigated genotype × environment interaction for 59 rice lines with different growing periods in three environments for traits related to grain yield. In this study, the first and second principal components justified 49.2% and 40.7% of the total data changes, respectively. Mohaddisi et al., [14] evaluated six promising lines of rice along with Shiroodi variety in two regions of Mazandaran during three years using GGE bi-plot method. In their research, the first two components explain 57% and 26.6%, respectively, and a total of 83.6% of the total data changes.

Six sections were formed based on the placement of genotypes in the obtained polygon in order to identify which-superior-where pattern, that the genotypes in each section are very similar to each other. Seven genotypes G1, G6, G9, G10, G12, G15 and G17 were placed at the polygon head

(Figure 1). The genotypes located at the polygonal head of each section are the superior cultivars of that section, and in other words, have a private adaptation to related environments. These lines are the best or the weakest in terms of performance in some environments or all environments, because they have the greatest distance from the biplot center. The lines located at the top are the most responsive cultivars, and in other words, they are considered the best cultivars in their respective sections. Finally, according to Figure 1, it can be concluded that genotype G1 in Chepressar, genotypes G9 and G12 in Rasht, and genotype G14 in Foman are the superior genotypes. Mostafavi et al., [15] identified three real big environments in order to select high-yielding and stable genotype in three years and three locations using the GGE bi-plot method and introduced genotype 12 as the superior and ideal genotype. Allahgholipour [15] used the GGE bi-plot method to investigate the interaction effect of genotype × environment of rice cultivars. By examining 10 local and modified rice varieties in three regions and two crop years, they identified two large and separate environments.

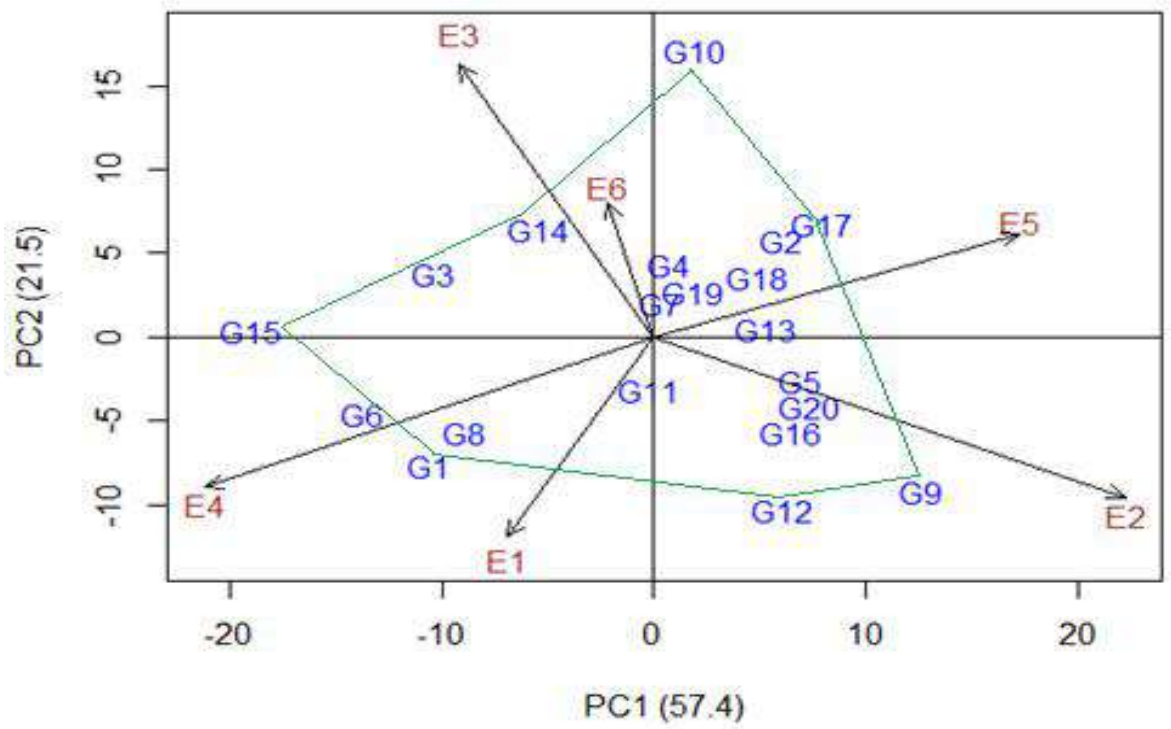

Fig.1- Polygon diagram of GGE biplot based on which-superior-where pattern for rice genotypes in different environments. Genotypes are indicated by the letter "G" and environments by the letter "E".

Conclusion

Based on the yield and the results of stability analysis of investigated lines, the best genotypes were DM300-40, HM60-7, AM290-15, AM50-5, DM300-39, BM310-16, HM60-2 and DM60-3, respectively. Considering other characteristics of selected genotypes such as plant height and early maturity, three genotypes DM300-40, DM300-39 and DM60-3 can finally be selected as superior genotypes for extension and agronomic research experiments.

References

[1] Anonymous (2022). Cereals in the mirror of statistics. Department of Statistics and Information of the Ministry of Jihad and Agriculture.

[2] Wang, L.Q. (1992). Advances in plant mutation breeding in China: a full analysis. Bulletin of Nuclear Agricultural Science. 13: 282-295.

[3] Chen H, and Lin, Y. (2013). Promise and issues of genetically modified crops. Current Opinion in Plant Biology. 2013;16(2):255–260.

[4] Ismachin, M. and Sobrizal A. (2006). a significant contribution of mutation techniques to rice breeding in Indonesia Plant Mutation Reports 1 18-21.

[5] Khanh, T.D.; Duong, V.X.;Nguyen, P.C.; Xuan, T.D.; Trung, N.T.;Trung, K.H.; Gioi, D.H.; Hoang, N.H.;Tran, H.-D.; Trung, D.M. (2021) Rice Breeding in Vietnam: Retrospects,Challenges and Prospects. Agriculture, 11, 397 .

[6] Panwar, L. L., Joshi, V. N. and Ali, M. (2008). Genotype x environment interaction in scented rice. Oryza 45, 103–109.

[7] Swamy, M.N. and Kumar, B.M.D. (2003) Stability analysis for grain yield and its components in rice. Karnataka J Agric Sci 16 (2) : 223-227

[8] Abebe, D., Mohammed, W. and Abebe, A.T. (2022). Genotype X environment interaction and stability analysis in upland rice (Oryza sativa L.) varieties in Ethiopia. Journal of Crop Science and Biotechnology, 1-12.

[9] Ebadi, A. A. and Rahmi M. R. (2021) Preliminary evaluation of selected mutant lines resulting from the mutation of local cultivars. Final report under registration number 62986 - Rice Research Institute of Iran– Rasht

[10] Juliano, B. O. (1971). A simplified assay for milled-rice amylose. Cereal science today, 16(10): 334-340.

[11] Little, R.R., Hilder, G.B. and Dawson, E.H. (1958). Differentioal effect of dilute alkali of 25 varieties of milled white rice. Cereal chemistery. 350: 111-126.

[12] Yan, W. and Tinker, N. (2005). A biplot approach for investigating QTL-by-environment patterns. Mol. Breed. 15 (1): 31-43.

[13] Jadhav, S., Balakrishnan, D., Shankar, V.G., Beerelli, K., Chandu, G. and Neelamraju, S. (2019). Genotype by environment (G×E) interaction study on yield traits in different maturity groups of rice. J. Crop Sci. Biotech. 22 (5): 425-449

[14] Mohaddisi, A., Erfani, R., Sharifi, P., Amin-Panah, H. and Abbasian, A. (2017). Studying the relationships between yield and yield components and stability of some of rice genotypes using biplot method. Cereal Research, 6(4): 411-421.

[15] Mostafavi, Kh., Hosseini Imeni, S.S. and Firoozi, M. (1993). Stability Analysis of Grain Yield in Lineas and Cultivars of Rice (Oriza sativa L.) Using AMMI (Additive Main effects and Multiplicative Interaction) Method. Iranian Journal of Field Crop Science, 45(3): 445-452.

[16] Allahgholipour, M. (2016). Genotype × environment interaction effect in rice genotypes using GGE Biplot. Cereal research, 6(1): 1-14.

ICNST 2024
International Conference on Nuclear Science and Technology
6- 8 MAY 2024 | Isfahan, Iran

Conceptual design of a three-phase flow meter based on the gamma backscattering technique (Paper ID : 1488)

Beigzadeh A. M., Sharifzadeh M. *, and Askari M.

Radiation Application Research School, Nuclear Science and Technology Research Institute, Tehran, Iran.

Abstract

Three-phase flow in the oil and gas industry is prominently displayed. Measuring this flow in transmission pipelines is of special importance for both monitoring and fiscal metering. Although three-phase flowmeters with online monitoring capability are commonly used, the high uncertainties associated with them have prevented flow separators from being replaced by them in custody transfer. In this article, the conceptual design of a three-phase flowmeter for online measurement of oil-water-gas flow in pipelines is proposed to provide the possibility of high-accuracy measurements using the backscattering gamma technique. At a fixed distance from the tube, this set scans half of it from the lowest point to the top and records the data related to counting the backscattered gammas. Finally, by comparing the count rate versus angle chart with the calibration data, the height of each component of the laminar flow inside the pipe will be calculated and their component fraction values will be reported.

Keywords: Conceptual design, Three-phase flow, Flowmeter, Gamma technique, Backscattering.

INTRODUCTION

Oil-gas-water three-phase flow is a common occurrence in production pipelines. However, accurately measuring the flow rate remains a challenge in the petroleum industry [1]. In well testing applications, it is important to achieve a desired accuracy level comparable to that of a well test separator, with a target of ±10%. Additionally, a minimum accuracy of 5% (with 1% as the ideal target) is sought for gas and, in some cases, hydrocarbon condensate allocation. Table 1 provides an illustration of typical process data for an offshore well testing application operating at 100°C and 150 bar [2].

Table 1. Gas condensate process data.

	Start of life	Mid life	End of life
Gas flowrate ($MMSm^3$)	0.5	1.3	0.8
Oil flowrate (m^3)	1830	900	200
WLR	0%	7%	64%
GVF	65%	90%	94%
Pressure bar a	150	150	150

As proposed by the American Petroleum Institute [3] and the Norwegian Society for Oil and Gas Measurement [4], one of the common strategies used to ensure an accurate measurement procedure is to separate the flow into liquid (oil plus water) and gas streams and measure them using either traditional two or single-phase flow meters.

The complete separation process is carried out by expensive, heavy and space-occupying systems. On the other hand, the partial separation process also faces systematic errors in measurement along with flow pressure drops and increased costs.

Therefore, one of the solutions for measuring three-phase flow is to emphasize the installation of meters in appropriate positions instead of using the separation process, which should ensure the laminar flow of fluid. In this situation, interfaces between three immiscible and incompressible fluids are laminar and the flow is characterized by a low-to-moderate Reynolds number. The density of each fluid is assumed to be constant, but there is no restriction on the density differences between the separate fluids. By using the principles of fluid mechanics and the condition that we face sufficiently large straight lengths before and after the placement of the meter, it is expected to reach a stratified three-phase regime with non-wavy boundaries [5].

This article investigates the possibility of detecting the boundary position between the three-phase flow components in the stratified regime by using the proposed gamma backscattering system embedded around the flow pipe in the MCNP Monte Carlo environment.

PROPOSED SETUP

To create various fractions of three-phase flow components under stratified regime conditions, a 32-inch pipe was filled with oil-water-air components at four different heights. The proposed three-phase flow meter, as shown in Figure 1, will be installed around the pipe to collect data on gamma scattering. The data will be collected in 5º increments from the bottom to the top of the pipe.

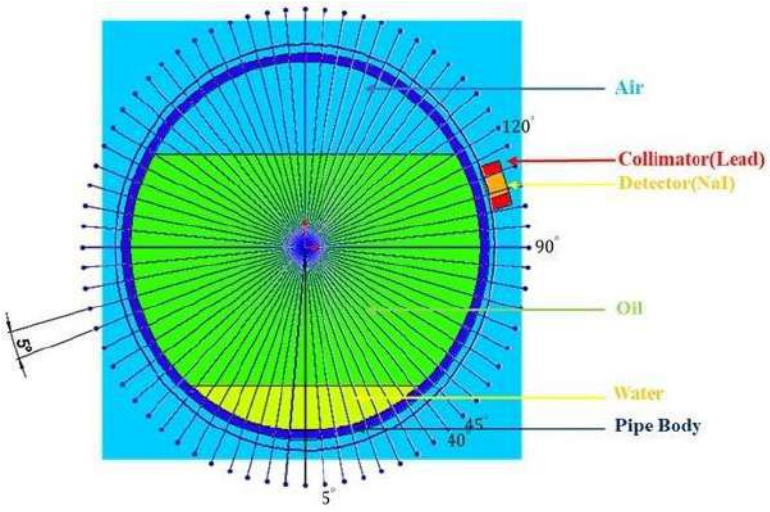

Fig. 1. The proposed three-phase flow meter setup uses the gamma backscattering technique.

MONTE CARLO SIMULATION

Through modeling and continuous simulation, engineers can optimize system design and make decisions before launching prototypes or costly implementations. One of the main reasons for the importance of simulation in engineering is its ability to predict and understand the behavior of complex systems [6].

Simulations allow them to observe how changes in a parameter affect the performance and end result of the system. This helps engineers evaluate different design options and make better design choices. In addition to design optimization, simulation helps improve efficiency and reduce costs [7]. In the nuclear industry, due to the use of radioactive sources and ionizing radiation generators, simulation becomes more important. Researchers can gain valuable experience working with various nuclear materials and instruments such as radioactive sources and detectors without the risk of exposure using simulation.

Monte Carlo codes are widely used for various applications that require the modeling of radiation interaction with matter. MCNP, as one of the powerful and versatile simulation Monte Carlo codes, is widely used for accurately modeling complex processes. It transports and tracks radiation through matter by considering scattering, absorption, and nuclear reactions. One of its key strengths is the ability to model a wide range of nuclear systems, including nuclear reactors, particle accelerators, radio medicine, and even space applications. This makes MCNP a valuable tool for researchers,

engineers, and scientists working in various fields of nuclear science and technology [8]. In this study, the modeling part consists of three main units: the radiation source inside the collimator, the process material, and the detection unit. The final design was simulated using the MCNPX Monte Carlo code. Figure 2 shows a view of the geometry of the proposed three-phase flow meter simulated in the Monte Carlo environment.

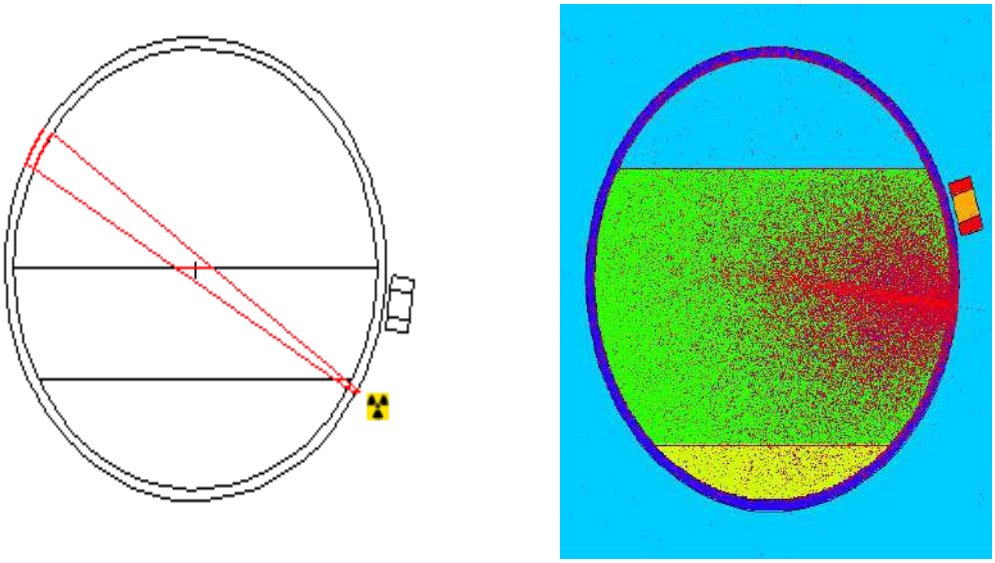

Fig. 2. The track of the radiation through matter is taken into account by considering gamma backscattering interaction in the proposed three-phase flow meter.

As depicted in Figure 3, the stratified regime of water-oil-gas three-phase in four different fractions is prepared and fed into the MCNP input file and the backscattered gamma is acquired at several angular positions.

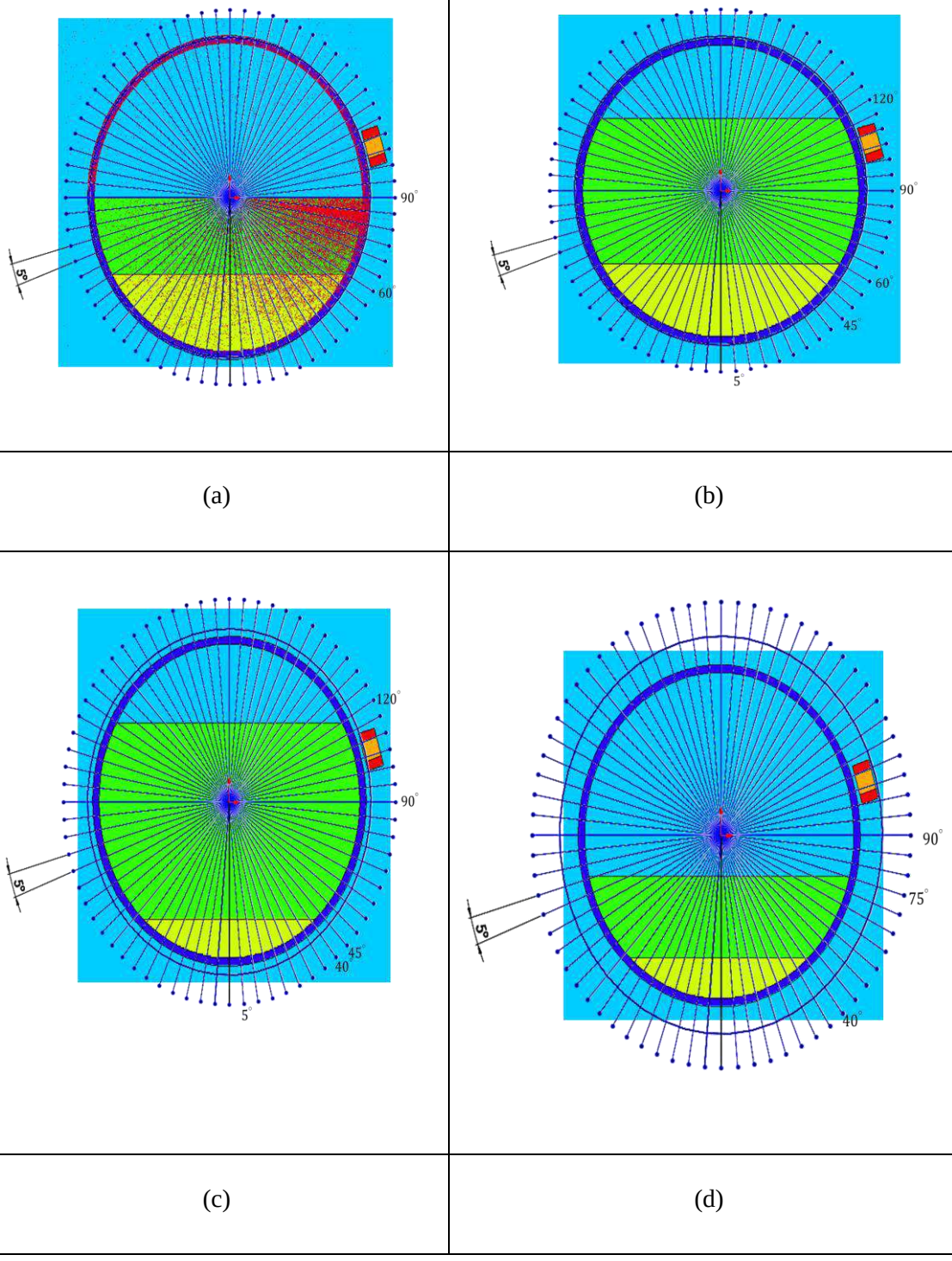

(a) (b) (c) (d)

Fig. 3. The different fractions of stratified water-oil-gas three-phase flow prepared and fed into the MCNP input file. (a) h_g=R, h_w = h_o =R/2, (b) h_g = h_w =R/2, h_o=R, (c) h_g=R/2, h_w = 5R/4, h_o =5R/4, (d) h_g=R/2, h_w = R/4, h_o =R/2. Consequently, the backscattered gamma was acquired in several angular positions.

To differentiate between the gas and liquid components in the three-phase flow, a ^{60}Co source was used. The average energy of the emitted gamma-rays, which is approximately 1250 keV, enables effective differentiation between the gas and liquid phases mainly through Compton scattering. Moreover, this energy range allows for a significant flux of gamma rays to pass through the pipe and reach the external detector. This method minimizes counting statistics errors to the greatest extent possible.

Results and discussion

Following the simulation, 37 input files corresponding to each of the four categories of the three-phase combination were prepared for the gamma transport and backscattered photon acquisition process. Figure 4 depicts a selection of diagrams obtained from a specific lens, allowing for a comparison of the results across different phase fractions.

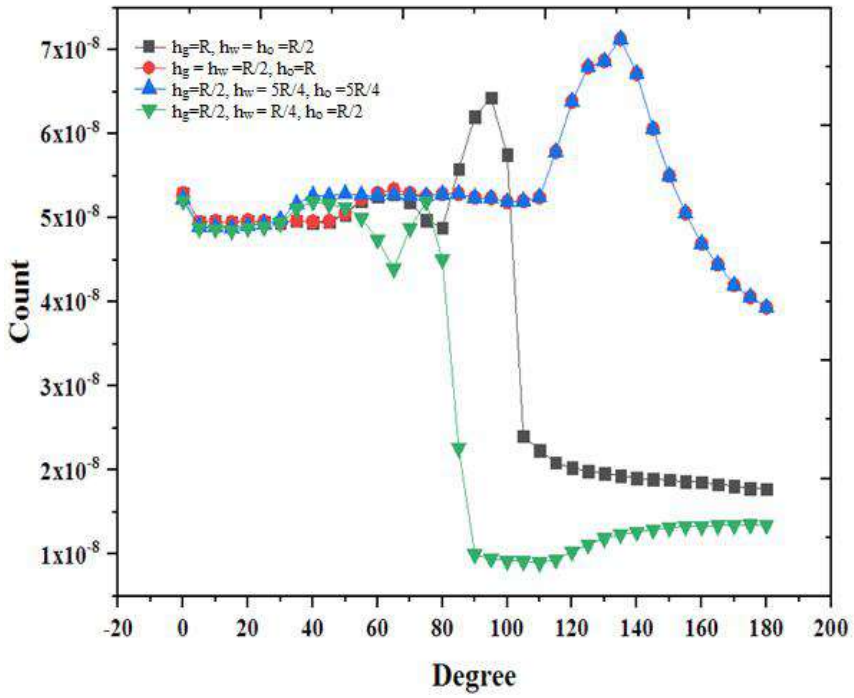

Fig. 4. The count vs angular position diagrams are related to four categories of the three-phase phase fractions.

As shown in Figure 4, two successive relative extrema can be seen. These extrema for each of the states a, b, c and d are in two consecutive angles of 65-95, 65-135, 40-135, and 40-75 respectively. In fact, and as a very important result, it is observed that there are two counting peaks at the boundary

of the separation of the flow components, and this means the ability to use the proposed system to separate the three-phase flow.

Comparing the true consecutive angles of 60-90, 60-120, 40-120, and 40-75, the highest and lowest matching error is related to the second and fourth states which have the lowest and highest amount of gas fraction.

Comparison of two states b and c with the maximum mismatch between simulation and real consecutive angles shows that error in the water-oil boundary distinction is reduced with the reduction of the water fraction as the densest phase in stratified three-phase flow.

According to the collected data, the liquid-liquid versus gas-liquid boundary distinction can always be done with less mismatch.

Finally, the system presented in this research work is able to distinguish liquid-liquid and gas-liquid phases of the stratified three-phase water-oil-gas fluid with a maximum uncertainty of 5 and 15 degrees relative to the center of the pipe, respectively.

Conclusions

The accurate measurement of the oil-gas-water three-phase flow rate is done by using expensive and bulky flow separators, which has made the use of online multiphase flowmeter systems highly desirable in the petroleum industry.

Finding a convenient location along the pipeline that ensures laminar flow of fluid, in addition to using the gamma backscattering technique, is proposed as a new solution in this study. This article investigates the possibility of detecting the boundary position between the three-phase flow components in the stratified regime by installing a coupled gamma source-scintillation detector around the pipe at different angles with the ability to count gamma rays backscattered by the fluid.

As the results show in Figure 4, it can distinguish liquid-liquid and gas-liquid boundaries with the highest and lowest matching error related to the second and fourth states corresponding to the lowest and highest gas fraction.

References

[1] Thorn, R., Johansen, G. A., & Hjertaker, B. T. (2012). Three-phase flow measurement in the petroleum industry. Measurement Science and Technology, 24(1), 012003.

[2] Couput, J., Gajan, P., De Laharpe, V., & Strzelecki, A. (2000, October). Wet Gas Metering in the upstream area: needs, applications & developments. In 18th North Sea Flow Measurement Workshop, Scotland (pp. 24-27).

[3] American Petroleum Institute. (2004). State of the Art Multiphase Flow Metering. API Technical Publication 2566.

[4] METERING, M. F. HANDBOOK OF MULTIPHASE FLOW METERING.

[5] Robert, W. F., Alan, T. M., & Philip, J. P. (2004). Introduction to fluid mechanics. John Wiley&Sons.

[6] Sinha, R., Paredis, C. J., Liang, V. C., & Khosla, P. K. (2001). Modeling and simulation methods for design of engineering systems. J. Comput. Inf. Sci. Eng., 1(1), 84-91.

[7] Rosova, A., Behun, M., Khouri, S., Cehlar, M., Ferencz, V., & Sofranko, M. (2022). Case study: the simulation modeling to improve the efficiency and performance of production process. Wireless Networks, 28(2), 863-872.

[8] Waters, L. S. (2002). MCNPX user's manual. Los Alamos National Laboratory, 124.

Kian is the first drought-tolerant cultivar in Iran by inducing mutation in local cultivars (Paper ID : 1489)

Ebadi A.A. [1*] Hallajian, M.T. [2] Khoshkdaman M. [1] Majidi F. [1] Mohammadi M. [1]

[1]*Rice Research Institute of Iran (RRII), Agricultural Research Education and Extension Organization (AREEO), Rasht, Iran.*

[2]*Nuclear Science and Technology Research Institute (NSTRI), Nuclear Agriculture Research School, Karaj, Iran.*

Abstract

Iranian local cultivars are sensitive to environmental stress, including water stress, while having very suitable cooking quality. In order to introduce drought stress tolerant variety, after determining the optimal dose of gamma radiation for the local Tarom variety, a mutant population was formed. The selection was carried out based on tolerance to drought stress and other agronomic characteristics during the years 2009 to 2011, which led to the selection of 56 promising drought tolerant mutant lines. Among these mutant lines, 14 lines were selected based on preliminary evaluation in two years (2012 and 2013) under normal and drought stress conditions. The stability of these 14 mutant lines were evaluated in three regions, Rasht (under normal conditions and drought stress at the end of the season), Chaparsar and Fars during the years 2014 to 2015. Based on this evaluation, the Kian variety (line TM8-B-7-1 or line MN5) was selected as the superior line in terms of yield and drought stress tolerance indices. Other characteristics of this variety are early maturity and good cooking quality. The application of 90 kg of nitrogen per hectare with a planting distance of 20 x 20 cm for this variety was determined based on the agronomic test. In 2017, the Kian variety was cultivated with the native Hashemi cultivar in three cities of Guilan province (Lashtenesha, Soumesara and Langrod) in the fields of leading farmers. The results showed that the average grain yield of Kian variety in all three cities was 5383 kg/ha under normal conditions and 4093 kg/ha under drought stress conditions, while the average grain yield of the Hashemi cultivar in the three cities under normal conditions was 3900 kg/ha. The length of the growth period from the time of sowing to the maturity stage was between 99-109 days in Kian variety and between 112-114 days in the Hashemi variety.

Key words: rice, local variety, drought tolerance, mutation.

INTRODUCTION

Rice or Oryza sativa is a member of the cereal family (Poaceae). This plant is one of the important grains that grows in one third of the areas under cereals cultivation and provides 21% of global energy and 15% of global protein. Rice is the plant that needs the most water among cereals. This plant needs about 8 to 20 thousand cubic meters and 700 liters of water to produce one kilogram of dry matter until the physiological maturation of seeds [1]. At the same time, water deficit stress is considered as one of the main limitations that reduce rice yield [2]. According to statistics, out of the 11.38 million hectares of crops in Iran, 52.9% is irrigated and 47.1% is rainfed. Out of this amount, the highest level of harvest belongs to the cereals group (71.86 percent), of which 44.52 percent is related to irrigated cereals. In the meantime, rice cultivation is irrigated in all regions of the country [3]. Identifying or creating drought tolerant genotypes with high yield, and using them in drought stress areas, will minimize the damage of water deficit and ensure the sustainability of rice production. Considering the limitation of irrigation water for most crops including rice, more useful use of irrigation water is considered one of the most important ways to deal with the water shortage crisis. Therefore, it is important to identify varieties with higher water use efficiency for use in future breeding programs to produce tolerant rice varieties. Drought stress, as one of the main limitations that reduces yield, can occur at any time from the beginning of the growing season to the filling of seeds. However, rice is most sensitive to drought stress in the reproductive stage [4]. According to estimates, 50% of global rice production is affected by drought [5]. Due to the fact that the probability of occurrence of drought stress is higher in the reproductive stage compared to the vegetative stage, and drought stress, especially in the reproductive stage, has a greater effect on the grain yield and its components. Usually, in the evaluation of rice genotypes, late-season drought stress is applied [6-8]. Considering that about 70% of paddy fields in Guilan are irrigated by the Sepidroud dam, and usually at the end of the growing season, the amount of water behind the dam greatly reduced. Therefore, when there is a problem of water shortage, usually the release of water is less at the end of the growing season, i.e. at the time of flowering and grain filling. And the areas that are located downstream have a water shortage and the paddy fields in these areas have drought stress. This is one of the main reasons for not cultivating late high-yielding cultivars in Guilan.

Local cultivars are of special importance due to the increase in grain length after cooking and having a very good taste. And for these reasons, the interest in cultivating these cultivars continues despite having many disadvantages, and most of the paddy fields are under the cultivation of these cultivars.

Therefore, improving local cultivars with different breeding methods can increase the average yield and total production of rice. One of the breeding methods to overcome the disadvantages of local cultivars is the use of mutation breeding. In this research, physical mutagen was used to provide the required diversity. Also, mutational breeding has been used to create new varieties with superior qualitative and quantitative traits in most regions of the world. However, due to the quantitative of the studied trait and the difficulties in producing drought-tolerant cultivars using gamma radiation, few works have been done in this field.

The lines evaluated in this research were obtained from the induced mutation of the local Tarom variety during the implementation of several joint projects between Rice Research Institute of Iran(RRII) and Nuclear Science and Technology Research Institute (NSTRI), [9, 10]. The Kian variety is drought stress-tolerant and has a shorter height and higher yield under normal and drought stress conditions. Also, this variety has the desirable characteristics of local varieties (amylose content 21, medium gelatinization temperature, good aroma, head rice percentage of 62% and cooking quality similar to local varieties).

Materials and Methods

In this research, the improved cultivars "Fajr" and "Khazar" and the local cultivars "Tarom Mahali" and "Hashmi" were used as plant materials. The optimal dose of gamma rays for irradiating the seeds of these cultivars was determined. And then, based on the results of irradiation and determining the optimal dose, in order to create the plant population of the M1 generation, the seeds of the main population of cultivars were irradiated with an optimal dose and a higher dose.

The seeds of all plants of the M1 generation were harvested. Plants of M2 generation were subjected to drought stress to screen the tolerant plants. Changes in soil moisture were periodically measured in plots under drought stress using a tensiometer. Water stress was applied in the field from about 10 days before flowering to 4 days after flowering for two weeks [11]. Phenotypic analysis of rice plants under drought stress was done based on IRRI standard evaluation systems [12]. All phenotypic analyzes of rice plants under drought stress during 2010-2012 were carried out in three generations of mutations in Tarom and Fajr, Hashemi and Khazar genotypes.

In 2013, 56 mutant lines of the M5 and M6 generations were obtained from the mutation of two local cultivars (Hashmi and Tarom Mahali) and two improved cultivars (Khazar and Fajr) along with the 4 mentioned parents and 4 cultivars of Sengjo, Baynam, Ali Kazemi and Sepidroud (as control cultivars tolerant to drought stress) were evaluated. This research was carried out in the form of two square lattice designs (8 x 8) with two replications in the experimental field of Rice Research Institute of Iran separately in two conditions of normal and drought stress. In the experiment related to drought stress, irrigation was completely stopped at the panicle initiation until harvesting.

Fourteen selected mutant lines (7 Hashemi mutant lines, 6 Tarom mutant lines and one Khazar mutant line) along with 4 cultivars (Hashmi, Tarom, Khazar and Gilaneh) in 3 locations (Rasht, Chapressar and Fars) during two years (2014- 2015) were evaluated. In Rasht, the lines were evaluated in two conditions, normal and under drought stress. In the experiment related to drought stress, irrigation was completely stopped at the panicle initiation until harvesting. During the growth period or after harvesting, traits such as grain yield (T/ha), number of panicle per plant, weight of one hundred seeds (gr), number of seeds per panicle, plant height (cm), panicle length (cm) and number of days until 50% flowering were done on 5 random plants in each plot. In addition, grain quality traits including amylose amount, gelatinization temperature, gel consistency, grain physical properties such as length, width, as well as elongation after cooking and head rice yield were measured.

The optimal planting distance and the appropriate amount of nitrogen fertilizer were determined for the Kian variety (promising line TM8-B-7-1 or MN5). A research in 2017 in the form of a factorial experiment based on RCBD in three replications using five levels of pure nitrogen fertilizer (zero, 60, 75, 90 and 105 kg/ha) and two levels of planting distance (20x15 and 20x20 cm) was implemented.

During the years 2016-2017, the Kian cultivar was cultivated in 500 square meters along with the Hashemi cultivar in three cities of Guilan province (Lashtenesha, Soumesara and Langrod) in the fields of leading farmers. During the growth period, important morphological characteristics (number of panicle, plant height, length of growth period and grain yield) were measured by taking the necessary number of samples. Statistical analysis including descriptive statistics, preparation of tables and graphs was performed using SAS ver 9.1 software.

Results and discussion

The results of the dose tests showed that the optimal dose for the local Tarem genotype is 230 Gy (Fig.1) and the optimal dose for Fajr genotype is between 200 and 230 Gy. The optimal dose is the dose that produces the highest mutation with the least damage to the plant. The optimal radiation dose of "Hashmi" and "Khazar" genotypes was determined to be 250 and 200 Gy, respectively. The pattern and level of sensitivity to gamma rays in native cultivars and genotypes (Taram Mahali and Hashemi) were somewhat different from improved cultivars and genotypes (Fajr and Khazar).

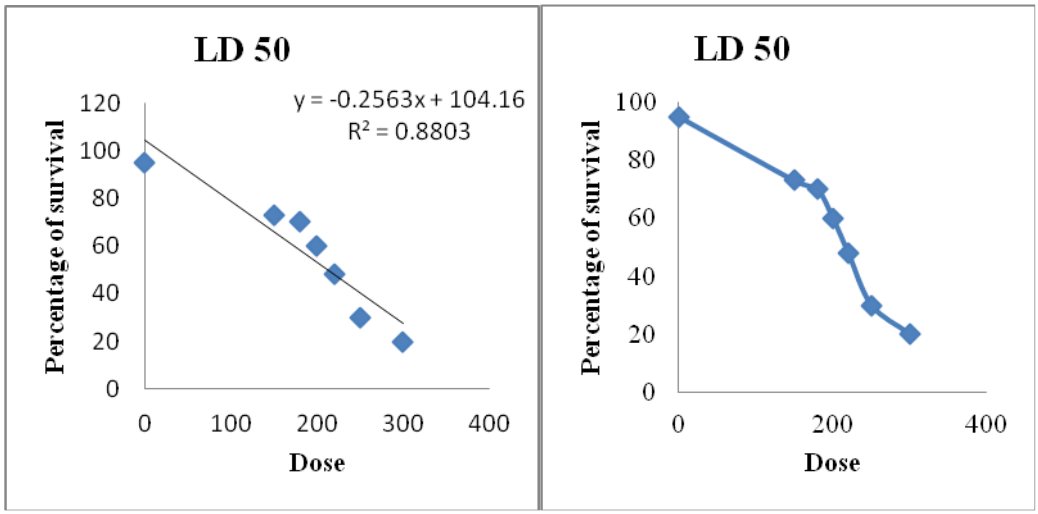

Fig.1- LD50 of seedling survival in "Taram Mohali" genotype

Two weeks after drought stress in the population of the M2 generation of Tarom mutant lines, 64 mutant plants tolerant to drought stress based on the leaf rolling scale and 81 early and very early mutant plants based on the flowering date (145 plants in total) was selected. After 2-3 weeks of drought stress, 49 tolerant lines based on leaf rolling scale and 5 early lines based on flowering date (54 plants in total) were selected from M3 generation population. In the M4 generation, about one month of drought stress was applied on the Tarom genotype mutant plants in the experimental field. 10 tolerant lines based on leaf rolling scale and 3 early lines based on flowering date (13 lines in total) were selected in M4 population.

In total, 56 promising mutant lines tolerant to drought stress were selected from the mutant plant populations of the M4 generation of local Tarom and Fajr cultivars and the M3 generation of Hashemi and Khazar cultivars, which performed well in comparison with the normal control. These drought stress resistant mutant lines were subjected to preliminary performance evaluation under normal and drought stress conditions. The comparison of the average traits in normal conditions showed that the Kian variety (promising line TM6-B-7-1) had the highest grain yield among all the

examined lines with 5861 kg/ha. The amount of yield under drought stress in Kian cultivar was 2217 kg/ha, which was statistically lower than only two lines number 12 and 43 and was placed in the second group.

After simple analysis of investigated traits in different places and years in 14 mutant lines along with 4 control numbers and checking the uniformity of experimental error variances for common traits measured in all three places and in both years, combined variance analysis was performed. The main effect of genotype in all investigated traits was significant at the level of 1%. The triple interaction effect of genotype by year at location was significant at the 1% level for all the studied traits. The height of the plant in Kian cultivar was 119 cm, which statistically had a significant difference with local Tarom and Hashemi cultivars. The average spike length trait in Kian cultivar was 24.86 cm, which was in the second group in terms of this trait. The number of healthy seeds in this variety was 89.05, which was not significantly different from the highest value of this trait among the studied varieties and lines. Of course, the average number of seeds in this cultivar was lower than the control cultivars. Also, the trait of fertility percentage was 91.35% in the Kian cultivar, which was more than the control cultivars and was not significantly different from the highest amount of this trait observed in line number 7. Kian cultivar with an average weight of 2.72 grams was among the lines of group one in this trait, which had a significant difference with the control cultivars. Kian variety had the highest average yield of paddy in three places and two years evaluated among the investigated genotypes with a rate of 5684 kg/ha.

In order to identify more stable genotypes, stability analysis using different statistics is needed. The stability parameters of intra-spatial variance and environmental variation coefficient showed that Kian variety (line no. 5) and lines no. 7, 12 and 8, having the lowest values of these indicators, are the most stable genotypes in terms of grain yield. Three indices of regression coefficient (bi), average performance of genotypes ($\bar{g}$) and average performance of total genotypes ($\bar{X}$) were used to classify genotypes in terms of stability. The Kian cultivar along with genotypes 1, 2, 7, 8, 12 and 18 had a regression coefficient less than one and the average yield was higher than the average of all genotypes. Among these genotypes, the amount of deviation from regression in Kian variety and genotype 12 was less than other genotypes. In total, Kian cultivar and genotype 12 with average grain yield higher than the total average, regression coefficient less than one, minimum deviation from regression, coefficient of environmental changes and low intra-spatial variance, were high-yielding genotypes with stable yield (Table 1). In accordance with this result, other researchers also

used the above parametric methods to identify stable genotypes of rice. So that Nahvi et al., [13] reported that line 424 (Darfak variety) is the most stable and productive variety due to having less mean square and coefficient of internal variation. Also, Sharifi et al., [14] with methods of stability analysis with environmental variance, coefficient of variation, variance and variance of Shukla deviation, Rick's equivalence, regression coefficient, detection coefficient, Eberhart-Russell variance analysis, performance stability statistic (YSi) and non-parametric methods of genotypes They identified stable. Sharifi and AminPanah [15] identified the most stable genotype with low intra-spatial variance and coefficient of variation parametric methods.

Table 1- Some parameters of grain yield stability of rice genotypes in three places and three years

Genotype	Grain Yield (kg/ha)	Regression Coefficient (bi)	Deviation from regression	Intra-spatial variance (Msy/l)	Environmental Coefficient Variation (CVy/i)
G1	4607	0.996	111284	412652	13.94
G2	4699	0.711	279690	391490	13.31
G3	4418	1.08	96356	453456	15.24
G4	4227	1.25	122539	608946	18.46
Kian	5684	0.69	72194	215927	8.18
G6	4237	0.795	47371	246212	11.71
G7	5009	0.265	113668	118698	7.02
G8	4466	0.0863	248161	206154	10.17
G9	4323	0.828	21113	227225	11.03
G10	4240	0.977	103534	394590	14.81
G11	4175	1.34	130530	686332	19.93
G12	5470	0.526	69483	149672	7.02
G13	4148	0.989	78619	382271	14.90
G14	3353	2.351	241389	2216414	44.40
Khazar	3252	2.72	283012	2603394	49.61
Hashemi	3908	0.774	97766	261180	13.08
Tarommohali	3883	0.789	34495	232571	12.42
Gilaneh	4504	0.71	260708	375491	13.60

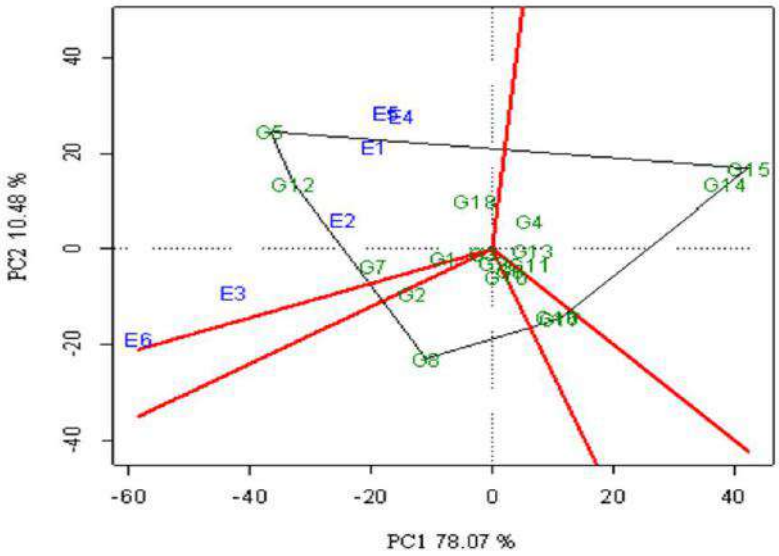

Fig.2- Polygon view of GGE biplot based on grain yield data of 18 genotypes in three locations and two years (6 environments).

As it is clear in the diagram, genotypes 5 (Kian number), 7 (promising line (HM8-250-5E-1-1) or MN7) and 12 with a higher average yield than the rest of the genotypes were more compatible for all 6 investigated environments. So that genotypes 7 and 12 were highly compatible with three environments (2, 3 and 6) and genotype 5 (Kian number) was more compatible with three environments (1, 4 and 5) (Fig.2).

The results of the evaluation of the important agronomic characteristics of Kian and Hashemi varieties in three different cities of Guilan province showed that under normal conditions, Kian had the highest seed yield in Soumesara city with 6400 kg per hectare and the lowest yield in Lashtnesha city with 4500 kg per hectare (Fig. 3). This difference in performance in two regions is mostly due to non-observance of agricultural tips and instructions in Lashtnesha and poor nutrition management in this city. Therefore, by following the agricultural guidelines, it is possible to have a very good performance for the Kian variety, on the other hand, this variety has a high yield potential compared to the local Hashemi variety, so that by changing the agricultural management, a higher performance can be obtained for this line. In all three studied cities, the Kian cultivar had a higher yield than the Hashemi cultivar. On the other hand, with the application of drought stress, the yield reduction in Kian cultivar was not high, so that after applying drought stress, the yield of this line was equal to that of Hashemi cultivar under normal conditions.

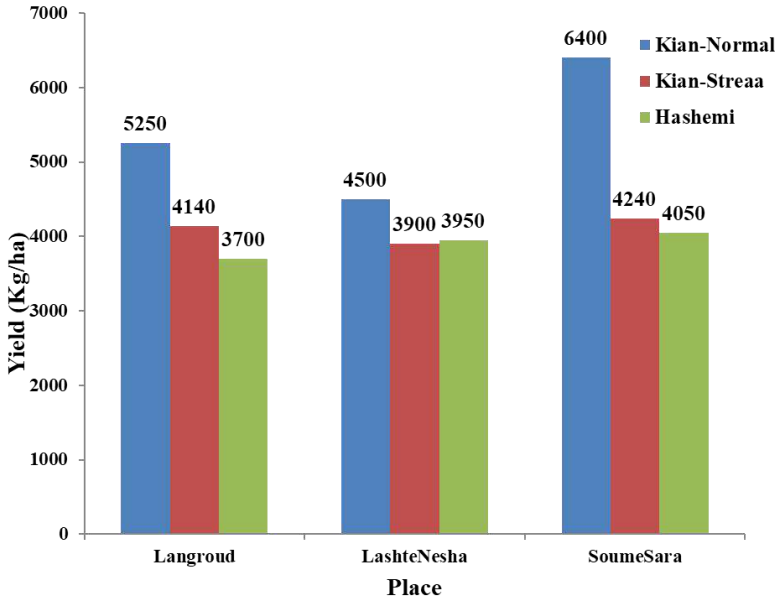

Fig. 3- Average grain yield (kg/ha) of Kian variety (under normal conditions and drought stress) and Hashemi variety in three different cities.

By evaluating the planting distances and different amounts of nitrogen for the Kian variety, it was found that the average seed performance in the planting distance of 20x20 cm was significantly higher than the planting distance of 15x20 cm. The harvest index, nitrogen recycling efficiency and agricultural efficiency of nitrogen application in the planting distance of 20x20 cm were significantly higher than the planting distance of 15x20 cm, but the amount of nitrogen absorption of straw in the planting distance of 20x15 cm was significantly higher than the planting distance of 20x20 cm. The highest seed yield was obtained from the application of 90 kg of nitrogen per hectare with a planting distance of 20 x 20 cm (4492 kg per hectare). Considering the fact that the performance of this treatment has a significant difference with other levels of nitrogen, the application of 90 kg of nitrogen per hectare with a planting distance of 20x20 cm is recommended for Kian variety.

The Kian cultivar is tolerant to drought stress induced by mutation (through gamma radiation) in the native cultivar. This variety has a yield of 5.5-6 tons per hectare, weight of 100 seeds is 3-2-8 grams, number of full seeds is 111-112 and height is 147-135 cm under normal conditions. Also, the yield is about 3.5 tons per hectare, the weight of one hundred seeds is 2.2-9.7 grams, the number of filled seeds is 92-97 and the height is 128-132 cm under drought stress conditions. In addition to being superior to its parent, this variety is considered one of the early and semi-short varieties and has the same cooking quality as local Iranian varieties. This line has wide leaves and this is a great advantage

for the plant in terms of more photosynthesis and higher yield. The germination of the seeds of this variety in the treasury, like other local varieties, has a high speed, and after planting in the main land, due to its long leaves, it creates good shading in the spaces between the bushes, and for this reason, it prevents the growth of weeds.

Substitution of Kian cultivar in 10% of the paddy fields of Guilan and Mazandaran provinces (about 40 thousand hectares) instead of local cultivars will result in an increase in production equivalent to 60 to 80 thousand tons of paddy. In other words, by cultivating this variety instead of native varieties such as Hashmi, about 750 to 1000 million Rials (1500 to 2000 kg of paddy more and the price of 500 thousand Rials per kg of paddy) will be more income for rice farmers. Of course, it should also be noted that in lands with water shortage problems, this variety can lead to the stability of production in these lands while preventing damage to rice farmers.

References

[1] Karimi, H. (1991). Agricultural plants. Tehran University Publications. Third edition. 387 pages.

[2] O,Toole, J. C. and Chang, T. T. (1979). Drought resistance in cereals. Rice: A case study. In: Messel, H. and R. C. Taples. (Eds.). Physiology of crop plants. John Wiley and Sons, New York. pp. 347-405.

[3] Anonymous (2022). Cereals in the mirror of statistics. Department of Statistics and Information of the Ministry of Jihad and Agriculture.

[4] Ji, K., Y. Wang, W. Sun, Q. Lou, H. Mei, Sh. Shen and Chen, H. (2012). Drought-responsive mechanisms in rice genotypes with contrasting drought tolerance during reproductive stage. J. Plant Physiol., 169 :336–344.

[5] Mostajeran, A. and Rahimi-Eichi, V. (2009). Effects of drought stress on growth and yield of rice (*Oryza sativa* L.) cultivar and accumulation of proline and soluble sugars in sheath and blades of their different ages leaves. American-Eurasian J. Agric. Environ. Sci., 5(2) : 269-272.

[6] Mushtaq, R., S. Katiyar and Bennett, J. (2008). Proteomic analysis of drought stress-responsive proteins in rice endosperm affecting grain quality. J. Crop Sci. Biotechnol., 11 (4) : 227 – 232.

[7] Rabello, A.R., Guimarães, C.M., Rangel, P.H., da Silva, F.R., Seixas, D., de Souza, E., Brasileiro, A.C., Spehar, C.R., Ferreira, M.E. and Mehta, A. (2008). Identification of drought-responsive genes in roots of upland rice (*Oryza sativa* L). BMC genomics, 9(1), p.485.

[8] Kumar, R. and Kujur, R. (2008). Role of secondary traits in improving the drought tolerance during flowering stage in rice. Indian J. Plant Physiol. 8: 236-240.

[9] Ebadi, A. A. and Halajian, M.T. (2013). Development of rice plants tolerant to drought stress using mutation breeding and proteomics techniques. Final report under registration number 46845 - Rice Research Institute of Iran - Rasht.

[10] Ebadi, A. A., Halajian, M.T., Qudsi, M. and Mohammadi, M. (2015). Preliminary evaluation of selective mutant lines resulting from the mutation of local and improved rice cultivars. Final report under registration number 5104- Rice Research Institute of Iran-Rasht.

[11] Saxena, N.P. and O'Toole, J.C. (2002). Field screening for drought tolerance in crop plants with emphasis on rice. In: Proceedings of an international workshop on field screening for drought tolerance in rice, 11-14 Dec, ICRISAT, Patancheru, India.

[12] IRRI (2002). Standard Evaluation Systems for Rice (SES). DescriptioNS, Scales and Codes. Drought sensitivity, http://www.irri.org.

[13] Nahvi, M., Allahgholipour, M. Mohammad Salehi, M. S. (2002). Studying the compatibility and sustainability of rice in different regions of Gilan province. Seed and Plant Journal, 18 (1):1-13.

[14] Sharifi, P., Aminpanah, H., Erfani, R., Mohaddesi, A., and Abbasian, A. (2017). Evaluation of genotype × environment interaction in rice based on AMMI model in Iran. Rice Science, 24(3), 173–180.

[15] Sharifi, P. and Aminpanah, H. (2017). Evaluation of genotype × environment interactions, stability and a number of genetic parameters in rice genotypes. Plant Genetic Researches.3 (2) :25-42.

ICNST 2024
International Conference on Nuclear Science and Technology
6- 8 MAY 2024 | Isfahan, Iran

Comparison of radiolabeled bisphosphonates in bone metastasis (Paper ID : 1490)

Erfani M.[1]*, Mikaeili A.[1], Goudarzi M.[1], Fallah Z.[1], Rezaei M.[1]

[1]*Radiation Application Research School, Nuclear Science and Technology Research Institute (NSTRI), Tehran, Iran*

Abstract

Bisphosphonates have a very high affinity for bone mineral because they bind to hydroxyapatite crystals. Based on this fact, it was hypothesized to evaluate bone uptake for $^{99m}Tc/^{188}Re$ radiolabeled bisphosphonates to determine the order of uptake in bone as agents for imaging or treatment of skeletal disorders.

Bisphosphonate samples were labeled by adding 185 MBq of $^{99m}Tc/^{188}Re$ in saline. $SnCl_2$, $2H_2O$ and ascorbic acid were used as reducing agents. Radioactive thin layer chromatography (RTLC) was used to determine the radiochemical purity. The stability of radio-complexes in saline and human serum was investigated. Bone uptake was evaluated through biodistribution experiments in normal mice.

A radiochemical purity of >90% was obtained for evaluated radiotracers. Bone accumulation and rapid renal excretion were observed in the biological evaluation 2 hours after injection for all evaluated bisphosphonates. Although bone uptake was desirable for investigated bisphosphonates, it appears that third-generation bisphosphonates have the potential to be used as novel bone imaging or therapeutic agents.

Keywords: Bisphosphonates; $^{99m}Tc/^{188}Re$; Radiochemical yield; Bone metastasis

INTRODUCTION

Bisphosphonates have been increasingly used for a variety of skeletal disorders. bisphosphonates have a very high affinity for bone mineral because they are attached to hydroxyapatite crystals [1]. Accordingly, skeletal bisphosphonate retention depends on the availability of hydroxyapatite binding sites. Bisphosphonates are preferentially incorporated into sites of active bone remodeling, as typically occurs in conditions accelerated by skeletal turnover [2]. The bisphosphonate that does not remain in the skeleton is quickly cleared from the circulation by renal excretion. In addition to their ability to inhibit calcification, bisphosphonates inhibit the breakdown of hydroxyapatite,

thereby effectively suppressing bone resorption [3]. Recently, it has been suggested that bisphosphonates also act to limit osteoblast and osteocyte apoptosis [4].

Technetium-99m has become the most important radionuclide for organ imaging due to its superior physical specifications and uncomplicated availability from a generator. Since it has been described that bisphosphonates had high affinity for bone mineral, several ^{99m}Tc-labeled phosphate compounds have been developed for skeletal imaging [5, 6]. Pyrophosphate has only two phosphate moieties

and is a simple polyphosphate. [^{99m}Tc]Tc-pyrophosphate is now rarely used for bone scanning due to its high soft tissue background activity, but is still used to determine myocardial infarction. Unfortunately, phosphating agents may be affected or damaged in vivo by enzymes such as alkaline phosphatase, thereby releasing free technetium from the complexes. ^{99m}Tc-labeled of 1-hydroxyethyliden-1,1-bisphosphonate (HEDP), as a new bone imaging agent showed significant bone tissue uptake compared to [^{99m}Tc]Tc-pyrophosphate [7, 8]. With raising of ^{99m}Tc-labeled methylene bisphosphonate (MDP) and hydroxymethylene bisphosphonate (HMDP), [^{99m}Tc]Tc-MDP and [^{99m}Tc]Tc-HMDP with superior biodistribution compared to [^{99m}Tc]Tc-HEDP, have been used as radiopharmaceuticals of choice for bone scintigraphy [9, 10]. However, their exact structure is still unknown because these compounds are a mixture of short and long chain oligomers and cannot exist as a single species. Furthermore, from the point of view of clinical studies, since ^{99m}Tc-labeled bisphosphonates show slow blood clearance, a delay time of 2-6 hours is required to initiate the bone scan. [11].

Rehenium-188 with properties such as half-life of 16.9 h and Eβ(max)=2.12 MeV is attractive for therapy. Additionally, its 155-KeV γ-emission (15% abundance) allows for imaging of its distribution to facilitate dose calculation. Moreover, like to the in-house use of the ^{99}Mo/^{99m}Tc generator for the preparation of different technetium-99m labeled diagnostic agents, rehenium-188 can be obtained from an alumina based ^{188}W/^{188}Re generator in nuclear medicine centers. Similar chemical properties between technetium and rhenium give rise to [^{188}Re]Re-HEDP, which has surprising properties as a bone-seeking agent [12]. However, previous studies have indicated that the in vivo decomposition of radio-complex into perrhenate cause unnecessary radiation to other organs and led to delay in blood clearance and high gastric uptake of radioactivity after injection [13]. So,

development of a new bone- specific radiopharmaceutical which has more potency, stability and greater accumulation in the bone is needed.

Preparation of a radiopharmaceutical with ideal characteristics such as higher absorption for bone, more rapid clearance from blood and enable imaging at an earlier time after injection is required accordingly and might be advantageous. In this regards the new generations of bisphosphonate tracers have been developed [14]. As well as some ^{99m}Tc-labeled second and third generation bisphosphonates analogues have been made ready and investigated [15]. Herein, in order to achieve a tracer with high bone uptake different labeled bisphosphonates with ^{99m}Tc/^{188}Re were compared in mice.

RESEARCH THEORIES

In according to the specific advantages of using ^{99m}Tc/^{188}Re in imaging and palliative radiotherapy of bone pain, the biological properties of the labeled bisphosphonates were compared.

EXPERIMENTAL

Materials and measurements

All chemicals reagents were purchased from Sigma/Aldrich and used without further purification. Technetium-99m and rehenium-188 were eluted from a commercial ^{99}Mo/^{99m}Tc and ^{188}W/^{188}Re generators (Iran, Tehran, Pars Isotope Co) with saline solution (0.9% NaCl). Radioactivity was determined in a dose calibrator (Isomed, Germany). Quantitative gamma counting was performed using a NaI(Tl) counter.

Labeling with ^{99m}Tc/^{188}Re

For radiolabeling with technetium-99m, solutions of the first and third-generation bisphosphonates (methylene bisphosphonate (5 mg/mL) and zoledronate (0.15 mg/mL)) were prepared by dissolving in the water and citrate buffer respectively. Ascorbic acid (0.2 mg) was combined in the vials. A solution of $SnCl_2$, $2H_2O$ in nitrogen-purged 0.1 M HCl, 0.1 mg and 0.2 mg) was added. 185 MBq of technetium-99m in saline was added to the final solution in the vials. The pH was adjusted to 3 and 6 for zoledronate and methylene bisphosphonate respectively. The mixture was shaken vigorously for 60 second. The incubation was carried out in sealed container for 20 minutes at room temperature.

Rehenium-188 radiolabeling was done through preparation of a solution containing second-generation bisphosphonate (pamidronate, 5 mg/mL) by dissolving in water. $SnCl_2.2H_2O$ (0.5 mg in nitrogen-purged 0.1 M HCl) and ascorbic acid (2.5 mg) were combined in a vial. To the vial was added 0.1 mg potassium perrhenate as a carrier and then was labeled by 185 MBq of rehenium-188 in 1 mL saline. Final pH was adjusted (pH=3) by addition of 1N HCl. The mixture was incubated in sealed container for 30 minutes at 100 °C.

Radiochemical analysis

The radiochemical purity of labelled bisphosphonates was determined by paper chromatography strips (Whatman 1) developed in acetone and water as solvents. About 5 µL radio-complex solution was applied at 1 cm from the bottom of paper stripes and after complete development, the chromatographic paper stripes were analyzed to determine the radiochemical purity. With the acetone as an eluting solvent, the free pertechnetate and perrhenate migrate with the solvent front, while the colloidal impurity and radio-complex both remain at the origin of the paper strip. With the water as an eluting solvent, the colloidal impurity remains at the origin of the paper strip, while pertechnetate, perrhenate and radio-complex move with the solvent front.

Stability of radio-complexes was evaluated in saline and human serum. Aliquots were taken out at different times post labeling and analyzed by paper chromatography strip. 50 µL of labeled formulations was added to 0.5 mL of freshly prepared human serum, and the mixture was incubated in a 37 °C. 50 µL aliquots were removed at the different time points after reaction and treated with 50 µL of ethanol. Samples were centrifuged for 5 min at 1000 rpm to precipitate serum proteins and for supernatants paper chromatography were performed.

Biodistribution in mice

Animal experiments were performed in compliance with the regulations of our institution and with generally accepted guidelines governing such work. Biodistribution experiments were performed with an intravenous administration of 50 µL of each diluted tracers' solution (1.85 MBq) to mice via a tail vein. Groups of at least 3 mice each were sacrificed and the tissues and organs of interest were collected, immediately weighed and counted in a NaI well-type γ-counter. Subsequently, percentage

uptake of radioactivity in one gram of the bone, blood, stomach, intestine, thyroid, liver, kidney of mice was calculated as the percentage of the injected dose per gram tissue (%ID/g tissue).

Imaging

The solutions containing approximate radioactivity of 1.85 MBq of radio-complexes were given as intravenous injection in the tail vein of mice. The bone radio-complexes uptake was assessed by planar scintigraphy using the single head gamma camera (small area mobile, Siemens, 140 keV high sensitivity parallel whole collimator and 15% window around 140 keV). Before the imaging mice were anesthetized with ketamine and xylazine intra-peritoneally. Scanning were performed for 5 min at 256×256 matrix size.

Results and discussion

Radiolabeling

Technetium-99m bisphosphonates were prepared via the decrease in oxidation state of $[^{99m}Tc]TcO_4^-$ by hydrous solvent of tin chloride (figure. 1). The amounts of reagents are important in labeling process to obtain the best labeling yields. In order to achieve maximum in vivo specific target uptake for labeled ligand against non-labeled ligand, high specific activity labeling of ligand is necessary. However, the sufficient amount of ligand in formulation must be presented yet to reach a high labeling yield complex formation.

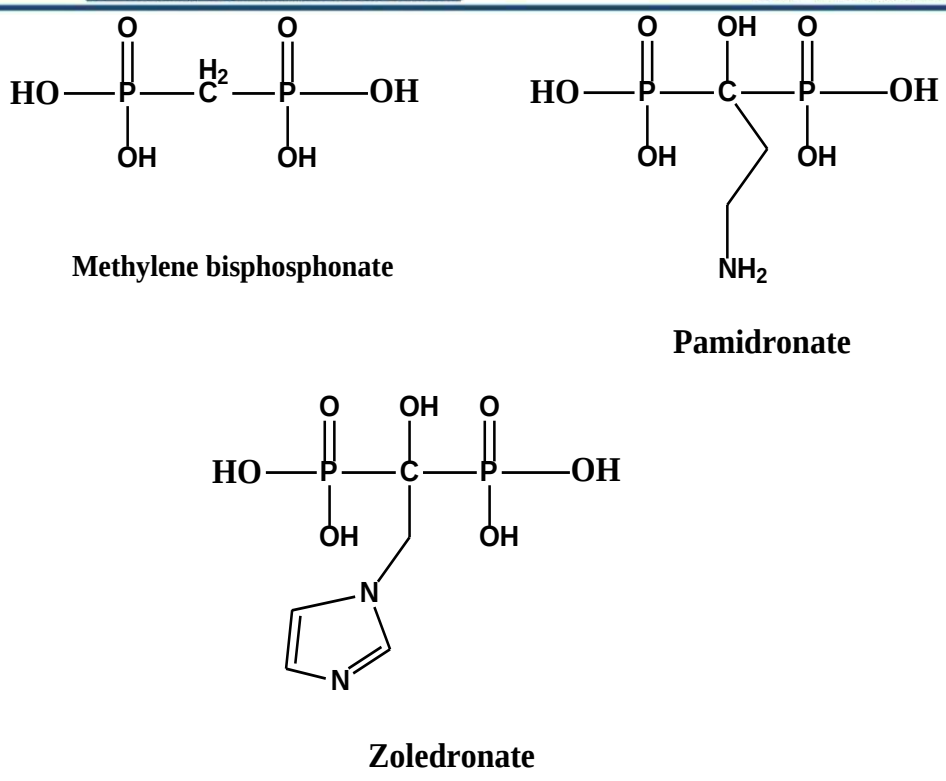

Fig. 1. Chemical structure of a first, second and third generation bisphosphonates.

Stannous chloride was used to reduce rehenium-188 to the lower oxidation stage which could be able to react with ligand. Rhenium is not as easily reduced as technetium, and once reduced, it tends to quickly revert to a higher oxidation state [16]. SnO_2 might be formed with excess tin and the labeling efficiency decreases. Ascorbic acid was used as an antioxidant and stabilizer of stannous ion. The low labeling yield at high pH could be attributed to colloid formation of SnO_2 at near neutral and elevated pH above 6 which in turn causes high liver and spleen uptake and trapping of particles in lung capillaries in biodistribution studies.

Paper chromatography measurement of labeled bisphosphonates showed that in the system acetone the Rf values were 0.9-1.0 for $[^{99m}Tc]TcO_4^-$ and $[^{188}Re]ReO_4^-$ while labeled bisphosphonates, $[^{99m}Tc]TcO_2$ and $[^{188}Re]ReO_2$ remained in the bottom. In the system water, $[^{99m}Tc]TcO_4^-$, $[^{188}Re]ReO_4^-$ and labeled bisphosphonates were in Rf 0.8-1.0 while $[^{99m}Tc]TcO_2$ $[^{188}Re]ReO_2$ remained in the bottom. Labeling efficiency of labeled bisphosphonates was >90% in paper chromatography (figure. 2). It is extremely important for radioconjugates that isotope chelation remain stable as time passes. The results for paper chromatography analyses showed that the radiolabeled bisphosphonates retaining a radiochemical purity >90% for 6 h in saline and serum.

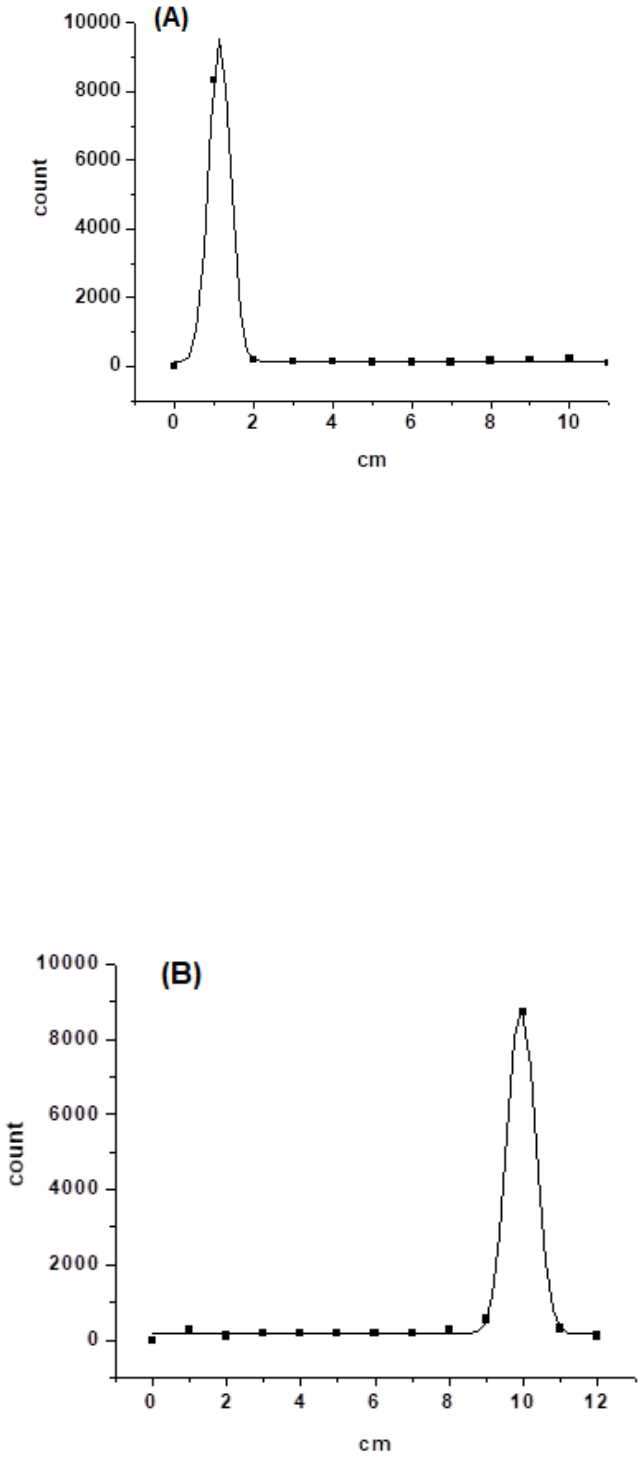

Fig. 2. Quality control of radiolabeled bisphosphonates by paper chromatography in acetone (A) and water (B) as a solvent.

Animal study

Biological evaluations of radiolabeled bisphosphonates were performed in mice. The results are shown in table 1 and figure 3. As results showed all radio-complexes mainly accumulated in the bone, kidneys and liver. In bone at 2 h post injection high level of uptakes including 3.86 ± 0.12 %ID/g, 4.19 ± 0.15 %ID/g and 0.74 ± 0.20 %ID/g were observed for [^{99m}Tc]Tc-methylene bisphosphonate, [^{99m}Tc]Tc-zoledronate and [^{188}Re]Re-pamidronate respectively. No significant concentration of radio-complexes in any other organs were obtained.

Table 1. Biodistribution of radioactivity after intravenous administration of labeled bisphosphonates in normal mice at 2 h post injection. (%ID/g ± SD, n=3)

Organs	Labeled bisphosphonates		
	[^{99m}Tc]Tc-methylene bisphosphonate	[^{99m}Tc]Tc-zoledronate	[^{188}Re]Re-pamidronate
Blood	0.66 ± 0.13	0.60 ± 0.10	0.23 ± 0.05
Kidneys	1.72 ± 0.08	2.65 ± 0.12	1.54 ± 0.22
Stomach	0.29 ± 0.05	0.17 ± 0.08	0.85 ± 0.06
Intestine	0.43 ± 0.02	0.46 ± 0.05	0.60 ± 0.15
Thyroid	0.26 ± 0.13	0.20 ± 0.14	0.15 ± 0.05
Liver	1.19 ± 0.27	0.36 ± 0.10	5.80 ± 1.12
Bone	3.86 ± 0.12	4.19 ± 0.15	0.74 ± 0.20

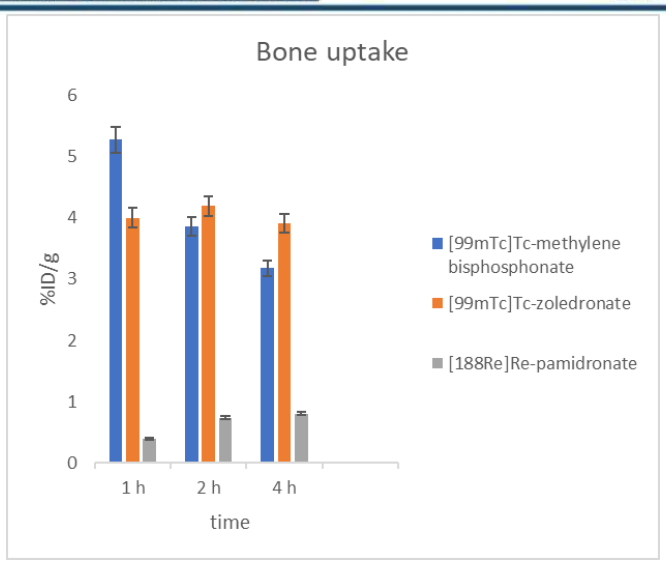
Bone uptake
%ID/g
6
5
4
3
2
1
0
1 h
2 h
4 h
time
[99mTc]Tc-methylene bisphosphonate
[99mTc]Tc-zoledronate
[188Re]Re-pamidronate

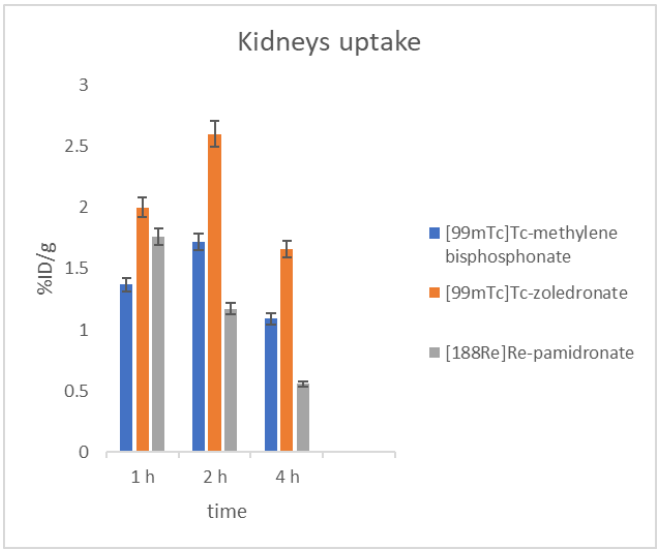
Kidneys uptake
%ID/g
3
2.5
2
1.5
1
0.5
0
1 h
2 h
4 h
time
[99mTc]Tc-methylene bisphosphonate
[99mTc]Tc-zoledronate
[188Re]Re-pamidronate

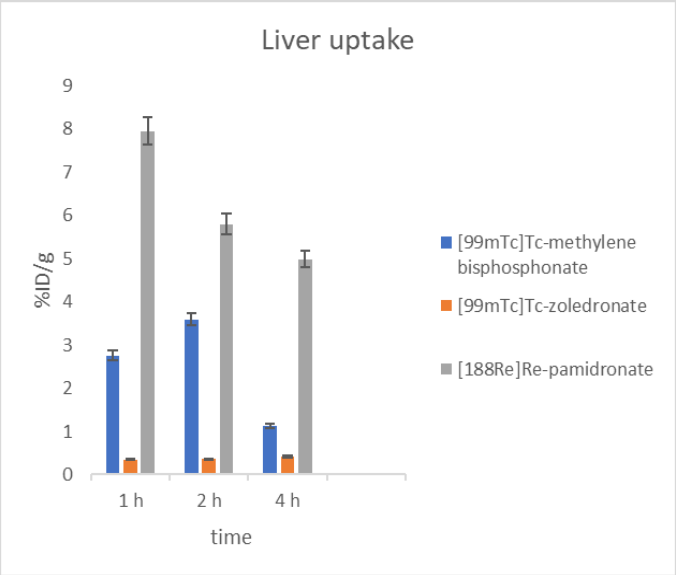

Fig. 3. Comparison of bone, kidneys and liver uptake for labeled bisphosphonates at different time after injection.

Based on the comparison results shown in figure 3, while [^{99m}Tc]Tc-methylene bisphosphonate showed rapid accumulation of activity in bone, [^{99m}Tc]Tc-zoledronate also showed significant bone uptake. Liver activity uptake of [^{99m}Tc]Tc-methylene bisphosphonate was higher and kidneys uptake value was lower than [^{99m}Tc]Tc-zoledronate. The results of biodistribution studies revealed bone uptake for [^{188}Re]Re-pamidronate and significant liver uptake.

According to the results, low blood activity uptake and fast blood clearance are the advantages of these radio-complexes. In addition, it should be noted that the significant kidneys uptake indicates the renal excretion of these radio-complexes and that the kidneys play a major role in their elimination. Remaining radioactivity in bone over time could be duo to binding with excellent retention and slow release. Significant liver uptake for [^{188}Re]Re-pamidronate may be explained by the aliphatic chain in the compound structure and pharmacokinetic properties of the prepared rhenium bisphosphonate chelate. As has been shown in figure 3, the main advantages of [^{188}Re]Re-pamidronate were the retention of activity in bone and decrease in liver uptake with the passing time after injection.

Through imaging it was observed that the radio-complexes mainly were accumulated in the skeleton and kidneys (figure. 4). Clear images of the mice skeleton were obtained which supported the results obtained by biodistribution studies. However, the quality of the [^{188}Re]Re-pamidronate image was significantly low, hypothesized to be due to the presence of scattered photons from high-energy gamma rays (i.e., 478, 633, 829, and 913 keV). Consequently, more activity and much contrast were necessary to obtain the same hot sphere detection capability compared to technetium-99m imaging.

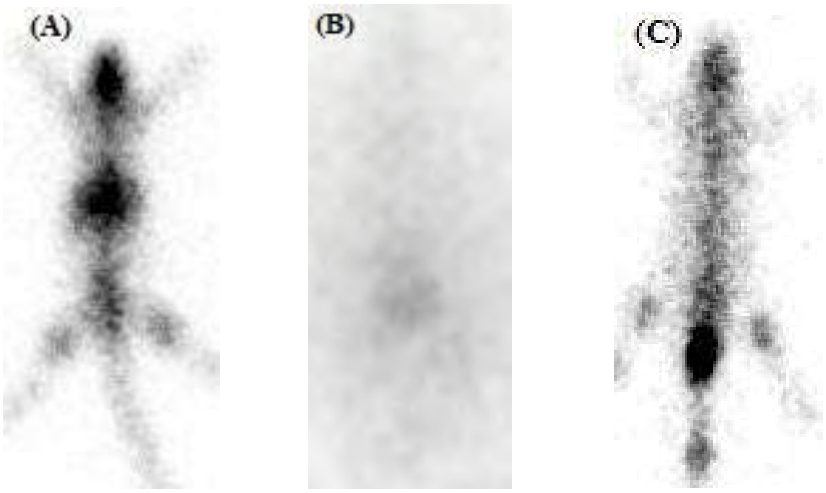

Fig. 4. Anterior image of radio-complexes ((A) [^{99m}Tc]Tc-methylene bisphosphonate, (B) [^{188}Re]Re-pamidronate and (C) [^{99m}Tc]Tc-zoledronate) in mice.

Conclusions

These finding suggest that addition of hydroxyl group at the central carbon is efficient to increase uptake in bones. Also, another side chain attached to the carbon also may taking part not only to the cellular but also to the physicochemical action of bisphosphonate. Furthermore, based on these results it is expressed that to evaluate the adsorption and retention of diphosphonate to hydroxyapatite the whole structure of molecule is necessary to be considered and it depends on both side chains structures.

Acknowledgements

We greatly appreciate the supports of this work by Nuclear Science and Technology Research Institute, Tehran, Iran.

References

[1] Russell, R.G. (2006). Bisphosphonates: from bench to bedside. Annals of the New York Academy of Sciences, 1068:367-401.

[2] Fleisch, H. Russell R.G. Straumann, F. (1966). Effect of pyrophosphate on hydroxyapatite and its implications in calcium homeostasis. Nature, 212(5065):901-903.

[3] Russell, R.G. Muhlbauer, R.C. Bisaz, S. Williams, D.A. Fleisch, H. (1970). The influence of pyrophosphate, condensed phosphates, phosphonates and other phosphate compounds on the dissolution of hydroxyapatite in vitro and on bone resorption induced by parathyroid hormone in tissue culture and in thyroparathyroidectomised rats. Calcified Tissue Research, 6(3):183-196.

[4] Plotkin, L.I. Weinstein, R.S. Parfitt, A.M. Roberson, P.K. Manolagas, S.C. Bellido, T. (1999). Prevention of osteocyte and osteoblast apoptosis by bisphosphonates and calcitonin. Journal of Clinical Investigation, 104(10):1363-1374.

[5] King, M.A. Weber, D.A. Casarett, G.W. Burgener, F.A. Corriveau, O.A. (1980). Study of irradiated bone. Part II: Changes in Tc-99m pyrophosphate bone imaging. Journal of Nuclear Medicine, 21:22-30.

[6] Valdez, V.A. Jacobstein, J.G. (1980). Decreased bone uptake of technetium-99m polyphosphate in thalassemia major. Journal of Nuclear Medicine, 21:47-49.

[7] Subramanian, G. McAfee, J.G. Blair, R.J. Mehter, A. Connor, T. (1972). ^{99m}Tc-EHDP: a potential radiopharmaceutical for skeletal imaging. Journal of Nuclear Medicine, 13(12):947-950.

[8] Castronovo, F.P. Callahan, R.J. (1972). New bone scanning agent: ^{99m}Tc-labeled 1-hydroxy-ethylidene-1, 1-disodium phosphonate. Journal of Nuclear Medicine, 13(11):823-827.

[9] Domstad, P.A. Coupal, J.J. Kim, E.E. Blake, J.S. Deland, F.H. (1980). ^{99m}Tc-hydroxymethane bisphosphonate: a new bone imaging agent with a low tin content. Radiology, 136:209-211.

[10] Mari, C. Catafau, A. Carrio, I. (1999). Bone scintigraphy and metabolic disorders. Quarterly Journal of Nuclear Medicine, 43(3):259-267.

[11] Love, C. Din, A.S. Tomas, M.B. Kalapparambath, T.P. Palestro, C.J. (2003). Radionuclide bone imaging: an illustrative review. Radiographics, 23(2):341-358.

[12] Elder, R.C. Yuan, J. Helmer, B. Pipes, D. Deutsch, K. Deutsch, E. (1997). Studies of the structure and composition of Rhenium-1,1-hydroxyethylidenediphosphonate (HEDP) analogues of the radiotherapeutic agent (186)ReHEDP. Inorganic Chemistry, 36:3055-3063.

[13] De Winter, F. Brans, B. Van De Wiele, C. Dierckx, R.A. (1999). Visualization of the stomach on rhenium-186 HEDP imaging after therapy for metastasized prostate carcinoma. Clinical Nuclear Medicine, 24:898-899.

[14] Erfani, M. Rahmani, N. Doroudi, A. Shafiei, M. (2017). Preparation and evaluation of rhenium-188-pamidronate as a palliative treatment in bone metastasis. Nuclear Medicine and Biology, 49:1-7.

[15] Golshaiyan, S. Erfani, M. Shamsaei, M. Shirmardi, S.P. Abodzadeh Rovais, M.R. Mikaeili, A. Goudarzi, M. (2023). An optimized formulation for [^{99m}Tc]Tc radiolabeling of zoledronic acid as bone imaging agent. Iranian Journal of Nuclear Medicine, 31(2):137-143.

[16] Deutsch, E. Libson, K. Vanderheyden, J.L. Ketring, A.R. Maxon, H.R. (1986). The chemistry of rhenium and technetium as related to the use of isotopes of these elements in therapeutic and diagnostic nuclear medicine. Nuclear Medicine and Biology, 4:465-477.

ICNST 2024
International Conference on Nuclear Science and Technology
6- 8 MAY 2024 | Isfahan, Iran

Production and Preclinical evaluation of the 67Ga-CHX-A-DTPA-trastuzumab for HER2+ breast cancer SPECT Imaging (Paper ID : 1493)

B. Alirezapour[1]*, M. Alizadeh[2], F. Badipa[1], F. Hooshmandan[1]

[1]*Radiation Application Research School, Nuclear Science and Technology Research Institute, Tehran, IRAN*

[2]Pars Isotope Company, Tehran, IRAN

Abstract

Radiolabeled monoclonal antibodies have shown great promise for cancer diagnosis and therapy. Breast cancer continues to pose a significant challenge in the field of healthcare, despite the remarkable strides made in cancer research. Approximately 15% to 20% of breast cancers exhibit an overexpression of a growth-promoting protein known as HER2. In the present study, we prepared Trastuzumab as an anti-HER2 antibody via identical chelator, CHX-A-DTPA (p-SCN-Bn-CHX-A-DTPA) labeled with ^{67}Ga [T1/2 = 78.3 hrs, EC, Eγ = 93 (40%), 184 (24%), 296 (22%) and 388 (7%) keV] and performed preliminary biodistribution studies in female Sprague Dowley rat. Trastuzumab was conjugated with CHX-A-DTPA (Macrocyclics B-355), the average number of the chelator conjugated per mAb was calculated and total concentration was determined by spectrophotometrically. CHX-A-DTPA–trastuzumab was labeled with ^{67}Ga (10 mCi, 375 MBq) then Radiochemical purity and immunoreactivity by SKBR3 cell line and serum stability of ^{67}Ga– CHX-A-DTPA–trastuzumab were determined. The biodistribution studies and radioimmunoscintigraphy were performed in female Sprague Dowley rat (^{67}Ga–CHX-A-DTPA–trastuzumab i.v., 200 microl, 200±20 mCi, 35±5 µg mAb , 4, 24, 48 and 72 h). ^{67}Ga– CHX-A-DTPA–trastuzumab was prepared (RCP>98% ± 0.5, Specific activity 4.1 ± 0.7 µCi/µg). Conjugation reaction of chelator (50 molar excess ratio) to antibody resulted in a product with the average number of chelators attached to a mAb (c/a) of 4.1 ± 1.2. Labeling yield with ^{67}Ga in 400µg concentration of bioconjugate was 92.5% ± 2.1. Immunoreaction of ^{67}Ga– CHX-A-DTPA– trastuzumab complex towards HER2 antigen was determined by RIA and the complex showed high immunoreactivity towards HER2. In vitro and in vivo stability of radioimmunoconjugate was investigated respectively in PBS and blood serum by RTLC method. In vitro stability showed more than 91% ± 2.6 in the PBS and 81% ± 1.8 in the serum over 24 h. The Immunoreactivity of the radiolabeled anti-HER2 towards SKBR3 cell line was done by using Lindmo assay protocol. Under these conditions, the immunoreactivity of the radioimmunoconjugate was found to be 0.84. The biodistribution of ^{67}Ga–CHX-A-DTPA-

trastuzumab complex in normal Sprague Dowley rat at 4, 24, 48 and 72 h after intravenous administration, expressed as percentage of injected dose per gram of tissue (%ID/g). Biodistribution studies at 24 and 48 h post-injection revealed the similar pattern to the other radiolabeled anti-HER2 immunoconjugates.

Keywords: HER2, Gallium-67, Trastuzumab, CHX-A-DTPA, Breast Cancer

INTRODUCTION

The HER2/neu antigen is a transmembrane receptor [1] overexpressed in 25–30% of breast cancers [2]. The overexpression has been implicated in the carcinogenesis of breast cancer and is an independent prognostic indicator of survival in patients [3]. Trastuzumab is a humanized IgG1 monoclonal antibody (mAb) recognizing an epitope in the extracellular domain of the receptor and is used for immunotherapy for HER2/neu-positive tumors [4]. Breast cancer radioimmunoscintigraphy targeting HER2/neu expression has been proposed by different research groups and could allow direct assessment of the receptor status of primary and metastatic lesions suggesting the effectiveness of Herceptin therapy. Herceptin and its fragments have been radiolabeled and used in the imaging of HER2/neu-positive tumors using In-111 [5], Y-90 [6], Y-86 [7], Br-76 [8], and Zr-89 [9]. ^{67}Ga [T1/2 = 78.3 hrs, EC, Eγ = Eγ = 93 (40%), 184 (24%), 296 (22%) and 388 (7%) keV, allows for SPECT imaging and follow up of the radionuclide therapy [10]. Due to the superior bioconjugation of DTPA bi-functional ligands p-SCN-Bn-CHX-A-DTPA was used as a bi-functional ligand [11]. This ligand has already shown good biological performance when used in protein conjugation of various radioisotopes such as Ac-225 [12], Lu-177 [13] and lead radioisotopes [14]. In order to develop Herceptin radioimmunoconjugates for using in imaging studies, CHX-A-DTPA -trastuzumab (Herceptin) was labeled by Ga-67 chloride for preliminary biodistribution studies in rats.

EXPERIMENTAL

Enriched zinc-68 chloride with a purity of more than 95% was obtained from Ion Beam Separation Group at Agricultural, Medical and Industrial Research School. 67Ga was produced in Radiation Application Research School, Karaj, Iran, by 68Zn(p,2n)67Ga reaction. p-SCN-Bn-CHX-A-DTPA (B-355) was purchased from Macrocyclics (NJ, USA). Trastuzumab (Herceptin) was a pharmaceutical sample purchased from Roche Co. Fetal Bovine Albumin (FBS), RPMI-1640

medium, and L-Glutamine were bought from Gibco Co. (Dublin, Ireland). PD10 De-salting column was inquired from Amersham Pharmacia Biotech; additional chemicals were purchased from Sigma Chemical Co. (MO, USA). Sprague-Dawley rats were obtained from Pasteur Institute (Tehran, Iran). A Bioscan AR-2000 radio TLC scanner instrument (Bioscan, Paris, France) was used for Radio-chromatography purposes. A p-type coaxial high-purity germanium (HPGe) detector (model: EGPC 80-200R) coupled with a multichannel analyzer card system and a dose calibrator ISOMED 1010 (Dresden, Germany) were utilized for the measurement of the activity. Calculations were carried out based on the 184 keV peak for 67Ga. The United Kingdom Biological Council's Guidelines on the Use of the Living Animals in Scientific Investigations, 2nd edition was used to determine the framework of animal experiments. Achieved results are displayed as mean ± standard deviation (Mean ± SD), and Student's T-test was used to compare the data based on statistical significance defined as $P < 0.05$.

Conjugation of p-SCN-Bn-CHX-A"-DTPA with the trastuzumab

The final concentration of trastuzumab mAb was measured by means of a biophotometric assay at 280 nm. About 4.0 mg of the antibody in a 1000 µl bicarbonate buffer was then added to 3 borosilicate vials containing 0.3 (1:25), 0.5(1:50), and 1.0 mg (1:80) of p-SCN-Bn-CHX-A"-DTPA and 400 µl bicarbonate buffer following gentle pipetting for 20–30 times. Afterward, each vial was shacked for 12 h at room temperature. Then, the mixture was transferred on a Vivaspin-2 cutoff filter (30 kDa) and centrifuged at 4000 rpm for 15 min. To terminate the conjugation step and providing appropriate conditions for radiolabeling, the upper fraction of the filter was washed by 2 mL of 2.0 M ammonium acetate buffer (pH = 5.5) In the last step, ammonium acetate buffer (1 ml) was added to the upper fraction to dissolve the conjugated antibody, followed by gentle pipetting for 10–20 times for the purpose of immunoconjugate dissolution. Then, the filter was centrifuged at 2.684 × g for 5 min upside-down to detach the conjugated antibody from the filter. The concentration of conjugated antibody was finally measured utilizing a biophotometer (Eppendorf) at OD = 280 nm.

Determination of the average chelator: MAb ratio

The number of p-SCN-Bn-CHX-A"-DTPA conjugated to each mAb was determined utilizing the Pippin method and in accordance with the previous researches [15]. 1.6 µM yttrium (III), 0.15 M sodium acetate buffer (pH 4.0), and 5.0 µM Arsenazo (III) were used to prepare Arsenazo yttrium (III) complex (2:1, 1 ml). The optical density of the prepared complex was measured by means of a biophotometer at 652 nm. A standard solution of 3 mM p-SCN-Bn-CHX-A"-DTPA in 0.15 M

sodium acetate buffer solution (pH 4.00) was supplied. Then, 15 µl of the standard solution was added to the Arsenazo yttrium (III) complex and the optical density was measured and documented. This procedure (adding the standard solution and measuring the optical density) was repeated four times. In the next step, the optical density of the 1:2 yttrium (III) complex of Arsenazo (1 mL) was measured at 652 nm in the presence of conjugation product to investigate the p-SCN-Bn-CHX-A"-DTPA-antibody attachment.

Radiolabeling of the p-SCN-Bn-CHX-A"-DTPA-trastuzumab conjugate with ^{67}Ga

Certain amounts of the p-SCN-Bn-CHX-A"-DTPA-trastuzumab conjugate (200, 400, and 600 µg) were added to the vials comprising 74 MBq of ^{67}Ga adjusted to the pH of 5.5 using acetate buffer. The mixture was incubated at 25°C for 1 h. Then, the radiochemical purity of the complex was investigated by instant thin-layer chromatography (ITLC) using Whatman No. 2 and 1 mM DTPA as the stationary and mobile phase, respectively. Whenever the optimum concentration was specified, experiments were performed to determine the suitable time for labeling. Ultimately ethylene di-amine tetra acetic acid solution (10 µl, 10 mM) was added to the labeling mixture and incubated for 10 min in order to scavenge the unlabeled ^{111}In cation. The mixture was then passed through a disposable PD10 desalting column to remove the impurities with small molecular weight and elevate the radiochemical purity. Finally, the mAb-containing solution was stored at 4°C to be used in further in-vitro and in-vivo studies.

Stability studies of the radiolabeled compound in PBS buffer and human serum

About 150 µL of the radioimmunoconjugate (with approximately 250 µCi (9.5 MBq activity) was added to the 500 µL of the PBS buffer and freshly prepared human serum while keeping at 4°C and 37°C, respectively. Samples were taken from the complex at 0,12, 24 and 48 h after preparation, and the radiochemical purity was assessed by means of the ITLC method using Whatman No. 2 and 1 mM DTPA solution.

Reactivity of the radiolabeled compound toward HER2 antigen using radioimmunoassay method

Three rows of eight wells of ELISA were selected. In the eight wells of the first row, 100 µl of BSA with the concentration of 0.6 µg/100 µl and in another eight wells, 100 µl of HER2 at 0.3 µg/100 µl were poured and then were incubated overnight at 37°C. The wells were washed three times with 10 mM phosphate buffer (containing tween 20) and after complete removal of water, all wells were

filled with bubble solution and incubated for 45 min at 37°C. ^{67}Ga-CHX-A"-DTPA-trastuzumab was then added with the concentration of 10 µg in 100 µl and incubated for 2 h and the wells were washed six times by washing buffer, after full water drainage, each of the wells was removed from the plate by breaking, and their activation was counted in the gamma counter. Each measurement was performed 3 times.

Immunoreactivity of radiolabeled mAb trastuzumab toward SKBR3 and CHO cell lines

Distinct numbers (5×10^6, 2.5×10^6, 1.25×10^6, 0.62×10^6, 0.31×10^6, and 0.15×10^6) of CHO and SKBR3 cells were put into the tubes and mixed with 30,000 cpm of the radiolabeled mAb trastuzumab. The tubes were incubated at 4°C for 3 h and the radioactivity of each tube was measured by means of a γ-counter. In the centrifuge of the tubes in 3000 ×*g*, the supernatant was disposed and respective radioactivities of the cell debris were determined. The immunoreactivity was ascertained utilizing a Lineweaver–Burk plot. Lindmo method was applied to analyze the data.

Biodistribution studies of ^{67}Ga-CHX-A"-DTPA-trastuzumab in normal Sprague Dowley rat

For biodistribution studies, ^{67}Ga-CHX-A"-DTPA-trastuzumab was administered to normal Sprague Dawley rats separately. A volume (150-200 µl) of final radioactive solution containing 200 ± 10 µCi radioactivity and 35 ± 5 µg of trastuzumab was injected intravenously to rats through their tail vein. The total amount of radioactivity injected into each rat was measured by counting the 1 ml syringe before and after injection in a dose calibrator with a fixed geometry. Biodistribution studies were performed using groups of 3 rats sacrificed at 4, 24, 48 and 72 hours after injection of each radiolabeled mAb trastuzumab. At each time point, rats were sacrificed using CO2 gas and normal organs (lungs, stomach, small and large intestine, spleen, blood, heart, kidneys, bone, feces, skin and liver) were excised. Organs were weighed and gamma counted with an HPGe detector counting the area under the curve of the 184 keV peak. The percentage of injected dose of radioisotope per gram (% ID/g) organ was calculated (after correcting for radioactive decay using an aliquot of the injected at each time point). Mean values and standard errors for each tissue and time point were plotted.

Statistical analysis

The experiments were performed three times for each test and final values were presented as the mean ± SD. Statistical analyses were performed using IBM Corp. Released 2010. IBM SPSS Statistics for Windows, Version 19.0. Armonk, NY: IBM Corp, U.S.A. 10.0 considering $P < 0.05$ as statistically significant. The paired *t*-test was used to compare the results of the two experiments.

Results and discussion

Conjugation of trastuzumab with p-SCN-Bn-CHX-A"-DTPA and radiolabeling of trastuzumab with ^{64}Cu

In order to overcome the effect of excipients and producing appropriate acidity for conjugation step the pharmaceutical sample was purified by ultra-filtration using cut-off filters followed by determination of the antibody concentration using spectrophotometry. In order to improve the conjugation step alkaline pH is necessary, thus bicarbonate buffer was used to reconstitute the antibody. The use of polymer tubes and other synthetic materials in the conjugation and labeling step interfered with the conjugation reaction, while borosilicate vials were the appropriate vessels. In order to remove the leftover of Bi-Functional Chelator in the reaction and concentrate the antibody, the cut-off filter was used once more (30kDa). At this stage, a pH 5.0 buffer was used to recover the antibody in order to terminate the conjugation step and provide the suitable radiolabeling pH, and for final fraction the quantity of the antibody was measured at OD = 280 nm. In order to estimate the number of CHX-A-DTPA prosthetic group on each antibody molecule, the arsenazo yttrium complex [$Y(AAIII)_2$] method was used. The absorbance of $Y(AAIII)_2$ at 652 nm decreases upon the addition of CHX-A-DTPA-trastuzumab while the corresponding absorbance of AAIII at 538 nm increases (Fig 1). The $Y(AAIII)_2$ and arsenazo III are the only absorbing species in solution; neither CHX-A-DTPA-trastuzumab nor its Y(III) complex have any absorbance in this wavelength region. The isosbestic point observed at 585 nm is consistent with only two absorbing species for reaction. The data demonstrated the CHX-A-DTPA:antibody ratio of 4.1±1.2:1(Table 1).

Kukis et al. observed that coupling of too many ligands to antibody leads to impairment of immunoreactivity. As described for the Lym-1 antibody [16]. Zimmermann et al. also found that unfavorable biodistribution were a more sensitive marker for over-substitution of the mAb than *in vitro* immunoreactivity. Whereas substituting 18 ligands per antibody molecule lead to an about 25% lower *in vitro* immunoreactivity, *in vivo* tumor uptake was decreased by 80%. At the same time accumulation of radioactivity in the liver was increased about 40%. A c/a ratio up to 11 seemed to be the limit for substituting mAbs without damage to immunoreactivity and effects on biodistribution [17]. Thus, in this study we optimized conjugation procedure to obtain a chelate-to-mAb molar ratio less than 11 (4.1±1.2:1 for instance), in order to minimize any immunoreactivity loss and unwanted liver uptake.

Radiochemical purity determination

By direct radiolabeling of the Conjugate in a simple and rapid manner, the radioimmunoconjugate was easily prepared in radiochemical purity of higher than 98%. The DTPA-trastuzumab conjugate was labeled with ^{67}Ga at Specific activity 4.1 ± 0.7 μCi/μg, and the radiolabeled mAb exhibited high *in vitro* serum stability and minimal loss of immunoreactivity. The effect of time on RCP was also studied and 30 min was considered as the best time. ITLC chromatogram of the radiolabeled compound and free ^{67}Ga are indicated in Figure 2. As a result of the experiments, the best conditions for radiolabeling were as follows: 400 μg of the bioconjugate was added to a vial containing 74 MBq of ^{67}Ga radionuclide and pH of the reaction mixture was arranged to 5.5 as keeping at 25°C for 30 min.

Stability of Radiolabeled Protein in presence of human serum and PBS

Table 2, presents the *in vitro* stability of radiolabeled mAb by using size exclusion chromatography using G-25 Sephadex at 37ºC after 0, 12, 24 and 48 h of incubation (in buffer and human serum). The results showed that After incubation of ^{67}Ga-CHX-A"-DTPA-trastuzumab (300 μCi) with freshly prepared human serum at 37°C for up to 48 h, more than 78% of total radioactivity eluted in the same position as ^{67}Ga-CHX-A"-DTPA-trastuzumab. Cole et al. reported that deacreases of stability in human serum resulted from mild transchelation of ^{67}Ga to serum components such as albumin [18], while Cooper et al. reported the high stability of macrocyclic immunoconjugates such as DOTA-mAb, DO3A-mAb and NOTA-mAb in serum over 48 h [19] which is in agreement with our data.

Reactivity of radiolabeled trastuzumab towards HER2/neu antigen by RIA

Reactivity of radiolabeled mAb trastuzumab towards the HER2/neu antigen (0.2 μg/well) and BSA (0.2 μg/well) was shown in Figure 3. The ^{67}Ga-CHX-A"-DTPA-trastuzumab showed high immunoreactivity towards HER2/neu antigen. This result also showed that the chemical binding of ^{67}Ga to mAb had no adverse effects on the immunoreactivity of antibody towards HER2/neu antigen.

Immunoreactivity of radiolabeled trastuzumab towards SkBr3 cell line

Zimmermann et al. reported that moderate increase of chelator to mAb ratio leads to slight decrease in immunoreactivity. Lewis et al also reported this slight decrease in immunoreactivity is likely due to non-specific conjugation of chelators to mAb, which possibly attaches a chelator in the region of the antigen binding site [20]. The Immunoreactivity of the radiolabeled trastuzumab (^{67}Ga-CHX-A"-DTPA-trastuzumab) towards SkBr3 cell line was determined under conditions of antigen excess in HER2/neu antigen-expressing SkBr3 human breast carcinoma cells by using a Lineweaver-Burk plot. Under these conditions, the immunoreactivity of radioimmunoconjugate was found to be 0.84 which is suitable for further imaging studies in animal models and possibly human trials. It seems that exact optimization of c/a ratio has led to such suitable immunoreactivity. Thus, conjugation and complexation procedures did not affect the affinity of mAb toward its antigen in this work (figure 4).

^{67}Ga-CHX-A"-DTPA-trastuzumab biodistribution in normal Sprague-Dawley rat tissues

Kokai et al. showed that during late gestation (Embryonic day 18) and during the early postnatal period (PND-1 and PND-5), two types of tissue expressed HER2/neu antigen (p185) in normal rat. Strong immunoreactivity was detected on epithelial cells of the intestinal villi, the skin, pulmonary bronchioles, and proximal renal tubules. Also, faint staining of connective tissue was observed. Staining in the nervous system could no longer be detected. In adult animals, immunoreactive p185 was limited to epithelial tissues, including the basal layer of skin, the mucosal epithelium of intestine, bronchiolar epithelium of lung, and proximal tubular epithelium of kidney. Connective tissue no longer expressed p185 [21]. As shown in Figure 5, biodistribution studies in adult normal Sprague-Dawely rats after injection of ^{67}Ga-CHX-A"-DTPA-trastuzumab demonstrated that uptake in intestine, skin and lung organs significantly increased during the study time also high uptake in kidney organ during the time study were observed which is due to the presence of HER2/neu antigens in mentioned tissues also leading to high colon and feces activity content, which is in agreement with the findings of Kokai and co-workers. This has been already shown by other groups, working with ^{125}I-anti-HER2 probes [22]. A significant kidney uptake of radiolabeled mAb trastuzumab is observed all time intervals, in Figure 5 possibly due to the presence of HER2/neu antigen. As shown in figure 5, accumulation of radiolabeled mAb trastuzumab in spleen and liver increases by the time

up to 24 h. This behaviour has been already shown to be consistent with half life of intact mAb in circulation like other radiolabeled mAb anti HER2 probes.

Table 1 Average numbers of chelators bound to each antibody (c/a) in different molar of chelator added to conjugation reaction (*n*=3)

Bifunctional chelator	Conjugate	Molar excess of chelator added to conjugation reaction	Average number of Chelators/mAb
p-SCN-Bn-CHX-A"-DTPA	CHX-A"-DTPA-trastuzumab	25	2.2 ± 0.4
		50	4.1 ± 1.2
		80	7.2 ± 0.9

Table 2. Stability of ^{67}Ga-CHX-A"-DTPA-trastuzumab in PBS at 4°C and human blood serum at 37°C at different times postlabeling (*n*=3)

	Radio-Chemical Purity (RCP)(%)	
Time post labeling (h)	PBS (4 °C)	Human Serum (37 °C)
0	98.0 ± 0.5	98.0 ± 0.5
12	95.5 ± 0.7	91.0 ± 1.1
24	91.1 ± 2.6	81.8 ± 1.8
48	90.5 ± 1.1	78.3 ± 0.9

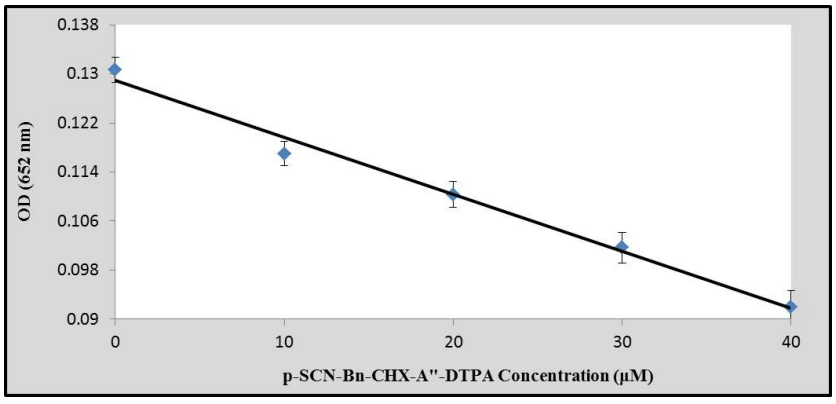

Fig. 1. The standard curve of the absorption of Arsenazo yttrium (III) complex against the concentration of p-SCN-Bn-CHX-A"-DTPA (*n* = 3)

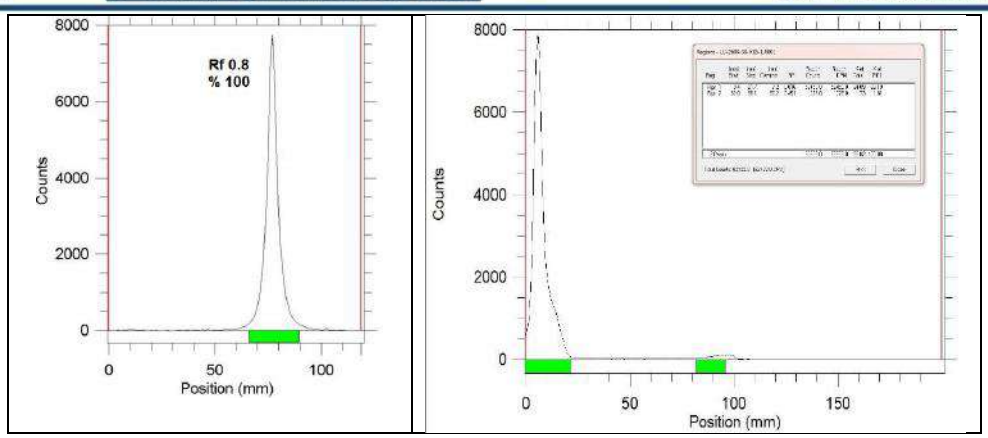

Fig. 2. Radiochromatogram of free ^{67}Ga (left) and ^{67}Ga-CHX-A"-DTPA-trastuzumab (right) using Whatman No. 2 in 1 mM DTPA, pH 5.0 (n=3).

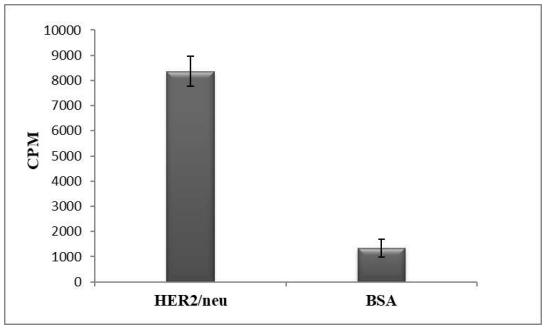

Fig. 3. Reactivity of ^{67}Ga-CHX-A"-DTPA-trastuzumab (10 µg/well) toward HER2 antigen (0.3 µg/well) and BSA (0.6 µg/well) using radioimmunoassay method (n = 3)

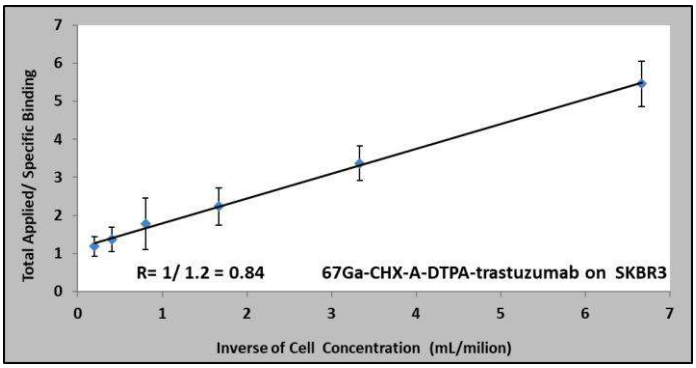

Fig. 4. Immunoreactivity of ^{67}Ga-CHX-A"-DTPA-trastuzumab (total applied/specific binding) toward SKBR3 cell line at different cell concentration (n = 3)

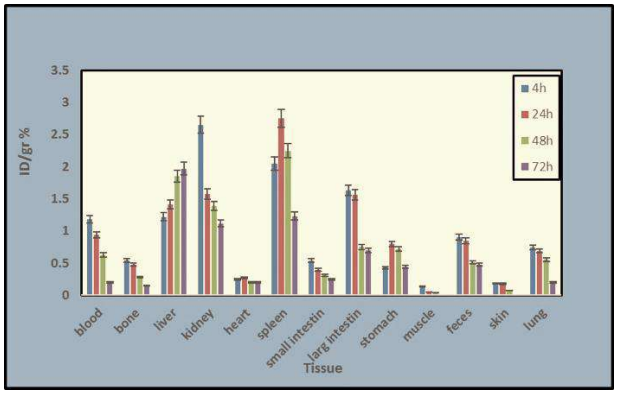

Fig. 5. Percentage of injected dose per gram (% ID/g) of ^{67}Ga-CHX-A"-DTPA-trastuzumab in normal Sprague-Dawely rat at 4, 24, 48 and 72 h postinjection(n = 3).

Conclusions

Radiolabeling, stability testing, radiochemical purity, reactivity, immunoreactivity and biodistribution study of ^{67}Ga-CHX-A"-DTPA-trastuzumab were determined followed by biodistribution studies in normal Sprague-Dawley rat tissues (200 ± 20 µCi, 4, 24, 48 and 72 h p.i.). The radioimmunoconjugate was prepared with a radiochemical purity of higher than 98 ± 0.5% (ITLC). The average number of chelators per antibody (c/a) for the conjugate used in this study was 4.1±1.2:1. The ^{67}Ga-CHX-A"-DTPA-trastuzumab showed high immunoreactivity towards HER2/neu antigen and SkBr3 cell line. *In vitro* stability of the labeled product was found to be more than 91% in PBS and 81.8 ± 1.8% in human serum over 48 hr. The accumulation of the radiolabeled mAb in liver, skin, intestine, lung, spleen, kidney and other tissues demonstrates a similar pattern to the other radiolabeled anti-HER2 immunoconjugates.

These data validate this radiopharmacutical for further clinical testing. Therefore ^{67}Ga-CHX-A"-DTPA-trastuzumab is a potential compound for molecular imaging of SPECT for diagnosis and follow-up of HER2 expression in oncology.

References

[1] Schechter AL, Stern DF, Vaidyanathan L, Decker SJ, Drebin JA, Greene MI, et al. The neu oncogene: an erb-B-related gene encoding a 185,000-Mr tumour antigen. Nature. 1984;312:513–6.

[2] Pauletti G, Dandekar S, Rong H. et al. Assessment of methods for tissue-based detection of the HER-2/neu alteration in human breast cancer: a direct comparison of fluorescence in situ hybridization and immunohistochemistry. J Clin Oncol. 2000;18:3651– 64.

[3] Slamon DJ, Godolphin W, Jones LA, et al. Studies of the HER-2/neu proto-oncogene in human breast and ovarian cancer. Science. 1989;244:707–12.

[4] Leonard DS, Hill ADK, Kelly L, Dijkstra B, McDermott E, Higgins NJO. Anti-human epidermal growth factor receptor 2 monoclonal antibody therapy for breast cancer. Br J Surg. 2002;89:262–71.

[5] Tang Y, Wang J, Scollard DA, Mondal H, Holloway C, Kahn HJ, Reilly RM, Imaging of HER2/neu-positive BT-474 human breast cancer xenografts in athymic mice using (111)In-trastuzumab (Herceptin) Fab fragments. Nucl Med Biol. 2005;32:51–58.

[6] Blend MJ, Stastny JJ, Swanson SM, Brechbiel MW, Labeling anti-HER2/neu monoclonal antibodies with 111In and 90Y using a bifunctional DTPA chelating agent. Cancer Biother Radiopharm. 2004;18:355– 63.

[7] Garmestani K, Milenic DE, Plascjak PS, Brechbiel MW, A new and convenient method for purification of 86Y using a Sr(II) selective resin and comparison of biodistribution of 86Y and 111In labeled Herceptin. Nucl Med Biol. 2002;29:599–606.

[8] Winberg KJ, Persson M, Malmstrfm PU, Sjfberg S, Tolmachev V, Radiobromination of anti-HER2/neu/ErbB-2 monoclonal antibody using the p-isothiocyanatobenzene derivative of the [76Br]undecahydro-bromo-7,8-dicarba-nido-undecaborate(1-) ion. Nucl Med Biol. 2004;31:425–33.

[9] Dijkers EC, Kosterink JG, Rademaker AP, Perk LR, van Dongen GA, Bart J, de Jong JR, de Vries EG, Lub-de Hooge MN.Development and characterization of clinical-grade 89Zr-trastuzumab for HER2/neu immunoPET imaging. J Nucl Med. 2009;50(6):974-81

[10] Firestone RB, Shirley VS, Baglin CM, Zipkin J, In: Table of isotopes. 8th edition, John Wiley and Sons, New York, 1996 :1447.

[11] Chappell LL, Ma D, Milenic DE, Garmestani K, Venditto V, Beitzel MP, Brechbiel MW. Synthesis and evaluation of novel bifunctional chelating agents based on 1,4,7,10-tetraazacyclododecane-N,N',N'',N'''-tetraacetic acid for radiolabeling proteins. Nucl Med Biol. 2003 ;30:581–595.

[12] McDevitt MR, Ma D, Simon J, Frank K, Scheinberg DA, Design and synthesis of 225Ac radioimmunopharmaceuticals. Applied Radiat Isotopes. 2002;57:841–847.

[13] Smith CJ, Galib H, Sieckmanc GL, Hayes DL, Owen NK, Mazuru DG, Volkert WA, Hoffman TJ, Radiochemical investigations of 177Lu-DOTA-8-Aoc-BBN[7-14]NH2: an in vitro/in vivo assessment of the targeting ability of this new radiopharmaceutical for PC-3 human prostate cancer cells. Nucl Med Biol. 2003;30:101–109.

[14] Chappell LL, Dadachova E, Milenic DE, Garmestani K, Wu C, Brechbiel MW. Synthesis, characterization, and evaluation of a novel bifunctional chelating agent for the lead isotopes 203Pb and 212Pb. Nucl Med Biol. 2000;27:93–100.

[15] Pippin CG, Parker TA, McMurry TJ, Brechbiel MW. Spectrophotometric Method for the Determination of a Bifunctional DTPA Ligand in DTPA-Monoclonal Antibody Conjugates. Bioconjugate Chem. 1992;3:342-345.

[16] Kukis DL, DeNardo GL, DeNardo SJ, Mirick GR, Miers LA, Greiner DP, et al. Effect of the extent of chelate substitution to the immunoreactivity and biodistribution of 2IT-BAT-Lym-1 immunoconjugates. Cancer Res. 1995;55:878–884.

[17] Zimmermann K, Grunberg J, Honer M, Ametamey S, Schubiger PA, Novak-Hofer I. Targeting of renal carcinoma with 67/64Cu-labeled anti-L1-CAM antibody chCE7: selection of copper ligands and PET imaging. Nucl Med Biol. 2003;30:417–427

[18] Cooper MS, Ma MT, Sunassee K, Shaw KP, Williams JD, Paul RL, et al. Comparison of 64Cu-Complexing Bifunctional Chelators for Radioimmunoconjugation: Labeling Efficiency, Specific Activity, and in Vitro/in Vivo Stability. Bioconjug chem. 2012;23(5):1029−1039

[19] Tolmachev V, Velikyan I, Sandström M and Orlov A. A HER2-binding Affibody molecule labelled with ^{68}Ga for PET imaging: direct in-vivo comparison with the 111In-labelled analogue. Eur. J. Nucl. Med. Mol. Imaging (2010)37:1356-1367.

[20] Spiridon CI, Sarah Guinn S and Vitetta ES. A Comparison of the in-vitro and in-vivo Activities of IgG and F(ab′)2 Fragments of a Mixture of Three Monoclonal Anti-Her-2 Antibodies. Clin. Cancer Res. (2004) 10: 3542-3548

[21] Costantini DL, Chan C, Cai1 Z, Vallis KA, Reilly RM. 111In-Labeled Trastuzumab (Herceptin) Modified with Nuclear Localization Sequences (NLS): An Auger Electron-Emitting Radiotherapeutic Agent for HER2/neu-Amplified Breast Cancer. J NUCL MED. 2007;48(8): 1358−1368.

[22] Kokai Y, Cohen JA, Drebin JA, Greene MI. Stage- and tissue-specific expression of the neu oncogene in rat development. Develop Biol. 1987;84:8498–8501.

ICNST 2024
International Conference on Nuclear Science and Technology
6- 8 MAY 2024 | Isfahan, Iran

Shielding design considering commercial parts for the LEO mission satellite using the SPENVIS software... (Paper ID : 1495)

Zahra Bokaei[1], Hamideh Daneshvar[2], Seyed Amir Hossein Feghhi [3], Ali Asghar Shokri[1]

[1]Payame Noor University, Tehran, Iran

[2]Radiation Application Research School, NSTRI, Tehran, Iran

[3]Department of Radiation Application, Shahid Beheshti University, Tehran, Iran

Abstract

Radiation damage has destructive effects on the electronic components of satellites. Due to economic reasons and the existence of various restrictions, the use of commercial components has become common in short-term and low-altitude missions. The most effective method of protection against radiation is the use of shields. The purpose of this work is to check the optimal shielding in a 3-year mission in LEO orbit by considering the radiation resistance of commercial parts using SPENVIS software, SHIELDOSE code, and MULASSIS software. The result of SHIELDOSE, MULASSIS calculations is that the amount of thickness of different materials for the radiation tolerance of commercial parts does not differ much in condensation thickness. Also, there is no need for complex protection and you can use the usual protections. A comparison of the calculations obtained from MULASSIS and SHILEDOSE to achieve the dose into the silicon target indicates that the values are very similar and if there is a limitation in each of the capabilities of MULASSIS and SHILEDOSE, another can be used as an alternative software.

Keywords: space radiation, radiation damage, commercial components, shielding

INTRODUCTION

The space radiation environment consists of trapped protons and electrons, solar protons, galactic cosmic radiation, and neutrons, which can cause the malfunction of electronic satellites [1][2]. The environmental effects of space radiation are classified into three general categories, total ionizing dose effects (TID), single-event effects (SEE), and displacement damage effects (DD) [3]. Radiation

has devastating effects on electronic components in satellites, so the selection of components has particular importance. In general, there are three types of component categories for space systems. Rad Hard, Rad Tolerant, and COTS. Rad-Hard Designed for the long haul, these devices are built to resist intense radiation levels over extended periods. These devices are heavyweights, designed to handle exceptionally high levels of radiation. Their structure and materials are chosen and optimized to endure the harshest radiation environments. No stone is left unturned when qualifying rad-hard devices. Every wafer lot undergoes rigorous testing, ensuring that each component meets the highest radiation resistance standards. Rad-Tolerant: Tailored for shorter stints, rad-tolerant electronics are perfect for missions or applications with a lifecycle of typically five years or less. They're more like sprinters, built to perform optimally in short, intense bursts. Rad-Tolerant: Suited for milder radiation climates, these devices can typically handle radiation exposure ranging from 10-30krad(Si). In some cases, they might be tweaked to withstand slightly higher doses, but they won't match the resilience of rad-hard devices. These devices undergo a more streamlined, automotive-like qualification process, with one-time radiation characterization. Although they are tested to ensure radiation tolerance, the process is less exhaustive than with rad-hard devices, reflecting their shorter operational expectancy and less demanding radiation specifications [4][5]. Commercial-Off-The-Shelf or commercially available off-the-shelf (COTS) products are packaged or canned (ready-made) hardware or software, which are adapted aftermarket to the needs of the purchasing organization. For some spacecraft manufacturers, the use of Commercial Off-The-Shelf (COTS) parts is the only option to meet the performance and cost needs of a mission. Today, many COTS devices are operating successfully in orbit. To achieve mission reliability, the location of COTS parts and sub-systems within the overall build is important and spacecraft modeling software such as TRAD's FASTRAD can help identify areas of the satellite structure that can offer improved levels of shielding from radiation [6].

Most COTS components are resistant to radiation up to 5 krad. Some of them fail before 1 krad. By the COTS method, commercial components and subsystems are purchased and they can be used in the satellite provided they meet other environmental requirements (vibration, temperature, etc.) [3]. The reasons to use COTS instead of space-class components are time-saving, up-to-date, and cost-effective, and they cannot access limitation, on the other hand, it is increased using these components in smaller satellites in LEO orbit. Most of the important components used in radiation systems have silicon bases and are fabricated on VLSI semiconductor technology, so the most studied radiation

damage is focused on silicon. The most effective way to protect against radiation is to use the shield. The protective effect of different materials can be studied using particle transport codes. For shielding, in addition to investigating the protective effect of different materials, it can be optimized on the layout and structure of the shield. Traditionally, aluminum has been the standard material used in space applications that meet radiation shielding and structural-functional requirements. But other materials are also used in this field, including polyethylene, thallium, etc. In this research work various types of materials have been used for shielding calculations [7][2][8]. Space radiation researchers have developed different models to simulate the elements of the radiation environment. These models are based on data sets of different space missions launched in different orbits [5]. The protective effectiveness of different materials can be evaluated using particulate transport codes. [6]. HZETRN, MCNP, GEANT4, and SHIELDOSE-2 CODES are available independently or in software packages such as OMERE and SPENVIS. In this work, SPENVIS is used. The SPENVIS system is developed by a consortium led by the Royal Belgian Institute for Space Aeronomy (BIRA-IASB) for ESA's Space Environments and Effects Section through its General Support Technology Programme (GSTP). The development team at BIRA-IASB maintains the system [9].

The Space Environment Information System (SPENVIS) is a web application that provides models and tools to space engineers and scientists to model the space environment around Mercury, Earth, Mars, and Jupiter but also in the interplanetary medium. In addition, it allows the users to combine and chain results between different models enabling them to calculate the potential effects of the environments specific to their (planned) mission. The effects are divided into the following categories: ionizing dose, non-ionizing energy loss, radiation damage in solar cells, single event upsets, spacecraft charging, atomic oxygen erosion, and meteoroid and debris models [10].

SHIELDOSE and MULASSIS are implemented in SPENVIS software. It is used this capability in this work. SHIELDOSE is a computer code for space-shielding radiation dose calculations. It determines the absorbed dose as a function of depth in shielding materials of spacecraft, given the electron and proton fluences encountered in orbit [9]. Mulassis allows the definition of a multi-layered, one-dimensional shield and incident particle source, and using the Geant4 toolkit simulates radiation transport through the geometry, treating electromagnetic and nuclear interactions. It started working in the field of space radiation as the country's attention to the design and construction of satellites. Most activity in this field is performed using the OMERE software for determination and

shielding calculations. This work aims to investigate the optimal shielding in LEO missions by considering the radiation resistance of COTS components using SPENVIS software.

RESEARCH THEORIES

As mentioned in the introduction, shielding is very important for the utilization of COTS parts, so to find a suitable shield, first, it is necessary to calculate and simulate different and appropriate materials. To consider the impact of TID against the shield, different shields such as aluminum, titanium, tantalum, iron, copper-tungsten alloy, and a bilayer shielding sample (consisting of aluminum and tantalum) have been studied and the amount of TID absorbed into silicon has been calculated for different thicknesses.

Table 3: Mission Orbit Specifications

Perigee altitude	500 km
Apogee altitude	500 km
Inclination	55^{0}
Mission start	01/01/2023
Mission end	31/12/2025

RESULTS

Protons and solar ions, trapped particles including electrons, protons, and galactic cosmic rays are considered the radiation sources of this orbit. The results of calculations using SPENVIS software are presented in this section. Differential and integral flux of solar protons via energy in this LEO mission is shown in Figure 1 and the differential and integral flux of trapped electrons in this LEO mission via energy is shown in

Figure **2**.

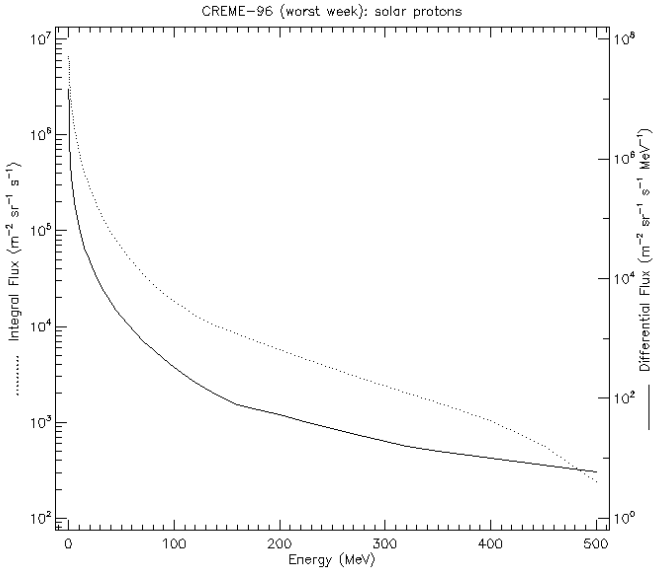

Figure 1- Differential and integral flux of solar protons via energy

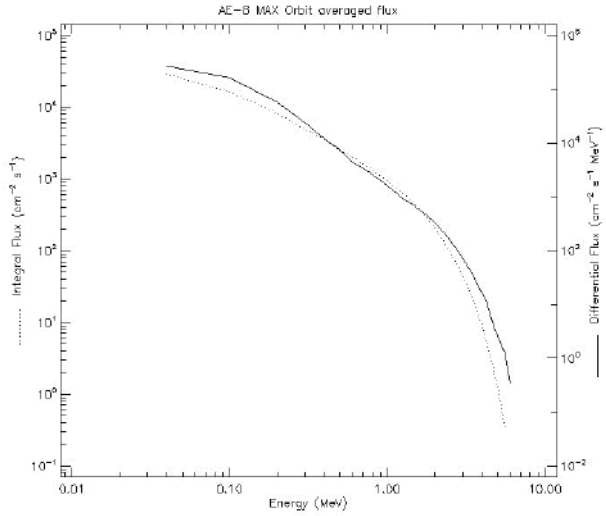

Figure 2- Differential and integral flux of trapped electrons via energy

According to the characteristics of the orbit and the radiation sources, the dose curve is drawn via thickness. In **Table 4**, a sample of the calculations performed using this software is displayed. The target material is silicone and the shield is intended to be flat. The obtained dose of trapped electrons, trapped protons, and solar protons and the total dose in silicon were calculated in terms of thickness. The output of these tables is the dose curve in terms of condensation thickness ($^{g}/_{cm^2}$). The red

horizontal line indicates the radiation tolerance of COTS components. The minimum amount of thickness is obtained from the intersection of two graphs. In

Figure **3**, the dose curve is displayed in terms of thickness for aluminum shielding. This work is repeated for Titanium, Tantalum, Iron, Al + Ta bi-layer, and CW80 Copper-Tungsten Alloy, and the results are summarized in Table 5. In Table 5, the minimum amount of condensation thickness ($^{g}/_{cm^2}$) for the radiation tolerance of COTSs for different materials in this mission is obtained.

Table 4: An Example of Calculation of Dose Determination via Thickness in SHIELDOSE Code

Eqv Al absorber thickness		Actual absorber thickness		Total	Trapped electrons	Brems-strahlung	Trapped protons	Solar protons	Tr. electrons+ Bremsstrahlung	Tr. el.+Bremss. +Tr. protons	Total (krad)
(mm)	(mils)	(g cm^{-2})	(mm)								
0.05	1.968	0.014	0.05	2.13E+04	2.04E+04	4.37E+01	0.00E+00	8.21E+02	2.05E+04	2.05E+04	2.13E+01
0.1	3.937	0.027	0.1	1.11E+04	1.06E+04	2.63E+01	0.00E+00	4.96E+02	1.06E+04	1.06E+04	1.11E+01
0.2	7.874	0.054	0.2	5.34E+03	5.03E+03	1.48E+01	0.00E+00	2.90E+02	5.05E+03	5.05E+03	5.34E+00
0.3	11.811	0.081	0.3	3.43E+03	3.22E+03	1.02E+01	0.00E+00	2.03E+02	3.23E+03	3.23E+03	3.43E+00
0.4	15.748	0.108	0.4	2.48E+03	2.33E+03	7.91E+00	0.00E+00	1.50E+02	2.33E+03	2.33E+03	2.48E+00
0.5	19.685	0.135	0.5	1.92E+03	1.79E+03	6.63E+00	0.00E+00	1.17E+02	1.80E+03	1.80E+03	1.92E+00
0.6	23.622	0.162	0.6	1.55E+03	1.44E+03	5.79E+00	0.00E+00	9.64E+01	1.45E+03	1.45E+03	1.55E+00
0.8	31.496	0.216	0.8	1.08E+03	1.01E+03	4.64E+00	0.00E+00	7.18E+01	1.01E+03	1.01E+03	1.08E+00
1	39.37	0.27	1	8.00E+02	7.39E+02	3.80E+00	0.00E+00	5.75E+01	7.43E+02	7.43E+02	8.00E-01
1.5	59.055	0.405	1.5	4.30E+02	3.88E+02	2.68E+00	0.00E+00	3.91E+01	3.91E+02	3.91E+02	4.30E-01
2	78.74	0.54	2	2.55E+02	2.23E+02	2.06E+00	0.00E+00	2.97E+01	2.25E+02	2.25E+02	2.55E-01
2.5	98.425	0.675	2.5	1.57E+02	1.32E+02	1.66E+00	0.00E+00	2.35E+01	1.34E+02	1.34E+02	1.57E-01
3	118.11	0.81	3	9.99E+01	7.93E+01	1.39E+00	0.00E+00	1.92E+01	8.07E+01	8.07E+01	9.99E-02
4	157.48	1.08	4	4.45E+01	2.95E+01	1.07E+00	0.00E+00	1.39E+01	3.06E+01	3.06E+01	4.45E-02
5	196.85	1.35	5	2.28E+01	1.13E+01	8.70E-01	0.00E+00	1.06E+01	1.22E+01	1.22E+01	2.28E-02
6	236.22	1.62	6	1.35E+01	4.33E+00	7.49E-01	0.00E+00	8.43E+00	5.07E+00	5.07E+00	1.35E-02
7	275.59	1.89	7	9.14E+00	1.62E+00	6.65E-01	0.00E+00	6.85E+00	2.29E+00	2.29E+00	9.14E-03
8	314.96	2.16	8	6.90E+00	5.80E-01	6.02E-01	0.00E+00	5.71E+00	1.18E+00	1.18E+00	6.90E-03
9	354.33	2.43	9	5.59E+00	1.94E-01	5.53E-01	0.00E+00	4.84E+00	7.47E-01	7.47E-01	5.59E-03
10	393.7	2.7	10	4.74E+00	5.79E-02	5.13E-01	0.00E+00	4.17E+00	5.71E-01	5.71E-01	4.74E-03
12	472.44	3.24	12	3.63E+00	2.37E-03	4.50E-01	0.00E+00	3.18E+00	4.52E-01	4.52E-01	3.63E-03
14	551.18	3.78	14	2.87E+00	1.48E-05	4.02E-01	0.00E+00	2.47E+00	4.02E-01	4.02E-01	2.87E-03
16	629.92	4.32	16	2.34E+00	1.29E-07	3.64E-01	0.00E+00	1.97E+00	3.64E-01	3.64E-01	2.34E-03
18	708.66	4.86	18	1.95E+00	0.00E+00	3.32E-01	0.00E+00	1.62E+00	3.32E-01	3.32E-01	1.95E-03
20	787.4	5.4	20	1.66E+00	0.00E+00	3.06E-01	0.00E+00	1.35E+00	3.06E-01	3.06E-01	1.66E-03

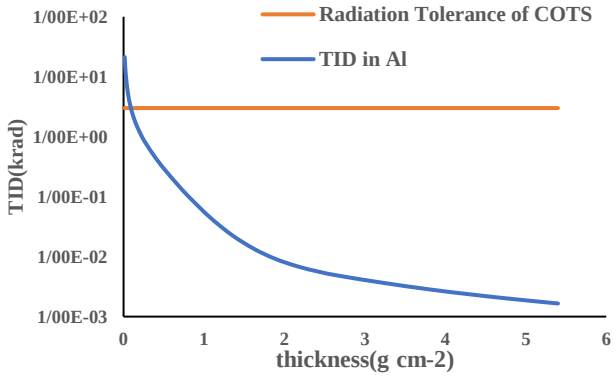

Figure 3- Total ionizing dose curve in terms of thickness for aluminum

Table 5- Minimum condensing thickness (g/cm^2) for radiation tolerance of COTS components for different materials

Shield material	Thickness (mm)	Condensation thickness (g/cm2)
Titanium	0.1798	0.0873
Tantalum	0.0485	0.0799
Iron	0.1029	0.0858
Al + Ta bi-layer	0.5000	0.1400
Aluminium	0.3000	0.0932
CW80 Copper-Tungsten Alloy	0.0520	0.0852

The minimum condensation thickness values for the radiation tolerance of commercial parts in different materials are presented in Figure 4. As shown in in Table 5 and Figure 4, the amount of thickness of different materials for the radiation tolerance of COTS components does not differ much in terms of condensation thickness in this mission. The lowest and highest thickness is related to Tantalum and Ta+Al(1mm) combined shields.

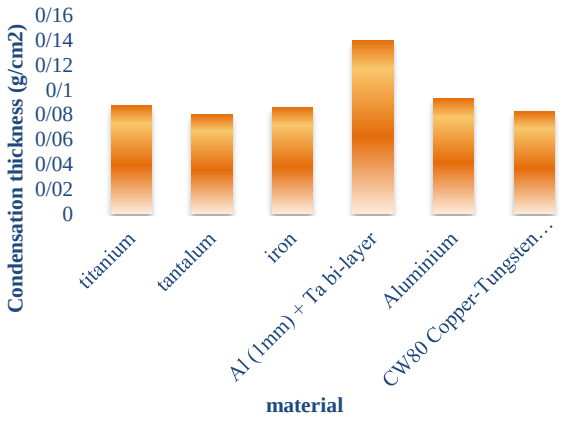

Figure 4- Comparison of the minimum amount of condensing thickness (g/cm^2) for radiation tolerance of different materials

To assessment dose quality, two capabilities of SPENVIS, MULASSIS and SHILDOSE have been used. To validate the two tools, the dose values are calculated in the same conditions. The results of this comparison are shown in Figure 5. As shown in this figure, the values obtained for the dose are almost close to each other in thicknesses of 2-8 mm and they have similar large magnitude.

Therefore, it can be concluded that if there is a limitation in any of the capabilities of MULASSIS and SHILEDOSE, another can be used as an alternative software.

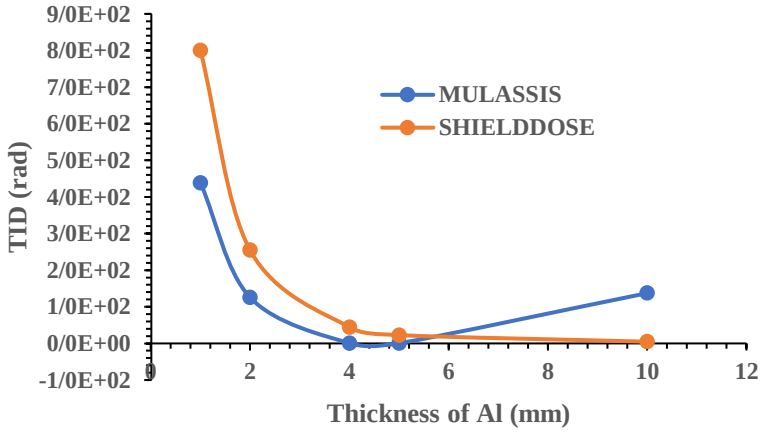

Figure 5- Comparison of total ionizing dose curve obtained from MULASSIS and SHIELDOSE calculations in terms of thickness for aluminum shielding in silicon

Conclusions

It is important to have a good understanding of these effects on the satellite in order to provide the required shielding for mission planning and design, Radiation damage has devastating effects on electronic components in satellites, and the selection of components has a particular importance. The most effective way to protect against radiation is to use a shield. The use of shields appears to be the only practical tool to reduce the impact of radiation on astronauts and satellite cargo. There are two transport radiation codes used in this study. The aim of this work is to investigate the optimal shielding in LEO mission by considering the radiation resistance of COTS components using SPENVIS software. It will be a three-year mission for a low-altitude orbit satellite (LEO). The results of SHIELDOSE2 calculations show that the amount of thickness of different materials, for the radiation tolerance of commercial parts, does not differ much in terms of condensation thickness in this mission. The lowest thickness is the tantalum. Comparison of the calculations obtained from MULASSIS and SHILEDOSE to achieve the dose into the silicon target indicates that the values are very similar and if there is a limitation in each of the capabilities of MULASSIS and SHILEDOSE, another can be used as an alternative software. The general conclusion of the conservation design

topics in this mission is that there is no need to use complex shielding and can also be used for this purpose.

References

[1] R. H. Maurer, M. E. Fraeman, M. N. Martin, a/ac D. R. Roth, 'Harsh Environments: Space Radiation', *Johns Hopkins APL Tech. Dig.*, rhif. 28, rhif. 1, t. 17, 2008.

[2] Astrium, 'Circumventing Radiations Effetcs by Logic Design - Executive Summary Report', 2001.

[3] Jet Propulsion Laboratory, 'Radiation Design Margin Requirement', NASA, 1999. [Arlein]. Ar gael: http://llis.nasa.gov/lesson/792.

[4] Nasa, 'Space Radiation Effects on Electronic Components in Low-Earth Orbit', *Orbit An Int. J. Orbital Disord. Facial Reconstr. Surg.*, rhif. April, 1996.

[5] C. Poivey, 'Total Ionizing and Non-Ionizing Dose Radiation Hardness Assurance for Space systems', *RADHARD Symposium*. 2017.

[6] K. Rojdev, A. J. Tylka, a/ac W. Atwell, 'Preliminary radiation analysis of the total ionizing dose for the resource prospector mission', yn *AIAA SPACE 2015 Conference and Exposition*, 2015, t. 4504, doi: 10.2514/6.2015-4504.

[7] M. M. Rahman, D. Shankar, a/ac S. Santra, 'Analysis of radiation environment and its effect on spacecraft in different orbits', yn *Proceedings of the International Astronautical Congress, IAC*, 2017, rhif. 12, tt. 8073–8079.

[8] T. F. Wrobel, 'On heavy ion induced hard-errors in dielectric structures', *IEEE Trans. Nucl. Sci.*, rhif. 34, rhif. 6, tt. 1262–1268, 1987, doi: 10.1109/TNS.1987.4337463.

[9] P. Truscott *et al.*, 'MULASSIS - Monte Carlo radiation shielding simulation for space applications made easy', yn *European Space Agency, (Special Publication) ESA SP*, 2003, rhif. 2003-Septe, tt. 191–196.

[10] 'The ESP models', [Arlein]. Ar gael: https://www.spenvis.oma.be/help/background/flare/flare.html#ESP.

ICNST 2024
International Conference on Nuclear Science and Technology
6- 8 MAY 2024 | Isfahan, Iran

Estimation of Defect Cluster Density and Elements Radiation-Induced Segregation in WWER-1000 Reactor Pressure vessel by RADIX Code (Paper ID : 1498)

Elaheh Moslemi Mehni*

**Corresponding author. E-mail: s9512423201@phd.araku.ac.ir*

Abstract: Irradiation damage is an important element in understanding the mechanism of nuclear materials performance. In the current study, radiation damage in the reactor pressure vessel (RPV) is re-assessed by computing the displacement per atom (dpa) cross-sections from the ENDF/B-VII.1 nuclear data library. An indigenous computer code, radiation damage induced by incident neutron flux (RADIX), is developed to compute elastic part of displacement cross section and dpa value of materials through new radiation damage model, a thermal recombination-corrected displacement per atom (arc-dpa). On the other hand, the non-elastic part of damage is extracted from the HEATR module of the NJOY code. According to the total dpa results and semi-experimental relations, some tensile properties and grain boundary concentrations of Cr, Ni, and Si are compared together. Also, defect cluster density obtained about 1.995E+23 (m^{-3}) during forty years of effective full power year (EFPY) operation of WWER-1000 reactor with the coolant temperature of 291 ˚C. Finally, this results are compared with the SPECTER/SPECOMP and NJOY code.

Keyword: Neutron radiation damage, Defect cluster density, Grain boundary concentration, Stainless steel 316

INTRODUCTION

Nuclear power plays a crucial role in global energy supply, accounting for approximately 17% of global electricity generation. As the industry continues to grow rapidly and face increased scrutiny, ensuring high reliability and safety becomes imperative. Understanding the impact of neutron radiation damage is a key factor in achieving safe and reliable operation throughout the lifetime of nuclear power plant instruments. Therefore, having a foundational knowledge of the neutron interaction mechanism, binary collision approximation, Monte Carlo method, angular distribution of reaction products, and secondary displacement models is essential as a starting point for studying neutron radiation damage.

During neutron irradiation, atoms undergo displacement from their original positions, referred to as primary knock-on atoms (PKA), resulting in a cascade of secondary displaced atoms. The minimum energy required to displace these atoms from their lattice positions is known as the threshold energy (Ed). As the cascade cools down, two types of defects are induced in the irradiated material: vacancies (vacant lattice positions) and interstitials (displaced atoms in interstitial lattice positions), collectively known as "Frenkel Pairs" (FP) [1].

The Norgette-Robinson-Torrens (NRT) model, developed based on Lindhard theory, has been widely utilized to estimate the displacement per atom (dpa) in computer codes such as SPECTER, SPECOMP, and SRIM codes [2-4]. However, some researchers have found that this model tends to overestimate the dpa value. To address this limitation, the athermal recombination-corrected (arc-dpa) model has been introduced, providing a more physically realistic description of primary radiation damage [5].

Austenitic stainless steels (SSs) are commonly used as structural alloys in the inner components of reactor pressure vessels (RPVs) due to their high strength, fracture toughness, and ductility. However, Extend neutron irradiation causes changes in the microstructure (radiation-induced hardening) and microchemistry (radiation-induced segregation) of these steels [6-8]. Additionally, irradiation-assisted stress corrosion cracking (IASCC) is another degradation process that affects RPV internal components exposed to neutron irradiation [8]. Some literature suggests that radiation enhances stress corrosion cracking (SCC) through four main mechanisms: hardening, relaxation, segregation, and radiolysis [9].

In this study, we aim to determine the defect cluster density and grain boundary concentrations of Cr and Ni (related to radiation-induced segregation) after forty years of operation of the WWER 1000 reactor pressure vessel. We calculate the neutron irradiation damage using the correction of the secondary displacement model (in dpa unit) and a semi-empirical method extracted from the same coolant irradiation conditional and temperature of various reactors.

RESEARCH THEORYS

2.1. Theory of damage cross section

According to the damage theory, the total dpa value during the exposure time t reads

$$dpa = t\int_0^{\infty} \sigma_D(E)\psi(E)dE \quad (1)$$

Where $\psi(E)$ is the incident neutron flux, $\sigma_D(E)$ is dpa cross section which is one of the primary parameters that is required to estimate the dpa value, given as

$$\sigma_D(E) = C_i(E)\int_{E_{R_{\min}}}^{E_{R_{\max}}} dE_R\ \sigma_i(E)\ \nu\left[T\{E_R\}\right]\ K_i(E,E_R) \quad (2)$$

$K_i(E,E_R)$, $\sigma_i(E)$ and $C_i(E)$ are respectively the kernel of energy transfer, cross section and normalization factor for specified reaction that is denoted by the suffix i as well as the ν parameter is the secondary displacement function which is briefly described in the next section. Here E_R is the recoil energy of displaced atom and the damage energy, $T(E_R)$ is energy available to generate atomic displacement (Robinson partition function) [10]. If the atomic mass (A) of each element and the displacement threshold energy (E_d) in the compound are approximately equal to those of the other elements, the dpa cross-section of impurity materials can be derived using the following equation:

$$dpa_T = \sum_i w_i D_i \quad (3)$$

Where w_i and Di represent the weight fractions (table 1) and displacement damage of each element (Eq. (2)) in a chemical composition.

Table 1. The weight percentage of the chemical composition for the first and second layers of stainless steel is provided, with iron (Fe) serving as the balancing element. [11].

Element	C	Si	Mn	Cr	Ni	Mo	Ti	Co	S	P	Cu	Sb	Sn
First layer SS	0.09	0.95	1.30	23.20	12.90	-	-	0.02	0.004	0.015	-	-	-
Second layer SS	0.05	0.07	1.50	19.01	9.80	0.03	-	0.016	0.005	0.005	0.08	-	-

2.2. Atomic displacement models

In particular, final radiation defects generated in energetic cascades is much smaller than simple linear collision cascade models such as the NRT-dpa prediction [5]. According to the equation 2, the ν parameter defined as:

$$\nu(T)=\begin{cases} 0 & T(E_R)<E_d \\ 1 & E_d \le T(E_R) \le \dfrac{2E_d}{\beta} \\ \dfrac{\beta\xi(T)T(E_R)}{2E_d} & T(E_R)\ge \dfrac{2E_d}{\beta} \end{cases} \quad (4)$$

Here β is the damage efficiency with a value of 0.8, and E_d is the average threshold energy.

$$\xi_{NRT}(T)=1 \quad (5)$$

$$\xi_{arc-dpa}(T)=\frac{1-C_{arc-dpa}}{\left(\frac{2E_d}{\beta}\right)^{b_{arc-dpa}}}T^{b_{arc-dpa}}+C_{arc-dpa} \quad (6)$$

Where $b_{arc-dpa}$ and $c_{arc-dpa}$ are dimensionless parameters obtained from molecular dynamics (MD) simulations and extensive experiments. Table 2 presents these parameters for specific elements.

Table 2. The dimensionless parameters used to calculate dpa cross-sections based on the arc-dpa model.[12].

Element	Fe	Ni	Cr	Mn
$c_{arc-dpa}$	0.286	0.23	0.37	0.33
$b_{arc-dpa}$	-0.568	-1.01	-1.0	-1.0

2.3. Tensile properties

Tensile properties data has been gathered for various grades of austenitic stainless steels, encompassing weld heat-affected zone (HAZ) material, weld metal, and CF-8 cast austenitic stainless steels. These materials were subjected to irradiation at temperatures ranging from 300 to

400 °C (from 572 to 752°F) in fast reactors and LWRs. The provided data represents an exponential equation that can be utilized to estimate the tensile properties based on the neutron dose:

$$Property = A_0 + A_1(1-\exp(-d/d_0)) \quad (7)$$

Where d represents the neutron dose in dpa, the coefficients A_0, A_1, and d_0 are provided in table 3.

Table 3: Equations describing the material properties of irradiated CW Type 316 stainless steel.

Property	Units	$Property = A_0 + A_1(1-\exp(-d/d_0)$		
		A_0	A_1	d_0
0.2% Yield Strength	MPa	500	470	3
Ultimate tensile strength	MPa	650	330	3
Uniform elongation	%	10	-9.7	2
Total elongation	%	18	-11	5

2.4. Simulation of the reactor core and pressure vessel utilizing MCNPX

The WWER-1000 reactor comprises 163 hexagonal fuel assemblies and has a 1/6 symmetric shape. It operates at a full power output of 3000 MWt. To maintain criticality, a concentration of 6.56 g/kg of boric acid is required. Under normal conditions, the reactor remains critical with a coolant temperature of 291°C. The pressure vessel is constructed from stainless steel, specifically using type 15Kh2NMFAA as the base metal and SV-09GNMTAA grade metal for the weld joint. The maximum flux rate is observed at a height of 180 cm on the inner surface of the reactor vessel. Figure 1 illustrates the neutron flux spectrum at a height of 180 cm on the inner surface of the RPV.

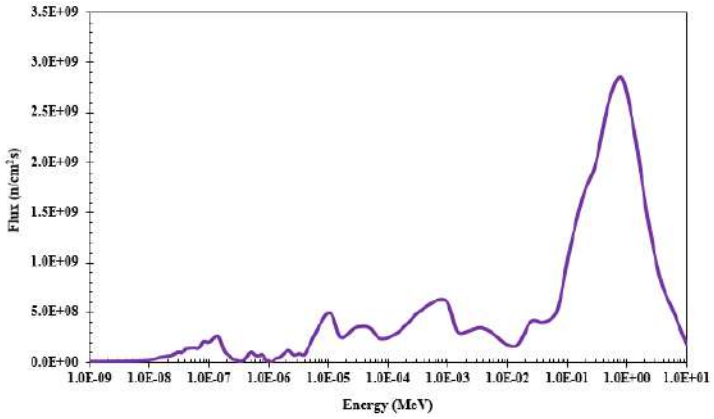

Figure 1: Neutron energy spectrum measured at a height of 180 cm from the pressure vessel.

2.5. Generating pointwise energy-damage cross-section utilizing the NJOY code

The NJOY code is a system that processes nuclear data in the ENDF format. It converts the data into usable formats for calculating parameters related to nuclear reactions, scattering theory and resonances. Within the NJOY code, RECONR reads an ENDF file (TAPE 20) and generates a common energy grid for a specified reaction by linear interpolation and writes the resonance cross sections onto a pointwise PENDF file (TAPE 21) for future use. The BROADR module reads the TAPE 21 file and applies the accurate point-kernel method to perform Doppler broadening on the data. After the broadening and thinning process, the summation cross sections are reconstructed using their respective components. Subsequently, the resulting data is written into a new PENDF file (TAPE 22). Then, HEATR module reads TAPE 22 file and applies energy-balance heating and produces a pointwise energy-damage cross-section for all reaction (such as elastic, inelastic, disappearance, and total interactions) and includes them in the PENDF tape (sections 444-447). The dpa results obtained from the HEATR module utilize nuclear data from ENDF/B-VII.1 and the NRT model. However, the code has not yet integrated the most recent secondary displacement models, such as the arc-dpa, for dpa cross-sections. At the end, under normal conditions (291°C) and neutron radiation exposure, the total dpa cross-sections (MT=444) of the constituent elements in the RPV

structure (Fe, Ni, Cr, and Mn) are derived from equations (1) and (3). These steps are depicted in figure 2.

Figure 2: Processing nuclear data using the NJOY code to quantify radiation damage on the inner surface of the pressure vessel.

2.6. Estimation of neutron radiation damage in the pressure vessel utilizing the SPECTER/SPECOMP

The SPECOMP code is specifically designed for the computation of compound dpa cross-sections for material combinations comprising up to five elements. Subsequently, these cross-sections are incorporated into the COMPOUND.DAT file of the SPECTER code. Figure 3 illustrates the simulation and calculation processes performed by the SPECTER and SPECOMP codes.

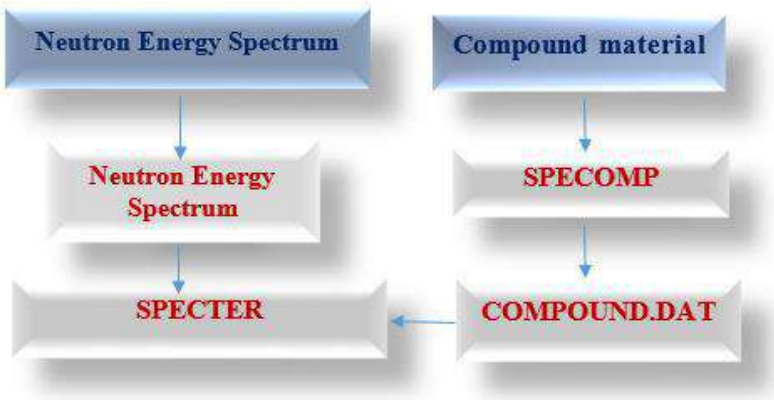

Figure 3: Processing Nuclear data using the SPECTER/SPECOMP to quantify radiation damage on the inner surface of the pressure vessel.

2.7. Estimation of neutron radiation damage in the pressure vessel utilizing the RADIX

As the elastic DPA cross-section plays a vital role in DPA calculation, a data processing program called RADIX has been developed to calculate the elastic DPA values for a pure material or a simple linear combination of materials. RADIX modifies the elastic calculation part of the HEATR module based on various displacement models. The non-elastic part of the DPA cross-sections from the PNDF tape (MT numbers 446 and 447) of the NJOY code can be easily incorporated into a file in the RADIX code. Moreover, the neutron flux, obtained from MCNP simulations, can be included in RADIX's input file, enabling automatic execution of DPA calculations for a compound (figure 4).

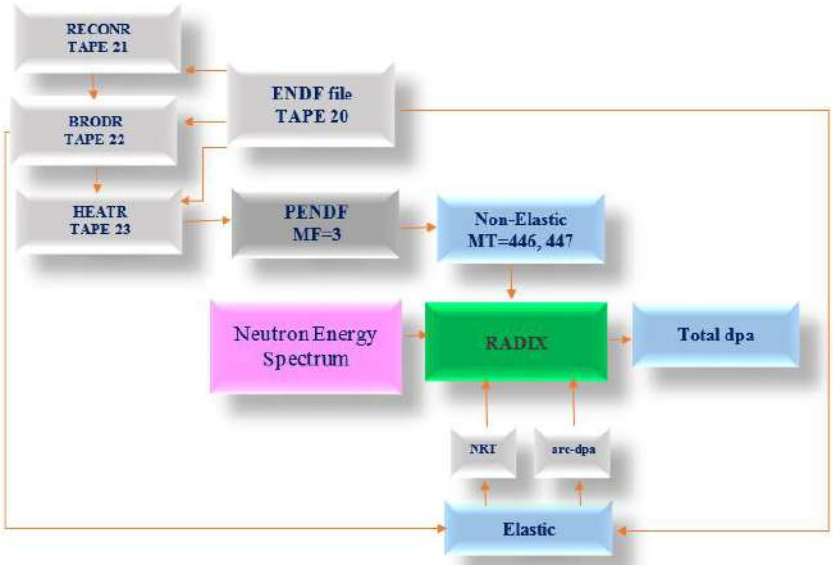

Figure 4: Processing nuclear data using the RADIX code to quantify radiation damage on the inner surface of the pressure vessel.

Results and discussion

3.1. Estimation of defect cluster density and grain boundary concentrations

Neutron irradiation significantly impacts the properties of stainless steel, including its mechanical properties and structural integrity like defect cluster density and grain boundary concentrations. The

defect cluster density and grain boundary concentrations of Cr, Ni, and Si in the vessel wall over a 40-year period have been determined through a variety of methods. These methods include the calculation of displacements per atom (dpa) using RADIX (arc-dpa)/HEATR, NJOY, and SPECTER/SPECOMP codes, as well as empirical relations derived from curve fitting with

experimental data (as presented in figures 5-8). The computed results for the inner surface of the RPV are presented in the table 4.

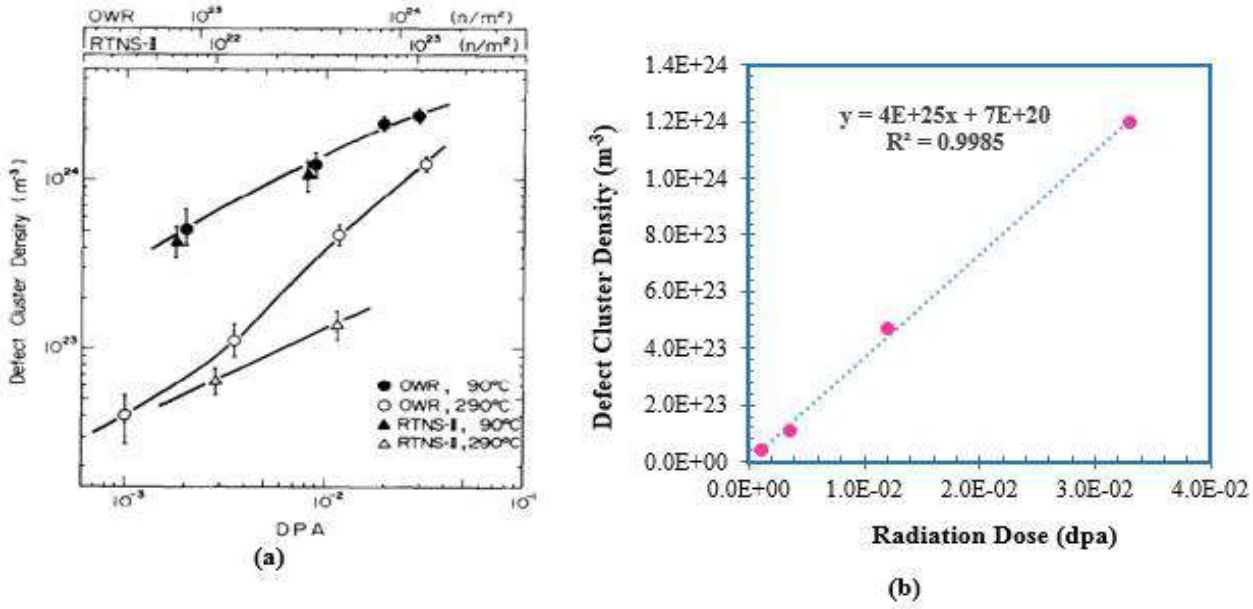

Figure 5: (a) Plot of defect cluster density versus displacement per atom (dpa) [6]. (b) Interpolation of experimental defect density data of stainless steel versus dpa.

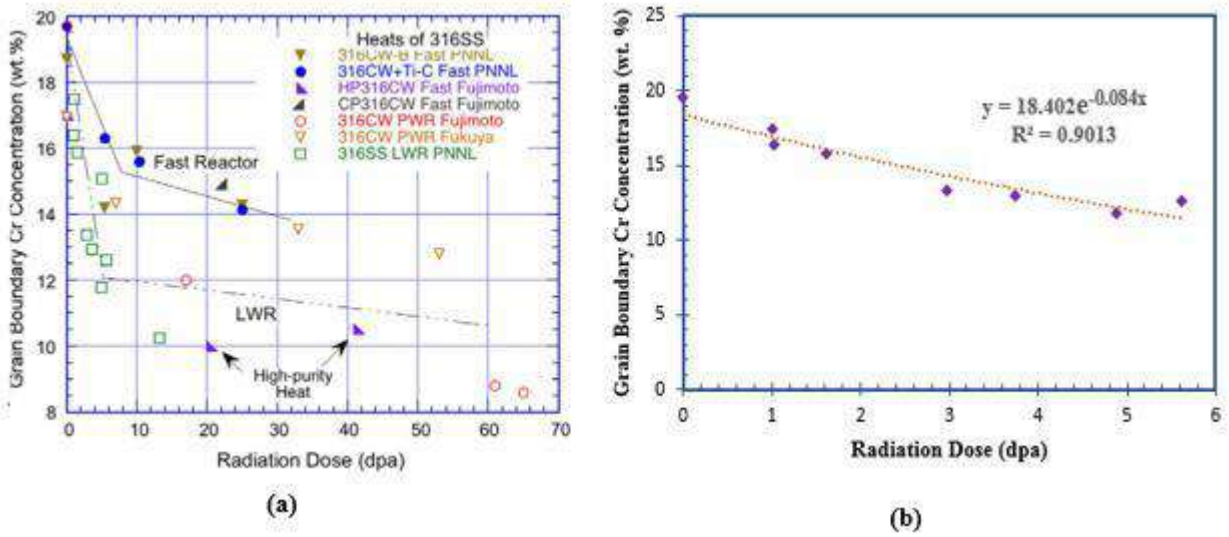

Figure 6: (a) Plot of grain boundary Cr concentration versus displacement per atom (dpa) [8]. (b) Interpolation of experimental grain boundary Cr concentration of stainless steel versus dpa.

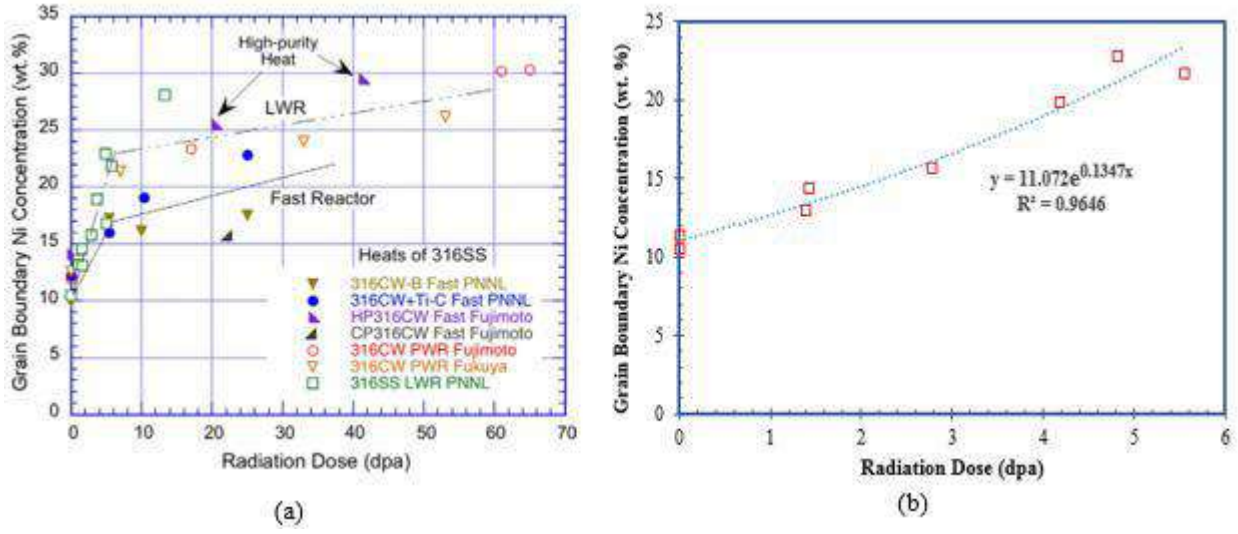

Figure 7: (a) Plot of grain boundary Ni concentration versus displacement per atom (dpa) [8]. (b) Interpolation of experimental grain boundary Ni concentration of stainless steel versus dpa.

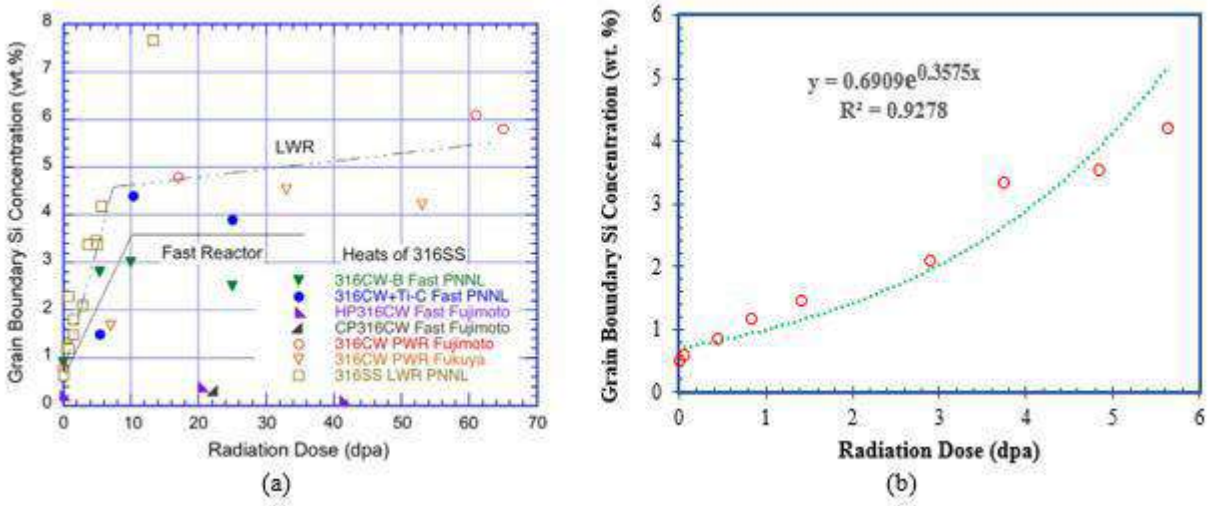

Figure 8: (a) Plot of grain boundary Si concentration versus displacement per atom (dpa) [8]. (b) Interpolation of experimental grain boundary Si concentration of stainless steel versus dpa.

Table 4: Evaluating dpa values, defect cluster density and Grain boundary concentration using RADIX/HEATR, NJOY and SPECTER/SPECOMP codes. $\phi_{tot} = 2.56E+10,\ t = 2.54016E+07s$

Property	Units	Computational Codes		
		RADIX	NJOY	SPECTER-SPECOMP
Radiation dose (40 EFPY)	dpa	4.97E-03	8.57E-03	7.47E-03

Defect cluster density	m^{-3}	1.995E+23	3.435E+23	2.99E+23
GB Cr Concentration	wt. %	18.394	18.388	18.390
GB Ni Concentration	wt. %	11.0794	11.0848	11.083
GB Si Concentration	wt. %	0.6921	0.6930	0.6927

3.2. Tensile properties of the irradiated CW type austenitic 316 stainless steel

The data pertaining to the 0.2% yield strength, ultimate tensile strength, uniform elongation, and total elongation were utilized in order to establish a fitting exponential equation (Equation 7). The calculation results for the inner surface of the RPV are presented in Table 5.

Table 5: Evaluating dpa values and tensile properties using RADIX/HEATR, NJOY and SPECTER/SPECOMP codes . $\phi_{tot} = 2.56E+10,\ t = 2.54016E+07s$

Property	Units	Computational Codes		
		RADIX	NJOY	SPECTER-SPECOMP
Radiation dose (40 EFPY)	dpa	4.97E-03	8.57E-03	7.47E-03
0.2% Yield Strength	MPa	500.78	501.34	501.16
Ultimate tensile strength	MPa	650.54	650.94	650.82
Uniform elongation	%	9.976	9.958	9.964
Total elongation	%	17.989	17.981	17.983

Conclusion

In order to accurately assess the properties of structural materials used in nuclear power plant equipment, it is crucial to determine their performance. As previously mentioned, one of the primary

factors that contributes to changes hardening and segregation within the reactor pressure vessel is the radiation-induced effect. Additionally, researchers have discovered that several parameters, such as the type of interaction between neutrons and atoms, atomic displacement model, and temperature, can significantly impact displacement damage. As a result, these parameters directly influence the strength of irradiated materials. The main objective of this study was to estimate the defect cluster density, tensile properties and grain boundary element concentration of the reactor pressure vessel. To achieve this goal, benchmark neutron spectra were obtained from the MCNPX code, and calculations of displacement damage were carried out on the inner surface of the RPV using the RADIX and NJOY computer codes. These calculations were conducted under normal operating conditions (291°C) and at a temperature of 0 K using the SPECTER/SPECOMP code. The discrepancy in the results, particularly with regards to the 0.2% yield strength and defect cluster density (as presented in tables 4 and 5), can be attributed to the implementation of the highly precise displacement model, arc-dpa, in the RADIX code calculations for the elastic part of radiation damage.

References

[1] Saha, Uttiyoarnab, K. Devan, and S. Ganesan. "A study to compute integrated dpa for neutron and ion irradiation environments using SRIM-2013." *Journal of Nuclear Materials* 503 (2018): 30-41.

[2] Greenwood, Lawrence R., and Robert K. Smither. *SPECTER: Neutron damage calculations for materials irradiations*. No. ANL/FPP/TM-197. Argonne National Lab.(ANL), Argonne, IL (United States), 1985.

[3] Greenwood, L. R. "Compound Displacement Damage Calculations with SPECOMP." *Informal Notes, Argonne National Laboratory,(February 1988)* (1988).

[4] J. F. Ziegler, M. D. Ziegler, and J. P. Biersack, "SRIM - The stopping and range of ions in matter (2010)," *Nuclear Instruments and Methods in Physics Research,* Vols. 268, no. 11–12, no. Section B: Beam Interactions with Materials and Atoms, pp. 1818-1823, 2010.

[5] Nordlund, Kai, et al. "Improving atomic displacement and replacement calculations with physically realistic damage models." *Nature communications* 9.1 (2018): 1084.

[6] Yoshida, N., et al. "Microstructure-tensile property correlation of 316 SS in low-dose neutron irradiations." *Journal of nuclear materials* 179 (1991): 1078-1082.

[7] Garner, F. A. "Radiation damage in austenitic steels." *Comprehensive nuclear materials* (2012): 33-95.

[8] Chopra, O. K., and A. S. Rao. "A review of irradiation effects on LWR core internal materials–IASCC susceptibility and crack growth rates of austenitic stainless steels." *Journal of Nuclear Materials* 409.3 (2011): 235-256.

[9] Was, G. S., and P. L. Andresen. "Irradiation assisted corrosion and stress corrosion cracking (IAC/IASCC) in nuclear reactor systems and components." *Nuclear Corrosion Science and Engineering*. Woodhead Publishing, 2012. 131-185.

[10] Moslemi-Mehni, Elaheh, et al. "Estimation of yield strength due to neutron irradiation in a pressure vessel of WWER-1000 reactor based on the correction of the secondary displacement model." *Nuclear Engineering and Technology* 55.9 (2023): 3229-3240.

[11] ARDEKANI, Seyed Fazel Ghazi; HADAD, Kamal. Monte Carlo evaluation of neutron irradiation damage to the VVER-1000 RPV. Nuclear Energy and Technology, 2017, 3.2: 73-80.

[12] SAHA, Uttiyoarnab; DEVAN, K.; GANESAN, S. Application of arc-dpa model to estimate the primary radiation damage of structural materials by neutrons and the necessity of rescaling dpa versus final experimental damage correlations. Journal of Nuclear Materials, 2019, 522: 86-96.

Improving classification of nodules using deep learning method (Paper ID : 1518)

S. Ghanbari mishamandani[1*], M. Zadnorouzi[b], A. Sadremomtaz[c]
[1,2,3]*Departement of Physics, University of Guilan, Rasht, Iran*

Abstract

Lung cancer has the highest death rate worldwide, because the symptoms of this disease appear late which causes the survival rate of patients to decrease. Therefore, early diagnosis of this disease is very important. Convolutional neural networks have a good ability to analyze images and automatically extract features from them and making them highly recommended
for the design of computer-aided diagnosis systems thanks to its promising results on medical image analysis. In the present study, deep convolutional neural networks (CNN) were suggested to improve the accuracy of nodule classification. Two pre-trained models based on ResNet50 and Xception, as well as and one light CNN were designed as feature extractors and feature fusion technique apply. Finally, machine learning classifiers were applied on the extracted features. the evaluations on LUNA dataset show the accuracy of 96.72, AUC of 96.14 and recall of 93.73. the metrics' value is

better than previous studies. the results of this study indicates the effectiveness of the proposed method compared to other studies.

Keywords: lung, nodule, classification, deep learning

INTRODUCTION

Lung nodules are small masses of tissue that appear in the lung due to various reasons. They appear as opaque white objects on a CT image and their sizes vary from 3 mm to 30 mm. There can be benign lung nodules and malignant (cancerous) lung nodules. In a few scans and subsequent analyses, a benign nodule can be misclassified as a cancerous lung nodule [1]. To avoid this error, an efficient classification scheme is needed. It is not easy to differentiate benign nodules and malignant nodules because both are having similar visual representations. Many CADs available in the literature are based on image processing and traditional machine learning techniques. recently, deep learning‐based CADs are being introduced in most of the areas for detecting the abnormalities in the medical images. The performance of classification system depends largely on features being selected. However, CNN includes both feature extraction and classification sequentially. CNN has also shown best results in bio- medical image classification. Some
of the benefits of using CNN in classifying the lung nodules based on malignancy are: (1) CNN has outperformed most of the conventional models in detecting the malignant lung nodules [2]. (2) The convolution, pooling and fully connected layer of CNN architecture concatenates the feature extraction and classification phases in lung nodule classification and hence does not require an additional feature extraction/feature selection stage. (3) Lung nodule classification using CNN has been found to be superior to other deep learning architecture.

RESEARCH THEORIES

In this paper, a feature fusion technique is proposed. The proposed ensemble learning based fusion technique is fusion based on averaging the prediction scores. First, the deep features are learned using two different state-of-the art DCNN architectures: ResNet50 and Xception as well as a proposed light CNN. Then the prediction results are obtained by training the SVM and AdaBoostM2 classifiers. After that, the performance of the above classifiers is analyzed and the predicted results of the two classifiers are fused by averaging the averaging of prediction scores of each classifier.

EXPERIMENTAL

The LUNA16 challenge dataset [3] is a subset of the LIDC-IDRI [4] database. The LIDC-IDRI database includes almost all special features of nodules such as nodule location, size, metastasis level and margin. This data set is annotated by four radiologists using a two-step image annotation process. We propose a fusion technique that incorporates the deep features of three DCNNs into a single framework.

The classic studies basically rely on segmentation of lung nodule for regional analysis. We address the raw nodule patches by a hierarchical learning framework to extract the discriminative features from, alternatively, stacked layers. The feature extraction is a major step in the nodule classification systems which effects the performance significantly. The features are extracted from the fully connected layer of the pre-trained ResNet50 and Xception models and proposed CNN for feature fusion and training the classifier.

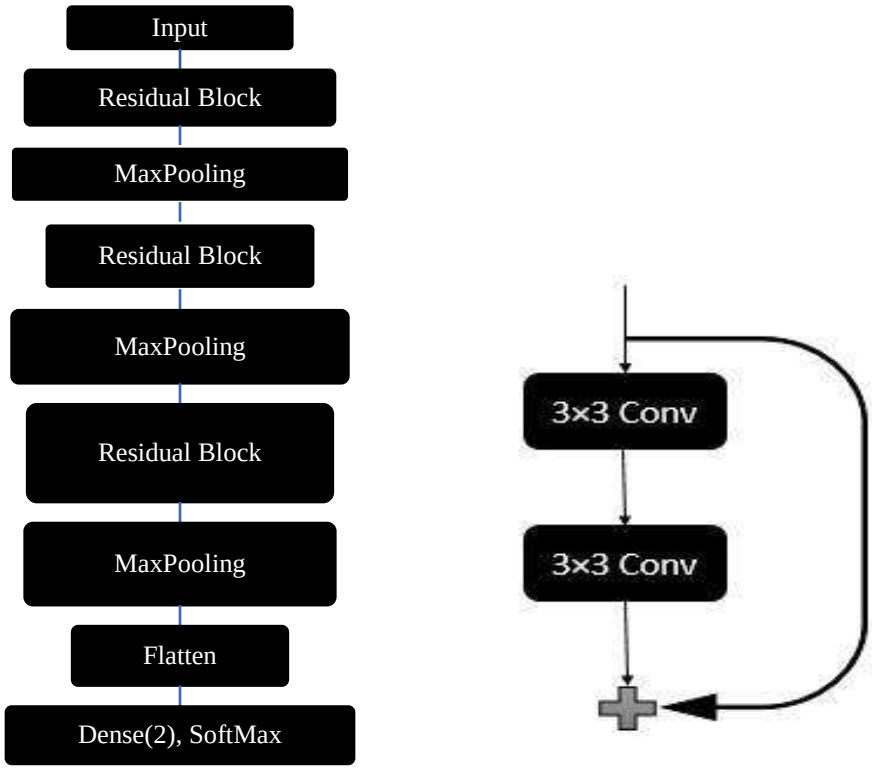

Fig. 1. The structure of proposed RSANet (a) Residual block (b)

Results and discussion

The proposed technique of fusion is based on averaging of prediction score. The classifier is trained on deep features separately, then fuse the results based on averaging of prediction scores of each classifier.

The quantitative performance of the proposed pulmonary nodule classification techniques is evaluated by using six different evaluation metrics, which are: Accuracy, F1-Score, Recall, and Precision. True positive (TP), true negative (TN), false positive (FP) and false negative (FN) are used to compute the evaluation metrics, as follows:

The fusion based on averaging of prediction score (AVG Predict) is applied by taking the average of predicted scores of SVM and AdaBoostM2 classifiers.

TABLE 1. Nodule classification results based on deep features.

Models/metrics	Accuracy	precision	Recall	F1	AUC
final predict	96.72	96.73	93.73	94.8	96.14

The feature fusion technique improves the classification performance as compared to the previous implemented technique whose results are given in Table 2.

TABLE 2. Comparison proposed fusion method with state-of-the-art techniques.

Year	Reference	Dataset	Recall	AUC	ACC
2023	Proposed method	LUNA16	93.73	96.14	96.72
2021	MUZAMMIL et al.[5]	LUNA16	-	-	95.59
2021	Ge Zhang[6]	LUNA16	87.00	-	92.4
2017	Nibali et al. [7]	LIDC-IDRI	91.07	94.59	89.90

In the table. 2, the comparison of the results of the proposed method with other studies on the LUNA16 dataset is given. As shown, the performance of the proposed model for nodule classification is better than other methods.

Conclusions

The ensemble learners can be built by fusing the prediction results of multiple DCNN learners for pulmonary nodule classification which leads to improved classification performance over a single model**.** The performance results were very promising and surpassed those of existing works.

Acknowledgements

The authors declare that they have no known competing financial interests or personal relationships that could have appeared to influence the work reported in this paper.

References

[1] Dhara AK, Mukhopadhyay S, Dutta A, Garg M, Khandelwal N. (2016). A combination of shape and texture features for classification of pulmonary nodules in lung CT images. J Digit Imaging, 29(1):466–75.

[2] Hua, K. L., Hsu, C. H., Hidayati, S. C., Cheng, W. H., & Chen, Y. J. (2015). Computer-aided classification of lung nodules on computed tomography images via deep learning technique. OncoTargets and Therapy, 8: 2015–2022.

[3] A. A. A. Setio et al. (2017). Validation, comparison, and combination of algorithms for automatic detection of pulmonary nodules in computed tomography images: The LUNA16 challenge, Med. Image Anal., 42: 1–13.

[4] S. G. Armato, III, et al. (2011). The lung image database consortium (LIDC) and image database resource initiative (IDRI): A completed reference database of lung nodules on CT scans," Med. Phys., 38(2): 915–931.

[5] I. Ali, M. Muzammil, I. U. Haq, A. A. Khaliq, and S. Abdullah. (2021). Efficient lung nodule classification using transferable texture convolutional neural network. IEEE Access, 8: 175859–175870.

[6] Y. Wang, H. Zhang, K. Chae, Y. Choi, G. Jin, and S. Ko, (2020). Novel convolutional neural network architecture for improved pulmonary nodule classification on computed tomography. Multidim Syst Sign Process, 31(5): 1163–1183.

[7] A. Nibali , Z. He, and D. Wollersheim, (2017). Pulmonary nodule classification with deep residual networks. International journal of computer assisted radiology and surgery, 12(10): 1799–1808.

ICNST 2024
International Conference on Nuclear Science and Technology
6- 8 MAY 2024 | Isfahan, Iran

Systematic investigation of pure beta sources to reduce breakdown voltage in x-band waveguide (Paper ID : 1519)

Mohammad Reza Kardgar[1*], R. Razavi [2,] M. Ramezani [3], A. Shekari [4]

[1] *Physics Science and Technology Center, Department of Physics, Imam Hossein University (AS), Tehran, Iran.*

Abstract

The radar receiver protector (RRP) is a vital and important part of the radar system that prevents electromagnetic interference on the radar receiver. In this paper, a novel method for designing and simulation a radiation-based RRP is used. In this method, pure beta sources with different half-lives and helium gas are used as the medium. Using the MCNPX code, the amount of deposited energy in the space of the RRP is calculated. Then, using the CST software, the electric field resulting from the ionization of the radiation sources at the X-band frequency is calculated.

The results demonstrate that radioactive sources can serve as a key parameter in reducing the breakdown voltage of the receiver protector. Notably, within the X-band and depending on the specific dimensions and structural features of the receiver protector, pure beta sources with lower energy exhibit superior performance in reducing breakdown voltage.

Keywords: Pure beta source, Deposited energy, MCNPX code, Waveguide

INTRODUCTION

Radar is a system based on radio frequency electromagnetic waves that plays a vital role by detecting, tracking and measuring objects. An important part of the radar system is the radar receiver, which receives and processes the reflected signals. The protection of the receiver against unwanted signals and destructive electromagnetic waves is the responsibility of the RRP.

To design and build RRP, one of the key parameters in the design of the RPP is breakdown voltage, which has a direct effect on the sensitivity and performance of the radar receiver. The receiver

protectors consist of a chamber with two electrodes, which by applying a voltage between these two electrodes and the presence of an incoming wave causes an electrical discharge between these electrodes. At the same time as a spark is created between the two ends of the electrode, noise is produced. If the discharge is too strong, the noise level may be high enough to reduce the sensitivity of the receiver and damage it. Another disadvantage of receiver protection is the need for a high voltage source. Another disadvantage of receiver protectors is their relatively short lifetime due to the erosion of electrodes due to electron and ion bombardment [1]. To overcome these disadvantages, radiation sources have been introduced as an auxiliary electron source in the receiver shield. Various theoretical and experimental studies on the use of radioactive materials in RRP have been investigated. In Nelson and Goldie's 1974 structure, beta radioactive material (tritium radioactive material is used) is placed near the tip of the cones on the screen and causes the breakdown voltage to decrease in the receiver protector [2]. In another invention made by Gang in 2013, radioactive material was used in two ways. In the first case, electron sources have been used on the tips of the cones. In the second case, the radioactive material is used as a plate next to the electrodes. These two modes are compared with each other. The radioactive substance used in this invention is Cobalt-60 and Nickel-63[3-4].

In this study, we explore the significance of five distinct pure beta sources in minimizing the breakdown voltage of the RRP. To achieve this, we analyze the dimensions and design of a commercially available receiver protector structure. Furthermore, we examine the impact of employing a radioactive beta source to lower the breakdown voltage.

Model and Simulation

In this section, we explain the simulation method of a radiation-based RRP using MCNPX, Solidworks, and CST software. First, we design the structure of the RRP using Solidworks. Then, we investigate five radioactive materials (pure beta sources) with MCNPX code. Finally, the results are used in the CST software to simulate the RRP. In Figure 1 the cross section of this structure is shown.

Waveguides, which are made in various structures such as rectangular, circular, and elliptical, are among the important structures in microwave engineering. Rectangular waveguides are more

commonly used than other shapes due to their simple construction. One of the common standards for this type of waveguide is WR90 for the X-band frequency, which has a window dimension of 0.9 inches (22.86 mm) by 0.4 inches (10.16 mm). We have used this standard waveguide in our structure. The length of the waveguide is considered 50 millimeters. In this structure, an attempt has been made to get closer to the real sample. The middle plate of the structure is 1 millimeter thick and consists of an iris plate (metal plates that are placed in the waveguide and change the effective resistance and inductance of the waveguide. This structure could be a passband filter). assembly and a cone system the angle of the cones is considered 60 degrees and the distance between the tips of the cones is 0.32 millimeters. In previous simulations performed by Yin et al., a conical structure was used in the waveguide [3].

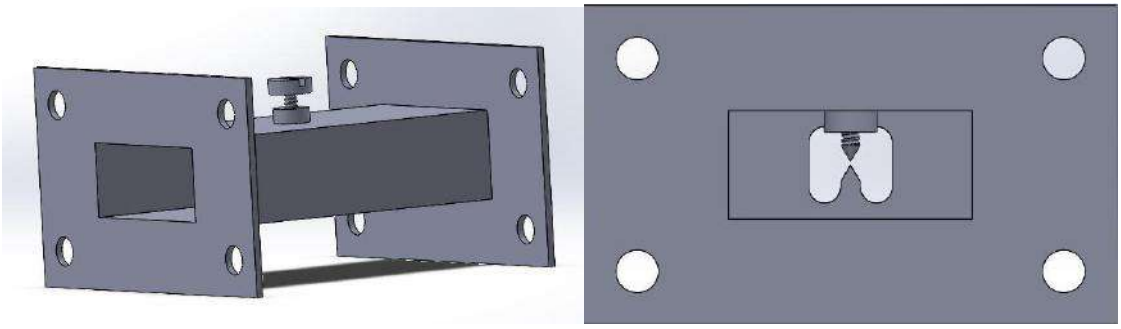

A section of the cross section in SolidWorks environment

In the MCNPX software, 5 sources of radiation (pure beta) are considered in terms of volume and energy distribution based on experimental data and the amount of energy stored in the environment, the amount of ionization and electric charge density, and the plasma frequency created by radiation can be obtained [6-13].

MCNPX is a computational code that is used to calculate the transfer parameters, energy, and momentum of neutrons, photons and electrons in different environments. Using MCNPX, we can model the shielding environment of the radar receiver using geometric shapes and calculate the amount of energy produced by the radiation sources and the energy absorbed by the Helium (He) gas. For this purpose, we have used MCNPX software version 2.6.

Results and discussion

Five radioactive materials (pure beta sources) have been selected. In Table 1 these radioactive sources are presented. The intensity for these sources in MCNPX software is considered to be one millicurie (mCi) Due to the safety and availability of the radioactive material in different intensities[4-5]. The simulation is done in standard temperature and pressure (STP) conditions and the gas inside the chamber is Helium (He). Radioactive sources are considered as gaseous and volumetric based on their respective energy spectrum in the space of the RRP.

Table 1. Pure beta sources and MCNPX result

ω_{pe}	$n_e(\frac{N}{m^3})$	Energy Deposited in cell (ev)	Half_life	Endpint energy for	Radioactive materials
294043851.8	2.72E13	7.77E9	14.28d	1.71	^{32}P
300460109.4	2.84E13	8.1E9	3.81 y	0.766	^{204}Tl
342948188.4	3.7E13	1.061E10	2.12E5 y	0.292	^{99}Tc

392238601.6	4.84E13	1.38E10	87.9 d	0.167	^{35}S
926423436.4	2.7E14	7.677E10	12.26 y	0.0186	^{3}H

To select the best source for use in the RRP device, several factors must be considered. These factors can include half-life, endpoint energy, and energy deposited in the cell.

Half-life: A source with a longer half-life can be used for a longer period. In this case, the ^{99}Tc source with a half-life of 2.12E5 years has the longest half-life.

Endpoint energy: This value can directly affect the efficiency of the source. A source with higher endpoint energy can provide the most power. In this case, the ^{32}P source with an endpoint energy of 1.71 eV has the highest endpoint energy. Considering that these sources are pure beta, it should be noted that due to the high mean free path, electron particles collide less with particles and transfer less energy.

Energy stored in the cell: This value shows how much of the source energy is stored in the cell. A source with more energy stored in the cell can have the most significant effect. In this case, the ^{3}H source with an endpoint energy of 0.0186 eV has stored the most energy in the cell. Considering the life and energy stored in the receiver protector, among the pure beta sources, the tritium source is the suitable source for reducing the breakdown voltage. For this reason, we have investigated the plasma frequency for different tritium intensities. Figure 2, examines the plasma frequency for the activity 0.1, 1 , 10 , 100 mCi of Tritium. It can be seen that with an increase in the activity of the source, the electron density and plasma frequency increase.

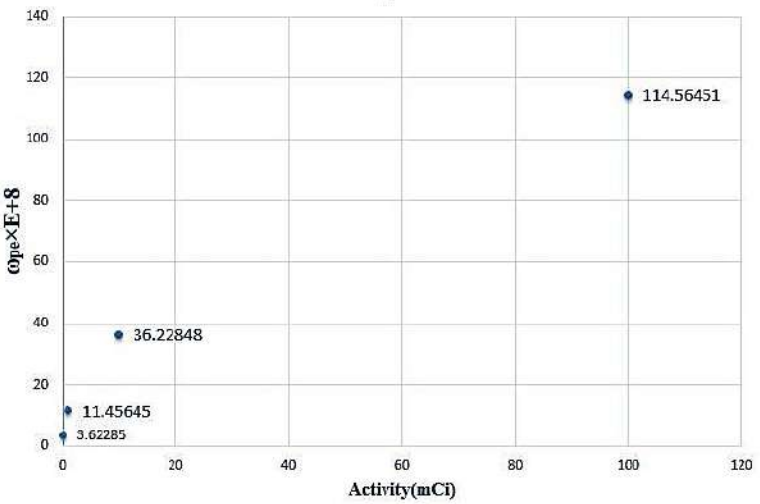

Plasma frequency according to the intensity of the tritium radiation source

In the ionized gas environment, based on the simulation results of MCNPX software and according to the ionization energy of helium gas (24.5 ev), the electron density resulting from ionization through radiation can be obtained. Plasma frequency and collision frequency can be calculated using the following relations.

$$\omega_{pe} = \sqrt{\frac{n_e e^2}{m_e \varepsilon_0}}$$

$$\gamma_c = 8.3\times10^5 \pi a^2 \sqrt{T}\, n_0$$

where n_e is electron density and e is the charge of the electron is equal to 1.6E-19 , m_e is the electron mass equal to 9.1E-31, a is the radius of the helium molecule and T is the temperature. Moreover, n_0 is the natural particle density of (He) and ε_0 is the vacuum permittivity [6].

We put the results in the CST software, then the electric field is simulated. The simulation is performed for the two cases; the simulation without the effect of radiation, and the simulation in the presence of radioactive material. Finally, we compare the results of these two cases. The figure below shows a longitudinal cut of the receiver protector in CST software.

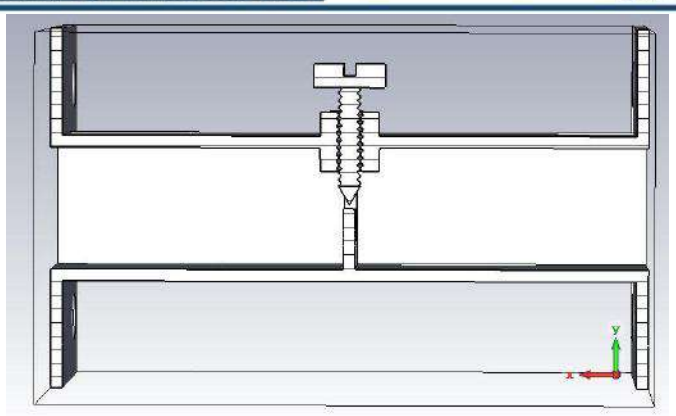

Cross-section of the receiver protector.

We use the radio frequency package and the Drude plugin, which describes the dielectric behavior of the ionized or plasma environment, and introduce the ionized environment (plasma) to the software using the values of plasma frequency and collision frequency derived earlier. Figure 4 shows the simulation of the ionized environment (He) in 8-GHz for the X-band frequency. The input wave enters the waveguide from the right side and exits from the left side.

In general, the waveguide acts as a wave filter. When the wave passes through the waveguide, In the presence of a radioactive material, a field in the opposite direction of the field caused by the input wave is formed in the ionized medium, which reduces the field intensity, which can be considered equivalent to an external applied voltage. For this ionized environment, we consider a tritium source with an intensity of one mCi and helium gas (He), and we obtain the value of the electric field in the

receiver protector. We do the same simulation is done with the same port but in the presence of the helium gas.

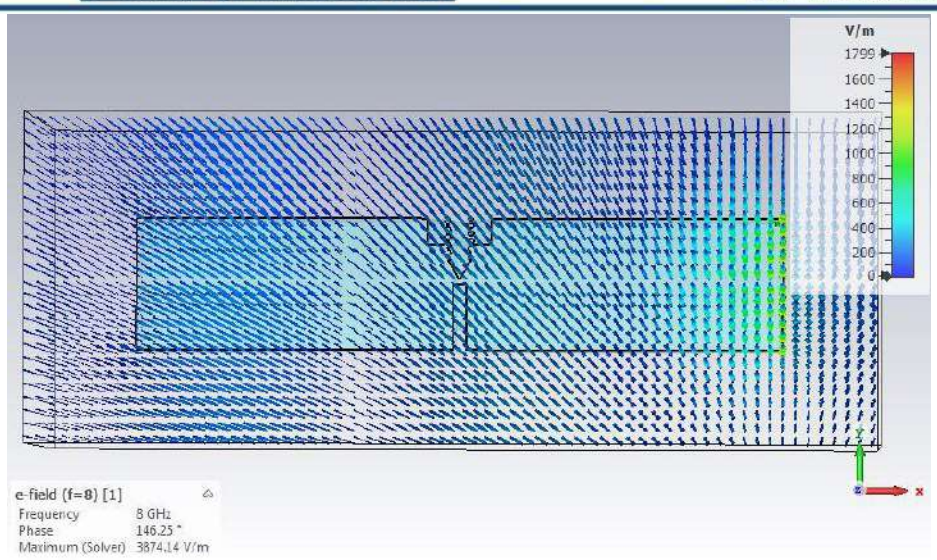

a)

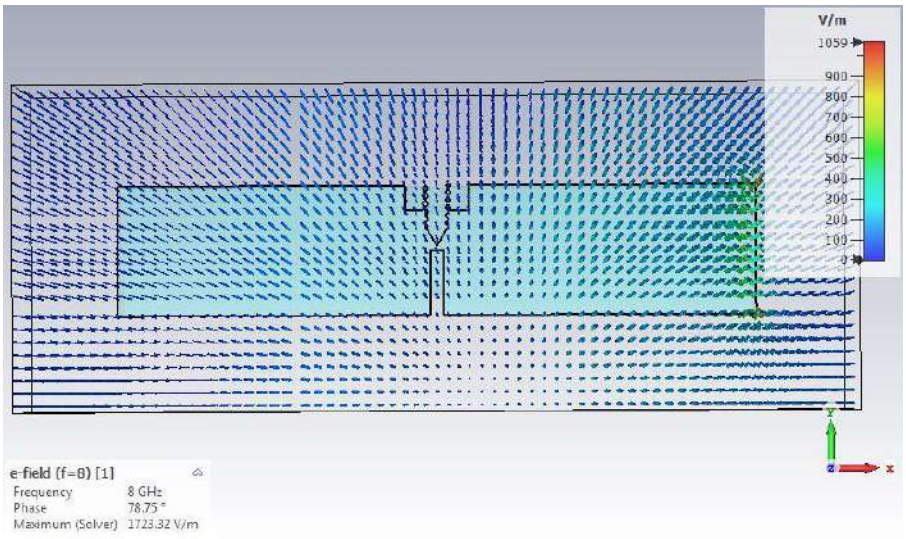

b)

Comparison of two simulation modes in CST software. a) RRP in the presence of tritium source b) RRP in the absence of radioactive material

As can be seen, the maximum electric field value for the helium gas is 1799 V/m, while for the exact same port, the maximum electric field value for helium gas with a tritium radiation source is 1059

V/m. Therefore, it can be concluded that the difference between these two electric field values is due to the effect of the radiation source in the direction of reducing the breakdown voltage. Therefore, this effect can be considered equivalent to an external applied voltage.

Conclusions

In this paper, we calculate the electric field caused by a mixture of pure beta radioactive sources with helium gas as an auxiliary electron voltage in a RRP. We use the MCNPX computational code to calculate the deposited energy and electron density at activity of 1 mCi by 5 pure beta sources and we have concluded that the tritium source has a particular advantage over other radioactive sources in term of lifetime and deposited energy in the RRP. We also investigated the electron density and plasma frequency resulting from radiation for this radioactive source at activities of (0.1, 1, 10, 100) mCi. The results show that the plasma frequency increases exponentially with increasing activity. Using the obtained plasma frequency and collision frequency, we simulated the mixed (ionized) environment using CST software and studied the electric field for the X-band input wave. The simulation results show that using a radioactive source act as a factor in reducing the breakdown voltage. By increasing the activity of the radioactive source, the deposited energy in the medium increases, then the electron density and plasma frequency in the protective environment of the receiver increase. This phenomenon can be used to improve receiver protection devices. By using radioactive material, we need less space for the RPP and its components and it also reduces the need for external high voltage.

References

[1] R. M. Harry Goldie, "RADAR RECEIVER PROTECTOR WITH AUXLARY SOURCE OF ELECTRON PRIMING," Westinghouse Electric Corp.Pittsburgh, Pa., 1978.

[2] H. Goldie, "Radioactive (tritium) ignitors for plasma limiter," IEEE Transactions on Electron Device, pp. 917-928, 1972.

[3] C.-g. a. L. S.-b. Yin, "Analysis on the effect of plasma on the transmission characteristics microwave transmit-receive switches," 2008 8th International Symposium on Antennas, Propagation and EM Theory, p. 2008, 1350-1353.

[4] "CPII," 2023. [Online]. Available: https://www.cpii.com/docs/related/4/Rad%20FAQs.pdf.

[5] N. P. &. S. W. T. Kherani, "Electron Flux at the Surface of Titanium Tritide Films," Fusion Technology, pp. 21(2P2), 334–339, 1992.

[6] V. Polyanskii, "Electromagnetic wave backscattering from a cloud of alpha-emitting radioactive elements in air," Technical Physics, vol. 27, pp. 274--276, 2000.

[7] H. Gang, "Gas discharge transmitting-receiving tube," Chengdu Guoguang Electric Co Ltd. CN103325641A. China.

[8] T. N. .. Goldie, "Receiver protection method and apparatus," CBS Corp-US3858125A, 1991.

[9] M. A. a. W. C. L. a. W. M. L. a. L. E. D. a. S. R. J. a. W. D. A. Prelas, "A review of nuclear batteries," Progress in Nuclear Energy, vol. 75, pp. 117--148, 2014.

[10] S. a. P. K. a. K. K. a. K. I. Pomm{\'e}, "On the interpretation of annual oscillations in 32Si and 36Cl decay rate measurements," Scientific Reports, vol. 11, p. 16002, 2021.

[11] J. a. M. M. I. Singh, "Challenges in Neutrino Mass Measurements," arXiv preprint arXiv:2305.12654, 2023.

[12] S. a. Z. N. a. S. S. a. A. A. a. G. N. a. F. M. H. a. T. B. a. G. P. a. S. H. a. A. M. R. Kaviani, "Design and development of a dedicated portable gamma camera system for intra-operative imaging," Physica Medica, pp. 889--897, 2016.

[13] A. a. M. A. a. B. D. a. S. E. a. K. M. a. G. G. Williart, "Study on Tl-204 simultaneous electron and photon emission spectra and their interaction with gold absorbers. Experimental results and Monte Carlo simulations," Nuclear Instruments and Methods in Physics Research Section A: Accelerators, Spectrometers, Detectors and Associated Equipment, vol. 927, pp. 435--442, 2019.

[14] G. F. Knoll, Radiation detection and measurement, John Wiley & Sons., 2010.

Iran & IAEA Project Achievement Report; Depletion of veterinary pharmaceuticals using Zinc-radioisotopes for global combatting antimicrobial resistance (Paper ID : 1528)

ICNST 2024
International Conference on Nuclear Science and Technology
6- 8 MAY 2024 | Isfahan, Iran

Yousef Fazaeli*[1], Gholamreza Shahhoseini[2], Alireza Neisi[2], James Jacob Sasanya[3], Parviz Ashtari[1], Shahzad Feizi[3]

[1]*Radiation Application Research School, Nuclear Science and Technology Research Institute (NSTRI), Moazzen Blvd., Rajaeeshahr, P.O. Box 31485-498, Karaj, Iran*
[2]*Nuclear Agriculture Research School, Nuclear Science and Technology Research Institute (NSTRI), Karaj, Iran*
[3]*Food Safety and Control Section, Joint FAO/IAEA Centre of Nuclear Techniques in Food & Agriculture, Vienna, Austria*

Abstract

Antimicrobial resistance (AMR) as one of the world's most development threats that affect public health in all regions and at all income levels. This issue needs concerted attention, because it has direct effect on the human healthcare, agriculture industries, and veterinary industries. According to World Health Organization announcement;" The misuse and overuse of antimicrobials in humans, animals and plants are the main drivers in the development of drug-resistant pathogens" (1). It was predicted by the world bank that by 2050 AMR would result in 1 trillion US$ additional healthcare costs (2). Determing the remaining residues of drugs in foods is essential in the fight against AMR. Herein, in cooperation with IAEA, new method for determining and visualizing the residues of a veterinary drug in animal matrices using zinc-radionuclides was introduced. This method is named as "Depletion Imaging". Amoxicillin was labelled with [^{62}Zn/^{65}Zn] $ZnCl_2$ and administrated to rainbow trout fish. In-vivo positron emission tomography (PET), evaluation of the amount of radiolabelled amoxicillin in fish using a high purity germanium (HPGe) nuclear detector, and Enzyme Linked Immunosorbent Assay (ELISA) technique were done. The results showed that depletion imaging and biodistribution study using zinc-62 and zinc-65 radionuclides, is a precise method for accurate determining of the drug's distribution, metabolic and excretory profile.

Keywords: Depletion imaging, zinc-65, zinc-62, antimicrobial resistance.

INTRODUCTION

According to the objectives of the Coordinated Research Project entitled "Depletion of Veterinary Pharmaceuticals and Radiometric Analysis of their Residues in Animal Matrices", prepared workplans and the 24th Codex Committee for Residues of Veterinary Drugs (CCRVDF) in foods in

[3]* Corresponding author E-mail address: yfazaeli@aeoi.org.ir

May 2018 (FAO/WHO, 2018) which identified some priority compounds for immediate attention including (but not limited to): a) Amoxicillin in goats, poultry; b) Ampicillin in cattle, pig, horse, goats, sheep, fish, poultry; c) trypanocides e.g. Diminazene in sheep, goats; d) Imidocarb in horse; Ivermectin in horse, goats, camel, poultry; e) Oxytetracyline in honey, camel, horse, and goats, this study present a new assessment protocol of Amoxicillin in fish using radiolabeled Amoxicillin. The main goal of presented project was to generate data on these scopes: (1) study on biodistribution of Amoxicillin in vital organs of fish, (2) assessment of the depletion of drug residues from edible tissues at varying time intervals following administration, (3) metabolic profile, detailed understanding of the individual components/residues of concern, (4) marker residue(s) for compliance/regulatory purposes and monitoring of appropriate drug used using novel nuclear techniques (PET Scan), and (5) identification of target tissue (s) relevant to national or regional monitoring/regulatory programs (VICH, 2012).

Amoxicillin is a penicillin antibiotic that fights bacteria and used to treat many different types of infection caused by bacteria, such as tonsillitis, bronchitis, pneumonia, and infections of the ear, nose, throat, skin, or urinary tract. Figure 1 shows the structure of Amoxicillin. Previous studies on radiolabeled amoxicillin like ^{99m}Tc-amoxicillin (short half-life radioisotopes), showed that these compounds can be suitable candidates for study of metabolic profile of amoxicillin [3]. On the other hand, utilizing of ^{65}Zn and ^{62}Zn in assessment of biological distribution of drugs help us to track the pharmaceuticals in body in both short and long time after administration [4,5]. It has already been proved that zinc cannot interfere in the action metabolism of Amoxicillin, so in this project, the radiolabeled Zinc complexes of Amoxicillin was studied [6].

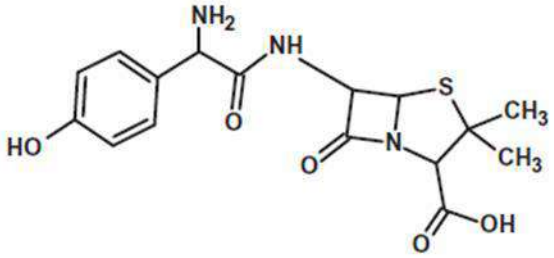

Fig. 1. Structure of Amoxicillin

EXPERIMENTAL

The preparation of pure zinc (62&65) radioisotopes, was done using pure electrodeposited copper on gold coated backings. Irradiations were carried out by means of a Cyclone-30 (IBA, Belgium) cyclotron machine in NSTRI facility in Karaj. ^{Nat} Cu(p, xn)^{62}zn/^{65}Zn was used as one of the best nuclear reactions for the production of radio-Zn. In this method impurities could be removed in the radiochemical separation process. The highly pure ^{62}Zn/^{65}Zn was eluted with 0.02 M HC1 from prepared Zn-62-Zn-65 /Cu-62 generators followed by evaporation and solving in 5mL of 2 M HCl. For radiolabeling, 0.1 ml of [^{62}Zn/^{65}Zn] $ZnCl_2$ (15 mCi) in 0.02 M HCl solution was labeled with 1.5 g of Amoxicillin. The active solution was checked for radiochemical purity by paper gamma chromatography [For detailed information please See:7]. The labeled compound was administered by oral gavage to each fish (with the mean weight of 300 g). Fish were sacrificed at different times after administration, followed by PET imaging of whole-body fish scan (Figure 2) and the internal

fish organs were taken immediately Samples of fillet (muscle) were weighed and rinsed with normal saline. The specific activities of fish fillet were determined with the HPGe detector.

Fig. 2. PET imaging of fish.

Results and discussion

Radionuclidic purity was evaluated using an HPGe γ spectrometry with characteristic peaks of ^{62}Zn at 549 keV and 596 keV and 1115 keV for ^{65}Zinc. ^{65}Zn cannot be observed after of the separation chemistry, due to the high yield of ^{62}Zn (a total yield of 5.5Ci). Results shows the highly pure ^{65}Zn (99.999%, Total yield of 19.2 mCi). The spectrum was taken 7 days after production of the radio-Zinc solution, when almost all ^{62}Zn had decayed[7].

The labelling yield of 100% is achieved. The radiochemical purity (more than 99%) of the $^{62/65}$Zn-Amox was determined by γ-paper chromatography. While the free zinc cations (in control solution) migrated to higher R_f (0.68-0.86), the Zn-Amox complex (in reaction vessel) remained at the base (Rf=0.00-0.015) Serum stability test results showed stability of the complex ([$^{65/62}$Zn] Zn-Amox).

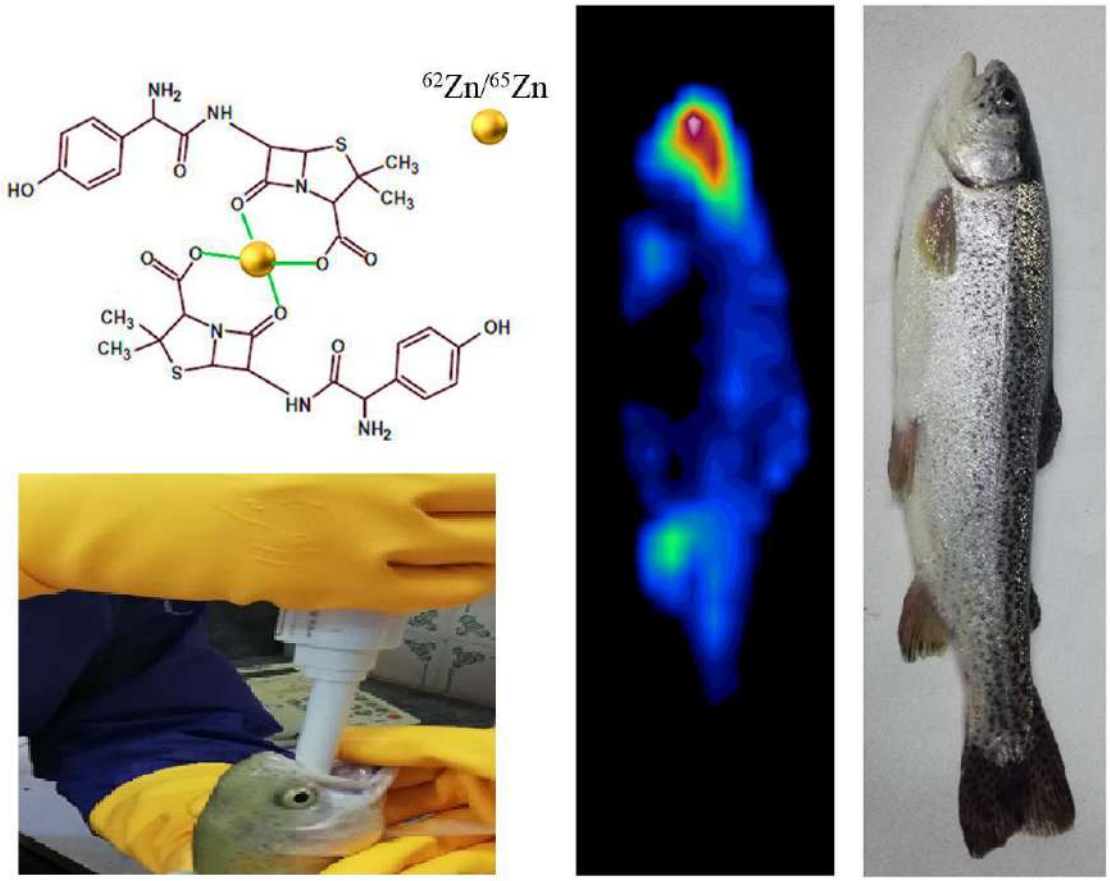

Fig. 3. Structure of Amoxicillin complex ([$^{65/62}$Zn] Zn-Amox), PET image of fish and gavage method.

Table 1, showed the remaining radiotracer and residues of Amox in fish fillet that illustrated very good correlation with residue levels of non-labelled Amox analyaed with ELISA method.

Table 1. Residues of amoxicillin (ELISA) and [$^{65/62}$Zn] Zn-Amox in fish fillet [7].

Times	30 min ^{62}Zn	60 min ^{62}Zn	120 min ^{62}Zn	180 min ^{62}Zn	210 min ^{62}Zn	24 hours ^{62}Zn	48 hours ^{62}Zn	72 hours ^{62}Zn	7 days ^{65}Zn	21 days ^{65}Zn
% of [$^{65/62}$Zn] Zn-Amox	7.2%	9.16%	14.5%	11.76%	9.1%	4.7%	2.145%	NA	0.925%	0.395%
Residues of Amox (µg/kg)	4200	3750	4050	3860	3260	3100	880	310	N.A	N.A

% of Amox	14%	12.45%	13.5%	12.86 %	10.8%	10.27%	2.93%	1.02%	N.A	N.A

Conclusions

This project introduces “Depletion imaging” for the first time according to the authors’ knowledge, as a new method for visualizing residues of veterinary drugs in animal matrices using radionuclides, while also determining total radioactive residue. The visualization method in correlation with HPGe γ-spectroscopy, showed that it is more sensitive than other routine techniques such as ELISA. This research encouraged other countries to use their cyclotrons (commonly used for human radiopharmacy) to produce radionuclides such as 62 Zn/65/Zn and facilitate radiolabelling and implementation of animal depletion studies, saving costs and time compared to the use of carbon and tritium radioisotopes. Radiolabelling with Zinc radioisotopes, depletion imaging and γ-spectroscopy are useful techniques for evaluation of depletion of veterinary pharmaceuticals. All the information about this project was now a head of print in Radiochimica acta journal [7].

Acknowledgements

This study was supported in part by the Joint FAO/IAEA Division (Centre) of Nuclear Techniques in Food & Agriculture, and Coordinated Research Project (CRP): D52043 entitled: “Depletion of Veterinary Pharmaceuticals and Radiometric Analysis of their Residues in Animal Matrices”.

References;

[1] a-https://www.who.int/news-room/fact-sheets/detail/antimicrobial-resistance,b-Antimicrobial Resistance Collaborators. (2022). Global burden of bacterial antimicrobial resistance in 2019: a systematic analysis. The Lancet; 399(10325): P629-655. DOI: https://doi.org/10.1016/S0140-6736(21)02724-0

[2] Drug-Resistant Infections: A Threat to Our Economic future (March 2027) https://www.worldbank.org/en/topic/health/publication/drug-resistant-infections-a-threat-to-our-economic-future

[3] Syeda KiranShahzadi (2019) , ^{99m}Tc-amoxicillin: A novel radiopharmaceutical for infection imaging, Arabian Journal of Chemistry, (12), 2533-2539.

[4] Ghandi M., Feizi Sh, Ziaea F, Fazaeli y, notash b (2014), Synthesis, characterization and in vivo evaluation of [62Zn]–benzo-d-sultam complex as a possible pet imaging agent, Ann Nucl Med, 28(9):880-90.

[5] McLean, J A (1985) , Elimination rate of 65Zn as a measure of food intake: a validation study in the mouse (Mus sp.) J Appl Physiol; 79(4):1361-9.

[6] https://www.drugs.com/drug-interactions/amoxicillin-with-zinc-187-0-2329-16534.

[7] Fazaeli, Y, Shahhoseini, Gh, Neisi, A, Sasanya, J., Ashtari, P and Feizi, Sh. (2024), "A novel method for evaluating the depletion of veterinary pharmaceuticals using radioisotopes" Radiochimica Acta, (aop). https://doi.org/10.1515/ract-2023-0249

ICNST 2024
International Conference on Nuclear Science and Technology
6- 8 MAY 2024 | Isfahan, Iran

Absorbed Dose Assessment of Human Organs for a Novel AntiMuc1 Radioimmunoconjugate (Paper ID : 1537)

Alirezapour B[1*], Akbari L[1]
[1]*Radiation Application Research School, Nuclear Science and Technology Research Institute, Tehran, IRAN*

Abstract

Breast cancer is the most common cancer among women worldwide. The early diagnosis of this cancer is a critical issue in treatment management. MUC1, overexpressed in the human breast ovary and other adenosarcomas, can be considered as a high potential to target this type of cancer. AntiMUC1, a newly introduced antibody which target MUC1, can effectively use for this purpose. This study aimed to estimate the human absorbed dose of the recently produced ^{111}In-DOTA-AntiMUC1 radioimmunoconjugate based on biodistribution data of the tumor-bearing mice. The radioimmunoconjugate was prepared with radiolabeling yield was > 95.0 ± 0.5% and specific activity was 170 ± 44 MBq/mg at optimized conditions and its radiochemical purity was assessed by the instant thin-layer chromatography (RTLC). Stability of the final radiolabeled complex was checked in PBS buffer (4 ºC) and human serum (37 ºC). Biodistribution of the final complex was studied in normal rats and tumor-bearing mice. Finally, the absorbed dose of human organs was estimated based on animals' data. The biodistribution study of the new radioimmunoconjugate demonstrated the high accumulation of the tracer in the MUC1+ breast tumors compared to other non-target organs at all intervals post-injection. The estimation of absorbed dose in human organs absorbed dose after injection of the complex showed the liver (0.376 mGy/MBq) and kidneys (0.237 mGy/MBq) have been received the highest amounts of the absorbed dose. Generally, it can be concluded that ^{111}In-DOTA-AntiMUC1 radioimmunoconjugate is a safe agent with a high potential for radioimmunoscintigraphy (RIS) of MUC1+ breast cancer.

Keywords: Breast Cancer, Radioimmunoconjugate, Radioimmunoscintigraphy, Absorbed dose, ^{111}In

INTRODUCTION

High incidence of breast cancer with increased mortality and morbidity along with invasive nature of this malignancy with early distant metastasis especially to the bone has been a challenge for early diagnosis and treatment. New diagnostic approaches such as radioimmunoscintigraphy (RIS) can take advantage of antibody specificity to tumor surface antigens as well as noninvasive emitted radiation from a radioisotope to the other non-target organs [1]. MUC1, a transmembrane protein

expressed on somatic cells of the secretory system, is overexpressed in the human breast ovary and other adenosarcomas and can be a suitable target to detect this type of cancer [2-4].

MUC1 is recognized by a series of antibodies, including AntiMUC1 which, was introduced by Paknejad et al.[3]. AntiMUC1 has high specific reactivity and also a high affinity to two peptides of TSA-P1-24 and A-P1-15 [3]. While, AntiMUC1 labeled ^{99m}Tc indicated good efficiency, the complex suffered from low immunoreactivity and in vitro stability in human serum [5].

Indium-111, a radionuclide-produced cyclotron, is an exciting radioisotope to radiopharmaceutical goals because of its physical properties, easy production, and availability [6]. It emits gamma photons of 173 and 247 keV; 89% and 94% intensity, respectively. Its half-life is 2.8 days that matches with monoclonal antibodies biologic half-live, makes it a favorable radionuclide in single-photon emission computed tomography (SPECT) [7-9]. The SPECT results of ^{111}In labeled bombesin, HIgG, DOTMP, and BPAMD show the usefulness of this radionuclide in the imaging detection process of SPECT [7-11]. Radiation absorbed dose defined as the amount of energy deposited in a unit mass of any organs, play a significant role in evaluating the risks associated with the administration of radiopharmaceuticals and also in determining the maximum amount of administrated activity[12]. After the development of the medical internal radiation absorbed dose (MIRD) method, as the primary method for calculating the absorbed dose, nowadays, some resources are available for this purpose. The radiation dose assessment resource (RADAR) is the most common source for the calculation of the absorbed dose [13].

In this piece of research work, the human absorbed dose of ^{111}In-DOTA-AntiMUC1, a newly developed RIS tracer, was estimated based on biodistribution studies in animals by the RADAR method. For this purpose, ^{111}In-DOTA-AntiMUC1 was prepared in optimal condition and its radiochemical purity, and in vitro and in vivo stabilities were studied. The final radiolabeled compound was injected into normal rats and tumor-bearing mice, and the biodistribution of the radioimmunoconjugate was assessed at different intervals up to 72 h post-injection. Finally, the human absorbed dose of the radiotracer was estimated based on the gathered data in animals according to the standard methods.

EXPERIMENTAL

Indium-111 was produced in Radiation Application Research School, Karaj, Iran, by 112Cd (p,2n) 111In reaction. p-SCN-Bn-DOTA (B-205)was purchased from Macrocyclics (NJ, USA). Fetal Bovine Albumin (FBS), RPMI-1640 medium, and L-Glutamine were bought from Gibco Co. (Dublin, Ireland). PD10 De-salting column was inquired from Amersham Pharmacia Biotech; additional chemicals were purchased from Sigma Chemical Co. (MO, USA). Sprague-Dawley rats were obtained from Pasteur Institute (Tehran, Iran). A Bioscan AR-2000 radio TLC scanner instrument (Bioscan, Paris, France) was used for Radio-chromatography purposes. A p-type coaxial high-purity germanium (HPGe) detector (model: EGPC 80-200R) coupled with a multichannel analyzer card system and a dose calibrator ISOMED 1010 (Dresden, Germany) were utilized for the measurement of the activity. Calculations were carried out based on the 245 keV peak for 111In. The United Kingdom Biological Council's Guidelines on the Use of the Living Animals in Scientific Investigations, 2nd edition was used to determine the framework of animal experiments. Achieved results are displayed as mean ± standard deviation (Mean ± SD), and Student's T-test was used to compare the data based on statistical significance defined as $P < 0.05$.

Production and quality control of $^{111}InCl_3$

Indium-111 was produced according to the previously reported procedure [14]. Briefly, cadmium was electroplated on a copper surface to be used as a target and irradiated by a 22 MeV proton at a 30 MeV cyclotron for 100 μAh to produce ^{111}In. Indium-111 was eluted with 1 N HCl (25 ml) as $^{111}InCl_3$ for labeling use. Radionuclidic purity of the final solution was measured by the HPGe detector. Chemical purity control was carried out to ensure that the amounts of cadmium (from target material) and copper (from target support) ions in the final solution are acceptable regarding the internationally accepted limits. Chemical purity was studied by differential-pulsed anodic stripping polarography. The radiochemical purity of the $^{111}InCl_3$ solution was also measured by the instant thin-layer chromatography method (ITLC).

Preparation and quality control of ^{111}In-DTPA-AntiMUC1

p-SCN-Bn-DOTA was conjugated with the AntiMUC1 according to the previously published method [15]. For the preparation of ^{111}In-DOTA- AntiMUC1 complex at optimized condition, 74 MBq of ^{111}In-$InCl_3$ (in 0.2 M HCl) was added to conical vials, and dried under a flow of nitrogen and gentle heating. Then, pH was arranged to 5.5 by ammonium acetate buffer. 400 μg of the bioconjugate was added to the vial and the sample was taken for 1 h at 38 °C. The radiochemical

purity of the final product was studied by instant thin-layer chromatography (ITLC) using a radio-TLC scanner (Whatman no. 2; 1 mM DTPA).

Stability tests

About 18.5 MBq of the final radioimmunoconjugate was added to the PBS buffer and freshly prepared human serum while keeping at 4°C and 37 °C, respectively. Samples were taken from the complex up to 72 h after preparation, and the stability of the final complex in PBS buffer and human serum was assessed by measuring radiochemical purity.

A mouse model with breast tumor

A few BALB/c mice with grade II/III invasive ductal carcinoma were provided from Pasteur Institute, Tehran, Iran. These mice breast tumor models were used for the development of the tumor allograft in other healthy BALB/c mice. The tumor was established by subcutaneous implantation of spontaneous breast tumor fragments (2–3 mm^3) in the right side of the abdominal region (Flank) of inbred female BALB/c mice (16–25 g, 6–8 weeks old). The bio-distribution and imaging studies were performed when the tumor volume reached 70–80 mm^3. All the animal experiments were approved by the Animal Care Committee of Tarbiat Modares University.

Biodistribution of ^{111}In-DOTA- AntiMUC1 in normal and tumor-bearing animals

3.7 MBq of ^{111}In-DOTA-AntiMUC1 was injected intravenously into Sprague-Dawley rats (140-160 g, 8-10 weeks' age) and tumoral BALB/c mice. The rats were sacrificed at 12, 24, 48, and 72 h post-injection (n=4). Their organs, including blood, liver, spleen, kidneys, stomach, small and large intestines, heart, lungs, muscle, skin, bone, and tumor were taken, rinsed with normal saline, weighted, and their activity was measured by a p-type coaxial HPGe detector. The activity of each tissue was calculated using Equation 1:[16]

$$A = \frac{N}{\epsilon\, \gamma\, t_s\, m\, k_1\, k_2 k_3\, k_4\, k_5} \qquad (1)$$

Where ε is the efficiency at photopeak energy, γ is the emission probability of the gamma line corresponding to the peak energy, t_s is the life time of the sample spectrum collection in seconds, m is the mass (kg) of the measured sample, k_1, k_2, k_3, k_4 and k_5 are the correction factors for the nuclide decay from the time the sample is collected to start the measurement, the nuclide decay during counting period, self-attenuation in the measured sample, pulses loss due to random summing and the coincidence, respectively. N is the corrected net peak area of the corresponding photopeak given as:

$$N = N_s - \frac{t_s}{t_b} N_b \qquad (2)$$

Where N_s is the net peak area in the sample spectrum, N_b is the corresponding net peak area in the background spectrum, and t_b is the life time of the background spectrum collection in seconds.

Accumulated activity calculation for animal organs

The non-decay corrected percentage of the injected activity versus time for different animal organs was plotted according to Equation 3.

$$\tilde{A} = \int_{t_1}^{\infty} A\,(t)\;dt \qquad (3)$$

Where *A(t)* is the activity of each organ at time t.

The curves were extrapolated to infinity by fitting the tail of each curve to a monoexponential curve with the exponential coefficient equal to the physical decay constant of the indium-111 radionuclide. Whereas the activity of blood at t=0 was considered the total amount of the injected activity, the activity of all other organs was assumed to be zero at that time.

Estimation of accumulated activity for human organs

Sparks et al. method was used to extrapolate the cumulated activity for animal organs to the cumulated activity for human organs (Equ. 4) [17]. The standard mean weights for each human organ were utilized for the extrapolation [18].

$$\tilde{A}_{Human\ organ} = \tilde{A}_{Animal\ organ} \times \frac{Organ\ mass_{human}/Body\ mass_{human}}{Organ\ mass_{animal}/Body\ mass_{animal}} \qquad (4)$$

Equivalent absorbed dose calculation

RADAR formalism was used for the calculation of the absorbed dose in human organs based on biodistribution data in rats:

$$D = \tilde{A} \times DF \qquad (5)$$

Where $\tilde{A}$ is the accumulated activity for each human organ, and DF is:

$$DF = \frac{k \sum_i n_i E_i \phi_i}{m} \qquad (6)$$

In this equation, n_i is the number of radiations with energy E emitted per nuclear transition, $E_i$is the energy per radiation (MeV), ϕ_i is the fraction of energy emitted that is absorbed in the target, m is the mass of the target region (kg), and k is some proportionality constant ($\frac{\mathrm{mGy,kg}}{\mathrm{MBq,s,MeV}}$). In this research, DFs presented in OLINDA/EXM software were employed[19].

Calculation of effective absorbed dose

The effective absorbed dose was calculated using Equation 7.

$$E = \sum_T W_T H_T \quad (7)$$

Where H_T is the equivalent absorbed dose for each organ and W_T is the tissue-weighting factor and obtained from the reported value in ICRP 103[20].

Results and discussion

Quality Control of ^{111}In chloride solution

The HPGe spectrum of $^{111}InCl_3$ showed the presence of 171 and 245 keV gamma energies, all originating from ^{111}In. The radionuclidic purity of > 99.9 % was demonstrated. The result of polarography showed the concentrations of cadmium and copper were below the internationally accepted levels, i.e., 0.1 ppm[21]**.** The radiochemical purity of the $^{111}InCl_3$ sample investigated by the ITLC method, showing a purity of more than 99 %. The free ^{111}In moves to higher Rf in the DTPA mobile phase and remains at the origin in the 10 % ammonium acetate:methanol mixture (1:1) solution.

Preparation and quality control of ^{111}In-DOTA-PR81

^{111}In-DOTA-AntiMUC1 was prepared with radiochemical purity of greater than 98 % at optimized conditions. ITLC chromatograms of ^{111}In and ^{111}In-DOTA-AntiMUC1 are indicated in Fig.1. While the free cation migrates to higher R_f (0.8), the radiolabeled compound remains at the origin (Fig.1).

Biodistribution of the Complex in normal and tumor-bearing animals

The percentage of the injected dose per gram in animal organs was calculated up to 72 h after injection of ^{111}In-DOTA-AntiMUC1. The non-decay corrected clearance curves from the main organ sources of the animals for the radiolabeled compound are shown in Fig. 2 that indicated high uptake of the tumor compared to other non-target organs.

Equivalent absorbed dose calculation

In this study, human organ absorbed dose was estimated based on the animals' data which is a prerequisite in radiopharmaceutical development and is suggested in the ICRP 62 recommendations[22, 23]. For this purpose, RADAR and Spark et al. methods were utilized in similarity to the previously reported literature [24, 25,26]. The values of absorbed dose in different human organs were represented in Table 1.

As shown, the highest amounts of the absorbed dose after injection of the radiolabeled compound was observed in the liver, kidneys, and spleen with 0.376, 0.237, and 0.143 mGy/MBq, respectively. Also, the effective absorbed dose in humans after injection of ^{111}In-DOTA-AntiMUC1 was estimated as 0.044 mGy/MBq. As a result, this new radiolabeled compound can be regarded as a safe complex and a suitable alternative for SPECT imaging of the MUC1+ breast tumors; however, further studies are still needed.

Table 1 Equivalent and effective absorbed dose delivered into human organs after injection of ^{111}In-DOTA-AntiMUC1

Target Organs	Equivalent absorbed dose in humans (mGy/MBq)	Wt[a]	Effective absorbed dose in humans (mSv/MBq)
Adrenals	0.087	0.12	0.0104
Brain	0.007	0.01	0.0001
GB Wall	0.112	0.12	0.0134
LLI Wall	0.058	0.12	0.0069
Small Int	0.027	0.12	0.0032
Stomach Wall	0.061	0.12	0.0073
ULI Wall	0.034	0.12	0.0041
Heart Wall	0.129	0.12	0.0155
Kidneys	0.237	0.12	0.0284
Liver	0.376	0.04	0.0150
Lungs	0.192	0.12	0.0230
Muscle	0.029	0.12	0.0035
Pancreas	0.079	0.12	0.0095
Red Marrow	0.035	0.12	0.0042
Bone Surf	0.041	0.01	0.0049
Spleen	0.143	0.12	0.0172
Testes	0.014	0.12	0.0017
Thymus	0.034	0.12	0.0041
Thyroid	0.014	0.04	0.0006
UB Wall	0.012	0.04	0.0005
Total Body	0.044		0.044

GW: Gallbladder Wall; LLI: lower large intestine; Int: Intestine; ULI: upper large intestine; UB Wall: Urinary Bladder Wall.

[a] Tissue weighting factors according to international commission on radiological protection, ICRP 103 (2007).

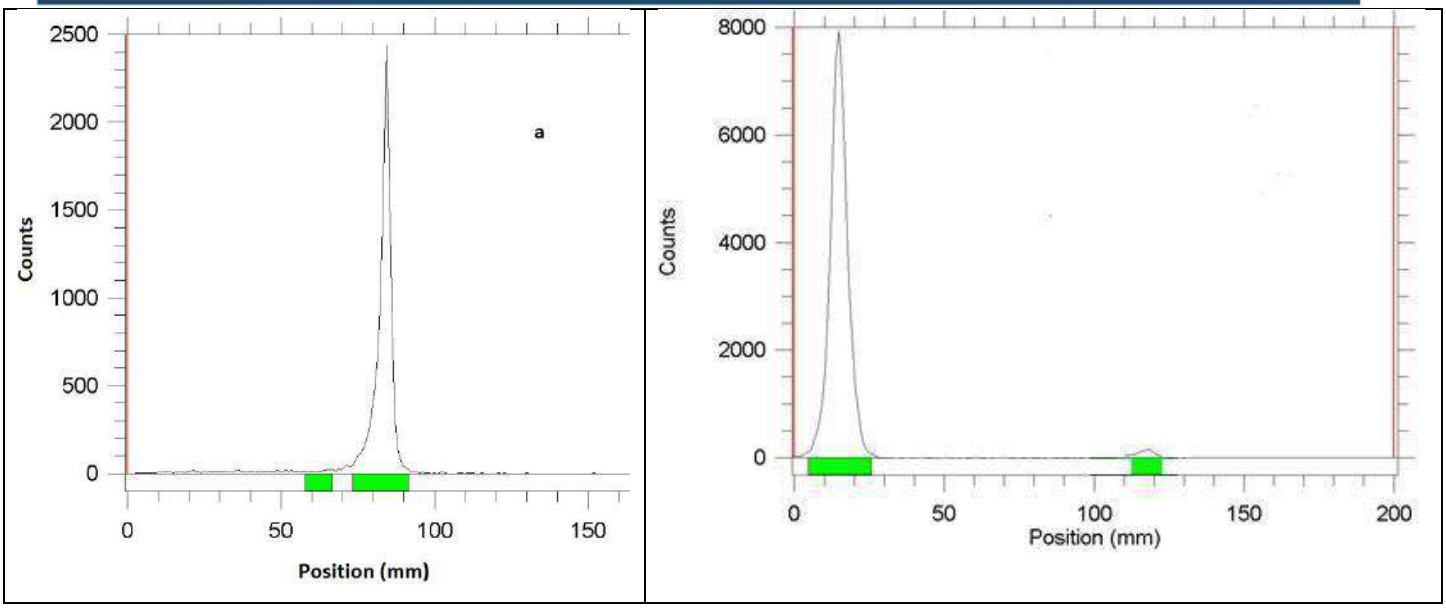

Fig. 1. Radiochromatogram of free $^{111}In^{3+}$ (a) and ^{111}In-DOTA-AntiMUC1 (b) using Whatman No. 2 in 1 mM DTPA, pH 5.0 (n=3).

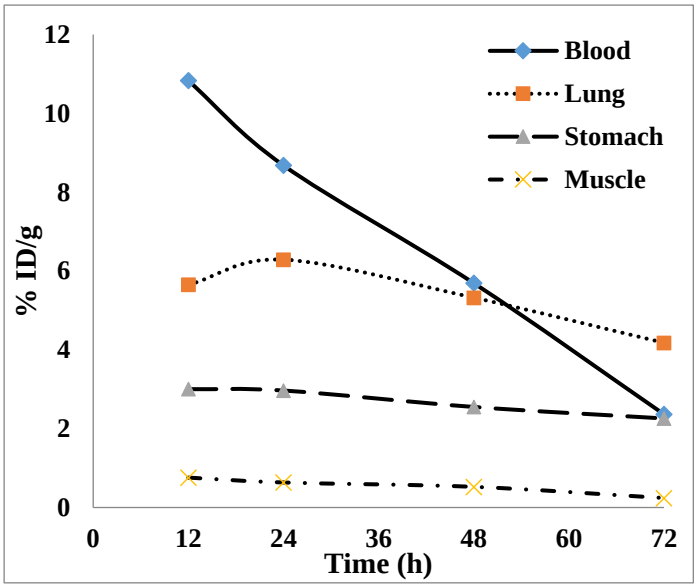

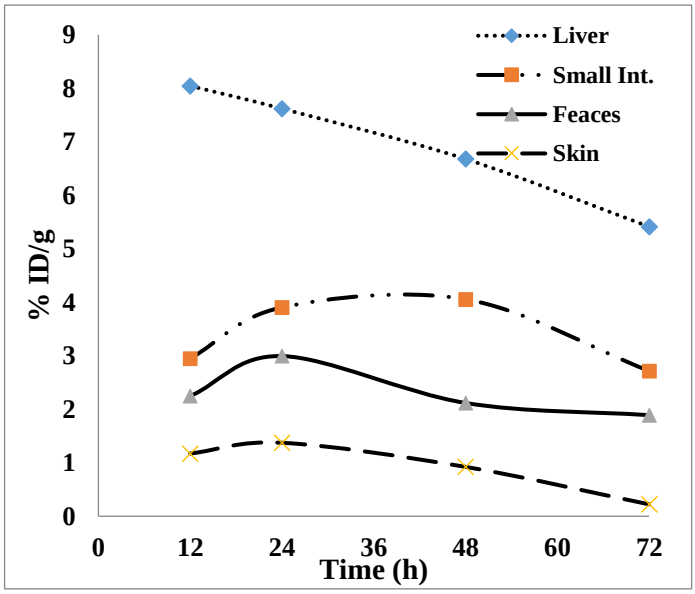

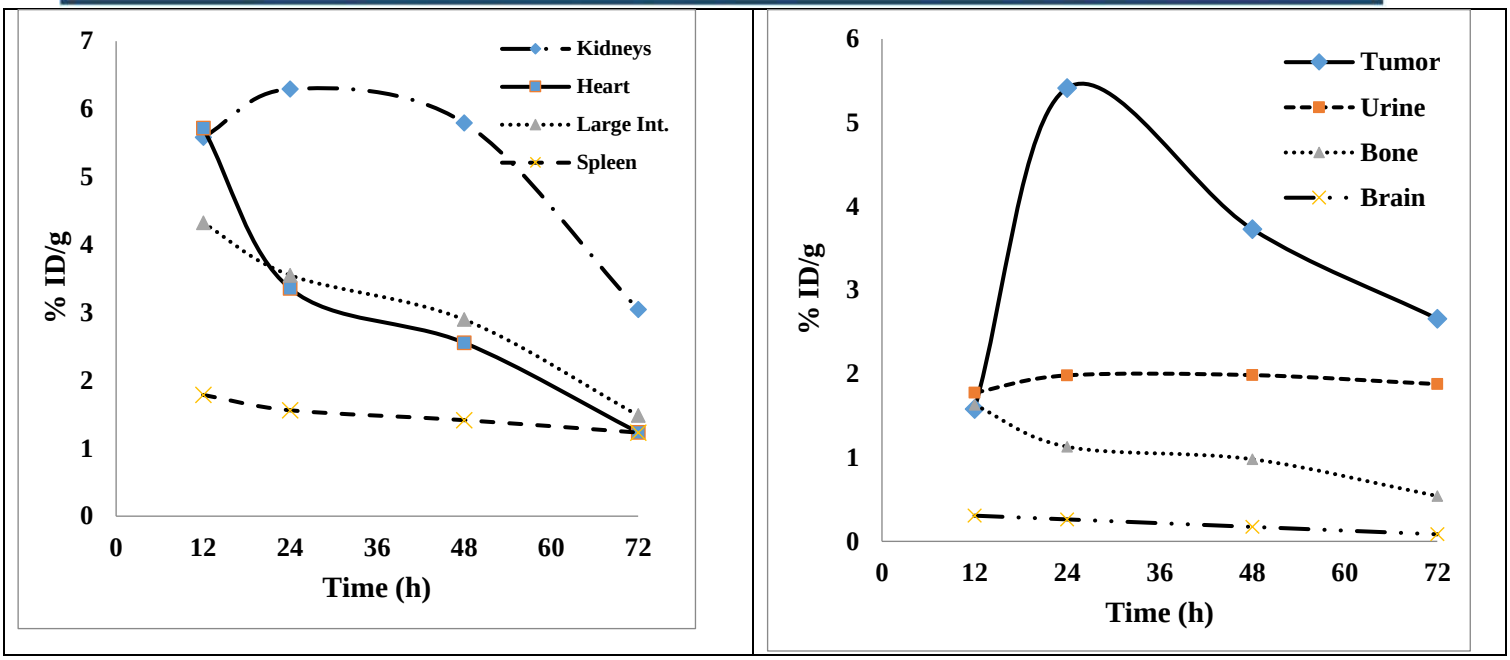

Fig. 2. Non-decay corrected clearance curves of the animals' organs after injection of ^{111}In-DOTA-AntiMUC1 complex

Differentradiopharmaceuticals,including 18F-FES, 18F-FDHT, 111In-trastuzumab, and 111In-pentetreotide have been developed and used for breast cancer imaging. The values of the effective absorbed dose and the absorbed dose of critical organs (who received the highest amount) after injections of these radiolabeled compounds are presented in Table 2

Table 2 The values of the effective absorbed dose and the absorbed dose of organs received the highest dose after injection of ^{18}F-FES, ^{18}F-FDHT, ^{111}In-trastuzumab, ^{111}In-pentetreotide and ^{111}In-DOTA-Anti-MUC1

Radiolabeled compound	Absorbed dose (mGy/MBq)	Effective absorbed dose (mSv/MBq)	Reference
^{18}F-FES	Liver: 0.13 Gallbladder: 0.10 Urinary bladder: 0.05	0.022	[27]
^{18}F-FDHT	Urinary bladder: 0.061	0.020	[28]

^{111}In-trastuzumab	Liver: 0.598 Spleen: 0.360	0.185	[29]
^{111}In-pentetreotide	Spleen: 0.57 Kidneys: 0.41 Liver: 0.1	0.054	[29]
^{111}In-DOTA-PR81	Liver: 0.376 Kidneys: 0.237 Spleen: 0.143	0.044	This study

Conclusions

In this study, ^{111}In-DOTA-AntiMUC1 was prepared with radiochemical purity of >98%. High uptake of the complex in MUC1+ breast tumors compared to other non-target organs shows that the radioimmunoconjugate is a beneficial agent for SPECT imaging of MUC1+ breast cancer. Human organs absorbed dose of the complex was estimated based on animals' data according to the RADAR and Spark et al. methods. The highest amounts of the absorbed dose are in the liver (0.376 mGy/MBq) and kidneys (0.237 mGy/MBq), respectively. ^{111}In-DOTA-AntiMUC1 radioimmunoconjugate is a high potential agent for MUC1+ breast cancer SPECT imaging, and estimated absorbed dose values could helpfully utilize for determining the maximum injectable dose.

References

[1] Clarke CA, Glaser SL, West DW, Ereman RR, Erdmann CA, Barlow JM, et al. (2002) Breast cancer incidence and mortality trends in an affluent population: Marin County, California, USA, 1990–1999. Breast Cancer Res, 4:1-7.

[2] Gendler S, Taylor-Papadimitriou J, Duhig T, Rothbard J, Burchell J. (1988) A highly immunogenic region of a human polymorphic epithelial mucin expressed by carcinomas is made up of tandem repeats. J. Biol. Chem, 263:12820-3.

[3] Paknejad M, Rasaee MJ, Tehrani FK, Kashanian S, Mohagheghi MA, Omidfar K, Bazl MR. (2003) Production of monoclonal antibody, PR81, recognizing the tandem repeat region of MUC1 mucin. Hybrid Hybridomics, 22:153-8.

[4] Salouti M, Babaei MH, Rajabi H, javad Rasaee M. (2011) Preparation and biological evaluation of ^{177}Lu conjugated PR81 for radioimmunotherapy of breast cancer. Nucl Med Biol, 38:849-55.

[5] Salouti M, Rajabi H, Babaei MH, Rasaee MJ. (2008) Breast tumor targeting with 99mTc-HYNIC-PR81 complex as a new biologic radiopharmaceutical. Nucl Med Biol, 35:763-8.

[6] Yousefnia H, Zolghadri S, Jalilian AR. (2015) Preparation and biodistribution assessment of 111In-BPAMD as a novel agent for bone SPECT imaging. Radiochim Acta, 103:653-61.

[7] Yousefnia H, Zolghadri S. (2015) Human Absorbed Dose Estimation of a New IN-111 Imaging Agent Based on Rat Data. JPMS, 9(10):627-31.

[8] Zhou Z, Wagh NK, Ogbomo SM, Shi W, Jia Y, Brusnahan SK, et al. (2013) Synthesis and in vitro and in vivo evaluation of hypoxia-enhanced 111In-bombesin conjugates for prostate cancer imaging. J Nucl Med, 54:1605-12.

[9] Nijhof MW, Oyen WJ, Kampen Av, Claessens RA, van der Meer JW, Corstens FH. (1997) Evaluation of infections of the locomotor system with indium-111-labeled human IgG scintigraphy. J Nucl Med, 38:1300-5.

[10] Lai J, Quadri SM, Borchardt PE, Harris L, Wucher R, Askew E, et al. (1999) Pharmacokinetics of radiolabeled polyclonal antiferritin in patients with Hodgkin's disease. Clin Cancer Res, 5:3315-23.

[11] Yousefnia H, Zolghadri S, Jalilian AR. (2015) Preparation and biodistribution assessment of ^{111}In-BPAMD as a novel agent for bone SPECT imaging. Radiochimica Acta, 103:653-61.

[12] Stabin M, Tagesson M, Thomas S, Ljungberg M, Strand S-E. (1999) Radiation dosimetry in nuclear medicine. Appl Radiat Isot, 50:73-87.

[13] Stabin MG, Siegel JA. (2003) Physical models and dose factors for use in internal dose assessment. Health Phys, 85:294-310.

[14] Yousefnia H, Jalilian AR, Zolghadri S, Mirzaei A, Bahrami-Samani A, Mirzaii M, et al. (2015) Development of ^{111}In DOTMP for dosimetry of bone pain palliation agents. J Radioanal Nucl Chem, 304-911-6.

[15] Alirezapour B, Rasaee MJ, Jalilian AR, Rajabifar S, Mohammadnejad J, Paknejad M, et al. (2016) Development of [64Cu]-DOTA-PR81 radioimmunoconjugate for MUC-1 positive PET imaging. Nucl Med Biol, 43:73-80.

[16] IAEA-TECDOC-1401.Quantifying uncertainty in nuclear analytical measurements Austria, Vienna: IAEA; 2004.

[17] Sparks R, Aydogan B. (1999) Comparison of the effectiveness of some common animal data scaling techniques in estimating human radiation dose: Oak Ridge Associated Universities, TN (United States).

[18] Yousefnia H, Zolghadri S, Jalilian AR, Tajik M, Ghannadi-Maragheh M. (2014) Preliminary dosimetric evaluation of 166Ho-TTHMP for human based on biodistribution data in rats. Appl Radiat Isot, 94:260-5.

[19] Stabin MG, Sparks RB, Crowe E. (2005) OLINDA/EXM: the second-generation personal computer software for internal dose assessment in nuclear medicine. J Nucl Med, 46:1023-7.

[20] The 2007 Recommendations of the International Commission on Radiological Protection. ICRP publication 103. Ann ICRP. 2007;37(2.4):2.

[21] United States Pharmacopoeia 28, NF 23, p.1895.

[22] Kesner AL, Hsueh W-A, Czernin J, Padgett H, Phelps ME, Silverman DH. (2008) Radiation dose estimates for [18 F] 5-fluorouracil derived from PET-based and tissue-based methods in rats. Mol Imaging Biol, 10:341-8.

[23] Radiological Protection in Biomedical Research. ICRP Publication 62. Ann. ICRP 1992;22 (3).

[24] Vaez-Tehrani M, Zolghadri S, Yousefnia H, Afarideh H. (2016) Estimation of human absorbed dose for 166Ho-PAM: comparison with ^{166}Ho-DOTMP and 166Ho-TTHMP. Br J Radiol, 89:20160153.

[25] Yousefnia H , Zolghadri S , Jalilian AR. (2015) Absorbed dose assessment of ^{177}Lu-zoledronate and 177Lu-EDTMP for human based on biodistribution data in rats. J Med Phys, 40: 102–8.

[26] Shanehsazzadeh S, Lahooti A, Yousefnia H, Geramifar P, Jalilian AR. (2015) Comparison of estimated human dose of (68)Ga-MAA with (99m)Tc-MAA based on rat data. Ann Nucl Med, 29:745-53.

[27]. McCall K, Abbott A, Hu J, Cheng SC, Kravets S, Dubey S, et al. Report on the PET/CT image-based radiation dosimetry of 18FDHT in women, an imaging agent with new applications for evaluation of androgen receptor status in patients with metastatic breast cancer. J Nucl Med. 2019;60:1630.

[28]. Gaykema SB, de Jong JR, Perik PJ, Brouwers AH, Schröder CP, Oude Munnink TH, et al. (111)In-trastuzumab scintigraphy in HER2-positive metastatic breast cancer patients remains feasible during trastuzumab treatment. Mol Imaging. 2014;13:1–6.

[29]. Bombardieri E, Ambrosini V, Aktolun C, Baum RP, Bishof-Delaloye A, Del Vecchio S, et al. 111In-pentetreotide scintigraphy: Procedure guidelines for tumour imaging. Eur J Nucl Med Mol Imaging. 2010;37:1441–8.

ICNST 2024
International Conference on Nuclear Science and Technology
6- 8 MAY 2024 | Isfahan, Iran

Determining the effective atomic number of some composite materials using MCNP simulation (Paper ID : 1541)

Sabouri Gerdeh H.[1*], Zolfagharpour F.[1], Jalili Torkamani M.[1]
1 Department of Physics, Faculty of Science, University of Mohaghegh Ardabili, Ardabil, Iran

Abstract

During the interaction of photons with matter, the effective atomic number (Z_{eff}) is an important factor in obtaining information about a sample. However, determining the Z_{eff} of alloys and low Z compound materials presents a challenging problem. While there are several methods available for calculating the Z_{eff} of compound materials, many of them are complex and destructive. In contrast, nuclear techniques are convenient and non-destructive. Furthermore, the Monte Carlo simulation method allows for the study of various materials and compounds without direct access to them. In this research, the MCNP simulation method was used to determine the Z_{eff} of compound materials. By scattering configuration in MCNP simulation, the R/C ratio of elements and compound materials extracted and their fit function calculated. Using this equation and the R/C ratio of compound materials, Z_{eff} was calculated for compound materials. The simulation results demonstrated a strong correlation with the theoretical data, indicating the effectiveness of the simulation method in determining the Z_{eff} of compound materials.

Keywords: MCNP, Effective atomic number, Photon scattering

INTRODUCTION

The fundamental interactions between photons and matter include photoelectric absorbtion, scattering (both coherent and incoherent) and pair production. During coherent scattering, the atomic bound electron absorbs the incident photon and emits it again with the same frequency. This occurs while the atom is neither ionized nor excited. In contrast, Compton scattering (incoherent scattering) is the interaction between an incident photon and an atomic free electron, during which the energy of the scattered photon changes and the atom is ionized.

The effective atomic number (Z_{eff}) is a crucial parameter for materials when interacting with radiation, which is used to determine their dosimetric properties [1]. Z_{eff} can be obtained for compound materials through various methods, such as X-ray fluorescence and fast neutron activator analysis [2]. However, many of these methods are destructive and complicated. Additionally, some of them are not able to accurately determine the Z_{eff} of light elements. In contrast, absorbtion and

scattering of radiation are nuclear techniques that are simpler than the aforementioned methods and are widely used to determine the effective atomic number of compound materials. The absorbtion method is commonly used to determine the effective atomic number (Z_{eff}) of materials by calculating the mass attenuation coefficient. However, this method has limitations due to the characteristics of the sample and experimental setup, making it difficult to accurately determine Z_{eff} for light elements and materials. In contrast, the scattering method, specifically the Rayleigh to Compton scattering ratio (R/C), is not affected by the physical properties of the materials or experimental geometry. Instead, it is highly sensitive to changes in the atomic number (Z) of the target material. These characteristics make the scattering method a suitable choice for investigating the Z_{eff} of materials [3,4]. Due to its simplicity and efficiency, the R/C method has been widely used by researchers for various medical and industrial purposes [5-7].

The simulation method provides a wide platform for researchers, enabling the use of various materials or sources with different energies based on our specific goals. One of the most frequently used nuclear simulation codes in this field is the Monte Carlo N particle transport code (MCNP). Researchers have also employed this code to calculate the Z_{eff} of compound materials [8,9], but all of them have used the absorbtion method.

In this study, our main goal is to determine the effective atomic number (Z_{eff}) of compound materials through the utilization of the MCNP code and R/C ratio method. The R/C ratio of elements and compound materials will be investigated using a 70 degree scattering configuration in the MCNP code. The Z_{eff} of compound materials will be determined by comparing the R/C ratio of known Z elements and their corresponding fit function.

RESEARCH THEORIES

Coherent scattering is most prominent in materials with high atomic numbers and at low energy and scattering angles. The differential Rayleigh scattering cross-section is obtained through the atomic form factor (F(x,z)) and the differential Thomson scattering cross-section per electron

$$\frac{d\sigma_R}{d\Omega} = \frac{d\sigma_T}{d\Omega}|F(x\ z)|^2 = \frac{{r_0}^2}{2}(1 + cos^2\theta)|F(x\ z)|^2 \quad (1)$$

Where r_0, θ, x are the classical radius of the electron, the scattering angle and the momentum transferred to the electron respectively.

The incoherent scattering cross-section is also obtained by modifying the Klein-Nishina relation for free electrons.

$$\frac{d\sigma_C}{d\Omega} = \frac{d\sigma_{KN}(\alpha\ \theta)}{d\Omega} S(x\ z) \quad (2)$$

In this equation, α is the incident photon energy in units of the electron rest mass energy and S(x,z) is the incoherent scattering function (correction factor). The R/C ratio is obtained as follows [10,11].

$$\frac{R}{c} = \frac{N_{coherent}}{N_{incoherent}} = \frac{d\,\sigma_R/d\,\Omega}{d\,\sigma_{KN}/d\,\Omega} \propto \frac{|F(x\ z)|^2}{S(x\ z)} \quad (3)$$

Where $N_{coherent}$ and $N_{incoherent}$ are the number of coherent and incoherent scattered gamma rays, respectively. Therefore, for constant energy and experimental setup, the R/C ratio will only be a function of a material's atomic number

$$\frac{R}{C} \propto F(z) \quad (4)$$

This equation shows a significant relationship between the R/C ratio and the atomic number.

Simulation

Our main objective is to determine the effective atomic number (Z_{eff}) of compound materials by extracting the R/C ratio of various materials through MCNP simulation. The MCNP code is widely used for simulating the transport of neutrons and photons, making it a valuable tool in various scientific and engineering fields. In this study, we utilized the MCNPX version, which includes a wide range of materials and their corresponding cross-sections. The simulation geometry is shown in Fig.1. We made efforts to closely match the simulation with the experimental conditions. To achieve this, we modeled the High Purity Germanium (HPGe) detector as a pure Ge cylinder, which was then covered with a lead shield. The radioactive source used was Americium-241, emitting 59.54 KeV gamma rays. These gamma rays were scattered from the sample at a 70-degree angle and then

detected by the HPGe detector for counting. To match our simulation with real conditions, we used F8 tally in code to get the gamma spectrum in output.

Fig.1. Configuration designed for MCNP simulation code

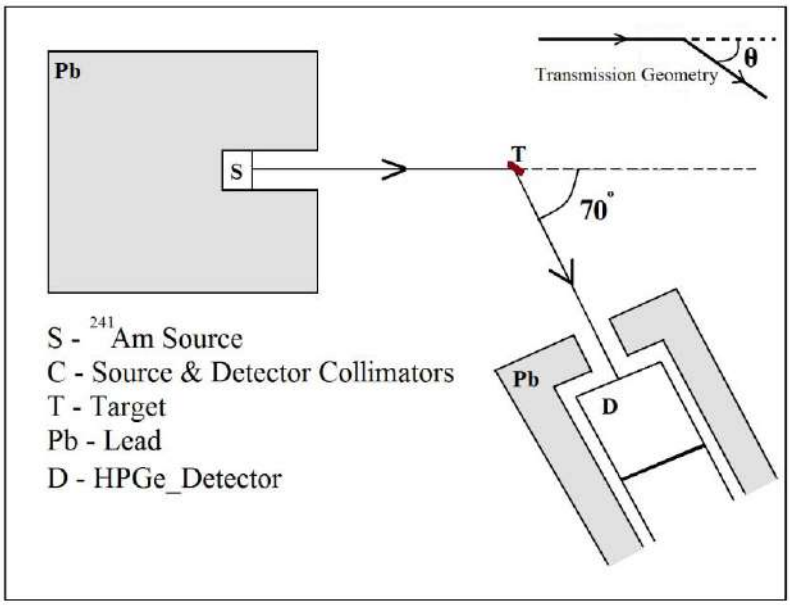

Indicator materials were selected from among 10 elements between 6<Z<82 (light to heavy elements). On the other hand, Brass, Solder, Bakelite, Glucose and Oxalic Acid were considered as compound materials. The R/C ratio of all elements and compound materials, which we introduced in the input of the MCNP code, was obtained from MCNP simulation results. From the results, the R/C ratio of the index materials was used to calculate the best fit function, which can be used to determine the Z_{eff} of compound materials.

Results and discussion

Using the spectrum obtained from the simulation results, we extracted the intensity of the photons that reached the detector after rayleigh and compton scattering at a scattering angle of 70-degrees, respectively, by calculating the area under the corresponding peaks. The ratio of these intensities, allowed us to calculate the R/C ratio for the target samples. This process was repeated for both individual elements and compound materials. Our comparison of the R/C ratios for the elements revealed that, as expected according to relation (3), the R/C ratio increases with increasing atomic number (Z). From this relationship, we then obtained the fit function through spectrum analysis

software. The best fit function, as shown below, includes a wide range of atomic numbers to present this relationship.

$$\frac{R}{C} = a + bz^3 + c\left(ln(z)\right)^2 \quad (5)$$

Where a, b, c are fitting constants that have the values of $-0{,}071\ \ 3{,}30 \times 10^{-6}\ \ 0{,}022$ respectively. The Z_{eff} value of the compound materials was determined using this fitting function, as shown in table.1. To validate our work, we compared our simulation results with theoretical and experimental results from other articles [2,12]. The percentage of the relative difference between theoretical and simulation results is presented in the last column of Table.1, which illustrates the good agreement between the two methods.

Table.1. MCNP, theory and Experimental values of Z_{eff} with the percentage of the relative differences between theory and simulation values

Compound	Experiment	Theory	ref	Our results	
				MCNP	Relative difference
Brass	27.60	29.10	[7]	29.61	1.76 %
Solder	64.90	66.40	[7]	63.79	3.93 %
Bakelite	5.50	6.60	[7]	6.48	1.82 %
Glucose	6.18	6.78	[22]	7.01	3.45 %
Oxalic Acid	7.37	7.28	[22]	7.82	7.40 %

Conclusions

This study presents a new method for determining the Z_{eff} of compound materials by calculating their R/C ratio through the MCNP code. The results of this method are in good agreement with theoretical values, with a relative difference of less than %8 and show an effective performance for low Z materials. Even in many compound materials, the simulation results are better than experimental data. The results demonstrate the effectiveness of the presented method in obtaining the Z_{eff} of compound materials.

References

[1] Thanh, T.T., Cuong, N.Q.B., Chuong, H.D., Thong, N.D., Nguyen, V.H., Ho, P.L., Tai, C.T. and Van Tao, C., 2020. Study of different methods to estimate the Rayleigh to Compton scattering ratio and the effective atomic number (10< Z< 30) using Si (Li) detector. Nuclear Instruments and

Methods in Physics Research Section A: Accelerators, Spectrometers, Detectors and Associated Equipment, 969, p.163995.

[2] Singh, M.P., Sandhu, B.S. and Singh, B., 2007. Measurement of the effective atomic number of composite materials using Rayleigh to Compton scattering of 279 keV gamma rays. Physica Scripta, 76(4), p.281.

[3] Schätzler, H.P., 1979. Basic aspects on the use of elastic and inelastic scattered gamma radiation for the determination of binary systems with effective atomic numbers of less than 10. The International Journal of Applied Radiation and Isotopes, 30(2), pp.115-121.

[4] Mossop, J.R., Kerr, S.A., Bradley, D.A., Chong, C.S. and Ghose, A.M., 1987. The use of coherent gamma-ray scattering for the characterisation of materials. Nuclear Instruments and Methods in Physics Research Section A: Accelerators, Spectrometers, Detectors and Associated Equipment, 255(1-2), pp.419-422.

[5] Pereira, M.O., de Carvalho Conti, C., dos Anjos, M.J. and Lopes, R.T., 2012. Correction of radiation absorption on biological samples using Rayleigh to Compton scattering ratio. Nuclear Instruments and Methods in Physics Research Section B: Beam Interactions with Materials and Atoms, 280, pp.39-44.

[6] Gobo, M.S., Soares, L.D.H. and Poletti, M.E., 2020. Effective atomic number of breast tissues determined by transmission and scattering methods. Radiation Physics and Chemistry, 167, p.108260.

[7] Antoniassi, M., Conceição, A.L.C. and Poletti, M.E., 2014. Rayleigh to Compton ratio scatter tomography applied to breast cancer diagnosis: A preliminary computational study. Radiation Physics and Chemistry, 95, pp.288-291.

[8] Rammah, Y.S., Mahmoud, K.A., Mohammed, F.Q., Sayyed, M.I., Tashlykov, O.L. and El-Mallawany, R., 2021. Gamma ray exposure buildup factor and shielding features for some binary alloys using MCNP-5 simulation code. Nuclear Engineering and Technology, 53(8), pp.2661-2668.

[9] Hamad, M.K., Mhareb, M.H.A., Alajerami, Y.S., Sayyed, M.I., Saleh, G., Maswadeh, Y. and Ziq, K., 2020. Radiation shielding properties of Nd0. 6Sr0. 4Mn1− yNiyO3 substitute with different concentrations of nickle. Radiation Physics and Chemistry, 174, p.108920.

[10] Duvauchelle, P., Peix, G. and Babot, D., 1999. Effective atomic number in the Rayleigh to Compton scattering ratio. Nuclear Instruments and Methods in Physics Research Section B: Beam Interactions with Materials and Atoms, 155(3), pp.221-228.

11] Hubbell, J.H., Veigele, W.J., Briggs, E.A., Brown, R.T., Cromer, D.T. and Howerton, D.R., 1975. Atomic form factors, incoherent scattering functions, and photon scattering cross sections. Journal of physical and chemical reference data, 4(3), pp.471-538.

[12] Hosamani, M.M. and Badiger, N.M., 2018. Determination of effective atomic number of composite materials using backscattered gamma photons–a novel method. Chemical Physics Letters, 695, pp.94-98.

ICNST 2024
International Conference on Nuclear Science and Technology
6- 8 MAY 2024 | Isfahan, Iran

Automatic segmentation of lung, bone and soft tissue based on CT scan images using deep learning (Paper ID : 1544)

Mohammad Mohammadian[1] Maryam Khazaee Moghadam[1*] Elham Saniei[1]

1 Department of Medical Radiation Engineering, Central Tehran Branch, Islamic Azad University, Tehran, Iran

Abstract

The segmentation of medical images is crucial for treatment planning and some diagnostic cases and many researches have been performed in this field. The aim of this study is to assess two convolutional neural network to segment different body tissues based on the CT scan images.

Materials and Methods: In this work the implemented supervised learning algorithms required organ masks for convolutional pixel-labeling. In order to pre-process CT scan images as input files to the neural network algorithm, 3d slicer software has been used to produce mask images of soft tissues, bones and lungs. To train the networks deeplabv3plus was used as the backbone and the Resnet50 and Xception architectures were fine-tuned in MATLAB._The accuracy,and IOU parameters were exploited at the end of each section to compare the network architectures.

Results: the accuracy, and IOU of Xception and Resnet50 neural networks is evaluated using test images. The results show that the accuracy of Xception and Resnet50 neural networks for bone semantic segmentation is 97% and 97%, respectively. For lung and soft tissue segmentation, the accuracy of Xception and Resnet50 neural networks is 96% and 96% (for lung) and 99% and 98% (for soft tissue), respectively.

IOU of Xception and Resnet50 neural networks for bone semantic segmentation is 84% and 80%, respectively. For lung and soft tissue segmentation, the IOU evaluation metric for Xception and Resnet50 neural networks was 91% and 92% (for lung) and 99% and 98% (for soft tissue), respectively.

Conclusion: It was presented that Xception neural network has a higher performance compared to Resnet50 network to CT scan images according to different evaluation criteria.

Keywords: segmentation, computed tomography, deep learning

Introduction

Computed Tomography (CT) images play a crucial role in medical diagnosis nowadays. In this

regard, accurate segmentation of bone, lung, and soft tissue structures based on the CT scan images which involves identifying and delineating regions of interest (ROI),is an important task in medical imaging analysis. The results of bone, lung, soft tissue segmentation could facilitate bone, lung, soft tissue disease diagnosis and post-treatment dosimetry assessment, and support planning and image guidance for many treatment modalities including surgery, interventional radiology, and radiation therapy. However, manual segmentation of bone, lung, soft tissue is time consuming and labor intensive. As a result, development of an automated bone , lung, soft tissue segmentation algorithm is highly desirable. The application of Threshold techniques the most commonly used semi-automatic segmentation model in bone, lung, and soft tissue [1, 2].

As the bone tissue has higher density compared to the other organs, bone segmentation based on the CT images is considered an easier task compared to the segmentation of the other organs such as lung, and soft tissue; however, there are some specific difficulties to be considered.[3] Bone and soft tissues have different shapes and various densities throughout the body which makes the definition of one or two thresholds to segment the aforementioned ROIs impractical.[4]

Novel advances using deep-learning-based methods have achieved considerable success in many different fields, including medical image segmentation[5, 6]. Several reports have investigated convolutional neural network (CNN)-based architecture for bone segmentation based on the CT images[7, 8].

The purpose of this study was to develop a compare two CNN-based models to perform bone, lung, soft tissue segmentation on whole-body low dose CT images, and to evaluate the accuracy and generalizability of these models.

Materials and Methods

The dataset included in this study contains 3,000 slices of CT images from 9 whole body CT scans that were obtained using Siemense Biograph CT scanner. Slice thickness was 3 mm, and axial in-plane image resolution was 0.41–0.68 mm.

Ground truth labels were established using 3d slicer: a software platform for analysis and visualization of medical images [9, 10]. First, the base labels were created with 3d slicer

segmentation tools such as thresholding, and then manual corrections were performed by medical experts using 3d slicer manual segmentation tool. Finally, the labels were verified and modified by a radiologist (25-years' experience in diagnostic imaging) for each scan.

In this study semantic segmentation network was used to classify every pixel in the CT image. In this regard, the data was split into validation data, training data and test data. The splitting task was randomly generated and scans from the same patient were not used in both the training and sets. A more specific explanation of the implementation is shown in (Fig. 1).

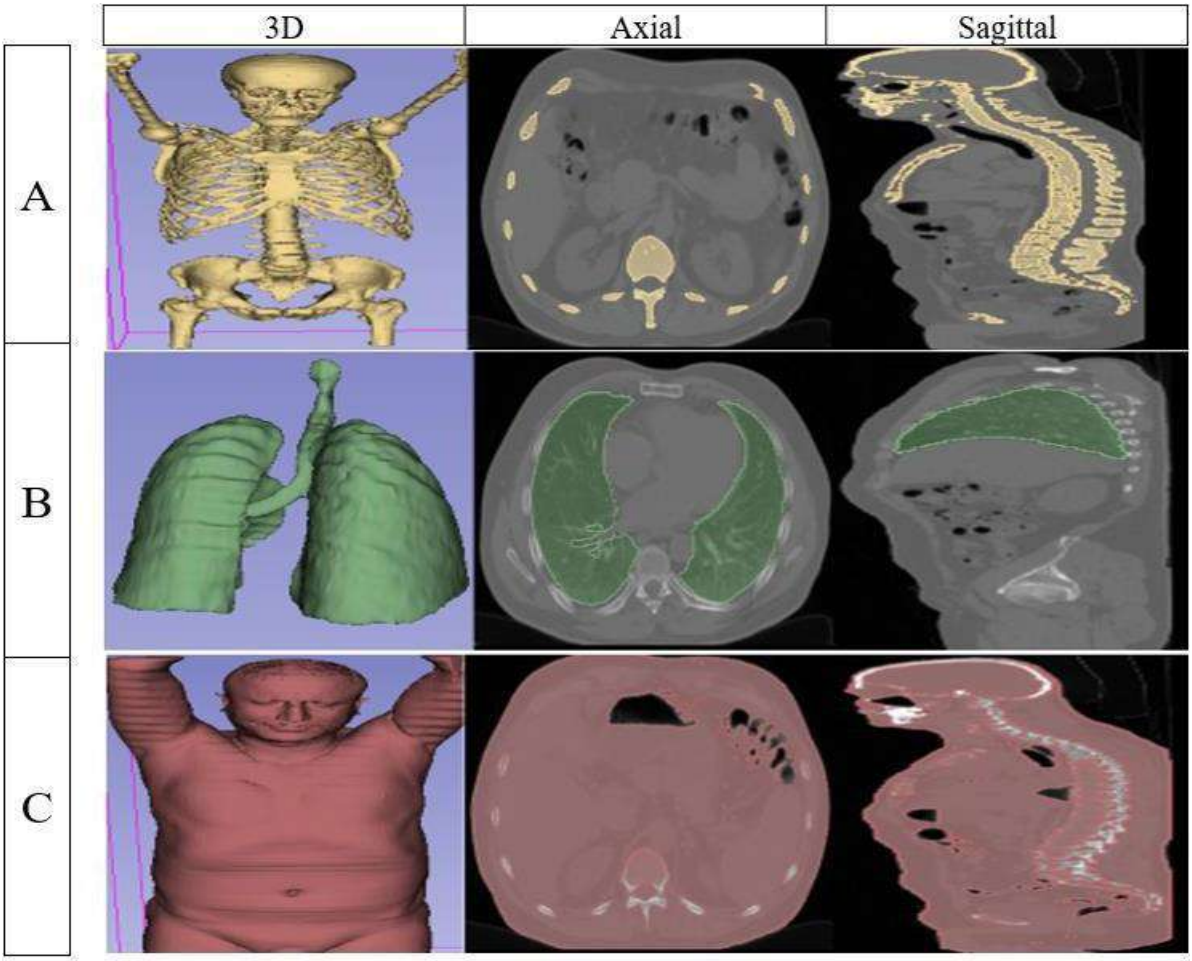

Fig. 1 An example of images divided by 3D Slicer software Bone (A) Lung (B) Soft tissue (C) In axial, coronal and sagittal view

Architecture A convolutional neural network, known as CNN[11, 12], with Resnet50 , and Xception pretrained models was implemented in MATLAB[2023].

For the presented semantic segmentation, deeplabV3+ backbone was used which is matched with limited pretrained networks. All the matched pretrained networks were evaluated and the two presented networks had higher accuracy compared to the other architectures. Moreover, ResNet50 is a popular convolutional neural network architecture known for its deep structure with skip connections (residual connections). These skip connections help in mitigating the vanishing gradient problem, making it easier to train very deep networks.ResNet50 has shown impressive performance on various computer vision tasks, particularly in image classification and object detection tasks.It strikes a balance between model complexity and performance, making it a suitable choice for many applications. On the other hand, Xception is another convolutional neural network architecture that is designed to be more efficient in terms of computation and parameter efficiency.Xception uses depthwise separable convolutions, which separate the spatial and channel-wise convolutions, leading to a significant reduction in the number of parameters compared to traditional convolutional layers. Xception has shown to perform well in tasks where computational efficiency is crucial, ResNet-50 and Xception used for transfer learning to initialize weights.[13]

ResNet-50 is a convolutional neural network with 50 layers, and it is a pre-trained network that was trained to classify images into 1000 different object classes. This network has an image input size of 224 x 224. As a result, the neural network has learned rich feature representations for a wide range of images figure 2.tt

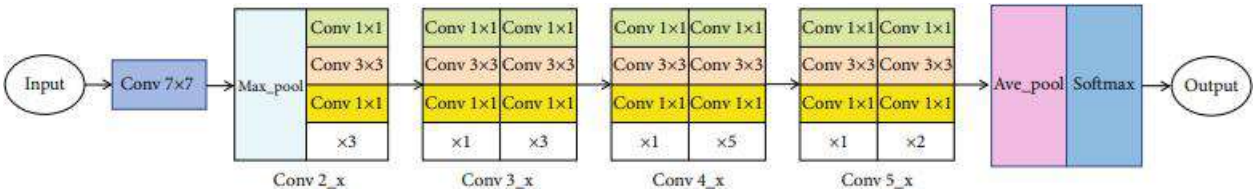

Fig. 2. Schematic illustration of the ResNet-50 architecture used in the present study[14].

Xception is a convolutional neural network that has 71 layers it is a pre-trained network that can classify images into 1000 different object categories. This network has an input image size of 299 x 299. The schematic illustration of the Xception architecture used in the present study is shown in figure3.tt

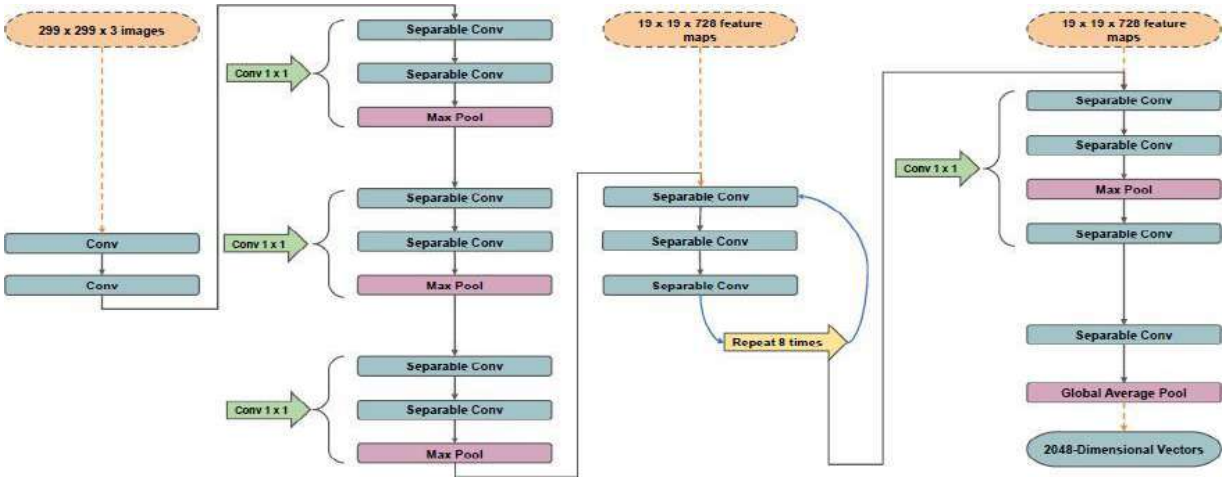

Fig. 3. Schematic illustration of the Xception architecture used in the present study[15].

To adjust the learning rate, a piece-time schedule was used. The selected learning rate decreases by 0.3 for every 10 periods. This results in the network learning more quickly with a higher initial learning rate. The network was tested against the validation data in each period by adjusting the "data validation" parameter. "Data Validation" is set to 4 in order to stop the training process earlier when the validation accuracy converges. This prevents overfitting the network to the training data set. The total body CT scan data included 6000 slices for both networks; which contains 3000 labeling image slices using 3D slicer software and 3000 raw image slices. The labeled images are divided into three categories: bone, soft tissue and lung for the neural network.[16-18].

Results

The execution results using the ResNet-50 and Xception neural networks are presented in Table .1. the diagram of the training process for ResNet-50 and the Xception neural networks is shown in Fig. 4 and Fig. 5 respectively.

Table 1. Neural network output parameters Resnet50, Xception

Heading	Iteration	Validation Accuracy	Validation Loss
Resnet50	1650	99.32%	0.0530
Xception	2750	99.36%	0.0624

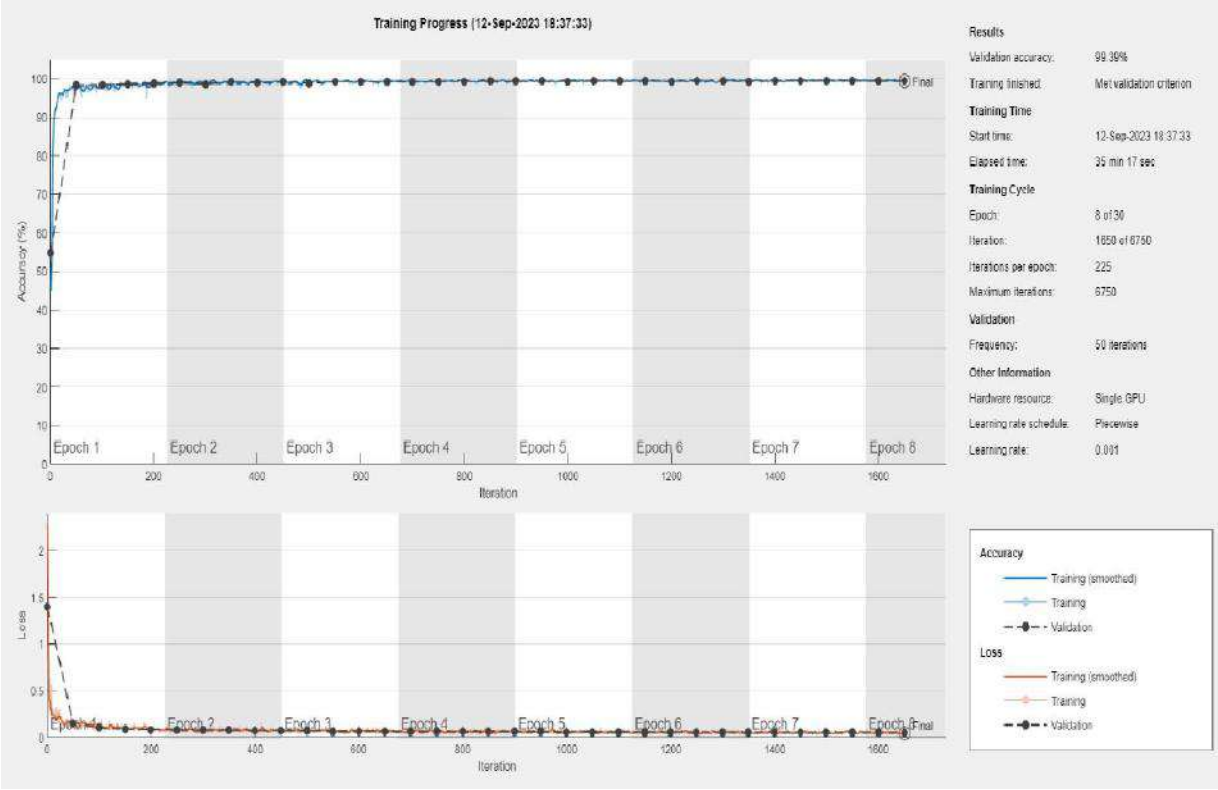

Fig. 4. Diagram of evaluation metrics (validation accuracy) of neural network using Resnet50

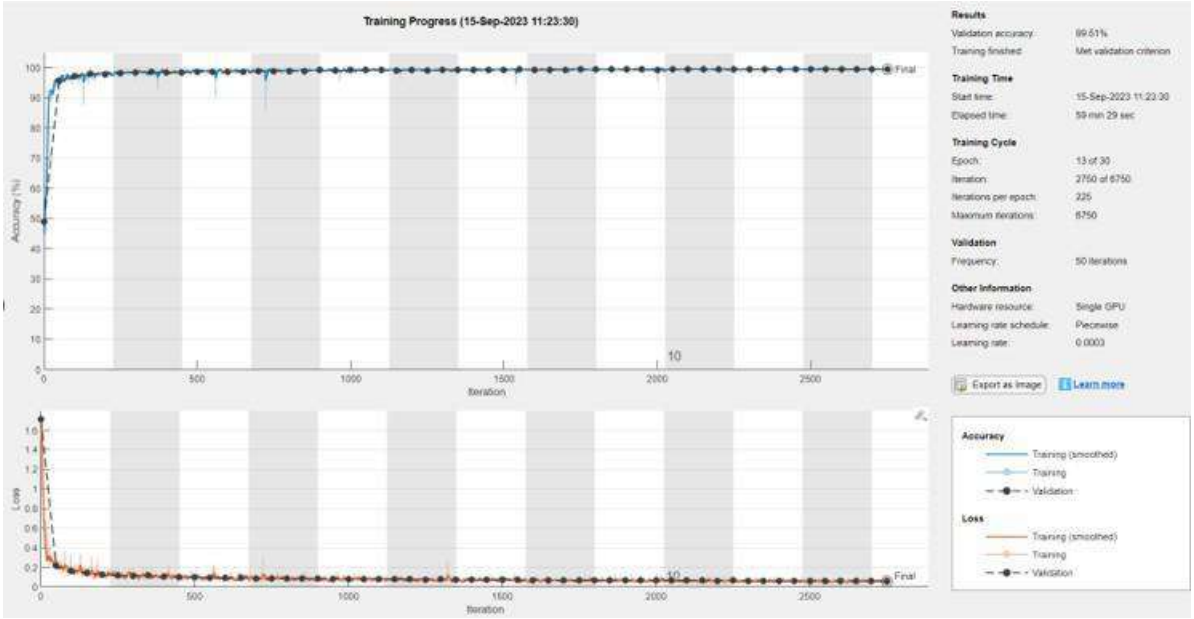

Fig. 5. Diagram of evaluation parameters (accuracy) of neural network Xception

In this study the network is trained using 70% of the total data images.[19] The rest of the images are divided into two groups of equal size for validation and testing. The code randomly divides the label and image data into a training, validation, and testing set.[7, 20].

Figure 6 shows the comparison between the results predicted by the model with the expected ground truth which was stored in Test data. The highlighted green and magenta region areas are the segmentation results which are different from the expected ground truth.

In the results obtained from the two networks in question, the areas marked by the network in purple are errors and the areas in green are not recognized by the network.

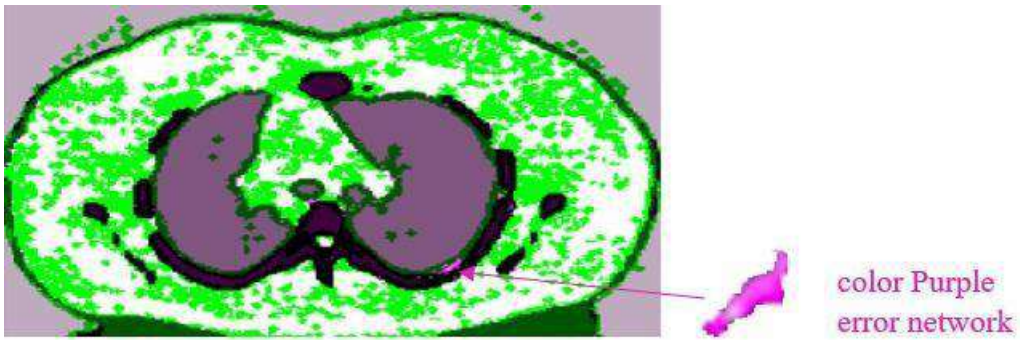

Fig. 6. Neural network test results Resnet50

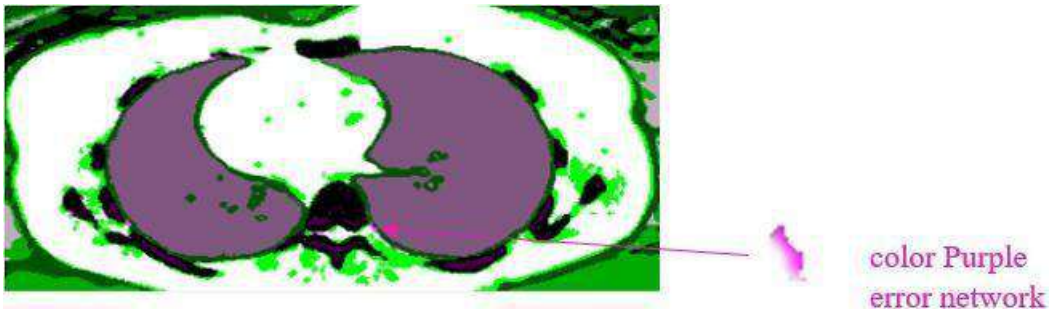

Fig. 7. Neural network test results for Xception model

To evaluate the networks The degree of overlap in each class can be measured using IoU, also known as the Jaccard index ,In each epoch, we test the model on the validation data and the accuracy of the model is obtained. As long as the error of the model on the training data is reduced, the error of the validation data is reduced. But from a certain point on when the model retains the training data, the excess of the model error on the validation data increases instead of decreasing, accuracy parameters for soft tissue, lung, and bone were calculated and compared for Resnet50 and Xception models (Table .2).

Table 2. Results of accuracy parameters for neural networks

RESNET50			Xception	
Heading	Accuracy	IoU	Accuracy	IoU
bone	0.98375	0.80356	0.97363	0.8434
lung	0.96969	0.92307	0.97363	0.91698
soft tissue	0.98706	0.986	0.99282	0.91698

The image size was adjusted to fits NVIDIA™ Titan X with 12 GB memory for training. The training time was 2 h per fold.

Discussion

The results of our study showed insight into deep neural networks applications to segment bone, lung and soft tissue on whole-body CT scan images. The performance was evaluated for two different pretrained network and achieved sufficient accuracy.

For decades, various techniques have been implemented for bone[1], lung[9] and soft tissue[21], segmentation on CT images. Of these methods, thresholding technique has been most widely applied[17, 22] .As bony structures have higher density levels, they are more specific on CT images and they can usually be separated compared to the soft tissue by thresholding.

Other methodologies such as edge detection are commonly combined with other techniques [18]and are seldom used independently. In addition, most of the aforementioned methods require some degree of manual input, which is laborious and depends on the experience in clinical practice. CNN-based methods have recently achieved strong results in various fields, including medical image segmentation[5, 6]. Several studies have investigated CNN-based architecture for bone, lung and soft tissue segmentation on whole-body CT.

Our model showed outstanding results in all calculated evaluation metrics (Dice coefficient, Jaccard index, sensitivity, and positive predictive value); which is considered to be attributable to segment images with high quality on various dataset.[23]. Image metrics using the defined model is rapid with a currently available GPU, requiring about 45 second to segment a whole-body CT of 329 slices.

Although segmentation accuracy with this model on different datasets was acceptable, some errors were found. Most common error sources are costal cartilage and intervertebral discs. Costal cartilage becomes calcified especially in elder patients and are presented similar to ribs shape and density in CT images. As a result, costal cartilage was not labelled as bone in the ground truth data.

Conclusions

We developed a fully automated network to segment bone, lung, and soft tissue using two pretrained CNN based on the low dose CT image dataset. The deeplabvthreeplus CNN was able to

detect and segment bone ,lung, and soft tissue structures with sufficient accuracy. The results showed that the pretrained Xception neural network has better results compared to the RESNET50 For lung bone and soft tissue. And we are investigating other models to choose architecture with better performance in MATLAB.

References

Noguchi, S., et al., Bone segmentation on whole-body CT using convolutional neural network with novel data augmentation techniques. Computers in biology and medicine, 2020. 121: p. 103767.

Van Eijnatten, M., et al., CT image segmentation methods for bone used in medical additive manufacturing. Medical engineering & physics, 2018. 51: p. 6-16.

Belal, S.L., et al., Deep learning for segmentation of 49 selected bones in CT scans: first step in automated PET/CT-based 3D quantification of skeletal metastases. European journal of radiology, 2019. 113: p. 89-95.

Gorman, K. and S. Bedrick. We need to talk about standard splits. in Proceedings of the conference. Association for Computational Linguistics. Meeting. 2019. NIH Public Access.

Zhang, Z. and E. Sejdić, Radiological images and machine learning: trends, perspectives, and prospects. Computers in biology and medicine, 2019. 108: p. 354-370.

Hesamian, M.H., et al., Deep learning techniques for medical image segmentation: achievements and challenges. Journal of digital imaging, 2019. 32: p. 582-596.

Klein, A., et al., Automatic bone segmentation in whole-body CT images. International journal of computer assisted radiology and surgery, 2019. 14: p. 21-29.

Minnema, J., et al., CT image segmentation of bone for medical additive manufacturing using a convolutional neural network. Computers in biology and medicine, 2018. 103: p. 130-139.

Skourt, B.A., A. El Hassani, and A. Majda, Lung CT image segmentation using deep neural networks. Procedia Computer Science, 2018. 127: p. 109-113.

Hu, Q., et al., An effective approach for CT lung segmentation using mask region-based convolutional neural networks. Artificial intelligence in medicine, 2020. 103: p. 101792.

Lee, M.S., et al., Deep-dose: a voxel dose estimation method using deep convolutional neural network for personalized internal dosimetry. Scientific reports, 2019. 9(1): p. 10308.

Liu, X., et al., Automatic organ segmentation for CT scans based on super-pixel and

convolutional neural networks. Journal of digital imaging, 2018. 31: p. 748-760.

Ioffe, S. and C. Szegedy. Batch normalization: Accelerating deep network training by reducing internal covariate shift. in International conference on machine learning. 2015. pmlr.

Renjun, X., et al., Fault detection method based on improved faster R-CNN: take ResNet-50 as an example. Geofluids, 2022. 2022: p. 1-9.

Wu, X., et al. An xception based convolutional neural network for scene image classification with transfer learning. in 2020 2nd international conference on information technology and computer application (ITCA). 2020. IEEE.

Jin, D., et al. CT-realistic lung nodule simulation from 3D conditional generative adversarial networks for robust lung segmentation. in Medical Image Computing and Computer Assisted Intervention–MICCAI 2018: 21st International Conference, Granada, Spain, September 16-20, 2018, Proceedings, Part II 11. 2018. Springer.

Rathnayaka, K., et al., Effects of CT image segmentation methods on the accuracy of long bone 3D reconstructions. Medical engineering & physics, 2011. 33(2): p. 226-233.

Krčah, M., G. Székely, and R. Blanc. Fully automatic and fast segmentation of the femur bone from 3D-CT images with no shape prior. in 2011 IEEE international symposium on biomedical imaging: from nano to macro. 2011. IEEE.

Tajbakhsh, N., et al., Convolutional neural networks for medical image analysis: Full training or fine tuning? IEEE transactions on medical imaging, 2016. 35(5): p. 1299-1312.

Takahashi, R., T. Matsubara, and K. Uehara. Ricap: Random image cropping and patching data augmentation for deep cnns. in Asian conference on machine learning. 2018. PMLR.

Lee, Y.S., et al., Deep neural network for automatic volumetric segmentation of whole-body CT images for body composition assessment. Clinical Nutrition, 2021. 40(8): p. 5038-5046.

Pham, D.L., C. Xu, and J.L. Prince, Current methods in medical image segmentation. Annual review of biomedical engineering, 2000. 2(1): p. 315-337.

Chang, H.-H., et al., Performance measure characterization for evaluating neuroimage segmentation algorithms. Neuroimage, 2009. 47(1): p. 122-135.

ICNST 2024
International Conference on Nuclear Science and Technology
6- 8 MAY 2024 | Isfahan, Iran

Evaluation of shielding properties of polymer-lithium tetra borate composite for neutron beams (Paper ID : 1555)

Ghaneamzadeh S.[1*], Aghamiri M. R.[1], Kashian S.[2], Malekie, S.[2]

Department of Medical Radiation Engineering, Shahid Beheshti University, Tehran, Iran.

Radiation Application Research School, Nuclear Science and Technology Research Institute, Tehran, Iran

Abstract

In this research, radiation shielding properties of the Bisphenol A/Lithium tetraborate (BPA/$Li_2B_4O_7$) composite against the neutron source of ^{241}Am-Be with an activity of 18 Ci were evaluated. The optimal weight fraction and thickness of the samples were simulated using the MCNP code. Due to high neutron absorption cross-section of the $Li_2B_4O_7$, this composite is expected to be used as an effective absorber for thermal neutrons. Based on the simulation results, it is observed that the sample containing 20 wt% $Li_2B_4O_7$ and 1 cm thickness can attenuate the thermal neutrons by ~90%. Therefore, this finding suggests the feasibility of using the BPA/$Li_2B_4O_7$ composite as a protective material against the thermal neutrons for achieving high performance.

Keywords: Neutron shielding, Polymer, Composite, MCNP code, Lithium Tetraborate.

Introduction

Exposure to neutrons can lead to metal breakage, brittleness and swelling, which causes problems especially for nuclear facilities and seriously limits their half-life. Sometimes there are more severe risks such as neutron activation, which is actually the ability of neutron radiation to induce radioactivity in most of the materials under this radiation, such as the body of people who deal with this radiation. This process occurs through the absorption of neutrons by atomic nuclei and their conversion to other nuclides, which are mostly radionuclides [1]. Advances in neutron science and technology have led to the release of unwanted neutron particles, which often occur in nuclear power plants, the medical sector, and the aerospace industry [2, 3].

Advances in the use of neutron sources such as neutron activation analysis, neutron radiography, active neutron recovery techniques, and neutron absorption therapy in the last two decades demonstrate its importance. During operating conditions in such applications, unwanted neutron particle radiation escapes and interacts with surrounding material atoms, making the medium radioactive [4]. Nuclear power plants are an alternative source of energy to traditional fossil fuels with negligible carbon emissions, so they are relatively clean and efficient. The neutron released in the reactors during the nuclear fission process must be shielded with suitable shielding materials. In particular, high- energy neutrons above 2

MeV during operation must be shielded to protect workers and the environment [5, 6]. Understanding the radiobiological effectiveness of byproduct neutron doses that occur during radiation therapy is important because of the public health implications [7]. The use of high-energy photon rays is one of the most useful methods in radiotherapy treatment in cases of tumors located in deep places. In such treatments, the neutron pollution caused by the interaction of high energy photons (greater than 8 MeV) is the most important issue to consider [8]. Most of the neutrons are produced on collimation systems, applicators and scattering foils in the accelerator. Metal and polymer-based shielding materials are provided to protect the patient from exposure to these neutron beams, and flexible materials are especially needed to protect ventilation ducts, air conditioners, etc. [9]. According to the mentioned problems, it can be stated that protective materials with structural integrity (uniformity) and performance are important for safer use of these applications. For example, nuclear equipment and instruments use a lot of neutron shielding materials. These are generally used for converging beam fields, shielding detectors and last but not least, protecting the environment in which researchers operate. Materials commonly used for this purpose are characterized by the relative abundance in atomic nuclei that have a high neutron absorption cross section. The physical properties of doped polymer composites can be tuned for a specific application by exposure to ionizing radiation such as electron beams, gamma-rays, etc. These changes primarily depend on the nature of the impurity as well as the polymer, as well as how the impurity reacts with the host polymer matrix. The most common types of reactions in irradiated polymers are cross-linking and chain scission [10]. Both of these reactions can significantly change the macroscopic properties of the polymer composite, i.e. electrical conductivity, optical properties, mechanical strength, etc. [11]. Lithium tetraborate $Li_2B_4O_7$ has special physical properties that are important for practical applications and finds wide application in various fields of science and technology. PVA composite films doped with lithium salt can be used in electrochemical cells, sensors, solid state batteries, etc. [12]. Lithium-6 (^{6} Li) has a large absorption cross-section of 940 b for thermal neutrons, and the absorption is mainly the (n, α) reaction without the production of gamma rays. Therefore,^{6}Li is commonly used for thermal- neutron shielding in medical and biological applications. The natural abundance of ^{6}Li is low, 7.5%, so enriched ^{6}Li (up to 96%) is commonly used [13].

Developments in the use of neutron beams in the last decade, such as neutron radiography and neutron absorption therapy (BNCT), show the necessity of using advanced neutron shielding materials. The

choice of neutron attenuation material depends on the incoming neutron energy. Neutron shielding

materials are mainly divided into concrete, metal and polymer composites. In concrete, heavy atomic fillers such as hematite, iron ore, etc. show more attenuation than very fast neutrons. Polymer-based

neutron shielding composites have several advantages, including light weight, ease of fabrication, better distribution of neutron absorbers, excellent chemical resistance, etc.

Kaur (2021) studied environmentally friendly bismuth-doped lithium borate glass system for structural shielding properties against gamma rays and fast neutrons. Densitometry, XRD, Raman, FTIR and UV-Visible spectroscopic techniques helped to understand the structure of bismuth-lithium-borate ternary glass system. It is found that the glass samples are amorphous in nature and the structure is mainly composed of BO4, BO3, BiO6, BiO3 and non-bridging oxygens (NBOs) units.

the prepared bismuth-lithium-borate glass system can be used for radiation protection applications [14]. Jurgen (2019) investigated the effect of borax (B_2O_3) on the gamma and neutron shielding properties of lithium borate glasses [15]. Ismail (2018) investigated the changes caused by electron beam in the microstructure of PVA/ $Li_2B_4O_7$ polymer layers: positron annihilation study. Films of 5% by weight lithium tetraborate ($Li_2B_4O_7$) doped with poly (vinyl alcohol) (PVA) were prepared by solution- molding method. The prepared films were irradiated with different doses of 8 MeV electron beam [12]. So far, many studies have not been reported on the investigation of the protective properties of lithium tetraborate-polymer composite against neutron rays.

In this research, the protective properties of polymer-lithium tetraborate composite for neutron rays are evaluated. In which, the 241Am-Be neutron source with 18 Ci activity, is simulated.

Material ad methods: Theoretical neutron absorption calculations

When a collimated beam of thermal neutrons with intensity of I_0, incident on the absorber with a thickness of x and the transmitted neutron intensity is measured (I) ,the removal of neutrons from the beam is given by :

$$I = I_0 e^{-N\sigma_{th} x} \quad (1)$$

Where N is the atomic number density and σ_{th} is the microscopic thermal neutron absorption cross-section. According to this relation, thermal neutron absorption cross-section ($\sum = N\sigma_{th}$) is depending on atomic number density and elemental composition of material [13,14].

Simulation

The flux of slow neutrons was calculated using Tally F4 using the MCNPX code. The geometry is depicted in Fig. 1.

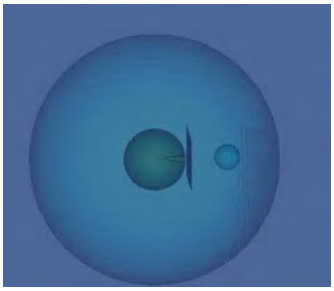

Fig. 1 Geometry of the problem in this work, containing neutron source, spherical ^{3}He detector, and nanocomposite shield.

Results and discussion

In Fig. 2, flux of thermal neutrons vs wt% is exhibited. It can be seen that for the 20 wt% sample with a thickness of 1 cm, the flux of thermal neutrons was decreased by about 90%.

Also, as can be seen from Fig. 3, a comparision of neutron flux vs. Li2B4O7 wt% for thermal and fast neutrons was assessed using the MCNPX code. It seems that the neutron flux for all composites is independant for fast neutrons, but for thermal neutrons, the flux is decreased as the concentrations of the inclusions is incresed.

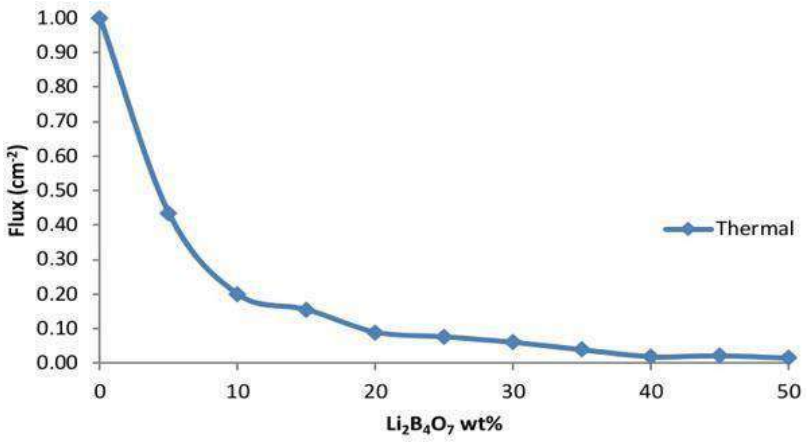

Fig. 2 Thermal neutron flux vs. Li2B4O7 wt% simulated using the MCNPX code in this work.

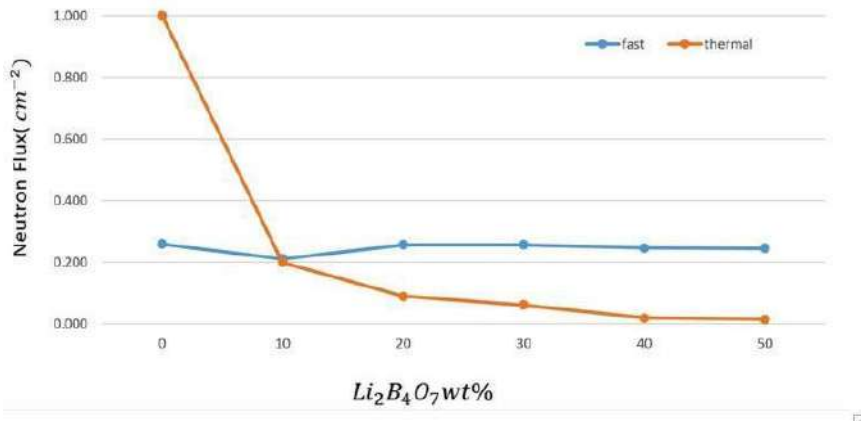

Fig. 3 Comparision of neutron flux vs. Li2B4O7 wt% for thermal and fast neutrons using the MCNPX code in this work.

Conclusion

Based on the simulation results, Bisphenol A /Lithium Tetraborate composite, at 20 wt% and 1 cm thickness, can attenuate 90% of the thermal neutrons of 18 Ci ^{241}Am-Be source, in which this material can be applied as an suitable absorber for thermal neutrons. Experimental work is in progress.

References

Beckurts K-H, Wirtz K. Neutron physics: Springer Science & Business Media; 2013.

Mozhayev AV, Piper RK, Rathbone BA, McDonald JC. Moderator design studies for a new neutron reference source based on the D–T fusion reaction. Radiation Physics and Chemistry. 2016;123:87-96.

Chandra S, Ahmad T, Barth R, Kabalka G. Quantitative evaluation of boron neutron capture therapy (BNCT) drugs for boron delivery and retention at subcellular-scale resolution in human glioblastoma cells with imaging secondary ion mass spectrometry (SIMS). Journal of microscopy. 2014;254(3):146-56.

Abdulrahman ST, Ahmad Z, Thomas S, Rahman AA. Introduction to neutron-shielding materials. Micro and Nanostructured Composite Materials for Neutron Shielding Applications: Elsevier .2020 ;p. 1-23.

Zinkle SJ, Was G. Materials challenges in nuclear energy. Acta Materialia. 2013;61(3):735-58.

Zinkle SJ, Busby JT. Structural materials for fission & fusion energy. Materials today. 2009;12(11):12-9.

Walsh L. Neutron relative biological effectiveness for solid cancer incidence in the Japanese A-bomb survivors: an analysis considering the degree of independent effects from γ-ray and neutron absorbed doses with hierarchical partitioning. Radiation and environmental biophysics. 2013.36-29:)1(52;

Banaee N, Goodarzi K, Nedaie HA. Neutron contamination in radiotherapy processes: a review study. Journal of Radiation Research. 2021;62(6):947-54.

Deng L, Zhou N, Chen Y-s, Tu Y. Photoneutron radiation field of ducts in barrier of 15 MV medical electron accelerators. Radiation Physics and Chemistry. 2017;140:340-4.

Rao RV, Rao PM, Shridhar M. Effect of electron irradiation on P4VP/PTSA complex and P4VP/Phthalocyanine composites. Nuclear Instruments and Methods in Physics Research Section B: Beam Interactions with Materials and Atoms. 2002;187(3):331-9.

Harisha A, Ravindrachary V, Bhajantri RF, Sanjeev G, Poojary B, Dutta D, et al. Electron irradiation induced microstructural modifications in BaCl2 doped PVA: A positron annihilation study. Polymer degradation and stability. 2008;93(8):1554-63.

Ravindrachary V, Sanjeev G, Praveena S. Electron beam induced modifications in the microstructure of PVA/ $Li_2B_4O_7$ polymer films: Positron annihilation study. Radiation Physics and Chemistry. 2018;151:69-76.

Eid G, El-Toony M, Kany A, Bashter I, SA E, Gaber F. Neutron shielding using Li3BO3/Epoxy composite. Researcher. 2011;3:85.

Kaur P, Singh K, Kurudirek M, Thakur S. Study of environment friendly bismuth incorporated lithium borate glass system for structural, gamma-ray and fast neutron shielding properties. Spectrochimica acta part A: molecular and biomolecular spectroscopy. 2019;223:117309.

ICNST 2024 International Conference on Nuclear Science and Technology
6- 8 MAY 2024 | Isfahan, Iran

Effect of different concentrations of boric acid on the moderator's neutronic parameters (Paper ID : 1556)

Karimi F.[1*], Zolfagharpour F.[1]
[1]*Faculty of Sciences, Mohaghegh Ardabili University, Ardabil, Iran*

Abstract

In this research, the effect of different concentrations of boric acid on neutron parameters has been experimentally investigated using a BF_3 neutron detector and a ^{241}Am-Be neutron source with an activity of 5.2 Curies. A boric acid solution with concentrations of 1.6, 3.2, 4.8, 6.4, and 8 g/cm^3; poured into a glass chamber at various thicknesses from 1 to 15 cm, was positioned in front of the neutron source.

A cadmium shield with a slot for specific angle reflection was employed to detect neutrons. The BF_3 neutron detector was placed within this cadmium shield and then positioned under the glass chamber containing the boric acid solution.

Subsequently, neutron spectra were recorded by conducting multiple trials with increasing thicknesses and concentrations. Finally, the changes in the area under the curve within a certain interval were discussed and analyzed.

Keywords: Boric acid, Neutron parameters, BF_3 neutron detector, ^{241}Am-Be neutron source

INTRODUCTION

Boron finds various applications in commercial nuclear power plants, serving as a chemical in the cooling process of the primary circuit in PWR-type power plants. Its acid solution can function as a coolant absorbent and an emergency controller, providing inherent safety measures for reactors. Boric acid is dissolved in the reactor coolant to regulate the flux rate and neutron reactions. As a soluble neutron absorber, it is referred to as a soluble poison.

The utilization of boric acid offers several advantages. It is highly soluble in water, facilitating the creation of required concentrations. Additionally, it exhibits adequate chemical and physical stability within the necessary temperature range and possesses a low tendency to combine with oxide layers on the reactor tank walls. Moreover, it does not induce corrosion in the tank, preserving the integrity of the reactor system.

Research and experimental studies have explored the diverse applications of boric acid in nuclear science, spanning various areas within the nuclear industry. These include its role in neutron radiation reduction and shielding, as well as its application in measuring and monitoring boric acid deposition. Studies have also delved into the effects of boric acid concentration within reactors, particularly in light water reactors. Investigations have examined its capacity to mitigate DNA chain breakage induced by thermal and fast neutrons, with boric acid acting as a protective agent for proteins responsible for DNA strand maintenance. Furthermore, research has focused on the impact of boric acid on the corrosion of light water reactor tube shell materials, as well as its mass transfer dynamics and accumulation in the fuel core during emergency conditions in nuclear power plants. These studies contribute to a deeper understanding of cooling system behavior in emergency scenarios, thereby enhancing the overall safety of nuclear power plants [1-8]. Given the diverse applications highlighted earlier and the crucial role of boric acid concentration in reactor coolant for ensuring reactor safety and regulating neutron flux to maintain criticality, this research aims to investigate the effect of boric acid concentration on the reactor moderator and neutron reflection [9].

EXPERIMENTAL

To conduct this research, a boric acid solution was first prepared at concentrations of 1.6, 3.2, 4.8, 6.4, and 8 g/cm^3. The laboratory setup includes a ^{241}Am-Be neutron source with an activity of 5.2 Curies, housed within a steel protection tank and an ultra-purified water tank. The water tank serves as a neutron moderator and provides protection against neutron radiation. Surrounding this setup is a 5 cm thick lead shield for gamma radiation protection, along with a glass container for holding various boron-containing solutions, a BF_3 neutron detector, and cadmium shielding for the neutron detector, as shown in Figure 1.

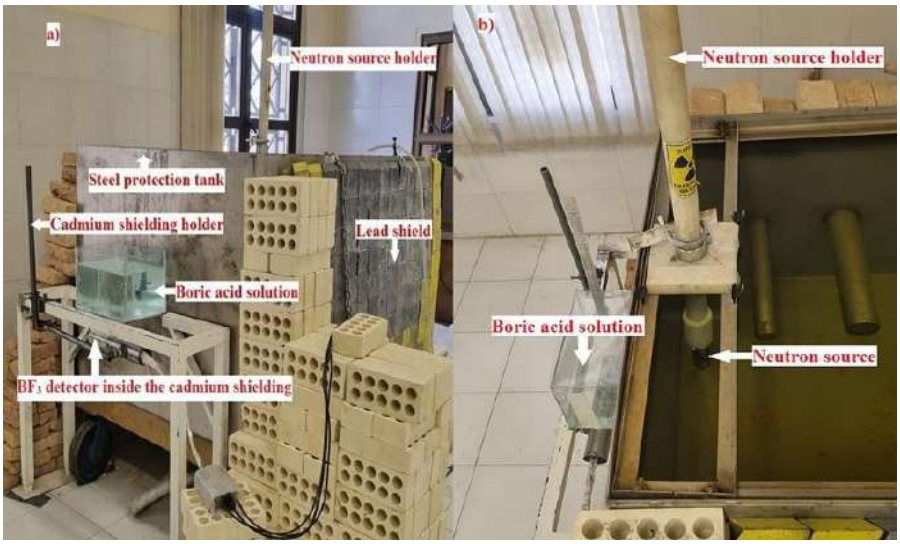

Fig. 1. a) The experimental setup includes a shielded water tank within ^{241}Am-Be source, BF_3 detector, cadmium shielding neutron detector, cadmium shielding holder; b) Viewed from above, the source is positioned inside the water tank by the holding rod, the experimental setup is placed outside the tank for measurement.

Measurement and calculation of neutron flux outside the containment tank were conducted using the BF_3 neutron detector, which was coated with cadmium to a thickness of 1.5 cm for protection. To measure the neutron albedo coefficient of boric acid solutions, glass containers containing solutions of varying concentrations of boric acid were prepared. The thickness of these solutions ranged from 1 to 15 cm, with a boric acid solution of known concentrations added in one-centimeter increments for each measurement step. Neutron flux was measured using the BF_3 detector, and these steps were repeated for other concentrations.

The BF_3 neutron detector used in the experiment had a diameter of 2.5 cm and a height of 20 cm, with an applied voltage of 2100 V. A multi-channel MCA analyzer and NTMCA software were employed to record the spectrum of reflected neutrons.

Results and discussion

The pulse height spectrum obtained from the BF_3 neutron detector using NTMCA software for boric acid solutions at various concentrations. One of this obtained spectrums for boric acid solutions with a concentration of 1.6 g/cm^3 is depicted in Figure 2 in different thicknesses from 1 to 15 centimeters as reflectors. The result of Figure 2 and other obtained results for concentration of 3.2, 4.8, 6.4, and 8 g/cm^3 used to calculate the area under the curve.

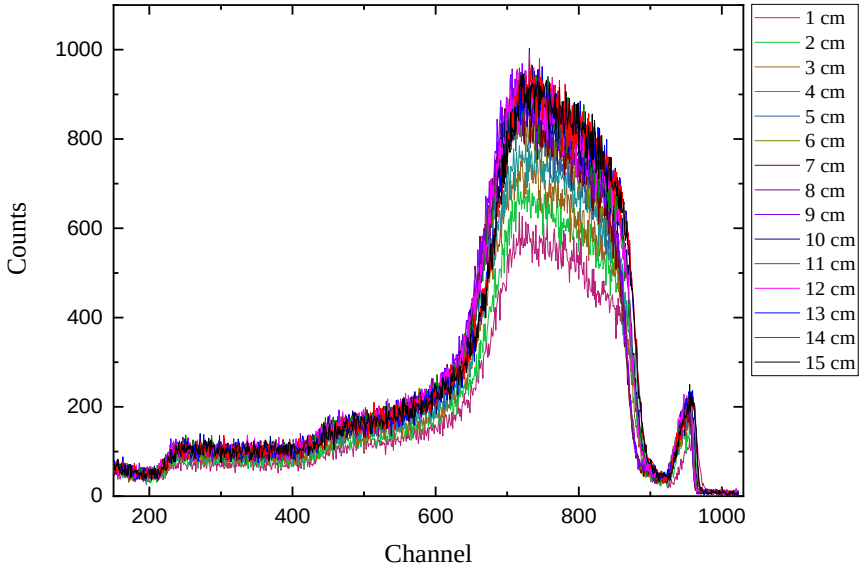

Fig. 2. The experimental spectrum was recorded by the neutron detector for boric acid solutions with specific concentration of 1.6 g/cm^3 at various thicknesses solution from 1 to 15 centimeters.

Additionally, Figure 3 illustrates the area under the curve from channel 210 to 1024 in all of the recorded spectra for different boric acid concentration separately.

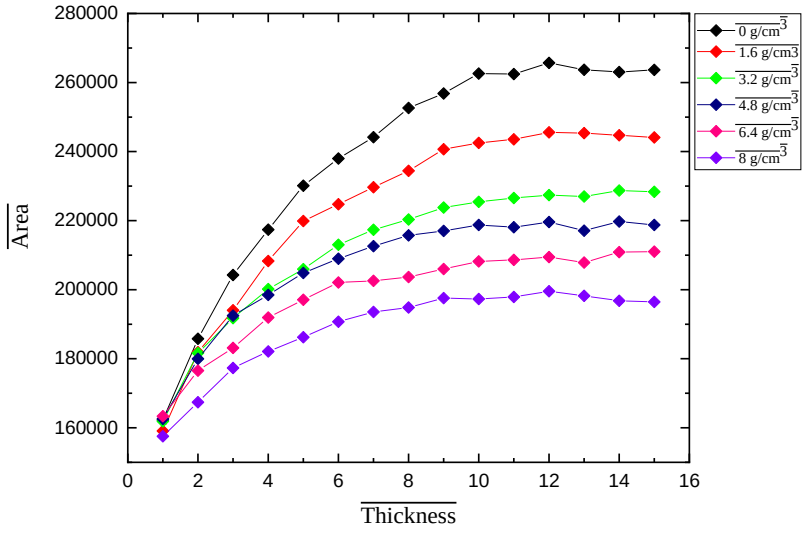

Fig. 3. The variations in the surface beneath the curve depict the spectrum of measured thermal neutrons, influenced by the thickness of the boric acid solution from 1 to 15 centimeters for different concentrations of the solution (1.6, 3.2, 4.8, 6.4, and 8 g/cm^3 shown in the figure by different colors).

As depicted in Figure 2, the number of thermal neutrons increases with the thickness of the boric acid solution at each specific concentration. Additionally, Figure 3 illustrates that increasing the thickness of the solutions leads to an increase in the area under the curve, reaching an approximate saturation level. Moreover, according to the Figure 3, increasing concentration of boric acid results cause reduction in level of the curves.

Conclusions

The results obtained from Figure 3 indicate that the saturation thickness of neutron reflection occurs at around 10 cm of boric acid solution for various concentrations. Increasing the concentration of the solution to 1.6 g/cm^3 reduces the neutron reflection by approximately 7% compared to using pure water instead of the solution and at a concentration of 8 g/cm^3, it decreases neutron reflection by about 25%.

The results obtained in this research demonstrate the impact of variations in the concentration and thickness of boric acid solution on the albedo coefficient of the moderator.

References

[1] Ramadan, W., Sakr, K., Sayed, M., Maziad, N. and El-Faramawy, N. (2020). Investigation of acrylic/boric acid composite gel for neutron attenuation. Nuclear Engineering and Technology, 52(11), 2607-2612.

[2] Vaghetto, R., Childs, M., Kee, E. and Hassan, Y.A. (2016). Observations and measurements of boric acid precipitation scenarios. Progress in Nuclear Energy, 91, 302-309.

[3] Özdemir, T., Akbay, I.K., Uzun, H. and Reyhancan, I.A. (2016). Neutron shielding of EPDM rubber with boric acid: mechanical, thermal properties and neutron absorption tests. Progress in Nuclear Energy, 89, 102-109.

[4] Jamsranjav, E., Ito, A., Kato, Y., Tatebe, Y., Takase, N. and Yoshida, S. (2019). DNA strand breaks induced by fast and thermal neutrons from YAYOI research reactor in the presence and absence of boric acid. Radiation Research, 191(5), 483-489.

[5] İçelli, O., Erzeneoğlu, S. and Boncukçuoğlu, R. (2004). Experimental studies on measurements of mass attenuation coefficients of boric acid at different concentration. Annals of Nuclear Energy, 31(1), 97-106.

[6] Park, J.H., Chopra, O.K., Natesan, K., Shack, W.J. and Cullen Jr, W. (2005), August. Boric acid corrosion of light water reactor pressure tank materials. In Proceedings of the 12th International Conference on Environmental Degradation of Materials in Nuclear Power System-Water Reactors, 459-468.

[7] Morozov, A.V., Sorokin, A.P., Ragulin, S.V., Pityk, A.V., Sahipgareev, A.R., Soshkina, A.S. and Shlepkin, A.S. (2017). Effect of boric acid mass transfer on the accumulation thereof in a fuel core under emergency modes at NPPs with WMR. Thermal Engineering, 64, 490-495.

[8] Uddin, Z., Yasin, T. and Shafiq, M. (2022). Development of novel silane modified boric acid/high density polyethylene composites for radiation shielding applications. Radiation Physics and Chemistry, 192, 109909.

[9] Myerscough, P. B. (1991). Nuclear power generation: incorporating modern power system practice. Pergamon.

ICNST 2024 International Conference on Nuclear Science and Technology
6- 8 MAY 2024 | Isfahan, Iran

Investigation the effect of the Pb2O3, WO3, and Bi2O3 of nanocomposites on the thermal, mechanical, and shielding properties of PVC-based nano composites (Paper ID : 1567)

Rahimi. S[1*], Jahanbakhsh. O [1], Ahadzadeh. I[2]

[1]*Department of physics, University of Tabriz, Tabriz, Iran*

[2]*Department of chemistry, University of Tabriz, Tabriz, Iran*

Abstract

This study investigated the effect of Pb_2O_3, WO_3, and Bi_2O_3 metal oxide nanoparticles on the thermal, mechanical and shielding properties of polyvinyl chloride (PVC) composites which have been proposed as efficient substitute for the traditional lead-based materials for shielding gamma and x-ray radiations. The mentioned nanoparticles were synthesized by using an electrochemical method and characterized by XRD and SEM analysis, which is uniformly dispersed in the polymer matrix by the casting method. The mechanical and thermal properties of the prepared samples were investigated by stress-strain and TGA analysis. The results of them demonstrate that the addition of the above metal oxide nanoparticles leads to decrease in thermal stability and increase in the rate of the weight loss of them. Also, as can be seen that the nanocomposites filled with metal oxide nanofillers, have higher tensile strength and modulus elasticity than the pristine polymer, and their shielding properties improved by increasing nanofiller content.

Keywords: Metal oxide nanoparticles, Electrochemical method, Stress-strain analysis

INTRODUCTION

Despite the harmful effects of ionizing radiation, their applications in various fields such as industry, medicine, agriculture, etc. have been increasingly developed. This doubles the importance of attenuating the ionization radiation and protecting people and their environment. Heavy and dense materials such as bismuth, lead, tungsten and barite are very suitable options for making radiation shields. But some challenges such as environmental pollution, toxicity, difficult manufacturing, high volume and weight, etc., make their use doubtful. In recent years, new materials known as composites have attracted the attention of researchers, which

often cover the above disadvantages. The use of these materials has been reported in various studies [1-3]. Metal oxide composites are the most suitable materials for making radiation shields. By selecting nanoparticles of heavy metals such as lead, bismuth and tungsten as fillers in the structure of composites, in addition to maintaining protective properties, light, economical and harmless protections for the environment and humans can be achieved. In the conducted research, the protective properties of nanocomposites have been investigated and the results indicate that compounds containing metal oxide nanoparticles with higher weight percentages have a higher radiation attenuation capability [4, 5]. This study investigates the physical properties of Pb_2O_3, WO_3 and Bi_2O_3 nanocomposites based on polyvinyl chloride at different weight percentages of additives. For this purpose, the electrochemical method was used to synthesize the nanoparticles, and the casting method was utilized to prepare the composite samples. Then, some mechanical, thermal, and shielding properties of the produced composites were investigated and discussed in detail.

MATERIALS AND METHODS

1. RESEARCH THEORIES

By using the mechanical analysis, in addition to guaranteeing the performance of materials in the design and production of parts, it is also possible to obtain the amount of strain and stress of the samples, which is a measure of the amount of pressure applied to the sample. These two parameters can be calculated from the following relations:

$$\boldsymbol{\sigma = \frac{F}{A}} \qquad (\mathbf{1})$$

$$\boldsymbol{\varepsilon = \frac{\Delta L}{L_0} = \frac{L - L_0}{L_0}} \qquad (\mathbf{2})$$

where σ is the stress of the samples, F is the force on the surface of the object, A is the area of the desired surface, ε is the strain of the samples, ΔL is the changes of length, L is the final length of the sample after applying tension and L_0 is the initial length of the samples.

2. EXPERIMENTAL

After studying different synthesis methods, the electrochemical method was chosen for the synthesis of metal oxide nanoparticles [6]. For this purpose, first, using pieces of lead, tungsten and bismuth metal as anode and a piece of stainless steel 316 as cathode, which were placed in the electrolyte solution of 30% weight-volume of sodium chloride. The arrangement of the electrochemical cell was prepared and an electric current of about 0.5 to 1 amp per unit of anode area was applied to it. In this process, the anode was corroded and the solutions containing metal oxide nanoparticles were obtained and then placed inside the oven. After drying the solutions, they were washed several times with deionized water and filtered and put back into the oven to obtain Pb_2O_3, WO_3, and Bi_2O_3 nanoparticles. Figure 1 shows the experimental setup of nanoparticles synthesis by the electrochemical method.

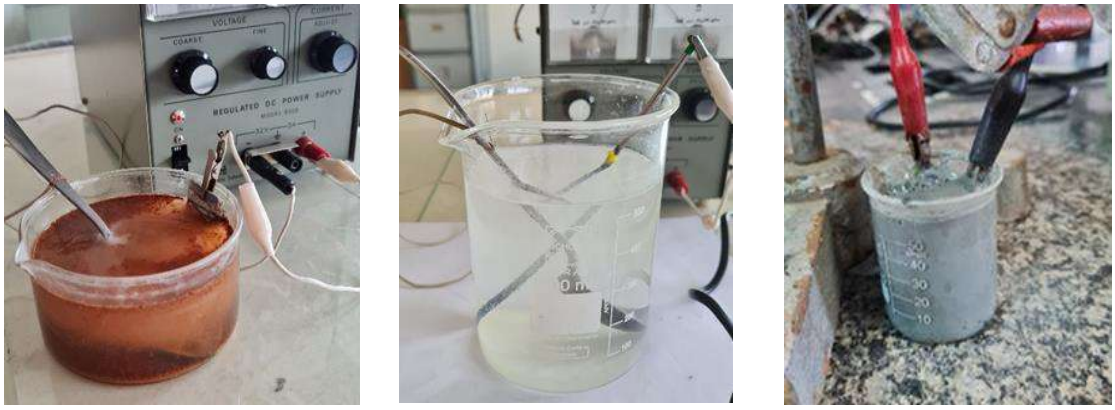

(a) (b) (c)

Fig.1. The experimental setup of the electrochemical cell for synthesis of (a) Pb_2O_3, (b) WO_3, and (c) Bi_2O_3 nanoparticles.

To make nanocomposites, PVC polymer as a matrix and synthesized metal oxide nanoparticles as nanofillers were mixed together to obtain a homogenous mixture. Due to the fact that nanoparticles have a good mixing ability in polymer bases, the molding method was chosen to prepare and manufacture composites containing

metal oxide nanoparticles. In the continuation of the work, the obtained uniform mixture was poured into the molds with desired shape and dimensions. The prepared samples were placed in the laboratory environment for 24 hours to harden completely. Various analysis was performed on the prepared nanocomposites to investigate the physical and mechanical properties of them. The results of which are given in the following sections.

3. CHARACTERIZATION

3.1. XRD, EDS and SEM analysis: The correspondence of the reference peaks and the peaks observed in the diffraction pattern (XRD) spectrum with the 2θ angle range from 20° to 80° indicates the successful synthesis of nanoparticles. The SEM images and the EDS analysis of the prepared nanocomposites indicate the proper distribution of nanoparticles in the polymer matrix and their homogeneity. Moreover, the EDS diagrams show that the elements used to prepare these samples have a semi-quantitative distribution and the availability of nanoparticles in the samples is evident. The results of mentioned analysis were in good agreement with similar researches.

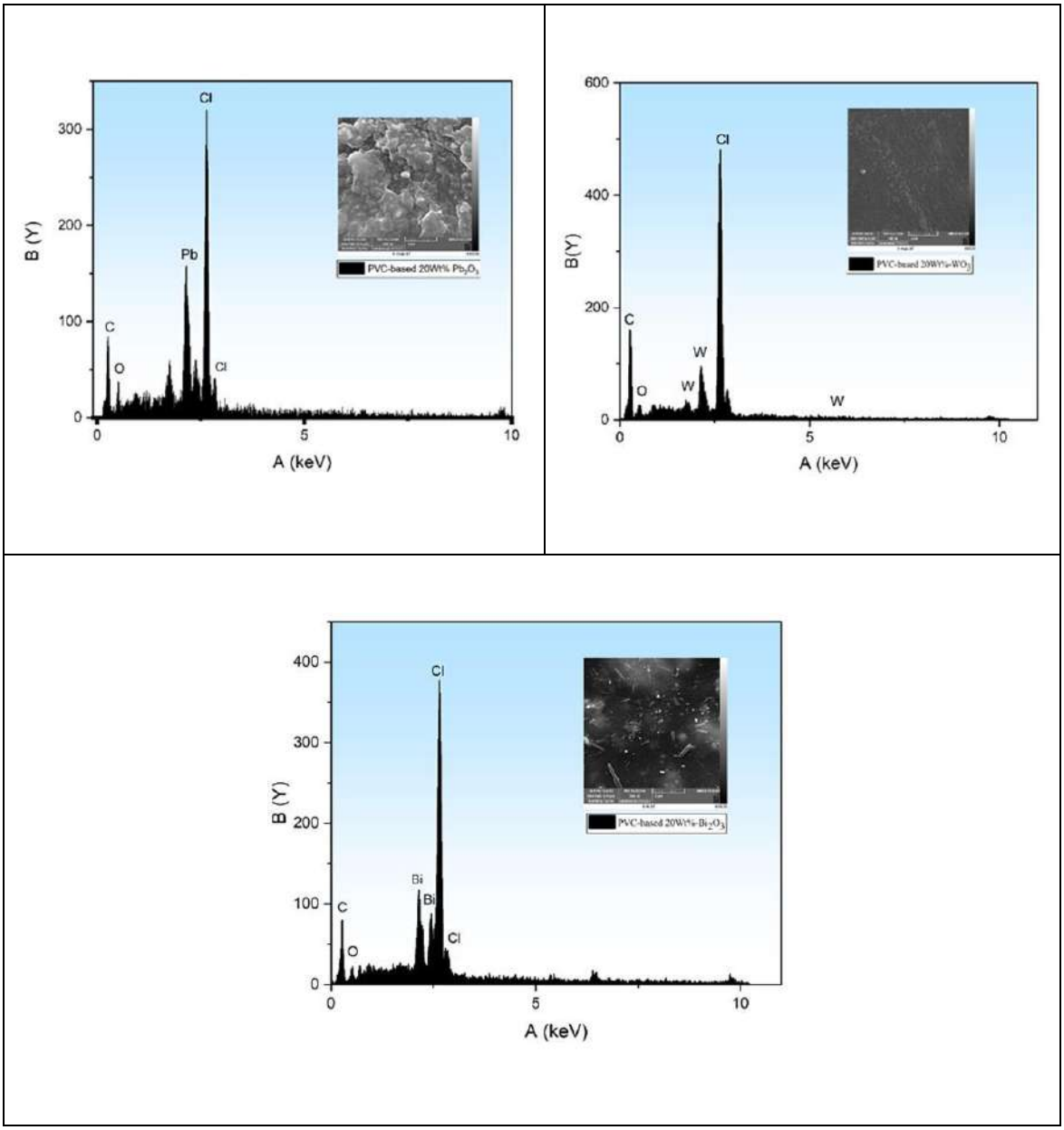

Fig.2 . SEM images of 20 Wt% of PVC-based nanocomposites and their EDS spectrum

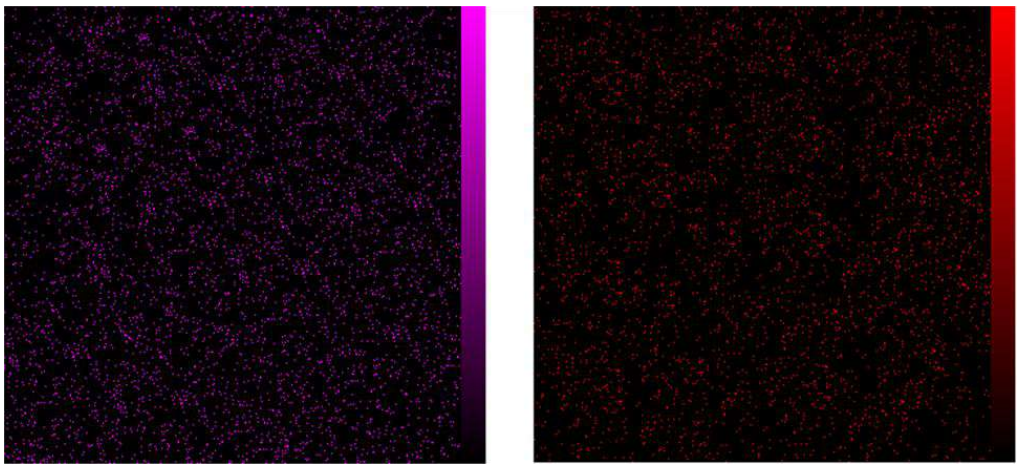

Fig.3 . EDS mapping of lead (violet) and oxygen (red) distribution in the PVC-based nanocomposites.

RESULTS AND DISCUSSION

1. RESULTS OF ANALYSIS

1.1. TGA analysis. The TGA analysis is one of the methods for measuring the thermal resistance of materials, which determines the stability and degradation temperature of different combinations of materials. In this research, the TGA analysis was performed on the pure PVC polymer and PVC-based nanocomposites in different weight percentages with Pb_2O_3, WO_3, and Bi_2O_3 nanofillers, in the temperature range of 25 to 600 °C in a nitrogen atmosphere and with a heating rate of 10°C/min in the LINSEIS® device, the results of which are shown in Figure 4. The results indicate that the PVC-based nanocomposites are more thermally stable than pure PVC. Also, as the percentage of nanofillers increases, the stability and degradation temperature of nanocomposites also increases. The manufactured samples show one-step thermal decomposition and due to the pyrolysis of polymer chains, they are almost completely decomposed at temperatures below 350°C for PVC and PVC-based nanocomposites.

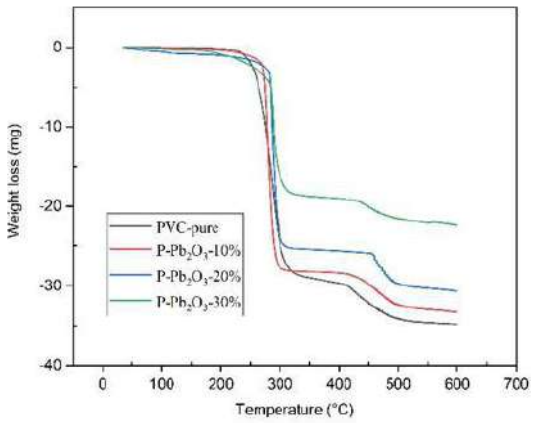

(a)

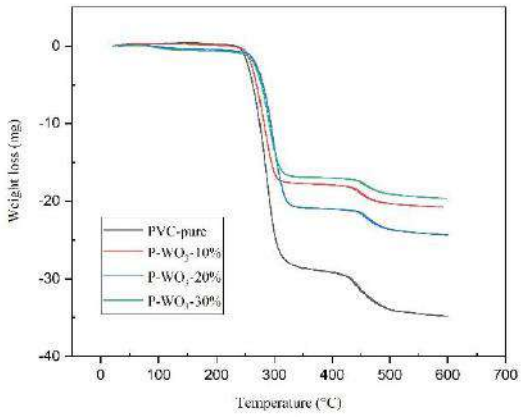

(b)

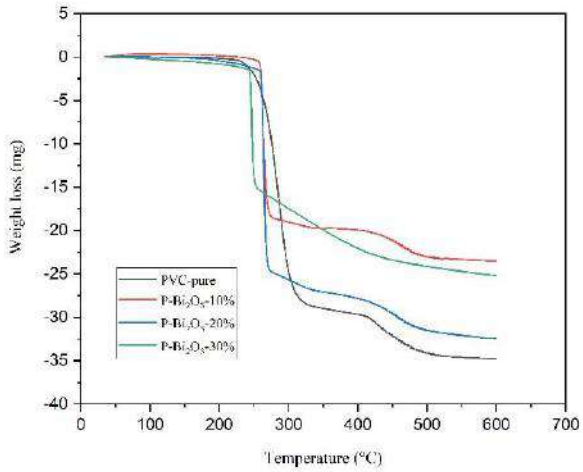

(c)

Fig. 4. TGA curves of pure and PVC-based nanocomposites filled with (a) Pb_2O_3, (b) WO_3 and (c) Bi_2O_3 nanoparticles.

1.2. Stress-strain analysis. The effects of incorporating Pb_2O_3, WO_3 and Bi_2O_3 nanoparticles on the tensile stress-strain behavior of the PVC polymers were investigated. As can be seen in the figure 8 and tables (1-3),

the added fillers improve the tensile properties of PVC composites. For example, adding 30% by weight of nanoparticles (the highest percentage of nanoparticles) to the PVC matrix significantly increases the tensile strength of the composites (80%).

Table1. Tensile properties of the pure and reinforced PVC with various concentrations of Pb_2O_3 nanofillers

Material properties	PVC-pure	PVC-based nanocomposites with Pb_2O_3 nanofiller		
		10 Wt%	20 Wt%	30 Wt%
Young's modulus, E_t (MPa)	10.90	18.48	34.14	122.56
Tensile strength, σ_t (MPa)	5.50	6.71	6.43	9.89
Tensile strain at break, ε_t (%)	198.95	142.21	162.94	99.75

Table2. Tensile properties of the pure and reinforced PVC with various concentrations of WO_3 nanofillers

Material properties	PVC-pure	PVC-based nanocomposites with WO_3 nanofiller		
		10 Wt%	20 Wt%	30 Wt%
Young's modulus, E_t (MPa)	10.90	8.47	21.63	29.70
Tensile strength, σ_t (MPa)	5.50	1.83	3.36	5.26
Tensile strain at break, ε_t (%)	198.95	107.07	110.94	207.16

Table3. Tensile properties of the pure and reinforced PVC with various concentrations of Bi_2O_3 nanofillers

Material properties	PVC-pure	PVC-based nanocomposites with Bi_2O_3 nanofiller		
		10 Wt%	20 Wt%	30 Wt%
Young's modulus, E_t (MPa)	10.90	10.49	21.68	123.79
Tensile strength, σ_t (MPa)	5.50	5.70	2.43	4.37
Tensile strain at break, ε_t (%)	198.95	162.93	165.75	55.95

The reason can be that in the PVC matrix that bears the force, due to the presence of nanoparticles, the effective cross-sectional area has decreased. In addition, the good and optimal distribution of nanoparticles leads to a more uniform distribution of stress in the polymer matrix [7]. Fig. 5 shows the stress-strain curves of the pure and the filled PVC-based nanocomposites for different weight fractions of Pb_2O_3, WO_3, and Bi_2O_3 nanoparticles.

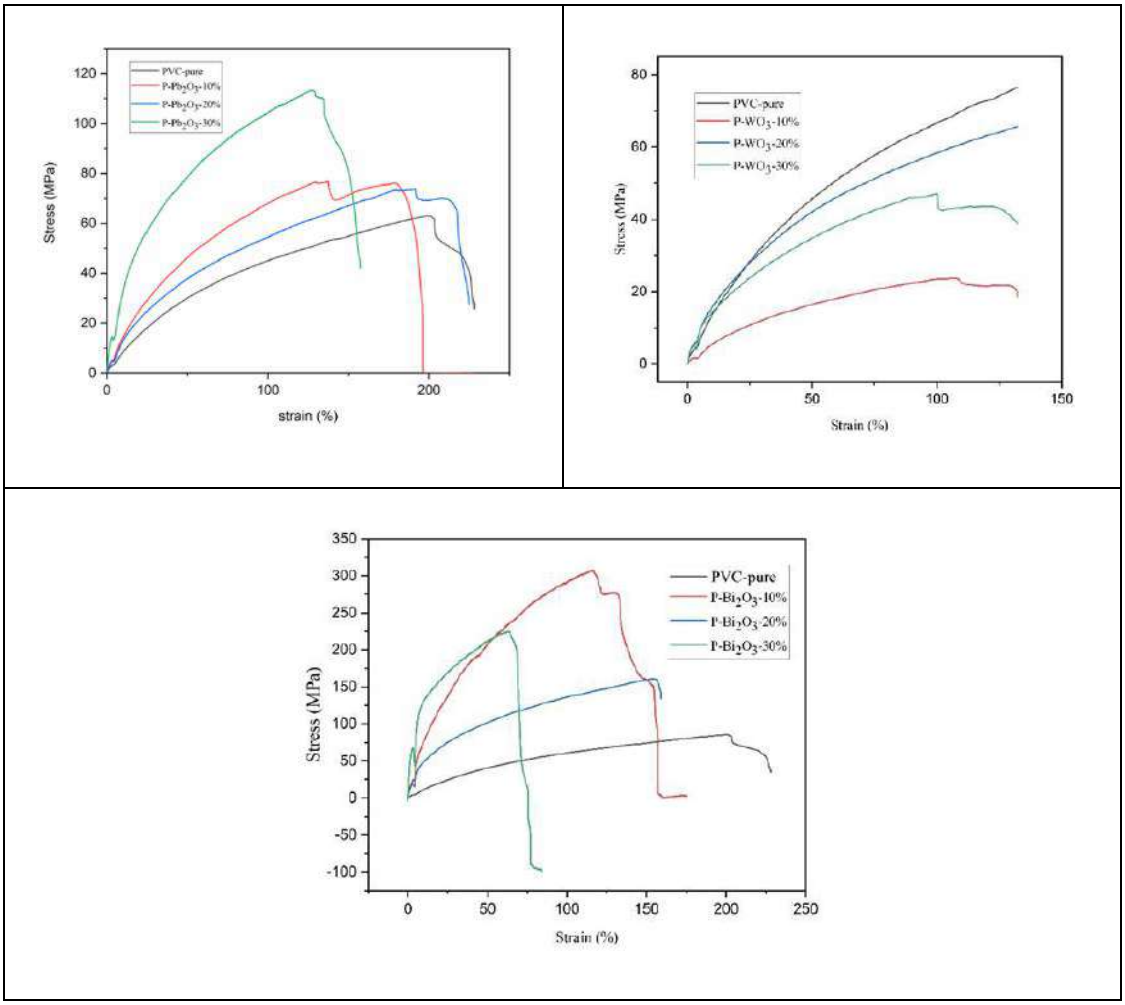

Fig. 5. Stress-strain curves of nano Pb_2O_3 , WO_3, and Bi_2O_3 filled PVC composites.

1.3. Shielding analysis. To evaluate the shielding performance of prepared samples, an experimental setup was utilized (Fig.6).

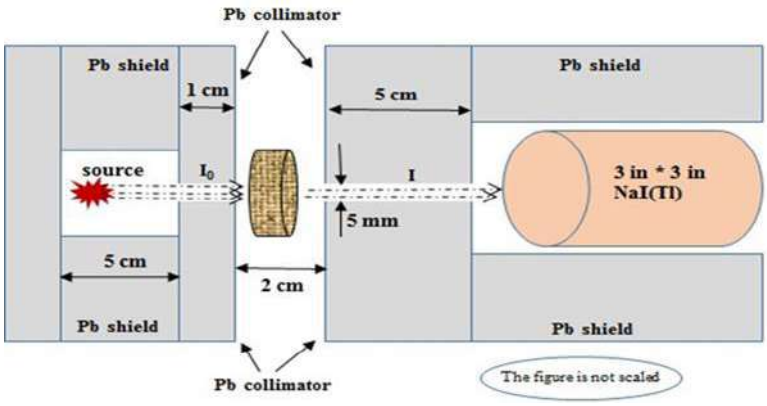

Fig. 6. Schematic setup of the experiment **[8]**

The results of tables 4-6 show that the linear attenuation coefficient (LAC) values increase, half value layer (HVL), and mean free path (MFP) values decrease with rising Pb_2O_3, WO_3, and Bi_2O_3 concentration in PVC-based nanocomposites.

Table 4. LAC values of PVC-based nanocomposite samples contained metal oxide nanoparticles in different energy values

Polymer	NPS	Wt% / E	LAC (cm^{-1})			
			60 keV	662 keV	1173 keV	1332 keV
PVC	Pb_2O_3	0	0.4629	0.1068	0.0809	0.0758
		10%	1.172	0.1232	0.0918	0.0827
		20%	2.061	0.1442	0.1048	0.0914
		30%	3.198	0.1682	0.1219	0.1030
PVC	WO_3	0	0.4629	0.1068	0.0809	0.0758
		10%	0.9152	0.1195	0.0889	0.0832
		20%	1.4537	0.1338	0.0973	0.0908
		30%	2.026	0.150	0.1073	0.1001
PVC	Bi_2O_3	0	0.4629	0.1068	0.0809	0.0758
		10%	0.5818	0.1183	0.0894	0.0840
		20%	1.979	0.1395	0.1086	0.0927
		30%	3.003	0.1608	0.1100	0.1030

Table 5. HVL values of PVC-based nanocomposite samples contained metal oxide nanoparticles in different energy values

Polymer	NPS	Wt% / E	HVL (cm)			
			60 keV	662 keV	1173 keV	1332 keV
PVC	Pb_2O_3	0	1.493	6.424	8.349	9.023
		10%	0.589	5.625	7.569	8.362
		20%	0.335	4.790	6.620	7.228
		30%	0.216	4.077	5.776	6.395
PVC	WO_3	0	1.493	6.424	8.349	9.023
		10%	0.7572	5.799	7.787	8.323
		20%	0.4767	5.179	7.124	7.624
		30%	0.3420	4.62	6.458	6.920

		0	1.493	6.424	8.349	9.023
		10%	1.191	5.854	7.744	8.248
PVC	**Bi_2O_3**	**20%**	0.3500	4.967	6.387	7.471
		30%	0.2307	4.309	6.297	6.722

Table 6. MFP values of PVC-based nanocomposite samples contained metal oxide nanoparticles in different energy values

Polymer	**NPS**	**Wt% E**	**MFP (cm)**			
			60 keV	**662 keV**	**1173 keV**	**1332 keV**
		0	2.160	9.367	12.36	13.19
PVC	**Pb_2O_3**	**10%**	0.849	8.117	10.89	12.09
		20%	0.485	6.939	9.551	10.94
		30%	0.312	5.942	8.233	9.702
		0	2.160	9.367	12.36	13.19
PVC	**WO_3**	**10%**	1.092	8.368	11.237	12.01
		20%	0.6878	7.473	10.280	11.002
		30%	0.4935	6.666	9.319	9.986
		0	2.160	9.367	12.36	13.19
PVC	**Bi_2O_3**	**10%**	1.718	8.448	11.175	11.901
		20%	0.5051	7.168	9.200	10.781
		30%	0.333	6.218	9.087	9.700

2. DISCUSSION: According to present study, the TGA results indicate that the adding of metal oxide nano fillers to the PVC matrix, improve the thermal stability of nanocomposites. Although both filled and unfilled samples do not experience any weight loss within the temperature range of 25°C - 250°C. It can be seen that the addition of metal oxide nanoparticles to the PVC-based nanocomposites increases the tensile strength which is in good agreement with recent studies [8, 9]. The protective properties of samples show significant improvement, especially in low energies, by adding the mentioned nanoparticles, as expected [10, 11].

Conclusions

This study aimed to investigate the thermal, mechanical, and shielding properties of Pb_2O_3, WO_3 , and Bi_2O_3 nanocomposites based on polyvinyl chloride at different weight percentages of the additives (10, 20, 30 wt%). A straightforward and low-cost electrochemical method was utilized to synthesize the mentioned nanoparticles, and the casting technique was used to prepare the composite samples. Various characterization techniques demonstrated that the nanoparticles were successfully synthesized and uniformly dispersed in the polymer matrix. The thermogravimetric results showed that the addition of metal oxide nanofillers cause the more stability of nanocomposites. Results showed that the percentage of nanoparticles in the composites had a direct effect on the tensile strength of PVC polymers, indicating that the interaction between nanoparticles and PVC is very strong, and therefore the nanocomposites have higher strength than the original polymer. The shielding properties of the nanocomposites were tested by placing them in front of radiation sources and measuring their shielding parameters in a laboratory. The results showed that the radiation performance of the nanocomposites demonstrate that the more nanofillers added, the better the shielding properties of the nanocomposites became [2, 5, 12, 13].

References

1. Mehnati, P., R. Malekzadeh, and M.Y. Sooteh, Application of personal non-lead nano-composite shields for radiation protection in diagnostic radiology: A systematic review and meta-analysis. Nanomed. J, 2020. **7**(3): p. 170-82.

2. Zali, V.S., O. Jahanbakhsh, and I. Ahadzadeh, Preparation and evaluation of gamma shielding properties of silicon-based composites doped with WO3 micro-and nanoparticles. Radiation Physics and Chemistry, 2022. **197**: p. 110150.

3. Özdemir, T., et al., Nano lead oxide and epdm composite for development of polymer based radiation shielding material: Gamma irradiation and attenuation tests. Radiation Physics and Chemistry, 2018. **144**: p. 248-255.

4. Ambika, M., et al., Preparation and characterisation of Isophthalic-Bi2O3 polymer composite gamma radiation shields. Radiation Physics and Chemistry, 2017. **130**: p. 351-358.

5. Muthamma, M., et al., Micro and nano Bi2O3 filled epoxy composites: Thermal, mechanical and γ-ray attenuation properties. Applied Radiation and Isotopes, 2021. **174**: p. 109780.

6. Maduraiveeran, G., M. Sasidharan, and W. Jin, Earth-abundant transition metal and metal oxide nanomaterials: Synthesis and electrochemical applications. Progress in Materials Science, 2019. **106**: p. 100574.

7. Chai, H., et al., Preparation and properties of novel, flexible, lead-free X-ray-shielding materials containing tungsten and bismuth (III) oxide. Journal of Applied Polymer Science, 2016. **133**(10).

8. Rahimi, S., O. Jahanbakhsh, and I. Ahadzadeh, Effects of Pb2O3 nanoparticles on thermal and mechanical properties of epoxy resin, silicone, and PVC-based nanoshields. Progress in Nuclear Energy, 2024. **169**: p. 105083.

9. Bhatia, S., S. Angra, and S. Khan. Mechanical and wear properties of epoxy matrix composite reinforced with varying ratios of solid glass microspheres. in Journal of Physics: Conference Series. 2019. IOP Publishing.

10. Oliver, N., R.M. Ramli, and N.Z.N. Azman, An empirical study on the X-ray attenuation capability of n-WO3/n-Bi2O3/PVA with added starch. Nuclear Engineering and Technology, 2022. **54**(9): p. 3459-3469.

11. Nambiar, S. and J.T. Yeow, Polymer-composite materials for radiation protection. ACS applied materials & interfaces, 2012. **4**(11): p. 5717-5726.

12. Sayyed, M., et al., The influence of PbO and Bi2O3 on the radiation shielding and elastic features for different glasses. Journal of Materials Research and Technology, 2020. **9**(4): p. 8429-8438.

13. Mahmoud, K., et al., The effect of CuO additive on the mechanical and radiation shielding features of Li2B4O7–Pb2O3 glass system. Boletin de la sociedad espanola de ceramica y vidrio, 2022. **61**(4): p. 275-283.

ICNST 2024
International Conference on Nuclear Science and Technology
6- 8 MAY 2024 | Isfahan, Iran

Measurement of the activity of soil samples in Shazand region with experimental and simulation methods (Paper ID : 1570)

Kiyani A.[1*], Mohebian M.[2], Salehi M.[3], Karimi M.[4]
[1,2]*Nuclear Physics, Arak University, Arak, Iran*
[3] *Nuclear Physics, Kashan University, Kashan, Iran*
[4] *Nuclear Engineering, Amirkabir University, Tehran, Iran*

Abstract

In order to investigate the effects of environmental pollution, it is essential to measure the amount of radiation accurately. A gamma spectroscopy system (HPGe detector) was utilized to determine the activity of soil samples in the Shazand region. For this purpose, a detector efficiency calibration curve using reference sources is required. Gamma rays are attenuated due to self-absorption, making it impossible to calculate the correct amount of gamma radiation. Therefore, it is necessary to consider the self-absorption correction factor to measure the activity of sample accurately. This article determined the amount of self-absorption correction using the ratio of simulation efficiency to experimental efficiency, and its dependence on energy was investigated. The International Atomic Energy Agency's (Standard Source) reported values served as the basis for the self-absorption correction coefficient evaluation and calculation. The investigation results show that the correction coefficient for self-absorption using Monte Carlo simulation methods depends on energy. Comparing the experimental results of the activity while considering the self-absorption correction factor shows good compatibility with the simulation, with a calculation error of less than 10%.

Keywords: Activity, Simulation, HPGe detector, self-absorption correction coefficient

INTRODUCTION

Quantitatively evaluating radiation levels in the environment is essential for a wide range of applications, including nuclear safety and environmental monitoring. The precise quantification of radioactive elements in environmental samples necessitates careful examination of multiple aspects that may impact the outcomes. Germanium detectors are widely recognized for their exceptional energy resolution, making them essential instruments for quantitatively examining radioactive elements. Nevertheless, quantifying radiation levels in environmental samples has several difficulties. There are numerous factors that can lead to measurement errors, including pile-up, dead time, background effects, interference effects, coincident summation effects, and single-escape and double-escape peak effects. It is of utmost importance to consider these parameters to ensure accurate measurement of activity levels [1, 2].

The HPGe detector manufactured by BSI was used. This detector's efficiency is 30%, and it is used in the nuclear laboratory of Arak University. The HPGe detector is p-type coaxial, and its entrance window is aluminum.This basic feature can improve the device's accuracy and performance and ensure its stability and high accuracy in radioactive measurements.Fig 1 shows a view of the detector used in the laboratory.

One viable strategy for improving precision entails using spectrum registration methodologies, which may be implemented by employing either an empty container or a container filled with distilled water. By incorporating spectrum analysis software, this approach facilitates enhanced measurement precision through background radiation adjustment. It is important to note that the background measurement length should match the spectrum counting period for the sample to maintain consistency and dependability. This is especially important for samples with minimal activity, such as distilled water [3, 4]. Efficiency plays a crucial role in the determination of activities. The process of calibrating the sample-detector system requires the achievement of chemical composition and density matching between the standard source and the sample. When this method is used, it guarantees that the gamma rays will be reduced fairly, which means that self-absorption correction factors in the specimen are not needed [5]. Nevertheless, when dealing with energies below 100 keV, such as those produced by ^{129}I, ^{210}Pb, or ^{241}Am, it becomes crucial to apply self-absorption correction. The relevance of this impact declines above a threshold of 100 eV [6, 7].

The experimental estimate of the self-absorption correction factor at energies of 295, 911, and 1461 keV supports the accuracy of activity measurements. Researchers have carefully calculated the correction factor using experimental and simulation techniques, leading to the development of equations that show a relationship between this factor and energy [8, 9]. This work aims to investigate the computation and importance of the self-absorption correction factor, elucidating its crucial function in enhancing the precision of radioactivity measurements. Through a thorough examination of the issues outlined earlier and the use of strong methodology, our goal is to make a valuable contribution to the progress of accurate environmental radioactivity assessment. This will ultimately promote improved safety and environmental responsibility.

RESEARCH THEORIES:

Geant4 (Geometry and Tracking) is a Monte Carlo simulation code developed and designed to simulate the propagation of particles or radiation across different materials. Due to its multifaceted functionalities, this software allows for the generation of simulations encompassing a diverse array of devices, detectors, and radiation sources. Additionally, it facilitates the documentation of specific outputs that illustrate the physical

quantities arising from the interactions between source particles and detector materials. The behavior of a high-purity germanium (HPGe) detector was simulated using Geant4 version 11.1.1 in this work. The electromagnetic interactions within the detector were modeled using the G4EmStandardPhysics_option4 package. The selection of this package was based on its remarkable accuracy and precision in the computation of low-energy interactions, hence guaranteeing dependable outcomes in our simulations [10, 11].

We employed the General Particle Source (GPS) type of particle source with predetermined volume parameters to simulate particle emissions from the radiation source. The utilization of this methodology enabled us to effectively depict the emission of particles in a spherical fashion, thereby conveying the complexities associated with particle propagation. In our experimental approach, we did not incorporate a filter into the code to analyze the spectrum within the active volume of the detector. The process of spectrum extraction was conducted with great attention to detail, utilizing the Event class, which facilitated an accurate examination of the identified radiation spectrum [12].

You can obtain the necessary spectrum in Geant4 by utilizing the optional classes.In this study, we used the Event class to compute the sub-photopic count, gathering the Total Energy Deposit value for each event in the detector's active volume and drawing its spectrum using the Root tool.To calculate the photopic efficiency, we must first determine the number of gamma rays released from the source volume.For this, we used the Steping class. We then calculated the efficiency using the following formula:

$$\varepsilon(E) = \frac{C}{C_0} \quad (1)$$

C: The number of gamma rays detected in the detector's active volume at energy E.

C_0: The number of gamma rays released by the source at energy E [13].

In addition, our work involved evaluating the efficiency of the detector-sample system and calculating the self-absorption coefficient for ambient samples using Geant4 modeling software. The purpose of using these algorithms was to gain a more profound understanding of the interaction between ambient samples and the detection system, with the ultimate goal of improving the accuracy and reliability of our data. Our research significantly contributes to radiation detection techniques, improving our understanding of environmental monitoring processes using Geant4 and precise simulation methodology.

EXPERIMENTAL

-Sampling and Sample Preparation: The sampling process involved selecting 10 soil samples randomly from sun-exposed orchard communities and slopes. A square area measuring one square meter, extending to a depth of 10 cm below the soil surface, consisted of four points at the corners and one point at the center of each sample location. For comprehensive details on the sampling regions Fig.2 and the steps involved in sample preparation, please see the reference [8].

Fig. 1. The gamma spectrum system utilizes HPGe detector and equipment

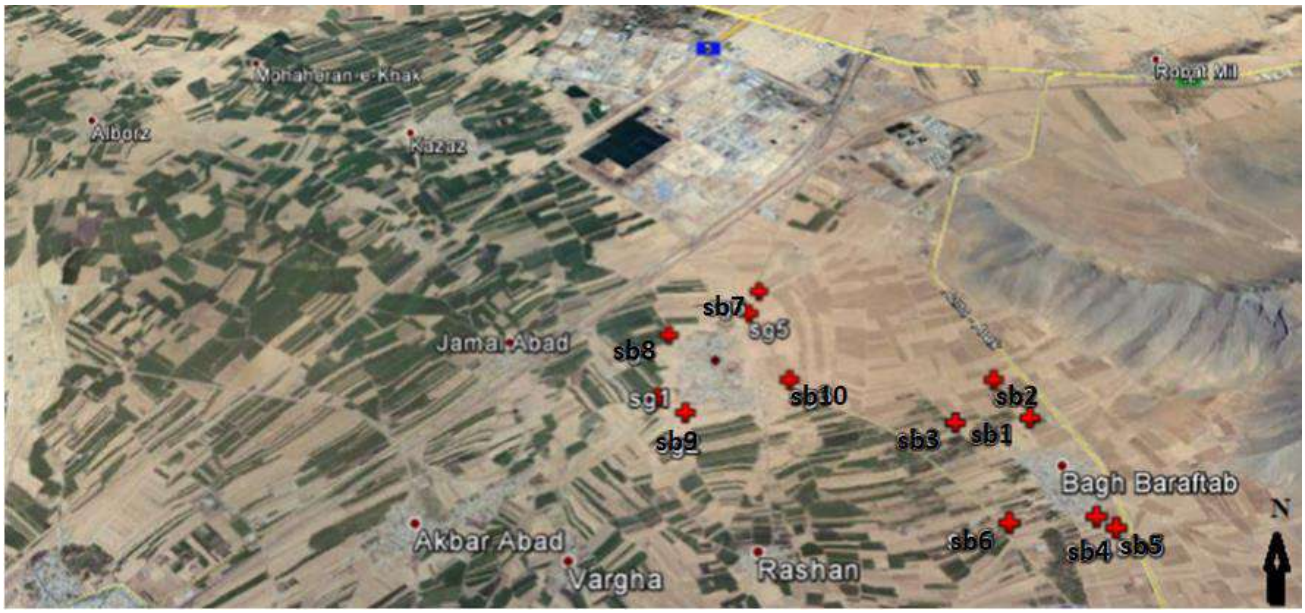

Fig. 2. Location of the research area and the sampling site marked with a red plus sign and black color

Measurement of Efficiency Using HPGe Detector: In this study, the efficiency of the detector-sample system was measured using reference materials and a high-purity germanium (HPGe) detector. The reference materials comprised RGU, which exhibited an average activity of 4940 Bq/kg, RGTh, which displayed an average activity of 3250 Bq/kg, and RGTh, which exhibited an average activity of 14000 Bq/kg. The employed detector exhibits a 30% efficiency and a 1.85 keV energy resolution.

In order to calibrate the energy of the system before spectrometry of the environmental sample, we rely on the crucial role of standard sources or reference materials such as (Reference Materials) RMs (RGU-1, RGTh-1, RGK-1). These materials, including uranium, thorium, and potassium reference materials (RGK-1, RGTh-1, and RGU-1), contain certain amounts of natural uranium (with radioactive daughter nuclei), natural thorium (with radioactive daughter nucleid), and potassium. The gamma spectrum of reference materials is in the energy range of 50 keV to above 2000 keV. The gammas from standard sources are well known and have precisely defined energies. RMs standard sources are one of the most important things due to having special nuclues with long half-life and low manufacturing cost. RMs contain special radioactive nuclei that cover gamma photons in the energy range from 46.5 keV (Pb210) to 2614Tl (208) keV[14].

-Calculation of Self-absorption Correction Factor: Analytical relationships based on the mass attenuation coefficient have been proposed by several scholars, such as Katchal, Roba, Ike, and Jadelowski, in order to ascertain the self-absorption correction factor [15, 16]. The present study employed the self-absorption correction factor, as defined by Jadelowski (2017), to calculate the self-absorption correction coefficient. The underlying assumption of this equation is that the efficiency of the standard sample is equivalent to the effective efficiency of the sample, as anticipated. The efficiency that needs to be estimated is represented by the calculated efficiency, which was acquired through simulation using the Geant4 approach [17, 18]. The equation obtained from Jadelowski's formulation can be applied to gamma detectors of any size, regardless of their non-cylindrical shape, and to any kind of gamma radiation. This approach provides a direct and effective way to calculate the self-absorption correction.

We estimated the empirical efficiencies for all 10 samples using an HPGe detector, which was based on the efficiency curve of reference materials [8]. The measurements were taken in eight gamma lines. Each sample had a weight of 300 grams and varied heights, leading to varying densities. Simulated calculations of the efficiency of 8 gamma lines took into account the soil's unique composition, height, and density. Following

this, the coefficient for self-absorption adjustment was calculated by dividing the simulated efficiency by the empirical efficiency [8] for all energy levels.

$$C_{SA} = \frac{\varepsilon_{sim}}{\varepsilon_{exp}} \quad (2)$$

In equation (2), C_{SA} stands for the self-absorption correction coefficient, ε_{sim} for the simulated efficiency obtained using the Geant4 simulation method, and ε_{exp} for the experimental efficiency as measured using the empirical approach. The gamma lines of 295.22, 911.25, and 1460.80 have been utilized to compute the activity of Ra-226, Th-232, and K-40, respectively. Table 3 displays the outcomes of computations and measurements, expressed in units of Becquerel per kilogram (Bq/kg). Without accounting for the correction factor and with accounting for the correction factor, respectively, A and A_{sa} denote the specific activity of Ra-226 (Th-232 and K-40) nuclei.

Results and discussion:

Two distinct approaches, namely the empirical method and the Geant4 simulation method, were employed to evaluate the efficiency of the detector-sample system. The empirical approach employed the calibration efficiency curve to quantify the efficiency of the system. Furthermore, the efficiency was calculated using the Geant4 simulation method, and the findings were then summarized in Table 4. Additionally, the self-absorption correction coefficient obtained from the Geant simulation is presented in Table 4. In this statement, the strategies utilized to assess the effectiveness of the detector-sample system are outlined, emphasizing both empirical and simulation-based approaches. The use of calibration efficiency curves and Geant4 simulations emphasizes how thorough the research is.

Table 1. For energy level 1460.83 physical property, efficiency, and specific activity in soil samples

Sample code	Density gr/cm^3	Efficiency		Correction Factor	Activity (Bq/kg)	
		Simulation	Experimental		A	A_{sa}
Sb1	1.36	0.006467	0.008009	0.8075	583.92±16.53	**723.12**
Sb2	1.33	0.006494	0.008009	0.8109	560.51±20.62	**691.22**
Sb3	1.41	0.006436	0.008009	0.8036	485.53±13.82	**604.19**
Sb4	1.43	0.006380	0.008009	0.7967	443.98±12.85	**557.27**
Sb5	1.35	0.006467	0.008009	0.8075	305.95±8.52	**378.89**

Sb6	1.34	0.006468	0.008009	0.8076	524.67±12.27	**649.67**
Sb7	1.39	0.006433	0.008009	0.8033	527.04±12.49	**656.09**
Sb8	1.33	0.006465	0.008009	0.8073	391.73±10.17	**485.23**
Sb9	1.36	0.006457	0.008009	0.8063	446.86±10.95	**554.21**
Sb10	1.40	0.006433	0.008009	0.8033	509.06±16.76	**633.71**

Table 2. For energy level 911.25 physical property, efficiency, and specific activity in soil samples

Sample code	Density gr/cm^3	Efficiency		Correction Factor	Activity (Bq/kg)	
		Simulation	Experimental		A	A_{sa}
Sb1	1.36	0.009244	0.011289	0.8188	32.99±2.53	**40.2894**
Sb2	1.33	0.009328	0.011289	0.8263	30.65±2.13	**37.0945**
Sb3	1.41	0.009199	0.011289	0.8148	26.65±2.02	**32.7058**
Sb4	1.43	0.00913	0.011289	0.8087	26.5±2.09	**32.7675**
Sb5	1.35	0.009247	0.011289	0.8191	18.63±1.79	**22.7447**
Sb6	1.34	0.009244	0.011289	0.8188	30.23±2.93	**36.9187**
Sb7	1.39	0.009202	0.011289	0.8151	33.93±2.81	**41.6265**
Sb8	1.33	0.009256	0.011289	0.8199	23.28±1.84	**28.3941**
Sb9	1.36	0.009229	0.011289	0.8175	25.07±2.53	**30.6668**
Sb10	1.40	0.009202	0.011289	0.8151	26.65±1.32	**32.6951**

Table 3. For energy level 295.22, physical property, efficiency, and specific activity in soil samples

Sample code	Density gr/cm^3	Efficiency		Correction Factor	Activity (Bq/kg)	
		Simulation	Experimental		A	A_{sa}
Sb1	1.36	0.02165	0.028606	0.756826	31.85±1.79	**42.0836**
Sb2	1.33	0.021834	0.028606	0.763266	29.75±1.92	**38.9772**
Sb3	1.41	0.021373	0.028606	0.74716	24.86±1.97	**33.2727**
Sb4	1.43	0.021021	0.028606	0.734836	25.95±2.15	**35.314**
Sb5	1.35	0.021614	0.028606	0.755563	16.87±1.89	**22.3277**
Sb6	1.34	0.021622	0.028606	0.755843	28.77±1.69	**38.0635**
Sb7	1.39	0.021353	0.028606	0.74646	26.91±1.42	**36.0502**
Sb8	1.33	0.021598	0.028606	0.755003	21.68±1.81	**28.7151**
Sb9	1.36	0.021485	0.028606	0.751081	26.09±2.05	**34.7366**
Sb10	1.40	0.021373	0.028606	0.74716	24.58±2.12	**32.8979**

Table 4. Calculated values in Geant4 simulation for output spectrum from reference sources

Sample code	Source	RMS (active volume)	Mean
Sb1	RGK	0.1866	0.03349
	RGTh	0.09255	0.01779
	RGU	0.05893	0.01066
Sb2	RGK	0.1870	0.03403
	RGTh	0.09272	0.01801
	RGU	0.05904	0.01068
Sb3	RGK	0.1862	0.03385

	RGTh	0.09235	0.01793
	RGU	0.0588	0.01062
Sb4	RGK	0.1859	0.03381
	RGTh	0.09224	0.01793
	RGU	0.05861	0.01059
Sb5	RGK	0.1866	0.03395
	RGTh	0.09254	0.01797
	RGU	0.05893	0.01065
Sb6	RGK	0.1866	0.03395
	RGTh	0.09253	0.01797
	RGU	0.05892	0.01065
Sb7	RGK	0.1862	0.03384
	RGTh	0.09235	0.01793
	RGU	0.05881	0.01062
Sb8	RGK	0.1866	0.03396
	RGTh	0.09253	0.01797
	RGU	0.05891	0.01065
Sb9	RGK	0.1864	0.03389
	RGTh	0.09249	0.01796
	RGU	0.05883	0.01063
Sb10	RGK	0.1862	0.03384
	RGTh	0.09238	0.01794
	RGU	0.05883	0.01063

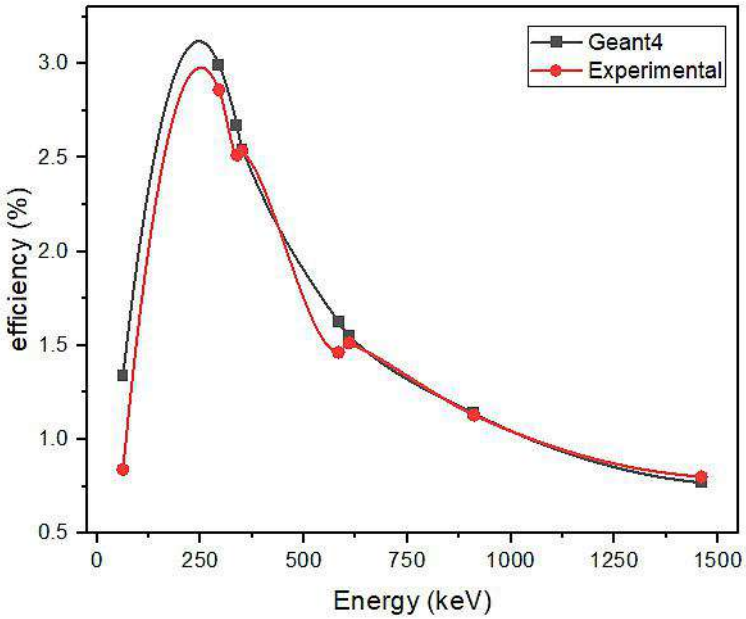

Fig. 3. Energy-based return chart (simulation and experience agree well)

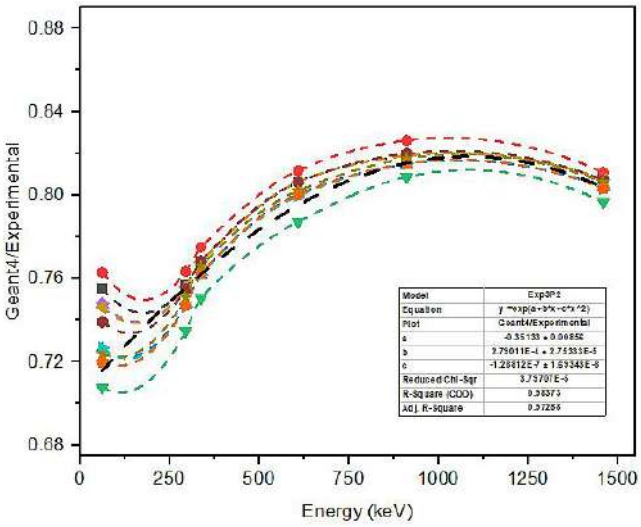

Fig. 4. Energy-adjusted decay curve with 10 samples and R-Square 0.97 fittings

Table 5. Compare the correction factor for various energies and their effect on activity

Sample code	Density gr/cm^3	Energy	Correction Factor	Activity (Bq/kg)	
				A	A_{sa}
Sb1	1.36	1460.83	0.8075	583.92	723.12074
		911.25	0.818826	32.99	40.2894
		295.22	0.756826	31.85	42.0836
Sb2	1.33	1460.83	0.8109	560.51	691.21963
		911.25	0.826268	30.65	37.0945
		295.22	0.763266	29.75	38.9772
Sb3	1.41	1460.83	0.8036	485.53	604.19363
		911.25	0.81484	26.65	32.7058
		295.22	0.74716	24.86	33.2727
Sb4	1.43	1460.83	0.7967	443.98	557.27375
		911.25	0.734836	25.95	35.314
		295.22	0.734836	25.95	35.314
Sb5	1.35	1460.83	0.8075	305.95	378.88545
		911.25	0.819092	18.63	22.7447
		295.22	0.755563	16.87	22.3277
Sb6	1.34	1460.83	0.8076	524.67	649.66568
		911.25	0.818826	30.23	36.9187
		295.22	0.755843	28.77	38.0635
Sb7	1.39	1460.83	0.8033	527.04	656.09361
		911.25	0.815106	33.93	41.6265
		295.22	0.74646	26.91	36.0502
Sb8	1.33	1460.83	0.8073	391.73	485.23473
		911.25	0.819889	23.28	28.3941
		295.22	0.755003	21.68	28.7151

Sb9	1.36	1460.83	0.8063	446.86	554.21059
		911.25	0.817497	25.07	30.6668
		295.22	0.751081	26.09	34.7366
Sb10	1.40	1460.83	0.8033	509.06	633.71094
		911.25	0.815106	26.65	32.6951
		295.22	0.74716	24.58	32.8979

Conclusions

In summary, the Fig 3 shows that the simulation results and experimental data agree well regarding the efficiency in terms of eight gamma lines.This agreement shows that the simulation model used to simulate soil samples can predict and produce results similar to accurate data.In this comparison, the standard source was used in both simulation and experiment, which confirms the excellent adaptation of simulation to experiment. the analysis of the simulated performance using Geant4 and the experimental data, as depicted in Table 5, demonstrates a level of compatibility within a 15% margin. Furthermore, the examination of self-absorption correction coefficients as presented in Table 5 reveals a noticeable correlation with energy. The average self-absorption correction factors derived across several samples exhibit significant variances, ranging from 0.7662 to 0.7933. The presence of an average coefficient of 0.7765 across all samples and energies in this observation highlights the significant influence of sample composition and energy levels on self-absorption. Moreover, a close study of how the self-absorption correction coefficient changes at gamma-ray energies of 295.22, 911.25, and 1460.80 eV (Table 3) shows that this correction coefficient is definitely affected by changes in energy variables. The Fig.4 displays the simulation-to-experimental ratio based on eight gamma lines for 10 soil samples.The diagram illustrates a consistent trend across all samples, with an R-squared value of 0.98, indicating a high degree of fitting for the data. Although there is overall consistency observed among the samples at these energy levels, sample Sb4 exhibits deviations mostly attributed to its increased density in comparison to the other samples. In conclusion, sample sb4's different self-absorption correction coefficients highlight the significance of sample density in influencing the effectiveness of gamma-ray detection. These findings emphasize the importance of taking into account both energy dependence and sample characteristics in the context of applying self-absorption adjustments in gamma-ray spectroscopy analysis.

References:

[1] Knoll, G. F. (2010). Radiation detection and measurement. John Wiley & Sons.

[2] Sima, O., & Arnold, D. (2000). Accurate computation of coincidence summing corrections in low level gamma-ray spectrometry. Applied Radiation and Isotopes, 53(1-2), 51-56.

[3] Pourimani, R., & Mohebian, M. (2021). Study of background correction of gamma-ray spectrometry using reference materials. Iranian Journal of Science and Technology, Transactions A: Science, 45(2), 733-736.

[4] Debertin, K., & Helmer, R. G. (1988). Gamma-and X-ray spectrometry with semiconductor detectors.

[5] Hubbell, J. H. (1982). Photon mass attenuation and energy-absorption coefficients. The International Journal of Applied Radiation and Isotopes, 33(11), 1269-1290.

[6].Berger, M. (2010). XCOM: photon cross sections database.
http://www. nist. gov/pml/data/xcom/index. cfm.

[7] Souci, S., Fachmann, W., & Kraut, H. (2011). Lebensmitteltabelle für die Praxis. Aufl. Wissenschaftl. Verlagsges. Stuttgart.

[8] Mohebian, M., Pourimani, R., & Modarresi, S. (2019). Using MCNP simulation for self-absorption correction in HPGe spectrometry of soil samples. Iranian Journal of Science and Technology, Transactions A: Science, 43, 3047-3052.

[9] Mostajaboddavati, M., Hassanzadeh, S., Faghihian, H., Abdi, M., & Kamali, M. (2006). Efficiency calibration and measurement of self-absorption correction for environmental gamma-spectroscopy of soil samples using Marinelli beaker. Journal of Radioanalytical & Nuclear Chemistry, 268(3).

[10] Incerti. (Incerti). Cern Wiki for GEANT4, 2023.
https://twiki.cern.ch/twiki/bin/view/Geant4/LowePhysicsLists

[11] Geant4. (2023). Geant4 User's Guide for Toolkit Developers, Release, 11.1.1.

[12] Allison, J., Amako, K., Apostolakis, J., Araujo, H., Dubois, P., & Asai, M. (2003). Geant4-a simulation toolkit. Nucl. Instrum. Meth. A, 506(3), 250-303.

[13] Lin, M., Wang, Y., & Qin, Z. (2023). Determination of detection efficiency on HPGe detector for point-like and volumetric samples based on Geant4 simulations. Applied Radiation and Isotopes, 200, 110989.

[14] Oddone, M., Giordani, L., Giacobbo, F., Mariani, M., & Morandi, S. (2008). Practical considerations regarding high resolution gamma-spectrometry measurements of naturally occurring radioactive samples. Journal of Radioanalytical and Nuclear Chemistry, 277(3), 579-585.

[15] Eke, C., Agar, O., Boztosun, I., Aslan, A., & Emsen, B. (2017). Determination of self-attenuation correction factor for lichen samples by using gamma-ray spectrometry. Kerntechnik, 82(1), 136-139.

[16] Cutshall, N. H., Larsen, I. L., & Olsen, C. R. (1983). Direct analysis of 210Pb in sediment samples: self-absorption corrections. Nuclear instruments and methods in physics research, 206(1-2), 309-312.

[17] Robu, E., & Giovani, C. (2009). Gamma-ray self-attenuation corrections in environmental samples. Romanian Reports in Physics, 61(2), 295-300.

[18] Jodłowski, P., Wachniew, P., & Nowak, J. (2017). Determination of the self-attenuation based on the sample composition in gamma-ray spectrometry of 210 Pb: requirements for the scope of chemical analyses. Journal of Radioanalytical and Nuclear Chemistry, 311, 1511-1516.

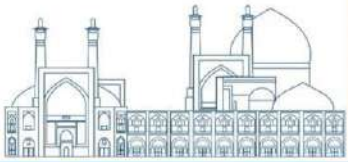

ICNST 2024 International Conference on Nuclear Science and Technology
6- 8 MAY 2024 | Isfahan, Iran

Image Quality Indicators implementation for High Energy Cargo Scanners (Paper ID : 1580)

Sadegh Yousefi[1*], Ali-Reza Homa[1], Hasan Fallahi [1], Seyed Mohammad Amin Hoseiny[1] Seyed Mohammad Mahdi Saadatmand[1], Masoud Ghorbani Qomi[1], and Amir Movafeghi[2]

[1*]*Fateh Scan Company, Qom University, Qom, Iran*
[2]*Reactor and Nuclear Safety Research School, Nuclear Science and Technology Research Institute (NSTRI), Tehran, Iran*

Abstract

The container and cargo inspection by high energy X-ray scanner is an effective way to control imported goods with containers. These scanners can prevent human smuggling and transportation of prohibited and restricted items without cargo unloading. Some of the important parameters of cargo inspection systems are including: the speed of scanning, the penetration of X-ray, imaging system spatial resolution and differentiating between different materials. Evaluation of different parameters of system is a necessary job that must be performed. The quality of final image has to be evaluated by using special objects. In this article, a specific image quality indicator object has been designed base on ANSI-N42.46 standard. Four different imaging tests have been defined for this quality testing object according to the standard. After initial design, other peripheral objects have been added to the test object. Different section of this imaging quality control object has been constructed and assembled. After that, this object has been used for testing of a high energy cargo scanner. The output images of the system were used for complete evaluation of cargo scanner specifications. The results show that this test object can be implemented effectively for the evaluation of different cargo scanner systems.

Keywords: Cargo scanner, Image quality test object, High energy X-rays, Penetrating power

INTRODUCTION

The rapid growth in international commerce has presented a significant challenge for cargo security, and one of the primary issues is the limited capacity to inspect and verify the contents of containers. Only a small percentage of containers are typically scanned or inspected thoroughly at ports and border crossings which leaves open the possibility of security breaches and smuggling activities[1].Countries' effective and efficient border security is becoming increasingly important in today's global world of economy and trade. To ensure these, customs organizations are responsible for the prevention of illicit goods' transportation across borders, particularly upon entry [2].

According to paragraph 22 of Art. 7 of the Budget act (1402) passed by the Islamic consultative assembly of Iran (Iranian Parliament), the Custom Organization of the Islamic Republic of Iran is obliged to equip the customs offices of the border provinces (with priority in Sistan and Baluchistan province) with x-ray inspection equipment. [3]. Therefore, in order to check the border customs of the country with the container inspection device (cargo), the accuracy of the operation of this device and the quality of its output image should be evaluated according to international standards. The international standard ANSI N42.46 measures the imaging performance characteristics of container (cargo) inspection devices [4]. Performing the tests mentioned in the objects that require the image quality assessment test should be available to the tester. Farafan Pajouhan Fateh Company has been the contractor for the construction of X-ray image quality evaluation objects for container (cargo) inspection devices for the honorable customs of the Islamic Republic of Iran. In this research, the process of designing and making test objects is reported in a brief way.

In recent years, measures have been taken to make this test object with different research purposes. C.H. Lim and et al calculated the X-ray irradiation angle-dependent changes in the contrast-to-noise ratio (CNR) of the images via Monte Carlo simulation. for this work they installed and evaluated A system based on the proposed dual-angle X ray imaging technology by scanning a real cargo container truck. For the evaluation, they designed test equipment based on the ANSI N42.46 report and examined the beam penetration power, contrast sensitivity, spatial resolution, and wire detectability of the developed system [5].

Kyungmin Oh et al measured the amount of radiation dose to adjust the feedback capacitance after the beam power of the dual energy x-rays and he distance from the source to the detector were set. In order to quantitatively evaluate the image after adjusting the feedback capacitance, they used a penetration test was carried out based on ANSI 42.46[6].

RESEARCH THEORIES

ANSI-N42.46-2008 standard is intended to be used to determine the imaging performance of x-ray and gamma-ray systems utilized to inspect loaded or empty vehicles, including personal and commercial vehicles of any type; marine and air cargo containers of any size; railroad cars; and palletized or unpalletized cargo larger than 1 m × 1 m in cross-section.

Test objects and measurement procedures may differ to some extent depending on the type of imaging system (e.g., transmission or backscatter) or system size. Test objects and procedures shall be consistent for all systems of similar type or size. The tests defined in this standard should be performed on the standard commercial product as provided by the manufacturer.

The procedures of this standard shall be used to measure the four characteristics of imaging performance or image quality: 1) Penetration 2) Spatial resolution 3) Wire detection 4) Contrast sensitivity.

all tests shall be performed at the two positions described below. Tests may also be performed at additional positions that shall be described in the test report. For example, if neither of the required positions corresponds to the location of maximum penetration, then additional tests may be performed at that location to demonstrate the system's maximum penetration performance. If performance at a position other than the two required positions is critical to a particular inspection location, then testing at one or more such additional locations may be specified. At each test position, the surface at the center of the test objects shall be oriented perpendicular to the radiation beam axis. For transmission imaging systems, the test object is placed behind the steel blocking plates; i.e., the blocking plates are between the energy source and the test object.

EXPERIMENTAL

In order to scientifically check and match the container scanner images with "ANSI-N42.46-2008" standards, four test objects have been designed and made. Maximum accuracy and effort have been used in the design and construction of these object tests so that the evaluation processes are carried out with the best accuracy and quality. The main effort of the experts of "Farafan Pajouhan Fateh" company has been to adapt the objects to "ANSI-N42.46-2008" standard as much as possible.

1.Making penetration test object

According to the investigations carried out by the company's experts, the penetration test object was made in accordance with the "ANSI-N42.46:2008" standard**.**

In the container scanner penetration detection test, it has been tried to include a suitable distance from the thickness to measure this important parameter. The thickness can be adjusted from one centimeter to thirty-five centimeters with steps of one centimeter. In fact, the number of 34 steel blocking plates (Fig. 1) plus one plate mounting the test object (Fig. 3) create the total thickness of this test object (Fig. 3). All plates have a thickness of one centimeter and are made of carbon steel and are plated to prevent rust. According to the standard text, the thickness of all plates are measured and certified before plating. The length and width of the plates are 60 cm x 60 cm**.**

Figure 1.Steel blocking plate

Figure 2. Mounting plate

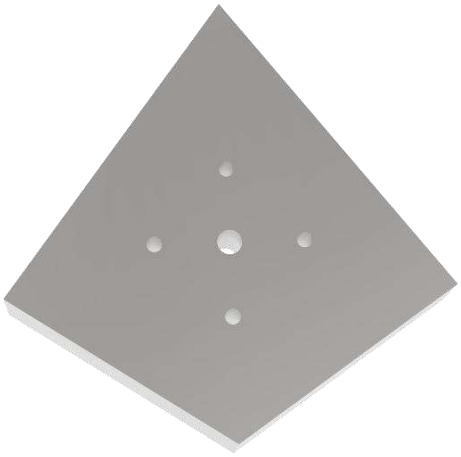

Figure 3.Arrow shape

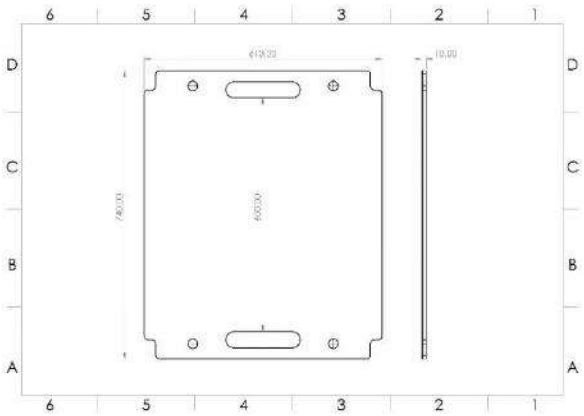

Figure 4. Steel blocking plate drawing

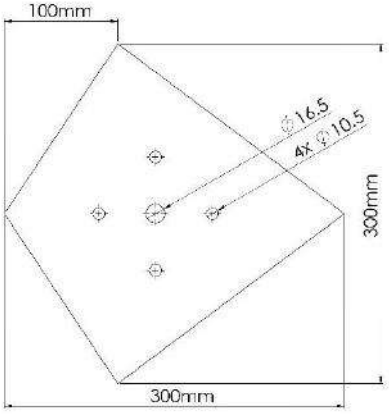

Figure 5. Arrow shape drawing

The test object mounting plate (Fig. 2) is made in such a way that it allows the installation of the penetration test object (Fig. 3), which is in the shape of an arrow. The important thing is that the relevant test object

should be installed in such a way that it does not provide any helpful information for diagnosis to the operator. the test object is placed behind the steel blocking plates according Fig 6.

The thickness of the penetration test object should be selected in such a way that 20% of the total thickness of the steel blocking and mounting plates. Therefore, this test object is made with thicknesses of 1, 2, 4, 5, 8, 10, 16 and 32 mm According to the Dimensions shown in Fig. 5 so that the desired thickness can be created by combining them. The mounting pin of this test object is located exactly on the center of its mass so that we do not have problems when changing the direction. Four smaller pins are intended to fix the direction of the arrow**.** The placement of the test object behind the blocking plate on the holder chassis is shown in Fig. 7.

Figure 6. Make of penetration test object

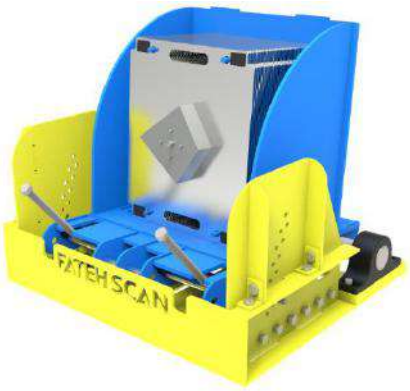

Figure 7. Representative test fixture for penetration and contrast sensitivity showing test object and steel plates

2. Making resolution test object

The spatial resolution test object is made according to the "ANSI-N42.46:2008" standard. In this test object, the number of three slots with the length of 10 cm and the width shown in Table (1) are placed side by side with an equal distance between the slots**.**

Table 6. Line-pair gauge feature sizes

Range of feature size d	Feature size increment
1 mm–10 mm	1 mm
10 mm–25 mm	2.5 mm
Greater than 25 mm	5 mm

This test object is made of carbon steel. The thickness of the sheet of each slot is equal to the width of that slot. In order to speed up the spatial resolution tests, all the sizes of the desired slots are installed on four planes, both horizontally and vertically according to Fig. 8 and 9. the horizontal spatial resolution test object Dimensions shown in Fig. 10 and 11. The placement of the horizontal spatial resolution test object on the holder chassis is shown in Fig. 12.

Figure 8. Horizontal spatial resolution test object

Figure 9. Vertical spatial resolution test object

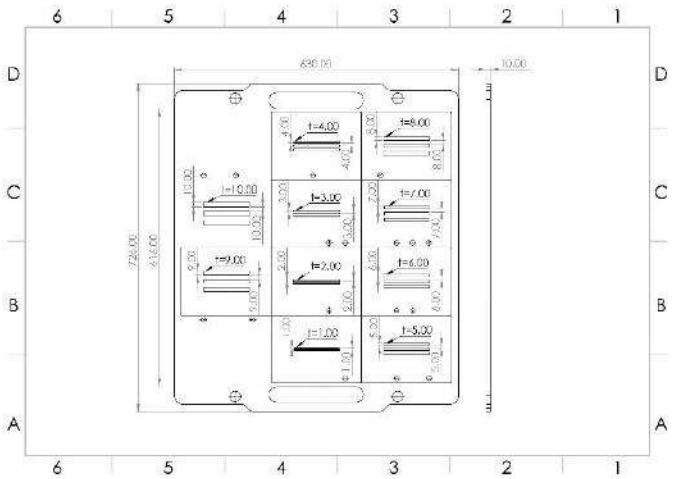

Figure 10. Drawing of horizontal spatial resolution test object

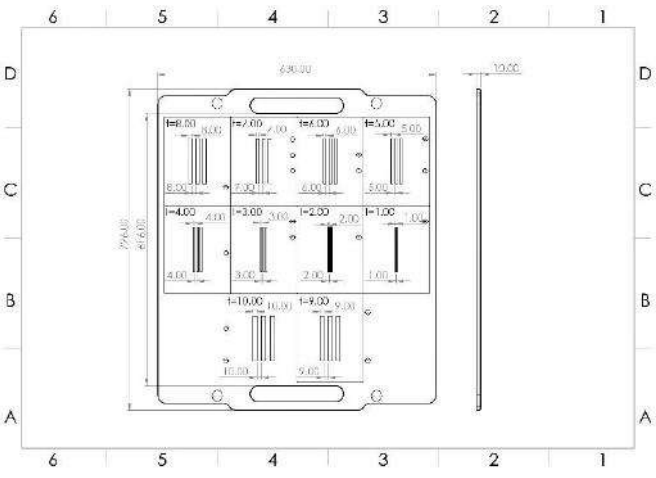

Figure 11. Drawing of vertical spatial resolution test object

Figure 12. Representative test fixture for spatial resolution showing test object

3. Making wire detection test object

The wire detection test object is made according to "ANSI-N42.46:2008" standard According to the Dimensions shown in Fig. 13. The diameter of the wires used in the AWG standard device is considered from number 10 to 24 in sinusoidal form with three periods. In order to perform this test, the wires are placed on three transparent X-ray sheets. The holder of the wires is a material with the atomic number of the machine selected**.** The placement of the wire detection test object on the holder chassis is shown in Fig. 14 .

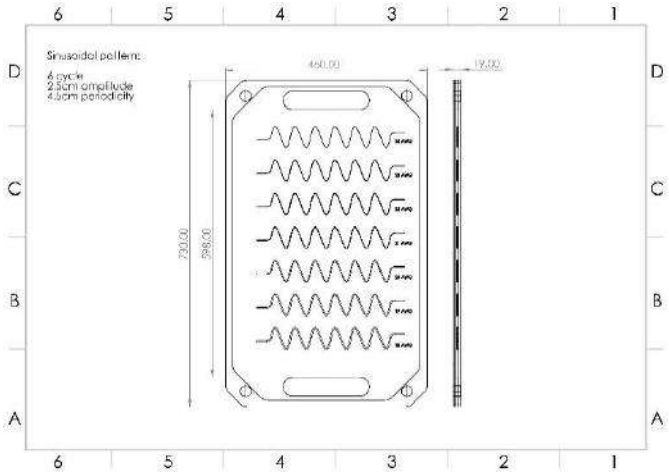

Figure 13. Drawing of wire detection test object

Figure 14. Representative test fixture for spatial resolution showing test object

4. Making contrast sensitivity test object

According to the studies and description of the standards, the contrast sensitivity test object is in accordance with the "ANSI-N42.46:2008" standard. The components used are the same components of the permeability test, and the only difference is the way they are used, which is explained in the theoretical basics section.

Results and discussion

We put all the image test objects on a main chassis(Fig. 15 and 16) with the ability to adjust the angle. The main chassis is inside a sturdy frame and its height is adjusted using a built-in jack.

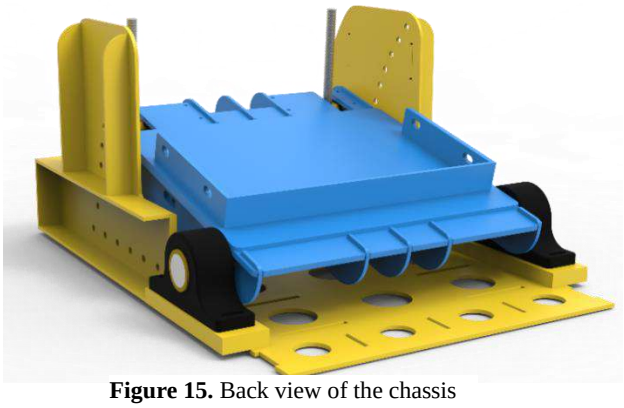

Figure 15. Back view of the chassis

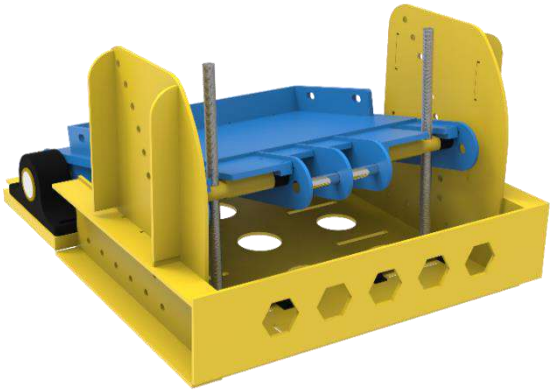

Figure16. Front view of the chassis

One of the important characteristics of the standard is to adjust the position of the test object in the height and width of the scanning area correctly. The design is such that it is possible to move the test object vertically and horizontally in a suitable interval. All the tests in the device evaluation process must be perpendicular to the output beam of the device. Therefore, the designed and built chassis is capable of verticalizing all the test objects.

Considering that the standard mentions that the tests should be carried out in conditions similar to reality, the main chassis is completely installed with a lifting jack on a 40-foot container accordint to Fig. 17, and the container is transported by a hydraulic crane and passes through the scanner gate. This condition simulates the reality that the examiner can easily perform the tests.

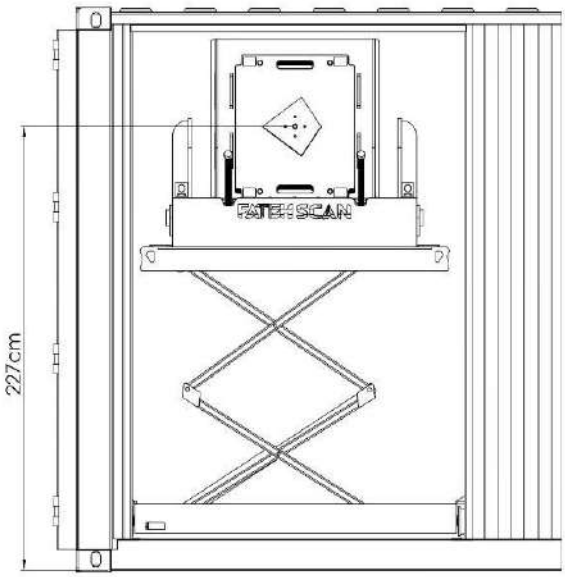

Figure 17. Test object adjust drawing

In the container, space is designed and built to store the test objects and its accessories from the crane family for transporting the test objects. the setup of the test object in the imaging position with the container x-ray inspection device is shown in Fig. 18. The location of the test object manufacturing at the site of Fateh company is shown in Fig. 19 . Also, the overview of the test object and its placement inside the container is shown in Fig. 20

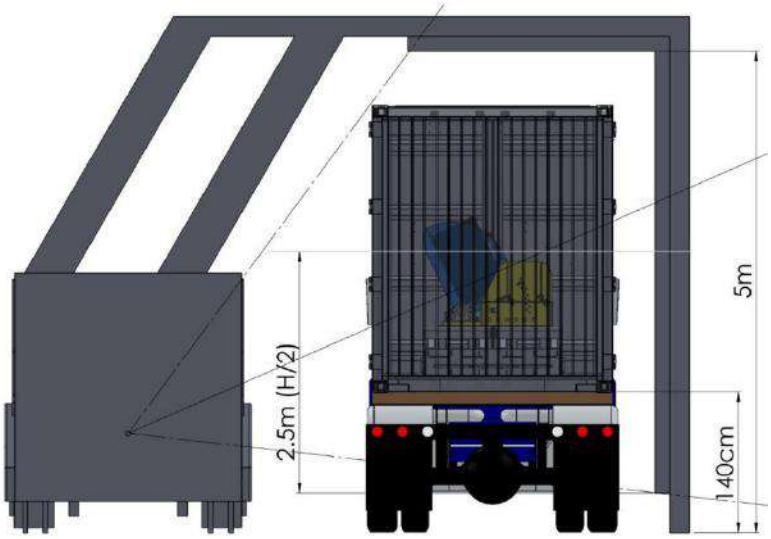

Figure 18. Overview of placing the test object in the container

Figure 19. Test object is made at the place of Fateh Scan company

Figure 20. Overview of test object in containers

Conclusions

In order to design, build and implement the performance test object of the container inspection device, based on "ANSI-N42.46:2008" standard, 8 specialists of Fateh Scan Company did this for the first time in the country within 4 months. The most important parameter in this project was the precision in making this test object. This test object with the container was delivered to the customs of the Islamic Republic of Iran to check the performance of the container inspection devices.

References

[1] Anzori Sh. Georgadze and Vitaly A. Kudryavtsev(2023). Geant4 simulation study of low-Z material detection using muon tomography, Journal of Instrumentation, Volume 18.

[2] Selina Kolokytha and et al (2017). Improving customs' border control by creating a reference database of cargo inspection X-ray images, Volume 2, Issue 3, Page No 60-66.

[3] https://rc.majlis.ir/fa/law/show/1775245

[4] American National Standards Institute (2008). American National Standard for Determination of the Imaging Performance of X-Ray and Gamma-Ray Systems for Cargo and Vehicle Security Screening,, ANSI N42.46-2008, 2008.

[5] C.H. Lim, J. Lee, Y. Choi, J.W. Park*b*, and H.K. Kim (2021). Advanced container inspection system based on dual-angle X-ray imaging method, Journal of Instrumentation, Volume 16.

[6] Kyungmin Oh and et al (2018). Evaluation and optimization of an image acquisition system for dual energy cargo inspections, IEEE

ICNST 2024 International Conference on Nuclear Science and Technology
6- 8 MAY 2024 | Isfahan, Iran

Investigation of Imaging Effects of ANSI-N42.46 Test Object Structure for High Energy Cargo Scanners by Monte-Carlo Simulation (Paper ID : 1582)

Sadegh Yousefi[1*], Ali-Reza Homa[1], Hosein Mashhadi[1], Masoud Ghorbani Qomi[1], and Amir Movafeghi[2]
[1*]*Fateh Scan Company, Qom University, Qom, Iran*
[2]*Reactor and Nuclear Safety Research School, Nuclear Science and Technology Research Institute (NSTRI), Tehran, Iran*

Abstract

The container and cargo inspection by high energy X-ray scanner is an effective way to control imported goods with containers. These scanners can prevent human smuggling and transportation of prohibited and restricted items without cargo unloading. ANSI-N42.46 standard is one of the published quality control standards for cargo scanner performance tests. This standard defines an imaging test object for quality evaluation of cargo scanner images. This test object has to be place by specific defined positioning before imaging. For holding the test object in these defined positions, it is necessary to use some mechanical positioning structures. These peripheral structure make some x-ray scattering and has some negative effects on generated images. Therefore investigation of this effect is important while using test object. In this research, the effects of presence of the container and mechanical structures of test object has been reviewed by simulation. This simulation was performed by a Monte-Carlo method. The simulation results showed that the presence of the container and the mechanical structures of the test object reduce the contrast to noise ratio (CNR) of x ray image.

Keywords: High energy cargo scanner, ANSI-N42.46 test object, Imaging effect, Monte-Carlo simulation

INTRODUCTION

The high energy cargo inspection systems are employed to inspect the inside of different cargo containers for unauthorized items, contraband items, or dangerous goods by using high energy photons from the outside, without accessing to inside or necessity for its opening. Ports or airports are equipped with cargo inspection systems for rapid and accurate inspection of cargo and postal items. Recently, cargo inspection systems have started using linear accelerators to generate high energy radiation. High energy x-rays having energy of several Mega Volts is generated in the linear accelerator and then irradiated on the container under inspection. The transmitted x-rays will reach to the detector arrays [1].

X-ray imaging detectors for the cargo container inspection using MeV-energy X-rays should accurately portray the internal structure of the irradiated container. Internal and external factors can cause noise, degrading image quality, and scattered radiation is the greatest source of noise. To obtain a high-quality transmission image, the influence of scattered radiation must be minimized [2].

The relative importance of scatter tends to increase as object size increases. The high energies used in cargo radiography mean that Compton scattering is the dominant interaction, both for photons that are scattered and photons that do not enter the detector or, more importantly here, for photons scatter but eventually deposit energy in the imaging detectors. This lies in contrast to lower energies (a few hundred keV and below) where photoelectric absorption dominates attenuation. It is thus important to assess the effect of scatter in typical cargo radiography systems [3]. In this research, we intend to investigate the effect of scattering on image quality. In recent years, various simulations have been carried out in order to check the effective parameters in the image quality of the container inspection device. C.H. Lim and et al calculated the X-ray irradiation angle-dependent changes in the contrast-to-noise ratio (CNR) of the images via Monte Carlo simulation [4]. Joseph Harms and et al used Monte Carlo simulations of a realistic imaging scenario with support from previous experimental measurements. They demonstrate how the use of monoenergetic photon beams in radiography can simultaneously reduce the radiation dose imparted to the cargo and any potential stowaways while increasing image quality [5].

METHODES

Monte Carlo Simulation by Geant4

Geant4 is a full object-oriented simulation tool that simulates accurately the passage of particles through matter. The code provides a complete range of functionalities including tracking, geometry and physics models, including electromagnetic and hadronic interactions. The code is being widely used in many different fields, such as nuclear and high energy physics, radioprotection, medical physics, accelerator design and astrophysics [6-7].

To perform a simulation in Geant4, it is necessary to write the codes describing basically the geometry, the materials used, the particles of interest, the physical processes of interaction and the main functions that indicates where the program will start and manage its execution. All the Geant4 MC calculations presented in this work have been performed using the 11.1.3 Geant version in a Linux system (Ubuntu) with Intel core i7 running at performance Cores: 6 cores, 12 Therads, 2.3 GHz Base, 4.7 GHz Turbo and Efficient Cores: 4 cores, 4 Therads, 1.7 GHz Base, 3.5 GHz Turbo. The physical model that was used the G4EmStandardPhysics_option4, G4EmStandardPhysics and G4OpticalPhysics.

For this simulation, the energy spectrum of the source was used according to the Fig. 1.

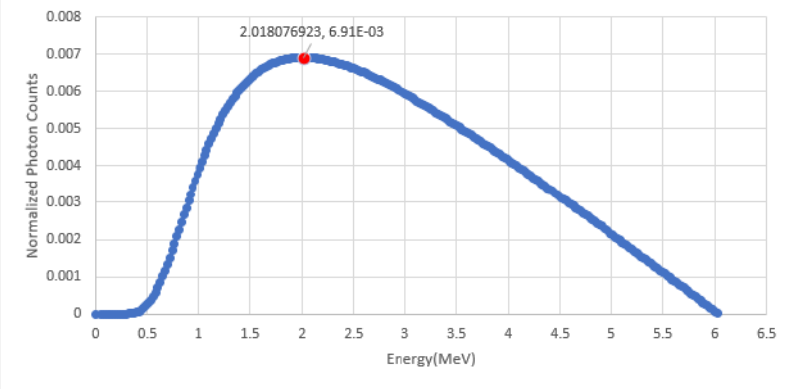

Fig. 1: the energy spectrum of the source

The horizontal axis of the graph shows the values of the energy spectrum and the vertical axis shows the normalaized photon counts. According to the diagram, the maximum energy of this spectrum is 6 MeV The maximum energy of cargo linear accelerators are usually 6 MeV and therefore 6 MeV was used for this simulation.. 2600 detectors are placed in both horizontal and vertical directions in an L shape for imaging**.** Each detector channel was composed of a CsI (2.5 mm × 2.5 mm × 2.5 mm) scintillator. The position of 1400 vertical detectors is in the direction y is positioned at (149,y,0) The position of the 1200 horizontal detectors is positioned along the x line at (x,175,0). To determine the position of the source and detector, we set the center of the container to the dimensions (236 cm, 273 cm, 1200 cm) as the coordinate origin. The spatial angles of the source beam in 50 degrees vertically and 2 degrees horizontal. The overview of the simulation in the Geant environment are shown in Figs 2 and 3. The trajectories of high energy photons are shown by green lines in the Fig. 2 and Fig. 3. They are shown by superimposed method. Test object holder is constructed according to the ANSI N42.46 satandard. test object for this simulation according to the ANSI N42.46 satandard is shown in Fig. 6.

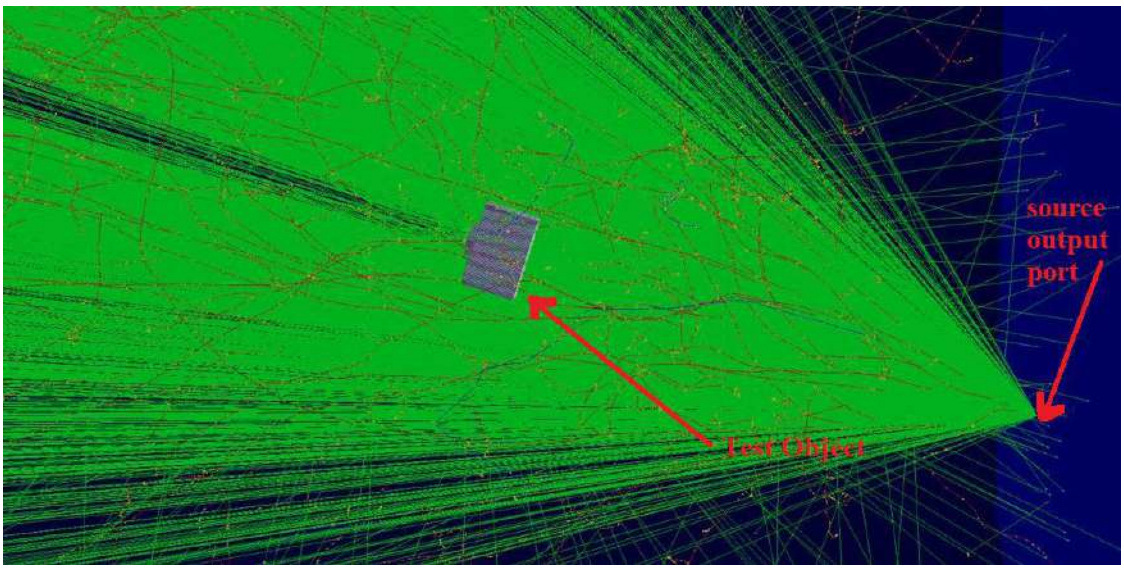

Fig. 2: The overview of the simulation in the Geant environment without container and test object holder

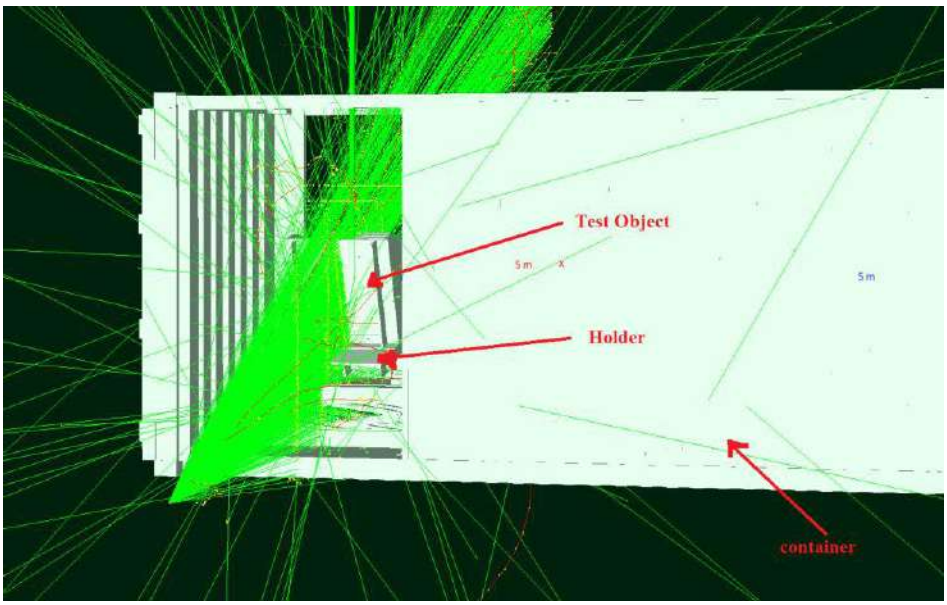

Fig. 3: The overview of the simulation in the Geant environment with container and test object holder

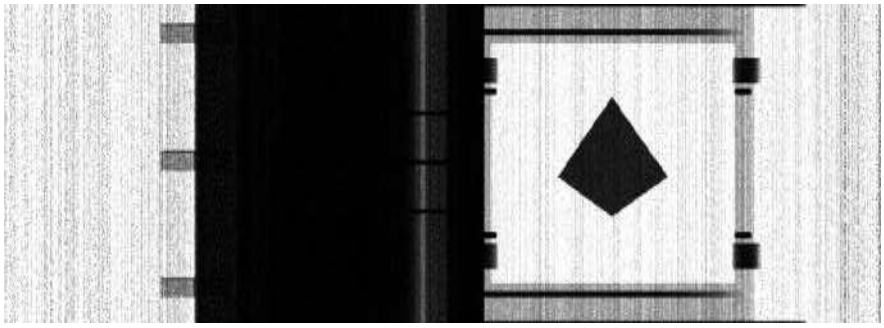

Fig. 5: X-ray image simulation with container and test object holder

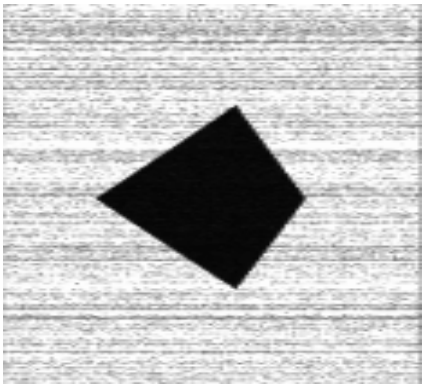

Fig. 4: X-ray image simulation without container and test object holder

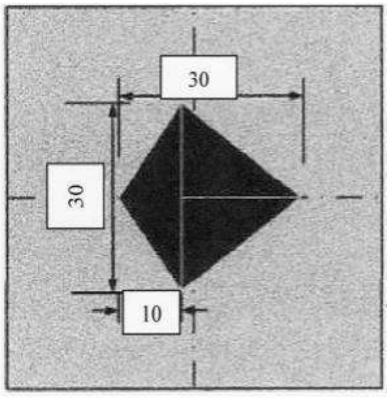

Fig. 6: test object in ANSI N42.46

Results and discussion

In order to quantitatively analyze the scatter effect in the x ray image, the contrast-to-noise ratio (CNR) was calculated, as shown in the equation (1)[4]. The contrast-to-noise ratio is a measure of how clearly the object (e.g., the arrow-shaped) appears in the x-ray image.

To calculate the CNR, the mean and standard deviation values(M_{obj}, σ_{obj}) of the arrow-shaped and the mean and standard deviation values (M_{SP}, σ_{SP}) of the steel plate were obtained from the Fig 4 and 5, as shown in table (1). To calculate this values using " Isee " software, we selected a region of interest(ROI) in two areas of the steel plate and the arrow-shaped.

$$CNR = \frac{|M_{SP} - M_{obj}|}{\sqrt{\sigma_{SP}^2 + \sigma_{Obj}^2}} \qquad (1)$$

Table 1: Parameters with and without container and test object holder

Without container and test object holder	With container and test object holder
M_{SP} = 246.2	M_{SP} = 245.6
M_{obj} = 26.49	M_{obj} = 26.71
σ_{SP} = 5.54	σ_{SP} = 5.78
σ_{obj} = 1	σ_{obj} = 2.04

By placing the values of Table(1) in relation(1), the amount of CNR was calculated in two radiation modes with the presence of container and test object holder and without container and test object holder. Without container and test object holder , the CNR value increased 10%.

Conclusions

The purpose of this research was to quantitatively show the radiation scattering effect caused by the presence of the container and test object holder. For this purpose, using Monte Carlo simulation, with a generalized energy spectrum and detector arrays from the ANSI-N42.46 standard penetration test object [8], imaging was done in two situations with and without a container and holder. According to the calculations, the scattering caused by the presence of the container and holder has a direct effect on CNR of image and reduce image quality. We used “Isee” software to calculate the CNR of the simulation images of the test object. After calculating the CNR in the absence of the container and test object holder, the CNR of image was increased 10%. It is shown that in the presence of container, the value of CNR reduces. so our simulation can be evaluated by this results. We can continue our work by investigation of different design parameters and their effects on image and CNR. This will be the topic of our future studies.

References

[[1] Kyungmin Oh and et al (2018). Evaluation and optimization of an image acquisition system for dual energy cargo inspections, IEEE Transactions on Nuclear Science, Volume 65

[2] Jeonghee Lee and et al (2017). The Effect of Grid Ratio and Material of Anti-scatter Grid on the Scatter-to-primary Ratio and the Signal to-noise Ratio Improvement Factor in Container Scanner X-ray Imaging, Journal of Radiation Protection and Research, 42(4):197-204**.**

[3] Erin A. Miller and et al (2011). Scatter in cargo radiography, Applied Radiation and Isotopes, Volume 69, Issue 11.

[4] C.H. Lim, J. Lee, Y. Choi, J.W. Park*b*, and H.K. Kim (2021). Advanced container inspection system based on dual-angle X-ray imaging method, Journal of Instrumentation, Volume 16.

[5] Joseph Harms, Luke Maloney and Anna Erickson (2019). Low-dose material-specific radiography using monoenergetic photons, National Institutes of Health (NIH), PLoS One.

[6] S. Agostinelli, J. Allison, K. Amako et al. (2003). Geant4 - A simulation toolkit, Nuclear Instruments and Methods *A*, 506 (3), pp. 250-303.

[7] J. Allison, K. Amako, J. Apostolakis et al. (2006). Geant4 development and applications", *IEEE* Transaction on Nuclear Science, 53 (1), pp. 270-278.

[8] American National Standards Institute (2008). American National Standard for Determination of the Imaging Performance of X-Ray and Gamma-Ray Systems for Cargo and Vehicle Security Screening,, ANSI N42.46-2008, 2008.

ICNST 2024 International Conference on Nuclear Science and Technology
6- 8 MAY 2024 | Isfahan, Iran

Feasibility of using correlation method in examining the images of contrast sensitivity and penetration tests in X-ray container devices according to ANSI N42.46 standard (Paper ID : 1585)

Sadegh Yousefi[1*], Ali-Reza Homa[1]Masoud Ghorbani Qomi[1], and Amir Movafeghi[2]
[1*]*Fateh Scan Company, Qom University, Qom, Iran*
[2]*Reactor and Nuclear Safety Research School, Nuclear Science and Technology Research Institute (NSTRI), Tehran, Iran*

Abstract

The container and cargo inspection by high energy X-ray scanner is a vital tool for security controls in borders. The quality control of this cargo scanner is a necessity for evaluating of generated radiography images. Contrast sensitivity and penetration tests are two fundamental tests in evaluating X-ray container devices based on the ANSI N42.46 standard. In these two tests, an arrow-shaped test tool is placed at different thicknesses along the X-ray beam. The aim of these two tests is to detect the direction of the arrow when the obstacle plates are placed between the X-ray source and the arrow-shaped test tool. According to the guidelines of these two tests, the criterion for accepting the test result is to detect the direction of the arrow. By increasing or decreasing the thickness of the obstacle plates, the two characteristics of the device's penetration and contrast sensitivity are recognized. According to the mentioned standard, the obstacle plates and the arrow-shaped test tool are made of carbon steel. The basis for detecting the direction of the test tool is the perception of the device operator. Therefore, the possibility of inconsistency in its detection and error in detection for different individuals arises. This article examines the possibility of using mathematical calculations of correlation coefficient for a better analyzing of these tests. The correlation coefficient expresses the relationship between two variables, By using four reference images, the direction of the arrow-shaped test tool in the unknown direction is examined. This can be done according to the directions of up, down, left, and right of the arrow-shaped test tool. It is shown that the correlation coefficient for the reference arrow-shaped test tool image and the unknown image in the same direction can have the highest precision.

Keywords: Correlation method, contrast sensitivity, X-ray penetration test, Cargo scanner, ANSI N42.46

INTRODUCTION

Over the past several years, x-ray cargo inspection has experienced tremendous growth. There are several hundred systems in use world wide and a few new units are installed every week. Fielded systems are mostly located in north and West Africa, Middle East, Europe (especially Russia), East Asia, and South

America[1].Cargo imaging is the industry of imaging large objects, such as cargo containers, trains, trucks or boats. It is mainly aimed at finding illegal goods, such as explosives, drugs, smuggled goods and even human trafficking. A cargo imaging system consists of an X-ray source, usually a linear accelerator (Linac) or a DC X-ray tube, collimators and beam filters, X-ray detectors, data acquisition electronics, control system, computers and radiation shielding. In order to spot items of interest from the images, the system must have adequate x-ray penetration power, contrast sensitivity and resolution[2].

Contrast sensitivity and penetration tests are two fundamental tests in evaluating X-ray container devices based on the ANSI N42.46 standard. In these two tests, an arrow-shaped test tool is placed at different thicknesses along the X-ray beam. The aim of these two tests is to detect the direction of the arrow when the obstacle plates are placed between the X-ray source and the arrow-shaped test tool. According to the guidelines of these two tests, the criterion for accepting the test result is to detect the direction of the arrow[3]. In this research, we intend to recognize the direction of the arrow in the X-ray image using the method of correlation coefficients. In recent years, research has been done in this direction in order to object detection using correlation coefficients.

Zheng and Elmaghraby propose a method for ATD(Anomalous Topic Discovery) in vehicles by detecting anomalous regions within images. They perform a window-wise correlation analysis comparing a fresh image of the vehicle to a historical image of the same vehicle stored in database. Images are split into 64 rectangular 4×16 pixel windows, and the correlation between the same windows in the fresh and historical image is computed. Correlation is also computed for fresh image windows with windows from different locations in the historical image, to account for goods that may have moved around inside the vehicle[4].

Maksym Zaliskyi and et al concentrates on the synthesis and analysis of methods for handgun recognition while operating the X-ray screening system..they use the correlation coefficient to recognize verified object similarity with etalons inside the database and define their mutual rotation and resizing[5].

RESEARCH THEORIES

Pearson’s Correlation Coefficient (PCC)

Pearson’s Correlation Coefficient (PCC) has been introduced by Karl Pearson in 1895. The Pearson's method is widely used in statistical analysis, pattern recognition and image processing. Applications on the latter include comparing two images for image registration purposes, disparity measurement, etc . It is described in (1):

$$r = \frac{\sum_i (x_i - x_m)(y_i - y_m)}{\sqrt{\sum_i (x_i - x_m)^2}\sqrt{\sum_i (y_i - y_m)^2}} \quad (1)$$

where x_i is the intensity of the i^{th} pixel in image 1, y_i is the intensity of the i^{th} pixel in image 2, x_m is the mean intensity of image 1, and y_m is the mean intensity of image 2. The correlation coefficient has the value r=1 if the the two images are absolutely identical. r=0 if they are completely uncorrelated and r=-1 If they are completely anti-correlated[6].

Contrast sensitivity test

according to ANSI N42.46 standard for Contrast sensitivity test, the test object is placed behind a total thickness of steel blocking plates and test object mounting plate equal to 10% of the maximum penetration. The orientation of the test object is randomly set with the arrow pointing up, down, left or right. The operator shall not be informed of the direction in which the arrow is pointed. After the steel blocking plates and test object are scanned, the operator examines the resulting image and reports the orientation of the arrow. The thickness of the test object is increased or decreased to recognize the minimum test object thickness at which the arrow orientation is correctly recognized [3].

EXPERIMENTAL

As mentioned in above the research theories section, the more the thickness of the steel plates increases, the more difficult it is for the examiner to recognize the direction of the arrow, to the extent that depending on the energy of the source, from one thickness onwards, in the X-ray image , the entire arrow is faded in the steel plate. Therefore, object detection algorithms and methods, which in this case is arrow direction detection, can be a practical tool to help evaluate the examiner in contrast sensitivity and penetration test. In this research, we used the native digital radiography device PX120D manufactured by Fateh Scan Company to simulate the x-ray images of the penetration and contrast sensitivity test of a ANSI N42.46 standard. We also made the steel blocking plates and the arrow-shaped object in smaller dimensions and thickness (Fig. 1) than what is mentioned in the ANSI N42.46 standard. Figs. 2 and 3 show the construction of arrow shape device. The setup of imaging with PX120D device is shown in Fig. 4. All the images taken in this research are with energy of 120 kev and a current of 1 mA with irradiation time of 10 s. The correlation relationship between two known and unknown X-ray images was used. An interpretation of the unknown image was presented. The unknown image is an image obtained according to penetration and contrast sensitivity tests.

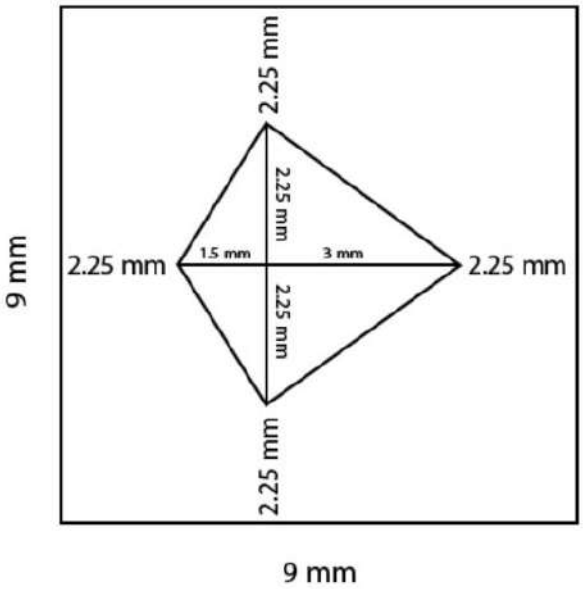

Fig. 1. drawing of arrow shape and blocking plate

Fig. 2. 3 arrow shape and 3 blocking plates that separate from each other

Fig. 3. 3 arrow shape and 3 blocking plate that stuck together

Fig. 4. setup of experimental

It consists of the superimposition of 3 blocking plates and 3 arrow plates in Fig. 2, Fig. 3. The thickness of each of the blocking plate and arrow-shaped plates is 1 and 0.2 mm, respectively. Therefore, the total thickness of the blocking and arrow-shaped plates is 3 mm and 0.6 mm, respectively. Fig. 5 is the output X-ray image from Fig. 4. As shown in Fig. 5, according to the ANSI N42.46 standard, the arrow-shaped plates are placed behind the blocking plates. Our goal is to be able to recognize the direction of the arrow in Fig. 5 automatically in the MATLAB software environment. The direction of the arrow in the X-ray image is downward.

Fig. 5. x ray image of three blocking plate and three arrow object

Another x ray images is necessay for calculating of the correlation coefficient, in addition to x ray image in Fig. 5. Since the difference between these two plates cannot be distinguished by increasing the thickness of the blocking plates and the arrow shape, reference images was usded so that the arrow direction of each unknown image can be recognized using them. Fig. 6 shows reference images obtained from blocking and arrow-shaped plates with thicknesses of 1 mm and 0.2 mm, respectively. To recognize the direction of the unknown image, it is enough to obtain its correlation coefficient with each of these reference images. The arrow direction in the unknown image is same to the arrow direction in the image with the highest correlation coefficient.

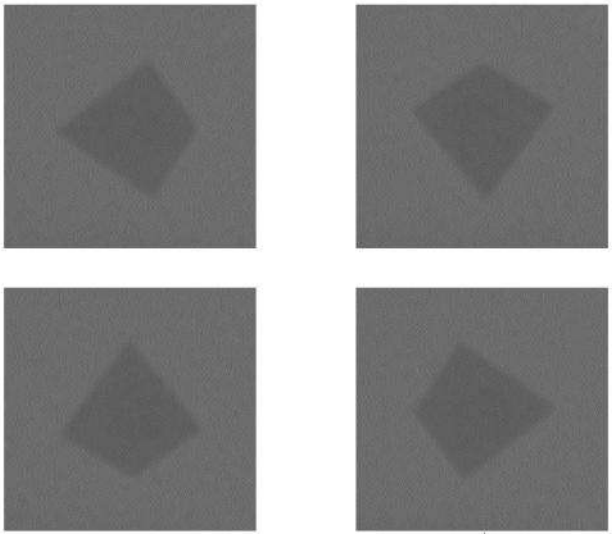

Fig. 6. reference x ray images

The image direction in Fig. 5 can be recognized by using the images in Fig. 6 in a simple manner. The problem will arise, where the unknown image is an image of thick blocking plate and a thick arrow. The images of Fig. 7 are obtained by changing the histogram of the image taken from an object consisting of 15 mm thickness of the blocking plate and 3 mm thickness of the arrow-shaped plate. As it is clear, its direction cannot be recognized in this image. In addition, by obtaining the correlation coefficient between this image and reference images, it is not possible to identify the correct direction of the arrow.

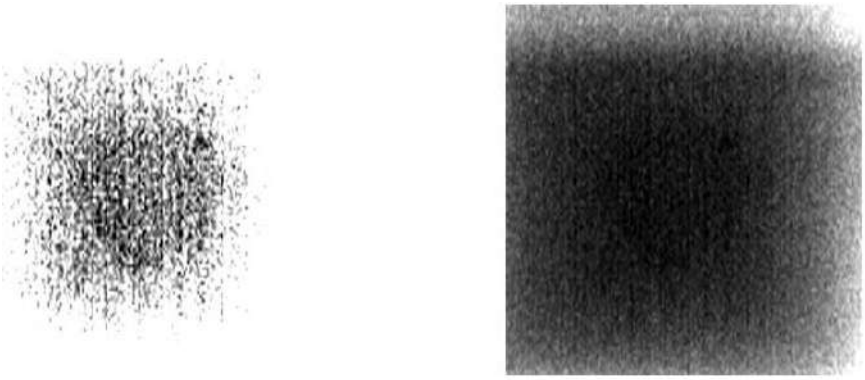

Fig. 7. changing the histogram of thick test object x ray image

The proper solution to solve this problem is to create a mask of the images in Fig. 6, like the images in Fig. 8, and then multiply each of the images in Fig. 8 by the image in Fig 5.

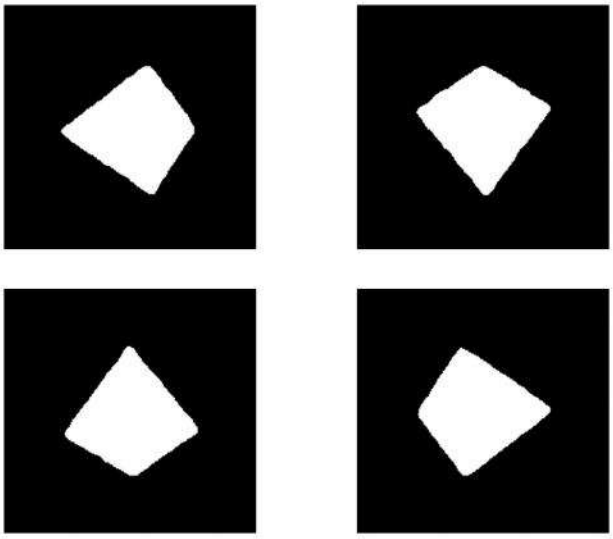

Fig. 8. masked images of fig. 6

Results and discussion

The result of multiplying Fig. 8 in Fig. 7 is shown in Fig. 9. Where it is known, image b is the only image that has a uniform image and they are matched. Therefore, the correlation coefficient of these images is higher than the correlation coefficient of the image in Fig. 5 and the other images in Fig. 9. Now with reference images, we know that the arrow direction of Fig. 5 is downwards. In the same way, the arrow direction can be recognized by calculating the correlation coefficient between the reference images and the images that consist of thick obstacles.

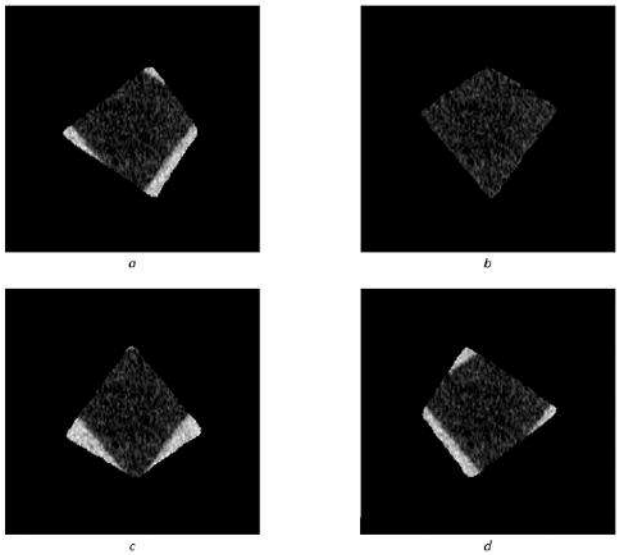

Fig. 9. multiplying Fig. 8 in Fig. 7

Conclusions

The purpose of this research was to provide an image processing method as an auxiliary tool for the examiner to recognizing the direction of the arrow in the ANSI N42.46 standard contrast sensitivity and penetration test object. There are several methods for recognizing patterns in images. One of the methods of pattern recognition in images is to use the correlation coefficient to measure the relationship between the reference image and the unknown image. In this research, we used the native digital radiography device PX120D manufactured by Fateh Scan Company to simulate the x-ray images of the penetration and contrast sensitivity test object of the ANSI N42.46 standard. We have shown that it is possible to recognize the direction of the arrow in the image of the thick blocking plate by calculating the correlation coefficient between an image of a thick blocking plate in which the direction of the arrow is not known with four masked images of a thin blocking plate in 4 directions up, down, left and right.

References

[1] Gongyin Chen and et al (2009). X-Ray Cargo Inspection: Status and Trends, Application of Accelerators in Research and Industry: Twentieth International Conference. AIP Conference Proceedings, Volume 1099. AIP Conference Proceedings, Volume 1099, Issue 1 [2] Gongyin Chen (2005). Understanding X-ray cargo imaging, Nuclear Instruments and Methods in Physics Research B," vol. 241, pp. 810-815.

[3] American National Standards Institute (2008). American National Standard for Determination of the Imaging Performance of X-Ray and Gamma-Ray Systems for Cargo and Vehicle Security Screening,, ANSI N42.46-2008.

[4] Y. Zheng and A. Elmaghraby(2013). A vehicle threat detection system using correlation analysis and synthesized X-ray images. In: Proceedings SPIE, 8709(2016):87090V. [5] Maksym Zaliskyi and et al (2023). Correlation Method of Dangerous Objects Detection for Aviation Security Systems. Workshop on Cybersecurity Providing in Information and Telecommunication Systems.

[6] A. Miranda Neto and et al (2013). Image Processing Using Pearson's Correlation Coefficient: Applications on Autonomous Robotics. 13th International Conference on Autonomous Robot Systems.

ICNST 2024 International Conference on Nuclear Science and Technology
6- 8 MAY 2024 | Isfahan, Iran

The Role of Nuclear Science in Advancing Public Health: A Comprehensive Review (Paper ID : 1599)

Zamani F. Correspondent[1*], Karimi Sabet J. Co-Author[2], Arkannia M.H. Co-Author[3]
[1]Nuclear engineering, shahid Beheshti University, Tehran, Iran [2]Nuclear Science and Technology Research Institute, Tehran, Iran [3]Energy engineering, Sharif University of Technology, Tehran-Iran

ABSTRACT

Health plays a fundamental role in at least 8 of the 17 Sustainable Development Goals. Because healthy people are the foundation of a healthy economy. Developed and developing countries pay special attention to improving the health of their society.

Nuclear technology is effective in various fields, including sterilization, food security, combating disease-carrying insects, desalination and water management, genetic and molecular research, diagnosis, treatment, etc., and improves the level of public health.

The International Atomic Energy Agency has developed a program called the "Human Health Program" focusing on prevention, treatment, and diagnosis.

According to the World Health Organization, by 2030, more than 21 million people will be diagnosed with cancer, and about 13 million of them (62%) will die. In Iran, cancer is the second cause of death after heart disease. The proportion of cancer deaths in developing countries is higher than in developed countries. However, the use of nuclear technology can reduce the number of casualties by 12.5%.

In this article, we examine the role of nuclear science and technology in improving the field of health and treatment, and after examining the dimensions of the use of nuclear medicine in cancer treatment, we examine Iran's situation in this field.

keywords: health, World Health Organization, cancer, Human Health Program, treatment, diagnosis.

1. INTRODUCTION

Health plays a role in at least 8 of the 17 goals of sustainable development. Zero hunger, ensuring a healthy life promoting well-being for all at all ages, ensuring access to water for all, and ensuring access to affordable, reliable, and sustainable energy are some of these. In explaining these cases, it is predicted that more than 600 million people around the world will face hunger and insecurity in a healthy and hygienic diet in 2030. Sustainable development makes a bold commitment to end the epidemics of AIDS, tuberculosis, malaria, and other communicable diseases by 2030. [1] On the other hand, access to safe and sanitary water is the most basic human need for health and well-being, and millions of people die every year due to water-related diseases such as malaria and diarrhea, unfortunately, in 2022, more than two

billion people will still do not have safe access to drinking water; And regarding the need to ensure access to affordable energy, it should be said that energy services are key to preventing disease and fighting epidemics. In this way, health is one of the most important topics of today's humanity, which is important to address, and what is more interesting is that nuclear science and technology also play a role in it. [2]

The two main and effective parameters of nuclear science and technology in the field of health are radiation and radioisotopes. [4]

1. Radioisotopes are atoms that contain an unstable combination of neutrons and protons or excess energy in the nucleus. Unstable isotopes can become stable by releasing different types of particles; This process is called radioactive decay and the elements that undergo this process are called radioisotopes or radionuclides. [3]

2. Alpha, beta, neutron, X, and gamma are ionizing rays whose types of interaction with the cell include both direct and indirect effects. Direct effects refer to cases of interruption in cell division, gene mutation, and chromosomal failure or changes in the composition and structure of damaged chromosomes and the production of abnormal daughter cells and cell death, and indirect effects include the breakdown of water molecules that make up the cell into ions or active radicals and compounds. It is the decomposed components with important molecules such as DNA (which causes disruption in the main function of DNA and causes direct effects). [3]

Therefore, in radiation treatments, the radiated radiation damages the cell by destroying all types of genetic material that controls the way cells grow and divide. The irradiated beam encounters two types of cells: healthy cells and cancer cells. Healthy cells can slowly repel much of the damage caused by radiation. But concerning cancer cells, a cancer cell whose DNA is less damaged only slows down its growth, and a cancer cell whose DNA is excessively damaged does not divide anymore or dies. Preventing cell division from the rapid effects of radiation and cell death are the results of high radiation. After death, the cell is decomposed and removed from the body, which is effective in radiation therapy and cancer treatment. For cancer cells, high-energy rays are generally used, which can target DNA in dealing with them. (X-rays were often used, but nowadays protons or other types are also used.) Therefore, considering the importance of health and the use of radioisotopes and radiation in this field, in this article, firstly, in section 2, we will examine the role of science. and nuclear technology in the promotion of health and treatment after examining the dimensions of the use of nuclear medicine in the treatment of cancer, in section 3 we will examine Iran's situation in this field and in the final section we will state the results. [5]

THE FUNCTION OF NUCLEAR SCIENCE AND TECHNOLOGY IN THE FIELD OF HEALTH

From the point of view of the International Atomic Energy Agency, the function of nuclear science and technology in the field of health and health is divided into the following: sterilization, food security, diagnosis, combating disease-carrying insects, desalination and water management, genetic and molecular research, help to reduce Climate change, treatment, dosimetry monitoring, and clean energy production. Among these, two parts of diagnosis and treatment under the title of nuclear medicine have been proposed, which are known as the most important functions of nuclear science and technology in this field. [1]

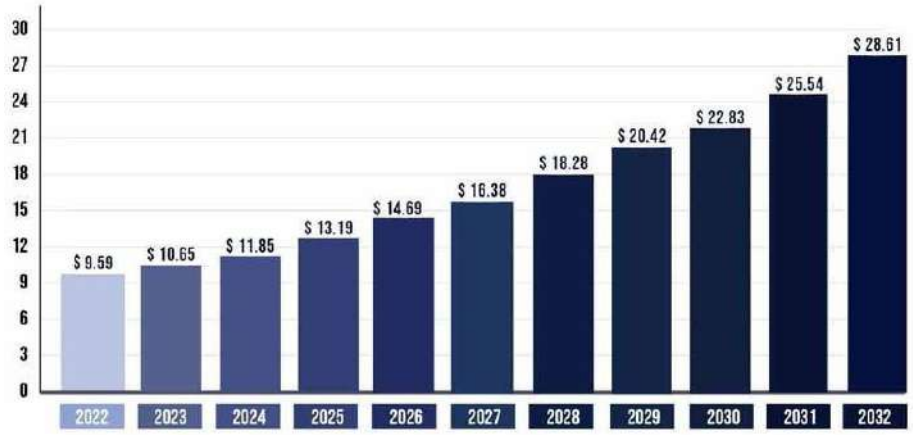

Figure 2. nuclear medicine market size 2022 to 20 32 (USD billion) [1]

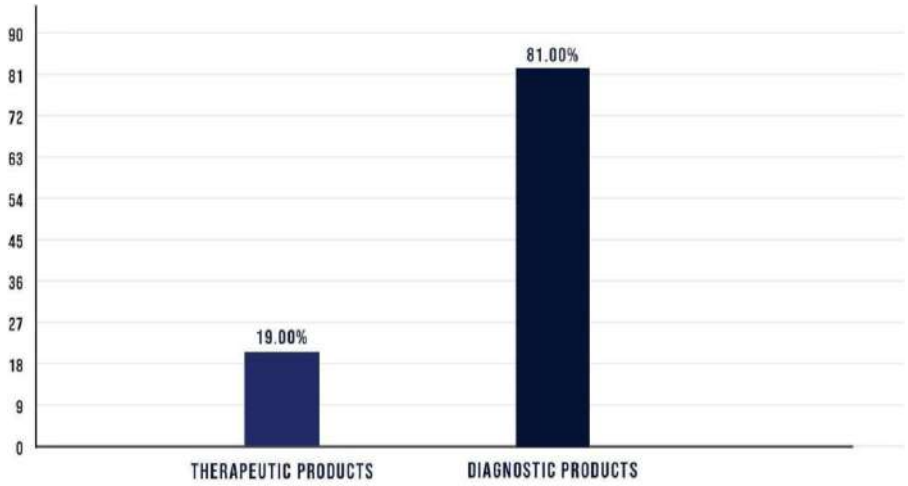

Figure 1. nuclear medicine market share by product 2021 (%)

The global nuclear medicine market capacity was more than $9.5 billion in 2022 and is expected to exceed $28 billion by 2032 (Figure 1). 81% of the nuclear medicine market volume belongs to the diagnostic field and North America has the largest nuclear medicine market share in the world (Figure 2). [1] According to statistics, it is predicted that by 2030, more than 21 million people will be diagnosed with cancer in the world and 13 million people will die due to this disease. On the other hand, in Iran, cancer is the second group of non-communicable diseases and the second cause of death after heart disease. [6]

According to the data of the World Cancer Observatory project, in 2020, more than 131 thousand new cases of diagnosis and more than 79 thousand deaths from cancer were reported in Iran. In a comprehensive modeled scale, nuclear medicine factors including imaging, treatment, and quality of care indicate a reduction of 55.9 million deaths from cancer worldwide. Therefore, the use of nuclear medicine becomes important. [7]

In nuclear medicine, very small amounts of radioactive materials are used inside the body to observe the function of organs or tissues (diagnosis) or to target and destroy damaged organs or tissues in a patient (treatment). Depending on the intended function and body tissue, various radiopharmaceuticals such as iodine, xinan, thallium, gallium, indium, technetium, etc. are used, some of which are given in Table 1.

Table 1. Some radiopharmaceuticals and their use

radiopharmaceutical's name	**Application**
Gallium Citrate Ga 67, Indium In 111 Oxyquinoline	Diagnosis of abscess and infection
Technetium Tc 99m Bicisate, Xenon Xe 133… ,	Diseases of blood vessels of the brain
Sodium Fluoride F 18, Technetium Tc 99m Medronate… ,	Bone diseases
Fludeoxyglucose F 18, Gallium Citrate Ga 67, Indium In 111 Pentetreotide… ,	cancer; Tumors
Technetium Tc 99m Albumin, Technetium Tc 99m Teboroxime… „	Heart disease

Therefore, radiopharmaceuticals are agents that are used to diagnose certain medical problems or treat certain diseases. [8]

DIAGNOSIS

Small amounts of radiopharmaceuticals pass through or are absorbed by an organ. (Depending on the type

of organ, a special radiopharmaceutical is used). Then the radioactivity is detected and images are produced by special imaging equipment. [9]

Single-photon emission computerized tomography (SPECT)

A nuclear medicine imaging technique that uses small amounts of a radioactive tracer and a specially designed camera to produce three-dimensional images of organs and tissues to diagnose disease or injury. What sets a SPECT scan apart from other imaging modalities is that it can show the function of specific organs. [10]

It is a type of nuclear medicine method that measures the metabolic activity of cells in body tissues. PET is actually a combination of nuclear medicine and biochemical analysis that is mostly used in patients with brain or heart diseases and cancer and can detect metabolism in body tissues

Also, PET can be used for better diagnosis with other diagnostic tests such as CT or MRI, such as PET/CT. Of course, the gamma camera system can scan faster and at a lower cost than traditional PET scanning. The most common use of PET is in cancer diagnosis and evaluation of cancer treatment; Other uses of PET include evaluating the treatment of cancer, hematoma, bleeding, or perfusion, determining the location of specific brain surgery, stroke, epilepsy, Huntington's disease, Parkinson's disease, etc.

Table 2 lists common diagnostic tests in nuclear medicine. Also, in Figures 3 and 4, you can see the distribution map of SPECT and PET devices in the countries of the world, respectively. [9]

Table 2. Common diagnostic tests in nuclear medicine

Test name	Target
Kidney scan	- Examination of the kidneys
	- Identifying any abnormality including irregular function or blockage of blood flow in the kidney
Thyroid scan	- Evaluation of thyroid function
	- Evaluation of thyroid nodule or mass

Bone scan	- Evaluation of destructive or inflammatory changes in the joints - Identification of bone diseases and tumors - Determining the cause of bone pain or inflammation
Gallium scan	- Diagnosis of active inflammatory or infectious diseases, tumors, and crimes
Heart scan	- Identification of irregular blood flow to the heart - Determining the extent of heart muscle damage after a heart attack Measurement of heart function
Brain scan	- Examining problems inside the brain or in the blood flow to the brain
Breast scan	- Often combined with mammography to locate cancerous tissue in the breast

Figure 3. Distribution map of SPECT devices in the countries of the world

Figure 4. Distribution map of PET devices in the countries of the world

treatment

Radiopharmaceuticals are used in larger amounts to treat certain types of cancer and other diseases. The radioactive agent is absorbed in the cancerous area and destroys the damaged tissue. Depending on the type of application, these radiopharmaceuticals can be used in different ways, such as intravenous or skin injection, tablet or liquid consumption, and inhalation. [10]

Nuclear medicine in Iran

For reasons such as the crystallization of the use of nuclear technology in human health in the field of nuclear medicine and its most important tool i.e. radiopharmaceuticals, the importance of radioactive materials and nuclear medicine in the diagnosis and treatment of diseases and deficiencies as a relatively cheap and quick solution and the special place of accelerators, radiation therapy, brake Therapy, and radiopharmaceuticals in the diagnosis and treatment of cancer as the second cause of death in Iran, nuclear medicine is also important in our country. [10]

Today, training in the field of nuclear medicine in Iran is carried out in the fields of nuclear medicine, nuclear medicine technology, nuclear medicine, radiation medicine, application of radiation, and health physics.

It is the government's responsibility to create and strengthen the infrastructure needed for the production of medicinal products and raw materials, vaccines, biological products, and medical supplies and

equipment in the form of international standards (paragraph 4 of the general policies of the system in the health sector, announced by the Supreme Leader), as well as the provision of medicines The needs of citizens are one of the most basic duties of the government. (Constitutional Law) and preparation and production of diagnostic and therapeutic radiopharmaceuticals including reactor radiopharmaceuticals, cyclotron, and radiopharmaceutical kits is the responsibility of the Atomic Energy Organization. (Clause H of Article 3 of the Atomic Energy Law) Therefore, the Atomic Energy Organization of Iran has put the following policies on its agenda:

Continuous efforts to provide radiopharmaceuticals needed by diagnostic and treatment centers

Speeding up the process of providing nuclear services required by the country's healthcare sector

Research and development in the field of new radiopharmaceuticals for timely diagnosis and reducing the suffering of patients with certain diseases, especially cancer. [11]

In this regard, Iran's Atomic Energy Organization has proudly carried out important activities in the field of promoting nuclear medicine, or is in the process of doing so; including the production and development of diagnostic and therapeutic radiopharmaceuticals, the export of radiopharmaceuticals and radiopharmaceutical kits, the construction of Iran's National Center for the Production and Development of Radiopharmaceuticals (Tetra), the construction of the National Ion Therapy Center,

the project to produce the medicinal radioisotope molybdenum-99 obtained from the fission of uranium, products derived from heavy water with applications in the field of health, localizing the technical know-how to produce all kinds of accelerators (linear and circular), using cold plasma to treat all types of cancer and chronic wounds, developing the use of medical lasers, manufacturing high- speed ultracentrifuge devices (tubular), etc. [12]

Currently, in line with the export of radiopharmaceuticals and pharmaceutical kits, Iran has been able to export to countries with knowledge and technology in order to increase the standards and quality of products, such as India (more than 80 hospitals), Egypt (more than 12 hospitals), Georgia, Turkey, New Zealand, Chile, Iraq, Syria, etc., as well as exporting to five continents for the first time on November 5, 2018, despite the animosity, sanctions and flight restrictions of the airlines.

The most important and practical nuclear medicine product is Technicim-99, in which more than 80% of nuclear medicine diagnoses, including the diagnosis of cardiovascular, pulmonary, renal, nervous,

inflammatory, infectious, etc. diseases, are performed with this radiopharmaceutical. For this reason, the production of the medicinal radioisotope molybdenum-99 will be important. In 2022, 250,000 tons of molybdenum were produced worldwide. 93% of this production was done in five countries.
China with 100,000 tons, Chile with 44,000 tons, America with 42,000 tons, Peru with 32,000 tons, and Mexico with 16,000 tons are ranked first to fifth. Meanwhile, Iran has taken the ninth place. [10]

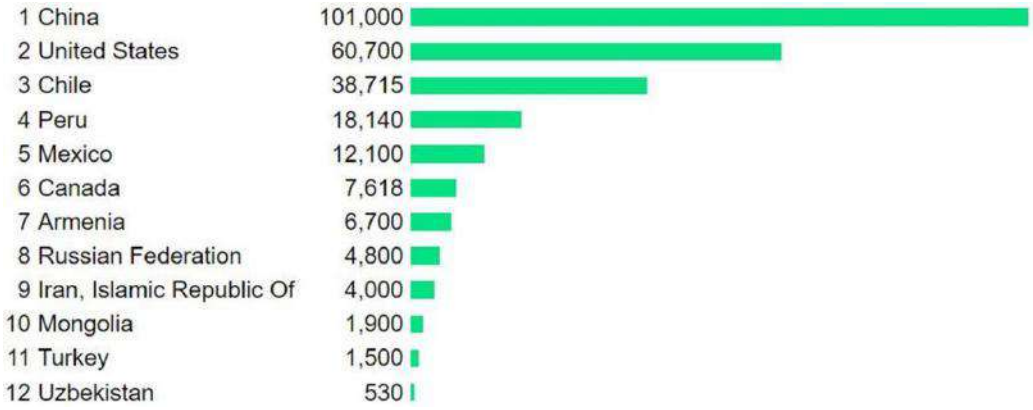

Figure 5. Molybdenum production rate worldwide in 2022, by countries

One of the honors of Iran in the field of nuclear medicine is the establishment of the National Ion Therapy Center. Most of the proton/ion therapy centers perform radiation therapy with only one type of radiation, and according to Figure 2.3, only 6 centers in the world with proton and carbon radiation capabilities are in operation, and Iran's National Ion Therapy Center is the seventh of them. The synchrotron accelerator in this center has been provided by the Austrian company Medastron (with the participation of Austria) and this complex can provide about 9000 radiation therapy sessions to more than 1200 patients annually. [9]

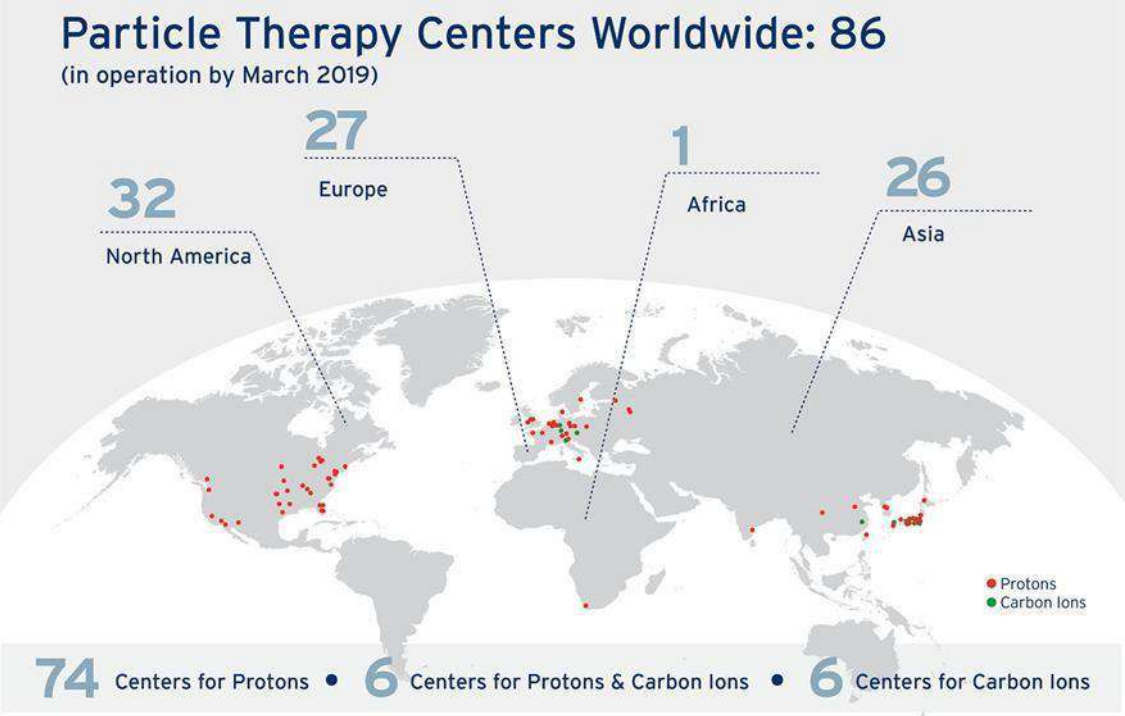

Figure 6. Distribution of proton/ion therapy centers in the world

Also, among the types of radiation therapy methods in cancer treatment are the X-ray method, electron beam method, and proton and ion therapy method, in line with the treatment of cancer with the help of radiation therapy using accelerators, the technical knowledge of producing all kinds of accelerators (linear and circular) has been localized. [12]

Conclusion

In the Sustainable Development Goals (SDGs), the international community has committed to reducing premature deaths from cancer and other chronic diseases by a third by 2030. Also, the International Atomic Energy Agency has presented the "Human Health Program" in order to promote public health. Our country has also carried out research and measures in this field with the power of research and is still in the process of research and development. Considering the early diagnosis of cancer (about 150 days earlier) compared to other diagnostic methods, our country also pays special attention to this field and has taken great steps in the development of new radiopharmaceuticals with the view of increasing the share of treatment and development of therapeutic radiopharmaceuticals. Currently, the share of the diagnosis sector is about 80% and the share of the treatment sector is 20%, and new products have been produced and offered, especially in the field of treatment. Some of the produced radiopharmaceuticals are part of some of the famous

products produced in the world and have been produced on a commercial scale by the Atomic Energy Organization.

References

www.grandviewresearch.com/industry-analysis/nuclear-medicines-market.

MEDICAL USES OF NUCLEAR TECHNOLOGY ROLE, CHALLENGES & PERSPECTIVES ANNEX, NUCLEAR MEDICINE EUROPE REPORT, 2021.

INTERNATIONAL ATOMIC ENERGY AGENCY IAEA BULLETIN, The flagship publication of the IAEA, 2017.

Nuclear Technology for a SUSTAINABLE FUTURE, IAEA REPORT, 2012.

The development status of nuclear technology applications in Iran and the world in the field of health, Report of Islamic Council Research Center, 2023.

Advancing Nuclear Medicine Through Innovation, The National Academy of Sciences, 2007.

Medical imaging and nuclear medicine: a Lancet Oncology Commission, Hedvig Hricak*, May Abdel-Wahab*, Rifat Atun*, Miriam Mikhail Lette, etc., 2021.

Lou R, Lalevic D, Chambers C, Zafar HM, Cook TS. Automated detection of radiology reports that require follow-up imaging using natural language processing feature engineering and machine learning classification. J Digit Imaging 2020; 3: 131–36.

Arunachalam SP, Asan O, Nestler DM, et al. Patient-care team contact patterns impact treatment length of stay in the emergency department. Annu Int Conf IEEE Eng Med Biol Soc 2019; 345–48.

Stolz LA, Muruganandan KM, Bisanzo MC, et al. Point-of-care ultrasound education for non- physician clinicians in a resource-limited emergency department. Trop Med Int Health 2015; 20: 1067– 72.

ICNST 2024 International Conference on Nuclear Science and Technology
6- 8 MAY 2024 | Isfahan, Iran

Unveiling the Multifaceted Applications of Nuclear Science: Beyond Electricity Generation (Paper ID : 1601)

Arkannia M.H. Correspondent[1*], Karimi Sabet J. Co-Author[2], Zamani F. Co-Author[3]
[1]*Energy engineering, Sharif University of Technology,*
Tehran-Iran [2]*Nuclear Science and Technology Research Institute, Tehran, Iran Nuclear engineering, shahid Beheshti University, Tehran, Iran*

Abstract

Contrary to the opinion of most people who have less knowledge about nuclear science and technology, it is not only limited to the production of clean nuclear energy from the two conventional methods of fission and fusion. Rather, this technology has its own applications in many other sectors, including healthcare, food security, management and desalination of water, environmental protection, archeology, propulsion, batteries, etc.

In this article, at first, an overview of the types of applications of nuclear science and techniques in these fields that they are related to the improvement of the quality level of human societies and citing examples of each is given, and then the current situation of Iran in the fields of non-power application is examined. In fact, this article is an attempt to briefly explain the various peaceful uses of nuclear energy other than electricity, which are generally unfamiliar to ordinary people and have less knowledge about them.

Keywords: Non power applications - food security - management and desalination of water – healthcare

1 . Introduction

Due to the nascent nature of nuclear science and technology compared to other existing sciences, there is less knowledge about it among the people, and most of them have no idea more than a nuclear bomb or eventually electricity production from it, and maybe few people know that nuclear science and technology can even be helpful and useful in the field of agriculture and animal husbandry or archeology. In this regard, the International Atomic Energy Agency provides programs, recommendations and researches and even supports active countries in these fields. For example, it supports adaptation efforts like plant breeding, soil and crop management, livestock production, and insect pest control. And performs some activities in this field such as support sustainable management of freshwater resources and agriculture systems, advise on and develop climate-smart agriculture methods including for soil, crop and water management, research and provide expertise on ecosystems and how to counter biodiversity loss, Study and provide guidance on ways to reduce the impact of climate-related severe weather on energy systems. [1]

Therefore, considering the importance of the application of nuclear sciences and techniques in non-power fields and the need to know and familiarize with them, this article has been written. in this Research, firstly, in part 2, we will get acquainted with the non-power applications of nuclear science and technology, and then in part 3, we will examine the current situation in Iran in these areas, and in the last part, we will express the results. [3]

2 . All kinds of non-power applications

If we divide nuclear applications into two groups of power and non-power, the power group will include fission and fusion that lead to the production of electricity and heat, and the non-power group will include applications in the fields of radioisotopes, environment, industry, agriculture, food and water, nuclear propellants and batteries, military, healthcare and archeology which we will discuss further.

2 . 1 . Nuclear agriculture

Pests and insects cause the destruction of one third of the world's agricultural products, and the high cost of chemical fertilizers and the lack of proper use of them due to the use of nitrogen 15 will cause damage to human health and the environment. On the other hand according to the reports of the Food and Agriculture Organization of the United Nations (FAO) and the United Nations (UN), about 795 million people (1 in 9 people) suffered from chronic malnutrition in 2014-16. Taking into account the mentioned cases, it is important to enter this field. Nuclear agriculture activities are generally classified into 5 areas: genetic and horticultural plant breeding, plant medicine and insect pest control (disinfection), production of plants with different ploidy levels, soil and water management and crop nutrition, genetic engineering and biotechnology studies. [5]

With the introduction of nuclear technology, 8 major changes have occurred in agriculture: 1. Increasing the health and production of animals: For example, in Cameroon, it improved, corrected and artificially inoculated and controlled animal diseases and tripled the milk production of animals from 500 to 1500 liters, which increased the income of an animal breeding farm by 110 million dollars in one year and reduced the contagious disease brucellosis in animals that consumed unpasteurized milk were infected.

2. Correcting water and soil balance using nuclear technology that doubled crops and reduced water by 55% (on a small scale) in Kenya. 3. Pest and disease control that the governments of Guatemala, Mexico, and the United States have been using it for decades to prevent the Mediterranean fly pest. 4. Food health, for example, in Pakistan, 50 companies using nuclear technology have the possibility of tracking drug residues and poisons in agricultural products. 5.Increasing the accountability of governments and

international institutions towards the people; In this regard, in 2011, in Japan, the United Nations World Food Organization and the International Energy Agency were able to identify and introduce contaminated food products caused by the leakage of nuclear materials using nuclear technology. 6. Increasing adaptability to climate change. 7. Preventing hunger and famine by increasing yield improvement; For example, in Bangladesh, thanks to the improvement of the early rice variety, the country's production increased from 26.8 million tons in 2004 to 33.8 million tons in 2013. 8. Reducing water consumption, in this context, the path of water can be traced in the ground and plants, so with this method, it is possible to prevent water wastage in the field. [2]

All these changes are done using three techniques of radiation, tracking and analysis by activation method.

2 . 2 . Food and water

By using the irradiation method, it is possible to improve the quality and increase the shelf life of food, as well as disinfecting and sterilizing it. According to the standards of the World Health Organization (WHO), the Food and Agriculture Organization (FAO) and the Food and Drug Administration (FDA), the recommended dose for irradiation in this field is a maximum of 10 KGy (equivalent to an increase of 2.4 ° in water temperature).

The advantage of this method is not to increase the temperature of the target material, as a result, compared to other methods, the reduction of nutrients will be very small. It is also worth mentioning that irradiation does not cause radioactivity in food; Because there is no direct contact with it. [4]

But in the case of water, nuclear has different applications in water resource management. including directing surface and underground water, identifying underground aquifers, leakage control and safety of dams, desalination of salt water and sea water, detection and control of pollution. For example, in the hydrology of surface water, it is possible to study the movement of water in lakes and reservoirs, water balance, determination of feeding sources and their areas, determination of sedimentation from dams and canals, feeding of rivers, determination of suspended load and sediment bed load, sedimentation rate, evaporation. and transpiration, water exchange between surface and underground water, determination of the source of pollution and its tracking, determination of water equivalent to snow and its measurement, determination of the share of snow in runoff or in meteorological hydrology, changes in environmental conditions, movement and displacement of clouds, changes in precipitation, and environmental pollution can be investigated. [6]

2 . 3 . Industry

Radioisotopes are used in industry in various cases, the principles of each of which have a detailed explanation, and here we will only mention the name of these cases: Discovery of rare elements in mines and leak detection in transmission pipes, Surface, thickness and densitometry systems, Inspection of welding in oil and gas pipes (by Iridium source), Tracer to monitor fluid flow and filtration, Measurement of wear and corrosion of engine equipment, Examining glass melting furnaces to determine their defects, Checking the levels of gases, liquids and solids. [1]

2 . 4 . Healthcare

In nuclear medicine, very small amounts of radioactive materials are used inside the body to observe the function of organs or tissues (diagnosis) or to target and destroy damaged organs or tissues in a patient (treatment). Depending on the desired function and body tissue, various radiopharmaceuticals such as iodine, xenon, thallium, gallium, indium, technetium and so on. Radiation therapy (for example, destruction of cancerous tumors with radiation), Preparation and production of radiopharmaceutical kits for use in nuclear medicine centers, Preparation and production of hormonal kits, Preparation and production of various radiopharmaceuticals (such as iodine 131), Gamma scan, Tomography using single photon radiation (SPECT), Nuclear sterilization and disinfection of medical devices and Bone scan are Part of the applications of nuclear technology in the field of treatment and diagnosis. [1]

2 . 5 . Nuclear propellants and batteries

This technology, which is the monopoly of Russia, England, France, America, China, India and Iran, has military applications including nuclear submarines, aircraft carriers and armed submarines that carry ballistic and cruise missiles and civilian ones, including commercial and icebreakers (especially in Russia). The advantage of using these propellants is increasing safety, reducing costs, and reducing the need for refueling, and not having to surface the submarine for ventilation. [2]

But in the case of nuclear batteries, whose technology is also the monopoly of Russia, England, France, America and Iran, atomic energy is directly converted into direct current electricity. The energy of these batteries is ten times more than chemical batteries and they have a lifespan of several tens of years.These types of batteries, which are used in people's lives, health (implanted in the body), industry, agriculture, oil and gas fields, and launching satellites in the fuel sector, are produced in three types: radioisotope batteries, liquid nuclear batteries, and diamond nuclear batteries. [3]

2. 6 . Environment

In this field of nuclear science and technology, to identify air, water and soil pollutants using accelerators, tracking ground pollutants, controlling fossil and biological pollutants in air and sewage and hospital waste, eliminating industrial and household waste. Disinfection of sensitive surfaces, geological investigations (study of soil erosion using nuclear methods), development and implementation of alternative technologies for decontamination of surface and underground water due to the accumulation of industrial waste and human activities, irradiation for cleaning industrial wastewater, Municipal water, underground water and drinking water, break down toxic organic compounds and biological pollutants and reduce the accumulation of greenhouse gases using nuclear reactors. [2]

2. 7 . Other applications of nuclear technology

Nuclear technology is also used in fields such as military, archeology and protection of endangered animals. It is used in the military field, for things like identifying anti-personnel mines and producing anti-armor weapons, in archeology for examining archaeological samples such as coins, pottery, etc., detecting counterfeit samples of ancient artifacts and fossils, and dating and analyzing ancient artifacts and fossils and in the area of protection of endangered animals, to inject into animals and monitor them. [4]

. Current situation in Iran
Agriculture and food

Currently, the amount of production of agricultural products in Iran is more than 121 million tons, of which approximately 30% of agricultural products amounting to 40 thousand billion Tomans are wasted in recent years. Considering that in Iran, 93% of water is used for agriculture; Of this amount, 50 to 60 percent is wasted due to improper use, to which 13 billion cubic meters of water that is the result of agricultural waste should be added. Iran has one third of the global average rainfall and according to forecasts, 12 provinces will have no water storage in the country in the next 50 years.

Separating the water challenge from the use of chemical fertilizers is another issue that highlights the role of using nuclear science and technology in the field of agriculture and food. Currently in Iran, with the import of 21,000 tons of poison per year in the country, that is, about half a kilogram of agricultural poison is consumed per Iranian, which exceeds the defined standards. Besides these challenges, Iran has a lot of potential in the field of agriculture. Iran is one of the largest pomegranate producers in the world; 18 kilos of pomegranate is equivalent to one barrel of crude oil. Meanwhile, in China, 110,000 hectares are under pomegranate cultivation, and this amount is 70,000 hectares in Iran. [10]

You should pay attention to this point only a limited part of conventional agricultural technology in developed countries can be used in other places, solving agricultural problems requires local research to use technology that is suitable for the climatic conditions and the needs of the country. [6]

In recent years, Iran has made many achievements in the field of agriculture, which include: Production of hygrometer in Iran (in monopoly of less than 10 countries), Production of two varieties of rice named (Poya) and (Tabesh) (in 1990) - lack of height problem and lack of resistance to pests, Solving the problem of the height of Tabasi wheat (nuclear wheat) - one of the most suitable wheat species for dry and salty regions of Iran - its use in some parts of the country, such as Tabas, resulted in a 70% increase in production, Also, using nuclear technology, research projects have been carried out in the field of reducing the microbial load of saffron, red meat, spices, cumin, dates, and increasing the storage of garlic, potatoes, onions, etc.

In the field of pest control of olive fly, pomegranate cutworm, bean plant root, etc., effective researches have been carried out and also Irradiation of agricultural products to increase shelf life and export (installation of portable irradiation system)

In relation to food as well, for example disinfection of spices, including heat treatment of disinfection with ethylene oxide and methyl bromide gas, was banned since 1998 due to the effect of changing the taste and smell, as well as having the effects of being carcinogenic. The researchers of Yazd Process Radiation Research and Application Center succeeded in achieving the technique of reducing the microbial consumption of spices by means of beam irradiation, which reached 10 mega electron volts, as a result, Iran succeeded in preparing the national standard of Iran under the title of “Spice Irradiation Procedures”. [7]

Water

In less than 10 years, 3.5 billion people in the world will face water problems, and Iran is already facing problems caused by drought. Iran has more than 2 thousand kilometers of water border, which has a great potential to solve the water challenge using nuclear science and technology. [8] While the initial capital for the construction of nuclear facilities for water desalination is 2 and 5 times that of using coal and oil, respectively, but its final cost is cheaper than fossil fuels. Saudi Arabia, Bahrain, Kuwait and the United Arab Emirates use very large water desalination plants to desalinate Persian Gulf water, while the water desalination plant of the Bushehr nuclear power plant produces 100,000 cubic meters of water per day, and Iran plans to build two nuclear power plants to produce 400,000 cubic meters of water per day. It has

a thousand cubic meters of water in its program. [7]

Healthcare

In the field of nuclear medicine research, the Islamic Republic was ranked seventh among 70 countries in 2006 and first among 85 countries in 2010. Domestic production of radiopharmaceuticals covers 90-95% of radiopharmaceutical consumption in Iran.

The latest radiopharmaceutical products of Iran are:

Strontium 90/Yttrium 90 generator for the treatment of prostate, breast, ovary, liver cell cancers, treatment of non-Hodgkin's lymphoma (malignant), joint inflammation and neuro-endocrine tumors.

Chromic phosphate to treat liver cancer

Iodine-125 brachytherapy spring for brain cancer treatment

Brombezin - Gallium 68 for the treatment of prostate, lung and breast tumors

It is worth mentioning that 95% of radiopharmaceuticals are produced in 5 nuclear reactors in Canada, Holland, Belgium, France and South Africa.

Currently, more than one million people in Iran use nuclear medicine such as radiopharmaceuticals every year. Most radiopharmaceuticals cannot be imported due to their short half-life, such as iodine 123, which has only 13 hours of life. right now in Iran, about 20 billion tomans of subsidies are allocated to domestic radiopharmaceuticals, which in case of import inevitably costs more than 100 billion tomans. Currently, radiopharmaceuticals are also produced in the research reactor of Tehran, which, due to the existing developments, the potential of exporting radiopharmaceuticals in Iran has been provided. It is expected that if the reactor under construction in Arak is started, the main burden of this task as well as the development of the nuclear medicine industry will be placed on this reactor. [9]

. Conclusion

Considering the extensive applications of nuclear science and technology in non-energy industries, it is clear that this technology has significant positive effects in improving people's lives and raising the level of development of societies. From nuclear applications in the field of agriculture and food security to improving health and medicine, from water and environment purification to industrial use, each of these applications bring positive effects in societies.

Considering that Iran also uses this technology in various fields, this country has many capacities to exploit non-energy applications of nuclear science and technology. From great successes in the field of agriculture and improving the health of plants and animals to significant advances in the field of medicine

and water purification, Iran has shown that it can take advantage of its capacities in this field and add to the progress of its society and country.

Finally, the examination of the non-energy production applications of nuclear science and technology shows that this technology can effectively help in solving various problems of modern societies and use it as a powerful tool in the direction of progress and development.

References

WHO Guidance on Exposure to Depleted Uranium For Medical Officers and Programme Administrators World Health Organization 2001

Depleted Uranium weapons in 2001-2002 Occupational, Public and Environmental Health Issues January 2002

FINAL REPORT OF THE DEPLETED URANIUM OVERSIGHT BOARD SUBMITTED TO THE UNDERSECRETARY OF STATE FOR DEFENCE February 2007

DEPLETED URANIUM With contributions of: Felicity Arbuthnot Rosalie Bertell Ray Bristow Peter Diehl Dan Fahey Henk van der Keur Daniel Robicheau Laka Foundation May 1999.

Shahzadi, S., Azimi, P., Zali, A. and Parsa, K., (2011). Outcomes of Stereotactic Brachytherapy (temporary 125Iodine seeds) for the treatment of low grade glioma tumors in Shohada-Tajrish Hospital between 2004 and 2011. Pajoohandeh Journal, 16(3), pp.105-111.

Hamta A, Hamidi S. (2013). Modeling Breast Cancer Using Chemical and Radiopharmaceutical Effect of P32 on Related Cancer Cells. Journal of Cell and Tissue (JCT), winter; 3(4): 345-350.

Cheung, J.Y., Yu, K.N., Yu, C.P. and Ho, R.T., (1998). Monte Carlo calculation of single-beam dose profiles used in a gamma knife treatment planning system. Medical physics, 25(9), pp.1673- 1675.

Khademian R, N.B. Jelodar. (2008). Nuclear technology applications in agricultural and gardening plant breeding.

Improving crop quality and stress tolerance in plants in Asia and the Pacific region. (2012) www.iaea.org.

Mousavi Shalmani, Mir Ahmad; Khorasani, Ali; Piervali Baeranvand, Nejat. (2008). Use of isotopic trace techniques to management of macro and micro elements in plant nutrition cycles.

ICNST 2024 International Conference on Nuclear Science and Technology
6- 8 MAY 2024 | Isfahan, Iran

Design and construction of permanent rings for an ECR plasma source with priliminary result of air plasm spectrum (Paper ID : 1608)

Asadi Aghbolaghi M.[1], Torabi M.[2*], Masoudi A.[3], Ghasemi M.[4], Keshavarz M.[3] and Arjhangmehr A.[1]

[1]*Department of Radiation Application, Faculty of Nuclear Engineering, Shahid Beheshti University, P.O. Box 19839-69411, Tehran, Iran*

[2]*Department of Physics, Shahid Beheshti University, P.O. Box 19839-69411, Tehran, Iran*

[3]*Department of Physics and Energy Engineering, Amirkabir University of Thechnology*

[4]*Department of Nuclear Engineering, Islamic Azad University Central Tehran Branch*

ABSTRACT

Electron cyclotron resonance plasma sources (ECRPS) is utilized in different applications such as neutron generators, ion implanters, coating devices etc. In this plasma source, when the electron Larmor frequency is the same as the microwave frequency (in the resonance zone), the electrons get heated to ionize the neutrals in the plasma bulk. In this work, the 48 N52 (NdFeB) permanent magnets with dimension of 2 cm×1 cm×1 cm are used to design and construct the magnet rings. The magnetic field profile with the resonance field value of 875 G is simulated by applying COMSOL Multiphysics and formed in the stainless steel plasma chamber with the length of 19.8 cm and the radius of 3.8 cm. The results show a good agreement between the simulation and experimental data measured by gauss meter. In addition, the optical emission spectra of air is measured by means of optical emission spectroscopy (OES) through the middle port on the chamber.

KEYWORDS: ECRPS, Permanent magnet, Resonance zone, COMSOL, OES

INTRODUCTION

ECR plasma source is one of the most useful devices to produce charge ions current for different applications in research institute, industries, etc. The main parts of this plasma source are: RF power supply (magnetron), RF line, plasma chamber, magnet structure and etc. In this work, The RF frequency and power are chosen to be 2.45 GHz and 1 kW, respectively, and RF line consist of directional coupler, circulator, wattmeter, water load, three-stub tuner and waveguide [1]. Additionally, stainless steel and quartz are selected as non-magnetized material for plasma chamber and pressure window, respectively. Finally, like Ref. [2] the permanent magnet rings are placed in the holder around the chamber. The aim of utilizing the

magnetic field is confining the electrons and ions around the field lines to ionize the plasma and lead them toward the extraction system. In this work, the magnetic field profile is simulated using COMSOL software and compared to experimental data measured by a standard gauss meter. In addition, the air spectra is obtained by OES method and shows an acceptable result of air atoms recognition.

RESEARCH THEORIES and EXPERIMENTAL

In this study the magnetic field profile is simulated by 24 N52 (NdFeB) permanent magnets with dimension of 2 cm×1 cm×1 cm and the schematic of structure is shown in Figure 1-a. The rings include 24 magnets are arrayed in 12 rows with equal spacing around the plasma chamber. The gauss meter is used or magnetic field measurement on the middle axis and the size step is chosen about 5 mm. Figure 1-b shows the setup of permanent magnets with their iron holder.

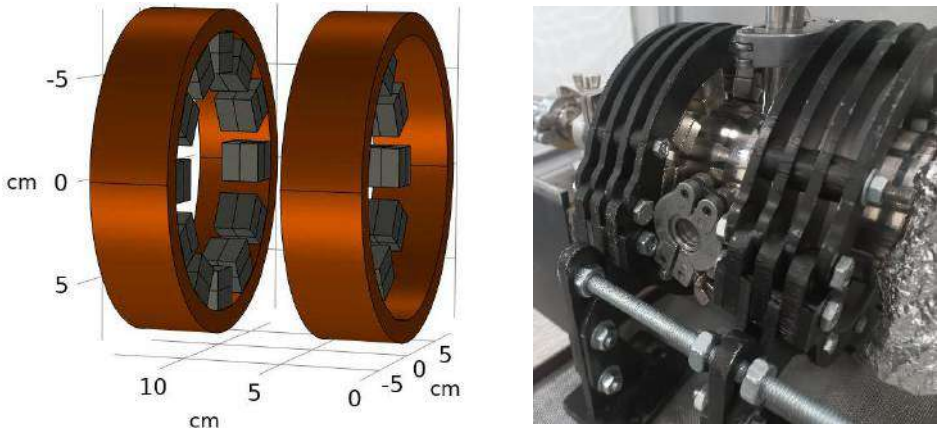

(a) (b)

Fig. 1. a) Schematic and b) magnet structure with plasma chamber.

RESULTS

The simulated and measured magnetic field profiles is shown in Figure 2-a. As one can see, there is a good agreement between both profiles. In addition, ECR plasma formation have been studied in the pressure range of $1 \times 10^{-2} - 3.3 \times 10^{-3}$mbar for different absorbed power for air gas by a CMOS based OES system. Air plasma is shown through a view port in Figure 2-b.

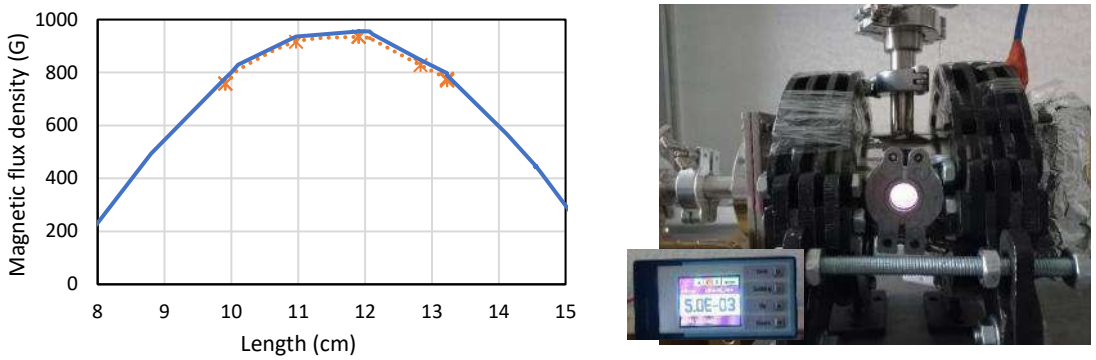

(a) (b)

Fig. 2. a) The simulated (blue solid line) and measured (star-dash line) magnetic field profiles and b) magnet structure with plasma formation in chamber.

Figure 3 show the air spectrum for around 300-watt microwave absorbed power in vacuum pressure of 5×10^{-3}mbar. It can be seen that like each conventional air microwave plasma the 1st- and 2nd positive series of excited molecular nitrogen are presented in the plasma [3]. More study result of ongoing work will be presented in the future publications.

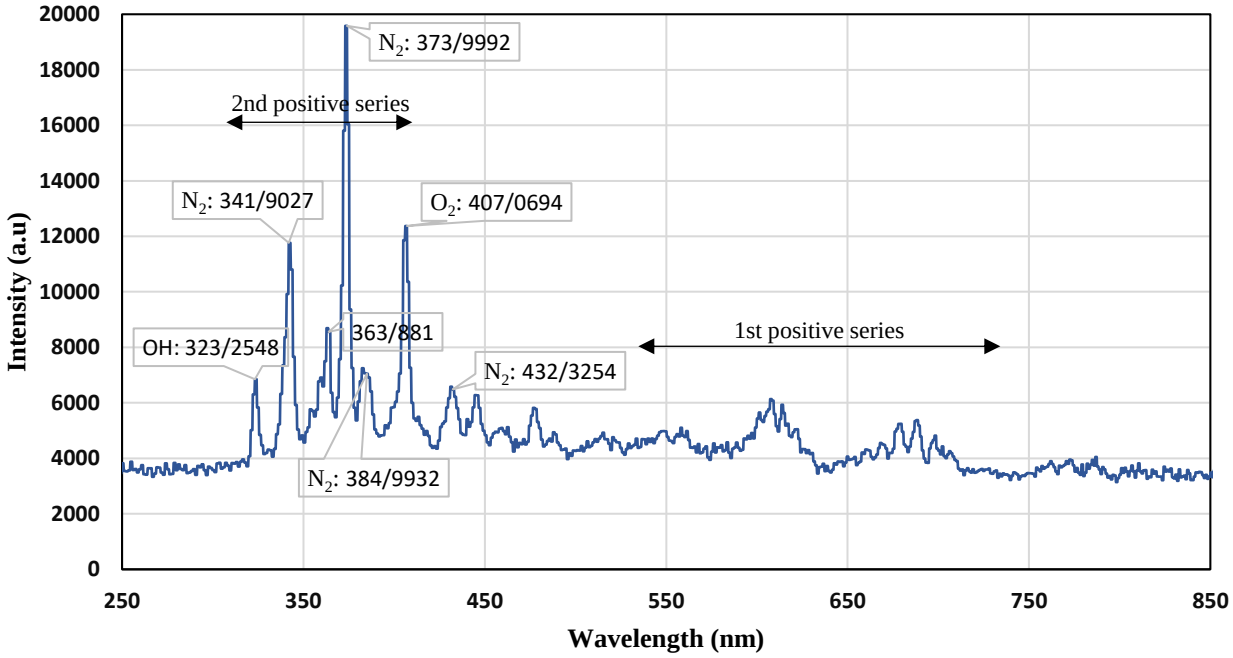

Fig. 3. Optical emission spectra of ECR air plasma source.

CONCLUSIONS

In this work, the magnetic field profile was produced with permanent magnet rings and the simulation shows a good agreement with experimental data measured by a standard gauss meter. In addition, the air spectra is obtained by OES method shows an acceptable result of air plasma.

REFERENCES

[1] Jin, Q. Y., Liu, Y. G., Zhou, Y., Wu, Q., Zhai, Y. J. and Sun, L. T. (2021). RF and Microwave Ion Sources Study at Institute of Modern Physics.

[2] Cho, Y. S., Kim, D., Kwon, H. J., Seol K. T. and Kim H. S. (2011). Microwave Ion Source with a Permanent Magnet Solenoid. Journal of the Korean Physical Society. 59(2):586-589.

[3] Hughes, W. C., Rowland, W. H., Johnson, M. A. L., Fujita, Sh., Cook, J. W. and Schetzina, J. F. (1995). Molecular beam epitaxy growth and properties of GaN films on GaN/SiC substrates. Journal of Vacuum Science & Technology.

ICNST 2024 International Conference on Nuclear Science and Technology
6- 8 MAY 2024 | Isfahan, Iran

Feasibility study on the using of Coded Aperture Mask in SPECT for Boron dose imaging in TRR-Based BNCT: Preliminary study (Paper ID : 1617)

Mansouri. P[1]. Rahmani. F. *[1]

[1] *Department of Physics, K. N. Toosi University of Technology, 16315-1618, Tehran, Iran*

Abstract

In this work, the feasibility study on using Coded-Aperture Imaging (CAI) based on Modified Uniformly Redundant Array (MURA) coded mask in Single Photon Emission Computed Tomography (SPECT) was investigated for boron dose measurement in Boron Neutron Capture Therapy (BNCT). In this preliminary study, a MURA rank 13 with a 2×2 mosaic configuration, and a CZT detector array mounted in a single mask were investigated using MCNPX2.7 simulations. This is the first investigation on the use of CAI for BNCT purposes. Also, Maximum Likelihood-Expectation Maximization (MLEM) was used for boron dose image reconstruction. Preliminary results show that SPECT with MURA masks can be an efficient and precise tool for boron dose measurement in BNCT.

Keywords: Boron dose imaging, Single Photon Emission Computed Tomography, Modified Uniformly Redundant Array, Boron Neutron Capture Therapy, Maximum Likelihood-Expectation Maximum.

INTRODUCTION

Boron Neutron Capture Therapy (BNCT) is one of the promising methods for treatment of Glioblastoma Multiform (GBM) tumors, which is based on the energy deposition of produced nucleons in the cell dimension due to thermal neutron capture in ^{10}B:

$$^{10}B + n_{th} \rightarrow \alpha + {}^{7}Li\ (94\%) + 478\ keV \qquad (1)$$

Two main keys in successive BNCT are providing ^{10}B drug with optimized deposition in tumor as well as appropriate thermal neutron flux in the tumor location. Characteristics of the appropriate therapeutic

neutron beam are defined in IAEA-1223 [1]. The appropriate boron dose distribution can be measured by real-time methods such as Prompt Gamma Neutron Activation Analysis (PGNAA) [2], and Single Photon Emission Computed Tomography (SPECT) [3], based on recording 478 keV gamma emission. SPECT has some disadvantages, such as the long time needed for boron dose imaging, and also the reduced intensity and spatial resolution due to long collimators between sample and detectors. In this work, a new method has been proposed to monitor boron dose distribution with the Modified Uniformly Redundant Array (MURA) [4], which has not been used and reported in BNCT yet. This feasibility has been tested for the designed therapeutic neutron beam in Tehran Research Reactor (TRR) using Monte Carlo simulation code, MCNPX2.7 [5].

Materials and methods

In this work, SPECT using a MURA-based mask for a TRR-based BNCT has been introduced.

BNCT in TRR

TRR is a 5 MW pool-type research reactor with low-enrich uranium fuel. Kinds of research related to BNCT have been performed in the past years [6-8]. The Thermal column has been selected for providing an appropriate neutron beam in the present project, which was shown the potential to be used for BNCT in our last project [7]. A therapeutic neutrons beam (Fig. 1) with an epithermal flux of about 6.5E8 n/cm^2.s can be provided at the BSA exit [7].

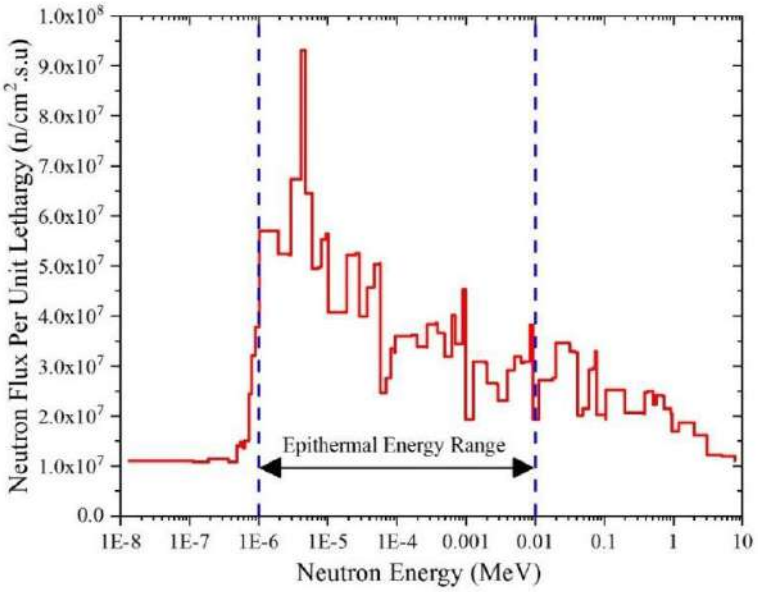

Fig.1. Therapeutic neutron spectrum at the BSA exit [7]

SPECT

In BNCT, the patient is positioned in front of a therapeutic beam for less than an hour. During BNCT, neutron capture in ^{10}B will produce 478 keV gammas, which intensities are proportional to boron concentration, so measuring and recording emitted gammas can provide some useful information about the position of gamma emission or local boron dose. A conventional SPECT array is an assembly of long collimators with detectors behind them [9], so the recorded gammas in the detector array can be interpreted as boron concentration and used for boron dose imaging [10-11]. A general SPECT array is shown in Fig. 2.

As shown, high-Z (such as platinum, gold, lead, or tungsten) collimators with hole diameter in the order of 4-5 mm and the length of 30-50 cm can be used for SPECT in BNCT. The dimension of the collimator (length and hole diameter) is dependent to the desired spatial resolution in the image. Semiconductor detectors such as CdZnTe (CZT), or CdTe, with a size as small as collimator hole, are common options. With these designs, spatial resolution of about 4-5 mm can be obtained. In addition, 5-9 degree of angular rotation is efficient for BNCT [11]. The duration for one complete rotation of SPECT array around the head should be less than the determined treatment time of BNCT (less than an hour), so it is different in each BNCT setup with dedicated treatment time. As stated before, imaging using conventional SPECT has some disadvantages such as low resolution, low S/N, and long-time needed for angular imaging around the head, which are important in BNCT due to low intensity 478 keV gammas.

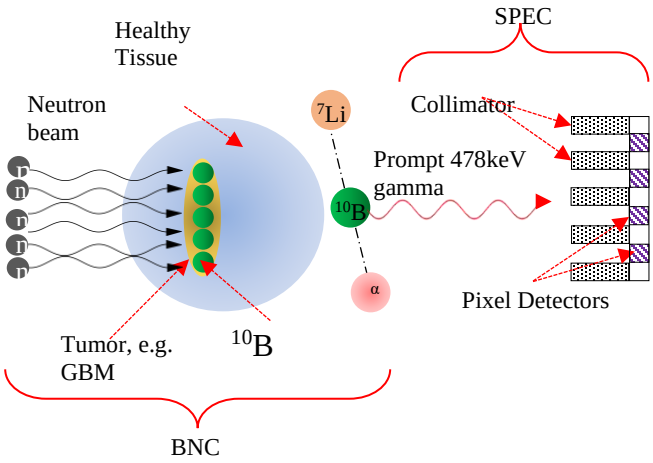

Fig. 2. General SPECT array in BNCT.

SPECT with MURA

Coded-Aperture Imaging (CAI) using a mask is applied in X-ray cameras and telescopes [4-12-13], and also in gamma-ray imagers for medical applications. CAI with MURA is proposed for BNCT for the first time in this work [4-14-15].

A coded-aperture mask can be assumed as a multiplexed pinhole collimator with a particular pattern, which allows improved system sensitivity and good spatial resolution, but they suffer from a trade-off between sensitivity and data ambiguity [9]. Mathematically, a mask is a binary array of opening and opaque pattern in the aperture. Uniformity in an opening distribution is necessary for image reconstruction. Therefore, uniformly redundant arrays (URAs) were introduced, and then, by changing URA's encoding algorithm, a Modified Uniformly Redundant Array (MURA) was developed [16]. These apertures can provide up to 50% transparency for the transmission of radiation. MURA masks are different in the arrangement of opening and opaque elements, as well as in the number of pixels, so they are classified according to the rank. Complete descriptions of new suggested and constructed arrays have been discussed in several litterateurs [16]. As mentioned about the number of pixels, and the rank applied in this work, the total number of elements for the MURA rank 13 with a 2×2 mosaic configuration are 625, which are arranged in a 25×25 matrix. A position-sensitive pixel detector is placed behind each of the open or opaque elements of MURA [17].

Dimension of elements in the mask have been selected according to the considered spatial resolution of boron dose imaging. In this work, spatial resolution of 0.8 cm has been determined, which was selected according to the aim of this work (feasibility study). It should be applied in a smaller size for further investigations.

High-Z materials such as tungsten (W) and lead (Pb) can be considered as appropriate candidates for gamma shielding, and the opaque part of the mask. In this project, W is selected for opaque parts of the mask. The dimension of pixels in mask has been selected equal to 0.8×0.8 cm^2, according to the considered spatial resolution of boron dose imaging, as stated before. To avoid shadowing in the opening element, the appropriate thickness of mask should be selected [9-18-19]. Conventional semiconductor solid-state detectors, such as CdTe and CdZnTe can be used in this manner. In this work, CZT has been selected due to its appropriate energy resolution in the range of 478 keV, and its separation capability from 511 keV [20]. Produced prompt gammas due to neutron capture in ^{10}B in phantom can pass through the opening elements of MURA and can be recorded in the position-sensitive CZT array. As mentioned before, neutron capture in ^{10}B produces 478 keV gammas with the intensity proportional to boron concentration, so the

recorded gammas in the detector array can be converted to the image. In gamma spectra recorded in the CZT, the net counting rate of photopeak (478 keV) is based on the integration of the counting rate in the Region Of Interest (ROI) in the range of 478± FWHM (keV), which FWHM of CZT detector for 478 keV gamma should be calculated.

Implementation in MCNPX2.7

To simulate the MURA rank according to the gamma energy used in BNCT rank 13 with a 2×2 mosaic mask and a block size of 0.8×0.8 cm^2 and a thickness of 1.3 cm with a 99.83% probability of not passing the beam and also a CZT pixel detector. It is simulated using

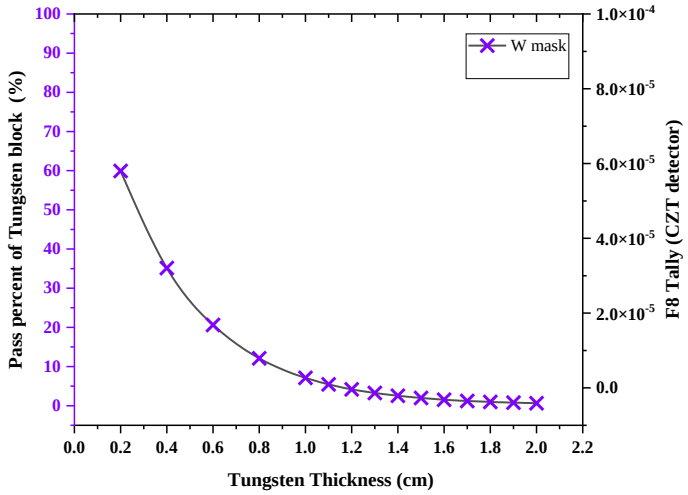

MCNPX2.7 with dimensions of 0.8×0.8 cm^2 with a thickness of 2 cm. Calculation of the pulse height, F8 Tally along with the energy, and GEB (Gaussian energy spread) card are used to record the gamma spectrum at each pixel of the CZT radiation detector. The GEB parameters in the GEB card can be adjusted using the incident gamma energy E as well as the corresponding full width FWHM at half maximum of the CZT radiation detector (FWHM of 478 keV in a CZT radiation detector of about 9.3 keV, and a corresponding energy resolution of about 1.94%). The thickness of tungsten (MURA Mask) should be selected to stop a significant percentage of 478 keV gammas. Therefore, a simple simulated setup, including a 478 keV beam, a box-shape tungsten (W) with various thicknesses, and a CZT detector has

been considered, then F8 tally within 478 keV ROI in the CZT detector has been calculated. It can be inferred from Fig. 3, for a thickness of 1cm (1.3 cm) of tungsten, 478 keV gammas will be attenuated by a factor of about 90% (95%). Therefore, the thickness of 1.3 cm has been chosen for the MURA mask.

An extended volumetric gamma source of 478 keV in one voxel of the tumor in a dimension of 1×1×1 cm^3 has been considered in front of the MURA mask, and the recorded gammas in the detector array have been considered. that the considered thickness of 1.3 cm for tungsten (MURA mask) is in compliance. Figure 4. shows the schematic view, as well as the simulated of a rank 13 with a 2×2 mosaic-MURA mask with a CZT detector array.

Therefore, Figure 5. Shows the MURA mask is positioned 10 cm above the voxelized cubic head phantom contained tumor (with 43 ppm ^{10}B) with a dimension of 4×4×4 cm^3 (in the middle of the cubic phantom) in front of the exit window of a therapeutic neutron beam. In addition, the CZT pixel detector is positioned 1 cm above the MURA mask, which leads to magnify the subtended solid angle between the CZT pixel detector and the MURA mask. Boron concentrations according to the ^{10}B in BPA has been selected 43 ppm in tumor and 15 ppm in normal tissue.

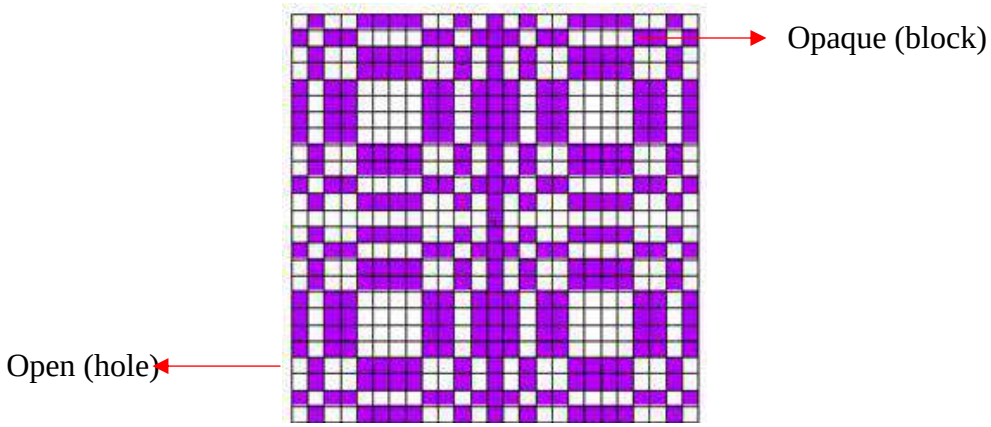

Fig.4. simulated MURA rank 13 with a 2×2 mosaic configuration in MCNPX2.7, violet and white blocks demonstrate opaque and open MURA elements, respectively – drawings are not in scale.

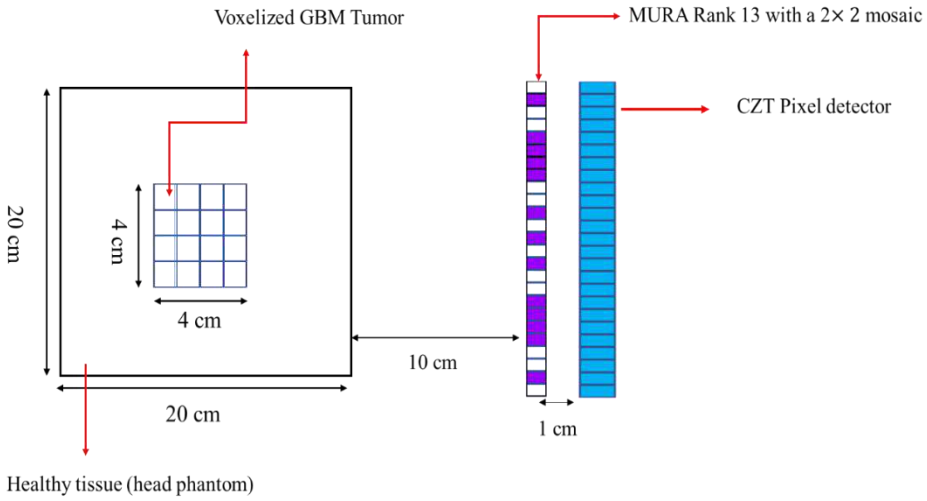

Fig.5. MURA mask array positioned above the head phantom (top view) – drawings and dimensions are not scale.

MLEM Method

For calculating the boron dose imaging or measurement of ^{10}B concentration in each voxel of head phantom (including tumor), the below matrix-equation must be solved for λ:

$$A\,\lambda = y \qquad (2)$$

where, A is the entire detector response matrix, y is the detector response matrix for an unknown ^{10}B concentration distribution in a head phantom, and λ is the considered answer, which contains information about the presence of ^{10}B in voxels.

A is usually a big matrix, and mostly its inverse (A^{-1}) cannot be simply calculated using conventional techniques, such as $\lambda = A^{-1}y$. Therefore, some advanced mathematical techniques such as Tikhonov regularization [21], Moore-Penrose Inverse method [22], and Maximum Likelihood Expectation Maximization (MLEM) [23-25] are suggested to solve such kinds of problems.

The MLEM [23-25] is a very flexible method regarding the sampling conditions based on the iteration selected for solving the voxel value matrix of λ as follows:

$$\lambda_j^{n+1} = \frac{\lambda_j^n}{\sum_i A_{ij}} \sum_i A_{ij} \left(\frac{y_i}{b_i + \sum_k \lambda_k^n A_{ik}} \right) \qquad (3)$$

As stated before, A is the entire detector response matrix, b is the background radiation and noise contribution, y is the detector response matrix for an unknown boron distribution in tumor and/or head phantom around the tumor, and λ_j^n is the probability of ^{10}B presence in a voxel j^{th} in the n^{th} iteration. However, the main concern about the MLEM method is its convergence speed, which is not always guaranteed.

In this study, the number of CZT detector pixels is 625. Tumor with 64 different distributions in voxels have been considered, therefore the A matrix has 625 rows and 64 columns, the b and y vectors have 625 rows in one column, as well as, the λ vector has 64 rows in one column.

The number of iterations is completely problem-dependent and usually, 100000 iterations are utterly adequate to converge. To construct the A matrix, each different distribution of the head phantom is considered with 478keV volumetric gamma-source, in such a way that the entire detector response related to each different distribution fills the corresponding column in A.

Monte Carlo MCNPX2.7 simulated characteristics for a MURA 2×2 mosaic mask Rank 13 as well as the CZT pixel detector are shown in Table 1.

Results

As mentioned before, the thicknesses of the MURA mask have been considered 1.3 cm to test the proposed method. For this investigation, two evaluations (examinations) are noticeable: case I) the extended 478 keV gamma source in one voxel of tumor, and case II) the extended 478 keV gamma source in multiple voxels of the tumor in front of the MURA. These multiple voxels can be considered as a closely neighboring voxels, or even multiple single-voxels far apart from each other in the tumor. In Fig. 6, the way of numbering the tumor voxels is depicted.

Case I is some of special situation having only a single voxel of borated-tumor with amount of ^{10}B that is rare. for showing the performance of the imaging system. Also, the general case II has been evaluated and studied. For example, if ^{10}B in all the tumor voxels have an equal concentration, calculated ^{10}B concentrations must be the same using the MLEM method. In Figs.7, 8 and 9, raw and reconstructed (by using MLEM) images are depicted which shows the reconstructed image is in good agreement with the above description.

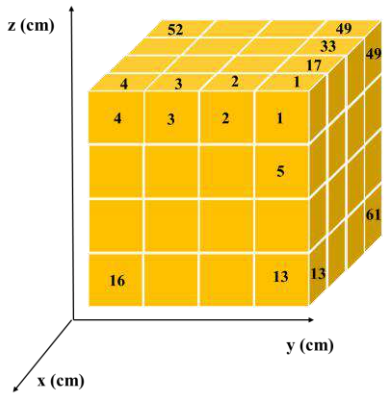

Fig.6. Numbering of tumor voxels from 1 to 64.

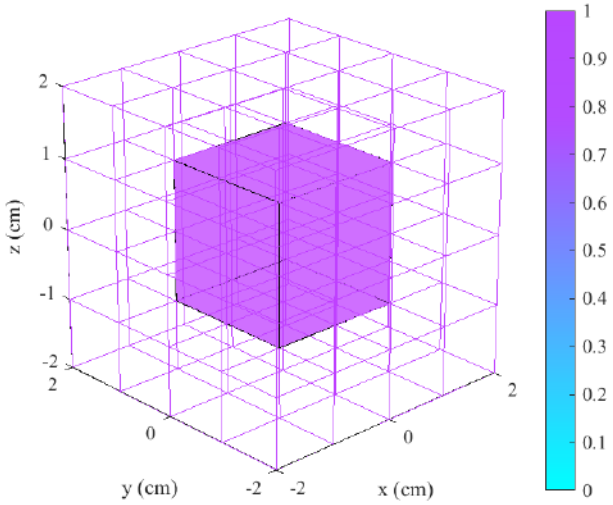

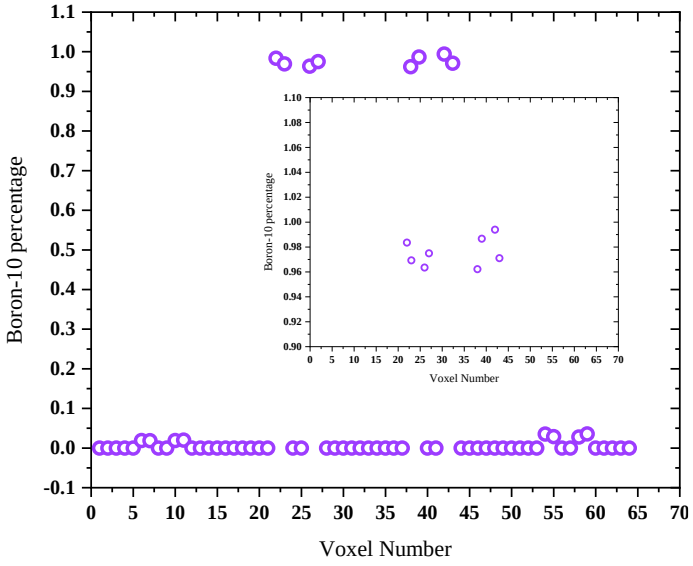

Fig.7. #1.Left) Relative ^{10}B percentages calculated by using MLEM method, Right) 3D illustration of reconstructed ^{10}B distribution in tumor voxels – purple color means the centers voxel filled completely with ^{10}B.

However, the slight differences between calculated relative ^{10}B percentages in tumor voxels can be seen in Fig.7 (left), which are better than the needed accuracy (recognition 1 ppm differences) for boron measurement. It should be noticed that these slight differences will also be disappeared by applying more iterations in MLEM method. A main reason for the mentioned small fluctuations can be related to different flight paths of 478 keV gamma rays from different depths of the tumor up to the CZT pixel detector. Another investigation to test the proposed methods is considering the different spatial distributions of ^{10}B in tumor

voxels. In Table 2, some special ^{10}B distributions are listed, and the accuracy of the proposed MURA mask with MLEM method has been tested as follows.

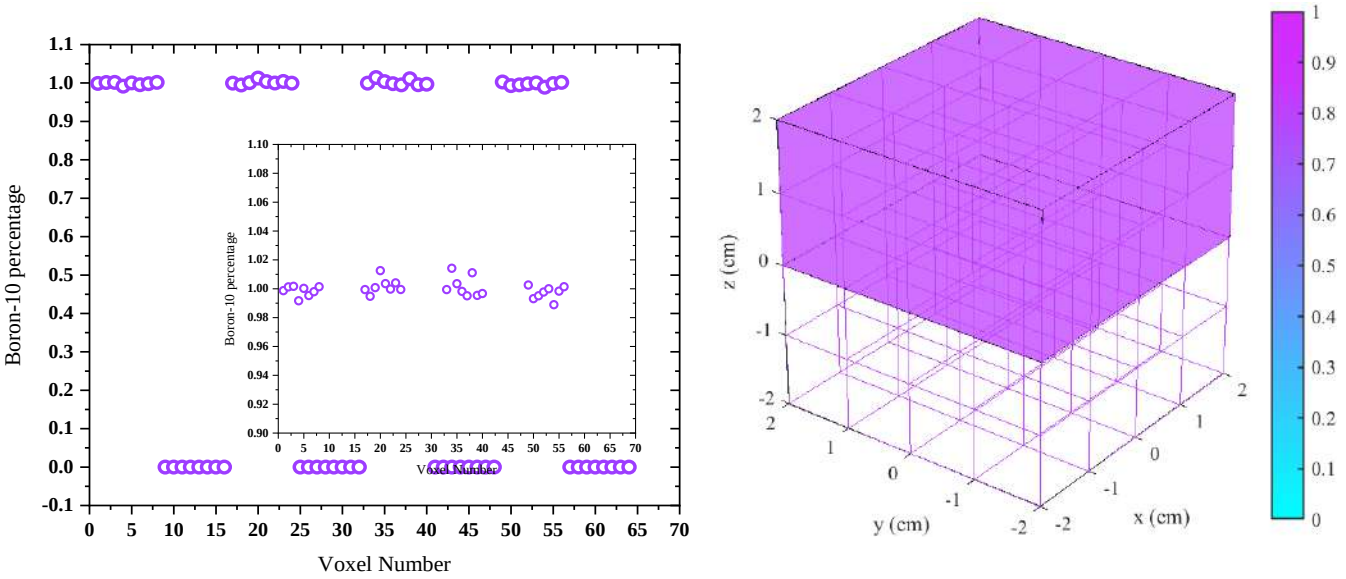

Fig.8. #2.left) Relative ^{10}B percentages calculated by using MLEM method, Right) 3D illustration of reconstructed ^{10}B distribution in tumor voxels – purple color means the upper voxels filled completely with ^{10}B.

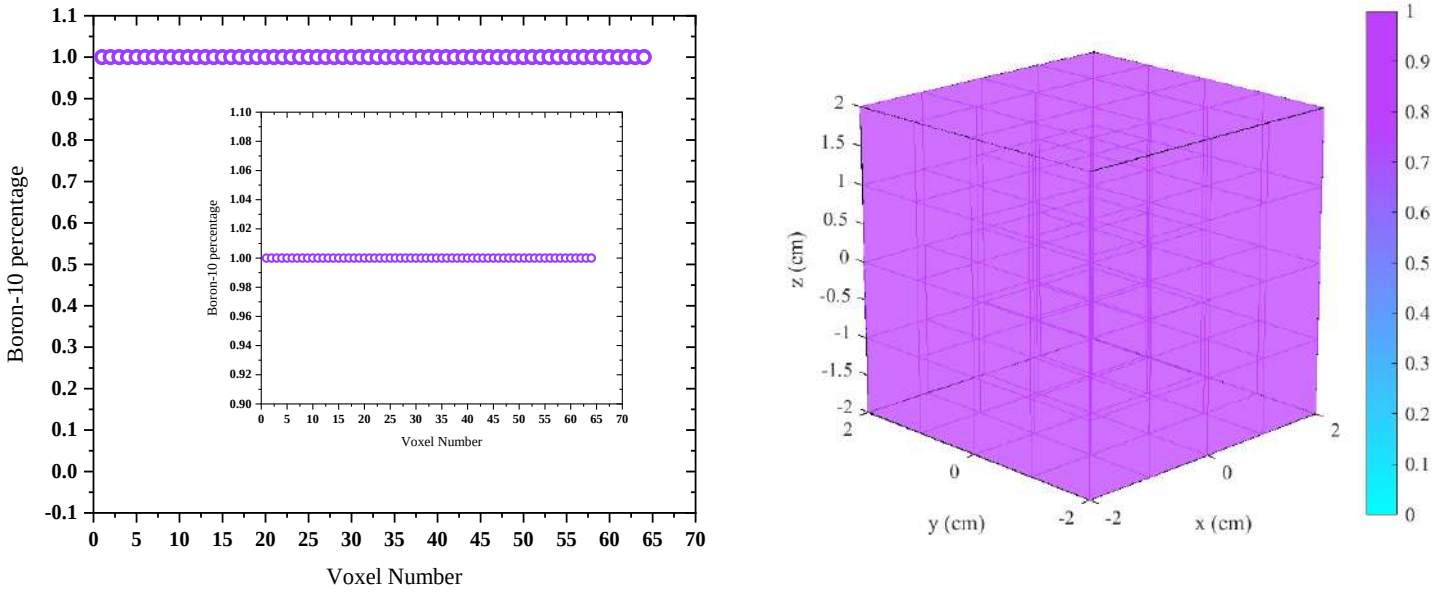

Fig.9. #3.left) Relative ^{10}B percentages calculated by using MLEM method, Right) 3D illustration of reconstructed ^{10}B distribution in tumor voxels – purple color means the total of tumor filled completely with ^{10}B.

Table 1. Characteristics of CZT pixel detector and MURA mask.

Characteristic	Material	Density (gr/cm^3)	Effective atomic Number	Dimension (cm×cm×cm)
MURA (mask)	Tungsten (W)	19.30	74	0.8×0.8×1.3
Detector	CZT	5.8	48.5	0.8×0.8×2

Table 2. Special ^{10}B distributions in tumor voxels (voxel numbers are listed according to the Fig.6).

Special ^{10}B distribution	Targeted voxels
#1	22, 23, 26, 27, 38, 39, 42, 43
#2	1 to 4, 5 to 8, 17 to 20, 21 to 24, 33 to 36, 37 to 40,49 to 52, 53 to 56
#3	1 to 64

Conclusion

In this research, preliminary study was performed to show the potential use of **Coded Aperture Mask,** MURA mask in boron dose distribution during BNCT.

It is obvious that geometry optimization should be considered for real application, but the advantage of MURA is evident in comparison to heavy SPECT systems. In further investigation, details of boron dose distribution in TRR-based BNCT will be reported.

References

[1] TECDOC, I. (2001). Current status of neutron capture therapy. TECDOC-1223.

[2] Babaeian, K., Rahmani, F., & Kasesaz, Y. (2019). Conceptual design of prompt gamma neutron activation analysis facility at Tehran Research Reactor for BNCT application. Nuclear Instruments and Methods in Physics Research Section A: Accelerators, Spectrometers, Detectors and Associated Equipment, 935, 185-190.

[3] Murata, I., Mukai, T., Ito, M., Miyamaru, H., & Yoshida, S. (2011). Feasibility study on BNCT-SPECT using a CdTe detector. Progress in Nuclear Science and Technology, 1.

[4] Cieślak, M. J., Gamage, K. A., & Glover, R. (2016). Coded-aperture imaging systems: Past, present and future development–A review. Radiation Measurements, 92, 59-71.

[5] Goorley, J. T., James, M. R., Booth, T. E., Brown, F. B., Bull, J. S., Cox, L. J., ... & Zukaitis, A. J. (2012). Initial MCNP6 Release Overview-MCNP6 Beta 3 (No. LA-UR-12-26631). Los Alamos National Lab.(LANL), Los Alamos, NM (United States).

[6] Kasesaz, Y., Khalafi, H., Rahmani, F., Ezzati, A., Keyvani, M., Hossnirokh, A., ... & Amini, S. (2014). Design and construction of a thermal neutron beam for BNCT at Tehran Research Reactor. Applied Radiation and Isotopes, 94, 149-151.

[7] Kasesaz, Y., Khalafi, H., & Rahmani, F. (2014). Design of an epithermal neutron beam for BNCT in thermal column of Tehran research reactor. Annals of Nuclear Energy, 68, 234-238.

[8] Kasesaz, Y., Khalafi, H., Rahmani, F., Ezzati, A., Keyvani, M., Hossnirokh, A., ... & Amini, S. (2014). Design and construction of a thermal neutron beam for BNCT at Tehran Research Reactor. Applied Radiation and Isotopes, 94, 149-151.

[9] Van Audenhaege, K., Van Holen, R., Vandenberghe, S., Vanhove, C., Metzler, S. D., & Moore, S. C. (2015). Review of SPECT collimator selection, optimization, and fabrication for clinical and preclinical imaging. Medical physics, 42(8), 4796-4813.

[10] Murata, I., Mukai, T., Nakamura, S., Miyamaru, H., & Kato, I. (2011). Development of a thick CdTe detector for BNCT–SPECT. Applied Radiation and Isotopes, 69(12), 1706-1709.

[11] Minsky, D. M., Valda, A. A., Kreiner, A. J., Green, S., Wojnecki, C., & Ghani, Z. (2009). Experimental feasibility studies on a SPECT tomograph for BNCT dosimetry. Applied Radiation and Isotopes, 67(7-8), S179-S182.

[12] Caroli, E., Stephen, J. B., Di Cocco, G., Natalucci, L., & Spizzichino, A. (1987). Coded aperture imaging in X-and gamma-ray astronomy. Space Science Reviews, 45(3), 349-403.

[13] Grindlay, J. E., & Hong, J. (2004, January). Optimizing wide-field coded aperture imaging: radial mask holes and scanning. In Optics for EUV, X-Ray, and Gamma-Ray Astronomy (Vol. 5168, pp. 402-410). International Society for Optics and Photonics.

[14] Alnafea, M., Wells, K., Spyrou, N. M., & Guy, M. (2007). Preliminary Monte Carlo study of coded aperture imaging with a CZT gamma camera system for scintimammography. Nuclear Instruments and Methods in Physics Research Section A: Accelerators, Spectrometers, Detectors and Associated Equipment, 573(1-2), 122-125.

[15] Alnafea, M., Wells, K., Spyrou, N. M., Saripan, M. I., Guy, M., & Hinton, P. (2006). Preliminary results from a Monte Carlo study of breast tumour imaging with low-energy high-resolution collimator and a modified uniformly-redundant array-coded aperture. Nuclear Instruments and Methods in Physics Research Section A: Accelerators, Spectrometers, Detectors and Associated Equipment, 563(1), 146-149.

[16] Gottesman, S. R., & Fenimore, E. E. (1989). New family of binary arrays for coded aperture imaging. Applied optics, 28(20), 4344-4352.

[17] Cieślak, M. J., Gamage, K. A., & Glover, R. (2016). Coded-aperture imaging systems: Past, present and future development–A review. Radiation Measurements, 92, 59-71.

[18] Lee, T., & Lee, W. (2014). Compact hybrid gamma camera with a coded aperture for investigation of nuclear materials. Nuclear Instruments and Methods in Physics Research Section A: Accelerators, Spectrometers, Detectors and Associated Equipment, 767, 5-13.

[19] Cieślak, M. J., Gamage, K. A., Glover, R., & Taylor, C. J. (2019). Gamma-ray modulation properties of tungsten coded apertures for a novel mixed-field imaging system. Journal of Instrumentation, 14(02), P02007.

[20] Knoll, G. F. (2010). Radiation detection and measurement. John Wiley & Sons.

[21] Golub, G. H., Hansen, P. C., & O'Leary, D. P. (1999). Tikhonov regularization and total least squares. SIAM journal on matrix analysis and applications, 21(1), 185-194.

[22] Katsikis, V. N., Pappas, D., & Petralias, A. (2011). An improved method for the computation of the Moore–Penrose inverse matrix. Applied Mathematics and Computation, 217(23), 9828-9834.

[23] Cui, J., Pratx, G., Meng, B., & Levin, C. S. (2013). Distributed MLEM: An iterative tomographic image reconstruction algorithm for distributed memory architectures. IEEE transactions on medical imaging, 32(5), 957-967.

[24] Mihlin, A., & Levin, C. S. (2013, October). An MLEM method for joint tissue activity distribution and photon attenuation map reconstruction in PET. In 2013 IEEE nuclear science symposium and medical imaging conference (2013 NSS/MIC) (pp. 1-3). IEEE.

[25] Carmi, R., Shapiro, O., & Braunstein, D. (2004, October). Resolution enhancement of X-ray CT by spatial and temporal MLEM deconvolution correction. In IEEE Symposium Conference Record Nuclear Science 2004. (Vol. 5, pp. 2765-2768). IEEE.

ICNST 2024 International Conference on Nuclear Science and Technology
6- 8 MAY 2024 | Isfahan, Iran

Rn monitoring in irradiation chamber using spark discharge assisted laser induced breakdown spectroscopy (SD-LIBS) (Paper ID : 1629)

Saeidi-babi R.[1,2], Shirafkan L.[1], Ahmadinouri F.[1], Norouzian D[1]., Khoshnevisan R.[1], Afarideh H.[1], Parvin P.[1]*

[1]*Department of physics and energy engineering, Amirkabir university of technology, Tehran, Iran*

[2]*Faculty of sciences and modern technologies, Graduate University of advanced technology, Kerman, Iran*

Abstract

Spark discharge assisted laser induced breakdown spectroscopy (SD-LIBS) has been investigated in both synthetic air and an environment containing radon trace mixed with air (Rn+air). SD-LIBS is realized by focusing the laser shots (10-100 *mJ/pulse*) at 1046 *nm* on the Pd target. The latter is a noble metal catalyst used to enhance the plasma emission. Palladium serves as the metal target in the Q-switched Nd: YAG laser-induced plasma. Regarding the synthetic air, the emission lines attributed to the metal species, N and O components exhibit significant enhancements. Subsequently various characteristic emissions stemmed from oxygen, nitrogen, and Pd species are observed within the controlled chamber. The notable reduction in the characteristic lines is consistent with the radon decay. Moreover, the plasma temperature is estimated through Boltzmann plot analysis, whereas the electron density is determined based on the Stark broadening. It is shown that plasma temperature linearly reduces against Rn specific activity.

Keywords: Rn monitoring, Spark discharge, Laser induced breakdown spectroscopy.

INTRODUCTION

The detection of noble gases in the environment faces several difficulties mainly due to their chemical or biological inertness. Most of the noble gases are not regarded as the pollutants while Rn is an exception. Radon is a colorless, odorless, tasteless, radioactive noble gas with most abundant isotope ^{222}Rn (half-life of 3.8 days). The environmental radon concentration is a function of time and climate conditions. Radon concentrations were found to vary from 0.1 Bq/m^3 above oceans or in Antarctica to 1 MBq/m^3 in unventilated uranium mines. The radon detection attracts significant attention because it is a naturally radioactive gas from uranium or thorium decay chain used as an indicator in mine explorations and earthquake predictions. It is well understood that the majority of radon gas from various cascade radioactive decays are trapped in the underground reservoirs, voids, and pits. Radon diffuses to the atmospheres via macro cracks especially after seismic events. It may be subsequently trapped inside the tunnels and underground channels at shallow depths. If inhaled by human, the hazardous radiation affects

the lung. In many countries, radon is the second cause of lung cancer after smoking. The proportion of the cancers linked to radon is estimated to be up to 14%, and varies due to local concentrations and the method of calculation. Since no safe level of exposure is established, even low concentrations of radon are risky for the cancer accurance. Furthermore, the radon daughters are solid and can stick to the air dust particles. If contaminated dust is inhaled, these particles can adhere to the airways of the lung and elevating the health risks[1,2].

The nuclear techniques for detection and measurement of Rn in air can be subdivided into active/passive methods. The former requires electric power and vacuum pump to collect the sample whereas the latter does not require complicated equipment. Nuclear track detectors are taken into account as the passive techniques vastly used for the diversity of applications such as alpha and neutron dosimetry, measurement of ultraviolet solar radiation (UVSR), and recently for the beam profile recording of UV excimer laser. The polymeric-solid state nuclear track detectors (SSNTDs) are also widely exploited for the radon measurements. Among the versatile SSNTDs, Lexan and CR-39 are well known alpha dosimeters. Those determine the radon concentrations by counting the developed latent tracks from the incident alpha particles. It is essential to obtain the track density, the exposure time and the calibration factor that converts the track density the radon concentration. Although the advantages include low cost and insensitivity to humidity and temperature as well as the background beta/gamma radiations, this technique suffers from sluggish collection time, taking several weeks of exposure and few days for developing and track counting[1,2].

SD-LIBS technique has found widespread applications for the elemental identification[3,4]. Unlike the other spectroscopic methods, it requires no preparation and a small amount of material is sufficient for sampling and analysis. In situ remote sensing via optical fiber is carried out allowing the measurements in hostile environments. Analytical findings of LIBS on solids are frequently reported similar to investigations on liquids and gaseous samples. Unambiguous identifications of gases are restricted to the monatomic species such as noble gases used as buffer gas in LIBS investigations. Among them, argon is a very popular buffer gas in laser ablation whose effect has been studied, as well as neon and helium. The detection of trace concentrations of helium and argon in the control chamber assisted with Q-switched Nd:YAG lasers has been previously reported.

We acknowledge there are a number of current articles investigating the potential of LIBS method on

various radioactive targets, but to our knowledge there is no report of study on spark discharge assisted laser induced plasma (SD-LIBS) in (Rn+air) environment using Pd catalyst. Here, the effects of heavy Rn species on the metal (and air) characteristic emission spectra were investigated. This work has focused on the enhancement of metal target and air characteristic lines rather than that of radon, which at its natural trace levels are not detectable by LIBS, where the (Rn+air) undergoes a smaller breakdown voltage against that of air.

EXPERIMENTAL

The experimental setup consists of an infrared coherent source, conducting and focusing optics, detector,

spectrometer, a processor, a pressure gauge and vacuum and gas dosing system, all shown in Fig. 1(a). A Q-switched Nd:YAG laser, 100 *mJ/pulse*, 10 *ns* duration, 5 *Hz* pulse repetition rate, has been exploited as the coherent source with the fundamental wavelength of 1064 *nm*, to generate the micro-plasma on the metal target inside the control chamber. A Balzer vacuum valve was connected to the chamber in order to maintain high vacuum within the chamber and block the atmospheric pressure. The vacuum and gas-dosing system consists of a Leybold D30A high vacuum pump (10^{-3} *mbar*, 10 m^3/hr) and a digital manometer (0.1 *mbar* precision). A BK7 lens (f = 150 *mm*) is situated in front of the beam in order to enhance the power density at the focal area on the target surface. The plasma light emission was collected by an optical fiber bundle. The fiber output was coupled to the entrance slit of a compact wide-range spectrometer 200–1100 *nm*, model Avantes, the AvaSpec-2048 fiber optic spectrometer, with 1.1 *ms* integration time, 0.4 *nm* resolution, and 2 μs delay time. A home-made six-outlet cross type irradiation chamber was constructed of stainless steel and three BK7 windows were installed; one for traversing the IR laser beam into the chamber, and a pair for viewing the plasma plume. A MgF_2 window was fixed on top for the collection of the plasma emissions, particularly in the UV–visible spectral range. One outlet was exploited to manipulate the orientation of the target holder, whereas another one was allocated for gas dosing.

The radon source consists of the synthetic dry radium in soil inside a closed container while a ventilator was installed to discharge radon in the safe atmosphere as seen in Fig. 1(b). In order to fill the control chamber with radon, it was first fully evacuated to 10^{-3} *mbar* using a rotary vacuum pump, then the air

and the Rn trace was allowed to flow into the chamber at atmospheric pressure. The Pd target was inserted inside the chamber and examined separately. Using metal assisted SD-LIBS, the laser energy required for the breakdown is significantly reduced due to higher electron density and electron mobility of metallic targets. Fig. 1(c) demonstrates the instantaneous optical and electrical signals, temporal voltage, and current waveforms during a typical SD-LIBS experiment.

To prepare the various radon concentrations, the (Rn+air) medium was partly discharged from the control chamber. According to Rn dilution method at constant pressure, the gas residual was compensated with the premixed synthetic air, maintaining the atmospheric pressure. Utilizing the ideal gas approximation, the corresponding concentration is determined from the proportion of the pressure after/before evacuation, multiplied by the initial concentration.

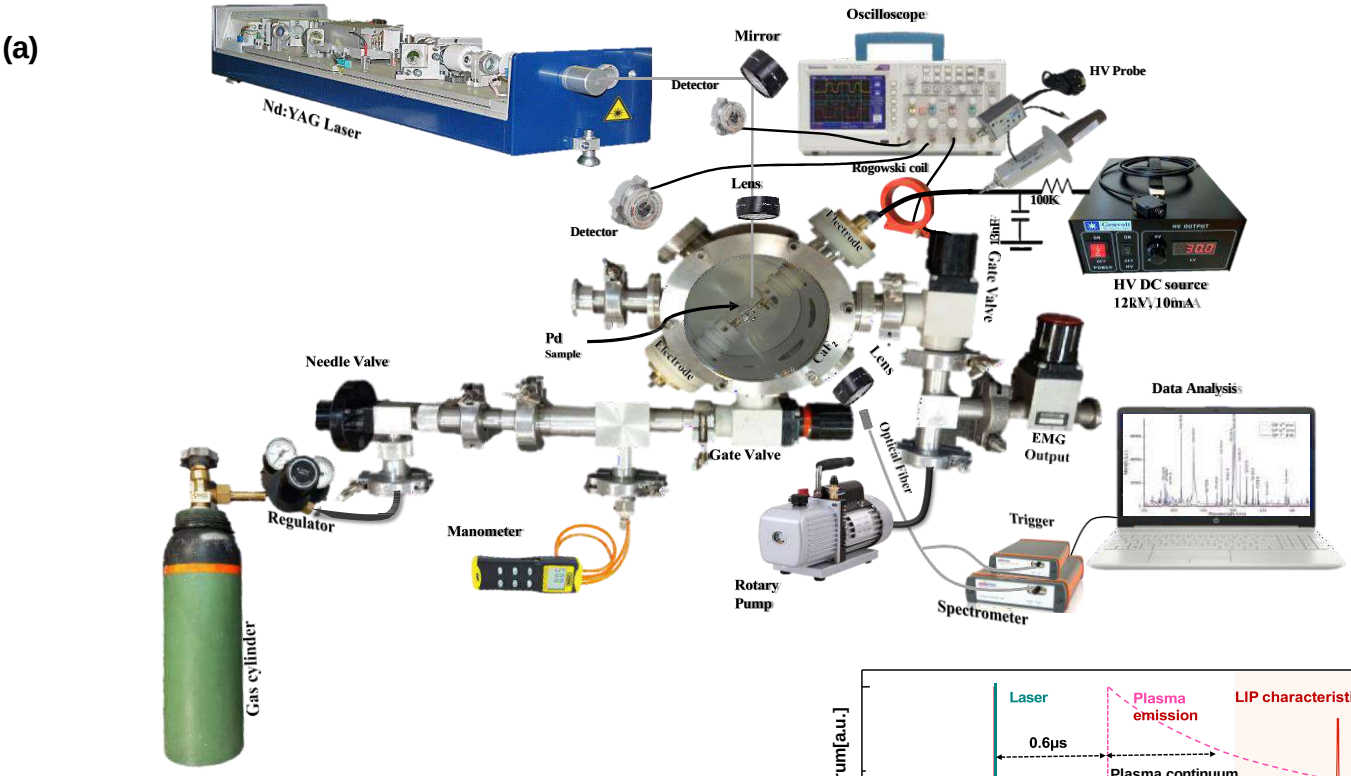

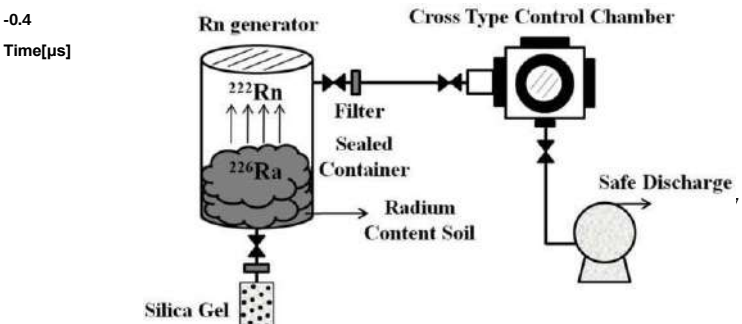

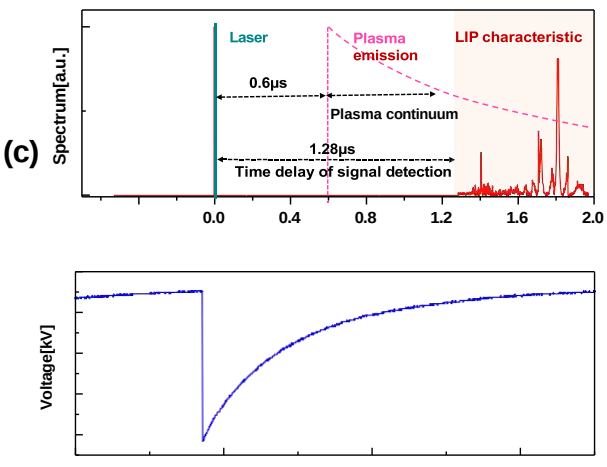

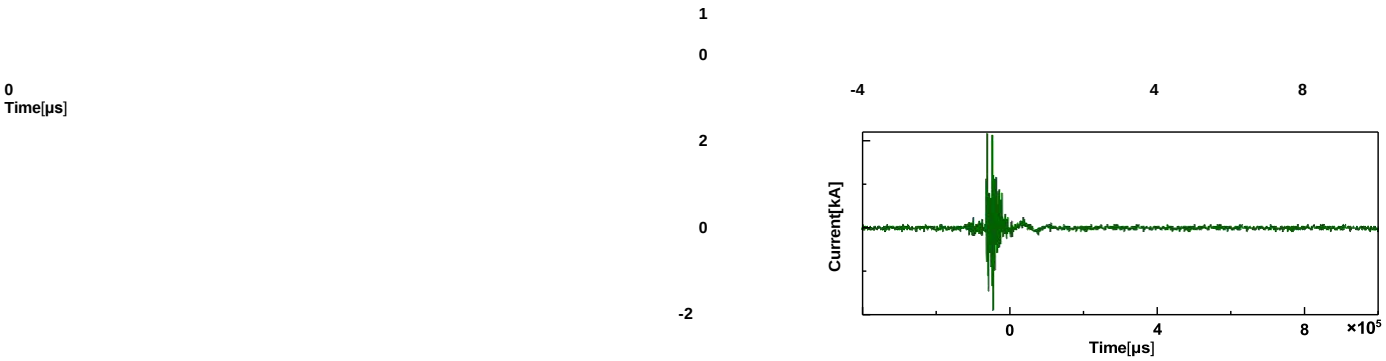

Fig. 1. (a) SD-LIBS arrangement for radon identification within a control chamber, and(b) Rn extraction and trapping process in the controlled chamber using Rn generator. (c) Instantaneous optical and electrical signals, temporal voltage, and current waveforms during a typical SD-LIBS experiment.

RESULTS AND DISCUSSION

Emission spectra

In this case, the required energy for the formation of each ion pair is ~35.5 *eV*. The alpha particles due to Rn decay easily supply adequate energy for the generation of many electron-ion pairs along their trajectory. The number of the ion pairs is determined based on the production rate of emitted alpha particles. Therefore, typically more than 4000 electrons are available per cm^3.sec in air due to 27 $kBqm^{-3}$ Rn trace in the air.

We note that this initial excess electron density from alpha radiation rises several orders of magnitude larger in the controlled atmosphere (Rn+air) compared to that in the synthetic air. This is the major difference for enhancing the inelastic collisions due to electron impact excitations to populate the transitions leading to the enhancement of characteristic emissions. This further population of the excited states leads to stronger characteristic lines when compared to plasma emissions taken in air particularly during SD-LIBS.

Radon with 5.48 *MeV* alpha energy generates a great number of electron-ion pairs within the control volume. This increases the initial electrons to facilitate the plasma generation. The laser induced plasma emission is predominantly based on the thermal electron impact excitations of atoms while the photo-excitation process causes a minor contribution.

SD-LIBS

The preparation of various radon concentrations is performed in several stages. Part of the (Rn+air) was discharged from the control chamber using a vacuum pump, and the remaining gas was supplemented with a premixed synthetic air until atmospheric pressure was regained. According to the ideal gas approximation, the new concentration is determined based on the pressure ratio after and before evacuation, multiplied by the initial concentration.

This re-emphasizes the role of Rn trace in plasma as a magnifying agent of the characteristic emissions. There is a large gap to reach the synthetic air by reducing the Rn trace, however here Rn concentration as low as 0.5 kBq/m^3 was easily achieved. The sensitivity is defined as the ratio of the signal amplitude over the Rn concentration. It depends on laser pulse to pulse stability, the sensitivity of detector array as well as the measurement accuracy of the pressure gauge during the preparation process of Rn trace in synthetic air using the barometric methods.

A better precision as low as 0.1 kBq/m^3 may be achievable by means of more stable laser and high sensitive detector arrays. The barometric method of preparation process of Rn trace in synthetic air may be improved using the pressure gauge with 0.1 *mbar* accuracy rather than 1 *mbar* in the current measurements.

Furthermore, Fig. 2(a) illustrate the emission spectra at atmospheric pressure for two cases of SD and SD-LIBS. Fig. 2(b) depicts the plasma temperature versus Rn activity in case of Pd target. The significant difference between (Rn+air) and synthetic air medium is in accordance with the previous measurements. In fact, the plasma temperature in (Rn+air) linearly decreases with the Rn activity. This is consistent with our previous results. Fig. 2 (c) illustrates the characteristic emission spectra at 510.554 and 521.820 *nm* in various sub-atmospheric pressures in the case (Rn+air).

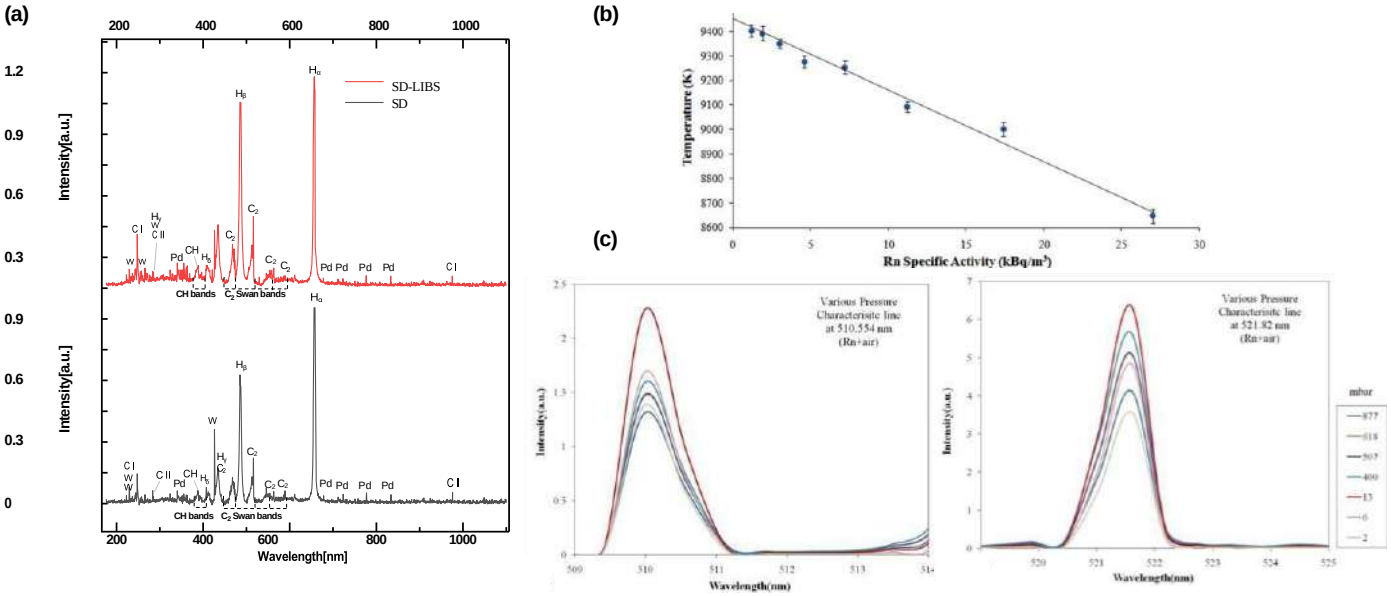

Fig. 2. (a) SD-LIBS and SD spectra in the attendance of Pd catalyst, (b) plasma temperature versus various Rn activities in atmospheric air, and (c) typical emission intensity at 510.554 and 521.82 nm in the various sub-atmospheric pressures in case of (Rn+air).

SSNTD

The radon activity (concentration) is determined via the Lexan detectors through the following expression:

$$C = \frac{D}{kt} \qquad (1)$$

where, k, C, D and t denote the calibration factor (*track.cm*$^{-2}$ per *Bq.m*$^{-3}$*.d*), standard radon concentration (*Bq.m*$^{-3}$), track density (*tracks.cm*$^{-2}$), and exposure time (d, day) respectively. Radon concentrations in air are seldom given in the ppm unit or lower. However, it can be calculated with those precisions using some assumption. In case of ^{222}Rn in air, a concentration of $27m^{-3}$ is carefully determined to be 0.5 *ppq* (parts per quadrillion, 10^{-15}). Evidently, no current optical spectrometer is able to detect such a low dose of radon trace in air; otherwise the inexpensive track detector could help by collecting the latent tracks of alpha particles on its surface over a long exposure time.

A number of Lexan pieces were utilized to detect the alpha emissions. At first, the background was counted and the net number of tracks was obtained after the alpha exposure. Fig. 3 illustrates the developed tracks on the Lexan surface due to 27 *kBq/m*^{3} activity. The track densities are proportional to the Rn activity. By counting the corresponding tracks in several optical desired fields and taking the average, the mean track density is determined. One of the drawbacks of this detector is the sensitivity variation which may be different from sheet to sheet in the same batch supplied by the manufacturer. To remedy this, the calibration curve is obtained using various activities accompanying the good statistics.

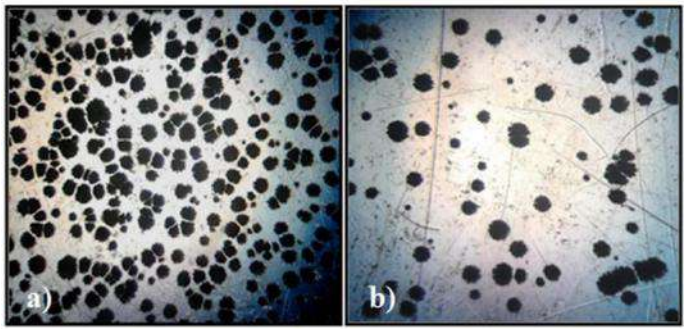

Fig. 3. Alpha tracks in Lexan due to Rn trace in air. a) 27 kBq.m^{-3} of Rn in the chamber at 1 atm., b) Background tracks (due to cosmic ray and other radionuclide traces).

Fig. 4 displays the calibration curve (track density versus the product of specific activity multiplied by exposure time) of Lexan whose calibration factor is obtained using Eq. (1). The calibration factor depends on the active volume of alpha monitoring device, the type of track detector, and the etching conditions. In practice, the alpha track density "D" was found to be a linear function of the products of "C.t".

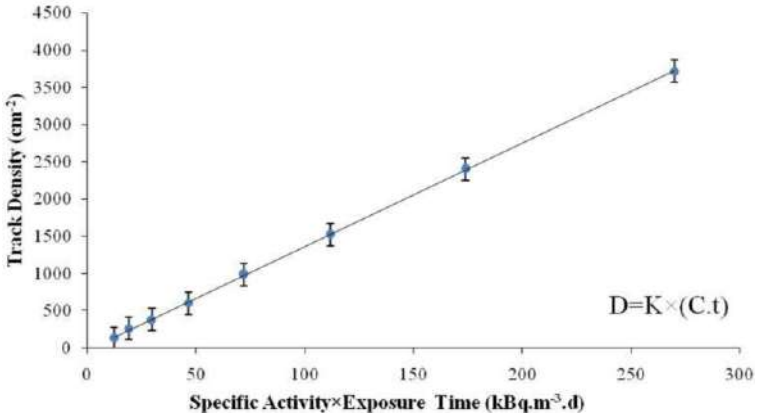

Fig. 4. Alpha track density "D" in terms of "C.t".

CONCLUSIONS

Several characteristic emission lines from the metal Pd target were investigated in trace presence of radon gas in the atmospheric air, using Q-SW Nd:YAG laser induced plasma inside a control chamber assisted by spark discharge. The emission lines of metal species are noticeably enhanced in (Rn+air), where smaller breakdown voltage is required to ignite the laser induced plasma relative to those in the synthetic air alone. Similar spectra were also taken in various sub-atmospheric environments in order to determine the optimum pressure for enhancement. Solid-state nuclear track detectors were also employed to count the tracks due to alpha particles for the activity assessment. The mean concentration of radon in atmosphere with specific activity of kBq/m^3 is too low to detect by LIBS however it can be discerned by SD-LIBS. In this work, we have shown that the characteristic emissions of metal species and air components increase in (Rn+air) compared to that in the atmospheric air. Although, the exact mechanisms are not well understood, it may arise from the fact that small amount of heavy species alter the plasma properties. In general, the increase of signal to noise ratio (SNR) originates from the plasma heating, which in turn leads to higher plasma temperatures.

Conversely, this work emphasizes that the rise of

signal amplitude is correlated with the radon activity in air leading to the corresponding increase of initial electrons. In fact, radioactive decays give out alpha particles with energy of 5.48 *MeV*, which create a noticeable number of electron-ion pairs in the control chamber.

The ionization of air by energetic alpha particles enhances the electron density in the chamber before plasma ignition. The plasma temperature and electron density of the (Rn+air) are estimated from the Boltzmann plot and Stark broadening respectively, which were given to be lower than those in pure air. Because of relatively high initial density of free electrons, the signal enhancement is therefore attributed to increase of the number of excited species in plasma and the volume of plasma itself, leading to subsequent decrease in electron density and temperature.

References

[1]M. M. Hashemi, P. Parvin, A. Moosakhani, S. Z. Mortazavi, A. Majdabadi, A. Reyhani, and S. Abachi. (2014).Characteristic emission enhancement in the atmosphere with Rn trace using metal assisted LIBS, AIP Adv. 4(6): 0–17.

[2]A. Moosakhani, P. Parvin, A. Majdabadi, and M. M. Hashemi. (2016). Radon decay monitoring in air using characteristic emission of species in metal-assisted LIBS, Radiat. Meas. 92: 39–48.

[3] F. Ahmadinouri and P. Parvin. (2024). Methane conversion using spark discharge-assisted laser-induced plasma (SD-LIP) with Pd catalyst: Non-oxidative hydrogen production, Chem. Eng. J. 149645.

[4]M. Habibpour, P. Parvin, and R. Amrollahi. (2021). Gold fineness measurement using single-shot spark assisted laser-induced breakdown spectroscopy. Appl. Opt. 60(5): 1099.

DIAL-Phoswich hybrid lidar for remote sensing of radioactive plume (Paper ID : 1630)

Norouzian D[1]., Shirafkan L.[1], Saeidi-babi R.[1,2], Ahmadinouri F.[1], Khoshnevisan R.[1], Afarideh H.[1], Parvin P.[1]*

[1]*Department of physics and energy engineering, Amirkabir university of technology, Tehran, Iran*
[2]*Faculty of sciences and modern technologies, Graduate University of advanced technology, Kerman, Iran*

Abstract

Radionuclide pollutants, released into the atmosphere are hazardous for human health. Thus, those must be identified and well protected. For this purpose, the activity and the radiation dose on the local area should be assessed carefully. Here, an efficient remote sensing system is designed and modeled for remote monitoring of the radioactive effluent from the nuclear sites into the atmosphere. It is based on the combination of DIAL-phoswich array system, using the phoswich detector to identify the characteristic hard X-ray emissions of the transuranium radionuclides to determine the radionuclides of interest. Then a differential absorption lidar (DIAL) coupled with a tunable UV/Vis laser, measures the plume location and the concentration/activity of the radionuclides. An interactive library is provided to interconnect the atomic/nuclear features of radionuclides accordingly. Here, the ability of the hybrid system for the prompt identification/quantification of the radiative effluents are verified, regarding the species energy of X-ray emission alongside the absorption cross-section as well as the corresponding spectral absorbance of trace elements. Subsequently, the atomic/nuclear characteristics of radionuclides of interest released from a typical reactor or precessing plant are obtained and the tunable laser is tuned for proper performance of DIAL.

Keywords: Differential Absorption Lidar (DIAL), Phoswich Detector, UltraViolate/Visible Tunable Laser

INTRODUCTION

The Chernobyl core meltdown accident showed that the scale of impact can be very large and the risk of remote nuclear sites should also be of considerable concern for the area. Thus, it is important to obtain the geographic distribution of the nuclear risk based on the external dose. Nuclear power plants usually release various gaseous and liquid effluents as well as highly radioactive mixture of fission products components in structural and cladding materials due to neutron activation as well as small amounts of long-lived transuranium elements (Z > 92) during their normal operation. The radionuclides discharge to atmosphere is evaluated to be ~1 *TBq/GW*. In both pressurized-water

reactors (PWR) and boiling-water reactors (BWR), the condenser steam-jet air ejectors and the turbine gland-seal system are two important sources that release gaseous radioactive products to the atmosphere through the stack. The individual dose is determined to be 0.2 *μSv/yr*, which is less than 0.1% of the background level radiation. They may emanate considerably more radioactivity higher than background level during the course of an accident, where especially radioactive gases are first released into the containment building and may leak to the atmosphere. It is well known that particulates in airborne dust which contain ^{238}U and its daughters and sometimes ^{232}Th and its daughters are hazardous to human health. Release from mining and milling facilities as well as effluents from fuel fabrication sites are estimated to be ~0.01–0.1 *ppb*. Comparably, the abundance of uranium in the earth crust is ~3–4 *ppm*, while ~1 *ppb* can be found in the human body[1].

The radioactivity from the ground is strongly varying, dependent on the living places. The radioactivity originates from long lived isotopes with lifetime of order 109 years, particularly for ^{232}Th, ^{235}U and ^{238}U. Predominant gaseous effluent from active uranium mine is ^{222}Rn in the ventilation from underground mine or released into the pits from surface mine. Release rate of radon per unit mass of ore were estimated to be ~1 *GBq/ton* in underground mine and about 0.1 *GBq/ton* from surface mine while natural radon density is reported to be of ~7 Bq/m^3 (107 *ppm*). In general, the average human being from those natural sources receives a dose equivalent of approximately 2 mSv/yr. Furthermore, cosmic rays act on nuclei in the atmosphere to produce other radionuclides, including ^{3}H, ^{7}Be, ^{10}Be, ^{14}C, ^{22}Na, ^{32}P, ^{39}Cl, and ^{33}P. The cosmic radiation from the space, including the radiation from the sun, consists mainly the highly energetic protons, alpha particles and to some extent of heavier charge particles to give a dose of about 10 *μSv/y* on the ground[2].

Here, the DIAL–phoswich hybrid system is introduced, which is potentially an advantageous technique to investigate the dynamic effluent parameters of a radioactive plume such as uranium. It consists of both passive nuclear and active atomic detection units. It is based on a phoswich detector array to trace species due to their characteristic hard X- and γ-ray emissions accompanying a differential absorption lidar coupled with a tunable UV/Vis laser. It is mainly useful for rapid identification of the unknown radioactive elements within the plume as well as the corresponding concentration, the exact location and external dose rate. We have shown that the application of the combined technique noticeably enhances the system efficiency. Indeed, the hybrid system is proposed here in order to act as a novel technique for the remote sensing of the radioactive plume, as to an efficient instrument for element tracing, uranium mine exploration and the health physics applications.

Consequently, the spacecraft equipped with the hybrid system enables the scientists to explore the radioactive sources in the solar system, such that a portable hybrid instrument mounted on a rover makes Mars mission more attractive.

RESEARCH THEORIES

Apparatus

The hybrid system includes a transmitter, a receiver, phoswich scintillators coupled with photomultiplier tubes (PMTs) array, pulse shape analyzer (PSA), anticoincidence unit, multichannel analyzer (MCA) and the data processor equipped with interactive software for real time control and data acquisition with the access to atomic/nuclear data libraries. The transmitter employs the pulsed tunable UV/Vis laser and the receiver consists of a Cassegrain telescope, a Lyot tunable birefringent filter or a Fabry-Perot interference filter and a PMT detector. The latter is generally used as a low noise and sensitive detector for UV and visible spectral region. It offers fast response and high gain as well as good quantum efficiency.

Phoswich detector array (PDA)

A phoswich detector is a combination of two dissimilar scintillators optically coupled to a single PMT, employing pulse shape analyzer (PSA) to suppress background in the counting X-ray. It consists of a typical thin Na I(Tl) and a thick Cs I(Tl) within different decay times, 0.25 μs and 1 μs, respectively, so that, the shape of the output pulse from the PMT is dependent on the relative contribution of scintillation light from the two scintillators. The Na I(Tl) and Cs I(Tl) crystals are designed to be ~3 and ~20 mm thick. Lightly penetrating radiations in spectral range ~30–300 keV, are stopped fully in the first scintillator, but more penetrating MeV photons may generate light in the thick one. PSA and pulse shape discriminator (PSD) unites identify the signals due to each scintillator. Those distinguish that the energy deposition in which scintillator occurs. The events generating light in both scintillators are denied to suppress the noise for X-ray counting.

EXPERIMENTAL

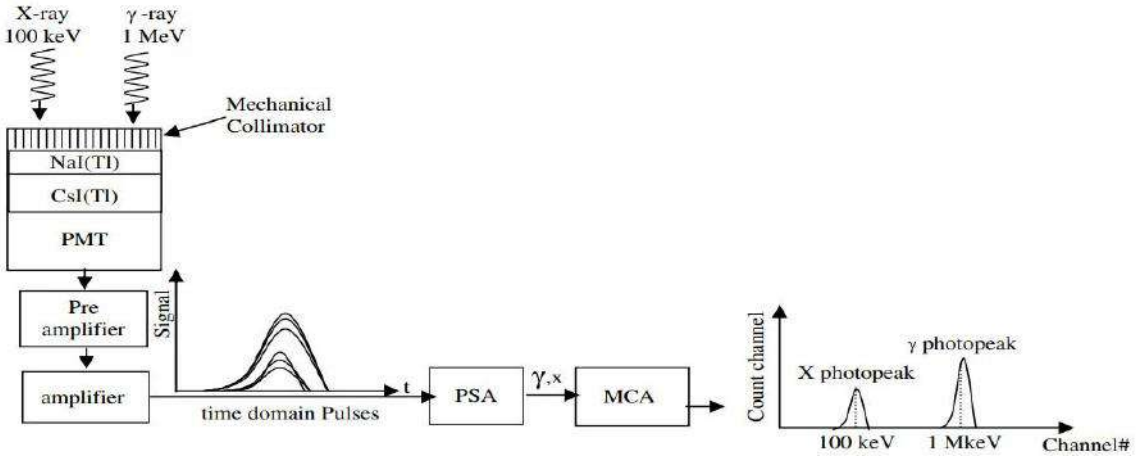

Fig. 1. Performance of phoswich dual energy analyzer.

Fig. 1 shows the performance of a typical PDA, including about 80 standard phoswich detectors each one having ~100 cm^2 area subtended together to constitute an array of 1 m diameter with the same area of telescope in DIAL unit. PSA unit discriminates between Na I events (left) and Cs I events (right) using an MCA. Events resulting in scintillations from both volumes can be recognized by their pulse shape and can thus be rejected for X-ray detection, whereas those scintillate simply in Cs I are accepted to detect γ photons. The electronics using PSA is capable of discriminating events in 30–300 keV X-ray energies and up to several MeV gamma photons. It is characterized by a couple of peaks, one due to Na I(Tl) and the other due to Cs I(Tl) events. The scale in abscissa is correlated with the decay time of the scintillation pulses. The selection of X-ray events is performed through PSD unit using the choice of lower and upper thresholds in the electronic unit.

Differential absorption lidar (DIAL)

High sensitivity with good spatial resolution for long-range dynamic monitoring of the plume constituents can be achieved by the combination of differential absorption and scattering. DIAL includes high degree of sensitivity per probe energy and the capability of wavelength scanning over a wide variety of molecules and atoms having absorption characteristic in the spectral range as well as the quantitative evaluation of desired species. A typical DIAL system often sends a pair of pulsed laser wavelengths into the atmosphere. Those are close to each other with a large absorption coefficient difference, one at the tuned line, λ_{on}, where the species under investigation absorb and the other at a nonabsorbing detuned line, λ_{off}. A couple of such wavelengths, rather than a single one, are needed

in order to strongly reduce the effect of the extinction in the atmosphere, mostly due to the scattering, and to correct the instrument calibration constant. When laser wavelength is much greater than the scatter size which is valid for the gaseous plumes, the Rayleigh scattering occurs with the backscatter cross-section proportional to λ^{-4}. Conversely, for water drops, clusters, dust, volcanic ashes, smokes or the aerosols under the condition that the scatter size is being greater than laser wavelength, the Mie scattering becomes dominant. The corresponding cross-section is more complex than Rayleigh scattering with wavelength dependence proportional to λ^{-x} where 0.4 < x < 0.5. The lidar equation is written as below[1]:

$$\boldsymbol{P_s(\lambda, R) = P_0 \frac{A_2}{R^2} \xi(\lambda)\beta(\lambda, R)\xi(R) \left(\frac{c\tau_1}{2}\right) \exp\left(-2\int_0^R \alpha(\lambda, R)dR\right)} \quad (1)$$

where P_s is instantaneous power received by the detector from the range R. P_0, τ_1, β, α, and A are the transmitted power, pulse duration, volume backscattering coefficient, extinction coefficient and telescope area, respectively. $\xi(\lambda)$ and $\xi(R)$ are defined to be the spectral gain coefficient of the receiver and the geometrical factor of the telescope, respectively. Usually, β and α consist of contribution from both air molecules and aerosols. By dividing the received power at λ_{on} over that of λ_{off} based on Eq. (2), the species concentration, $N(R)$, can be simplified as[1]:

$$\boldsymbol{N(R) \approx \frac{1}{2\Delta\sigma}\frac{d}{dR}\left(\ln\frac{P_s(\lambda_{off},R)}{P_s(\lambda_{on},R)}\right)} \quad (2)$$

This equation is known as the DIAL equation. In the atomic remote sensing of uranium element, the absorptive and nonabsorptive wavelength are tuned at λ_{on}= 351.46107 *nm* and $\lambda_{off} = 352.26107$ *nm*. Thus, we can neglect the noise caused by ozone compared to the uranium concentration above stacks of the nuclear site which is reported to be ~ 0.01–0.1 *ppb*. In addition, the probe lines λ_{on} and λ_{off} are close together such that their difference is slightly greater that Doppler-limited linewidth ($\lambda_{off} = \lambda_{on} \pm 2\delta\lambda_D$), where $\delta\lambda_D \approx 0.75$ *pm*. By definition, λ_{off} lies in the tail of absorption spectrum and λ_{on} represents the peak.

Broadband tunable UV laser

In atomic absorption remote sensing, a laser should be reliable and possesses characteristics such as wide wavelength tuning range from the visible to the deep UV, narrow spectral linewidth, high repetition rate, compactness, and a relatively low price. Various coherent sources, such as dye, diode and Ti:Al_2O_3 lasers as well as the optical parametric oscillator (OPO) have been employed. Among those lasers, OPO does not fit wide application in high resolution atomic spectroscopy mostly due to the lack of frequency and linewidth stability in order of atomic linewidth ~0.01 cm^{-1}. In addition, the excimer and the higher harmonic Nd:YAG lasers are taken into account as the alternatives to monitor some of radionuclides. For long-range remote sensing, the multistage amplifiers of dye or Ti:Al_2O_3 lasers can be exploited to scale up the pulse energy of the laser probe.

Broadband dye and Ti:Al_2O_3 gain media are often desirable to tune a specific wavelength over the bandwidth without changing the cavity mirrors. The dye laser pumped by SHG of Nd:YAG laser offers a wide tunability mainly by changing the dye solutions such as Coumarin and Rhodamine with the spectral emission at 400– 500 *nm* and 570–610 *nm*, respectively. The higher harmonic of those lasers covers the spectral range of 200–400 *nm*. The Ti:Al_2O_3 laser, pumped by a frequency stable SHG Nd:YAG laser at 532 *nm*, is mostly used as a tunable NIR laser with very broad emission bandwidth 660–1180 *nm* to generate *ns* short pulses. The higher harmonic generations of those lasers lie within the attractive UV spectrum of the atomic absorption. For instance, the corresponding UV absorption lines (λ_{on}) of 238U are 351.46107, 356.18038, and 358.48774 *nm*, which lie on the SHG spectrum of Ti:Al_2O_3 laser. Similarly, the remote sensing of 230Th is performed at 371.94347 *nm* using SHG of that laser and 234Pa from uranium chain may be traced at the corresponding absorptive lines of 398.223. XeF laser at 351 *nm* is also the other choice for uranium remote sensing. During emergency conditions of an operating reactor, the leakage of Samarium drastically increases due to LOCA. The strong samarium absorption line at 463.2320 *nm* can be matched well with the fundamental harmonic of coumarin laser as well.

It is understood that the narrow linewidth of the absorption spectra of atoms is Doppler-limited which is about 0.01 cm^{-1}or about 1 *pm* at 300 *nm* with a corresponding isotope shift is in order of 0.1 cm^{-1}. In addition, the hyperfine structure due to the presence of nuclear spin is much smaller than the splitting caused by electron spin. Various arrangements, such as Hansch array, DoubleQuartet prism method and Littman setup are available to perform tuning the emission of tunable lasers. Littman setup is chosen mainly because of easy alignment to achieve single mode with spectral width as narrow as 0.01

cm^{-1}. For the additional linewidth narrowing, intracavity Fabry-Perot etalons or birefringent crystal waveplates can be utilized. The diffraction grating used in Littman arrangement operates as a beam expander and a dispersion element simultaneously, so that the dispersion power becomes two times higher than that of the Littrow mount.

RESULTS AND DISCUSSION

Radioactive pollutants which are released from the waste or the probable explosion of nuclear site during the accident are known to be extremely hazardous for human health, therefore those must be quickly identified and well protected. Here, a new method is investigated for remote sensing of an unknown radioactive plume having gamma or X emitter radionuclides including uranium chain or transuranium elements to help ensure that nuclear power plants operate safely to be non-detrimental to human and environmental well-being. Hybrid system can be used for continuous, atmospheric mapping and systematic monitoring of radioactive plume constituents based on the optical remote sensing DIAL and phoswich detector arrangements.

In a reactor accident, the radionuclides such as fission products are first released into the containment building and subsequently may leak to the atmosphere. The activity of the resulting effluent depends on the rate at which this leakage occurs. In addition to the released gaseous products such as I, Xe, Kr and, Sm which easily escape the nuclear power plant containment, the other radionuclides, such as U and Pu can also be released, because of the fuel evaporation due to high temperature.

In general, interaction of laser with plume released above the stack at reactor normal operation could be Rayleigh scattering. However, the concentration of the effluents increases to become noticeable above background level when an accident such as LOCA occurs. Power excursion is categorized as another major accident in the reactors, when steam explosion of the pressure vessel leads to the release of heavy plume including various nuclides with a dense cloud to such an extent that Mie scattering becomes dominant. The tuned laser probe can be used for the prompt identification and quantification of the accidental radioactive leakage to the atmosphere as well as normally radionuclide release in *ppb* (or less) around the stacks of nuclear power plant or radioisotope labs, reprocessing plant and the conversion facilities.

The interactive performance of the hybrid system is shown in Fig. 2. The arrangement includes two main sections of phoswich detector array and DIAL system which interact with each other through a processor unit to operate simultaneously. Field of view of phoswich array is aligned to the top of the reactor stack to determine the radioactive plume. The processor unit commands to phoswich detector

array to integrate the signal in the definite time interval along plume direction. The process carries out by detecting γ/Xray photopeaks, using nuclear library, then the radionuclide species and their half-life can be determined. If there is more than one radionuclide, those can be identified by searching photopeak energies on MCA. In the stage of *X/γ* detection, using phoswich, the photopeaks of the characteristic hard X-ray of transuranium (30–300 *keV*) elements can be identified, if available within the radioactive plume. For instance, the typical photopeaks of 241Am, 239Pu and 235U denote to be 59.5, 38.7 and 11.5 *keV*, respectively.

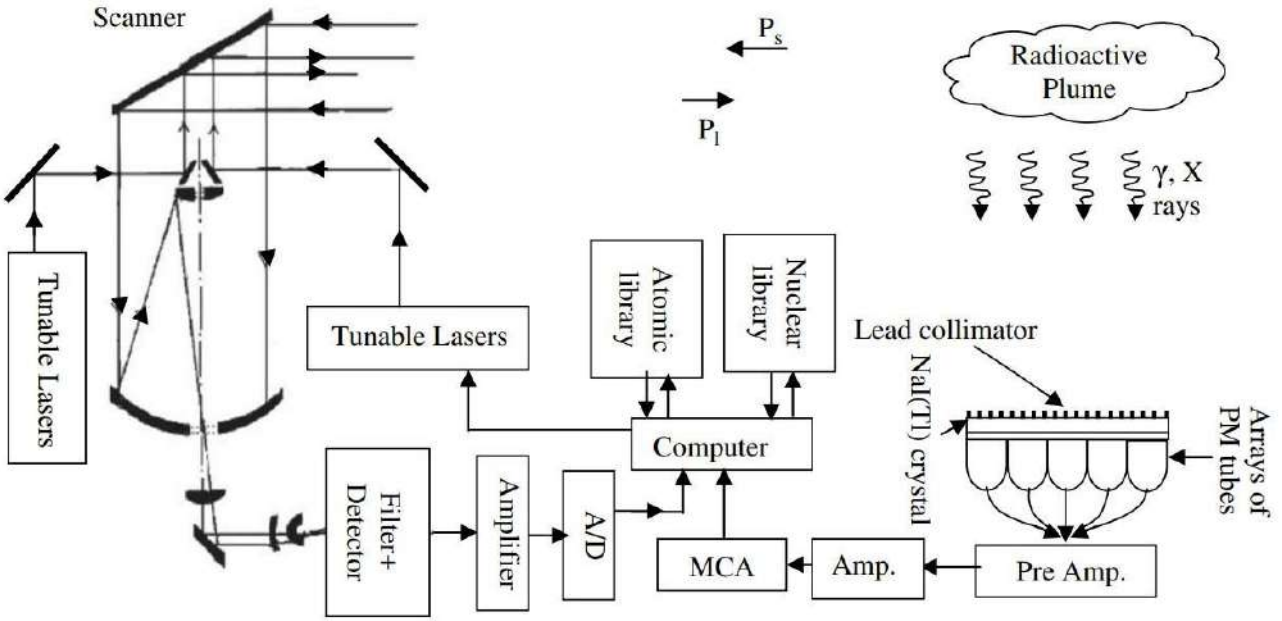

Fig. 2. Performance of phoswich–DIAL hybrid system.

Fig. 3 illustrates DIAL range in the clean atmosphere that is achievable up to several *km* using the oscillator–amplifier array. However, the effective range of interactive hybrid system is limited to the phoswich performance to a few *km*.

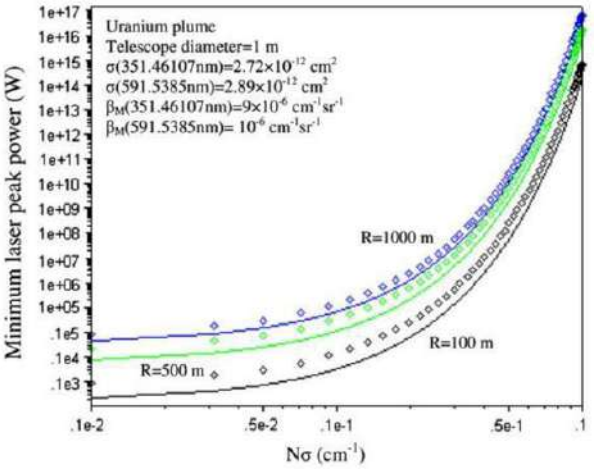

Fig. 3. Minimum laser peak power versus absorption coefficient, Nσ, in order to detect the released uranium into the atmosphere. Solid line and dashed line represent lon ¼ 351.46107 and 591.5385 *nm*, respectively.

CONCLUSIONS

Radioactive pollutants which are released into the atmosphere are known to present a hazard to human health; therefore, they must be identified and well protected. Here, an improved remote sensing system is investigated for monitoring radioactive plumes released into the atmosphere from nuclear sites. It is based on the combination of DIAL technique with a phoswich detector array. The DIAL, using a tunable UV/Vis laser, measures the concentration of the radionuclide and the plume distance, whereas the phoswich detects characteristic hard X/γ ray emissions. Here, we have shown the ability of a hybrid system for the prompt identification and quantification of the effluents containing the uranium radionuclide, using the parameters of uranium such as absorption cross-section, absorption spectrum and density.

In this work, the feasibility of hybrid system to sense a remote uranium plume was investigated, using the uranium absorption spectrum with hyperfine structure, the corresponding absorption cross-section as well as the nominal concentrations above the stack in the normal and accidental conditions. Moreover, the serious incapability of phoswich for pointing and identification of an unknown radioactive plume in the atmosphere, as depicted, has been strongly improved using DIAL–phoswich combination, and the graphical representation. The hybrid system functions as an interactive process including a slow response, time integrated phoswich array and a fast, real time DIAL. A certain phoswich counting, at a chosen integration time, may be due to a high active source with low γ energy emission or oppositely a dilute radioactive plume emitting high energy photons. Moreover, it may be due to a dense plume afar or a weak effluent nearby for the identical X/γ energy emissions.

Alternatively, the hybrid system exhibits a linear correlation between the counts and the concentration of the species. It indicates a unique counting corresponding to a certain activity owning the potential to resolve X/γ energies effectively at longer ranges. Finally, despite phoswich is unable to determine the external dose, however, the hybrid system does.

References

[1] G. Shayeganrad and P. Parvin. (2009). DIAL-phoswich hybrid system for remote sensing of radioactive plumes in order to evaluate external dose rate. Prog. Nucl. Energy **51**(3):420–433.

[2] H. Kariminezhad, P. Parvin, F. Borna, and A. Bavali. (2010). SF6 leak detection of high-voltage installations using TEA-CO2 laser-based DIAL. Opt. Lasers Eng. **48**(4): 491–499.

ICNST 2024
International Conference on Nuclear Science and Technology
6- 8 MAY 2024 | Isfahan, Iran

Identification of uranium ores using spark discharge assisted laser induced breakdown spectroscopy (SD-LIBS) (Paper ID : 1632)

Shirafkan L.[1], Norouzian D[1], Saeidi-babi R.[1,2], Moafi A.[1], Afarideh H.[1], Parvin P.[1]*
[1]*Department of physics and energy engineering, Amirkabir university of technology, Tehran, Iran*
[2]*Faculty of sciences and modern technologies, Graduate University of advanced technology, Kerman, Iran*

Abstract

The natural uranium foils have been examined using laser-induced breakdown spectroscopy (LIBS) and then by means of spark discharge (SD) assisted LIBS in order to analyze the samples of interest. Regarding the strict health physics and safety regulations of radiation protection, the natural uranium specimens are placed in a control chamber and the experiments are carried out. A Q-switched Nd:YAG laser, 100 mJ/shot, 10 ns duration with 1-5 HZ PRR is employed for the target ablation and the subsequent plasma emission carrying out in the controlled irradiation chamber at atmospheric pressure. Afterward, the significant characteristic emission fingerprints of U^{235}/ U^{238} have been revealed in favor of U I at 424.41 nm/ 424.44 nm, respectively. Furthermore, a Geiger detector is coupled with the chamber to measure the number of counts in the course of the laser ablation and the subsequence-induced plasma emission. In fact, the characteristic lines and the corresponding amplitude of plasma emission are employed to assess the plasma parameters in favor of the uranium contents of the ore in the ambient atmosphere. Eventually, we have proposed that the SD-LIBS benefits larger signals against the traditional LIBS in various uranium ores, to emphasize the ability to detect the minimum ppb limit of detection (LOD).

Keywords: Uranium ore, Spark discharge, Laser-induced breakdown spectroscopy.

INTRODUCTION

The development of compact laser-induced breakdown spectroscopy (LIBS) and high-resolution spectrometers enable us to screen nuclear facilities in the context of health physics. The presence of uranium and plutonium as well as the radiological materials can be determined by monitoring the elemental emission spectra using relatively low-resolution spectrometers. In addition, uranium compounds in nuclear fuel processing can be identified by applying chemometric analysis to the laser-induced breakdown (LIB) spectra recorded by the spectrometers[1–3]. For nuclear applications, however, U and Pu isotopes and other elements, require higher resolution spectrometers given the narrow magnitude of isotope shifts for some of these elements. High-resolution spectrometers are preferred for several

reasons but these must be realized at first[4,5].

The hand-held LIBS instrumentation probe combined with a couple of relatively high-resolution spectrometers with typical resolving power of 45000-75000, give us the potential to meet the field-band analysis needs. Here, an evaluation of the SD-LIBS probe combined with a high-resolution spectrometer proposed the rapid detection of uranium isotopes in the ore, and is also capable to use after some processing.

EXPERIMENTAL

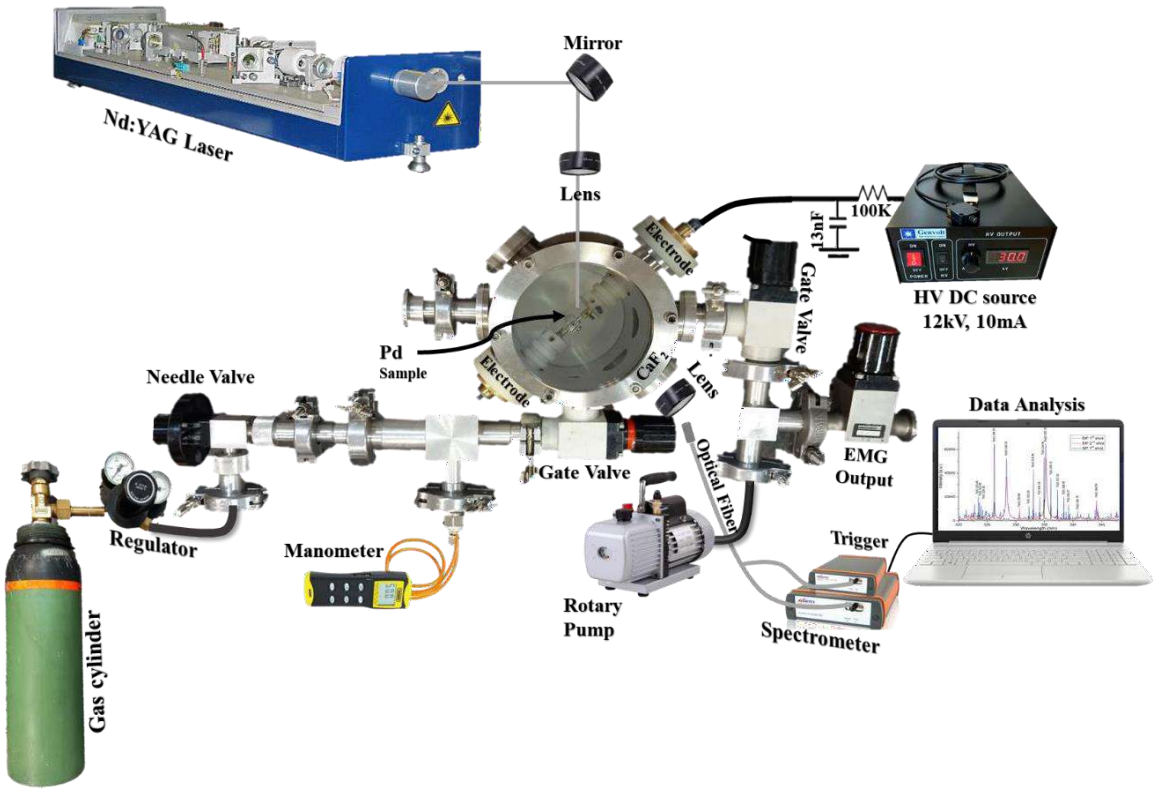

Fig. 1. SD-LIBS arrangement for the detection of $^{235}U/^{238}U$ isotopes using a high resolution. Etchellon spectrometer (40000-70000)

An etchellon spectrometer is employed with an ICCD detection system having a resolution of 6 pm with a 1-10 μs delay time. Note that both high-resolution, Czerny-Turner and etchellon spectrometers are able to resolve the isotope shift of interest. The Czerny-Turner one may achieve up to 40000 resolving power, however, it is better to employ the etchellon spectrometer with 75000 resolving power using large diffraction order. Furthermore, its optimal spectral resolution (6pm) can be easily achieved by means of

the mentioned spectrometer. Samples of different natural isotope enrichments can be prepared by using a mixture of U_3O_8 where the natural abundance of U^{235} is ~0.7%. Note that the homogeneity of the samples suggests to be good using visual inspection. The U_3O_8 samples are placed in an irradiation chamber with a 7.5 mm diameter, ~2mm thick made of quartz window which is sealed using silicon sealant. The strongest reproducible U signals are determined by monitoring the uranium peak intensity from replicate measurements. The detection limits for trace elements Al, Ca, Cr, Cu, Mg, Na, and V in U_3O_8 were determined using standard certified references. Linear calibration curve was prepared and detection limits were determined. The natural uranium foils (0.7% U^{235} and 99.3 U^{238}) are used as the target samples. The U_3O_8 samples are fixed in a stable matrix having a 2 cm diameter disk and 3 mm thick to evaluate uranium isotope detection using LIBS. The samples were prepared in the health physics facility of AEOI and the initial set of test samples are delivered to us to carry out a series of LIBS. The visual coupling of the laser pulse into the sample targets and the strength of the emission signal is proportional with U_3O_8 concentration. The emission signals are useful to monitor the uranium spices as low as ppm level. Fig. 1 illustrates the SD-LIBS arrangement for isotope shift measurement of uranium species.

RESULTS AND DISCUSSION

The etchellon spectrometer is able to discern both isotopes taken from laser-induced plasma emission. The typical laser energy shot of 100 mJ/pulse at 1064 nm of Nd-YAG Q-switched laser is employed to ignite the plasma emission. An etchellon spectrometer coupled with ICCD succeeds in fulfilling the real-time spectroscopy of uranium isotopes. The higher harmonics of the Nd:YAG laser are also examined to verify the findings, however, there is no significant discrepancy between the fundamental laser beam (1064 nm) and SHG at 532 nm for this purpose. The detection limits are computed using the absolute areas of the element emission line by rationing the element line area to the area of a nearby uranium line. The resolution of a couple of Ar I lines from a low-pressure Ar discharge lamp is also inspected.

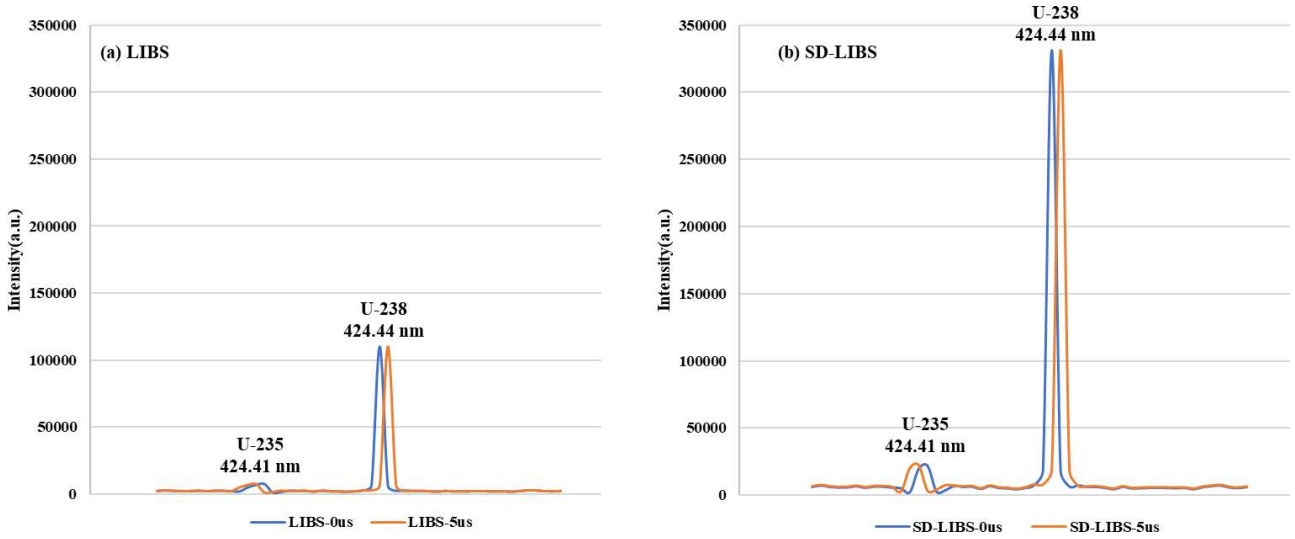

Fig. 2. U^{235}/ U^{238} emission spectra and corresponding isotope shift using (a) traditional LIBS and (b) SD-LIBS. Note that SD-LIBS enhances the spectral emission of the characteristic line up to 3 folds due to the more energetic plasma during spark discharge to elevate the plasma emissions consequently.

The comparison of the U^{235}/ U^{238} lines at 424.41 nm and 424.44 nm are determined as a function of time delays 0 and 5 µsec. The U^{235} isotope shift is ~ 25 pm to the blue whereas this takes place ~ 6 pm to the red in favor of U^{238} isotopes. With the normalized line intensity, Fig. 2 shows the isotope shifts varying with time delay. As the delay time increases to 5 µsec, the width of the line changes from 6-11 pm for the samples of interest.

The Geiger counter (Noro 2511) is employed to detect the relative counting of radionuclides of interest. The alpha radiation was counted to be 2324±58 and 371±25 when the distances between the probe and the U foils is set 1 and 30 mm, and the background radiation was measured to be 35 ± 6. Note that plasma temperature (Te) is determined using the Boltzmann equation and the electron density (Ne) is estimated according to Stark broadening [6]. Here, the traditional LIBS gives out typical Te=11.3 *kK* and Ne=1.7×10^{17} cm^{-3}, whereas those of SD-LIBS notably elevate as high as 12.8 *kK* and 2.4×10^{17} cm^{-3}, respectively.

Consequently, LIBS and SD-LIBS have been carried out to highlight a notable enhancement of uranium characteristic lines due to the spark discharge events. Fig. 2 illustrates U^{235} and U^{238} spectra at 424.2 nm as well as a certain isotope shift of ~0.251 *A*° is determined that is resolved with a high-resolution spectrometer with 75000 resolving power.

CONCLUSIONS

Here, the isotope ratio in U^{235}/U^{238} uranium samples in the air at atmospheric pressure using a high- resolution spectrometer has been demonstrated. A 100 mJ/shot energy of laser can induce sufficient excitation of the target uranium samples. We have highlighted that SD-LIBS enhances the characteristic emission against traditional LIBS, which allows to detection of LOD as low as possible. Moreover, the isotope shifts between U^{235}/U^{238} slightly change as a function of time delay ~25 pm to ~31 pm. The present proposal will be further developed in the near future to realize a hand-held high-resolution probe for the prompt detection of the radionuclides of interest.

Reference

1. G. C.-Y. Chan, I. Choi, X. Mao, V. Zorba, O. P. Lam, D. K. Shuh, and R. E. Russo, "Isotopic determination of uranium in soil by laser induced breakdown spectroscopy," Spectrochim. Acta Part B At. Spectrosc. **122**, 31–39 (2016).
2. R. C. Chinni, D. A. Cremers, L. J. Radziemski, M. Bostian, and C. Navarro-Northrup, "Detection of uranium using laser-induced breakdown spectroscopy," Appl. Spectrosc. **63**(11), 1238–1250 (2009).
3. J. E. Barefield II, E. J. Judge, K. R. Campbell, J. P. Colgan, D. P. Kilcrease, H. M. Johns, R. C. Wiens, R. E. McInroy, R. K. Martinez, and S. M. Clegg, "Analysis of geological materials containing uranium using laser-induced breakdown spectroscopy," Spectrochim. Acta Part B At. Spectrosc. **120**, 1–8 (2016).
4. D. A. Cremers, A. Beddingfield, R. Smithwick, R. C. Chinni, C. Randy Jones, B. Beardsley, and

   L. Karch, "Monitoring uranium, hydrogen, and lithium and their isotopes using a compact laser- induced breakdown spectroscopy (LIBS) probe and high-resolution spectrometer," Appl. Spectrosc. **66**(3), 250–261 (2012).
5. P. Parvin, B. Sajad, K. Silakhori, M. Hooshvar, and Z. Zamanipour, "Molecular laser isotope separation versus atomic vapor laser isotope separation," Prog. Nucl. Energy **44**(4), 331–345 (2004).
6. F. Ahmadinouri and P. Parvin, "Methane conversion using spark discharge-assisted

laser-induced plasma (SD-LIP) with Pd catalyst: Non-oxidative hydrogen production," Chem. Eng. J. 149645 (2024).

Porous glasses in the 21st century- Nuclear applications (Paper ID : 1640)

Hamnabard Z. Correspondent[1*], Maghsoudipour A.[2]

[1]*Radiation Applications, Syclotron Radioisotope & Radiopharmaceuticals research School, NSTRI, Karaj, Iran*
[2]*Ceramics Division, Materials & Energy Research Center(MERC), Karaj, Iran*

Abstract

Porous glass is a material that contains pores in the nano/micro metre range. Porous glasses can be synthesized by different methods; conventional method such as foaming, phase separation and leaching process, sol-gel method and alteration process of volcanic materials such as allophones.

In this paper we will discuss different features of porous glasses related to their properties and possible applications with emphasis on nuclear applications such as biomaterials, host matrices for nuclear wastes, precursors for special glasses, bioglass and glass for hydrogen storage.

One of the most famous methods for preparation of porous glasses can be achieved through phase separation of alkali borosilicate glasses. In this method, porous glass can be prepared by an acid or alkaline leaching treatment of phase-separated alkali borosilicate glasses. The interconnected structure of the alkali-rich borate phase in the pure SiO_2 phase is an important precondition for mechanically stable of porous glasses.

In this way, our work reports preparation of porous silica glass via phase separation of an alkali borosilicate glass composition with addition of ZrO_2 and TiO_2. Results showed that tendency of crystallization decreased with increasing the amount of ZrO_2 due to increase in viscosity. By increasing the amount of TiO_2 in the mother glass, phase separation was achieved. In the next step, the acid leaching process of phase separated glasses was performed. Porosity analyzes and measurement of specific surface area of BET were performed on acid leached samples.

Keywords: Nuclear Materials- Porous Glass- Phase Separation- Vycor Glass

Introduction

A porous material is defined by IUPAC[i] as "Any solid material which contains cavities and channels may be regarded as porous[1]. The physical properties of a solid material, such as density, thermal conductivity, strength and chemical durability depend largely on pore structure. Therefore controlling the porosity is of great importance in managing the properties of a solid material. in recent years, due to the influence of pores on controlling properties of solids and physical interaction with gasses and liquids, porous materials has great interest in research and industry.[2,3,4]

Pores can be classified according to their availability to an external fluid. Using this approach, pores can be categorised in two types; open pores and closed pores. According to Fig.1 Closed pores are shown as region (a) and open pores in regions (b), (c),(d), (e) and (f).

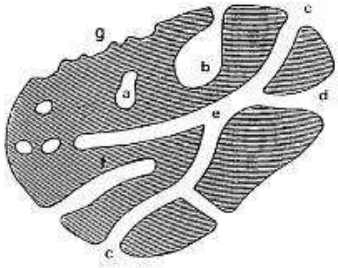

Fig 1: Schematic cross-section of porous solid[5]

Glass and its products have played an important role in materials science. Porous glass has gained new interest in recent years because of its importance in nuclear, chemical, pharmaceutical, and biological applications. For the first time in 1944, Nordberg introduced porous glass. Porous glass is a porous material with SiO_2 as its skeleton and a nano-connected structure. This material can be classified in different ways. According to the pore size, porous glass can be divided into microporous glass, mesoporous glass and macroporous glass. Table 1 shows classification of pore according to the pore-width.

Table 1: Classification of pore according to their pore-width[5]

Pore type	Pore-width (nm)
Microporous	< 2
Mesoporous	2 – 50
Macroporous	> 50

Porous glass can be produced by different methods such as using foam agents to glass powder, conventional leaching phase separated alkali borosilicate glass, sol-gel process and alteration process of volcanic materials such as allophones. Porous glass prepared with silica exhibits high resistance to chemicals and solvents. This properties combined with their high mechanical and thermal stability, makes it suitable to a wide variety of applications. In general porous silica can be used for the following nuclear applications:[5]

1- Material for the encapsulation of nuclear waste
2- Gas separation membranes
3- Catalyst supports
4- Nanoporous silica based bioactive glass for drug delivery systems
5- Hydrogen storage

This present work was performed to investigate the phase separation of an alkali borosilicate glass composition containing TiO_2 and ZrO_2 to produce nanoporous silica glass. In this respect, a glass composition was chosen to examine how its microstructure is modified by adding different TiO_2 and ZrO_2 oxides. Studying the effect of these well-known phase seperation agents will be a helpful and suitable approach to understand the devitrification behavior of an alkali borosilicate glass composition in the SiO_2-B_2O_3-Al_2O_3-CaO-Na_2O system used for nuclear applications.

Experimental

Glass specimens were prepared using conventional melt quenching method in the SiO_2-B_2O_3-Al2O_3-CaO-Na_2O system. Raw materials used were reagent pure chemicals Belgium 99.9% SiO_2 powder, H_3BO_3, Al_2O_3, $CaCO_3$, Mg $(NO_3)_2.6H_2O$ and K_2CO_3. Amounts of 0.5, 1.5, 2.5 and 3.5% mole of TiO_2 (Merck 8557502) and $ZrSiO_4$ (Aldrich 383287) were added to the base glass named as CZ and CT. Table 2 shows the chemical compositions of the investigated glasses.

Table 2: Chemical compositions of the investigated glasses

Glass		Composition (mole%) SiO_2	B_2O_3	CaO	MgO	Na_2O	Al_2O_3	K_2O	MoO_3	TiO_2	ZrO_2
Base	C	51.23	14.81	14.20	7.41	5.55	4.94	1.85	-	-	-
C Z	C0.5Z	50.97	14.74	14.13	7.37	5.52	4.92	1.84	-	-	0.5
	C1.5Z	50.47	14.59	13.99	7.30	5.47	4.87	1.82	-	-	1.5
	C2.5Z	49.98	14.45	13.85	7.23	5.41	4.82	1.80	-	-	2.5
	C3.5Z	49.50	14.31	13.72	7.16	5.36	4.77	1.79	-	-	3.5
C T	C0.5T	50.97	14.74	14.13	7.37	5.52	4.92	1.84	-	0.5	-
	C1.5T	50.47	14.59	13.99	7.30	5.47	4.87	1.82	-	1.5	-
	C2.5T	49.98	14.45	13.85	7.23	5.41	4.82	1.80	-	2.5	-
	C3.5T	49.50	14.31	13.72	7.16	5.36	4.77	1.79	-	3.5	-

Fifty grams of a dry mixture of raw materials were melted in a high alumina crucible at 1400°C for 3 hours and cast in a stainsteel mold. The obtained glasses were melted, heat-treated at 580°C for 2 h, and then cooled naturally to room temperature. The glass heat treatment of glass samples was performed inspecified intervals of 620, 650, 680, 710 ° C. The phase analysis and microstructure of the glasss pecimens was characterized by X-ray diffraction and scanning electron microscope (SEM) analyzer. In the next step, acid leaching was carried out in two steps: 0.5M HCl, 15h and 0.1M NaOH, 0.5 h for removing soluble-acid phases and colloidal silica. Brunauer–Emmett–Teller (BET) analysis was performed for pore size and specific surface area of phase separated glasses. Figure3 shows a schematic diagram of the typical process for making porous borosilicate glass.

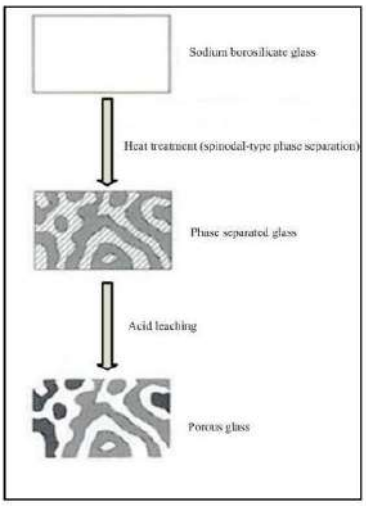

Fig 3: Schematic preparation procedure of porous glass

Results and discussion

Fig. 4 shows the XRD pattern of the base glass. It is seen that the base glass has an amorphous structure, no crystalline phase appeared in this sample and the homogeneous glass was prepared successfully.

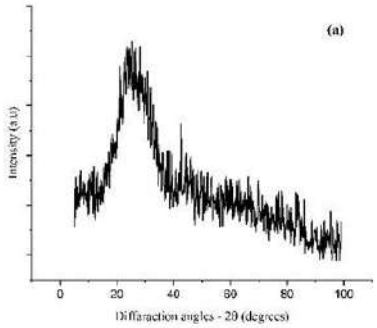

Fig 3: XRD pattern of glass sample

Using DSC technique, temperature range of heat treatment was determined. DSC was performed both for bulk and powder forms, Tg was detected only in the powder state. Fig 4 show the results of DSC analysis of glass samples (powder and bulk form).

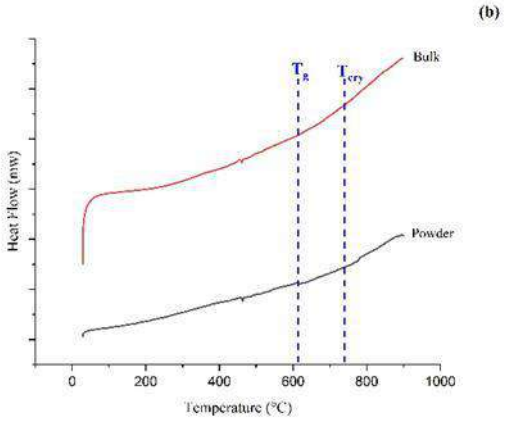

Fig 4: Differential Thermal Analysis of glass sample

Fig 5 shows SEM analysis of glass sample containing different amounts of ZrO_2 and TiO_2 heat treated at different temperatures.

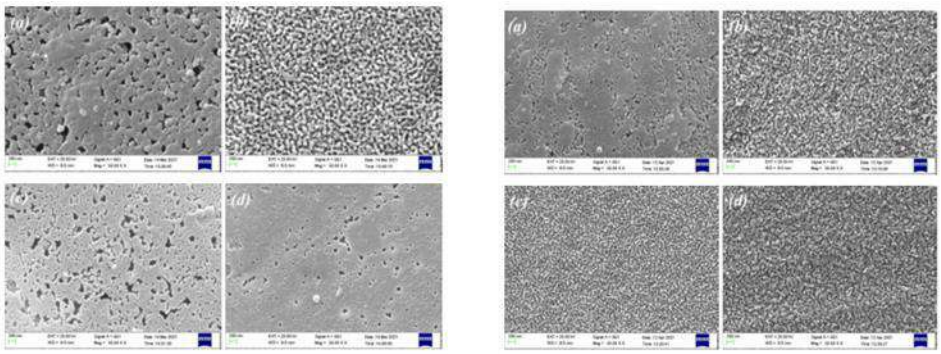

Figure 5(A). SEM images (a) C0.5T-680HT, (b) C1.5T-680HT, (c) C2.5T-680HT, (d) C3.5T-680HT
(B). SEM images (a) C0.5Z-710HT, (b) C1.5Z-710HT, (c) C2.5Z-710HT, (d) C3.5Z-710HT

As it can be seen, with increasing of titanium oxide percent, the microstructure becomes finer. In cases of sample 0.5 mol% of titanium oxide, increasing the activation energy cause to the rate of nucleation and growth is low, so these glasses need more energy for phase separation. In the glass samples containing ZrO_2, two phases of the structure are evident, and according to the uniformity of the structure it seems that this separation is of the spinodal type.[5]

Conclusions

Porous glasses have been applied in many different fields, such as adsorption, ion exchange, membrane technology, drug delivery, solid phase biochemistry, catalysis. But for more than 60 years, porous glasses on the basis of phase-separated alkali–borosilicate glasses have been prepared. However, this does not mean that all problems concerning the preparation, modification and characterization of porous glasses are solved. In recent years, the special properties of porous glasses have led to new applications as components of optical chemosensors, as host materials for immobilization of nuclear waste, Hydrogen storage, porous-wall hollow glass microspheres for drug delivery.[3]Furthermore, porous glassware as a host of luminescent materials for environmental and biological sensors. It seems that the interest of science and industry in porous glasses will continue in the next century.

References

[1] S. Schuller et al.,'Phase separation and crystallization of borosilicate glass enriched in MoO_3, P_2O_5, ZrO_2, CaO' J. Non-Crystalline Solids 354,2008, 296–300.

[2] Z. Hamnabard et al.,'Preparation and Characterization of Nano porous Silica Glasses for Nuclear

waste Immobilization' J. Nuclear Research and Applications, 3(2)2023, 27-31.

[3] R. Reisfeld et al., 'Porous glasses as a host of luminescent materials, their applications and site selective determination' J. of Luminescence, 169(B)2016,440-444.

[4] D. Arcos,' Bioceramics for drug delivery' Acta Materialia 61,2013, 890–911.

[5] M. Hasanuzzaman,' Investigation of porous glasses based on sodium borosilicate glass system, PhD Thesis, DUBLIN CITY UNIVERSITY, March 2013

[1-] IUPAC: International Union of Pure and Applied Chemistry

ICNST 2024
International Conference on Nuclear Science and Technology
6- 8 MAY 2024 | Isfahan, Iran

Extraction of Ce144/Ce141 from Lanthanide Fission Products Simulated Waste in the Process of Molybdenum-99 Production (Paper ID : 1647)

Iman Dehghan1*, Ali Bahrami-Samani1, Simindokht Shirvani-Arani1, Seyed Milad Miremad

[1]*Nuclear Science and Technology Research Institute (NSTRI), Tehran, Iran*

Abstract

The radioisotope ^{141}Ce, with a half-life of 508.32 days, undergoes beta decay with maximum and average energies of 580.8 keV and 145.22 keV, respectively. The radioisotope ^{141}Ce, with a half-life of 9.284 days, exhibits beta decay energies of 318.7 keV (maximum) and 82.25 keV (average). These radionuclides hold promise for various medical and industrial applications. In this study, an extraction chromatography process using α-HIBA solvent is reported for the separation of Ce144/Ce141 from fission products. Based on MCNPX calculations, an equivalent solution was experimentally prepared to mimic the waste solution from the 99-Mo production process via the fission method. Suitable radioisotope tracers were added to the simulated waste solution for radiochemical process analysis.The results demonstrated a radionuclidic purity of 97% and a radiochemical purity exceeding 99% for radiocerium.

Keywords: Ce144/Ce141, chromatographic process, fission products, α-HIBA

INTRODUCTION

Most fission products and their daughters find valuable applications in medicine, industry, and nuclear analysis. Additionally, radiochemical separation of fission products has been of interest for long-term nuclear waste management resulting from the fission of ^{235}U. This separation aims to reduce the radioactivity of waste and measure various fission products with lower yields. Notably, when the infrastructure for separating a fission product, such as ^{99}Mo, already exists, the separation of other fission products becomes simpler, more attractive, and achievable. This article investigates the extraction chromatography process using α-hydroxyisobutyric acid (α-HIBA) solvent for the recovery of Ce-144/Ce-141 radioisotopes as byproducts in the production of ^{99}Mo. The Ce-144/Ce-141 radioisotopes are relatively high-yield products in nuclear fission. Their radioactivity data are presented in Table 1.

Table 1. Radioactive data of ^{141}Ce and $^{144}Ce^{*}$

NO	Radioisotope	half life (day)	Decay mode	Beta Spectrum		Discrete gamma ray with maximum intensity		Cumulative fission yield (For thermal neutron incident with 235U)
				End point Energy (keV)	Mean Energy per disintegration (keV)	E(keV)	I(%)	
1	141Ce	32.51	β-	580.8	145.22	145.44	48.29	0.05847
2	143Ce	1.38	β-	1461.5	404.9	293.27	42.8	0.05956
3	144Ce	284.9	β-	318.7	82.25	133.52	11.09	0.055

*The data provided from: [ref: Janis-ENDF/B-VIII.0 library]

The radioisotope Ce144 has several practical applications, including: Standard Sources: It is used for calibrating detectors, Burn-Up Monitoring: Ce144 serves as a monitor for determining the burn-up of nuclear fuel, Decontaminability Evaluation: It helps evaluate the decontaminability of materials used to cover surfaces exposed to radioactive substances. Moreover, 144Ce finds attractive medical applications, such as the preparation of plaques for eye-cancer radiotherapy.

The choice of separation method depends on the required purity, which is specified by the intended use of the radioisotope. Cerium radioisotope separation has been the focus of numerous studies. The most widely used methods include solvent extraction, extraction chromatography, and electrochemical separation [1-10].In this study, we first calculated the isotopes/radioisotopes produced through irradiation of Low-Enriched Uranium (LEU) targets in the Tehran Research Reactor (TRR) for ^{99}Mo production. We employed the MCNPX Monte Carlo code for this purpose. Subsequently, a simple MATLAB code was used to apply separation coefficients to alumina adsorbent. This allowed us to determine the isotopic content of the liquid waste resulting from the separation step in ^{99}Mo production, where an alumina column captures ^{99}Mo. The waste solution is a rich, valuable source of radio-lanthanides, and its content is directly affected by irradiation time, cooling duration, storage time, and separation coefficients. Stable isotopes and radioisotopes of each element were added by the code to obtain the elemental inventory of the liquid waste. Based on the results, we prepared a 1:100 scale-down equivalent waste solution using suitable salts. The appropriate amount of simulated element composition was then irradiated in TRR to produce corresponding radiotracers via the

neutron activation method. Considering the different isotopes of an element, further investigations are warranted.

2.Materials and methods

Natural isotopes in forms of oxide or salt were prepared from analytical grade from Sigma/Aldrich and were used without any further purification. To perform chromatographic separations, a Peristaltic pump (Langer basic series model BT100-2J, China), a Dowex 1X8 anionic resin (Sigma Aldrich Canada), a Dowex 50WX8 resin (Dow Chemical Company, Midland, Michigan), Merck nitric acid 65% and hydrochloric acid 35%, α-HIBA (α-Hydroxyisobutyric acid, Sigma-Aldrich Chemie GmbH Eschenstrasse). Gamma-ray spectroscopy was performed using a p-type coaxial high-purity germaniumdetector125 (HPGe, EGPC 80-200R) coupled with a multichannel analyzer and Gamma 2000 software126 (Silena). In order to provide the simulated ^{99}Mo production waste solution, the stock solution of the related tracers was first prepared using natural salts and oxides according to Table 2, See result and discussion section.

Table 2. Element inventory of considered waste solution

Element	m (gr)	Element	m (gr)	Element	m (gr)	Element	m (gr)
Al	391.2	Ti	0.2995	Sr	5.61E-03	Se	2.91E-04
Mg	3.40401	Zr	0.019781	Pr	5.55E-03	Eu	1.98E-04
Si	2.043189	Nd	0.017816	Y	2.89E-03	Nb	1.79E-04
Fe	1.392055	Ce	0.013819	Sm	2.30E-03	Sn	1.25E-04
Cu	0.936	Br	1.11E-04	Rh	2.12E-03		
Cr	0.6637	Ru	7.99E-03	Rb	2.08E-03		
Zn	0.4969	Ba	6.49E-03	Te	1.92E-03		
Mn	0.2995	La	6.05E-03	Pd	9.82E-04		

The contents of stable isotopes and radioisotopes in the considered waste solution were calculated using the **MCNPX Monte Carlo code** and a custom **MATLAB code**. Precise determination of parameters such as the characteristics of local Low-Enriched Uranium (LEU) targets, reactor operational power, irradiation and cooling times, geometrical details of the irradiation position in the Tehran Research Reactor (TRR) core, radiochemical process properties for **^{99}Mo** separation, and storage duration of the waste solution is essential for estimating the element inventory. The isotope inventory of irradiated LEU targets can be calculated using the **BURN card** in MCNPX. The waste solution's inventory

depends on the properties of the selected radiochemical process for **^{99}Mo** production. Additionally, during the decay-delay time (including cooling time, **^{99}Mo** separation duration, and storage period), the waste solution's inventory evolves. Considering the radioisotope half-lives and their decay chains, we determine the point at which the radioisotope of interest (RIOI) reaches its highest content, and the separation of RIOI is performed accordingly. As previously mentioned, our goal in this study is to separate **^{144}Ce** as a byproduct of the Fission-Molly process (the process of **^{99}Mo** production via **235U** fission). In Iran's Fission-Molly process, irradiated **U_3O_8Alx** is dissolved in **6 M HNO_3** and loaded onto an alumina column to retain **^{99}Mo**. The remaining acidic waste solution serves as a rich source of radioisotopes, including **^{144}Ce**. Based on previous calculations and simulations, it is necessary to have **24 domestically manufactured targets** (containing a total of **27 g of uranium-235**) in the channel to produce the desired radioisotopes. To meet Iran's medical demand for 99Mo, which amounts to 100 Ci (6 days) per week, we considered the following parameters:Irradiation Channel: D6 channel, Operational Power of TRR: 4 MW, Irradiation Time: 100 hours. A simple MATLAB code was developed to apply the separation coefficients of the alumina column used in the radiochemical process of 99Mo production to the isotope inventory calculated by MCNPX. The radioactivity variations of three comparable radioisotopes (141Ce, 144Ce, and 147Pm) existing in the acidic waste of the alumina column were studied for storage periods of 70, 180, 300, and 400 days (as illustrated in Fig. 1).

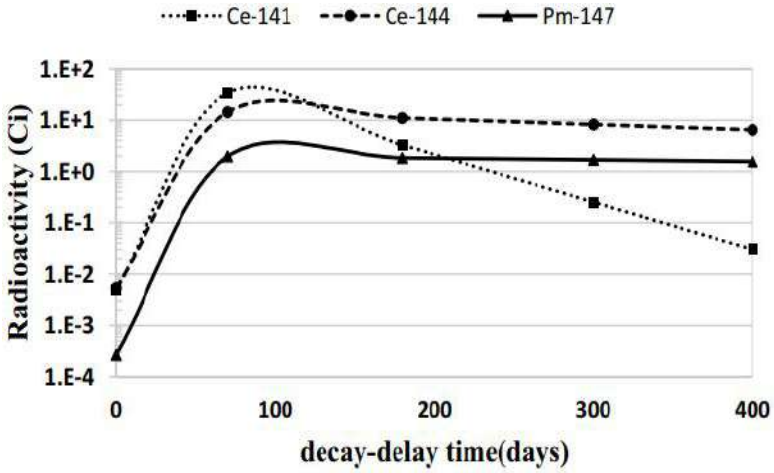

Fig. 1. ^{141}Ce, ^{144}Ce, and ^{147}Pm radioactivity variations in acidic alumina waste solution up to 400 d cooling period [11]

Radioactivity Trends: Initially, 141/144Ce and 147Pm radioactivity levels are low, followed by a peak after approximately 70 days of decay-delay time.

- Subsequently, 141Ce radioactivity decreases with a steeper slope than 144Ce and 147Pm, primarily due to its lower half-life.

- Consequently, the waste solution with 300 days of decay-delay time could serve as a suitable source for 144Ce separation.

3.Experimental

3.1. Preparation of equivalent waste solution. The estimated volume of 99Mo production waste was approximately eight liters. Due to limitations related to handling high radioactivity materials and the potential gamma emission peak overlaps from fission products, separating 144Ce from such a volume on a laboratory scale was not feasible. A solution containing uranium/aluminum in a 1:100 ratios was prepared. Then, 2 mL of the prepared tracer solution (see "Waste Solution Inventory Calculation" section) was added to create a simulated fission-molly-waste solution. By scaling down to a 1:100 ratios. Specifically, one-hundredth of the element inventory of the considered waste was mixed with salt composition and dissolved in 80 mL 6 M HNO3. This solution served as the basic solution for Ce separation and purification processes.

3.2.The preparation of radiotracer solution. A small amount of equivalent salt composition from the considered waste was poured into quartz glass and placed in a suitable aluminum can. After conducting a leakage test, the can was irradiated in the Tehran Research Reactor (TRR) for 24 hours. Following a 10-day cooling period, the hot salt composition was dissolved in 6 M HNO3. This resulting solution is referred to as the radiotracer solution. For each experiment, a portion of this composition was added to the basic solution to create the feed solution. Sampling was performed at different process steps. The gamma rays emitted from each sample were recorded using a high-purity germanium (HPGe) detector. The analysis was conducted by identifying the suitable radiotracer based on the recorded gamma spectrum of the samples. in the analyzed sample, radioisotopes of lanthanides such as La140, Ce141, and others, as well as impurities like Cs137 and Se75, have been reported.

This process is utilized to separate 144Ce from the simulated waste solution. Subsequently, we outline an approach that leverages two-step extraction chromatography as a modified separation method. After preparing the dissolution solution containing fission products (a simulated waste solution mimicking the waste from the 99Mo separation process), which contains radio-lanthanides in the form of neutral nitrate complexes, we follow the process flow shown in Figure 3 to convert it from the nitrate form to the chloride form. This transformation allows the removal of impurities such as uranium, aluminum, tellurium, and ruthenium, which

form anionic complexes and are adsorbed onto the Dowex 1-X8 anion exchange resin column. The lanthanides, which remain in their cationic form, pass through the column. Subsequently, the evaporated solution is dried, and the residue is washed with 100 mL of 10 M hydrochloric acid. The solution is initially passed through a polyethylene column (10 cm in height) containing Dowex 1-X8 anion exchange resin using a peristaltic pump at varying flow rates (1, 1.5, and 3 mL/min). The output solution from this column must be converted from the chloride form back to the nitrate form. To achieve this, the process is repeated by evaporating the output solution from the anion exchange column, followed by washing the residue with 50 mL of 0.5 M hydrochloric acid. The remaining radioisotopes, including radio-lanthanides, are then converted from the chloride form to the nitrate form. This conversion occurs using a peristaltic pump at different flow rates (1, 1.5, and 3 mL/min) through a polyethylene column containing Dowex 50W-X8 cation exchange resin. For the specific separation of Ce141 from other impurities, the eluted solutions from the cation exchange column (which contain the highest amount of Ce141) are dissolved in 10 M hydrochloric acid to break down the α-HIBA complex. The resulting solution is subsequently converted to a chloride salt in the aqueous phase by passing it through a column containing DGA resin (at flow rates of 1, 1.5, and 3 mL/min). This process allows cerium to be absorbed while potential impurities like promethium pass through the column. To ensure the successful separation of cerium, the procedure for separating Ce141 from the mentioned column involves washing it several times (specifically, four times) with M05/0HCl ml20. Important Note: For lanthanide group analysis (specifically Ce141), the samples are diluted at a ratio of 1:10 using an HPGe system, and the experiments are repeated three times.

Table 3. Chromatographic conditions in Dowex50W-X8 cation exchange column

Chromatography conditions	Important parameters in chromatography column
9 gr	Amount of resin
0.9*10 Cm	Polyethylene column dimensions
100 ml	The volume of input feed to the column
3M	pH of input feed to the column
1.5 ml/min	flow rate of input feed to the column (Flow from top to bottom)

100 ml	Volume of solution removed from column
50 mL HNO_3 0.5M	Type and volume of washing solution
180 mL α-HIBA (0.1-0.9 M)	Type and volume of elushion solution
4 – 4.5 M	pH of elushion solution
80 mL HCL (0.05 M)	Type and volume of resin DGA -containing column washing solution
25 ^{0}C	The temperature of the experiments

4. Results and discussion

Figure 2 compares the spectra recorded by the HPGe detector for the feed solution (a simulated waste solution resembling the waste from the 99Mo production process) and the optimal eluent solution (0.8 M α-HIBA). Despite removing certain impurities present in the initial feed using α-HIBA, lanthanides such as Ce141 and other impurities like Cs137 are also detected in the extraction chromatography product. Continuing, to create a Ce141 salt solution and liberate it from the complex, we added concentrated solutions of α-HIBA (ranging from 0.7 M to 0.9 M) and concentrated HCl (10 M). Subsequently, the solution was passed through a column containing DGA resin, followed by four washing steps with dilute HCl (0.5 M) on the same column. The results indicate that the highest ^{141}Ce separation percentage is achieved in the first elution step at different loading rates (1, 1.5, and 3 mL/min). The separation percentages for all mentioned stages align with those in Tables 4 .

Table 4. Conditions and Results of Cerium-141 Separation using Extraction Chromatography (First Method) - Loading rate: 1 milliliter per minute (Gamma radiation energy of Cerium-141 is approximately 145 KeV

Percentage separation ^{141}Ce	CPS	Washing volume (ml)	washing solution
100	198.18	100	Column input Dowex 1-X8
99.01	157.08	100	column output Dowex 1-X8
90.83	143.99	100	Column input Dowex 50W-X8
0	0	100	column output Dowex 50W-X8
6.30	20.01	50	Wash with HNO_3 - 0.5 M
0.35	27.87	20	elushion with 0.1M α-HIBA
0	0	20	elushion with 0.2 M α-HIBA
0	0	20	، elushion with 0.3 M α-HIBA
0	0	20	elushion with 0.4 M α-HIBA
0	0	20	elushion with 0.5 M α-HIBA

0	0	20	elushion with 0.5M α-HIBA
11.45	907.85	20	elushion with 0.7 M α-HIBA
20.05	1590.01	20	elushion with 0.8 M α-HIBA
14.58	1155.96	20	elushion with 0.9 M α-HIBA
43.36	42.96	20	DGA resin column input
0	0	20	DGA resin column output
22.35	1772.09	20	First washing with 0.05 M HCl
0	0	20	Second washing with 0.05 M HCl
0	0	20	Third washing with 0.05 M HCl
0	0	20	Fourth washing with 0.05 M HCl

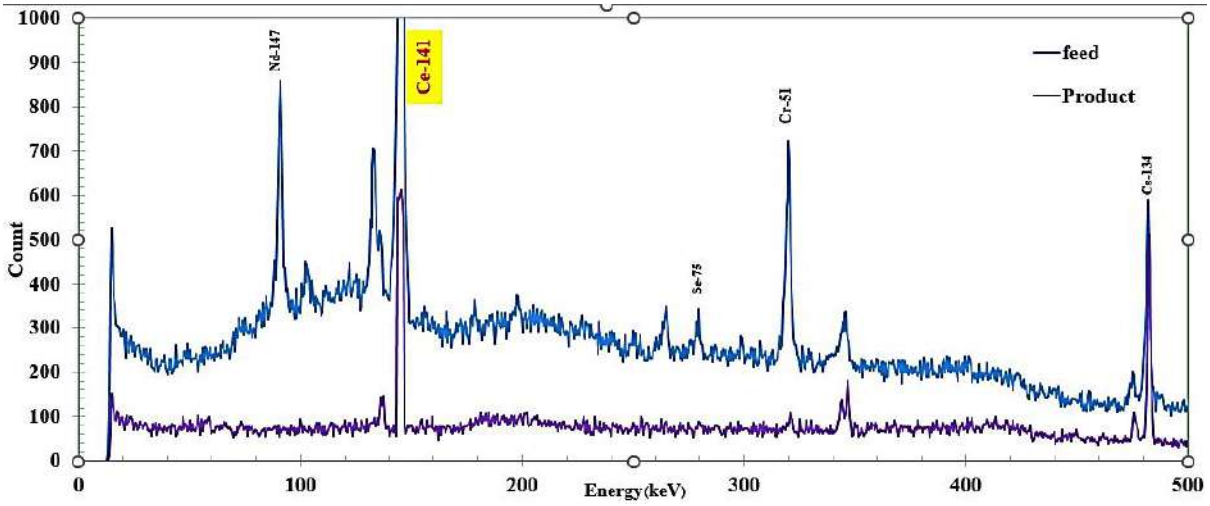

Fig. 2. Comparison of gamma emission spectrum for the feed solution and the isolated product

4. Conclusion

In this method, a simulated solution of the waste from the production process of molybdenum-99, containing radionuclides, passes through an anion exchange column and is then passed through a cation exchange resin bed in the ammonium form. The lanthanides will be absorbed by the cation exchange resin. To separate each of the lanthanide radioisotopes, their various affinities with a complexing agent are utilized in the solution. Exchange agents in ion exchange chromatography have lower selectivity and higher capacity, whereas in extraction chromatography, they exhibit greater selectivity and lower capacity. In extraction chromatography, free electron pairs and ligand atoms in the solvent containing the complexing agent form a dative bond with the vacant orbitals of 3-valent lanthanides. Passing the solution containing the complexing agent through the column, the lanthanides form stable complexes with it. A competitive interaction between the aqueous phase and the resin begins, resulting in continuous exchange of lanthanide ions between the complexing agent and the resin. Due to differences

in complex formation constants, lanthanides with higher formation constants move more rapidly downward through the column (and separate earlier). In various studies on lanthanide separation, the solution containing the complexing agent used in this method is α-Hydroxyisobutyric Acid (α-HIBA) with an approximate concentration of 2.1 molar (48.12 grams of α-HIBA in 100 milliliters of water) at a pH of 5.4

The findings indicate that Ce-141 can be separated from nuclear fission products using the solvent α-Hydroxyisobutyric Acid (α-HIBA) in the extraction chromatography method, particularly at high concentrations of the mentioned solvent. Additionally, apart from lanthanides, the cation exchange column also absorbs other impurities (such as cesium-134), which compete during the separation process with Ce-141 using α-HIBA. However, despite the successful separation of Ce-141 by the extraction chromatography method using α-HIBA and its purification relative to other impurities, the efficiency of this method is not very desirable. Therefore, I recommend that future research explore alternatives, such as replacing the cation exchange column with an Ln-resin column in extraction chromatography, and consider using different solvent solutions for this method.

References

[1] Horner DE, Crouse DJ, Brown KB, Weaver B (1963) Fission product recovery from waste solutions by solvent extraction. Nucl Sci Eng 17(2):234–246.
[2] Glendenin LE, Flynn KF, Buchanan RF, Steinberg EP (1955) Radiochemical determination of cerium in fission. Anal Chem 27(1):59–60.
[3] Moore FL, Jurriaanse A (1967) Separation of californium from curium and berkelium from cerium by extraction chromatography. Anal Chem 39(7):733–736.
[4] Ejaz M, Carswell DJ (1975) Amine oxides as solvents for uranium, thorium and some fission products. J Inorg Nucl Chem 37(1):233–237.
[5] Sarkar, S., & Ohuchi, A. (1997). Separation of rare earths and transuranium elements from spent nuclear fuel solution by high performance liquid chromatography.
[6] Lee CS, Wang YM, Cheng WL, Ting G (1989) Chemical study on the separation and purification of promethium-147. J Radioanal Nucl Chem 130:21–37
[7] Vasudevan S, Sozhan G, Mohan S, Pushpavanam S (2005) An electrochemical process for the separation of cerium from rare earths. Hydrometallurgy 76(1–2):115–121.
[8] Han Q, Du M, Guan Y, Luo G, Zhang Z, Li T, Ji Y (2020),Removal of simulated radioactive cerium (III) based on innovative magnetic trioctylamine-polystyrene composite microspheres.
Chem Phys Lett 741:137092.
[9] Alqahtany FZ, Khalil M (2021) Adsorption of 140 La and 144Ce radionuclides on ZnO nanoparticles: equilibrium and kinetics studies. J Radioanal Nucl Chem 327:91–104.
[10] Brown, M. A., Servis, A., & Tkac, P. (2020). Development and Optimization of a Purification Process to Recover 99Mo from Low-enriched Uranium (No. ANL-20/83). Argonne National Lab. (ANL), Argonne, IL (United States).

[11] Hosseini SE, Ghannadi-Maragheh M, Bahrami-Samani A, Shirvani-Arani S (2021) Evaluation of promethium-147 production as a by-product of the fission molybdenum-99 process in Tehran research reactor. Radiochim Acta 109(4):295–300.

Overview of radioisotope based technique applications for industrial process diagnostics (Paper ID : 1656)

QUANG NGUYEN H., DUY DANG NGUYEN T., CHAU NGUYEN T.,

LAMACO Company Ltd., A13- Khu quy hoach vien hat nhan, Hung Vuong Rd., Ward 11, Dalat City, VIETNAM
Email: nhquang.dalat@gmail.com

Abstract.

In process industries such as petrochemical plants, the timely identifition of the problem for remedial action and optimization of the plant performance bring great benefits through reducing operational downtime, maintaining operational efficiency, ensuring safety and prevent environmental disasters. Over decades of application, the radioisotope based techniques such as radiotracers and sealed radiation sources have proven themselves to be the effective diagnostic tools in troubleshooting and optimization of industrial processes thus leading to high economic benefits. The most obvious advantage of radioisotope techniques is based on the penetrating properties of radiation, which allows observing the structure and fluids inside the process equipment with measuring devices placed outside the wall while the equipment is operating. Radiotracer techniques are used to identify the malfunction or the leak in process equipment by injection of the suitable radioisotope tracer into the inlet and detection of tracer transport through the system by detectors placed at the outlets. Gamma scanning techniques are also the unique tool to determine the internal structure of fluids distribution in the process equipment or to identify the corrosion and deposit in the pipeline. Neutron backscattering is the useful method to determine moisture in the insulation and hydrocarbon/water liquid levels.

Because practical applications are so numerous, this overview presents typical examples to illustrate the application of radiotracer techniques and sealed radiation sources in industrial process diagnostics. The benefit of the such applications is also illustrated by examples of solved problems.

I. Introduction

In the large scale process industry such as petrochemical plants, the successful operation depends on the timely identifition of the problem for remedial action and optimization of the

plant performance. Over decades of application, the radioisotope based techniques such as radiotracers and sealed radiation sources have proven themselves to be the effective diagnostic tools in troubleshooting and optimization of industrial processes thus leading to high economic benefits. The most obvious advantage of radioisotope techniques is based on the penetrating properties of radiation, which allows observing the structure and fluids inside the process equipment with measuring devices placed outside the wall while the facility is operating.

The principles and practical applications of radioisotope techniques for diagnostics in troubleshooting and industrial process optimization can be found in a number of IAEA publications and related journals. Some popular documents are listed in the References section.

Radioisotope based techniques used for industrial inspection may also include Radiographic Testing as in Nondestructive Testing (NDT) and Nucleonic Gauge but those techniques are not used for diagnostics of system in operation. Therefore, in this paper we focus on the in-situ techniques including radiotracer, gamma scan and neutron backscattering which are used frequently in diagnostics for troubleshooting and optimization of the system.

II. Principles of radioisotope based technique applications

2.1. Tracer technique [1,2,3]

The principle of tracer application in process diagnostics is illustrated in Figure 1. Tracer material is injected at the inlet of the system as the pulse and tracer movement through the system is detected by using detector placed outside the wall and at the outlet. Tracer data are radioactivity counts versus time elapsed since injection.

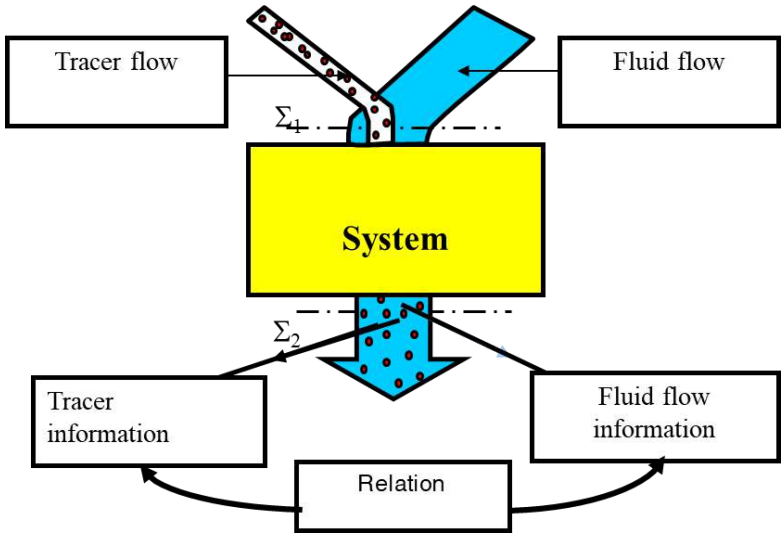

Figure 1. The principle of tracer application in process diagnostics.

Most application of tracer in process investigation works on the principle of phase tracing. In practice, by selection of the appropriate tracer for a particular application the criteria for suitable phase tracing is can be met by radiotracers as clarified below:

- The tracer behaves in the same way as the material under investigation. For example, tracers can be a compound soluble in water, organic or gas phase which is tagged with the radioisotope.
- Tracer movement in the system can be easily detected at low concentrations without disturbing the system. By using the appropriate specific radioactivity, the mass of tracter used in application is quite small to disturb the tracing fluid. On the other hand, the radioisotope is selected as gamma emitter, for example Br-82 in Dibromobenzene, which is detected by using out wall gamma detector.
- The residual tracer radioactivity in the product from the system should be

  minimal in radiation safety consideration; This criteria can be achieved by

using short half-live radioisotope and let the tracer stay enough long time in the system for decaying and dilution.

- No significant absorption on the wall and thermal/chemical inert.

In general, the factors which are important in the selection of the tracer are half-life, specific activity, type of radiation, radiation energy and physical and chemical form. The commonly used radiotracers for process investigation are listed in the Table 1. Tracer materials are usually prepared in two ways: direct irradiation in a nuclear reactor or synthesis of radioactive tracer compounds by a tagging procedure. For example, Methyl Bromide (Br-82) is synthesized from Potasium Bromide (Br-82) after activation in a neutron flux; Argon-41 is produced directly by neutron activation of Argon gas.

Table 1. Commonly used radiotracers in process investigation

Isotope	Half-life	Gamma radiation energy, MeV	Chemical form	Tracing phase
Sodium-24	15 h	1.37 (100%) 2.75 (100%)	Sodium Chloride, Iodide Chloride NaCl, NaI	Aqueous
Bromine-82	36 h	0.55 (70%) 1.32 (27%)	Dibromobenzene Ammonium bromide Methyl Bromide	Aqueous Organic Gas
Lanthanium-40	40 h	1.16 (95%) 0.92 (10%) 0.82 (27%) 2.54 (4%)	Lanthanium Chloride	Solid (absorbed)

				Activated intrinsic tracer such as catalyst
Gold-198	2,7 days	0.41 (100%)	Chloauric acid	Solid (absorbed) Organic (colloidal)
Iodine-131	8.04 days	0.36 (80%) 0.64 (9%)	Potasium or Sodium Iodide Iodobenzene	Aqueous Organic
Krypton-79	35 h	0.51 (15%)	Krypton	Gas
Argon-41	110 min	1.29 (99%)	Argon	Gas

Tracer radioactivity amount A (Bq or milicurie) for injection into the system is estimated based on specific activity which detector can detect and on flow rate as described in the following formula:

$$A = Q.K^{-1}\int_0^{\infty} r(t)dt$$

where, Q (m3/s) is flow rate at detector position, r(t) is count rate at time t (counts/s), K is detection efficiency (counts.m^3/Bq.s) determined by laboratory experiment.

Because the amount of tracer material is very small, the tracer solution is prepared by diluting it with a non-radioactive carrier before injecting it into the system which mixes well the tracer solution with bulk fluids.

The tracer is injected into the system in pulse mode, meaning that the time of injection is very short compared to the traveling time in the system.

Residence Time Distribution [2]

Continuously processing systems are designed to have either plug flow or well mixed flow patterns. In case of malfunction, the deviation from designed patterns is considerable and of a direct bearing on the process efficiency and product quality. The formation of damage, leakage, blockage, deposit… inside the equipment are the factors create the malfunctions such as fouling, channeling, by-passing, maldistribution etc. The malfunction of the real system can be assessed by analysis of RTD for interpretation of the actual flow pattern.

With assumption that tracer following consistently with tracing fluid, the actual RTD of a flow system can be obtained from the normalized tracer response to an impulse injection of tracer stimulant. If an impulse of tracer is injected at the inlet of the system at time t=0 and its radioactivity is measured as a function of time at the outlet C(t), then Residence Time Distribution E(t) is determined as:

$$E(t) = \frac{C(t)}{\int_0^\infty C(t)dt}$$

E(t)dt represents the fraction of the tracer having residence time between time interval (t, t+dt) or probability for a tracer element to have a residence time in the system between interval (t, t+dt). Thus:

$$\int_0^\infty E(t)dt = 1$$

In principle, any flow system can be described by composing the ideal elementary models – the perfect mixers (or perfect mixing tank) in series model. The RTD function can be expressed in tank number j and time domain as bellows.

Perfect mixers (j=1): $E(t) = \frac{1}{\tau}\exp\left(-\frac{t}{\tau}\right)$

Perfect mixers in series (j>1): $E(t) = \left(\frac{J}{\tau}\right)^{J} \frac{t^{J-1}\exp\left(-Jt/\tau\right)}{(J-1)!}$

Different perfect mixers in series models and plot of according E(t) are illustrated in Figure 2.

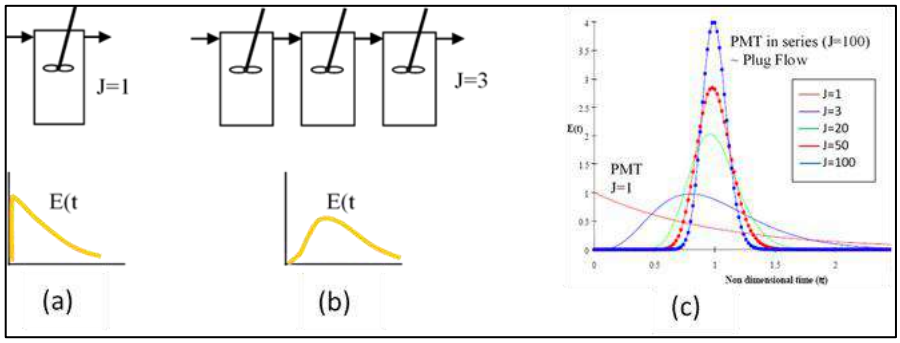

Figure 2. Perfect mixers in series models and their RTD curves. (a) – Perfect mixer, (b) – Three perfect mixers in series and (c) – RTD curves of perfect mixers in series as function of mixer (tank) number J. When the number of mixers is large (>20), the flow is almost plug flow.

Examples of description of a real flow system by composing elementary models is given in Figure 3. During diagnostics, the tracer response curve provides the experimental RTD and the actual flow pattern of the system is approached by fitting the calculated RTD to the experimental RTD curve.

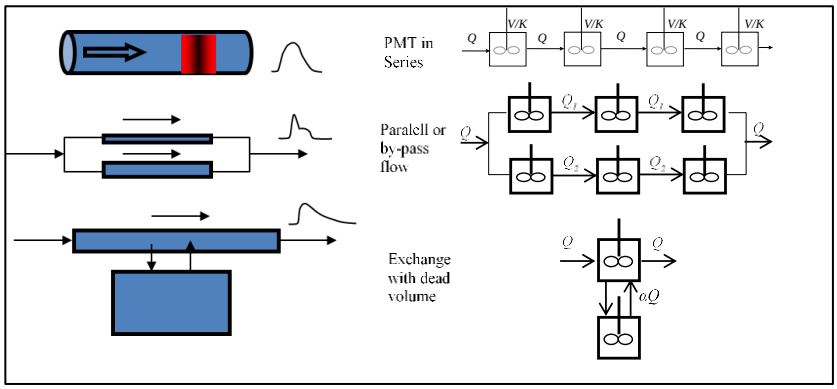

Figure 3. Examples of description of the real system by composing the

2.2. Gamma scanning techniques [3]

The intensity of gamma radiation absorbed in the material between the radioactive source and detector is described by the transmission law.

$$I = I_o.\exp(-\mu.p.x)$$

where: I: the intensity of radiation transmitted through the material

I_0: the intensity of incident radiation

μ: the mass absorption coefficient of the test material

ρ: the density of material

x: thickness of material

This basic equation is used for experimental design, measurment, data processing

and interpretation of gamma-ray absorption scans in column, vessels and pipes. In principle, backscatter gamma scanning can also be used. However, the wall thickness and large size of industrial facilities are obstacles to the practical application of this method.

Column scan is the most common application of transmission gamma scanning technique. With a collimated symmetric source and detector configuration moving along the column body, the count attenuation profile gives information about the internal structural condition as well as the fluid distribution of the distillation or adsorption columns. Figure 3 introduces principle of column gamma scan. In fact, gamma scan gives quick results on the site about the malfunction such as tray collapse, clogging, flooding, fooling, foaming in distillation towers or liquid maldistribution, channeling, pack material loss in packed column. The gamma scanning findings are very useful in provision of the fact for diagnostics in troubleshooting and treatment that brings a great benefit from minimizing downtime, optimizing operation optimization and avoiding accident.

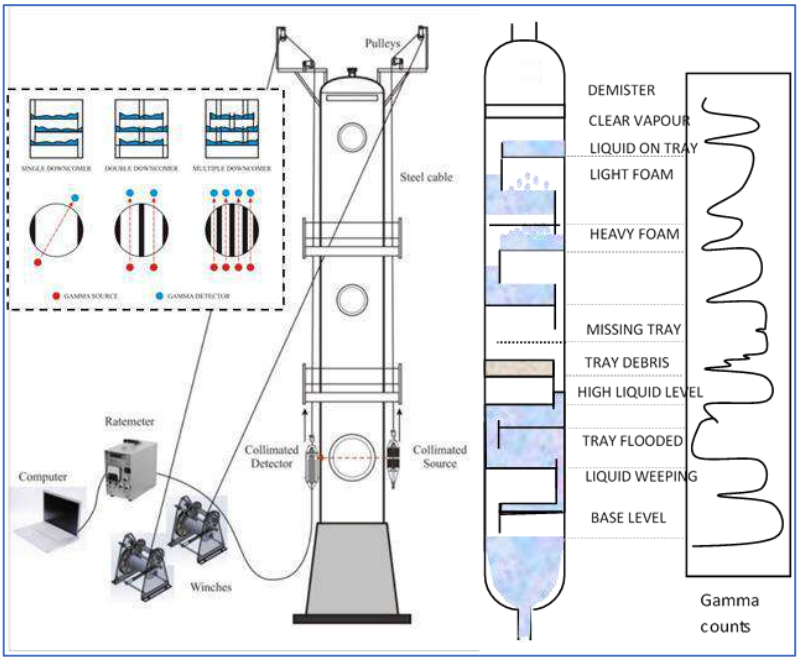

Figure 3. Principle of column gamma scanning technique.

2.3. Neutron backscattering technique [3]

In addition to the gamma scan, the neutron scattering measurement technique can be applied in determining water, hydrocarbon liquid levels and deposit, blockage by the hydrocarbon material. The principle of neutron scattering measurement is based on the slowing down (moderation) of fast neutrons emitted from the source into thermal neutrons that are sensitive to the hydrogen concentration in the material. The equipment consists of a neutron

source and neutron counter (He-3 or BF_3) placed next to each other. Since detector counts only thermal neutron backscattering from the material of hydrogen composition due to moderation of the fast neutron, the counting rate will reflect content of hydrogen in material. Hydrocarbon materials have higher hydrogen content than water, so they give a higher counting rate than water. Figure 4 describes the principles of neutron backscattering gauge in level measurement.

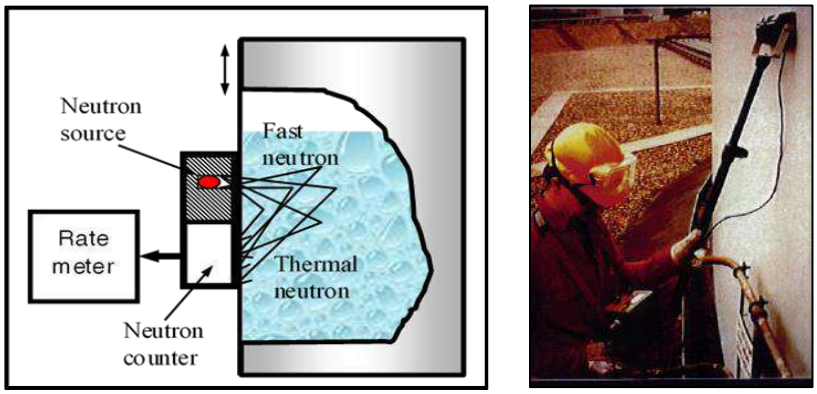

Figure 4. Principle of neutron backscattering measurement in level detection.

2.4. Industrial Computed Tomography [4]

The gamma scanning technique has the advantage of being simple and quick giving results of surveying the condition of process equipment on site. However, gamma scanning results based on the attenuation of the transmitted gamma ray beam only provide information about the total density of material along the scanning path. That in some cases is not enough to understand the

detailed condition of the fluid or defect inside the tower. Computed Tomography is a solution that can provide cross-sectional images of the process equipment. Using the image reconstruction algorithm, the data of the gamma scanning lines around the object are processed to give a cross-sectional reconstructed image of the internal density distribution. The Industrial CT device can be installed on site to survey the damage, cracking state of refractory inside column, blockages or corrosion inside pipes. Figure 4 depicts the configuration of different generations of CT and photos of Industrial CT equipments designed and fabricated in the Centre for Applications of Nuclear Technique in Industry (CANTI, Viet Nam) [5].

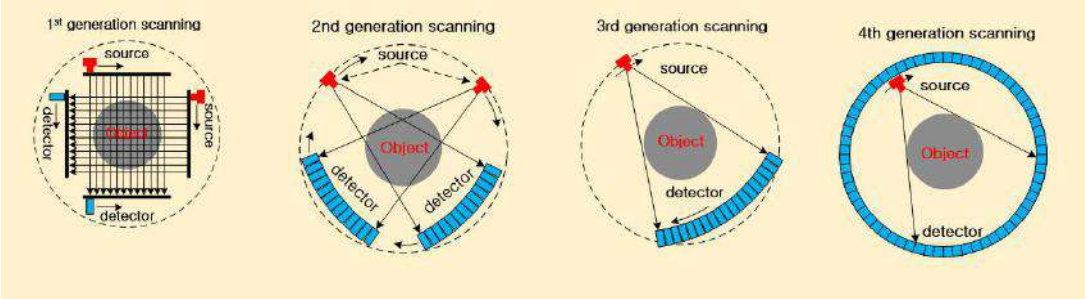

Figure 4a. Configuration of different generations of Computed Tomography

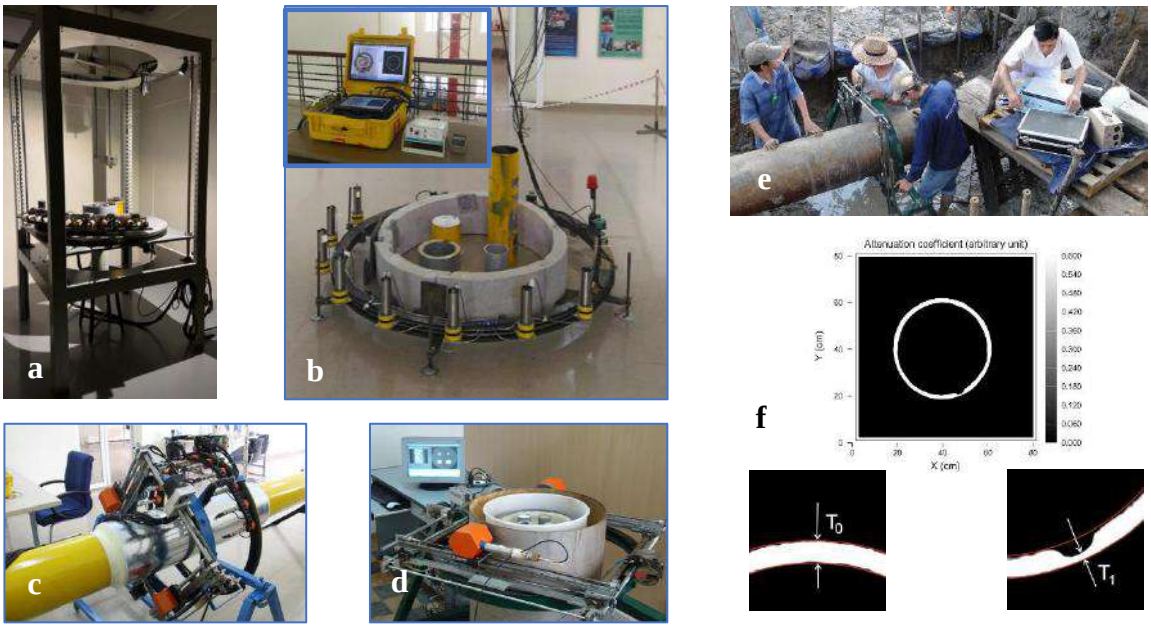

Figure 4b. Photos of different industrial CT equipments. G-COMET – the 3rd generation CT equipment for flow model study (a); g-OCTOPUS – the improved 3rd generation portable CT system for large scale scanning (b); g-SPIDER – the portable CT equipment combined 1st and 3rd generation (c); GORBIT – the 1st generation portable CT equipment (d) and photos of CT application on the site for detection of pipe corrosion (e, f) – CANTI' s photos [5].

III. Industrial applications

3.1. Radiotracers for study of catalyst distribution and flow pattern in Fluidized Catalytic Cracking Unit in a Refinery

In cracking unit using catalyst, the axial catalyst distribution and flow pattern in FCCU riser are of great concern of operator to ensure the process efficiency. Radiotracer was applied to investigation of the flow dynamics of catalyst in the Riser of FCCU. The following case study was reported in the IAEA/RCA Project

RAS/08/107/9002/01- Technical Meeting on New Developments in Radiotracers and Sealed Source Applications [6].

Radioisotopic tracer La-140 for solid catalyst tracing is prepared by neutron activation of catalyst powder. The experiment arrangement is showed in Figure 5.

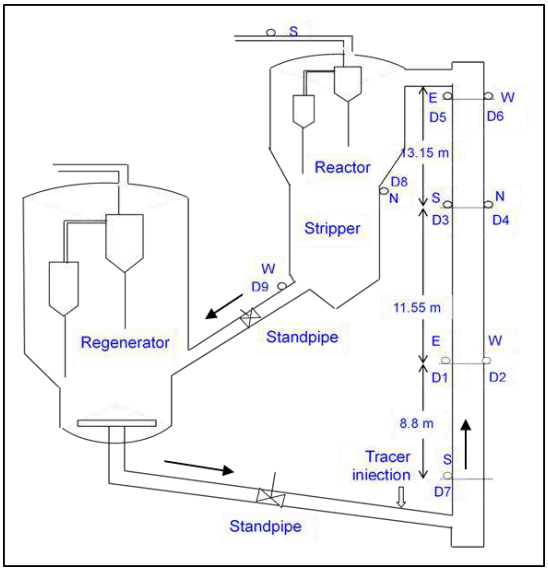

Figure 5. Arrangement of experiment.

D1 – D9: detector position

S, W, N, E: location in the direction around the system

Tracer injection point was located at the catalyst inlet of the riser. Detector D7 is to detect the tracer input. Detectors were placed in three section of the riser where, D1 and D2 are to observe tracer movement in the East and West, D3, D4 in the South and North and D5, D6 in the East and West of the riser. All detectors are NaI 2" x2" collimated by lead shield. Radioactivity counts were collected by the Data Acquisition System with 0.1s reading. The obtained experimental RTD curves were fitted with the model RTDs for interpretation of flow pattern (Figure 6).

The experiment results of Mean Residence Time, velocity, Peclet number and flow pattern in each section of riser are summaried in Table 2.

The obtained RTD curves of each couple of detectors are almost concided to each other that shows good radial distribution in all three sections of riser. RTD analysis also shows flow pattern in each section that the catalyst flow in form of near plug flow from the inlet (D7-D1D2) and the next section (D1D2-D3D4) to the intermediate mixing (D5D6) and to the near well mixing in the last section. That means the riser operated well in the condition at the experiment carried out. However, the experiment should be continued with different conditions to optimize the operations of the riser.

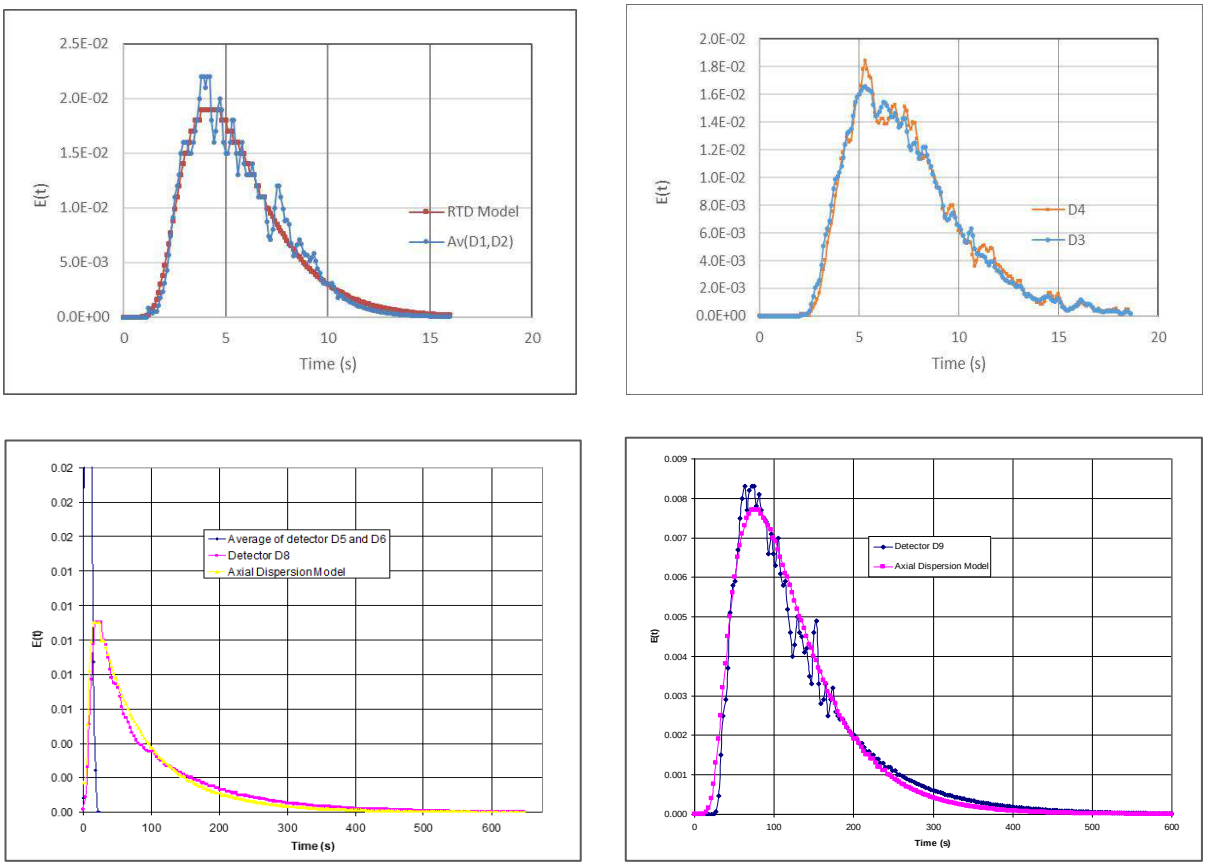

Figure 6. Experimental RTD and modeled RTD curves of catalyst tracer at observation locations.

Table 2. Results of catalyst tracer measurement in Riser

Parameters	Between detector locations					
	D7-D1D2	D1D2-D3D4	D3D4-D5D6	D5D6-D8	D8-D9	D7-D9
Radial distribution	Good	Good	Good			
Expt MRT(s)	3.65	1.4	2.6	96	50	132
Velocity U(m/s)	2.4	8.25	5.0			
Model MRT(s)	3.7	1.55	2.5	81.5	41	123

Peclet Number	9.5	7.12	10	2.95	5.7	5.7
Flow pattern	Plug flow	Intermediate mixing flow	Plug flow	Near well mixing flow	Intermediate mixing flow	Intermediate mixing flow

3.2. Column scan for monitoring heavy foaming in absorption column

The impurity of the product was found in absorption column in DQ Refinery. The gamma scans were carried out to investigate the inside column status. The gamma scanning diagram is depicted in Figure 7 in which the gamma source is located in the Northeast and the detector is in the Southwest.

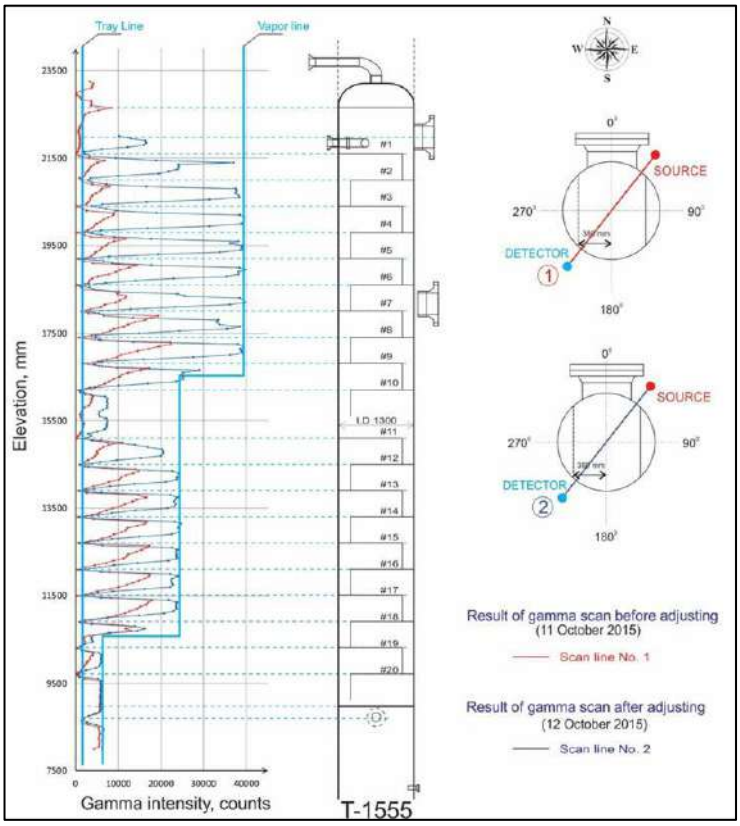

Figure 7. Gamma scanning application for monitoring heavy foaming in the absorption column of DQ Refinery.

Scan results (Scan Line #1) show that all trays are in good condition, however low gamma counts indicate high liquid density in all trays with the potential for heavy foaming.

After receiving the scan results, the operator adjusted the operating parameters and requested a re-scan. The second scan results (Scan Line #2) showed that there was no thick foam phenomenon, and the liquid inside was likely in vapor form as usual. The product obtained is of good quality. The investigation was completed in just 2 days. The cost of the investigation was not high, but the benefits from restoring the process are huge because the cost of downtime runs into millions of US dollars per day.

3.3. Investigation of malfunction in the condensate stabilizer of NCS Plant by using Radiotracers, Gamma Scan and Neutron Backscattering Techniques [8]

NCS condensate stabilizer was found to be malfunctioning. Column pressure increases as production increases, causing a suspected blockage problem in Bed #3 or from the trap out tray to the product drainage pipe. Condensate flow blockages can be detected with a gamma scan, but the cause of the blockage may be from Bed #3 that should be investigated with tracers.

The diagram of Stabilizer and gamma scan, tracer application is shown in Figure 8.

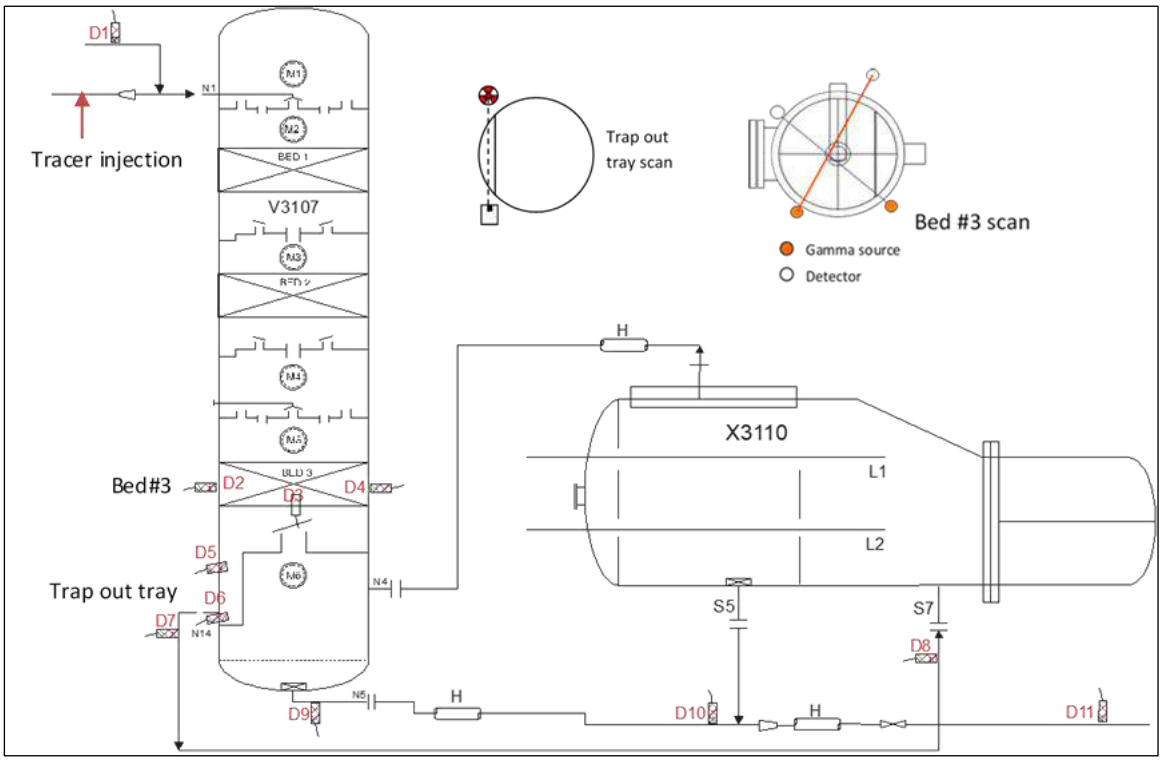

Figure 8. Diagram of NCS Condensate Stabilizer and gamm scan, tracer application.

Gamma scans were applied for Bed #3, Trap out Tray and the Pipe connect to Trap out Tray at 3 operation regimes 40 m3/h, 20 m3/h and 0 m3/h. Bidirectional scanning results showed no abnormalities detected in Bed No. 3 (Figure 9, left). However, the scan results in the Trap out Tray show different condensation levels depending on the operating flow of 40

m3/h, 20 m3/h and 0 m3/h respectively, very high levels even upto the chimney, medium level and no condensate. Additionally, scanning in the Trap out Tray and pipe scanning detected an area of build up in the Tray with material of higher density than the condensate extending from the elevation of 120 cm down to the pipe connected to the Tray (Figure 9, left). This finding was confirmed by cross checking with neutron scan.

With the assumption that the material accumulating in the tray could be from Bed #3, the tracer in form of organic colloid Au-198 was injected into the system to investigate the condensate distribution across the bed. Monitoring results showed an uneven distribution of condensate in the zone of detector D3, towards the Downcomer, where the condensate amount was 1.5 times higher than in other zones, which is believed to have less packing material (Figure 10).

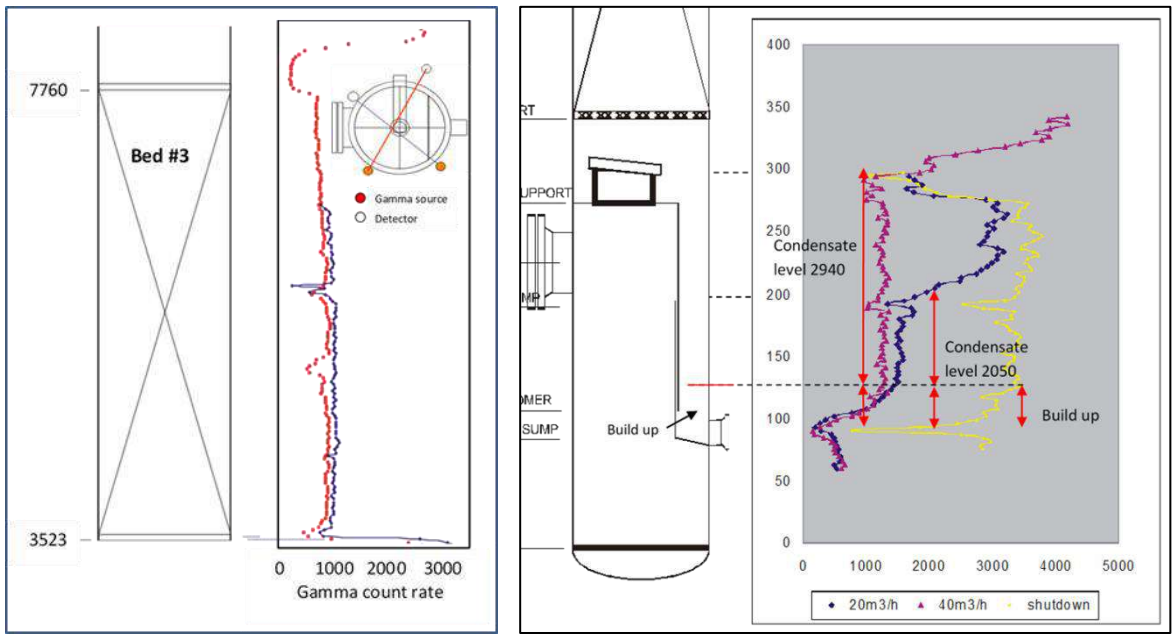

Figure 9. Scanning results in Bed #3 (left) and Trap out Tray (right).

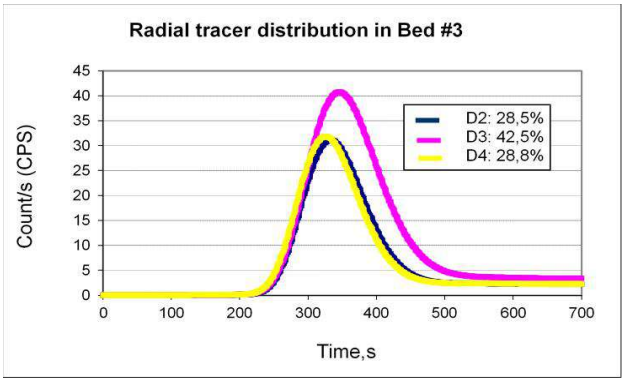

Detector	MRT, s	Tank number	Tracer recovery
D2	206	21	28.5%
D3	220	18	42.0 %
D4	198	20	28.8%

Figure 10. Radial tracer distribution in Bed #3.

IV. Concluding remarks

Over decades of application, the radioisotope based techniques such as radiotracers and sealed radiation sources have proven themselves to be the effective diagnostic tools in troubleshooting and optimization of industrial processes thus leading to high economic benefits [9]. Thanks to the unique ability to "look inside the system", in the context of increasing competition from modern technologies, radiation techniques such as gamma scanning, neutron scanning and tracer are still being applied in diagnostics investigation of industrial processes. Research to improve methods, modernize measuring equipment, and use new technologies such as wireless transmission and artificial intelligence in result interpretation is still continuing in many laboratories.

References

[1]. Radiotracer applications in industry – a guide book, Technical Report Series No. 423, IAEA, Vienna, 2004.

[2]. "Radiotracer Residence Time Distribution Method for Industrial and Environmental Applications", Training Course Series No. 31, IAEA, 2008.

[3]. Charlton J. S., Radioisotope techniques for problem-solving in industrial process plants, Leonard Hill, London, 1986.

[4]. Industrial Process Gamma Tomography, Final report of a Coordinated Research Project, 2003-2007, IAEA TECDOC – 1589, IAEA 2008.

[5]. Unpublished document of development of Industrial Computed Tomography, CANTI.

[6]. IAEA/RCA Project RAS/08/107/9002/01- Technical Meeting on New Developments in Radiotracers and Sealed Source Applications.

[7]. Service contract report on investigation of absorption column in DQ Refinery, CANTI (unpublished)

[8]. Service contract report on investigation of malfunction of the condensate stabilizer of NCS Plant, CANTI (unpublished)

[9]. Fries B.A., Newman A.M, Economic Benefits of Tracer Applications in Petroleum Refining, Isotopenpraxis 26 (1990) 9, pp. 414-418

Investigation the Properties of Polyaniline-Tin Oxide Nanocomposite under Gamma Radiation (Paper ID : 1657)

Varmazyar Gh.[1*], Tohidi T. [2], Jamshidi-Ghaleh K.[1], Tohidi S.[3]

[1] Department of Physics, Azarbaijan Shahid Madani University, Tabriz, Iran

[2] Northwest Research Complex (Bonab), Radiation Applications Research School, Nuclear Science and Technology Research Institute (NSTRI), Tehran-Iran Abstract

[3] Faculty of Physics, Tabriz University, Tabriz-Iran

Abstract

In this study, the PANI/SnO_2 nanocomposite was synthesized using the combination of hydrothermal and chemical polymerization methods. SnO_2 nanoparticles, with 30% of the weight, were dispersed in polyaniline. The samples were then exposed to gamma irradiation at

three different doses of 10, 20, and 30 kGy. The morphology, structure, and optical characteristics of the samples were analyzed using the X-ray diffraction (XRD), UV-vis absorption spectroscopy, photoluminescence (PL) emission spectroscopy, energy dispersive X-ray analysis (EDX) and scanning electron microscopy (SEM). Photoluminescence spectroscopy and UV-vis absorption spectrum were utilized to examine the electron transitions and optical properties, respectively. It was observed that gamma radiation is increasing the uniformity and density of the particles, significantly impacting the structure and morphology of the sample surface without altering the phases. Optical absorption and photoluminescence peak intensities increased at higher gamma irradiation doses. For 30 kGy irradiation dose, the photoluminescence peak shifted from 420 nm to 416 nm in comparison of the non-irradiated sample (blue shift). The direct band gap decreased from 2.58 eV to 2.47 eV as the gamma dose increased from 0 to 30 kGy.

Keywords: Polyaniline-tin oxide nanocomposite, Chemical polymerization, Nanocomposite, Gamma rays

INTRODUCTION

In recent decades, advancements in modern science have led to the emergence of new studies in the field of nanotechnology, sparking a revolution in device manufacturing and material property examination at the nanoscale. The rules of nanotechnology have also highlighted the interest in the physical properties of materials. Therefore, it is crucial to find a cost-effective, convenient and rapid method for producing nanoparticles. Nanoscale materials display optical and electrical behaviors that differ from those of the same materials in lager structural dimensions. Conductive polymers are particularly noteworthy for their potential applications in chemical and biological sensors, solar cells and other areas, thanks to their affordability, flexibility and capabilities.

Easy and fast processing has garnered a lot of attention [1]. The flexibility and environmental stability of polyaniline are considered advantageous [2], as well as the use of nanoparticles due to their high surface-to-volume ratio and modification of optical, electrical and other properties related to conductive polymers. Additionally, polyaniline holds a special position due to its lower price. One of the most important metal oxides is SnO_2. Pure tin dioxide SnO_2 is a crucial n-type wide band semiconductor with a wide band gap (3.6 eV) [3]. Dispersion of nanoparticles in a suitable environment is a new technique for preparation, resulting in a nanocomposite [4].

Nanocomposites can be prepared by combining SnO2 nanocrystalline particles in the form of a colloidal suspension [5].

It is widely understood that exposure of any solid material to ionizing radiation (such as X-rays, gamma rays, etc.) causes a change in the materials microstructural properties, subsequently affecting its overall properties. This change depends on two factors: the irradiation dose and the thickness of the layers. The higher doses and the thinner layers, the more intense the destruction will be.

Previous research has explored the effects of gamma radiation with different doses on the electrical, optical, and structural properties of hybrid PANI/ZnO and tellurium dioxide, investigating its applicability in gamma dosimetry. This research focuses on the investigation of a polyaniline-tin oxide nanocomposite and the study of the effect of gamma radiation on the properties of the composition. In this study, a PANI/SnO_2 hybrid nanocomposite was prepared using the combination of chemical and hydrothermal polymerization methods and its properties were examined for the first time under gamma radiation, showcasing its potential as a new material in dosimetry.

EXPERIMENTAL

Synthesis of SnO_2 nanomaterials by hydrothermal method

For the synthesis of SnO_2, the hydrothermal method was utilized with chemicals of 99% purity. A 981.68 mg of tin chloride was dissolved in 70 ml of deionized water and 8 g of glucose was added. The solution was stirred until clear. Next, 104.24 ml of phosphoric acid was added drop by drop, and the mixture was stirred with a magnetic stirrer for 20 minutes. The solution was then transferred to a Teflon autoclave and placed in an oven at 140 degrees for 24 hours. The settled powder was centrifuged, dried in an oven at 80 degrees for 12 hours, and then placed in a furnace at 550 degrees Celsius for 3 hours to enhance crystalline conditions.

Synthesis of PANI-SnO_2 nanocomposite

PANI-SnO_2 nanocomposite films were synthesized using the chemical polymerization method. The synthesis involved two separate vessels, A and B. In vessel A, a mixture of 0.5 mmol of ammonium persulfate and 30 ml of dilute hydrochloric acid was stirred for 30 minutes. In vessel B, tin dioxide nanoparticles (30% by weight) and 30 ml of dilute hydrochloric acid were combined and stirred with an ultrasonic device for 10 minutes. Then, 0.5 mmol of aniline was

added and mixed thoroughly. The contents of vessel A were added drop by drop to vessel B and placed in an ice bath for 2 hours. The sediment was allowed to settle for 30-40 minutes, then washed multiple times with distilled water to remove impurities. The sediment was then dried and ground with a mortar to obtain the PANI-SnO_2 nanocomposite sample with 30% tin oxide by weight. The resulting nanocomposites were characterized using spectroscopic devices [6].

Results and discussion

Figure 1 shows the XRD diffraction patterns of the composite sample of polyaniline with 30% tin oxide (PANI/SnO_2 (30%)) under different doses of gamma radiation. From bottom to top, the patterns represent the sample without gamma radiation, the sample irradiated with a dose of 10 kGy, the sample irradiated with a dose of 20 kGy, and finally the sample with a radiation dose of 30 kGy. It is evident that the application of radiation doses did not alter the phases of the sample which is consistent with previously published results [7]. In all cases, the sample exhibited two main phases: PANI and SnO_2 in their pure forms. The polyaniline phase possesses a monoclinic crystal system with an index peak at a diffraction angle of 25.52º, categorized as plates with the Miller index (200). The tin oxide phase, on the other hand, features a tetragonal crystal system with an index peak at a diffraction angle of 26.54º, categorized as plates with the Miller index (110). Upon comparison of the diffraction patterns, it is apparent that the sample without gamma radiation shows the sharpest SnO_2 peaks with the highest intensity. With the application of gamma radiation and an increase in dose from 10 to 30 kGy, the intensity of the SnO_2 phase peaks gradually diminishes.

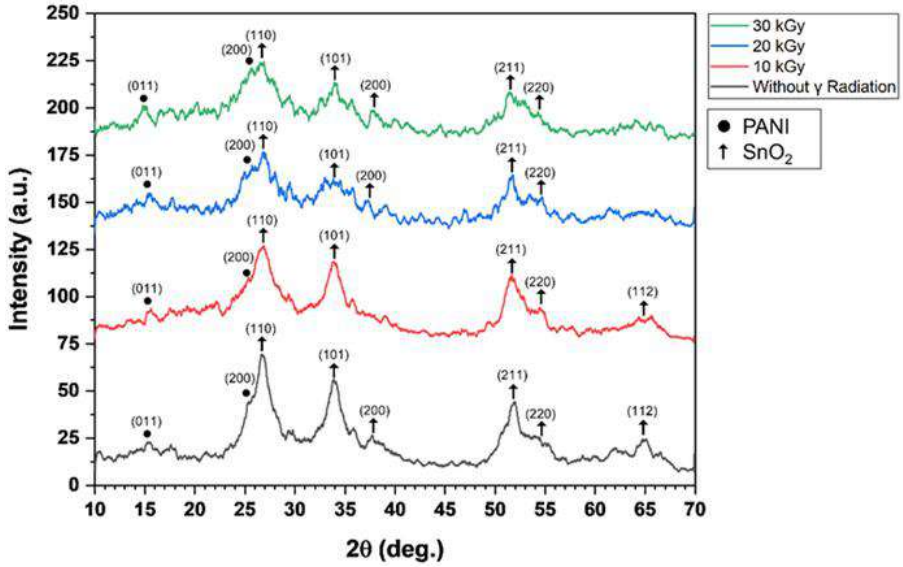

Fig.1. XRD pattern of the nanocomposite (30%) PANI/SnO_2 under gamma radiation at doses of 10, 20 and 30 kGy

As shown in Table 1, the size of crystals in PANI/SnO_2 (30%) increased as the radiation dose of gamma rays increased from 10 kGy to 20 kGy. However, when the radiation dose was increased to 30 kGy, the size of the crystals decreased. Figure 2 depicts the non-irradiated (30%) PANI/SnO_2 nanocomposite, irradiated under gamma rays at doses of 10, 20 and 30 kGy. The nanocomposite film (30%) of PANI/SnO_2 demonstrates that SnO_2 nanoparticles are evenly dispersed in the polyaniline matrix [8] and PANI interacts with tin oxide crystals [9]. By analyzing the shape and calculating the particle size using Scherer's formula, it is evident that the particle size of PANI/SnO_2 increases with the radiation dose reaching 20 kGy, resulting in enhanced uniformity and density of the particles. However, when the radiation dose is increased to 30 kGy, both the density and size of the particles decrease, corroborating the findings of X-ray diffraction. The crystals tend to aggregate after gamma irradiation, leading to the formation of larger crystals, which is in good agreement with previously reported results [10].

Table 1. Particle size of PANI/SnO_2 (30%) in XRD spectrum after gamma ray irradiation at different doses

D ($\mathring{A}$)	$\beta_{struct.}$ (degree)	2θ (degree)	β_{std} (degree)	β_{obs} (degree)	K	λ ($\mathring{A}$)	Phase name	Gamma dose

40	2.080	34.100	0.020	2.100	0.9	1.5406	SnO_2	30 kGy
87	1.010	51.630	0.020	1.030	0.9	1.5406	SnO_2	20 kGy
71	1.170	33.940	0.020	1.190	0.9	1.5406	SnO_2	10 kGy

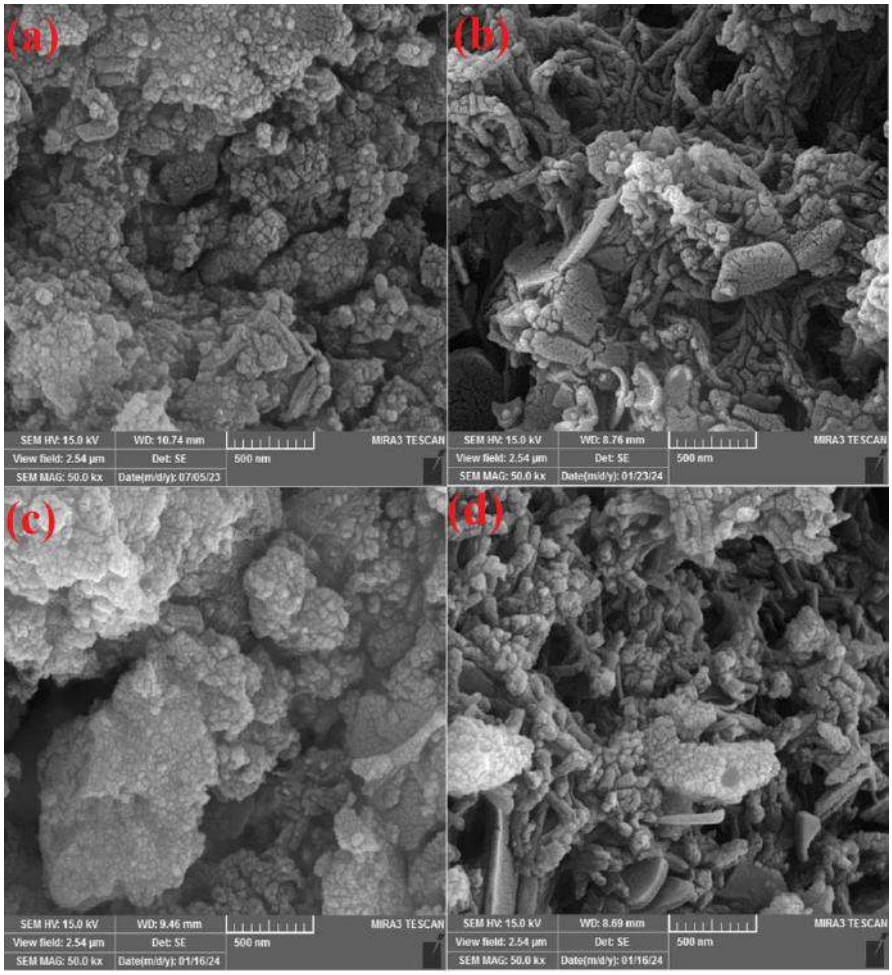

Fig.2. SEM images of 30% PANI/SnO_2 before and after irradiation at different doses: (a) before irradiation (b) after 10 kGy (c) after 20 kGy and (d) after 30 kGy

Figure 3, shows the EDX spectrum of the PANI/SnO_2(30%) nanocomposite. The weight and atomic percentage of elements are listed in the inset of figure.

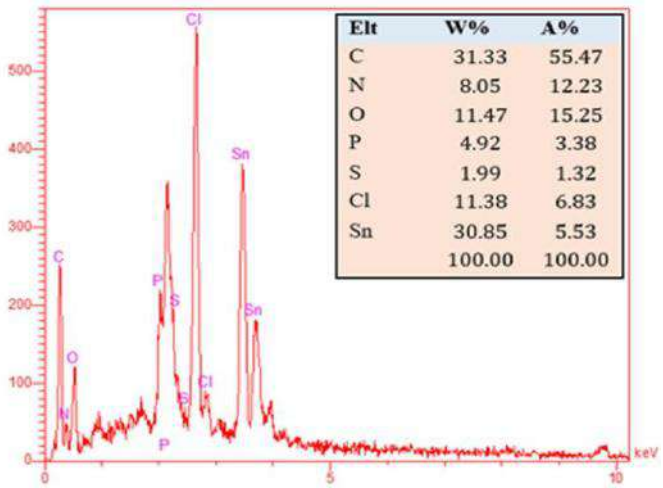

Fig.3. EDX of PANI/SnO_2 nanocomposite (30%). The inset shows the atomic and weight percentage of the elements.

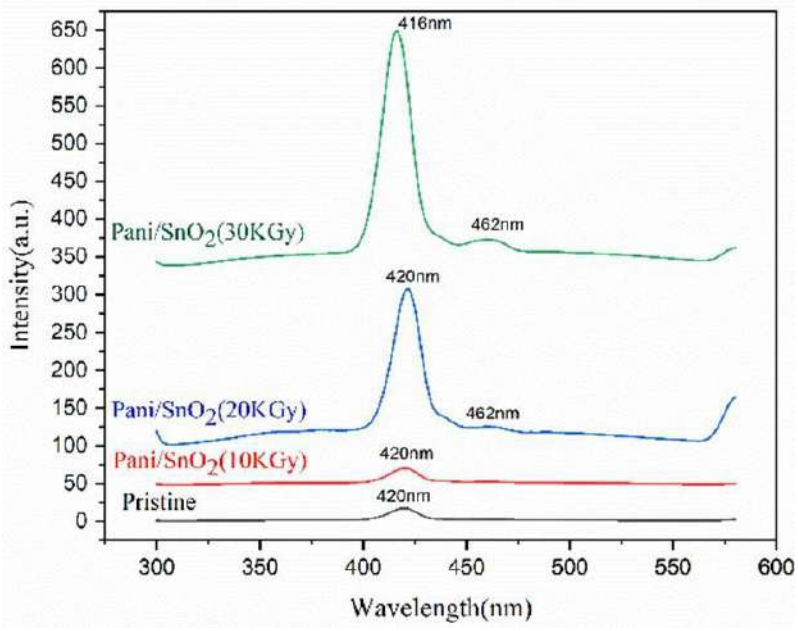

Fig.4. Photoluminescence spectrum of PANI/SnO_2 nanocomposite (30%) with different dosages

Figure 4 shows the photoluminescence spectrum of PANI/SnO_2 under varying doses of gamma rays. The intensity of the PL peak changed after exposure to gamma radiation, with the peak intensity increasing as the radiation dose increased. This increase in intensity is likely a result of the filled cavities increasing with the gamma dose, causing the release of charge carriers through thermal excitation and subsequent recombination with their counterparts. At a dose of 30 kGy, the photoluminescence spectrum underwent significant changes, shifting towards shorter wavelengths [7]. The peak of the spectrum shifted from 420 nm to 416 nm, indicating

a blue shift. Figure 5(a) and (b) show the values of absorption edge and band gap energy for the synthesized compounds after gamma irradiation. As the radiation dose increased, so did the absorption and absorption edge shift. This shift and increase in absorption after gamma radiation can be attributed to the increase in grain size [11, 12].

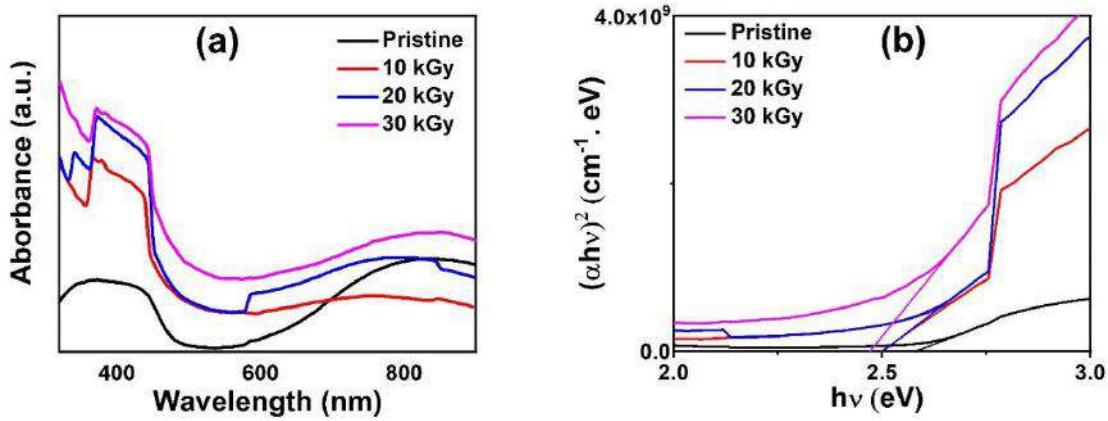

Fig. 5. Absorption spectrum (a) and band gap (b) of nanocomposite with 30% PANI/SnO_2

It can be observed that prior to gamma radiation, the energy gap increased by adding SnO_2 to PANI. After irradiation, a trend of decreasing energy gap with increasing radiation dose is evident. This means that as the radiation dose increases, the energy gap decreases, aligning with results from the nanocomposite (PANI/ZnO). The decrease in energy gap after gamma radiation can be explained by the simple charge transfer model. According to this model, the Fermi levels in the samples after irradiation have increased compared to pre irradiation samples, resulting in a reduction of the optical energy gap. Additionally, absorption peaks broaden with higher gamma doses, likely due to the creation of defects such as organic components, radicals or radiation-induced color centers that form new energy levels. Table 2 shows the band gap values of the PANI/SnO_2 nanocomposite sample (30%) before irradiation and after various doses of gamma radiation.

Table 2 Measured band gap energies (eV) of PANI/SnO_2 sample (30%) at different doses

30 kGy	20 kGy	10 kGy	0 kGy	Sample
2.47	2.49	2.50	2.58	PANI/SnO_2(30%)

Conclusions

The PANI/SnO_2 nanocomposite was synthesized using a combination of hydrothermal and chemical polymerization methods. SnO_2 nanoparticles, accounting for 30% of the weight, were dispersed in polyaniline. The prepared samples were exposed to gamma irradiation at three different doses of 10, 20, and 30 kGy. The morphology, structure, and optical characteristics of the samples were investigated using XRD, UV–vis absorption spectroscopy, PL, EDX, and SEM. It was observed that gamma radiation increased the uniformity and density of the particles and significantly affected the structure and morphology of the sample's surface, without changing the phases. The intensity of the optical absorption spectrum and photoluminescence peak intensity increased with increasing gamma irradiation doses.

The particle size of the PANI/SnO_2 nanocomposite increased from 71 to 87 angstroms by increasing the radiation dose from 10 to 20 kGy. However, at 30 kGy irradiation dose, it decreased to 40 angstroms. Additionally, the band gap decreased from 2.58 to 2.47 as the gamma dose increased from 0 to 30 kGy.

This proves that gamma radiation can be an effective tool for adjusting the characteristics of the surface.

References

[1] Nasirian, S. and Moghaddam, H.M. (2014). Effect of different titania phases on the hydrogen gas sensing features of polyaniline/TiO_2 nanocomposite. Polymer, 55(7):1866-1874.

[2] Hu, Z.-A. et al. (2009). Polyaniline/SnO_2 nanocomposite for supercapacitor applications. Materials Chemistry and Physics, 114(2-3):990-995.

[3] Khuspe, G. et al., (2013). Facile method of synthesis of polyaniline-SnO_2 hybrid nanocomposites: Microstructural, optical and electrical transport properties. Synthetic metals, 178:1-9.

[4] Parvin, M.H. Pirnia, M. and Arjomandi J. (2015). Electrochemical synthesis, in situ spectroelectrochemistry of conducting indole-titanium dioxide and zinc oxide polymer nanocomposites for rechargeable batteries. Electrochimica Acta, 185:276-287.

[5] Dutta, K. and De, S. (2007). Optical and nonlinear electrical properties of SnO_2–polyaniline nanocomposites. Materials letters, 61(27):4967-4971.

[6] Nadaf, L. et al. (2016). Poly-aniline-Tin oxide nanocomposites: synthesis and characterization. IOSR Journal of Applied Chemistry, 9(2):55-61.

[7] Sen, S.K. et al. (2020). Influence of total absorbed dose of Co-60 γ-radiation on the properties of h-MoO_3 thin films. Thin Solid Films, 693:137700.

[8] Khuspe, G. et al. (2014). Camphor sulfonic acid doped polyaniline-tin oxide hybrid nanocomposites: synthesis, structural, morphological, optical and electrical transport properties. Ceramics International, 40(3):4267-4276.

[9] Karim, M.R. et al. (2007). Synthesis of core-shell silver–polyaniline nanocomposites by gamma radiolysis method. Journal of Polymer Science Part A: Polymer Chemistry, 45(24):5741-5747.

[10] Ali, S.M. et al. (2020). Gamma dose dependent structural, optical and current-voltage characteristics of CdS/p-Si heterojunction. Materials Chemistry and Physics, 240:122243.

[11] Guimarães, N.E. et al. (2023). Electrical and optical properties of Poly (vinyl chloride)/ZnS nanocomposites exposed to gamma radiation. Materials Research, 26:e20220308.

[12] Issa, S.A. et al. (2021). Structure, optical, and radiation shielding properties of PVA–$BaTiO_3$ nanocomposite films: An experimental investigation. Radiation Physics and Chemistry, 180:109281.

ICNST 2024
International Conference on Nuclear Science and Technology
6- 8 MAY 2024 | Isfahan, Iran

Effect of gamma irradiation on the physical properties of CdS/PVA nanocomposite thin films prepared by CBD method (Paper ID : 1663)

Tohidi T.*, Taghavi M., Rahmatallahpur Sh., Saei Zavoshti I., Heidari S.

Northwest Research Complex (Bonab), Radiation Application Research School, Nuclear Science and Technology Research Institute (NSTRI), Tehran, Iran

Abstract

Polymer nanocomposites are considered promising candidates for device applications in various fields. The physical properties of polyvinyl alcohol (PVA) are the subject of active research, as it is a distinguished base material with natural properties that make it a good host matrix for embedding nanoparticles. CdS/PVA nanocomposites have garnered significant attention due to the wide direct band gap of 2.42 eV of CdS, coupled with the good mechanical, acoustic, and elastic properties of PVA. We present the preparation of CdS/PVA nanocomposite thin films on a glass substrate using the chemical bath deposition (CBD) method. The temperature, deposition time, and pH value of the bath were 80˚C, 1 hour, and 11, respectively. The resulting films were uniformly homogeneous, smooth, and firmly adhered to the substrate. Subsequently, the samples underwent gamma irradiation at five different doses: 10, 40, 70, 100, and 150 kGy. Characterization was conducted using scanning electron microscopy (SEM) and energy dispersive X-ray spectroscopy (EDS). The I-V characteristics of the samples were also examined. It was noted that gamma radiation increased the grain size and had a significant impact on the I-V characteristics. The I-V plots before and after gamma irradiation displayed linearity, with an increase in current post-irradiation.

Keywords: Thin films, CdS/PVA nanocomposite, Chemical bath deposition, Electrical properties, Gamma rays.

INTRODUCTION

Recently, much attention has been given to the physics of the semiconductor-polymer nanocomposites materials that are very attractive owing to their potential applications in various fields such as optoelectronic applications, transistors, and biological imaging. Due to interactions between polymer molecules and nanoparticles surfaces, both the characteristics of nanoparticles and the host polymeric matrix can be considerably changed. The polymer as a host material exhibits high stability, flexibility, and processability combined with the

functional tenability and also can be used to control the growth of nanoparticles during the synthesis of the nanocomposites [1]. Among inorganic semiconductors, cadmium sulfide (CdS) nanoparticles are a technologically important material, with a direct wide band gap semiconductor (E_g=2.42 at 300 K). In the past several years, synthesis and characterization of nanocrystalline cadmium sulfide (CdS) thin films have been attracting wide attention due to their unique size dependent properties and great potential in several applications such as semiconductor nonlinear optical devices, semiconductor lasers, gas sensors, thin film transistors, light emitting diodes, solar cells and photo detectors [2, 3]. Besides, polyvinyl alcohol (PVA) is one of the most common everyday life polymers that are characterized by their widespread applications due to its interesting chemical and physical properties, excellent thermal stability, high chemical resistance, high mechanical strength, and water solubility. It is a semicrystalline material exhibits certain physical properties resulting from the crystal-amorphous interfacial effect. Its structure reveals a carbon backbone with hydroxyl groups attached to methane carbons. These hydroxyl groups can be a source of hydrogen bonding. PVA is a distinguished base material that has natural properties providing a good host matrix for the embedding of nanoparticles. PVA has gained attention due to its nontoxicity and its reduction ability [4].

CdS-PVA nanocomposites were studied extensively by various researchers due to the CdS wide band gap, with excellent elastic mechanical properties of PVA. The various deposition methods such as spin coating, thermal evaporation, spray pyrolysis, electro deposition, dip coding and chemical bath deposition (CBD) were proposed to prepare CdS/PVA thin films. Among these various thin film deposition methods, the chemical bath deposition process is a simple, easy to handle and cost effective method. Additionally, it is a very interesting chemical technique because it can be used easily at low temperatures with inexpensive processes for large-area depositions. By using of CBD method, the surface density and dimensions of nanoparticles can be tuned. Therefore, it can be employed to prepare high-performance nanocrystalline films. In this method, for the preparation of thin films with special applications, it is necessary to control the deposition parameters such as materials concentration, pH and temperature of the bath, reaction time, stirring duration and the amounts of introduced dopants and complexing agents [5].

It is shown that ionizing radiation (like γ-ray) changes the microstructural features of thin film materials and then varies their electrical, optical and physical properties. The changes strongly

depend on the internal structure of the exposed films as well as the energy and dose of ionized radiation. Electron excitation or ionization, structure transformation and displacement of atoms inside the lattice are among the changes. Due to this, some new electronic states may be formed and dramatically change the physical properties of the materials under irradiation. Ionizing radiations have numerous applications in many areas, such as nuclear power plants, industry, military, medicine, particle accelerators and scientific research. Knowledge of the physical modifications of the sample under radiation is important in designing gamma dosimeters based on thin film structures. Thin films as a new generation of radiation sensors are of particular interest in recent years. Many studies have been conducted to enhance the performance of the thin film-based radiation sensors by improving both the properties of the materials and the manufacturing technology. The threshold dose at which radiation is harmful, depends on some factors including the coating technique, structure and thickness of thin films. A more intense degradation occurs when the doses are higher and films are thinner [6].

There are multi studies for the effect of ionizing radiation that have proceeded via the polymeric materials. Ionizing radiation appears to be the appropriate technique for modifying natural polymers as well as biodegradable artificial polymers. Ionizing radiation might be applied to induce degradation, cross-linking or grafting in the systems containing polysaccharide or PVA. Benthami et al. [7] have investigated the effect of gamma radiation on optical and color properties of polyvinyl alcohol-Sodium lignosulfonate-Cadmium sulfide (PVA-LS/CdS) nanocomposite films. Abdel-Galil et al. [1] have investigated the gamma radiation effect on conductivities (DC/AC) and dielectric properties of cadmium sulfide/polyvinyl alcohol (CdS/PVA) nanocomposites films prepared by a solution casting method. Nouh et al. [4] have prepared the ZnS/PVA Nanocomposite films by casting method. The effect of gamma radiation on the structural and optical properties of ZnS/PVA have investigated using XRD and UV–vis spectroscopy.

This research focused on preparation CdS/PVA nanostructure thin films on a glass substrate using chemical bath deposition. The study aimed to investigate the impact of gamma radiation on electrical properties. This method allows for the preparation of smooth, compact films with linear I-V characteristics, making them suitable for dosimetry applications.

Experimental details

To have uniform films and effective deposition the substrate must be cleaned carefully. Contamination on the surface of the substrate, creates unwanted nucleation sites, leading to nonuniform growth of films. The glass slides with dimensions of 25×75×1 mm^3 were washed by a liquid detergent. Next, they were immersed in dilute nitric acid over 24 hours. Then, distilled water was used to clean them. Subsequently, ultrasonic agitation was used to treat the substrates in acetone. After that, isopropyl alcohol was used to rinse the substrates and finally, they were dried in oven at 70-80 °C for 15 min.

All reagents were of analytical grade and used as received without further purification. Double distilled water was used throughout the experiments. CdS/PVA nanocomposite thin films were deposited on glass substrates by CBD technique using cadmium chloride [$CdCl_2$] as Cd^{2+} ion source and thiourea [$CS(NH_2)_2$] as S^{2-} ion source. Polyvinyl alcohol (PVA) was used as a basic polymer controller matrix. The preparation details of the CdS/PVA nanocomposite thin films are as follows:

Add 5.3×10^{-5} mol of PVA and 0.0011 mol of cadmium chloride to 200 ml of double distilled water. Bring the temperature of the resulting solution to 70-80 ˚C and stir for 3 hours using a stirrer. Remove the solution from the heater stirrer and let it sit for 24 hours to allow the aging process to occur. Take 50 ml of the solution and pour it into a beaker in a bathroom at 80 ˚C. Dissolve 0.013 mol of ammonium chloride in 1.3 mol of NH_4OH solution and add it to the solution in the beaker. Lastly, dissolve 0.0132 moles of thiourea in a few cc of water and add it to the solution as well. The solution was brought to a final volume of 100 ml by adding distilled water. Place the slides in the beaker and allow the deposition process to take place.

The surface morphology of deposited films was characterized using the EVD 18 SEM (Carl Zeiss). KEITHLEY 6485 Picoammeter was used to measure electric current.

Results and discussion

The SEM micrographs of the prepared samples are presented in Figure 1, showing the surface morphology of the CdS/PVA nanocomposite thin film before and after irradiation at different doses. The results show the formation of spherical nanoparticles in shape with relatively homogenous distribution. These figures indicate that the spherical nanoparticles have a mean grain size in the range of 121 nm for the nonirradiated sample and 136 nm, 288 nm, 156 nm,

157 nm, and 145 nm for the irradiated samples, respectively, as shown in Table 1. The increase in the grain size of CdS/PVA films after gamma irradiation is related to the large amounts of energy transferred to the structure within a short time interval. These results indicate that gamma irradiation can be an effective tool for tailoring surface characteristics.

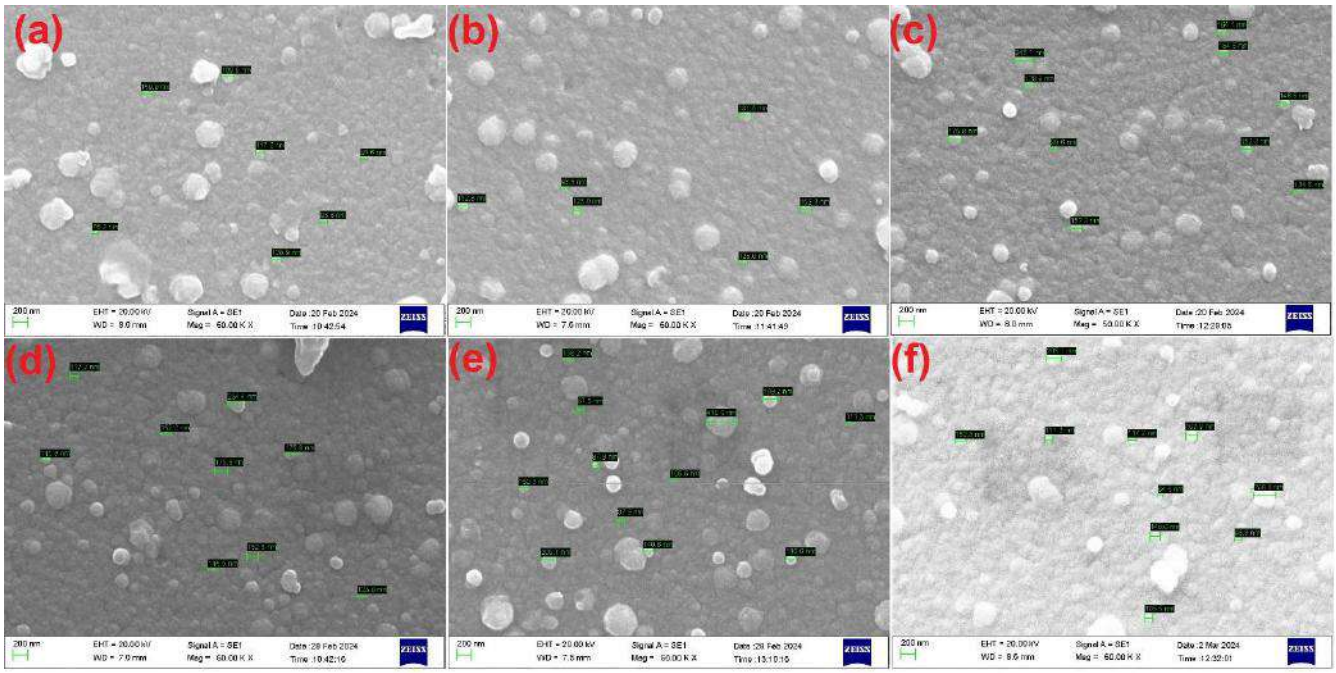

Fig.1. SEM images of CdS/PVA nanocomposite (a) before irradiation and after irradiation (b) 10 kGy, (c) 40 kGy, (d) 70 kGy, (e) 100 kGy, (f) 150 kGy

Table 1. Mean grain size of samples before and after irradiation

Sample	0 kGy	10 kGy	40 kGy	70 kGy	100 kGy	150 kGy
Mean grain size (nm)	121	137	288	156	157	145

Figure 2 showes its cross-sectional view of CdS/PVA before irradiation. According to the figure, it can be seen that the thickness of the thin film is about 170 nm and it has a uniform and smooth surface.

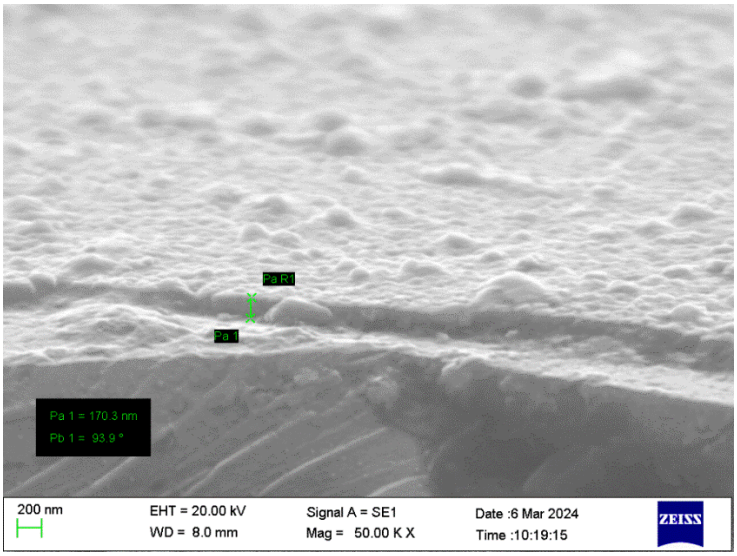

Fig.2. Cross section of CdS/PVA nanocomposite

Figure 3, shows the EDX spectrum of the CdS/PVA nanocomposite. The weight and atomic percentages of elements are listed in the inset of the figure, including C, Cd and S elements. Other peaks are related to the substrate.

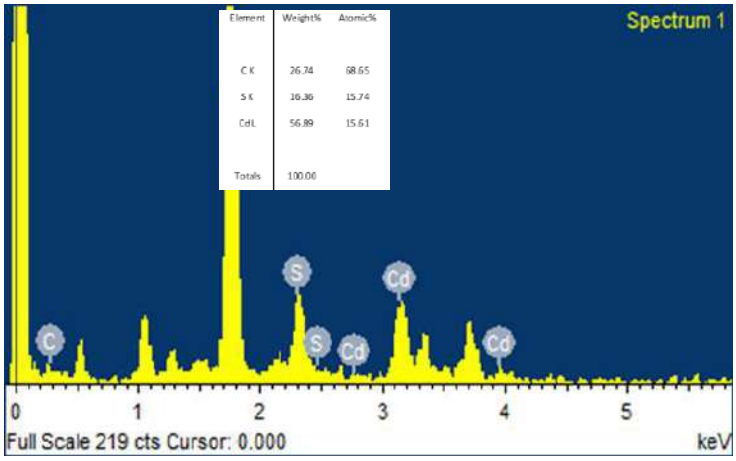

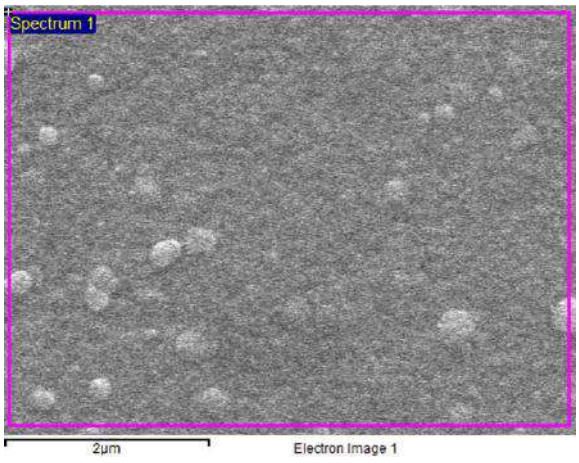

Fig.3. EDX of CdS/PVA nanocomposite. The inset shows the atomic and weight percentage of the elements

Figure 4a depicts the current-voltage curve for CdS/PVA thin film before and after irradiation at doses of 10, 40, 70, 100 and 150 kGy. It can be obsorved that the electric current increases linearly with the voltage for irradiated and unirradiated samples. A comparison of the curves reveals that radiation dose impacts the current of the samples. Figure 4b shows the current versus dose at constant voltages of 10 V, 20 V, 30 V, and 40 V. As shown in these figures, the current increases after gamma irradiation for CdS/PVA nanocomposite film. Based on Figure 4b, it can be seen that the relationship between electric current and dose is non monotonic, but linear within certain ranges (for example 0-10 kGy).

This effect may be due to the cross-link process and the increase of the CdS grain size as a result of gamma irradiation. In addition, the gamma irradiation can enhance the incorporation between PVA and CdS nanoparticles and hence increase of the electrical conduction of CdS/PVA nanocomposites films [1]. Also, this phenomenon can be attributed to the creation of inherent crystalline defects during thin film deposition. When gamma radiation interacts with the film, additional defects are introduced, altering the film's structure. The number of defects post-irradiation (induced and residual intrinsic) is lower than the initial intrinsic defects due to recombination. Recombination of crystalline defects reduces film resistance, leading to increased current [8].

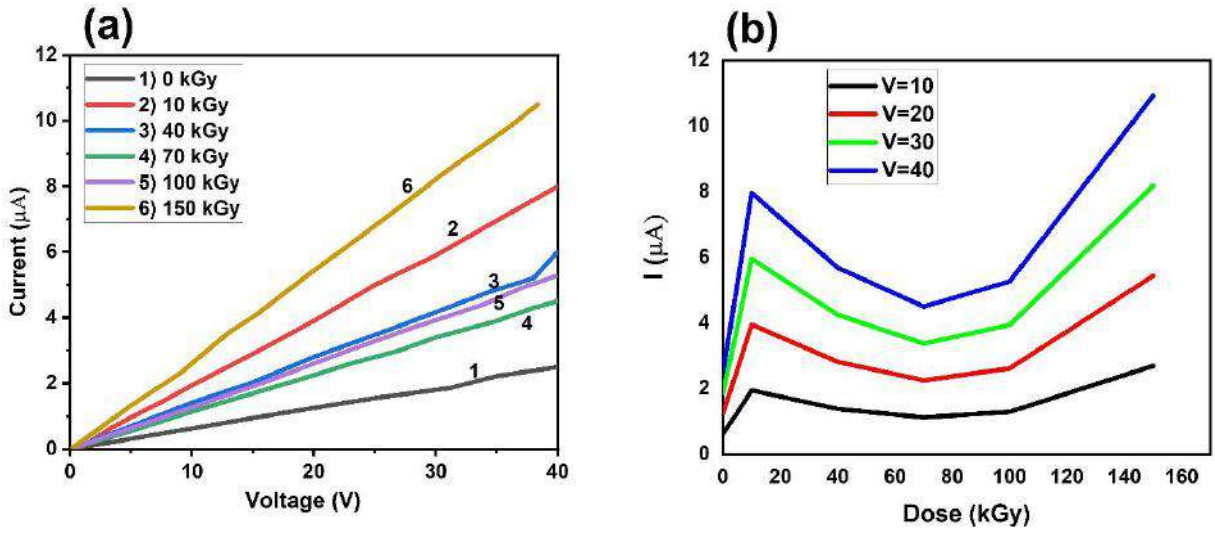

Fig.4. The I-V characteristics of CdS/PVA before and after irradiation in different doses.

Conclusions

A CdS-PVA nanocomposite film was deposited using the simple CBD method. The prepared sample was exposed to gamma irradiation at five different doses: 10, 40, 70, 100 and 150 kGy. The effects of gamma rays on its morphology and electrical properties were investigated. SEM images showed that the size of the particles increased after irradiation and ranged from 122 to 290 nm. The results indicated that gamma ray irradiation at different doses altered the electrical properties of the sample, resulting in an increase in current value after gamma radiation.

References

[1] Abdel-Galil, A., Balboul, M.R. and Ali, H.E. (2020). Synthesis and Characterization of γ-Irradiated Cadmium Sulfide/Polyvinyl Alcohol Nanocomposites Films. Journal of Electronic Materials, 49(3):2222–2232.

[2] Su B. and Choy K.L. (2000). Microstructure and properties of the CdS thin films prepared by electrostatic spray assisted vapour deposition (ESAVD) method. Thin Solid Films, 359(2):160.

[3] Rengaraj S., Ferancora A., Jee S.H., Vengataraj S., Kim Y., Labuda J. and Sillanpaa M. (2010). Physical and electrochemical characterization of CdS hollow microspheres prepared by a novel template free solution phase method. Electrochimica Acta, 56(1):501.

[4] Nouh S.A., Benthami K. (2019). Gamma induced changes in the structure and optical properties of ZnS/PVA nanocomposite. Journal of Vinyl and Additive Technology, 25(3):271-277.

[5] Tohidi T., Yousefpour Novini N., Jamshidi-Ghaleh K. (2024). Effect of Gamma irradiation on optical characteristics of Fe-doped CdS thin films prepared using chemical bath deposition. Optical Materials, 151:115394.

[6] Al-Zahrani J.H., EI-Hagary M. and EI-Taher A. (2015). Gamma Irradiation Induced Effects on Optical Properties and Single Oscillator Parameters of Fe-doped CdS Diluted Magnetic Semiconductors Thin Films. Materials Science in Semiconductor Processing, 39: 74-78.

[7] Kaoutar A.B., Somayah M.S., Asmahan M.Al-K., Shahad K.Al-H. and Samir A.N. (2023). Optical and Color Properties of Gamma Irradiated Polyvinyl Alcohol-Sodium lignosulfonate-Cadmium sulfide Nanocomposite Films. Journal of Macromolecular Science B, 62(2):39-53.

[8] Abhirami K.M., Sathyamoorthy Asokan R.K. (2013). Structural, optical and electrical properties of gamma irradiated SnO thin films. Radiation Physics and Chemistry, 91:35–3

Production of Medical Radionuclides at RIAR JSC (Paper ID : 1680)

P.S. Butkaliuk[1], O.I. Andreev[1]

[1] *Research Institute of Nuclear Reactors, State Scientific Centre, Joint-Stock Company, Dimitrovgrad, Russia*

Abstract

State Scientific Centre Research Institute of Nuclear Reactors (RIAR) produces radiochemicals and radioactive sources for more than 40 years. The production capabilities are based on RIAR's unique reactors allowing for accumulation of a wide range of radionuclides with high specific activity. Radionuclides are accumulated in five research reactors, including reactor SM, one of the world's highest flux reactors. The SM core was refurbished in 2020, and the number of irradiation cells with ultra-high thermal neutron flux density ($\geq 1 \cdot 10^{15}$ $cm^{-2}c^{-1}$) has been twice increased: from 27 to 57. Extraction of accumulated radionuclides from irradiated targets, their purification and production of sealed radioactive sources and radiochemicals are performed in radiochemical laboratories in hot cells and shielded boxes. Today, RIAR produces more than 30 different radionuclides. Some of them are supplied as sealed radioactive sources, like ^{60}Co used for contact and intracavitary therapy and gamma knife installations, and ^{252}Cf used for brachytherapy of radioresistant malignant neoplasms. The majority of medical radionuclides is supplied as radiochemicals. ^{89}Sr, ^{99}Mo, ^{106}Ru, ^{125}I, ^{131}I, ^{131}Cs, ^{177}Lu and ^{188}W are produced on a regular basis.

In 2022-2023, a new area was arranged to produce medical short-lived alpha emitters ^{223}Ra, ^{227}Th and ^{225}Ac from generators based on long-lived parent isotopes ^{227}Ac and ^{229}Th. Test supplies of long-lived radionuclide ^{228}Th are made to organizations which produce short-lived daughter products ^{224}Ra and ^{212}Pb. Special attention is paid to quality control of products. The analysis methods developed for the certification make it possible to determine the content of radioactive impurities (especially long-lived isotopes) at a level of 10^{-3} – 10^{-4}% of the total activity.

Key words: Reactor produced radioisotopes, radionuclide generators, quality control

Sources production

RIAR produces the unique ^{252}Cf based sealed neutron sources, which are used for contact and intracavitary therapy of radioresistant malignant neoplasms. Production process of

^{252}Cf is long and multi-staged. A full cycle takes 7–8 years and involves manufacture and irradiation of targets from ^{240}Pu, mixtures of heavy isotopes of Pu, Cm and its mixtures with Am, heavy isotopes of Cm as well as several radiochemical reprocessing when transuranium elements are purified from fission fragments. A technological process has recently been developed to obtain additional quantities of ^{252}Cf from ^{249}Bk which was previuosly considered as a by-product during Cf production.

RIAR also produces ^{60}Co based sources for intracavitary brachytherapy and gamma knife installations (Fig. 1, Table 1). High-flux channels used for ^{60}Co accumulation enable to obtain cores with high specific activity (more than 200 Ci/g).

Fig. 1. Outer capsule (top) and inner capsule (bottom) of GC60T0 source model

Table 1. Specification of Co-60 sealed radioactive sources

Тип источника	**Application**	**Equivalent activity, Bq**		**Size, mm**	
		min	max	diameter	length
GC60M11, GC60M12	Interstitial brachytherapy	$7.5\cdot10^{7}$	$1.15\cdot10^{8}$	1.0	25; 35
GC60M41	Intracavitary brachytherapy	$2.0\cdot10^{8}$	$3.5\cdot10^{8}$	2.0	16
GC60T01÷ GC60T06	Teletherapy	$1.27\cdot10^{14}$	$5.55\cdot10^{14}$	13.65÷23.6	22.5; 33; 36.9
GC60T1÷ GC60T7	Gamma knife	$1.11\cdot10^{12}$	$1.94\cdot10^{14}$	6.8÷27.8	26÷57.5

Radiochemicals production

The radiochemicals based on ^{89}Sr, ^{99}Mo, ^{106}Ru, ^{131}I, ^{131}Cs, ^{177}Lu and ^{188}W are extracted from the irradiated targets and supplied on a regular basis. Not only neutron capture reactions

of the thermal spectrum are used to accumulate target radionuclides, but also threshold reactions on fast neutrons and extraction from fission products. For example, RIAR performs extraction of fissile ^{99}Mo from the irradiated U-Al targets and ^{106}Ru from the irradiated Pu and Cm targets. Here ^{106}Ru is an additional product extracted from fission products fraction after separation of the target isotopes (Am, Cm and Cf). Due to asymmetry of charge-mass distribution of light fragments, the yields of ^{106}Ru during the fission of Pu and Cm isotopes are more than one order higher than the corresponding values for U isotopes (Fig. 2) [1].

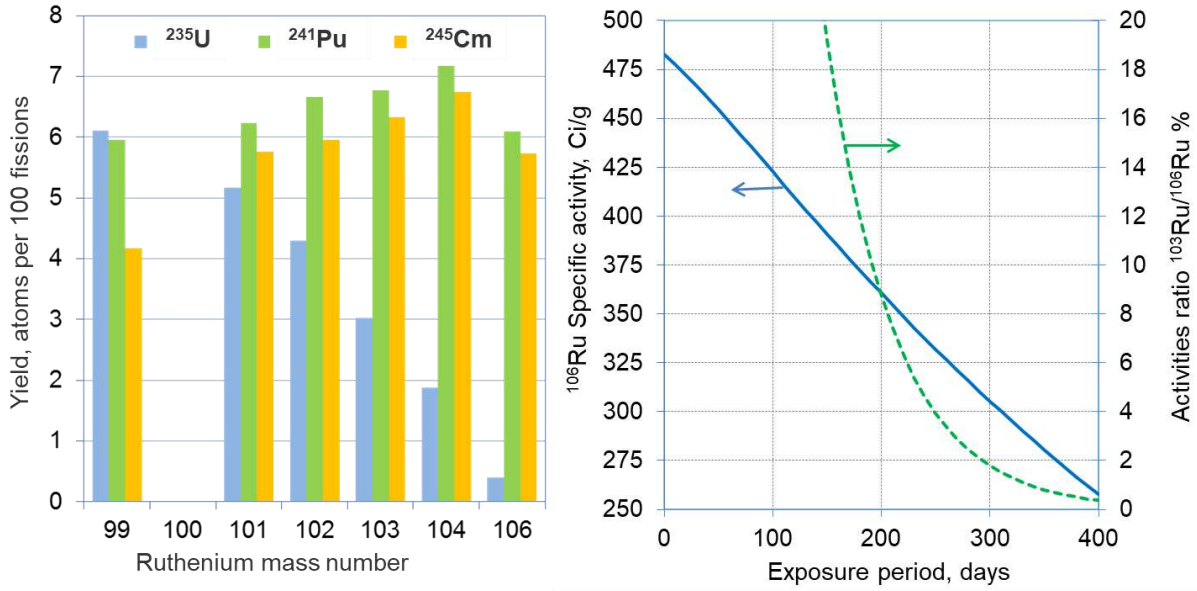

Fig. 2. The isotopic composition of reactor produced ruthenium

Irradiation of targets with TeO_2, which processing is much easier than irradiated uranium, is used for ^{131}I production instead of fission products extraction. The radioactive isotope ^{125}I is produced using the loop installation, stationary mounted in SM reactor reflector channel. This method enables signifciantly to reduce the content of ^{126}I impurity due to sorption on special filters. As a result, radionuclide ^{125}I is produced only by decey of purified ^{125}Xe in special cryogenic traps.

Two technological processes were devepoled for ^{89}Sr production: from irradiated $^{88}SrCO_3$ with thermal neutrons and from Y_2O_3 irradiated in the fast BOR-60 reactor. In the second case, ^{89}Sr is produced by the reaction ^{89}Y(n,p)^{89}Sr and the manufactured chemical has a specific activity close to a theoretical possible one. Now ^{89}Sr is mainly produced from ^{88}Sr due to economic reasons.

Not only direct methods are used for radionuclide production. Radioisotope ^{131}Cs successfully uses in brachytherapy to treat prostate cancer is produced via irradiation of barium carbonate enriched ^{130}Ba in SM reactor. Due to ^{131}Ba /^{131}Cs half-lives ratio (11.5 and 9.7 days) more than one ^{131}Cs separation is pefrormed form each barium batch (Fig. 3).

In 2022-2023 regular production of medical short-lived alpha emitters ^{223}Ra and ^{225}Ac was started. These isotopes are obtained from generators based on long-lived parent isotopes ^{227}Ac and ^{229}Th. The scheme for ^{223}Ra manufacture from ^{227}Ac includes ^{227}Th isolation and purification (Fig. 4). That makes possible supplies of ^{227}Th test batches for preclinical trials. Also test batches of long-lived radionuclide ^{228}Th are supplied to organizations producing its short-lived daughter products ^{224}Ra and ^{212}Pb.

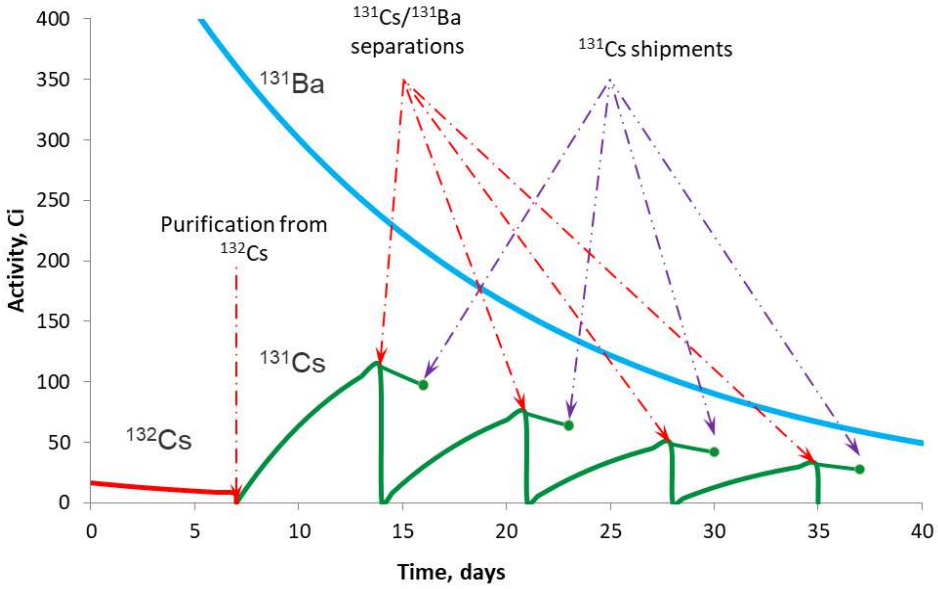

Fig. 3. ^{131}Cs production from ^{131}Ba

The quality control is an important part of all technological processes. It may includes alpha- and gamma-spectrometry, liquid scintillation spectrometry, mass-spectrometry, spectral analysis and others analytical methods. Special attention is made to determination of radionuclidic impurities. Content of long-lived radionuclides (such as ^{227}Ac or ^{228}Th) in some medical radiochemicals shouldn't' exceed 10^{-3} – 10^{-4}% of the total activity (table 2). In some cases, it is possible only after the chemical extraction of trace amounts of impurity radionuclide from the radiochemical aliquot [2].

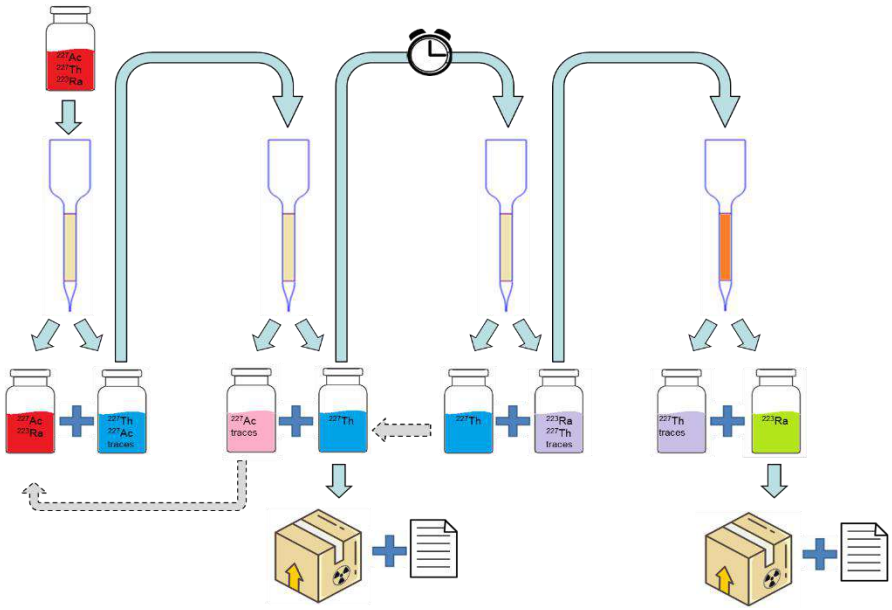

Fig. 4. Generation ^{227}Th and ^{223}Ra from ^{227}Ac

Table 2. Specification of short-lived alpha emitters for medical use

^{227}Th		^{223}Ra		^{225}Ac	
Parameter	Value	Parameter	Value	Parameter	Value
Chemical form	$^{227}Th(NO_3)_4$	Chemical form	$^{223}RaCl_2$	Chemical form	$^{225}AcCl_3$
Solvent	4 M HNO_3	Solvent	0.1 M HCl	Solvent	0.1 M HCl
Activity conc.	≥ 1 mCi/mL	Activity conc.	≥ 1 mCi/mL	Activity conc.	≥ 2 mCi/mL
Impurities		Impurities		Impurities	
^{227}Ac	≤ 0.0001%	^{227}Th	≤ 0.01%	^{224}Ra	≤ 0.002%
other radioactive	≤ 0.01%	^{227}Ac	≤ 0.001%	^{225}Ra	≤ 0.02%
				^{228,229}Th	≤ 0.0007%
non-radioactive	≤5 μg/mCi	non-radioactive	≤20 μg/mL	non-radioactive	≤10 μg/mL

Conclusions

JSC «SSC RIAR» is one Russia's largest manufacturer of radionuclides, which are widely used in various areas, including diagnostic and effective medical treatment. Nowadays RIAR develops new radioisotopes production technologies and expands its product line. The current work is to increase our production capabilities for ^{177}Lu and medical alpha emitters.

References

[1] Toporov, Yu.G., Tarasov, V.A., Kupriyanov, A.V. et al. (2018) Production of high specific activity ruthenium-106. Collected papers of Joint Stock Company “State scientific Center-Research Institute of Atomic Reactors, (2), 29-33 (in Russian).

[2] Butkalyuk, P. S., Butkalyuk, I. L., Andreev, O. I. et al. (2022) Production of pilot batches ^{223}Ra and ^{227}Th of medical purpose. Applied Radiation and Isotopes, 184, 110205.